

PROCEEDINGS OF SPIE



SPIE—The International Society for Optical Engineering

Contract F61708-97-W0098

CSP 97-1044

ROMOPTO '97

Fifth Conference on Optics

Valentin I. Vlad
Dan C. Dumitras
Chairs/Editors

9-12 September 1997
Bucharest, Romania

Sponsored by

Romanian Ministry of Research and Technology
Romanian Academy, Division of Physics
Romanian Ministry of Education
SPIE—The International Society for Optical Engineering
SPIE/RO—SPIE Romanian Chapter
EOARD—European Office of Aerospace Research and Development
ICTP—International Center for Theoretical Physics
ICO—International Commission for Optics
EOS—European Optical Society
Institute of Atomic Physics, Bucharest



19981029 092



Volume 3405
Part Two of Two Parts

REPORT DOCUMENTATION PAGE

Form Approved OMB No. 0704-0188

Public reporting burden for this collection of information is estimated to average 1 hour per response, including the time for reviewing instructions, searching existing data sources, gathering and maintaining the data needed, and completing and reviewing the collection of information. Send comments regarding this burden estimate or any other aspect of this collection of information, including suggestions for reducing this burden to Washington Headquarters Services, Directorate for Information Operations and Reports, 1215 Jefferson Davis Highway, Suite 1204, Arlington, VA 22202-4302, and to the Office of Management and Budget, Paperwork Reduction Project (0704-0188), Washington, DC 20503.

1. AGENCY USE ONLY (Leave blank)	2. REPORT DATE 8 October 1998	3. REPORT TYPE AND DATES COVERED Conference Proceedings	
4. TITLE AND SUBTITLE 5th Conference on Optics: ROMOPTO'97		5. FUNDING NUMBERS F6170897W0098	
6. AUTHOR(S) Conference Committee			
7. PERFORMING ORGANIZATION NAME(S) AND ADDRESS(ES) Institute of Atomic Physics IPTRD-Laser Department, P.O. Box MG-36 Bucharest R-76900 Romania		8. PERFORMING ORGANIZATION REPORT NUMBER N/A	
9. SPONSORING/MONITORING AGENCY NAME(S) AND ADDRESS(ES) EOARD PSC 802 BOX 14 FPO 09499-0200		10. SPONSORING/MONITORING AGENCY REPORT NUMBER CSP 97-1044	
11. SUPPLEMENTARY NOTES Came as two volumes.			
12a. DISTRIBUTION/AVAILABILITY STATEMENT Approved for public release; distribution is unlimited.		12b. DISTRIBUTION CODE A	
13. ABSTRACT (Maximum 200 words) The Final Proceedings for 5th Conference on Optics: ROMOPTO'97, 9 September 1997 - 12 September 1997 These are available as SPIE Proceedings vol 3405, parts one and two. lasers and radiation sources; lasers in material science; nonlinear, quantum and information optics; laser spectroscopy; biophotonics; optoelectronics; optical sensors and metrology; optical components; and optics in environmental research			
14. SUBJECT TERMS EOARD Adaptive Optics, Fibre Optics, Imaging, Lasers, Optical Components, Detector Technology, Non-linear Optics, Medical applications		15. NUMBER OF PAGES 1232 16. PRICE CODE N/A	
17. SECURITY CLASSIFICATION OF REPORT UNCLASSIFIED	18. SECURITY CLASSIFICATION OF THIS PAGE UNCLASSIFIED	19. SECURITY CLASSIFICATION OF ABSTRACT UNCLASSIFIED	20. LIMITATION OF ABSTRACT UL

NSN 7540-01-280-5500

Standard Form 298 (Rev. 2-89)
Prescribed by ANSI Std. Z39-18
298-102

PROCEEDINGS OF SPIE



SPIE—The International Society for Optical Engineering

ROMOPTO '97

Fifth Conference on Optics

Valentin I. Vlad
Dan C. Dumitras
Chairs/Editors

9–12 September 1997
Bucharest, Romania

Sponsored by
Romanian Ministry of Research and Technology
Romanian Academy, Division of Physics
Romanian Ministry of Education
SPIE—The International Society for Optical Engineering
SPIE/RO—SPIE Romanian Chapter
EOARD—European Office of Aerospace Research and Development
ICTP—International Center for Theoretical Physics
ICO—International Commission for Optics
EOS—European Optical Society
Institute of Atomic Physics, Bucharest



Volume 3405

Part Two of Two Parts

SPIE is an international technical society dedicated to advancing engineering and scientific applications of optical, photonic, imaging, electronic, and optoelectronic technologies.



The papers appearing in this book comprise the proceedings of the meeting mentioned on the cover and title page. They reflect the authors' opinions and are published as presented and without change, in the interests of timely dissemination. Their inclusion in this publication does not necessarily constitute endorsement by the editors or by SPIE.

Please use the following format to cite material from this book:

Author(s), "Title of paper," in *Fifth Conference on Optics (ROMOPTO '97)*, Valentin I. Vlad, Dan C. Dumitras, Editors, Proceedings of SPIE Vol. 3405, page numbers (1998).

ISSN 0277-786X
ISBN 0-8194-2857-4

Published by
SPIE—The International Society for Optical Engineering
P.O. Box 10, Bellingham, Washington 98227-0010 USA
Telephone 360/676-3290 (Pacific Time) • Fax 360/647-1445

Copyright ©1998, The Society of Photo-Optical Instrumentation Engineers.

Copying of material in this book for internal or personal use, or for the internal or personal use of specific clients, beyond the fair use provisions granted by the U.S. Copyright Law is authorized by SPIE subject to payment of copying fees. The Transactional Reporting Service base fee for this volume is \$10.00 per article (or portion thereof), which should be paid directly to the Copyright Clearance Center (CCC), 222 Rosewood Drive, Danvers, MA 01923. Payment may also be made electronically through CCC Online at <http://www.directory.net/copyright/>. Other copying for republication, resale, advertising or promotion, or any form of systematic or multiple reproduction of any material in this book is prohibited except with permission in writing from the publisher. The CCC fee code is 0277-786X/98/\$10.00.

Printed in the United States of America.

Contents

xxi	Conference Committee
xxiii	Introduction

Part One

SESSION 1 LASERS AND RADIATION SOURCES

- | | |
|----|---|
| 2 | Q-switch regime of 3-μm erbium lasers (Invited Paper) [3405-01]
S. Georgescu, V. Lupei, C. Hapenciuc, National Institute for Laser, Plasma, and Radiation Physics (Romania) |
| 10 | Stabilization of unstable states in a modulated noisy CO₂ laser (Invited Paper) [3405-02]
V. Ninulescu, P. E. Sterian, M. A. Dumitru, M. C. Piscureanu, Politehnica Univ. of Bucharest (Romania) |
| 17 | Beam optimization of a TEA-CO₂ laser [3405-03]
T. Groß, D. Ristau, G. Wallas, Laser Zentrum Hannover eV (FRG); G. Dumitru, D. G. Sporea, C. A. Timus, National Institute for Laser, Plasma, and Radiation Physics (Romania) |
| 24 | Modeling optical amplification in Er³⁺-doped LiNbO₃ waveguides [3405-04]
N. N. Puscas, Politehnica Univ. of Bucharest (Romania); R. Girardi, CSELT (Italy); D. Scarano, Pirelli Cavi (Italy); I. Montrosset, Politecnico di Torino (Italy) |
| 32 | Output beam characteristics of a Nd:YVO₄ miniature laser [3405-05]
N. I. Pavel, National Institute for Laser, Plasma, and Radiation Physics (Romania); T. Taira, M. Furuhashi, T. Kobayashi, Fukui Univ. (Japan) |
| 39 | Bound-state excitation in ion-ion collision as related to the modeling of x-ray lasers with Li-like ions [3405-06]
V. Stancalie, National Institute for Laser, Plasma, and Radiation Physics (Romania); A. Sureau, Univ. Paris-Sud (France); V. M. Burke, DRAL Daresbury Labs. (UK) |
| 45 | Nd:YAG linear resonator using an external stimulated Brillouin scattering Q-switching mirror [3405-07]
A. Mocofanescu, National Institute for Laser, Plasma, and Radiation Physics (Romania), V. Babin, S. Miclos, A. Farcas, National Institute of Optoelectronics (Romania) |
| 51 | Excitation upconversion by sensitized photon avalanche [3405-08]
V. Lupei, E. Osiac, National Institute of Atomic Physics (Romania); T. Sandroch, E. Heumann, G. Huber, Univ. Hamburg (FRG) |
| 58 | Medium-power stabilized laser diode [3405-09]
E. Smeu, N. N. Puscas, I. M. Popescu, Politehnica Univ. of Bucharest (Romania); Gr. I. Suruceanu, Technical Univ. of Moldova; R. G. Ispasoiu, Politehnica Univ. of Bucharest (Romania) |
| 65 | High-resolution spectral analysis of a pulsed CuBr laser [3405-10]
E. Scarlat, L. Preda, C. P. Cristescu, A. M. Preda, Politehnica Univ. of Bucharest (Romania) |

- 70 **Influence of active-medium properties on high-power solid state laser beam characteristics** [3405-11]
N. I. Pavel, National Institute for Laser, Plasma, and Radiation Physics (Romania); T. Taira, Fukui Univ. (Japan); T. Dascalu, V. Lupei, National Institute for Laser, Plasma, and Radiation Physics (Romania)
- 75 **Degradation effects in pulsed AlGaAs large optical cavity (LOC) structure laser diodes** [3405-12]
R. V. Ghita, National Institute of Materials Physics (Romania); E. Vasile, METAV SA (Romania); V. Cimpoca, National Institute of Materials Physics (Romania); N. Baltaneanu, National Institute for Laser, Plasma, and Radiation Physics (Romania)
- 81 **Performance of a pump system for diode-pumped lasers** [3405-13]
A. Stratan, C. G. Fenic, R. V. Dabu, N. Herisanu, C. Luculescu, D. G. Sporea, G. Dumitru, National Institute for Laser, Plasma, and Radiation Physics (Romania); G. Iordache, National Institute of Materials Physics (Romania)
- 85 **Medium-power cw He-Se laser** [3405-14]
M. Ristici, I. Ristici, V. R. Medianu, National Institute for Laser, Plasma, and Radiation Physics (Romania)
- 89 **Pump distribution effects on photon avalanche in fiber lasers** [3405-15]
V. Lupei, E. Osiac, Institute of Atomic Physics (Romania)
- 99 **High-quality beam transversal gas transport cw CO₂ laser** [3405-16]
I. Gutu, V. R. Medianu, P. Cristian, National Institute for Laser, Plasma, and Radiation Physics (Romania)
- 106 **Comparison between method of lines and time domain method in evaluating the large signal responses of Fabry-Perot semiconductor lasers** [3405-17]
A. L. Braverman, Politehnica Univ. of Bucharest (Romania)
- 112 **Generalized model for cw three-micron emission in concentrated Er systems** [3405-18]
V. Lupei, S. Georgescu, National Institute for Laser, Plasma, and Radiation Physics (Romania)

SESSION 2 LASERS IN MATERIAL SCIENCE

- 122 **Synthesis, characterization, and mechanical properties of carbide and nitride films prepared by pulsed-laser-deposition method (Invited Paper)** [3405-19]
A. Kumar, H. L. Chan, Univ. of South Alabama (USA); R. Alexandrescu, National Institute for Laser, Plasma, and Radiation Physics (Romania)
- 130 **Deposition of CN thin films by reactive pulsed laser ablation (Invited Paper)** [3405-20]
A. Perrone, Univ. degli Studi di Lecce (Italy) and Istituto Nazionale per la Fisica della Materia (Italy)
- 143 **Laser diagnostics in flame deposition of diamond (Invited Paper)** [3405-21]
R. J. H. Klein-Douwle, J. J. ter Meulen, Univ. of Nijmegen (Netherlands)
- 153 **Synthesis of nanosize powders by pulsed laser ablation and related plasma diagnostics (Invited Paper)** [3405-22]
K. Yatsui, W. Jiang, K. Nishiura, T. Yukawa, Nagaoka Univ. of Technology (Japan); C. Grigoriu, I. Chiş, A. Marcu, D. Miu, National Institute for Laser, Plasma, and Radiation Physics (Romania)

- 162 **X-ray micromachining with a laser-plasma source at 1-nm wavelength (Invited Paper)** [3405-23]
I. C. E. Turcu, C. M. Mann, Rutherford Appleton Lab. (UK); S. W. Moon, Rutherford Appleton Lab. (UK) and Korea Institute of Science and Technology; B. J. Maddison, R. M. Allott, N. Lisi, S. E. Huq, Rutherford Appleton Lab. (UK); N. S. Kim, Rutherford Appleton Lab. (UK) and Kumho Information and Telecommunication Lab. (Korea)
- 174 **Preparation of metal oxides by laser versus thermal processes (Invited Paper)** [3405-24]
R. Alexandrescu, I. G. Morjan, National Institute for Laser, Plasma, and Radiation Physics (Romania); C. R. Popescu, LACECA Research Ctr. (Romania); I. N. Voicu, National Institute for Laser, Plasma, and Radiation Physics (Romania)
- 182 **New studies of reactive pulsed laser deposition (Invited Paper)** [3405-25]
I. N. Mihailescu, E. Gyorgy, National Institute for Laser, Plasma, and Radiation Physics (Romania); V. S. Teodorescu, National Institute of Materials Physics; G. Marin, National Institute for Laser, Plasma, and Radiation Physics (Romania); D. Pantelica, National Institute of Nuclear Physics and Engineering Horia Hulubei; A. Andrei, Institute of Nuclear Research (Romania); J. Neamtu, Univ. of Craiova (Romania)
- 188 **Discharge-aided reactive laser ablation for ultrafine powder production (Invited Paper)** [3405-26]
I. Chis, National Institute for Laser, Plasma, and Radiation Physics (Romania); A. Marcu, Nagaoka Univ. of Technology (Japan); D. Miu, National Institute for Laser, Plasma, and Radiation Physics (Romania); T. Yukawa, Nagaoka Univ. of Technology (Japan); D. Dragulinescu, C. Grigoriu, National Institute for Laser, Plasma, and Radiation Physics (Romania); W. Jiang, K. Yatsui, Nagaoka Univ. of Technology (Japan)
- 199 **Deposition of carbon nitride thin films by IR-laser-induced reactions in carbon-nitrogen gas-phase compounds** [3405-27]
A. Crunteanu, R. Alexandrescu, R. Cireasa, S. Cojocar, I. G. Morjan, National Institute for Laser, Plasma, and Radiation Physics (Romania); A. Andrei, Institute of Nuclear Research (Romania); A. Kumar, Univ. of South Alabama (USA)
- 205 **Influence of thermal annealing on optical properties of porous silicon films** [3405-28]
I. Baltog, M. L. Ciurea, G. Pavelescu, E. Pentia, G. Galeata, National Institute of Materials Physics (Romania); J. P. Roger, Ecole Supérieure de Physique et de Chimie Industrielles (France)
- 211 **Optical devices with silica-gel small spheres** [3405-29]
A. M. Preda, E. Scarlat, L. Preda, I. M. Popescu, Politehnica Univ. of Bucharest (Romania)
- 218 **Growth of polycrystalline hydroxyapatite thin films by pulsed laser deposition and subsequent heat treatment in air** [3405-30]
V. D. Nelea, National Institute for Laser, Plasma, and Radiation Physics (Romania); C. Ghica, National Institute of Materials Physics (Romania); C. Martin, A. Hening, I. N. Mihailescu, National Institute for Laser, Plasma, and Radiation Physics (Romania); L. C. Nistor, V. S. Teodorescu, National Institute of Materials Physics (Romania); R. Alexandrescu, National Institute for Laser, Plasma, and Radiation Physics (Romania); J. Werckmann, Institute of Physics and Chemistry of Materials (France); E. Gyorgy, G. Marin, National Institute for Laser, Plasma, and Radiation Physics (Romania)

- 225 **Mechanisms of droplet formation in pulsed laser growth of thin oxide films [3405-31]**
V. Craciun, D. Craciun, National Institute for Laser, Plasma, and Radiation Physics (Romania); M. C. Bunescu, E. Vasile, A. Ioncea, METAV SA (Romania); R. V. Dabu, National Institute for Laser, Plasma, and Radiation Physics (Romania); I. W. Boyd, Univ. College London (UK)
- 233 **Nd:YAG laser surface texturing [3405-32]**
M. Poterasu, T. Dascalu, A. Marian, D. Buca, National Institute for Laser, Plasma, and Radiation Physics (Romania)
- 241 **Investigation of $\text{HgBr}_x\text{I}_{2-x}$ using confocal laser scanning microscopy and x-ray diffraction [3405-33]**
G. A. Stanciu, Politehnica Univ. of Bucharest (Romania); J. L. Oud, Univ. of Amsterdam (Netherlands); E. K. Polychroniadis, M. Daviti, Aristotle Univ. of Thessaloniki (Greece); A. Stanciu, National Institute of Microtechnology (Romania); C. Miu, Politehnica Univ. of Bucharest (Romania)
- 246 **Lasers for material processing [3405-34]**
A. Nichici, I. David, E. F. Cicala, Politehnica Univ. of Timisoara (Romania)
- 252 **Effects of UV laser radiation on the surface defects of NiO catalysts [3405-35]**
E. Ivana, V. Lăcătușu, M. Chelu, M. Craiu, Institute of Physical Chemistry (Romania); C. G. Fenic, A. Stratan, National Institute for Laser, Plasma, and Radiation Physics (Romania); L. C. Nistor, C. Ghica, National Institute of Materials Physics (Romania); P. Mărginean, Institute of Isotopic and Molecular Technology (Romania)
- 258 **Modeling of chalcogenide glass structures before and after laser illumination, based on mass spectroscopy data [3405-36]**
A. M. Andriesh, Ctr. of Optoelectronics (Moldova); A. I. Buzdugan, V. Dolghier, Ctr. of Metrology (Moldova); M. S. Iovu, Ctr. of Optoelectronics (Moldova)
- 262 **Ionic space-charge-limited currents in natural quartz crystal [3405-37]**
I. Enculescu, B. Iliescu, National Institute of Materials Physics (Romania)
- 267 **Compacting of metallic powder by using Nd:YAG laser [3405-38]**
A. Marian, D. Buca, T. Dascalu, M. Poterasu, National Institute for Laser, Plasma, and Radiation Physic (Romania)
- 272 **Microstructure of hydroxyapatite thin layers grown by pulsed laser deposition [3405-39]**
D. Craciun, V. Craciun, C. Martin, I. N. Mihailescu, National Institute for Laser, Plasma, and Radiation Physics (Romania); M. C. Bunescu, E. Vasile, A. Ioncea, METAV SA (Romania); I. W. Boyd, Univ. College London (UK)
- 278 **Computing coupling coefficients in transmission systems [3405-40]**
V. Calian, M. Ursache, C. Sarpe-Tudoran, M. Socaciu, Univ. of Craiova (Romania)
- 282 **Effect of pulsed-laser deposition parameters on plasma expansion studied by fast-framing photography [3405-41]**
D. Miu, A. Marcu, National Institute for Laser, Plasma, and Radiation Physics (Romania); T. Yukawa, Nagaoka Univ. of Technology (Japan); C. Grigoriu, I. Chis, National Institute for Laser, Plasma, and Radiation Physics (Romania); K. Yatsui, Nagaoka Univ. of Technology (Japan)

- 288 **Synthesis of europium-activated calcium tungstate phosphor [3405-42]**
E.-J. Popovici, F. Forgaciu, M. Nemes, Institute of Chemistry Raluca Ripan (Romania); V. Ursu, Institute of Physical Chemistry I.G. Murgulescu (Romania)
- 293 **Off-line multiresponse optimization of gas-jet-assisted CO₂ laser cutting of polymetacrylate [3405-43]**
E. F. Cicala, D. Zsivanov, A. Nichici, Politehnica Univ. of Timisoara (Romania)
- 299 **Establishing the regression polynomials for the objective function that defines dimensional accuracy in the case of laser drilling [3405-44]**
I. David, E. F. Cicala, Politehnica Univ. of Timisoara (Romania)
- 305 **Theoretical model for the reactive pulsed deposition process: application to the case of ablation of a Ti target in low-pressure N₂ [3405-45]**
J. Neamtu, Univ. of Craiova (Romania); I. N. Mihailescu, National Institute for Laser, Plasma, and Radiation Physics (Romania)
- 311 **Pulsed-laser and alpha particle irradiation effects in Fe-based glassy ferromagnets [3405-46]**
M. I. Toacsan, D. Barb, National Institute of Materials Physics (Romania); M. Sorescu, Duquesne Univ. (USA); B. Constantinescu, National Institute of Nuclear Physics and Engineering Horia Hulubei (Romania); L. Jeloica, National Institute of Materials Physics (Romania)

SESSION 3 NONLINEAR, INFORMATION, AND QUANTUM OPTICS

- 320 **Quantum optics of a single atom (Plenary Paper) [3405-47]**
H. Walther, Univ. München (FRG) and Max-Planck-Institut für Quantenoptik (FRG)
- 335 **Optical properties of quasi-periodic (self-similar) structures [3405-48]**
M. Bertolotti, C. Sibilio, Univ. degli Studi di Roma La Sapienza (Italy), Gruppo Nazionale di Elettronica Quantistica e Plasmi (Italy), and Istituto Nazionale per la Fisica della Materia (Italy)
- 353 **Novel femtosecond optical solitons in weakly excited semiconductors (Invited Paper) [3405-49]**
D. Mihalache, Institute of Atomic Physics (Romania); I. V. Mel'nikov, General Physics Institute (Russia); N.-C. Panou, New York Univ. (USA)
- 363 **Various approaches for optical implementation of the wavelet transform (Invited Paper) [3405-50]**
E. Marom, D. Mendlovic, Z. Zalevsky, Tel-Aviv Univ. (Israel)
- 375 **Radiation spectrum and thermodynamics of the quantum cubic cavities (Invited Paper) [3405-51]**
V. I. Vlad, N. Ionescu-Pallas, National Institute for Laser, Plasma, and Radiation Physics (Romania)
- 385 **Photoinduced phenomena in chalcogenide glasses and their application in optoelectronics (Invited Paper) [3405-52]**
A. M. Andriesh, Institute of Applied Physics (Moldova)
- 393 **Thermo-optic dispersion formula of AgGaSe₂ and its applications to thermal lensing effects (Invited Paper) [3405-53]**
E. Tanaka, Keio Univ. (Japan); K. Kato, Japan Defense Agency

- 399 **Possibility of two-photon superradiance in microcavities** [3405-54]
M. Macovei, N. A. Enaki, Institute of Applied Physics (Moldova)
- 406 **Nonlinear excitonic susceptibilities of semiconductors at high levels of excitation** [3405-55]
P. I. Khadzhi, D. V. Tkachenko, Trans-Dniester State Univ. (Moldova)
- 411 **Appearance and suppression of stochastic self-pulsations of coherent excitons and biexcitons in condensed matter** [3405-56]
V. Z. Tronciu, Technical Univ. of Moldova; A. H. Rotaru, State Univ. of Moldova
- 418 **Novel approaches in morphological correlations** [3405-57]
D. Mendlovic, A. Shemer, Z. Zalevsky, E. Marom, G. Shabtay, Tel-Aviv Univ. (Israel)
- 425 **Rotation-invariant pattern recognition using circular harmonics and synthetic discriminant functions** [3405-58]
D. Cojoc, Politehnica Univ. of Bucharest (Romania)
- 432 **Surface study of laser-induced charge gratings in $\text{Bi}_{12}\text{SiO}_{20}$ with an atomic force microscope** [3405-59]
E. Soergel, W. Krieger, Max-Planck-Institut für Quantenoptik (FRG); V. I. Vlad, Institute of Atomic Physics (Romania)
- 439 **Optical bistability in short-external-cavity DBR semiconductor lasers** [3405-60]
V. B. Guja, Politehnica Univ. of Bucharest (Romania); I. Montrosset, Politecnico di Torino (Italy); O. D. Iancu, Politehnica Univ. of Bucharest (Romania)
- 446 **Nonlinear optical properties of noncrystalline semiconductors** [3405-61]
V. N. Chumash, Institute of Applied Physics (Moldova)
- 454 **LBO optical parametric oscillator pumped by second harmonic of a Nd:YAG laser** [3405-62]
R. V. Dabu, C. G. Fenic, A. Stratan, C. Luculescu, National Institute for Laser, Plasma, and Radiation Physics (Romania); G. L. Muscalu, Pro Optica SA (Romania)
- 462 **Enhanced internal second harmonic generation in InGaAs/GaAs/AlGaAs strained single-quantum-well buried-heterostructure laser diodes** [3405-63]
R. G. Ispasoiu, N. N. Puscas, E. Smeu, C. E. Botez, Politehnica Univ. of Bucharest (Romania); V. P. Yakovlev, A. Z. Mereutza, G. I. Suruceanu, Technical Univ. of Moldova
- 469 **Resonatorless optical bistability in a thin semiconductor film** [3405-64]
S. L. Gaivan, P. I. Khadzhi, Institute of Applied Physics (Moldova)
- 473 **Nonlinear transmission of ultrashort light pulses by a thin semiconductor film in the exciton range of the spectrum** [3405-65]
P. I. Khadzhi, S. L. Gaivan, Institute of Applied Physics (Moldova)
- 477 **Cryptographic mixing transformations for image applications** [3405-66]
A. Vlad, M. Mitrea, Politehnica Univ. of Bucharest (Romania)
- 483 **Characterization of the silicon guided-wave optical couplers and Mach-Zehnder interferometers** [3405-67]
N. N. Puscas, G. Nitulescu, V. V. Gherman, A. Ducariu, Politehnica Univ. of Bucharest (Romania)

- 489 **Holographic interferometry study of interphase mass transfer [3405-68]**
L. Stefan, Univ. of Bucharest (Romania); A. Guzun-Stoica, Politehnica Univ. of Bucharest (Romania); M. Kurzeluk, Technical Univ. of Civil Engineering (Romania)
- 494 **Nonlinear processes in laser radiation absorption on metallic surfaces [3405-69]**
M. Ursache, V. Calian, M. Socaciu, C. Sarpe-Tudoran, Univ. of Craiova (Romania)
- 498 **Construction of the first-order stochastic nonlinear differential equations in the modeling of stimulated scattering of optical fields [3405-70]**
V. Babin, M. Grigore, L. Cojocaru, S. Ersen, A. Moldovan, National Institute of Research and Development for Optoelectronics (Romania)
- 504 **Spectral Jones vectors and spectral coherence matrices in analyzing modulated light [3405-71]**
T. S. Tudor, I. Vinkler, Univ. of Bucharest (Romania)
- 511 **Fidelity evaluation of the conjugated wavefront in photorefractive crystals using direct spatial phase demodulation of optical interferograms [3405-72]**
V. I. Vlad, A. Petris, A. Jianu, National Institute for Laser, Plasma, and Radiation Physics (Romania)
- 517 **Talbot moiré deflectometry with direct spatial reconstruction of optical phase [3405-73]**
A. Jianu, A. Petris, National Institute for Laser, Plasma, and Radiation Physics (Romania); C. Popa, D. Popa, Politehnica Univ. of Bucharest (Romania); V. I. Vlad, National Institute for Laser, Plasma, and Radiation Physics (Romania)

SESSION 4 LASER SPECTROSCOPY

- 524 **Competitive processes in a nonisothermal plasma by deconvolution of low-intensity spectral lines (Invited Paper) [3405-74]**
I. Iova, Gh. Ilie, M. Băzăvan, C. Biloiu, I. Gruia; I. Chera; Univ. of Bucharest (Romania); M. Cristea, T. Constantinescu, Politehnica Univ. of Bucharest (Romania)
- 533 **Formation of nonlinear optical MQD (metal quantum dot) in waveguides and modification by high-power laser irradiation (Invited Paper) [3405-75]**
G. Battaglin, Istituto Nazionale per la Fisica della Materia (Italy) and Univ. degli Studi di Venezia (Italy); E. Borsella, G. De Marchi, F. Gonella, G. Mattei, P. Mazzoldi, Istituto Nazionale per la Fisica della Materia (Italy) and Univ. degli Studi di Padova (Italy); A. Quaranta, Istituto Nazionale per la Fisica della Materia (Italy) and Univ. degli Studi di Trento (Italy)
- 541 **Optical pumping via a velocity-selective state (Invited Paper) [3405-76]**
N. Leinfellner, L. Windholz, Technische Univ. Graz (Austria); I. E. Mazets, A.F. Ioffe Institute of Physics and Technology (Russia)
- 548 **Linear and nonsaturating effects in atomic multiplets subjected to three strong electromagnetic fields of resonance (Invited Paper) [3405-77]**
F. F. Popescu, F. Marica, G. Radu, Univ. of Bucharest (Romania)

- 556 **Multicomponent trace gas analysis with a CO-laser-based photoacoustic detector: emission of ethanol, acetaldehyde, ethane, and ethylene from fruit** [3405-78]
F. J. M. Harren, J. Oomens, S. Persijn, Univ. of Nijmegen (Netherlands); R. H. Veltman, H. S. M. de Vries, Agrotechnological Research Institute (Netherlands); D. H. Parker, Univ. of Nijmegen (Netherlands)
- 563 **Spectroscopy of Yb³⁺ codoped Pr³⁺:YAG laser crystals** [3405-79]
A. Lupei, V. Lupei, A. Petraru, Institute of Atomic Physics (Romania)
- 570 **Effects of resonant electron-phonon interactions for the RE³⁺ ions in laser crystals** [3405-80]
V. N. Enaki, Chisinau State Univ. (Moldova); A. Lupei, V. Lupei, C. Presura, Institute of Atomic Physics (Romania); V. E. Ciobu, Chisinau State Univ. (Moldova)
- 578 **Laser photoacoustic detection of the essential oil vapors of thyme, mint, and anise** [3405-81]
A. M. El-Kahlout, M. M. Al-Jourani, Keele Univ. (UK); M. I. Abu-Taha, Al Quds Univ. (Israel); D. C. Lainé, Keele Univ. (UK)
- 584 **Coherent Raman scattering on light-induced optical gratings prepared by adiabatic population transfer** [3405-82]
N. Leinfellner, L. Windholz, Technische Univ. Graz (Austria); I. E. Mazets, A.F. Ioffe Institute of Physics and Technology (Russia)
- 589 **Energy transfer processes in Cr³⁺, Nd³⁺:YAG** [3405-83]
A. Lupei, V. Lupei, A. Petraru, M. Petrache, Institute of Atomic Physics (Romania)
- 596 **Infrared photochemistry of trichloroethylene in the presence of oxygen** [3405-84]
C. Ungureanu, Institute of Isotopic and Molecular Technology (Romania); M. Ungureanu, Gh. Lazar College (Romania)
- 603 **Excited xenon(1s₄) atom detection by modulation laser absorption spectroscopy** [3405-85]
Y. Sakai, Hokkaido Univ. (Japan); M. A. Bratescu, G. Musa, National Institute for Laser, Plasma, and Radiation Physics (Romania); K. Miyamoto, Hokkaido Univ. (Japan); M. Miclea, National Institute for Laser, Plasma, and Radiation Physics (Romania)
- 612 **Multiphonon transitions and heating effects in Er:YAG laser rods** [3405-86]
S. Georgescu, V. Lupei, National Institute for Laser, Plasma, and Radiation Physics (Romania)
- 619 **Determination of phase transitions in liquid crystals by optical absorption spectroscopy** [3405-87]
C. Sarpe-Tudoran, M. Socaciu, M. Ursache, J. Neamtu, G. Bratulescu, S. Radu, Univ. of Craiova (Romania)
- 623 **Photoluminescence decay in porous silicon films** [3405-88]
I. Baltog, M. L. Ciurea, G. Pavelescu, L. Mihut, M. Baibarac, National Institute of Materials Physics (Romania)
- 627 **Photoacoustic detection of ethylene released by biological samples under stress conditions** [3405-89]
S. M. Cristescu, D. C. Dumitras, D. C. A. Dutu, National Institute for Laser, Plasma, and Radiation Physics (Romania)

- 632 **Luminescence properties of some double-activated zinc-sulphide-type phosphors [3405-90]**
E.-J. Popovici, M. Aneculaese, Institute of Chemistry Raluca Ripan (Romania); V. Ursu, Institute of Physical Chemistry I.G. Murgulescu (Romania)
- 636 **Correlation of some radiative processes resulting from electronic and vibrational spectra of a CN molecule excited in an electric arc discharge [3405-91]**
I. Iova, M. Băzăvan, C. Biloiu, Gh. Ilie, M. Bulinski, Univ. of Bucharest (Romania)

Part Two

SESSION 5 BIOPHOTONICS

- 642 **Laser-based assessment of lipid peroxidation in humans (Invited Paper) [3405-92]**
G. Giubileo, ENEA (Italy)
- 654 **CO₂ laser ablation of biological tissue (Invited Paper) [3405-93]**
D. C. Dumitras, D. C. A. Dutu, C. E. Matei, National Institute for Laser, Plasma, and Radiation Physics (Romania)
- 665 **Laser method for corneal structure investigation (Invited Paper) [3405-94]**
M. L. Pascu, National Institute for Laser, Plasma, and Radiation Physics (Romania); B. Carstocea, Central Military Hospital (Romania); G. Popescu, National Institute for Laser, Plasma, and Radiation Physics (Romania); L. Gafencu, S. Apostol, Central Military Hospital (Romania); N. Moise, M. Roman, C. M. Ticos, National Institute for Laser, Plasma, and Radiation Physics (Romania)
- 673 **Electronic-beam analysis of excimer lasers used for photorefractive keratotomy (Invited Paper) [3405-95]**
C. B. Roundy, Spiricon, Inc. (USA)
- 678 **UV laser radiosensitivity of normal and tumoral chromatin [3405-96]**
L. Radu, Victor Babes Institute (Romania); I. N. Mihailescu, National Institute for Laser, Plasma, and Radiation Physics (Romania); V. Preoteasa, I. Radulescu, D. Gostian, Victor Babes Institute (Romania); A. Hening, National Institute for Laser, Plasma, and Radiation Physics (Romania); S. Radu, Polytechnia Univ. of Bucharest (Romania)
- 686 **Observations concerning the use of rMuIFN- γ -activated macrophages by intra- and peritumoral perfusion combined with laser therapy in animals with carcinosarcoma [3405-97]**
V. F. Dima, Cantacuzino Institute (Romania); V. V. Vasiliu, National Institute for Laser, Plasma, and Radiation Physics (Romania); D. Laky, Victor Babes Institute (Romania); S. V. Dima, Ctr. Medico-Chirurgico S.I.S. Hahnemann (Italy)
- 692 **Influence of the laser beam wavelength on the gonarthrosis treatment: a preliminary comparative study [3405-98]**
G. Brojbeanu, St. Suteanu, Clinical Hospital Dr. Ioan Cantacuzino (Romania); M. V. Udrea, V. V. Vasiliu, National Institute for Laser, Plasma, and Radiation Physics (Romania)
- 696 **Value of low-power lasers in the treatment of symptomatic spondilosis [3405-99]**
C. Antipa, Coljea Clinical Hospital (Romania); V. Moldoveanu, Bagdazar Clinical Hospital (Romania); N. Rușca, Genesis srl (Romania); I. I. Bruckner, M. Vlăiculescu, E. Ionescu, Coljea Clinical Hospital (Romania); V. V. Vasiliu, National Institute for Laser, Plasma, and Radiation Physics (Romania)

- 702 **Dependence of the ablative effect of nanosecond laser pulses at the surface of dentine samples on laser wavelength [3405-100]**
C. G. Fenic, I. Chiş, R. V. Dabu, A. Stratan, I. G. Apostol, R. Stoian, C. Luculescu, National Institute for Laser, Plasma, and Radiation Physics (Romania); C. Ghica, L. C. Nistor, National Institute for Materials Physics (Romania)
- 708 **Comparison of the effect of UV laser radiation and of a radiomimetic substance on chromatin [3405-101]**
I. Radulescu, L. Radu, Victor Babes Institute (Romania); R. Serbanescu, Univ. of Bucharest (Romania); V. D. Nelea, C. Martin, I. N. Mihailescu, National Institute for Laser, Plasma, and Radiation Physics (Romania)
- 713 **Laser therapy in ocular tumors [3405-102]**
B. Cârstocea, O. L. Gafencu, S. Apostol, M. Ioniţă, Central Military Hospital (Romania); A. Moroşeanu, T. Dascălu, V. Lupei, National Institute for Laser, Plasma, and Radiation Physics (Romania); V. Ioniţă-Mânzatu, Biotechnos SA (Romania)
- 717 **Laser-induced fluorescence of atherosclerotic plaques [3405-103]**
N. Moise, M. L. Pascu, National Institute for Laser, Plasma, and Radiation Physics (Romania); C. Carp, C. Volvoreanu, Institute of Cardiology (Romania)
- 722 **Determination of size-shape distribution of biological particles from light-scattering measurements [3405-104]**
N. E. Mincu, Institute of Optoelectronics (Romania); M.-A. Popovici, Politehnica Univ. of Bucharest (Romania); M. Dobre, Carol Davila Medical Univ. (Romania)
- 727 **Photodynamic therapy using hematoporphyrin derivative and He-Ne laser irradiation in Erlich tumor: an experimental study on mice [3405-105]**
M. Radu, National Institute for Research and Development of Optoelectronics (Romania); D. Ciotaru, Victor Babes Institute (Romania); M. Calin, National Institute for Research and Development of Optoelectronics (Romania); G. Savi, Victor Babes Institute (Romania); M. Bota, Univ. of Southern California (USA); C. Stroila, Victor Babes Institute (Romania)
- 733 **Comparative study of the thermal effects generated by laser irradiation for medical applications [3405-106]**
M. Calin, M. Tomescu, R. N. Radvan, M. Radu, T. Necsoiu, National Institute for Research and Development of Optoelectronics (Romania)
- 739 **Low-power laser efficacy in peripheral nerve lesion treatment [3405-107]**
C. Antipa, Colţea Clinical Hospital (Romania); M. Nacu, N. Malaxa Clinical Hospital (Romania); I. I. Bruckner, Colţea Clinical Hospital (Romania); D. Bunilă, Plastic Surgery Hospital (Romania); M. Vlaiculescu, Colţea Clinical Hospital (Romania); M. L. Pascu, National Institute for Laser, Plasma, and Radiation Physics (Romania); E. Ionescu, Colţea Clinical Hospital (Romania)
- 747 **Low-power laser use in the treatment of alopecia and crural ulcers [3405-108]**
T. Ciuchiţă, Military Hospital Pitesti (Romania); M. Uşurelu, Military Hospital Cluj (Romania); C. Antipa, M. Vlaiculescu, E. Ionescu, Colţea Clinical Hospital (Romania)

SESSION 6 OPTOELECTRONICS

- 756 **Applications of infrared, heterodyne detection systems (Invited Paper) [3405-109]**
M. Strzelec, Z. Puzewicz, Institute of Optoelectronics (Poland); M. Kopica, Military Univ. of Technology (Poland)
- 762 **Characterization of integrated optical waveguides based on oxidized porous silicon (Invited Paper) [3405-110]**
M. Balucani, V. Bondarenko, Istituto Nazionale per la Fisica della Materia (Italy) and Univ. degli Studi di Roma La Sapienza (Italy); N. Kasuchits, Belarusian State Univ. of Informatics and Radioelectronics; G. Lamedica, Istituto Nazionale per la Fisica della Materia (Italy) and Univ. degli Studi di Roma La Sapienza (Italy); N. Vorozov, Belarusian State Univ. of Informatics and Radioelectronics; A. Ferrari, Istituto Nazionale per la Fisica della Materia (Italy) and Univ. degli Studi di Roma La Sapienza (Italy)
- 768 **Electronic laser beam profile measurement (Invited Paper) [3405-111]**
C. B. Roundy, Spiricon, Inc. (USA)
- 779 **Satellite remote sensing data applied for seismic risk assessment of Vrancea region (Invited Paper) [3405-112]**
M. Zoran, C. L. Braescu, C. Aiftimiei, Institute of Optoelectronics (Romania)
- 784 **Amorphous silicon photodetectors for optical integrated circuits [3405-113]**
M. Balucani, Istituto per la Fisica della Materia (Italy) and Univ. di Roma La Sapienza (Italy); V. Bondarenko, Istituto per la Fisica della Materia (Italy) and Belarusian State Univ. of Informatics and Radioelectronics; G. Lamedica, A. Ricciardelli, A. Ferrari, Istituto per la Fisica della Materia (Italy) and Univ. degli Studi di Roma La Sapienza (Italy)
- 790 **Properties of polymer compositions for recording and copying optical images [3405-114]**
V. V. Bivol, Ctr. of Optoelectronics (Moldova); N. A. Barba, S. V. Robu, B. M. Ishimov, L. A. Vlad, State Univ. of Moldova; A. M. Prisacari, G. M. Triduh, E. A. Akimova, Ctr. of Optoelectronics (Moldova)
- 796 **Electro-optic response of some chiral liquid crystals with high spontaneous polarization [3405-115]**
C. Dascalu, C. Motoc, E. Petrescu, C. Rosu, Politehnica Univ. of Bucharest (Romania); H. D. Koswig, U. Labes, Technische Univ. Berlin (FRG)
- 801 **Fluid optical components and their applications in optoelectronics [3405-116]**
R. N. Rădvan, M. Călin, R. Savastu, M. Robu, M. Radu, National Institute for Research and Development of Optoelectronics (Romania)
- 807 **Optical fiber multiplexed image transmission system [3405-117]**
S. Micloș, T. Zisu, B. Robea, Institute of Optoelectronics (Romania)
- 813 **Cylindrical piezoceramic transducer for remote optoelectronic system [3405-118]**
I. Chilibon, M. Robu, Institute of Optoelectronics (Romania)
- 819 **Optical systems for night vision devices [3405-119]**
G. Copot, R. Copot, Institute of Optoelectronics (Romania)
- 825 **Optical beacon for pointing and tracking systems for free-space communications [3405-120]**
P. E. Sterian, Politehnica Univ. of Bucharest (Romania); P. P. Digulescu, Technical Military Academy (Romania); R. V. Ivan, Politehnica Univ. of Bucharest (Romania)

- 831 **Laser treatment of a-SiC:H thin films for optoelectronic applications [3405-121]**
D. Ghica, N. E. Mincu, National Institute for Research and Development of Optoelectronics (Romania); C. A. Stanciu, G. H. Dinescu, E. Aldea, National Institute for Laser, Plasma, and Radiation Physics (Romania); V. Sandu, National Institute of Materials Physics; A. Andrei, Institute of Nuclear Research (Romania); M. Dinescu, National Institute for Laser, Plasma, and Radiation Physics (Romania); A. Ferrari, M. Balucani, G. Lamedica, Istituto per la Fisica della Materia (Italy) and Univ. degli Studi di Roma La Sapienza (Italy)
- 837 **Gamma-induced transparency loss of thick quartz fibers [3405-122]**
E. M. Gasanov, E. M. Ibragimova, B. S. Yuldashev, Institute of Nuclear Physics (Uzbekistan); M. Kh. Ashurov, I. R. Rustamov, Scientific Association Phonon (Uzbekistan)
- 846 **Electrical and optical characterization of PbTiO₃/Si heterostructures for applications in optoelectronics [3405-123]**
V. Dragoi, L. Pintilie, I. Pintilie, D. Petre, I. Boerasu, National Institute of Materials Physics (Romania); M. Alexe, Max Planck Institute of Microstructure Physics (FRG)
- 852 **Optical integrated circuits [3405-124]**
O. D. Iancu, D. Pircălăboiu, Politehnica Univ. of Bucharest (Italy)
- 860 **Optical properties of polycrystalline In_xGa_{1-x}Sb (x=0.20) from 15 to 30 μm [3405-125]**
C. A. E. Grigorescu, Institute of Optoelectronics (Romania); S. A. Manea, National Institute of Materials Physics (Romania); M. F. Logofatu, I. I. Munteanu, B. Logofatu, Univ. of Bucharest (Romania); M. Calin, M. Radu, National Institute for Research and Development of Optoelectronics (Romania); M. F. Lazarescu, National Institute of Materials Physics (Romania)
- 865 **Verifying a model for statistical hypothesis in detection of noncoherent radiation [3405-126]**
V. Babin, S. Ersen, A. Moldovan, National Institute for Research and Development of Optoelectronics (Romania); N. Iftimia, Military Research and Development Institute (Romania)
- 873 **Characterization of ion-exchanged waveguides from near-field measurements [3405-127]**
D. Pircălăboiu, Politecnico di Torino (Italy) and Politehnica Univ. of Bucharest (Romania); G. Motta, G. Perrone, I. Montrosset, Politecnico di Torino (Italy)
- 877 **Non-Markovian effects in dissipative systems [3405-128]**
E. N. Stefanescu, National Research Institute of Microtechnology (Romania); P. E. Sterian, Politehnica Univ. of Bucharest (Romania)
- 883 **Optoelectronic micropositioning device with a piezoceramic transducer [3405-129]**
I. Chilibon, M. Robu, Institute of Optoelectronics (Romania)
- 887 **Spectroellipsometric characterization of multilayer systems containing Ni and Bi [3405-130]**
V. Hutsanu, Univ. of Bucharest (Romania); M. Gartner, C. Ghita, Institute of Physical Chemistry (Romania); V. Dolocan, Univ. of Bucharest (Romania)
- 891 **Orthorectification of radar (SAR) data: synergism and complementariness with optical (Landsat TM) data [3405-131]**
C. L. Brăescu, M. Zoran, C. Aiftimiei, A. Stoica, Institute of Optoelectronics (Romania); D. Răducanu, Technical Military Academy (Romania)

- 897 **Al₂O₃ single-crystalline substrates for optoelectronic applications [3405-132]**
C. Logofatu, National Institute for Lasers, Plasma, and Radiation Physics (Romania); B. Iliescu, I. Enculescu, National Institute for Materials Physics (Romania); C. A. E. Grigorescu, Institute of Optoelectronics (Romania); S. A. Manea, National Institute of Materials Physics (Romania)
- 902 **Optical light modulation in planar As₂Se₃Sn_x waveguides [3405-133]**
A. A. Popescu, A. I. Albu, A. Tsaranu, Ctr. of Optoelectronics (Moldova)
- 906 **Approximate solutions of the eigenvalue equation near cutoff for TE_{0m} and TM_{0m} modes for a step index fiber optic: new forms and considerations [3405-134]**
C. L. Schiopu, P. Schiopu, Politehnica Univ. of Bucharest (Romania)
- 912 **Concept of WDM-HD: WDM for increasing the information capacity of fiber optic communication systems [3405-135]**
P. Schiopu, Politehnica Univ. of Bucharest (Romania); L. Dragnea, Institute of Microtechnology (Romania)
- 916 **Modeling the passive and active LiNbO₃ optical waveguides [3405-136]**
N. N. Puscas, I. M. Popescu, Politehnica Univ. of Bucharest (Romania)
- 922 **Effective index method for the computation of the propagation constant and electromagnetic field distribution in z-uniform dielectric or semiconductor waveguides [3405-137]**
M. Dumitrescu, Tampere Univ. of Technology (Finland); M. Guina, Politehnica Univ. of Bucharest (Romania)
- 926 **Real performance of image intensifier systems for night vision [3405-138]**
M. Mirzu, L. Cosereanu, M. Jurba, Army Institute for Research and Development (Romania); G. Copot, D. Ralea, R. Marginean, Institute of Optoelectronics (Romania)
- 930 **Control of laser spiking in Nd:YAG lasers with saturable absorbers [3405-139]**
M. Jurba, Army Institute for Research and Development (Romania); V. Babin, Institute of Optoelectronics; N. Baltateanu, National Institute for Laser, Plasma, and Radiation Physics (Romania); I. Gherghina, V. Jipa, E. Popescu, L. Cosereanu, M. Mirzu, Army Institute for Research and Development (Romania)
- 936 **Optical transmission of ZnO thin films [3405-140]**
I. I. Rusu, Bacău Univ. (Romania); I. D. Bursuc, Al. I. Cuza Univ. (Romania); I. Vascan, Bacău Univ. (Romania)
- 941 **Magneto-optical behavior of ferronematics [3405-141]**
C. Motoc, E. Petrescu, C. Dascalu, Politehnica Univ. of Bucharest (Romania)
- 946 **Optical bistability using nematic liquid crystals and polymer-dispersed liquid crystals [3405-142]**
D. Manaila-Maximean, C. Rosu, R. Bena, A. M. Albu, I. M. Popescu, Politehnica Univ. of Bucharest (Romania)
- 951 **IR absorption of TiO₂ thin films [3405-143]**
M. D. Stamate, Bacău Univ. (Romania); G. I. Rusu, Al. I. Cuza Univ. (Romania); I. Vascan, Bacău Univ. (Romania)

- 955 **Computerized lateral-shear interferometer [3405-144]**
S. A. Hasegan, A. Jianu, V. I. Vlad, National Institute for Laser, Plasma, and Radiation Physics (Romania)
- 960 **Amorphous Se/CdSe and SiO_x/CdSe multilayers [3405-145]**
M. A. Popescu, F. Sava, A. Lörinczi, National Institute of Materials Physics (Romania); E. Vateva, D. Nesheva, G. Tchaushev, Institute of Solid State Physics (Bulgaria); I. N. Mihailescu, Institute of Atomic Physics (Romania); P.-J. Koch, S. Obst, H. Bradaczek, Freie Univ. Berlin (FRG)
- 965 **Aluminophosphate glass with CdS_xSe_{1-x} microcrystallite for optoelectronics [3405-146]**
R. Rogojan, M. Elisa, MATPUR SA (Romania); P. E. Sterian, Politehnica Univ. of Bucharest (Romania)

SESSION 7 OPTICAL SENSORS AND METROLOGY

- 972 **New principle for self-calibration techniques in phase-shift interferometry (Invited Paper) [3405-147]**
A. Dobroiu, D. Apostol, V. Damian, V. Nascov, National Institute for Laser, Plasma, and Radiation Physics (Romania)
- 978 **Instruments and standard measurement procedures for laser beam characterization (Invited Paper) [3405-148]**
R. Mästle, C. Schmitz, F. Varnik, A. Giesen, H. Hügel, Univ. Stuttgart (FRG)
- 990 **Laser frequency comparisons involving Romanian length standard and traceability (Invited Paper) [3405-149]**
G. Popescu, National Institute for Laser, Plasma, and Radiation Physics (Romania); J.-M. Chartier, Bureau International des Poids et Mesures (France); F. Bertinetto, Istituto di Metrologia G. Colonnetti (Italy); F. Petru, Institute of Scientific Instruments (Czech Republic)
- 999 **All-direction localizer of pulsed optical sources [3405-150]**
P. P. Digulescu, Technical Military Academy (Romania); P. E. Sterian, Politehnica Univ. of Bucharest (Romania)
- 1007 **UV radiation sensors with unitary and binary superficial barrier [3405-151]**
V. Dorogan, T. Vieru, V. Kosyak, Technical Univ. of Moldova; I. Damaskin, Institute of Applied Physics (Moldova); F. Chirita, Technical Univ. of Moldova
- 1013 **New type of sensor of radiation in a wide range of energy [3405-152]**
A. M. Andriesh, S. A. Malkov, V. I. Verlan, M. G. Bulgaru, Institute of Applied Physics (Moldova)
- 1022 **Interference devices for noncontact diagnostics of arbitrarily shaped rough surfaces [3405-153]**
P. P. Maksimyak, Chernivtsy Univ. (Ukraine)
- 1027 **Optical studies on sedimentation of suspensions [3405-154]**
S. Anghel, Univ. of Pitești (Romania); I. Iova, Șt. Levai, Univ. of Bucharest (Romania); I. Iorga Simăn, I. Iosub, Univ. of Pitești (Romania)

- 1032 **Quadrant detector based on InGaAsP heterostructures [3405-155]**
V. Dorogan, V. Brynzari, T. Vieru, V. Kosyak, Technical Univ. of Moldova
- 1039 **Photothermal method using a pyroelectric sensor for thermophysical characterization of agricultural and biological samples [3405-156]**
A. Frandas, D. Dadarlat, M. Chirtoc, Institute of Isotopic and Molecular Technology (Romania); H. Jalink, Ctr. for Plant Breeding and Reproductive Research (Netherlands); D. D. Bicanic, Wageningen Agricultural Univ. (Netherlands); D. Paris, J. S. Antoniow, M. Egee, Univ. de Reims (France); C. Ungureanu, Institute of Isotopic and Molecular Technology (Romania)
- 1045 **Techniques for accurately measuring laser beam width with commercial CCD cameras [3405-157]**
C. B. Roundy, Spiricon, Inc. (USA)
- 1056 **Definition of a robust measurement of similarity for the localization of small shapes in scenes [3405-158]**
X. Fernández, Industrias de Optica, SA (Spain); J. Ferré-Borrull, S. Bosch, Univ. de Barcelona (Spain)
- 1063 **Light scattering in liquid crystals [3405-159]**
M. Ursache, M. Socaciu, C. Sarpe-Tudoran, Univ. of Craiova (Romania)
- 1067 **Digital laser powermeter [3405-160]**
E. Smeu, N. N. Puscas, I. M. Popescu, Politehnica Univ. of Bucharest (Romania)
- 1074 **Structured light in visual inspection [3405-161]**
C. Blănuș, V. V. Vasiliu, National Institute for Laser, Plasma, and Radiation Physics (Romania)
- 1078 **Romanian primary length standards involved in international comparisons [3405-162]**
G. Popescu, National Institute for Laser, Plasma, and Radiation Physics (Romania)
- 1083 **Calibration procedures for a 10.6- μ m laser calorimeter [3405-163]**
M. Kennedy, D. Ristau, Laser Zentrum Hannover eV (FRG); G. Dumitru, D. G. Sporea, C. A. Timus, National Institute for Laser, Plasma, and Radiation Physics (Romania)
- 1088 **Estimation of some physical characteristics of metallic powders using VIS reflectance measurements [3405-164]**
M. Nicola, E. Darvasi, D. Gomoiescu, E. Cordoș, Research Institute for Analytical Instrumentation (Romania)
- 1094 **Method for small birefringence evaluation [3405-165]**
A. M. Beldiceanu, Pro Optica SA (Romania)
- 1100 **Circularity measurement by laser triangulation [3405-166]**
V. Damian, C. Blănuș, D. Apostol, A. Dobroiu, V. Nascov, National Institute for Laser, Plasma, and Radiation Physics (Romania)

SESSION 8 OPTICAL COMPONENTS

- 1106 **Polarizing interference coatings made with anisotropic thin films (Invited Paper) [3405-167]**
F. Flory, C. Defay, Ecole Nationale Supérieure de Physique de Marseille (France)

- 1114 **Special mirrors for cw CO₂ high-power lasers (Invited Paper) [3405-168]**
R. V. Medianu, I. Gutu, G. Georgescu, National Institute for Laser, Plasma, and Radiation Physics (Romania); M. F. Lazarescu, National Institute of Materials Physics (Romania)
- 1120 **Spectrophotometry, ellipsometry, and computer simulation in thin film developments (Invited Paper) [3405-169]**
S. Bosch, Univ. de Barcelona (Spain)
- 1132 **Structure investigations of optical coatings on GaAs substrate (Invited Paper) [3405-170]**
C. A. Timus, R. V. Medianu, G. Georgescu, National Institute for Laser, Plasma, and Radiation Physics (Romania); E. Vasile, METAV SA (Romania)
- 1137 **Characteristics of a carbon/nickel multilayer structure for soft x-ray optics deposited by rf magnetron sputtering [3405-171]**
M. Ulmeanu, G. Georgescu, R. V. Medianu, National Institute for Laser, Plasma, and Radiation Physics (Romania); N. Nastase, National Institute of Microtechnology (Romania); C. Ghica, National Institute of Materials Physics (Romania); V. V. Vasiliu, National Institute for Laser, Plasma, and Radiation Physics (Romania)
- 1143 **New method for automatic optimization of glass combination in optical systems working in the visible range [3405-172]**
D. Ralea, R. Marginean, Institute of Optoelectronics (Romania); M. Marzu, Army Institute for Research and Development (Romania)
- 1150 **Interferometric characterization of GRIN lenses for ophthalmic uses [3405-173]**
J. R. de F. Moneo, I. P. Juvells, S. R. Vallmitjana, S. Bosch, A. Carnicer, I. Labastida, J. Pérez, Univ. de Barcelona (Spain)
- 1156 **Ray tracing for ophthalmic optics: specific developments for GRIN materials [3405-174]**
J. R. de F. Moneo, I. P. Juvells, S. R. Vallmitjana, S. Bosch, A. Carnicer, I. Labastida, J. Pérez, Univ. de Barcelona (Spain)
- 1162 **Solutions of single-layer synthesis with symmetrical three-layer periods [3405-175]**
A. G. Dincă, P. T. Miclea, V. Lupei, National Institute for Laser, Plasma, and Radiation Physics (Romania); M. P. Dincă, Univ. of Bucharest (Romania)
- 1167 **Yield optimization of multilayer optical coating by modeling of the monitoring process [3405-176]**
G. L. Muscalu, Pro Optica SA (Romania)
- 1173 **Interferential filter design with continuously variable refractive index [3405-177]**
A. G. Dincă, V. Lupei, National Institute for Laser, Plasma, and Radiation Physics (Romania); M. P. Dincă, Univ. of Bucharest (Romania)
- 1178 **Filters with induced transmission [3405-178]**
Gh. Honciuc, Pro Optica SA (Romania)
- 1183 **Software for optical coating design [3405-179]**
Gh. Honciuc, Pro Optica SA (Romania); Gh. Singurel, Al. I. Cuza Univ. (Romania)
- 1189 **Electrostatically driven dynamic focus system [3405-180]**
H. Tojia, M. Micluța, National Institute for Laser, Plasma, and Radiation Physics (Romania)

SESSION 9 OPTICS AND ENVIRONMENT

- 1194 **III-V compounds and piezoelectric ceramic thin films deposited by reactive PLD: application to sensor building (Invited Paper) [3405-181]**
M. Dinescu, Nationa Institute for Laser, Plasma, and Radiation Physics (Romania); P. Verardi, F. Craciun, CNR Institute of Acoustics (Italy); C. A. Stanciu, R. Dinu, National Institute for Laser, Plasma, and Radiation Physics (Romania); C. Gerardi, L. Mirengi, PASTIS CNRSM (Italy); M. Gartner, Institute of Physical Chemistry I.G. Murgulescu (Romania); V. Sandu, National Institute of Materials Physics (Romania)
- 1202 **Laser monitoring of pesticides in water (Invited Paper) [3405-182]**
M. L. Pascu, N. Moise, L. Voicu, National Institute for Laser, Plasma, and Radiation Physics (Romania); T. Negoita, Polar Research Ctr. (Romania); G. Manolescu, Institute of Physical Chemistry (Romania); A. Smarandache, National Institute of Materials Physics (Romania)
- 1215 **Detection of atmospheric pollutants by pulsed photoacoustic spectroscopy [3405-183]**
M. Roman, M. L. Pascu, A. Staicu, National Institute for Laser, Plasma, and Radiation Physics (Romania)
- 1220 **Modeling of atmospheric effects on the angular reflectance characteristics of vegetation canopies [3405-184]**
G. Stancalie, National Institute of Meteorology and Hydrology (Romania)
- 1228 *Author Index*

SESSION 5

Biophotonics

Laser based assessment of lipid peroxidation in humans.

Gianfranco Giubileo

ENEA - Dipartimento Innovazione, Divisione Fisica Applicata
Centro Ricerche Frascati, Via E. Fermi, 45 - 00044 Frascati (Rome), Italy
Phone: 39-6-9400-5768, Fax: 39-6-9400-5334
e-mail: giubileo@frascati.enea.it

ABSTRACT

Infrared absorption spectroscopy can be performed at very high resolution by tunable diode laser (TDL) based optical systems for any gas with well resolved absorption spectra. In a double beam setup atmospheric trace gas concentration can be measured down to ppb levels. The analysis of trace gases may have useful applications in detecting chemicals in the human breath for non invasive medical diagnostic. The capability of TDL based breath analysis was well demonstrated by monitoring ammonia and methane. In the human body the formation of free radicals does induce oxidative degradation of polyunsaturated fatty acids (lipid peroxidation) which is a damage for cells and organs in the organism. Specific volatile hydrocarbons generated as end product by lipid peroxidation (LP) can be found inside circulating blood and expired breath. TDL based analysis of those specific hydrocarbons (ethane and pentane) in the expired breath can allow a non invasive assessment of the LP extent.

Keywords: laser spectroscopy, breath alkanes, lipid peroxidation, free radicals

1. INTRODUCTION

The oxidative modification of biological molecules is an essential part of the normal biological activity in the human organism, but an excess in some oxidant activities does cause injury to cells and tissues. Particular attention is devoted to the oxidant activity of free radicalic species. It is known that an increased free radical formation in the organism is involved in the pathophysiology of several diseases, consequently a measurement of the oxidative damage that a human is undergoing will be helpful in clinical diagnosis. Standardized methods for measuring the free radicals activity in humans are not yet established, so the development of reliable measures is desirable.

To perform such a measure we need a test effect. One of the events generated by free radicals interaction with biomolecules is the oxidative degradation of fatty acids. The phenomenon of free radical induced peroxidation of fatty acids is ubiquitous in the organism. Every living cell possesses an active boundary (the cytoplasmic membrane) on which many chemical and physical phenomena take place. The structure of any biological membrane is based on a bilayer of lipids which carry fatty acid molecules. Under chemical attack by oxidative free radicals the fatty acids in the membrane lipids undergo a chemical decomposition working out through many chained chemical reactions. This process is named lipid peroxidation (LP). The ultimate step in the peroxidative chain reaction is the formation of different hydrocarbons molecules, depending on the molecular arrangement of the fatty acid involved. In the human body, the fatty acids inside the membrane lipids are mainly linolenic acid and arachidonic acid. The peroxidation of these fatty acids does produce two volatile alkanes, ethane and pentane respectively. Both of them are considered in literature to be good markers of free radical induced lipid peroxidation in humans.

Such gases diffuse inside body tissues and are convected through haematic flow towards the lungs. In the lungs they are excreted in the expired breath. An increase in the free radical activity determines an increase in the lipid peroxidation which is detectable by an excess in the breath ethane and pentane. So the extent of unrecovered lipid peroxidation may be estimated by the measurement of ethane and pentane exhaled in the breath, a non-invasive analysis.

In healthy people the normal breath concentration of these alkanes is about 1 ppb (nmoles/liter) as order of magnitude. Due to their low concentration hydrocarbons in the expired breath can be well analyzed by a spectroscopy of absorbing lines in the infrared region through an appropriate light source. Single mode tunable diode lasers (TDL) were proved to be good light sources in the high resolution infrared spectroscopy for gas with well resolved absorption spectra. They have

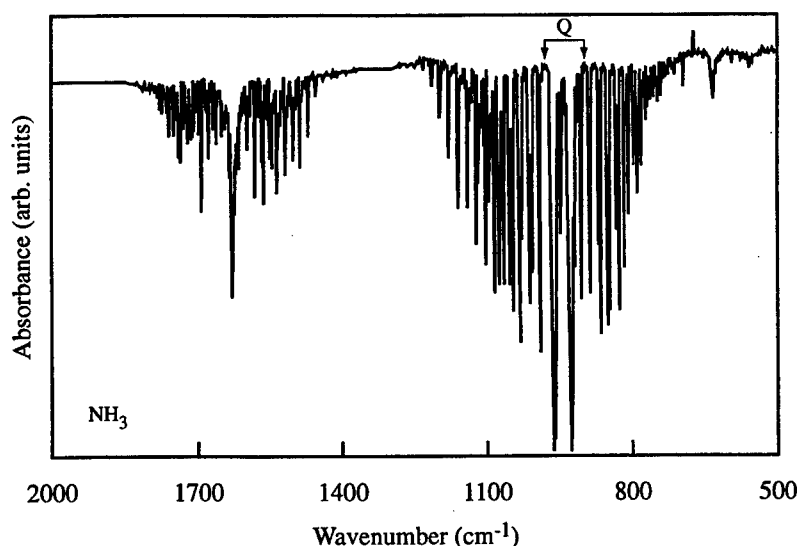


Fig. 1. IR Absorption spectrum of ammonia (NH₃) between 500 cm⁻¹ and 2000 cm⁻¹ (see Ref. 1)

been already successfully used in trace gas analysis applied to atmosphere and expired breath and may be applied in the just outlined assessment. In the following the laser based breath analysis and the LP test effect will be described.

2. LASER BASED ANALYSIS

2.1 IR molecular spectroscopy.

Infrared spectroscopy is based on selective molecular absorption of IR radiation when a gas mixture is exposed to light. The infrared absorption spectrum of molecules is normally determined by transitions between series of vibrational-rotational energy levels. For every chemical species a well defined set of narrow width absorption lines in the IR spectrum does exist, differing from each molecular species to other likewise a fingerprint. Besides, when an atom in a molecule is replaced by another isotope of the same element, there is a shift in the energy levels due to a change in the atomic masses, and consequently there is a shift in the spectral lines. This resulting frequency shift in the IR absorption spectrum forms the basis of the isotope laser spectroscopic analysis. An example of an IR absorption spectrum is reported in fig.1. The IR spectrum of ammonia shown in this picture was detected by a classical spectrophotometer based on a black body light source, so it has a relatively low resolution (around 1 cm⁻¹).

An increase of several order of magnitude in the resolution can be obtained by using a laser source¹ because of its high brightness, high space-time coherence and monochromatic emission. High sensitivity optical systems have been realized based on a single mode tunable diode lasers (TDL) as radiation source. The spectral resolution of a diode laser based system can be better than 10⁻³ cm⁻¹, which is smaller than the absorbing linewidth and the line spacing in the IR spectra we need to acquire, allowing us to resolve a single transition line. By selecting an appropriate spectral region the probability of interference between absorption lines of different gas species in the same mixture can be reduced greatly, and very low gas levels are detectable. In fig.2 an high resolution spectrum is reported as recorded by a TDL based system; the fine structure of a small portion of the NH₃ absorption spectrum near 937 cm⁻¹ (the branch Q in the ν₂ band pointed out in fig.1) has been resolved. The same portion of ammonia spectrum has been calculated and is shown in fig.3, where a computer simulation is given by the HITRAN-PC database².

2.2 TDL sources.

A typical diode laser is a ternary lead salt structure with built in a p-n junction. The IR coherent radiation is emitted during the charge recombination inside the p-n junction area, the total output power being nearly 1 mW at a work temperature lower than 100 K and diode injection current around 1 A. The frequency of the emitted radiation is depending on the diode temperature and for this kind of laser falls in the wavelength range between 3 and 30 μm (3,300-300 cm⁻¹).

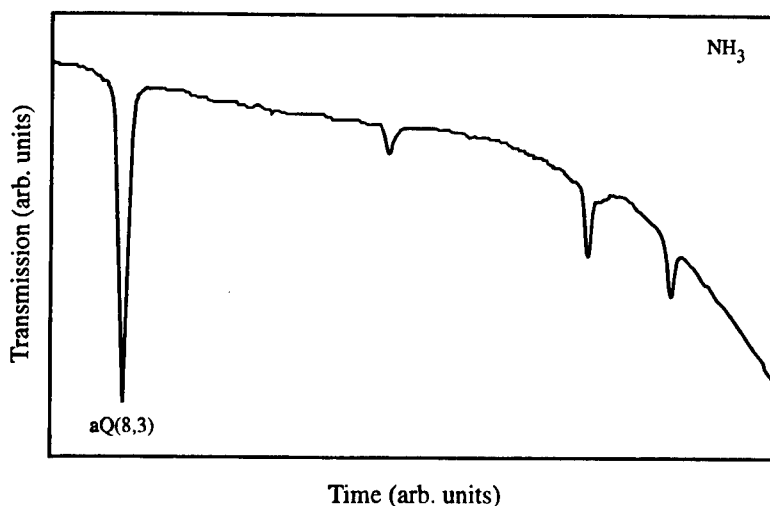


Fig. 2. IR spectrum of ammonia between 937.5 cm^{-1} and 937.8 cm^{-1} as recorded by a TDL system. The more intense line is named aQ(8,36) and is located at 937.515 cm^{-1}

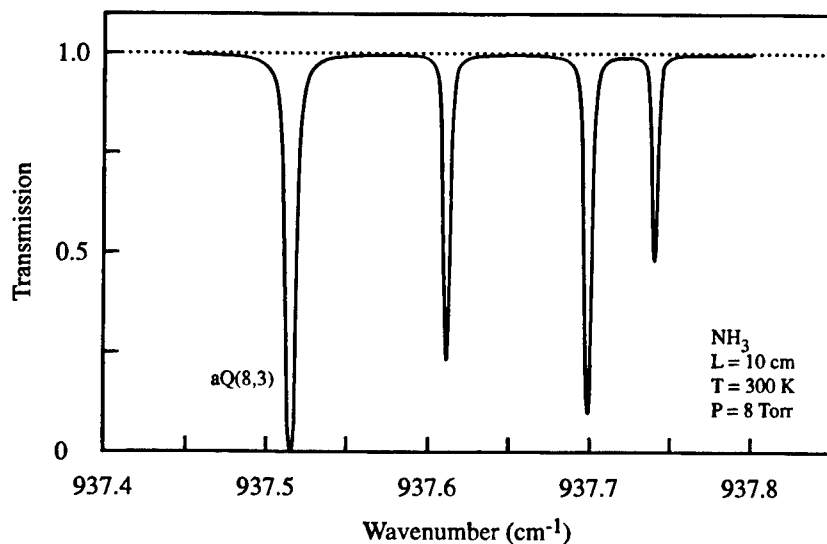


Fig. 3. Fine structure of a small portion of ammonia spectrum as calculated by HITRAN-PC database

The radiation frequency of a given TDL is continuously tunable for about 100 cm^{-1} by acting on laser temperature and diode injection current.

The emission mode is selected by fixing the laser work temperature through a cold finger connected to a closed-cycle liquid nitrogen cooler. The continuous tuning is obtained by modulating the injection current of the diode; the tuning rate is around $1 \text{ cm}^{-1}/\text{mA}$. When the modulating current does increase linearly from a minimum toward a maximum we have a gradual heating of the laser structure and a related variation in the radiation frequency, the order of magnitude of the variation being $1 \text{ cm}^{-1}/\text{K}$. The laser light frequency depends on the temperature following the curve reported in fig.4. The

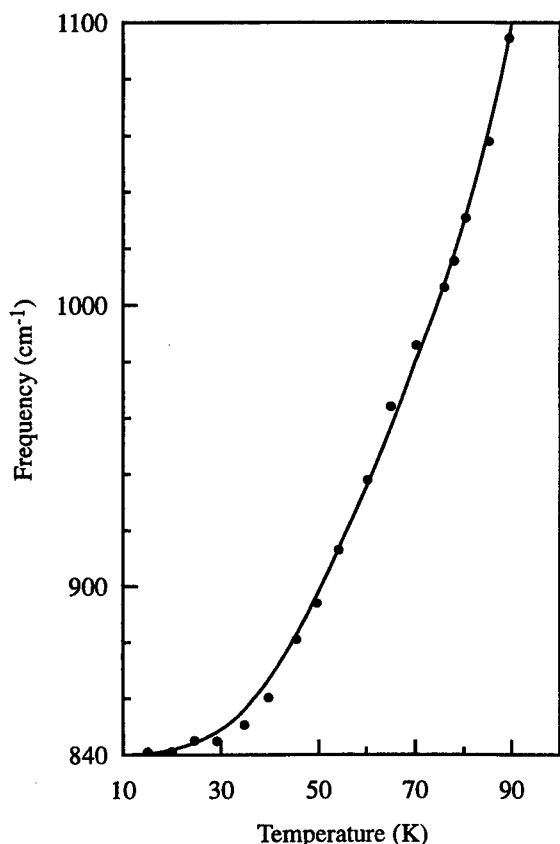


Fig. 4. Frequency of emitted radiation vs diode temperature for a TDL

current modulation is repeated periodically to fulfil a periodical scanning of a spectral range centred on the desired absorption line of the chemical species we are interested.

The spectral linewidth of a diode laser emitted radiation is almost 10^{-6} times the line frequency. Both the narrowness of the emission lines of the laser radiation and the possibility of a continuous frequency modulation of the radiation itself determine the spectroscopic capability of a diode laser based optical system. Allowing the frequency modulated laser beam to pass through a gas mixture, the fraction of beam energy absorbed for each frequency can be recorded.

2.3 Experimental apparatus.

A schematic view of our experimental setup is reported in fig.5. The optical system consists of TDL radiation source, beam transport devices, gas filled cells, radiation detectors and data acquisition system. The radiation source does comprise the laser structure, the temperature control system and the power supply.

The apparatus is a double beam setup. The laser light, comes out of the cold head through an IR window (ZnSe) and is divided into two beams by a beam splitter. The first beam passes through an interferometer (germanium etalon) and a reference cell and then is focused into an IR detector. The second beam passes through a sample cell and is focused into another IR detector. Both signals are collected by the electronic acquisition system. The reference cell containing the pure gas is used for mode selection and for calibrating the signal amplitude. The other cell (the measurement one) is filled with the examined gas sample. The insertion of an etalon on the beam line does allow the determination of spectral distances on the spectrum, the distance between two consecutive fringes being known. The laser light is selected

at the right frequency for the molecular transition to be detected by fixing the work temperature of the thermostate and then, to record the absorption spectrum, it is allowed to pass through the absorbing gas (inside reference cell) while tuning the light frequency over the spectral region. The waveform of the pulsed modulating current is a triangular one. The intensity of the transmitted beam energy versus the radiation frequency is displayed on a CRT. The optical absorbance is depending on the optical path of the laser beam inside the absorbing gas and on gas concentration. So in a calibrated system the amount of absorbed energy is a measure of the gas concentration inside the examined mixture. Although the rate of frequency change is not linear with temperature it does not affect the absorption measurements.

An example of a typical laser mode transmitted through pure ammonia gas is shown in fig.6 together with the unperturbed laser mode. The two detected absorption lines are aQ(8,5) at 933.8260 cm^{-1} and aQ(4,1) at 933.8424 cm^{-1} , which means a line separation of 0.0164 cm^{-1} . Transmission through a germanium etalon is also reported in fig. 6, the spacing between two consecutive fringes being 0.01631 cm^{-1} . The lines aQ(8,5) and aQ(4,1) as simulated by HITRAN database are reported in fig.7.

2.4 Gas trace detection.

The described method may be applied to any gas with a suitable IR absorption spectrum. The spectroscopic capability of TDL based systems has been already used to reveal small traces of gases in the atmosphere to very low levels,³ for example NO, NO₂, HNO₂, H₂O₂. In Table I some detection limits are listed for selected molecules that are detectable by TDL spectroscopy. It is apparent that this method has a very good sensitivity and in reality for many substances the theoretical sensitivity limit is below 1 part over 10^9 (1 ppb).

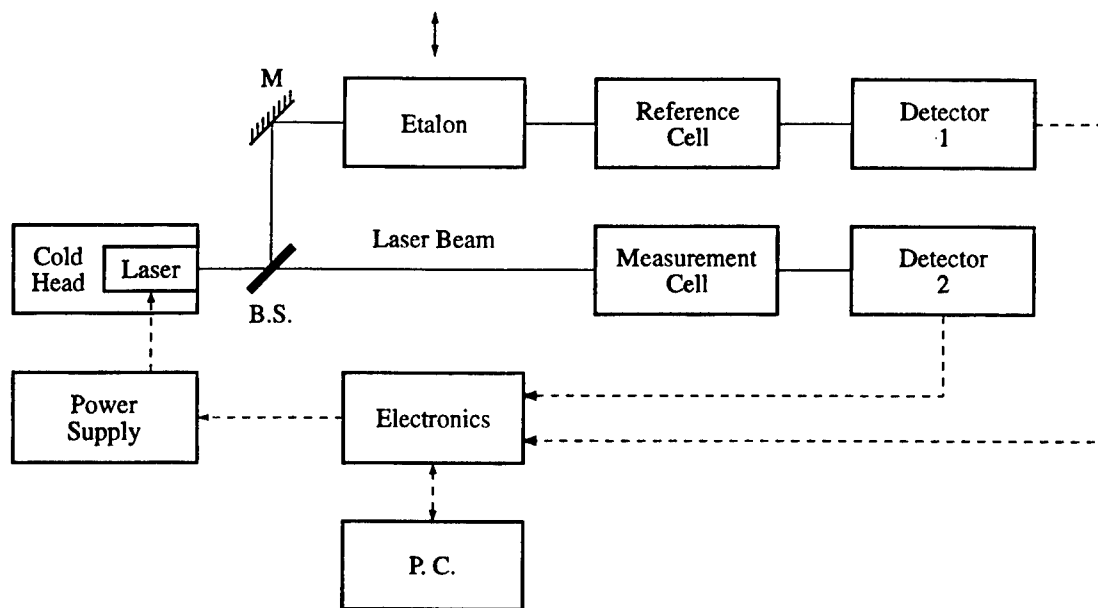


Fig. 5. Schematic diagram of the diode laser analysis system

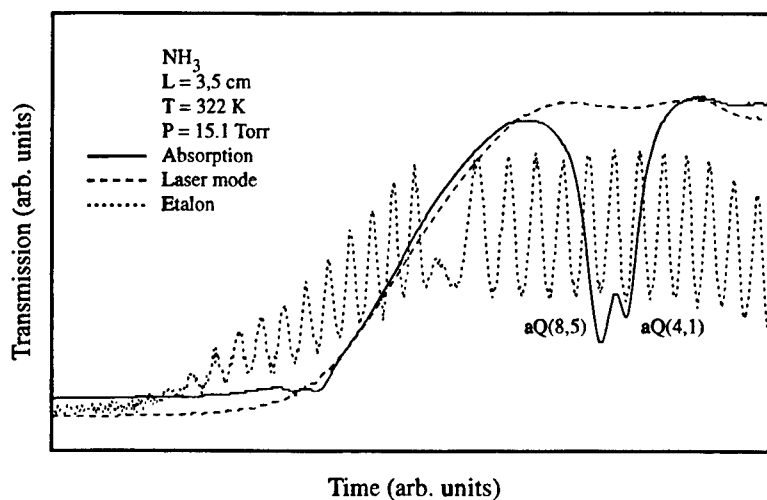


Fig. 6. Transmission of a laser mode through pure ammonia gas with absorption at 933.8260 cm^{-1} (line aQ(8,5)) and 933.8424 cm^{-1} (line aQ(4,1)). The unperturbed laser mode and the etalon fringes are reported too. The spacing between two consecutive fringes is 0.01631 cm^{-1}

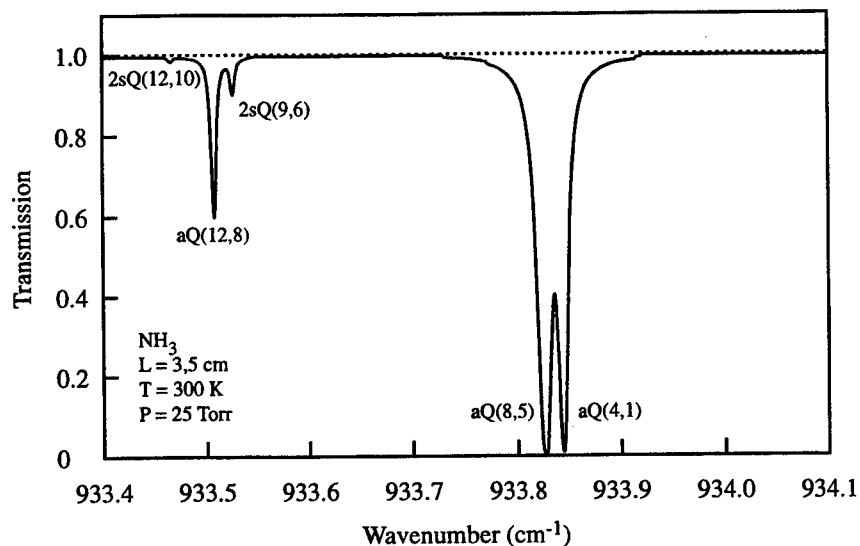


Fig. 7. The absorption lines aQ(8,5) and aQ(4,1) of ammonia simulated by HITRAN-PC database

Table I - Measured (a) and calculated (b) detection limits of TDL absorption spectroscopy for selected molecules⁴. 1 ppbv= 1/10⁹ volume ratio

Molecular species	Minimum detectable concentration (p.p.b.v.)	
	(a)	(b)
H ₂ O ₂	0.1-0.6	0.160
NO	0.1-1.5	0.096
NO ₂	0.025-0.2	0.032
HNO ₃	0.35	0.048
N ₂ O	0.04-1	0.024
NH ₃	0.1	0.016
O ₃	0.5	0.230
CO	1	0.030
CH ₂ O	0.04-0.3	0.128
SO ₂	0.2-3	0.096
HCl	0.25-50	0.012

Also a TDL based spectroscopic system has been used to detect trace components in the human breath.⁴⁻⁷ The human organism makes use for its living processes of chemicals that are introduced with the food or the air and, after sometimes intricate biochemical processes, they are converted into other chemical species. Such transformations and their products are assumed as indicators of the body health and used in medical diagnostics. The measure of the naturally produced chemicals, or the ones produced after the intake of a substance enriched with a particular isotope, may reveal an actual illness or bad functioning.

The indicators are currently measured by nuclear methods or mass spectrometry by invasive analysis. Part of them are gas and are expelled in small amount with breathing. Detection of these gases may be performed directly on the exhaled breath in a non invasive analysis by the spectroscopic method above described. In our laboratory in Frascati we possess a good experience of this kind of measurements. The concentration of the expired gas is generally very low (around ppm) anyway, because of the high sensitivity of the method, useful informations can be derived by collecting only one exhalation.

Substances like CO, CO₂, CH₄, NH₃, and other gases produced inside human body, have already been detected and measured in several medical studies. In the next section the origin, the detection and the diagnostic utility of some hydrocarbons in the expired breath will be discussed.

3. LIPID PEROXIDATION AND TEST EFFECT

3.1 Lipids in living cells.⁸

Every living cell is bordered by a cellular membrane based on a twofold layer of phospholipids which are bonded each other by Van der Waals bonds. Phospholipids are part of a more general class of organic compounds (lipids) not soluble in water and working inside human body likewise metabolic fuel storage system, metabolic fuel transport system and basic components in cellular membrane structure.

In a block diagram (see fig.8) the general structure of a phospholipid can be viewed as an assembly of different molecular groups. They are a glycerol molecule bonding a phosphate-alcohol and 1-3 fatty acids. The alcoholic group has a strong polarity, while the fatty acid tails are not polar groups. So in hydrated environment like a biological system the natural arrangement of phospholipids is a twofold layer (thickness 8 nm) with the polar heads directed toward the water and the fatty acid tails along the opposite direction toward the inner side of the membrane. In fig.9 one of the most common fatty acid is shown.

Fatty acid molecules are long hydrocarbon chains. Most of carbon in the chain are linked to two hydrogen and two carbon by simple covalent bonds (-CH₂-CH₂-); sometimes a double bond can be observed between two adjacent carbon atoms in the same chain (-CH=CH-). Hydrocarbon chains with one or more double bond are known like unsaturated, while chains without double bond are told saturated. Many different fatty acids do exist in nature inside living cells, the chain length ranging between 14 and 22 atoms of carbon.

In principle any fatty acid chain may take part in the structure of a lipid, but in nature the unsaturated species are found more abundant then the saturated one. In particular the oleic acid, linoleic acid, linolenic acid and arachidonic acid are the more abundant fatty acids in the human organism. Their molecular composition has been reported in Table.2.

3.2 Lipid peroxidation.

Lipid molecules can be chemically disassembled through peroxidative pathways started by interaction with free radicals. Free radicals are atoms or molecules possessing one or more unpaired electrons. They are produced either by an oxidation-reduction process or by transferring sufficient energy to a molecule to cause unimolecular dissociation at a covalent bond, so that one of the bonding electrons remains with each molecular fragment.

Free radicals are generally electrically neutral and often extremely reactive. Their inevitable production in human body may be endogenous or exogenous as well. A peroxidative degradation takes place when a oxidant radical does react with a biomolecule. We are concerned with peroxidative degradation of PoliUnsaturated Fatty Acids (PUFA) in phospholipids, owing to the specific chemical species released as end-product, this process being named lipid peroxidation (LP).

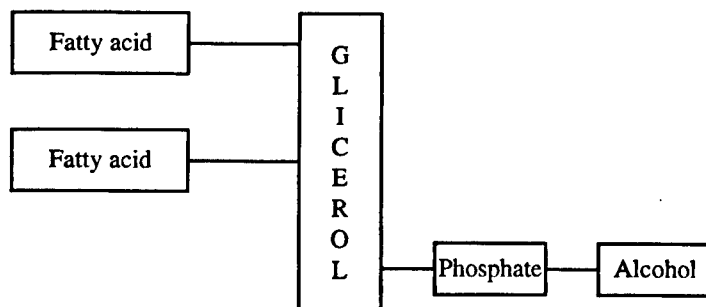


Fig. 8. General molecular structure of phospholipids

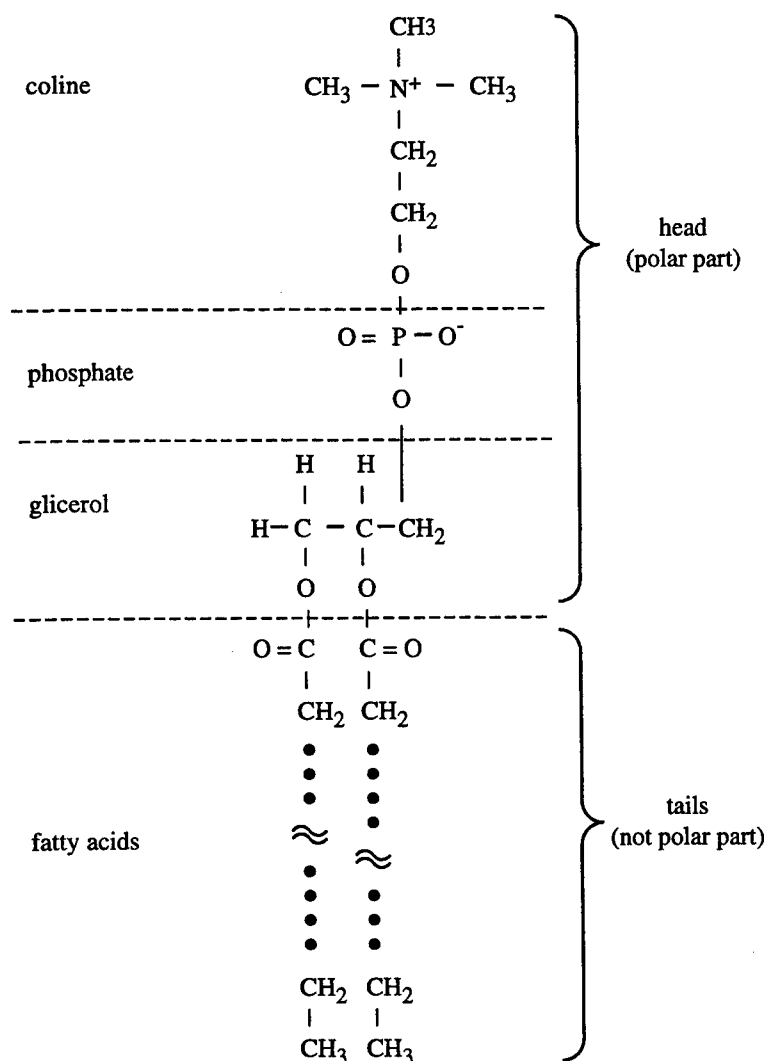


Fig. 9. Molecular structure of phosphatidilcoline (see Ref. 8)

Table II. Molecular structure of the more abundant fatty acids

Fatty acid	Molecular Structure
oleic acid	CH ₃ (CH ₂) ₇ CH=CH(CH ₂) ₇ COOH
linoleic acid	CH ₃ (CH ₂) ₄ CH=CHCH ₂ CH=CH(CH ₂) ₇ COOH
linolenic acid	CH ₃ CH ₂ CH=CHCH ₂ CH=CHCH ₂ CH=CH(CH ₂) ₇ COOH
arachidonic acid	CH ₃ (CH ₂) ₄ CH=CHCH ₂ CH=CHCH ₂ CH=CHCH ₂ CH=CH(CH ₂) ₃ COOH

Lipid peroxidation starts when an oxidant radical reacts with a PUFA. As consequence of this reaction the hydrogen atom nearest to one of the unsaturated bonds is abstracted from the hydrocarbon chain leaving a second generation reactive

radical. The oxidative process of radical formation may be repeated one or more times between adjacent species disrupting many biological macromolecules in a time as short as a microsecond. This process is catalized both by enzymes and transition metals and is a major cause of cell and biomembrane disruption in human organism.

3.3 Production of ethane and pentane.

The chain reaction may follow different pathways depending on the molecular composition of the chemical species surrounding the reaction site. Among them, the peroxidative pathways leading to the formation of alkanes have been well studied. In fig.10 a simplified scheme of the formation of alkanes by lipid peroxidation is reported, showing the formation of pentane (C_5H_{12}) through the peroxidative degradation of arachidonic acid. Starting with linolenic acid a similar set of chained reactions leads to the formation of ethane (C_2H_6).

The correlation between hydrocarbons production and lipid peroxidation was theoretically discussed in 1961 and it was experimentally verified in vitro in 1964. In 1974 the production of ethane due to lipid peroxidation in vivo was described for the first time. In the subsequent years it was experimentally proved that the peroxidation of ω -3 family of PUFAs (i.e. linolenic acid and its derivative) does end principally with generation of ethane and, by a similar process, the peroxidation of ω -6 family of PUFAs (i.e. linoleic acid and arachidonic acid) does end principally with generation of pentane. Today ethane and pentane are universally accepted as the best markers of in vivo LP.⁹⁻¹⁰

At body temperature these alkanes are volatile gases and not soluble in water because they are nonpolar molecules. After generation by LP they diffuse easily through the living tissue and enter the circulating blood and then they are convected to the lungs by the haematic flow and are expelled with the expired breath. A sample of expired breath can be collected and examined to determine the hydrocarbon concentration.

The process of peroxidative hydrocarbon release could be modelled, but a computer simulation is difficult to achieve because hydrocarbon production is not the only possibility as conclusion of a LP event and numerical value of branching ratios are not well known. On the other hand the significant experimental knowledge on alkanes generation by lipid peroxidation can be summarized through the following statements.

1. In the major part of in vitro processes 1 to 10 percent of LP events do end with hydrocarbon release.
2. Low amounts as small as 0.03% of overall ω -3 fatty acids peroxidation have been detected in vitro by monitoring the ethane evolution.
3. The hydrocarbon emission is reduced in vivo due to several metabolic factors. Nevertheless the expelled amounts are still measurable.
4. In rats, pentane as detected in vivo ranges around 0.2 millimoles/liter for one mole of peroxidated lipids.
5. In the man, numerical values are not well defined due to obvious difficulty in performing experimental study; anyway normal levels of alkanes emission are known. In healthy people normal values for ethane and pentane in the breath are 0.3-1.7 nanomol/liter and 0.1-4.9 nanomol/liter respectively.

3.4 Breath test.

The minimum of the above mentioned normal values in healthy people is equivalent to something like 1 ppb which is the smallest amount that must be well measurable in a breath specimen by any adopted analytical system to appreciate pathological changes in the lipid peroxidation extent.

Both ethane and pentane show many absorption lines in the infrared spectrum. To check the experimental feasibility of a TDL based breath alkanes study, we intend to perform experiments on ethane emission. An accurate selection of the spectral range is necessary in order to reduce the superposition with lines of other human breath components absorbing in the same region.

The ethane pure gas shows three absorption bands at approximately 825, 1475 and 2950 cm^{-1} .¹¹ Many intense lines are located in the band at 2950 cm^{-1} . By first study through the HITRAN database it appeared that the more intense ethane absorption lines are located near 2973 cm^{-1} . This small portion of the spectrum as calculated by HITRAN was reported in fig.11. Consequently we are performing a feasibility study of the high resolution IR spectroscopy ethane detection by a TDL emitting at around 3.4 μm .

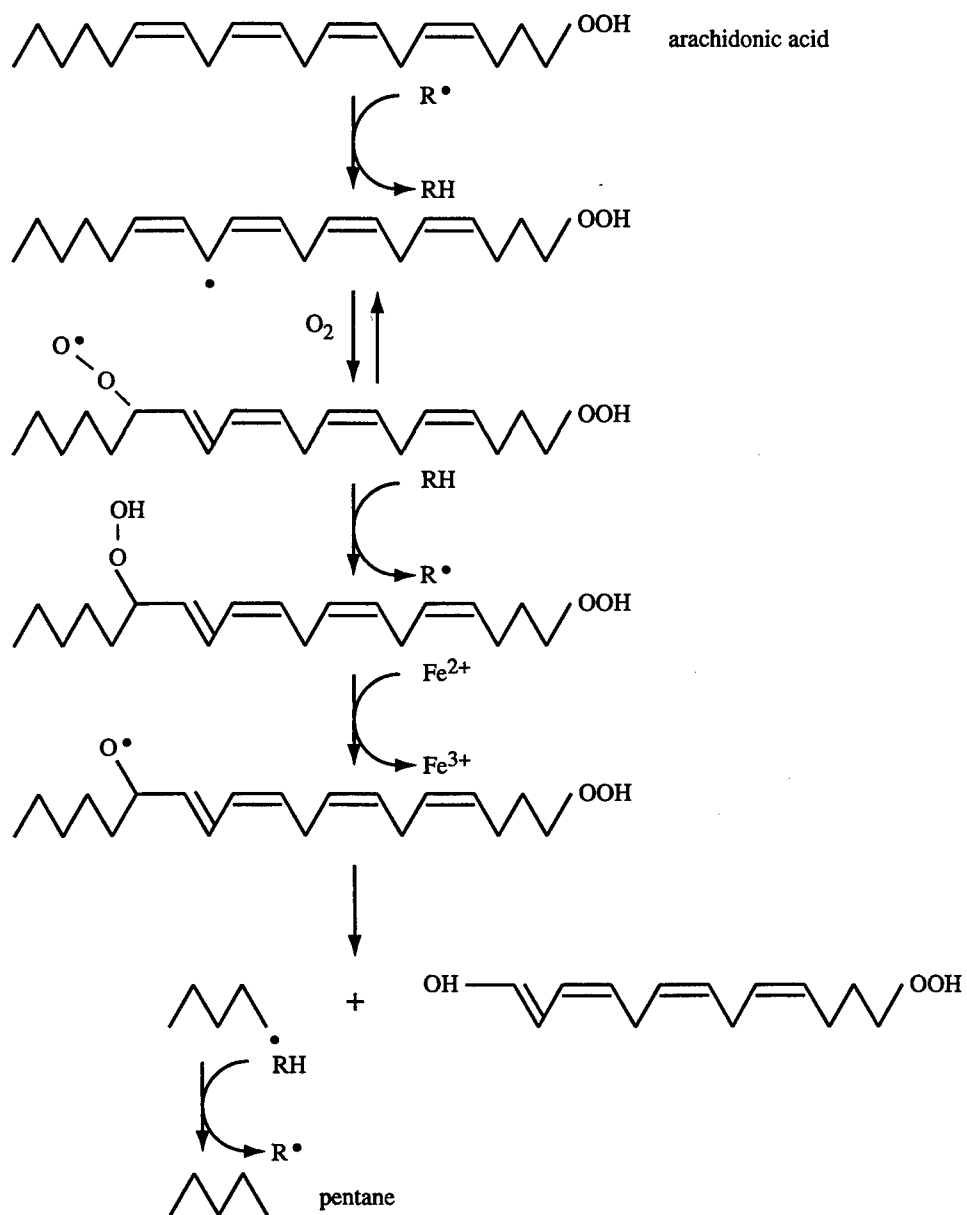


Fig. 10. A simplified scheme of the chemical conversion of arachidonic acid to pentane (see Ref. 9)

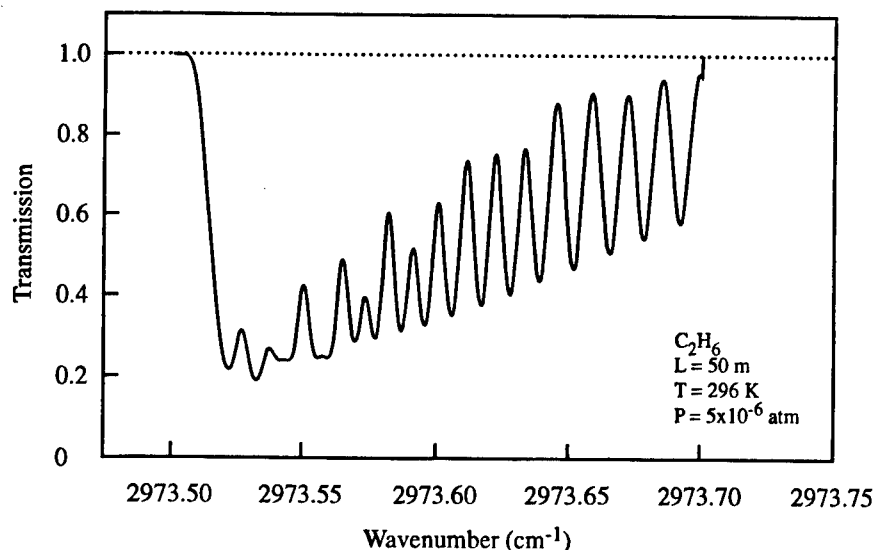


Fig. 11. A small portion of ethane absorption spectrum simulated by HITRAN-PC database

4. CONCLUSION

Specific hydrocarbons (ethane and pentane) are bred as end product of lipid peroxidation in vivo; they are expelled with the expired breath allowing a non invasive assessment of lipid peroxidation. Alkanes breath test is a promising non-invasive method for the detection and follow-up of lipid peroxidation involving diseases in clinical practice.

High resolution IR absorption spectroscopy has been applied in detecting trace gases in the atmosphere. TDL systems have been proved to be reliable to detect ppb of the trace substances. Trace gas analysis in the breath has been proved to be accurately performed by TDL based spectroscopy. Our experimental apparatus was applied successfully in monitoring expired methane and ammonia. Experiments on laser based ethane and pentane analysis in human breath have to be performed.

5. REFERENCES

1. W.Demtroder, Laser Spectroscopy, cap.6, Springer-Verlag, Berlin, 1982
2. HITRAN-PC 92, Copyright University of South Florida, 1992
3. P.Werle, "High Frequency Modulation Spectroscopy: A Sensitive Detection Technique for Atmospheric Pollutants", SPIE, vol.2092 Substance Detection Systems, 4-15, 1993
4. G.Baldacchini, A.Bellatreccia, L.Nencini, "Applicazioni e prospettive della spettroscopia molecolare con diodi laser accordabili", ENEA Report RT/TIB/89/29 (1989)
5. G.Baldacchini, A.Bellatreccia, F.D'Amato, P.K.Chakraborti, E.Righi, "Rivelazione di tracce di metano nell'atmosfera per scopi medici", ENEA Report RT/INN/91/18 (1991)
6. G.Baldacchini, F.D'Amato, G.Giubileo, S.Martellucci, "Tunable Diode Laser Detection of Small Traces of Gases for Medical Diagnostics", NATO ASI Series, Serie E: Applied Sciences, **325**, 185-195, 1996

7. U.Lachish, S.Rotter, E.Adler, U.El-Hananay, "Tunable Diode Laser Based Spectroscopic System for Ammonia Detection in Human Respiration", Rev.Sci.Instrum., **58**, 923-927, 1987
8. A.L.Lehninger, Biochemistry, cap.10, Worth Publisher, 1970
9. C.M.F.Kneepkens, G.Lepage, C.C.Roy, "The Potential of the Hydrocarbon Breath Test as a Measure of Lipid Peroxidation", Free Radic.Biol.Med. **17**, 127-160, 1994
10. C.S.Smith, "Correlations and Apparent Contradictions in Assessment of Oxidant Stress Status in vivo", Free Radic.Biol.Med., **10**, 217-224, 1991
11. C.D. Craver (Editor) *A Special Collection of Infrared Spectra*, Copyright 1983, The Coblentz Society, Inc. (USA) Catalog Card No. 83-70287

CO₂ laser ablation of biological tissue

Dan C. Dumitras, Doru C. A. Dutu, Consuela E. Matei

Department of Lasers, National Institute for Laser, Plasma and Radiation Physics,
P. O. Box MG - 36, Bucharest, Romania

ABSTRACT

This paper presents a comprehensive review of the CO₂ laser ablation of biological tissue. Based on energy balance for modelling laser ablation, the thermal relaxation time and the ablation threshold are determined. Laser ablation of biological tissue is related to the spatial coherence of laser beams, so that the propagation of laser beams, the beam quality and the focusability of laser beams are taken into consideration. To achieve the ablation threshold, the laser irradiance in the focal zone is computed as a function of laser parameters. The advantages of pulsed operation of the CO₂ laser for minimum residual thermal damage of the tissue are stressed. The strengths and the weaknesses of the CO₂ laser ablation are finally discussed.

Keywords: laser ablation, CO₂ laser, biological tissue, laser irradiance and radiant exposure, thermal damage

1. INTRODUCTION

Laser interaction with biological tissue has been a subject of ongoing research since the operation of the first laser in the early sixties. Of the various laser systems currently used in medical practice, the CO₂ laser has proved itself as one of the most efficient surgical instruments¹. The CO₂ laser has been used for many years in surgery, where laser induced destructive macroeffects are remarked. When a pulsed CO₂ laser is used, ablation (explosive evaporation) of the biotissue can be the decisive physical process, while for a standard surgical continuous wave (cw) CO₂ laser, the power density reached at the tissue stays below the threshold for tissue ablation. The necessary condition for laser assisted ablation of biotissue is to make the substance in the irradiated tissue volume go to an overheated metastable state within a time interval shorter than that required for heat to diffuse from this volume.

During the pulsed laser ablation of biological tissue, the following fundamental phenomena were experimentally observed: (1) the presence of an ablation threshold for the laser pulse fluence; (2) the formation of shock waves; (3) the gasdynamic sputtering of the ablation products with supersonic velocities; and (4) the dependence of the ablation efficiency and threshold fluence on the attenuation coefficient of the tissue². The ablation of tissue by pulsed laser radiation can be explained by the photochemical, photothermal or photomechanical mechanisms.

One of the most important problems in laser ablation is that of maximizing ablation rates, while simultaneously minimizing collateral damage, enhancing selectivity and improving precision of the interaction process. The ablation threshold plays an important role in characterization of tissue effects. Below threshold, there is heating of the tissue resulting in sequence denaturation of enzymes and losing of membranes (40 - 45°C), coagulation and necrosis (60°C), drying out (100°C), carbonization (150°C), and finally, pyrolysis and vaporization (above 300°C). In contrast to the cw CO₂ laser, the pulsed CO₂ laser vaporizes tissue water instantly, involving minimal thermal injuries. In this case, the heating is strong enough and is accompanied by a substantial pulsed pressure rise. Above ablation threshold, the exploding water vapor consumes thermal energy, suppressing heating of the surrounding tissue. So, the ablation threshold, depending on the laser fluence and the time of exposure, will determine whether the thermal energy will be transported to surrounding tissues or not.

In real experimental conditions, the ablation threshold can be surpassed by adjusting the laser parameters, such as power or energy, spot size, pulse duration, pulse repetition rate, and total delivery time. By focusing the laser beam, the irradiance may vary enormously, depending on the distance of the lens to the tissue. Also, the irradiance in the center of a laser beam may reach the ablation threshold, while the flanks stay below. In the following, we shall clarify all these aspects, and we shall establish the conditions when the ablation threshold is reached, resulting a charless crater in the tissue surface.

2. LASER ABLATION MODELLING

2.1 Energy balance

One widely used approach for modelling laser ablation uses energy balance³. In this model, the ablation rate is:

$$R = \rho A (F - F_{th}) / H \quad (1)$$

where R is the ablation rate expressed in mass ablated per pulse, ρ is the density of the target, A is the area irradiated by the laser, F is the delivered radiant exposure (fluence) per pulse, F_{th} is the threshold radiant exposure, and H is the heat of ablation (specific evaporation energy). Ross et al.⁴ have investigated the *in vitro* effects of a pulsed CO₂ laser on pig skin using pulsewidths of $\tau_p = (0.25 - 10)$ ms. Mass loss was measured with an analytical balance over a range of radiant exposures and pulse durations. The slope of the mass of pig skin removed per pulse vs. the incident radiant exposures varies between 3.0 and 2.4 $\mu\text{g} \cdot \text{cm}^2/\text{J}$, when the pulse duration is increased from 0.8 to 10 ms. Using Eq. (1), H and F_{th} can be derived. The ablation threshold increases from 5 J/cm² at $\tau_p = 0.8$ ms to 15.2 J/cm² at $\tau_p = 10$ ms, while the heat of ablation using the average of the calculated heats of ablation from mass loss experiments is $H_a = 3.4$ kJ/cm³.

The increase in ablation threshold at longer pulse durations is caused by thermal diffusion during the pulse. However, the heat of ablation did not change as a function of pulse duration since once the threshold was reached, the ablation front outpaced thermal diffusion.

2.2 Thermal relaxation time

The complex tissue optical properties can be predicted from the component contributions of cellular chromophores (absorption) and cellular structures (scattering). In the infrared spectrum, at the CO₂ laser wavelength ($\lambda = 10.6$ μm), the scattering coefficient is enough small and can be neglected.

The definition of the absorption coefficient α [cm⁻¹] is based on the transmission through a pathlength L in a medium:

$$T_a = \exp(-\alpha L), \quad \alpha L \ll 1 \quad (2)$$

and T_a is the probability that a photon will transmit through a pathlength L without any interaction with the medium. Absorption occurs due to coupling photon energy at a particular frequency with the energy of electronic or vibrational transitions. In the near-infrared and mid-infrared spectrum, the strong absorption is due to water. Jacques⁵ has summarized some of the major absorbers in biological tissues. At the CO₂ laser wavelength, he indicates $\alpha = (450 - 560)$ cm⁻¹ for skin with 75% water. The absorption coefficient is related to the optical penetration depth, δ [cm⁻¹], by:

$$\delta = 1 / \alpha \quad (3)$$

For the CO₂ laser wavelength and skin, δ is approximately 20 μm .

The absorption characteristics of biotissue leads to a spatially nonuniform distribution of heat released inside as a result of absorption of pulsed CO₂ laser radiation. Prahl⁶ has generated charts that allow to make rapid estimates of the spatial and temporal thermal distributions following laser irradiation for arbitrary pulse durations and absorption coefficients. In our case, the following three characteristic times are of importance:

- a) τ_p - the laser pulse duration;
- b) $\tau_s = \delta / v_s$ - the time it takes for sound to propagate with a velocity v_s beyond the optical penetration depth δ (thickness of the heated zone), i. e. the relaxation time of the pressure resulting from the pulsed local heating;
- c) $\tau_R = \delta^2 / 4k$ - the time it takes heat to propagate by diffusion beyond the optical penetration depth, i.e. the thermal relaxation time of pulsed heating; k is the thermal diffusivity. For skin, k has been estimated to be $1.3 \cdot 10^{-3}$ cm²/s, so that the thermal relaxation time is 600 - 950 μs .

2.3 Ablation threshold

An ablation threshold can be established in terms of the ablation and heat conduction velocities. The velocity of ablation, v_a , is simply:

$$v_a = \frac{I}{H_a} \quad (4)$$

where I is the local irradiance and H_a is the experimentally determined heat of ablation. For an usual irradiance of 10 kW/cm², the velocity of ablation is 3 cm/s.

The effective heat conduction velocity, v_c , is given by:

$$v_c = \frac{d}{t_d} \quad (5)$$

where d is the minimum depth of histologically identifiable thermal damage ($\sim 80 \mu\text{m}$) and t_d is the time required for heat conduction over this distance: $t_d = d^2/4k$ (12.3 ms). By introducing t_d in Eq. 5, the term for v_c reduces to: $v_c = 4k / d$, which has a value of 0.65 cm/s.

To assure minimal thermal damage, the velocity of ablation must exceed the heat conduction velocity. In other words, for any CO₂ laser that achieves $v_a \geq v_c$, minimal thermal damage will be observed. The threshold irradiance for achieving ablation with minimal thermal damage, I_{th} , is reached when $v_a = v_c$. This gives:

$$I_{th} = \left(\frac{d}{t_d} \right) H_a \quad (6)$$

Inserting the experimentally determined values for H_a , d and τ_d , we obtain: $I_{th} = 2.2 \text{ kW/cm}^2$. This value of the ablation threshold compares reasonably well with the values measured experimentally by Ross et al.⁴ for F_{th} ($I_{th} = 2F_{th} / \tau_p$).

We can explain the different aspects of the laser-produced craters in biotissues, when the irradiance varies over a large range. During high irradiance ablation ($>2.2 \text{ kW/cm}^2$), tissue is removed at a rate that is higher than the thermal diffusion rate, regardless of pulsewidth, and therefore residual thermal damage approaches a theoretical minimum of 50 μm . Usually, the thermal damage at the centers of craters is independent of pulse duration, because the irradiance is higher than the ablation threshold. At the crater edges where lower irradiances are effective (irradiances under the ablation threshold), experimental results showed that thermal damage increased with pulse duration.

The importance of the calculation of laser irradiance in the focal zone on both longitudinal and transversal directions and its dependence on laser parameters now becomes evident.

3. SPATIAL COHERENCE OF LASER BEAMS

3.1 Propagation of a gaussian beam

To understand the focusability of laser beams and hence the irradiance in the focal zone it will be useful to recall first the free-space propagation formulae for an ideal lowest-order or TEM₀₀ gaussian beam. The spot-size propagation formula for a gaussian beam is well known⁷ (the square of the beam diameters increases linearly with the square of the distance away from the waist):

$$w^2(z) = w_0^2 \left[1 + \left(z / z_R \right)^2 \right] \quad (7)$$

$$z_R = \frac{\pi w_0^2}{\lambda} \quad (8)$$

where w_0 is the beam waist, z is the propagation distance measured from the waist, z_R is the Rayleigh range and λ is the wavelength. $w(z)$ and w_0 are the radii of the laser spot (the beam diameter is the distance between the points where the intensity falls to $1/e^2$ of peak value). The Rayleigh range (the range over which the beam is considered to be collimated) is the propagation distance from the waist location in which the beam diverges to twice the area at its waist.

The beam contour of a gaussian beam as it propagates from its waist is a hyperbola, with asymptotes inclined at an angle θ (far-field, half-angle divergence, in radians):

$$\theta = \frac{\lambda}{\pi w_0} \quad (9)$$

This relation shows that there is a minimum possible product of waist diameter times divergence, corresponding to a diffraction-limited beam (uncertainty principle).

3.2 Beam quality

The laser beams often are not pure modes (gaussian beams), but mixtures of transverse modes, in a superposition of multiple-peaked profiles. Higher-order mode components produce a larger divergence than a single-mode beam.

To characterize multimode laser beams, the constant M^2 (coefficient of beam quality) was introduced⁸, defined as the product between beam's minimum diameter and divergence angle:

$$M^2 = \frac{\pi}{\lambda} w_{0R} \theta_R \quad (10)$$

where the index R stands for "real" beams. This constant is a measurable quantity describing beam propagation as well as beam quality (beam's mode content and focusability). For a gaussian beam, $M^2 = 1$; beams with larger constants are described as being "several times the diffraction limit". M^2 increases for modes of greater divergence or greater focal area. The inverse of M^2 constant is the propagation factor ($K = 1 / M^2$).

The spot-size propagation formula for an arbitrary real laser beam is:

$$w_R^2(z) = w_{0R}^2 \left[1 + \left(\frac{M^2 \lambda z}{\pi w_{0R}^2} \right)^2 \right] \quad (11)$$

Putting:

$$w_{0R} = M w_0 \quad (12)$$

there follows:

$$w_R^2(z) = M^2 w^2(z) \quad (13)$$

and

$$\theta_R = \frac{M^2 \lambda}{\pi w_{0R}} = M \theta \quad (14)$$

These relations show that a high order mode that has a waist radius M times larger than the waist of the fundamental mode of the same resonator, will have a beam M times larger everywhere.

3.3 Focusability of laser beams

Laser ablation of biological tissue requires a minimum spot-size. There are a number of factors that affect the spot-size of focused beams, the most important being the laser mode (M^2), diffraction and spherical aberration.

Diffraction is a natural and inescapable result of the wave nature of light. It causes light beams to spread transversely as they propagate. The spot size (radius) due to diffraction, w_{0D} , is given by the following formula:

$$w_{0D} = \frac{2\lambda f}{\pi D} \quad (15)$$

where f is the lens focal length and D is the beam diameter at the lens (at the $1/e^2$ points). The spot size due to diffraction increases linearly with focal length, but is inversely proportional to beam diameter. Thus, the spot size decreases due to lower diffraction as the input laser beam diameter increases for a given lens or as the focal length decreases for a given laser beam diameter.

Spherical aberration causes rays impinging near the edge of the lens to cross the optical axis closer to the lens than those going through the center of the lens. It has the effect of increasing spot size. The spot size (radius) due to spherical aberration, w_{0S} , is:

$$w_{0S} = \frac{aD^3}{2f^2} \quad (16)$$

where a is a function of the index of refraction. For a ZnSe plano-convex lens which focuses a CO_2 laser beam ($\lambda = 10.6\mu\text{m}$), a is 0.0286, while for a meniscus, a is 0.0187.

The spot size radius due to diffraction and spherical aberration is:

$$w_0 = w_{0D} + w_{0S} \quad (17)$$

The minimum spot-size for a given lens is obtained by balancing the increase with f/D of the spot-size due to diffraction and its decrease with f/D due to spherical aberration. For a plano-convex lens with $f = 127 \text{ mm}$ (5") and a CO_2 laser beam with $D = 7 \text{ mm}$, $w_0 = 122 \mu\text{m}$.

For a lens with fixed focal length, the optimum input beam diameter is:

$$D_{\text{opt}} = \left(\frac{4\lambda M^2 f^3}{3\pi a} \right)^{1/4} \quad (18)$$

In this case,

$$w_{0\text{opt}} = w_0(D_{\text{opt}}) = \frac{8\lambda f}{3\pi} \left(\frac{3\pi a}{4\lambda f^3} \right)^{1/4} \quad (19)$$

For the same plano-convex lens with $f = 127 \text{ mm}$, we get an optimum input beam diameter d_{opt} of 9.8 mm, which provides a $191.8 \mu\text{m}$ focal spot diameter ($2w_{0\text{opt}}$). If the input beam diameter obtained from this calculation does not closely match the existing beam diameter in the system, then we can expand or contract the laser beam to this size.

Conversely, when lens input beam diameter is fixed, the optimum focus length can be determined:

$$f_{\text{opt}} = \left(\frac{\pi a D^4}{2 \lambda M^2} \right)^{1/3} \quad (20)$$

For $D = 7 \text{ mm}$, f_{opt} is 21.6 mm.

As can be seen from the preceding discussion, there is a limit on the focal spot size which can be achieved when either focal length or input beam diameter is imposed, which is the usual case in laser surgical applications. At any rate, one can calculate and choose the right focusing lens to obtain a minimum focal spot diameter and consequently, a higher irradiance.

4. LASER IRRADIANCE IN THE FOCAL ZONE

4.1 Irradiance, brightness and radiant exposure

The irradiance (sometimes called intensity) of a gaussian beam that propagates along the z axis is given by:

$$I(x, y, z) = I_0 \exp \left[-2(x^2 + y^2) / w^2(z) \right] \quad (21)$$

where I_0 is the maximum irradiance and $w(z)$ is given by Eq. (7) or (11). The integral of $I(x, y)$ over all area is the power in the beam. At beam waist ($z = 0$), we have:

$$P = \frac{\pi w_0^2}{2} I_0 \quad (22)$$

Therefore,

$$I_0 = \frac{2P}{A} \quad (23)$$

where $A = \pi w_0^2$ is the beam area.

For a real beam, w_0 is replaced by w_{OR} and the irradiance is inverse proportional to M^2 .

Brightness is defined as the ratio between the intensity and the solid angle:

$$S = \frac{I}{\Omega} \quad \left[W / (m^2 \cdot sr) \right] \quad (24)$$

where $\Omega = \lambda^2 / (2w_0)^2$.

Radiant exposure (or laser fluence) is the product of laser power times pulse duration over beam area:

$$F = \frac{P \tau_p}{A} \quad (25)$$

Radiant exposure is related to maximum irradiance simply by

$$F = \frac{I_0 \tau_p}{2} \quad (26)$$

4.2 Distribution of the Irradiance

In the following, we shall discuss the longitudinal and transversal distribution of the irradiance in the focusing region, using Eq. 21 in one transverse coordinate (x). One can see that the irradiance depends on laser power, beam area and beam divergence. The last two parameters also depend on the coefficient of beam quality.

The transversal distribution as a function of z axis near the waist location, for lines of constant irradiances and the spot-size propagation of the gaussian beam (dotted line) are presented in Fig. 1. We have used the parameters of our surgical CO₂ laser unit BILAS-10^{9, 10}, namely $P = 10$ W, $M^2 = 1$, $D = 7$ mm and a focusing lens of 127 mm. There results: $w_0 = 0.122$ mm, $A = 0.046$ mm² and $I_0 = 42.8$ kW/cm². Responsible for laser ablation is not the Rayleigh range (4.4 mm), nor the gaussian beam distribution, but an area with a constant beam irradiance. The contour of the beam where the power density exceeds the ablation threshold ($I_{th} = 2.2$ kW/cm²) is defined as the "ablating beam"¹¹. This means that the spot-size of the laser beam near the focus is not representative for the actual area of the ablated tissue. The ablating beam area will be larger if the power of the laser pulse is higher. The shape of this beam depends on laser parameters.

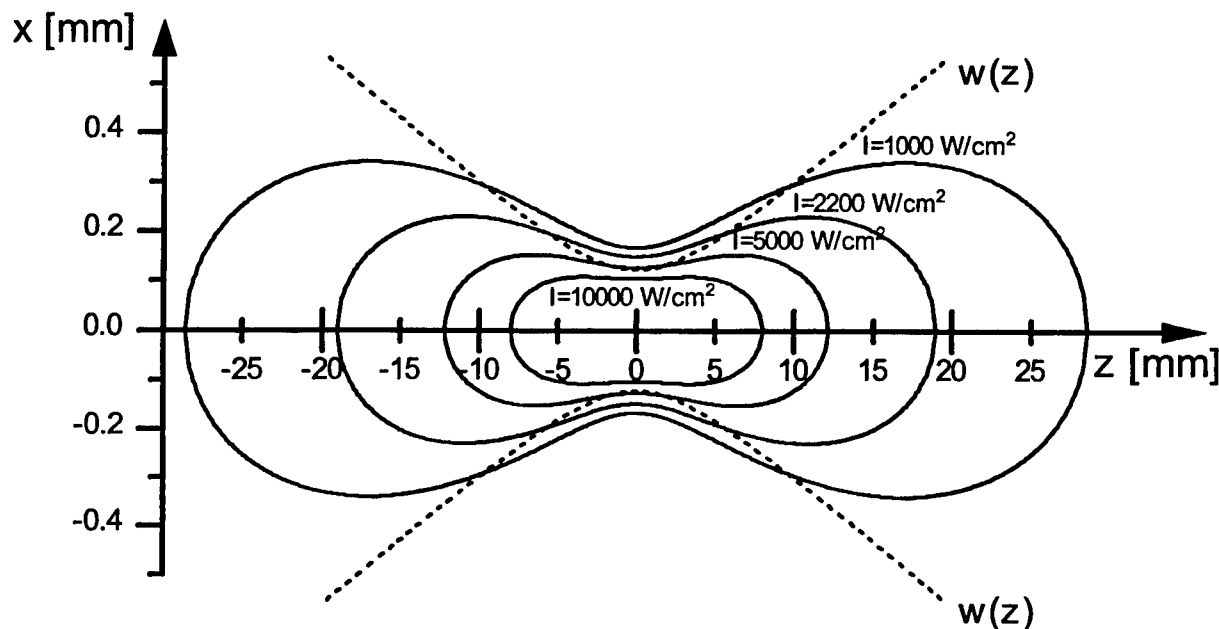


Fig. 1 The transversal distribution of the laser beam near the focus, for lines of constant irradiances

Another two features can be remarked from this representation. First, the transversal dimension of the ablating beam is much smaller than the axial one near the waist location (0.4 mm compared to 38 mm in the above case). This means that surgeons have the possibility to adjust the distance between the handpiece of the CO₂ laser surgical instrument and the tissue in a range which is not very critical. Second, the ablating beam can be larger than the theoretical shape of the gaussian beam. In contrast to the gaussian beam shape, the ablating beam depends on laser power. This is evident from Fig. 2, which is a close-up picture of Fig. 1 near the focus, for different power levels.

Another interesting characteristic is the fact that the maximum extension of the ablation beam in the transversal direction is not at the waist location ($x_{z=0}$), but at an axial distance of $\pm (10 - 20)$ mm (x_{max}), depending on laser power. This situation is depicted in Fig. 3. If the surgeon will use a defocused beam, he will obtain a maximum ablated area per pulse.

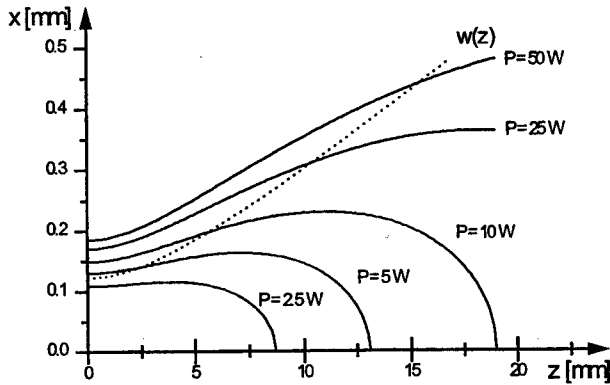


Fig. 2 The ablating beam for different laser power levels compared to gaussian beam (dotted line) near the focus

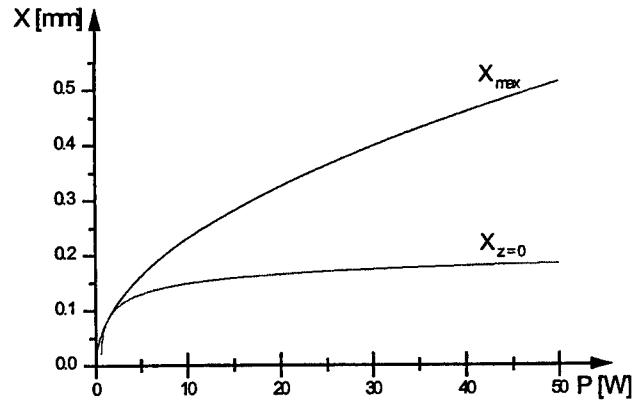


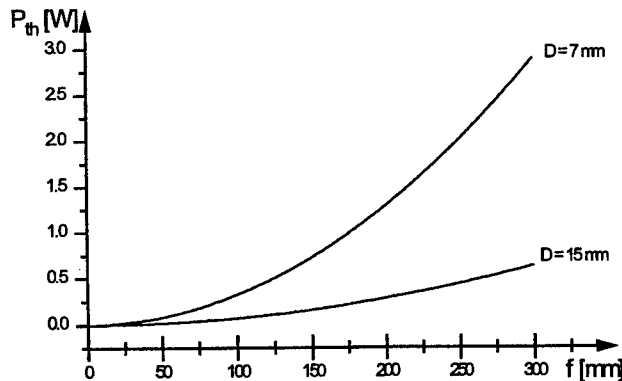
Fig. 3 The transversal dimensions of the ablating beam as a function of laser power, at the waist location ($x_{z=0}$) and at its maximum (x_{max})

Nevertheless, one must be careful of the following consequence. If we have, for example, a laser power of 10 W and we are working with a defocused beam at $z = 15$ mm, three regions can be discriminated in Fig. 2: a) a region between $x = 0$ and $x = 0.2$ mm where there is the ablating beam (full ablating beam region); b) a region between $x = 0.2$ mm and $x = 0.43$ mm, that is between the ablating beam and the gaussian beam, where the ablation threshold is not reached and the gaussian beam will induce carbonization; c) a region with $x > 0.43$ mm where no effect is encountered. From the point of view of the residual thermal damage of the tissue, this situation is disadvantageous. At the beam focus ($z = 0$), the ablating beam is usually higher than the gaussian spot in the waist and scarring will be avoided.

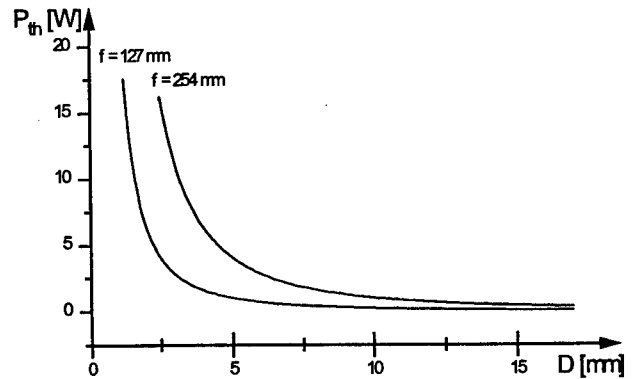
4.3 Dependence on laser parameters

Focusing handpieces used for beam delivery in CO₂ laser surgical systems allow to modify the irradiance in a large range, depending on the distance to the tissue (z near focus) and the beam waist at the focus (depending on the lens focal length, f , and beam diameter at the lens, D). Alternatively, collimated handpieces (with a telescope lens system) can control the beam divergence, θ , and the beam diameter, D , but offer less flexibility in changing tissue effects (the residual thermal damage is usually higher).

The power threshold is simply related to the irradiance threshold by Eq. (22). We must recall here that laser power in this case is the peak power of a pulsed CO₂ laser. The dependence of power threshold on lens focusing length and on beam diameter are presented in Fig. 4. By changing the beam diameter or lens focal length, it is possible to reach the power threshold easily.



(a)



(b)

Fig. 4 The power threshold dependence on lens focusing length (Fig. 4a) and on beam diameter (Fig. 4b)

There are several laser systems that produce pulses useful for ablation. The so-called super-pulsed systems generate pulses with a steep rise and a slower decay and a length of 50 μ s to several ms. The ultra-pulsed systems produce pulses with peak-power of 200-800 W and duration of 1 μ s to 1 ms, which are block shaped. Another approach is to use a computer-assisted laser scanner¹². In this case, the focused CO₂ laser beam is swept over a tissue area from several mm² to several cm², with a dwell time on each tissue point of less than 1 ms (smaller than the thermal relaxation time). The key for homogeneous vaporization in this case is to keep a constant tangential linear velocity.

We have calculated the laser power dependence of z_{\max} (maximum axial distance of the ablating beam) and x_{\max} (maximum transversal spreading of the ablating beam), for different input beam diameters and lens focal lengths. The results are presented in Fig. 5.

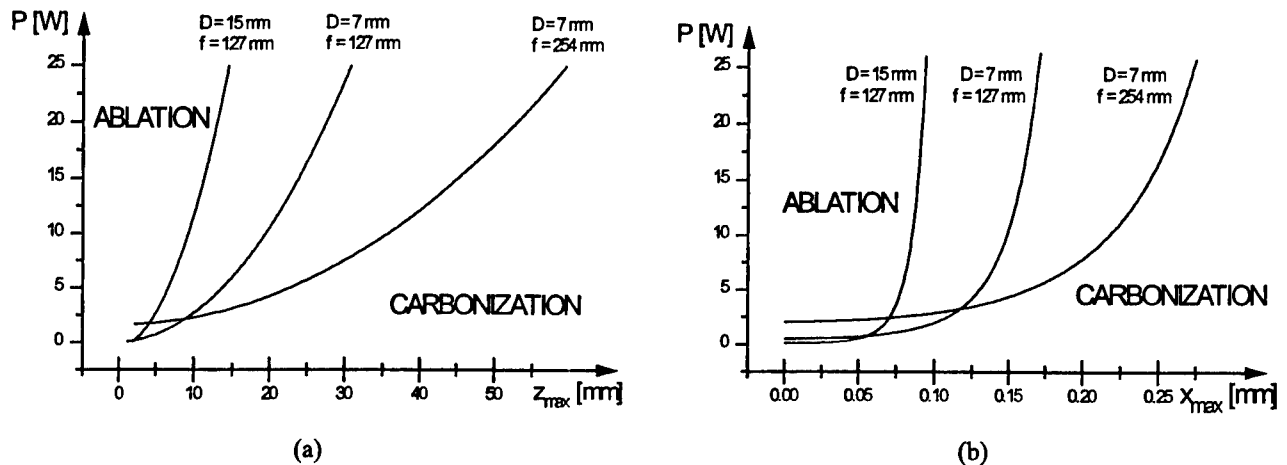


Fig. 5 The laser power necessary to reach the ablation threshold as a function of z_{\max} (Fig. 5a) and x_{\max} (Fig. 5b)

One can distinguish two important zones: the ablation zone (at the left of the curves), where the irradiance is higher than the ablation threshold and the carbonization zone, where the irradiance is below the ablation threshold. The power necessary to reach the threshold is minimum when the beam waist is located at the surface of the tissue ($z=0$). If the surgeon works with a defocused beam, the ablation threshold can be reached even at a distance of 30-50 mm from the beam waist, depending on power and lens focal length. Also, by choosing a set of given f and D parameters, one can modify the diameter of the crater burned in the tissue with an ablating beam by changing the beam power.

Sometimes, it is easier to use the radiant exposure or laser fluence (Eq. 25 and 26), instead of laser power or irradiance. The threshold radiant exposure function on laser pulsewidth is given in Fig. 6.

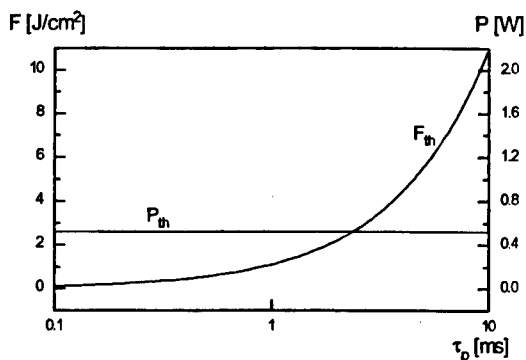


Fig. 6 The dependence of the threshold fluence and the power threshold on laser pulsewidth ($f = 127$ mm, $D=7$ mm)

Pulses with a duration of 0.1 to 10 ms are characteristic for the laser ablation of biotissue. As a comparison, the power threshold is also depicted and it does not depend on laser pulsewidth. Experimentally, a radiant exposure threshold of 3 J/cm² was measured¹¹. Here is an example. A commercial ultra-pulsed CO₂ laser system (Coherent 5000) produces pulses with a peak power of 800 W and a rise time of several microseconds. For a pulse duration of 1 ms, an energy of 250 mJ can be reached. If the beam is focused with a 119 mm handpiece at a preset spot-size of 1 mm, then the radiant exposure is near 8 J/cm², which is over the ablation threshold. When the collimated handpiece with a particular diameter of 3 mm is used, the radiant exposure is under the threshold (0.9 J/cm²) and residual thermal effects are expected.

The collimated handpiece is sometimes advantageous, because it allows the surgeon to change the distance from the target tissue without varying the spot-size or power density.

5. DISCUSSION

The pulsed CO₂ laser can lower or eliminate the risk of burning and therefore scarring, and has been shown to cause minimal thermal injury, because the high energy pulses produce laser ablation. This is accomplished by removing a specific amount (depth) of about 100 - 150 μm of tissue on each pass as determined by the irradiance on the surface. As we have already shown, the irradiance can be modified over a wide range by the delivery mode of the particular laser and handpiece. To control all these parameters precisely, the surgeon must be intensive and properly trained.

Ross et al.⁴ have measured the depth of residual thermal damage at edge of the ablation crater through histology. By varying the CO₂ laser pulsewidth between 0.25 and 10 ms and the radiant exposure between 7.5 and 14 J/cm², they measured a depth of residual thermal damage between 83 and 124 μm (a smaller range if the radiant exposure is higher). Irrespective of radiant exposure or pulsewidth, the depth of the residual thermal damage were equal at the centers of the craters. The edges showed significantly increased thermal damage for pulsewidths longer than 1 ms. It is thus clinically advantageous to restrict laser pulsewidth to less than the thermal relaxation time (τ_R), so that thermal damage is consistent for both the ablation center and the crater edges.

For pulses longer than τ_R , a larger zone of thermal damage is observed because significant thermal diffusion occurs during the pulse. Consequently, the efficiency of ablation is not controlled by the total energy deposited, but rather by the energy deposited per unit time, i.e., the power¹³. In order to predict the width of the zone of thermally altered tissue, one must always specify the particular target tissue and its thermodynamic properties. For example, the zone of thermal damage for aorta and myocardium is less than that for skin and cornea¹³ (the major constituent for skin and cornea is collagen, while for aorta and myocardium the major constituents are elastin and muscle, respectively; the denaturation temperatures of elastin and muscle have been measured to be 90°C and > 90°C, respectively, compared to 65°C for collagen).

Thermal damage produced by continuous wave CO₂ laser ablation of tissue was measured to be thinner than 100 μm by using single laser pulses¹⁴. Multiple pulses can lead to increased damage. The damage-zone thickness was approximately constant around the periphery of the cut, consistent with a model of thermal damage in which a liquid layer, produced by laser heating, stores heat, and displaced to the sides of the cut by radial pressure gradients, acts as a thermal reservoir which mediates damage.

In practice, the pulsed CO₂ laser uses pulse duration from 0.5-1 ms and radiant exposures from 3.5-7.1 J/cm². The ablation threshold could be easily determined just by listening to the sound (a very discrete snapping) coming from the tissue (explosive evaporation). Usually only 2-3 passes of the laser beam are used to eliminate a defect (e.g. a wrinkle). Besides ablation, another potential mechanism is the contraction of irradiated areas (desiccation and collagen shrinkage).

We can now discuss the strengths and the weaknesses of the CO₂ laser ablation. Where there is ablation, energy can be deposited in a small area of tissue with minimal scarring due to heat conduction to the surrounding tissue. The pulse duration is not critical in this case, since there is a rapid temperature drop just below the moving ablation front. Without ablation, the temperature profile under the tissue decays more slowly and can extend unacceptably deep into the adjacent structures, resulting undesired charring that leads to scarring.

Layer by layer peeling of the tissue can be achieved by laser ablation without leaving extensive thermal necrosis and resultant scarring with profound pigmentary changes. Another benefit of CO₂ laser-assisted surgery is less bleeding during and after surgery, because small blood vessels are sealed, resulting shorter surgical time. Post-operative crusting may also be minimal or non-existent, improving post-operative appearance. The expense of pulsed CO₂ laser techniques appears to be the main drawback.

In conclusion, we have shown that irradiance can be used as an independent parameter in predicting the effects of pulsed CO₂ lasers and in determination of the ablation threshold. Thanks to the development of safer and more effective laser instruments, tools and techniques, a revival of CO₂ laser surgery is underway.

6. REFERENCES

1. D. C. Dumitras and D. C. A. Dutu, "Surgical properties and applications of sealed-off CO₂ lasers", *NATO - A.S.I. Series E: Applied Sciences*, Vol. 325, pp. 231-239, 1996.
2. V. S. Letokhov, "Some future trends of laser biomedicine", *NATO-A.S.I. Series E: Applied Sciences*, Vol. 325, pp. 3-20, 1996.
3. J. Walsh and T. Deutsch, "Pulsed CO₂ laser ablation: Measurement of the ablation rate", *Lasers Surg. Med.*, Vol. 8, pp. 264-275, 1988.
4. E. Victor Ross, Y. Domankevitz, M. Skrobal and R. Rox Anderson, "Effects of CO₂ laser pulse duration in ablation and residual thermal damage: Implications for skin resurfacing", *Lasers Surg. Med.*, Vol. 19, pp. 123-129, 1996.
5. S. L. Jacques, "Modelling light propagation in tissues", *NATO - A.S.I. Series E: Applied Sciences*, Vol. 325, pp. 21-32, 1996.
6. S. A. Prahl, "Charts to rapidly estimate temperature following laser irradiation", *Proc. SPIE 2391*, pp. 499-511, 1995.
7. D. C. Dumitras, "Gas Lasers", Romanian Academy Publishing House, Bucharest, 1982.
8. A. E. Siegman, "New developments in laser resonators", *Proc. SPIE 1224*, pp. 2-14, 1990.
9. D. C. A. Dutu, D. C. Dumitras and L. Danaila, "The microsurgical CO₂ laser scalpel BILAS-10 and its applications in neurosurgery", *Rev. Roum. Phys.*, Vol.30, pp. 863-876, 1985.
10. V. G. Artjushenko, L. Danaila, E. M. Dianov, D. C. Dumitras, D. C. Dutu, V. I. Konov, S. M. Nikiforov, A. M. Prokhorov, M. M. Sargin, I. Ursu and S. Usov, "Surgical CO₂ laser units with specialized beam delivery systems", *Proc. SPIE 1066*, pp. 242-251, 1989.
11. R. M. Verdaasdonk, C. F. P. van Swol and J. Coates, "Characterization of handpieces to control tissue ablation with pulsed CO₂ laser", *Proc. SPIE 2391*, pp. 358-365, 1995.
12. D. C. A. Dutu, D. C. Dumitras and S. Ghetie, "Computer assisted CO₂ laser scanning system for surgical techniques", *Proc. SPIE 2774*, pp. 581-589, 1996.
13. J. T. Walsh, T. J. Flotte, R. Rox Anderson and T. F. Dentsch, "Pulsed CO₂ laser tissue ablation: Effect of tissue type and pulse duration on thermal damage", *Lasers Surg. Med.*, Vol. 8, pp. 108-118, 1988.
14. K. T. Schomacker, J. T. Walsh, T. J. Flotte and T. F. Deutsch, "Thermal damage produced by high-irradiance continuous wave CO₂ laser cutting of tissue", *Lasers Surg. Med.*, Vol. 10, pp. 74-84, 1990.

Laser method for corneal structure investigation

M.L. Pascu, B. Carstocea*, G. Popescu, Luiza Gafencu*,
S. Apostol*, N. Moise, Miruna Roman, C.M. Ticos

National Institute for Lasers, Plasma and Radiation Physics, Bucharest, Romania

* Central Military Hospital, Clinic of Ophthalmology, Bucharest

ABSTRACT

This paper reports a laser method for corneal structure investigation which allows to obtain images of corneal layers as well as information about dimensions of the endothelium and basal epithelium cells. The method's principle is based on the laser radiation reflection at the interface between ocular media having different refractive indices. So, the laser incident beam on the cornea is multiply reflected and refracted within it, since the cornea is a superposition of several transparent layers with different refractive indices. If observed on a screen, the radiation reflected by a certain corneal layer forms on it the image of corneal cell structure. Because of cornea curvature, the reflected beam which contains information about corneal structure- becomes strongly divergent; therefore the experimental set-up forms the cell images big enough to be seen directly by eye.

There were used both a HeNe (632.8 nm) and a Ar⁺ (488.514 nm) lasers at a power level less than 0.1 mW. The reflected beam, strongly divergent because of the corneal curvature of the rabbit eye, allows to obtain the corneal cell images on a screen mounted at a variable distance with respect to the eye. The observed images were recorded either photographically or using a video-camera.

The reflection corresponding to epithelium and endothelium leads to a superposition of images originated in these two corneal layers. In the central zones of the images, the epithelial cells prevail, showing a less regular structure. Towards the peripheral zone of the image, the endothelial cells replace the epithelial ones, but the intracellular membrane may be seen less intense.

Using a model of image formation which takes into account the optical phenomena appearing within the cornea, we have calculated the magnification factor of the system, and finally, the typical values of 35 μ m for endothelial cell dimensions were obtained.

The great advantage of this method for corneal structural study is, besides its simplicity, the capacity to provide images from a large surface of a corneal layer (limited only by laser beam cross section), without asking an electronic reconstruction of these images.

Keywords: laser, cornea, epithelium, endothelium.

1. INTRODUCTION

This paper reports a laser method for corneal structure investigation which allows to obtain images of corneal layers as well as information about dimensions of the endothelium and basal epithelium cells.

The endothelium is the most profound corneal layer; it is in direct contact with the aqueous humour and represents the most important component to maintain corneal transparency. At the other surface (towards the exterior of the eye) it is limited by Descemet membrane. The endothelium is a monolayer with a refractive index of 1.376 which for an young adult contains about 500,000 flat, regular, hexagonal cells 6 μ m high and 18-20 μ m long [1]; at the peripheral zone, the cells become progressively irregular.

From the point of view of the clinical medical practice, the study of the endothelium has a great importance since it is a cellular puzzle of hexagonal cells without replication power, so that with age a gradual diminishing of the cell number is observed, with implications on eye health state; an image of this layer allows to obtain information about the shape of cells and their density.

The principle of method is based on the laser radiation reflection at the interface between ocular media having different refractive indexes. So, the laser incident beam on the cornea is multiply reflected and refracted within it, since the cornea is a superposition of several transparent layers with different refractive indexes. If observed on a screen, the radiation reflected by a certain corneal layer forms on it the image of corneal cell structure. Because of cornea curvature, the reflected beam -which contains information about corneal structure- becomes strongly divergent; therefore the experimental set-up forms the cell images big enough to be seen directly by eye.

Using a model of image formation which takes into account the optical phenomena appearing within the cornea, we have calculated the magnification factor of the system (the diameter of image cell reported to that of real cell) as a function of incident beam divergence. Thus, measuring the diameter of an image cell, it can be deduced with a good approximation the diameter of the corresponding real cell.

2. EXPERIMENTAL SET-UP

The experimental arrangement used to obtain the images is shown in Fig. 1.

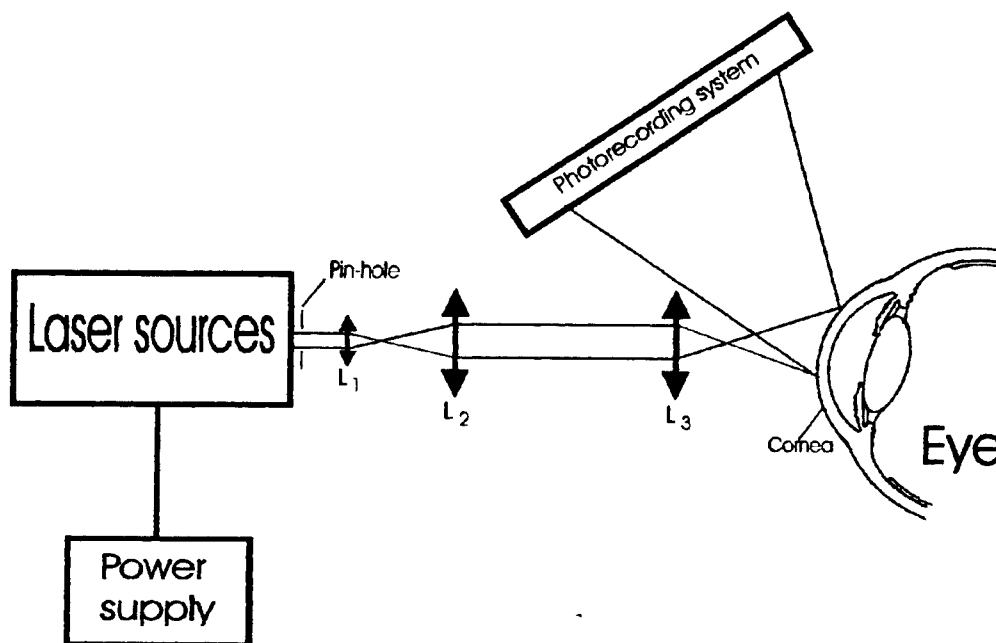


Fig. 1 Experimental set-up

A HeNe laser (632.8 nm, cw) was the first light source utilised; the laser worked on fundamental mode TEM_{00} and the radiation was attenuated until the beam power was less than 0.05 mW, assuring a non-invasive eye exposure. A diaphragm of maximum diameter 2 mm was mounted at the laser output to allow working with gaussian beams, since the experiments have shown that the intensity distribution within a cross section of the laser beam has a significant influence on the obtained image contrast.

The lens system L_1 / L_2 made the HeNe laser beam parallel. For further divergence variation, a set of convergent lenses L_3 with focal distances ranging respectively from 4 mm to 150 mm was used; L_3 was mounted to allow placing the focal spot in front of the cornea in order to obtain a laser beam maximum divergence of 0.4 rad.

The reflected beam, strongly divergent because of the corneal curvature, allowed to obtain the corneal cells images on a screen mounted at a variable distance with respect to the eye. The arrangement made possible adjusting the distance cornea-screen to obtain the best image quality. The studies were performed on rabbit eye in vivo, anaesthetising the rabbit in accordance with the standard procedure used in such experiments. The observed images were recorded either photographically or using a video-camera [2].

Another light source introduced in the experimental arrangement was an Ar^+ laser from which the 514 nm (green) radiation and 495 nm-514 nm (blue-green) radiation were used at power levels lower than 0.05 mW. The images obtained in this case exhibited, in average, a better contrast than the pictures obtained with the HeNe laser beam.

3. THEORETICAL APPROACH

The reported measurements and the obtained images are based on the reflection of the laser radiation at the interfaces between ocular media with different refractive indexes.

The laser beam incident on the cornea is multiply reflected and refracted within the cornea; this may be considered, in general terms, as a sandwich of several transparent layers with different refractive indexes. The radiation reflected by a certain corneal layer forms on the screen the image of its cell structure. Because of the cornea's curvature (for the rabbit eye, the measured radius of a vertical section through the cornea, at epithelial level is 8.08 mm and the same for the horizontal section is 8.36 mm) the reflected beams which contain information about corneal structure become strongly divergent.

The magnification depends on the depth the light is reflected from and the divergence of the incident beam. It is known that the reflection coefficient corresponding to a reflection from an interface between two media of refractive indexes n_1 and n_2 , respectively, is:

$$r = \left(\frac{n_2 - n_1}{n_2 + n_1} \right)^2 \quad (1)$$

Thus, the greater the difference between the two indexes of refraction, the higher laser beam intensity will be reflected.

For in vivo cornea, the images of greatest interest we obtained originated from lachrymal film-epithelium and endothelium-aqueous humour interfaces. Thus, the best images we obtained were those of epithelium and endothelium.

In order to find a theoretical formula for the optical magnification (the diameter of an image cell to the real cell diameter) we considered the cornea as an homogeneous spherical shell with concentric inner and outer surfaces which is a good enough approximation if one considers only the corneal central region.

The optical path of the laser radiation within the experiment is shown in Fig. 2 where the outer surface has the curvature radius R and the inner surface the radius $r=R-e$ (e is the cornea thickness). In Fig. 2, one considers a light ray incident on the corneal surface and its optical path within the cornea, showing only the ray obtained after the reflection on the inner corneal surface; O is the point in which the incident ray intersects the eye optical axis and, in the same time, the origin of a rectangular co-ordinate system XOY (the eye optical axis is the abscissa of the system); C is the curvature centre of both inner and outer corneal surfaces.

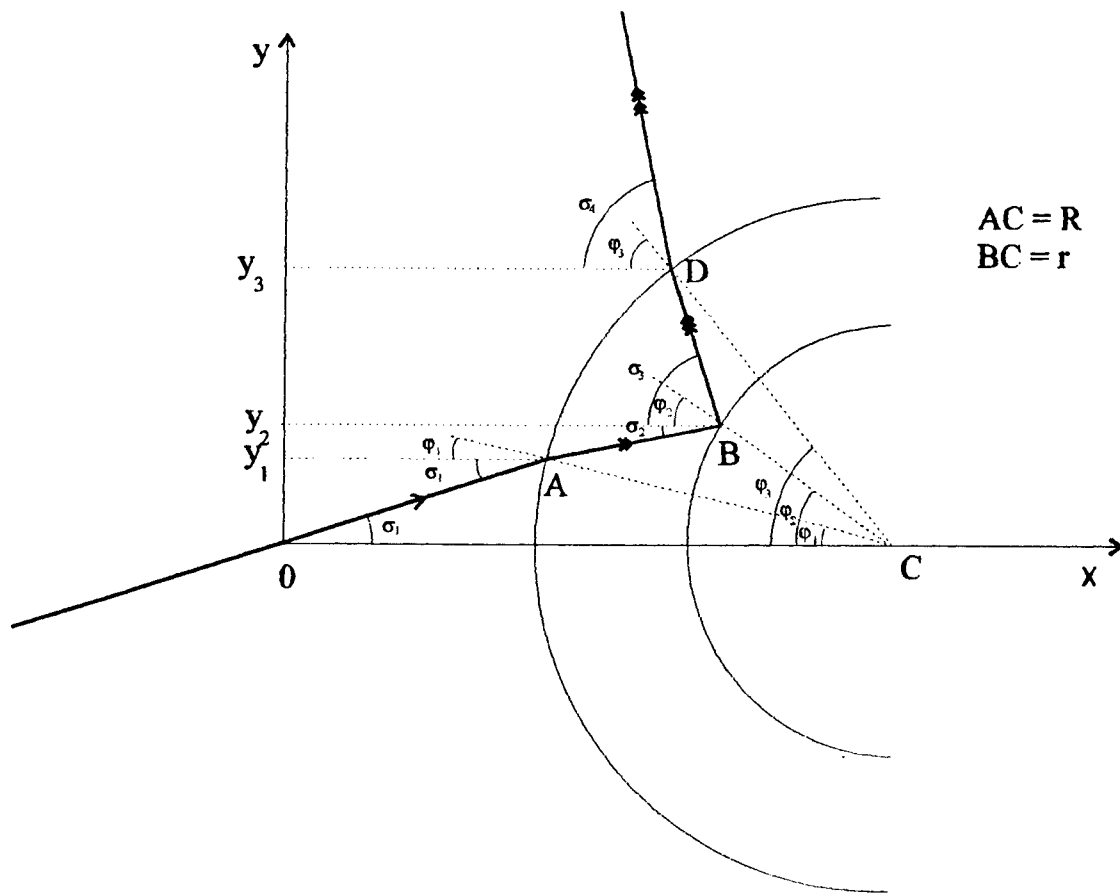


Fig. 2 Optical scheme for image formation

The points where the incident ray intersects the two surfaces are noted (Fig. 2) A, B and D; the angles are noted σ_k , $k=1..4$ for the angles between the rays and optical axis, i_j , $j=1..5$ for angles between rays and the normals at the surfaces and φ_i , $i=1..3$ for the angles between the surfaces normals (in the incident points) and optical axis. The values y_k , $k=1..3$ are the ordinates of the incident points.

Our first aim is to determine -within the approximation of small angles- a relationship between the tilt angle of the incident ray (σ_1 , Fig. 2) and that of the emergent ray (σ_4). From the refraction law applied in point A, B and D it can be deduced:

$$\sigma_4 = \sigma_1 + 2 \cdot n \cdot \varphi_2 - (n-1) \cdot (\varphi_1 + \varphi_3) \quad (2)$$

Within the small angles approximation and assuming $e \ll R$ and $e/R \approx 1$, the relation becomes after differentiating:

$$d\sigma_4 = d\sigma_1 + 2 \cdot d\varphi_2 \quad (3)$$

Integrating equation (3) over an interval corresponding to a single cell, on the inner surface:

$$\Delta\sigma_4 = \Delta\sigma_1 + 2 \cdot \Delta\varphi_2 \quad (4)$$

Keeping the small angles approximation:

$$\begin{aligned}\Delta\varphi_2 &= \frac{\Delta y}{r} \\ \Delta\sigma_4 &= \frac{\Delta Y}{L}\end{aligned}\quad (5)$$

where Δy is the real diameter of cell and ΔY is the diameter of image cell; $\Delta\sigma_1$ is the divergence of the beam that illuminates a single cell and it can be expressed as a function of the divergence of the incident beam, α :

$$\Delta\sigma_1 = \frac{\Delta y}{\omega} \cdot \alpha \quad (6)$$

where ω is the diameter of the incident beam at the cornea surface.

The second aim of these computations is to find the expression of the optical magnification β . By definition,

$$\beta = \frac{\Delta Y}{\Delta y} \quad (7)$$

and, consequently, for the endothelial cell, the magnification β_{en} is:

$$\beta_{en} = \frac{L}{\omega} \cdot \alpha + \frac{2 \cdot L}{r} \quad (8)$$

An analogue expression is found for epithelial cells:

$$\beta_{ep} = \frac{L}{\omega} \cdot \alpha + \frac{2 \cdot L}{R} \quad (9)$$

The equations (8) and (9) show the dependence of the magnification on both the distance L between the screen and the cornea and the divergence of the incident laser beam.

4. EXPERIMENTAL RESULTS

Fig. 3 represents the image obtained using a HeNe laser with collimated beam.

The reflection corresponding to epithelium and endothelium lead to a superposition of images originated in these two corneal layers. In central zone of the image, the epithelial cells prevails, showing a less regular structure. Towards the peripheral zone of the image, the endothelial cells replace the epithelial ones, but the intracellular membrane may be seen less intense. The reflected light comes predominantly from endothelium at the peripheral zone because here the incidence angle is greater, closer to the limit reflection angle. From our computations, this angle is approximately 78° .

In Fig. 4, it can be seen more clearly the endothelial image obtained using an Ar^+ laser beam of the 84 mrad divergence. In this case, the incidence was made at a greater angle leading to a better image of the more profoundly located cells. Nevertheless, one observes a central superposition (epithelial and endothelial cell images) zone.

Figure 5 shows the result obtained with an Ar^+ (514 nm) laser beam.



Fig. 3. Corneal endothelium; image obtained with a HeNe collimated laser beam



Fig. 4 Image obtained using the radiation of 488 nm from an Ar^+ laser

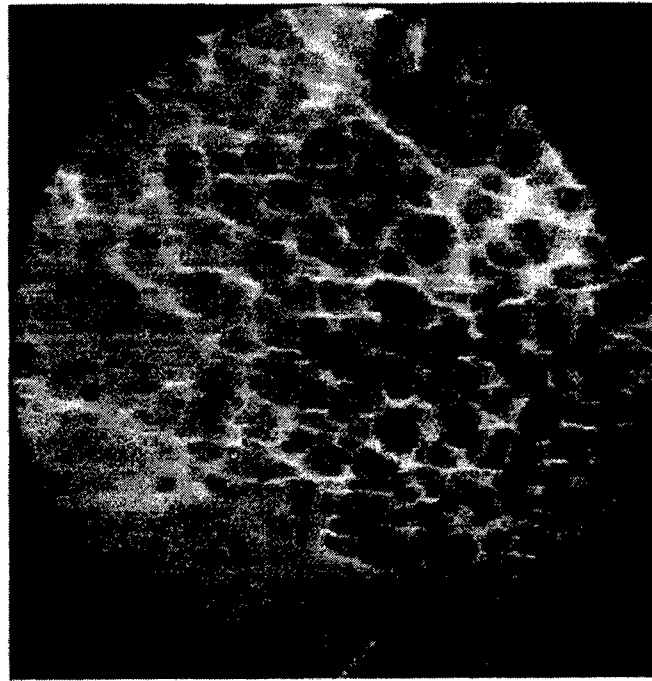


Fig. 5 Superposition of corneal layers obtained with 514 nm Ar⁺ radiation

It was not accounted a great difference between images obtained using either of the two laser sources (HeNe and Ar⁺), but with the Ar⁺ laser, the images obtained have a slightly better contrast because the interference patterns that inherently appear are more confined.

The dimensions of cells was determined projecting the reflected beam on the screen covered by scaled paper. Thus, the diameter of any image cell could be measured with a reasonable accuracy. This operation was developed for several values of incident divergence and distance. For any configuration we considered the average value of cell diameters calculated as an arithmetical mean of several cell diameters randomly chosen .

The data are summarised in Table 1.

Table 1.

Distance D(cm)	Divergence α (mrad)	Magnification β	Image diameter ΔY (mm)	Real diameter Δy (μ m)
40	0	114	2	18
40	86	149	2.5	18
40	400	247	5.5	20
50	0	143	3	21
50	86	186	4	22
50	400	342	8	23

An important source of errors is the lack of good enough precision in measuring experimentally the divergence and the incidence angle of the incoming beam. While divergence may be measured in far field with a relatively good precision, the incidence angle on the rabbit eye, in vivo, is difficult to be known exactly. The errors in real cell resulting

diameters due to the divergence and incidence angle errors are in the range $\pm 10\%$, out of which the errors in incidence angle are dominating. Another source of errors is the approximate measurement of the cell image diameters within the observation plane and respectively the distance from the rabbit eye to the observation plane; this accounts for a total error of at most $\pm 10\%$.

The above mentioned sources of errors are originating in the working experimental conditions; as for the computational sources of errors, the most important seem to be the approximations made in evaluating the magnification factor which is responsible for $\pm 1\%$ error.

Considering all the errors sources, the overall error on the values of the real cells diameters shown in Table 1 is in the range of $\pm 21\%$.

5. DISCUSSION

The images of inner cornea layers, presented in Fig. 3, 4 and 5 provide information about its structural zones profoundly located. Depending on laser beam divergence and incident angle, it can be obtained images from different depths of cornea. Of special interest for clinical investigation, endothelium prevails in Fig. 4 because of the appropriating conditions of illuminating.

Nevertheless, we faced the problem of image stability. It is known that the eye exhibit rapid rotations upon different axis so that the images become unsteady and unclear. It seems that using a flash illuminating, this problem would be solved.

The image construction, described in Chap. 3, leads to a relationship among the divergence of the beam, the distance at which the projection is made and magnification factor (formula 8, 9). Further, an evaluation of endothelial cell diameter was made starting from the parameters above. Since the measuring method of image cell diameter imply some errors, the real endothelial cell dimensions are not deducted with a great accuracy. However, the results present interest allowing to perform a relative investigation of different zones of corneal endothelium.

The great advantage of this method for corneal structural study is, besides its simplicity, the capacity to provide images from a large surface of a corneal layer (limited only by beam cross section), without demanding an electronic reconstruction of these images.

6. REFERENCES:

1. Patel S.: Refractive index of the mammalian cornea and its influence during pachometry. *Ophtal. Physiol. Opt.* 7: 503-506, 1987.
2. B.Carstocea, O. Gafencu, S. Apostol et al. Preliminary studies of rabbit corneal structure using laser beams, *Proc. SPIE, BIOS 1996 Conference*, vol. 2930.

Electronic beam analysis of excimer lasers used for photorefractive keratotomy

Carlos B. Roundy

Spiricon, Inc.
2600 North Main, Logan, UT 84341, USA

ABSTRACT

Excimer lasers are an excellent instrument for performing photorefractive keratotomy, PRK. The UV light from the laser causes an ablation of the cornea in proportion to the intensity of the light. The primary characteristic essential to successful PRK is the uniformity of the Top Hat, or working portion of the laser beam. In order for this intensity profile to be sufficiently uniform for PRK, it is essential to periodically measure the quality of the laser beam profile. This ensures that the laser continues to operate properly and provide the expected performance.

Excimer laser beams can be made extremely uniform. When the beams are monitored, it is possible for the operator to ensure the quality of the intensity distribution throughout the operation, as well as throughout the life of the laser. However, a laser beam can deteriorate to the point that it is unsatisfactory for PRK. For example, a beam that is not flat, but has a 50% tilted top hat, could correct part of the cornea by 1 diopter, and the opposite side by 1.5 diopter. This would leave the patient not only without corrected vision, but with uncorrectable or blurred vision.

Electronic beam analysis is a tool that enables very rapid identification of unsuitable beams. It enables the operator to clearly visualize the fluence or energy density over the usable area of the laser beam and to take corrective action when necessary. The numerical analysis that is available from electronic beam analyzers can assist in determining in advance when the beam is beginning to deteriorate to the point that it is unsuitable for PRK surgery.

Spiricon application engineers have analyzed and measured the beam intensity profile of many excimer lasers, from many manufacturers. This includes lasers for PRK, as well as for other industrial and scientific applications. It is our experience that all the brands of lasers we have tested can perform well when properly maintained. We have also observed miss-aligned and poor performance of laser beams from most manufacturers. The following figures show typical examples of both good and bad laser beams from excimer lasers being used for PRK.

Keywords: excimer laser, laser beam profile diagnostics, UV laser, pyroelectric, PRK, photorefractive keratotomy

1. EXAMPLES OF ELECTRONIC LASER BEAM DIAGNOSTICS

The following beam profiles have been obtained using a pyroelectric camera to measure the beam uniformity from the PRK excimer lasers. They illustrate how uniform the beam can be, and also how electronic beam analysis can very quickly identify and define potential problems.

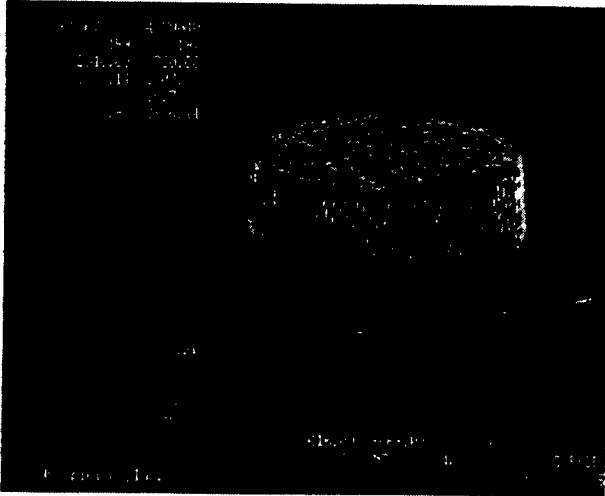


Figure 1. Uniform excimer laser beam.

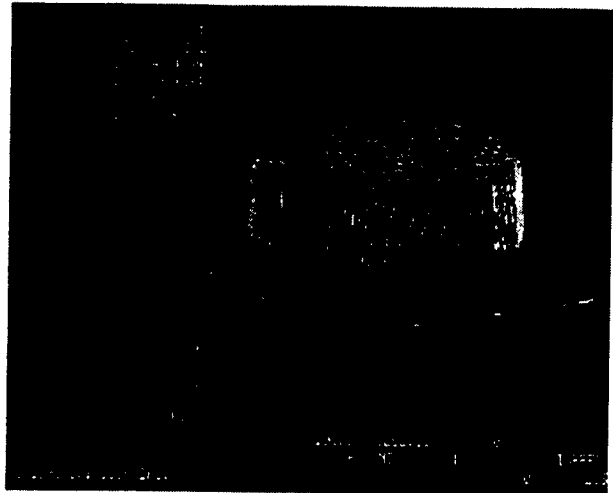


Figure 2. Excimer laser with slight dimple.

Figure 1 shows the beam profile of a very uniform excimer laser beam. Notice that it is nearly flat on top. If you looked at it from the top you would see that the beam perimeter is nearly perfectly round. This is the ideal PRK excimer laser beam which would perform an even and controlled corneal ablation.

Figure 2 is very similar to Figure 1. Notice, however, a very slight dimple near the center and just off to the right. This dimple may not be sufficient to cause uneven ablation, resulting in an unsatisfactory photorefractive keratotomy. Nevertheless it shows how fine a measurement the electronic laser beam analyzer can make. It is interesting to note that in Figure 1 the standard deviation across the top was only 2 counts out of a maximum of 197. In Figure 2 the standard deviation is 3 counts. Here the numerical analysis is able to show one beam being slightly better than the other.

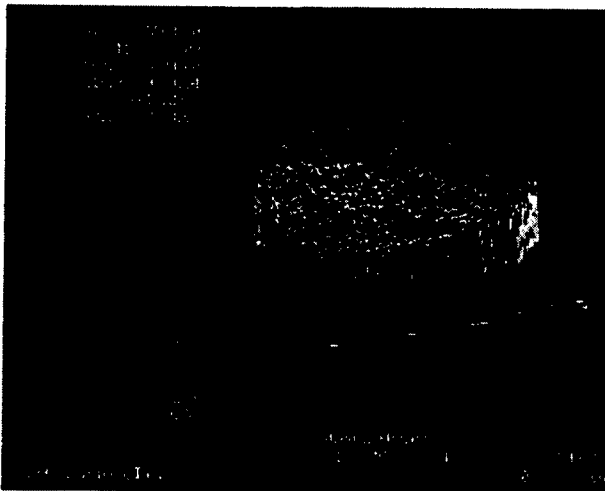


Figure 3. Excimer laser with misaligned delivery system.

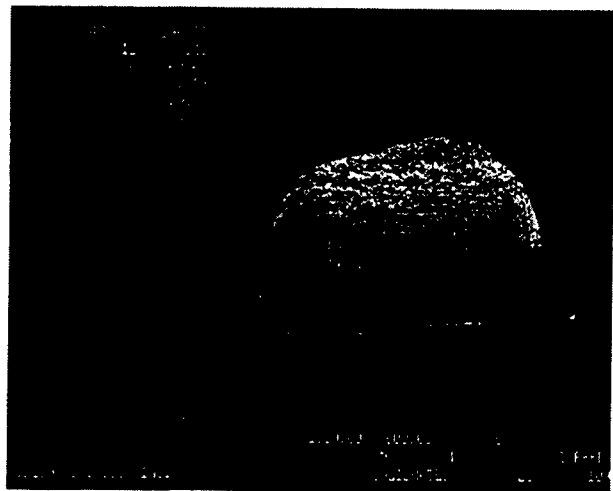


Figure 4. Excimer laser with rounded edges.

Figure 3 shows the beam profile of a poorly aligned delivery system from the excimer laser. Because of this poor alignment the laser is not Flat Top at all, but has a triangular wave form. The beam intensity at one edge is nearly double the beam intensity at the opposite edge, as is easily seen by a beam diagnostics user. The standard deviation has risen to 20 counts. This laser would cause uneven correction across the cornea, resulting in blurred vision.

Figure 4 shows a different kind of Flat Top beam. Notice here that the edges of the beam are rounded, rather than sharp and square, as they were in the first three figures. Nevertheless, even with the slight rounding of the edges, this beam is fairly uniform on top. It has a standard deviation of 4, illustrating the difference in the uniformity caused by the round edges. When the laser operator or physician can see and know the laser beam shape, he can design the treatment with that shape in mind.

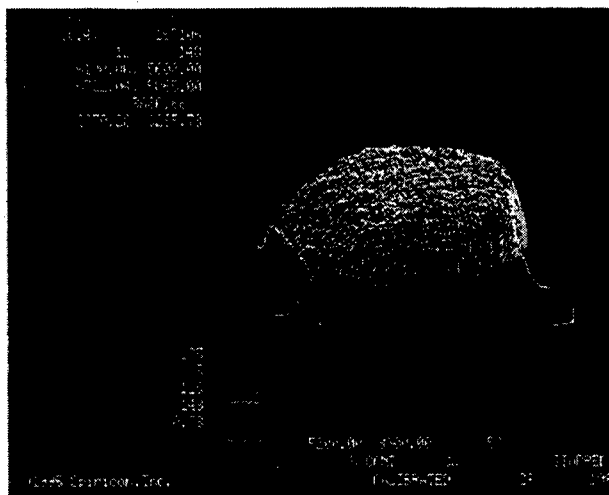


Figure 5. Excimer laser with misaligned optics.

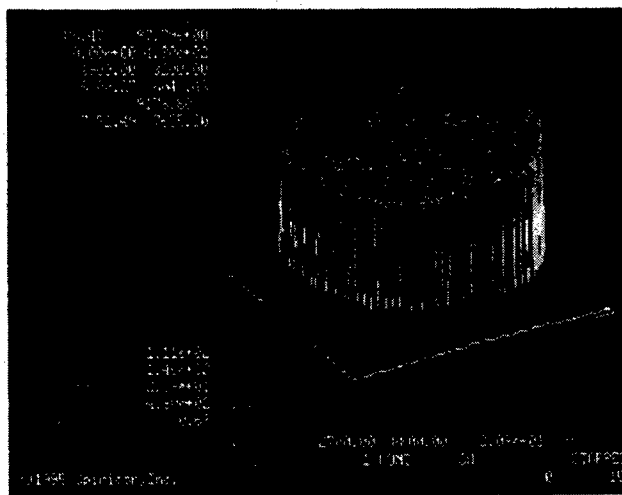


Figure 6. Laser with diffraction from aperture optics.

Figure 5 shows a beam from a similar laser as Figure 4, but now misalignment in the optics has caused one edge of the beam intensity profile to drop off considerably. This laser beam would give non-uniform ablation in PRK, resulting in uncontrolled corneal sculpting and blurred vision.

A problem opposite of that shown in Figure 5 is shown in Figure 6. In this case the aperture used to limit the size of the beam is causing diffraction around the edges of the beam. Thus the intensity of the laser beam is slightly higher around the edges. A measurement of this intensity shows that at the edges the intensity is 10-20% higher than it is in the middle. This would cause a ring of deeper ablation of the cornea, resulting in potentially blurred vision.

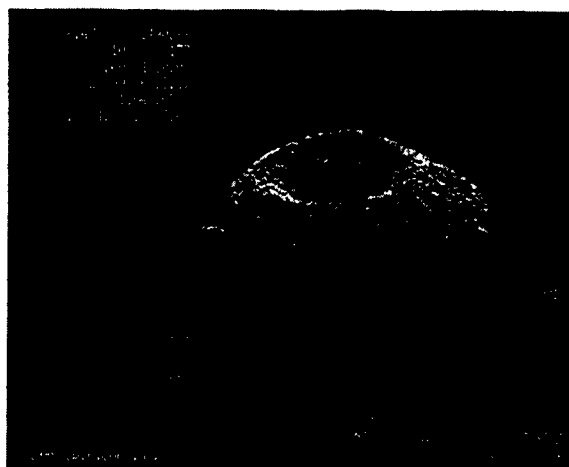


Figure 7. Laser with burned optics in delivery system.

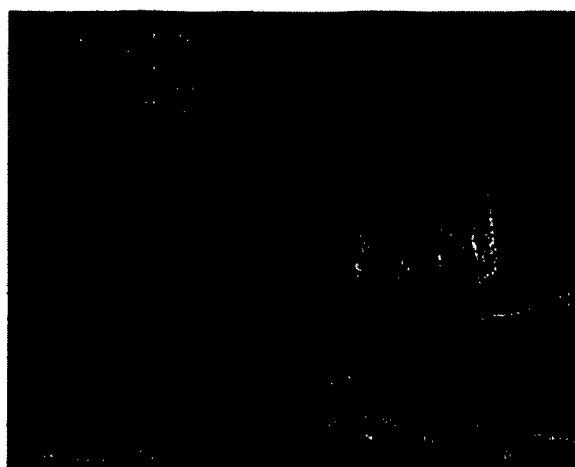


Figure 8. Poorly aligned excimer laser.

Figure 7 is an illustration of things that can go wrong. In this case, a mirror in the delivery system has a burn spot on it. Thus the excimer laser had a hole in the middle of its intensity pattern. This hole would cause very serious problems. The center of the cornea would not be ablated as expected, and proper vision correction would not be achieved.

Finally, Figure 8 shows a very poorly aligned beam. There is a very high amount of structure with 4 major peaks, and a valley through the middle. There is also structure out in the wings of the beam. It is of low intensity, but enough that it could cause problems with multiple pulse treatment. A patient treated in PRK with this laser beam would end up with extremely blurred vision.

2. EXCIMER LASER BEAM MEASUREMENT METHODS

There are a number of methods currently in use to measure the intensity uniformity of PRK excimer laser beams. They vary greatly in the degree of resolution and clarity provided. The two major categories are non-electronic and electronic methods.

2.1 Non-electronic methods

Presently used non-electronic methods to measure the energy distribution of the excimer laser include the use of: thermal fax paper, and metalized plastic blocks. The thermal paper technique provides minimal spatial information and size, and very poor qualitative information. It provides a dynamic range of only about 3. Thus it is possible to see only gross variations in intensity within the spot and no quantitative intensity information. An example of thermal paper burns is shown in Figure 9.

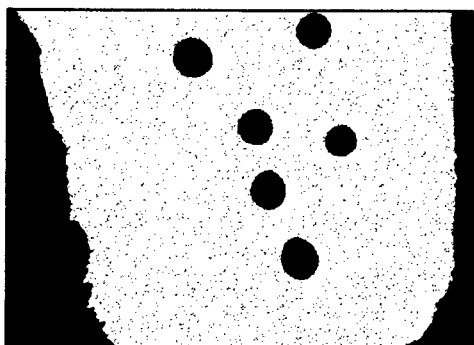


Figure 9. Thermal paper with laser burn spots.

Metalized plastic blocks are also used to measure the intensity distribution. To measure beam intensity the metalized block is ablated with the laser beam until a small portion of the metalization is initially removed. The operator counts the number of pulses it takes to first ablate through the metal to the plastic substrate. He then counts the successive number of pulses that are required until the metalized surface is completely ablated. The degree of uniformity is calculated from the ratio of the number of pulses required for each step. This method provides minimal quantitative information, and is very crude and cumbersome.

2.2 Electronic beam profiling methods using CCD cameras

CCD cameras can be used for electronic beam profiling of excimer lasers. These CCD cameras overcome many of the drawbacks of the thermal paper and metalized blocks, but also have some drawbacks. The main advantage of CCD cameras is that they give high resolution, quantitative beam intensity information. Up to 512 X 480 pixel resolution can be obtained with measurements of about 1% accuracy in magnitude.

Drawbacks of CCD cameras are as follows. First, they are too sensitive, and require at least 8 orders of magnitude attenuation. While this is possible using optical beam sampling techniques, the problems associated with attenuating a beam are proportional to the amount of attenuation required. Secondly, the laser beam is usually too large to fit on the CCD sensor area and must be resized for measurement. In some cases the CCD sensor is not uniform in response across the surface to UV radiation. Also, UV radiation degrades the silicon sensor's performance. This includes bleaching, wherein some of the areas of the CCD sensor are reduced in sensitivity. Another problem is ablation, where some of the silicon material is removed from the CCD array, leading to eventual failure.

There are secondary imaging techniques used with CCD cameras that overcome some problems, but introduce new ones. This includes down-converting the UV radiation to visible light. This is done by using phosphor paints deposited on a surface, or thin scintillation crystals. These techniques give reduced spatial resolution, due to the blurring in the conversion media. Also, down-conversion systems suffer from limited dynamic range of the useable linear range of the down-converting medium.

2.3 Excimer beam analysis using Spiricon's pyroelectric camera

Spiricon's Pyrocam I solid-state pyroelectric camera overcomes many of the disadvantages of CCD cameras. First, it provides spatial resolution of a 124X124 matrix with 0.1 mm pixels, a dynamic range in excess of 1000 (which is approximately 10 times greater than CCD cameras), and high saturation thresholds (approximately 10^6 greater than CCD cameras). With lower sensitivity the Pyrocam I requires only 2 orders of magnitude attenuation, or a 1% beam sampling. This is easily accomplished using modern dichroic mirror coatings. No ablation or long term bleaching effects have been observed on these pyroelectric cameras with the application of the excimer laser. Thus there is no danger of degradation with time and use. The pyroelectric camera sensitive area is 12.4 mm, which is large enough to accept most of the excimer lasers used in PRK, without having to resize the beam.

All of the beam profiles shown in Figure 1 through 8 were measured with the Pyrocam I camera. These figures illustrate the resolution and clarity that the camera provides.

3. CONCLUSIONS

Excimer lasers have been shown to produce a very uniform beam intensity that seems to work well for photorefractive keratotomy, PRK. However, it is possible for the laser and/or the delivery optics to deteriorate to the point that the beam intensity is no longer uniform. Beam uniformity measurements are necessary to insure that the laser is operating satisfactorily.

Electronic beam uniformity measurements excel over non-electronic measurements. Electronic measurements provide a better view of the beam pattern, showing even minor deviations in the uniformity. Electronic measurements also provide accurate quantitative analysis that helps to reduce operator error and misjudgment, and to define standards for the uniformity.

UV laser radiosensitivity of normal and tumoral chromatin

Liliana Radu, I. Mihailescu^x, V. Preoteasa, Irina Radulescu, Doina Gostian, A. Hening^x, S. Radu^{xx}

Molecular Genetics & Radiobiology Department, Victor Babes Institute, Spl. Independentei 99-101,
Bucharest 76201, Romania

^x Laser Department, Institute of Physics and Technology of Radiation Devices, MG-6, Bucharest, Romania

^{xx} Computer Science Department, Polytechnic University, Spl. Independentei 313, Bucharest 77703, Romania

ABSTRACT

A normal and a tumoral chromatin radiosensitivity to an UV laser radiation was determined.

The characteristics of these chromatin samples were established by the analysis of the absorption and emission spectra of chromatin complexes with a specific DNA ligand - ethidium bromide, by Scatchard representations of ligand binding to chromatin and by the Förster energy transfer efficiency determination between two fluorescent ligands coupled at chromatin: dansyl chloride and acridine orange.

The effects of excimer laser beam with $\lambda = 248$ nm on chromatin structure were analysed by the above methods and also by the establishment of the intrinsic chromatin fluorescence and of the excited state lifetimes of a specific DNA ligand.

keywords: UV laser, chromatin, absorption and emission spectroscopy, Scatchard representations, Förster energy transfer, time resolved spectroscopy

1. INTRODUCTION

The chromatin is the complex of deoxyribonucleic acid (DNA) with basic proteins (histones) and acidic proteins (nonhistones), that exists in eukaryotic cells nuclei.

In the last time, an important progress has been made in the establishment of the structure of nucleohistones complexes - the nucleosomes^{1,2,3}. However, some aspects of chromatin structure are still undetermined. Our previous studies were oriented towards the analysis of chromatin structure from normal tissues and from experimental tumors by methods of thermal transition, precision calorimetry, isotope uptake and ¹H-NMR spectroscopy^{4,5}.

In this paper we present the results of the study of a normal and a tumoral chromatin by: the determination of absorption and emission spectra of chromatin complexes with a specific DNA ligand - ethidium bromide, the Scatchard representations of ligand binding process and the establishment of the Förster energy transfer efficiency between two ligands coupled at chromatin.

As regards the laser action on biological materials, it presents great importance the action on DNA and chromatin. The majority of papers deals with the action of visible lasers^{6,7}, and studies of UV laser action were performed only on DNA^{8,9}. Our previous studies were oriented on the laser action on DNA¹⁰ and on normal chromatin¹¹.

In this paper we present a comparative study of laser action on a normal tissue-livers of Wistar rats and on a tumoral tissue - the Walker carcinosarcoma maintained on Wistar rats. The utilized methods were: the analysis of absorption and emission spectra of the complexes of chromatin with the ligand with specificity for DNA - ethidium bromide and the establishment of relative contributions of excited state lifetimes of the ligand. Also the chromatin intrinsic fluorescence and the energy transfer efficiency between a pair of fluorescent ligands coupled at chromatin versus laser dose were determined.

2. MATERIALS AND METHODS

The chromatin was extracted from livers of Wistar rats and from Walker carcinosarcoma, maintained on Wistar rats, by a combined method^{12,13,14}, that use treatments with EDTA-Na dithionite, that inhibits the action of endogenous nucleases and proteases. Also, a supplementary nuclei purification was realized by passing through a layer of 1 M sucrose.

The chromatin purity was verified by an absorption test¹⁵. The chromatin samples with 2.5×10^{-4} M DNA concentration were used. The ligand with DNA specificity -ethidium bromide ($\lambda_{\text{excitation}} = 480$ nm, $\lambda_{\text{emission}} = 600$ nm) was used in 10^{-5} M concentration.

An ultraviolet laser radiation with $\lambda = 248$ nm from an Iofan 1701 model excimer laser with Kr (p=100 Torr), F (p=125 Torr) and He (p=1600 Torr) was used. A 25 mJ dose/pulse and $\nu = 50$ Hz were utilized and the irradiation doses were between 0.5 and 3 MJ/m².

The Scatchard representations were realized using absorption data. The values of E_1 - the extinction of the free ligand, of E_2 - the extinction of the bound ligand and of E - the extinction of the mixture of free and bound ligand were determined. The fraction of the bound ligand - α - is :

$$\alpha = r T_A / T_L = (E_1 - E) / (E_1 - E_2)$$

where r is the ratio of the bound ligand to macromolecule quantity, T_A is the total macromolecule concentration and T_L is the total ligand concentration.

The equilibrium concentration of free ligand is :

$$[L] = T_L (1 - \alpha)$$

According to the Scatchard equation :

$$r / [L] = k (1 - n \times r) \{ [1 - n \times r] / [1 - (n - 1) \times r] \}^{n-1}$$

in the representation $r / [L]$ versus r , the intersection with the r axis gives the value of $1 / n$ and the intersection with the $r / [L]$ axis gives the value of k , where n is the number of the binding sites of the ligand on macromolecule and k is the binding intrinsic constant.

The Förster energy transfer efficiency between dansyl chloride -donor- ($\lambda_{\text{ex}} = 323$ nm, $\lambda_{\text{em}} = 505$ nm), covalently bounded at chromatin proteins and acridine orange -acceptor- ($\lambda_{\text{ex}} = 505$ nm, $\lambda_{\text{em}} = 530$ nm) intercalated between DNA base pairs, was determined as :

$$E = (I_A^D / I_A - 1) \times \epsilon_A / \epsilon_D$$

where I_A and I_A^D are the relative fluorescence intensities of the acceptor in the absence and respectively in the presence of the donor and ϵ_A and ϵ_D are the molar extinction coefficients of the acceptor and of the donor at excitation wavelength.

The energy transfer efficiency is related to the distance r between donor and acceptor by the expression

$$E = r^{-6} / (r^{-6} + R_0^{-6})$$

where R_0 - the distance at which the efficiency is 50% - can be computed as:

$$R_0 = (J \times K^2 \times Q_0 \times n^4)^{1/6} \times 9.73 \times 10^3$$

where: K^2 is the orientation factor, n is the refraction index of the medium, Q_0 is the quantum yield of the donor in absence of the transfer and J - the overlap integral - is :

$$J = \frac{\int_0^\infty F(\lambda) \epsilon(\lambda) d\lambda}{\int_0^\infty F(\lambda) d\lambda}$$

where $F(\lambda)$ is the donor fluorescence intensity at λ and $\epsilon(\lambda)$ is the molar extinction coefficient of the acceptor at λ .

Time resolved fluorescence lifetime measurements were carried out using a time correlated single photon counting system. The fluorescence decays were fitted to double exponential functions by the method of iterative conduction.

For the chromatin intrinsic fluorescence determinations, $\lambda_{ex} = 290$ nm and $\lambda_{em} = 345$ nm were used.

A Perkin Elmer spectrophotometer, an Aminco SPE 500 spectrofluorimeter and a time-resolved fluorimeter FL 900 CD, Edinburgh Analytical Instruments were used.

3. RESULTS AND DISCUSSION

3.1. The normal and tumoral chromatin characteristics

3.1.1. Spectrophotometric analysis of chromatin - ligand complexes

In table 1 are represented the parameters deduced from the spectrophotometric analysis of the complexes with the ligand ethidium bromide of chromatin from livers and from Walker carcinosarcoma: the relatives values at the absorption maximum (E_r) and the red shift of $\lambda_{maximum}$ ($\Delta\lambda$). These parameters are strictly dependent on the DNA concentration in chromatin samples. By comparison with the values of E_r and $\Delta\lambda$ obtained for DNA-ethidium bromide complexes¹⁶, percentage values of DNA available for ligand binding in chromatin samples were deduced to be 33.5% for liver chromatin and 41.2% for Walker carcinosarcoma chromatin. The difference between the percent of DNA available value for the two types of chromatin are due to the greater quantity of euchromatin regions (with a genic activity more intense) in tumoral chromatin.

Table 1. The parameters : E_r - relative extinction , $\Delta\lambda$ -maximum absorption displacement and $\%DNA_{av}$ - percent of DNA available for ligand binding, deduced from spectrophotometric analysis of the complexes of ethidium bromide with chromatin samples from Wistar rats livers and from Walker carcinosarcoma.

Chromatin	$c_{DNA}(\mu g/ml)$	E_r	$\%DNA_{av}$	$\Delta\lambda$ (nm)	$\%DNA_{av}$	$\overline{\%DNA_{av}}$
Liver	60	0.892	33.3	41.0	33.33	33.54±0.35
Liver	80	0.821	33.12	42.0	32.50	
Liver	100	0.750	35.00	44.0	34.00	
Walker	25	0.964	40.00	38.5	44.00	41.27±0.62
Walker	75	0.785	40.66	43.0	40.00	
Walker	150	0.607	41.00	48.5	42.00	

3.1.2. Spectrofluorimetric analysis of chromatin - ligand complexes

Table 2 includes the values of the fluorescence intensities of the complexes of chromatin with ethidium bromide.

Table 2. The parameters : I_{rel} - relative fluorescence intensity and $\%DNA_{av}$ - percent of DNA available for ligand binding , deduced from spectrofluorimetric analysis of the complexes of ethidium bromide with chromatin samples from Wistar rats livers and from Walker carcinosarcoma.

Chromatin	$c_{DNA}(\mu g/ml)$	I_{rel}	$\%DNA_{av}$	$\overline{\%DNA_{av}}$
Liver	50	2.25	35.00	32.91±0.46
Liver	70	2.36	31.42	
Liver	100	2.61	33.00	
Walker	47.5	2.27	37.89	40.06±0.53
Walker	95	2.78	43.15	
Walker	142.5	3.08	38.94	

Also, as compared to the values obtained for the DNA - ethidium bromide complexes case¹⁶, the proportion values of DNA available for ligand binding were deduced for the two types of chromatin. They are very close to those established from the spectrophotometric determinations.

3.1.3. Parameters deduced from Scatchard representations

From the Scatchard representations of the binding to chromatin of the ligand ethidium bromide, the values of the number of binding sites and of the coupling constant were obtained (table 3).

Table 3. The values of the n - number of binding sites and K - coupling constant for the complexes with ethidium bromide of DNA, liver chromatin and Walker chromatin.

Sample	n	$K(\text{mol}^{-1})$
DNA	4.00	$3.72 \cdot 10^5$
Liver chromatin	9.09	$3.20 \cdot 10^5$
Walker chromatin	7.46	$3.45 \cdot 10^5$

The value $n = 4$ for ethidium bromide binding to DNA indicates the coupling stoichiometry: a ligand molecule to four nucleotides.

The bigger values for n in chromatin cases are due to the existence of bounded proteins on DNA in chromatin structure and thus to the reduction of the ligand coupling possibility. The value $n = 7.46$ for Walker chromatin, as compared to the value $n = 9.09$ for liver chromatin, also indicates the greater ligand coupling availability in tumoral chromatin, due to a higher euchromatin proportion, than in normal chromatin.

The less values for the coupling constant in chromatins than in DNA case is as also explained by the chromatin structure.

3.1.4. Energy transfer between fluorescent ligands coupled at chromatin

The emission spectrum of dansyl chloride is superposed on the excitation spectrum of acridine orange and an energy transfer takes place between these two ligands¹¹. The values obtained for the energy transfer efficiency between the two fluorescent ligands and for the mean donor-acceptor distance for liver chromatin and for Walker chromatin are included in table 4.

Table 4. The energy transfer efficiency (E_f) between dansyl chloride and acridine orange and the mean distance donor-acceptor (r) for liver chromatin and for Walker chromatin.

Chromatin	E_f	$r(\text{\AA})$
Liver	0.274 ± 0.004	49.48 ± 0.012
Walker	0.187 ± 0.006	57.14 ± 0.015

The lower energy transfer efficiency and the higher donor-acceptor distance in the Walker chromatin, as compared to the liver chromatin, is an indication of a less compact structure of tumoral chromatin, due to the intense genic activity in this cells type.

3.2 The laser radiation effects on normal and tumoral chromatin

3.2.1. Absorption spectra of chromatin - ligand complexes

In figure 1 are represented the values of red λ shifts for the absorption maximum of ethidium bromide intercalated between DNA base pairs of laser irradiated chromatin (for liver chromatin and for Walker carcinosarcoma chromatin).

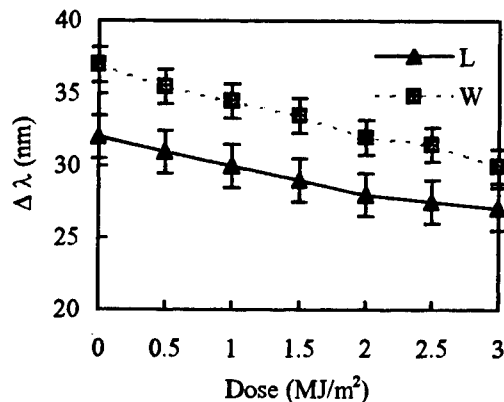


Figure 1. The difference between absorption maximum wavelength of chromatin - ethidium bromide complexes and that of free ligand, versus laser dose (L - liver chromatin, W - Walker chromatin).

The decrease of $\Delta\lambda$ values with laser dose indicates the damages produced in chromatin DNA, that prevent the ligand intercalation.

3.2.2. Emission spectra of chromatin - ligand complexes

In figure 2 are represented the variation of the relative fluorescence intensities of ethidium bromide - chromatin complexes, (for the normal tissue chromatin -L- and for the tumoral chromatin -W) with the laser dose.

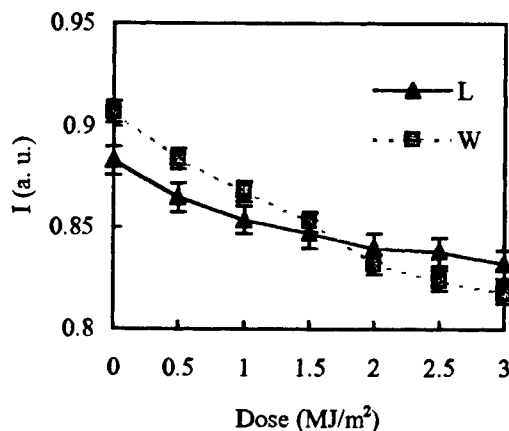


Figure 2. The relative fluorescence intensities of ethidium bromide - chromatin complexes versus laser dose (L - liver chromatin, W - Walker chromatin).

The spectrofluorimetric analysis of chromatin - ligand complexes, like the spectrophotometric one, gives informations on chromatin DNA structure. The decrease of the fluorescence intensities with the laser dose indicates the diminution of DNA double helix proportion in chromatin. On UV laser action, single and double DNA strand breaks are produced, with the reduction of DNA double helix quantity.

The variation of relative fluorescence intensities on the 0 - 3 MJ/m² domain is bigger for Walker chromatin, than for liver chromatin, that indicates a greater UV laser susceptibility of tumoral chromatin.

The same type of DNA modifications were observed under the action of X-ray irradiation¹⁷ or on fast neutrons action^{18,19}, with the production of DNA strand breaks and the decrease of DNA double helix proportion.

3.2.3. Time resolved fluorescence of chromatin - ligand complexes

The fluorescence decay curves of free (unbound) ethidium bromide presents a 2 ns lifetime⁵. The intercalated ligand in chromatin DNA has a 24 ns lifetime. The variation with laser dose of the relative contribution f (%) of the excited state lifetime of bound ligand was determined (figure 3).

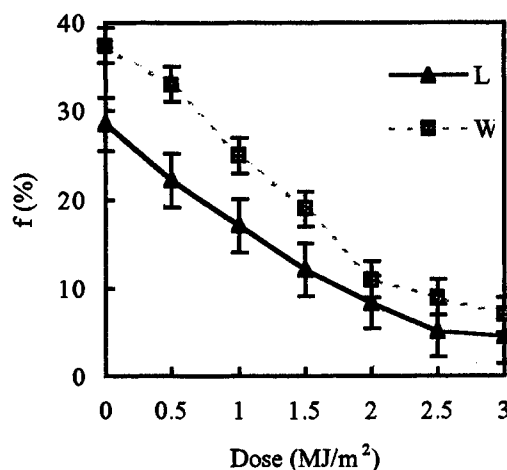


Figure 3. The relative contribution of the excited state lifetime of bound ethidium bromide in chromatin, versus laser dose (L - liver chromatin, W - Walker chromatin).

The lifetimes of the excited states establishment is a precise method for the analysis of chromatin structure modification. The decrease of the relative contribution of the lifetime of bound ligand in chromatin indicates the exact quantity of chromatin DNA destruction produced by UV laser action.

Also, the laser action on the tumoral chromatin is more efficient than on the normal one.

3.2.4. Chromatin intrinsic fluorescence

Figure 4 presents the intrinsic fluorescence intensities versus UV laser dose.

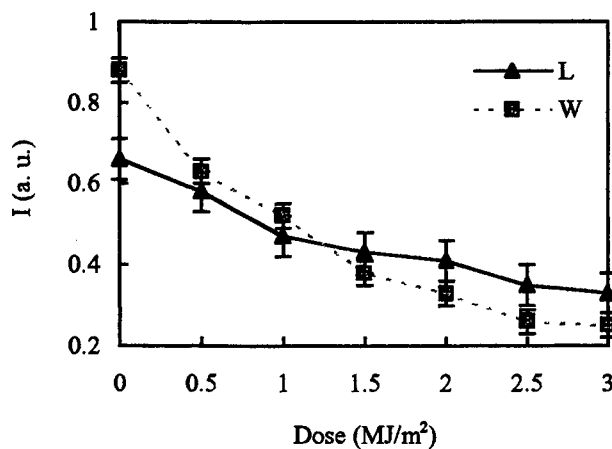


Figure 4. The chromatin intrinsic fluorescence versus laser dose (L - liver chromatin, W - Walker chromatin).

In the tumoral chromatin case, the intrinsic fluorescence for unirradiated sample, is bigger than for the normal chromatin. This result is due to a greater acidic proteins proportion in tumoral chromatin, because of an intense genic activity, that is performed by tumoral cells.

The decrease of the intrinsic fluorescence with the UV laser dose denotes the destruction of chromatin proteins. The variation of the intrinsic fluorescence is also higher for the tumoral chromatin, indicating a greater susceptibility to UV laser radiation.

3.2.5. Förster energy transfer efficiency between a pair of ligands coupled at chromatin

In figure 5 is represented the efficiency of Förster energy transfer between the pair of fluorescent ligands coupled at chromatin: dansyl chloride and acridine orange, versus UV laser dose.

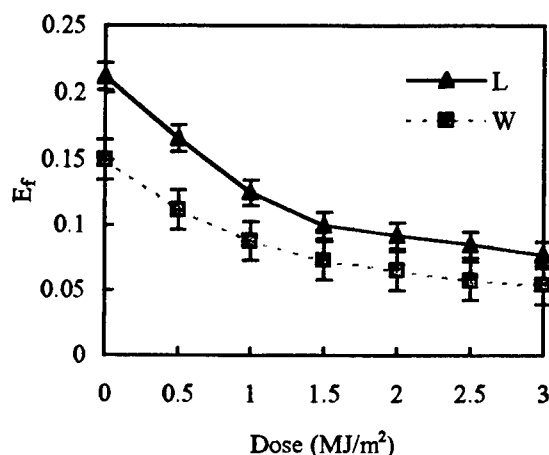


Figure 5. The energy transfer efficiency versus laser dose (L - liver chromatin, W - Walker chromatin).

The energy transfer efficiency decreases with the UV laser dose. This behaviour indicate a more unstabilised chromatin tertiary structure on the UV laser action, that determine as the energy transfer to be produced with less intensity. The diminution of the energy transfer efficiency is due to an increase of the donor-acceptor distance.

4. CONCLUSIONS

1. The presented methods (the analysis of the absorption and emission spectra of the chromatin complexes with a DNA ligand, the determination of the relative contributions of the ligand excited state lifetimes, the Schatchard representations of the ligand binding process, the chromatin intrinsic fluorescence measurement and the Förster energy transfer efficiency establishment) allow to determine the chromatin characteristics and also the chromatin UV laser radiosensitivity.

2. The accessibility for interactions with chromatin DNA was deduced to be 33.2 % for liver chromatin and 40.6 % for Walker carcinosarcoma chromatin, deduced from the spectrophotometric and spectrofluorimetric analysis of chromatin - ligand complexes.

3. The 248 nm laser beam produces complex modifications in chromatin structure :

- changes of chromatin global conformation
- DNA strand breaks with the reduction of the double helix DNA proportion
- acidic and basic proteins destruction

4. The UV laser effects on chromatin are proportionally to the dose on the domain 0 - 3 MJ/m².

5. The tumoral chromatin has a greater UV laser radiosensitivity than a normal chromatin, because of the greater euchromatin proportion.

6. The UV laser action on chromatin present similarities with the ionising radiation action.
7. The effects on chromatin of UV laser gives indications for the utilisation of this laser in radiochemiotherapy in medical applications.

5. REFERENCES

1. R. Kornberg, "Chromatin structure: a repeating unit of histones and DNA", *Science*, **184**, 868-871 (1974)
2. J. J. Hayes, T. D. Tullius, and A. P. Wolffe, "The structure of DNA in a nucleosome", *Proc. Natl. Acad. Sci. USA*, **87**, 7405-7409 (1990)
3. B. Lewin, "Chromatin and gene expression: constant questions, but changing answers", *Cell*, **79**(4), 397-406 (1994)
4. L. Radu, V. Preoteasa, and Z. Lenghel, "The action of anticancer drugs thiotepa and lomustine and of E and A vitamins on tumor chromatin, analysed by thermal transition, fluorescence methods and ^1H -NMR spectroscopy", *J. Molec. Struct.*, **348**, 29-32 (1995)
5. L. Radu, V. Preoteasa, I. Radulescu, and S. Radu, "Fluorescence lifetime and precision calorimetry in the study of normal and tumoral chromatin structure", *J. Molec. Struct.*, in press (1997)
6. T. Karu, "Photobiology of low-power laser effects", *Health Physics*, **56**(5), 691-704 (1989)
7. D. Schulte-Frohlinde, M.G. Simic, and H. Görner, "Laser-induced strand break formation in DNA and polynucleotides", *Photochem. Photobiol.*, **52**(6), 1137-1151 (1990)
8. I.E. Kochevar and A. Buckley, "Photochemistry of DNA using 193 nm excimer laser radiation", *Photochem. Photobiol.*, **51**(5), 527-532 (1990)
9. O.I. Kovalsky and E.I. Budowsky, "Laser (two-quantum) photolysis of polynucleotides: quantitative processing of results", *Photochem. Photobiol.*, **51**(5), 659-665 (1990)
10. L. Radu, M. Stirbet, V. Preoteasa, O. Hörer, D. Gostian, and G. Ganciu, "The effect of laser radiation on DNA", *Stud. & Res. Physics*, **10**, 553-557, (1991)
11. L. Radu, V. Preoteasa, I.N. Mihailescu, and B. Constantinescu, "Photolysis of chromatin by UV laser irradiation at 248 nm", *Rom. J. Biophys.*, **5**(4), 383-389, (1995)
12. B.L. McConaughy and B.J. McCarthy, "Fractionation of chromatin by thermal chromatography", *Biochem.*, **11**, 998-1007 (1972)
13. R.D. Kornberg, J.W. LaPointe, and Y. Lorch, "Preparation of nucleosomes and chromatin", *Meth. Enzym.*, **170**, 3-14 (1989)
14. N.L. Oleinick and S.-M. Chiu, "Nuclear and chromatin structures and their influence on the radiosensitivity of DNA", *Radiat. Prot. Dosim.*, **52**(1-4), 353-358 (1994)
15. E. Gajewski, G. Rao, Z. Nackerdien and M. Dizdaroglu, "Modification of DNA bases in mammalian chromatin by radiation-generated free radicals", *Biochem.*, **29**, 7876-7882 (1990)
16. L. Radu, I. Moraru, V. Gheorghe, A. Stirbet, and V. Preoteasa, "A spectrophotometric, spectrofluorimetric and calorimetric study of the modifications of chromatin structure by the carcinogen thioacetamide", *Rev. Roum. Biochim.*, **22** (2), 129-137, (1985)
17. C. Baumstark-Khan, U. Griesenbach, and H. Rink, "Comparison of DNA strand break induction in CHO cells measured by alkaline elution and by fluorometric analysis of DNA unwinding", *Fre Rad. Res. Comms.*, **16**(6), 381-389 (1992)
18. M. Spothem-Maurizot, J. Franchet, R. Sabattier, and M. Charlier, "DNA radiolysis by fast neutrons. II. Oxygen, thiols and ionic strength effects", *Int. J. Radiat. Biol.*, **59**(6), 1313-1324, (1991)
19. L. Radu, I. Mihailescu, B. Constantinescu, O. Gostian, "Absorption and emission spectroscopy in the analysis of laser radiation and fast neutrons action on chromatin", *J. Int.Soc.Opt.Engin.*, **2461**, 405-407, (1995)

Observations concerning the use rMuIFN - gamma activated macrophages by intra and peritumoral perfusion combined with laser therapy in animals with carcinosarcoma

V.F.Dima, V.Vasiliu*, D.Laky**, and S.V.Dima***

Cantacuzino Institute, *National Institute for Laser, Plasma and Radiation Physics,

**Victor Babes Institute, Bucharest - Romania

***Centro Medico-Chirurgico S.I.S. Hahnemann, Rome - Italy

ABSTRACT

Experiments were performed on five batches of inbred rats with Walker-256 carcinosarcoma receiving sole treatment photodynamic therapy (PDT), rMuIFN - gamma activated macrophages (AMØ) or associated therapy (PDT+ AMØ - A; PDT+ AMØ - B) and the control batch (saline) consisting of animals with untreated Walker - 256 tumors.

These experimental observations demonstrate that "combined" photodynamic therapy with immunotherapy stimulates cell-mediated antitumoral activity, increased survival rates and reduces incidence of Walker - 256 carcinosarcoma in rats.

Key words: He-Ne laser, Photofrin II, Activated macrophages, Photodynamic therapy, Walker - 256 tumor cells.

1. INTRODUCTION

Experimental approaches and clinical investigations have shown that the association of two or more means for cancer treatment such as antitumoral agents¹, radiation, hyperthermia, bacterial extract², endotoxin³, lymphokines and photodynamic therapy⁴ in animals and human present evident advantages and has become a frequently accepted treatment.

Photodynamic therapy of malignant tumors includes biological, photochemical and photophysical processes. These processes involve: (i) absorption of photosensitizing agent; (ii) selective retention of the photosensitizer in tumors and (iii) irradiation of sensitized tumor by laser radiation⁵.

In the last decade, human and murine macrophages differentiated from blood monocytes and activated with interferon-gamma have been used in adoptive immunotherapy^{6, 7}. Some investigators have demonstrated that photodynamic therapy stimulates lymphocytes and activated macrophages, resulting in immunologically beneficial effects to the hosts.

In the present work, we have studied the effects of interferon activated macrophages associated with photodynamic therapy upon evolution of carcinosarcoma and immunological reactivity after local exposure to combined therapy.

2. MATERIALS AND METHODS

2.1 Animals and tumor implantation

The tumor used in these studies was the Walker-256 carcinosarcoma cells obtained from the Oncology Institute, Bucharest and maintained by serial transplantation in inbred Wistar-R8 rats. Tumoral

suspension (0.2 ml) was subcutaneously injected in the dorsal region of syngeneic animals. Tumor were visible 7 days after transplantation.

2.2. Drug exposure

Photofrin II (Photofrin Medical Inc. Cheetkowage, NY.). Rats were intraperitoneally injected with a drug dose of 20 mg/kg body mass. Twelve hours post-injection, rats were irradiated with He-Ne laser.

2.3. Light source

The light source was a divergent beam from a LG - 6 He-Ne laser (632.8 nm, 10 mW) whose output was checked with a Spectra Physics C power meter.

2.4. Cells and cell culture

Murine blood monocytes (Mo) were obtained from tumor bearing rats and prepared by the method described by Bartholeyns et al⁶. Monocytes were grown on Pyrex bottles at 37°C in a humidified 5 % CO₂ / 95 % air incubator. Cells differentiated into macrophages after 10 days of culture. The effector cells were activated by exposure to 400 units / ml of recombinant interferon-gamma (rMuIFN-gamma) (5x10⁶ U/mg, Genetech Inc. South San Francisco, U.S.A) for 24 hours.

2.5. In vivo experiments

Five different treatments were evaluated in rats with Walker-256 carcinosarcoma. Photodynamic therapy (PDT) in five fractionated, 60 min. each (batch I); rMuIFN-gamma activated macrophages (AMØ / batch II) given intratumorally in five doses (5 x 10⁶ cells / dose / animal) every four days; PDT+AMØ - A (intratumoral perfusion - batch III); PDT+AMØ - B (intra and peritumoral) perfusion batch IV and saline injection (control batch V). Fraction irradiation of animals in batch I, III and IV was performed at 3 days intervals, followed next day by AMØ perfusion. The animals were followed up 52 days.

The efficacy of activated macrophages (AMØ) sole or associated with PDT was estimated by means of the following parameters: (1) in vivo effects of AMØ on tumor development; (2) immunological tests and (3) histopathological observations.

2.6. Immunological Tests

2.6.1. Mitogenic response

The mitogenic activity of spleen cells was assayed by the method described by Csako et al.⁸ Radioactivity was read in a Beckman-model CPM-100 scintillation counter. Results were calculated from the uptake of ³H-thymidine by the cells and were expressed as mean uptake in cpm / well.

2.6.2. Assesment of cytotoxicity

Cytotoxicity of effector cells was assayed by ³H-Uridine method of Nishimura et al.⁹. Target cell lysis was calculated by the following equation: % cytotoxicity = 1 - (cpm in culture of effector and target cells / cpm culture of target cells alone) x 100.

The lines K562 (human myeloid tumor cells) was used as target cells. The cells were maintained at 37°C in a humidified atmosphere of 5% CO₂ in RPMI 1640 medium (Gibco, Grand Island, N.Y.).

2.7. Histopathology

Tumors were removed from animals used for immunological tests after twenty-eight days of treatment alone are combined, fixed in buffered formalin, sectioned and stained with hemotoxylin-eosin (HE).

2.8 Statistical analysis

Data were expressed as arithmetic mean and standard error (S.E.).

Significance of differences between groups was calculated by the Kruskal-Willis test.

3. RESULTS

3.1 In vivo antitumor effects of combined therapy

In animals exposed to photodynamic treatment, associated with interferon activated macrophages, the values of investigated experimental parameters (mortality, progressive evolution and complete tumoral regression) were superior as compared to values noticed in other batches.

Table 1. Enhanced antitumor efficacy of the combination of PDT with activated macrophages in Wistar R8 tumor bearing rats

Treatment batch:	Percentage and number of dead rats during experiments	Tumor incidence ^a	
		Percentage of rats with progressive tumor	Percentage of rats in which tumor regressed completely
I ^b	46.6 (7/15) ^c	26.7 (4/15)	26.7 (4/11)
II	55.5 (10/18)	11.1 (2/18)	33.3 (6/18)
III	20.0 (4/20)	30.0 (6/20)	50.0 (10/20)
IV	7.4 (2/27)	7.4 (2/27)	85.2 (23/27)
V	83.3 (15/18)	16.7 (3/18)	- -

a - Tumor incidence is based on the total number of rats alive in each group at 52 days after treatment

b - Batches: I (PDT); II (AMØ); III (PDT+ AMØ-A); IV (PDT+ AMØ-B); V (Control untreated animals)

c - Numbers in parantheses denote number of rats

These facts demonstrate the efficacy of PDT treatment associated with activated macrophages in experimental rats carcinosarcoma.

3.2. Mitogenic response of spleen cells

The values of ³H-thymidine incorporation after lymphocyte stimulation with Con A, 14 and 28 days after treatment, are presented in Fig. 1. After 14 days, we noticed a superior response post-Con A stimulation in all studied batches, as compared to values found in batch V (saline) and healthy rats. Significant values were found in batches III and IV, receiving associated treatment (PDT+ AMØ-A and PDT+ AMØ-B) (Fig. 1). Twenty-eight days post-treatment, cpm values found after lymphocyte stimulation with Con A were significantly higher to those after 14 days, as compared to control batches.

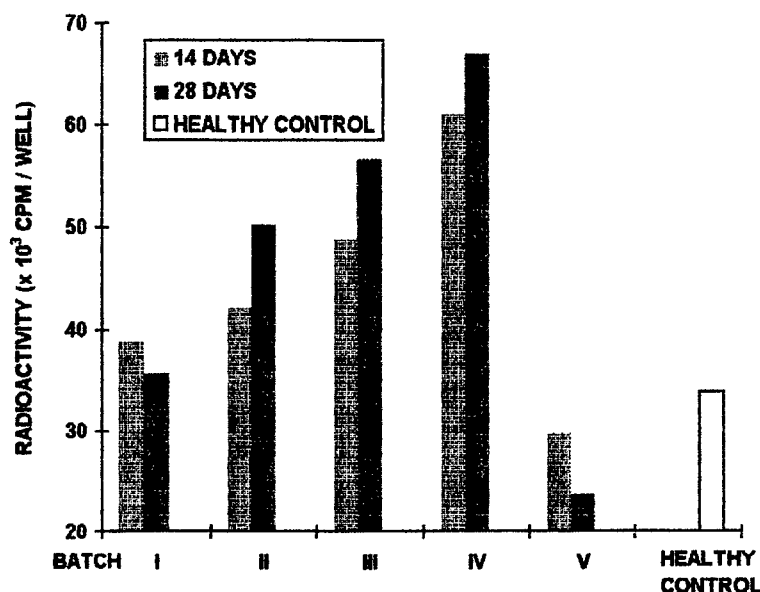


Fig. 1. Response of lymphocytes to Con A in carcinosarcoma of rats receiving sole and combined therapy. (For details see Table 1)

3.3. Cytotoxicity Assays

The results of cytotoxicity tests are presented in Table 2. Percentage values found for anti-K562 activity of spleen cells from the treated animals batch were superior to control values (saline), 14 days post-treatment; the following four group: I (PDT); II (AMØ); III (PDT+ AMØ-A) and IV (PDT+ AMØ-B) had a significant anti-K562 activity, compared to the controls. The batches exposed to combined treatment had higher cytotoxicity values in comparison with control animals. Twenty eight days post-treatment, in all studied batches a increase of splenic cell cytotoxicity was noticed, against K562 target cells, in comparison with the values determined 14 days after post-treatment. Anti-K562 cytotoxic activity in batches where activated macrophages were associated with PDT was superior to the other animal batches (Table 2)

Table 2. Results of cytotoxicity assay using splenic cells from carcinosarcoma treated rats

Batch:	Percentage of cytotoxicity against K562 target cells	
	14 days after treatment	28 days after treatment
I	22.8±2.34	28.3±1.55
II	25.1±2.97	27.9±2.08
III	28.5±3.14	31.7±2.59
IV	33.9±2.76	42.9±3.22
V	16.3±1.29	17.1±0.58

Healthy control animals: 22.7±1.22 percent

3.4. Histopathological Examination

Morphological changes appeared in tested animals and controls presenting Walker-256 carcinosarcoma were studied four weeks post-treatment. In animal from control batch V (saline-injected) we noticed: small cells, oval or rounded, presenting nuclei with rich chromatin, comparatively with reduced cytoplasm; here and there larger cells with multiple nuclei, presenting characteristic atypia for tumor cells; in the tumor mass we noticed unequal zones of necrosis, leading to the conclusion that the tumor was weakly differentiated tumor of sarcomatoid type. In animals from batch III exposed to PDT associated with intratumoral perfusion of AMØ (PDT+ AMØ-A) we noticed: histological variations could be seen from one zone to another with alterative tumor cells with vacuolar and dystrophic lesions; lymphocytes and macrophages elements, vasodilatation and edema were observed. In animals from batch IV, exposed to PDT associated with activated macrophages (PDT+ AMØ-B) intra and peritumorally perfusion, we noticed large hemorrhagic regions, marked vasodilatations, extended necroses with few isolated tumor cells; macrophages infiltration in the tumor center and periphery are in small or large groups. No tumoral proliferation was detected.

4. DISCUSSION

In this paper, we noticed that association of photodynamic therapy with interferon-activated macrophages significantly reduced mortality, and tumor incidence in inbred with Walker-256 carcinosarcoma. Tumoral incidence decrease both as progression and regression, was assigned to exposure to photodynamic therapy but also to recombinant murine interferon-gamma activated macrophages association, increasing cell-mediated immune response.

The results showed that 14 and 28 days after treatment initiation T-splenic lymphocytes significant reacted to Con A stimulation, in comparison with healthy control animals. The cells giving the best response were from rats which received combined treatment.

Lymphocytes from animals exposed to "associated" treatment demonstrated an increase anti-K562 activity, compared to saline injected controls and healthy animals at 14 and 28 days post-treatment. This increased cytotoxic activity could be assigned to three factors: (i) stimulation with tumoral antigens; (ii) cytokine production after He-Ne laser irradiation and (iii) direct cytotoxic activity of activated macrophages by releasing products such as: TNF-alpha, neutral proteases, oxygen metabolites and complement components.

The morphological and immunological changes noticed in these experiments, after exposure to PDT, are in full agreement with previous observations of the other authors referring to mechanisms which are probably involved in photodynamic therapy¹⁰⁻¹³.

Besides the PDT mechanisms we could add the following antitumoral effects of activated macrophages such as: (a) cytotoxicity mediated by monokines in membrane associated or soluble forms; (b) killing and ingestion of tumor cells by phagocytosis and probably apoptosis¹⁴⁻¹⁶; (c) cytokine "cascade" is responsible for immune response amplification, involving various kinds of soluble factors produced by a variety of immuno-competent cells¹⁷.

Summing up, this work demonstrates that combined photodynamic therapy with interferon activated macrophages stimulates cell-mediated antitumoral activity, increased survival rates and reduces incidence of carcinosarcoma in animals.

5. REFERENCES

1. D.Spaeth, T.Conroy, I.Krakovski, L.Geoffrois, and M.V.Berns, "Cisplatin and long term continuous infusion of Fluorouracil in the treatment of advanced breast cancer: Advanced breast cancer-a retrospective study of 77 patients," *Bull du Cancer*, Vol.80, pp.351-356, 1993.
2. V.F.Dima, V.Vasiliu, D.Laky, A.Popa and M.Stirbet, "Response of murine mammary adenocarcinoma to photodynamic therapy and immunotherapy," *Laser Ther.*, Vol.2, pp. 153-160, 1990.
3. V.F.Dima, V.Vasiliu, D.Laky, M.D.Ionescu and S.V.Dima, "Treatment of rat Walker-256 carcinosarcoma to photodynamic therapy and endotoxin irradiated with high energy electrons," in *Photodynamic Therapy of Cancer.*, Julio Jori, Johan Moan, Willen M.Star, Editors, Proc. SPIE 2078, pp. 547-557, 1994.
4. C.J.Gomer, N.Ruker, A.Ferrario and S.Wong, "Properties and applications of photodynamic therapy," *Radiation Res.*, Vol.120, pp. 1-18, 1989.
5. S.Kimel, J.P.Tromberg, G.W.Roberts and M.V.Berns, "Singlet oxygen generation of porphyrins, chlorides and phtalocyanines," *Photochem. Photobiol.*, Vol. 50, pp. 175-183, 1989.
6. J.B.Bartholeyns, M.Lopez and R.Andreesen, "Adoptive Immunotherapy of Solid Tumors with Activated Macrophages: Experimental and Clinic Results," *Anticancer Res*, Vol.11, pp.1201-1204, 1991.
7. R.Andreesen, B.Hennemann, "Adoptive immunotherapy with autologous macrophages : Current statusn and future perspectives," *Pathobiol.*, Vol. 51, pp. 259-263, 1991.
8. G.Csako, E.A.Suba, A.Ahlegren, C.M.Tsai and R.J.Elin, "Relation of structure to function for the U.S.reference standard endotoxin after exposure to ⁶⁰Co radiation," *J. Infect. Dis.*, Vol. 153, pp. 98-108, 1986.
9. T.Nishimura, Y.Togashi, M.Goto, H.Yagi, Y.Uchiyama and Y. Hashimoto, "Augmentation of the therapeutic efficiency of adoptive tumor immunotherapy by in vivo administration of slowly released recombinat interleukin 2," *Cancer Immunol. Immunother.*, Vol.21, pp. 12 - 18, 1986.
10. J.Moan and S.Sommer, "Oxygen dependence of the photosensitizing effect of hematoporphyrin derivative in NHIK 3025 cells," *Cancer Res.*, Vol.454, pp. 1068-1073, 1985.
11. K.Chaudhuri, W.R.Keck and S.H.Selman, "Morphological changes of tumor microvasculature following hematoporphyrin derivative sensitized photodynamic therapy," *Photobiol.*, Vol. 46, pp. 823-827, 1987.
12. G.Jori, "Response of tumor tissues to photodynamic therapy," in *Photodynamic Therapy of Cancer.*, Julio Jori, Johan Moan, Willen M.Star, Editors, Proc. SPIE 2078, pp. 286-292, 1994
13. J.O.Funk, A.Kruse and H.Kirchner, "Cytokine production after Helium-Neon laser irradiation in cultures of human peripheral blood mononuclear cells," *J. Photochem. Photobiol. B: Biol.*, Vol. 16 pp. 347-355, 1992.
14. J.B.Bartholeyns and M.Lopez, "Immune control of neoplasia by adoptive transfer of macrophages: Potentiality for antigen presentation and gene transfer," *Anticancer Res.*, Vol.14, pp.2673-2676, 1994.
15. C.Zhou, C.Shunji, D.Jinsheng, L.Junlin, G.Jori and C.Milanesi, "Apoptosis of mouse MS-2 fibrosarcoma cells induced by photodynamic therapy with Zn(II)-phthalocyanine," *J.Photochem-Photobiol.B: Biol*, Vol. 33, pp. 219-223, 1996.
16. J.A.Hickman, "Apoptosis chemotherapy resistance," *Eur.J.Cancer*, Vol. 12A, pp. 921-926, 1996.
17. G.Boccoli, R.Masciulli, E.M. Ruggeri, P.Carlini, G.Gianella, E.Montesoro, G.Mastroberardino, G.Isacchi, U.Testa, F.Calabresi and C.Peschle, "Adoptive immunotherapy of human cancer: The cytokine cascade and monocyte activation following high-dose interleukin 2 bolus treatment", *Cancer Res.*, Vol.50, pp.5795-5800, 1990.

Influence of the laser beam wavelength on the gonoarthrosis treatment
- a preliminary comparative study -

Gabriela Brojbeanu, St.Sutearu, M.V.Udrea*, V.Vasilu*

Clinical Hospital "Dr.Ioan Cantacuzino", Romania

*Institute of Laser and Plasma Physics, Department of Lasers, PO Box MG-36, Bucharest, Romania

ABSTRACT

A comparative study on four groups of patients which have been exposed to laser radiation was performed. Three wavelength were used (633, 670 and 830 nm). The fourth group received only laser placebo. Every group is composed by 20 people homogeneously selected from the point of view of age, sex and clinical and paraclinical parameters. The irradiation dose was kept almost the same, i.e. 15 J/cm². The dependence of subjective and objective indicators on the laser wavelength were put into evidence.

Keywords: photodynamic therapy, HeNe laser, diode laser.

1. INTRODUCTION

The well known therapeutically and biostimulating effects of the laser radiation on living tissues were successfully put into evidence by our team during the experiments of last years. The researches have been performed comparatively on different groups of patients with the same rheumatological disease, using different types of lasers. Usually, one group has received classical medication, a second one has received classical medication in addition with laser radiation and the third one has received only placebo effect.

The results of our studies being encouraging, we have started a systematic study in order to evaluate the dependence of the dynamics of the treatment on the laser wavelength. More, we have used only laser treatment without ordinary medication.

2. METHOD AND TOOLS

This study is based on the analgesic and anti-inflammatory effects of laser therapy. The lasers we have used to perform this study have the following characteristics:

a. HeNe laser, continuous laser beam at 633 nm wavelength, 5 mW power;

b. GaAs laser diode, continuous beam at 670 nm wavelength, 5 mW power;

c. GaAs laser diode, continuous beam at 830 nm wavelength, 30 mW power;

The spot area of these beams are approximately the same, i.e. 0,2 cm². The distance from the laser generator and the patient was about 0,5 m. Taking into consideration that the irradiation dose was chosen to be the same (about 3 J) for all three kinds of lasers we have used it results a density of irradiation of 15 J/cm².

The standard procedure consists of: medical examination (estimation of the pain with mechanical character in the knee), paraclinical tests, radiographic aspects which are typical for gonoarthrosis consisting in one or more characteristics: asymmetrical narrowing of articulator space, sharpening of the tibia spines \pm marginal osteophytes).

The study is performed on 80 female patients from the Clinic of Internal Medicine and Rheumatology of the Hospital Dr.I.Cantacuzino. All of them had the diagnosis of gonoarthrosis already established. Their age is from 39 to 75 years.

We have split this lot into four groups as following:

Group A, 20 patients : placebo, the patients were suggested to be exposed to a laser diode but the laser power supply was not switched on;

Group B, 20 patients: a 5 mW, 633 nm HeNe laser was used;

Group C, 20 patients: a 5 mW, 670 nm (red) laser diode was used;

Group D, 20 patients: a 30 mW, 830 nm (infrared) laser diode was used, maintaining an irradiation dose similar to group B and C;

The average ages of group A is 55,2 years, of group B is 53,8 years, of group C is 52,5 years and of the group D is 54,3 years.

Seven irradiation seances were daily performed. We have irradiated 5 points on the knee, for 2 minutes per point in the case of 5 mW lasers and about 20 seconds in the case of 30 mW diode laser.

We have excluded from our experiment the patients which other kinds of lesions (suppuration, neoplasm) or articulator diseases.

The evaluation of the effectiveness of laser therapy was performed checking three parameters:

1. the pain score (a subjective indicator);
2. the angle of the flexion movement of the knee;
3. the time needed to cover a given distance (15 m);

The level of the pain score before the treatment was registered as 10 and 0 is the score for complete removal of the pain. Every patient is questioned about the pain score in the 1st, 4th, and 7th day of treatment. Then the pain score is divided 3 levels:

0 - 3, marked effectiveness;

4 - 7, effectiveness;

8 - 10, ineffectiveness;

The angle of the flexion movement of the knee and the 15 m walk test were measured on the first and the seventh day of the treatment.

3. RESULTS AND DISCUSSION

The evolution of the mean pain score for every group of patients is presented in fig.1.

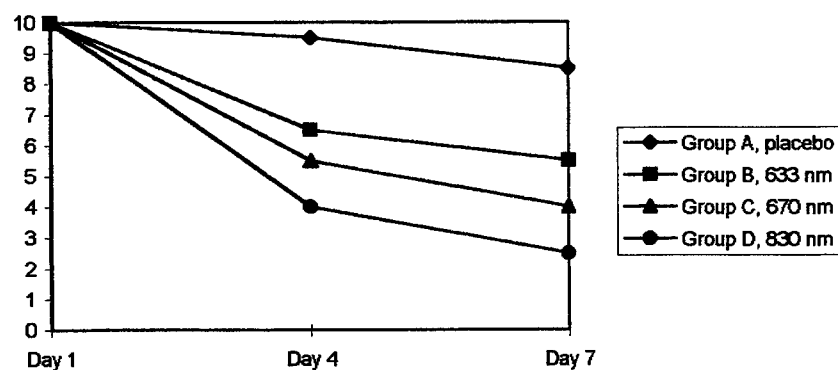


Fig.1 The pain score dependence on the laser wavelength

	Day 1	Day 4	Day 7
Group A, placebo	0%	5%	15%
Group B, 633 nm	0%	35%	45%
Group C, 670 nm	0%	45%	60%
Group D, 830 nm	0%	60%	75%

Table 1 The percent of improvement of the pain score

It should be put into evidence the high efficiency (75%) of the infrared beam after 7 days of treatment in comparison with the 670 nm diode laser (60%) and HeNe laser (45%).

In the followings we present the comparative effect of irradiation by means of the three types of lasers on the knee flexion ability:

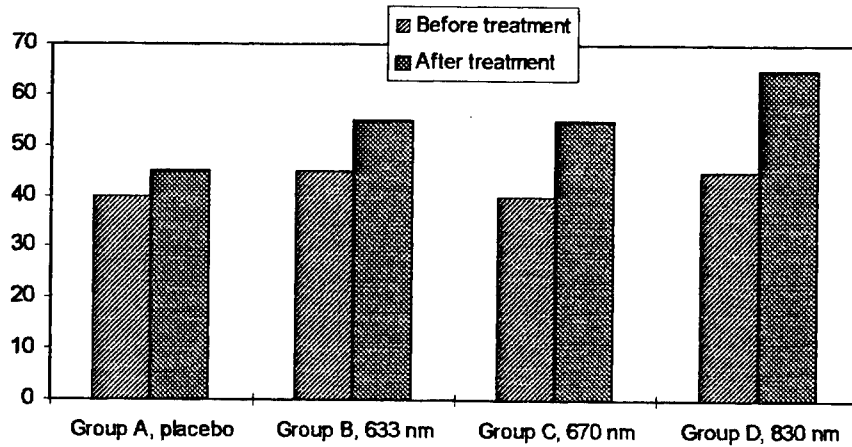


Fig.2 The dependence of the angle of flexion on laser irradiation

The third parameter which has been taken into consideration was the time which is necessary for a 15 m distance walk. It has to mention that the patients are free of pulmon, heart, or neuralgic disease which might influence the measurements.

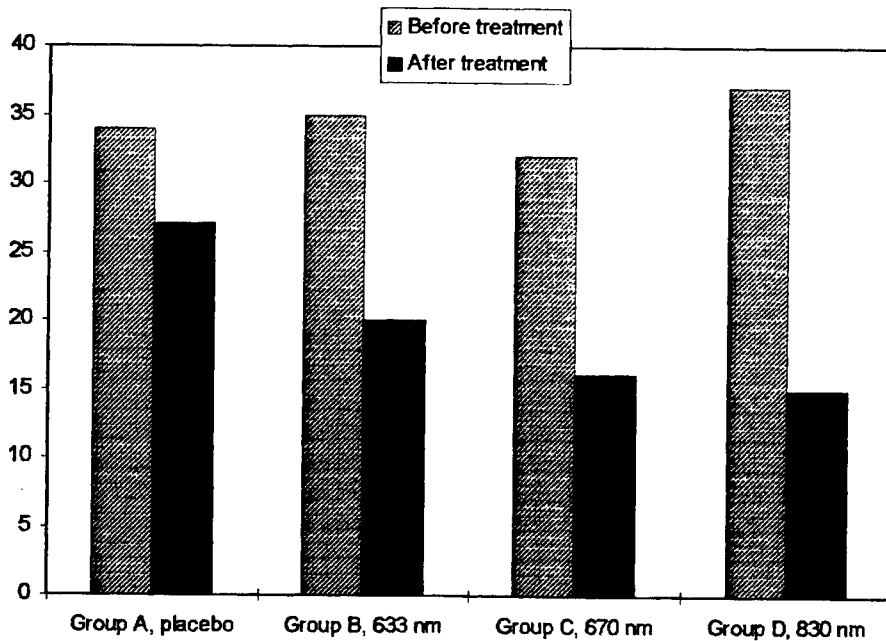


Fig.3 The walking time for 15 m before and after the treatment

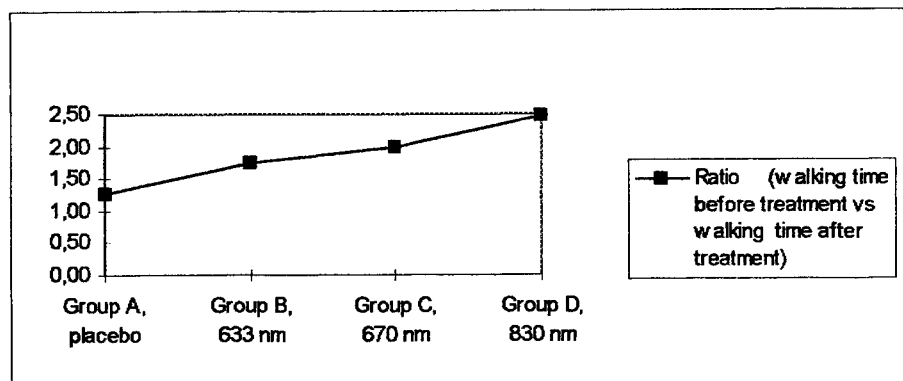


Fig.3 The ratio between the walking time before and, respectively, after the treatment

4. CONCLUSIONS

The laser diode based therapy is one of the medical recommendation as a low level laser therapy (LLLT). It has been reported to be very effective in removing a large variety of pains. The mechanism of pain removal or attenuation is discussed. LLLT may act on the metabolism of the algassic substances, may raise in the individual's pain threshold. Also, might be occurring an increase in the neural transfer of natural substances coupled with a block of the pain transmitters at the synaptic gate.

LLLT has also been shown to enhance the permeability of the vessel wall to possible anti-inflammatory agents.

The pain score method was decided on to evaluate the effectiveness of pain removal due to its simplicity of administration and ease of patient response. It is true that it is a purely subjective assessment and may thus be influenced by intellectual and emotional level of the patient or the way the questions are asked by the assessor. But, it is also true that we used other two objective methods: improvement of the flexion movement and 15 meters walktime, where significantly improvements were noticed.

The structure of the knee suffers the most intensive arthritic process. With the first signs of gonarthrosis, the prevention of obesity and abnormalities of static, the prevention of trauma, the laser radiation have a good effectiveness and prevent the enhancing of degenerative process.

None of the laser - treated patients have had bad side effects or complications as a consequence of laser therapy.

The irradiation must be delivered by spots in the painful points which are determined at clinical examination. The time of irradiation per point were of about 1 - 2 minutes and the energy density is between 10 - 15 J/cm².

If the time from the beginning of the disease is not so long the improvement is significant, especially with near infrared radiation whose penetration depth is higher (about 50 - 50 mm). The effectiveness is decreasing as the abnormalities are more important.

In the spite of the fact that the LLLT is not a total remedy it might be considered as a very useful adjutant of the classical therapy.

5. REFERENCES

1. K.Asada, Y.Yutani and A.Shimazu, " Diode laser therapy for rheumatoid arthritis: a clinical evaluation of 102 joints treated with low reactive level laser therapy (LLLT)", *Laser Therapy*, vol.1, no.3, sept.1989.
2. T.I.Karu and V.S.Letokhov, " Biological action of low intensity monochromatic light in the visible range", *Laser Photobiology and Photomedicine*, Plenum Press, edited by S.Martelucci and A.N.Chester, 1985.
3. T.I.Karu, L.V.Pyalibrat, G.S.Kalendo, R.O.Esenaliev, " Effects of monochromatic low intensity light and laser irradiation on adhesion of HeLa cells", *Lasers in Surgery and Medicine*, **18**, 171-177 (1996).

Low power lasers value it the treatment of symptomatic spondilosis

Ciprian Antipa¹, Vladimir Moldoveanu², Nicolae Rușcă³, Ion Bruckner¹, Mihaela Vlăiculescu¹, Elena Ionescu¹, Virgil Vasiliu⁴

1 - Colțea Clinical Hospital

2 - Bagdazar Clinical Hospital

3 - Genesis srl

4 - IFTAR Măgurele

Abstract

Low power laser (LPL) use in the treatment of arthrosic rheumatism is well known. From a total number of 280 patients with symptomatic spondilosis we finally selected 66, with changes of the EEG colour mapping. Theese investigation was done before and after treatment in order to obtain an objective method to appreciate the results. The patients were splited in laser group (36 patients treated with HeNe and IR diode LPL) and control group (30 patients treated with placebo laser). The results indicate a significant improvment of the symptoms at 77% of the patients from laser group as compared with 33% favourable results at the placebo laser. The EEG mapping improved at 58% patients from laser group as compared with 20% at the control group.

In conclusion LPL proves to be very efficient in the treatment o cervical spondilosis and EEG color mapping can be an useful method for the results control.

Keywords: low power laser, spondilosis, EEG mapping.

Even controversial, the low power laser (LPL) is used in the treatments of different kind of rheumatisms. The most importants objections against this therapy are the unknown intimal mechanism of action and the lack of objective appreciation of the results^{1, 3, 4, 10, 11}. The aim of the study is to increase the credibility of thees therapy.

1. Patients, Lasers and Method.

From an initial number of 280 patients with the diagnostic of cervical spondilosis (arthrosis of the cervical spine) claining pain and/or dizzines, we finally selected 66 patients of both sexes, age between 38 to 72 years. All thees 66 patients prezented EEG colour mapping changes.

We divided the patients into: laser group (36 of them) treated with lasers mentioned below and control group, 36 patients treated with placebo laser.

Lasers used were:

- Helium Neon (HeNe) laser, the wavelength 632,5 nm, with continuous emission in red, 2 mW power and spot size about 4 mm.

- Infrared diode laser, the wavelength 767 nm, with continuous emission, 3,5 mW power, skin application and spot size of 5 mm.

Laser irradiation was performed succesively with both lasers (the HeNe first) in 9 cervical points 1 minutes per points for every daily sessions, and also moved along some cervical circuits. The total number of session varied function of the clinical respons, between 6 to 10. (Fig. 1)

Results evaluation was done in two ways:

a) Self evaluation of every patient of the pain and dizziness scale with 10 points, before and after the treatment on a scale.

We consider results to be positive only if the individual difference was bigger than 3 points.

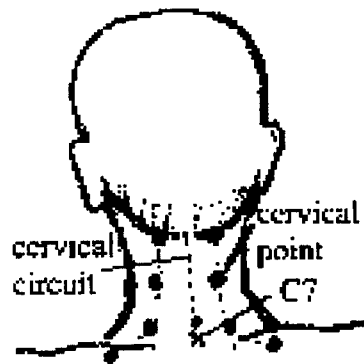


Fig. 1 Cervical points and circuits to irradiate

b) EEG colour mapping

In order to evaluate in objective manner the treatments' efficacy, we used the pathological relationship between morphological abnormalities produced by spondylotic process on the cervical vertebres and its effects on vertebrobasilar haemorheology.

The two groups of subjects were especially tested during resting periods, with extreme lateral rotation of the neck to the left or to the right, for one minute, in order to obtain the maximal subclinical vertebral artery dysfunction before and after the treatment.

The power of the electrophysiological data were analysed, on the four classic bands of frequency: delta (0-3 Hz), theta (3-8Hz), alfa (8-12Hz), beta (12Hz). We used the classic quantification of neurophysiologic expression because of sensitive relation between slow wave cerebral activity and regional dysfunction in cerebral blood flow⁹.

In order to avoid individual variations we used neurometrics techniques: all neurophysiological data from each group were added and averaged to obtain a general portrait of each group of subjects. On the resulting average colour group map we made comparisons regarding physiological conditions of the patients, before and after the treatment.

Statistical analysis of the clinical results was performed by a significancy test with the level of significance at 0,01 ($p < 0,01$).

2. Results

At the end of the study, clinical results of the HeNe and IR lasers regarding pain and dizziness, were good and very good, at 28 from the 36 patients of the laser group, meaning 77%, as compared to placebo laser group, 10 patients meaning 33%, have had good results (Fig. 2)

This difference between laser and placebo laser groups was statistically significant $p < 0,01$.

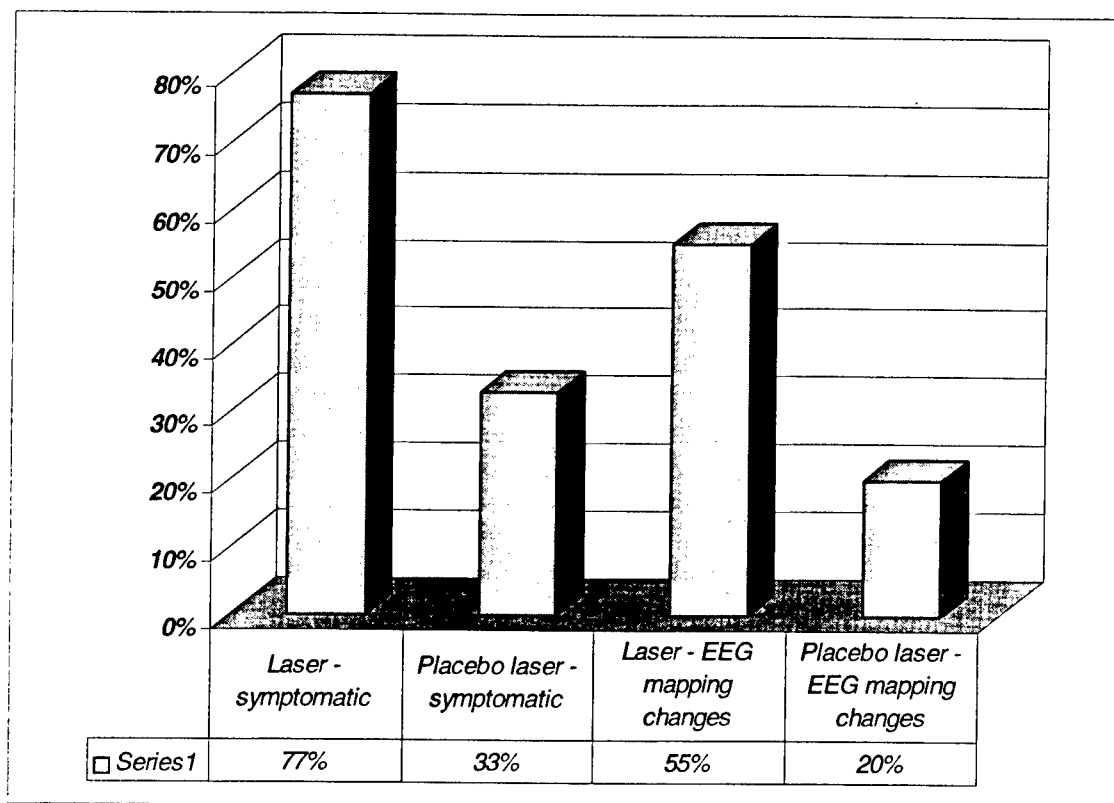


Fig. 2. Comparativ improvments of symptoms and EEG mapping for both groups

Regarding EEG average colour mapping, we noticed significant changes at 20 patients from laser group meaning 55%, as compared to placebo group 6 patients meaning 20%. The significant EEG mapping changes were founded at laser group in teta and delta domain (Fig. 3). At this moment, we have no satisfactory explanation for this.

We didn't find any side-effects on laser groups.

There were no radiological changes observed after the treatment at any of the groups. We also didn't note any difference of the therapeutical responses between male and female patients.

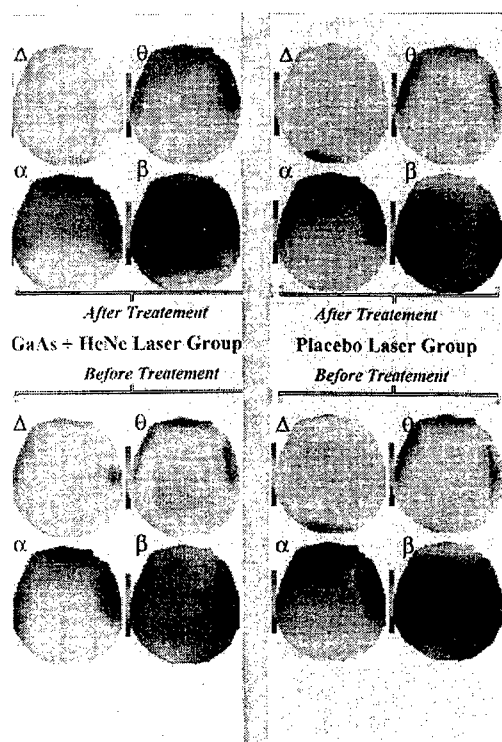


Fig. 3. Average group EEG colour mapping

3. Discussion

In spite of the relative small number of patients we can say the LPL treatment have good and very good results compared with placebo therapy^{2, 3, 5, 7}.

The results of the HeNe and GaAs groups could be explained by the possible rise of the optical window of the skin, by the engerical cumulative aport of the two lasers stimulating diffent photoreceptors, and by different photochemical wavelength depending effects in practically the same time^{1, 6}.

We think that an explanation of the low lasers favourable effects on pain could be the increase of the sensitive pain threshold, due to known effect of LPL on the diminution of the prostaglandine synthesis^{5, 1, 2}.

We used as an additional method for objective evaluation of the treatments effects, on cervical spondylosis exploiting the pathologic interference with vertebral arteries blood flow. The subclinical haemorheological dysfunction is amplified by peculiar position of cervical spine: maximal sustained lateral rotation for 1 minute. The cerebral electrophysiological expression of blood flow reduction as changes in EEG power spectra: from normal distribution to slow wave rising incidence where transient ischemic condition is accomplished.

By means of neurometrics techniques on the resulting colour maps before and after the treatment as an average group image, we objectively quantify the changes at cerebral level of the vertebral artery dysfunction, expressed especially in the theta and delta wave domain (see Figure 3). At the placebo laser group we couldn't notice any significant changes.

In other words, between the two groups, laser and placebo laser, we found obvious differences before and after treatment situations.

4. Conclusions

1. LPL treatment proved to be a very useful therapeutical method for cervical spondylosis, especially when used the association HeNe and IR diode. The percentages were 77% (laser group), as compared with 33% (placebo laser), with statistical significance.

2. We didn't found any side-effects at the patients treated by laser irradiation.

3. As a preliminary observation, EEG mapping seems to be an useful and objective method for the evaluation of the cervical spondylosis treatment efficiency, for the patients with vertebrobasilar haemorrhagic modifications.

5. References

1. C.Antipa, C.Moldovan, A.Podoleanu, -"Low Energy Lasers in Medicine and Biology" - in *Laser and Technology*, vol.4,3,:51-62,1994.

2. G.Galletti, L.Bolognani and G.Ussia Eds. - "*Laser Application in Medicine and Surgery*", Monduzzi, Bologna, 1992.

3. G.D.Baxter - "*Therapeutic Lasers - theory and practice*", C.Livingstone, 1994.

4. J.R.Basford - "Low Intensity Laser Therapy: still not an Established Clinical Tool" - in *Lasers in Surgery and Medicine*, 16,4,:331-342,1995.

5. C.Antipa, I.Bruckner, N.Crîngulescu, C.Moldovan, A.Podoleanu, Viorica Stănciulescu, Elena Ionescu - "Our clinical experience in low energy laser medical treatments" - in *Optical Engineering*, 35(5):1367-1371, May, 1996.

6. C.Antipa, V.Moldoveanu, N.Ruşcă, I.Bruckner, A.Podoleanu, V.Stănciulescu: "Low Energy Lasers treatment in rheumatic diseases - a long term study" - in *Laser-Tissue Interaction VI*, Steven L.Jacques edit., vol.2391:658-662,1995.

7. A.Amano, K.Miyagi, T.Azuma, Y.Ishira, S.Katsube, I.Aoyama, I.Saito - "Histological Studies on the Rheumatoid Synovial Membrane Irradiated with Low Energy Laser" - in *Lasers in Surgery and Medicine*, 15:290-294,1994.

8. B.Mokhar, G.D.Baxter, D.M.Walsh, A.J.Bell, J.M.Allen - "Double-Blind, Placebo-Controlled Investigation of the Effect of Combined Phototherapy/Low Intensity Laser Therapy Upon Experimental Ischaemic Pain in Humans" - in *Lasers in Surgery and Medicine*, 17:74-81,1995.

9. T.Iwase, N.Hori, T.Morioka, D.O.Carpenter - "Low Power Laser Irradiation Reduces Ischemic Damage in Hippocampal Glias in Vivo" - in *Lasers in Surgery and Medicine* 19:465-470,1996.

10. T.Karu - "Interaction of monochromatic visible light and near infrared radiation with cells: currently discussed mechanisms" - in *Laser Tissue Interaction VI*, S, Jacques and A.Katzireds, Pro SPIE - 2391, 576-580,1995.

11. M.G.Bouma, W.A.Bunmam, F.van den Wildenberg - "Low Energy Laser Irradiation Fails to Modulate the Inflammatory Function of Human Monocytes and Endothelial Cells" - in *Lasers in Surgery and Medicine* 19:207-215,1996.

12. N.Shimizu, M.Yamaguchi, T.Goseki, Y.Shibata, H.Takiguchi, T.Iwasawa, Y.Abiiko - "*Inhibition of prostaglandin E2 and interlenkin 1-beta production by low-power laser irradiation in stretched human periodontal ligament cells*" J-Dent-Resch 74(7):1382-8,jul.1995.

The dependence of the ablative effect at the surface of dentine samples, of the nanosecond laser pulses, on the laser wavelength.

C. Fenic, I. Chiş, R. Dabu, A. Stratan, I. Apostol, R. Stoian, C. Luculescu
National Institute for Laser, Plasma and Radiation Physics.

C. Ghica, L. Nistor
National Institute for Materials Science.

ABSTRACT

A Q-switched Nd:YAG laser beam and its second (SH) and fourth (FH) harmonics are focused onto the polished surface of dentine samples in order to compare the ablative effect for the three wavelengths. A photoacoustic technique is applied for the ablation threshold determination. The Scanning Electronic Microscope (SEM) images of the produced craters are investigated and the volume of ablated material is determined. The necessary optical constants for the ablation calculation are experimentally determined.

Keywords: thermoelastic regime, ablation regime, volume ablation, ablation threshold.

1. INTRODUCTION

The dental hard tissue is part of the dental enamel or of the dentine. The main constituent of both of them is the hydroxiapatite, whose concentration varies from 85% for enamel to 70% for dentine. This concentration is responsible for the difference in the hardness of the two tissues. We focused our investigation on the dentine ablation with a Q-switched Nd:YAG laser and with its second and fourth harmonics, in order to describe the phenomena in the laser-interaction with a such non homogenous material.

The ablation threshold was determined using a photoacoustic technique¹. Because the dentine samples required by this technique must be larger than a normal human tooth could supply, we used animal (swain) biological material, quite similar to human structure. The dentine samples were cut normal on the tooth axis with a diamond disc. It assures a good surface quality necessary to compare the ablation effect of the three laser wavelengths. The TEM₀₀ pulsed Nd:YAG laser and its harmonics are focused a little bit behind the surface of the sample, to avoid the air break-down. The small craters are analysed with a Scanning Electronic Microscope (SEM) type JEOL JEM 200CX. The depth of the craters was measured with a optical microscope Carl Zeiss Jena type NU 2.

2. EXPERIMENTAL SETUP.

The experimental arrangement, Fig.1, for the investigation of the dentine ablation threshold and of the dentine ablation, uses an oscillator-amplifier Nd:YAG laser configuration with TEM₀₀ output², equiped with a KTP II doubling crystal for SH generation and with an ADP I quadrupler for 4H generation.

The dentine sample DS is fixed in a special mechanical mount that allows the sample to be precisely translated by three micrometric screws in x, y, z directions.

The laser beam is focused by a quartz lens QL with a 30mm focal length on the dentine sample DS. A BaTiO₃ acoustic detector AD is attached at the rear side of the dentine sample for the ablation threshold determinations. A quartz beam splitter BS is used to illuminate a calibrated photodetector P for the pulse energy measurement. The calibration of the photodetector is made for the every wavelength using a TRG102 calorimeter. This signal triggers also a digital 200MHz TEK and the detected acoustic signal is aquired on a PC.

Special 1 mm thick dentine samples of human tooth are used in the focus of the QL lens to compare the ablative effect of the three wavelengths high above the ablation threshold of the UV radiation. For this purpose the output laser energy is

adjusted for the three wavelengths in the limit of (10-20)mJ per pulse, to allow a good comparison of the effects. After each pulse the sample is translated in XY plane with 300 μ m. So, for every wavelength there are a few small craters very well separated.

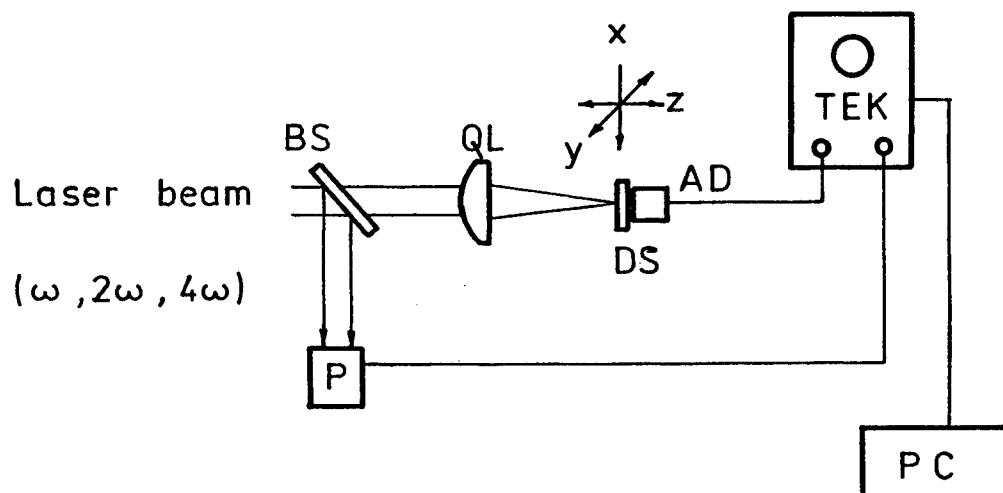


Fig.1 Experimental setup for the dentine ablation investigation

3. EXPERIMENTAL RESULTS

The optical reflectivity and absorption coefficient are experimentally determined using the three wavelengths of the Nd:YAG laser, in a very simple configured experimental setup, Fig.2.

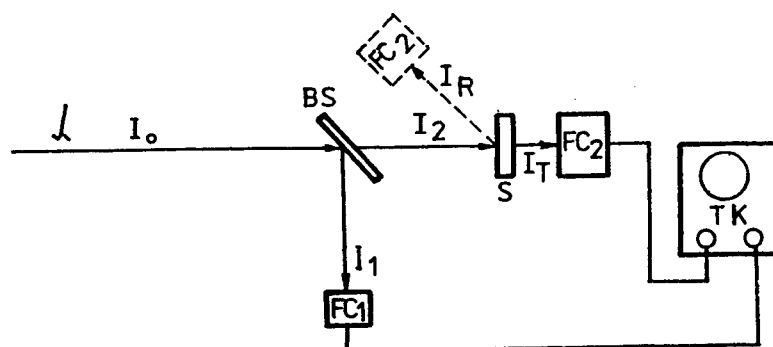


Fig.2 Experimental setup for dentine reflectivity and absorption coefficient measurements.

A 1 mm polished dentine sample S is used. With two ICCE large area silicon photocells, FC₁ and FC₂, type DFR-01 are measured the incident and reflected or transmitted intensities. It is supposed that the photocells have the same linear dependence of the output signal with the light intensity in the measured domain. The reference intensity I₁ registered with FC₁ is a measure of the I₂, incident on the surface of the sample. The calibration coefficient $k = I_2/I_1$ is determined for the three wavelengths. For the reflectivity measurements the deflection angle was under 30° to diminish the errors due to polarisation. The reflectivity is given by

$$R = I_R/I_2 = I_R/kI_1 \quad (1)$$

where I_R is the reflected beam measured with FC_2 . For the absorption measurements the sample is put very close to the detector surface, to diminish the scattering losses. The absorption coefficient α is given by

$$\alpha = (1/d) \ln [(1-R) k I_1 / I_T] \quad (2)$$

where d is the thickness of the sample and I_T the transmitted beam measured with FC_2 . The measured optical reflectance and absorption coefficient are given in the Table 1.

Table 1. The general data involved in the dentine ablation experiments

λ nm	R	α cm ⁻¹	E 10 ⁻³ J	τ ns	energy fluence 10 ³ Jcm ⁻²	power fluence 10 ¹¹ Wcm ⁻²	I_T μ m	d μ m	V_a 10 ⁻¹⁵ m ³	V_{em} 10 ⁻¹⁵ m ³
1064	0.1	8.1	20	15	6.3	4.2	2.3	70	1008	732
532	0.01	0.9	10	10	12	12	1.9	25	22	65
266	0.03	36.3	8	7	1	1.5	1.6	16	441	15

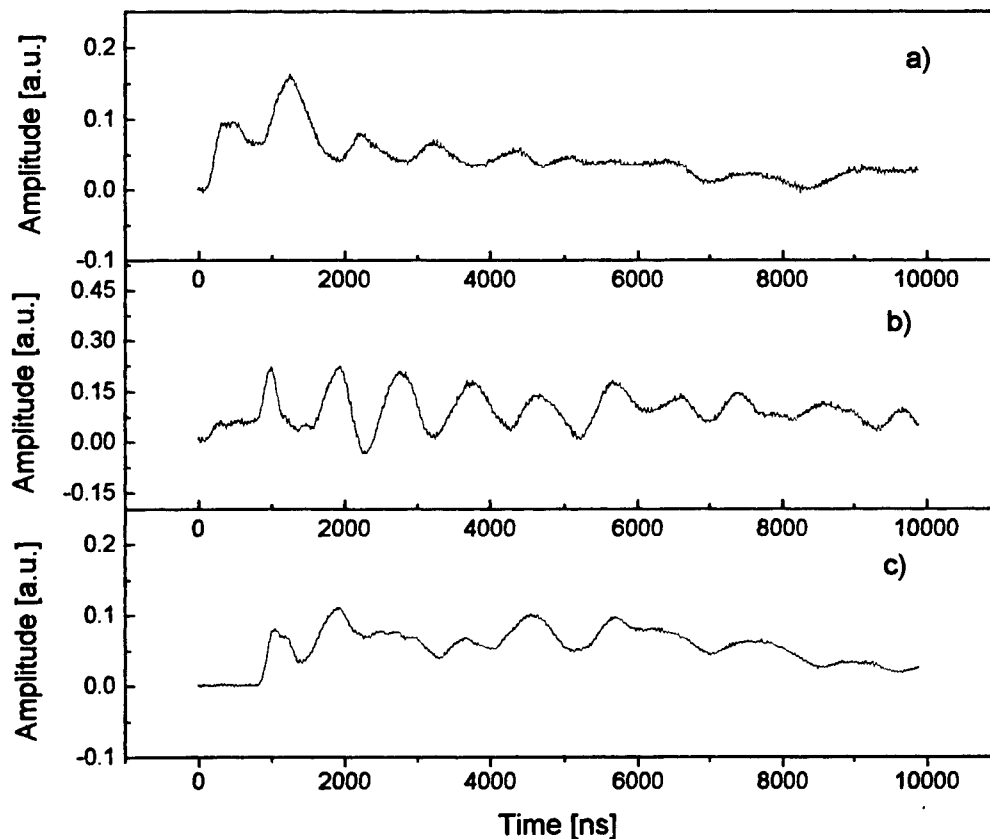


Fig.3 The acoustic signal in the ablative regime for the laser-dentine interaction.

a) $\lambda = 1064$ nm; b) $\lambda = 532$ nm; c) $\lambda = 266$ nm. The small delay of the acoustic signal in a) and b) suggests the ablation occurs close to the rear surface of the sample, near the piezoelectric detector.

The transparency of the dentine material, as shown in the Table 1, suggests that only UV radiation could give an ablative effect. The suggestion is confirmed by the photoacoustic technique used for the ablation threshold determination. Due to the small absorption coefficients, in case of the 1064nm and 532nm wavelengths the ultrasounds source generated by the laser pulse in the sample material take place in the volume, near the rear surface of the sample, close to the piezoelectric detector. This is proved by the small delay between the laser pulse and the acoustic signal, Fig.3a,b, which means the propagation distance is small comparing to the sample thickness. For the UV radiation at 266nm, where the absorption coefficient is

higher, the acoustic source will be formed just beneath the irradiated surface, so there will be a significant delay between those two signals, due to the propagation time of the elastic wave in the material bulk, Fig.3c.

The dependence of the amplitude of the first peak in the acoustic signal train on the laser fluence, registers a change in the slope value. This point gives the ablation threshold, when the thermoelastic effect of the laser pulse near the surface of the sample changes to an explosive one, with material removal. The same ablation point could be more precisely revealed by the so called "slope change", a parameter which describes the evolution in the acoustic waveform shape in the thermoelastic and ablation regimes. The transition from the thermoelastic to the ablation regime appears in the structure of the acoustic signal, where a particular position at sheare arrival of the acoustic train changes the slope. The phenomena is described in detail in the reference 1.

Fig.4a shows the waveforms of the acoustic signal for UV irradiation in the thermoelastic and ablative regime. Fig.4b shows the ablation threshold determined from the dependence of the amplitude of the acoustic signal on the laser fluence and from the "slope change" evolution as well. On the slope change-energy representation one can notice the negative evolution until the ablation source will compensate and then dominate the thermoelastic one, when a positive growth will take place. The ablation threshold was considered at the point where the "slope change" curve crosses the $y = 0$ axis and becomes positive, which means the positive slope of the ablation source will cancel the negative slope of the thermoelastic source. It could be seen that for the UV radiation the ablation threshold is reached at an energy fluence of 10 J/cm^2 . This value is an order of magnitude higher than the one reported for amorphous hydroxiapatite³, the main constituent of dentine, where it is in crystalline shape.

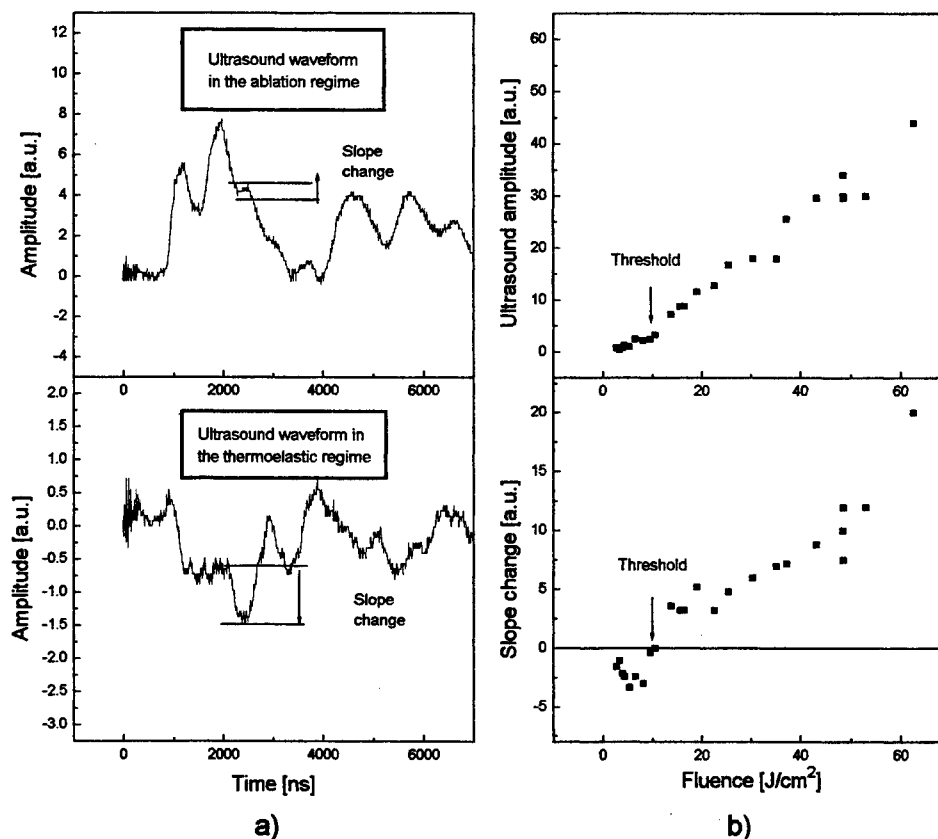


Fig.4 a) The acoustic waveform for UV irradiation in thermoelastic and ablative regime. The "slope change" estimation. b) The ablation threshold from the dependence of the acoustic amplitude and of the "slope change" on the laser fluence.

4. ABLATION RATE ESTIMATION

The hydroxiapatite, in the shape of amorphous, sintered material, is very absorbent ($\alpha=910\text{cm}^{-1}$) and with a high reflectivity ($R=0.7$)⁴. In spite of the high concentration of hydroxiapatite in the dentine material, dentine is quite transparent, even for the UV radiation, because of the microcrystalline structure of the hydroxiapatite in a collagen compound. The ablation mechanism in this circumstances can not be assimilated with none of the classical (surface) ablation modeling: thermal ablation⁵ or ablation pressure model⁶. This could be applied if

$$l_T = 2(D\tau)^{1/2} \gg 1/\alpha \quad (3)$$

where l_T is called the thermal length of the material, τ the pulse duration and α the absorption coefficient of the dentine, given in the Table1. D is the thermal diffusivity of the material given by

$$D = k_T / \rho c_p \quad (4)$$

where $k_T = 10^{-2} \text{ Wcm}^{-1}\text{K}^{-1}$ is the thermal conductivity coefficient⁴, $c_p = 0.772 \text{ J/g } ^\circ\text{K}$ the specific heat⁷ and $\rho = 1.4\text{gcm}^{-3}$ the dentine density experimentally determined. For k_T and c_p were taken the values given in the references 4 and 6 for hydroxiapatite, considering its high concentration in the dentine material.

With these values $D = 9.2 \cdot 10^{-3} \text{ cm}^2\text{s}^{-1}$. From the values calculated for l_T (Table1) it results that the condition (3) is not fulfilled for any of the three wavelengths.

In our experiments irradiation fluences are more than two orders of magnitude higher than the ablation threshold, evidenced for UV radiation with the described photoacoustic technique. The craters obtained in this conditions are the result of a volume absorption, near the surface of the sample, where the laser beam is focused. The effect is called by analogy "volume" ablation. This mechanism implies vaporisation of the material, break of clusters, chemical decomposition and explosive ejection of particles. The absorption of laser energy in this cloud leads to a evolution of an ablated plasma in free atmosphere with an increasing of the plasma density in the path of the beam, the enhancing of photon absorption and decreasing of laser-target coupling.

The above mentioned ablation models being inoperable to the volume absorption, evidenced in our experiments, we estimate the ablation rate considering the microscopic measured crater depth d given in Table1 and the energy absorbed in target up to this depth. A rough approximation was made neglecting the losses in the generated plasma and target bulk. The heat equation implied in volume ablation leads to the an ablation rate given by

$$V_a \cong E(1-R)\alpha d / \rho c_p \Delta T \quad (5)$$

where E is the laser pulse energy given in Table1, $\rho = 1.4\text{gcm}^{-3}$ the dentine density experimentally determined, $c_p = 0.772\text{J/g } ^\circ\text{K}$ the specific heat⁷ and $\Delta T = 900^\circ\text{C}$, the temperature for chemical decomposition of hydroxiapatite⁴, lower than vaporisation temperature. The enthalpy was neglected because the hydroxiapatite is a complex molecule with a supposed low dissociation energy value.

From the SEM images of the small craters produced by the three wavelengths of the Nd:YAG laser, one can see that due to the non homogeneous structure of the dentine, the shape of the craters differs from a pulse to other. To compare the calculated ablated volume with the real volume of the craters, experimentally determined V_{exp} , it was taken into account a averaged size of the crater, assimilated with a circular cone with a averaged diameter of the base and a averaged highest. Fig.5 shows some of the SEM images of craters produced with the three wavelengths. In Table1 are compared the experimental values of ablated volumes and those calculated with relation (5).

The relatively good agreement between the calculated and experimental values of ablated volumes for infrared and visible radiation, suggests that the volume ablation with a low absorption of laser radiation in the generated plasma is a good supposition for dentine material interaction with these wavelengths. The major discrepancy in the case of UV interaction is a proof for a strong absorption of this radiation in the relatively dense plasma generated near the surface of the target (evidenced and by the photoacoustic technique), decreasing the pulse energy coupling to the target and increasing the internal energy of the plasma species. For the IR and green photons main absorption occurs at the critical density surface,

most of it being transferred to the target by superheated plasma. Another fact, difficult to estimate, occurring in transparent materials⁸, is the increasing of the absorption coefficient after the structural changes initiated in the laser-target interaction. This fact we suppose to be a possible explanation for the relatively high difference between the calculated and experimental ablated volumes in the interaction with green radiation, where α has the lowest value for dentine material.

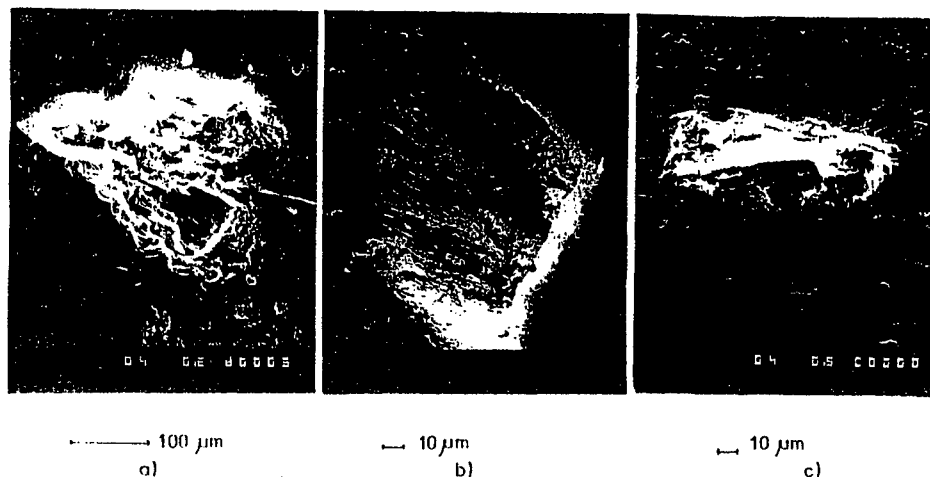


Fig.5 SEM images of some craters produced by laser pulses of a) 1064nm, b) 532nm, c) 266nm

5. CONCLUSIONS

A relatively difficult to investigate material like dentine was ablated with the fundamental wavelength, the second and the fourth harmonics of an Q-switched Nd:YAG laser. Some opto-physical data were experimentally determined in order to calculate the ablated volume after a simple volume-ablation model proposed, neglecting the absorption in the generated plasma. A relatively good agreement with the experimentally determined ablated volumes was obtained for infrared and green radiation. A photoacoustic technique was used for ablation threshold determination.

REFERENCES

1. I. Apostol, R. Stoian, R. Dabu and A. Stratan, "Optical and photoacoustic studies of target ablation for LPVD of YBCO thin films", *Journal of Alloys and Compounds*, vol.251, pp.48-55, 1997.
2. A. Stratan, C. Fenic, R. Dabu, I.V. Grozescu and L. Muscalu, "TEM₀₀ Nd:YAG lasers with dynamic stable resonators", in *Proc. SPIE* vol. 2461, pp. 47-49, 1995.
3. V. N. Bagratashvili, E. N. Antonov, E. N. Sobol and V. K. Popov, "Macroparticle distribution and chemical composition of laser deposited apatite coatings", *Appl. Phys. Lett.*, vol. 66, pp. 2451-2453, 1995.
4. L. Torrisi and R. Setola, "Thermally assisted hydroxiapatite obtained by pulsed-laser deposition on titanium substrates", *Thin Solid Films*, vol. 227, pp. 32-36, 1993.
5. Bauerle, "Laser Processing and Chemistry", Springer Verlag Berlin, 1996.
6. C. R. Phipps et al, "Impulse coupling to targets in vacuum by KrF, HF and CO₂ single-pulse lasers", *J. Appl.Phys.*, vol. 64, pp. 1083-1096, 1988.
7. E. P. Egan, T. Wakefield, and K. L. Elmore, "Low Temperature Heat Capacity and Entropy of Hydroxiapatite", *J. of Am. Chem. Soc.*, vol.73, pp. 5579-5583, 1951.
8. L. L. Chase, "Laser Ablation. Principles and Applications", ed. J. C. Miller, Springer-Verlag Berlin 1994.

Comparison of action on chromatin of an UV laser radiation and of a radiomimetic substance

Irina Radulescu, Liliana Radu, Ruxandra Serbanescu*, V. D. Nelea**, C. Martin**, I. N. Mihailescu**

Molecular Genetics & Radiobiology Department, Victor Babes Institute, Spl. Independentei 99-101, Bucharest, 76201, Romania,

*Biophysics Department, Faculty of Physics, Bucharest, Romania

**National Institute for Lasers, Plasma and Radiation Physics, Department of Lasers, Bucharest MG-36, 76900, Romania

ABSTRACT

The damages of the complex of deoxyribonucleic acid (DNA) and proteins from chromatin, produced by the UV laser radiation and/or by the treatment with a radiomimetic substance, bleomycin, were compared.

The laser radiation and bleomycin effects on chromatin structure were determined by the static and dynamic fluorimetry of chromatin complexes with the DNA specific ligand - proflavine and by the analysis of tryptophan chromatin intrinsic fluorescence.

Time resolved spectroscopy is a sensitive technique which allows to determine the excited state lifetimes of chromatin - proflavine complexes. Also, the percentage contributions to the fluorescence of proflavine, bound and unbound to chromatin DNA, were evaluated.

The damages produced by the UV laser radiation on chromatin are similar with those of radiomimetic substance action and consists in DNA and proteins destruction.

The DNA damage degree has been determined. The obtained results may constitute some indications in the laser utilisation in radiochemotherapy.

Keywords: chromatin DNA, bleomycin, UV laser, fluorimetry, time resolved spectroscopy

1. INTRODUCTION

The extensive laser utilisation in biomedical applications requires the elucidation of laser action mechanisms on cellular compounds and especially on chromatin, DNA and proteins, which exists in eukaryotic cells.

Up to now, there are few data about the effects of high intensity UV laser on polynucleotides, plasmid DNA and nucleoproteins¹⁻³, but some aspects concerning the UV laser mechanisms and effects are still unknown.

The irreversible photoproducts formation, due to multiphotonic excitation is the effect of high intensity UV laser irradiation of DNA. These photoproducts are similar to those produced by ionising radiation¹.

The radiomimetic substance bleomycin has a citotoxic action due to the attachment to DNA of bleomycin - Cu²⁺ or Fe³⁺ complexes and, as a result, the DNA break-up.

Our previous studies were done on laser action on DNA⁴ and on normal and tumoral chromatin^{5,6}, by methods of absorption and fluorescence spectroscopy, by precision calorimetry, by determination of the susceptibility to DN - ase and by H-NMR spectroscopy.

In this paper we investigate the excimer laser - chromatin interactions by a more sensitive method - the determination of dynamic characteristics (fluorescence lifetimes of excited states and the percentage contributions to the fluorescence) of chromatin - ligand complexes and by the intrinsic fluorescence determinations. The damages induced by UV laser radiation and by bleomycin action were compared.

2. MATERIALS AND METHODS

Some lots of Wistar rats were pre-treated with the radiometric substance bleomycin (0.33 mg/Kg body). The chromatin was extracted⁷ from rats livers (submitted to 24 h partial hepatectomy).

The used concentrations were 2.5×10^{-4} M for chromatin DNA, $(0.5 \pm 2.5) \times 10^{-4}$ M for DNA (Sigma) and 3×10^{-5} M for proflavine (Sigma).

An UV laser radiation with $\lambda = 248$ nm, from an Iofan 1701 laser, with 100 mJ dose/pulse and $\nu = 50$ Hz was used in doses of 0.5 - 3.0 MJ/m². All irradiations were done at room temperature.

The chromatin - proflavine complexes fluorescence ($\lambda_{ex} = 444$ nm, $\lambda_{em} = 510$ nm) and the intrinsic fluorescence of chromatin tryptophan ($\lambda_{ex} = 290$ nm, $\lambda_{em} = 345$ nm) were determined with an Aminco - Bowman spectrophotofluorimeter.

The fluorescence decay profiles were recorded by means of a time resolved fluorimeter FL - 900 CD (Edinburgh Analytical Instruments) based on time correlated single photon counting method. A hydrogen flash lamp with a 1 ns FWHM at 39 KHz frequency was used as a light source with excitation wavelength set at 444 nm. The fluorescence intensity decays were least - squares fitted to single or double exponential functions by the Marquardt deconvolution method⁸. The χ^2 value (≈ 1), standard deviations in the weighted residuals, autocorrelation function and Durbin - Watson parameter were inspected for the fit test. The samples were measured in a 1 cm optical path quartz cell at room temperature ($20 \pm 3^\circ\text{C}$).

3. RESULTS AND DISCUSSIONS

3.1 Static fluorimetry

According to the state (bound or unbound to chromatin DNA), the used ligand (proflavine) shows different fluorescence parameters. At constant ligand concentration, the relative fluorescence intensities of DNA - proflavine decrease with the DNA concentration. By 444 nm excitation of chromatin - proflavine sample was obtained the fluorescence quenching of the ligand. This fact is due to the formation of DNA - proflavine complexes which have a very low quantum yield, compared to that of free ligand. The relative fluorescence intensities of chromatin - proflavine complexes are higher than those corresponding to DNA concentration within chromatin samples. This is explained by the hindrance of ligand binding to chromatin DNA, due to the existence of proteins. By comparison with relative fluorescence intensities of DNA - proflavine complexes, was deduced the available DNA proportion for ligand coupling to be 33,2 %.

Figure 1 presents the relative fluorescence intensities (the intensities of irradiated samples divided by this of unirradiated chromatin - ligand sample) of proflavine complexes with laser irradiated chromatin with and without radiomimetic substance bleomycin.

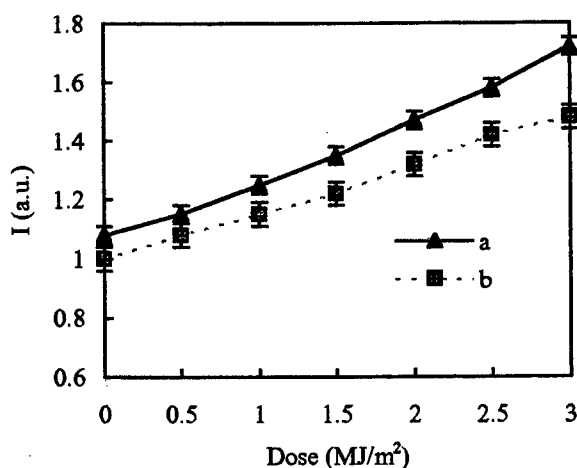


Figure 1. The effect of UV laser radiation on the relative fluorescence intensities of chromatin - proflavine complexes, with (a) or without (b) treatment with bleomycin

The relative fluorescence intensities of chromatin - proflavine complexes increase with laser dose, indicating the laser action on chromatin DNA: the decrease of the chromatin DNA double helix proportion. The estimation of DNA lesions proportion is possible because of proflavine capacity to bind only to undamaged DNA. The damage of DNA is the

result of UV laser irradiation and /or of the treatment with bleomycin, which has a cvasianalogue effect. For unirradiated samples, the relative fluorescence intensity increases with 32% by treatment with bleomycin. The variation of fluorescence intensity values with laser radiation dose is greater in bleomycin case, because the UV laser and treatment with bleomycin actions were cumulated. A 58.7% decrease of the proflavine bound proportion in the chromatin - bleomycin sample irradiated with 3 MJ/m^2 is produced. For smaller doses, the protective effect of proteins and of the compactness degree of DNA within chromatin was important.

By UV laser irradiation of chromatin, damages not only on chromatin DNA level, but also on chromatin proteins were produced. This is based on intrinsic fluorescence analysis of chromatin.

In figure 2 are presented the tryptophan intrinsic relative fluorescence intensities dependence on UV laser dose, for chromatin with or without treatment with bleomycin (the intrinsic fluorescence intensities of irradiated samples divided by this of unirradiated chromatin sample).

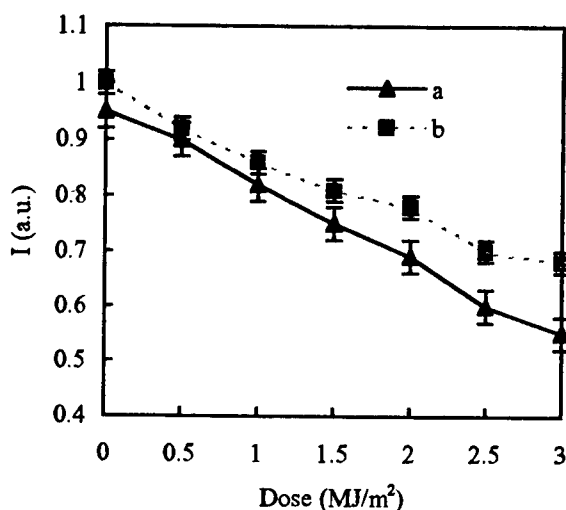


Figure 2. The effect of UV laser radiation on the intrinsic fluorescence intensities of chromatin tryptophan, with (a) or without (b) treatment with bleomycin

The decrease of intrinsic fluorescence intensities with laser dose denotes a destruction of chromatin proteins, which determine the modifications in tryptophan environment, followed by a nonradiative deexcitation process. The effect is emphasised with 15% by treatment with bleomycin. For this result, the supplementary protein lesions produced by radiomimetic substance are responsible. The 10 nm redshift of the emission peak for chromatin treated with bleomycin and 3 MJ/m^2 irradiated, indicates the tryptophan localization near the protein - solvent interface, so a unpacked chromatin structure.

3.2 Time resolved fluorimetry

Time resolved fluorescence studies indicate the existence for chromatin - ligand samples of two fluorescence lifetimes of excited states of proflavine: free ($\tau_1 = 5.38 \pm 0.04 \text{ ns}$) and bound to chromatin DNA ($\tau_2 = 1.09 \pm 0.09 \text{ ns}$). By the deconvolution method, the fluorescence decay curves of chromatin - proflavine samples, with or without radiomimetic substance, were fitted to double-exponential functions (fig. 3).

No significant differences of lifetime values for pre-treated chromatin have been observed, as compared to the fluorescence lifetimes for normal chromatin (table 1). One can notice the decrease of bound state lifetime for laser doses over 2 MJ/m^2 . That is explained by the conformational changes of whole chromatin after irradiation; the presence of proteins in chromatin is not enough to protect DNA against UV laser high doses.

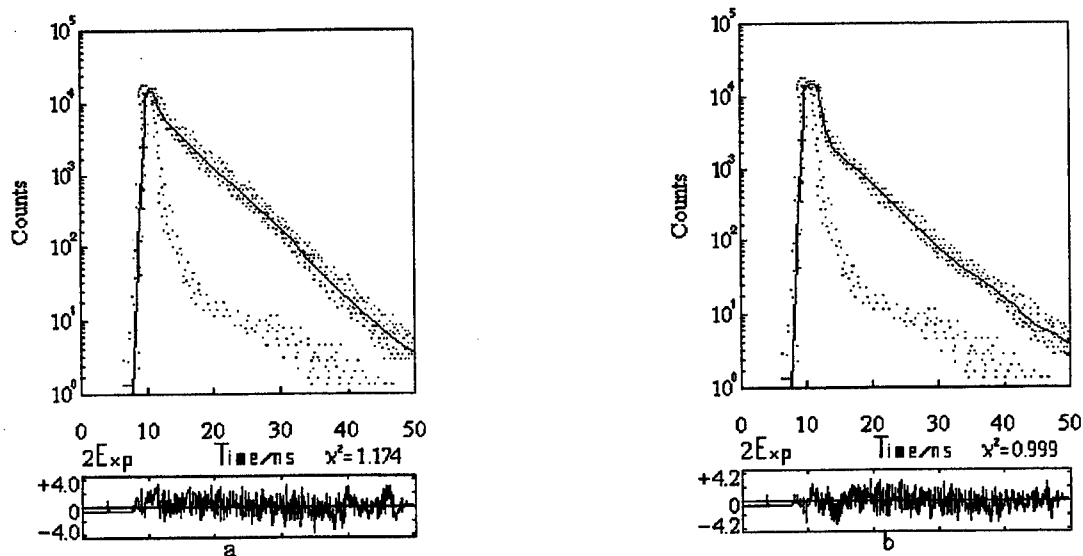


Figure 3. The fluorescence decay curves of chromatin - proflavine samples, with (a) and without radiomimetic substance (b), (for 3 MJ/m² UV laser dose) fitted to double exponential functions. Below the decay curves, standard errors of the fit were presented.

Table 1. The fluorescence lifetimes ($\tau_1 \pm 0.05$, $\tau_2 \pm 0.1$)(ns) for chromatin samples UV laser irradiated, with or without treatment with bleomycin.

Dose (MJ/m ²)	with treatment		without treatment	
	τ_1 (ns)	τ_2 (ns)	τ_1 (ns)	τ_2 (ns)
0	5.21	0.98	5.38	1.09
0.5	5.18	1.04	5.22	1.05
1	5.28	1.01	5.35	0.98
1.5	5.35	0.89	5.27	1.02
2	5.40	0.80	5.33	0.86
2.5	5.31	0.62	5.28	0.77
3	5.38	0.48	5.40	0.65

The DNA damage percent was defined as:

$$\% \text{ DNA damage} = \frac{f_2(0) - f_2^{a,b}(\text{dose})}{f_2(0)},$$

where $f_2(0)$ and $f_2^{a,b}(\text{dose})$ were the percentage contributions to the fluorescence of bound ligand, for unirradiated chromatin sample and irradiated chromatin samples, respectively (^a with and ^b without bleomycin).

The DNA damage percent versus laser dose is represented in figure 4. An increasing dependence of proflavine accessible DNA damage with the UV laser dose was obtained. By treatment with bleomycin, a 8.2% DNA damage was determined. For irradiated chromatin pre-treated with bleomycin, the DNA damage was 22% bigger comparatively with the DNA damage of untreated chromatin after UV laser irradiation (3 MJ/m²).A 54.2% DNA damage in bleomycin -

chromatin sample irradiated with 3 MJ/m^2 was obtained. An intensified destructive action of UV laser radiation is produced in chromatin DNA structure by bleomycin. For low doses, the chromatin proteins have an important role in protection.

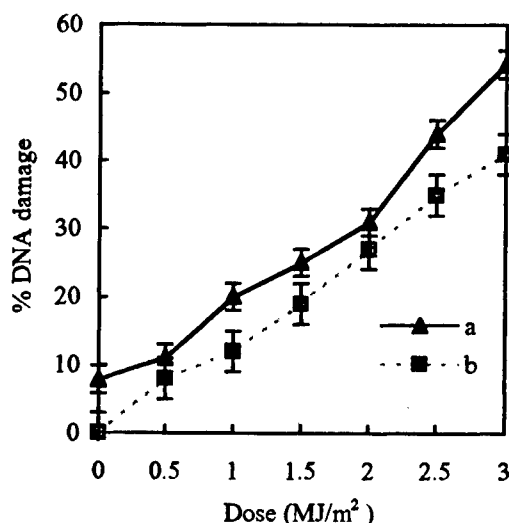


Figure 4. The effect of UV laser radiation on chromatin DNA accessible for the ligand, with (a) or without (b) treatment with bleomycin

4. CONCLUSIONS

By static fluorescence and especially by time resolved spectroscopy, the chromatin damage after UV laser irradiation has been precisely established. The effects of UV laser radiation on chromatin were: conformational changes of whole chromatin, chromatin DNA strand breaks with the reduction of the DNA double helix proportion, damage of chromatin proteins. These effects are most important in case of treatment with bleomycin, not only on chromatin DNA, but also on chromatin proteins. The protective role of proteins within chromatin is important.

5. REFERENCES

1. D. Schulte-Frohlinde, M.G. Simic and H. Gerner, "Laser induced strand break formation in DNA and polynucleotides," *Photochem. Photobiol.* **52** (6), 1137-1151 (1990).
2. D.T. Croke, W. Blau, C. OhUigin, J.M. Kelly and D.J. McConnell, "Photolysis of phosphodiester bonds in plasmid DNA by high intensity UV laser irradiation," *Photochem. Photobiol.* **47** (4), 527-536 (1988).
3. O. Kovalsky and E.I. Budowsky, "Laser (two-quantum) photolysis of polynucleotides: quantitative processing of results," *Photochem. Photobiol.* **51** (5), 659-665 (1990).
4. L. Radu, M. Stirbet, V. Preoteasa, O. Horer, D. Gostian and G. Ganciu, "The effect of laser radiation on DNA," *Stud.&Res. Physic* **10**, 553-557 (1991).
5. L. Radu, V. Preoteasa and Z. Lenghel, "The action of anticancer drugs thiotepa and lomustine and of E and A vitamins on tumor chromatin, analyzed by thermal transition, fluorescence methods and ^1H -NMR spectroscopy," *J. Molec. Struct.* **348**, 29-32 (1995).
6. L. Radu, V. Preoteasa, I. Radulescu and S. Radu, "Fluorescence lifetime, precision calorimetry and fluorescence energy transfer measurements in the study of normal and tumoral chromatin structure," *J. Molec. Struct.*, in press.
7. R.D. Kornberg, J.W. LaPointe and Y. Lorch, "Preparation of nucleosomes and chromatin," *Meth. in Enzym.* **170**, 3-14 (1989).
8. J.R. Lakowicz et al., *Topics in Fluorescence Spectroscopy*, Vol. II, Plenum Press, New York, 1991.

Laser Therapy in Ocular Tumors

B. Cârstocea, O. Gafencu, S. Apostol, M. Ioniță

Ophthalmology Clinic, Central Military Hospital (CMH),
Plevnei St., No. 36, Bucharest, Romania

A. Moroșeanu, T. Dascălu, V. Lupei

National Institute for Lasers, Plasma and Radiation Physics
NILPRP, Bucharest-Magurele, P. O. Box MG-36, Romania

V. Ioniță-Mânzatu

Biotechnos S. A., Dumbrava Roșie St., No. 23, Bucharest, Romania

ABSTRACT

The medical laser equipments made at NILPRP have been exploited intensively for more than 10 years at CMH. The availability and reliability of the first like-on equipment have increased, following improvements in optical delivery system and cooling circuit. This paper shows the impact of technical advances on the development of ophthalmologic laser therapy. Intraocular tumors pose special problems of diagnosis and treatment. Diagnostic methods include addition to systemic and ophthalmologic examinations, ancillary examinations, such as transillumination, fluorescence angiography, ultrasonography, radioactive phosphorus uptake tests, radiology, computerized tomography and fine-needle aspiration biopsy with cytological analyses. The enucleation of the involved eye used to be a generally accepted management of malignant tumors. Improved therapeutic methods such as photocoagulation and better surgical techniques now provide a variety of therapeutic alternatives. This study covers 31 cases of intraocular tumors that were managed either by Argon Laser photocoagulation and/or by Nd:YAG laser surgical treatment. Four cases were intraocular metastases and 17 cases were primitive intraocular tumors. Argon laser therapy proved to be totally ineffective for intraocular metastases but very adequate therapy for primitive tumors. Tumor extirpations (choroidal, ciliary body or iris tumors) using Nd:YAG laser lancet proved to be more suitable than classic surgery.

Keywords: medical laser, ophthalmology, laser therapy, intraocular tumors, photocoagulation, laser surgery

1. INTRODUCTION

Intraocular tumors pose special problems of diagnosis and treatment. Since the therapy of intraocular neoplasm varies greatly according to the type of tumor, it is important first to determine the correct diagnosis.¹

Diagnostic methods include in addition to systemic and ophthalmologic examinations, ancillary studies such as transillumination, fluorescent angiography, ultrasonography, radioactive phosphorus uptake tests, radiology, computerized tomography and fine-needle aspiration biopsy with cytological analysis.

Important factors in making a therapeutic decision include: type of tumor and whether it is benign or malignant, location of the lesion, age and health of the patient, condition of the fellow eye.

Benign tumors are, generally, managed more conservatively than malignant ones. Tumors located near the fovea or optic disc causing visual loss are often managed differently from similar, but asymptomatic tumors located in the peripheral fundus. Treatment is also different for chronically ill elderly patients or for those with the tumor in their only useful eye.

2. EXPERIMENTAL RESULTS

Last year, newly developed methods of treatment improved a lot. Previously, enucleation of the involved eye was the generally accepted management of malignant tumors. That is not satisfactory for benign tumors, or monophthalmic patients or small malignant tumors. It is also well known that even a benign tumor can determine significant visual loss from secondary complications.

Improved therapeutic methods such as irradiation, photocoagulation and cryotherapy and better surgical techniques, combined with improved understanding of the biological behavior of various types of tumor, now provide a variety of therapeutic alternatives.^{2,3}

Depending on the overall clinical situation, a particular tumor may now be managed by simple observation, photocoagulation (xenon arc or argon laser), cryotherapy, diathermy, local resection, enucleation, chemotherapy or immunotherapy, or by a combination of these methods, or irradiation with a cyclotron-emitted proton beam.

All these arguments determined us to apply laser therapy in a few cases of intraocular tumors.^{4,5}

Our study consists of 4 cases of intraocular metastasis (three of them with the origin in a breast neoplasm and one in a bronchopulmonary neoplasm), 5 cases of primary intraocular tumors (probably melanoma) and 12 cases of small intraocular neoplasm in adult patients.

All these patients suffered argon laser photocoagulation. The uselessness of this type of therapy was demonstrated in metastatic tumors (all 4 patients died within a period of time of 6-12 months of either metastase or cachexy).

The rest of 17 cases were monitored for a long period of time (2-9 years). The diagnosis was based on angiography, clinical appearance and other paraclinical investigations. We completed these investigations with ultrasound sonography A & B, in order to eliminate the possibility of extraocular extensions of the tumor, and leukocyte adherence inhibition (LAI) test (an immunological test of malignancy).

Photocoagulation was carried out using argon laser Coherent 900, in several sessions, around the margins of the tumors using a spot size of 500 μm , with duration of 0.2-0.5 seconds and a power setting of 500-1000 mW. The intensity of the visible coagulation effect varies with the degree of pigmentation of the fundus. The purpose of this photocoagulation is to obtain an area of chorioretinal atrophy with the destruction of choroidal blood supply.⁶

Another session of treatment, using the same instrument setting, is done to cover the surface of the tumor about three weeks after the first session. This time the laser spots must be confluent. A small flat area of pigmentation often remains in the center of the scar. This central area is studied by fluorescent angiography and when it is hypofluorescent no further treatment is necessary.

During the surveillance period, patients supported several fluorescent angiographies and LAI tests, that were necessary for the identification of the active areas.

In 15 of these 17 cases there was no extension, in surface or in thickness, of the tumor.

One case 2 years after photocoagulation, was enucleated (the tumor was more prominent and much more extended).

The histopathological examination showed a choroidal melanosarcoma. Although the photocoagulation was carried out before enucleation there were no coagulated cells. The patient survived 2 years after surgery.

A similar case (the 17-th) was, in fact a metastatic tumor of an unknown pulmonary neoplasm and the patient died 6 months after enucleation.

Argon laser photocoagulation proved to be one of the most adequate therapeutic solutions in small intraocular tumors (smaller than 3 papillary diameters and maximum 3-4 D thickness). This therapy should be associated with non-specific Calmette-Guerinebacillus (CGB) desensitization.

An interesting case is that of a patient enucleated 20 years ago that developed in his only eye an intraocular tumor associated with secondary retinal detachment. In this case we decided surgical treatment chorioretinal resection by Nd:YAG laser.

We used the medical laser LCY-FT with the following characteristics:

- type of laser Nd:YAG in continuous wave at 1.064 μm ;

- laser power—variable up to 48 W multimode;
- transmission system—quartz fiber water cooled, with the core diameter of 600 μm and sapphire terminals.

Using a conic sapphire terminal with a sharp edge the radiation is reflected within core.

Therefore, a great quantity of energy is concentrated at the edge of the sapphire, reaching 1800–2000° C (below the melting point of the sapphire).

We performed a preparatory photocoagulation to produce a chorioretinal adherence 2–3 mm around the tumor, ophthalmoscopy and transillumination, in order to localize the tumor. We also marked the margins of the neoplasm by diathermy.

Sclerochoroidal resection consists of:

- scleral flap corresponding to the tumor
- deep linear sclerotomy by laser vaporization;
- vaporization of the tumor by intratumoral balancing of the sapphire edge;
- suture of the sclerotomy;
- suture of scleral flap;
- cryotherapy around the scleral flap.

Postoperative evolution was spectacular, with a fibrous scar corresponding to the tumor (the lens and vitreous body remained clear). A pre-existent optic atrophy, due to secondary glaucoma, determined us to associate vitaminotherapy and vasodilator drugs.

We applied this method to 2 other cases, one a monophthalmic patient and the other one with a prominent metastatic tumor. Six months after operation, the monophthalmic patient showed a secondary retinal detachment (probably due to an incorrect intraocular manipulation of the sapphire edge).

The surveillance period of these 3 patients was from 6 to 14 months. Their spectacular evolution and the success of this therapy determine us to declare that, in spite of technical impairment, laser therapy seems to be a very efficient instrument for intraocular tumor management.⁷

In the last 2 years our experience has enlarged by 7 cases of primary tumors of the iris and ciliary body. Our option was that of surgical treatment—iridocyclectomy (surgical removal of part of the iris and ciliary body).

Prior to operation, we performed iris Argon laser non perforating photocoagulation, in order to obtain an avascular area around the tumor.

Iridocyclectomy consists of:

- a fornix based conjunctival flap to expose the sclera and localization of the tumor by transillumination;
- an anteriorly hinged scleral rectangular flap, of 3/4 depth with 2 mm margin around the tumor;
- diathermy on the remaining scleral fibers surrounding the tumor;
- tumor extirpation in one piece with Nd:YAG laser;
- iridoplasty;
- suture of the scleral flap and conjunctiva.

The anatomic and functional postoperation recovery was reasonable.

The surveillance period was 2 years, and patients suffered several fluorescein angiographies, ultrasound examinations and LAI tests.

Only one case developed a complicated cataract (probably iatrogenic), that was removed by extracapsular extraction and anterior chamber intraocular lens (IOL) implantation, with total functional recovery.

There were no signs of extending tumors.

3. DISCUSSIONS

Laser therapy (photocoagulation) is useful in small choroidal tumors with maximal 3 papillary diameters long and 3–4 D thickness. Otherwise, since 1976, J. Francois, has noted in his studies a favorable evolution using Xenon arc photocoagulation in similar cases.

1. Choroidal tumor extirpation using laser lancet is better than classic choroidectomy or that done by diathermy. The high temperature (1800–2000° C) developed by laser beam stops intraoperation hematogenic dissemination of tumoral cells.
2. Laser therapy is suitable in small preecuatorial tumors (smaller than 3 papillary diameters, 3–4 D thickness). Complications can occur and include vitreous hemorrhage or retinal detachment.
3. Iris and ciliary body laser extirpation seems to be a more effective therapeutic alternative than classic iridocyclectomy.

REFERENCES

1. B. Cârstocea, "Applications of laser in treatment of ocular and annexa tumors", *Lasers and medicine, Achievements and new directions - National Conference*, Institute of Atomic Physics, Bucharest, pp. 27–33, (1991).
2. B. Cârstocea, "Romanian Lasers in Ophthalmology", PhD. Thesis, University of Medicine and Pharmacy, Bucharest, (1990).
3. V. Lupei, I. Ursu, "Medical solid-state lasers", *Achievements and trends in laser field - National Conference*, Institute of Atomic Physics, Bucharest, pp. 421–445, (1990).
4. V. Cotea, A. Cotea, B. Cârstocea, "Trends of development in ophthalmologic treatment and diagnosis with lasers", *Oftalmologia*, **3**, pp. 254–261, (1994).
5. M. Predescu, A. Moroşeanu, "L'utilisation du Diode Laser dans la Medecine Energetique", *Applications des Lasers en biologie - Colloque Franco-Roumain*, Institute of Atomic Physics, Bucharest, pp. 74–75, (1995).
6. B. Cârstocea, O. Gafencu, S. Apostol, M. Ioniţă-Mânzatu, V. Lupei, A. Moroşeanu, V. Ioniţă-Mânzatu, "Laser Treatment of Ocular Annex Tumors", *BIOS Europe '96*, Conference on lasers in Ophthalmology, Vienna, (1996).
7. B. Cârstocea, O. Gafencu, S. Apostol, M. Ioniţă-Mânzatu, V. Lupei, A. Moroşeanu, "Laser Treatment of Intraocular Tumors", *1st Balkan Congress of Oncology*, Athens, (1996).

Laser-induced fluorescence of atherosclerotic plaques.

N.Moise*, M.L.Pascu*, C.Carp**, C.Volvoreanu**

*National Institute for Laser, Plasma and Radiation Physics, PO Box MG-36,
Bucharest, 76911, Romania.

**Institute of Cardiology, Department of Cardiology, Fundeni Way 256, Bucharest, Romania

ABSTRACT

In vitro laser-induced fluorescence (LIF) spectra and lifetimes of normal and atherosclerotic tissues are reported. The experimental arrangement conceived to measure LIF contained a 700 ps nitrogen pulsed laser (337.1 nm) and two quartz optical fibres to induce and respectively collect the fluorescence of normal and diseased samples. With UV laser excitation we found prominent differences both in spectral and temporal range between normal artery and atherosclerotic plaques which was standard pathological classified in five types such as: normal artery, fibrous plaque, atherosclerotic plaque, calcified plaque and ulcerated plaque.

As for statistics, the total number of measurements performed on each of the five mentioned types of tissues was 25.

Keywords: laser, fluorescence, spectroscopy, atherosclerotic plaques.

1.INTRODUCTION

LIF spectroscopy has proved to be one of the most sensitive detection methods and became a powerful tool in the field of analytical chemistry¹, environmental monitoring². During the last ten years LIF spectroscopy has been increasingly used in biomedical studies³⁻⁴, both at cell level and for human tissues diagnostics and therapy, particularly, for cardiovascular diagnosis and therapy.

Low power laser radiation induces tissue fluorescence without tissue damage and can be used for diagnostic fluorescence spectroscopy. Fluorescent substances have long been identified in atherosclerotic plaques^{5,6} and numerous studies⁷⁻¹⁰ have shown that normal and atherosclerotic arterial fluorescence differ both in spectral and temporal range.

This difference between the LIF spectra of atherosclerotic plaque and normal arterial tissue has been proposed as the basis for developing a "smart" laser angioplasty system. This system would incorporate fluorescence spectroscopical feedback to guide high power laser energy so that only tissue with the fluorescence characteristics of atherosclerotic plaque would be ablated.

2.MATERIALS AND METHODS

The arterial samples were excised from fresh cadaveric human aortae at less than 12 h post mortem. After excision, all samples were cleaned and rinsed with saline solution to remove contaminants such as hemoglobin and oxyhemoglobin which can influence the measurements of fluorescence. Samples were stored in normal saline solution at 4C until use.

The vessels were opened longitudinally to expose the intimal surface and approximately 1.5 x 1.5 cm specimens were isolated for analysis. Following pathological gross inspection performed to confirm tissue structure, the samples were classified in five types such as normal, and the rest as various degrees of atherosclerosis (fibrous plaque, atherosclerotic plaque, calcified plaque, and ulcerated plaque).

The lumen side of each sample was secured flush against a face of a quartz lamella, providing a well-defined surface from which to observe fluorescence and to decrease the scattered UV laser light.

LIF was obtained using a nitrogen pulsed laser working at atmospheric pressure; the laser radiation wavelength was 337.1 nm and the emitted energy per pulse was about 350 μ J. The laser pulse time width was approximately 700 ps and the pulse repetition rate was chosen between 0.5 pps and 10 pps. The laser beam power fluctuations were less than 5%, inducing relatively small fluctuations of fluorescence signal. In the experimental measurements, the fluorescence excitation of arterial samples was achieved using a quartz optical fibre (0.8 mm diameter); a second optical fibre (1 mm diameter) was used to collect the fluorescence signal.

The experimental set-up is shown in Fig.1. To focus the laser radiation on the optical fibre input, a system of spherical lenses was mounted allowing the transmission of 70% - 80% from the laser incident beam power into the optical fibre. The fluorescence emission was collected by the second fibre with a greater diameter and numerical aperture to collect a greater part of the fluorescence emission. The excitation/detection geometry of the two optical fibres ends was chosen so that an optimum signal/noise ratio (fluorescence/UV scattered light ratio) was obtained. The second optical fibre transmitted the fluorescence radiation to the entrance slit of a monochromator. An UV blocking filter was introduced

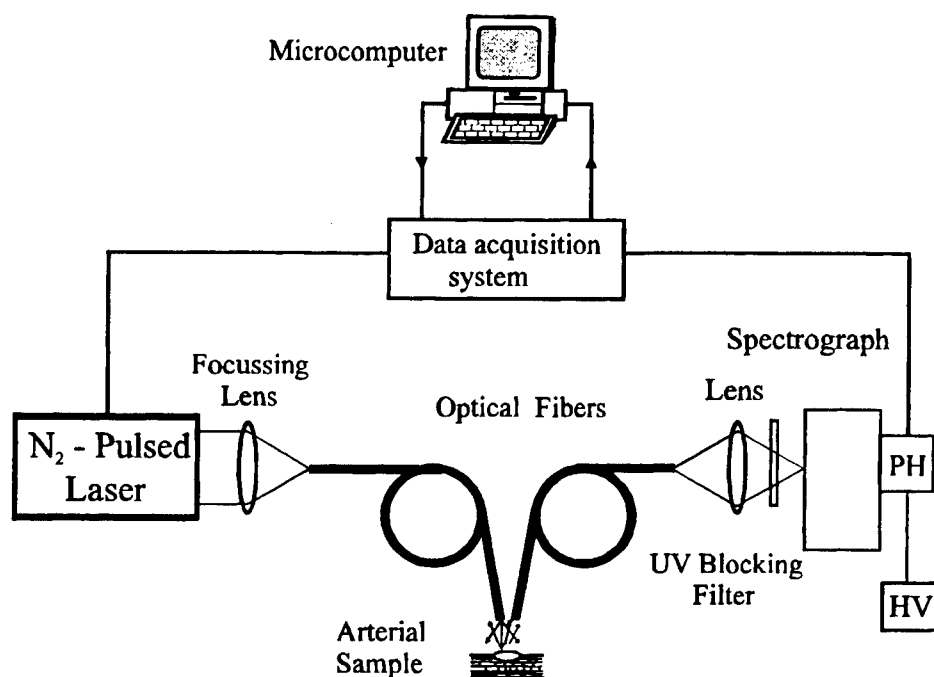


Fig.1 Experimental set-up for LIF measurements.

before the monochromator entrance slit, avoiding UV radiation input into the monochromator; the fluorescence spectra reported further are corrected taking into account the transmission characteristics of the filter. The electrical signal of the photomultiplier is further processed by a data acquisition system installed on a microcomputer. The nitrogen laser pulses are controlled also by the same microcomputer.

The experimental set-up to measure the LIF lifetimes of the arterial samples is similar with the one described above except the monochromator and photomultiplier which are removed. The fluorescence signal was applied on a fast PIN photodiode with a rise time of 0.2 ns. The photodiode yielded signal was observed on a TDS 530 digital Tektronix scope.

The image obtained on the scope screen reproduces the time behavior of fluorescence intensity. From the fluorescence intensity decay, which is proportional to the excited state population, one estimated the fluorescence lifetime as the time required for the intensity to decay to $1/e$ of its initial value.

3. RESULTS

With UV laser excitation at 337.1 nm we found proeminent differences between normal artery samples and atherosclerotic samples. The atherosclerotic samples were classified in four types such as fibrous plaque, atherosclerotic plaque, calcified plaque and ulcerated plaque. The ability to differentiate normal from atherosclerotic tissues with different stages in the progression of atherosclerosis using fluorescence spectra or /and lifetimes is suggested and depends by their composition, specifically by the differences in the concentration and the nature of the fluorophores.

Normal aortic samples displayed two maxima at 395 nm and 455 nm, separated by a minimum at 415 nm which shows clearly the strong hemoglobin reabsorption although the samples were rinsed from blood with saline solution. We noticed that the second maximum is higher than the first. The full width at half maximum (FWHM) is approximately 130 nm. The LIF spectrum of normal aortic sample is shown in Fig.2.

Typical fluorescence spectrum for fibrous plaque is more structured than for normal samples exhibiting two maxima located also at 395 nm and 455 nm, and the third at 500 nm separated by two minima at 415 nm and 485 nm. The mentioned differences are identifiable on the plots shown in Fig.3. The FWHM is greater than for normal sample and is approximately 160 nm.

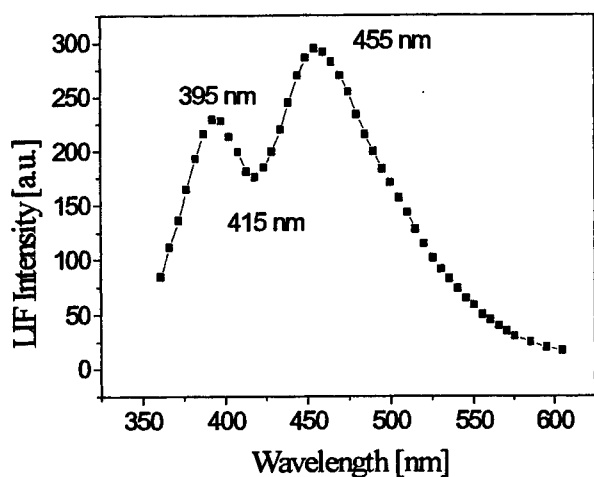


Fig.2 LIF spectrum of normal artery.

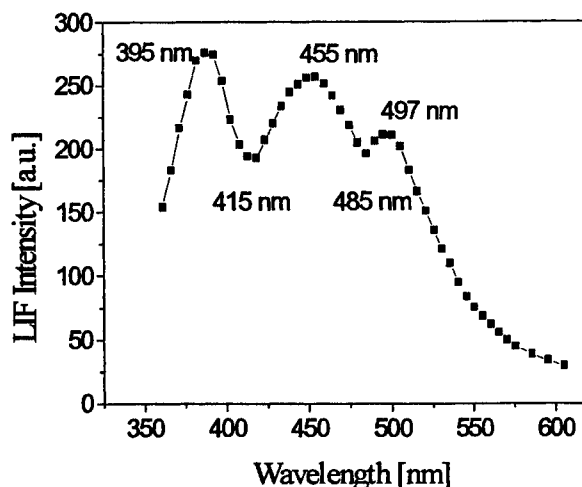


Fig. 3 LIF spectrum of fibrous plaque.

LIF spectra of the atherosclerotic plaques (Fig.4) present two approximately equal maxima located at 395 nm and 455 nm with a weak shoulder at 500 nm, separated by minimum at 430 nm. The FWHM is about 135 nm. Typical fluorescence spectra of calcified atherosclerotic plaques (Fig.5) have a main maximum located at 395 nm and two secondary maxima at 455 nm and 500 nm. The FWHM is about 120 nm.

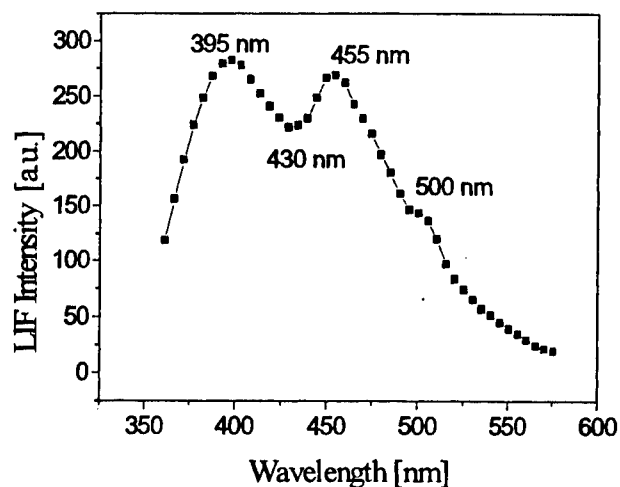


Fig.4 LIF spectrum of atherosclerotic plaque.

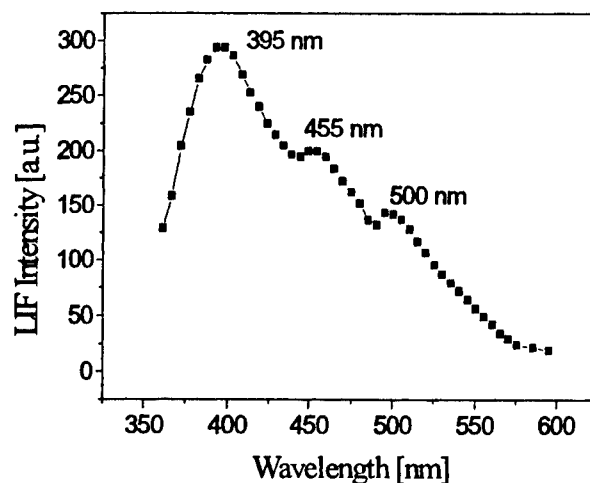


Fig.5 LIF spectrum of calcified plaque.

The fluorescence spectra of ulcerated plaques (Fig.6) have a main maximum shifted at greater wavelength at 490 nm and a minor maximum at 395 nm separated by a minimum at 425 nm. Other essential difference is that the value of the fluorescence intensity is ten times smaller than any other sample.

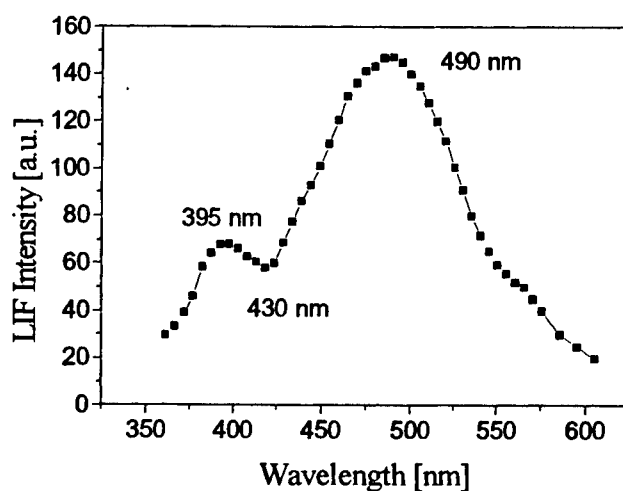


Fig.6 LIF spectrum of ulcerated plaque.

Measurements of LIF lifetimes were performed using a fast PIN photodiode obtaining values of approximately 5 ns for normal samples, 7.2 ns for fibrous and atherosclerotic plaques, 6 ns for calcified plaques and 3.6 ns for ulcerated plaques.

As for statistics, the total number of measurements performed on each of the five mentioned types of tissues was 25.

4. CONCLUSIONS

LIF has great potential for arterial wall diagnosis due to its sensitivity, and its ability to be monitored remotely using optical fiber probe. Since fluorescence emission is affected by the fluorophores nature and concentration, and their surrounding environments, normal and diseased plaque tissues are expected to yield different fluorescence behavior both in wavelength and time.

From the measured LIF spectra we noticed that all these samples are composed by three fluorescent specimens with emissions at three different wavelengths 395 nm, 455 nm and 500 nm and in different proportions. All the atherosclerotic samples have the first maximum greater than the second.

One may conclude that LIF techniques may be used for diagnosis of atherosclerotic plaques, based on the spectral characteristics and temporal behavior of the LIF signals.

5. REFERENCES

1. V.S.Letokhov, Ed., *Laser Analytical Spectrochemistry*, Adam Hilger, Bristol, 1985.
2. R.M.Measures, *Laser remote Sensing: Fundamentals and Applications*. Wiley, New York, 1984.
3. R.R.Alfano, B.T.Darayash, J.Cordero, P.Tomashefsky, F.W.Longo, and M.A.Alfano, "Laser-induced fluorescence spectroscopy from native cancerous and normal tissue," *IEEE J.Quantum Electron.*, Vol. 20, pp.1507-1511, 1984.
4. J.R. Lakowicz (ed.), *Time-Resolved Laser Spectroscopy in Biochemistry (I and II)*, *Proc. SPIE*, Vol. 1204, 1990.
5. I. Banga, M. Bihara-Varga, " Investigations of free and elastin bound fluorescent substances present in the atherosclerotic lipid and calcium plaques," *Connect. Tiss. Res.*, Vol. 2, pp.237-241, 1974.
6. M.R. Prince, T.F. Deutsch, Matthews-Roth, " Preferential light absorption in atheromas in vitro," *J. Clin. Invest.*, Vol. 78, 295-302, 1986.
7. T.G. Papazoglou, "New Trends in Photobiology (Invited Review) - Malignancies and Atherosclerotic Plaque Diagnosis - Is Laser-Induced Fluorescence Spectroscopy the Ultimate Solution ?," *J. Photochem. Photobiol. B-Biology*, Vol. 28, pp. 3-11, 1995.
8. L.I.Deckelbaum, J.K. Lam, H.S. Cabin, "Discrimination of normal and atherosclerotic aorta by laser-induced fluorescence," *Laser Med. Surg.*, Vol. 4, pp.171-181, 1989.
9. L.I.Laifer, K.M.O'Brien, M.L.Stetz, G.R.Gindi, T.J.Garrand, L.I.Deckelbaum, " Biochemical basis for the difference between normal and atherosclerotic arterial fluorescence", *Circulation*, Vol.80, No.6, pp.1893-1901, Dec.1989.
10. A.L.Alexander, C.M.Connor Davenport, and A.F.Gmitro, "Fluorescence spectroscopy of normal and atheromatous human aorta: Optimum illumination wavelength," *SPIE*, Vol. 1425, pp. 6-15, 1991.

N. Mincu, Maria-Ana Popovici*, Mara Dobre**

Institute of Optoelectronics, 1 Atomistilor St, P.O. Box MG-22, 76900 Bucharest, Romania

Fax: (401) 420.86.32, e-mail: raduc@roifa.ifa.ro

* "Politehnica" University, Physics Dept., 13 Splaiul Independentei, Bucharest, Romania

** Carol Davila Medicine and Pharmacy University, Microbiology Dept.,
37 Dionisie Lupu St., Bucharest, Romania

ABSTRACT

We present static light scattering measurements of size-shape distributions of biological particles in suspension. Results are compared to the Rayleigh -Debye-Gans theory predictions. They are inverted to retrieve the geometrical parameters of the suspended particles and their size-distribution function. The inversion of data is performed by a combined method using normalized cubic B spline functions and linear programming, which is firstly applied to different sets of simulated data, to study its efficiency and stability in the presence of experimental noise.

Keywords: elastic light scattering, size distribution function, biological particles

1. THEORY

The intensity of the radiation scattered by a particulate sample contains information about the physical properties of the sample. Determination of sizes, size distribution functions and optical properties is possible by means of elastic laser light scattering measurements¹. The angular dependent intensity $I(m, \theta)$ scattered by a collection of polydisperse particles suspended in a homogenous medium can be considered as linear combination of Lorentz - Mie form factors $F(\kappa, r, \theta)$, where $\kappa = 2\pi m / \lambda_0$ is the wave vector, λ_0 is the incident radiation wavelength in vacuum, m is the relative refractive index of the particles in a certain solvent, r is the particle radius and θ is the scattering angle^{2,3}:

$$I(m, \theta) = \int_{r_{\min}}^{r_{\max}} w(r) F(\kappa, r, \theta) n(r) dr. \quad (1)$$

In equation (1), $w(r)$ is a weighting factor depending on the type of $n(r)$ the size distribution function which is to be retrieved, r_{\min} and r_{\max} are the limits of the size range.

The Rayleigh - Debye - Gans (RDG) theory is a special case of the Lorentz - Mie theory, which is valid for $|m-1| \ll 1$ and $\kappa d |m-1| \ll 1$, where d is a characteristic linear dimension of the scattering centre. The RDG expression of the form factor $F(\kappa, r, \theta)$ in terms of the scattering matrix elements depending on the particle geometry can be obtained¹. For spherical particles, the form factor - written as a function of the scattering vector length $x = \frac{4\pi m r}{\lambda_0} \sin\left(\frac{\theta}{2}\right)$ - is given by:

$$F(x) = \left[\frac{3}{x^3} (\sin(x) - x \cos(x)) \right]^2. \quad (2)$$

For rod-like particles, $x = \frac{4\pi m l}{\lambda_0} \sin\left(\frac{\theta}{2}\right)$, where l is the length of the rod, and the form factor is:

$$F(x) = \frac{2}{x} \int_0^x \frac{\sin \xi}{\xi} d\xi - \left[\frac{2}{x} \left(\sin \frac{x}{2} \right) \right]^2. \quad (3)$$

2. SIMULATIONS OF LIGHT SCATTERING DATA

Simulated light scattering data were obtained for particle distributions of an increasing complexity: Gaussian monomodal, bimodal and trimodal. In each case, the simulated size distribution function $n_{\text{sim}}(r)$, which represents the number of particles per unit volume with radii between r and $r+dr$ is taken in equation (1) together with equation (2) or (3) to get values of the scattered intensity $I_{\text{sim}}(\theta)$ by collections of spherical or rod-like particles at different angles. Equation

(1), which from a mathematical point of view is a Fredholm integral equation of the first kind is inverted to retrieve the size distribution function $n(r)$. Then the input and output distributions are compared.

The inversion procedure was fully described by us in a recent paper⁴. First, the size distribution function $n(r)$ is considered as a linear combination of normalized cubic B spline functions, then linear programming is used to retrieve the coefficients of the combination, by minimizing the sum of measurement errors. The coefficients are used to reconstruct $n(r)$. This method proved to present a very good stability with respect to the noise level of data, which makes it well suited for processing experimental data.

The simulated values of the intensity scattered by a suspension of particles characterized by a Gaussian monomodal size distribution function, at large scattering angles are presented in Figure 1 concomitantly with the fitted curve. In Figure 2 we represented the corresponding input and retrieved distribution functions. Other parameters of the simulated sample are the concentration $c=10^4 \text{ cm}^{-3}$ and the refractive index $m=1.08$. The fit corresponds to a number $s=30$ cubic splines.

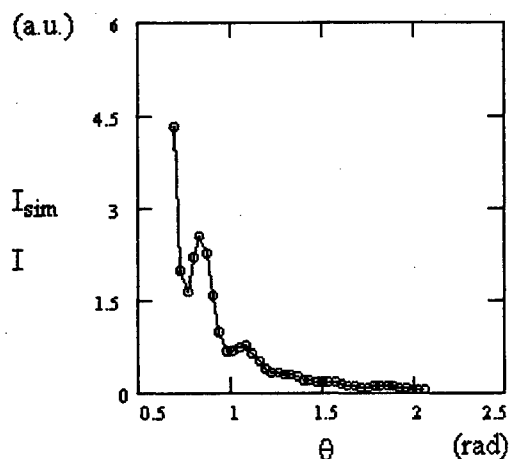


Figure 1. Simulated (circles) and retrieved (line) values of light intensity scattered by a Gaussian monomodal size distribution function, at angles between $\theta_{\min} = 40 \text{ deg}$ and $\theta_{\max} = 120 \text{ deg}$

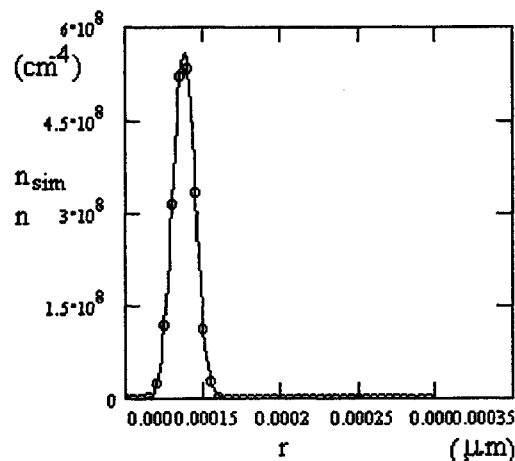


Figure 2. Simulation and results of inversion for a Gaussian monomodal size distribution function characterized by $\bar{r} = 1.4 \mu\text{m}$ mean value and $\sigma = 0.056 \mu\text{m}$ standard deviation.

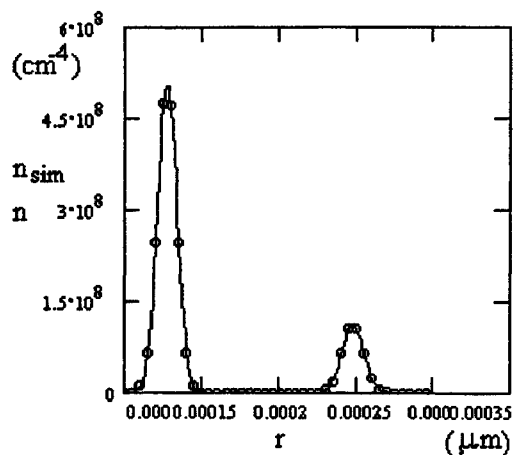


Figure 3. Bimodal Gaussian size distribution function. $\bar{r}_a = 1.3 \mu\text{m}$, $\bar{r}_b = 2.5 \mu\text{m}$, $\sigma_a = 0.03 \mu\text{m}$, $\sigma_b = 0.05 \mu\text{m}$

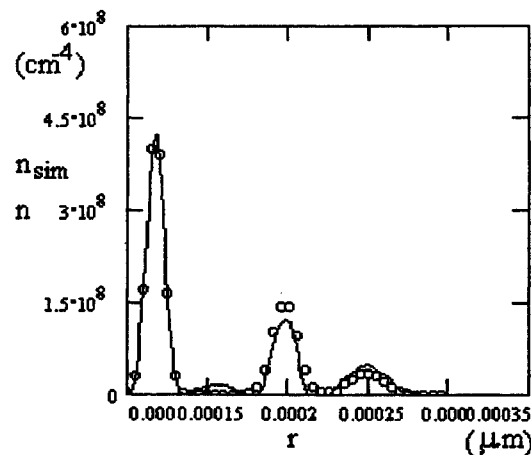


Figure 4. Trimodal Gaussian size distribution function $\bar{r}_a = 1.2 \mu\text{m}$, $\bar{r}_b = 2 \mu\text{m}$, $\bar{r}_c = 2.5 \mu\text{m}$, $\sigma_a = 0.024 \mu\text{m}$, $\sigma_b = 0.06 \mu\text{m}$, $\sigma_c = 0.1 \mu\text{m}$

We also performed simulations involving more complex size distribution functions. The simulated and retrieved bi- and trimodal distributions are presented in Figure 3 and Figure 4. Each time, a Gaussian background noise of null mean value and 3% root mean square was added.

3. EXPERIMENTAL SETUP

Elastic laser light scattering data were collected in two different ways. First, we measured scattered intensities at very low angles, then at large angles. The experimental setup which we used for near-forward scattering experiments is presented in Figure 5. The laser beam is passed through a device which expands it and also performs spatial filtering so that the divergence (measured in the far field) of the incident beam on the sample is $\theta = 0.2$ mrad and the diameter is 8 mm. The scattering cell is 2.5 mm thick (multiple scattering is negligible), has flat entrance and exit windows, with a diameter of 15 mm- much larger than that of the incident beam, to avoid edge effects and losses of the incident power. The focal length of the collecting lens is 63 mm, which is adequate for measuring particles in the size range $[1\mu\text{m}, 100\mu\text{m}]$ ⁵.

Beam masking is absolutely necessary due to the fact that the unscattered intensity is three orders of magnitude larger than the scattered intensity, which results in the saturation and even damaging of any photo-device. We use a knife-edge beam mask, placed right in front of the video camera. The CCD video camera is connected to a frame grabber operating at 15 MHz. The data, consisting in matrices of 512×480 numbers (if the acquisition system works in the high resolution regime) are stored on disk and introduced in the programs for data processing.

One of the advantages of using a CCD camera for recording scattered light is the possibility of measuring large particles (aggregates) which scatter mainly in the near forward direction. On the other hand, if it is necessary to measure small particles, there exists the possibility of moving the camera. The precision of its positioning is of $5\mu\text{m}$. Another advantage is that one can get many data points in a comparatively small range of angles. This results in a finer size distribution, i. e. particles with little differing sizes can be observed. Simulations show that complex size distribution have the effect of "smoothing" the scattered intensity. So, the higher the resolution in scattering angle range is, the more accurate results you get. The errors that limit the minimum scattering angle available for reliable measurements are connected to the divergence of the incident beam on the sample and to the diffraction effects on the beam mask. The maximum value of the scattering angle is limited by the background noise.

The setup for measuring light scattered at large angles is a conventional goniometric system in which the photosensitive device is also a CCD video camera connected to a frame grabber and a personal computer. In this case we use a cylindrical

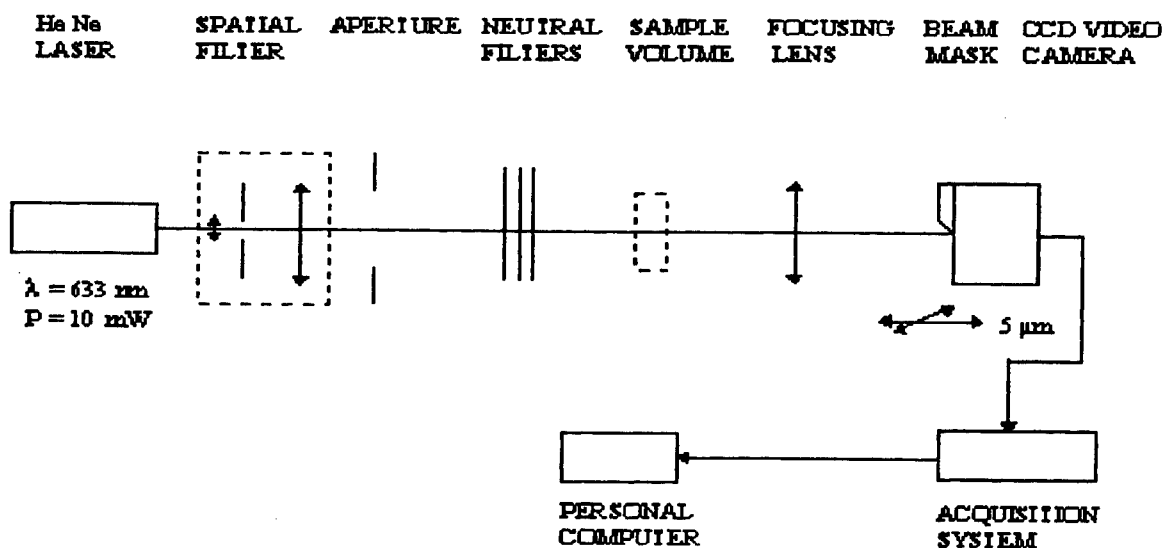


Figure 5. Experimental setup for near-forward scattering measurements

scattering cell, with two flat entrance and exit windows designed to reduce stray light scattering and back reflection in the system, an opaque side wall to minimize the reflected light from the sample cell. The focal length of the collecting lens is $f = 200 \text{ mm}$.

If the light source presents short time power fluctuations one can use the possibility of averaging as many recorded frames as necessary to minimize their effect on the results. On the contrary, if long time fluctuations are present, than a single frame will give the necessary information on the collection of scatterers.

4. RESULTS

The experiments have been carried out using two kinds of particles within the same size range 1 - 1.5 μm , with different shapes (spherical and rod-like) and a number concentration of 10^6 particles/ml. In the first case we studied a suspension of cocci (spherical particles) in 0.85% saline solution, thermally inactivated. The second sample was a suspension of *Pseudomonas Aeruginosa* bacilli (rod-like particles), also inactivated by thermal treatment, in the same 0.85% saline solution.

In Figure 6 and Figure 7 the results obtained inverting near-forward scattering data are presented.

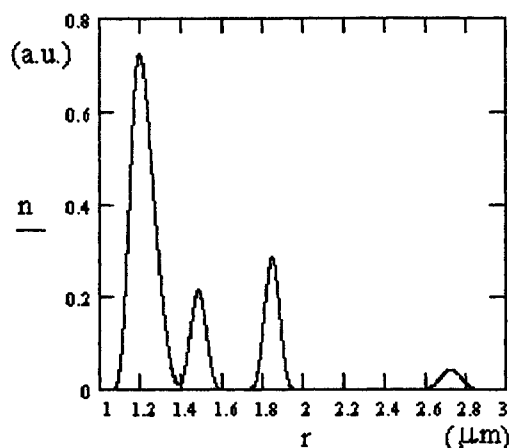


Figure 6. Retrieved size distribution function of a suspension of cocci in 0.85% saline solution. r is the radius of particles.

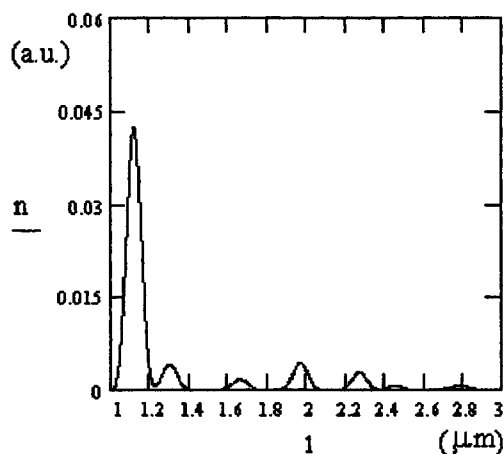


Figure 7. Retrieved size distribution function of a suspension of *Pseudomonas Aeruginosa* bacilli in 0.85% saline solution.

In comparison to these, we present the results of light scattering measurements at large angles by the same types of samples.

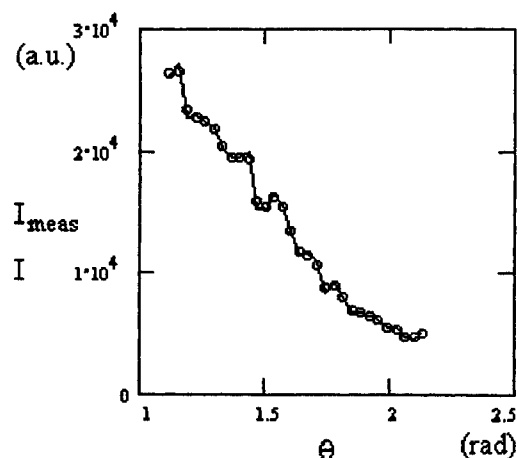


Figure 8 . Measured scattered intensity from coccus particles .

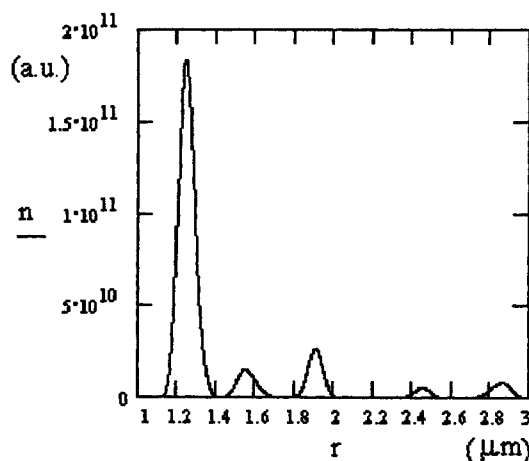


Figure 9. Size distribution function of cocci obtained from scattering measurements at large angles.

The results present a good similarity to those obtained by optical microscopy. The refractive index was obtained as the parameter for which the best fit was obtained. We got $m=1.02$ for the coccus particles and $m = 1.08$ for the bacilli. We notice that apart from the main peak, each size distribution function also reveals the presence of larger particles. These are clusters which existed in the samples although they were placed in an ultrasonic bath before the measurements.

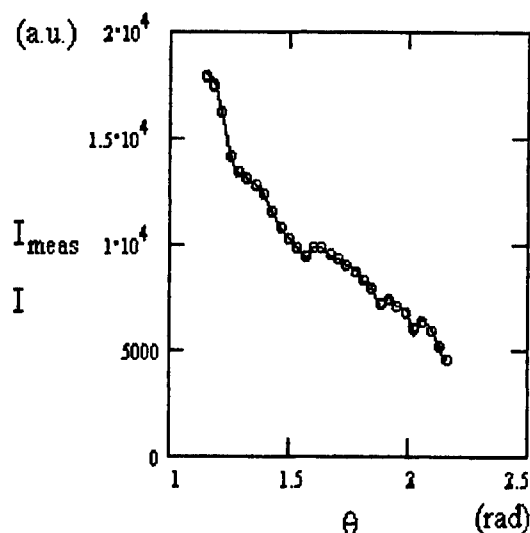


Figure 10. Measured scattered intensity from *Pseudomonas Aeruginosa* bacilli.

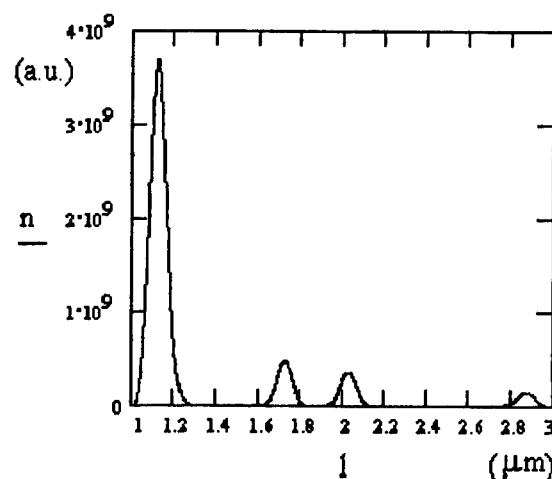


Figure 11. Size distribution function of *Pseudomonas Aeruginosa* bacilli obtained from scattering measurements at large angles.

Actually, these clusters were observed by microscope too. They are a result of the bacterial division process which, when the suspension is thermally treated, is stopped. Consequently, the culture will be "frozen" in a certain growth phase and, beside isolate bacteria, one will be able to observe groups of 2, 4, 6, 8,...etc. specimens. Using the methods presented in this paper, we can detect them and compute the relative weight of each cluster in the studied growth phase. The possibility of measuring such complex continuous size distribution functions is one of the major advantages of our method of measuring and processing elastic laser light scattering data.

5. REFERENCES

1. C. Bohren and D. Huffman, "*Absorption and Scattering of Light by Small Particles*", J. Wiley, New York, 1983.
2. O. Glatter "Modern Methods in Data Analysis in Small Angle Scattering and Light Scattering", *Modern Aspects of S.A.S.*, NATO Sci. Series, Kluwer Publ., 1995.
3. H. Schnablegger and O. Glatter, "Optical sizing of small colloidal particles: an optimized regularization technique", *Appl. Opt.* **30**(33), 4889-4896 (1991).
4. M.A. Popovici, N. Mincu and C. Plosceanu, "Using linear programming in near forward light scattering data processing", *Romanian J. Optoelect.* **5**(3), 43-48 (1997).
5. K.A. Kusters, J.G. Wigers and D. Thoenes "Particle sizing by laser diffraction spectrometry in the anomalous regime", *Appl. Opt.* **30**(33), 4839-4848 (1991).

Photodynamic therapy using hematoporphyrin derivative and He-Ne laser irradiation in Erlich tumor.
An experimental study on mice.

Mihaela Radu*, D. Ciotaru**, Mihaela Calin*, G. Savi**, M. Bota***, Carmen Stroila**

* National Institute of Research and Development for Optoelectronics, P. O. Box MG 22, Magurele, Bucharest
76900, Romania

** Victor Babes Institute, Department of Immunopathology, Bucharest, Romania

*** USC LA, Department of Brain Research, California, USA

ABSTRACT

In vitro (absorption spectroscopy) and in vivo (fluorescence microscopy) studies before and after the uptake of intraperitoneal injected Hematoporphyrin Derivative (HpD) were made in mice. The absorption spectrum of HpD is characterized by four bands in the visible region with decreasing absorption towards longer wavelengths (510 nm, 540 nm, 568 nm and 621 nm). These spectra were obtained only at low concentration (10^{-5} M). After (15 - 30) minutes postirradiation (He-Ne laser, 1 mW) the features of curves were the same with those of nonirradiated samples but with a displacement of wavelengths. The presence of laser emitting products was pointed out by fluorescence microscopy (cryostat section in fluorescence microscopy).

Keywords: *photodynamic therapy, hematoporphyrin derivative, fluorescence microscopy, spectrophotometry.*

1. INTRODUCTION

The sensitizing hematoporphyrins and related species used in Photodynamic Therapy (PDT) were revealed to be complex mixtures of monomers, dimers (mainly dihematoporphyrin ether or ester) and aggregates. They are widely used in clinical experiments of PDT. The mechanism and efficiency of the photosensitizing action of porphyrins are dependent on the large variety of parameters. The monomeric and aggregated species of porphyrins have different photophysical properties and exhibit different photosensitizing activities. The mechanism of photosensitizing and efficiency of the photosensitizing action of porphyrin are dependent on the aggregation states of porphyrins. These aggregation states appear to be active species in sensitizing tumor cells.

The aim of this work is to determine the efficiency of HpD photoproducts in vitro and in vivo treatment of Erlich tumor cells (in cultures systems and intraperitoneal in mice). The PDT was applied by many years ago but in spite of many works about it, there are still unclarified aspects and therefore it is not a current therapy.

2. MATERIALS AND METHODS

The animals (30) used in this experiment were Balb mice, divided into three groups:

- the control group, containing normal mice with no tumors;
- the second group, containing mice with Erlich tumor;
- the third group, containing mice with Erlich tumor injected with HpD and irradiated with a He-Ne laser (SPECTRA PHYSICS, 1 mW).

Tumor: Erlich ascitic tumor cells, intraperitoneal administrated in two concentrations (10^8 cells/ml and 10^4 cells/ml). Erlich tumor cells culture in C. I. (Cantacuzino Institute) medium, PBS buffered at pH=7.2, antibiotic supplementation.

Methods: Spectroscopy: HpD spectra were recorded by means of a SPECORD M 40, before and after irradiation;
Trypan blau exclusion dye coloration for cell viability;
Fluorescence microscopy.

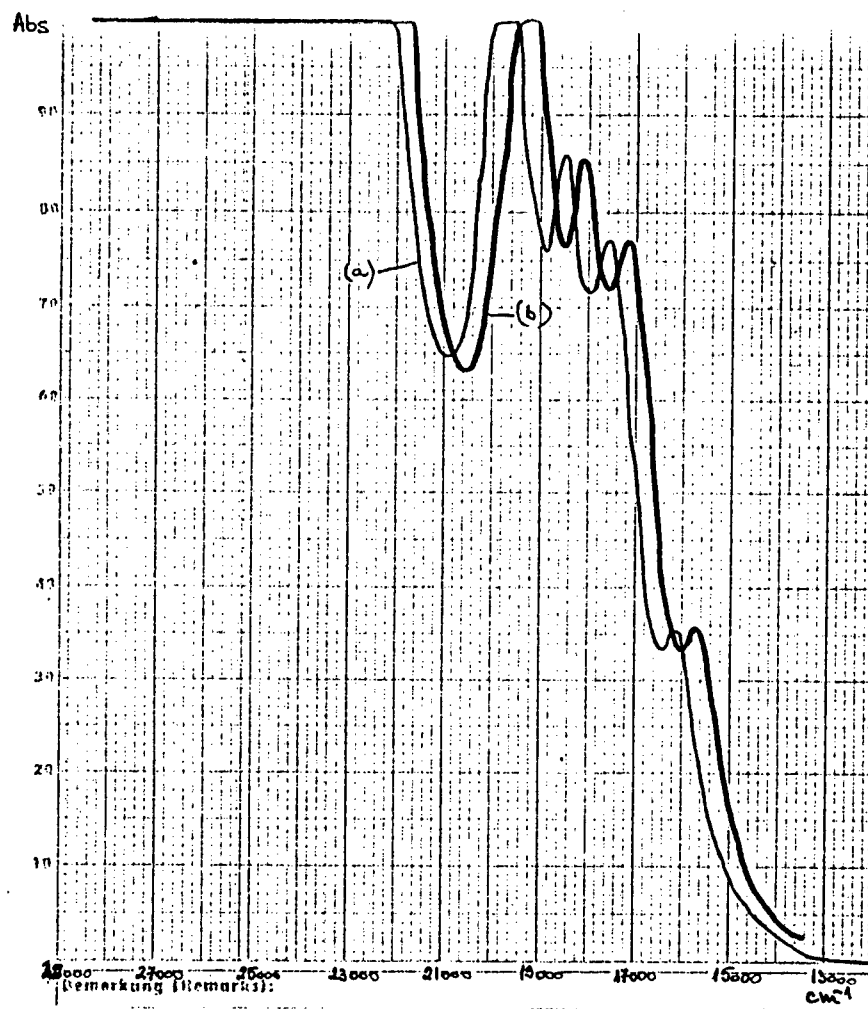


Fig. 1. The absorption curves of HpD before (a) and after (b) irradiation

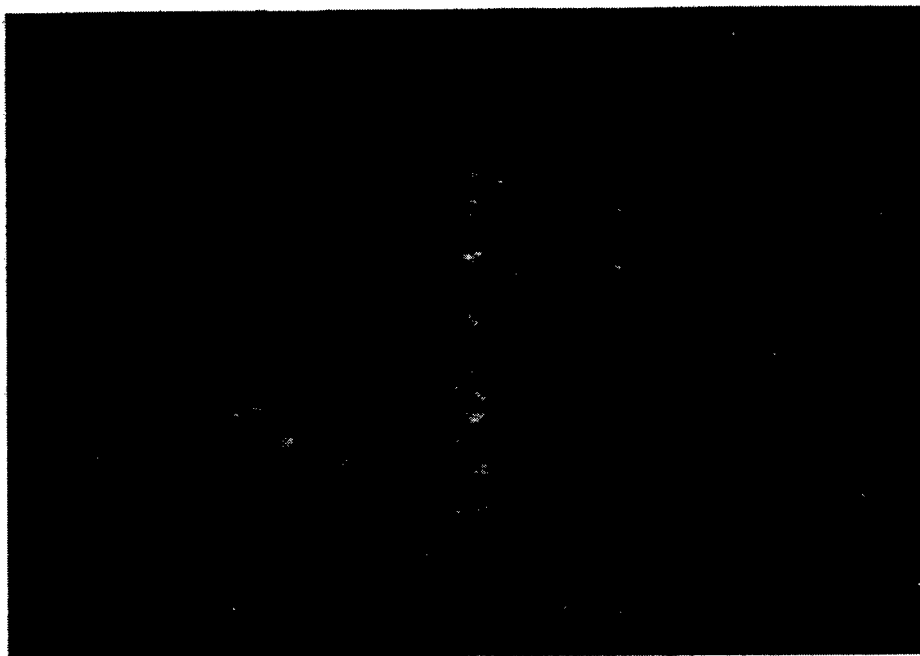


Photo 1a: The peritoneum aspect after HplD intraperitoneal administration (10x)

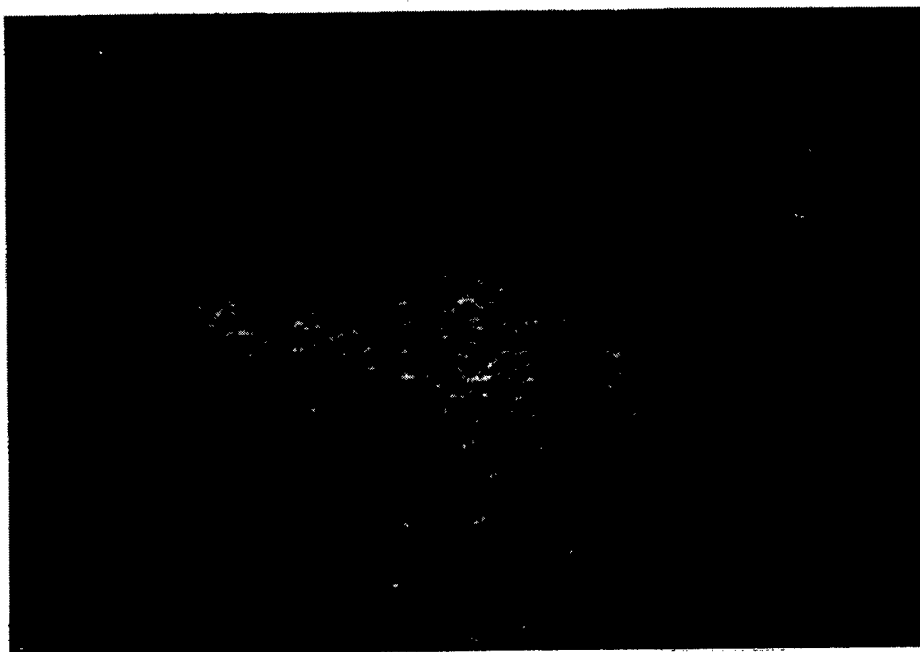


Photo 1b: The fluorescence after laser irradiation (10x)

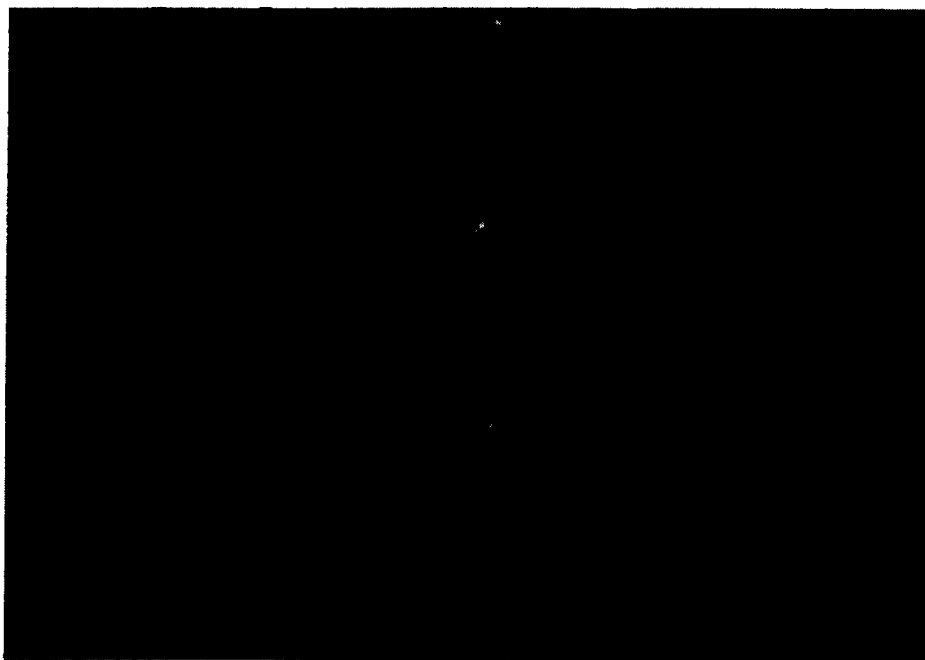


Photo 2a: Erlich tumor cells in single and agglutinated cells recolted after intraperitoneal HpD administration (10x)



Photo 2b: Erlich tumor cells after HpD intraperitoneal administration and He-Ne laser irradiation (10x)

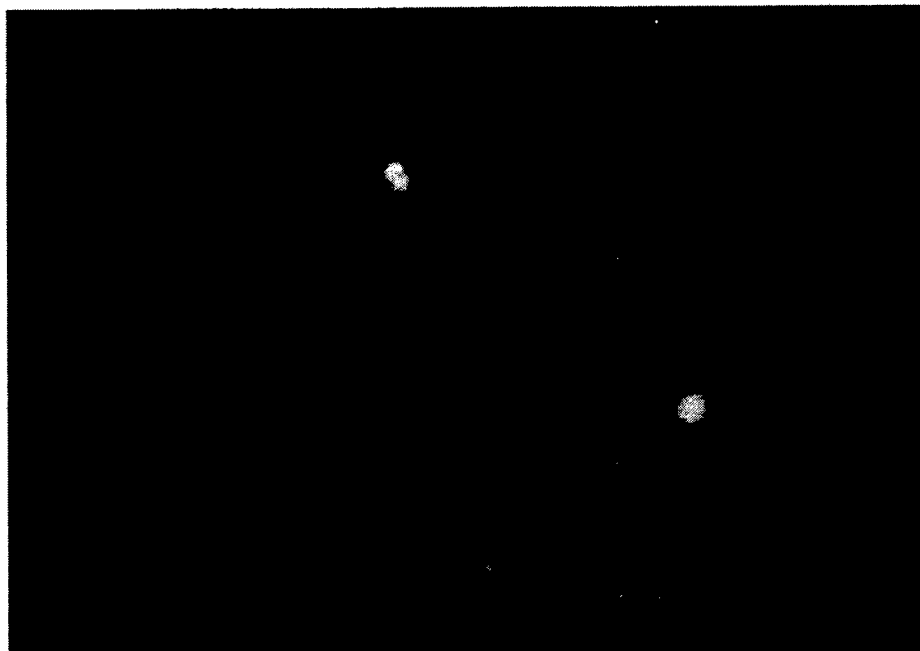


Photo 3: Erlich tumor cells after He-Ne laser irradiation (20x)

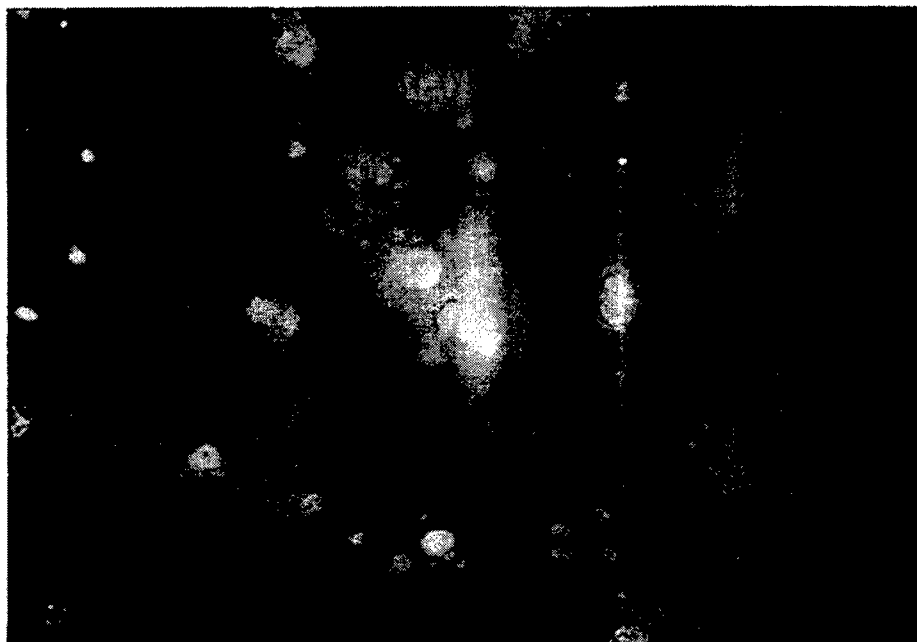


Photo 4: Erlich tumor cells after He-Ne laser irradiation (40x)

Following an interval of 24 h from the administration of the sensitizer, during which the animals were kept in a dark room we irradiated the animals using a He-Ne laser (1 mW), two times per day with a break of 30 min. The duration of each irradiation was 15 min.

3. RESULTS

The absorption curves of HpD before and after irradiation are presented in Figure 1. The absorption spectrum of HpD is characterized by four bands in the visible region with decreasing absorption towards longer wavelengths (510 nm, 540 nm, 568 nm and 621 nm). These spectra were obtained only at low concentration (10^{-5} M) and after (15 - 30) minutes postirradiation (He-Ne laser, 1 mW). The features of curves were the same with those of nonirradiated samples but with a rightwards displacement of wavelengths: 525 nm, 555 nm, 584 nm and 641 nm.

The life span of treated mice was not semnificative increased; they lived two or three days more than the untreated mice.

In Erlich tumor cells culture, after HpD and He-Ne irradiation, the viability was not significantly modified, but in vivo after intraperitoneal administration of Erlich tumor cells, the viability of cells was significantly decreased (by trypan blau exclusion dye coloration).

Photo 1a shows the peritoneum aspect after HpD intraperitoneal administration and Photo 1b shows the fluorescence after laser irradiation (objective 10x)

Photo 2a presents Erlich tumor cells single or agglutinated cells recolted after intraperitoneal HpD administration; Photo 2b presents Erlich tumor cells after HpD intraperitoneal administration and He-Ne laser irradiation (objective 10x).

Photos 3, 4 present Erlich tumor cells after He-Ne laser irradiation (objective 20x and 40x). The fluorescence surrounding cells is the fluorescence of HpD photoproducts (Photo 4).

4. CONCLUSIONS

From the obtained results, there are two facts which are remarkable for future researches. It seems that Erlich tumor cells are more resistant at the PDT than Walker 256 tumor¹ because, at the same doses of HpD, in the case of Erlich tumor the treatment was not so efficient as in the case of Walker 256 tumor.

The differences between in vivo and in vitro are, perhaps, due to immunostimulatory and antitumor activities by an induction of Interleukin-1 (Il-1) and Tumor Necrosis Factor (TNF) by the immunocompetent cells².

5. REFERENCES

1. D. Ciotaru, Dana Necsoiu, Mihaela Radu and Carmen Stroila, "Photodynamic therapy (PDT) using hematoporphyrin (HP) and He-Ne laser irradiation in Walker 256 tumor. An experimental study on rats", *Lasers in the Life Sciences*, Vol. 7(3), pp. 167 - 172, 1997.
2. V. I. Gorbach et al., "New glycolipids (chitooligosaccharide derivatives) possessing immunostimulating and antitumor activities", *Carbohydrate Research*, Vol. 260(1), pp. 73 - 82, July 1994.

Comparative study of the thermal effects generated by laser irradiation for medical applications

Mihaela Calin, M. Tomescu, Roxana Radvan, Mihaela Radu, T. Necsoiu

National Institute of Research & Development for Optoelectronics
INOE 2000, Bucharest, PO Box MG 22, 76900, Romania

ABSTRACT

The medical laser applications use the thermal effects of laser irradiation. The present work contains applications of the thermovision. This method offers the following advantages recording and processing of the thermal distribution on the irradiated zone. The study has in view the development of an algorithm of work for an useful data base regarding the laser application in medicine. The experiments used Ar laser, laser diode and some kinds of biological tissues. The paper presents some thermal distributions before, during and after laser irradiation and the images processing.

Keywords: *thermal effects, thermovision, laser-tissue interaction, images processing.*

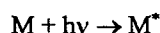
1. INTRODUCTION

The interaction between laser radiation and biological tissues generates complex phenomena which depend by laser parameters (power, spot dimensions, pulse duration, wavelength) and, also, by the tissue's properties.

If a laser beam is directed toward the tissue, it will be : reflected, scattered, transmitted or absorbed. Of course, the absorption depends significantly by the wavelength of the laser beam and by the nature of tissue. This work presents some aspects concerning thermal effects induced by different laser radiations.

2. THERMAL EFFECTS

The thermal effect is a process described by following model¹ : an absorbant molecule (M) takes the energy from a photon (hv) so that it will be risen to an excited state M*:



Within 10^{-6} s to 10^{-9} s following excitation, the energy is lost, most often as heat, and the molecule M* relaxes to its former state:



Relaxation may, also, result from photochemical decomposition of the molecule, fluorescent or phosphorescent reemission of the photon.

Due to the absorption of the laser energy the following biological changes occur: warming $(37 - 60)^{\circ}\text{C}$, coagulation $(60 - 65)^{\circ}\text{C}$, protein denaturization $(65 - 90)^{\circ}\text{C}$, drying $(90 - 100)^{\circ}\text{C}$, vaporization, carbonization $(>100^{\circ}\text{C})$. Ideally, from the clinical point of view is to determine exactly these domains, very important for efficient therapies.

3. METHODS AND EQUIPMENT

Telethermography means the recording and/or the visualization of the thermal state of the body using the IR radiation emitted by this body².

After the thermal image processing, the following results can be obtained:

- the isotherm curves with the possibility to select the lower or higher temperature points;
- the temperature profile drawing ;

- computing and displaying of the temperature differences between simetric points relative to a reference region;
- mixing, filtration, color processing for an easily interpretation of the image.

We used, to obtain the thermal images, a thermal imaging system LORIS (LORIS (Long Range Infrared System) model IRTV- 445L made by Inframetrics Inc. The recorded images using this system are processed by a specialised hard-software system Thermagram.

The lasers used in our experiments are the following :

- Ar laser (514.5 nm and 488nm);
- He-Ne laser (633 nm);
- GaAs diode laser (904nm).

Irradiated targets used are : paraffin, gelatine and human tissue (arm).

4. RESULTS

Figure 1 presents the thermal images of the paraffin irradiated with Ar laser ($\lambda=514.5\text{nm}$, $P=1\text{W}$) recorded at different exposure times (3min, 6min).

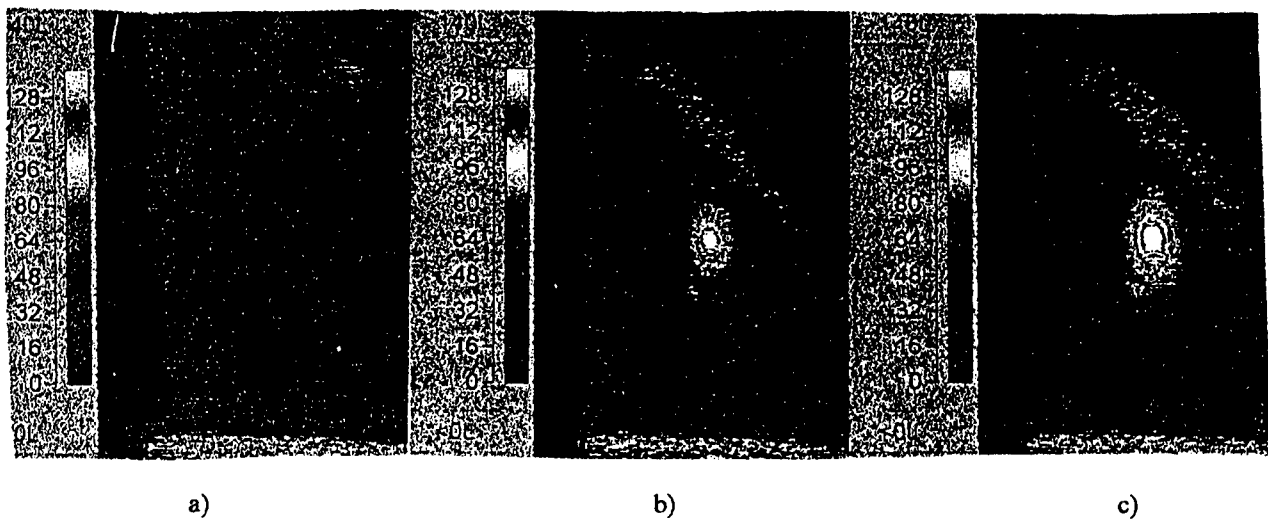


Fig.1 Thermal effects generated in paraffin under the Ar laser beam ($\lambda=514.5\text{nm}$, 1W) at different exposure times a) $t_0=0\text{min}$ (the reference image); b) $t_1=3\text{min}$; c) $t_2=6\text{min}$.

One can observe that within the irradiated region temperature decreases from the centre to the outside. The maximum temperature is located in the middle of the laser spot.

The heating of the surfaces by the laser beam depends by the irradiation time and by the thermal conductivity of the matter.

Figure 2 presents the thermal images of the paraffin irradiated with Ar laser ($\lambda=488\text{nm}$, $P=1\text{W}$) recorded at different exposure times (3min, 6min, 9min).

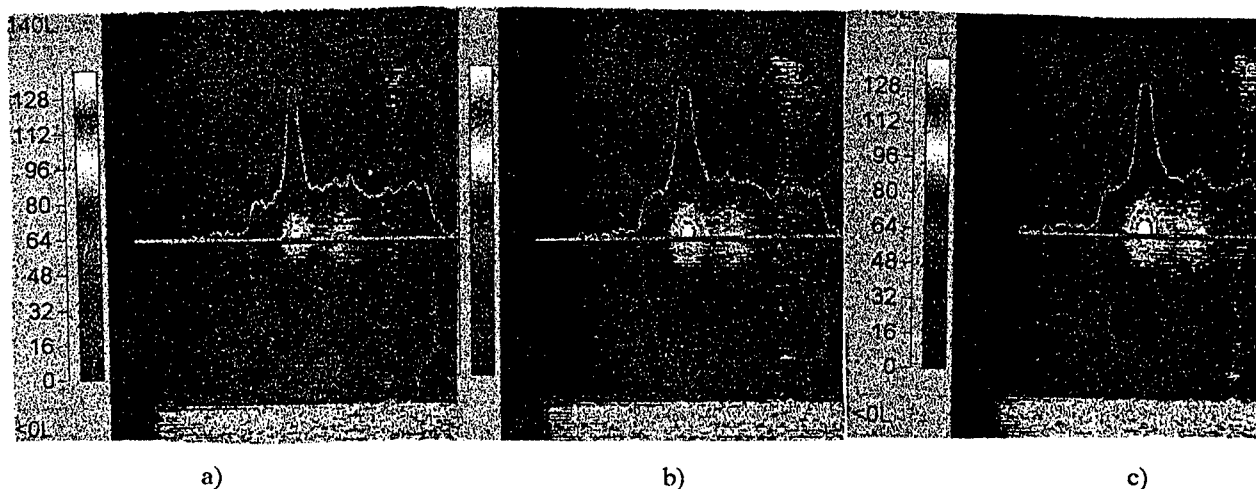


Fig.2 Thermal effects generated in paraffin under the Ar laser beam ($\lambda=488\text{nm}$, $P=1\text{W}$) at different exposure times a) $t_1=3\text{min}$; b) $t_2=6\text{min}$; c) $t_3=9\text{min}$.

In this Figure it is shown the spatial distribution of the temperature on the irradiated region and the diagrams of energetic brightness.

Thermal effects induced in gelatine due to irradiation by Ar laser ($\lambda=514.5\text{nm}$ and $\lambda=488\text{nm}$, $P=1\text{W}$) at different exposure times are presented in Figures 3 and 4.

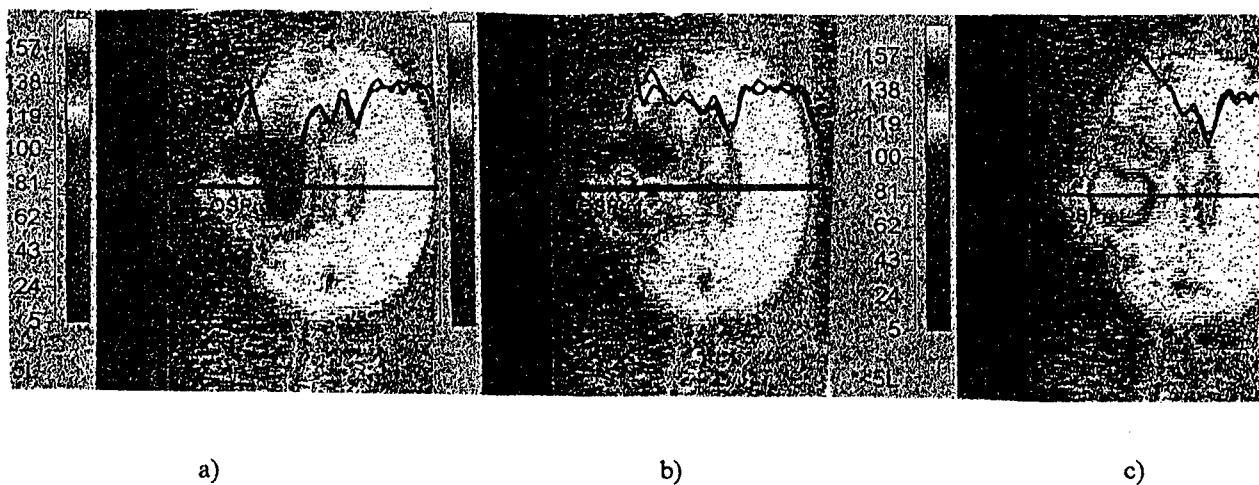


Fig.3 Thermal effects generated by Ar laser beam ($\lambda=488\text{nm}$, $P=1\text{W}$) on gelatine at different exposure times a) $t_1=1\text{min}$; b) $t_2=3\text{min}$; c) $t_3=5\text{min}$.

Figure 3 shows that depending on the exposure time the results are successive circunambient regions as the heat is dissipated.

The energetic brightness diagrams point out the evolution of the thermal state of the irradiated region. Conductibility of the paraffin is less than gelatine's conductivity.

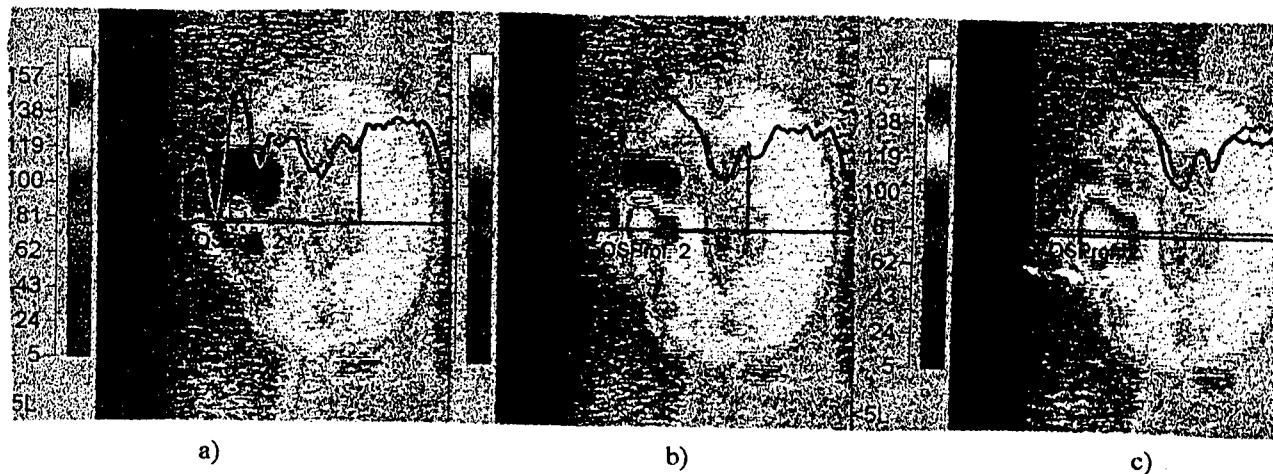


Fig.4 Thermal effects generated by Ar laser beam ($\lambda= 514.5\text{nm}$, $P=1\text{W}$) on gelatine at different exposure times a) $t_1=1\text{min}$; b) $t_2=3\text{min}$; c) $t_3=5\text{min}$.

Using the He-Ne laser ($\lambda=633\text{nm}$, $P=15\text{mW}$) for the irradiation of the gelatine determines the thermal effects presented in Figure 5 for the exposure times : 1min, 3min and 5min. The thermal effects due to laser irradiation, in this case, have less intensity than in the case of using the Ar laser.

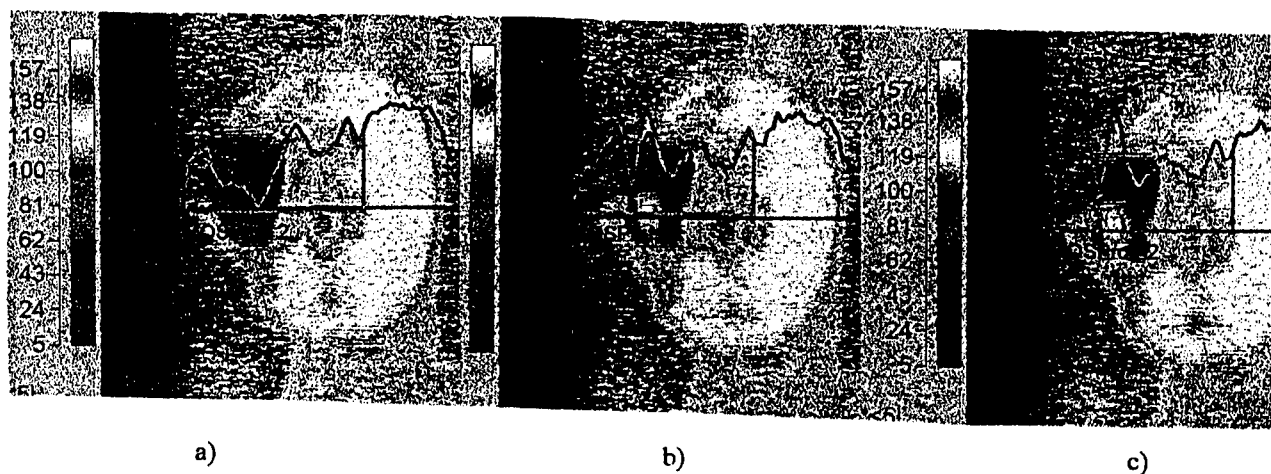


Fig.5 Thermal effects generated by He-Ne laser beam ($\lambda= 633\text{nm}$, $P=15\text{mW}$) on gelatine at different exposure times a) $t_1=1\text{min}$; b) $t_2= 3\text{min}$; c) $t_3=5\text{min}$.

The thermal effects on human tissue induced by GaAs diode laser ($\lambda=904\text{nm}$, $P=9\text{W}$) for 2 min exposure time are presented in Figure 6.

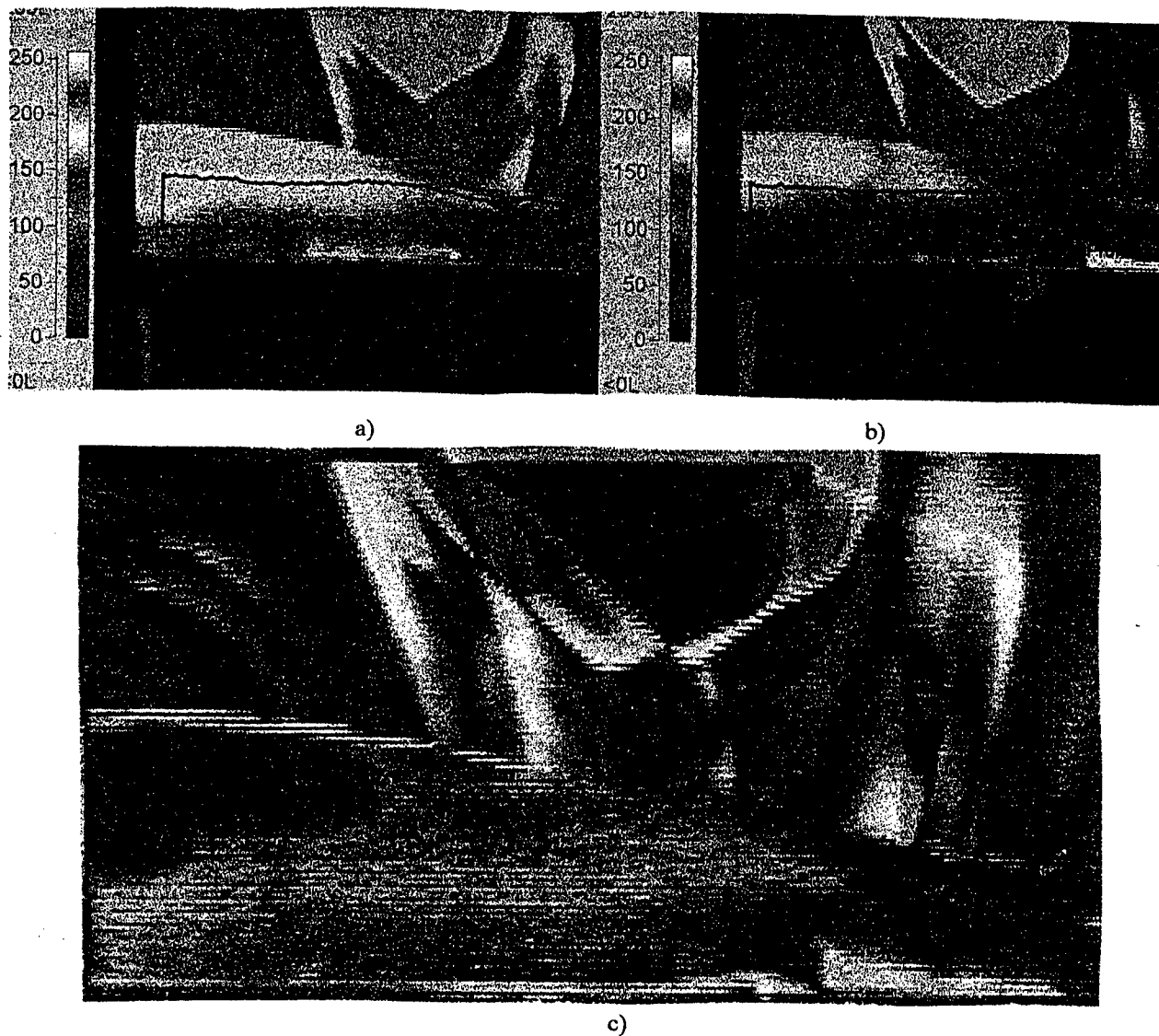


Fig. 6 The thermal effects on human tissue induced by a laser diode beam, a) before irradiation, b) after $t=2\text{min}$, c) the difference between the previous two images (a-b).

Figure 6.a represents the thermal images of arm before laser irradiation and Figure 6.b the thermal images after laser irradiation. The study of these two images shows an increasing of the energetic brightness after the laser irradiation.

Using the specialised hard-software Thermagram system it was realised the image difference between the thermal images taken before and after laser irradiation. This image-difference presents the exactly induced thermal effect by laser irradiation.

5. CONCLUSIONS

Our experience presented in this paper allows us to evaluate easily, in real time and without no risk, in future, the thermal effects induced by laser beams in living tissues Telethermography presented as a method for monitoring the thermal response of biological tissue could be used during medical treatments to give information regarding the temperature distribution of the irradiated tissue. These information are useful for the physicians to confine the heating process to any one of thermal ranges to produce the desired result.

6. REFERENCES

1. L. Goldman, *Laser non surgical medicine. New challenges for an old application*, Ed. Technomic Publising Co. Inc. Lancaster-Basel, 1991.
2. M.P. Popescu, I. Mogos, N. Nicolau, Nicoleta Labusca-Tebeanu, "Thermography as a method for ocular tumor diagnosis" (rom.), *Oftalmology (rom.)*, Vol. XX, No. 4, pp 311 - 314, 1976.
3. L. Miro, "Effets tissulaires du laser", *Angéiologie*, Vol. 37, No. 1, pp. 29 - 36, 1985.
4. A. Dallozo-Bourguignon, "Place de la thermographie dans l'appréciation diagnostique et thérapeutique", *Méditerranée Médicale*, Vol. 1, No. 232, pp. 81 - 82, 1984.

Low power laser efficacy in peripheral nerves lesions treatment

Ciprian Antipa, Mihaela Nacu, Ion Bruckner, Daniela Bunilă, Mihaela Vlaiculescu,

Mihai Pascu, Elena Ionescu

(AC, IB, MV, EI, Colțea Clinical Hospital, University of Medicine, Bucharest, Romania)
(MN, "N.Malaxa" Clinical Hospital Bucharest, Romania) (DB, Plastic Surgery Hospital, Bucharest
Romania) (MP, National Institute of Laser, Plasma and Radiation Physics, Bucharest, Romania)

ABSTRACT

In order to establish the low energy laser (LEL) effects on nervous tissue regeneration in clinical practice, we evaluated in double blind, placebo controlled study, the efficacy of LEL in the functional recovery of 46 patients with distal forearm post-traumatic nerve lesion, after surgical suture. The patients were divided into two groups: A-26 patients were treated with LEL; B-20 patients, as control, were treated with placebo lasers and classical medical and physical therapy. Lasers used were: HeNe, 632.5 nm wavelength, 2 mW power, and GaAlAs diode laser, 880 nm wavelength, pulsed emission with an output power about 3 mW. Before, during and after the treatment, electromyography (EMG) and electroneurography (ENG) were done in order to measure objectively the efficacy of the treatment.

We obtained good results after 4-5 months at 80.7% patients from group A and about the same results at 70% patients from group B, but after at least 8 months. The good results were noticed concerning the improvement of EMG and ENG registrations and on the involution of pain, inflammations, movements and force of the fingers. Finally we can say that the favourable results were obtained in at least half the time with LEL treatment faster than with classical therapy.

Keywords: low energy laser, nerve lesion recovery

Previous studies demonstrated good results on nerve regeneration when nerve is stimulated with low energy laser (LEL)^{7,9}. Best results were obtained when laser irradiation was done soon after the nerve's lesion^{3,10,11,12}. This time we tried to verify the efficiency of LEL in the functional recovery of the posttraumatic distal forearm nerve lesion after surgical suture, in a double blind placebo controlled study.

1. PATIENTS, METHOD AND MATERIAL

An initial number of 46 patients were divided in two groups: A (laser) with 26 patients treated with LEL and medical therapy; B (control) with 20 patients treated with placebo laser and classical medical and physical therapy. All the patients were young, between 18 and 34 years old, without other diseases, 19 men and 27 women. The type and gravity of the lesions were similary distributed into the two groups.

Only one physician knew which was the laser or placebo group and which was real laser or placebo laser apparatus.

1.1. Operative technique

Surgical intervention was done immediately after the injury and was predicted for the primary repairs of all the elements involved: bones, tendons and nerves. The trauma agents were cutting agents in most of the injuries and some crushes in others. The first step was to establish the priorities in the case of the acute hand injured with the overall goal of maximum function at the earliest possible time.

One of the major priorities was early establishment of accurate anatomic bone and joint architecture, usually aided by internal fixation.

Skin coverage, the other major priority, contributed significantly to early healing of all injured parts. We preferred to apply the basic techniques for skin coverage, with the best functional result. Prompt skin and soft tissue healing over the repaired deep tissues remains the basic priority. Such healing will allow an early active mobilization program and attains the maximum functional result for the patient.

The priority of nerve repair is the next consideration, because the quality of the sensory and/or motor return is a major factor in the final usefulness of the injured hand. We practiced the primary repair of the nerve, when it is cut by a sharp edge, such as a knife or piece of glass. We preferred the external epineurial suture of the bundles of fasciculi, and sometimes both external and internal epineurium. The ideal location for sutures is in the intraneural epineurium, the tissue that both surrounds and separates bundles.

The priority for tendon injury is considered last in the analysis of injury, not because it is the least important in a functional sense but because the success of any tendon repair depends primarily on the restoration of the surrounding tissues (bone, skin coverage, soft tissue bed, and sensibility), and not of the tendon repair itself. We always prefer the primary repair of both flexor and extensor tendons (Bunnel technique) in all anatomic zones of the hand in all the patients, with the restoring, as nearly as possible, of a functional gliding mechanism.

After surgery we used early mobilization which was a passive one. In order to prevent adhesions of the tendons, we controlled the passive motion with a dorsal block splint. The splint was removed after 3 weeks and then we started laser, and medical and physical therapy. At this moment we also started active mobilization (2 times a day).

1. 2. Lasers and other therapeutical means

For study group (A) we used two kinds of lasers:

a) Helium-Neon (HeNe) one, 2 mW power with a continuous emission in red, 633 nm wavelength and with a spot size about 0.5 cm.

b) Gallium Aluminium Arsenide (GaAlAs) with infrared, non-collimated, pulsed emission and skin application. The wavelength was 890 nm, with 200 ns pulsed, the spot size about 0.5 cm, and the output power about 3mW. The two kinds of lasers were applied successively at the same point, first HeNe laser, during 60-90 sec per point for each laser, in 8-10 points, per session. All the points were situated at the forearm and the hand level. At the end of every session, both lasers were also applied in an active way, along some circuits in the same anatomic area during 1 min per every laser. The total energy dose used was between 4.8 J/cm^2 and 13.5 J/cm^2 per session. The number of sessions per serie was 10-12 and we used three series at 1-2 months, 4-5 months and 7-8 months^{2, 4, 5, 11}, after surgery.

In B group (control), the patients were "treated" in the same way but with placebo laser who looked like a real laser. We couldn't let these patients without treatment, so we also added medical procedures consisting in some drugs and physical therapy (ultrasound at the affected hand level) and massage in three series, of about 10 sessions each, at the same intervals as group A. The drugs administered were vitamins, vasodilators,

antiinflammatory and also antihistaminic, antibiotics and analgesics. The massage and antihistaminic, antibiotics and analgesics were given also to the patients from A group.

In order to respect ethical medical procedures every patient gave his writing aproaval for the experiment.

1.3. Evaluation of the results

In order to evaluate the efficacy of the treatment in an objective way, we mainly took into account the results obtained by electromiography (EMG) and electroneurography (ENG), measurements done to all the patients: a) after surgical suture before the beginning of any kind of treatments; b) after first series of treaments (1-2 months); c) after second series of treatments (4-5 months); d) after the third series of treatment (7-8 months).

We choose the following parameters obtained by EMG technique measurements¹:

1. Spontaneous activity of the muscle, which is normally absent, (long abduction for the radial nerve and short abductor for the medial nerve) and which was detected by concentric needle electrode. It is also absent 2-3 weeks after the nerve section. In case of favourable evolution of the nerve regeneration, spontaneous activity became present, expressed by fibrillation potential which diminishes in amplitude and frequency following favourable evolution.

2. After maximal muscular contraction, the analysis of the electric changes obtained also by concentric needle electrode, took into account the following aspects:

- a) general image which normally is interferential, after nerve damage became simple or intermediary (Figure 1);
- b) measurement of the motor unit potentials (MUP) parameters: amplitude, duration and morphology.

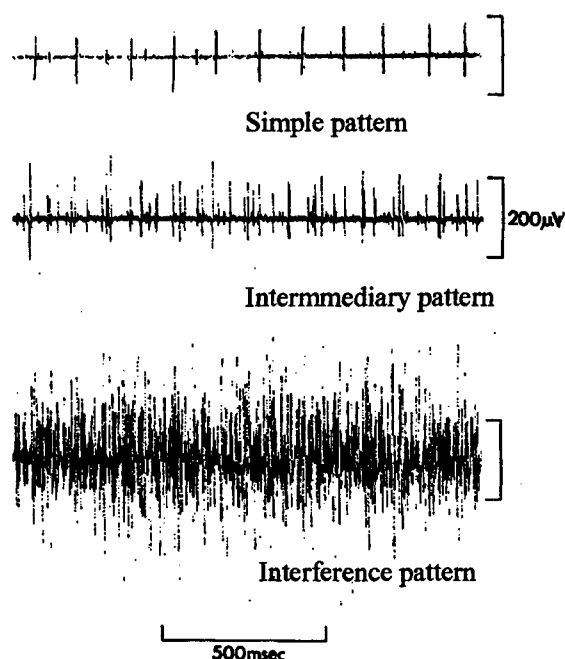


Figure 1. Motor unit activity during increasing voluntary

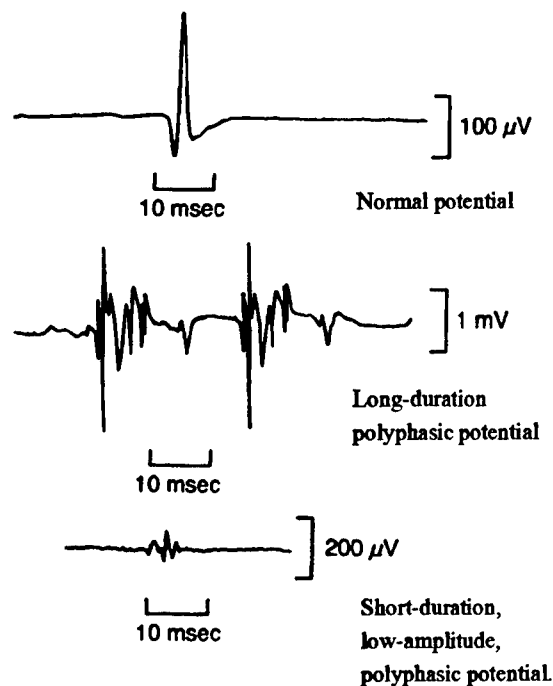


Figure 2. Motor unit potentials.

When patients couldn't realize maximal muscular contraction we used ENG, meaning electric nerve stimulation by a surface electrode, thus obtaining the same parameters of MUP (Figure 2).

3. Motor conduction velocity and distal latency detected by a surface electrode (ENG).

We also detected nerve degeneration reaction (classic EMG) but because of the lack of accuracy of the parameter, we didn't consider it in the results appreciation.

We also followed a less important way to appreciate the results: the subjective measurement on a 10 points scale of pain (done by the patients itself) and appreciation of the weakness of the fingers' muscles, swellings and articular movements (done by the physicians). The measurements were done at every stage of our study and we took into account only a difference over 3 points on this scale².

Of course, the neurophysiologist who interpreted the results didn't know to which group every patient belonged.

When clinical and EMG measurements weren't quite concordant we gave more credit to EMG measurements.

We want to underline the fact that, trying to eliminate some possible error factors, we include in both groups only young patients and without any other diseases such as diabetes mellitus, alcoholism, hepatic diseases, immunological disease, etc., which could alter EMG and ENG results¹.

Possible errors can be due to the little number of patients, local peripheral temperature and local vascularization of the nervous branches of the examined areas^{7,8}.

2. RESULTS AND DISCUSSIONS

The EMG and ENG parameter measurements as well as clinical and subjective observation were done four times, after approximately three weeks from surgical suture moment, before any medical or laser treatment. Second measurement was done after 1-2 months, after the first series of treatments (laser or classical), third measurement after 4-5 months (second series of treatments) and the fourth after 7-8 months (third series of treatment).

2. 1. Before treatments (after surgery)

The measurements for all 46 patients showed the following:

- a) spontaneous activity was absent. In fact it is too soon for such an activity to appear.
- b) MUP-amplitude parameter: a variation between 300 μ V and 900 μ V with an average of 650 μ V:
 - duration: a variation between 3-8 msec with an average of 5 msec;
 - morphology: polyphasic potentials, in a percentage of 20%, present at 11 patients (from the total number of 38) and, in a percentage between 12-15%, the rest of the 27 patients.
- c) MCV (motor conduction velocity) was varied from 24 to 40 m/sec with an average of 32 m/sec and DL (distal latency) varied from 4 to 10 msec with an average of 7.5 msec (table 1).

After any kind of treatment, these average value parameters have no useful significance for appreciation of the results, because of the great individual numerical variety. So we used the percentage of the patients with favourable evolution. This was considered to be a function of the good evolution of the mentioned parameters' values, measured and described at each stage.

Clinical examination found important weaknesses of the fingers' muscles, swelling, stiffness of the joint, lack of local sensitivity and pain. Each of these clinical troubles found before treatments was considered to be a comparison term for the future appreciations of their evolution after any kind of treatment.

Table 1. Comparison between normal values and average pathological values
(after surgical suture) of the mentioned parameters of all patients

Parameters	Normal values	After surgery but before treatment (average)
MUP (motor unit potentials) • Amplitude: • Duration: • Morphology: (polyphasic potentials)	200 μ V - 2 mV 5-8 msec <10-12%	650 μ V 4-5 msec 11 patients: 15-20% 27 patients: 12-15%
MCV (motor conduction velocity)	57-60 m/sec	32 m/sec
DL (distal latency)	2.5-4 msec	7.5 msec

2.2. After the first series of treatments (2 months)

Group A (laser): 10 patients (38.46%) had good pattern improvements such as: fibrillation potentials as a spontaneous activity and intermediary pattern at maximal muscular' contraction. MUP had (average): amplitude

about 1.8 mV, duration 7 msec and morphology with polyphasic potential between 15-20%. MCV at these 10 patients was (average) 40 m/sec and distal latency (average) 5 msec.

Clinically we noticed significant improvement of swelling motility and local sensitivity, as well as diminishing of pain.

For the other 16 patients (61.54%) the average of the parameters' changes were less significant: very frequent fibrillation potential and simple electric pattern after maximal contraction; PUM had amplitude 2 mV, duration 6-8 msec and polyphasic potential over 20%; MCV was under 40 m/sec and distal latency 6-7 msec. Also clinical changes were less significant. Generally we consider their results as stationary.

Group B (control): In this group we found only 5 patients (25.0%) with significant improvements and 13 patients with an evolution considered to be stationary (65.0%), the numeric average being similar with those of patients from group A. We noticed 2 patients (10.0%) clinic and EMG aggravation (table 2).

Table 2. Results after the first series of treatments (approx. 2 months)

Patients	Ameliorated	Cured	Stationary	Agravated
Group A	38.46% (10 patients)	0	61.54% (16 patients)	0
Group B	25.0% (5 patients)	0	65.0% (13 patients)	10.0% (2 patient)

2. 3. After the second series of treatments (4 months)

In **Group A:** 7 patients (26.93%) were considered to be cured because their clinical and EMG parameters were almost normal. 14 patients (53.84%) were treated as ameliorated because: we found rare fibrillation potentials and at maximal contraction the pattern was intermediary; MUP have had amplitude 1.9 mV, duration 6 msec and morphology with polyphasic potentials of 12-15%; MCV was about 47 m/sec and distal latency 4.5 msec. 5 patients (19.23%) have had their parameters almost unchanged.

In **Group B:** only 1 patient (5%) was considered cured, 9 patients (45%) ameliorated, and 9 patients (45%) with stationary evolution (table 3). At 1 patient (5%) the clinical and EMG measurements were still considered as aggravated. The average values were inferior to those obtained from the Group A patients.

Table 3. Results after the second series of treatments (approx. 4 months)

Patients	Ameliorated	Cured	Stationary	Agravated
Group A	53.84% (14 patients)	26.93% (7 patients)	19.23% (5 patients)	0
Group B	45.0% (9 patients)	5.0% (1 patient)	45.0% (9 patients)	5.0% (1 patient)

2. 4. After the third series of treatments

For **group A** patients, results remained almost the same as after the second series of treatments with the exception of one patient from the ameliorated group who was cured, and the percentage became 30.77%.

For group B: 10 patients (62.5%) were considered ameliorated and 2 (12.5%) cured, 3 patients (18.7%), remaining stationary. The average values of the analyzed parameters were similar with those described at the group 4 after four months. The patient considered aggravated also remained in this bad condition (table 4).

Table 4. Results after the third series of treatments (approx. 8 months)

Patients	Ameliorated	Cured	Stationary	Agravated
Group A	50.0% (13 patients)	30.77% (8 patients)	19.23% (5 patients)	0
Group B	55.0% (11 patients)	15.0% (3 patients)	25.0% (5 patients)	5.0% (1 patient)

In a synthetic image as a percentage of the patients' favourable final results (amelioration and cured cases) of the laser group (A) and control group (B), it is obvious that LEL treatment is more efficient than medical and physical therapy in the recovery of the peripheral distal forearm nerve lesion after surgical suture (figure 3). It can be remarked that the results were comparable without statistical significance for both groups after 2 and 8 months. The greatest difference ($p < 0.05$) was noticed after the second series of treatments (4 months), 80.77% vs. 50% (control group). The good results obtained with LEL therapy after 2nd series of treatment (4 months) are comparable with those obtained with classical therapy but after 8 months.

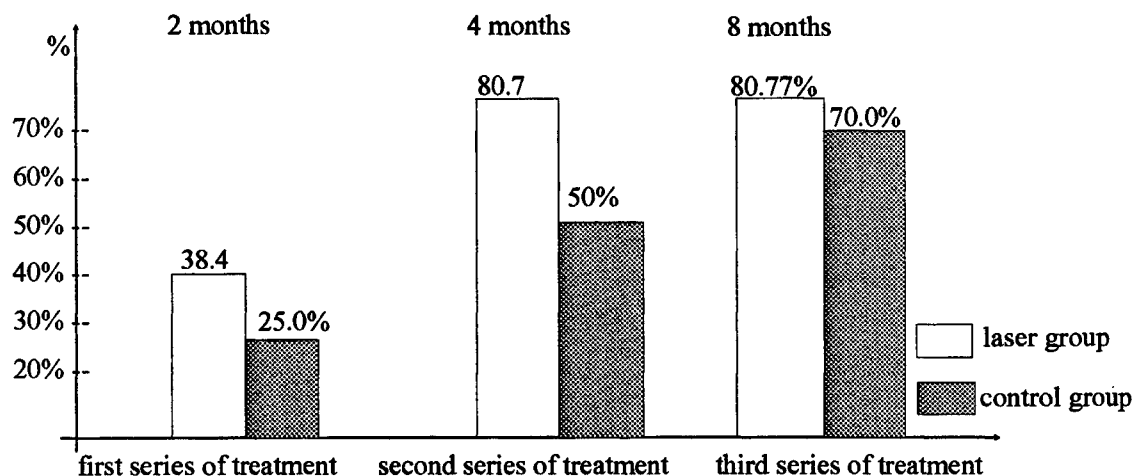


Figure 3. Comparison between the two groups favourable final results after each series of treatment (ameliorated and cured).

In fact we proved that with LEL therapy could be obtained better results and in at least half the time versus classical medical and physical therapy. Normally, without LEL therapy, the recovery begin at 4-5 months and is almost complete after 8-12 months (sometime after two years). Thus, we have twice shortened the time needed for recovery. We noticed a correlation between improvement EMG and ENG parameters and clinical status (swelling, sensitivity, mobility and pain) of the patients.

These better results obtained with LEL could be due to more rapid decrease of the swelling and inflammation, development of the local microcirculation^{3, 4, 5, 6, 12}, but we think that the main mechanism is the acceleration of the nerve myelin sheath restoring, because the very good results were obtained in reducing distal latency.

Speaking about recovery results we didn't find any differences between the affected nerves or different type of the initial lesions (cutting or crushing). We also didn't find any differences between male and female patient recovery.

We want to underline that we didn't notice any side effects of the LEL therapy.

So we showed, in our double blind placebo controlled study, that LEL therapy is at least, twice more efficient than other classical therapeutical means in the recovery after posttraumatic distal forearm lesion and surgical suture of the local peripheral nerve.

3. REFERENCES

1. M.J.Aminoff "Electromyography in clinical practice" - Churchill Livingstone, New York, 1987.
2. C.Antipa, C.Moldovan, A.Podoleanu "Low energy laser use in medicine and biology" in *Laser and Technology*, 4: 51, 1994.
3. K.Atsumi "Low power laser applications in medicine and surgery" in *Surgical and medical Lasers*, vol. 2, 4: 254, 1989.
4. J.S.Basford, H.O.Hallman, J.Y.Matsumoto, S.K.Moyer, J.M.Buss, G.D.Baxter "Effects of 830 nm Continuous Wave Laser Diode Irradiation on Median Nerve Function in Normal Subjects" in *Lasers in Surgery and Medicine*, 13:597, 1993.
5. G.D.Baxter "Therapeutic lasers - theory and practice", Churchill-Livingstone Edit., 1994.
6. T.I.Karu "Interaction of monochromatic light and near IR/radiation with cells: currently discussed mechanisms", in *Proceedings of the Photonic West Biomedical Optics '95, San Jose, CA, 2391 B-59, 1995*.
7. *** *Laser Application in Medicine and Surgery* - Galletti, Bolognani, Ussia - ed., Monduzzi, Bologna, 1992.
8. A.S.Lowe, G.D.Baxter, D.M.Walsh, J.M.Allen "Effect of Low Intensity Laser (830 nm) Irradiation on Skin Temperature and Antidromic Conduction Latencies in the Human Median Nerve: Revelance of Radiant Exposure", in *Lasers in Surgery and Medicine*, 14:40, 1994.
9. S. Rochkind, "Clinical and Experimental Aspects of Laser Therapy in the Neurosurgical and Neuro-Rehabilitation Fields", *Proceedings of the XI Congress, International Society for Laser Surgery and Medicine, Buenos Aires, p.99, 1995*.
10. S. Rochkind, G.E.Quakmne "Microsurgical Reconstruction of the Peripheral Nerve and the Brachial Plexus Followed by Laser Therapy", *Proceedings of the XI Congress, International Society for Laser Surgery and Medicine, Buenos Aires, p.105, 1995*.
11. M.Rosner, M.Caplan, S.Cohen, R.Duvdevani, A.Solomon, E.Assia, M.Belkin, M.Schwartz "Dose and Temporal Parameters in Delaying Injured Optic Nerve Degeneration by Low-Energy Laser Irradiation", in *Lasers in Surgery and Medicine*, 13:611, 1993.
12. M.Schwartz, E.Yoles, A.Solomon et al "Low energy laser irradiation as a neuroprotective modality" in *Laser Tissue Interaction II, SPIE, 2391: 627, 1995*.

Low power laser use in the treatment of alopecia and crural ulcers

Tavi Ciuchiță, Mircea Ușurelu, Ciprian Antipa, Mihaela Vlaiculescu, Elena Ionescu

(T.C. – Military Hospital, Pitești, Romania, M.U. – Military Hospital Cluj, Romania,
C.A., M.V., E.I. – Colțea Clinical Hospital, Bucharest, Romania)

ABSTRACT

The authors tried to verify the efficacy of Low Power Laser (LPL) in scalp alopecia and crural ulcers of different causes. Laser used was (red diode, continuous emission, 8mW power, wave length 670 nm spot size about 5 mm diameter on some points 1-2 minutes per point. We also use as control classical therapy. Before, during and after treatment, histological stamples were done for alopecia. For laser groups (alopecia and ulcers) the results were rather superior and in a three or twice time shorter than control group.

We conclude that LPL therapy is a very useful complementary method for the treatment of scalp alopecia and crural ulcers.

Keywords: low power laser, scalp alopecia, crural ulcers

In dermatology, the low power lasers (LPL) were used about 20 years ago.

The possible efficacy of LPL in the treatment of alopecia of the scalp, or crural ulcers, either singular or associated with the classical treatment, represents the aim of this work.

1. PATIENTS, MATERIAL AND METHOD

During two years, the utility of the LPL therapy applied alone or in association with the classical treatment in the androgenetic alopecia stages I-III, or unique or multiple-plaque-pelade, was verified on 60 patients (34 men and 26 women). In the same period, 24 patients (14 men and 10 women), with crural ulcers of diabetic, varicosis or artheritic causes were also treated with LPL.

Patients were distributed into two groups: the control group treated with classical therapy and the laser group, which were similar as regards the diagnostic, the stage of disease, the age and the sex. So the patients of both diseases were divided into control and laser groups.

For androgenetic alopecias and single or multiple plaques pelades the control group included 27 patients treated only by classical therapeutic well known drugs general or topical. The laser group included 33 patients treated with the laser after the therapeutic protocol mentioned above. Because we noticed that after stopping laser therapy there was at some patients a tendency of relapsing we associated laser with classical therapy.

For crural ulcers of various causes the control group of 11 patients was treated with classical dermatological therapy and the laser group (15 patients) was treated with the laser mentioned above. We also treated five of the 11th patient of the control group with placebo laser but only for a week for ethical reasons.

The patients of the control group were monitored every month for a period of 180 days of classical treatment. After this time interval independence of the clinical results obtained individually, either the treatment was carried on, or the patient was monitored with respect to the post-therapeutic course.

After the end of the classical treatment period, patients were monitored monthly for a period of 90 - 160 days, during which the possible appearance of post-therapeutic relapses and side-effects was followed-up.

Laser used was a red diode laser, wavelength 670 nm, spot size 5 mm, continuous emission, and 8 mW power. For both diseases, LPP was applied in a variable number of points (8-to 40) and for 1 - 2 minutes per points depending on type and extension of lesions. The points were situated contouring and inside the lesion at maximum 1 cm between them. Every daily session finished by 2 - 5 minutes of scaming the lesion.

Before starting the LPL treatment and after the end of the LPL therapeutic protocol, to all patients with alopecia were performed target biopsies.

It should be mentioned that the therapeutic protocol was unmodified when associating the LPL therapy with the classical treatment and the administered doses.

So the final results were analyzing by measuring the dimensions of the lesions and by histological proofs.

2. RESULTS

At the patients with alopecia, in the control group at 14 of them (52%) the stopping of the hair loss was obtained after 120 days and the growth of vellus type and mature hair, in 180 - 210 days (on the average in 195 days).

At these patients with favourable effects of the classical therapy, the monthly monitoring performed for 90 - 180 days detected the occurrence of a post-therapeutic relapse after 90-120 days (the loss of more than 80-100 hairs/24 hours reappeared), requiring the resumption and carrying on of the treatment.



Fig.1 Histological samples before laser therapy

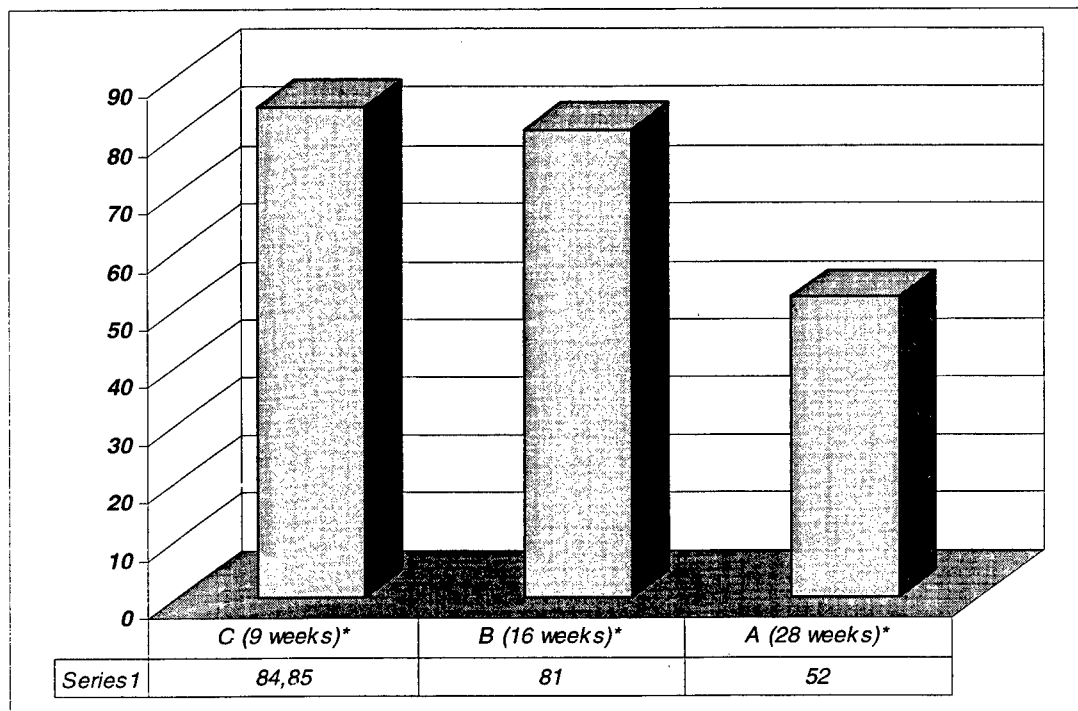


Fig.2 Histological samples after laser therapy

In the LPL group at 27 patients (81,4%), the stopping of hair loss was obtained in 45 days. That means a significant shortening of the time interval required for the appearance of favourable effects on pilogenesis as compared to the classical treatment (120-195 days).

The histopatological examinations (Fig. 1, 2) preformed before and after the LPL treatment confirmed in 27 cases (81,41%) the histopatological criteria marking a favorable course of LPL treated alopecias of the scalp, whereas in 6 cases (18,58%) these histopatological criteria were absent.

The monthly monitoring for 90 days of the 27 patients (81,41%) with favourable effects of the LPL treatment detected a post-therapeutic relapse after 45-60 days since the last LPL session. The time interval required for the hair regeneration by the LPL method was by 50% shorter in comparison with the control group. (Fig. 3)



*A = 52% regeneration ≈ 195 days (classical treatment)

*B = 81,41% regeneration ≈ 75 days (LPL treatment)

*C = 84,85% regeneration ≈ 60 - 65 days (LPL and classical treatment)

Fig. 3. Regeneration of hair follicles by the classical method, LPT and the combined method in alopecia of the scalp.

The associated LPL treatment with the classical therapy, applied to the 33 patients (55%) of the laser group, led to the following results:

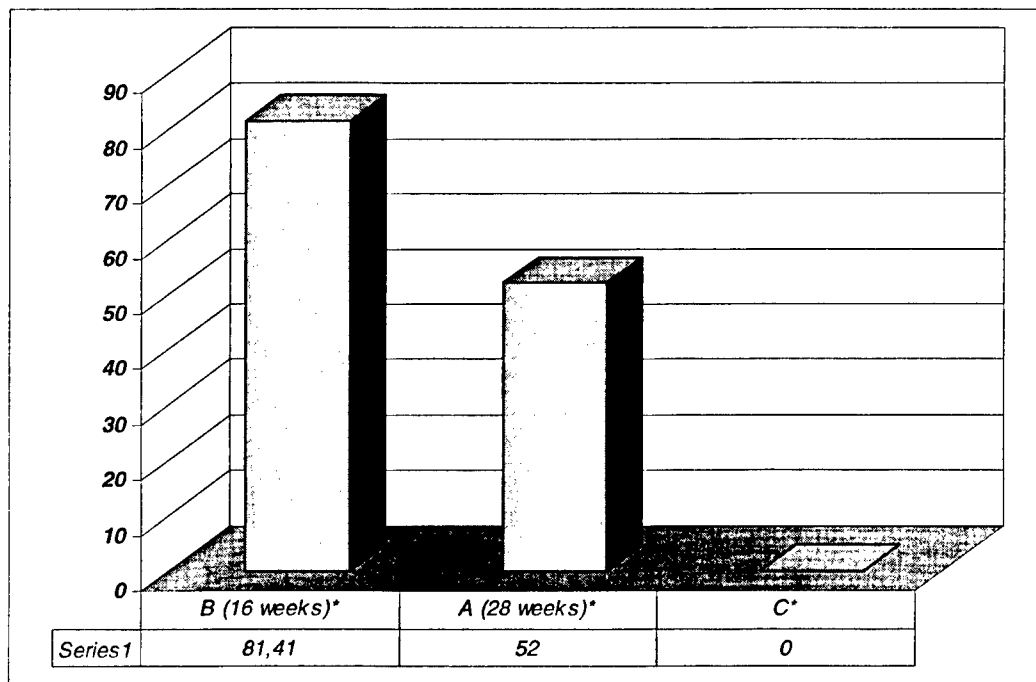
In 28 patients (84,8%), the stop of hair loss was obtained within 40 days (the equivalent of 44 - 47 LPL sessions). These results are better in comparison with the result of LPL treatment but without statistical significance. (Fig. 4)

In exchange, the results obtained with LPL single or with classical therapy were significantly better ($p>0,001$) than classical therapy alone.

The histopathological examination confirmed in 28 cases (84,85%) the presence of histopathological criteria of a favourable course after the associated treatment, the absence of the histopathological criteria being recorded only in 5 caeses (15,15%) treated by association of LPL with the classical treatment.

Speking about crural ulcer the average result were obtained in at least three time shorter with LPL than classical therapy as we can see in fig 5.

At the begining of the laser treatment the favourable changes. Were more impresive especially characterised by the regeneration of the border of the lessions.



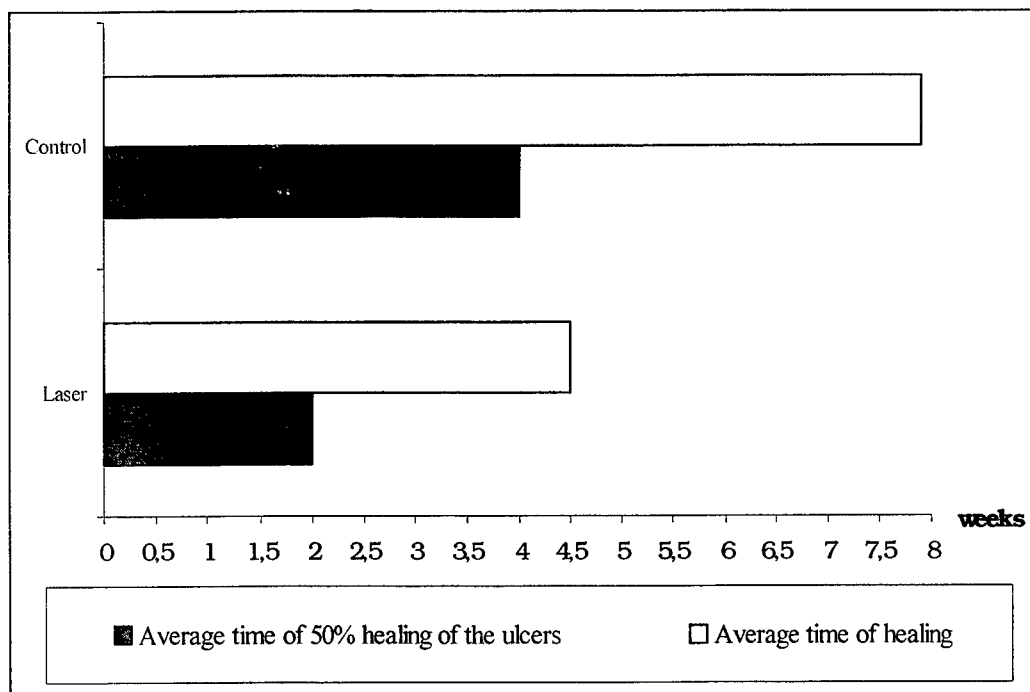
*A = 52% post-therapeutic relapse in classical treatment (90-120 days)

*B = 81,41% post-therapeutic relapse in LPT treatmet

*C = 0% post-therapeutic relapse in LPL and classical treatment after 90 days

Fig. 4. Post therapeutic relapse in alopecia of the scalp.

Fig. 5. Time of the crural ulcers healing



3. DISCUSSION

The LPL action on the hair follicle regeneration in the alopecia of the scalp and on healing of the crural ulcers, is probably determined by the synergism of the following effects:

- The trophic LPL effects stimulated the hair follicle regeneration in the alopecias and pelades of the scalp in the patients of the laser group, at calculated values from $E = 0,36$ to $0,48 \text{ J/cm}^2$ session.
- The anti-inflammatory effect of LPL is probably due to lowering the PGE2 secretion (useful especially in pelades of the scalp) or by diminishing the inflammatory oedema through histamine release as a consequence of mastocyte degranulation.
- The biostimulating effect of LPL which acts in several directions:
 - Stimulation of the protein synthesis by increasing the RNAm and DNA synthesis, respectively by enhancing the mitochondrial activity through the increase of ATP utilization and the acceleration of the respiratory chain in cytochrome.
 - Increase of the cell interferon synthesis.
 - Stimulation of mitoses, but without inducing nuclear mutations.
 - Stimulation of the capillary shunt opening by the lymph drainage.

Thus, the most rapid hair follicle regeneration was obtained by the association of LPL with the classical treatment in 28 days (84,85%) in the laser group within 65 days, this period being significantly shorter than that of hair regeneration in the 14 patients (52%) of the control group treated by the classical method for alopecia of

the scalp and rather comparable with the duration of regeneration obtained by the LPL treatment in 27 patients (81.84%) of the laser group (75 days).

The follow-up of the post-therapeutic results showed the absence of clinical relapses in 28 patients (84.85%) treated by LPL association with the classical treatment, for a period of 90 days, this result being superior in comparison with the appearance of the clinical relapse in the patients of the group within a time interval by 50% shorter (5-60 days) than in the patients of the control group, who responded favourably to the classical therapy (14 patients – 52%, 90 – 120 days).

The favourable post-therapeutic course was histopathologically objectified on the basis of specific criteria of the pelade, as well as of the androgenetic alopecia.

A therapeutic "resistance" of male patients treated for androgenetic alopecia was observed in comparison with the patients treated for unique or multiple pelade, regardless of the method of treatment used. On the other hand, age-differences in the therapeutic efficacy were not observed.

For crural ulcers the final results were superior when LPL, the regeneration time being, about three time shorter without relation with the cause of the ulcer. We remarked that after only two or three sessions, the border of the lesion started to regenerate.

We didn't noticed any side effect of the laser treatment.

In conclusion:

The regeneration of hair follicles in the LPL treated alopecia of the scalp is earlier obtained by the LPL therapy (75 days) in comparison with the results obtained by the classical treatment (95 days).

The persistence over time of the hair regeneration in the LPL treated alopecia of the scalp is by 50% shorter (45 – 60 days) in comparison with the results of the classical treatment (90 – 120 days).

The association of the two methods in this treatment of the alopecia of the scalp led to superior results in comparison with each method separately.

The LPL laser therapy proved to be very useful in the treatment of crural ulcers shortening significantly the time of heading.

4. REFERENCES

1. D.G. Baxter, "*Therapeutic Lasers – theory and practice*" – C. Livingstone - edit., 1994.
2. C. Bodemir, "Pelade a l'Anglaise", *Abs. Derm.* 1996, 303, 23-25.
3. P. Bouhana, "Cheveux - les racines du progres", *Abs. Derm.* 1996, 303, 24-25.
4. J.L. Boulinois, P. Richand, "Rayonnement laser et matière vivante", *Cahier de Bother*, 1981, 72: 56-59.
5. P. Couche, "*L'Énergie douce face à la douleur*", Lyon, 1993, 7-34.
6. P.J. Chavoine, "Effets thérapeutiques des lasers", *Colloque Genie Biol.Med. Toulouse*, 1982, 27, 10.
7. I.C. Elio Paulos, Trikhos, "Le journal du cuir chevelu", *Abs. Derm.* 1994, 204, 19-22.
8. J.P. Jacobs, "Use of tropical minoxidil therapy for androgenic alopecia in women", *J.Dermatol.*, 1993, 32, 10, 758-762.

9. R.I. Kelly, "Complications of artificial hair implantation", *J. Royal Soc.Med.*, 1994, 67, 291-292.
10. F. Laffitte, "Principes generas du laser". Reunion: laser en pathologie cutanée, Toulouse, 1983.
11. E. Mester, "L'aspect biostimulant du rayon laser", *Cahier de Biother*, 1983, 77, N Sup.: 59-65.
12. L. Miro, "Les effets tissulaires du rayonnement laser", Reunion laser en pathologie cutanée, Toulouse, 1983.
13. M. Nut Brown, Trikhos, "Le journal du cuir chevelu", Reunion annuelle de l'European hair research society, Stockholm, 1993, *Abs. Derm.*, 1994 208/209, 15-22.
14. V.A. Randall, "A comparison of the culture and growth of dermal papilla cels from hair follicles from non-balding and balding (androgenetic alopecia) scalp", *BR. J. Dermatol*, 1996, 134: 434-444.
15. R. Thill, "Alopecie au feminin", *Abs. Derm.*, 1994, 210, 18-19.

SESSION 6

Optoelectronics

„Applications of infrared, heterodyne detection systems”

M. STRZELEC, Z. PUZEWICZ*, M. KOPICA

Institute of Optoelectronics, * Team of Quantum Electronics

Military University of Technology, 01-489 Warsaw,

2, Kaliski Str., Poland

SUMMARY

Paper presents the theoretical and practical solutions of infrared, heterodyne detection systems applied in the pollution monitoring, methane detection, industry as well as laser spectroscopy. The utilization of stabilized laser diodes, coherent pumped solid state lasers as well as CO₂ lasers with conversion of generation frequency covers the broad band of infrared region especially interesting for detection of different atmosphere pollutants or gas contaminants. Low cost heterodyne vibrometers, velocimeters or rangefinders can find wide industrial or metrological applications.

1. INTRODUCTION

Investigations of sensitive, heterodyne, infrared systems, started in IOE MUT in the early 80-ties [1-3], allowed the development of several laboratory devices for laser ranging and pollution monitoring [4-6], utilizing the CO₂ laser transmitter and pulse compression detection techniques. In the last two years, due to the fast improvements of technology of different laser sources, detectors of laser radiation as well as electronic subassemblies, it was possible to project and develop heterodyne systems utilizing different wavelengths in the infrared region with wide applications.

In a typical heterodyne detection system, the transmitted laser beam, backscattered on the object, returns to the detector as the signal beam. At the same time, another beam is sent directly to the detector (local oscillator beam), emitted by the same or by another laser, but phase coupled with the first one. One of these beams has a frequency offset, achieved, for example, using A-O modulator. Both signals interfere on the detector surface and the resultant signal is proportional to the incident beam intensity in the bandwidth of the frequency offset. For frequency offset $\Delta F = 0$ (Fig. 1.), system works in homodyne regime, useful for example in vibration sensing. If the frequency shift, introduced by object is very big (fast moving objects), the post-detector electronics can track this frequency shift, preserving low bandwidth of detection (low noise), which is the equivalent of audio super-heterodyne systems. The idea of heterodyne detection of laser radiation is presented on fig. 1.

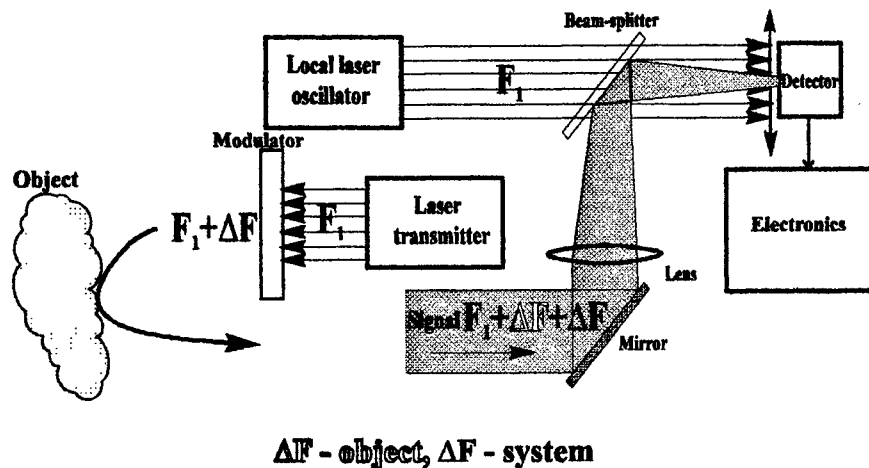


Fig. 1. The idea of heterodyne detection of laser radiation.

Laser diodes as well as diode pumped solid-state lasers can serve now as efficient sources of radiation in the near infrared region. The decreasing of production costs in connection with the increasing of wavelength stability and frequency tunability allows to cover the wide band of spectrum as well as to build low-cost measuring devices. The wavelength of CO₂ lasers, after detuning or frequency doubling/mixing (nonlinear crystals) can be utilized for the detection of many species present in the atmosphere. As an example the region of 9-11 μm is convenient to measure SO_x, NO_x concentrations and wavelength around 3.4 μm is characteristic for methane absorption. Heterodyne detection of scattered or reflected laser radiation increases the range and resolution of these measurements.

2. APPLICATIONS OF HETERODYNE LASER SYSTEMS

Fig.2 shows study, research and development works on heterodyne systems, performed in IOE MUT during last 15 years. Most of them utilized CO₂ laser transmitters and were connected with military applications.

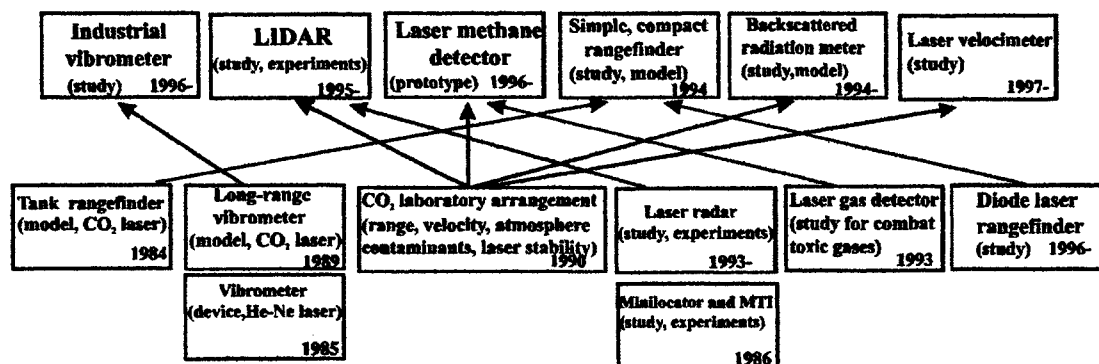


Fig.2. List of developed military systems and their possible conversion to civilian applications.

2.1. Vibrometers.

The idea of optical, laser measurements of vibrations isn't new and is represented on the market by He-Ne laser systems [7]. As compared with the visible range, utilization of middle infrared radiation can improve the range of system and penetration in bad weather conditions or in industrial dust. Important is also eye-safety of backscattered radiation. The optical layout of a simple CO₂ laser vibrometer is shown on fig.3.

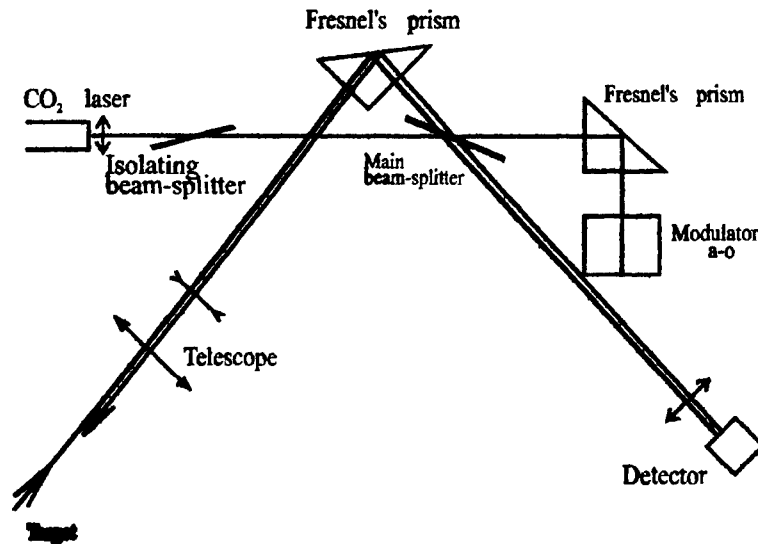


Fig.3. Optical scheme of simple infrared heterodyne vibrometer.

Several elements of the system (reflective a-o modulator, prism polarizers,) were developed earlier for laboratory heterodyne arrangement [1]. The reference beam is formed by small reflection of radiation from main beam-splitter placed almost at Brewster angle. Changes of polarization due to Fresnel's prisms allow to direct radiation into the proper axes.

System, tested outside the laboratory, have shown possibility to detect vibrations of diffuse target (amplitude of 1mm, audio frequency) in the range up to 500 m using uncooled HgCdTe photodiffusion effect detector and in the range up to 2000 m. for thermoelectrically cooled HgCdTe photodiode.

2.2. Laser methane detectors

Natural gas leakages are dangerous for environment, residents and industrial plants. Gas industry is looking for compact, sensitive and low-cost devices, able to detect and measure natural gas leaks, indicating the real place of gas leakage, measuring the level of gas flight in all-weather conditions. Up to date, market offers chemical or semiconductor transducers, combustion or spectroscopy gas analyzers, able to detect and measure gas existence in the place of measurement. These devices work for external temperatures above 0°C and are not able to indicate the real place of gas leakage. The progress in laser and optoelectronic technology allows to build the simple, portable gas analyzers fulfilling the demands of

end users. Heterodyne detection of scattered laser radiation can significantly improve the performance of these devices.

Figure 4 shows the absorption spectrum of methane, the main component of natural gas. From the point of view of absorption coefficient, the most interesting are absorption bands around 1.6 μm ., 2.3 μm ., 3.4 μm . and 7.6 μm . but the final selection should be based also on the availability of laser sources, sensitivity and costs of detection systems.

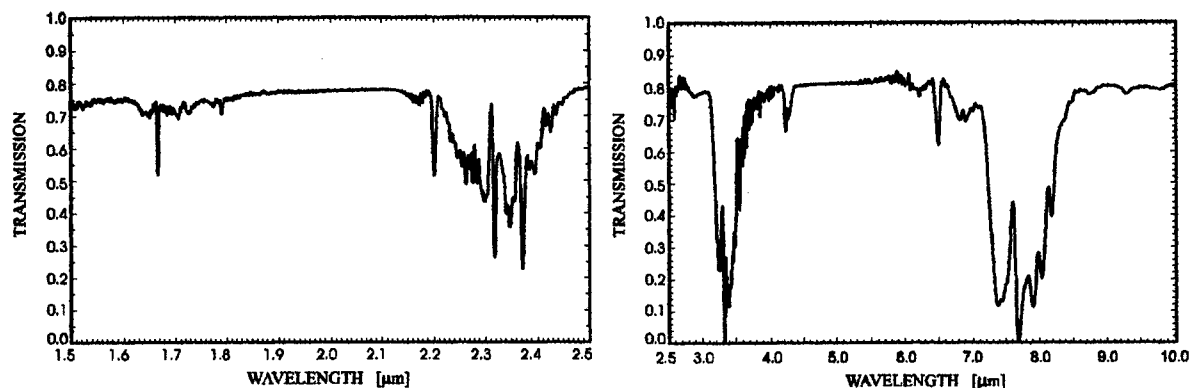


Fig.4. Absorption spectrum of methane.

The idea of active, laser gas analyzer (DIAL principle) is shown on fig.5. The utilization of differential detection, when one wavelength of radiation is absorbed by methane, and second one is the reference beam, as well as heterodyne detection for both wavelengths significantly improves the sensitivity (range) of the system.

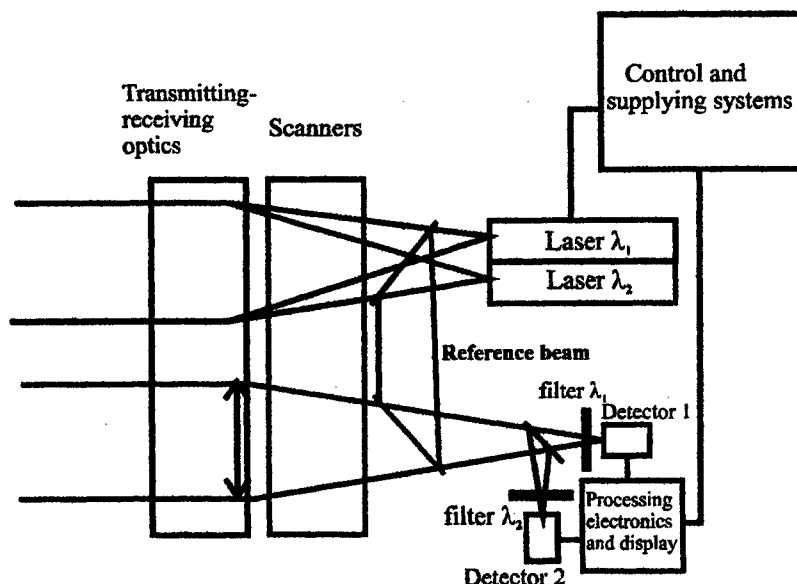


Fig.5. Differential absorption laser gas detection system.

Wavelength conversion of laser radiation using nonlinear crystals is one of the methods allowing to obtain higher output power of laser transmitter as compared to natural generation wavelength of another laser. Second harmonic generation and frequency summing of CO₂ laser radiation (fig.6) secures several times higher resulting output power in the 3.4 μm band of methane (ethane) absorption than output power of infrared He-Ne laser [8].

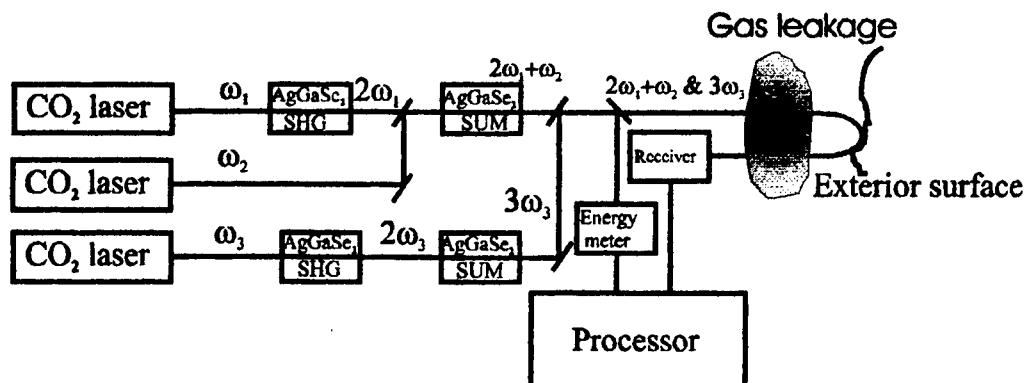


Fig.6. DIAL system utilizing three CO₂ lasers and wavelength conversion for ethane (methane) detection.

The big progress in the technology of diode lasers as well as coherent pumped solid-state lasers enables to develop heterodyne systems in the 1.6 μm. absorption band of methane (infrared laser diode, diode pumped YAG:Er laser).

2.3 Scattered radiation analyzers.

Although all heterodyne systems work on the principle of detection of scattered radiation, in some applications the amount of backscattered radiation can be the measure of surface or material parameters. Two heterodyne systems, utilizing CO₂ lasers and room-temperature HgCdTe detectors were developed on the base of universal arrangement, presented in [1]. The first application was connected with the measurement of diffuse reflection coefficient of coal. During laboratory experiments it was found, that reflection coefficient is connected with the ash contents in coal, a parameter important for mining industry and users. The relation was nearly linear, but varied in dependence on place of mining. After scaling of results from every coal-mine and generating data base it was possible to determine the ash contents with the accuracy of about 0.5% in a fast measurement. The standard procedure (burning in a stabilized furnace) takes several ours. In the second application, system tested the uniformity of calorimeter discs, black covered to absorb radiation.

3. CONCLUSIONS

This brief review shows, that laser heterodyne systems can find many, sometimes unexpected applications. In many cases sufficient are simple, compact lasers with low cost uncooled detectors. As a result of big interest of end users, special attention was paid to gas leaks detection and measurement.

Initial experiments and model investigations have shown advantages of heterodyne systems in distant, sensitive methane effusion discovery.

4. ACKNOWLEDGEMENTS

The partial support of research funds, especially in the field of methane detection, by Masovian District Gas Works from Warsaw, Poland are gratefully acknowledged.

REFERENCES

- [1]-M. Kopica, M. Strzelec, Z. Trzęsowski et al "Laboratory system for heterodyne detection of 10.6 μm radiation", *Optoelectronics Review*, February 1993.
- [2]-M. Strzelec, "Laser and optoelectronic research in Poland", invited lecture, *Proceedings of 1st International Symposium on Laser Spectroscopy*, Korea, Nov. 1993.
- [3]-Puzewicz Z., Strzelec M., Trzęsowski Z., Kopica M., Noga J., Zawadzki Z., „Detection of infrared radiation - selected results of investigations”, *Fourth Conference in Optics ROMOPTO'94*, Bucharest 5-8 Sept. 1994, invited paper, *Proc. SPIE* vol. 2461.
- [4]-N. Iftimia, M. Strzelec, M. Kopica et al "Active remote sensing using heterodyne technique", *Proceedings of SPIE, CLEO-94 Conf.*, June 1994
- [5]-Zbigniew Puzewicz , Marek Strzelec, Zdzisław Trzęsowski, Mirosław Kopica, Zbigniew Zawadzki, Arkadiusz Mazierski, „Selected results of investigations of infrared heterodyne detection systems”, *SPIE Conf. „Optical Velocimetry”*, May/June 1995
- [6]-Strzelec M., Puzewicz Z., Kopica M., „Heterodyne infrared detection system”, *XXIII National Symposium „Optics and Optoelectronics”*, *Technical Papers p.3*, March 14- 16, 1996, Dehra Dun, India.
- [7]-Catalog. Polytec Pl., Inc.
- [8]-J.Leonelli et al., *SPIE* vol.1062, 1989.

CHARACTERISATION OF INTEGRATED OPTICAL WAVEGUIDES BASED ON OXIDISED POROUS SILICON

M. Balucani¹, V. Bondarenko¹, N. Kasuchits², G. Lamedica¹, N. Vorozov², and A. Ferrari¹

¹ INFN Unita di Roma, Dipartimento di Ingegneria Elettronica, Universita 'La Sapienza' di Roma, Via Eudossiana 18, 00184 Roma - Italy

² Belarusian State University of Informatics and Radioelectronics, P. Brovki 6, 220027 Minsk, Belarus

ABSTRACT

Integrated optical waveguides based on oxidized porous silicon were fabricated by means of traditional silicon technology. Near-field pattern and out-of-plane scattering losses were measured to characterize optical properties of the waveguides. Strong confinement of light within the core of the waveguides as well as optical losses of about 5 dB/cm have been demonstrated in the visible range. The achieved results make the waveguides promising in optoelectronics use.

Keywords: integrated waveguide, optical losses, oxidized porous silicon.

1. INTRODUCTION

Optical technologies are becoming increasingly important in areas that were traditionally the domain of electronics. In particular, silica-based optical waveguide fibers are used in long-distance telecommunications and local networks. Recently important developments have been made on smaller scale - in optoelectronic integrated circuits in which planar optical waveguides on a semiconductor substrate are employed for optical interconnections between active devices (lasers, detectors, light-emitting diodes, etc) and also in passive devices such as splitters, filters, couplers, etc.

Fabrication of optical components on a silicon substrate provides a possibility of their integration with electronic devices fabricated on the common substrate. There are at least two ways for organizing the architecture of optoelectronic circuits in silicon wafer. The light from light emitting device (LED) has to go through silicon or the dielectric waveguiding layer and has to be adsorbed in the photodetector (PD) active region, resulting in a change of its electrical characteristics. The first way proposes the organization of optical interconnections between LEDs and PDs directly in silicon wafer. The second way proposes the use of the dielectric layers for optical interconnections between LEDs and PDs. In order to provide confinement and propagation of light within the waveguide (WG), the guiding region has to have a higher refractive index than the surrounding cladding regions. Standard dielectric materials of integrated optical waveguides are phosphosilicate glasses, silicon nitride, and different plastics. Silicon dioxide is the best material due to its excellent optical and thermo-mechanical characteristics and compatibility with silicon technology. But silicon dioxide has a refractive index lower than silicon, so silicon dioxide layer should be additionally doped with phosphorus, nitrogen, etc. to be used as a waveguide. Besides, thick silicon dioxide layers cannot be formed by thermal oxidation or deposition techniques because of too high mechanical stress level, cracking, and poor optical properties.

In 1993 an idea to use the oxidized porous silicon (PS) layers as waveguiding layers in silicon wafer was proposed and light guiding through thermally oxidized porous silicon was demonstrated [1,2]. White light of tungsten lamp as well as red light of He-Ne laser were easily observed by end-fire coupling into the mirror-like cleaved end of a waveguide via microscope. The oxidized porous silicon waveguide fabrication process is short and simple. Moreover, porous silicon regions can be formed in certain regions of silicon substrate. These regions are defined by masking or local doping of silicon. Importantly these WGs do not require epitaxy or implantation processes and therefore offer significant processing and cost advantages over other technologies. Similar to the thermal silicon dioxide, oxidized porous silicon exhibits high hardness and thermal stability. WGs based on oxidized PS can be fabricated even at the beginning of the optoelectronic integrated circuit manufacturing cycle and withstand all technological steps.

Preliminary results on optical investigation of the oxidized porous silicon WGs have been reported by several groups [3-7]. Achieving low optical losses is essential to the success of this WG technology and by optimizing the oxidation process, the oxidized porous silicon layers have to achieve low optical losses in waveguides easily fabricated using simple anodisation technique and conventional thermal oxidation. The present contribution is aimed at a deeper optical characterization of these WGs, including scattering losses and near-field measurements.

2. EXPERIMENTAL

The process of waveguide fabrication consists of four main steps (Fig.1): (a) silicon nitride mask deposition and patterning to define waveguide configuration; (b) selective anodization of silicon through the mask; (c) chemical removal of mask and cleaning of porous silicon; (d) thermal oxidation of porous silicon and densification of oxidized porous silicon.

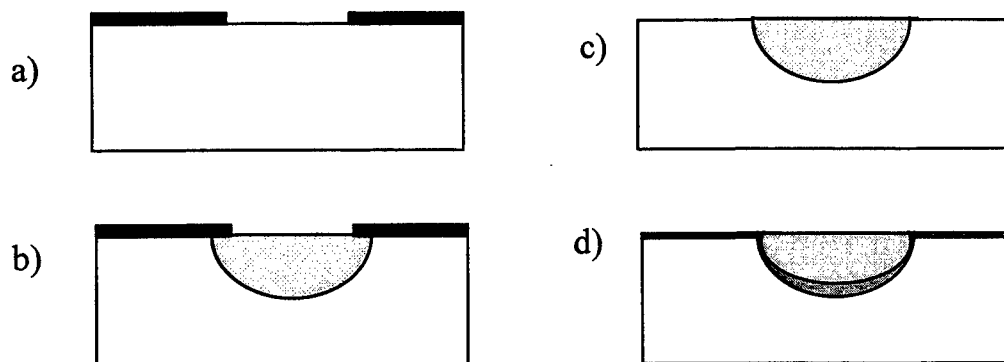


Figure 1. Process sequence for fabricating waveguides:
a) masking; b) silicon anodization; c) mask removal; d) porous silicon oxidation/densification.

2.1. Anodization

Boron-doped silicon (100) wafers of 0.01 Ohm-cm resistivity were used as initial substrates. Selective anodization of the wafers through the 0.2 μm thick silicon nitride mask was performed in HF/alcohol electrolyte under anodic current density of 10-30 mA/cm^2 . As a result, local porous silicon layers of single fiber or Y-shape waveguide topologies were formed. The waveguides had a length of 1.5-3.0 cm, a width of 10-30 μm and thickness of 5-15 μm . After anodization the silicon nitride mask was removed in 48% HF bath. Then the wafers were subjected to standard chemical cleaning, rinsed in deionized water and dried in nitrogen.

2.2. Oxidation

Thermal oxidation of PS was performed in a diffusion furnace by a three-step process. First, the structure of porous material was stabilized and prevented from sintering by low-temperature oxidation at 300°C for 1 h in dry oxygen. Optical properties of porous silicon are strongly dependent on the regime of its oxidation. In this work porous silicon was fully oxidized using a steam ambient at 900°C. Then a temperature was raised up to 1150°C during 25 minutes, and thermal densification of oxidized porous silicon in wet oxygen-nitrogen atmosphere was performed to improve optical properties of the material obtained. Finally, a temperature was reduced up to 850°C during 30 min before unloading. These soft regimes together with proper choice of porous silicon parameters provided low mechanical stress level of the waveguide structures, absence of cracks and dislocation slip lines. Thin a-Si:H layer was deposited on the surface of some samples to investigate the light linkage from the top of WG into amorphous layer.

2.3 Optical measurements

To study the optical properties of oxidized porous silicon layers, the samples were prepared by way of cleaving of silicon wafers with waveguides. The cleaved surfaces were studied through the use of optical and scanning microscopes. To provide the interferometric measurements, thin slices were prepared through the cutting followed by mechanical polishing. The thickness of the slices was of 150-200 μm .

The most widely used method for measurement of the attenuation of a waveguide is the measurement of the transmitted power as a function of waveguide length. In this method, all the energy flowing through the guide must be collected in the detector. In [5,7] optical losses of WGs based on porous and oxidized porous silicon were determined by end-fire coupling light into and out of the cleaved samples. The samples of different lengths were prepared using the cut-back method. However, this method is complex and hardly controlled. In the present work, out-of-plane scattering losses

were measured by scanning the surface of the waveguide using an optical fiber as a probe. The optical fiber mounted on a micrometric stepper motor scanned the distribution of the scattered light along the length of the waveguide perpendicularly to the surface. The probe angle and its distance from the waveguide were maintained constant. The optical signal was detected by a photomultiplier in conjunction with a lock-in technique, to increase the signal-to-noise ratio. Light was introduced in the waveguide by end-fire coupling, while a rutile prism was used as output to control the light coupling through the presence of m-lines.

To excite different guided modes, near-field pattern from end-fire output was measured by prism coupling input. Due to the difference in the refractive index between rutile prism and oxidized porous silicon layer, the angle between the laser beam and the silicon surface was close to 90° (the apex angle of the used prism was 45°). This prevented direct measurement of the input laser beam. The output beam from the end of the waveguide was magnified by a $50\times$ Leitz objective and detected by a silicon photodiode equipped with a pinhole of $50\text{ }\mu\text{m}$ in diameter. Both experiments were performed using He-Ne ($\lambda = 632.8\text{ nm}$) not intentionally polarized laser light.

3. RESULTS AND DISCUSSION

Microphotographs of the cleaved surface of silicon wafer with oxidized porous silicon WG are shown at Fig.2. Either white light of tungsten lamp or red light of He-Ne laser were easily observed via microscope from the cleaved ends of waveguide. As seen from Fig.2, the light was guided through the core part of the waveguide. Lightguiding was observed in the whole visible range. The output beam due to white light introduced in the oxidized porous silicon WG did not present any appreciable spectral difference.

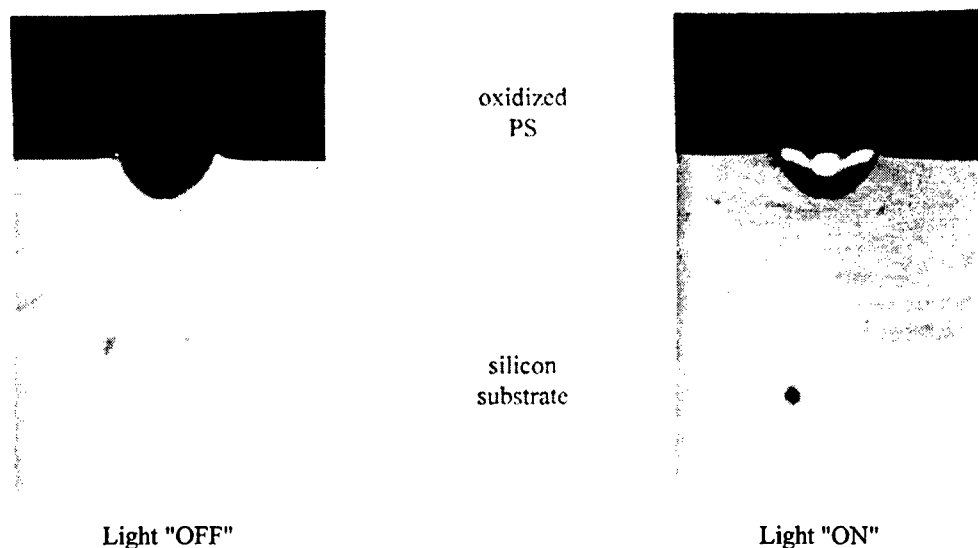


Figure 2. Cross section microphotographs of the waveguide based on oxidized porous silicon.

Fig. 3 shows an SEM microphotograph of the WG cross section. The border between silicon and porous silicon regions is evident at around $15\text{ }\mu\text{m}$ depth, at the center of the waveguide. The width of the porous layer is larger with respect to the starting nitride mask, reaching about $30\text{ }\mu\text{m}$. This is expected from previous experimental results and is due to the low degree of anisotropy (i.e. the ratio between lateral spreading and penetration depth) of the used anodization process [8]. The oxidized porous silicon WG surface refractive index, as determined by the interferometric method, was $n = 1.458$, that is very close to the quartz refractive index. As a matter of fact, near-field measurements show a very high output beam confinement in a smaller section with respect to the physical dimensions of the initial waveguide, as evidenced in Fig.3. This can be explained by the presence of a lower refractive index buffer layer between the dense oxidized porous silicon core and the bulk silicon, which presents a refractive index of about 4 in the visible range.

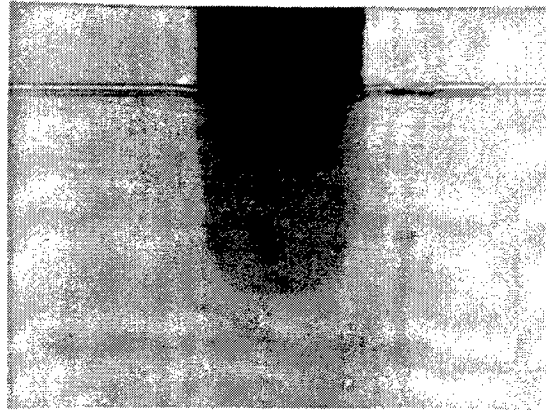


Figure 3. Scanning electron microscopy photograph of waveguide cleaved surface.

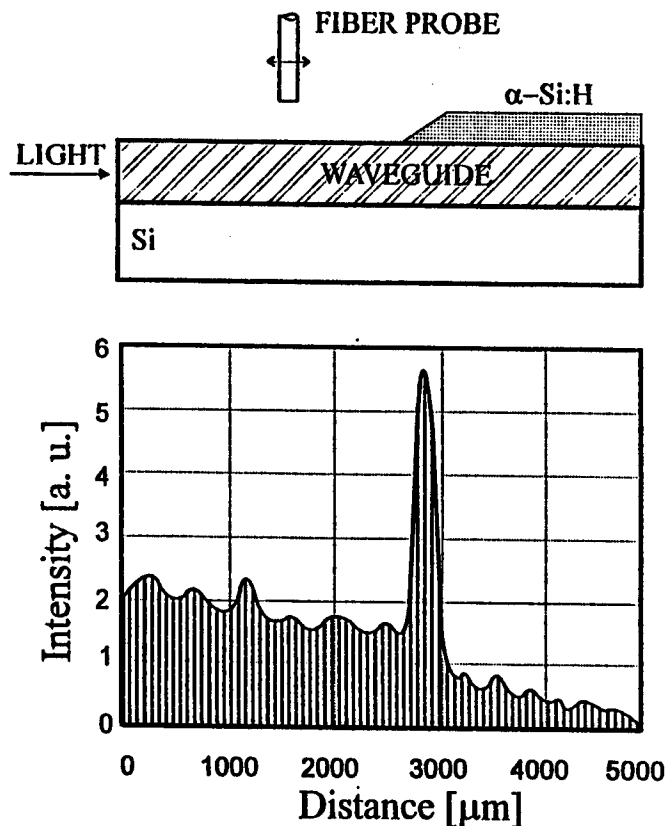


Figure 4. A scheme of the out-of-plane scattering losses measurement and a plot of scattered light intensity versus distance along the waveguide.

Fig. 4 demonstrates a scheme of the out-of-plane scattering losses measurements and a plot of scattered light intensity versus distance along the structure. Scattering losses from the surface of the oxidised porous silicon were determined to be of about 5 dB/cm on almost 5 mm waveguiding length, at $\lambda = 632.8$ nm exciting wavelength. This result is quite promising for optoelectronic applications [9]. We expect light-guiding propagation losses to be sufficiently lower in the infrared range, due to the one order of magnitude lower Rayleigh scattering losses in the same range. As seen from Fig.4, an increased scattering takes place at the beginning of α -Si:H layer. The reason is that amorphous silicon has higher refractive index than air allowing the light to exit from the waveguide. The border of α -Si:H layer is not sharp but has a certain slope due to a shadow mask deposition. When the layer thickness is small, the light goes out effectively from the waveguide. As soon as

the thickness of a-Si:H layer becomes higher, the attenuation of scattered light takes place due to absorption in amorphous silicon. As a result, rather sharp maximum of scattered light intensity is observed in the position corresponding to the angle border of a-Si:H layer. Further attenuation of optical signal is observed in the region of a-Si:H layer constant thickness: the slope of scattered light intensity plot is about 22 db/cm there. The observed strong attenuation of optical signal in the part of the waveguide covered by amorphous silicon provides a good background for the development of effective a-Si:H photodetector integrated with optical waveguide made of oxidized porous silicon and embedded into silicon substrate.

Fig.5 shows two cross sections of the measured near-field patterns, in the directions parallel (Fig. 5a, x-direction) and perpendicular (Fig. 5b, y-direction) to the surface and crossing at the maximum of output light intensity. A symmetric, gaussian profile accounts well for the distribution of light intensity along the direction parallel to the surface. In the other direction, the effect of the strong confinement due to the abrupt index change at the waveguide surface is well evidenced by the asymmetric shape of the near-field pattern; nevertheless, a gaussian profile fits well that part of experimental data resulting from regions of smoother index change toward the bulk of the substrate.

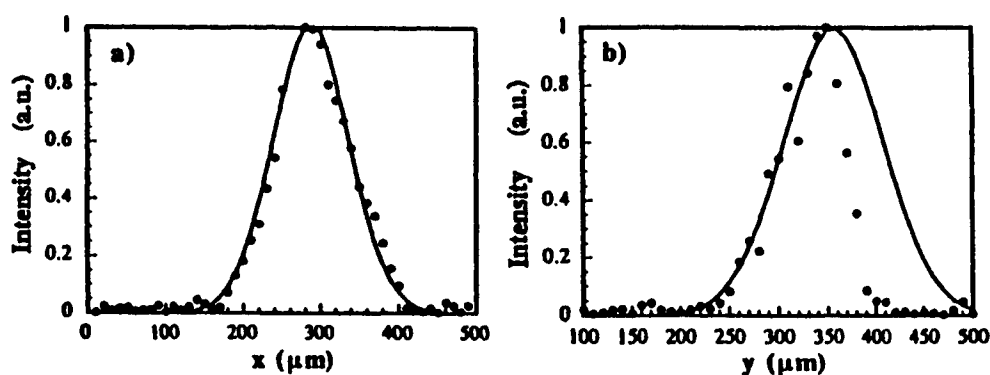


Figure 5. Cross-sections of the near-field pattern: (a) x-direction; (b) y-direction. Full circles are the measured data, while the continuous lines represent the gaussian best fit.

The overall shape of the reported near-field pattern accounts for a low-order guided mode. Nevertheless, changing slightly the input angle from the prism, to excite different modes, resulted in almost the same shape at the output. This fact can be due to the exchange of energy between different modes during the propagation in the long waveguide (mode mixing) which can be promoted by the presence of inhomogeneities. Considering the $50\times$ objective magnification of the experimental set-up, the FWHM of the output beam is about 4-5 μm .

A possible model of the waveguide structure is reported in Fig. 6. During the high temperature oxidation of porous silicon, the oxide growth rate is enhanced in proximity to the surface where oxygen can easily penetrate inside pores while a sintering process occurs in the bulk of porous silicon. The process of porous silicon sintering [10] is determined by the temperature and duration of the thermal treatment, whereas oxidation is due to both temperature and oxygen content. For this reason, the subsurface PS region is oxidized, while deeper zones can be sintered. Sintered PS consists of monocrystalline silicon with isolated voids. As a result of the competition of the two different processes, a buffer layer composed of low-density oxidized porous silicon can be formed. This porous oxide layer should have a refractive index value between 1.45 (SiO_2) and 1 (air) allowing the strong light confinement resulting from near-field measurements.

Optical properties of oxidized porous silicon can be drastically changed by rare-earth elements doping and thermal treatment. In particular, oxidized porous silicon doped with erbium was shown [11] to exhibit sharp (FWHM of ~ 0.01 eV at 77 K) luminescence at 1.54 μm . Such PS:Er waveguide structures are promising for integrated optical filters, amplifiers/modulators, light-emitting diodes and other optoelectronic devices.

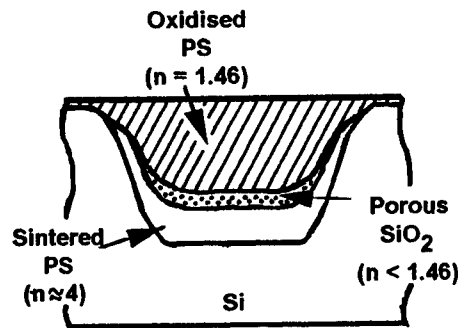


Figure 6. Schematic model of oxidized porous silicon WG.

4. CONCLUSION

Integrated optical waveguides based on oxidised porous silicon have been fabricated and characterised. Near-field and refractive index measurements suggest the presence of a lower refractive index layer between the oxidised porous silicon core and the bulk silicon. This porous oxide layer is responsible for the guiding performances of the structure. Optical losses of about 5 dB/cm have been demonstrated in the visible range wavelengths, supporting the possible utilization of such devices in optoelectronics.

5. ACKNOWLEDGMENTS

The authors thank Leonid Dolgyi, Alexander Dorofeev, and Valentina Yakovtseva of Belarusian State University of Informatics and Radioelectronics, Minsk, Gabriella Maiello of University 'La Sapienza', Rome, Lorenzo Masini of Terza University degli Studi, Rome for participation in fulfillment of experiments and useful discussion. This work was partially supported by NATO LINKAGE GRANT HTECH.LG 951231.

REFERENCES

1. V.P.Bondarenko, V.S.Varichenko, A.M.Dorofeev, N.M.Kazuchits, V.A.Labunov, V.F.Stelmakh "Integrated optical waveguide fabricated with porous silicon", *Tech.Phys.Lett.* vol.19, p.463-464, 1993.
2. V.P.Bondarenko and A.M.Dorofeev "Why porous silicon for SOI?" In: "Physical and Technical Problems of SOI Structures and Devices", edited by J.P.Colinge, V.S.Lysenko and A.N.Nazarov. NATO ASI Series, Series 3: High Technology - Vol.4. Kluwer Academic Publishers, Dordrecht, The Netherlands, p.15-26, 1995.
3. V.P.Bondarenko, A.M.Dorofeev, and N.M.Kazuchits "Oxidized porous silicon based waveguide for optical interconnections" *Proc. ECIO'95*. Ed. by L.Shi et al, April 3-6, 1995, Delft, The Netherlands, p.291-294.
4. V.P.Bondarenko, A.M.Dorofeev, and N.M.Kazuchits "Optical waveguide based on oxidized porous silicon", *Microelectronic Engineering*, vol.28, p.447-450, 1995.
5. A.Loni, L.T.Canham, M.G.Berger, R.Arens-Fisher, H.Munder, H.Luth, H.F.Arrand, T.M.Benson "Porous silicon multilayer optical waveguides", *Thin Sol.Films*, vol.276, p.143-146, 1996.
6. G.Maiello, S.La Monica, A.Ferrari, G.Masini, V.P.Bondarenko, A.M.Dorofeev, N.M.Kazuchits "Light guiding in oxidised porous silicon optical waveguides", *Thin Sol.Films*, vol.297, p.311, 1997.
7. A.Loni, R.J.Bozeat, M.Krueger, M.G.Berger, R.Arens-Fisher, H.Munder, H.Luth, H.Arrand, T.M.Benson "Application of porous silicon technology to optical waveguiding", *IEE Colloq. 'Microengineer. Appl. in Optoelectr.(UK)*, p.8/1, 1996.
8. V.P. Bondarenko " Investigation of porous formation process and its application for intercomponent isolation in semiconductor IC's" Ph.D. Thesis, Minsk, Minsk Radio-Engineering Institute, 1980.
9. R.Soref "Silicon -based optoelectronics", *Proc. IEEE*, vol.81, No.12, p.1687-1706, 1993.
10. V.Labunov, V.Bondarenko, L.Glinenko, A.Dorofeev, L.Tabulina "Heat treatment of porous silicon", *Thin Sol.Films*, vol.137, p.123-129, 1976.
11. V.Bondarenko, L.Dolgyi, A.Dorofeev, N.Kazuchits, A.Leshok, G.Troyanova, N.Vorozov, G.Maiello, G.Masini, S.La Monica, A.Ferrari "Porous silicon as low-dimensional host material for erbium-doped structures", *Thin Sol.Films*, vol.297, p.48-52, 1997.

Electronic laser beam profile measurement

Carlos B. Roundy

Spiricon, Inc.

2600 North Main, Logan, Utah 84341, USA

ABSTRACT

Because the spatial beam structure is the most critical element of a laser, measurement of this beam structure is indispensable in laser design, development, and manufacture. Since measurement of the beam structure inside the cavity is impractical, if not impossible, the beam profile structure outside the laser provides the only real insight into cavity structure. It is critical that profile measurements outside the cavity be as precise and illuminating as possible. Electronic measurement of the output beam profile is the only method that gives sufficiently accurate and illuminating beam structure analysis.

Non-electronic methods of beam profile measurement include burn spots on paper, viewing of a beam on a reflecting surface, and acrylic mode burns. All of these methods supply very low contrast because the dynamic range is low, and measurement accuracy is very poor. Electronic beam measurement, on the other hand, provides beam profile views with a dynamic range greater than 200. It also provides beam parameter measurements with less than 5% error.

Clearly seeing the laser beam profile provides the majority of information necessary for cavity alignment and optimization. Immediate real time feedback enables tuning and adjusting for optimum laser performance. Beam profile measurement accuracy less than 5% error enables quantitative evaluation of performance progress. Items such as beam width, uniformity of the beam, beam divergence, mode structure, and centroid pointing stability, all require large dynamic range and accurate measurements.

CCD and pyroelectric solid-state cameras are the most useful general purpose beam profile measurement instruments. They provide 2D simultaneous measurement of the entire laser beam, operate with pulsed, as well as CW lasers, and have a large linear dynamic range. In addition, they interface to computers for accurate data analysis, storage, and profile display. The current state-of-the-art beam profilers include framegrabbers that operate on the new high performance PCI bus in Pentium 100MHz and faster computers. They operate under Windows 3.1x and Windows 95. The performance of these beam analyzers is increasing directly with the increased speed of computers. For visible and near IR lasers, CCD cameras with 8-bit resolution usually suffice. While these cameras have some problems with noise and baseline offset, Spiricon's recent invention of Ultracal solves these problems. For lasers beyond 1.1 μ m, and into the far IR, pyroelectric solid-state cameras provide extremely linear and accurate beam profile measurement.

Keywords: laser beam profile diagnostics, beam profiler, pyroelectric, CCD, computer

1. INTRODUCTION

1.1 Obsolete beam profiling methods

Applications of lasers are becoming sufficiently complicated that the quality of the laser beam profile must be closer to the desired ideal to achieve success. Traditional measurement methods such as burn spots, mode burns, and viewing the reflected beam, do not provide sufficient information to enable a scientist to achieve optimum laser performance. Many of the emerging laser technologies would not be possible without more sophisticated electronic beam profile measurement.

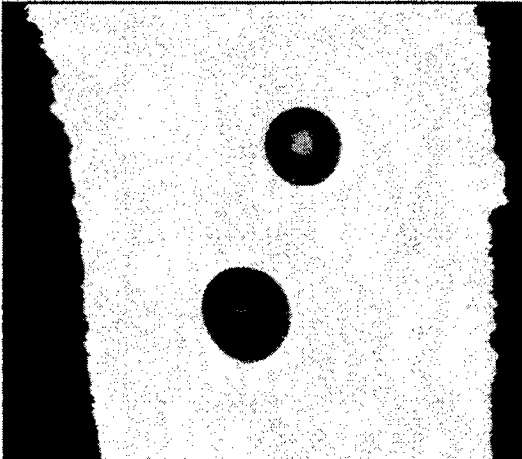


Figure 1. Burn Spots On Thermal Paper.

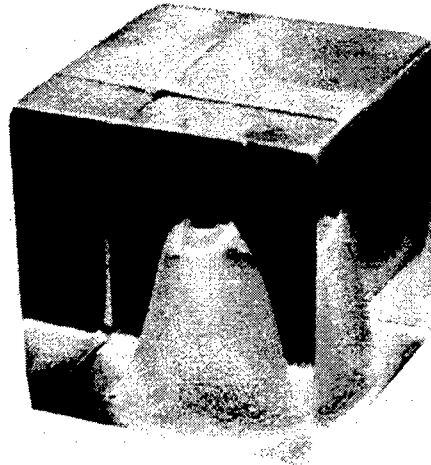


Figure 2. Acrylic Mode Burns.

1.2 Electronic beam profiling accomplishments

The availability of electronic laser beam diagnostics instrumentation has enabled scientists and engineers to tune lasers to much higher standards. Two properties of electronic beam diagnostics facilitate this increased laser performance. The first is the ability to provide illuminating beam profile displays. These displays, in both 2D and 3D beam views, often provide sufficient intuition to enable the laser operator to make significant improvements to the laser beam in a very short time.

The other property of electronic beam profile analysis which has had a high impact on laser performance is the higher accuracy with which laser beam properties are measured. Precise measurements, especially the precise measurement of the laser beam width, are major keys in enabling a laser designer or user to maintain optimum performance. Electronic laser beam diagnostics provides other measurements of the laser properties, such as Gaussian fit of near Gaussian beams, Top Hat measurements of flat top beams, divergence, M^2 , and statistical measurements to determine the stability of many beam properties.

1.3 Modern applications demand better laser beams

The property of lasers that makes them useful in nearly every application is the high energy density of light that is provided. If the intensity distribution, or beam profile, is not as expected, the performance of the laser will be substandard. In research and development with lasers, the reaction to the laser light is often proportional to the intensity squared or cubed. Imagine a beam profile pattern that has deteriorated to the point that much of the energy is in the wings of the beam rather than in the peak, such that the peak is 20% lower than expected. The result would be a conversion efficiency of only 64% to 50% of what is expected. Most research and development applications require better than 5% accuracy to have meaningful results. This accuracy can be achieved only with the latest electronic beam profile instrumentation with sophisticated profiling algorithms.

More and more laser users are demanding that the laser manufacturer provide a laser beam that is uniform within very tight limits. The laser manufacturers are being forced to perform accurate beam profiling measurements to ensure that they meet

the requirements of their customers. Manufacturers are now using beam profiling instrumentation on the production floor to assure that lasers being shipped to customers meet the specifications of the contract.

Medical applications of lasers are often in the public limelight, and have significant potential of improving the quality of life for everyone. Often these medical applications require a very careful characterization of the laser beam in order for the medical operation to be applied successfully.

Industrial applications with Nd:YAG and CO₂ lasers are used widely in metal processing and other industrial processes. For years many of the industrial job shops have used the method of burn spots and mode burns to characterize the laser beam. However, increasing numbers are realizing that these methods are inadequate. They do not provide instantaneous views of beam profiles on a shot-to-shot basis. By seeing the beam on a frame by frame basis with electronic profilers the operator can tell when the laser is erratic, and thus produce less scrap and higher profits for the user.

2. ACCURATE LASER BEAM WIDTH MEASUREMENTS

2.1 Importance of beam width measurement

The property of lasers that makes them useful in nearly every application is the high energy density of light that is provided. If the intensity distribution of this high power is not as expected the performance of the laser will be substandard. Three laser beam properties that are more important than any others are the total power or energy in the laser beam, the temporal pulse width, and the spatial width of the laser beam. Power and energy measurements, and temporal width can be measured accurately with a variety of commercial instruments. On the other hand, the spatial width of a laser beam is extremely difficult to measure. The difficulty in measuring laser beams arises from the fact that energy extends far out into the wings of the beam, and makes it difficult for an instrument to calculate or define what is the actual beam width. The ability to accurately measure the beam width enables a scientist or engineer to determine precisely the quality of the beam and how well it will focus or propagate.

2.2 Beam width measurement methods

The knife-edge beam width measurement method has traditionally been used with mechanical instruments, but is also very effective when used with camera based electronic beam profilers. A correction factor is used to convert from the typical 10% - 90% measurement to the $1/e^2$ width. The biggest difficulty with knife-edge measurements is that depending on the mode content of the beam, the clip level definition and correction factor can introduce error into the measurement.

Laser propagation theory indicates that the true measure of a laser beam width is the Second Moment, or D4 σ method. Second Moment is a method that integrates energy vs. distance from the centroid of the beam to obtain a properly weighted beam width. However, if there is diffraction in the beam, such as caused by an aperture, then there can be considerable energy in the wings that is not a functional part of the laser beam. Also, noise from the CCD camera has made it difficult to accurately measure the D4s laser beam width. Thus even though the Second Moment method is theoretically the most representative, it has, until now, been impossible to use for accurate measurements.

3. NOISE INDUCED ERRORS IN D4 σ MEASUREMENTS

3.1 Beam width accuracy simulations

One problem that has existed in defining the calibration accuracy of a beam is that no standard is available. One method of beam width measurement calibration has been to first measure a beam under the most ideal conditions of being at nearly saturation of the camera, and nearly filling the aperture of the camera. Afterwards the beam intensity is reduced, and/or the beam pixel count in the camera is reduced, for the same size beam, and measurements made to see how much the beam width calculation changes from the original. Beam width accuracy calculations are then based on the standard from the most ideal measurement and then extrapolation from that point.

Spiricon engineers have created a mathematically derived perfect Gaussian beam in a computer in the same format that a camera would provide. Computer generated random noise with a Gaussian distribution similar to the noise in a camera is added to the derived beam. Under these conditions the accuracy or beam width measurement algorithms can be calculated precisely because the original beam width is known, having been computer generated.

Using the computer generated beams, the accuracy of various algorithms for calculating beam widths was tested. Figure 3 illustrates the beam width measurement error of the Second Moment $D4\sigma$ measurements and the knife-edge beam width measurements. These calculations were performed in a 512 X 512 camera matrix, with the computer generating beams varying in size inside this matrix. It is seen that as soon as the beam is as small as 64 X 64 pixels, the $D4\sigma$ calculation creates an error of an astonishing 60%. This is in contrast to the knife-edge method, which creates only about 3% error at a beam size of 64 X 64 pixels. (In all calculations the signal magnitude was 256 counts, equal to saturation of an 8 bit digitizer, and the baseline had no offset or shading.) Figure 3 shows why the knife-edge method has given accurate beam width measurements, whereas the Second Moment method has been impossible to use with CCD cameras.

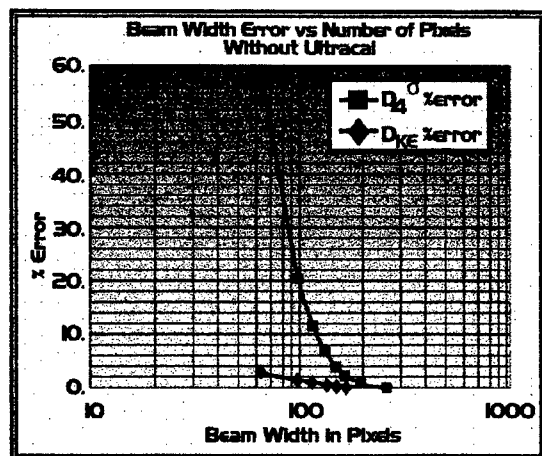


Figure 3. Beam Width Measurement Error Without Ultracal.

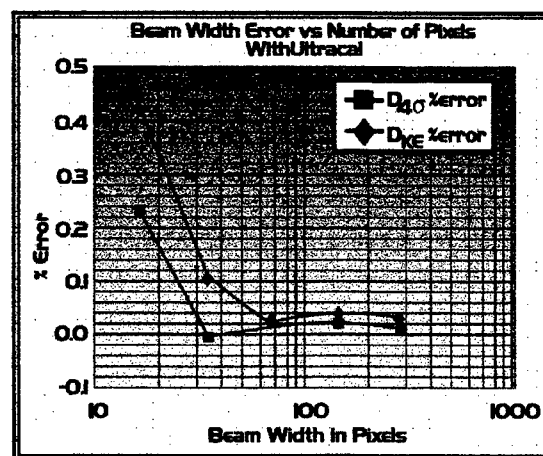


Figure 4. Beam Width Measurement Error Using Ultracal.

3.2 New measurement algorithms

Spiricon engineers have developed a new calculation algorithm that enables accurate Second Moment measurements in the presence of camera noise. These algorithms are incorporated into patented algorithms called "Ultracal". Under the same conditions of noise and signal of the simulations of Figure 3, the simulated measurement accuracy of the new algorithms is shown in Figure 4. With these new algorithms beam widths can be measured in the presence of noise with essentially no error. In a 512 X 512 camera field with a beam size of 64 X 64 pixels, the measurement error is now calculated to be less than 0.1%, whereas it was formerly 60%. Even with a beam width as small as 16 X 16 pixels, the measurement error is less than 0.3%. Using these new algorithms, the Second Moment measurement makes more accurate beam width measurements than the knife-edge method with a measurement error of 0.45% for a 16 X 16 beam. The simulated measurement accuracy is improved by more than a factor of 200.

3.3 Beam width measurements

The new algorithms have been tested with a real laser beam on a CCD camera. Conditions of varying the number of pixels in the beam and varying the beam intensity were evaluated for both Second Moment and knife-edge measurements. Figures 5 and 6 illustrate the accuracy capability of beam width measurements using these algorithms. Figure 5 shows that a beam width as small as 6 camera pixels can be measured with better than 1% error. Even with 3 pixels in the beam a 3% measurement can be made. Figure 6 shows that when the beam peak intensity is as low as 25 digital counts, or 10% of the saturation level, the width can be measured with less than 1% error. As shown in the next section with summing signal processing it is possible to measure a beam width with only 5% error when the beam peak is less than 1% of saturation.

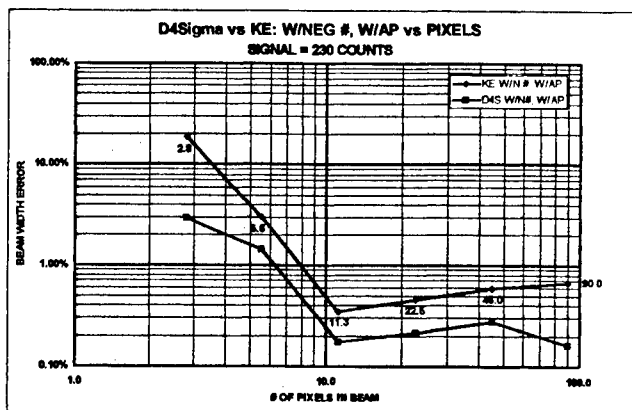


Figure 5. Comparison of the accuracy of $D4\sigma$ vs. knife-edge measurement versus number of pixels in the beam.

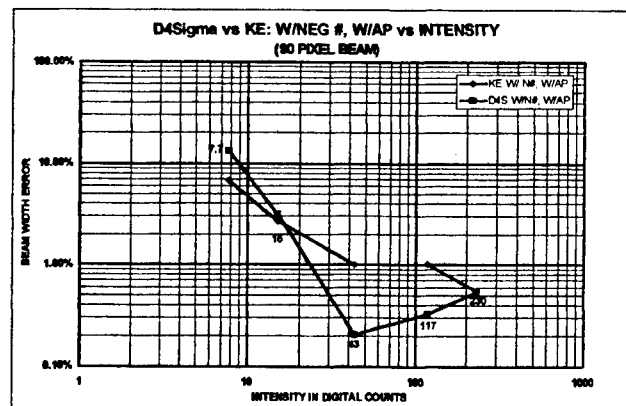


Figure 6. Comparison of the accuracy of $D4\sigma$ vs. knife-edge measurement versus intensity of the beam.

4. UNIQUE SIGNAL PROCESSING

4.1 Frame summing

One feature of the new algorithms is retaining the negative noise in the camera baseline field, which enables signal processing that would not otherwise be possible. One example of this processing is frame summing. When the negative noise components are eliminated, as is the case with most digitizers, frame summing causes all of the positive noise components to continually add, and ultimately produce a net positive baseline offset. However, with negative noise retained, the negative noise components subtract from the positive noise components on a frame-by-frame basis and keep the mean noise distribution near zero. The total noise adds roughly as the square root of the number of frames summed, the signal grows as the number of frames, which gives a signal-to-noise ratio improvement roughly as the square root of the number of frames summed. Summing is used in the following example to show the dramatic effect that can be obtained with the retention of the negative noise.

4.2 Low intensity beam

The utility of frame summing signal processing is shown with a low intensity laser beam that was attenuated until it was buried in the noise so that the peak was approximately 1 digital count. The noise was approximately ± 3 digital counts. The signal-to-noise ratio at the beam peak is therefore about 0.3, and 0.003 in the wings of the beam. The beam was not even visible in the display. For reference, Figure 7 shows a 3D picture of the beam at its full intensity.

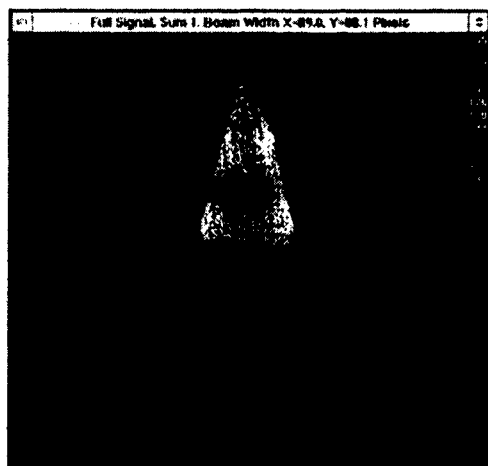


Figure 7. HeNe laser near Gaussian beam measured and displayed at full camera intensity.

4.3 Summing random noise

The accuracy of the baseline calibration is illustrated with the beam blocked and the baseline summed over 256 frames. Figure 8 shows a 3D picture of this noise field. The negative noise components are shown in gray, going below the colored positive noise components. The LBA-300PC produces a histogram of all signals. Figure 9 shows the histogram of the 256 sum of noise baseline from Figure 8. The histogram shows that the noise is centered at zero, with roughly a Gaussian distribution.

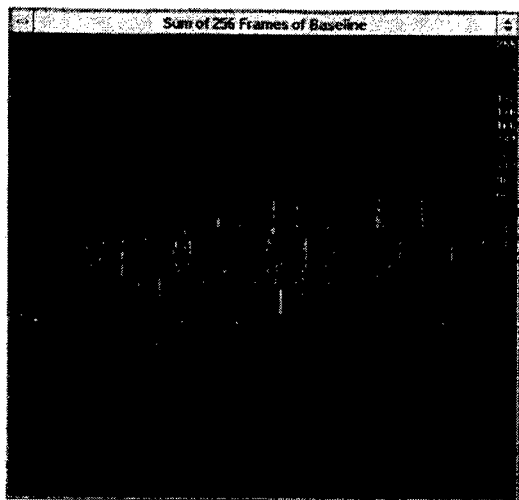


Figure 8. 3D display of noise field with summing

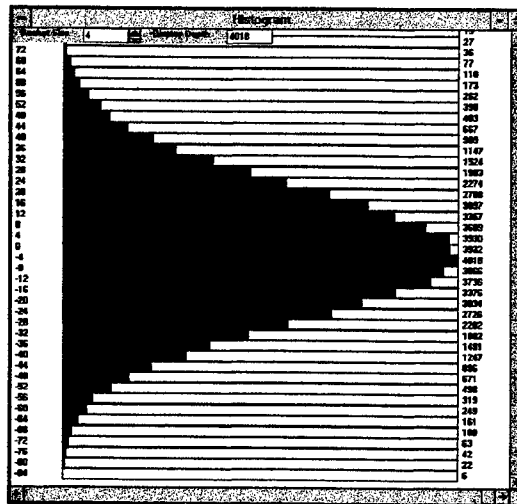


Figure 9. Histogram of the noise of Figure 8. of 256 frames. (Histogram shows the number of pixel counts at each intensity level.)

4.4 Beam with 256 frame summing

Another Ultracal was performed, then immediately afterwards the 1 count beam was unblocked, and a sum of 256 frames of that beam was made. This beam profile is shown in Figure 10. The laser beam rises up out of the noise. The Ultracal algorithm enables fairly accurate beam width measurement even in this instance. The computed beam width error, from the unattenuated beam, is less than 5%.

One feature of the LBA-300PC is to average adjacent pixels for display purposes only. Thus with a 256X240 camera field, you can average 4X4 pixels into a single pixel, and display it as 64X60. This is shown in Figure 11. The beam of Figure 10 is now clearly discernible above the noise. One reason the knife-edge measurement algorithm can measure the beam accurately is that it uses an averaging technique to measure beam width. This figure illustrates why it is able to find and measure a beam in the midst of such large noise.

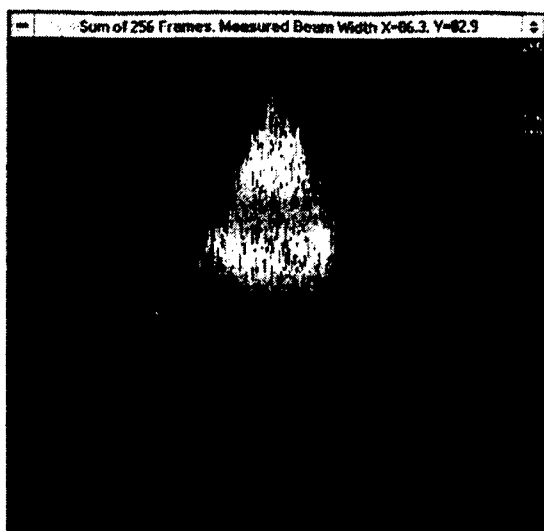


Figure 10. 3D image of laser beam of about 1 count intensity after 256 frames of summing.

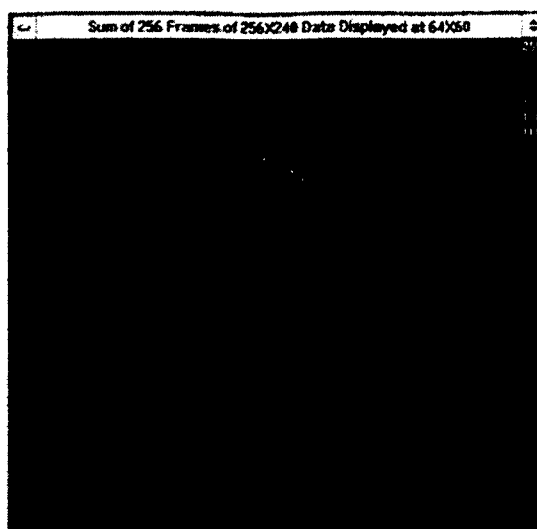


Figure 11. The beam of Figure 10 displayed with a 4X4 pixel averaging to create a single pixel.

4.5 Convolution algorithm

The LBA-300PC has other signal processing algorithms that can be used to improve the measurement of beams and other objects. One of these is convolution, which can be used to suppress noise. Figure 12 shows the beam of Figure 10, with a convolution of 7X7 pixels. This clears up the noise extremely well, by the processing of adjacent positive and negative noise components.

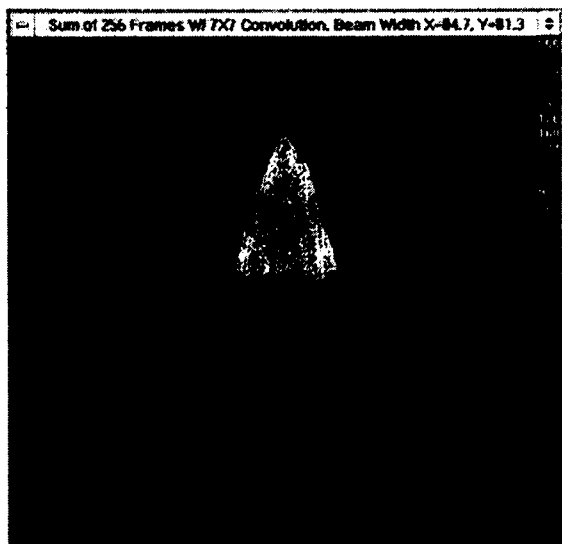


Figure 12. Convolution of 7X7 pixels of the beam of Figure 10.

5. EXAMPLES OF BEAM PROFILING APPLICATIONS

5.1 Industrial Nd:YAG laser

Nd:YAG lasers were used in an industrial application for cutting metal. The machine shop had one laser that cut differently in the X and Y directions. Using mode burns on pieces of metal it was not possible to tell any difference between the X and

the Y axis width. However the beam profile of Figure 13 made it obvious that a turning mirror was out of alignment. Within a few minutes a non-clipped beam of Figure 14 was obtained and the laser gave excellent performance.

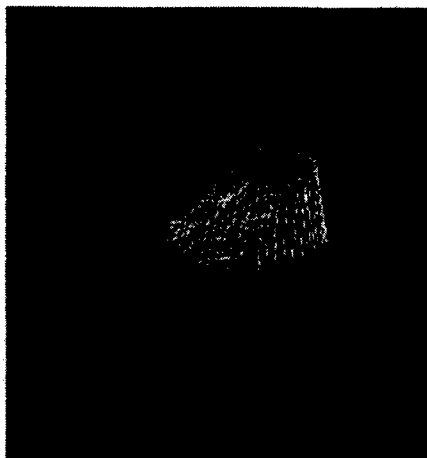


Figure 13. Misaligned Industrial Nd:YAG Laser.

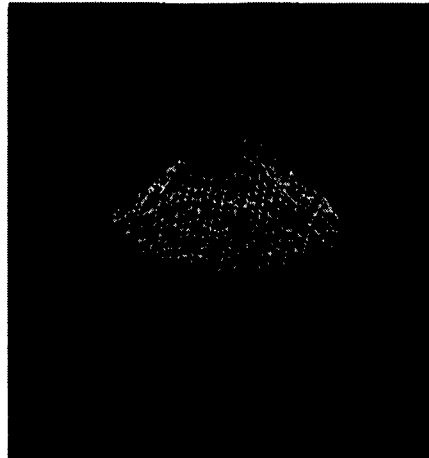


Figure 14. Realigned Nd:YAG laser.

5.2 Industrial CO₂ laser

Figure 15 shows the beam profile of an industrial CO₂ laser that did not operate as well as most lasers in the job shop. This laser had significant structure in the beam profile that gave erratic ablation on a ceramic wafer. Being able to see the beam enabled the decision that the laser needed factory maintenance, rather than have the laser technician continue to work on cavity alignment. Figure 16 shows the beam profile of other lasers in the shop that were operating properly.



Figure 15. CO₂ Laser With High Mode Structure.



Figure 16. Beam Profile of Good CO₂ Laser

5.3 Fiber optic alignment

Figure 17 shows the beam profile of a laser diode being used as an optical input to a single mode fiber. The beam was collimated with a lens to bring it to a relatively uniform round profile, rather than the usual rectangular beam profile emitted by laser diodes. The focused spot of the laser diode was then coupled into an optical fiber. This coupling is critical in all three axes, X, Y, and Z.

Figure 18 shows the diode when it is coupled properly in the X and Y direction, but not in Z. In this case the focus is behind the surface of the fiber, so much of the beam energy is being coupled into the cladding, rather than the center of the fiber. Thus the output of the fiber appears as in Figure 18 with a significant amount of energy not in the central beam. The energy that is not in the central beam is diverging at a much higher rate than the central lobe, and would be easily lost in

the application of this fiber. Figure 19 shows much better Z axis alignment of the diode into the fiber. In this case much more of the energy is in the central lobe. This type of alignment is greatly facilitated by the clear view of the beam that is provided by electronic beam diagnostics.



Figure 17. Laser Diode Beam Profile. (Input Beam to Fiber)



Figure 18. Fiber Output With Input Beam Poorly Aligned.

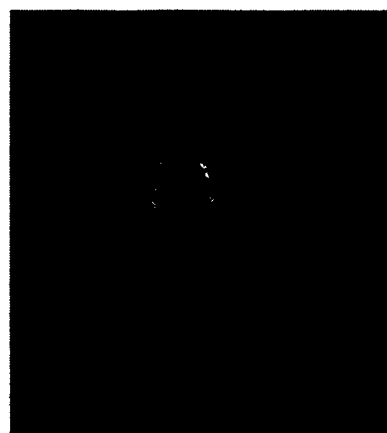


Figure 19. Fiber Output With Input Beam Well Aligned.

5.4 CO₂ laser waveguide medical delivery system

Figure 20 shows the output of a flexible waveguide delivery system for CO₂ lasers in a medical application. When the waveguide is held straight the beam is quite uniform. Figure 11 shows the beam pattern with slight bending of the waveguide. Notice that the beam is broken into many lobes and hot spots. However, these hot spots move around very rapidly with only slight bending of the waveguide delivery system, and thus a fairly uniform average energy is applied to the patient.

Figure 21, however, shows the same waveguide with heavy waveguide bending. Now the beam has become much less uniformly distributed, and the hot spots are coming together and leaving cold spots with large areas of low energy. In this case the motion did not make up for the poor distribution of energy, and uneven processing was performed with the laser. The hot spots became too concentrated to obtain uniform delivery to the patient. Electronic analysis of this waveguide system with a pyroelectric solid-state camera greatly enhanced the evaluation of the laser product.



Figure 20. CO₂ Waveguide Delivery System Output. (Slight Waveguide Bending)



Figure 21. CO₂ Waveguide Delivery System Output. (Heavy Waveguide Bending)

5.5 Pulsed Nd:YAG flat top laser

Figure 22 is a pulsed Nd:YAG laser used for thick film trimming. A hybrid semiconductor manufacturer was using this to trim active circuits. Burn spots of this laser appeared uniform, though obviously the intensity distribution is far from uniform. Other Nd:YAG lasers in the same facility had very flat top beams. As soon as electronic diagnostics were used to observe this beam, the alignment problem in the laser was rectified, and a uniform flat top and achieve reliable operation from the laser was achieved.

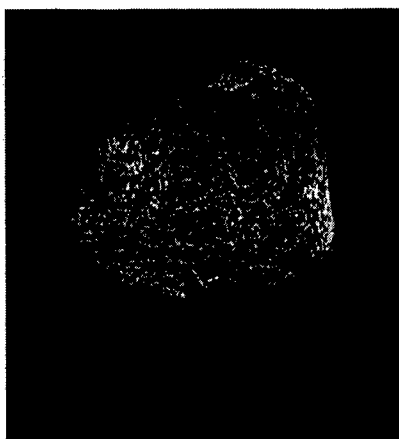


Figure 22. Pulsed Nd:YAG Laser For Thick Film Trimming.
(Desired Beam Was A Flat Top)

5.6 Optical parametric oscillator OPO at 3 μ m

Optical Parametric Oscillators are extremely useful lasers in that the wavelength can be changed over a fairly wide range. The output of OPOs is typically a strong function of the quality of the input laser beam. Figure 23 shows the output of an OPO that is being pumped by a high quality input beam, and thus has an output with a Gaussian fit of about .85, which is quite good for an OPO.



Figure 23. Output of OPO With High Quality Beam.

5.7 Human tissue welding at 1.5 μ m

A CW Erbium YAG laser in the 1.5 μ m range was used in a medical application for tissue welding. It was found that with exactly the right energy density at this wavelength, animal tissue could be welded together. Figure 24 shows the output of this beam with poor alignment of the delivery system. Using this beam the tissue welds were very poor, and failed under a very small amount of stress. Figure 25 shows the same laser with the delivery system properly aligned. In this case the beam is a nice uniform flat top, and it gave excellent performance.

In laboratory experiments this laser was used to weld together a severed vein in a mouse's leg. It was determined that using a well aligned beam, the vein could be welded such that the weld area was as strong as the rest of the vein. With poor alignment of the laser, the veins ruptured very quickly under very low pressure.

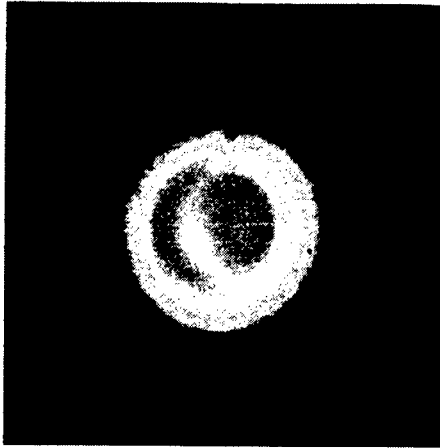


Figure 24. 1.5 μ m YAG Laser With Poor Top Hat Structure. (Used for Tissue Welding)

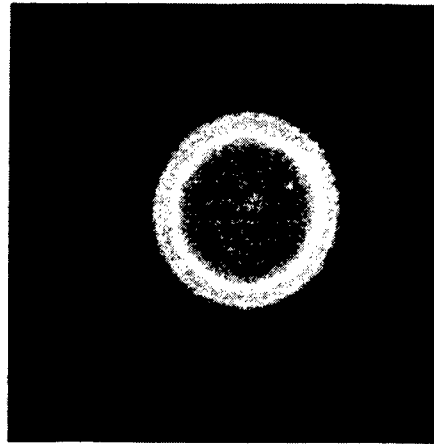


Figure 25. 1.5 μ m YAG Laser With Good Top Hat Structure. (Needed for Good Tissue Welding Results)

5.8 Free electron laser

Figure 26 shows the output of a free electron laser at 100 μ m. This laser was measured with a pyroelectric matrix array camera. This was the first time that the scientists using this laser had ever seen the beam profile. They were quite thrilled to see that the intensity profile was as close to Gaussian as is illustrated in this beam display.

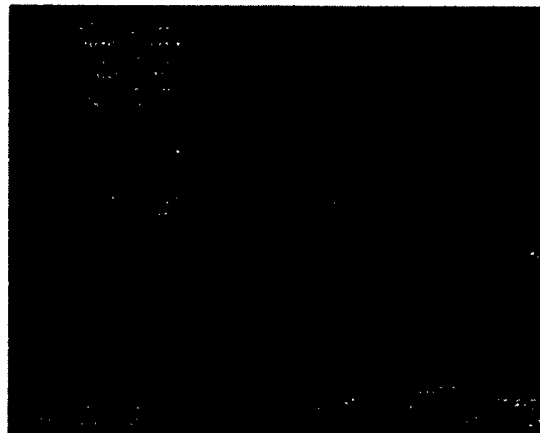


Figure 26. Output of Free Electron Laser Focused Beam At 100 μ m Wavelength.

6. CONCLUSIONS

Laser properties have improved dramatically in the last 5-10 years. Gains are increasingly made in many aspects. Pulses are getting shorter, wider wavelength range is achieved, higher powers and intensities are gained, and many other performance characteristics have improved. One of the major gains has been improvement in the beam profile so that the intensity pattern performs its job better than previously possible. Electronic beam profile analysis has contributed significantly to this improvement in lasers.

**SATELLITE REMOTE SENSING DATA APPLIED
FOR SEISMIC RISK ASSESSMENT OF VRANCEA REGION**

Maria Zoran, Cora Lucia Braescu, Cristina Aiftimiei
Institute of Optoelectronics, Remote Sensing Department
PO Box MG-22, 76900 Bucharest-Magurele, Romania

ABSTRACT

The aim of this study is to present the results of the application of remote sensing techniques for seismic risk analysis, which estimate the geographic distribution, frequency, and intensity of seismic activity, without attempting to predict specific events.

This method is based on the recognition of the active faults, which are defined as breaks along which movement has occurred in Holocene time (past 11,000 years).

Remote sensing analysis and field studies of active faults can provide a geologic history that overcomes many of the shortcomings of instrumental and historic records.

The majority of strong Romanian earthquakes has the origin in Vrancea region, a distinctive active zone of the Alpine orogenic belt placed at the Eastern Carpathians Arc Bend with extensive macroseismic area.

Many seismological researches revealed two kinds of mechanisms involved in the occurrence of intermediate earthquakes having a Vrancea focus: one has a NW-SE oriented compression axis (the fault plane direction is NE-SW) while the other has a NE-SW orientated compression axis (the fault plane direction is NW-SE). Subduction of the Black Sea Sub-Plate under the Pannonian Plate produces faulting processes. The fault plane is oriented approximately parallel to the Carpathian Bend, i.e. NE-SW. The Black Sea Sub-Plate would have a NW displacement along "the markers" formed by the Moesian and Eurasian Sub-Plates admitting of another fault plane, oriented NW-SE, approximately perpendicular to the first.

Landsat images are excellent for recognising the continuity and regional relationships of faults, but the spatial resolution is not so good to distinguish topographic features indicative of active faults.

SAR ERS-1 data are more useful for this purpose.

This also allows a more precise characterization of lineament structures, especially in cloud and soil covered areas, where the lack of data reduces the tectonic analysis. An on-going evaluation of all data will lead to a better understanding of the stress field which controlled the tectonic movements.

The results obtained from the remotely sensed data have shown a good concordance with the available "in-situ" data implying that remote sensing techniques provide a means for locating, identifying and mapping certain terrain features and aspects of geologic structures.

Further methodical work on Landsat TM and ERS-1 and ERS-2 SAR data will be useful to elaborate even physical parameters for the discrimination of different lithological units.

Keywords: seismic risk assessment, Vrancea, Landsat TM, ERS-1 SAR, methodology, remote sensing.

1. INTRODUCTION

Romania's territory, placed at the border of the great East-European Platform, is a region of a complex geological structure dominated by the presence of the Alpine Orogenic Belt of the Carpathian Mountains. This mountains arc has a spectacular change of direction just above the well-known Vrancea seismic region, very important seismic area of Europe, remarkable by the uncommon energy of earthquakes¹.

The Vrancea earthquakes are produced by the release of stress that has built up in the earth's crust. Some zones of maximum earthquake intensity and frequency occur at the boundaries between the moving plates that form the crust of the earth.

Subjection of the Black Sea Sub-Plate under the Pannonian Plate produces faulting processes. The fault plane that results is oriented approximately parallel to the Carpathian Bend, i.e. NE-SW. The Black Sea Sub-Plate would have a NW

displacement along the "markers" formed by the Moesian and Eurasian Sub-Plates only provided that we admit of another fault plane, oriented NW-SE, approximately perpendicular to the first ².

The Variance earthquakes are produced by the release of stresses that is accumulating in time along some fracture lines belonging to one of the first or second fault-planes.

From depth distribution point of view, Variance earthquakes foci are classified in three distinct zones: a zone of crust earthquakes with focal depth not exceeding 40-45 km; an aseismic zone up to 7-80 km; and a zone of intermediate earthquakes with focal depth between 70-80 km and approximately 200 km.

This finding suggested a new seismotectonic model of the Variance region, a model that implied, among others, the hypothesis that the subducted plate was torn in this region long time ago and the intermediate earthquakes were connected with the lithospheric "slab" (torn off the plate) remained in the mantle, the spatial distribution of Variance earthquakes' hypocentres being in a relationship with structural tectonic systems involved in continental and oceanic crust, subcrustal lithosphere and asthenosphere³.

Remote sensing techniques are very useful for seismic risk analysis, which estimates the geographic distribution, frequency, and intensity of seismic activity without attempting to predict specific events⁴.

Such analysis are essential for locating and designing dams, electric and nuclear-electric powerplants as well as different other projects in seismic areas.

Seismic risk analysis based on satellite remote sensing methods is based on the recognition of tectonic active faults, which are defined as breaks along which movement has occurred in Holocene time (past 11,000 years).

remote sensing analysis and "in situ" studies of active faults are able to provide a geologic history better than instrumental and historical records.

ERS-1 SAR is an active remote sensing system which has his own source of illumination in the microwave region of the electromagnetic spectrum. Due to the used range of wavelengths radar has advantages compared with optical systems (Landsat TM, SPOT). Radar is independent of sun light, therefore data acquisition is possible 24 hours a day. It has an all-weather capability, since there is only few scattering through clouds and precipitation. Finally radar data shows only minimal atmospheric absorption. The C-band frequency, the VV polarization and the small incidence angle qualify ERS-1 SAR data especially for the mapping of tectonic structural features. The intensity of the radar backscatter is a complex function of the interaction between terrain and radar pulse. Especially in semiarid and arid areas the penetration depth of the radar can be half of the wavelength. Therefore covered morphological features, which can not be discerned by optical systems are detectable by microwave. The radar signal depends mainly on three factors: surface roughness, topography (slope effect on the backscattering) and moisture. These factors make radar indispensable for a wide range of geological applications, such as to discriminate different surface lithologies as well as to discern the structural inventory of certain areas.

Our studies have been centered on estimating of geologic features and environmental parameters from multispectral data supplied by satellite sensors. As there is a great variety of sampling strategies, digital image processing techniques, and procedures for finding the relationship between the images and environmental parameters, we have found it necessary to develop a methodology best suited for our case study.

We have also investigated the potential of merging satellite Synthetic Aperture Radar (SAR) data with optical data, to get complementary information.

Remote sensing studies based on color analysis and supervised classification, vegetation stress and vegetation cover, have been performed to obtain a processing methodology suitable for seismic risk assessment analysis. Thematic maps have been produced to control the parameters under consideration during the study periods.

2. TEST SITE DESCRIPTION AND SATELLITE DATA USED

It was analyzed Vrancea - Focsani seismic region. This area is structurally and seismically complex area, bounded by latitudes 45.6 °N and 46.0 °N and longitudes 26.5 °E and 27.5 °E (Fig.1).

The Peceneaga-Camena Fault, a deep crustal fracture with dextral slip, is considered to be North-Eastern boundary of the Mason Platform. The Eastern unit of the Moesian Sub-Plate is characterized by a series of principal faults with a North-Western orientation and by a secondary system of faults orientated NE-SW. NW trending crustal fractures are also evidenced East of the Peceneaga-Camena Fault, within our test area.

An ERS-1 SAR image and a multispectral Landsat TM data set was used. Their characteristics are the following:

Landsat TM
 Acquisition date : 10. 14. 1989
 Path/ Row : 182 / 28
 Processed scene center
 latitude 46,0333406
 Processed scene center
 longitude 27,4253400

ERS-1 SAR
 Acquisition date : 11. 06. 1992
 Orbit/Frame : 6851 / 2691
 Frequency : 5.3 GHz
 Track : 193

All image enhancement steps were performed on a TITAN 3000 station , using a EASI/PACE image processing software package as well as own developed algorithms.

ERS-1 SAR data were acquired in PRI format and Landsat TM data at "system corrected" level. We used too topographic maps over the selected area.

In order to better manage all the informations available on the study area, data acquired have been integrated in an unique data base. This information consists of thematic maps from cartography, land use map from classification of remotely sensed data .

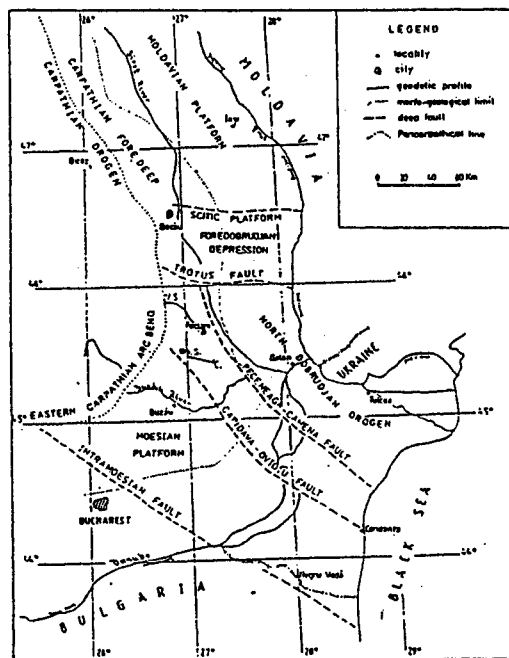


Fig.1. Tectonic faults for seismic region Vrancea

3. METHODOLOGY

The methodology used consists in the following steps :

- Reading the satellite data from the CCT magnetic tapes and including these in PCIDSK databases .

- Applying of atmospheric corrections.

- "De-speckling " of the SAR ERS-1 images was performed by using a 7x7 Frost filter, and a Lee filter too.

Reducing the speckle makes the discrimination of different lithological units easier and highlights more efficient textural features in radar images. This requires that the applied filters reduce the speckle without lowering thematic information. Comparing the best algorithms it appears that Lee filters reduce speckle most operative and run the procedure in the shortest computing time. Whereas the use of Frost filters highlights better textural features and there seems to be more efficient when a merge will be done in a further step. The slight structures are better emphasized as by Lee filter.

- Data conversion from 16 bits radar data to 8 bits images using AVS (Application Visualization System) from EASI/PACE software.

- To geometrically correct and geocode the images we have use a 1 : 100000 scale topographic map . 20 ground control points have been selected and second order polynomials were used to perform the image -map registration (the total RMS error was of 0,535 pixels).

- The registration-synergism between the Landsat TM geocoded image and SAR ERS-1 image was subsequently performed.

- Analysis of Landsat TM image processing :

The use of Landsat TM5 visible bands 1, 2, 3 , (0,452 - 0,518 μm ; 0,528- 0,609 μm ; 0,626 - 0,693 μm allows to represent with good correlation , the chromatic components of the observed area ⁷.

Analogously to the possibility to emphasize spatial and linear structures by filtering in the spatial domain, spectral characteristics of multispectral data can be enhanced by the adaptation of the adequate filters as linear transformation. Two different approaches were used : Principal Component Analysis and Relative Channel Analysis. By comparing the two processing procedures it can be stated that Principal Component Analysis as well as "Spectral Mean Value" show the same thematic information content concerning tectonic structures. Supplementary , the TM relative band 3 was taken for lineation mapping because a maximum of linear structures was emphasized in this channel.

- Data analysis:

Landsat TM and SAR ERS-1 data were use to identify linear features by visual interpretation (Fig. 2 and Fig. 3). Lithological units were differentiated By several Landsat TM RGB- processing. Finally the lineaments were digitized separating different stratigraphical units , in order to distinguish the tectonic structures in time and space.

4.RESULTS

The comparative analysis of ERS-1 SAR and Landsat TM data shows that linear features in TM images appear shorter and denser distributed , whereas ERS-1 images are dominated by the principal structures. In certain cases they complete the lineaments and lineament patterns derived from TM data .

Radar enables the interpretation of partly clouded zones for which Landsat TM are not available.

The method of seismic risk analysis and assessment is based on the recognition of the active faults . Comparison of the Landsat and SAR ERS-1 images of Vrancea- Focsani region with the topographic map and the map of faults indicates that the most of these faults are evident on the Landsat Tm and SAR ERS-1 images.

A fault zone includes the entire belt of active and inactive faults that may be hundreds of kilometers in length and several kilometers in width. The fault trace is the surface expression of the individual active faults.

Landast and SAR ERS-1 images are excellent for recognizing the continuity and regional relationships of faults, but the spatial resolution is too low to recognize any but the largest topographic features indicative of active faulting. The higher resolution of Skylab and aircraft photographs as well as SAR ERS-2 interferometric data are ideal for mapping of these features.

The most promising data are SAR ERS-1 and ERS-2 interferometric to measure tiny movements in the Earth's surface caused by shifting geological faults or volcanic activity.

Radar interferometry relies on taking two images on the same area from slightly different orbits of the satellite. The phase difference from one image is then superimposed by computer onto the phase information of the other. The phase values for

each corresponding picture element, or pixel , of the two images are subtracted, leaving an image , known as a interferogramme, that records only the differences in phase between the two.

These phase differences give the variations in altitude of each pixel. The effect is identical in principle like stereo vision.

The result is a computer relief map known as a digital elevation model, very useful for inaccessible parts of the world.

Differential radar interferometry is based on taking three images of the same area. The first two are subtracted to form an interferogramme , then the second and third are subtracted to form another interferogramme. The two interferogrammes are then subtracted from each other to make a final one which shows up with great accuracy and changes between the original three images.

Such researches will be very useful too for seismic risk assessment of Romanian Vrancea area.

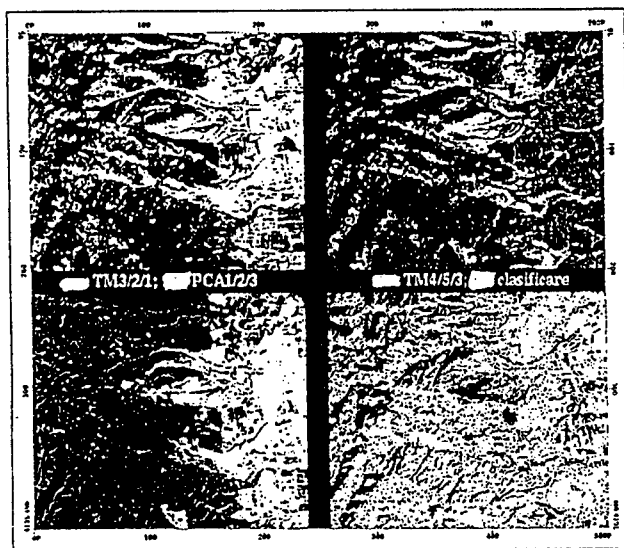


Fig.2 Landsat TM images for Vrancea region

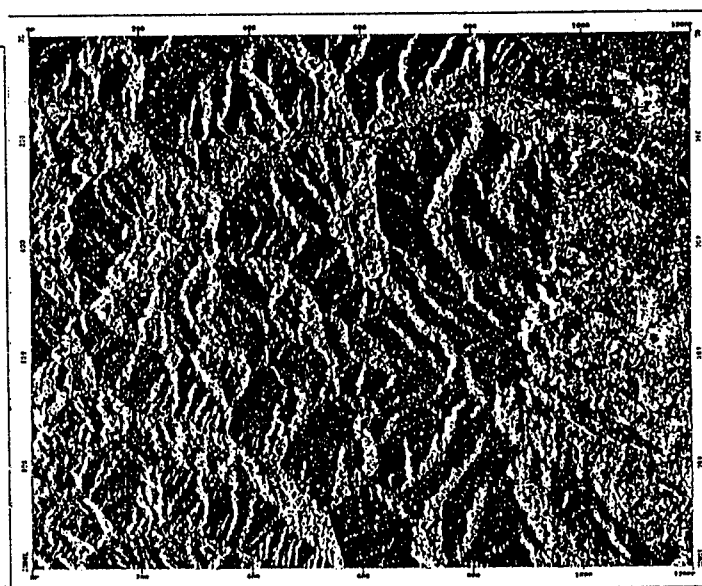


Fig.3 SAR ERS-1 image for Vrancea area

REFERENCES

1. V.Mocanu et al, Litospheric structure of Romania and recent crustal movements-Geodynamic Connections, Rev.Roum.Geophysique, Bucharest, 35, p 3-13, 1991 .
2. D.Zugravescu et al.,Romanian territory geodinamics, Rev.Roum.Gcol., Geophys.,Geogr.-Geophysique, 29, p 3-8, Bucharest, 1985.
3. D.Enescu et al., Tectonics and geodinamical evolution of the romanian territory,Rev.Roum.Geol.,Geophys.,Geogr. - Geophysique, 26, p 29-36, Bucharest, 1982.
4. F. Sabins, "Remote Sensing Principles and Interpretation", ed. Freeman , San Francisco, p. 363,1978.
5. C.Braescu, M.Zoran, F.Serban, et. al,An investigation of the potential of merging SAR ERS data with optical data, "Progress in Environmental Remote Sensing Research and Applications", Parlow (ed), Balkema, Rotterdam, ISBN 90 5410 5984, p.277-285, 1996.
6. F.Serban, C.Braescu, M.Zoran , et al.,Black Sea coastal study by use of Landsat and ERS-1 data, "Progress in Environmental Remote Sensing Research and Applications", Parlow(ed), Balkema, Rotterdam, ISBN90 5410 5984, p. 291-301.
7. M.Ippoliti, U.Poli, Use of Landsat and ERS-1 data for mediterranean coast,Remote Sensing 96, Spiteri(ed), Balkema, Rotterdam, ISBN 90 54 10 855X, p.141-144,1997.

AMORPHOUS SILICON PHOTODETECTORS FOR OPTICAL INTEGRATED CIRCUITS

M. Balucani¹, V. Bondarenko², G. Lamedica¹, A. Ricciardelli¹, and A. Ferrari¹

¹ INFN Unita di Roma, Dipartimento di Ingegneria Elettronica, Università 'La Sapienza' di Roma, Via Eudossiana 18, 00184 Roma - Italy

² INFN Unita di Roma, Belarusian State University of Informatics and Radioelectronics, P. Brovki 6, 220027 Minsk, Belarus

ABSTRACT

The first successful attempt to integrate on-chip optical waveguides based on oxidized porous silicon and amorphous silicon photodetectors have been demonstrated. Buried channel waveguides were performed by thermal oxidation of porous silicon. Amorphous silicon photodetectors were fabricated on the waveguides. Different device structures as well as their performance attributes are exhibited. The devices were demonstrated to have photocurrent characteristics promising for optoelectronic applications.

Keywords: amorphous silicon, integrated photodetector, integrated waveguide, oxidized porous silicon.

1. INTRODUCTION

Integrated optoelectronics is a fast growing industry with applications in many areas from watches and television to laser communications. At the heart of optoelectronic system are three main components, namely, light emitting device (LED), photodetector (PD) and waveguide (WG). LED and PD, useful as they are as discrete devices, form a system called as optoelectronic circuit when optically connected via WG and electrically connected with electronic components. It is of first importance that conventional silicon technology to be applicable for fabrication of the components. In that case, the possibility exists to integrate all optical and electronic components on-chip. As a result, the benefits will come from the increased functionality and reliability, and the corresponding reduction in cost.

Recently different optical integrated circuits in which planar optical waveguides on a semiconductor substrate are employed as optical interconnects between active devices (lasers, detectors, LEDs, etc.) have been presented [1-3]. We have developed an original method to confine the light in monocrystalline silicon wafers by using dense thermally Oxidized Porous Silicon Waveguides (OPSWG) [4,5]. The silicon oxide obtained by thermal oxidation of porous silicon shows suitable characteristics for optical applications, such as low losses and strong confinement [6]. The use of these waveguides as interconnections makes the fabrication of optical-electrical transducers necessary. Hydrogenated amorphous silicon (α -Si:H) has been demonstrated to be a suitable material to convert the optical signal to electrical signal because of its very high absorption coefficient for the light in the visible range [7,8]. This property allows to fabricate high efficiency photodetectors using thin layers (about 1 μ m thick).

Since integration and compatibility of individual optoelectronic components with one another is of the first important, photodetectors using α -Si:H as active layer for the detection of the optical signal passing through OPSWG were investigated in the present work.

2. EXPERIMENTAL

Boron-doped, 0.01 Ohm cm resistivity silicon was used as a starting material. Porous silicon channels were formed by selective anodization of silicon wafers using 0.2 μ m thick silicon nitride mask. Anodization was performed in HF/alcohol solution under a current density of 20 mA/cm². Then the wafer was chemically cleaned and rinsed in deionized water. It resulted in the formation of a channel porous silicon waveguide of a width of about 30 μ m, and a thickness of about 15 μ m. In order to obtain waveguiding properties in the visible range, porous silicon channel waveguides must undergo some farther technological processes. Thermal treatment in oxidizing atmosphere allows to create a dense silicon oxide core within the channel. The OPSWGs were located beneath the surface of silicon wafer.

To form photodetectors, a layer of hydrogenated amorphous silicon was deposited upon the waveguide by Plasma Enhanced Chemical Vapour Deposition technique. The deposition was performed in a parallel plate glow discharge reactor operating at a frequency of 13.56 MHz. The deposition time and substrate temperature were set in order to obtain films of undoped α -Si:H 1 μ m thick. Aluminum was then deposited over the α -Si:H layer by evaporation. Pads for electrical contacts were defined by conventional photolithography. Aluminum and amorphous silicon form a Schottky barrier making available a device which is known to be faster than p-n or p-i-n diodes [7,8]. Three different types of photodetectors were designed and investigated in the work.

* **Coplanar Photoresistive Detector (CPD).** The schematic representation and the optical microphotography of a CPD are shown in Fig.1(a). The operation of the device is based on the change of conductivity of α -Si:H induced by the absorption of the light which is lost by the waveguide. The gap between the contacts is $100\text{ }\mu\text{m}$, while contact length is 3 mm .

* **Pass-Through Detector (PTD).** This device (Fig.1b) is based on the direct illumination of the Schottky junction formed by aluminum and amorphous silicon: the light is lost by the guide because of the higher refractive index of α -Si:H and is then absorbed by the device. The second contact can be another Schottky contact formed on a separate or can be the bulk silicon under the guide. This second approach results in an high-pass behavior of the detector.

* **End-Fire Detector (EFD).** This device (Fig.1c) is based on a peculiar characteristic of OPSWG technology: the possibility to introduce a 90 degrees bending of the guided light beam. So the output of the guide is directly coupled with the active layer of the Schottky junction. We expected this device to have a greater efficiency (in terms of signal per device area) than the other devices. On the other side we have to say that this geometry can be used only in correspondence of the terminal section of the guide.

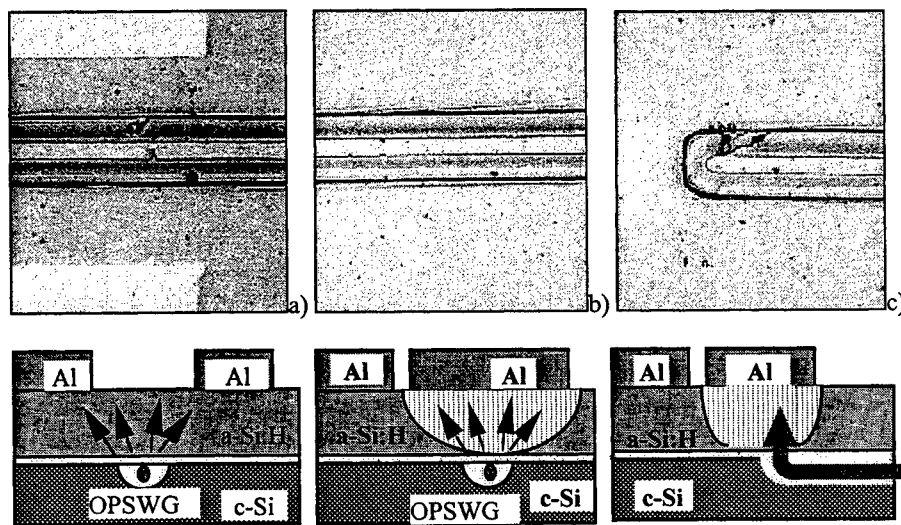


Figure 1. Top view pictures of the CPD(a), PTD(b) and EFD(c). On the bottom side the corresponding schematic cross sections are reported.

3. RESULTS AND DISCUSSION

We tested the devices presented in the preceding paragraph introducing the light in the OPSWG by end-fire coupling with a He-Ne ($\lambda = 632.8\text{ nm}$) or Argon ($\lambda = 488\text{ nm}$) laser and then measuring the photocurrent with a lock-in technique.

3.1. CPD - Coplanar Photoresistive Detector

Current-voltage characteristics of the CPD are shown in Fig.2 for different laser intensities. The photoresistive behavior of the device is appreciable only for voltages large enough to breakdown the double backward connected diodes present at the contact pads. At lower voltages the blocking characteristic of the diode is dominating in the device's behavior.

3.2. PTD - Pass-Through detector and EFD - End-Fire Detector

The photocurrents generated in the PTD and EFD devices as a function of the voltage applied to the Schottky junction are shown in Fig.3. The level of light intensity is the same for the two curves. As expected, for both devices the collection efficiency is greatly augmented by a reverse bias applied to the junction up to the saturation of photogenerated carriers (unity collection). From the comparison of the two characteristics we can see that stronger coupling makes EFD

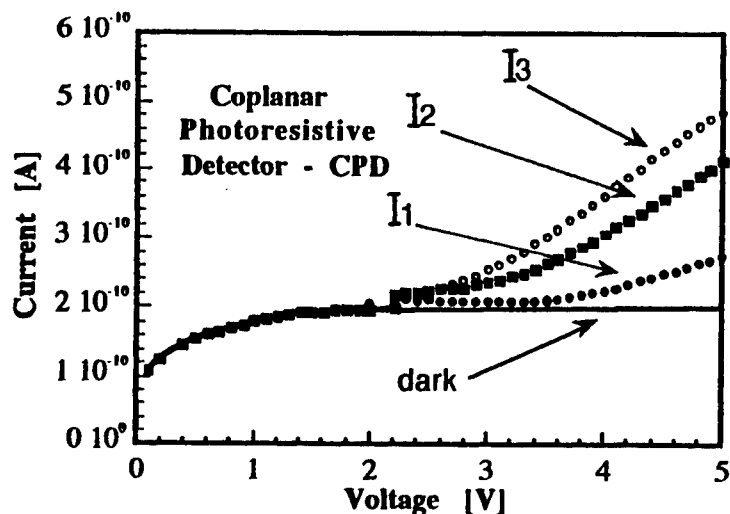


Figure 2. Current-voltage characteristics of CPD in the absence (dark) and for different levels of guided light intensity.

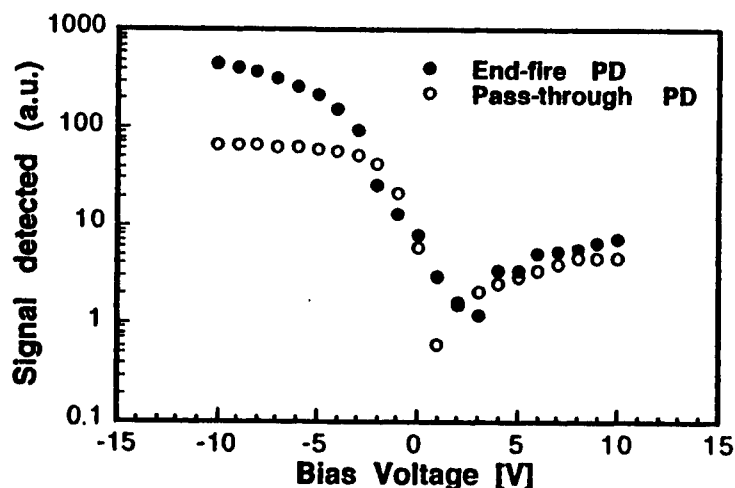


Figure 3. Photocurrent generated by PTD and EFD devices as a function of the applied voltage.

better than PTD by almost an order of magnitude in the saturated collection efficiency. However the PTD presents a very interesting characteristic not possessed by the EFD: indeed, you have not to place PTD device at the end of the OPSWG, it is possible to take advantage from the distributed way in which the waveguide leaks the light towards the α -Si:H layer. This feature could make possible to introduce several photodetectors along the waveguide length, each one absorbing just a fraction of the guided light and distributing the signal to different parts of the circuit. Further investigations have then been made upon PTD detector preparing another sample in which a photolithographic process was performed before the deposition of the α -Si:H in order to open a window in the oxide layer, preventing at the same time the destruction of the waveguide by HF etching. So we have now two different topologies for the PTD detector: type A which maintains the

oxide layer insulating the α -Si:H film from the highly conductive p-type silicon substrate and type B in which α -Si:H is in direct contact with crystalline silicon. The two devices are shown in Fig.4.

In Fig.5 we show the current-voltage characteristics of A and B devices in dark conditions with the positive side set on the ohmic contact in both cases. Type A sample shows the typical curve of an Al/undoped α -Si:H junction with a high series resistance due to the distance of some hundreds micrometer between the photodiode and the reference pad. The parameters of this curve resulted to be: saturation current $J_0 = 1.3 \cdot 10^{-10}$ A/cm², series resistance $R = 320$ MOhm, and quality factor $n = 13$. The graph for B type sample shows that in this device the high series resistance is practically absent. This is due to the vertical geometry of the device.

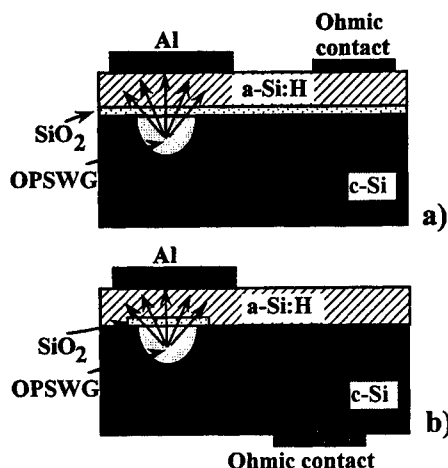


Figure 4. PTB devices of type A and type B.

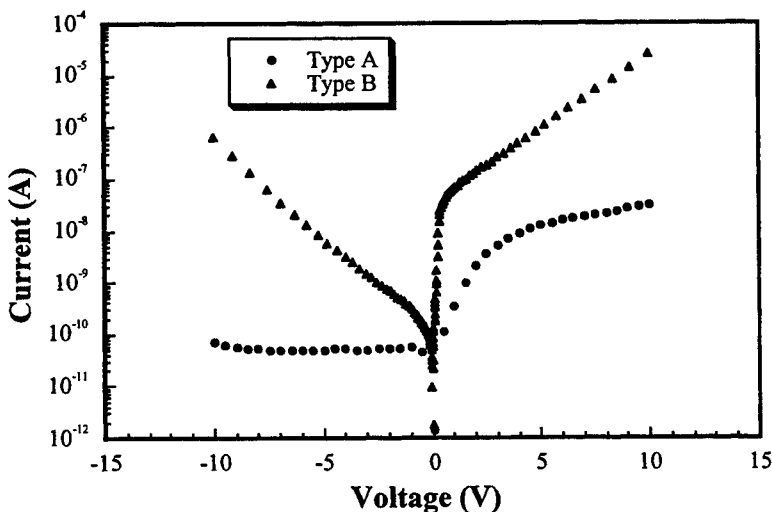


Figure 5. Dark current-voltage characteristics of type A and B devices.

The photocurrents for type A and type B devices are reported respectively in Fig.6 and in Fig.7 for different laser intensities (measured at the laser output, ignoring losses due to end-fire coupling and scattering). Both devices present a saturation behavior under reverse bias. The photocurrent increases with light intensity following a power law $I = A I_0^\gamma$ with $\gamma = 0.48$ for A type and 0.76 for B type. Under forward bias the A type device shows photoresistive behavior with a gain of about 70.

In A type samples the current is controlled by the Al/a-Si:H junction while in B type ones the photocurrent is controlled by the heterojunction c-Si/a-Si:H [15]. It is now important to understand the frequency limits of these devices.

Clearly B type devices, being not limited by the series resistance, are more promising for high frequency applications. Indeed the B type device showed flat response up to 10 kHz (maximum testing frequency used in our experiments); However, the results of a numerical simulation reported in [10] shows that response speed in the GHz range can be achieved in amorphous silicon detector with vertical structure. These results make samples of type B very interesting for high frequency optoelectronic applications.

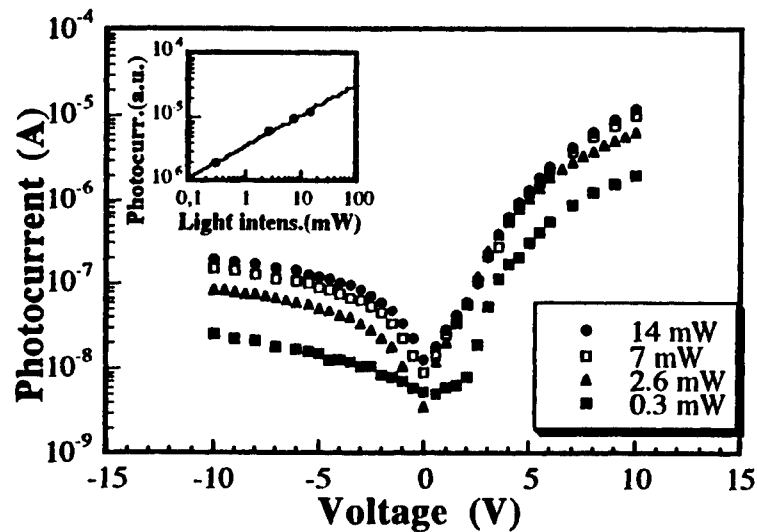


Figure 6. Photocurrent as a function of bias voltage for type A samples. In the inset photocurrent measured with a forward bias of 10 V versus laser light intensity is reported.

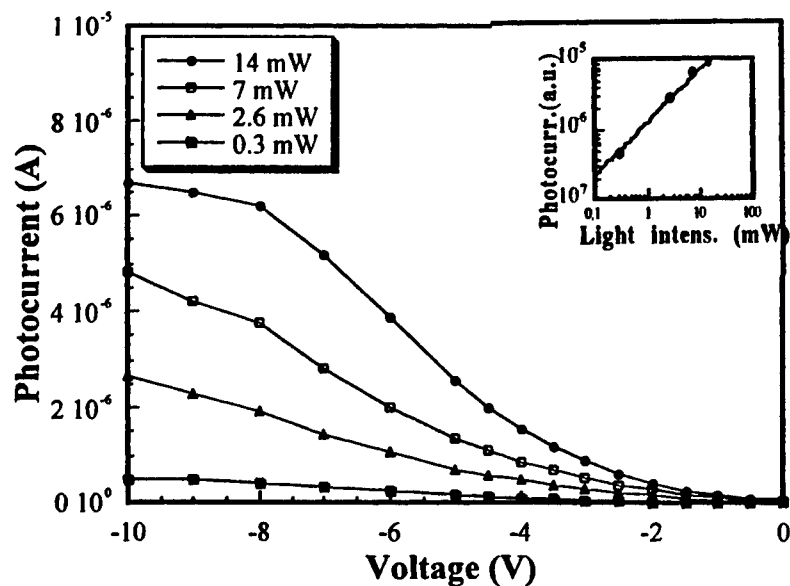


Figure 7. Photocurrent as a function of bias voltage for type B samples. In the inset photocurrent measured with a forward bias of 4 V versus laser light intensity is reported.

4. CONCLUSIONS

In this work we presented performance of different amorphous silicon photodetectors used to sense the light guided by oxidized porous silicon waveguides buried in silicon wafer. The geometric characteristics of PTD device seems to make the realization of various photodetectors upon the same waveguide possible. First results of frequency measurements make these systems promising for high frequency optoelectronic interconnections in silicon technology.

5. ACKNOWLEDGMENTS

The authors thank Valentina Yakovtseva of Belarusian State University of Informatics and Radioelectronics, Minsk, Gabriella Maiello of University 'La Sapienza', Rome, Lorenzo Masini of Terza University degli Studi, Rome for participation in fulfillment of experiments and useful discussion. This work was partially supported by NATO LINKAGE GRANT HTECH.LG 951231.

REFERENCES

1. R.Soref "Silicon -based optoelectronics", Proc. IEEE, vol.81, No.12, p.1687-1706, 1993.
2. J.T. Boyd Integrated Optics: Devices and applications, New York, 1990.
3. U.Hilleringmann and K.Goser "Optoelectronic system integration on silicon: waveguides, photodetectors, and VLSI CMOS circuits on one chip", IEEE Transactions on Electron Devices, vol.42, No.5, p.841-845, 1995.
4. V.P.Bondarenko, V.S.Varichenko, A.M.Dorofeev, N.M.Kazuchits, V.A.Labunov, V.F.Stelmakh "Integrated optical waveguide fabricated with porous silicon", Tech.Phys.Lett. vol.19, p.463-464, 1993.
5. V.P.Bondarenko, A.M.Dorofeev, and N.M.Kazuchits "Optical waveguide based on oxidized porous silicon", Microelectronic Engineering, vol.28, p.447-450, 1995.
6. G.Maiello, S.La Monica, A.Ferrari, G.Masini, V.P.Bondarenko, A.M.Dorofeev, N.M.Kazuchits "Light guiding in oxidized porous silicon optical waveguides", Thin Sol.Films, vol.297, p.311, 1997.
7. S.M. Sze Physics of Semiconductor Devices, Wiley, New York, 1981.
8. J. Kanicki Amorphous & Microcrystalline Semiconductor Devices, Hartech House, p.189, 1992.
9. G. Masini, A. Ferrari, M. Balucani, S. La Monica, G. Maiello, V.P. Bondarenko, A.M. Dorofeev, V. Filippov, and N.M.Kazuchits "Amorphous silicon photodetectors for Oxidised Porous Silicon based optical interconnections", NATO Advanced Research Workshop 1996, Kishinau, 1997.
10. D.S. Shen, and S. Wagner, J. Appl. Phys., vol.79, p.794, 1996.

Properties of polymer compositions for recording and copying optical images

Bivol V. V., Barba N. A. *, Robu S. V. *, Ishimov B. M. *,
Vlad L. A. *, Prisacari A. M., Triduh G. M., Akimova E.A.

Center of Optoelectronics, Academy of Sciences of Moldova,
*State University of Moldova,
1 Academiei Str., MD-2028 Chisinau, Moldova Republic

ABSTRACT

In this paper we present the experimental results of the investigation of relief recording of the information with application of the media based on thermoplastic materials and synthesized organic photopolymers. We present also the results concerning the possibilities of strengthening of polymer media with the scope to improve mechanical properties of the relief image (hardness, strength, adhesive stability) and the possibilities to make copies by stamping method. Also we examine the possibility to increase the sensitivity of photothermoplastic media by addition of the injector chalcogenide layers.

Keywords: Thermoplastic, polymer, optical image, holography, recording, information, photochromatic, sensibility, stability.

1. INTRODUCTION

During the last years the methods of optical registration of information are used in high technology equipments. These methods include also holographic registration on the layers of chalcogenide vitreous semiconductors (CVS) thin films [1,2] and sensitive photothermoplastic media (PTM) [3], which are characterized by high optical parameters (efficiency is more than 10% and the resolution power - more than 1000 mm^{-1}). A metallic matrix is deposited on the relief image received on CVS or on PTM by laser illumination. From this matrix we can get copies by stamping on the transparent thermoplastic layers.

The method for metallic matrixes preparation is very complex and the technological problems based on the reaction between the CVS and electrolyte cause many difficulties.

With the view to facilitate the multiplication of hologram copies, which were initially recorded on CVS (for example As_2S_3 , As_2Se_3) or on others substrates, the images were transferred by the method of hot stamping: mechanical pressing on the thermoplastic layers, prepared from copolymers or other compositions, which contain chemically active liaisons of 4-aminostyrol I or hlycedilmetacrylat II.

2. EXPERIMENTAL RESULTS AND DISCUSSION

The thermoplastic layers were prepared by the pouring method on the polyetilenteretalat (terilen) basis, which was previously specially treated to improve the adhesive. The thickness of the recording thermoplastic layer depends on the concentration of the polymer solution and constitutes 6 - 8 μm . After drying in the air and then in a vacuum drying box at the temperature of 40°C until the stage of constant mass, these materials were used to multiply copies.

The stamping was carried out with the equipment similar mechanical pressing at the softening temperature of the thermoplastic layer 83 - 85°C for thermoplastic I and 65 - 67°C for thermoplastic II. The thermoplastic layers with relief images can be crosslinked under the action of ultraviolet light or under the action of chemical agents, for example the ephyrat BF₃ vapor. As a result the polymer layers with the image become mechanical hard, strength and adhesive stable.

During the copying process from CVS film the original of the image is totally transferred on the thermoplastic layer. During this proces the detachment of the CVS layer takes place. This CVS layer is subsequently removed by the simple edging in 5% alkaline solution. The relief image is washed with distillate water, etched and then illuminated by the ultraviolet light during 2 - 3 hours (for thermoplastic layers I). The thermoplastic layers II are treated by ephyrat BF₃ vapor during 1 - 1,5 hours. The crosslinking process in both the cases was determined as a loos of solubility in organic solvents (toluol, chloroform), or as a preservation of the relief image during a long time at high temperature (80 or 100°C) without deterioration of the image characteristics, and also with the Infrared spectroscopy, detecting the change in the intensity of the absorption band in the region at 913 cm⁻¹, which is characteristic for the epoxygroup (Fig. 1). As we can see on the Fig. 1, the increase of the temperature from 25°C to 50°C accelerates the crosslinking process more than by 4

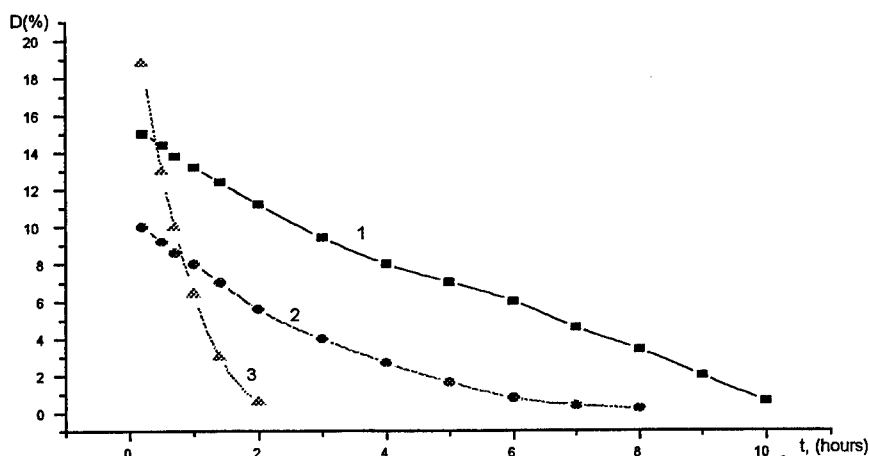


Fig. 1. The dependence of absorption of the epoxygroup at 913 cm⁻¹ versus treatment time in (C₂H₅O)₂BF₃: 1- room temperature (d_{layer}=50 μm); 2- room temperature (d_{layer}=20 μm); 3- T=50°C (d_{layer}=55 μm)

times. The second polymer matrix based on the thermoplastic layers I and thermoplastic layers II can be used for the multiplication of the copies on the special thermoplastic material, prepared on the base of butadiene copolymers. The ability for multiplication of the second polymer matrix based on copolymers of hlicedilmetacrilat is higher and we can get the number of about 100 copies without significant changes of its characteristics. With the view to improve the contrast the copies are used with a reflection metal layer (AlCr), that preserve them from mechanical damages.

For elaboration of new media for optical recording of the information we have synthesized the photothermoplastic materials based on copolymers of N-carbazoliletilmetacrylat [4] with glycedilmetacrylat III, which gives the possibility to record of relief images by the method of potential relaxation [3].

The elaborated PTM sensitized by 2,4,7-threenitrofluorenon has the photosensitivity approximately 10⁵ m²/J (approximately the same as widely used PTM materials), the resolution more than 1000 mm⁻¹ and the diffraction efficiency 10%. Besides these advantages our PTM are crosslinked in epherat (BF₃) vapor. After

crosslinking the samples with image can be used at higher temperature (60-80 °C) without damaging of image quality, and also as a matrix for duplication of copies.

To increase the photosensitivity the polymer layers were additionally sensitized by use of injecting sublayers made from CVS As_2S_3 , As_2Se_3 with the thickness of 0,3-0,5 μm

Evolution of the electrophotosensitivity photopolymers layers with injector and free of injector was carried out by the method of potential relaxation, by registering the time of decrease down to one half of the surface potential on the illuminated photopolymer layer, according to the relation for the sensitivity $S = (1/Et)$ $(\text{lx s})^{-1}$. Illumination on the layer was about 80 lx.

Experimental investigations the photosensitivity (Fig.2) shown that the photopolymer layers with an injector substrates (3,4) in the interval of 20-100°C is 5-10 times higher than the photosensitivity of the films without an injector (1,2). We suppose that the enhancement of the photosensitivity in the polymer with injection layers is due to the injection of the charge carriers from the chalcogenide layer. These layers are characterised by the obvious growth of polyepoxipropilencarbazole with a rich content of carbazole nucleus.

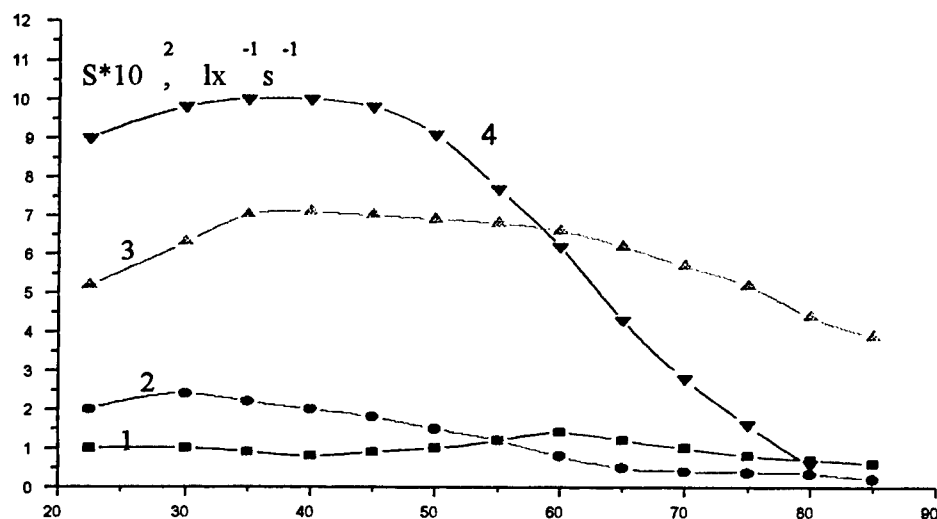


Fig.2. The temperature dependence of photosensitivity of photopolymers films without injection layer (1,2) and with injection layer (3,4).

The photothermoplastic film structures can be used for recoding of images, including holographic angles with the space frequency of 1000 mm^{-1} and with the diffraction efficiency of 8-10%. Its sensitivity for $l = 0.5 \text{ mm}$ is more than 10-15 times than the corresponding value for the structures without injective layer.

The spectral and kinetic characteristics of photodarkening (coloring) and photobleaching (relaxation) of photochromatic layers have been studied in details for elaboration of information media for holographic image registration with a resolution $\sim 5000 \text{ mm}^{-1}$.

The measurements were carried out with spectra-photometers SPECORD UV-VIS, SPECORD 61IR and on the special device with similar optical set-up.

It was determined that development time of photodarkening process for polymer layers constitutes about 20-25 s, and the relaxation time varies from several seconds to several hours and even more. These facts allow to use these films for information registration. The stability of photochromatic layers to UV-light in cycles "photodarkening-photobleaching" was determined and the possibility to stabilize the photochromatic layers by aromatic oxiceeton additions and other stabilizers was studied.

For preparing the photochromatic layers we have preliminary prepared the solutions-composition from copolymer styrol with butilmetacrylat (50:50 mol.%) and photochromatic substances in toluol. The content of photochromatic additions constitutes 6-8% from the quantity of copolymer. This concentration choice of photochromatic materials is due to the fact that in the case of small contents the intensity of coloring is not considerable, and in the case of high concentration the photochromatic additions are crystalized and the layers loosed the optical transparency. Actually, it was possible to add plastificator in the solution or different stabilizing additions. After the dissolution (seldom it is necessary to heat) and filtration of the solution we can depozit photochromatic layers both on the rigid substrate from optical glass as well as on an elastic substrate from optically transparent polyetilentereftalat (terilen). The thickness of the photochromatic layers depends on the polymers concentration in the solution and constitutes 10-20 μm . After drying of photochromatic layers in the air and then in the vacuum chamber at the temperature of 40°C for about of 5 hours, the layers were used for measurements. In the view to prevent scratches or other mechanical defects the photocromatic layers can be placed between optical glasses.

The spectral characteristics in the visible and IR range of spectrum of polymeric photochromatic layers were studed. The polymers are transparent in the visible range, but after ultra-violet illumination they become colored and exhibits a deep maximum of absorption in the range 550-600 nm (Fig.3, curve 1-3), which does not depend significantly on the position of NO_2 -group in the structure of photochromatic substance. The most pronounced effect was observed for photochromatic layers of 1,3,3-threemethyl-6-indolinospirobenzopiran, that accumulate intensively the cherry color and the maximum absorption attains 100% (Fig.3).

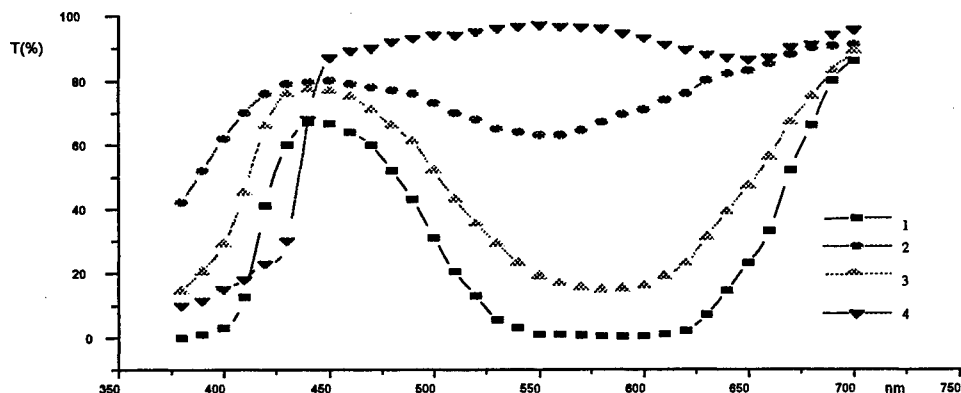


Fig.3. The spectral characteristic of photochromatic layers:

1 - 1,3,3-three methyl-6-nitroindolinospirobenzopiran I; 2 - 1,3,3-three methyl-8-indolinospiro-benzopiran II; 3 - Mixture I and II (1:1); 4 - 1,3,3-three methylindolinospiroantroxazin IY.

The study of spectral characteristics of photochromatic layers based on antratsen-oxazin dye-stuffs (curve 4) showed, that the maximum of absorption depends on the chemical structure of photochromatic layers. From the spectral characteristics we have evaluated the photodarkening and photobleaching time. All layers have a time of colouring in the range of 20-30 s, but the relaxation time is different. For example, the oxazin layer (IY) has the relaxation time of several seconds, and benzopiran dye-stuffs has the relaxation time of several hours and even about 24 hours.

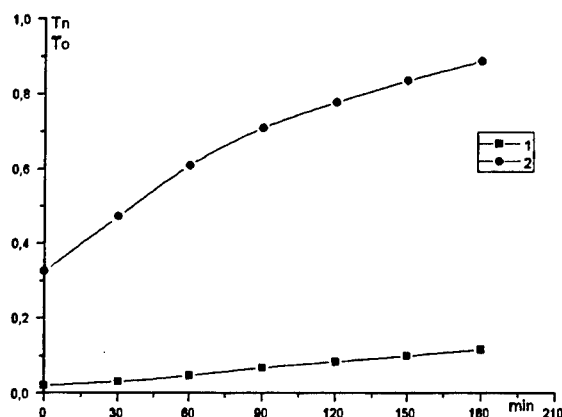


Fig. 4. The dependence of transparency at 590 nm for the photochromatic layer without plastificator diontiltalat (1) and with 5 mas % of plastificator (2).

The photodarkening time and especially the relaxation time depend on the presence in the composition of the polymer layer of plastificator addition (5-10%). Fig. 4 show the change of the optical transparency T_n/T_0 in dependence on the relaxation time at room temperature. It can be seen that the layers which contain 5-6% of plastificator have the relaxation time much more long then the usual photochromatic layer. This effect is due to the increase of the elasticity of polymer macromolecule and facilitation of conformation transformations of photochrom (Fig. 4).

Investigation of photostability of photochromatic layers was carried out with an experimental set up similar to the spectrophotometer. The characteristic curves of photodarkening and relaxation was registered on recording device H-338. The photochromatic characteristics and the photostability of photochromatic layers were evaluated from these measurements.

As a criterion for the stability evaluation we considered the change of maximum current of the photodiode I_{fmax} which corresponds to relaxation level of coloring and I_{fmin} , which respectively corresponds to the level of darkness of layers (Fig. 5).

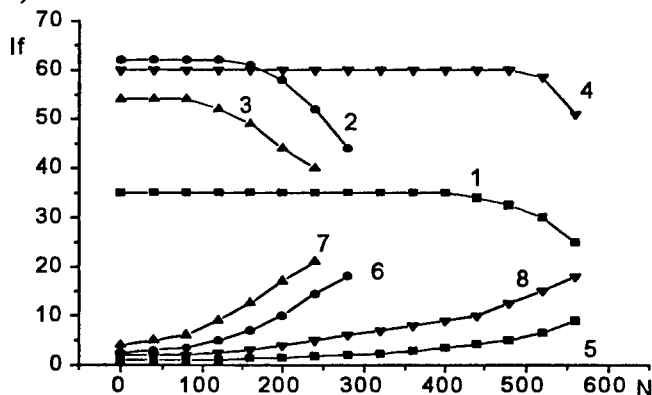


Fig. 5. Changes in the photodarkening (1-4) and relaxation (5-8) in dependence of the numbers of cycles (N) of UV-irradiation:
1,5 - photochrom IY; 2,6 - photochrom I; 3,7 - photochrom II; 4,8 - the stabilized photochrom I.

The investigation of the polymer layers photostability shows, that the maximum stability in ultraviolet light have the layers made from photochrom IV (curve 1-5), which attain ~500 total cycles of photodarkening-relaxation. The indolinospirobenzopirans' photochrom (curve 2-6 and 3-7) has a less photostability (~150 cycles), but it was possible to increase this stability by 2.5 - 3 times with different stabilizers (curve 4-8). The effect of the photostabilizers concentration on the photochromatic characteristics of layers was studied. It was established that the optimal concentration for the photostability of photochromatic layers was about 2.0-2.5 %. We suppose that the layer photoaging is due to the accumulation of molecules of photochrom which is determined by the stable conformation or destruction on the initial products during prolong illumination.

Investigation of the photoaging process by ultraviolet spectroscopy showed, that after prolong ultraviolet irradiation of photochromatic materials the concentration of -CH=CH- groups decreases and a new absorption band around $1700\text{-}1710\text{ cm}^{-1}$ appears, which is due to the aromatic aldehydes. This fact allows to make the conclusion about the dissociation of photochromatic substances on the initial compounds.

3. CONCLUSIONS

The obtained results allow us to make the following conclusions.

1. Thermoplastic media I and II from copolymer composition 4-aminostyrol and glycidylmetacrylate are developed for registration and duplication of images. It was found that the optical information is transferred from chalcogenide semiconductor layer on polymer layer by stamping without losses, and the secondary polymer matrix showed no damage after ~100 cycles of duplication.

2. Photothermoplastic media III based on cyclic copolymers carbazotrimetacrylate was developed too. It has a photosensitivity more than $10^5\text{ m}^2/\text{J}$ and a possibility to crosslink in BF_3 vapor. Sensitization of photopolymer layers by injection layers causes an increasing of photosensitivity by about 10 times, especially at softening temperature of photopolymers.

3. Optical properties and stability of indolinospirobenzopyran and indolinospiroantratsenoxazin photochrom layers have been investigated for creation of a new information media with high (more than 5000 mm^{-1}) resolution.

4. REFERENCES

1. Galpern A.D. and Smaev V.P. Method of registration and multiplication relief-phase image holograms. *Opt. Mech. Ind.*, 11, 49-56 (1988) (Rus).
2. Panasiuc L.M., Ishimov V.M., Robu S.V., Obruchkov G.S. *Conference of State University of Moldova*, Chisinau, p.126, 1995 (Rus).
3. Kartujanski A.L. *Perspectives and possibilities of unsilver photography*, Leningrad, 1988 (Rus).
4. Barba N.A., Dragalina G.A., Robu S.V. *Photosensitive polymeric materials based on carbasol*. Shtiintsa, Chisinau, p.69, 1991 (Rus).
5. *Organical photochroms*. M., "Chemistry", 1982 (Rus).

A study of the electro-optic response of some chiral liquid crystals with high spontaneous polarization

Constanta Dascalu , Cornelia Motoc , Emil Petrescu, Constantin Rosu,
H. D. Koswig* and U. Labes*

University " Politehnica "Bucharest, Department of Physics, Splaiul Independentei 313, 77206 Bucharest, Romania

*¹) Technische Universitat Berlin, Iwan-Stranski-Institut, Arbeitsgruppe Flussigkristalle, Hausvogteiplatz 5-7, D - 10117
Berlin, Germany

ABSTRACT

The electrooptical properties of some SSFLC devices with high spontaneous polarization liquid crystals are presented. The switching time was determined as function of electric field strength and a.c. frequency. Using the switching time the rotational viscosity γ_p was determined. The results are explained by considering the spectacular molecular relaxation, known as Goldstone mode. The surface stabilized ferroelectric liquid crystal (SSFLC) devices offer memory (bistable) capability, fast response speed and sharp threshold and have a variety of applications in electronics.

Keywords: ferroelectric liquid crystal, SSFLC, electro-optic response time, rotational viscosity

1. INTRODUCTION

One of the most promising ferroelectric smectic device, termed SSFLC was proposed in 1980 by Clark and Lagerwall¹. It consists of a thin film with smectic layers standing perpendicular to indium tin oxide (ITO) glass plates in the so called "bookshelf geometry". Under such circumstances the helix pitch of a chiral phase is parallel to the electrodes and the molecules are forced to lie in the plane of the plates displaying two possible orientations corresponding to the tilt direction. If the cell is thin enough (of the order of magnitude of the pitch, i.e. a few μm) the boundary conditions will suppress the antiferroelectric helix. An external electric a.c. field will switch the molecules from one tilt direction to the other and the polarization vector, which is normal to the plates, will be able to have two opposite direction "UP" and "DOWN". Under crossed polarisers the optical effect will consist in switching from extinction to transmission when the electric field is reversed. The switching mechanism of this device was explained first by considering the equilibrium of the viscous, ferroelectric and dielectric torques.^{2,3,4} More accurate estimations for the switching time were obtained by using the Landau model.⁵

SSFLC devices offer memory (bistable) capability, fast response speed and sharp threshold and have a variety of applications in electronics.^{6,7}

It is aim of this paper to examine the electrooptical properties of two ferroelectric liquid crystals (Mohr8 and Mohr10) exhibiting high spontaneous polarization⁸ in a high temperature range.

2. EXPERIMENTS

The electrooptical properties were studied using SSFLC cells consisting of two Indium-Tin Oxide coated glass plates which were previously covered by a rubbed polyimide layer (when assembling the cell, the rubbed directions of the two plates were antiparallel). To obtain thin cells, spacers of SiO were evaporated on the glass plates. The thicknesses of the cells was about $2\ \mu\text{m}$ and the active area was $0.16\ \text{cm}^2$. The liquid crystals Mohr8 and Mohr10 were introduced by capillarity into the cells; we used a Kofler hot bench to allow the liquid crystals heated up to temperatures into the isotropic phase.

In order to obtain a good planar alignment ("the bookshelf structure") the cells were cooled down from the isotropic phase to the SmC* phase with a rate of $0.3\ ^\circ\text{C}/\text{min}$. in the presence of a low frequency ($\sim 10\ \text{Hz}$) alternative electric field ($2.5\ \text{V}\mu\text{m}^{-1}$).

The textures and transition temperatures of the mesophases were examined by polarising optical microscopy using a "Jenapool"- Carl Zeiss Jena polarising microscope linked to a Mettler FP82 Hot Stage and a LINKAM hot stage temperature controller.

The optical response was controlled with a charge couple device (CCD camera (Hitachi KP-C551) with video recording of the microscope picture and the optical transmission change by a photodetector connected with an oscilloscope. All the equipment was interfaced to a microcomputer. The electrooptical switching time τ_{10-90} (the time corresponding to a change in the intensity of light transmitted from 10% to 90% when the polarity of the applied electric field is reversed) was determined.

The spontaneous polarization was determined by the well-known current -pulse technique.⁹ A triangular wave form for the applied voltage was used ($20V_{rms}$; 50Hz) for cells with thickness of about $2 \mu m$. The magnitude of the spontaneous polarization is obtained directly from the area of the induced current "bump" as a result of polarization reversal.

3. RESULTS AND DISCUSSIONS

The electrooptic response in the electrooptical effects in FLCs is determined by the rotational viscosity which characterises the energy dissipation accompanying the director reorientation process.

According to the ferroelectric liquid crystal (FLC) symmetry, two viscosity coefficients should be taken into account, γ_θ and γ_φ , which determine the corresponding response rates with respect to the director angles θ and φ (Fig.1).

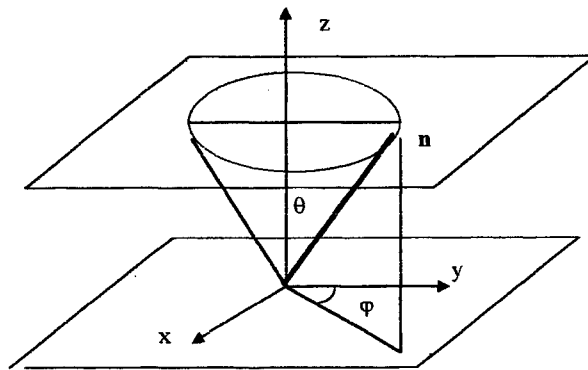


Fig.1. The orientation of the director n in the smectic ferroelectric layer.

It was shown¹⁰ that the relevant dynamic equations take the form :

$$\gamma_\theta \frac{d\theta}{dt} + A\theta = 0 \quad \tau_\theta = \gamma_\theta / A \quad (1)$$

$$\gamma_\varphi \frac{d\varphi}{dt} + P_s E \sin \varphi = 0 \quad \tau_\varphi = \gamma_\varphi / P_s E \quad (2)$$

where $A=2a(T_C-T)$, ($a>0$) is an effective elastic modulus for the tilt. The viscosity coefficient γ_φ can be written as :

$$\gamma_\varphi = \gamma_0 \sin^2 \theta \quad (3)$$

where γ_0 is independent of the angle¹¹. According to Eq. 3, $\gamma_\varphi \rightarrow 0$ when $\theta \rightarrow 0$, i.e., γ_φ is very low for small tilt angle θ . Far from the phase transition temperature (T_C) it is reasonable to consider only the azimuthal director angle φ because θ is frozen. Variations of the angle result in a density change, which is energetically unfavourable.¹² According to Ec.2 the rotational viscosity γ_φ is determined for a sufficiently high electric field E from the experimental dependence of electrooptical response as follow:

$$\gamma_\varphi = P_s E \tau_\varphi \quad \tau_\varphi = \frac{t_{90} - t_{10}}{1.8} \quad (4)$$

where t_{90} and t_{10} are the corresponding time for 90% and 10% light transmission from the maximum level. between crossed polarisers. The switching time τ_{φ} was determined at different temperatures when using a.c. fields of different frequencies and strengths.

The temperature dependence of the switching time τ_{φ} is shown in Fig.2 for the compound Mohr 8.

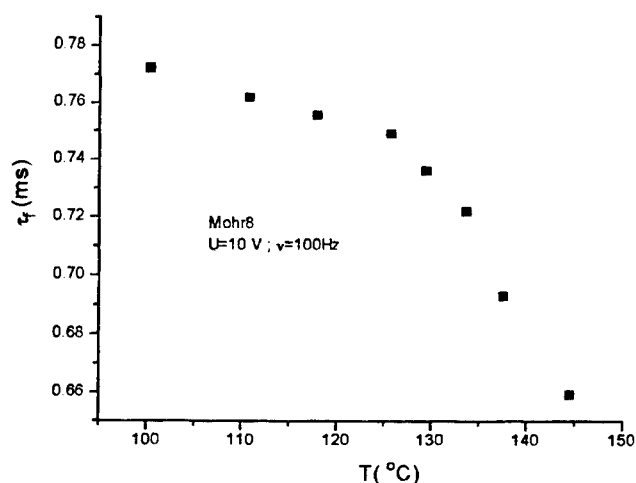


Fig.2. The temperature dependence of the electrooptic switching time τ_{φ}

The switching time τ_{φ} decreases when the temperature is increased, the highest values being obtained in the vicinity of crystal phase - smectic C chiral phase (SmC*) transition temperature. The switching time cancels at the temperature corresponding to SmC*-cholesteric transition. Using Eq.2 the response times in SSFLC cells is determined. The value of $t_{90} - t_{10}$ were determined experimentally and τ_{φ} was estimated considering Eq.4. This relationship indicates that the temperature behaviour of γ_{φ} and P_s are very important in determining the variation with temperature of the switching time.

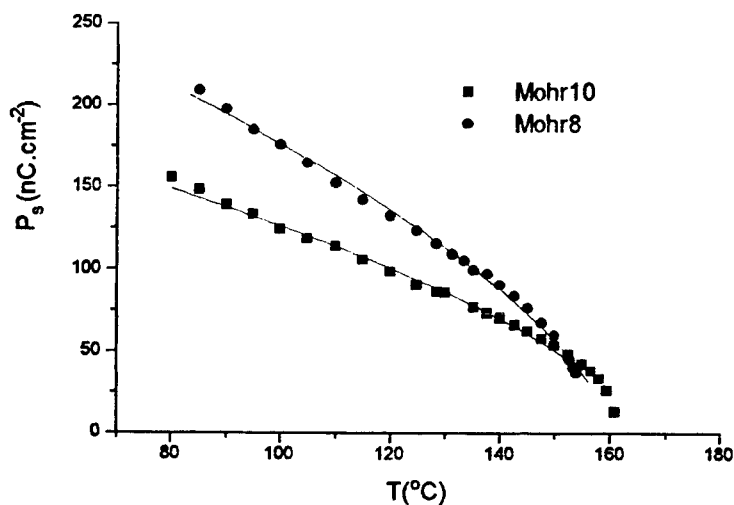


Fig.3. The temperature dependence of the spontaneous polarization for Mohr8 and Mohr10. Theoretical curve is indicated by a solid line.

The temperature dependence of the spontaneous was determined using the polarization reversal method described earlier. The results obtained for Mohr 8 and Mohr10 are given in Fig. 3 . Both compounds exhibit rather high spontaneous polarization , their highest values being in the vicinity of SmC*-solid transition temperature. The spontaneous polarization decreased slowly when the temperature is increased. The behaviour of P_s in vicinity of the SmC* - cholesteric transition point indicates that a first- order transition is involved. This results are similar to those obtained for other ferroelectric liquid crystals.^{9,12} For both substances the temperature dependence of the spontaneous polarization are described well by the relationship:

$$P_s(T) = P_0(T_c - T)^n \quad (5)$$

We get $P_0=12.7$, $T_c=160$, $n=0.64$ for the compound Mohr8 and $P_0= 164.5$, $T_c=12.7$, $n=0.61$ for the compound Mohr10. The theoretical curves are plotted as the solid lines in Fig. 3 and good agreement with experimental data was obtained. As the spontaneous polarization decreases slowly when the temperature is increased, we may conclude that the rotational viscosity γ_ϕ is the prevailing factor which makes τ_ϕ to decrease with temperature.

The viscosity is associated with the molecular mobility in the sample. It is well known that when the temperature is decreased an increase in viscosity is to be expected. From independent experimental measurements of the spontaneous polarization and of the switching time we can determine the rotational viscosity γ_ϕ of the liquid crystalline material (Eq.4). The results are shown in Fig. 4.

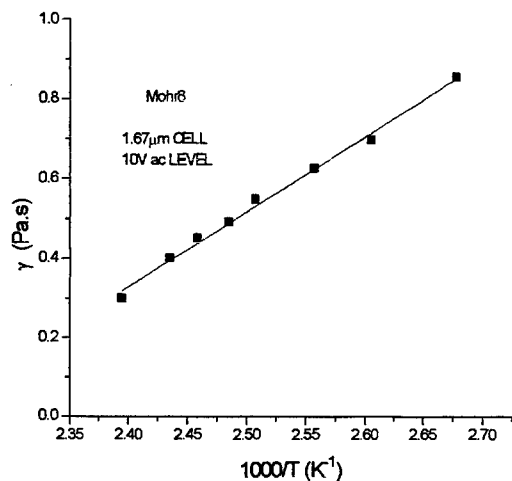


Fig.4. The Arrhenius plot of the rotational viscosity γ_ϕ for Mohr8

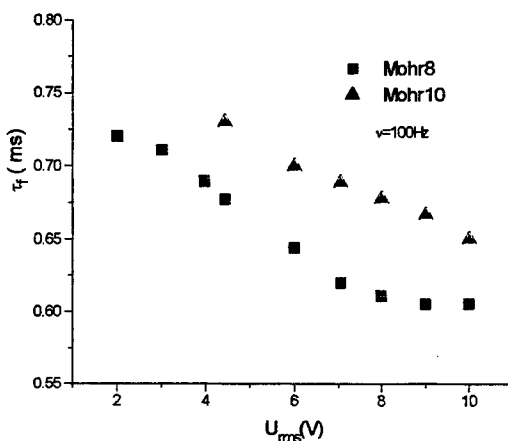


Fig.5. The electrooptic switching time as function of the applied electric field strength

The electrooptic switching time as function of applied a.c. field is illustrate in Fig.5. It follows that its temperature dependence may be described by an Arrhenius law. When plotting γ_ϕ (T) vs. $1000/T$ a straight line is obtained. The activation energy for this thermal process is $E_A=3.34\text{eV}$.

It may be noticed that within the voltage range ($4 \div 7\text{V}$ for Mohr8) and ($5\text{-}10\text{ V}$ for Mohr10) the switching time decreases when the applied voltages are increased according to the law $\tau_\phi \approx 1/E$ which agrees with the general relationship given by Eq.2. Fig. 6 gives the dependence on frequency of the electrooptic switching time for a SSFLC cell containing Mohr8, subjected to a square-wave voltage of 8V_{rms} .

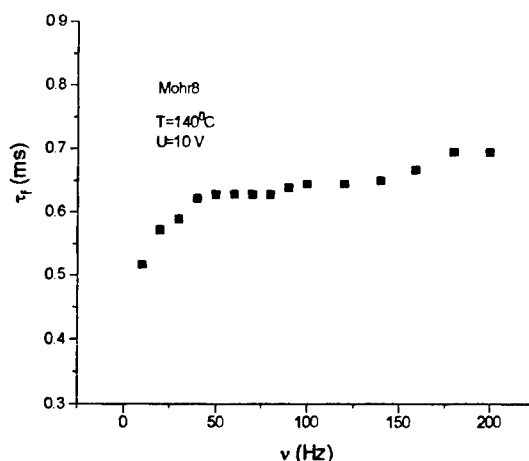


Fig.6. The frequency dependence of the electrooptic switching time.

An increase in the electrooptic switching time occurs when the frequencies of the a.c. fields are increased. To explain this we have to consider that in the SmC* phase a specific molecular motion, termed Goldstone mode is effective between a few Hz and about 100kHz. It is due to the phase fluctuations in the azimuthal orientation of the director. Usually it is assumed that the director moves around a cone described by the tilt angle θ , characteristic for the smectic C phase. The movement of the director on the cone will be in phase with the applied voltages when the frequencies are low and out of phase when the frequencies are high. This leads to an increase in the switching time when high frequencies are used.

4. ACKNOWLEDGEMENT

The financial support of the Deutsche Forschungsgemeinschaft is acknowledged. The authors wish to thank Ch. Selbmann and G. Hauck for help in experiments.

5. REFERENCES

1. N.A.Clark and S.T.Lagerwall, "Submicrosecond bistable electrooptic switching in liquid crystals", *Appl.Phys.Lett.* 36, pp. 899, 1980.
2. S.T.Lagerwall, B.Otterholm and K.Skarp "Material properties of ferroelectric liquid crystals and their relevance for applications", *Mol.Cryst.Liquid Cryst.* Vol.152, pp. 503, 1987.
3. N.A.Clark, M.A.Handschy and S.T.Lagerwall "Ferroelectric liquid crystal electro-optics using the surface stabilised structure", *Mol.Cryst.Liq.Cryst.* Vol.94, pp. 213, 1983.
4. I.Dhal, S.T.Lagerwall, K.Skarp "Simple model for the polarisation reversal current in a ferroelectric liquid crystal", *Phys.Rev.A*, Vol.36, pp. 4380, 1987.
5. Yu P.Kalmykov, J.K.Vij. "On the relationship between electro-optic and dielectric parameters of a smectic C* ferroelectric liquid crystal", *Liquid Crystals*, Vol.71, pp.741, 1994.
6. M.Schadt "Linear and non-linear liquid crystal materials, electro-optical effects and surface interactions. Their application in present and future devices", *Liquid Crystals*, Vol.14, pp.73, 1993.
7. P.Maltese "Advances and problems in the development of ferroelectric liquid crystal displays", *Mol.Cryst.Liq.Cryst.*, Vol.215, pp.57, 1992.
8. K.Mohr, S.Kohler, K.Worm, G.Pelzl, S.Diele, H.Zaschke and D.Demus, "A family of ferroelectric liquid crystals with very high spontaneous polarisation", *Mol.Cryst.Liq.Cryst.*, Vol.146, pp. 151, 1987.
9. K.Skarp, I.Dahl, S.T.Lagerwall and B.Stebler, "Polarisation and viscosity measurements in a ferroelectric liquid crystal by the field reversal method", *Mol.Cryst.Liq.Cryst.*, Vol. 114, pp. 283, 1984.
10. L.M.Blinov, V.G.Chigrinov, "Electrooptic effects in liquid crystal materials", ed. G.W.Taylor, Gordon, 1994.
11. K.Skarp, "Rotational viscosities in ferroelectric smectic liquid crystals", *Ferroelectrics*, Vol. 84, (1988).
12. P.G.de Gennes, J.Prost, "The physics of liquid crystals", Second edition, Clarendon Press, Oxford 1993.

Fluid optical components and their applications in optoelectronics

Roxana Rădvan, Mihaela Călin, Roxana Savastru, Maria Robu, Mihaela Radu

National Institute for Research & Development for Optoelectronics, Romania
INOE 2000, Bucharest, PO Box MG 22, 76900, Romania

ABSTRACT

This work presents some contribution in the non-conventional optical components field. The idea is concerning to fluid optical components, having in view to elaborate a documentation - like a catalogue of optical fluids - for optical system design. The using of optical fluids represents a new method of attaining apochromatic color correction in refractive optical systems.

Keywords: *optical fluid, component, apochromatic, correction, refractive index.*

1. INTRODUCTION

An important category of non-conventional optical component - fluid - occupy more and more time from research activity in the field. The liquid filters and lenses have specific important technical features and, especially, different motivations.

Due to some technological causes the application of fluid elements was postponed. Today, technological impediments (i.e. air-tighting, water-tighting, stability of the matter etc.) can be passed.

2. FLUID LENSES

A new method of attaining apochromatic color correction in refractive optical systems has been developed. Common, low-cost glasses and abnormal dispersion optical liquid are combined to produce optical systems that have a degree of color correction which previously was possible only by using abnormal dispersion glasses or crystals¹.

Figure 1 shows the chromatical aberration of the position for achromatical system (a) and for apochromatical system(b).

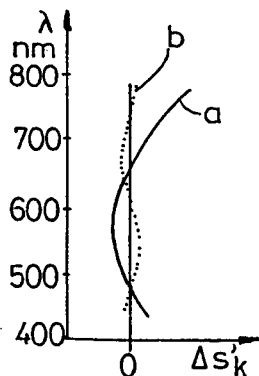


Fig. 1 Chromatical aberration of the position for achromatical system (a) and for apochromatical systems (b)

The conditions for a corrected system are:

$$\sum_{i=1}^k \frac{\phi_i'}{v_i} = 0 \quad (1)$$

where : $\phi_i' = \frac{1}{f_i'}$ [m⁻¹]. - for each lens of the system, and

v_i - is the coefficient of dispersion (Abbe number) for each lens. Usually, Abbe number takes values between 20.9 and 105.0.

$$v_d = \frac{n_d - 1}{n_F - n_C} \quad \text{or} \quad v_e = \frac{n_e - 1}{n_F - n_C} \quad (2)$$

Optical materials with normal dispersion are placed on the D line (fig. 2) and some other material with abnormal dispersion have places far from the D line.

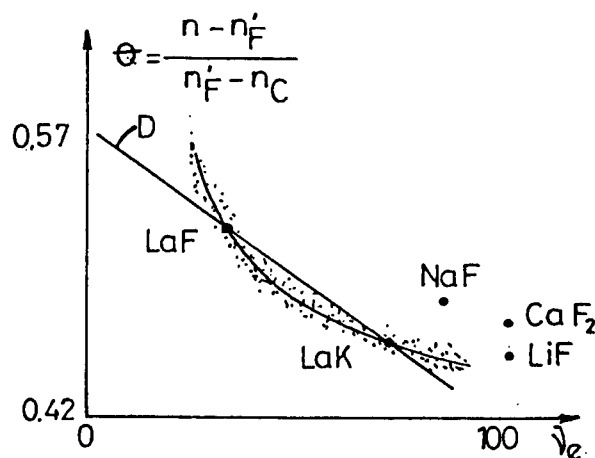


Fig. 2 Optical materials with normal and abnormal dispersion

The development and evaluation of glass-liquid apochromat has revealed that:

1. Many commercially available liquids have been found that have the abnormal dispersion properties required for high performance apochromatic optical systems;
2. The color correction of the lens systems designed with inexpensive normal dispersion glasses and certain abnormal dispersion liquids has been shown to be greatly superior to that obtained with conventional normal dispersion achromatic glass or glass-crystal combinations;

3. As a result of the availability of these abnormal dispersion liquids and the small volumes required much of the cost and size limitations associated with traditional glass apochromats are eliminated. Apochromatic color correction can now be achieved at a cost that is only slightly greater than of an all glass achromat;

4. The glass-liquid interferences efficiently dissaper due to index matching. This means that manufacturing tolerances are radii and surface figure are greatly increased, anti-reflection coating are not required, and surface scattering of light is essentially eliminated;

5. Small-scale thermal degradation of optical performance such as convection effects were not observed unless the lenses were subjected to phatological temperature environments. Large-scale thermal degradations such as focal length were predictable and usually refocusable. The athermalization scheme using two liquids proven effective in maintaining performance over modest temperature changes.

Some studies about the evolution of functional parameters - like focal length - in concordance with temperature variation show an evident difference between estimated and measured Δf . The stability of f increases when the liquid lenses are done like a mixture of two liquids or more.

Important observation is that is considerably greater in UV range and $\Delta f \rightarrow 0$ in IR range, when temperature variation is about 5°C .

3. FLUID FILTERS

Their using is not easily, having in view the mentioned disadvantages. In add, due to the heating of the fluid matters under the irradiation effect, the homogeneousness of the substance is modified. But even that disadvantage can be turned into an advantage when the equipment have to realize the variation of a physical parameter.

An important characteristic of the equipment is the possibility to have a continuous modification of the filter's thickness. Our study presents the specifical transmittance for some chemical substance and solution in already performed experimental condition. Table 1 presents the analysed liquids and some observation about them.

Table 1. The extinction for some analysed liquids

No	Liquid	Wavenumber (cm^{-1})	Extinction (Absorbance)
1	Nickel Sulfate (NiSO_4)	49000	0.9193
	(c =49.20 g/l)	48000	0.5817
		46000	0.3525
		44000	0.1918
		42000	0.0884
		40000	0.0417
		38000	0.0206
		36000	0.0084
		28000	0.0277
		27000	0.0914
		26000	0.2047
		25000 (max)	0.2313
		24000	0.1368
		23000	0.0354
		22000	0.0057
		17000	0.0066
		16000	0.0454
		15000	0.0793
		14000 (max)	0.0942
		13000	0.0699
		12000	0.0253

2	Copper Sulfate (CuSO_4)	38000	1.0730
	(c = 4.56 g/l)	36000	0.4398
		34000	0.1042
		32000	0.0028
		16000	0.0109
		15000	0.0577
		14000	0.1322
		13000	0.2076
		12000 (max)	0.2189
		11000	0.1987
3	Cobalt Sulfate (CoSO_4)	50000	1.3600
	(c = 11.28 g/l)	48000	0.3290
		46000	0.0618
		44000	0.0067
		22000	0.0361
		21000	0.0637
		20000 (max)	0.0878
		19000	0.0836
		18000	0.0187
4	Potassium Dichromate	50000	1.3290
	($\text{K}_2\text{Cr}_2\text{O}_7$)	49000	1.1070
	(c = 10.80 g/l)	48000	0.8872
		46000	0.5164
		44000	0.3522
		42000	0.3329
		41000	0.3591
		40000	0.3956
		39000 (max)	0.4218
		38000	0.4191
		37000	0.3926
		36000	0.3518
		35000	0.2955
		34000	0.2195
		32000	0.1053
		30000	0.2200
		29000	0.2944
		28000 (max)	0.3254
		27000	0.2947
		26000	0.2067
		25000	0.0862
		24000	0.0304
		22000	0.0105

The following diagrams show the transmittance (T%) and, respectively, the absorbance (ABS) of the experimented liquids in concordance with the wavenumber. The transmittance (T%) is represented by curve (a) and the absorbance (ABS) by curve (b) from the Figure 3.

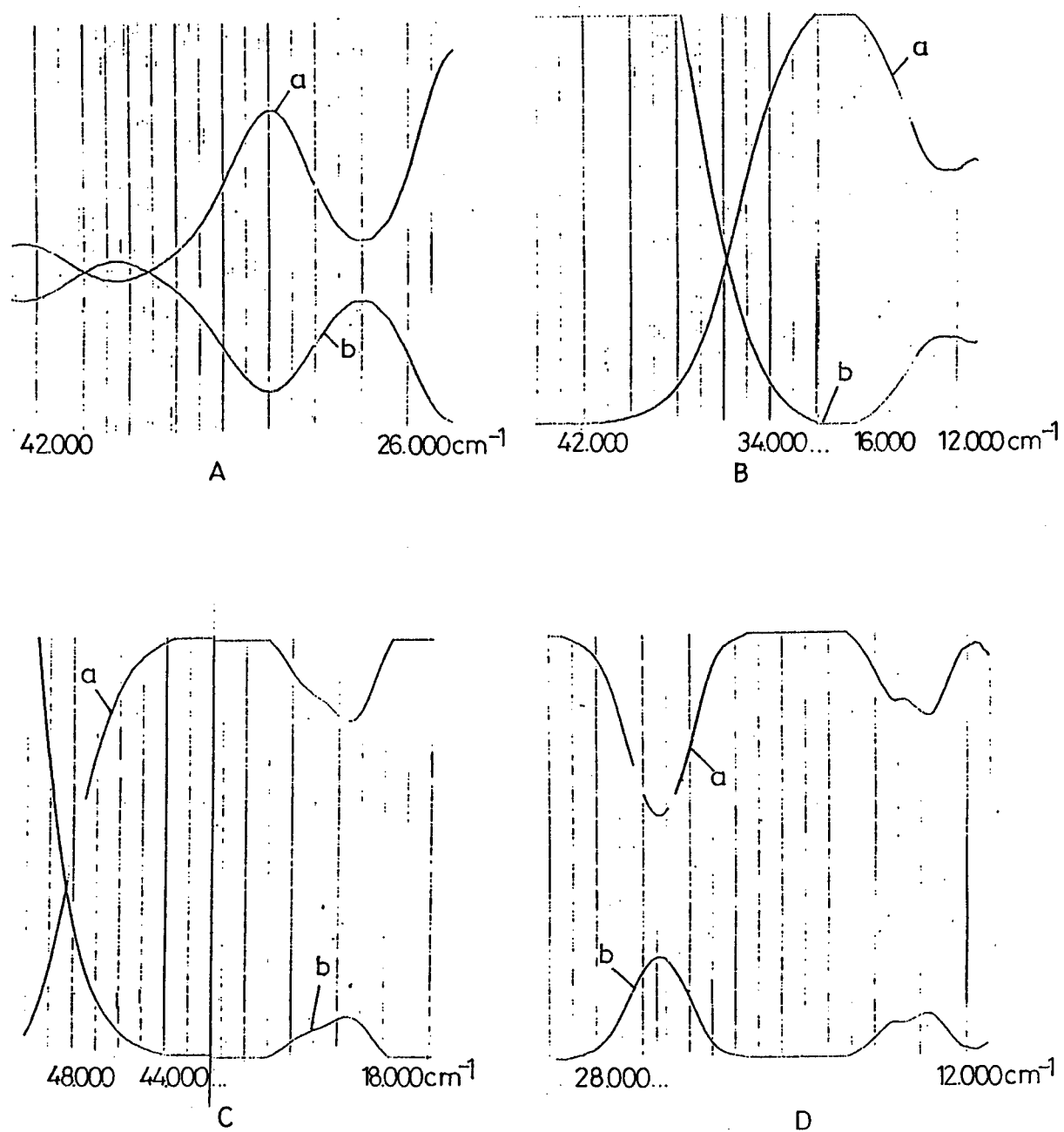


Fig. 3. Transmission (a) and Absorption (b) spectra.
A. Potassium Dichromate; B. Copper Sulfate; C. Cobalt Sulfate; D. Nickel Sulfate

The measured liquid matters are :

- a) nickel sulfate (NiSO_4)
- b) copper sulfate (CuSO_4) presents a strong absorbtion in UV region and a peak in VIS region at $\nu_{\text{max}} = 12000 \text{ cm}^{-1}$
- c) cobalt sulfate (CoSO_4) presents a strong absorbtion in UV region and a peak in VIS region at $\nu_{\text{max}} = 20000 \text{ cm}^{-1}$
- d) potassium dichromate ($\text{K}_2\text{Cr}_2\text{O}_7$) presents two absorption peaks : 39000 cm^{-1} , 28000 cm^{-1}

4. CONCLUSIONS

Some aspects of the glass - liquid apochromatic optical system have yet to be addressed. Little is presently known about the long-term stability of the liquid optical properties or on the long-term integrity of the seals, but these issues and others are currently being investigated and will be reported on in the future.

5 REFERENCES

1. M. Herzberger and H.Jenkins, " Color Correction in Optical Systems and Types of Glass", *J. Opt. Soc. Am.* , Vol. 39, pp. 984 - 989, 1989.
2. R. Rădvan, R. Savastru, "Modern Technologies for Optical Components with Special Dimensions Manufacturing", *Rev. "Optoelectronica"*, Vol. 1; nr. 4, pp. 156 - 162,1993.
3. I. Iizuka, "Engineering Optics", *Springer Series in Optical Sciences* ,1983.

Optical fiber multiplexed image transmission system

Sorin Micloș, Tudor Zisu, Bogdan Robea

National Institute of Optoelectronics - INOE 2000, 1, Atomistilor St., Bucharest, Romania

ABSTRACT

An optical fiber multiplexed image transmission system can be used in dangerous and low accessible environments, such as in nuclear or high explosion risk environments because the optical fiber cable is insensitive to the electromagnetic disturbances and, when an appropriate optical fiber is used, it withstands the gamma radiation. The system has the capability to simultaneously transmit, by using the video signals switch, the image from four CCD cameras placed in the dangerous environment to a remote surveillance center, at 2 km distance.

Keywords: Fiber optics, optical fiber data transmission

1. INTRODUCTION

Optical fiber image transmission systems offers a large range of advantages in respect to other transmission systems (radio, electric cable) due to some features^{1,2}, as :

- low transmission losses for wide bandwidth;
- small size and weight;
- immunity to electromagnetic interference ;
- electrical isolation
- signal security
- inexpensive raw material

A standard monochrome or color video signals transmission system consists of :

- CCD camera
- optoelectronic emitter
- optical cable
- optoelectronic receiver
- video signals switch
- TV monitor

The system (Fig. 1) has the capability to simultaneously transmit, by using the video signals switch, the image from four CCD cameras placed in the dangerous environment to a remote surveillance center, at 2 km distance.

To set up the system, the following devices were procured :

- CCD camera, WAT-310 type, manufactured by WATEC CO. LTD, Japan
- video signals switch, QUADRASPLIT 660, manufactured by Advanced Technology Video Inc., USA
- 12" (30 cm) black/white TV monitor

2. THE OPTOELECTRONIC EMITTER

Two variants were in view for the optoelectronic emitter: the first, using an IR (850 nm) LED, CQDP 07 F (Poland) and the second, using an IR (1300 nm) laser diode, EDL 1300 F (EPITAXX).

Fig. 2 presents the electrical diagram of the LED optoelectronic emitter. The input signal is a video complex signal of 1 V_{pp} amplitude at an impedance of 75 Ω and bandwidth of 6.5 MHz. The Q1 transistor is a voltage amplifier stage, and the transistors Q2 and Q3, in Darlington connection, form a current amplifier. By means of the R3 resistor, a parallel voltage reaction appears (sampling and comparison in node), providing the stability of the whole circuit. It can be noticed that the resistors R8 and R9 limit the DC component of the LED current up to a value of about 20 mA.

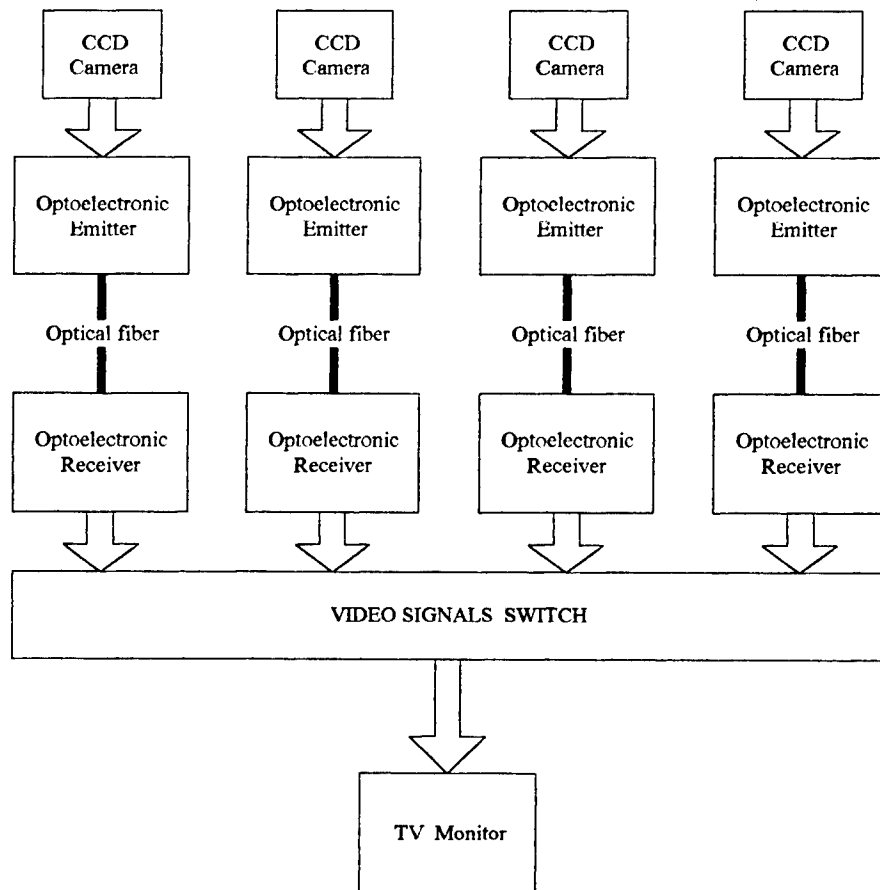


Fig. 1. The block diagram of the optical fiber multiplexed image transmission system

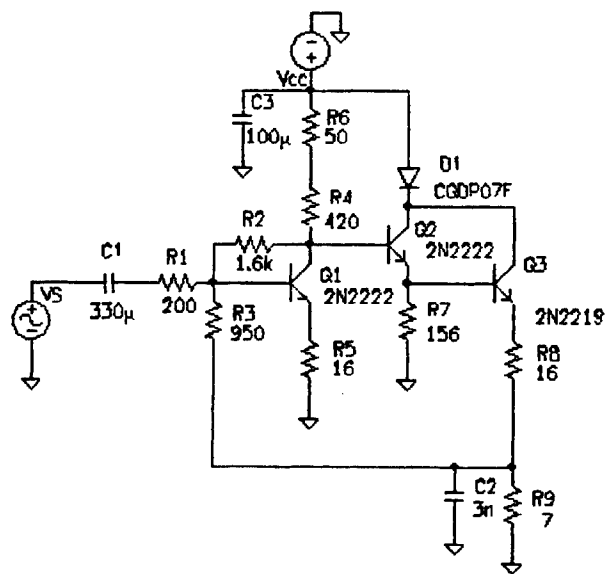


Fig. 2 The electrical diagram of the LED emitter

The frequency response analysis of the LED emitter is presented in Fig. 3.

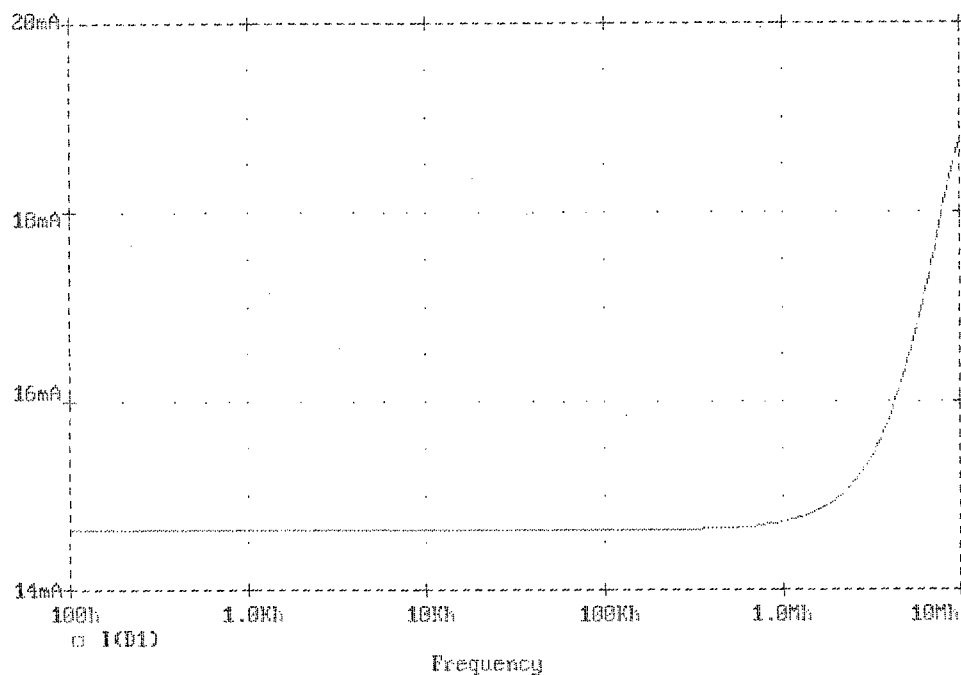


Fig. 3. The frequency response analysis of the LED emitter

Fig. 4 presents the electrical diagram of the laser diode optoelectronic emitter. The input signal is a video complex signal of 1 V_{PP} amplitude at an impedance of 75 Ω and bandwidth of 6.5 MHz. The Q1 transistor is a voltage amplifier stage, the Q2 transistor represents a repetitor stage and the Q3 transistor represents a distributed charge amplifier. By means of the R2 resistor, a parallel voltage reaction appears (sampling and comparison in node), providing the stability of the whole circuit.

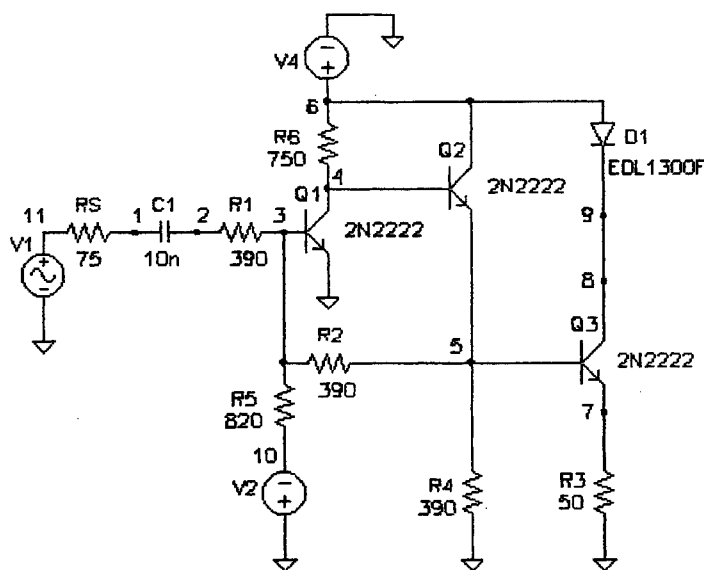


Fig. 4. The electrical diagram of the laser diode emitter

3. THE OPTOELECTRONIC RECEIVER

The receiver consists of an photodetector, a preamplifier (a transimpedance amplifier), a wideband amplifier, a low-pass filter (LPF) and an emitter repeter stage.

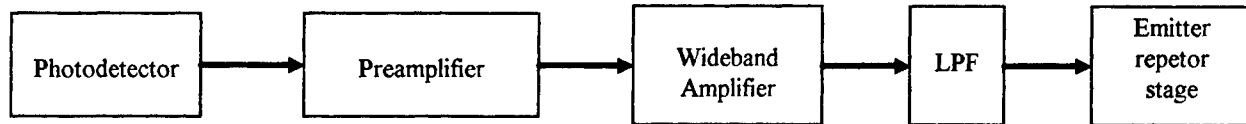


Fig. 5. The block diagram of the optoelectronic receiver

The electrical diagram of the front section of the optoelectronic receiver is presented in Fig. 6.

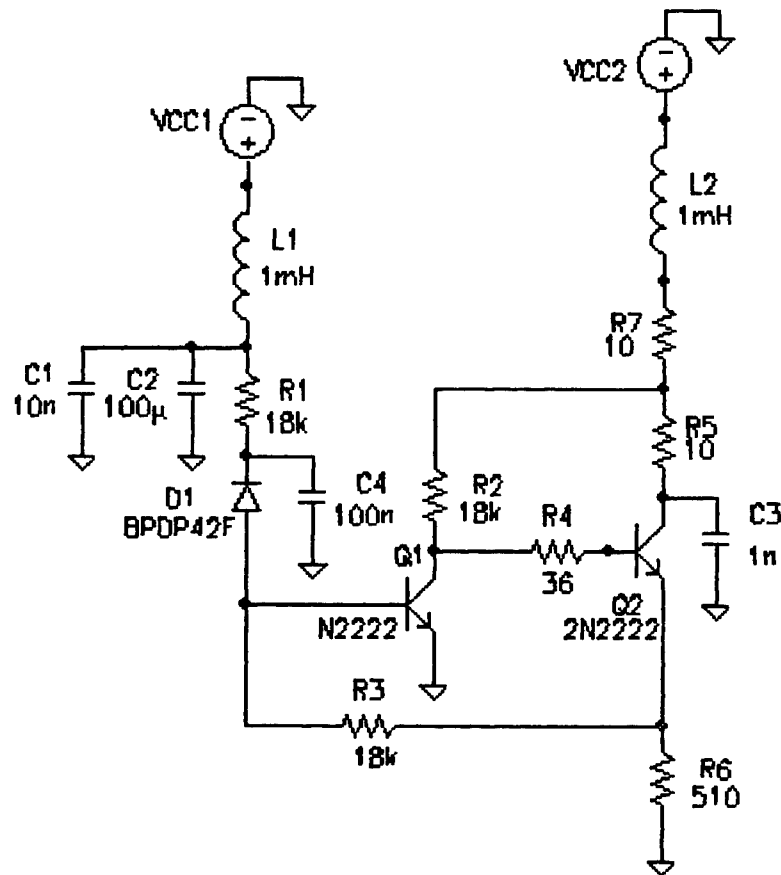


Fig. 6. The electrical diagram of the front section of the optoelectronic receiver

The photodetector is a PIN photodiode, BPDB 42 F type, the transimpedance amplifier ($R_f = 18 \text{ k}\Omega$) consists of two transistors, Q1 and Q2, the wideband amplifier is a two - stage one (based on the ROB 733 video amplifier integrated circuit) providing a total amplification of 100 (40 dB). The low - pass filter has an insertion attenuation of 3 dB.

Fig. 7 presents the transient analysis of the optoelectronic receiver.

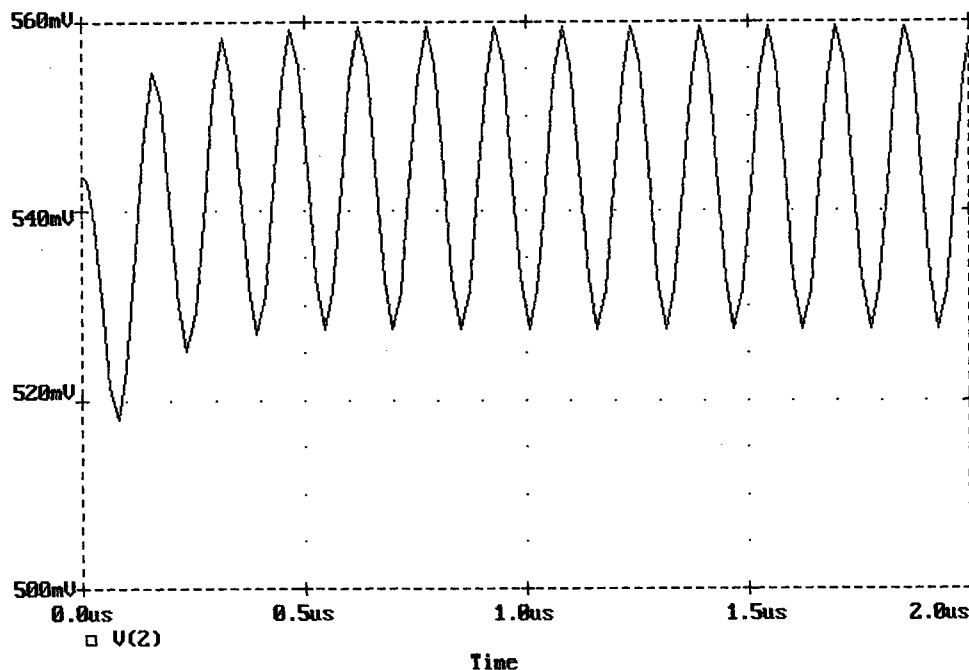


Fig. 7. The transient analysis of the optoelectronic receiver

4. THE SYSTEM FEATURES

The main features of the optical fiber multiplexed image transmission system are presented in Table 1.

Table 1. The main features of the system

Type	Parameter	Value
Electrical	Power supply	12 V _{DC}
	Emitter input level	1 V _{PP}
	Receiver output level	1 V _{PP}
	Emitter input impedance	75 Ω
	Receiver output impedance	75 Ω
	SNR	> 43 dB
	Bandwidth	6,5 MHz
	Gain control	AGC
	Connector	BNC
Optical	Wavelength	890 nm
	LED output power	65 μ W
	Receiver sensitivity	-30 dBm
	Optical fiber attenuation (for 2 km)	7 dB
	Connector	FC-PC

The losses along the transmission line can be accurately estimated by computing the "power budget"². The diagram is presented in Fig. 8 and the data in the Table 2.

Both variants of light sources are presented : one using the LED (the dashed line) and the other using a laser diode (continuous line). The LED power is 65 μ W (-12 dBm) and the laser diode power is 100 μ W (-10 dBm). The splice losses are of about 1 dB, the insertion losses of the connectors are 1 dB for each connector.

Table 2 The Power budget of the transmission line

THE BUDGET ELEMENT	LED	LASER
Emitted power [dBm]	-12	-10
Connector splice losses [dB]	1	1
Connectors insertion losses (4 pieces) [dB]	4	4
Fiber attenuation losses (3,5 dB/km) [dB]	7	7
Photodiode received power [dBm]	-24	-22
Receiver sensitivity [dBm]	-30	-30
Receiver power margin [dB]	6	8

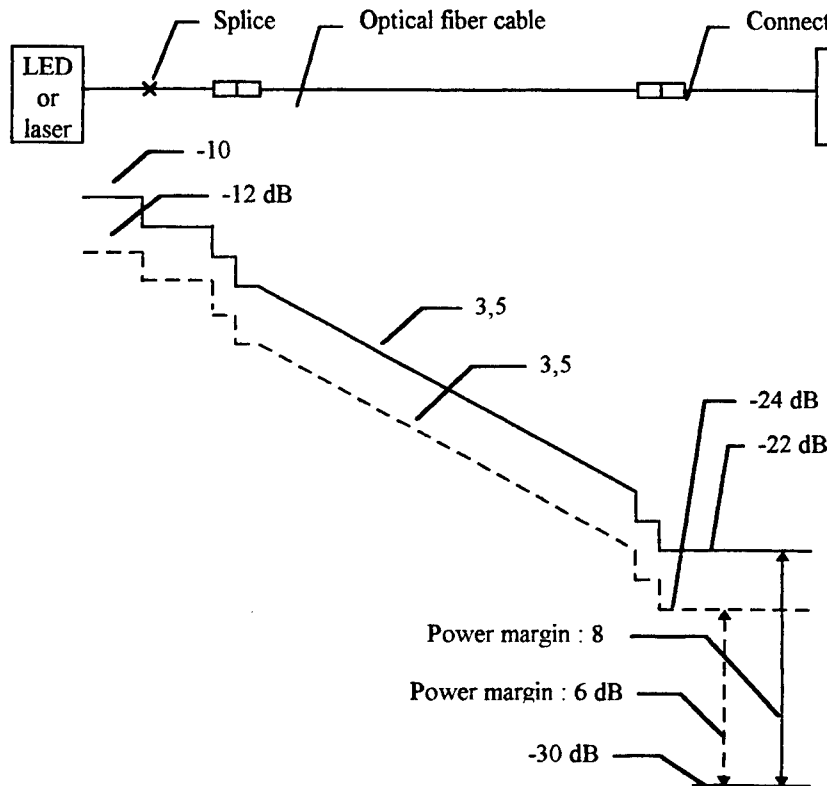


Fig. 8. The power budget of the system

This analysis proves that, even in the case of the maximum length of the transmission line (i.e. 2 km), there is still a considerable power margin of 6 dB when the LED is used, respectively 8 dB when laser diode is used. The system satisfies the requirements to be used in a nuclear power plant or in a reactor, when video image transmission is needed at ranges up to 2 km.

5. REFERENCES

1. J. Wacker, "A basic fiberoptic communication system", *Optical Communication Workshop*, TH Darmstadt, p. 1/1, Bucharest, 17-21May 1993
2. H. Jung and O.K. Tonguz, "Comparison of fibre and coaxial link for acces network in microcellular PCS", *Electronics Letters*, Vol. 32, No. 5, pp.425-426, February 1996
3. J. Wacker, "Optical time domain reflectometer", *Optical Communication Workshop*, TH Darmstadt, p. 3/7, Bucharest, 17-21May 1993

Cylindrical piezoceramic transducer for remote optoelectronic system

Irinela Chilibon, Maria Robu

Institute of Optoelectronics, R-76900, PO Box MG 22, Bucharest, Romania

ABSTRACT

This paper presents an experimental study on the behaviour of cylindrical piezoceramic transducers exposed to dynamic mechanical shocks. The piezoceramic materials under study are solid solutions of $\text{Pb}(\text{Zr}_x\text{Ti}_{1-x})\text{O}_3$ and present direct piezoelectric effect. In the laboratory were made experiments with cylinders of BaTiO_3 and PZT ceramics, for determination of their behaviour at mechanical shocks. The shocks resistance of piezoceramic materials is essential in those applications that involve dynamic stress. The tests on ceramics have sought to establish the capacity of a piezoceramic element to resist at recurrent hits and to absorb energy.

Keywords: PZT, piezoceramic transducer, mechanical shock, stress

1. INTRODUCTION

The piezoceramic materials under study are solid solutions of $\text{Pb}(\text{Zr}_x\text{Ti}_{1-x})\text{O}_3$, present direct piezoelectric effect. The shocks resistance of such materials is essential in those applications that involve dynamic stress. The tests on ceramics have sought to establish the capacity of a piezoceramic element to resist at recurrent hits and to absorb energy.

The magnitude of the electric charges was proportional with the mechanical shocks. The electric voltage was quite sufficient for supplying an electronic circuit with a laser diode. When a mechanical shock is applied on piezoceramic transducer the laser diode starts emitting a light beam at distance and then, a light sensor can received it. Then the optical signal can be easy prelucrated with an other electronic circuit.

The piezoelectric phenomenon consists in the appearance of an electric polarisation on the surfaces of a piezoelectric transducer when a force is focused on it; the polarisation is proportional with the force applied and it changes its sign with the direction of the applied force. The piezoelectric effect can be explained the deformation of the crystal lattice and by an electric disturbance of its atoms. The resistance at mechanical shocks of such materials is essential in those applications that involve dynamic strains. The tests on ceramics have sought to establish the capacity of a piezoceramic element to resist at recurrent hits and to absorb energy.

If the transducer is subjected to an accelerated displacement, its mass creates a mechanical stress on the piezoelectric crystals connected in parallel and, by direct piezoelectric effect the crystals get polarised. On the electrodes an electric charge, proportional with the acceleration, appears. According to the reciprocity principles, an analogy between the mechanical and electrical magnitudes of an electromechanical system can be done.

2. EXPERIMENTAL RESULTS

The piezoceramic materials under study are solid solutions of $\text{Pb}(\text{Zr}_x\text{Ti}_{1-x})\text{O}_3$ obtained by classic technology [1] in laboratory, using as raw materials oxide powders of PbO , TiO_2 , ZrO_2 . Such piezoceramic materials are important [2] in the field of applications, as they present piezoelectric effects.

The piezoelectric ceramics are crystallite conglomerate ferroelectrics materials with random orienting. The piezoceramic material utilised is type PZT (lead titanate zirconate) with various additions (Ni, Bi, Mn) and presents piezoelectric and dielectric characteristics like: 7.2 g/cm^3 density, 1000 permittivity, 70 quality factor, 0.55 coupling factor, $20 \times 10^{-12} \text{ m}^2 \text{N}^{-1}$ compliance constant, etc.

PZT piezoelectric ceramics utilised were $\text{Pb}(\text{Zr}_{0,53}\text{Ti}_{0,47})\text{O}_3$, with $\text{Pb}(\text{Zr}_x\text{Ti}_{1-x})\text{O}_3$ phase diagram of solid solutions shown in Figure 1. The Curie temperature is dependent of Zr/Ti compositional report and can be in the domain of 230°C and 480°C .

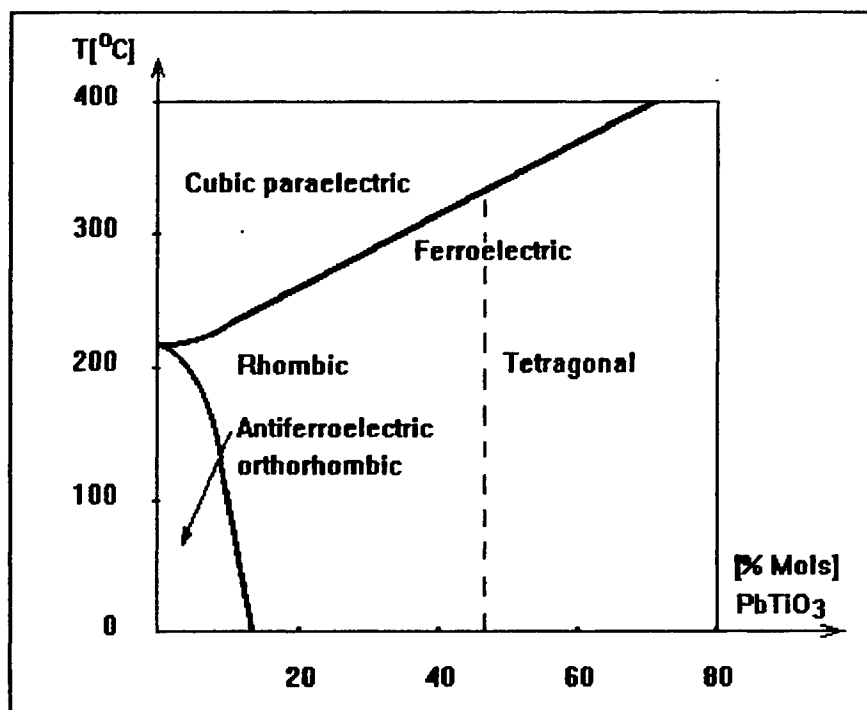


Figure 1 $\text{Pb}(\text{Zr}_x\text{Ti}_{1-x})\text{O}_3$ phase diagram of solid solutions

In the Table 1 we present the main characteristics of piezoceramic materials made in our laboratory, having special properties and high piezoelectric coefficients, and in the Figure 2 is shown the scheme of measurement for the main characteristics of piezoceramic materials.

Table 1 PZT materials, electrical and dielectric characteristics

No. crt.	PZT materials	C [nF]	$\tan \delta \times 10^3$	ϵ	Q	k_p
1	1M	2,79	13,70	1020	150	0,40
2	3M	2,26	19,47	1060	120	0,50
3	5M	2,22	16,60	1270	180	0,60
4	6M	1,92	14,58	1170	85	0,45
5	7M	1,97	17,76	1190	70	0,50
6	9M	1,84	18,48	1060	80	0,45
7	10M	2,05	16,58	1135	95	0,50
8	11M	2,26	18,58	1160	100	0,45
9	13M	3,00	12,00	1090	75	0,45
10	16M	2,59	14,67	1230	80	0,55
11	T	2,21	1,80	800	310	0,30
12	D	1,80	21,70	1000	50	0,40

where: C is the static capacity of the piezoceramic disk, $\tan \delta$ loosing factor, ϵ dielectric permittivity, Q mechanical quality and k_p electromechanical coupling coefficient.

The piezoceramic materials realised in laboratory, type 5M \div 7M, 10M, 11M and 16 M have high dielectric permittivity and electromechanical coupling coefficients.

This ceramics, type PZT present high mechanical resistance, they do not absorb humidity, and are very stable in time. The mechanical tests, realised on cylindrical piezoceramic devices, with various dimensions, have shown this materials present high mechanical resistance ($R_c = 3900 \div 4800 \text{ daN/cm}^2$ compression resistance and $R_b = 600 \div 710 \text{ daN/cm}^2$ bending resistance).

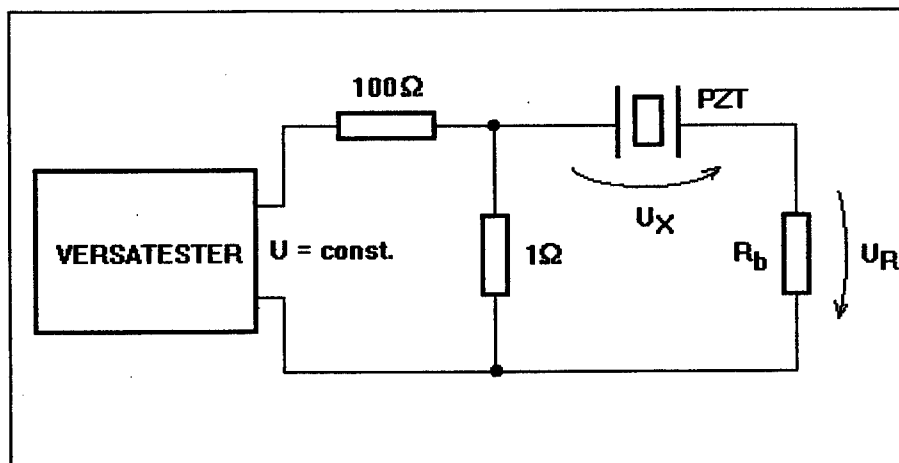


Figure 2 Scheme of measurement for the main characteristics of piezoceramic materials

In the laboratory were made experiments with cylinders of PZT ceramics, for determination of their behaviour at mechanical shocks. The magnitude of the electric charges was proportional with the mechanical shocks.

We have utilised piezoceramic cylinders realised of BaTiO_3 and PZT materials with $\rho_{\text{BaTiO}_3} = 5.1 \text{ g.cm}^{-3}$ and $\rho_{\text{PZT}} = 7.5 \text{ g.cm}^{-3}$ density values.

In the Table 2 we present the main electric and dielectric characteristics of piezoceramic cylinders, put inside the transducer (Figure 3), which receives mechanical shocks.

Table 2 Electrical characteristics of piezoceramic cylinders

Cylinder	U_m [mV]	f_m [kHz]	f_n [kHz]	Δf [kHz]	G [μS]	C [pF]
A	1,9	196	204	8	0,02	116
B	1,0	123	133	10	0,02	105

where: A is BaTiO_3 cylinder ($\Phi 10 \times 10$) mm; B PZT cylinder ($\Phi 11 \times 10$) mm; U_m measure voltage; f_m resonance frequency; f_n antiresonance frequency; Δf frequency range; G electrical conductance and C static capacity.

We have made experimental studies with a pendulum, for the determination of transducer behaviour at mechanical shocks. The tests were made utilising the fooling arm of a pendulum, supplied with different weights.

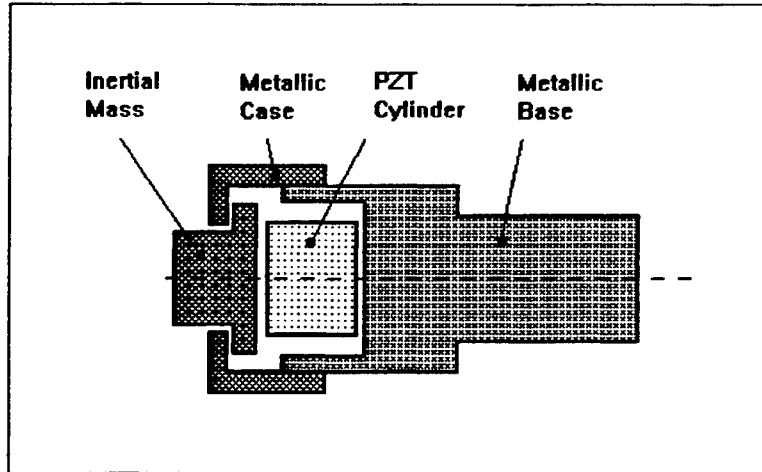


Figure 3 Experimental device with cylindrical piezoceramic transducer

When a mechanical shock was applied on the transducers, an electric charge appears on the electrodes, proportional with the acceleration (Figure 4).

Due to the piezoelectric effect, the mechanical shock applied on the transducer creates an electrical charge on piezoceramic cylinder surfaces, which have been seen at the screen of the Tektronix 2432 A oscilloscope with memory.

The electric charge can be measured by means of an amplifier with high input impedance and the output signal can be calibrated in acceleration units. If the output voltage is analogically integrated, it obtains a magnitude proportional with the velocity, and if this magnitude is integrated again, results the displacement of the transducer.

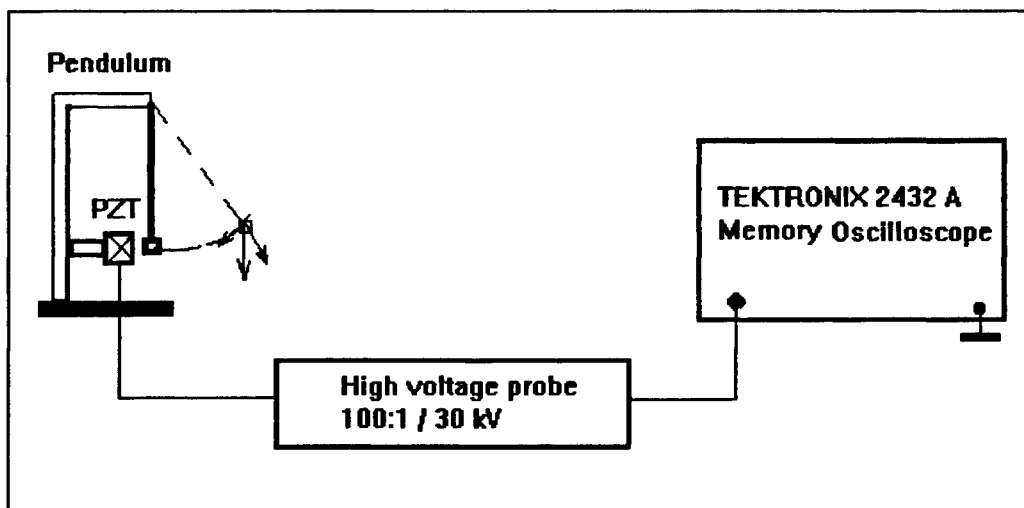


Figure 4 Experimental measurements at mechanical shocks, applied with pendulum

When a mechanical shock is applied on the surface of the transducers, an electric charge appears at the electrodes, proportional with the acceleration, (Figure 5) and the crystalline structure of piezoceramic material begins to vibrate, the electrical signal decreased in some hundred seconds.

The electric voltage was quite sufficient for supplying an electronic circuit with a laser diode. When a mechanical shock is applied on piezoceramic transducer the laser diode starts emitting a light beam at distance and then, a light sensor can received it. Then the optical signal can be easy prelucrated with an other electronic circuit ([3] and [4]).

The direct piezoelectric effect was utilised in manufacturing of a system with piezoceramic transducer hit with mechanical shocks, for remote commands in optoelectronic systems (Figure 6).

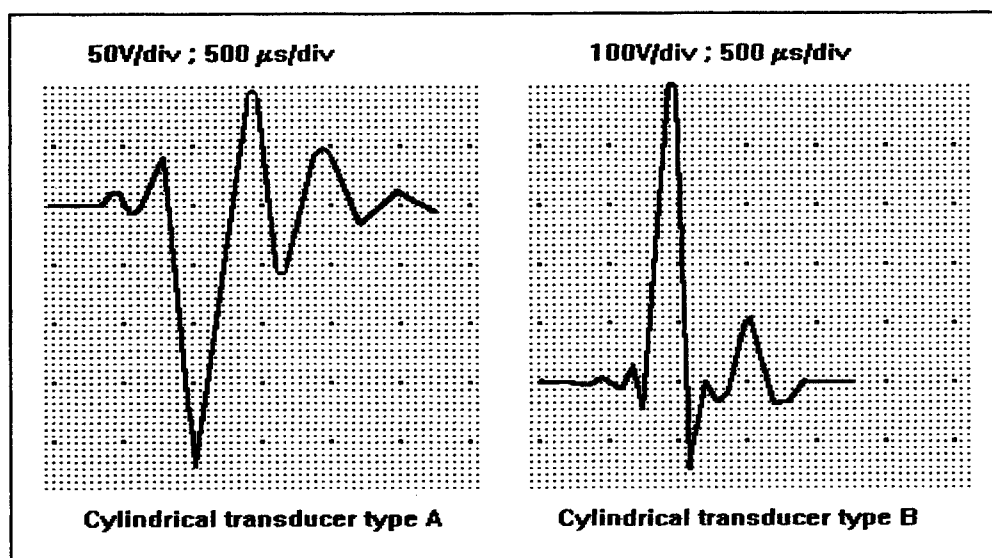


Figure 5 Electrical signals on the electrodes of cylindrical piezoceramic transducers at mechanical shocks

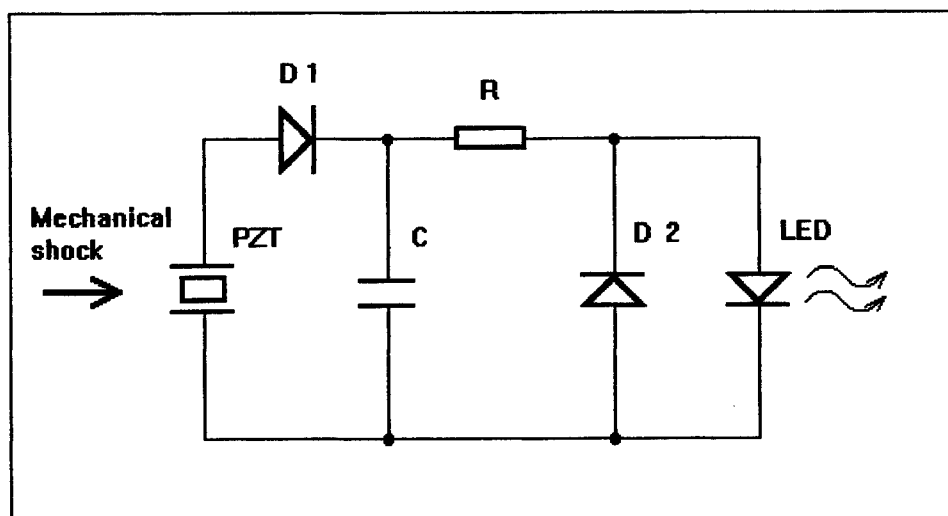


Figure 6 Optical system with piezoceramic transducer for mechanical shocks

3. CONCLUSIONS

The paper presents a study about the behaviour of piezoceramic materials type PZT realised in laboratory, at mechanical shocks. We have obtained electrical impulse of 1000 V electrical magnitude, for PZT cylinders hit with a pendulum.

Due to the piezoelectric effect, the mechanical shocks create electric charges into the transducer on the surface of ceramic disks. The magnitude of the electric charges is proportional with the mechanical shock.

The experimental tests have relieved that the cylinder made of PZT ceramics are more resistant at mechanical shocks then BaTiO₃ cylinder.

The direct piezoelectric effect can be used in manufacturing piezoceramic transducers for remote commands in optoelectronic systems, to produce sparks for sensing light at distance ignition of diverse gaseous combustibles, etc.

4. REFERENCES

1. K. Okazaki, "*Technologia keramiceskih dielektrikov*", Moskva, 1976.
2. M. Brissaud, "Characterisation of Piezoceramics", *IEEE Trans. on Ultrasonics*, Vol. 38, No. 6, Nov. 1991.
3. I. Chilibon, M. Robu, "Some considerations about cylindrical piezoceramic transducers in mechanical shocks systems", *Romanian Journal of Optoelectronics*, 5(2), 89-92 (1997).
4. I. Chilibon, M. Robu, "Piezoceramics for optoelectronic applications", *Romanian Journal of Optoelectronics*, 5(2), 86-88 (1997).

Optical systems for the night vision devices

Gheorghe Copot, Rodica Copot

Institute of Optoelectronics, 1 Atomistilor Street, Magurele, Bucharest, fax 4208632

ABSTRACT

The paper is the result of the studies made to establish criteria for the designing and the assessment of the optical systems for the night vision devices so that the ratio between the performances and the manufacture costs is best. These criteria were used to check optical systems of the existing night vision devices and to design new optical systems.

Keywords: image intensifier tube, recognition range, focal length, field of view, F/number, resolution, modulation transfer function, luminance, illuminance, differential threshold of luminance.

1. INTRODUCTION

In order to establish the criteria for the designing of the optical systems for the night vision devices (NVD) one must consider the main tactical characteristics which are required:

- a) recognition range;
- b) field of view;
- c) overall dimensions;
- d) weight.

Their share vary with the destination of the device, but in the most situations the leading requirement is to obtain the largest recognition range.

In our former studies we have correlated within the framework of an algorithm the recognition range and the intrinsic parameters of the apparatus, namely the technical characteristics of the objective and of the image intensifier tube (IIT). The algorithm also takes into account the characteristics of the target and the conditions of the observation.

This algorithm offer the possibility to analyse in order to get the optimum limiting values of the optical parameters which are to be observed during the optical computation and the design of the optical assemblies.

The essential factor in this analyse is the human eye capability of perception of the limiting threshold of the contrast which is a function of the scene luminance.

The modality of the transference of the contrast from the target to the observer's eye by the agency of the night vision device entails a study which is materialized in the designing of more objectives from which the best one is chosen.

To design an objective with a certain destination means to find the optimum set of values for the:

- a) focal length;
- b) field of view;
- c) F/number;
- d) modulation transfer function (MTF).

2. FOCAL LENGTH AND FIELD OF VIEW

The focal length of the objective (f') and the field of view (2ω) are correlated according to the formula:

$$\omega = \arctg \phi_{\text{IIT}} / 2f' \quad (1)$$

where

ω = half angular field;

ϕ_{IIT} = available diameter of the IIT.

But the focal length of the objective (f') is also correlated with the recognition range (D) according to the formula:

$$D = f' \cdot H \cdot R / N_p \quad (2)$$

where

H = critical dimension of the target;

R = resolution of the IIT corresponding to the illumination level of the photocathode and the value of the contrast of the target;

N_p = needed number of the resolution elements included in the critical dimension of the target for its recognition with the probability P. ²

A large recognition range entails a large focal length and a large focal length entails a small field of view and this introduces a contradiction.

Both the recognition range and the field of view are requested tactical characteristics but they also depend on the restricting series of the types of image intensifier tubes.

That is why the optimization of the values of these parameters is subject for the renegotiation between the designer and the beneficiary.

3. F / NUMBER

F/ number is the opposite parameter of the relative aperture and therefore its value causes the illumination level on the photocathode of the IIT and, implicitly, the resolution of the NVD.

For a concrete example of target and conditions of observation, with the next characteristics:

- critical dimensions of the target 2.3 m
- reflectivity of the target 0.15
- reflectivity of the background 0.32
- contrast of the target 0.36
- illumination level 1 lx
- recognition probability 0.8
- normal atmospheric visibility,

the values of the recognition range are calculated for different objectives (pairs of focal length and F/number) and are presented in Table 1.

Table 1. Recognition range

Focal length (mm)	Recognition range (m)						
	F/ number						
	1.8	1.7	1.6	1.5	1.4	1.3	1.2
100	418	434	444	453	466	477	480
105	439	456	466	474	485	499	505
110	458	476	486	496	508	523	529
115	479	497	508	519	527	546	553
120	499	519	530	534	550	568	575
125	520	536	552	559	573	592	598

The computing of the above values has used the technical characteristics of the standard IIT, second generation Plus, XX1410 family, 18mm.

We see that for a certain value of the recognition range there are more pairs of values (focal length / F/number). For example, for the focal length of 115 mm and the F/number of 1. 8, one obtains the same recognition range as for the focal length of 100 mm and the F/number of 1. 2.

The choose of the pairs of values (focal length / F/number) relies on the tactical requirements of the overall dimensions and weight. If the dimensions of the objective 100 mm / 1. 2 are considered to be the unit it has been found that for the objective 115 mm / 1. 8 the length is 1.15 and the diameter is 0.7, with the adequate decrease of the weight.

In order to obtain a smaller cost price the objectives with bigger focal length and F/ number are preferred, and an optimum F/ number is placed between 1. 5 and 1. 7.

4. MODULATION TRANSFER FUNCTION (MTF)

Modulation transfer function is a realistic criterion for the assessment of the correction level of the optical systems, and for its establishment it is necessary to analyse:

- the answer of the IIT to the real conditions of use;
- the human eye perception of the image on the screen of the IIT.

During the use in the terrain:

- the NVD with the objective 100 mm/ 1. 5
- at average reflectivity of 0. 2; 0. 5; 0. 8

the illumination levels on the photocathode don't exceed 10^{-2} lx .

The resolution of the IIT and the luminance of the screen are presented in Table 2.

Table 2. Resolution of the IIT and luminance of the screen

Illumination level of the background	Average reflectivity	Illumination level of the photocathode	Luminance of the screen	Resolution of the IIT	
				for C=1	for C=0.36
lux	-	lux	cd/m ²	lp/mm	lp/mm
1.00E-04	0.2	1.49E-06	-	< 9	5.4
	0.5	3.72E-06	-	10.4	6.3
	0.8	5.95E-06	0.02	12	7.2
1.00E-03	0.2	1.48E-05	0.07	13.8	8.3
	0.5	3.71E-05	0.12	15.7	9.4
	0.8	5.94E-05	0.2	17	10.2
1.00E-02	0.2	1.48E-04	0.75	20	12
	0.5	3.71E-04	1.1	22.3	13.4
	0.8	5.94E-04	2	24.2	14.6
1.00E-01	0.2	1.48E-03	2	27	16.2
	0.5	3.71E-03	2	28	16.8
	0.8	5.94E-03	2	28.5	17.2

It follows that usually the IIT doesn't operate at maximum resolution, even at high illumination levels, except the theoretical situation when the contrast is 1, but this value is not reached in practice.

The perception of the human eye is described by the differential threshold of luminance (χ) which is defined as:

$$\chi = \Delta B / B \quad (3)$$

where

B = average luminance of the screen;

ΔB = difference of the luminance between 2 next points which are resolved by the eye.

For the values of illumination from Table 2, the differential threshold of luminance varies as it is described by the curve in Figure 1.

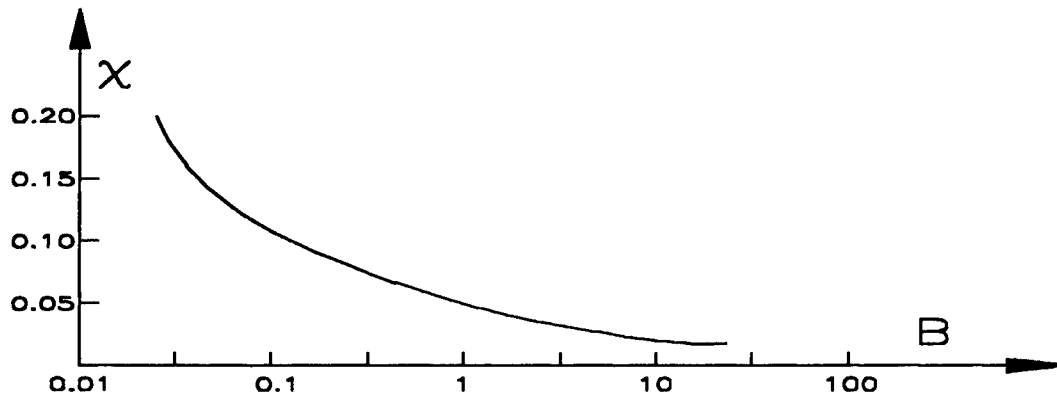


Figure 1. Differential threshold of luminance

This parameter (χ) represents a contrast threshold of the image, for which the human eye can resolve 2 areas having different luminance.

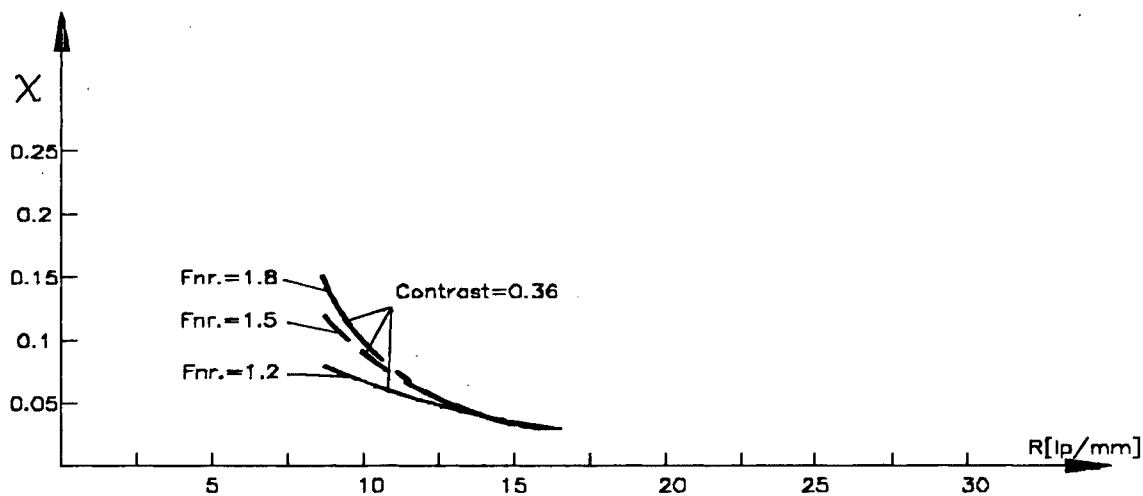


Figure 2. Variation of the perceived contrast with respect to the spatial frequency of the object

In this area of luminance, the visual acuity of the human eye is better than the apparent angular dimension of the target. Under these circumstances, we can consider the variation of the perceived contrast with respect to the spatial frequency of the object (the image on the IIT screen); the corresponding curve is presented in Figure 2.

By its aspect and significance, this curve is to be considered a limiting transfer function for the night vision device (NVD) and it is named pseudo MTF of the NVD.

Because MTF permits cascading the effects of the several major components of a system in determining a measure of resolution of the overall system, it is assumed that these limiting values of the contrast are reached with the contribution of the MTF of the optical systems and of the IIT.

5. CONCLUSION

According to these one can use a nomograph similar with that presented in Figure 3 , in order to establish the acceptable MTF for the optical systems. The nomograph is built up using the values of the pseudo MTF of the NVD and the values of the MTF of the IIT as presented in Table 3.

Table 3. Resolution of the IIT and differential threshold of luminance

Illumination of the target	F/number	Illumination of the photocathod	Luminance of the screen	Resolution of the IIT	Differential threshold of luminance
lux	-	lux	cd/m ²	lp/mm	-
1.00E-03	1.8	1.30E-05	0.06	8.2	0.2
	1.5	1.90E-05	0.085	8.7	0.12
	1.2	2.94E-05	0.18	9.2	0.08
1.00E-02	1.8	1.30E-04	0.7	11.7	0.065
	1.5	1.90E-04	0.9	12.4	0.055
	1.2	2.94E-04	1	13.1	0.045
1.00E-01	1.8	1.30E-03	2	15.9	0.03
	1.5	1.90E-03	2	16.2	0.03
	1.2	2.90E-03	2	16.5	0.03

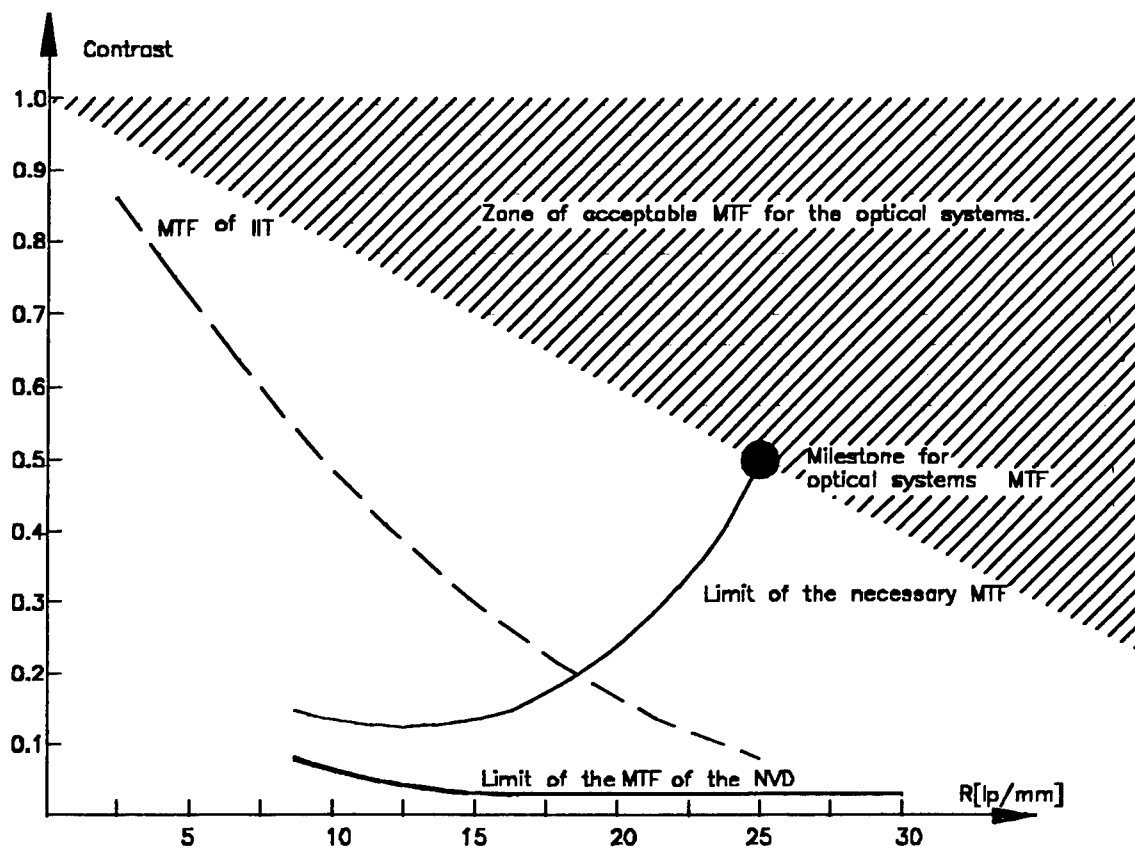


Figure 3. Nomograph to establish the acceptable MTF for the optical systems

6. REFERENCES

1. G. Copot, R. Copot, "Studies on the observation range of the night vision devices", *Proceedings SPIE*, vol. 2461, pp. 491-493, 1995.
2. John Johnson, "Analysis of image forming systems", *Image intensifier symposium*, UK, October 6-7, 1958.
3. ***, *Electro-Optics Handbook*, Section 11, Technical Series EOH-11, RCA Corp., 1974.
4. Gh. I. Mitrofan, *Digital television (from Romanian "Televiziune digitala")*, pp. 26-31, Romanian Academy Publishing House, Bucharest, 1986.

Optical beacon for pointing and tracking systems for free-space communications

P. E. Sterian

Department of Physics, "Politehnica" University,
313 Splaiul Independentei, Bucharest, Romania

P. P. Digulescu

Department of Electronics and Computer Science,
Technical Military Academy, 81-83 Regina Maria, Bucharest, Romania

R. V. Ivan

Department of Physics, "Politehnica" University,
313 Splaiul Independentei, Bucharest, Romania

ABSTRACT

A bi-directional pointing and tracking system is needed in order to establish the optical link between two optical transceivers located in two separated points at the ground or on satellites. That usually suppose the presence of a separate laser transmitter an optical beacon used for pointing and tracking purposes. The major stages of the pointing and tracking process were analysed based on a mathematical model presented in references. In order to increase the reliability of optical links a new optical beacon is purposed and, consequently a new pointing and tracking method is developed. This method requires only communication laser transmitters and uses their optical beams for pointing and tracking process, additionally giving the possibility to increase the signal to noise ratio at the communication receiver. A mathematical model of such a system is developed and an analysis of the method is performed.

Keywords: optical beacon, pointing and tracking system, free-space optical communications

1. INTRODUCTION

Communication from any place to another on the earth is an attractive goal that concentrate many research and development resources. One method to achieve this aim is by satellites networked together that cover the globe (Fig. 1). In this method, the information is transferred from the ground to the nearest satellite above and then propagate between the satellites to the satellite above the destination. This last satellite then transmits the information down to the destination.¹

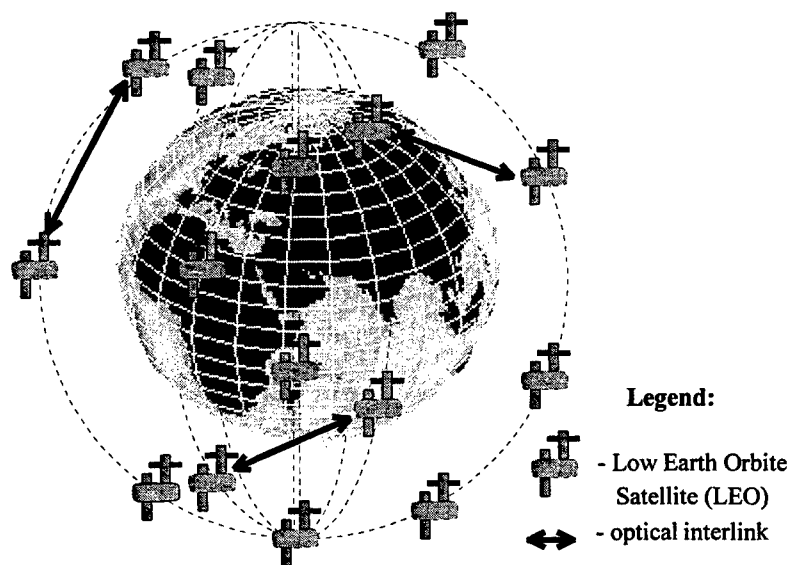


Fig. 1 Network of free-space optical communications satellites

Such a network may be complementary and networked to the existing networks at the earth surface. Concerning these last ones it is well known that the transmission of communication signals by light through optical fibres has, since 1980, been steadily replacing that of electrical signal through metal wires. Optical communications have already surpassed the bandwidth capabilities of metal wires and yet, today, the most advanced systems deployed only uses 0.1% of the intrinsic capacity of optical fibre. 2 By the other part, the communication between satellites and between any satellite and the earth surface stations is yet performed by microwave signals.^{3,4,5}

In these conditions, when is talking about "all optical networks", it is not far a real conflict between the optical communication capabilities at the surface and the capabilities of the microwave signals used at the satellite constellations in order for routing the information to it's destination. In this situation many scientists have been concentrate their attention to the problems that occur when using free optical beams instead the microwave beams.

2. OPTICAL BEACON FUNCTION

In Ref. 1 are analysed the advantages and disadvantages of the use of optical intersatellite links compared to microwave intersatellite links: smaller size and weight of the terminal, less transmitter power, higher immunity to interference, larger data rate and, smaller transmitter beam divergence angle. The main disadvantage of optical intersatellite links is the complexity of the pointing system. This complexity derives from the necessity to point from one satellite to another satellite from a distance of thousands of kilometres with a beam divergence angle of microradians when the satellites move and vibrate. The pointing system must compensate the predictable movement of the satellites using the known ephemerides data. Then, the tracking system must maintain the pointed satellite in the middle of the communication beam. At the other satellite the situation is the same.

Because the complexity of such a system and the high sensitivity to orientation and to environmental conditions especially vibrations, satellite-based laser communication is still an experimental technology implemented in laboratory conditions. Many theoretical and experimental progresses are reported in the literature¹. Basically, a pointing and tracking system (PAT) for satellite optical communication purposes includes a quite sophisticated electro-mechanical and optical system capable to ensure the appropriate paths for some transmitted or received optical beams used for pointing and tracking purposes. The communication optical transmitter and, respectively, optical receiver use the same optical system that is, they have the same optical axis with the pointing and tracking system and, may or may not contribute to the pointing process.

Usually, in a PAT exists a special optical transmitter called "optical beacon" by analogy with the radio beacons used in aviation. The beacon placed into any of the two systems involved in the optical link, called "primary station" (PS), has the role to transmit an optical beam that are used by the other system, called "remote station" (RS). The attributes "primary" or "remote" are conventional and, may switch reciprocally, depending of the point of view.

From the models reported in the literature, a prototype of a pointing, acquisition, and tracking (PAT) system developed by Ball Aerospace Corporation, described in Ref. 6, was considered in this paper as a reference system for the mathematical model, and electrical/mechanical analysis. Anyway, this model is not very different from the recent and so called "semiconductor laser intersatellite experiment" (SILEX) of the European Space Agency concerning the optical beacon role.

The aim of a PAT station is to exactly point the RS with the communication laser beam from the PS and, reciprocally, to position the communication laser beam from the RS on the communication receiver of the PS (Fig. 2). In order to avoid a greater and superfluous complexity, figure 2 illustrates only the optical beams and the wide field of view of the PS.

The primary and remote PAT stations include three electro-optical sub-systems responsible for three principal tasks (corresponding to three stages of positioning process): initial orientation of the coarse steering mirror, coarse steering and fine steering. The first stage of positioning employs the image created by beacon light-emitting diodes of the RS. This image is captured by the optics of a wide field of view camera and is used to define the coordinates of the target and to coarse point to it with the communication beam. The next stage imply a more accurate positioning of the communication laser using a close-loop control electronics. The final stage uses the incoming beacon beam to provide the precise position information and to maintain the appropriate orientation by a second closed-loop control electronics.

Two of the three stages of the positioning process are based on a laser transmitter of an optical beacon beam, separate from the communication transmitter. Four NIR wavelengths are used in the system. The positioning process is developed

autonomously at each station without any intercommunication data related to the actual position of the optical axe, except for the simple presence of the beacon beam.

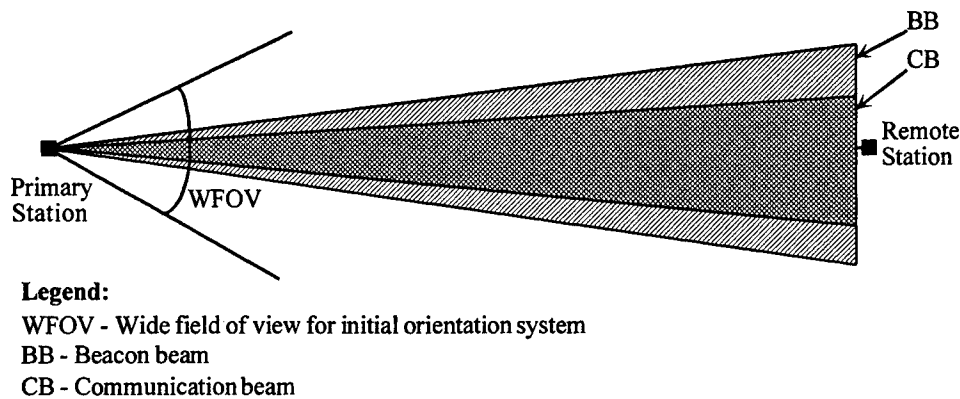


Fig. 2 Schematics of the optical beams transmitted from the primary station

The absence of the communication between the PS and the RS related to their reciprocal position, make both the systems very vulnerable to the perturbations. The tracking process is highly dependent on the beacon beam of the correspondent. Actually, each of them suppose that the correspondent is perfect aligned and, using the beams transmitted from this, try itself to remove any orientation error in order to obtain the maximum of the received signal amplitude. Even the alignment is perfect for one of them, no tracking occurs if the other do not point to it. In the next, a method to reduce this dependence such as providing a criteria at each station to correctly make the decision if it is aligned or not will be found.

3. AEROPLANE LANDING APPROACH - A SIMILAR PROBLEM

The landing of a plane is a similar problem. In this case the pilot of the incoming plane to the runway must be informed if his position in the space is correct or it is not. In order to achieve a good landing, the plane must be along the axis of the runway in the horizontal plane and, more, it must be at an altitude dependent of the distance to the runway. Actually, for an ideal landing the plane have to fly along to a line called "landing lane". The Instrumental Landing Systems (ILS), or similar, the Microwave Landing Systems (MLS), by theirs beacon aparature, ensure an electronic materialisation of this line. In order to "inform" about the vertical plane containing the runway axis, two beams with different modulation are transmitted such as they have the same amplitude of the signal in this plane. The situation is similar for the inclined plane. As a result we have an "equal signal line" identical to the desired landing line. Appropriate receivers exist on the plane and by the comparison between the previous mentioned modulated signals make possible to detect the position error of the plane relate to the landing lane. The information is displayed to the pilot and he knows what he has to do.

The similitude of the landing systems with the pointing and tracking systems is immediate. The role of the PS in the communication systems is played by the ground-based aparature in ILS or MLS. Something different is that the landing aparature always points the same fixed direction with the equal signal line of the transmitted beam. An other consists in the transmission of four beams with their patterns equally decalated from the landing line. The role of RS in the communication systems is played by the plane. This, using only the information received from the ground based landing aparature, try to be exactly pointed by the equal signal line, that means it is at the appropriate position. More, no transmitters exist on board for this problem.

In the case of pointing and tracking systems, the problem is more complicated a bit because both stations are moving objects but on the preimposed trajectories (orbits). Only rotation movements are permitted in order to ensure the pointing process. The plane in the landing process is in advantage because it can move in order to find it's correct position. The model of the landing systems is still valid in the problem of pointing and tracking process because in this case may exist a communication between the two stations involved.

Actually, the main aim of the system is to assure the communication between them. So that, if an appropriate receiver exists on the RS and this detects its self position in the beam transmitted from the PS then, this positioning information may be transmitted to the PS where it may be used for remove the positioning error. The situation may be the same for the positioning information detected by the PS and transmitted to the RS. In such a way, because on each station is permanently known from the other the positioning error of its beam then, the positioning process is accelerated.

4. NEW BEACONING METHOD ANALYSIS

The main advantage of the previous purposed positioning method consists in the possibility to determine the relative position of the optical axis of the correspondent station and to communicate this information as a signal error to that station for a faster correction of the positioning error.

Basically, this method suppose a four-beam transmission of the communication data, each of the having a specific modulation, different from the others, and an appropriate corresponding optical receiver. The beams used are geometrically shifted from the ideal optical axis of the optical system giving the possibility to determine the error angle relate to the ideal optical axis and to transmit a signal error to the PS, via the communication data. For simplicity, only a plane analysis for a two beam system is performed. In Fig. 3 is shown a plane section diagram which illustrate the position of the RS detectors relate to the PS transmitter beam patterns. The two beams illustrated here have the same divergence angle θ and, are symmetrically shifted from the optical axis by the angle of $\theta/2$.

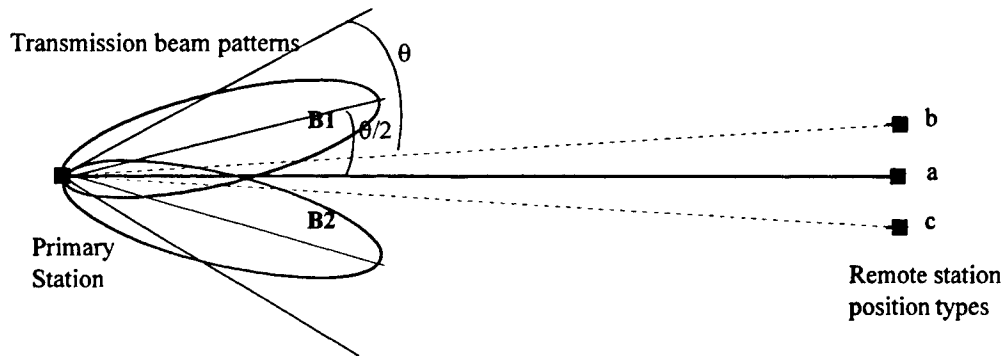


Fig.3 Plane section of the transmitted beam pattern and three different positions of the remote station

As in Fig. 3, if RS position is a) then the signals amplitudes provided by the two beams B1 and B2 are identical. In a position of b) type the signal provided by the beam B1 is larger than the signal provided by the other beam and reversal in a position of c) type. By the comparison of the two signals at RT it is possible to establish the position of the middle of the composed beam transmitted from PS. Any positioning error is transmitted to PS in order to remove it.

This multi-beam method present a series of advantages: (1) give the possibility to action only at the station where it is necessary, (2) for a given divergence angle of each beam used, let be θ this angle, the tracking stage is assured inside a 2θ angular sector and, (3) for a given output power of each transmitter, the signal to noise ratio increase at the receiver. More, the same transmitters may be used for all communication purposes and consequently, reducing the system complexity.

For a given gaussian beam pattern, with the standard deviation δ , one may write the next equations for the received optical power at RT, where P_0 is the maximum optical power that may be received from any of the two beams:

$$P_1(\alpha) = P_0 \cdot \exp\left(-\frac{(\alpha-\theta)^2}{\delta^2}\right) \quad (1)$$

$$P_2(\alpha) = P_0 \cdot \exp\left(-\frac{(\alpha+\theta)^2}{\delta^2}\right) \quad (2)$$

Actually, at RT a sum and a difference between the two signals may be performed, as in the following equations:

$$P_{\Sigma}(\alpha) = P_0 \cdot \left[\exp\left(\frac{(\alpha+\theta)^2}{\delta^2}\right) + \exp\left(\frac{(\alpha-\theta)^2}{\delta^2}\right) \right] \quad (3)$$

$$P_{\Delta}(\alpha) = P_0 \cdot \left[\exp\left(\frac{(\alpha+\theta)^2}{\delta^2}\right) - \exp\left(\frac{(\alpha-\theta)^2}{\delta^2}\right) \right] \quad (4)$$

Equation (3) may be used for information communication and, equation (4) for positioning error determination. In fact, the equations (3) and (4) transform the two transmitted beam pattern into two received beam pattern, sum beam pattern and difference beam pattern as in the next figure.

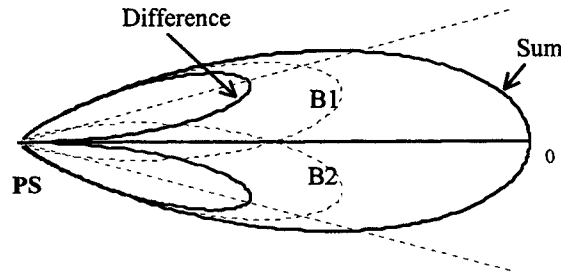


Fig. 4 Sum and difference beam patterns

5. IMPLEMENTATION

No major modifications in the basical optical system of a station are required. In order to simultaneously transmit the four beam required by the method, four laser transmitters with different wavelengths are used for generating the beams. If each laser transmitter is appropriately and slowly shifted from the focal point of the optical systems then the beams are angularly dcalated from the optical axis of the optical system and paired two by two in the perpendicular planes. Let be λ_1 and λ_2 the wavelength used for the horizontal plane as in Fig. 4.

The block diagram of a circuit that may solve the reception problems may be as in the next figure, where some appropriate filters are implicit at the top of each of the fotodetectors used, FD1 and FD2.

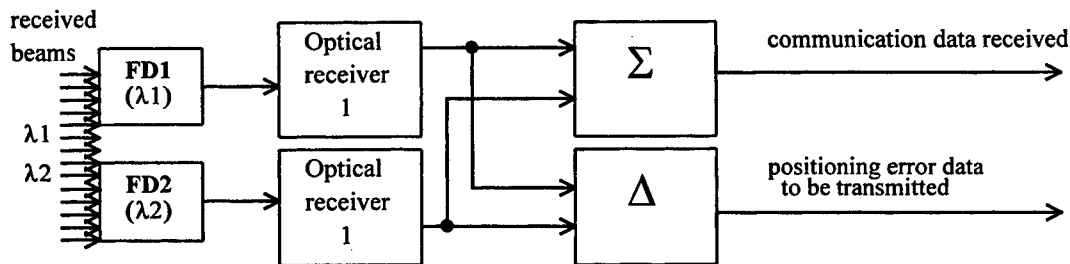


Fig. 5 Block diagram of the receiving circuit of a PAT station

The subtraction of the output signals of the optical receivers corresponding to λ_1 and λ_2 , we obtain as result a signal proportional with the angular error. The sum of the signals represent communication data.

Resulting from the positioning-data exchange between the secondary and the primary stations, via the intercommunication channel, a close-loop positioning system that include the both stations is obtained.

6. REFERENCES

1. S. Arnon, N. S. Kopeika, "Performance limitations of free-space optical communication satellite networks due to vibrations - analog case", *Opt. Eng.* **36**(1), 175-182, 1997.
2. T. Unter, "Optical Systems get the Glory ... Component to the Work", *Alcatel Telecommunications Review*, 85-86, 2-nd Quarter 1996.
3. B. L. Schwartz, "The future of satellite communications", *Alcatel Telecommunications Review*, 82-84, 2-nd Quarter 1997.
4. J. C. Hudson, "Satellite Constellations - A new frontier for telecommunications in space", *Alcatel Telecommunications Review*, 85-90, 2-nd Quarter 1997.
5. H. Sorre, P. Sourisse, "Skybridge: a broadband access system using a constellation of LEO satellites", *Alcatel Telecommunications Review*, 91-96, 2-nd Quarter 1997.
6. V. A. Skomin, C. R. Herman, M. A. Tascillo, D. N. Nicholson, "Mathematical modelling and simulation analysis of a pointing, acquisition, and tracking system for laser-based intersatellite communication", *Opt. Eng.* **32**(11), 2749-2763, 1993.
7. V. A. Skomin, M. A. Tascillo, T. E. Busch, "Adaptive jitter rejection technique applicable to airborne laser communication systems", *Opt. Eng.* **34**(5), 1263-1268, 1995.

Laser treatment of a-SiC:H thin films for optoelectronic applications

D.Ghica¹, N.Mincu¹, C.Stanciu², G.Dinescu², E.Aldea², V.Sandu³, A.Andrei⁴, M.Dinescu²,
A. Ferrari⁵, M.Balucani⁵, G.Lamedica⁵

¹ National Institute of Optoelectronics, Bucharest, P.O. Box MG-22, RO-76 900, Romania

² National Institute of Laser, Plasma and Radiation Physics, Bucharest, P.O. Box MG-16, RO-76900, Romania

³ National Institute of Materials Physics, Bucharest, P.O.Box MG-7, RO-76 900, Romania

⁴ Institute for Nuclear Research, Pitesti, Romania

⁵ INFN Unità di Roma, Dipartimento di Ingegneria Elettronica,
Università 'La Sapienza' di Roma, Via Eudossiana 18, 00184 Roma -Italy

ABSTRACT

Amorphous and hydrogenated (a-SiC:H) as well as crystalline silicon carbide are widespread materials for optoelectronic applications. In this paper, we studied the effect of the laser / RF plasma jet treatment of a-SiC:H thin films deposited by Plasma Enhanced Chemical Vapor Deposition (PECVD), on Si wafers. A Nd:YAG laser ($\lambda=1.06\text{ }\mu\text{m}$, $t_{\text{FWHM}}=14\text{ ns}$, $E_0=0.015\text{ J/pulse}$) was used with a fluence of 4 mJ/cm^2 incident on the sample, the number of pulses being varied. Plasma treatments were performed in a plasma jet generated by a capacity coupled RF discharge in N_2 . Different analysis techniques were used to investigate the films, before and after the irradiation: X-ray diffraction (XRD), X-ray photoelectron spectroscopy (XPS) and transmission electron microscopy (TEM). We followed the modification of their structure and composition as an effect of the laser/plasma treatment. A comparison with the excimer and also with the RF treatments was performed.

Keywords: a-SiC:H thin films, laser / plasma treatment

1. INTRODUCTION

Amorphous hydrogenated silicon carbide (a-SiC:H), as well as the crystalline silicon carbide continues to be of great interest from both fundamental and applicative viewpoints. Due to their special optical, electrical and mechanical properties, a-SiC:H and SiC thin films cover a wide range of applications such as optoelectronic devices, high-temperature and high power electronic devices, coating materials¹⁻⁸. Solar cells, UV photodetectors and blue light emitting devices (LED's) are important optoelectronic devices based on a-SiC:H and SiC films.

In the last years, many works were reported on laser treatment of a-SiC:H films⁹⁻¹¹, and on pulsed laser deposition of SiC layers¹²⁻¹⁴. We have previously carried out a parametric study of excimer (KrF) laser treatment of a-SiC:H thin films^{9,10}. Depending on the carbon content of the films and on the addition of H_2 inside the reactor during the initial film deposition by PECVD, the best regimes for crystallization and stoichiometry changing of the film were identified. "As deposited" films consist in SiC and unbounded Si and C. The KrF laser treatment revealed not only the crystallization of the layer, but also an increasing in the amount of SiC in the film. An explanation could be that the activation energy for Si-C reaction in solid phase (around 5 eV) is closed to the photon energy of the KrF laser. We also performed RF plasma jet treatments in N_2 or NH_3 atmosphere of a-SiC:H thin films¹⁵. Depending on treatment conditions (gas nature, temperature) and/or initial composition, different compounds are favored to appear in the film, for the same experimental parameters: the evolution of treated samples containing less carbon, towards a compound rich in SiN was

evidenced and on the samples having a higher carbon content, an upper layer rich in Si-C and sometimes even in C-N bonds was identified.

With the present experiments we intended to study the effect of the irradiation with a different laser wavelength on the a-SiC:H thin films (prepared in the same conditions as in our previous experiments^{9,10,15}), for several numbers of subsequent laser pulses, in the presence of RF plasma jet or only in N₂ atmosphere.

2. EXPERIMENTAL

a-SiC:H films, of around 6000 Å thickness, were grown on Si(111) wafers by PECVD, with or without hydrogen addition during deposition. The carbon content in the films varied in function of the deposition conditions, from 30% to 45%.

The RF plasma jet treatment was performed in a dedicated reactor (RF generator 13.56 MHz, 100 W). The discharge zone was placed outside the reactor and is limited by two electrodes spaced at 1-2 mm. The sample was placed in the downstream plasma at a distance of 100 mm from the nozzle, parallel to it. The irradiation time was varied with the number of the laser pulses.

The Nd:YAG laser treatments were performed either in nitrogen atmosphere or simultaneous with the RF plasma jet treatment (Fig.1). We used a Nd:YAG laser ($\lambda=1.06 \mu\text{m}$) of $E_0=0.015 \text{ J/pulse}$, $\tau_{\text{FWHM}}=14 \text{ ns}$ and 1 Hz repetition rate. The fluence on the surface of the sample was set to 4 mJ/cm^2 . Series of 200, 500 and 1000 subsequent laser pulses were directed to the same location on the sample. The irradiation parameters were chosen so that the material will not be molten by heating during the laser pulse (low fluence) or by the build up of heat due to the average power dissipation (low repetition rate).

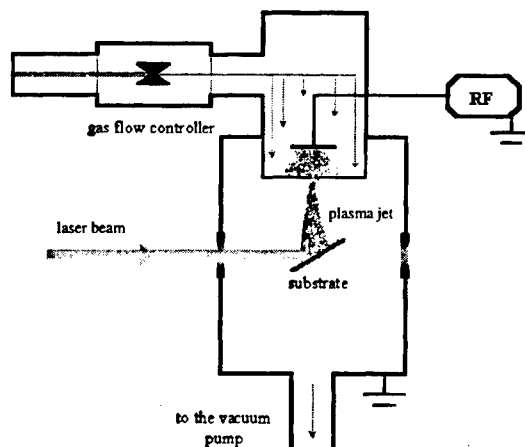


Fig.1. Experimental set up used for laser/plasma treatments of a-SiC:H films

Before and after the treatment the samples were investigated by X-ray diffraction (XRD), X-ray photoelectron spectroscopy (XPS), Transmission Electron Microscopy (TEM). XRD analyses were conducted with an URD6 apparatus with nickel filter, using Cu-K α line ($\lambda = 1.54 \text{ Å}$). X-ray photoelectron spectroscopy analyses were performed with a VG ESCALAB MK II spectrometer, using the Al-K α radiation (1486.6 eV) for excitation. TEM images were obtained with a JEOL 200 CX microscope operating at 200 kV.

3. RESULTS AND DISCUSSIONS

3.1. X-ray diffraction

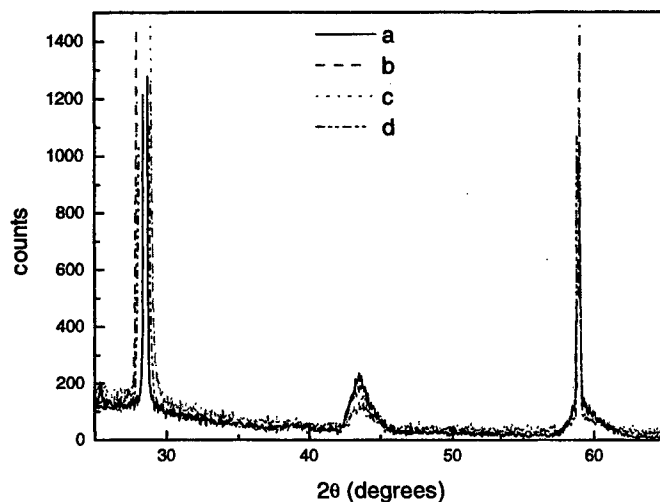


Fig.2. XRD spectra for a-SiC:H samples with 40-45% C content:

- a - untreated
- b - treated by 200 laser pulses at 1064 nm in the presence of RF plasma jet in N_2 atmosphere
- c - treated by 500 laser pulses at 1064 nm in the presence of RF plasma jet in N_2 atmosphere
- d - treated by 1000 laser pulses at 1064 nm in the presence of RF plasma jet in N_2 atmosphere

Figures 2 and 3 present the behavior of a-SiC:H samples with 40-45% C content under IR laser treatment in the presence of RF plasma jet working in N_2 atmosphere and in N_2 atmosphere, respectively. The most intense peak (at 28.4°) corresponds to the substrate, Si(111). The quite broad peak centered at 43.5° could be an envelope of different peaks corresponding to a mixture of α -SiC (centered at 43.51°) and silicon dioxide (centered at 43.33° and 43.71°) present into the films. The signal centered at 59° is split into two peaks, one corresponding to the SiO_2 (at 58.94°) and the other one corresponding to α -SiC (centered at 59.15°).

The laser/plasma treatment does not dramatically modify the general structure of the layer. An increasing of the crystallized amount of SiO_2 can be deduced from the behavior of the peak centered at 58.94° . On the other hand, the peak situated at 43.5° evidenced a systematic decreasing. This can be explained as a slight amorphization of the α -SiC compound together with a crystallization of the oxides present at the surface of the film. No nitrogen incorporation into the films occurred (as observed in plasma treatments), probably because of the shorter treatment time (up to 17 min) with respect to the previous plasma treatments (up to 90 min)¹⁵.

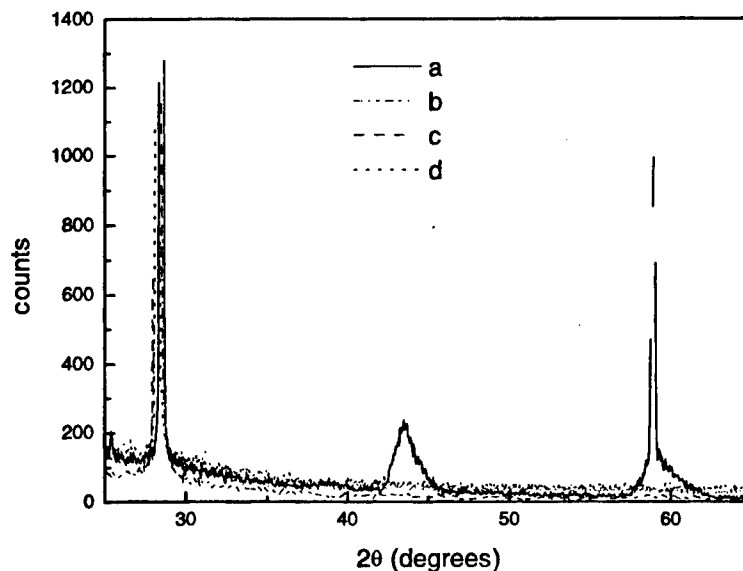


Fig.3. XRD spectra for a-SiC:H samples with 40-45% C content:
a - untreated
b - irradiated by 200 laser pulses at 1064 nm in N₂ atmosphere
c - irradiated by 500 laser pulses at 1064 nm in N₂ atmosphere
d - irradiated by 1000 laser pulses at 1064 nm in N₂ atmosphere

Laser treatments at 1064 nm in nitrogen atmosphere do not induce the crystallization of the amorphous thin films, as in the case of UV irradiation^{9,10}. From the disappearance of the peaks situated around 59° (Fig.2) an amorphization can be supposed. This can be a consequence of the low laser fluence, but also of the inappropriate laser wavelength.

The irradiation of the films for different incident laser fluences were also performed in orders to identify a possible threshold for laser crystallization. No crystallization as an effect of laser treatment was evidenced, even just below the ablation threshold or in the zones situated on the border of the ablation crater and investigated by TEM. Generally, the TEM images reveal only the amorphous phase. We can say that at 1064 nm, laser irradiation of the a-SiC:H films produces only amorphization, at any laser fluence.

3.2. X-ray photoelectron spectroscopy

Figure 4 presents results of XPS investigations in Si2p region for a-SiC:H samples before and after the laser/plasma treatments.

For the Si2p electrons, standard peaks at 99.7 eV from Si and 100.3 eV from SiC are reported¹². In our spectra (Fig.4) the Si peak was shifted toward the SiC peak, particularly after laser/plasma treatments. An oxidation effect is also evident from the increasing of SiO₂ peaks (situated at higher energies). C1s spectra recorded on the same samples confirm the Si2p spectra information, that the laser/plasma treatments lead to films with higher SiC content than the as deposited films.

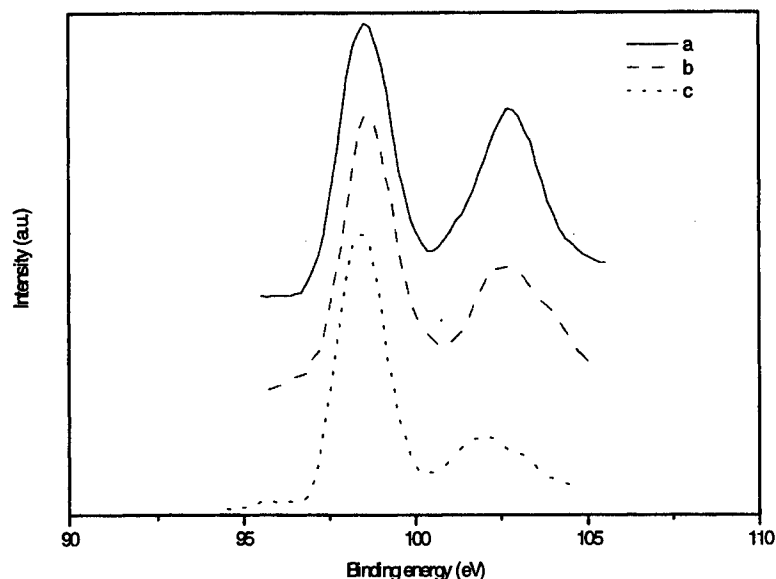


Figure 4. XPS spectra in Si2p region for a-SiC:H samples with 40-45% C content:
a - irradiated by 1000 laser pulses at 1064 nm in the presence of RF plasma jet in N₂ atmosphere
b - irradiated by 1000 laser pulses at 1064 nm in N₂ atmosphere
c - not irradiated

4. CONCLUSIONS

With the experiments presented in this paper we have studied the effect of the irradiation with 1064 nm laser wavelength on the a-SiC:H thin films, for several numbers of subsequent laser pulses, in the presence of an RF plasma jet or only in N₂ atmosphere.

Laser treatments at 1064 nm lead to the amorphization of the films for any laser fluence, even at the ablation threshold. Compared to the absorption coefficient for 248 nm, the absorption of 1064 nm is much weaker, the IR laser treatment leading to a higher absorption length, so that thermal effects occur at the interface SiC-Si. We can say that the vaporization threshold, which is reached at the interface (most probable in the silicon substrate), produces bulk (explosive) ablation, without significant thermal effects in the solid state film. In conclusion, no crystallization can be produced at any laser fluence.

The RF plasma jet in N₂ atmosphere seems to work as a shield for the 1064 nm wavelength, as the amorphization was weaker in this case. Laser/plasma treatments lead to films with a slightly higher SiC content than the as-deposited films. In all cases, no nitrogen incorporation in the films was observed by XPS investigations, probably due to the short time of the surface processing.

5. REFERENCES

1. H.Morkoc, S.Strite, G.B.Gao, M.E.Lin, B.Sverdlov, M.Burns, "Large-band-gap SiC, III-V nitride and II-VI ZnSe - based semiconductor device technologies", *J.Appl.Phys* **76**, 1363-1398, (1994)
2. J.A.Powell, L.G.Matus, "Recent developments in SiC (USA)", in *Springer Proceedings in Physics*, Vol. **34**, 2-12, Amorphous and Crystalline Silicon Carbide, Springer Verlag, Berlin-Heidelberg, (1987)
3. P.A.Glasow, "6H-SiC studies and developments at the Corporate Research Laboratory of Siemens AG and the Institute for Applied Physics of the University in Erlangen (FRG)", in *Springer Proceedings in Physics*, Vol. **34**, 13-33, Amorphous and Crystalline Silicon Carbide, Springer Verlag, Berlin-Heidelberg, (1987)
4. N.T.Tran, "Amorphous Silicon Carbide thin films produced in the glow discharge deposition system", in *Springer Proceedings in Physics*, Vol. **34**, 134-141, Amorphous and Crystalline Silicon Carbide, Springer Verlag, Berlin-Heidelberg, (1987)
5. H.Matsunami, "Crystalline SiC on Si and high temperature operational devices", in *Springer Proceedings in Physics*, Vol. **43**, 2-7, Amorphous and Crystalline Silicon Carbide, Springer Verlag, Berlin-Heidelberg, (1988)
6. T.Nakato, K.Koga, Y.Matsushita, Y.Ueda, T.Niina, "Single crystal growth of 6H-SiC by a vacuum sublimation, and blue LEDs", in *Springer Proceedings in Physics*, Vol. **43**, 26-34, Amorphous and Crystalline Silicon Carbide, Springer Verlag, Berlin-Heidelberg, (1988)
7. A.Suzuki, K.Furukawa, Y.Fujii, M.Shigeta, S.Nakajima, "Crystal growth of β -SiC on Si and its application to MOSFETs" in *Springer Proceedings in Physics*, Vol. **56**, 101, Amorphous and Crystalline Silicon Carbide, Springer Verlag, Berlin-Heidelberg, (1990)
8. V.E.Chelnokov, "Development prospects for SiC bipolar transistors and thyristors" in *Springer Proceedings in Physics*, Vol. **56**, 125, Amorphous and Crystalline Silicon Carbide, Springer Verlag, Berlin-Heidelberg, (1990)
9. G.De Cesare, S.La Monica, G.Maiello, E.Proverbio, A.Ferrari, M.Dinescu, N.Chitica, I.Morjan, A.Andrei, "Crystallization of amorphous silicon carbide thin films by laser treatment", *Surface and Coatings Technology* **80**, 237, (1996)
10. G.De Cesare, S.La Monica, G.Maiello, G.Masini, E.Proverbio, A.Ferrari, N.Chitica, M.Dinescu, R.Alexandrescu, I.Morjan, E.Rotiu, "Crystallization of silicon carbide thin films by pulsed laser irradiation", *Appl.Surf.Sci.*, **106**, 193, (1996)
11. S.P.Lau, J.M.Marshall, T.E.Dyer, "Structural and electrical transport properties of excimer (ArF)-laser-crystallized silicon carbide", *Philosophical Magazine* **B 72**, 323, (1995)
12. M.A.Capano, S.D.Walck, P.T.Murray, D.Dempsey, J.T.Grant, "Pulsed laser deposition of silicon carbide at room temperature", *Appl.Phys.Lett* **64** (25), 3413, (1994)
13. T.Zehnder, A.Blatter, A.Bachli, "SiC films prepared by pulsed excimer laser deposition", *Thin Solid Films*, **241**, 138, (1994)
14. V.E.Bondybey, "Laser vaporization of silicon carbide: lifetime and spectroscopy of SiC₂", *J.Phys.Chem*, **86**, 3396, (1982)
15. A.Ferrari, G.Maiello, S.La Monica, E.Proverbio, G.Dinescu, M.Dinescu, N.Chitica, A.Andrei, V.Sandu, M.Gartner, G.Masini, "Capacity coupled RF discharge plasma jet treatment of a-SiC:H structures", *Thin Solid Films*, **296**, 23, (1997).

Gamma Induced Transparency Loss of Thick Quartz Fibres

Gasanov E.M., Ibragimova E.M and Yuldashev B.S.
Institute of Nuclear Physics, P.Ulugbek, 702132 Tashkent, Uzbekistan

Ashurov M.Kh. and Rustamov I.R.
Scientific Association "Phonon", S. Yusupov st.50, 700054 Tashkent, Uzbekistan

ABSTRACT

Radiation response of thick multimode *Ge*, *P*, *F*-doped quartz fibre has been examined after exposure to ^{60}Co gamma-source within a dose interval of $10 - 10^7$ Gy at a dose power of 2.3 and 24 Gy/s at 300 K. The induced transparency losses A at the wave length of $1.06 \mu\text{m}$ do not exceed 0.2 after a dose of 10^6 Gy and reach a saturation, while the fibres are closed for visible light after a smaller dose. Varying focus and an angle of leading a probe light beam in fibre, the core modes were found to close at a dose of 10^4 Gy due to radiation induced colour centres of *Ge* and non-bridging oxygen O^- , and the clad modes were suppressed at 500 Gy by the expense of *Al* impurity colour centres. Key words: quartz fibre, laser beam, optical loss, colour centres, gamma radiation hardness.

2.INTRODUCTION

2.1 Requirements to fibres as a part of calorimeters in high energy experiments

A study of radiation response of optical fibres to a mixed flux of high energy particles is necessary for designing and optimal choice of fibre material for calorimetry in experiments at colliders. This problem became especially important for collider experiments with very high energies and luminosities when secondary particles cascading in the detector material produce high fluxes of neutrons and gammas which could damage the fibres used to collect a light from scintillation crystals. For example, in CMS detector which will be used in experiments at Large Hadron Collider at CERN the maximal dose per year for the luminosity of $10^{34} \text{ n/cm}^2\text{s}$ is expected to be $3-4 \cdot 10^5$ Gy (30-40 MRad) and in some experiments - above 1 GRad, and the maximal annual fluence of neutron is near 10^{15} n/cm^2 [1,2]. Use of the scintillation doped fibres in this case is limited by a level of radiation damage at doses of ~ 0.1 GRad, however several high pure and transparent dielectrics like quartz are radiation hard even at doses about 1 GRad [3,4].

Normally, in high energy detectors, the quartz fibres are put inside of an absorber at a low angle to an incident beam. So, exploring thick quartz fibres might be preferential if they appear to be radiation hard as well. Preliminary results were published by us in [5].

2.2 Radiation characteristics of quartz fibres

Influence of ^{60}Co gamma-rays and neutrons on optical properties of thin quartz fibres were studied intensively [6-11]. Eight types of radiation colour centres have been found in the induced absorption spectra within $0.3 - 1.9 \mu\text{m}$ of quartz fibres of $\text{SiO}_2 - \text{SiO}_2:\text{B}_2\text{O}_3$ after ^{60}Co gamma irradiation doses of 3 - 100 Gy at temperatures of 77 and 300 K [6,7]. These centres anneal at different temperatures and are bleached by laser illumination. The "effect of transfer" of UV-band at $0.34 \mu\text{m}$ into IR-band was discovered under pumping with the 3-rd harmonics of *YAG:Nd* laser followed by recovering at 300 K. The induced band at $0.67 \mu\text{m}$ was found to be discoloured by *He-Ne* laser irradiation. Also relaxation (anneal) of the colour centres is accompanied sometimes by luminescence, which should be taken into account in the scintillator's response. The induced losses at $1.3 \mu\text{m}$ were examined with a high accuracy and were proved to be proportional to a gamma dose rate and unstable [8]. Moreover, the losses in IR-region turned to be equal for 14 MeV neutrons and ^{60}Co gammas, provided with the same ionization dose [9]. Therefore the

authors concluded that the radiation response of the fibre is due presumably to ionization effects and is determined by an accumulated dose and not by structure changes from neutron induced atom displacements. This conclusion was confirmed by calculation of elastic and inelastic losses in quartz fibre after reactor exposure [11]. Radiation testing the fibre with pure quartz core and doped quartz clad, explored as an element of photometer in the region of 400-900 nm [10], after gamma-irradiation to the dose of 8×10^5 Gy (80 MRad) showed the maximal induced loss $\sim 2-3$ dB/m at 600 nm, the band being caused by the colour centre of non-bridging oxygen O' .

As far as the radiation induced loss in quartz fibres depends strongly on their composition and processing technology, it was necessary to carry out a comparative analysis of absorption spectra within 200-700 nm of the fibres having different content of OH-groups at γ -irradiation to a dose of 10^7 Gy, at a dose rate of 6.4 Gy/s. It has been accomplished lately by [12] for the Cherenkov radiation calorimeter based on quartz fibre. A strong absorption at 350 and 630 nm and luminescence at 670 nm appear at a dose of 10^5 Gy, depending on OH- group concentration. The higher content of OH, the more intensive absorption at 630 nm, but the weaker absorption at 400 nm. Thick fibre might possess a bigger radiation induced loss than thin one.

Thus, it is important to investigate both the radiation induced absorption (optical loss) and luminescence, including time parameters (dose rate dependence and relaxation), in order to determine a contribution from atomic and ionization energy losses into defect production and to predict the radiation hardness of fibres under the mentioned conditions.

The aim of this work was to study radiation hardness and radiation induced loss at a wave length of 0.35, 0.53, 0.63 and $1.06 \mu\text{m}$ of the gradient quartz fibres of a large diameter under effect of ^{60}Co γ -radiation at the temperature of 300 K, in a wide range of integral absorbed doses $10 - 10^7$ Gy at a dose power of 1.3 and 24 Gy/s. Using both pulse lamp and laser as a probing light enables to separate the optical loss of core and clad modes.

3. EXPERIMENT

3.1 Characteristics of fibres

Objects were quartz gradient multimode fibres, the core of which is of $530 \mu\text{m}$ in a diameter and made of pure SiO_2 with uncontrolled impurities of $10^{-6} - 10^{-7}$ wt.percent. The gradient of refraction index is conditioned by adding of GeO_2 component from 0 to 10 wt.percent to the core, the clad with a diameter of $1050 \mu\text{m}$ is made of two- component silica glass $\text{SiO}_2:F(0.02) \text{P}_2\text{O}_5(0.001-0.002)$ and the total diameter including a polymer cover is $1480 \mu\text{m}$. The numerical aperture is 0.22 and the initial optical loss κ for the wave length of $0.85 \mu\text{m}$ is 2.8 dB/km, $1.3 \mu\text{m} - 0.5$ dB/km and $1.55 \mu\text{m} - 0.25$ dB/km, the temperature of drawing is 2100°C . As far as the drawing condition is the chemical precipitation from a gas phase, a concentration of OH-groups is supposed to be high and therefore absorption in the region of 350 and 630 nm can be correspondingly high. So a length of the fibre samples was chosen to be 10 cm for a visible spectrum and 50 cm for IR-region where the optical loss are much less.

3.2 Conditions of irradiation

^{60}Co γ - radiation source, designed at the Institute of Nuclear Physics, Uzbekistan Academy of Sciences, allows to carry out irradiation of different size objects with different fluxes of the gammas in ambient (air) and inert environment. Specimens of 10 or 50 cm long fibres were inserted into a glass tube and placed inside a stainless steel hermetic cylindrical chamber with an inner diameter from 7 to 60 cm and a height from 20 to 70 cm. The chamber is installed into a water filled basin of 5 m depth, with the isotope capsules surrounding the chamber and providing with a homogeneous irradiation and several kinds of in-

situ measurements. Three samples with the ends broken off normally to fibre axis were exposed sequentially to doses from 10 to 10^5 Gy at a dose rate of 2.3 Gy/s and from 10^3 to 10^7 Gy at 24 Gy/s with an accuracy of 15 % at 300- 350 K depending on a dose rate. Therefore there was an opportunity to examine the dose rate dependence of the gamma-induced loss within the interval of 10^3 - 10^5 Gy/s, if any, and to compare with the results of experiments done at 6.4 Gy/s by [6,7,11,12]. The optical loss was measured 10 minutes later the irradiation, so this could include a sufficient part of the radiation induced centres unstable at 300 K.

3.3 Optical loss measurements

The experimental set-up is shown in Figure 1. It includes the table (8) with the freedom degrees for fitting and tuning a fibre sample (7), short-focal lenses (6) for entering and leading the probe light out off the fibre, neutral filters (3) for attenuation of the reference beam, optical detectors based on photodiode PD-10g (9) and calorimeter IMO-2 with digital registration of a signal amplitude (10), sources of a probing light (1) based on the *He-Ne* laser with the wavelength of $\lambda = 0.63 \mu\text{m}$, the power of ~ 30 mWt and *YAG:Nd* laser with the 1-st harmonics at the $\lambda_1 = 1.06 \mu\text{m}$ and the 2-nd one at the $\lambda_2 = 0.53 \mu\text{m}$, operating in the regime of free generation and modulation by *LiF:F₂⁻* providing with a pulse of 20 ns. The optical loss at the wave lengths of 0.35 and $0.53 \mu\text{m}$ were also taken by means of the pulse lamp INP-3/45 with a condenser (2) and the proper colour filters as an incoherent light source (labelled as Lamp). So far as the thick gradient multimode fibre has a different composition of it's core and clad, it should expect a different response to irradiation depending on an entrance angle of probing light. The entry angle varied by different lenses, and axial and cladding modes were distinguished at an image of the fibre's end [5]. If the probing light passes throughout the fibre's core, the output signal is maximal. If the light's path includes the fibre's clad, the image is like a ring. Laser beams passed preferentially through the core and incoherent light of the lamp can pass both the core and the clad of fibres. The quasi two beam scheme was used for determining the initial intensity of the passed light, I_1 , which was detected and memorised by the oscilloscope after being weakened by the proper neutral filters till the level of the signal, I_2 attenuated by the radiation induced absorption of the fibre examined. The optical loss as a function of a probing wave length, $A(\lambda)$, in the units of dB/m for a fibre of L meters long was calculated as follows:

$$A(\lambda) = (10/L) \log \{ I_2(\lambda) / I_1(\lambda) \}$$

The initial apparatus value of the light beam attenuation was measured in arbitrary units of $k = I/I_0$ by the ratio of an incident and outlet beam, which varied within 0.01. The attenuation of neutral light filters for conforming amplitudes of the reference and the sample signals was defined with the same accuracy. The measured γ - dose dependencies of the light attenuation coefficient and the calculated optical loss for different wave lengths and the conditions for leading the light beam into the fibre are shown in Figures 2-4.

4. RESULTS AND DISCUSSION

The *Ge* doped quartz fibre has rather high loss in visible range due to the radiation induced absorption bands at 290 and 540 nm. Besides, *OH*-groups give rise to absorption at 630 nm, so the experiments were started on fibres of 0.1 and 0.5 m length respectively at the laser wave length of 0.63 and $1.06 \mu\text{m}$. Gamma dose rates of 2.3 and 24 Gy/s were chosen for determining a starting dose of detectable radiation coloration, i.e. the radiation hardness of the fibres at the above mentioned wavelengths. Figure 2 shows dependencies of the optical loss A at a wavelength of 0.63 and $1.06 \mu\text{m}$ on the logarithm of integral gamma- dose (scale $\lg(D_\gamma)$) in the range of $1 - 1.5 \times 10^6$ Gy: doses $1 - 10^3$ Gy were accumulated at the dose

rate of 2.3 Gy/s and $10^3 - 10^6$ Gy were at 24 Gy/s. Solid and dashed curves indicate A values taken at the two different dose rates and demonstrate a weak dose rate dependence of the loss at 633 nm for this fibre. At a dose as small as 500 Gy the $0.63\mu\text{m}$ laser gets 3 times weaker and at a dose of 10^6 Gy a value of $k = 0.005$ or 240 dB/m. The radiation induced absorption at $0.63\mu\text{m}$ is due to the well-known centre of non-bridging oxygen [7,12] and a tail of the band at 540 nm of Ge-center. As it should be expected, the induced losses in the near IR-region are getting noticeable at the dose of 10^4 Gy and don't exceed 15-20 dB/m at 10^6 Gy - the saturation level keeping till 1.5 MGy. This fact implies suppression of the metal containing hole $O_2^{3-} M^+$ centres causing a wide stable absorption band about $1\mu\text{m}$ attributed to absorption of self-trapped holes in quartz [13]. Then the observed luminescence at 670 nm of the non-bridging oxygen centres makes unstable the self-trapped hole centres and diminishes the radiation induced losses in IR- region [14].

Figure 3 demonstrates the loss at the wavelength of $0.53\mu\text{m}$ (the 2-nd harmonics of laser radiation in the regime of 20 ns pulses at 25 Hz) within an expand dose range from 5 Gy to 1 MGy. As soon as different kind of colour and glow centres can contribute to this spectral region, it was of particular importance to separate the light beams passed through the core and the clad of the fibres. This was achieved with several means of focusing beam also unfocused one. There were observed visually uncoloured core of $\sim 100\mu\text{m}$ in diameter and rings at boundaries of layers with different composition. As it was supposed, the central part of the core containing the minimal trace of impurities appeared to be the most radiation hard till doses as high as 10 MGy, therefore at a rigid ($F=0.5$ cm) focusing beam into the fibre's core the registered losses are minimal (dashed curves). While the gradient layers drawn from $SiO_2:GeO_2$ glass have the γ - induced hole absorption both at 0.44 and $0.63\mu\text{m}$ due to the non-bridging oxygen and at $0.53\mu\text{m}$ due to Ge -centres. The clad has a coloration quite different from that of the gradient Ge part. The absorption is supposed to be due to fluorine centres substituting the non-bridging oxygen and aluminium centres substituting in SiO_2 tetrahedrons and P_2O_5 octahedrons. Therefore without focusing (circles) when the laser beam passes mainly through the clad, the induced losses are maximal (solid curves). One should expect the dose rate dependence of radiation induced losses within the dose interval of $10^2 - 10^5$ Gy. At the rigid focusing into the core some dose power dependence was found at 1.3 and 24 Gy. While at the soft focusing involving the core and the clad the dependence is not obvious within the measured interval of $5 \times 10^2 - 5 \times 10^4$ Gy. For a better comparison with the data available [6,12] the losses were measured with the lamp illuminator glow filtered in $0.50 - 0.55\mu\text{m}$, as shown in Fig.3 as well (solid curves). As the incoherent lamp light (530 nm) can't be focused rigidly into the fibre's core, the dose dependent losses were even higher than those at the soft focusing of laser beam (532 nm). Fig.4 displays the losses in the near UV-region obtained by filtration of the pulse lamp illuminator light within $0.33 - 0.37\mu\text{m}$ and $0.53\mu\text{m}$ at 10-100 Gy. As usual, unfocused beam passes the fibres with a larger losses. The losses at 530 and 330-370 nm seem to come from the Ge- doping colour centre. More moderate dose dependence at 630 nm relates to the hole centre of non-bridging oxygen, and the weakest dose dependence does to the unstable hole centres in the near IR-region $\sim 1\mu\text{m}$.

5. CONCLUSIONS

The experimental techniques used here allowed to measure separately the radiation induced losses in the core and the clad of the fibre, as they have different colour centres. At the dose region of $5 \times 10^2 - 10^5$ Gy the dose rate dependence of radiation induced losses can be studied, when the same doses are accumulating at dose rates differ by one order. There was not any noticeable dose rate dependence of the losses at the wavelengths of 0.63 and $1.06\mu\text{m}$, although it was at $0.53\mu\text{m}$ due to different contributions from the core and the clad [5]. Presence of Ge dopant and non-bridging oxygen in the core and F , Al

impurity in the clad cause the observed high level of the γ -induced losses ~ 100 dB/m at 0.53 and $0.63\mu\text{m}$ after a dose of 10^4 Gy in the core and as small as 500 Gy in the clad. The tested fibre has the satisfying radiation hardness only at the wavelength of $1.06\mu\text{m}$, with the saturated losses being less than 10 dB/m after a dose of 10^6 Gy.

6. REFERENCES

1. D. Acosta et al, *NIM A* **294**, 193 (1990); *NIM A* **305**, 55 (1991).
2. G. Stevenson, "New dose calculations for LHC detectors", *Proc.LHC Workshop*, Aachen, 4-9 Oct. 1990, CERN 90-10, Vol.III, p.566, 1990.
3. Gorodetzky, B. Grosdidier and D. Lazic, *Radiat.Phys.and Chem.* **4** (1992) 253.
4. Arrington, D. Kefford, P.Podrasky, C.Sanzeni et al, "A Preliminary Study for CMS Very Forward Calorimetry", CMS TN/94 - 327, CERN, 1994.
5. Yuldashev B.S., Gasanov E.M., Ibragimova E.M, Ashurov M.Kh. and Rustamov I.R., *Abstracts of MRS-95 Spring Meeting*, April 1995, San Fransisco
6. E.Dianov, L. Kornienko, E. Nikitin et al, *Sov. Quant. Electr.* **10** (3), 473 (1983).
7. E.Dianov, V.N. Karpechev, L.S. Kornienko, A.O.Rybaltovsky and P.V. Chernov, *Sov. Quant. Electronics*, **11**, 2480 (1984).
8. Y. Chigusa et al, *IEEE Trans.on Nucl. Sci.* **35**, 894 (1988).
9. T. Iida et al, *ibid*, p.898.
10. J.B. Chesser, *IEEE Trans. on Nucl.Sci.* **40**, 307 (1993).
11. D.E. Holcomb and D.W. Miller, *J.of Nucl.Mater.* **203**, 136 (1993).
12. V. Gavrilov, S. Kuleshov, Yu.Chumarovskii et al, "Study of Quartz Fibre Radiation Hardness", CMS TN-94-324, CERN 1994.
13. K. Tanimura, T. Tanaka and N. Itoh, *NIM B*, **1**, 187 (1984).
14. E.M. Ibragimova and V.N. Stepanov, *Phys.stat.sol.(a)* **115**, K255 (1989).

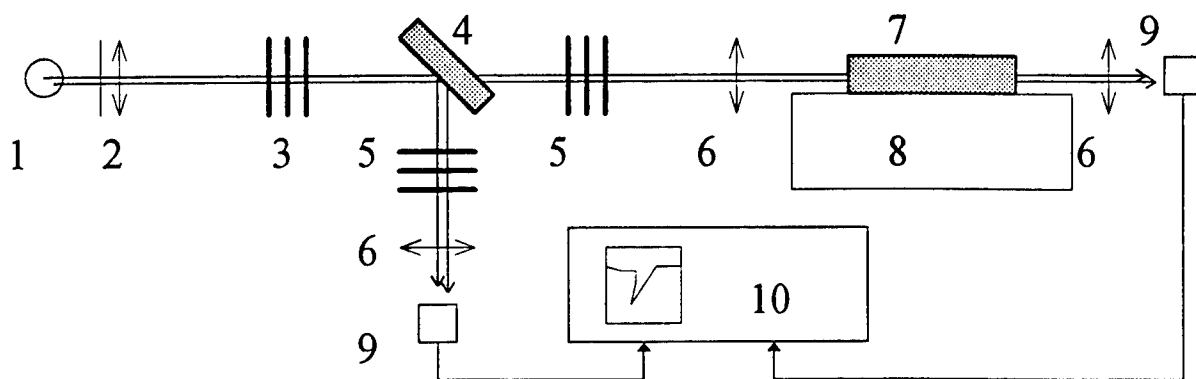


Fig.1 Experimental setup. (Explanation is in text)

Figure 2. Gamma-dose dependence of optical transmittance at different dose rates and wavelengths indicated

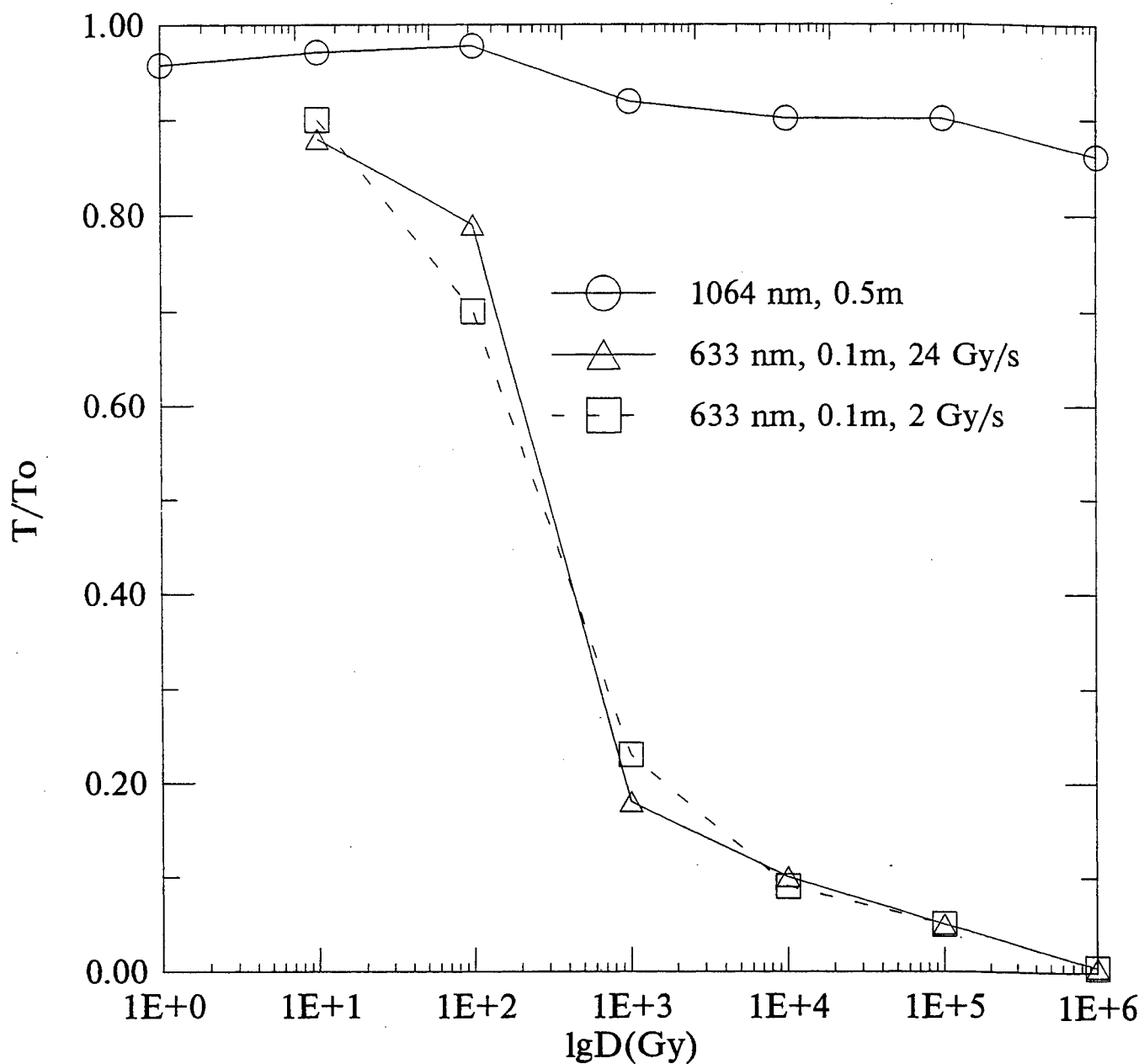


Figure 3. Gamma-dose dependence of optical transmittance at different dose rates and beam focusing at a wavelength of 532 nm.

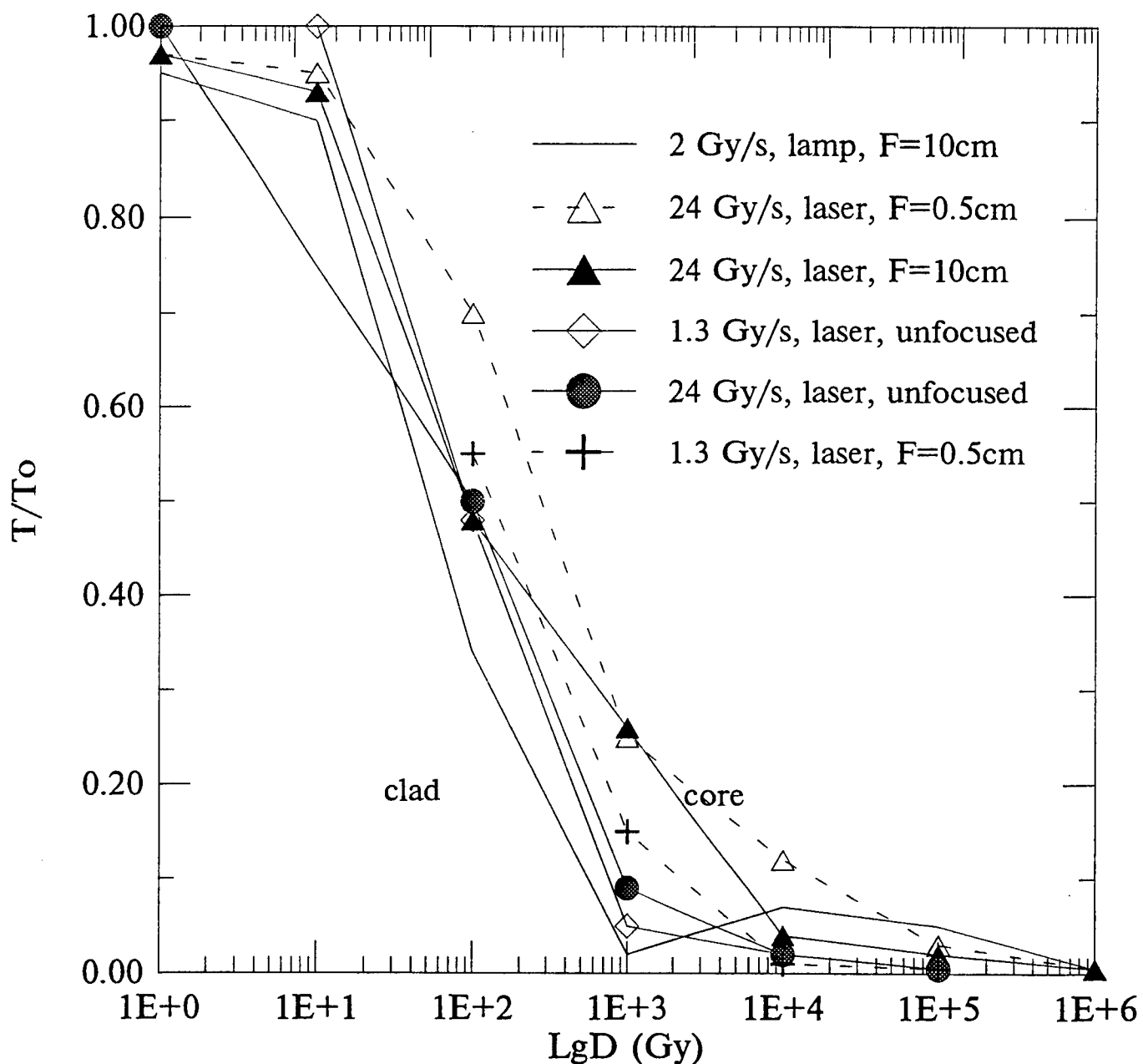
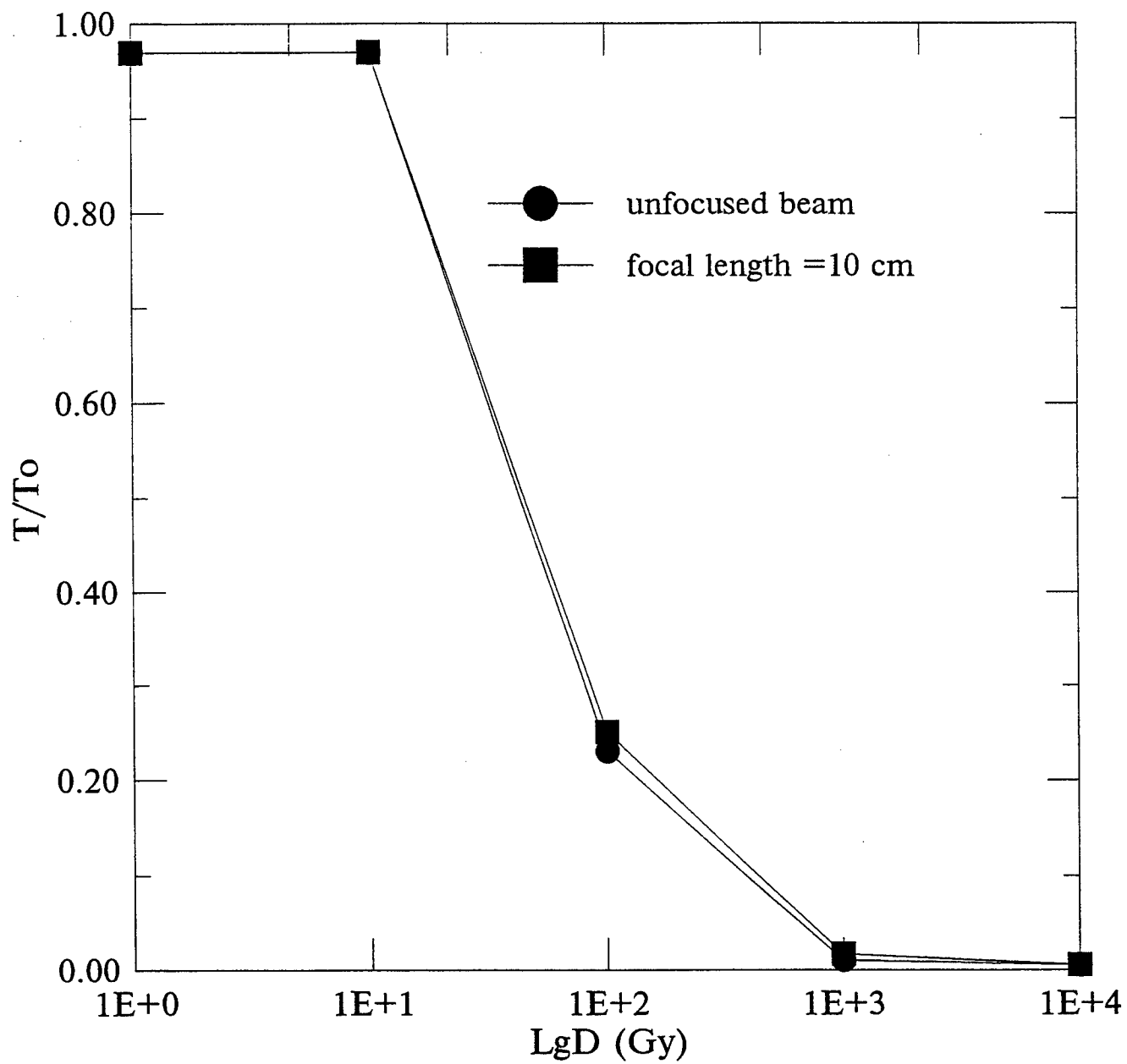


Figure 4. Gamma dose dependence of optical transmittance at the lamp wavelengths of 330 nm at the low dose rates of 1.3 Gy/s and 2 Gy/s and under different focusing.



V. Dragoi, L. Pintilie, I. Pintilie, D. Petre, I. Boerasu and M. Alexe*

National Institute of Materials Physics Bucharest, P.O.Box MG-7, R-76900, Romania

*Max Planck Institute of Microstructure Physics, D-06120 Halle, Germany

ABSTRACT

The ferroelectric/semiconductor heterostructures were fabricated by sol-gel deposition of lead titanate (PT) thin films on a single-crystalline p-type Si wafers. The PT films were crystallized by a conventional thermal annealing for 30 min at temperatures ranging from 575°C to 675°C. Current-voltage and capacitance-voltage characteristics show a hysteresis which can be due to the spontaneous polarization of PbTiO_3 . The current-voltage characteristics exhibit a diode behaviour while the capacitance-voltage exhibits a large memory window, up to 3.5 V, for the films annealed at 600-650°C. At the illumination with modulated light, a.c. photovoltage was detected on a broad range of wavelengths ($0.35\pm 4\ \mu\text{m}$) for all samples. The spectral distribution of the photoelectric signal in the UV-Vis-IR domain shows two local maxima. A model is proposed to explain the observed experimental results.

Keywords: sol-gel, ferroelectric/semiconductor heterojunctions, photoelectric effect, pyroelectric effect

1. INTRODUCTION

During the last decade a special interest was focused on the applications of the ferroelectric thin films, especially of solid solutions with perovskite structure, such as $\text{PbZrO}_3\text{-PbTiO}_3$ (PZT). They include devices for infrared detection¹⁻³, electro-optical devices⁴, high density dynamic random access memories (DRAMs)⁵ and non-volatile random access memories with low switching voltage (NVRAMs)⁶.

The present paper presents some results regarding the electrical and photoelectrical properties of sol-gel fabricated lead titanate/silicon heterostructures. The obtained results help in understanding of complex phenomena taking place at the ferroelectric/Si interface and can be explained if the spontaneous polarization and the high dielectric constant of ferroelectric thin film are taken into account.

2. SAMPLES PREPARATION

The PT films were deposited onto (111) oriented p-type silicon by the sol-gel method. The sol was prepared using lead acetate and titanium n-butoxide as raw materials and 2-methoxyethanol as solvent. The films were deposited by spinning at 2000 rpm for 60 s, followed by pyrolysis for 3 min. in air at 400°C. To obtain a 0.8 μm final thickness for the amorphous film, the sequence spinning - pyrolysis was repeated 10 times. Finally, the PT thin films were crystallized by conventional thermal annealing in air, for 30 minutes, at temperatures ranging from 575°C to 675°C.

Electrical and photoelectrical measurements were performed on metal-ferroelectric-silicon (MFS) structures. The MFS structures were obtained by deposition of aluminium electrodes of about 2000 Å thickness on the back silicon surface and semitransparent gold electrodes, of about 600 Å thickness, on the top PT surface. The gold electrodes were shaped into rectangles of 1,25x1,5 mm² by evaporation through a metallic mask.

3. STRUCTURAL AND ELECTRICAL CHARACTERIZATION

After annealing, the structure of the annealed films was investigated by X-ray diffraction. The study of the θ -2 θ diffraction patterns for all the samples revealed thin films fully crystallized into the perovskite phase without foreign phases. For the sample annealed at 600°C the mean crystallite size is about 200 Å and for the sample annealed at 625°C is about 300 Å.

The electrical characterization was performed by measuring the current-voltage (I-V) and the capacitance-voltage (C-V) characteristics of the metal-ferroelectric-semiconductor (MFS) structures (Au/PT/Si)⁸. The I-V characteristics were determined by applying the d.c. voltage from a Keithley 241 d.c. power supply and measuring the current flowing through the heterostructure using a Keithley 642 electrometer. For the samples annealed at temperatures up to 625°C, the I-V characteristics are diode type characteristics (as is shown in Fig. 1), the heterostructure being reverse biased when a negative voltage is applied on the Si substrate and forward biased when a positive voltage is applied on it. A small hysteresis appears in the forward current⁹, which may be a consequence of the hysteretic behaviour of the spontaneous polarization existing in the ferroelectric film.

The capacitance-voltage characteristics of the PT/Si heterostructure were determined by using a Hewlett Packard 4194A Impedance/Gain Analyser. The frequency of the measuring signal was 100 kHz and the amplitude 0.1 V. A typical C-V characteristic is presented in Fig. 2 for PT/Si heterostructure annealed at 625°C. The C-V characteristics reveal a clockwise hysteresis loop¹⁰, which is due to the existence of the spontaneous polarization in the PT film. The direction of the loop gives information about the existence of spontaneous polarization in the PT thin film. For the p-type Si, the clockwise loop is due to the existence of the spontaneous polarization in PbTiO₃¹¹, while a loop in the other sense is due to the electric conduction in the oxide¹².

As it is shown in Fig. 3, the memory window¹³ (which is the difference in the flat band voltages for the two sweeping directions) decreases with increasing of the annealing temperature. This could be due to a reaction between PT and Si occurred at PT-Si interface which develops a low permittivity layer between Si and ferroelectric.

The capacitance measured under accumulation conditions, which can be related with the oxide capacitance only, increases with the increasing of annealing temperature. This could be a result of the increasing of the crystallites size during the annealing. The interface reaction influences the total capacitance of the structure and the polarization of the ferroelectric film as it is shown by comparing the actual experimental value of the relative permittivity, about 20, with the known value (80) from literature¹⁵.

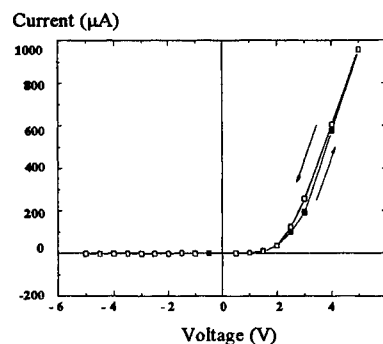


Fig. 1. The I-V characteristics for the sample annealed at 625°C.

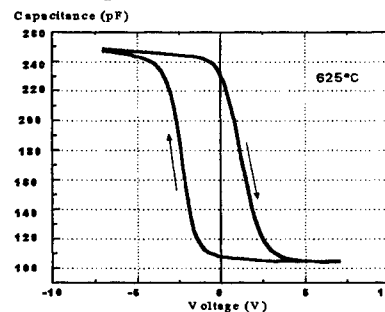


Fig. 2. The C-V characteristics for the sample annealed at 625°C

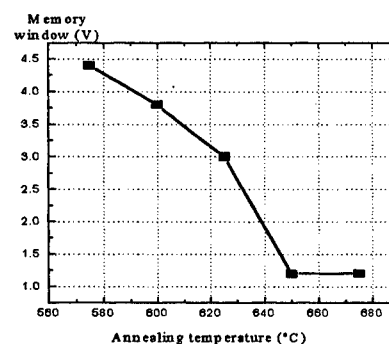


Fig. 3. The memory window versus the annealing temperature

4. PHOTOELECTRIC AND PHOTOVOLTAIC EFFECTS IN PT-Si HETEROJUNCTIONS

The photoelectric properties were investigated for the best sample, annealed at 650°C. These measurements were performed on a broad range of wavelengths using two light sources: a Nernst glower for the 0.5–4 μm range and a Xe lamp, XBO 101, for the 0.35–1 μm range. To raise spectral distributions, the light beam was passed through a Carl Zeiss monochromator or through interferential metal filters. The photoelectric measurements were performed in two cases of illumination: modulated light (using an ITHACO 383A mechanical chopper), and continuous light.

4.1. Measurements in modulated light.

The a.c. open-circuit voltage was measured using an UNIPAN 233 selective nanovoltmeter. The spectral distribution of this photoelectric voltage, measured at 160 Hz, is presented in Fig. 4. Two local sensitivity peaks appear in the normalized spectral distribution, at wavelengths around 0.38 μm and 0.95 μm. The energy gap can be determined from the relation:

$$E(\text{eV}) = \frac{1.25}{\lambda(\mu\text{m})} \quad (1)$$

The gap energies, estimated using the wavelengths of the two local maxima, are 3.33 eV and 1.12 eV. These values are comparable with values known from literature 3.4–3.5 eV for PT¹⁶ and 1.12 eV for Si. It can be readily assumed that the two maxima are associated to band-to-band electron excitation in the two materials. Moreover, a long tail can be observed in the long wavelength region (1 μm to 4 μm). In this region, the photovoltage is about 10⁴ times smaller than in the 0.35–1 μm region. We can suppose that this small signal is a pyroelectric signal which is developed by the PbTiO₃ film. The long wavelengths light is absorbed in the PT film, leading to a temperature variation and, therefore, to a variation of the spontaneous polarization (i.e. pyroelectric effect).

The frequency characteristics of the a.c. open circuit photovoltage were raised for different wavelengths of the incident light. From Fig. 5 and 6, which present the frequency characteristics of the a.c. open circuit photovoltage, it can be easily observed that the shape of the frequency characteristic depends on the light wavelength.

The frequency characteristic has a maxima for illumination with 0.35 μm wavelength light, while for 1 μm wavelength the photovoltage increases with increasing frequency until it reaches an approximately constant value. For 0.35 μm and 1 μm wavelengths, the shape of the curve is similar to the shape of a photoelectric signal, and at 2 μm wavelength, the frequency characteristic has again a maxima at low frequencies (80 Hz) and the shape is definitely similar to the frequency characteristics of a pyroelectric signal¹⁷.

As it was shown above, the PT/Si heterostructure is generating a photoelectric signal on a large wavelength range (UV to middle IR). It can be assumed that for the UV range, the signal generation mechanism is the

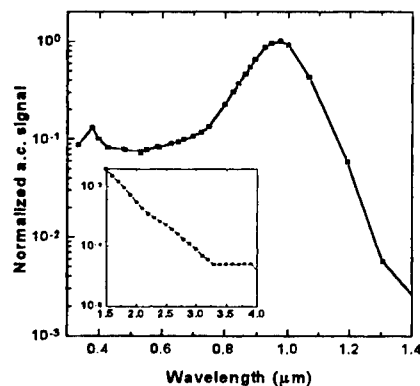


Fig. 4. The spectral characteristics of the photoelectric signal for the sample annealed at 650°C.

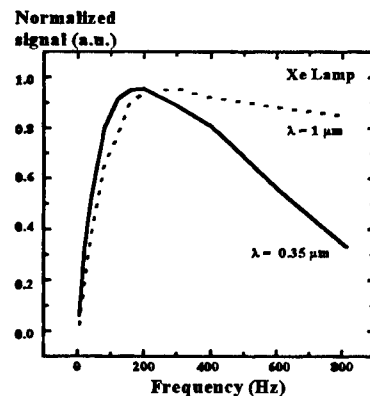


Fig. 5. The frequency characteristics of the a.c. open circuit photovoltage (Xe lamp).

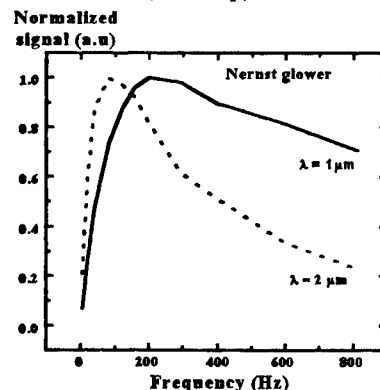


Fig. 6. The frequency characteristics of the a.c. open circuit photovoltage (Nernst glower).

photoelectric effect in the ferroelectric film. For the Vis-IR domain the signal is generated by internal photoelectric effect in Si. For wavelengths above 1.2 μm , the signal is due the pyroelectric effect in the PT film.

4.2 Measurements in continuous light.

For the MFS structures annealed at 650°C d.c photoconductive current was measured directly using an electrometer. The sample was reverse biased by applying a d.c. voltage of -2V and the spectral distribution of the generated photocurrent was raised. The spectral distribution for the photoconductive signal (d.c. photocurrent) is shown in Fig. 7.

One can observe that the two sensitivity peaks situated around 0.38 μm and 0.95 μm are present again, but the long tail which was present in the long wavelengths region when the sample was illuminated with modulated light has disappeared. This is a direct confirmation that long wavelength signal is due only to the pyroelectric effect. This effect is active only when the sample is illuminated with modulated light, while in case of continuous light illumination the pyroelectric signal is zero and the measured photosignal is due only to the photogenerated carriers.

The dependence of the photocurrent on the applied reverse voltage is presented in Fig. 8. A non-linear dependence, no matter the wavelength, can be observed. The photocurrent increases with increasing the applied voltage and tend to saturate. The non-linear behaviour might be a consequence of the non-linear dependence of the ferroelectric polarization on the applied electric field.

The time dependence of the generated photocurrent on the applied voltage and on the light intensity, respectively, were studied. In both cases, it was put into evidence that at the switch of the light on and off, the kinetics of the transitional signal upon switching the light are usual for photoferroelectrics and are determined by the Maxwellian relaxation of the photovoltaic current associated with the formation of space charge in the ferroelectric film¹⁸. For high light intensities, this usual behaviour vanishes, and the photocurrent reaches the steady-state value without any relaxation.

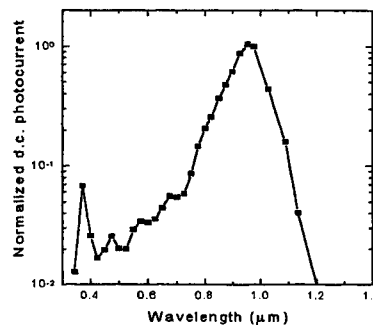


Fig. 7. The generated photocurrent vs. the radiation wavelength (d.c. reverse bias: -2V)

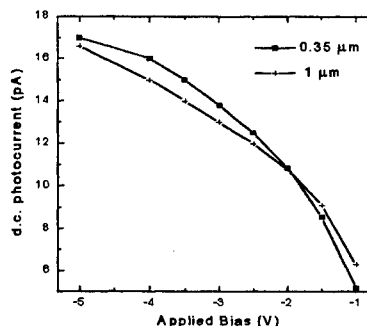


Fig. 8. The d.c. photocurrent versus the inverse voltage.

5. DISCUSSIONS

A band structure model like the one from Fig. 9 can help to explain the observed experimental results in the PT/Si heterostructure. We assumed that the ferroelectric polarization is oriented from the metal electrode to the Si substrate. In this case, the film surface is negatively charged at the metal-ferroelectric interface and positively charged at the PT/Si interface. Thus, a depletion layer will be induced in Si, near the PT/Si interface. If the ferroelectric polarization is oriented in an opposite direction, the film surface at the PT/Si interface will be negatively charged setting the Si into accumulation conditions. Anyway, no independently to the orientation of the ferroelectric polarization, an internal electric field will appear in Si.

When the I - V characteristic was raised, the applied

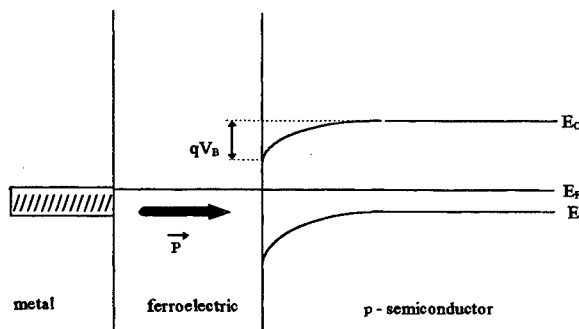


Fig. 9. The band structure for the classic metal/ferroelectric/semiconductor heterostructure

voltage had lead to the polarization of the ferroelectric film. If the applied voltage is positive, the ferroelectric polarization is oriented from the Si substrate to the metal electrode. An accumulation layer appears in Si and the structure is forward biased. Increasing the applied voltage, the ferroelectric polarization reaches saturation, but the current increases very quickly due to charge injection from the Si into the PT film. If the voltage is decreased but is positive, the forward current will decrease by passing through other values than in the case when the voltage is increased (see Fig. 1). A hysteresis will appear in the forward current due to the hysteretic behaviour of the ferroelectric polarization. If the voltage applied on the structure is negative, the ferroelectric polarization is oriented from the metal electrode to the Si substrate. A depletion layer will appear in Si and the structure appear to be reverse biased. In this case, the value of the measured current is very small (about 10^{-10} A) and is practically independent on the value of the applied voltage. After removing the applied voltage the ferroelectric film remains polarized, the value of the remanent polarization depending on the available compensation charge from the Si substrate. In our case it is expected that the value of remanent polarization is higher when positive voltage is applied on the structure (holes concentration higher than electron concentration). The I-V characteristics were raised in such a way that finally the ferroelectric polarization is oriented from the metal electrode to the Si substrate.

At the beginning of each photoelectric measurement, the ferroelectric polarization was intentionally oriented from the metal electrode to the Si substrate having the Si in depletion conditions. If the heterostructure is illuminated with light having energy higher than the Si gap, it will be absorbed at the Si surface creating electron-holes pairs. The generated carriers will be separated by the internal electric field and a photovoltage will appear. If the wavelength of the incident light is sufficiently small to generate carriers in the PT film, then these carriers will be separated by the depolarization field. The depolarization field exists as long as the ferroelectric polarization exists, but it is shielded by the compensation charges from the metal electrode and from the Si substrate. The depolarization field will separate the photogenerated carriers and also a photovoltage will appear. In this way, a photovoltaic signal will appear as long as the energy of the incident light is sufficiently high to produce non-equilibrium carriers either in Si or in the PT film.

The light with long wavelengths (small energy) can be absorbed in the PT film producing pyroelectric effect. The pyroelectric effect exists at all wavelengths, but at wavelengths shorter than $1.2 \mu\text{m}$ the pyroelectric effect is superimposed over the photovoltaic effect. At wavelengths higher than $1.2 \mu\text{m}$, only the pyroelectric effect exists. This effects superposition could be the reason of the tail in the spectral distribution of the a.c. photovoltage and the difference in shapes of the frequency characteristics raised at different wavelengths. When the structure is illuminated with light of $0.35 \mu\text{m}$, the light is strongly absorbed in the PT films and both, pyroelectric and photovoltaic, effects appear. The frequency characteristic could be a combination of the frequency characteristics of the two types of signals. At $1 \mu\text{m}$, the light is strongly absorbed in Si, ferroelectric film being transparent in that wavelength region. The photovoltaic effect in Si will be dominant but its frequency characteristic will be affected by the presence of the capacitive impedance represented by the PT film. This is the cause for the fact that at all small frequencies the signal increases with increasing frequency. Being known that $X_c \sim 1/2\pi f$, it results that increasing the modulation frequency, f , X_c will decrease and the measured photovoltage will increase. The frequency characteristic will be similar to a high pass filter manufactured from a resistance (the depleted region from the Si substrate) and a capacitance (the ferroelectric film) connected in series. At $2 \mu\text{m}$, the incident light can produce only pyroelectric effect and the frequency characteristic confirm this fact (see Fig. 6).

For the sample illuminated with continuous light the influence of the ferroelectric film is present only when the light is switched on/off. When the light is switched on, charge carriers are generated, supposing that the energy of the incident light is sufficiently high to produce non-equilibrium carriers. These carriers will modify the internal electric field, the charge from the interface and the value of ferroelectric polarization. A transient current peak will appear until a new equilibrium state is reached under illumination. Similar phenomena happen when the light is switched off.

6. CONCLUSIONS

Electrical and photoelectrical properties of a PT/Si heterostructure were studied. The experimental results impose the following conclusions:

- The PT/Si heterostructure has a current-voltage characteristic of diode type, with a small hysteresis in the forward current.

- The capacitance-voltage characteristic exhibits a large hysteresis loop, confirming the presence of ferroelectric state in the lead titanate film.

- For metal/ferroelectric/semiconductor structures with the PT film annealed at 650°C, a.c. open-circuit photovoltage was measured for a broad range of wavelengths (0.35 μm –4 μm). The measurements under modulated and continuous light and frequency characteristic of the a.c. photovoltage for different wavelengths showed that two types of effects can contribute to the measured photovoltage: pyroelectric and photovoltaic. The two effects overlap when the sample is illuminated with short-wavelength radiation, while at long wavelengths only the pyroelectric effect is active.

Beside the classical integrated pyroelectric sensors, a novel application of the PT-Si heterostructures is an UV-Vis photoelectric sensor¹⁹. For the practical applications one has to optimise the structure in order to maximize the signal in the UV region and to eliminate the parasitic interface effects. The UV sensitivity can be improved by doping the ferroelectric film and the interface effects can be diminished by choosing an appropriate thermal annealing process or by using other preparation methods for ferroelectric-semiconductor silicon, such as direct wafer bonding²⁰.

7. REFERENCES

1. R. Takayama, Y. Tomita, K. Ijima and I. Ueda, *J. Appl. Phys.* **61**, 411 (1987)
2. R. Takayama, Y. Tomita, K. Ijima and I. Ueda, *J. Appl. Phys.* **63**, 5868 (1988)
3. K. Ijima, S. Kawashima and I. Ueda, *Jpn. J. Appl. Phys.* **24-2**, 482 (1985)
4. S. Y. Wu, W. J. Takei and M. H. Francombe, *Ferroelectrics* **10**, 209 (1976)
5. K. Okamoto, Y. Nasu and Y. Hamakawa, *IEEE Transactions on Electron Devices* ED-28, 698 (1981)
6. J. F. Scott and C. A. Paz de Araujo, *Science* **246**, 1400 (1989)
7. J. I. Lanford, R. Delhez, T. H. de Keijser and E. J. Mittemeijer, *Aust. J. Phys.* **41**, 173 (1988)
8. M. Alexe, M. Popescu, V. Dragoi and C. Tanasoiu, *Proc. of 18th Annual Semicond. Conf., Sinaia, Romania*, pp. 725, October 1995
9. Y. Watanabe, *Appl. Phys. Lett.* **66**, 28 (1995)
10. J. K. Park and W. W. Grannemann, *Ferroelectrics* **10**, 217 (1976); J. F. Scott, in: *Ferroelectrics Ceramics*, edited by N. Setter and E. L. Colla (Birkhauser, Basel, 1993), p. 194.
11. J. K. C. Panitz and C. C. Hu, *Ferroelectrics* **27**, 161 (1980)
12. A. S. Grove, B. E. Deal, E. H. Snow and C. T. Sah, *Solid State Electronics* **8**, 145 (1965)
13. K. Aizawa and H. Ishiwara, *Jpn. J. appl. Phys.* **33**, 5178 (1994)
14. M. Alexe, *Proc. of 17th Annual Semicond. Conf., Sinaia, Romania*, pp. 713, October 1994
15. D. L. Polla, "Science and technology of electronic thin films", Kluwer Academic Publishers, pp. 413, 1995
16. S. E. Bernacki, *Mat. Res. Soc. Symp. Proc.*, **243**, 135 (1992)
17. S. B. Lang, "Source-book of pyroelectricity", Gordon and Breach, 1974
18. V. M. Fidkin, *Photoferroelectrics*, Springer-Verlag Berlin, 1979
19. M. Alexe, L. Pintilie, *Infrared Phys. & Techn.* **36**, 949-954 (1995)
20. M. Alexe, G. Kästner, D. Hesse, and U. Göesele, *Appl. Phys. Lett.* **70**, 3416 (1997).

Optical Integrated Circuits

Ovidiu Iancu, Daniel Pircălăboiu,

TEF Department, Faculty of Electronics and Communications,
"Politehnica" University of Bucharest
Armata Poporului 1-3, 77202, Bucharest 6
Fax +401-4107845, e-mail opto@joe.tehfi.pub.ro

ABSTRACT

The notorious implication of integrated optics in the nowadays communication systems makes more interesting the development of optical integrated devices and circuits. The evolution of the communication systems was sustained by the integrated optics and it is obvious that the actual interests in the optical communications are also transferred and adapted to integrated optics. The presentation of actual state-of-art in this field is a good opportunity both for an evaluation on the above mentioned evolution and for discerning the actual trends and their perspectives. These trends, guided by applicative goals, have to be discussed not only from the theoretical point of view but also from a practical one.

Keywords: optical guided communications, optical integrated circuits, wavelength division multiplexing

1. INTRODUCTION

The imminent arriving of the III^d millennium reveals to humanity a fundamental aspect of his evolution: the necessity to manage continuously increasing amounts of information.

On the bussines sector, the necessity of a rapid local access at the information resources is vital as well as the fast running of the on-line applications, multimedia services and so on. In the last years, as the Figure 1 shows, a big interest was polarized around the Internet network. The long-distance access, the specific communication tools, the voice and video conferencing, the possibilities to access and to share information anywhere, in any moment, with anyone throughout the world, are the advantages we are allways looking for and this segment of the communications named Internet has all the above features.

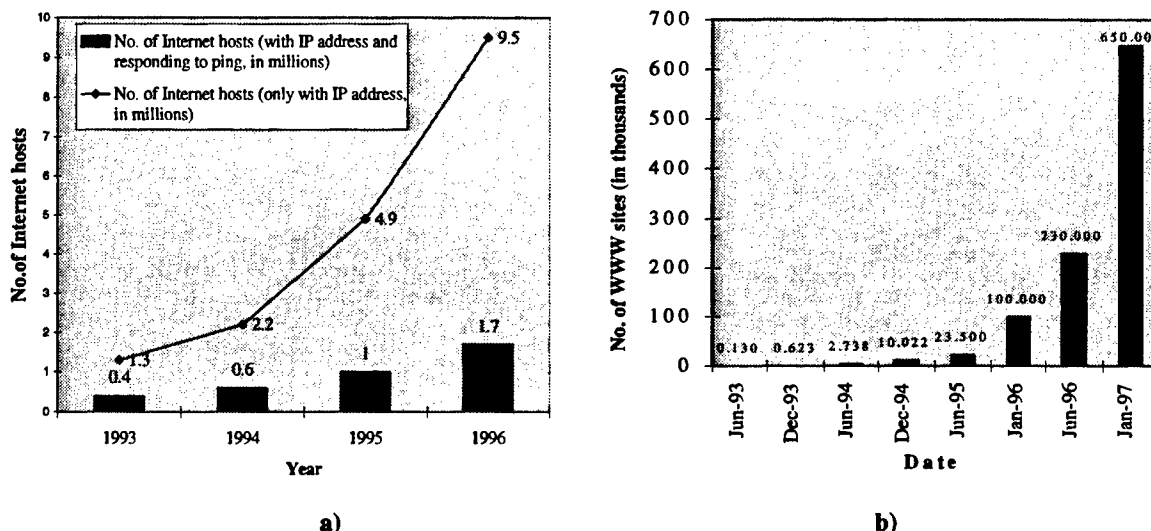


Figure 1 The growth of (a) Internet and (b) WWW, according to Matthew Gray (Massachusetts Institute of Technology).

On the residential front, apart from the classical interests for telephony, television and Internet connection, the rapid rise of the video-on-demand/interactive video services and the real-time distance video-game playing are generating an interesting combination of optimism and concern (because they need Broadband to the Home - BTTH - links).

The integration of the information sources, the technological development and the adaptation of a large part of human activities to this environment supplies the research "engines" in the communications domain and, in particular, in the optical ones.

The beginnings of the guided optical communications can be temporally placed in 1966 when Kao, Hockam [1] and Werts proposed a "glassy material constructed in a cladded structure [...] representing a possible practical waveguide with important potential as a new form of communication medium", which is the well-known now as the optical fiber. The multiple improvements of the optical fibers allowed the actual use of commercial products with linear attenuation less than 0.2 dB/km. Simultaneously with the improvement of the transmission medium, another important part of the communication systems was developed - the light sources. The advent of semiconductor laser sources was the initial kick for the development of the optical communication systems. The first such system that had better performances than a classical one was realised with devices working at 0.85 μm . Performances like 100 Mbit/s transmission rates, with 10 km repeaters spacing were considered a good level for such a technology. The second generation of systems introduced the single-mode optical fibers and changed the working wavelength toward 1.3 μm . This was possible because of availability of InGaAsP laser sources and Ge-based detectors. Consequently, the transmission rate achieved was as high as 200Mbit/s. In the next step the operating wavelength was pushed to 1.55 μm and the goals proposed were the compensation of the fiber dispersion (of about 17 ps/nm.km) and the monochromaticity of sources. The use of DFB and DBR lasers became fundamental. The performances reported (500 GHz frequency tunable DBR lasers, enabling to transmit 80 high definition TV channels to 2000 subscribers) are relevant for the efficiency of such a system.

The integrated optics was strongly connected to all these achievements. This domain followed and supported the systemic efforts by permanent adapting and improving its devices and circuits to the communicational needs. The evolution started with the first semiconductor laser sources, continued with the connecting aspects and focused on the device problems (it is wellknown that a large part of optical integrated devices and circuits serve the communication needs; filters, gratings, splitters, couplers, polarization splitters, circulators, mixers, are just few examples).

Another group of communications interests is the systemic one. It very actual and is related to Wavelength Division Multiplexing (WDM) systems. These systems are arrived from the intention to overcome the inherent electronic limitations and from the benefit of great transmission potential (expressed by the large optical fiber bandwidth). Early WDM systems have demonstrated a good perspective in this sense (62 Gbit/s) but the implementation of optical fiber amplifiers (since 1987) and, more recently, the monolithic multi-wavelength integration and the multisection alternative of DBR lasers were two major breakthroughs that made WDM much more interesting. Concerning the last one, the development of integrated star-couplers and multiple junctions (splitters/combiners) seems to be equally important for integrated optics, both from materials and technology and from device design point of view. Related to the material problems, another interesting group of devices is that of the nonlinear optical devices, naturally linked with the solitonic transmission of light.

On principle, from the architectural point of view, two are the interesting kinds of links in the actual communication systems: point-to-point links and the multiple-point links (access networks).

2. POINT-TO-POINT LINKS

This class of links is destined to the long-distance high-speed connections between two distribution/concentration nodes. The high-speed goal is achieved by a wavelength distribution of the information channels over the entire accessible optical spectrum following the wavelength-division-multiplexing principle. The bandwidth could be even better filled if the use of a supplementary Time Division Multiplexing (TDM) is made. As the Figure 2 suggests, there are some key components for the system. The laser sources must be tunable, monochromatic, amplitude (and, sometimes, phase) stabilized and must present a good fiber coupling efficiency and the highest modulation bandwidth achievable.

From the enormous number of semiconductor laser types, the Hybrid Distributed Bragg Reflector Laser (H-DBR laser) seems to fully accomplish the before mentioned requirements. The Bragg reflector made in a tapered-fiber has at least two advantages. Firstly, the emission wavelength position and its width are now controlled. The second is related to the high coupling with the optical fiber and is possible even to improve it, if a Spot-Size Converter (SSC) is used. HDBR [2] structures with emission wavelength λ in the 1.55 μm window, with line width less than 40 kHz, temperature-stabilized ($\Delta\lambda/\Delta T=400$ MHz/ $^{\circ}\text{C}$) and modulation bandwidth up to 40 MHz are already in use. For applications with the bit rates higher than 50 Gb/s, the external modulation seems to be the inherent solution.

The M \times N star coupler is an essential component since multiplexing/demultiplexing are based on such structures. We will mention only the fact that the two multiple junctions working in the TDM section (a splitter and a combiner) are operated at a fixed wavelengths and thus, their wavelength non-uniformities are less important for the system.

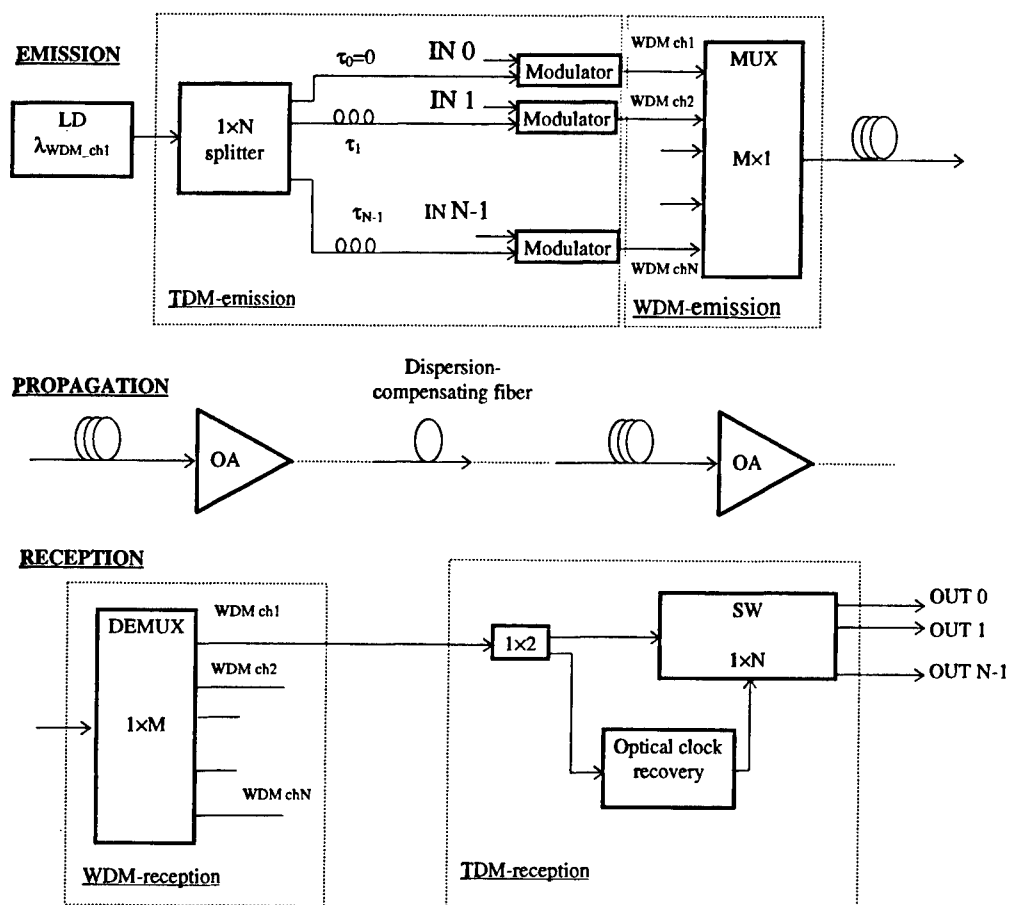


Figure 2. The architecture of a point-to-point link.

The other components of the system are fiber-based (the delay lines, the transmission fiber and the optical fiber amplifiers OA). For long distance transmission a part of these components must be optimized (i.e., the dispersion management is achieved by means of the insertion of the dispersion-compensating fibers, the gain of OA is equalised with an adequate filter, etc.).

3. THE MULTIPLE POINT LINKS

As the information needs seized on the mass attention, a number of access technologies has been developed (see Table I). The first solutions pointed on the existing structures (telephony and CATV plants). As an example, the Asymmetric Digital Subscriber Line (ADSL) technology uses the lowest frequency spectrum part (4 KHz) of the plain old telephone service. The rest of the usable spectrum (10KHz-1MHz) is managed using the Discrete MultiTone (DTT) technology. This technique divides the frequency interval in 256 subchannels (each 4KHz wide) and periodically assigns the data transfer rates upon the channel quality tests. The Switched Digital Video (SDV) and Hybrid Fiber-Coax (HFC) technologies are interesting solutions because they introduced and/or replaced high-speed fiber-optic links in the existing communication network. These implementations are an important step toward Passive Optical Networks (PONs) and must be encouraged because the actual estimations on the nature of transmission medium show that the rapport of lengths of mondial twisted-pair cooper cables and hybrid fiber-coax cables is 100:1 (20:1 in the USA). The efforts to change this fraction (a great advantage for the Digital Subscriber Line DSL technologies) are impressive but is not likely to reach parity in the near future (6 to 10 years).

The group based on the "air-transmission" is currently used for providing the basic (temporary) telephone connection for the new builds. Due to the narrow communication bandwidth, this group is not well-suited to broadband services and there are not many arguments for a future mass spreading.

The long-term solution for the communication systems is the group of PONs mainly because of their potential “infinite” bandwidth. For silica optical fibers a low attenuation over a 0.2 μm wavelength interval, centred on 1.55 μm , leads to a workable bandwidth of 25 THz ! Not many years ago, such a bandwidth was considered as impossible to fill up.

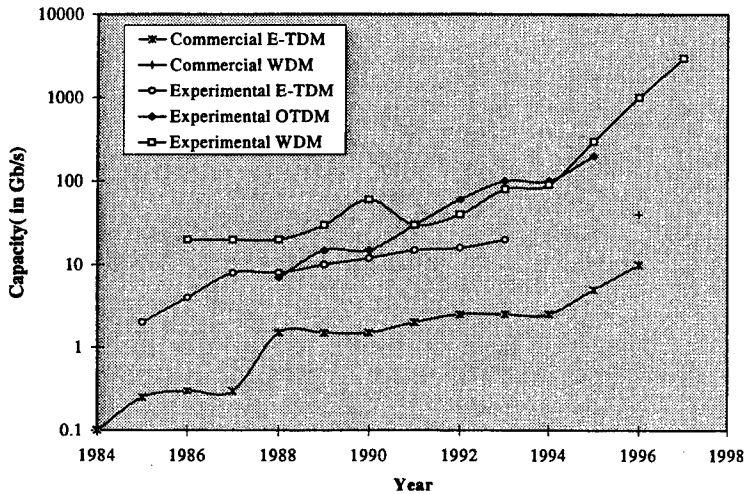


Figure 3. The optical networks evolution.

The PON's transmission capacity in time is having a spectacular evolution (see Figure 3). However, The difference between the experimental and commercial systems are of the order of 6-7 years. The PONs commercially available are (in the major part) TDM-based and the downstream/upstream services are rather narrowband based. This fact is due to the (still) low mass diffusion of the broadband applications and the availability of low-cost components. However, the currently TDM PON systems will migrate [3], in time, versus the pure WDM systems (passing through a hybrid TDM/WDM phase) as in Figure 4. This figure presents a WDM-based system in which an Optical Cross Connect unit (OXC) assures a higher connectivity to the network, a dispersion compensation circuit (eventually integrated on an optical chip), a monitoring system and an Optical Network Unit (ONU) based on filters and reflectors, are the new units to elaborate. Each of these units/circuits/components will be available in an optical integrated version (monolithic or hybrid).

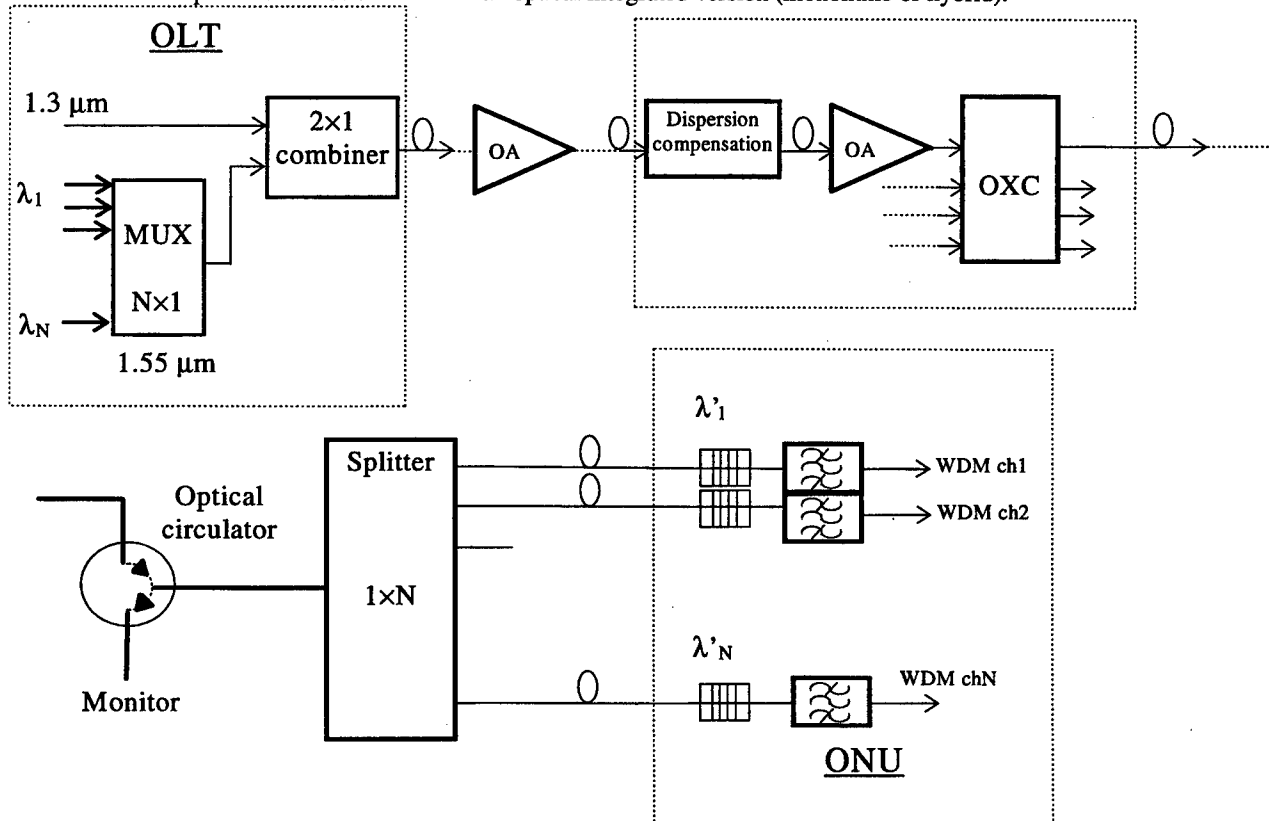


Figure 4. The WDM-based PON architecture.

TABLE I Current access technologies

Access type ^{*)}		Transmission medium	Transmission speed	Typical applications	Cost	Comments
DSL	ADSL	twisted pair	1.5-51Mb/s	telephony, video-on-demand (VoD), computer data	low	use the existing plant
	SDSL	twisted pair	<500Kb/s	telephony, video-on-demand, computer data	low	use the existing plant
HFC		fiber+coax	30Mb/s (downstream) <10Mb/s (upstream)	telephony, CATV, digital video, data	medium	use the existing plant, uses frequency division multiplexing
SDV		fiber, coax, twisted pair	<1Gb/s	telephony, broadcast video, VoD, data	expensive	baseband digital transmission the high speed segment is between central unit and ONU
PON		fiber	"infinite"	telephony, broadcast video, VoD, data, entertainment	medium	long-term solution
MMDS		air	-	broadcast video, VoD, data, entertainment	expensive	covers a radius of 25-30 km no upstream capabilities; combine with ADSL)
LMDS		air	<40Mb/s	broadcast video, VoD, data, entertainment	expensive	smaller coverage than MMDS
DBS		satellite	<40Mb/s	broadcast video, VoD, data, entertainment	expensive	broad coverage
***		air	<5Gb/s	broadcast video, VoD, data, entertainment	expensive	

^{*)} DSL - digital subscriber line; ADSL - asymmetric digital subscriber line; SDSL - symmetric digital subscriber line; HFC - hybrid fiber-coax; SDV - switched digital video; PON - passive optical network; MMDS - multichannel multipoint distribution service; LMDS - local multipoint distribution service; DBS - direct broadcast satellite.

TABLE II Typical speed specifications for demultiplexers

Parameter	AT&T	PIRI	Alberta
No. of channels	8	32	60
Center wavelength λ_0	1.550 nm band	1.550 nm band	1.550 nm band
Temperature stability / sensitivity	± 0.5 dB (+4+70 °C) / <0.1 nm	≤ 0.5 dB (+0+60 °C) / -1.4GHz/ °C	-
Optical insertion loss	<10dB (optical fiber excluded)	7-9dB (fiber-to fiber)	18.6-29.8dB (fiber-to fiber)
Optical crosstalk	-25dB	-25dB	-9dB
3dB bandwidth	>0.9nm	40% of channel spacing	0.09nm
20dB bandwidth	<2.2nm	~ the channel spacing	-
Polarization sensitivity	<0.07nm	< ± 0.05 nm	-
Polarization dependent loss	1.0 dB	0.3dB	-
Return loss	<22dB	≥ 40 dB	-

4. OPTICAL INTEGRATED DEVICES AND CIRCUITS FOR GUIDED OPTICAL COMMUNICATIONS

4.1. Optical integrated de/multiplexers

Many principles have been proposed and reported for the implementation of this function. The most interesting, as far, is the solution based on PHASed-Arrays (PHASAR), also called Arrayed Waveguide Gratings (AWG). The typical configuration is depicted in the Figure 5 and typical commercial specifications are presented in the Table II.

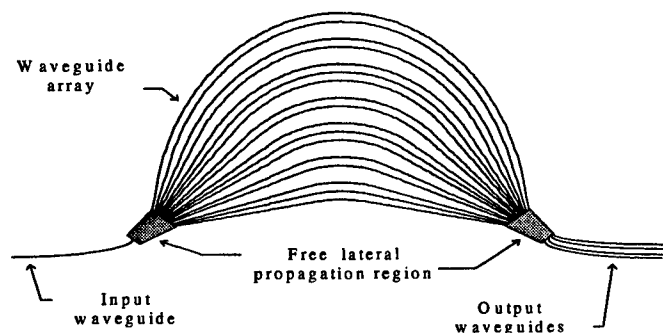


Figure 5. Schematics of a PHASAR demultiplexer.

Devices reported up-to-day are mainly silica or InP-based structures. The silica-based devices have less possibilities to integration (due to the large size) and limited potential of active devices too. The InP devices are more suited to integration and, despite the fiber coupling difficulties and propagation losses, the total loss remains acceptable [4].

The design of these structures is concentrated on the improving of the following parameters:

- the insertion loss of the central channel is due, in the major part, to the undesired diffraction on the higher diffraction orders. This effect is attenuated by a reduced spacing of the waveguides in the output aperture zone (easier for InP, which has a better confinement of the modal field and, thus, a reduced coupling); however, the best results reported on semiconductors are of the order of 2 dB [4];
- the bandwidth comes from the overlapping of the modal field (of the output waveguides) with the focal field of the PHASAR; the 1dB bandwidth is about $0.31 \cdot \Delta f_{ch} = 31\text{GHz}$ for the channel spacing $\Delta f_{ch} = 100\text{GHz}$ (ITU recommendations);
- the flattened response can be obtained using multimode output waveguides, shaping the phase transfer or using a MMI device for a "camel-shaped" propagating field [5];
- the channel crosstalk has multiple sources; actually, the crosstalk is limited not by design but by technological imperfections;
- the polarization dependence is due to the different propagation constants for TE-TM polarizations; in InP, because the waveguide has a stronger asymmetry birefringence, this effect is more evident than in silica-based devices. The polarization dependence is corrected by an adequate channel waveguide design, by the order matching technique (m-th TE coincides with m-1-th TM), using a halfwave plate (excellent method but with technological complications) or using a polarization splitter (in input, causing an initial relative shift).

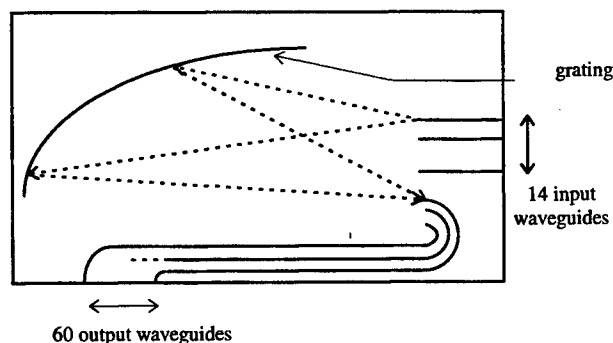


Figure 6. Concave-grating demultiplexer.

An interesting demultiplexer is the concave grating-based [6]. The principle is illustrated in the Figure 6 and the specifications are presented in the Table II. The waveguides were realised in $\text{SiO}_2/\text{SiON}/\text{SiO}_2$ on a Si substrate by Reactive Ion Etching (RIE). The concave grating is designed for the 75-th order of diffraction. The 60 WDM channels achieved in this manner are a demonstration of the advantages of microoptics, even if the actual performances are not competitive with the silica devices. Those remain the most widely studied, produced and used in this moment but, with a promising future, seems to be interesting the InP version, especially for the large level of integration.

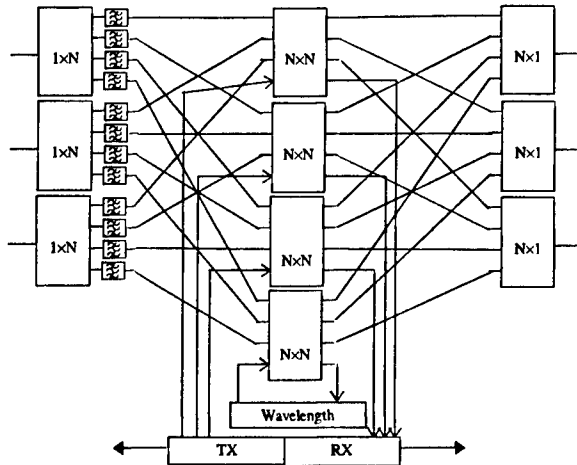


Figure 7. The schematics of an optical cross connect unit

and, simultaneously, impose supplementary requirements for the adjacent devices (e.g., for the filters - their crosstalk and transfer function shape [7]).

The various and frequent reports on implementations of the optical switching elements are a good indication about the interest gravitating around them. The Table III gives us an idea about the optical switches technologies [7].

TABLE III Implementations of guided optical switching devices.

laboratory	material	switching ^{*)}	in×out	size [mm ²]	insertion loss [dB]	crosstalk [dB]	drive
AT&T	Ti:LiNbO ₃	EO-DC	8×8	-	9	-22	9.4V
Ericsson	Ti:LiNbO ₃	EO-DOS	8×8	80×15	14.6	-15.5	±105V
NTT	Si/SiO ₂	TO-MZI	16×16	72×88	17.5	-17.3	0.46W
Akzo Nobel	polymer	TO-DOS	8×8	80×65	10.7	-	92mW
NEC	GaAs/AlGaAs	EO-DC	4×4	17×1.4	1.6 (fiber coupling not included)	-	13.5V
Alcatel	InP/InGaAsP	CI-DOS	4×4	20×2.25	<15	-12	-
ETHZ	InP/InGaAsP	EO-MZI	2×2	20×5	5	<-15	4.5V
NTT	GaAs/InGaAs	SOAG	4×4	1.2×1.7	0	<-30	16mA
Ericsson	InP/InGaAsP	SOAG	4×4	6.7×3.0	0	-30	50mA
Ericsson	InP/InGaAsP	SOAG	4×4	6.7×3.0	<2	-	32mA
Delft	InP/InGaAsP	EO_MZI	2×2	8×2	5.5	-26	6.5V
Bell	Ti:LiNbO ₃		4×4	80×8	12	-16	48V

*) EO - electro-optic; DC - directional coupler; DOS - digital optical switch; TO - thermo-optic; CI - carrier injection; MZI - Mach-Zehnder interferometer; SOAG - semiconductor optical amplifier gate.

From the integration point of view (see the size column) the differences between the listed switches are important.

Considering implicit the presence of optical amplifiers in these systems, the insertion loss column becomes less critical than the crosstalk one. The crosstalk requirements must be as restrictive as possible (since a repeated pass through the switch is always possible). Regarding this parameter, the best switches are the matrices of SOAG and EO-MZI in InP/InGaAsP.

4.3. Guided optical tunable filters.

The future pure WDM transmission, previously exposed in Figure 4, assigns the task of the channel demultiplexing to a filter placed in the optical network unit (ONU), practically in the subscriber's equipment. The correct reception of a WDM channel will occur when the optical filter isolates the desired channel and filters out all others. The Table IV lists the current optical filters together with their characteristics [8].

A future circuit which will require a high level of integration is the OXC unit. As the Figure 4 showed, this circuit will be essential for the future optical access network. It allows to manipulate the distribution of the information carried over the optical fiber: the wavelength routing, the channel removal (drop) and the channel addition (add). Apart from the input splitters and the output star-coupler (which can be an AWG), such a circuit needs (Figure 7), also, the integration of optical filters, switching modules and interfacing with electronics (data and commands).

4.2. Optical switching devices

Used in present only in TDM PONs, the optical switching devices could become a necessity for the OXC units in the future, as we mentioned above. Their characteristics are: the insertion loss, the optical bandwidth, the crosstalk, the input power dynamic range, the polarization dependence, etc. The particular position of an optical switch in an OXC gives more weight to some of these characteristics

TABLE IV Achievable characteristics for tunable optical filters

Filter type	No. of resolvable channels in the 200nm bandwidth	Tuning time	Attenuation at peak [dB]
Fiber Fabry-Perot	100	1ms	1
Fabry-Perot Interferometer	100	1ms	3
Mach-Zehnder Interferometer chain	128	1ms	5
Acousto-optic double wedge	600	2 μ s	9
Bulk acousto-optic	22	3 μ s	5
Acousto-optic Polarization Beam Splitter	90	6 μ s	3
Electro-optic Polarization Beam Splitter	80	0.1 μ s	4
Switched gratings	70	0.1 μ s	5

Considering the low attenuation interval for the silica optical fiber (i.e., 1545-1565 nm) and a channel spacing of 100 GHz (according to ITU recommendations), the optical filters must do a tuning over 200 nm and must have a bandwidth greater but close to the channel width (0.8 nm). The major part of the filters listed fulfils these requirements.

4.4. The system monitoring feature

The use of a part of the optical amplifiers' bandwidth to implement the monitoring feature of the WDM system was a consequence of the particular gain shape (see Figure 8). The left part, strongly not-uniform, is not used for transmissions and thus, can be used for various tests (the continuity, estimations on attenuation, chromatic dispersion, etc.). With a fiber grating carefully designed and realised, a "flat" gain can be obtained. In addition, according to a recently reported optical fiber amplifier [9], the gain can be obtained over a 52nm bandwidth (instead of the "classical" 30nm). In the cases with a large number of channels (more than 60), when all the flat band is used, an adjacent one can be allocated to these services.

The monitor channels are launched in OLT together with the downstream channels, then reflected on the correspondent gratings at ONU and deviated by the optical circulator to the monitoring system.

5. REFERENCES

1. K.C. Kao, G.H. Hocham, "Dielectric fiber surface waveguides for optical frequencies", *Proceedings IEE*, Vol.113, No. 7, pp1151-1158, 1968;
2. G. Oliveti, "Laser ibrido a cavita esterna H-DBR: Applicazioni a basso costo per la rete di accesso", *Dispositivi a reticolo in fibra ottica per applicazioni in sistemi WDM e OTDM -Technical Seminar*, pp. 40-48, Torino- June 1997;
3. F.M. Fenton, J.D. Sipes, "Architectural and technological trends in access: an overview", *Bell Labs Technical Journal*, pp.3-9, Summer 1996;
4. M.K. Smit, C. Dam, "Phasar-based WDM-devices: principles, design and applications", *IEEE Journal of selected topics in quantum electronics*, Vol. 2, No. 2, pp. 236-250, June 1996;
5. H. Uetsuka, L.J.Mara, K. Akiba, K. Morosawa, H. Okano, S. Takasugi, K. Inaba, "Recent improvements in arrayed waveguide grating dense wavelength division multi/demultiplexers", *Proceedings of ECIO '97*, pp. 76-79;
6. Z.J. Sun, K.A.M. Greer, J.N. Broughton, "Integrated concave grating WDM demultiplexer with 0.144nm channel spacing", *Electronics Letters*, Vol. 33, No. 13, pp. 1140-1142, June 1997;
7. M. Gustavsson, L. Gillner, C.P. Larsen, "Network requirements on optical switching devices", *Proceedings of ECIO '97*, pp. 10-15;
8. P.E. Green, "Tunable filters", *Fiber optic networks*, Prentice Hall, New Jersey, pp. 101-152, 1993;
9. H. Masuda, S. Kawai, K.I. Suzuki, K. Akida, "Wideband, gain-flattened, erbium doped fibre amplifiers with 3 dB bandwidth of >50nm", *Electronics Letters*, Vol. 33, No. 12, pp.1070-1072, June 1997.

Optical properties of polycrystalline $\text{In}_x\text{Ga}_{1-x}\text{Sb}$ ($x=0.20$) over 15-30 μm

¹Cristiana E. A. Grigorescu, ²S. A. Manea, ³Michaela Logofatu, ³I. Munteanu,
³B. Logofatu, ⁴Mihaela Calin, ⁴Mihaela Radu, ²M.F. Lazarescu

¹Institute of Optoelectronics, Bucharest, PO Box MG-22, 76900 Romania

²National Institute of Material Physics, Bucharest, PO Box MG-7, 76900 Romania

³Condensed Matter Department, University of Bucharest, PO Box 15-105, Bucharest, Romania

⁴National Institute of Optoelectronics, Bucharest, PO Box MG-22, 76900 Romania

ABSTRACT

This paper reports on the optical properties of polycrystalline p-type $\text{In}_x\text{Ga}_{1-x}\text{Sb}$ ($x=0.20$) over the wavelength range 15-30 μm , at room temperature. The material was obtained by direct synthesis from the elements and rapidly crystallized following a particular temperature regime. Transmittance and reflectance measurements were performed at room temperature by using a SPECORD M80 spectrophotometer. From the resulted values we calculated the absorption coefficient α as a function of the photon energy. Considerations are made concerning the peculiarities involved by the polycrystalline structure and the surface imperfections on the absorption phenomena over the mentioned wavelength range.

Keywords: *InGaSb, ternary compound, polycrystalline structure, optical properties, IR absorption coefficient*

1. INTRODUCTION

The actual trends in quantum optics and optoelectronics are claiming for special materials, among which the semiconductors, either as binary or ternary compounds, represent a particular group.

Tailoring gap III-V semiconductor compounds are of major interest for various optoelectronic devices and that is why a key point for the device development stays in the optical and electrical properties of the starting materials.

In this respect, in our former works^{1,2} we estimated that polycrystalline $\text{In}_x\text{Ga}_{1-x}\text{Sb}$ ($x=0.20$) (InGaSb) with highly uniform composition would find applications as photovoltaic (PV) infrared (IR) detectors and substrates for various heterostructures. Our prediction has been successful, taking into account that recent research³ on InAs/GaSb superlattices (SL) IR detectors demonstrate the particular value of $\text{In}_x\text{Ga}_{1-x}\text{Sb}$ in the design of these devices.

This paper deals with the study of the peculiarities of the optical properties of $\text{In}_{0.20}\text{Ga}_{0.80}\text{Sb}$ over 15-30 μm at room temperature, mainly of absorption, accounting for the results² obtained for the optical coefficient behavior within the range 3-14 μm too. In our former work² we supposed that the diffuse absorption edge around 5 μm could be attributed to the high content in gallium⁴ of this compound; the absorption measurements were extended towards lower photon energy values to put into evidence various absorption mechanisms involved.

2. EXPERIMENTAL

The ternary compound $\text{In}_{0.20}\text{Ga}_{0.80}\text{Sb}$ was obtained by direct synthesis from the elements and the rapid crystallization followed an original thermal regime². Structural characterisation of the polycrystalline ingots was performed by Neutron Activation Analysis and X-ray diffraction using the Vegard rule approximation^{2,4}. A highly uniform composition in respect of the ingot length was found.

The Hall - effect measurements revealed a p - type material, with an average acceptor concentration of $2 \times 10^{18} \text{ cm}^{-3}$ and a band gap value of 0.548eV at 300K.

Samples of polycrystalline $\text{In}_{0.20}\text{Ga}_{0.80}\text{Sb}$ 3mm in thickness and 11mm in diameter were chemically polished in a CP - 4 mixture. Transmission and reflection measurements were carried out at room temperature by using a SPECORD M 80 spectrophotometer. The corresponding curves of transmissivity and reflectivity over the wavelength range 15-30 μm are shown in Fig. 1.

With the values in Fig.1 we calculated the absorption coefficient as a function of the photon energy within the wavelength range 15 - 30 μm . To make a better idea about the absorption phenomena arising in the investigated ternary compound a plot of the absorption spectrum over the extended range 3 - 30 μm is shown in Fig.2

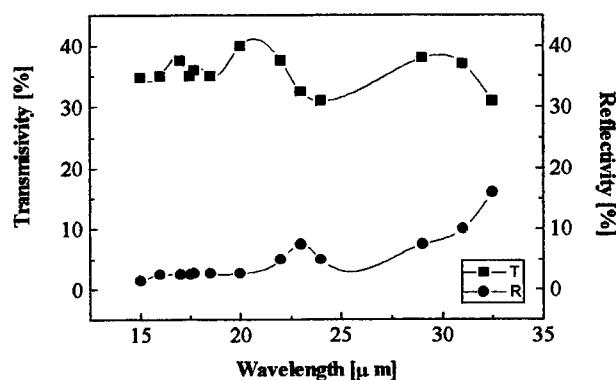


Fig. 1 Transmission and reflection spectra of $\text{In}_{0.20}\text{Ga}_{0.80}\text{Sb}$ at 300K

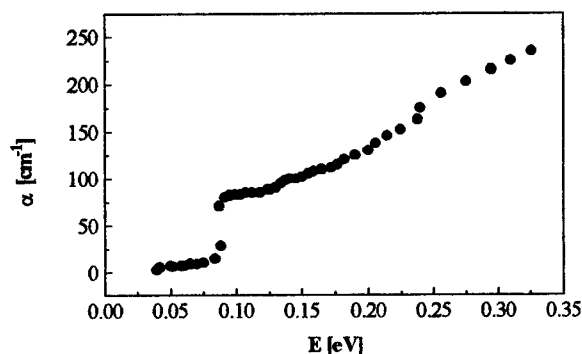


Fig. 2 Absorption spectrum of $\text{In}_{0.20}\text{Ga}_{0.80}\text{Sb}$ at 300 K

One should observe that polycrystalline $\text{In}_{0.20}\text{Ga}_{0.80}\text{Sb}$ exhibits more intensive absorption at higher photon energy as well as an absorption step around 15.5 μm . The very diffuse absorption edge around 5 μm , remarked in our former work², is put into evidence too, which might be explained by the occurrence of different absorption mechanisms.

The next section provides some fundamental data on the energy band structure of InGaSb and possible occurring absorption mechanisms over the IR range.

A discussion on the absorption and reflection spectra of polycrystalline $\text{In}_{0.20}\text{Ga}_{0.80}\text{Sb}$ in order to make clear the influence of the material structure on its optical properties will follow.

3. FUNDAMENTALS ON InGaSb

A review of fundamental data regarding the energy band structure of $\text{In}_x\text{Ga}_{1-x}\text{Sb}$ is strictly necessary to enable the explanation of the experimental results obtained for some optical properties of the material with $x=0.20$.

The III - V ternary compounds, e.g. $\text{In}_x\text{Ga}_{1-x}\text{Sb}$, have a band structure very similar to the binary compounds. A difference is found in the variation of the characteristic parameters of the energy bands with the composition parameter x , which is continuous, while for the binary compounds it is discrete⁵. $\text{In}_x\text{Ga}_{1-x}\text{Sb}$ has an energy band

structure very close to those of InSb and GaSb - the binary compounds from which it originates: the maximum of the valence band is found at $\mathbf{K}=0$, the band splitting into two branches (excepting for the spin) with the maxima being in the Brillouin zone center. Most important information concerning a ternary semiconductor compound refers to the dependence of the energy gap on the composition parameter x , plotted in Fig. 3

The simplest and most direct method to check the band structure of semiconductors consists in measurements of the absorption spectra.

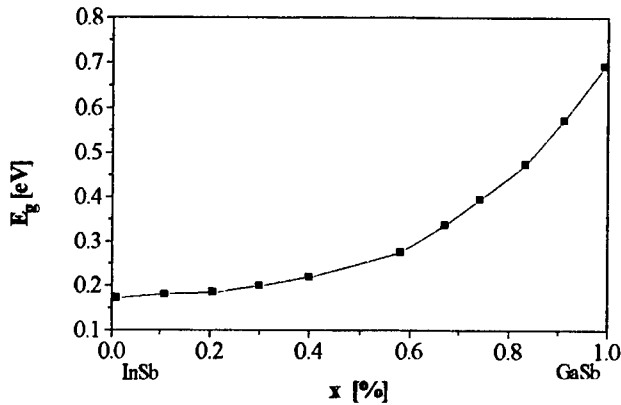


Fig. 3 The dependence of the energy gap of InGaSb on the composition parameter x at room temperature

In what follows some absorption mechanisms, the occurrence of which might be assessed for our material, are briefly mentioned with the aim to open a pertinent discussion on the basis of the experimental data regarding $\text{In}_{0.20}\text{Ga}_{0.80}\text{Sb}$.

The first mechanisms to be considered is the fundamental absorption, which refers to band-to-band or to exciton transitions. Because the momentum of a photon is very small in comparison with the crystal momentum, the photon-absorption process should conserve the electron momentum. The absorption coefficient is given by:

$$\alpha(h\nu) = A \sum P_{ij} n_i n_j,$$

where $h\nu$ is the photon energy, P_{ij} - the probability of transition from the initial state (i) to the final state (j); n_i and n_j - the density of electrons in the initial state and of available final state, respectively.

For simplicity it is assumed for an undoped semiconductor at 0 K that the states in the valence band are all empty.

Between two direct valleys where all the momentum-conserving transitions are allowed, the transition probability does not depend on photon energy. A rapid rise in absorption is observed in the spectrum and the absorption coefficient has values of the order 10^4 and even higher.

Data about GaSb rich alloys such as $\text{In}_x\text{Ga}_{1-x}\text{Sb}$ ($x=0.20$) make witness of a complicated behavior of the band gap⁵, most probably caused by the very short distance between the conduction band minima $\Gamma_{111\frac{1}{2}}$ ($\mathbf{K}=0$ valley) in GaSb and by an ordering effect characteristic to the mentioned alloys.

4. DISCUSSION AND CONCLUSIONS

From the electromagnetic theory of light arises that the reflectivity R for normal incidence may be written as⁶:

$$R = \frac{(n-1)^2 + \frac{\lambda^2}{16\pi^2} \alpha^2}{(n+1)^2 + \frac{\lambda^2}{16\pi^2} \alpha^2} \quad (1)$$

where n is the refractive index of the material, α - its absorption coefficient and λ the radiation wavelength. From eq. (1) it follows the proportional increase of the reflectivity with the absorption coefficient. When comparing the reflection spectrum in Fig.1 with the absorption one over the corresponding wavelength range in Fig.2, it obviously results that eq.(1) does not holds for the polycrystalline material investigated in this work. To make an appropriate interpretation, one should keep in mind that the absorption coefficient is actually a combination of partial absorption coefficients, corresponding to absorption centers of various nature, each with its own effective cross section, which depends, among others, on the photon energy. Concerning the optical absorption of the bulk ternary compound $\text{In}_{0.20}\text{Ga}_{0.80}\text{Sb}$ it should be accounted for both structural defects and impurity content when analyzing the spectra in Figs. 1 and 2. The grain boundaries exhibited by the polycrystalline structure as well as the imperfection of the sample surface might explain the low reflectivity values for an increasing absorption coefficient by the radiation scattering over the mentioned defects.

Over the wavelength range 3 - 30 μm it is no question to claim for intrinsic (fundamental) absorption at 300 K; it could take place only below 2.6 μm taking into consideration the connection between photon energy and energy gap of the material, which in our case is 0.548 eV:

$$\frac{hc}{\lambda} \geq E_g \quad (2)$$

At higher photon energy radiation absorption by free carriers takes place via lattice field and scattering by optical vibrations and impurity ions should be considered too in regards of the behavior of absorption coefficient of polycrystalline $\text{In}_{0.20}\text{Ga}_{0.80}\text{Sb}$ over 0.10 - 0.24 eV.

The absorption of radiant energy by free charge carriers is caused by the electric field of the radiation wave, the energy of which is converted into Joule heat; thus the absorption coefficient in this case is proportional to the electrical conductivity σ of the material⁷:

Actually, the transition of the free carriers from an energy level to another is entailed by the absorption of the radiant energy. Therefore the scattering mechanisms on grain boundaries and lattice defects should be considered when setting the dependence type of absorption coefficient on the wavelength as it is shown in Fig. 2.

For an electrically active impurity the absorption spectrum may be observed under very low temperature conditions when the free charge carriers are "frozen" on the impurity level. Since our measurements were carried out at room temperature only, no comment can be done in this respect. Although a rough estimation might be obtained if taking into account our Hall-effect measurements formerly performed⁴ at liquid nitrogen temperature: the free acceptor concentration at 77 K is by one magnitude order lower than at 300K and therefore a diminishing of the absorption coefficient should be expected in the lower temperature range.

5. REFERENCES

1. C. Grigorescu, A.S. Manea, M. Logofatu, M. Cruceru, B. Logofatu, M.F. Lazarescu, "Structural characterization of $\text{In}_x\text{Ga}_{1-x}\text{Sb}$ ternary compound bulk crystals", *Optoelectronica*, **2**(4), 31-34 (1994)
2. A.S. Manea, I. Munteanu, C. Grigorescu, M.F. Logofatu, M.F. Lazarescu, "On the uniform composition of $\text{In}_x\text{Ga}_{1-x}\text{Sb}$ ($x=0.20$) bulk crystals for special optoelectronic devices", *Opt. Eng.* **35**(5), 1356-1359 (1996)
3. *** Fraunhofer Institut für Angewandte Festkörper Physik - Freiburg, Germany, *Annual Report*, 1996
4. A.S. Manea, I. Munteanu, M. Logofatu, M.F. Lazarescu, M. Cruceru, C. Grigorescu, " $\text{In}_x\text{Ga}_{1-x}\text{Sb}$ of highly uniform composition", *IEEE-ISC CAS'95*, 297-300, Sinaia 1995
5. D. Long, *Semiconductor and Semimetals*, Vol. 1, p.145, Academic Press, New York, 1966
6. A. Anselm, *Introduction to Semiconductor Theory*, MIR Publishers, Moscow, 1981
7. P.S. Kireev, *Semiconductor Physics*, p. 515, MIR Publishers, Moscow, 1974

Verifying model for statistical hypotheses in detection of noncoherent radiation

*V. Babin, *S. Ersen, *A. Moldovan, **N. Iftimia

* National Institute for Research & Development for Optoelectronics INOE 2000
Bucharest 76900, P.O.BOX MG22, Romania,
** Military Research and Development Institute
Bucharest, Romania

ABSTRACT

A model of quantic detection for noncoherent optical radiation at noise limit is presented. Using the representation on coherent state of density matrix operators (ρ) and of detection operators (π), the detection probability (Q_d), false alarm probability (Q_o) and signal - noise ratio (S/Z), are estimated, as function of the number of freedom degrees of temporal oscillation modes (M_t) and of the spatial oscillation modes (M_s). A validation algorithm of statistical hypotheses, resulted from noncoherent optical field analysis, is made using Neyman -Pearson criterion.

Keywords: quantic detection, noise limit, statistical hypotheses

1. INTRODUCTION

The aim of the paper is to build a algorithm for the detection and characterisation of the non-coherent (thermal) optical field, at the noise limit. Using the specific instruments of the quantum mechanics, we get more "analytical transparency" when characterising the thermal field. We decompose the electromagnetic field on temporal modes and space normal modes, as follows:

$$\begin{aligned}\vec{B}(\vec{r}, t) &= \sum_k q_k(t) \cdot \vec{\nabla} \times \vec{U}_k(\vec{r}) \\ \vec{E}(\vec{r}, t) &= -\sum_k P_k(t) \cdot \vec{U}_k(\vec{r})\end{aligned}\quad [1]$$

We attach to a normal mode of oscillation the concept of quantum harmonic oscillator, by quantifying the electromagnetic field in the Hilbert space (H_S) of the "number of particles" eigen vectors ($|n\rangle$), by using creation (C_k^+), and annihilation operators (C_k^-), which leave invariant the space (H_S).

We use the property of thermodynamic equilibrium of the optical field with the matter and we suppose that the detection is made by means of a very narrow bandwidth filter (detection of an almost-monochromatic radiation) and a polariser, for the selection of a linearly polarised radiation. In this case the field operator takes the form:

$$\hat{\phi}(\vec{r}, t) = \sqrt{\frac{1}{2}} \hbar \Omega Z_0 \sum \hat{C}_{pm}^- \cdot \eta_p(\vec{r}) \cdot \vec{g}_m(t) e^{-i\Omega t} \quad [2]$$

where: (Ω) (the mid-frequency of the optical filter;

(Z_0) = $\sqrt{\frac{\mu}{\epsilon}}$ \rightarrow the impedance of the propagation medium;

($\vec{g}_m(t), \eta_p(\vec{r})$) (the eigen - function associated with temporal and space modes

The correlation function has the expression:

$$\Gamma(\vec{r}_1, \vec{r}_2; t_1, t_2) = \frac{2}{Z_0} T_r \left[\hat{\varphi}^-(\vec{r}_2, t_2) \hat{\rho} \hat{\varphi}^+(\vec{r}_1, t_1) \right] \quad [3]$$

From [3] it results that on the surface (A) of the reception aperture, and during the time of irradiating the detector (0, T'), we have:

$$C_{pm}^{\wedge-} = \frac{1}{\sqrt{\frac{1}{2} h \Omega Z_0}} \int_0^{T'} \int_A \eta_p^*(\vec{r}) g_m^*(t) e^{i \Omega t} \cdot \hat{\varphi}^-(\vec{r}, t) \cdot d^2 \vec{r} \cdot dt \quad [4]$$

where: $d^2 r = dx \cdot dy$;

By putting the condition of thermodynamic equilibrium for the thermal field:

$$T_r \left[\hat{\rho} \hat{\varphi}^-(r, t) \right] = 0 \quad [5]$$

it results:

$$T_r \left[\hat{\rho} \hat{C}_{pm}^{\wedge-} \right] = 0 \quad [6]$$

In accordance with Helstrom¹ and Glauber⁴ we obtain:

$$\Gamma(\vec{r}^{\rightarrow}_1, \vec{r}^{\rightarrow}_2; t_1, t_2) = \Gamma_1(\vec{r}^{\rightarrow}_1, \vec{r}^{\rightarrow}_2; t_1, t_2) + \Gamma_0(\vec{r}^{\rightarrow}_1, \vec{r}^{\rightarrow}_2; t_1, t_2) \quad [7]$$

where: (Γ_1) (the correlation function of the thermal field subject to detection)
 (Γ_0) (the correlation function of the background radiation)

We define the elements of the correlation matrix, taking into account [7]

$$\varphi_{pm, qn} = T_r \left[\hat{C}_{pm}^{\wedge-} \hat{\rho} \hat{C}_{qn}^{\wedge+} \right] = \varphi_{pm, qn}^{(1)} + \varphi_{pm, qn}^{(0)} \quad [8]$$

When detecting a monochromatic radiation, it results:

$$\Gamma_1(\vec{r}^{\rightarrow}_1, \vec{r}^{\rightarrow}_2; t_1, t_2) = \varphi_1(\vec{r}^{\rightarrow}_1, \vec{r}^{\rightarrow}_2) \chi(t_1 - t_2) e^{i \Omega(t_1 - t_2)} \quad [9]$$

The correlation matrix associated to the signal will have the form:

$$\varphi_{pm, qn}^{(1)} = \left\{ \frac{1}{h \Omega} \int_0^{T'} \int_0^{T'} g_m^*(t_2) \chi(t_1 - t_2) g_n(t_1) dt_1 \cdot dt_2 \right\} \cdot \left\{ \int_A \int_A \eta_p^*(\vec{r}^{\rightarrow}_2) \varphi_1(\vec{r}^{\rightarrow}_1, \vec{r}^{\rightarrow}_2) \eta_q(\vec{r}^{\rightarrow}_1) d^2 \vec{r}^{\rightarrow}_1 \cdot d^2 \vec{r}^{\rightarrow}_2 \right\} \quad [10]$$

The correlation matrix associated to the signal will have the form:

$$\varphi_{pm, qn}^{(0)} = N \cdot \delta_{pq} \cdot \delta_{mn} \quad [11]$$

As the detection of the thermal radiation is made at low signals (at the background radiation limit), we shall look for statistical strategies based on Neyman - Pearson criterion, in order to separate statistical hypotheses (H_0 , H_1), as follows::

$$H_0 : \varphi_{pm,qn} = \varphi_{pm,qn}^{(0)} \quad (\text{only the background radiation is detected})$$

$$H_1 : \varphi_{pm,qn} = \varphi_{pm,qn}^{(0)} + \varphi_{pm,qn}^{(1)} \quad (\text{there are detected the background radiation and the thermal field subject to detection})$$

We associate to these two statistical hypotheses (H_0 , H_1), the density matrix operator ($\rho_0^\wedge, \rho_1^\wedge$) and the detection operator (Π^\wedge).

We define the detection probability:

$$Q_d \stackrel{\text{Def.}}{=} P_r[H_1 | H_1] = T_r[\rho_1^\wedge \Pi^\wedge] \quad [12]$$

and the false alarm probability:

$$Q_0 \stackrel{\text{Def.}}{=} P_r[H_1 | H_0] = T_r[\rho_0^\wedge \Pi^\wedge] \quad [13]$$

From [11] can notice that the average number of photons emitted by background in (N). The average number of photons emitted by the target subject to detection, shall be:

$$N_s = \frac{1}{h\Omega} \int_A \int_0^{T'} I(\vec{r}, t) d^2\vec{r} \cdot dt \quad [14]$$

where:

$$I(\vec{r}, t) = \Gamma(\vec{r}, \vec{r}; t, t)$$

2. THE INFLUENCE OF SPACE AND TEMPORAL COHERENCE ON EFFICIENCY CHARACTERISTIC

We associate to the thermal field a Hilbert space (H_s) of eigen -vectors ($|v_{pm}\rangle$) where (v_{pm}) is the number of photons in the space mode (p) and temporal mode (m).

We also shall have:

$$(C_{pm}^{\wedge-}, C_{pm}^{\wedge+}) : H_s \rightarrow H_s \quad [15]$$

We define in the Hilbert space (H_s) the ortonormalization relation:

$$\sum_{v_{pm}} \left(\prod_p \prod_m |v_{pm}\rangle \langle v_{pm}| \right) = I^\wedge \quad [16]$$

(ρ = the unity operator defined in (H_s))

Using [15], on (H_S) we build the eigen-value equation:

$$\hat{C}_{pm}^+ \hat{C}_{pm}^- |v_{pm}\rangle = v_{pm} |v_{pm}\rangle \quad [17]$$

The probability of detection of (v_{pm}) photons in the space-temporal mode (p, m) in the case of the two hypotheses (H_0, H_1) has the form (the thermal field being considered as a set of quantum harmonic oscillator at the equilibrium):

$$H_k : P_k(\{v_{pm}\}) = P_r(\{v_{pm}\} | H_k) = \prod_p \prod_m P_{pm}^{(k)}(v_{pm}) \quad [18]$$

for: $k = 0, 1$;

where:

$$P_{pm}^{(k)}(v) = [1 - v_{pm}^{(k)}] \cdot [v_{pm}^{(k)}]^v \quad k = 0, 1$$

$$v_{pm}^{(k)} = \frac{N_{pm}^{(k)}}{1 + N_{pm}^{(k)}} \quad k = 0, 1$$

[19]

For the two statistical hypotheses, we have ²:

$$H_0 : N_{pm}^{(0)} = N;$$

$$H_1 : N_{pm}^{(1)} = N + h_p \chi_m N_S$$

[20]

One can notice that $(N_{pm}^{(0)})$ and $(N_{pm}^{(1)})$ are the diagonal elements of the correlation matrix, in the case of the two statistical hypotheses ¹; (χ_m, h_p) (are eigen values for temporal and spatial mode) In accordance with the Neyman-Pearson criterion, we define the plausibility ratio:

$$\Lambda(\{v_{pm}\}) \stackrel{Def.}{=} \prod_p \prod_m \frac{P_{pm}^{(1)}(v_{pm})}{P_{pm}^{(0)}(v_{pm})} \quad [21]$$

We also define by (g) the statistic utilised to "separate" the two statistical hypotheses, as:

$$g \stackrel{Def.}{=} \ln \Lambda(\{v_{pm}\}) = \sum_{p,m} \left[v_{pm} \ln \left(1 + h_p \chi_m \frac{N_S}{N} \right) - (v_{pm} + 1) \ln \left(1 + h_p \chi_m \frac{N_S}{1 + N} \right) \right] \quad [22]$$

From [22] one can obtain at the noise limit:

$$N_S \rightarrow 0 \quad [23]$$

the statistics:

$$U \cong \sum_{p,m} h_p \cdot \chi_m \cdot v_{pm} ; \quad [24]$$

We define probability:

$$P_r \left(\{v_{pm} \in W\} | H_0 \right) = \alpha \quad [25]$$

The meaning of [25] is: the probability for number of photons received to belong to a set (W), in the statistical hypotheses (H_0), is equal to (α), who has the threshold of meaning of the statistical test for separating the two statistical hypotheses (H_0, H_1). The value (α) has also the meaning of "the producer's risk", a concept utilised when verifying, in a statistical manner, the reliability parameters. For the separation to be complete, we similarly define the probability³:

$$P_r \left(\{v_{pm} \in W\} | H_1 \right) = 1 - \beta \quad [26]$$

This probability has also the meaning of a "power function" of the statistical test for separating the two statistical hypotheses (H_0, H_1). The value (β) has also the meaning of "the customer risk", a concept used in reliability studies.

The set of values (W) used in [25] and [26] represents "the critical region in the observations space" (of the number of detected photons on the spatial - temporal modes (p,m)).

From [25], [26] and [18] it results that:

$$H_0 : P_0 \left(\{v_{pm}\} \right) = P_r \left(\{v_{pm} \in W\} | H_0 \right) = Q_0 = \alpha ; \quad [27]$$

$$H_1 : P_1 \left(\{v_{pm}\} \right) = P_r \left(\{v_{pm} \in W\} | H_1 \right) = Q_d = 1 - \beta$$

The statistical strategy for separating the two statistical hypotheses consists, in this case, of determining the best regions in observables space (W^*) and so, for any critical region (W), one has:

$$P_r \left(\{v_{pm} \in W^*\} | H_1 \right) \geq P_r \left(\{v_{pm} \in W\} | H_1 \right) \quad [28]$$

if, for a set of measurements (\bar{v}_{pm}) we verify the statistical hypotheses (H_0), so the absence of the thermal source:

$$\bar{v}_{pm} = N \quad [29]$$

(\bar{v}_{pm} = the average number of photons detected experimentally) compared to the alternative statistical hypotheses (H_1) of presence of the source of thermal field, then

$$\bar{v}_{pm} > N \quad [30]$$

there exist the most powerful test to validate (separate) these two hypotheses (H_0, H_1). If, in the case of the statistical hypotheses (H_1) there exist:

$$N_{pm}^{(1)} > N_{pm}^{(0)} \quad [31]$$

condition confirmed by [20], it results the most powerful test of separating the hypotheses (H_0, H_1), when there exist:

$$\Lambda(\{v_{pm}\}) > \lambda \quad \left| \quad v_{pm} \in W^* \right. \quad [32]$$

From [22] we obtain:

$$\Lambda(\{v_{pm}\}) \Big|_{v_{pm} = v_{pmc}} = \lambda \quad [33]$$

hence the best critical region for separating the hypotheses (H_0, H_1) has the form:

$$W^* = \{v_{pm} \mid v_{pm} > v_{pmc}\} \quad [34]$$

The set of values (W^*) maximises (Q_d) compared to (Q_0) in the plane of characteristic. It also results:

$$\begin{aligned} P_r(\{v_{pm} > v_{pmc}\} \mid H_1) &= Q_d = 1 - \beta \\ P_r(\{v_{pm} < v_{pmc}\} \mid H_0) &= 1 - \alpha = 1 - Q_0 \end{aligned} \quad [35]$$

3. CONCLUSIONS

The separation algorithm of the statistical hypotheses (H_0, H_1) (and hence the capacity of a detection system to select signals from noise) is completely characterised equation of detection or, equivalently, by the efficiency characteristic $(Q_d = Q_d(Q_0))$. For big values of (μ, N) , the thermal radiation loses the “quantum” statistical character and gets a “classical” statistical character. For instance by, using Poisson distribution, when ⁵:

$$\begin{aligned} \mu N &\gg 1 \\ \mu N + N_s &\gg 1 \end{aligned} \quad [36]$$

the probabilities (P_0, P_1) get a Gaussian character:

$$\begin{aligned} P_0(x) &= \frac{1}{\sqrt{2\pi\mu N}} e^{-\frac{(x - \mu N)^2}{2\mu N}} \\ P_1(x) &\cong \frac{1}{\sqrt{2\pi\mu N}} e^{-\frac{(x - \mu N - N_s)^2}{2\mu N}} \end{aligned} \quad [37]$$

if the plausibility ratio has the value (λ) , from the Neyman - Pearson criterion, it results a threshold::

$$\frac{P_1(X_c)}{P_0(X_c)} = \lambda \quad [38]$$

and hence:

$$X_c = \frac{2\mu N \cdot \ln(\lambda) + [(\mu N + N_s)^2 - (\mu N)^2]}{2\mu N} \quad [39]$$

The best critical region will be:

$$W^*: X > X_c \quad [40]$$

if we write:

$$\Phi(X) = 1 - \text{erfc}(X) \quad [41]$$

$$\text{and:} \quad U_\alpha = \Phi^{-1} = X; \quad \Phi(X) = \alpha \quad [42]$$

it results the decision threshold:

$$X_c = \mu N + (\sqrt{\mu N}) \cdot U_{1-Q_0} \quad [43]$$

Hence, the decision threshold depends only the probability of false alarm and the value of (μN) . Also, from the definition equation for (Q_d) , we obtain :

$$N_s = \sqrt{\mu N} [U_{1-Q_0} + U_{Q_d}] \quad [44]$$

from the "classical limit", knowing that:

$$Q_0 = \alpha = \text{erfc} \left[\frac{X_c - \mu N}{\sqrt{\mu N}} \right] \quad [45]$$

$$Q_d = 1 - \beta = \text{erfc} \left[\frac{X_c - \mu N - N_s}{\sqrt{\mu N}} \right]$$

So we establish an interesting relation for the signal-to-noise ratio:

$$\left(\frac{S}{Z} \right) = \frac{N_s}{\sqrt{\mu N}} = U_{1-Q_0} + U_{Q_d} \quad [46]$$

with characteristics:

$$\begin{aligned}
\left(\frac{S}{Z}\right) \rightarrow 0 &\Rightarrow \begin{cases} Q_0 = Q_d \\ 1 - \beta = \alpha \end{cases} \\
\left(\frac{S}{Z}\right) \rightarrow 1 &\Rightarrow \begin{cases} U_{1-\beta} = 1 + U_\alpha \\ U_{Q_d} = 1 + U_{Q_0} \end{cases} \\
\left(\frac{S}{Z}\right) \rightarrow \infty &\Rightarrow \begin{cases} Q_d = Q_0 \\ 1 - \beta = \alpha \end{cases}
\end{aligned} \tag{47}$$

We conclude that quantities $\left[\left(\frac{S}{Z}\right); Q_0; Q_d\right]$ are the key - parameters when designing the system for detection the thermal field.

4. REFERENCES

1. C.W.Hestrom, *Quantum detection and estimation theory*, Mathematics in science and engineering, Vol. 123, Academic Press, New York, 1976.
2. R.G.Gallager, *Information theory and reliable communication*, New York, 1968.
3. A.J.F. Siegert, "A systematic approach to a class of problems in the theory of noise and other random phenomena", Part II, *Trans IRE*, IT-3, pp. 38-44, 1957.
4. R.J.Glauber, "The quantum theory of optical coherence", *Phys.Rev.* **130** (6), pp. 2529-2539, 1963.
5. V.Babin, *Determinist and stochastic models in stimulated diffusion (Brillouin) and detection of optical radiation*, Doctoral Thesis, Bucharest, 1997.

Characterization of ion exchanged waveguides from near-field measurements

Daniel Pîrcălăboiu¹, Gabriella Motta, Guido Perrone and Ivo Montrosset

Dipartimento di Elettronica - Politecnico di Torino

Corso Duca degli Abruzzi 24, 10129 Torino, Italy

tel. +39-11-564-4146 email: perrone@polito.it

ABSTRACT

The refractive index distribution is a key parameter not only to characterize the technological process but also for any integrated optical simulator. In this paper we propose a new algorithm to reconstruct the refractive index profile from the near-field measurements. The technique is based on the matching of the measured intensity profile with a computed one, varying the maximum index change and the diffusion depth.

Keywords: integrated optics, planar waveguides, near-field measurements, refractive-index profiles

1. INTRODUCTION

The modern integrated optical applications require increasingly complex devices, so to obtain high performances it is necessary to run many simulations whose reliability depends on the accuracy of the model used to describe the waveguide characteristics and in particular the refractive index distribution.

The problem of the determination of the refractive index profile with non destructive techniques has been already addressed in the literature. Among the various solutions proposed, one of the most popular is the Inverse WKB (IWKB) method (such as the version proposed by Chiang [1]) applied to the modal effective indexes measured with the prism coupling setup. However, this method can be applied only to highly multimode waveguides because, to give accurate results, it requires that at least three modes are above the cut-off. The refractive index profile of single mode waveguides - that are also the most interesting for practical applications - is usually reconstructed deriving twice the near field intensity [2]. This method is very sensitive to noise (because the square root operation and the double derivative are "amplifying" the existing noise) so critical and time consuming filtering procedures are necessary.

In this paper we propose a new method to retrieve the refractive index profile and we demonstrate it in planar waveguides obtained by ion exchange.

2. THEORETICAL CONSIDERATIONS

Several fabrication processes for optical waveguiding structures lead to graded refractive-index profiles in the depth direction (Figure 1).

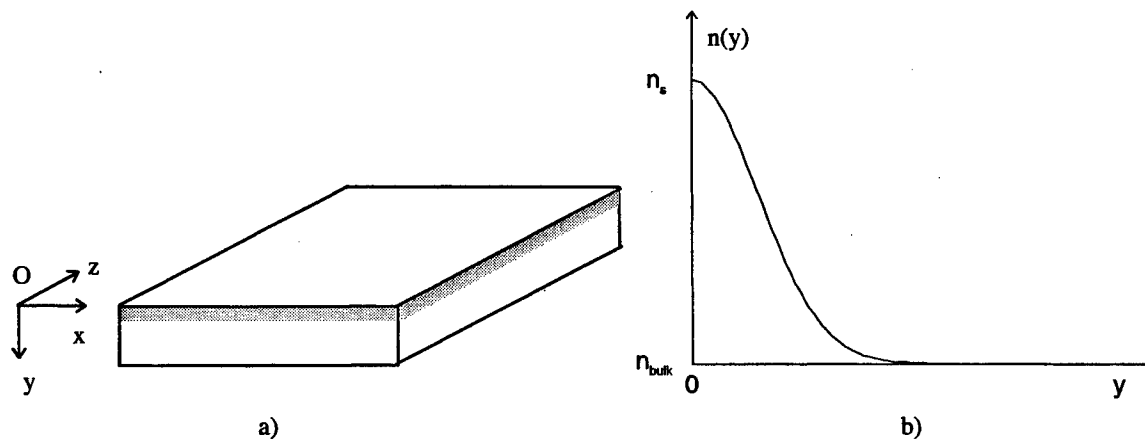


Figure 1. a) The planar waveguide geometry; b) the depth refractive-index profile

¹ Also with TEF Department, "Politehnica" University of Bucharest, Romania.

The wave equation which describes the depth (Oy direction, as depicted in Figure 1a) behavior of TE polarization (E_x component) in the planar waveguide is

$$\frac{d^2 E_x}{dy^2} = (\beta^2 - n^2(y) k_0^2) E_x \quad (1)$$

where β and k_0 are the propagation constants in the waveguide and in the air, respectively.

The refractive-index profile recovery method we propose in this paper is based on the fitting of the measured near-field distribution with a modal field computed from a supposed given refractive index shape with two free parameters. To simplify the modal field numerical evaluation, we assumed that the actual refractive index distribution can be approximated with a function derived from the well-known "1/cosh²" profile so that an analytical solution for the modal field $E_x(y)$ exists [3]. The actual refractive-index profile is an asymmetric one (as in Figure 1b) so we assumed

$$n^2(y) = \begin{cases} 1, & y < 0 \\ n_{bulk}^2 + \frac{2n_{bulk}\Delta n_y}{\cosh^2\left(\frac{2y}{h}\right)}, & y \geq 0 \end{cases} \quad (2)$$

The solution is derived from the exact solutions available for the symmetric "1/cosh²" profile, supposing the correspondence of the symmetric and asymmetric profiles mode orders being $2\nu_{asym} + 1 = \nu_{sym}$ and the zero values of E_x for $y \leq 0$ (in air). For the above refractive-index profile the expression of the modal field is

$$E_x(y) = \begin{cases} 0, & y < 0 \\ \frac{\sinh\left(\frac{2y}{h}\right)}{\cosh^s\left(\frac{2y}{h}\right)}, & y \geq 0 \end{cases} \quad (3)$$

$$\text{where } s = \left(\sqrt{1+V^2} - 1\right)/2, \quad V = k_0 h \sqrt{2n_{bulk}\Delta n_y} \quad (4)$$

The assumption of zero field in air is always checked estimating the field at air-waveguide interface:

$$E_x(0) = \frac{1}{\sqrt{\beta^2 - k_0^2}} \left(\frac{dE_x}{dy} \right)_{y=0} \quad (5)$$

The fitting consists in the maximization of the overlap integral

$$\eta = \frac{\int E_{x,meas}(y) E_x(y) dy}{\sqrt{\int E_{x,meas}^2(y) dy \int E_x^2(y) dy}} \quad (6)$$

by a two-dimensional scanning for the two free parameters Δn_y and h introduced above.

3. THE EXPERIMENTAL SETUP

Several single moded (at $\lambda=633$ nm) planar waveguides have been prepared in commercial soda-lime glasses by immersion in pure KNO_3 melted at 390 °C for 40 minutes. Then the samples have been cut and end face polished to an optical quality.

For the optical waveguide characterization, a He-Ne laser butt coupled to the waveguide with a single-mode fiber is used (Figure 2). The near-field intensity distribution is picked-up by a high magnification and NA microscope objective. The resulting beam is projected through a Glan-Thompson polarizing prism (in order to select the desired polarization) on a CCD camera connected both to a monitor and to an acquisition card that allows the post-acquisition numerical processing step.

In order to have a correct scale factor for the near-field distribution, an initial calibration step was performed using a reference reticule (2 μ m/division) in the focal plane of the microscope objective.

The bulk refractive-index has been estimated using the Brewster's angle measurement, in a setup involving an accurate collimated laser beam and a high precision rotating stage.

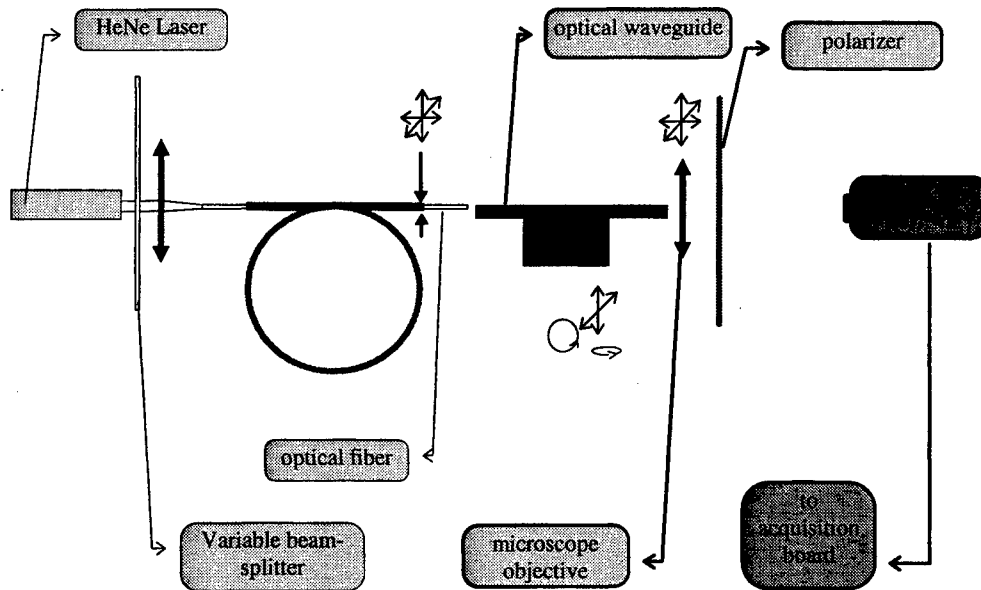


Figure 2. The near-field measurements setup.

For the real-time displaying of the near-field intensity distribution, a dedicated application was developed. This software allows the detection of the correct focusing position, of the CCD saturation effects and of situations with coarse resolution (few digitizing levels in intensity) and thus, the elimination of bad measurements.

4. RESULTS

The proposed method consists in the following steps:

- multiple image acquisition of the near-field intensity distribution;
- temporal filtering on acquired distribution averaging over 100 acquisitions;
- dimensional scaling of the field distribution using a calibration multiplication coefficient, previously obtained imaging a reference reticule with the same optical setup;
- starting the field fitting procedure.

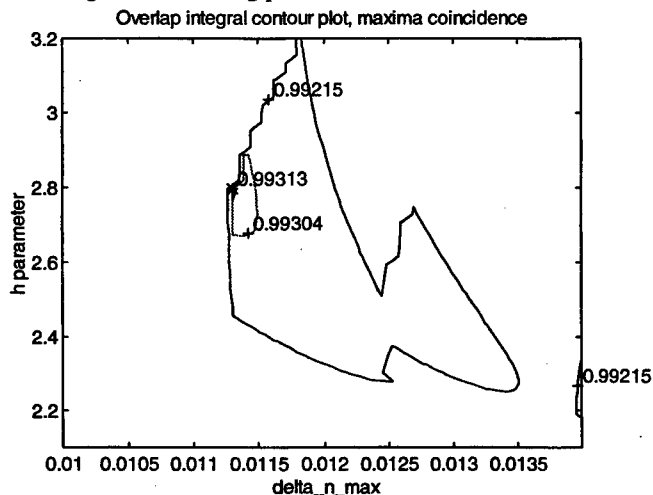


Figure 3. The two-dimensional scanning domain and the relevant contour plot of the overlap integral.

The fitting procedure is simply organized as a double loop. However, some precautions were taken on the integration domain in calculating the overlap integral (eq. 6) and on the verification of the “zero-field” hypothesis at the air-waveguide interface. For the cases we considered, the interface field is under 5% of the maximum, which is a value below the noise level of our measurements.

The two-dimensional scanning in the $(\Delta n_y, h)$ plane (Figure 3) is done with a cell dimension discretization of $2.2 \cdot 10^{-2} \mu\text{m}$ for h and $8 \cdot 10^{-5}$ for Δn_y . The maximum of the overlap integral is reached for $h = 2.8 \mu\text{m}$ and $\Delta n_y = 1.13 \cdot 10^{-2}$. These values are in a good agreement with the data of similar waveguides found in the literature [4] [5].

The measured and the best field fit obtained in this way are presented in Figure 4. Thanks to a good choice of the integration interval, a good fit is obtained even in a high noise level condition.

The refractive-index profile based on eq. (2) with the above reported best fitting parameters is shown in Figure 5.

The accuracy of the reconstructed refractive-index profile was tested calculating the modal effective-index and comparing with the value obtained from an "M-lines" measurement setup. The calculated effective-index is $n_{eff, fit} = 1.51413$ and its difference with respect to the "M-lines" measurements made on the same sample (at the same wavelength, in the same temperature conditions) is lower than 0.07%, which means an good agreement.

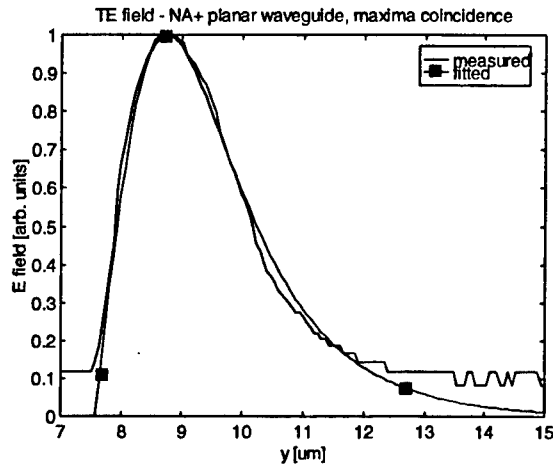


Figure 4. The best fitting of experimental data.

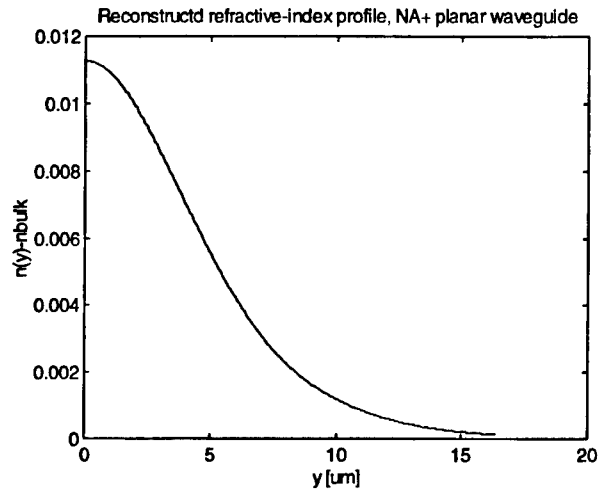


Figure 5. The reconstructed refractive-index profile.

5. CONCLUSIONS

An alternative method for refractive-index profile reconstruction was proposed and applied in the case of single-mode ion-exchanged glass optical waveguides. The proposed method is based on the fitting of the measured near-field distribution with an analytical one. This fact permits a very fast algorithm for the numerical implementation. A good accuracy of the results was achieved with a very low sensitivity to noise.

6. REFERENCES

1. K.S. Chiang, "Construction of refractive-index profiles of planar dielectric waveguides from the distribution of effective indexes", *Journal of Lightwave Technology*, vol. 3, No.2, pp. 385-391, 1985;
2. L. McCaughan, E.E. Bergmann, "Index distribution of optical waveguides from their mode profile", *Journal of Lightwave Technology*, vol. 1, No.1, pag. 241-244, 1983;
3. H. Kogelnik, "Theory of dielectric waveguides", *Integrated optics*, Springer -Verlag, New York, pp. 53-61, 1982;
4. G.L. Yip, J. Albert, "Characterization of planar optical waveguides by K+-ion exchange in glass", *Optics. Letters*, vol. 10, pag. 151-153, 1985;
5. S.I. Najafi, *Introduction to glass integrated optics*, vol. 27, pag. 3728-3731, 1988.

Non-Markovian effects in dissipative systems

Eliade Stefanescu and Paul Sterian*

National Research Institute for Micro-Technology,
72996 Bucharest, Romania

*Physics Department, Polytechnical University of Bucharest,
77206 Bucharest, România

ABSTRACT

In a unitary approach generally used in quantum optics, we consider Lindblad's Markovian master equation and the non-Markovian master equation of Ford, Lewis and O'Connell. We show that the second-order master equation in the hierarchy obtained from a Krylov-Bogoliubov expansion corresponds to the Born approximation. By time averaging, and neglecting the rapidly varying terms, Lindblad's master equation is obtained. With these two equations, we calculate the decay spectrum. We find that for rather low dissipated energies, only the non-Markovian master equation provides correct results. Based on the independent oscillator model of the dissipative coupling, explicit expressions of the dissipative coefficients are obtained.

Keywords: transition spectrum, master equation, the independent-oscillator model

1. INTRODUCTION

Dissipation is responsible for essential characteristics of a quantum system time evolution: energy decay, spectral broadening and shift, thermal fluctuations, etc.^{1,2,3}. A consistent description of the dissipative systems in quantum optics and nuclear physics is based on Lindblad's Markovian master equation⁴⁻⁹. This equation has been derived by Lindblad⁹, in the framework of a generalized quantum mechanics, where the evolution operators are no more dynamical groups, as in the conventional quantum mechanics, but semigroups¹⁰⁻¹². For a one-dimensional system with the coordinate x , and the momentum p , Sandulescu and Scutaru¹³ found a form of this equation with friction and diffusion coefficients. It has been shown that for these parameters, microscopic expressions can be obtained¹⁴.

Using this approach, the Bloch-Feynman equations have been generalized, obtaining a coupling through the environment of the polarization with the population⁶. Also, an enhancement of the dissipative tunneling^{7,8}, in a very good agreement with experimental data for the cold fission of the heavy nuclei, has been obtained⁹.

Generally, it is believed that the Markovian master equations provide correct descriptions of the optical or nuclear dissipative phenomena. However, when one calculates the diagonal elements of the density matrix, a Markovian master equation leads to a huge difficulty. As one can easily notice, solving such an equation with the initial state $|0\rangle\langle 0|$ of energy E_0 , non-zero occupation probabilities appear for final states with energies $E_i > E_0$. In principle, the Markov hypothesis, could seem somehow abstract and unphysical.

A more physical theory, taking into account in detail the time-evolution of a system, has been developed by Ford, Lewis and O'Connell¹⁵⁻¹⁸. Using an expansion of the density matrix according to a method of Krylov and Bogoliubov, they obtained a hierarchy of non-Markovian master equations¹⁸. The essential advantage of this theory is that it provides microscopic expressions of the dissipation parameters.

In this paper we calculate the decay spectrum with Lindblad's master equation and with the non-Markovian master equation of Ford, Lewis and O'Connell. In Sec.2, we show that the Born approximation leads to the second order master equation in the hierarchy of Ford, Lewis and O'Connell. Lindblad's master equation is obtained only by a time averaging process and neglecting the rapidly varying terms. In Sec.3, from the two master equations we calculate the diagonal elements of the density matrix and compare the two spectra. Sec.4 is for conclusions.

2. QUANTUM MASTER EQUATIONS

We consider a system with the Hamiltonian H_0 , coupled to a dissipative environment with the Hamiltonian H^E . The method of quantum master equations is in fact a technique of replacing the environment observables q_j, p_j of the environment, by their correlation functions, which, finally, are connected to phenomenological parameters like decay rates, temperature, etc. Generally, in the total Hamiltonian H of the system, we can distinguish three terms: 1) a term \bar{H}_0 , depending only on the system operators s_a , 2) a term H^E , depending only on the environment operators q_j, p_j , and 3) an interaction term V . Here, we have taken into account that the term \bar{H}_0 contains not only the system Hamiltonian H_0 , but also an additional term depending on the masses of the environment particles.

As in [3], we consider the interaction Hamiltonian V and the total density operator $\chi(t)$ of the form:

$$\left\{ \begin{array}{l} V = \hbar \sum_a s_a \Gamma_a \\ \chi(t) = \rho(t) R_0, \end{array} \right. \quad (1)$$

where Γ_a are operators of the environment, $\rho(t)$ is the density operator of the system, and R_0 is the density operator of the environment. We consider quasi-equilibrium processes, when R_0 is diagonal, corresponding to the Gibbs energy distribution. From the equation of motion

$$\dot{\rho}(t) = -\frac{i}{\hbar} [\bar{H}_0, \rho(t)] - \frac{1}{\hbar^2} \int_0^t e^{-\frac{i}{\hbar} \bar{H}_0 t} [V(t), [V(t'), \tilde{\chi}(t')]] e^{\frac{i}{\hbar} \bar{H}_0 t} dt', \quad (2)$$

we obtain a general non-Markovian master equation:

$$\begin{aligned} \dot{\rho}(t) = & -\frac{i}{\hbar} [\bar{H}_0, \rho(t)] + \sum_{a,b} \int_0^t \{ C_{ab}(t, t') [e^{-\frac{i}{\hbar} \bar{H}_0 (t-t')} s_a \rho(t') e^{\frac{i}{\hbar} \bar{H}_0 (t-t')}, s_b] + \\ & + C_{ba}^*(t, t') [s_a, e^{-\frac{i}{\hbar} \bar{H}_0 (t-t')} \rho(t') s_b e^{\frac{i}{\hbar} \bar{H}_0 (t-t')}] \} dt', \end{aligned} \quad (3)$$

with the dissipative kernels

$$\begin{aligned} C_{ab}(t, t') & \doteq \text{Tr}_E \{ \Gamma_a(t') R_0 \Gamma_b(t) \} = \sum_{mn} e^{-i\omega_{mn}^E (t-t')} \langle m | \Gamma_a | n \rangle R_0^{(n)} \langle n | \Gamma_b | m \rangle, \\ C_{ba}^*(t, t') & = C_{ab}(t', t) \doteq \text{Tr}_E \{ \Gamma_a(t) R_0 \Gamma_b(t') \} = \sum_{mn} e^{i\omega_{mn}^E (t-t')} \langle m | \Gamma_a | n \rangle R_0^{(n)} \langle n | \Gamma_b | m \rangle, \end{aligned} \quad (4)$$

where the hermiticity of the operators Γ_a, Γ_b has been taken into account. In these expressions, $\omega_{mn}^E = \omega_m^E - \omega_n^E$, are the transition frequencies between the states $|m\rangle$ and $|n\rangle$ of the environment, and $R_0^{(n)}$ are the occupation probabilities of the states $|n\rangle$.

Previously¹⁴, we showed that considering δ -functions instead of the rapidly varying terms in (4), Lindblad's master equation is obtained. However, as it is shown in [18], based on the independent oscillator model [15]-[18], the dissipative kernels can be calculated explicitly, and the non-Markovian master equation can be used. Considering the masses m_j and the frequencies ω_j of the dissipative oscillators, Eq.(3) takes the form:

$$\begin{aligned} \dot{\rho}(t) = & -\frac{i}{\hbar}[\bar{H}_0, \rho(t)] + \frac{1}{2\hbar} \int_0^t \{C(t, t') [e^{-\frac{i}{\hbar}\bar{H}_0(t-t')} x \rho(t') e^{\frac{i}{\hbar}\bar{H}_0(t-t')}, x] + \\ & + C^*(t, t') [x, e^{-\frac{i}{\hbar}\bar{H}_0(t-t')} \rho(t') x e^{\frac{i}{\hbar}\bar{H}_0(t-t')}] \} dt', \end{aligned} \quad (5)$$

with the dissipative kernel

$$C(t, t') = \frac{1}{\pi} \int_0^\infty \zeta(\omega) \omega \left\{ \coth \left(\frac{\hbar\omega}{2kT} \right) \cos[\omega(t-t')] - i \sin[\omega(t-t')] \right\} d\omega + B(t, t'), \quad (6)$$

where $\zeta(\omega)$ is the dissipative function defined by the relation

$$\sum_j m_j \omega_j^2 = \frac{1}{\pi} \int_0^\infty d\omega \zeta(\omega), \quad (7)$$

and

$$\begin{aligned} B(t, t') = & \frac{2}{\pi^2 \hbar} \int_0^\infty d\omega \zeta(\omega) \omega \int_0^t x(\tau) \sin[\omega(t-\tau)] d\tau \cdot \\ & \cdot \int_0^{t'} d\omega' \zeta(\omega') \omega' \int_0^{t'} x(\tau') \sin[\omega'(t'-\tau')] d\tau'. \end{aligned} \quad (8)$$

We notice that the term $B(t, t')$ of the dissipative kernel $C(t, t')$ depends on the system observables $x(\tau)$, $x(\tau')$. This term, being proportional to ζ^2 , describes only small oscillations that can be neglected - the Born approximation. One can notice that Eq.(5), with the dissipative kernel (6) in the Born approximation, is the master equation of the second-order in the hierarchy of master equations derived in [18]. Eliminating the rapidly-varying terms, for a harmonic oscillator with the renormalized frequency $\bar{\omega}_0$, we obtain the Markovian master equation in [18] of the form:

$$\begin{aligned} \dot{\rho}(t) = & -\frac{i}{\hbar}[\bar{H}_0, \rho(t)] - \frac{\zeta(\bar{\omega}_0) \bar{\omega}_0}{4\hbar} \frac{1}{2} \left\{ \coth \left(\frac{\hbar\bar{\omega}_0}{2kT} \right) \left[[x, [x, \rho(t)]] + \frac{1}{m^2 \bar{\omega}_0^2} [p, [p, \rho(t)]] \right] + \right. \\ & \left. + \frac{i}{m\bar{\omega}_0} \left[[x, p\rho(t) + \rho(t)p] - [p, x\rho(t) + \rho(t)x] \right] \right\}. \end{aligned} \quad (9)$$

This equation is exactly the quantum master equation derived by Sandulescu and Scutaru¹³ from Lindblad's master equation,

$$\begin{aligned} \frac{d\rho}{dt} = & -\frac{i}{\hbar}[H, \rho(t)] - \frac{i\lambda}{2\hbar}([x, p\rho + \rho p] - [p, x\rho + \rho x]) - \frac{D_{pp}}{\hbar^2}[x, [x, \rho]] - \frac{D_{xx}}{\hbar^2}[p, [p, \rho]] \\ & + \frac{D_{xp}}{\hbar^2}([x, [p, \rho]] + [p, [x, \rho]]), \end{aligned} \quad (10)$$

but with microscopic expressions of the friction and diffusion coefficients:

$$\lambda = \frac{\zeta(\bar{\omega}_0)}{4m}, \quad D_{pp} = \frac{\hbar\lambda m\bar{\omega}_0}{2} \coth\left(\frac{\hbar\bar{\omega}_0}{2kT}\right), \quad D_{xx} = \frac{\hbar\lambda}{2m\bar{\omega}_0} \coth\left(\frac{\hbar\bar{\omega}_0}{2kT}\right), \quad D_{xp} = 0. \quad (11)$$

3. DISSIPATIVE TRANSITIONS AS MARKOVIAN AND NON-MARKOVIAN PROCESSES

In this section we discuss additional effects described by the non-Markovian master equation (5) in comparison with the system evolution described by the Markovian master equation (9).

Calculating the diagonal matrix elements $\rho_{ii}(t)$ from (9), with a pure initial state $\rho_{00}(0) = |0\rangle\langle 0|$, we obtain the transition rates from the state $|0\rangle$ to the states $|i\rangle$:

$$\Gamma_i \doteq \frac{\rho_{ii}(t)}{t} = \frac{\zeta(\bar{\omega}_0)}{4m} \left[(\alpha x_{0i}^2 + \alpha^{-1} s_{0i}^2) \coth\left(\frac{\hbar\bar{\omega}_0}{2kT}\right) - 2x_{0i}s_{0i} \right], \quad (12)$$

where $\alpha \doteq \frac{m\bar{\omega}_0}{\hbar}$, $x_{0i} \doteq \langle 0|x|i\rangle$, $s_{0i} \doteq \langle 0|\frac{d}{dx}|i\rangle$. The transition spectrum has an amplitude proportional to the dissipative coefficient $\lambda = \frac{\zeta(\bar{\omega}_0)}{4m}$ and a shape depending of the matrix elements x_{0i} , s_{0i} .

A similar expression can be derived also from the non-Markovian master equation (5). Calculating the diagonal elements of the density matrix, we obtain:

$$\begin{aligned} \frac{d\rho_{ii}}{dt} = & \frac{x_{0i}}{\pi\hbar} \int_0^\infty \zeta(\omega)\omega \left[\langle 0|\rho(0)|0\rangle \left(\frac{\sin[(\omega - \omega_i)t]}{\omega - \omega_i} - \frac{\sin[(\omega + \omega_i)t]}{\omega + \omega_i} \right) - \right. \\ & \left. - \int_0^t \frac{d\langle 0|\rho(t-\tau)|0\rangle}{d\tau} \left(\frac{\sin[(\omega - \omega_i)\tau]}{\omega - \omega_i} - \frac{\sin[(\omega + \omega_i)\tau]}{\omega + \omega_i} \right) d\tau \right] d\omega, \end{aligned} \quad (13)$$

where $\omega_i = \bar{\omega}_0 - \bar{\omega}_i$ is the transition frequency between the eigenstates $|0\rangle$, $|i\rangle$ of \bar{H}_0 . For rather long times, the time dependent functions become proportional to δ -functions, and Eq.(13) can be integrated. We obtain the transition rates:

$$\Gamma_i \doteq \frac{1}{\rho_{00}(t)} \frac{d\rho_{ii}(t)}{dt} = \frac{1}{\hbar} \zeta(\omega_i) \omega_i x_{0i}^2. \quad (14)$$

Since the function $\zeta(\omega)$ is defined only for positive frequencies ω , the transition rates take non-zero values only for negative final energies $= E_i = \hbar\bar{\omega}_i - \hbar\bar{\omega}_0 = -\hbar\omega_i$, or for positive dissipated energies $\hbar\omega_i$. This

essential property is not described by the Markovian expression (12) that yields positive transition rates also for positive final energies E_i .

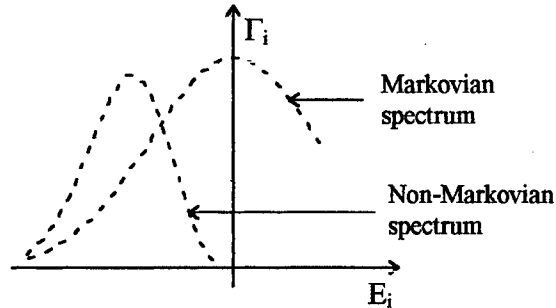


Fig. 1 The decay spectrum obtained with the Markovian expression (12) and with the non-Markovian expression (14).

In comparison with (12), the new expression (14) contains dissipative coefficients depending on the final energies $E_i = -\hbar\omega_i$. From (7) we find the explicit expression:

$$\zeta(\omega_i) = \frac{m_i \omega_i^2}{\delta \omega_i}, \quad (15)$$

where $\frac{1}{\delta \omega_i}$ is the density of the final states, m_i are the masses of the environment oscillators and ω_i are the transition frequencies. We find also a simple expression for the dissipative coefficient

$$\lambda = \frac{m_0 \omega_0^2}{4m \delta \omega_0} \quad (16)$$

of the Markovian master equation (10). In this expression, the mass m_0 and the density of states $\frac{1}{\delta \omega_0}$ are the values of m_i and $\frac{1}{\delta \omega_i}$, corresponding to the frequencies $\omega_i \approx \omega_0$ of the dissipative oscillators.

4. CONCLUSIONS

In this paper we considered two of the most remarkable master equations for a correct description of the dissipative phenomena: Lindblad's Markovian master equation and the non-Markovian master equation of Ford, Lewis and O'Connell. We reobtained them in an unitary approach, well-known in quantum optics, and calculated the dissipation spectrum. We found similar results only for rather high values of the dissipated energy. For final energies not very far from the initial energy of the system, the results of the two equations are different. The non-Markovian master equation provides the correct result that the transition rates decrease to zero when the dissipated energy approaches to zero, and are zero for final energies of the system higher than the initial energy. At the same time, the Markovian master equation yields increasing transition rates to energies approaching to zero, and non-zero transition rates to higher energies, that are not real.

We conclude that the Markovian master equations, generally used in optics and nuclear physics, are an appropriate tool only for decay processes, where rather high dissipated energies are involved. For processes at approximately the same energy, like spectral broadening or quantum tunneling, a non-Markovian

master equation is much more appropriate. Using the independent oscillator model of Ford, Lewis and O'Connell, we obtained an explicit expression of the decay spectrum, as a function of the transition elements of the coordinate, the density of the final states, the masses of the environment oscillators, and the transition frequencies.

5. REFERENCES

1. Ke-Hsueh Li, "Physics of Open systems", *Phys.Rep.* **134**(1), 1-85 (1986).
- 2 M.Razavy, A.Pimpale, "Quantum Tunneling: A General Study in Multidimensional Potential Barriers with and without Dissipative Coupling", *Phys.Rep.*(6) **168**, 305-370 (1988).
3. H.Carmichael, *An Open Systems Approach to Quantum Optics*, in *Lecture Notes in Physics* **m18**, Springer Verlag, Berlin, Heidelberg, New York, 1993.
4. A.Isar, A.Sandulescu, H.Scutaru, E.Stefanescu and W.Scheid, "Open Quantum Systems", *Int.J.Mod.Phys. E* **3**(2), 635-714 (1994).
5. W.Scheid, A.Isar, A.Sandulescu and E.Stefanescu, "Application of Lindblad theory to problems of nuclear dissipation", *International Research Workshop on Heavy Ion Physics at Low, Intermediate and Relativistic Energies, Poiana Brasov (7-14 Oct. 1996)*, to be published.
6. A.Sandulescu, E.Stefanescu, "New Optical Ecuations for the Interaction of a Two-Level Atom with a Single Mode of the Electromagnetic Field", *Physica A* **161**, 525-538 (1989).
7. E.Stefanescu, A.Sandulescu and W.Greiner, "Quantum Tunneling in Open Systems", *Int.J.Mod.Phys. E* **2**(1), 233-258 (1993).
8. E.Stefanescu, A.Sandulescu and W.Greiner, "Analytical model for quantum tunneling with dissipation through a fission-like barrier", *J.Phys.G: Nucl.Part.Phys.* **20**, 811-828 (1994).
9. E.Stefanescu and W.Scheid, A.Sandulescu and W.Greiner, "Cold Fission as Cluster Decay with Dissipation", *Phys.Rev. C* **53**(6), 3014-3021 (1996).
10. G.Lindblad, "On the Generators of Quantum Dynamical Semigroups", *Comm.Math.Phys.* **48**, 119-130 (1976).
11. E.B.Davies, *Quantum Theory of Open Systems*, Academic Press, London, New York, San Francisco, 1976.
12. R.Alicki and K.Lendi, *Quantum Dynamical Semigroups and Applications*, in *Lecture Notes in Physics* **286**, Springer Verlag, 1987.
13. A.Sandulescu and H.Scutaru, "Open Quantum Systems and the Damping of Collective Modes in Deep Inelastic Collisions" *Ann.Phys.* **173**(2), 277-317 (1987).
14. E.Stefanescu, P.Sterian, Opt.Eng. "Exact Quantum Master Equations for Markoffian Systems" **35**(6), 1573-1575 (1996).
15. G.W.Ford, J.T.Lewis, R.F.O'Connell, "Quantum Langevin Equation", *Phys.Rev. A* **37**(11), 4419-4428 (1988).
16. R.F.O'Connell, "Dissipation and Fluctuation Phenomena in Quantum Mechanics", *Int.J.Q.Chem.* **58**(6), 569-581 (1996).
17. G.W.Ford, R.F.O'Connell, "There is No Quantum Regression Theorem", *Phys.Rev.Lett.* **77**(5), 798-801 (1996).
18. G.W.Ford, J.T.Lewis, R.F.O'Connell, "Master Equation for an Oscillator Coupled to the Electromagnetic Field", *Ann.Phys.* **252**, 362-385 (1996).
19. Claude Cohen-Tannoudji, Jaque Dupont-Roc, Gilbert Grynberg, *Atom-Photon Interactions* p.267, John Wiley & Sons, Inc., New York, 1992.
20. Mitchel Weissbluth, *Photon-Atom Interactions*, p.288 Academic Press Inc., Boston, San Diego, New york, 1989.

Optoelectronic micropositioning device with piezoceramic transducer

Irinela Chilibon, Maria Robu

Institute of Optoelectronics, R-76900, PO Box MG 22, Bucharest, Romania

ABSTRACT

This paper presents an experimental study on the behaviour of piezoceramics type PZT, having a high compliance, and their application for an optoelectronic micropositioner device with piezoceramic transducer.

The piezoelectric ceramics are crystallite conglomerate ferroelectrics materials with random orienting. In the laboratory we have realised PZT ceramics with various additions (Ni, Bi, Mn), presenting high compliance; for optoelectronic micropositioning device in micrometry displacements. The experimental transducers, realised like stacks of $30 \div 35$ pieces of PZT thin disks, supplied with $0 \div 1000\text{V}$ voltages, have produced $0 \div 15\text{ }\mu\text{m}$ displacements.

Keywords: PZT, piezoceramic material, displacement transducer, optoelectronic micropositioning device

1. INTRODUCTION

The piezoelectricity phenomena, discovered in 1880 by the Curie brothers, presents two complementary aspects : stress - electricity. So, in the direct effect, the application of a mechanical stress determines the reorientation of internal electrical dipoles, resulting a volume polarisation and a induced electrical voltage ; in the reverse effect, the application of an electrical field produces the material deformation.

The piezoceramic materials under study are solid solutions of $\text{Pb}(\text{Zr}_x\text{Ti}_{1-x})\text{O}_3$ obtained by classic technology in laboratory, using as raw materials oxide powders of PbO , TiO_2 , ZrO_2 . Such piezoceramic materials are important in the field of applications ([2] and [3]), because they present piezoelectric effects.

This piezoceramic materials type PZT with high compliance and electrostrictive coefficients, have a large domain of applications in electromechanical transducers for optoelectronics as: low power bimorph piezoceramic transducers for optical vibrating systems, interferometer with laser, remote commands in optoelectronic systems, bare code systems and micropositioners for laser systems.

In the laboratory we have realised a transducer, like stacks of many thin piezoceramic rings, supplied with electrical continuous voltage. This electromechanical transducer works on the basis of the reverse piezoelectric effect, converting an electrical power into a displacement in the range of tens microns.

2. EXPERIMENTAL RESULTS

In the laboratory we have made experimental researches for obtaining PZT materials, with high electrostrictive coefficients and compliance.

The Table 1 shows the main physical, electrical and dielectric characteristics for 6 types of PZT materials realised in the laboratory. The measurements were made on the PZT disks with $\Phi 25\text{ mm}$ diameter and 2 mm thickness, where: C is the static capacity, $\tan \delta$ dielectric loss factor, ϵ dielectric permittivity, Q quality mechanical factor and k_p electromechanical coupling factor. The mechanical impedance Z_m can be decreased using a piezoceramic material type PZT with high density, piezoelectric voltage and dielectric constants, and also high electromechanical coupling factor.

For establishing the elasticity characteristics of piezoceramic materials we have applied electrical voltages of 1000V , 1500V and 3000V on disks and rings made of PZT, with $1,2\text{ mm} \div 6,5\text{ mm}$ thickness.

Table 1 The main characteristics of PZT materials

No. crt.	PZT materials	C [nF]	$\tan \delta \times 10^3$	ϵ	Q	k_p
1	5M	2,22	16,60	1270	180	0,60
2	7M	1,97	17,76	1190	70	0,50
3	10M	2,05	16,58	1135	95	0,50
4	11M	2,26	18,58	1160	100	0,45
5	16M	2,59	14,67	1230	80	0,55
6	T	2,21	1,80	800	310	0,30

The experimental measurements were made with an interferometric system with He-Ne laser ($\lambda = 632.8$ nm). In the Table 2 we present the thickness deformations Δh of piezoceramic elements (expressed in number of fringes f , $1f = 0,316$ nm and in μm), function of the thickness h and the electrical voltage applied on the electrodes U .

The application of an electrical voltage U in the polarisation direction of the piezoceramic element produces an elastic deformation of it Δh (stretching or compressing).

The active element of the device with piezoceramic transducer is a sandwich of piezoceramic thin rings (Figure 1). This electromechanical transducer works on the basis of the revers piezoelectric effect, converting an electrical power into a mechanical displacement in the range of tens microns.

Table 2 The deformations of piezoceramic elements function of electrical voltages

PZT elements	h [mm]	Fringes number f	Δh [μm]	U [V]
1	1,2	2f	0,632	1500
2	4,0	2f	0,632	1000
3	4,0	5f	1,580	3000
4	5,5	2f	0,632	3000
5	6,0	1f	0,316	1000
6	6,0	4f	1,264	3000
7	6,5	3f	0,948	3000

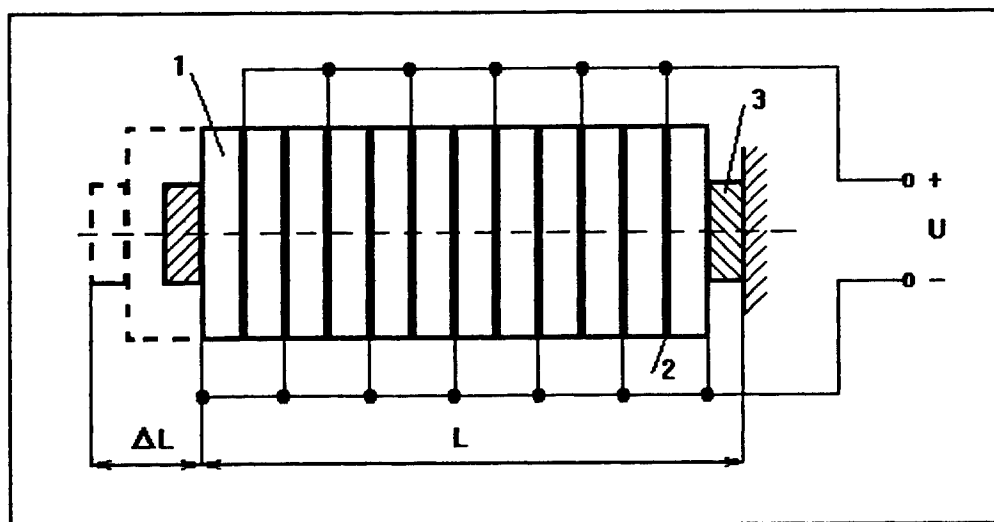


Figure 1 Piezoceramic stack: 1 - PZT element, 2 - electrode, 3 - metallic element for holding

The total displacement ΔL for a stack of n piezoceramic pieces with L length is function of d_{33} piezoelectric constant of PZT material, and the relationship between them is:

$$\Delta L = d_{33} \cdot n \cdot U$$

In the Table 3 we present the length deformation ΔL of the experimental piezoceramic stack, function of continuous electrical voltage U , applied in parallel on the 30 PZT thin rings.

Table 3 The deformations of piezoceramic stack function of electrical voltages

U [V]	Δh [μm]	U [V]	Δh [μm]	U [V]	Δh [μm]	U [V]	Δh [μm]
100	0	700	8,0	1100	16,2	500	7,7
200	1,2	800	9,8	1000	15,1	400	5,8
300	2,3	900	11,5	900	13,9	300	3,9
400	3,6	1000	13,4	800	12,3	200	2,2
500	4,9	1100	15,1	700	10,7	100	0
600	6,6	1200	17,8	600	9,3		

The displacements for a PZT element of 1 mm thickness, supplied with 1000V, was $0,3 \div 0,6$ mm. The experimental transducers, realised like stacks of $30 \div 35$ pieces of PZT thin disks, supplied with $0 \div 1000$ V voltages, have produced $0 \div 15$ μm displacements.

The experimental piezoceramic stack has the mechanical deformation - electrical voltage diagram (Figure 2) with cu maximum hysterezis of $2,7$ μm , and the sensitivity of the device of $14,3$ nm/V.

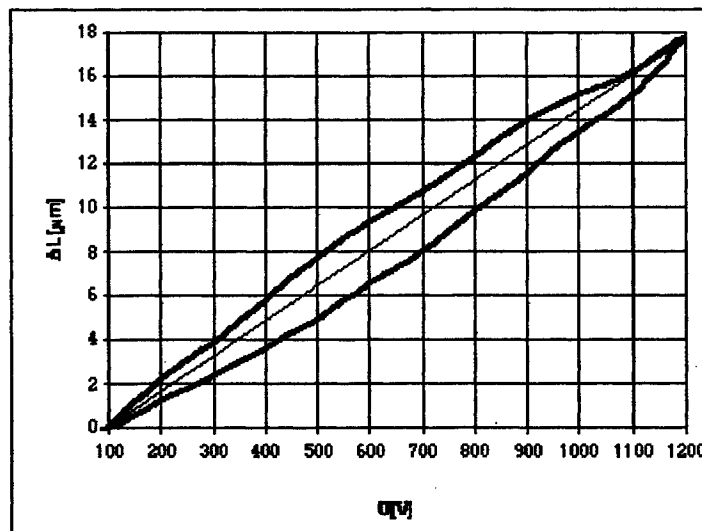


Figure 2 Mechanical deformation - electrical voltage diagram of piezoceramic stack

When alternative voltage is applied on the device it vibrates mechanical $\pm \Delta L$ amplitude. The transducer is an important device for optoelectronic applications, because it has small dimensions and can be easy implemented into a laser system (Figure 3), ([2] and [3]).

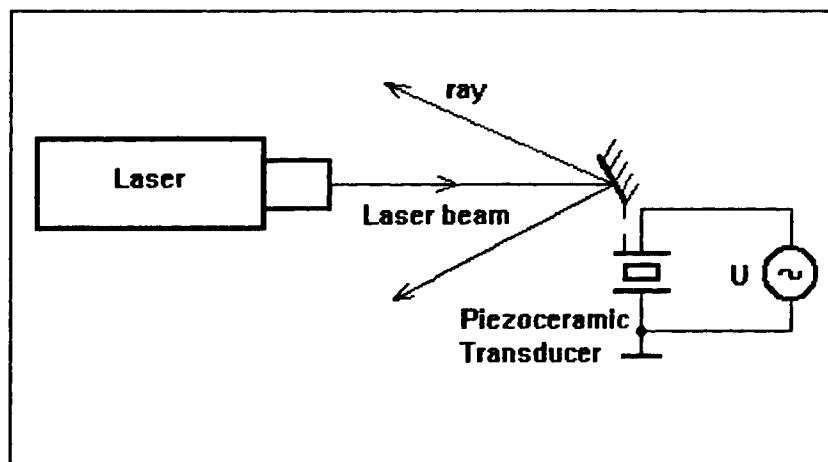


Figure 3 Laser system with displacement piezoceramic transducer

3. CONCLUSIONS

The reverse piezoelectric effect can be used in manufacturing piezoceramic transducers for optoelectronic micropositioning device.

The sandwich piezoceramic transducer realised in laboratory, with high electrostrictive coefficients and compliance PZT materials is an important device for optoelectronic applications, because it has small dimensions and can be easy implemented into a laser system.

4. REFERENCES

1. K. Okazaki, "Developments in fabrication of piezoelectric ceramics", *Ferroelectrics*, Vol. 41, pp. 77-96, 1982.
2. M. Brissaud, "Characterisation of Piezoceramics", *IEEE Trans. on Ultrasonics*, Vol. 38, No. 6, 1991.
3. M. Robu, I. Chilibon, "Materiaux piezoceramiques pour des transducteurs de déplacement", *X Symposium FASE 1993*, Academia Română, Bucuresti, pp. 169-171, 1993.
4. M. Robu, I. Chilibon, "Piezoceramic transducers for optoelectronic systems" (from Roumanian), *"Optoelectronica"* 1(4), 131-133 (1993).

Spectroellipsometric characterization of the multilayer systems containing Ni and Bi

V. Hutsanu, M. Gartner*, C. Ghita*, and V. Dolocan

Faculty of Physics, University of Bucharest, Dept. of Solid State Physics,
P.O. BOX MG-11, R-76900, Bucharest-Magurele, Romania

* Institute of Physical Chemistry, Splaiul Independentei 202, 77208 Bucharest, Romania

ABSTRACT

In this paper an optical evaluation of the system Ni,Bi/Cu,ITO/glass system, prepared by electrochemical method is presented. Among various factors that affect the optical and structural properties of the multistructure systems we focus on the influence of the substrate and the interfacial oxidic layers. To this end we used the Spectroellipsometric (SE) method in VIS-NIR spectral range.

The SE results show that the electrochemical deposited films (Ni,Bi) are porous and their refractive index depends strongly on the substrate.

Keywords : ellipsometry, multilayer structure, electrochemical method, giant magnetoresistance

1. INTRODUCTION

The metal multilayered structures with the nanometric layer thickness are of a considerable interest due to their mechanical, electrical and magnetic properties. Short-period metal/metal superlattices manifest some new phenomena that differ significantly from those of bulk materials. One of these phenomena is the GMR (giant magnetoresistance)¹⁻² whose continue to be the subject of a large scientific effort both at a fundamental level and at the level of its technological applications to magnetic recording technology. For GMR to be observed a fair control over the deposition parameters is needed, since rough interfaces between subsequent layers can influence the effect. That is why most of the samples which exhibit large coupling strengths and high MR values have been prepared by sputtering, molecular beam epitaxy (MBE), or other vacuum based techniques³. Recently, some authors⁴⁻⁸ have reported giant magnetoresistance in multilayers grown by electrodeposition.

Electrodeposition has some obvious advantages over trivial techniques, since the experimental apparatus required is considerably simpler (and cheaper) than those for techniques which require high or ultrahigh vacuum. This work is our first step made to realize fine short period superlattices by electroplating from new materials. We study a multistructure system consisting of a sandwich of Ni and Bi films formed by electrochemical (EC) deposition.

The physical and chemical properties of these films are strongly influenced by the method of deposition, its technological parameters and the substrate type. The Ni/Bi and Bi/Ni films were supported on different substrates that do not influence the magnetic measurements (as ITO/glass) or which can be removed before these measurements (as Cu/glass).

For the optical characterisation of these systems we used the spectroellipsometric (SE) method, which is a sensitive and non-destructive technique, suitable for the study of surfaces and thin films. Using a suitable theoretical model, one can have a qualitative and quantitative assessment of the composition and structure of the sample under investigation (sub-layers and the composition of each sub-layer)

2. EXPERIMENTAL

Bi-Ni structures have been prepared from two separate electrolytic solutions, the first used for Bi deposition and the second for Ni deposition. All the depositions were carried with potentiostatic control in standard 3 -electrodes geometry shown in Fig. 1.

A potentiostat (Taquselle model PR-20X) maintains the potential of the film substrate (the cathode) at the desired value relative to the standard calomel saturated reference electrode by varying the potential between the film substrate and a platinum auxiliary electrode.

The electrolyte solution for Bi deposition contains 40 g/l Bi₂O₃, 104 g/l HClO₄, 0.03 % glue, 0.08 % b - naftol and has a pH = 1.5. Ni deposition electrolyte solution contains Nickel sulfate NiSO₄ × 7H₂O - 150 g/l, Boric acid B(OH)₃ - 10

g/l and has a pH = 5.5. All chemicals were p.a. grade with the balance of the solution being distilled water. All the depositions were carried at room temperature without any agitation of the solution.

We deposited our films using cathode potentials of - 0.292 V for Bi, - 1.320 V for Ni measured relative to a saturated calomel electrode (SCE).

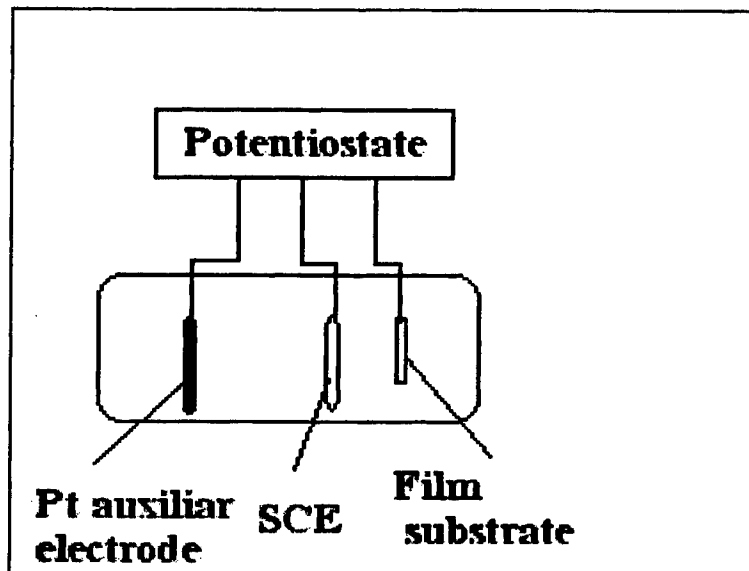


Fig.1

Schematic diagram of electrolytic cell for multilayer samples preparation.
SCE - saturated calomel electrode

The thickness of the deposited films depends direct on the length of the time impulse which is controlled by a time adjustable relay (TR). This TR permits to adjust different deposition times for each substance deposition.

Spectroellipsometric measurements were made at 70° angle of incidence in visible spectral range ($0.4\mu\text{m}$ - $0.7\mu\text{m}$) at 10 nm intervals. The ellipsometer used was in polarizer -compensator-sample-analyzer arrangement. A 150 W xenon lamp was used to the light source. The SE data were obtained at room temperature. Measurements were carried out after cleaning the surface with ethanol.

3. RESULTS AND DISCUSSIONS

In order to calculate the real thickness of each layer from the measurement of the passed charge during electrodeposition, it is necessary to know the effective current efficiency. This was defined by us as the ratio of the real thickness of an electrodeposited film to its nominal thickness (the thickness calculated assuming bulk densities and 100% current efficiency). The weighting of the thick layers prepared from the same solution and in the same conditions shows a high current efficiency. On the other hand, to compare the real thickness of deposited Bi and Ni layers with the nominal values computed from the Faraday law, spectro-ellipsometry was used. Table 1 displays the results of this comparison.

The samples for spectroellipsometry were prepared on two types of substrates using the same electrolyte. An ITO (InSnO_2) layer of 2000 Å dc sputtered on glass was used as a substrate for electrodeposition because due to its low conductance the necessity of dissolving the substrate vanishes and because of its perfect optical surface favorable for ellipsometry. The second type of substrate used is a Cu vacuum evaporated 9800 Å thick on glass. Results presented in Table 1 show a greater than 90% current efficiency for Ni deposition but a lower efficiency for Bi deposition. This is due to the growth mechanism of Bi layer. For example we could not obtain the compact Bi layer on the ITO substrate from this electrolyte solution.

Theoretical model applied on ellipsometric measurements assumes a multilayer system with multicomponent layers. The experimental values are compared with the simulated ones obtained using the Bruggemann's Effective Medium Approximation (EMA)⁹ with the layer thickness and the volume fractions of the components as fitting parameters. The dielectric constants used in the modelling (glass, Cu, CuO, Cu_2O , Ni, NiO, Bi, Bi_2O_3 , ITO) were taken as bulk values given in the literature^{10,11}.

Table 1 Real and nominal thickness of Ni layers and its porosity.

Sample	Substrate	Porosity ellipsometric measured (%)	Real thickness ellipsometric measured (Å)	Nominal thickness calculated (Å)	Current efficiency (%)
Ni 1	ITO/glass	30.97	753	830	90.72
Ni 2	ITO/glass	33.67	300	300	100
Ni 3	ITO/glass	25.56	310	314	98.72
Ni 4	Cu/glass	44.27	275 (without CuO)		94.17
		43.19	253 + 65 (CuO)	290	85.45
Ni 5	Bi / Cu / glass	1.00	300	500	60

In the Bruggemann/EMA each composite layer was modelled as a simple physical mixture of components. This approximation requires that the grains of each constituent in the composite material are randomly mixed and the grain size are smaller than wavelength of light. On the other hand the light has to penetrate the sample until substrate in order to obtain an complete information on the entire system. In the same time, the grain size must be large enough for an correct macroscopic evaluation of optical parameters.

Because it is expected that each metallic film is oxidized when the structure is transferred in air, the modelling of our systems must contain an interfacial oxide layer between two metallic layers. Therefore the best theoretical fit of the experimental spectra is reached for the following model : Ni/Bi_xO_y/Bi/Cu_xO/Cu/glass.

The optical constants (n,k) were calculated taking in account the thickness (d) and the volum fractions of each layer from this best fit (Fig.2).

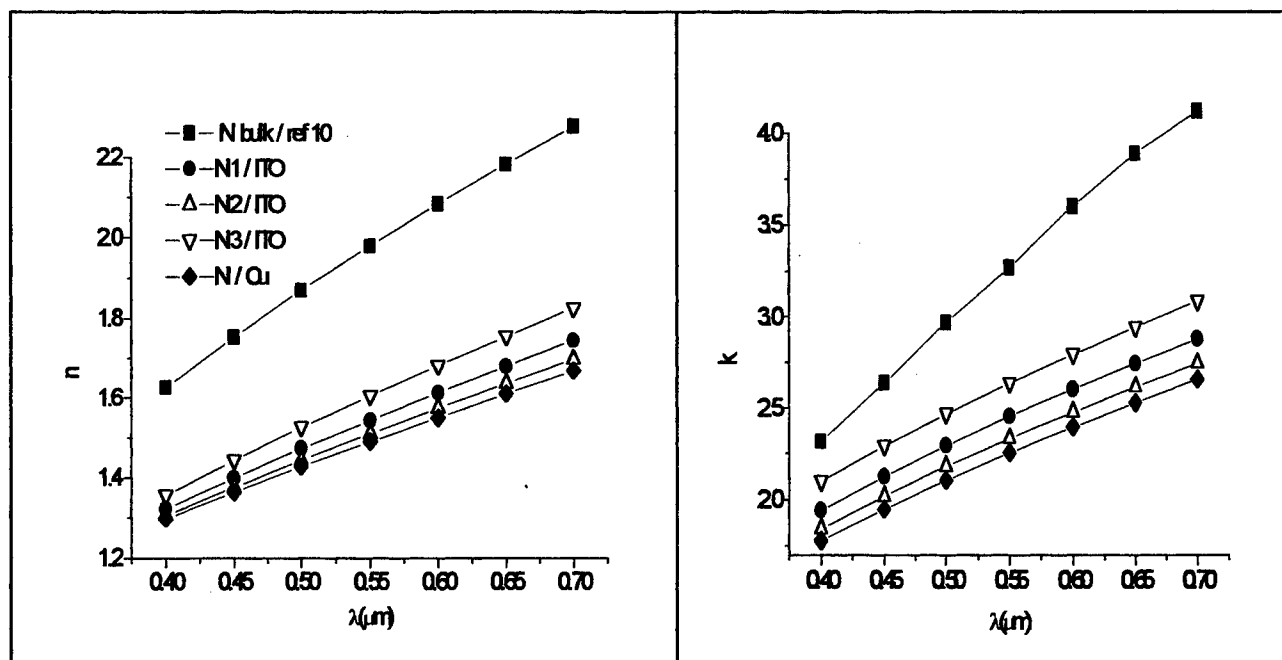


Fig.2. Optical constants (n and k) of Ni films (with Ni thickness : 1 - 830Å; 2 - 276 Å; 3 -290Å) deposited on ITO/glass, Cu/glass and Bi/glass substrates

Ellipsometric results show that :

- the films thickness measured by SE is about the same with the computed thickness from technological parameters of deposition

- our electrochemically deposited films are more porous (the refractive indices (n) are smaller) than that obtained by another type of deposition. An example is shown in Fig.2 for the Ni films deposited by (EC) and by reactive sputtering (ref.10). The porosity of our films are shown in Table 1.

- the refractive index of the films depends strongly on the substrate (Fig.1). Thus, for the Ni films deposited on the ITO refractive index is bigger than for Ni film deposited on Cu and much bigger than Ni deposited on Bi.

A reason for this is the surface conditions of substrates which affect the orientation and packing of film molecules¹². The films deposited on substrates with tighter packing will be also tighter packed and will have a higher index of refraction (ITO has a refractive index higher than Cu which, in its turn, is higher than Bi)

4. CONCLUSIONS

The electrochemical deposition method was used to prepare binary metallic multilayer systems. Two separate electrolytes were used to obtain Bi-Ni samples. The thickness of the layers were investigated by spectro-ellipsometry which shows a good agreement with nominal (calculated) values for Ni deposition. The porosity of these films obtained by EC are higher than of the films obtained through another methods of preparation and it is due to substrate influence.

5. ACKNOWLEDGMENTS

We are thanking to Dr. I. H. Plonski for letting us to use her experimental equipment to prepare our samples.

6. REFERENCES

1. M.N. Baibich, J.M. Broto, A. Fert, F.Nguyen Van Dau, F. Petroff, P. Eitenne, G. Creuzet, A. Friederich and J. Chazelas, "Giant magnetoresistance of (001)Fe/(001)Cr magnetic superlattices," *Phys.Rev. Lett.* **61**, 2472-2475 (1988).
2. S.S.P. Parkin, R. Bhandra and K.P. Roche, "Oscillatory magnetic exchange coupling through thin copper layers," *Phys. Rev. Lett.* **66**, 2152- 2155 (1991).
3. J.A.C. Bland and B. Heinrich, eds., *Ultrathin Magnetic Structures I and II*, Springer, Berlin-Heidelberg, 1994.
4. M. Alper, K. Attenborough, V. Baryshev, R. Hart., D.S. Lashmore and W.J. Schwarzacher, "Giant magnetoresistance in electrodeposited Co-Ni-Cu/Cu multilayers," *J. Appl. Phys.* **75**(10), 6543-6545 (1994).
5. M. Alper, K. Attenborough, R. Hart, S.J. Lane, D.S. Lashmore, C. Younes and W. Schwarzacher, "Giant magnetoresistance in electrodeposited superlattices," *Appl. Phys. Lett.* **63**(15), 2144-2146 (1993).
6. S. Z. Hua, D. S. Lashmore, L. Salamanca-Riba, W. Schwarzacher, L. J. Swartzendruber, R. D. McMichael, L. H. Bennet and R. J. Hart, "Giant magnetoresistance peaks in CoNiCu/Cu multilayers grown by electrodeposition," *J. Appl. Phys.* **76**(10), 6519-6521 (1994).
7. S.K.J. Lenczowski, C. Schönenberger, M.A.M. Gijs and W.J.M. de Jonge, "Giant magnetoresistance of electrodeposited Co/Cu multilayers," *J. Magn. Magn. Mater.* **148**, 455-465 (1995).
8. K. Attenborough, R. Hart, S.J. Lane, M. Alper and W. Schwarzacher, "Magnetoresistance in electrodeposited Ni-Fe-Cu/Cu multilayers," *J. Magn. Magn. Mater.* **148**, 335-336 (1995).
9. C. Flueraru, M. Gartner, C. Rotaru, D. Dascalu, G. Andreescu, P. Cosmin, "Spectro-Ellipsometric Investigations of Polycrystalline Silicon Surface Roughness," *Microelectronic Eng.*, **31**, 309-316 (1996).
10. E.D. Palik, "Handbook of Optical Constants of Solids", Academic Press, New York, 1985.
11. M. Ylilammi, "Thin Film Technology VTT Electronic Materials and Components," VTT Electronics, PL. 1101, 02044 Finland.
12. B.E. Yoldas, "Deposition and properties of optical oxide cloudings from polymerized solution," *Appl. Optics*, **21**, 2960-2964 (1982).

Orthorectification of radar (SAR) data.
Synergism and complementarity with optical (Landsat TM) data

Cora Lucia Brăescu, Maria Zoran, Cristina Aiftimiei, Axente Stoica
Institute of Optoelectronics, Remote Sensing Department
PO Box MG-22, 76900 Bucharest-Magurele, Romania

Dan Răducanu
Technical Military Academy, Bucharest, Romania

ABSTRACT

The integration of digital remote sensing data from either airborne or spaceborne platforms and normal line or thematic maps has become increasingly significant to a varied field of applications, from geology to municipal mapping. To take full advantage of this data source, it must be overlayed to existing map data. The geometry and projection information must be equivalent, in other words they must be an orthogonal projection or correlation between the point on the ground and some reference surface. This process is referred to as rectification. The output satellite or airphoto images are referred to as orthorectified images or ortho images.

The particular data we have used - SAR (Synthetic Aperture Radar) have several characteristics which we had to take into account in order to produce the orthorectified images. The main problem is the geometric distortion (layover, shadowing effects) due to the oblique viewing of the antenna. Another problem met was the "speckle" type perturbation, due to the coherence of the radar signal. An orthorectification procedure for radar data (SAR-ERS-1) over a mountainous zone in Romania (Buzau) is presented, also a registration procedure with optical (Landsat TM) data and a complementarity study.

Keywords: orthorectification, SAR (Synthetic Aperture Radar), complementarity, synergism.

1. INTRODUCTION - SAR IMAGES CHARACTERISTICS

Real aperture (SLAR - Side Looking Airborne Radar) and synthetic aperture (SAR - Synthetic Aperture Radar) radars are side-looking, microwave imaging systems. The radar beam is transmitted, in a fixed direction, at right angles to the flight direction, thereby illuminating, in pulses, a patch of ground to the side and below the aircraft or satellite. Ground features closest to the sensor reflect the pulses first, while echoes from those farthest away are received last. The resultant image is therefore one in which the cross-track axis is measured in the travel time of the pulse out and back from the sensor and the along-track axis is measured in terms of distance travelled by the vehicle. Knowing the speed of propagation of electromagnetic radiation and the speed of the vehicle, these axes can both be translated into distances.

The resolution of the system across-track (range) is given by the pulse width: $R_r = \frac{\tau \cdot c}{2 \cdot \cos \gamma} \cong 23\text{m}$ for SAR. ERS-1

with τ the pulse width and γ the depression angle. The resolution of the system along-track (azimuth) is determined by the angular width of the radar beam for a real aperture radar. For synthetic aperture radars the Doppler principle is used in order to acquire a good resolution regardless of the width of the beam.

The main geometric distortions characterising radar images are:

- radar shadowing - appears due to the oblique illumination of the surface and depends on the local angle of incidence. In the shadowed areas, information is lost (and combination between radar and optical data is best suited).
- radar foreshortening - is determined by the time a surface is illuminated by the radar beam.
- radar layover - appears mainly in the mountainous regions - the peak appears farther away from the centre of the image than it is on a proper map.

The texture is defined as the frequency of tonal change on an image (its roughness and smoothness). It is the aggregate of unit features such as tree leaves and leaf shadows. As the scale of an image is reduced, the texture becomes progressively finer and disappears. In SAR imaging, much of texture is caused by "speckle". It is caused by the random effect of many small individual reflectors within a given pixel. The overall effect is an image which gives a "pepper and salt" texture, causing a distraction to the interpreter. The way to get rid of this appearance is by filtering the image. Usually adaptive filters are used (Lee, Kuan, Frost etc.).

Radar image processing comprises geometric correction, radiometric corrections, enhancements and classification and multi-channel classification, synergism with other data types. In this study we will focus on the geometric corrections of radar images and their synergism with optical data.

2. SATELLITE DATA USED

Date	Data type	Path/Row		
27.03.1989	Landsat TM	183/29		
		Frame	Orbit	Node
06.11.1992	SAR.PRI.ERS-I	2691	6851	descendant

From the Landsat TM image, a subimage of 1000x1000 pixels (30kmx30km) was chosen, covering the West part of Buzau (see figure 1). From the SAR.ERS-I image, a subimage of 2000x2000 pixels (25kmx25km) was read from tape, covering the same test area (see figure 2).

3. METHODOLOGY

In order to rectify the radar image, the following steps were followed:

3.1. Creating the DEM (Digital Elevation Model)

A topographic map, Long/Lat projection, 1:100000 scale was used to digitize contour levels and terrain features (water courses, roads and railroads). The corners of the selected area were:

1. Up left: 26d30'00"E/45d20'00"N
2. Up right: 26d50'40,55"E/45d19'58,09"N
3. Low right: 26d50'49,28"E/45d03'43,82"N
4. Low left: 26d30'00"E/45d03'41,18"N

The digitizing precision has been of 0,3 mm - that is about 30 m in terrain - spatial resolution, which is comparable to the satellite images resolution (30m - Landsat TM and about 25m SAR). The altimetric resolution is of 5 m.

After digitizing the contour levels from the map, the PROCONV program has been used to transform the data into UTM coordinates. GRDVEC and GRDINT programs have been used to transform the vector data into raster and then to interpolate the height values into a digital elevation model (the conic interpolation method was used). We have obtained a DEM in UTM coordinates. An image of the DEM in 3D is shown in figure 3.

3.2. SAR image simulation

For investigations regarding SAR images, especially layover and shadow, the EASI/PACE package contains a SAR simulator, which delivers an image which is dependent on the elevation model and the viewing geometry of the sensor. The backscattering properties of the surface are not taken into account and only the terrain features are simulated. As in mountainous areas the terrain is the dominating factor, the simulated and the real image are similar (if the DEM is accurate enough).



Fig.1 Landsat 5 TM(1) - West of Buzau (30x30km²)

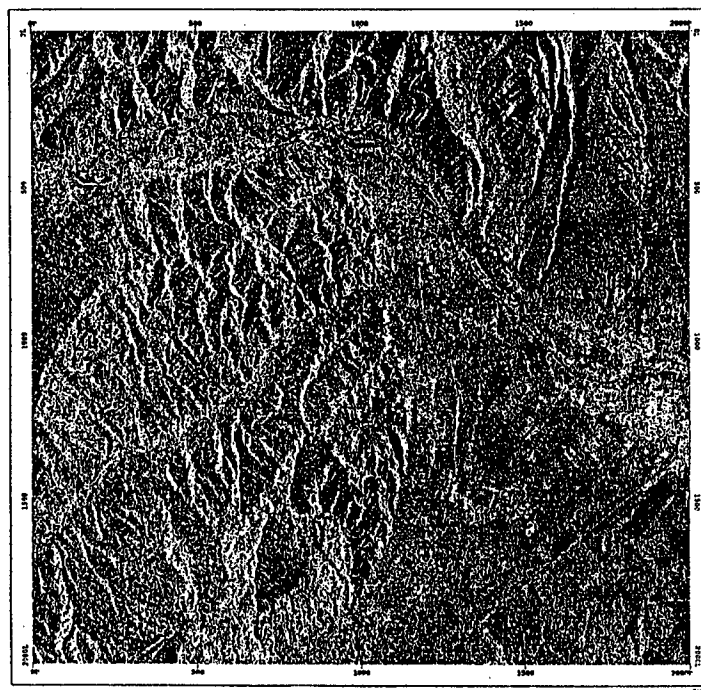


Fig.2 ERS-1.SAR.PRI image (25x25km²)

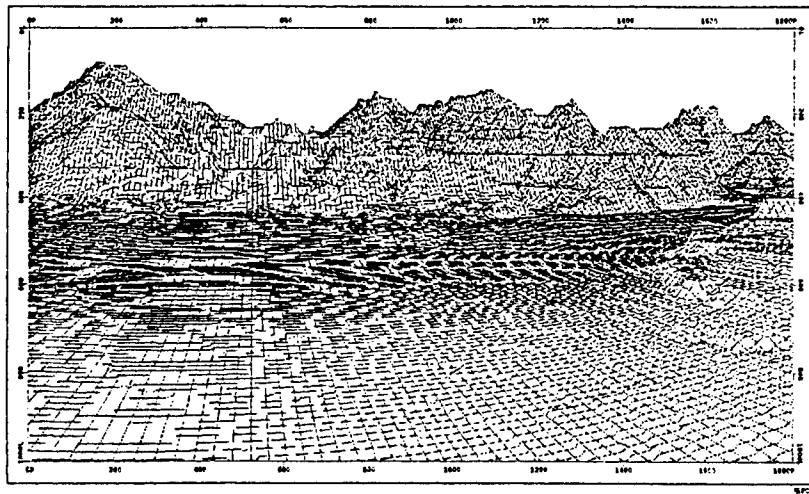


Fig.3 Digital elevation model (detail)

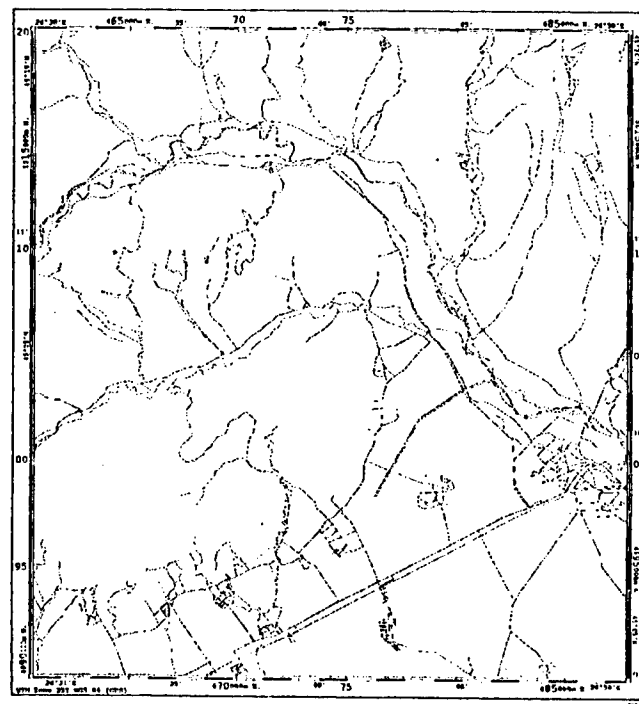


Fig.4 Digitized vectors

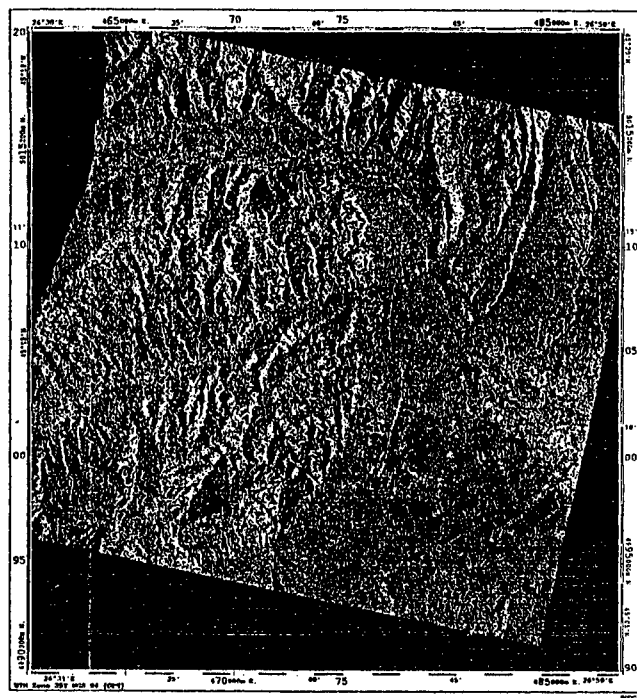


Fig.5 Orthorectified radar (ERS-1 SAR) image

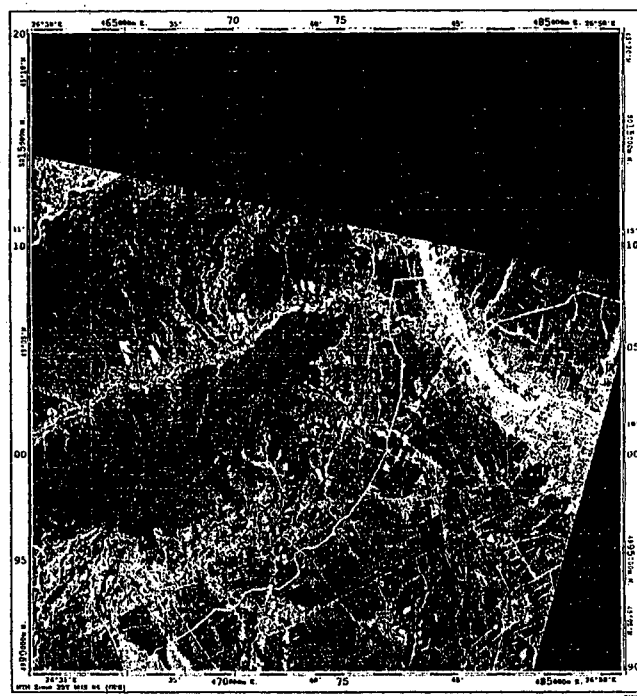


Fig.6 Geocoded optical (Landsat) image

3.3. SAR image registration

The real image can be further geocoded, by collecting ground control points (GCP) between the real and simulated radar images. The application of a mathematical model achieves the coordinate system change.

The detection of GCPs in a digital image is rather difficult, as the aspect of the synthetic (simulated) image only makes possible to take GCPs on the crest lines with a high accuracy, while no precise topographical details can be seen in valleys. The principal aim is to select GCPs spread over all the image in a regular spatial distribution. As the synthetic image, obtained from the DEM was not sufficient, we have looked for improvements. We have digitized vectors representing water courses, roads and railroads (see figure 4) and attributed them with artificial heights in order to include them into the simulated image. We have obtained thus a simulated image containing also information regarding special targets (roads, railroads and rivers - which were visible in the radar image).

GCPs were selected from comparing the radar image and the simulated one. A total of 29 GCPs (with a root mean square (RMS) error of 2.7 pixels) were selected and the SARGE program was used to register the SAR image to the DEM and thus obtain the radar ortho-image (see figure 5). The SARGE program applies the reverse model deduced from the direct model that produced the synthetic view.

3.4. Optical image registration and data integration

The registration between the optical Landsat (TM) image to the digitized vectors was performed with 29 selected GCPs, RMS of 0.9 pixels, first order polynomials and the nearest neighbour resampling method, resulting a geocoded optical image of the tested area (see figure 6).

The geometrical quality of the ortho-image has been tested by superimposition with the optical geocoded image together with the digitized vectors. Also the complementarity information is exploited. The thematic information is enhanced by the support of the optical channel, while the relief is enhanced by the microwave channel. The shadow areas on the simulated image have been transferred on the ortho-image and masked. The optical image has been superimposed on the radar image under the masked zones.

4. CONCLUSIONS

The proposed methodology yielded a good quality orthorectifying procedure for SAR images over mountainous zones. The quality of the registration constitutes an excellent starting point for the user of pixel basis fusion of Landsat TM and ERS-1 data. The complementarity between information provided by SAR and optical data can be studied.

Establishing methods for operational geocoding and image-fusion will lead to effective systems for monitoring alpine regions. This is expected to be an important step forward in environmental surveillance and planning.

5. REFERENCES

1. *Scientific Achievements of ERS-1*, ESA SP-1176/I, pp.125-131, 1995.
2. I. Dowman, et al., "Preliminary studies on the application of ERS-1 data to topographic mapping", *Proceedings of the First ERS-1 Symposium - Space at the Service of our Environment*, Cannes, France, pp.543-550, 1992.
3. F. Perlant, "Example of SPOT/ERS-1 complementarity", *Proceedings of the First ERS-1 Symposium - Space at the Service of our Environment*, Cannes, France, pp.563-568, 1992.
4. S. Quegan, R.G. Caves, R.G. White, "The structural content of ERS-1 images and its implications", *Proceedings of the Second ERS-1 Symposium - Space at the Service of our Environment*, Hamburg, Germany, pp.623-628, 1993.
5. R. Kallian, W. Kellerer-Pirklbauer, "Implementation and exploitation of a geocoded multi-sensor dataset in alpine environment", *Progress in Environmental Remote Sensing Research and Applications - Proceedings of the 15th EARSeL Symposium - Basel, Switzerland*, pp.87-90, 1995.
6. L. Castagnas, "Ortho-image SAR in mountainous areas", *Progress in Environmental Remote Sensing Research and Applications - Proceedings of the 15th EARSeL Symposium - Basel, Switzerland*, pp.119-123, 1995.

Study of Al_2O_3 single crystalline substrates for optoelectronic applications

¹C. Logofatu, ²Brandusa Iliescu, ²I. Enculescu, ³Cristiana E. A. Grigorescu, ²S. A. Manea

¹National Institute for Lasers, Plasma & Radiation Physics, Bucharest, PO Box MG-36, 76900 Romania

²National Institute for Physics and Technology of Materials, Bucharest, PO Box MG-7, 76900 Romania

³Institute of Optoelectronics, Bucharest, PO Box MG-22, 76900 Romania

ABSTRACT

These paper reports on controlled electric and optical properties of single crystalline sapphire for substrates use. The crystals were grown by the Czochralski method from a graphite crucible by using an original non-conventional crystal growth assembly. We paid a special attention to the homogeneity of the crystal. A new model for the electric conduction mechanisms is considered, the validity of which was confirmed by experimental measurements.

1. INTRODUCTION

The combination of desirable optical and mechanical properties in sapphire crystal makes it the material of choice in a variety of modern high technology applications, from environmental, space and military optical systems to high - power laser optics, high - pressure components and semiconductor substrates.

Sapphire maintains its strength at high temperatures. It has good thermal properties, excellent electrical and dielectric properties and is resistant against chemical corrosion. Its transmission spectrum is broader than that of quartz and is comparable to that of light fluorides. These properties encourage the use of sapphire in aggressive environment where reliability, optical transmission and strength are required.

Applications of sapphire in optoelectronics are claiming for single crystalline material, to achieve transparency, homogeneity and mechanical integrity. The aim of this paper is to study the optical and electrical properties of sapphire grown in a new non-conventional crystal growth assembly which provides a cost-effective technique¹.

2. OBTAINING AND CHARACTERIZATION OF THE SAPPHIRE CRYSTAL

Sapphire single crystals were grown by the Czochralski method from a graphite crucible² in a crystal growth system with traveling reflectors¹, under argon atmosphere. The melting / crystallization temperature of 2030°C was provided by a graphite heater surrounded by a complex screening system as described in our previous works^{1,2,3}. A pulling rate of 6mm/min was found suitable to obtain sapphire ingots of satisfactory crystalline properties.

In view of the crystal characterization samples 2mm thick were cut perpendicularly to the growth axis, which were plan/parallel lapped and optically polished.

From X-ray diffraction study a single crystalline orientation along [0001] axis was found as well as impurity peaks attributed to molybdenum and carbon which originates in the growth system.

An original technique was used to check the homogeneity of the sapphire crystals, by measuring the distribution of the refractive index over the cross section of the crystal. To this end, a HeNe laser was used as radiation source together with a diffraction assembly and an image acquisition and processing system (SPIRICON).

The variation of the refractive index over a 13.5 μm diameter area in the central and peripheral zones, respectively, of the cross section of the sample is shown in Figs. 1 (a) and (b), correspondingly. It can be observed that the central zone of the crystal is highly homogeneous while the peripheral one exhibits different values of the refractive index due to the staking faults at the crystal edge.

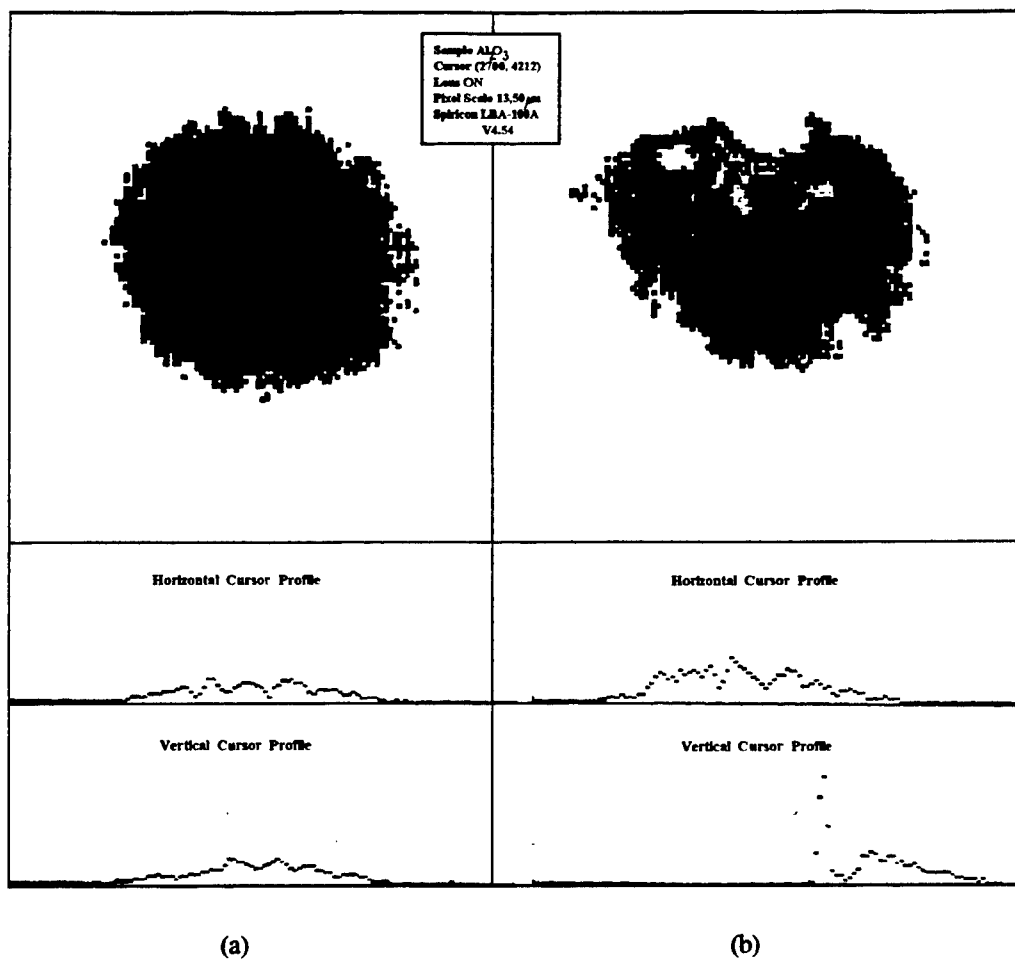


Fig. 1 The distribution of the refractive index over: (a) a central area of the sample, (b) the peripheral area of the sample

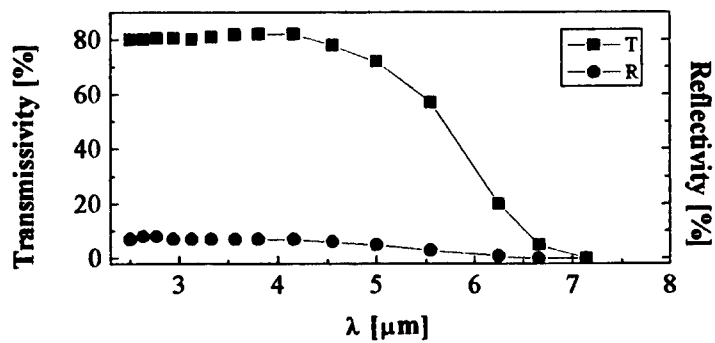


Fig. 2 Transmission and reflection spectra of the sapphire crystal grown in a graphite crucible

Transmission and reflection spectra at room temperature for the RI range (2-10 μ m) were obtained with a SPECORD M 80 spectrophotometer (Fig. 2). The transmissivity value lays around 80% which meets the most restrictive requirements for high technology optoelectronics applications.

D.c. conductivity measurements were performed in air (27% O₂) within the temperature range 300 - 1000°C, with a Lemuzy Picoampermetre type PA 15B. The electric field was 600 V/cm and the temperature was raised at a rate of 50°C/h. Platinum sheets 0.2 mm in thickness were used as electrodes. Details on the measuring setup are given in a previous paper⁴.

With the experimental data Arrhenius plots were represented and compared with already published results⁵ for pure sapphire crystals, as it is seen in Fig. 3. It is remarkable that the activation energy of our crystal, calculated from the slope of the corresponding Arrhenius plot, is of the same magnitude order as those attributed to the pure material by many authors.

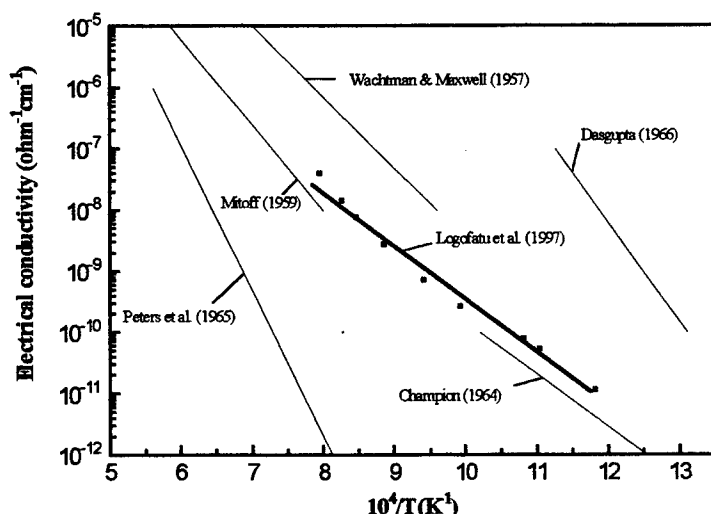


Fig. 3 Electrical conductivity of single crystalline Al₂O₃ as a function of reciprocal absolute temperature

3. A MODEL FOR THE CONDUCTION MECHANISMS

The electric conductivity and the optical properties of the sapphire crystal are strongly influenced by its impurity content and the native defects. It is of high importance to account for the concentration of both oxygen and aluminum vacancies when estimating the electrical conductivity of Al₂O₃ based crystals and for the major effect resulting from the type and concentration of the impurity, being known that a good control of the mentioned properties will provide high accuracy in the prediction of the device performance.

Our generalized model is worked out with respect to the electric conduction in Al₂O₃ which is controlled by double ionized oxygen vacancies, triple ionized aluminum vacancies and various impurity types.

The following defect reactions are considered, by using the conventional denotations⁶:

- generation and removing of oxygen vacancies:



where O_o is the oxygen atom on its lattice site, $V_o^{\bullet\bullet}$ is the double ionized oxygen vacancy, e' the electron

- generation and removing of aluminum vacancies, V_{Al}''' :



where h is the hole

- intrinsic thermal generation:



- donor ionization:



where D is the donor impurity and \dot{D} the ionized donor

- acceptor ionization:



where A is the acceptor impurity and A' the ionized acceptor

The equilibrium equations corresponding to the mentioned defect reactions are written below using the conventional denotations⁶:

$$[\ddot{V}_o] n^2 p_{O_2}^{1/2} = k_{vo}^0 \exp\left(-\frac{E_1}{kT}\right) \quad (6)$$

$$[V_{Al}''] p^3 = k_{Al}^0 \exp\left(-\frac{E_2}{kT}\right) p_{O_2}^{3/4} \quad (7)$$

$$np = k_i^0 \exp\left(-\frac{E_g}{kT}\right) \quad (8)$$

$$[\dot{D}] n = k_D^0 \exp\left(-\frac{E_3}{kT}\right) [D] \quad (9)$$

$$[A'] p = k_A^0 \exp\left(-\frac{E_4}{kT}\right) [A] \quad (10)$$

where $[]$ denotes the concentration of the corresponding quantities, n and p - the free electron and hole concentration, respectively, p_{O_2} - oxygen pressure, k - the equilibrium constants of the corresponding reactions, E_1 - E_4 the activation energies, respectively, E_g - the energy gap.

The upwritten equations together with the neutrality condition :

$$n + 3[V_{Al}''] + [A'] = p + 2[\ddot{V}_o] + [\dot{D}] \quad (11)$$

This model enabled us to make an appropriate interpretation of the experimental data. From the electrical conductivity measurements an activation energy of about 4 eV resulted, which is very close to that of the pure crystal. By accounting for this fact and for the value of the oxygen pressure used during the experiments equation. (11) turns into:

$$3[V_{Al}''] \approx p \quad (12)$$

In this case our model provides for the energy gap a value of 9.1 eV which is in a good agreement with the values previously reported by various authors⁷.

4. CONCLUSIONS

Sapphire single crystals were obtained using a new non-conventional assembly which provides a cost-effective technique.

From the investigation of their optical properties over the IR range a transmissivity of about 80% , a reflectivity of about 7% and a homogeneous distribution of the refractive index in the center of the crystal resulted, which reveals it most suitable for optoelectronic applications.

From electrical conductivity measurements (Arrhenius plots) an activation energy value close to that reported for pure sapphire was obtained, which might be evidence for the low impurity content in the investigated crystal.

A new, complex, theoretical model for the electrical transport phenomena was worked out, which enabled an appropriate interpretation of the experimental data.

To better knowledge of the material properties and a deeper understanding of the complicated transport mechanisms further experiments under various oxygen pressure and temperature conditions will be performed in the near future.

5. REFERENCES

1. C.E.A. Grigorescu, A.S.Manea, "Heating and melting system", Romanian Pat. No. 108 423/1984.
2. C.E.A. Grigorescu, A.S.Manea, C.Logofatu, "Crystal growth thermal fields control by travelling reflectors", submitted to *J. Crystal Growth*.
3. A.S. Manea, C.E.A. Grigorescu, "Heater for the melting of high purity materials", Romanian Pat. No. 102 049/1990.
4. B.Iliescu, A.Vedda, G.Spinolo, "Alkali defect center and current density peaks in quartz sweeping", *Cryst. Res. Technol.*, **31**, pp. 215-218, 1996.
5. P.Kofsad, *Nonstoichiometry, Diffusion and Electrical Conductivity in Binary Metal Oxides*, p. 344 Wiley Interscience, New York, 1972.
6. P.Kofsad, *Nonstoichiometry, Diffusion and Electrical Conductivity in Binary Metal Oxides*, p. 25, Wiley Interscience, New York, 1972.
7. O.T. Özkan, A.J. Moulson, "The electrical conductivity of single-crystal and polycrystalline aluminum oxide", *J. Phys. D: Appl. Phys.*, **3**, pp. 983-987, 1970.

Optical light modulation in planar $\text{As}_2\text{Se}_3\text{Sn}_x$ waveguides

A. Popescu, A. Albu, A. Tsaranu

Center of Optoelectronics, Academy of Sciences of Moldova

1 Academiei Str., MD-2028 Chisinau, Moldova

ABSTRACT

The modulation of infrared radiation ($\lambda=1150\text{nm}$) in waveguides of glassy semiconductors As_2Se_3 and $\text{As}_2\text{Se}_3\text{Sn}_{0.175}$ has for the first time been investigated experimentally. The measurement of frequency-response characteristic shows that there are two relaxation constants-fast and slow.

The rise time of optical modulator with arsenic selenide waveguides having tin additions is nearly 10^{-3}s . The origin of additional absorption can be explained in the framework of two-steps transition models.

The first one is the excitation of excess carriers into the conducting band by highly absorbed pump beam and their partial capturing on localized states. The second is the re-excitation of trapped carriers and restoration of optical absorption by signal waveguided beam.

Keywords: integrated optics, light modulation, chalcogenide glasses, optical properties of amorphous semiconductors.

1. INTRODUCTION

The photoinduced changes of refractive index and optical absorption in chalcogenide glassy semiconductors are widely studied both for elucidating physical mechanisms and applied purposes. The photoinduced changes which are maintained after interrupting the influence and are related to the structural changes have been widely investigated. At the same time a dynamical effect involved in the transport phenomena of glassy semiconductors or energetical spectrum filling occurs. The value of the dynamical effect is one-two orders smaller than the stationary one, but can be more sensitive to the influencing optical radiation. Photoinduced optical absorption in amorphous semiconductors was explained for the first time by Kastner¹ involving the population of localized states. These ones can be modified by thermal or optical activation². Andriesh et al.³ propose a more complex model taking into account multiple trapping on shallow and deep states. This model explains not only the restoration but also the enhancement in certain conditions of optical absorption in chalcogenide glass fibres.

This effect is of interest in creating active opto-electronic components. So, integrated optical switches⁴ and modulators⁵ of the type "light-light" in planar As_2S_3 waveguides of glassy semiconductors had been investigated earlier, but the time of their response turned out to be enough great ($\sim 20 \cdot 10^{-3}\text{s}$). The decrease of time relaxation is to be expected in semiconductors of this class but with a smaller width of the forbidden zone. The aim of this paper is to study the characteristics of full light waveguide modulator based on As_2Se_3 glassy semiconductor.

2. EXPERIMENTAL PART

As_2Se_3 forms a multicomponent glassy alloy when tin is added. The thin films of these compounds obtained by using the method of thermal vacuum evaporation create a planar waveguide structure on the polished glassy substrates. The thickness of the films is 1-2 μm . The experimental set-up is showed on fig.1. The infrared radiation of the He-Ne laser with the wavelength of 1150 nm and 10 mW power was let in and out of the planar waveguide using two gallium - phosphide prisms. This radiation serves as a signal beam. The beam is sine-modulated by a chopper at the frequency of 4 kHz in order to avoid D.C. shift and measure low level intensities. The focusing lens is used to achieve better coupling of the radiation into waveguide. The transformed beam size is $\phi 0,2\text{ mm}$ at the entrance of the prism. The estimated coupling efficiency is 10-20% and waveguide losses 2-5 dB/cm. The output signal registered by the photodiode after amplifying it with the selective voltmeter was sent to the self-recorder.

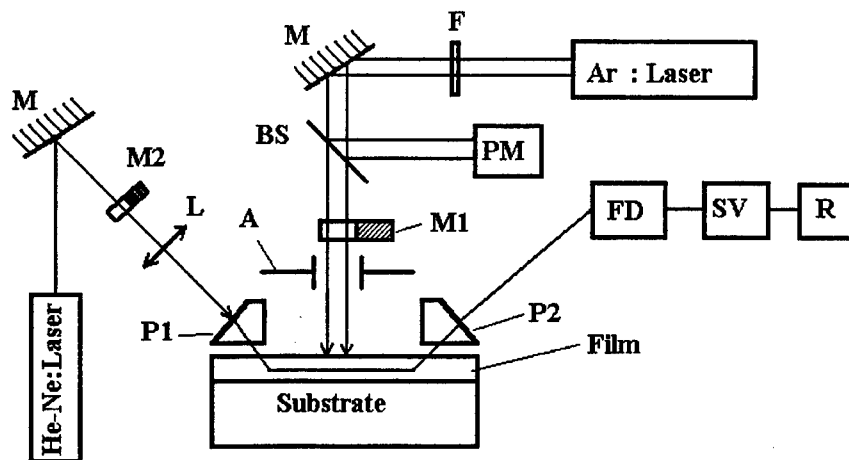


Fig.1 Experimental setup for investigation of light by light optical modulation: M-mirrors, F-optical filter, BS-beam splitter, PM-power meter, FD-photo receiver, SV-selective voltmeter, R-recorder, M1,M2-mechanical modulator, L-focusing lens, P1,P2-coupling GaP prisms, A-limiting aperture

The modulating beam of the argon laser having the wavelength of 514 nm and the power of 40 mW is directed towards the area between the prisms perpendicular to the planar waveguide plane. Its radiation can be attenuated with optical filters and modulated using mechanical switch. The incidente power of pump beam is measured by an power-meter.

3. EXPERIMENTAL RESULTS

Figure 2 shows the typical modulation curves of the waveguide radiation under the influence of a single rectangular impulse, the duration of which is 10 and 20 s (curve 1). Curve (2) corresponds to the waveguide of As_2S_3 and curve (3) to the one of $\text{As}_2\text{Se}_3\text{Sn}_{0.175}$.

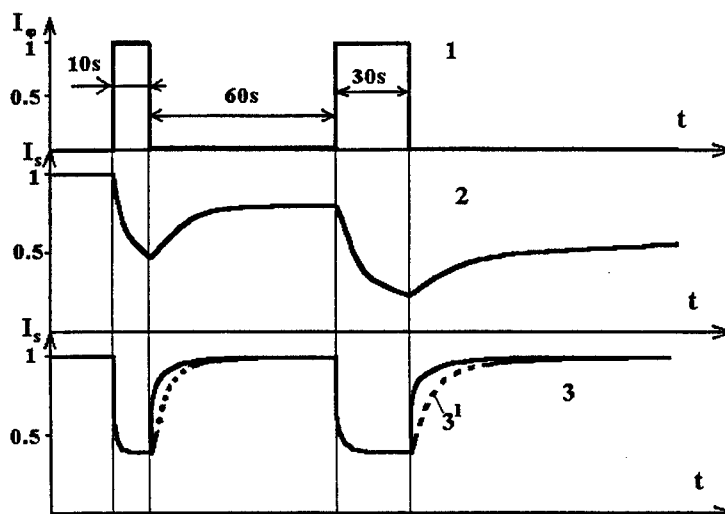


Fig.2 Light modulation in planar waveguide for $\text{As}_2\text{S}_3\text{Sn}_{0.175}$ film (3,3'), As_2S_3 film (2). Curve (1) is the pump beam shape.

From the given figure it is seen that the time of switching on and off for arsenic sulphide is much longer than for arsenic selenide with tin additions. Besides that it turned out that in the case of As_2S_3

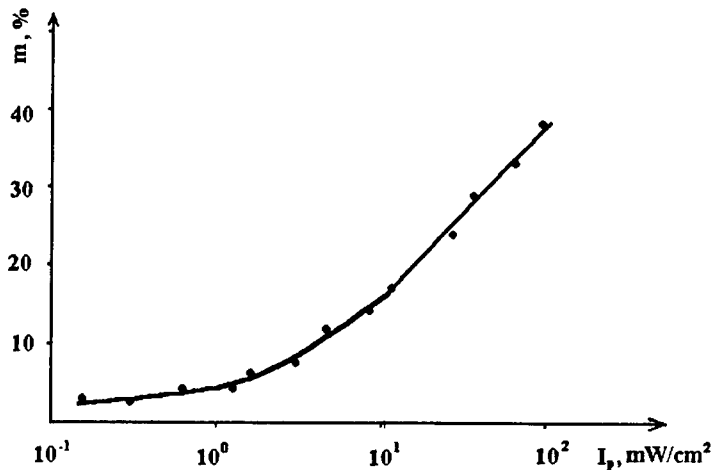


Fig.3 The modulation coefficient versus pump beam intensity for $\text{As}_2\text{Se}_3\text{Sn}_{0.175}$ waveguide

waveguide there occurred a decreasing of the initial level during the next radiation cycles which is indicative of the taking place structural changes and induced light scattering. Such a transition for $\text{As}_2\text{Se}_3\text{Sn}_{0.175}$ was not observed. It must be mentioned that the restoration time of optical absorption increase when the intensity of waveguide signal decrease (see curve 3').

The analysis of the modulation curves shows that they can't be described by only one time relaxation constant. Therefore the amplitude-frequency characteristics of the modulation coefficient $K_m = \lg(I_f/I_0)$ for the periodical modulated pump beam has been

measured. Here I_f is the modulation amplitude at f frequency, but I_0 is the modulation amplitude at the frequency close to zero. The results given in fig.3 shows these dependences for waveguide travelling of signal beam (curve 2) and for transverse travelling of pump beam (curve 1).

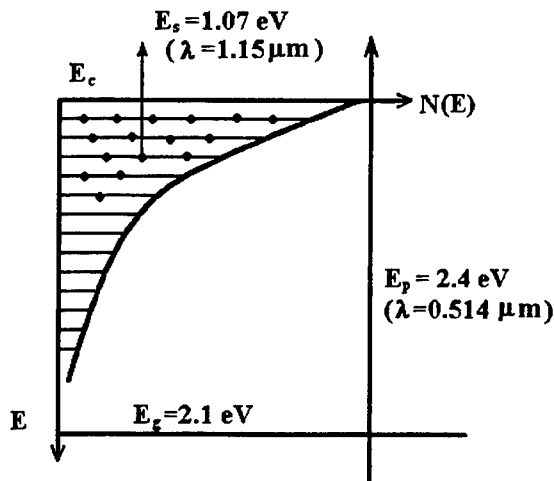


Fig.5 Model of photoinduced absorption in chalcogenide glasses

In both cases the modulation coefficient doesn't change up to the frequency of 150 Hz. However,

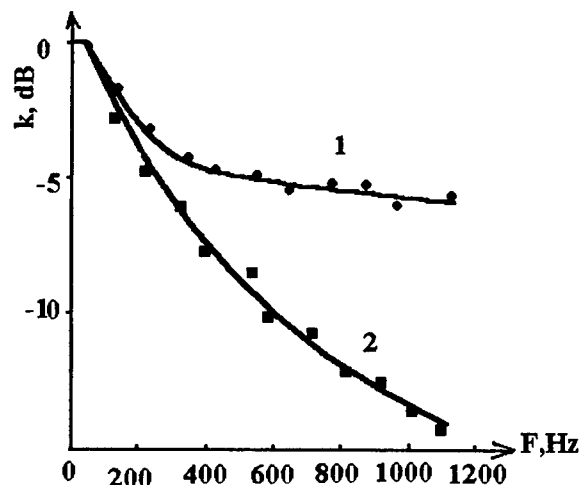


Fig.4 The frequency-response characteristic of the $\text{As}_2\text{Se}_3\text{Sn}_{0.175}$ waveguide structure for transverse propagation (2) and waveguide propagation (1) of the signal.

afterwards, the modulation coefficient for transverse travelling sharply falls while for arsenic selenide with tin additions does not exceed 5.5 dB at the frequency of 1000 Hz, this corresponding to the speed of response of the order 10^{-3} s. As can be seen from fig.4, the dependence of the coefficient of modulation versus the intensity of pump beam turned out to be rather linear in the range of 5 to 100 mW/cm^2 . There also occurs threshold intensity (about 1 mW/cm^2) smaller than that there is no modulation. This fact is indicative of the two-cascade mechanism of light absorption.

4. DISCUSSION

The experimental results can be explain in the base of diagram fig. 5 taking in account the follow conditions:

1. In chalcogenide glasses there are exponential distributed states in the forbidden band. The band gap energy E_g is 2.1 eV for arsenic selenide.

2. The pump beam have quantum energy $E_p = 2.4$ eV , intensity $I_p = 10^{-1}$ W and absorption coefficient $\alpha_p = 10^4$ cm $^{-1}$

3. The signal beam have the parameters quantum energy $E_s = 1.1$ eV , waveguide intensity $I_s = 10^3$ W/cm 2 and, absorption coefficient $\alpha_s = 1$ cm $^{-1}$.

The excess carriers excited in the conduction band quickly reach the bottom of the band ($\tau \sim 10^{-12}$ s). This carriers partialy recombine and partialy are trapped on the localized states in forbiden zone. There are two kind of states - shallow states with the energy band $\Delta E \sim kT$ and deep states. The signal beam can't be absorbed directly because $E_s < E_g$. It can be absorbed only by the excess traped carriers. So there is a self induced restoration of optical absorption with rise time $\tau \sim I_s^{-1}$. The self induced restoration dominate the thermal activation even at the ambient temperature because the signal intensity is rather high. This can be seen on fig. 2: curve 3 and 3' are for two different signal intensity. The model also predict a threshold signal power witch corespond to the case when the thermal activation with the subsequent recombination dominate the process of creating the exces carriers.

5. REFERENCES

1. G. Orenstein and M. Kastner, Phys. Rev. Lett. **46**, 1421 (1979).
2. V. Arhipov and E. Emilianov, Phys. Technol. Semicond. (Moscow) **25**, 1792, (1991).
3. A. M. Andriesh et al. J. Non-Cryst. Solids, **189**, 147-153, (1995).
4. Ke. Tanaka, Y. Imai and A. Odajima J.Appl.Phys., **57**(11), 4897, (1985).
5. A. M. Andriesh, O. V. Bolshacov, V.V.Zhitar, A.A.Popescu. J. Non-Cryst. Solids, **90**,565, (1987).

Approximate Solutions of the Eigenvalue Equation Near Cut-off for TE_{0m} and TM_{0m} Modes for a Step Index Fiber Optic - New Forms and Considerations

Schiopu Carmen Liliana, Schiopu Paul

University "Politehnica", Department of Electronic Engineering, Bucharest, România

ABSTRACT

In this work the authors intend to present a new approximate technique of solving the characteristic (eigenvalue) equation for a step index fiber optic near cut-off. To illustrate this new method, there are presented (and demonstrated) two particular forms, corresponding to the case $v = 0$ (TE_{0m} and TM_{0m} modes). Solutions of these equations are compared with other solutions suggested by Marcuse and - also - it is analysed the accuracy of our results compared with the general solution of the characteristic equation.

Keywords : step index fiber optic, characteristic equation, approximative solutions near cut-off

1. THEORETICAL CONSIDERATION

Because the well-known eigenvalue exact equation - for modes of optical fibers having an uniform core made from a glass of refractive index n_1 (constant) embedded in a large cladding glass of index n_2 ($n_2 < n_1$, $n_2 \neq n_1$) - is a rather complicated transcendental equation^{*}:

$$\left[\frac{J'_v(u)}{uJ_v(u)} + \frac{K'_v(w)}{wK_v(w)} \right] \cdot \left[n_1^2 \cdot \frac{J'_v(u)}{uJ_v(u)} + n_2^2 \cdot \frac{K'_v(w)}{wK_v(w)} \right] = \left(\frac{\beta v}{k_0} \right)^2 \cdot \left(\frac{V^2}{u^2 w^2} \right)^2 \quad (1)$$

it is very difficult to find exact solutions. Many authors^{1,2,3,4} try to solve this problem using approximation of the true modes. Most frequently, this simplification consists in the weakly-guiding approximation $n_1 - n_2 \ll n_1$ ($n_1 - n_2 \leq 0,1 \cdot n_1$). Another method applied in solving the eigenvalue equation having the form (1) consists in rewriting this equation near or far from cut-off, because in these special frequency ranges can be used approximation for the $J_v(u)$ Bessel function and the modified Bessel function of the second kind $K_v(w)$ of small or large argument. In this paper, the authors try to approach some important problems and questions connected with solving the eigenvalue equation near cut-off in a particular case: TE_{0m} and TM_{0m} modes ($v = 0$).

I. The first step consists in writing the eigenvalue equation in accordance to the imposed value $v = 0$, which represents a special case (we obtain two different equations, corresponding to the modes designated as TE_{0m} and TM_{0m}).

II. Because the cut-off condition is $w = 0$ ($u = V_c$), near cut-off we have the inequality: $w \ll 1$ ($w \rightarrow 0$), so it can be used the following approximation for the Bessel function of the second kind of small argument:

$$\lim_{w \rightarrow 0} \frac{K_1(w)}{wK_0(w)} = \frac{1}{w^2 \cdot \ln(2/\gamma w)} \quad \text{with } \gamma = 1,781672 \quad (\text{Euler's constant}) \quad (2)$$

III. When $w \rightarrow 0$, $u \rightarrow V = V_{c, \text{mode}}$, so that near cut-off we can use an approximate form for the other parameters used in the eigenvalue two equations:

$$\left. \begin{array}{l} u^2 = V^2 - w^2 \\ w \rightarrow 0 \Rightarrow V \rightarrow V_c \end{array} \right\} u = V \sqrt{1 - \frac{w^2}{V^2}} \approx V \left(1 - \frac{w^2}{2V^2} \right) \quad (3) \quad \text{so that} \quad u \approx V - \frac{w^2}{2V} \quad \text{and} \quad u - V_c = (V - V_c) - \frac{w^2}{2V}$$

^{*} We use the usual definitions of $u^2 = a^2 \cdot (k_0^2 n_1^2 - \beta^2)$, $w^2 = a^2 \cdot (\beta^2 - k_0^2 n_2^2)$ and $V^2 = u^2 + w^2$ representing the normalised frequency.

We try to expand Bessel function of first kind near cut-off in terms of Taylor's series, using only the first two terms (considering $u - V_c \leq 0,1$):

$$J_v(u) \approx J_v(V_c) + (u - V_c)J'_v(V_c) \quad \text{but} \quad J'_v(V_c) = -\frac{v}{V_c}J_v(V_c) + J_{v-1}(V_c) \quad \text{and also} \quad J'_v(V_c) = +\frac{v}{V_c}J_v(V_c) - J_{v+1}(V_c)$$

so it results :

$$\begin{cases} J_v(u) = J_v(V_c) \left[1 - \frac{v}{V_c} \left(V - V_c - \frac{w^2}{2V} \right) \right] + \left(V - V_c - \frac{w^2}{2V} \right) J_{v-1}(V_c) \\ J_v(u) = J_v(V_c) \left[1 + \frac{v}{V_c} \left(V - V_c - \frac{w^2}{2V} \right) \right] - \left(V - V_c - \frac{w^2}{2V} \right) J_{v+1}(V_c) \end{cases} \quad (4.a) \quad (4.b)$$

The accuracy of this approximation depends on the w/V range values. If we define the relative error of the series expansion of the radical (3) in terms of $\varepsilon_r = f(x) = \left| \sqrt{1-x} - (1-x/2) \right| / \sqrt{1-x}$, with $x = w^2/V^2$, it can be demonstrated that for $w/V \leq 0,8$ the relative error ε_r is less than 10 %. Also, we can demonstrate that the influence of the third term of the Bessel expand in Taylor's series is insignificant ; so the Eq. (4.a) and (4.b) may be considered enough accurately to be used further.

IV. Taking into account all this consideration , now we can analyse separately the two eigenvalue equations , having the purpose of finding the most appropriate approximate forms which can allow approximate - but as accurately as possible - solutions.

1.1. Approximate solutions of the Te_{cm} modes

The particular characteristic (eigenvalue) equation can be written [replacing the approximations (2) and the condition $v=0$ in Eq. (1)] in the form :

$$\frac{J_1(u)}{uJ_0(u)} + \frac{K_1(w)}{wK_0(w)} = 0 \quad \Leftrightarrow \quad \frac{J_1(u)}{uJ_0(u)} + \frac{1}{w^2 \ln(2/\gamma w)} = 0 \quad (5) \quad \text{with the cutoff condition } J_0(V_c) = 0$$

Because we have (see Eq. (4)) :

$$J_0(u) = J_0(V_c) - J_1(V_c) \left(V - V_c - \frac{w^2}{2V} \right) = -J_1(V_c) \left(V - V_c - \frac{w^2}{2V} \right)$$

$$J_1(u) = J_1(V_c) \left[1 - \frac{1}{V_c} \left(V - V_c - \frac{w^2}{2V} \right) \right] + J_0(V_c) \left(V - V_c - \frac{w^2}{2V} \right) = J_1(V_c) \left[1 - \frac{1}{V_c} \left(V - V_c - \frac{w^2}{2V} \right) \right]$$

and $u \approx V - (w^2/2V)$, if we substitute this partial results in the Eq. (5) results the approximate form of the characteristic equation near cut-off:

$$-\frac{w^4}{2V} \left[\frac{1}{V_c} \cdot \ln\left(\frac{\gamma w}{2}\right) + \frac{1}{2V} \right] + w^2 \left[1 - \frac{V_c}{2V} - \frac{2V_c - V}{V_c} \cdot \ln\left(\frac{\gamma w}{2}\right) \right] - V \cdot (V - V_c) = 0 \quad (6)$$

where $V_c = V_{cm} = K_{1cm} \cdot a = \rho_{0m}$. This equation permits the following observations :

- V (normalised frequency, imposed by the generator) has a known value ;
- V_c (for a certain mode) is one of the Bessel function roots ;
- the only unknown value of the Eq. (6) is w ; it can be determined by numerical (computational) analyse (anyway, we expect a very small value !);
- from $u^2 + w^2 = V^2$ we can calculate the numerical value of u (which is in the proximity of V_c value) ;
- if all this numerical values are known, all the other parameters (especially the propagation coefficient β) can be determined, so the theoretical problem is solved.

Because the Eq. (6) differs from another approximate forms proposed by Marcuse (the only one who try to find equivalent / simplified forms for the characteristic equation near cut-off), such of :

$$w^2 = \frac{2V_c(V - V_c)}{1 - 2 \ln(\gamma w/2)} \quad (7.a) \quad (\text{Marcuse I}^5)$$

$$w^2 = \frac{-V_c(V - V_c)}{\ln(\gamma w/2)} \quad (7.b) \quad (\text{Marcuse II}^6)$$

we try to compare and analyse in detail - using a special computer program - the solution of Eq. (6) and (7). The numerical results are presented as function $w = f(V)$. The equation $u = \sqrt{V^2 - w^2}$ allows the next results, presented as function $u = g(V)$. All this graphical dependencies (results) for TE_0 mode can be watched in Figure 1.

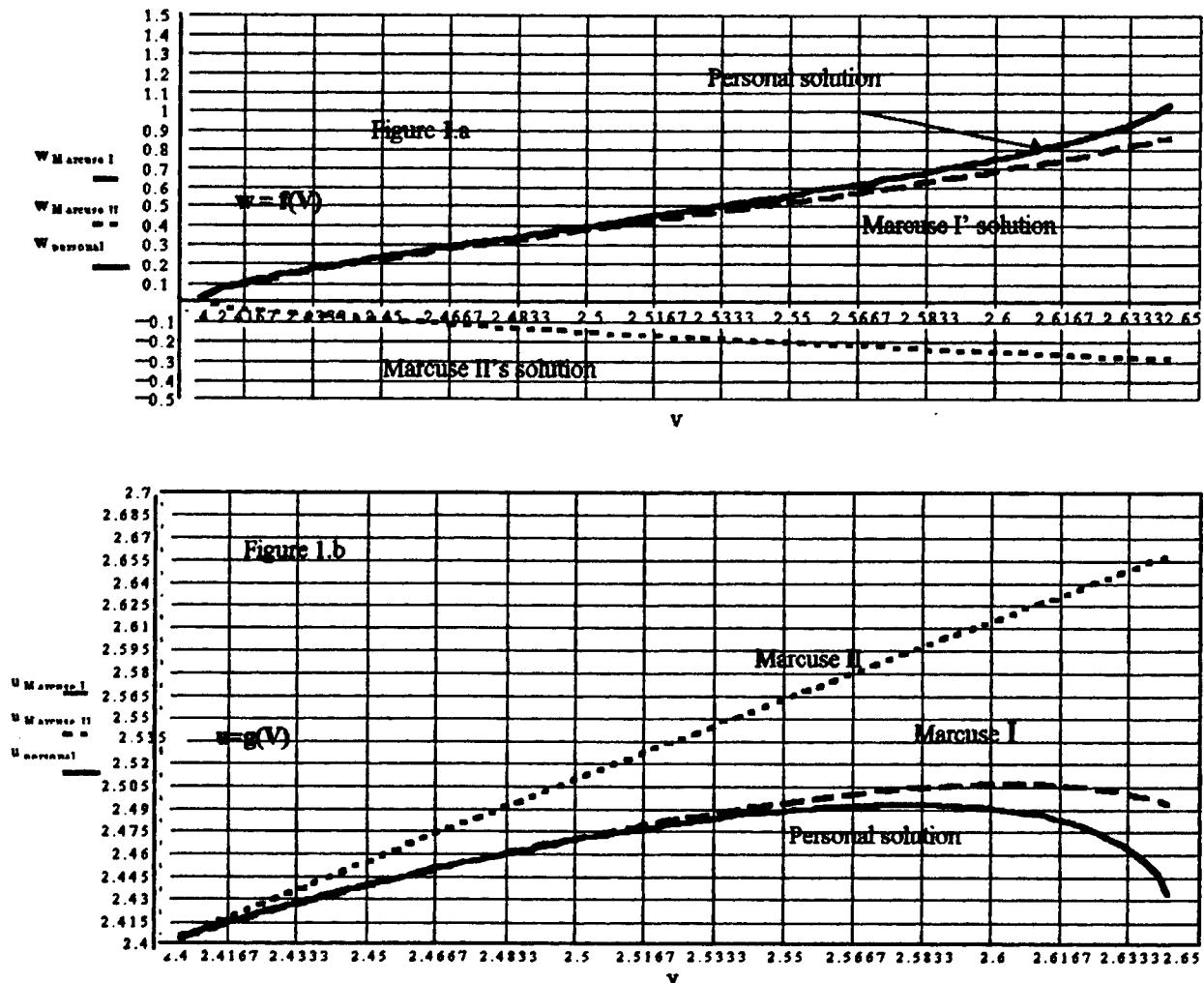
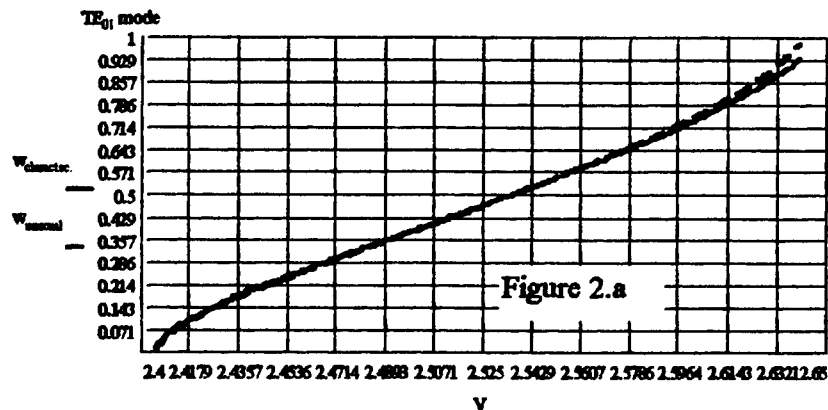


Figure 1.a and 1.b. Comparative solutions for the TE_0 mode ($V_c = 2,4048$)



Because all the other dependencies (obtained for TE_{02} and TE_{03} modes) has similar and different forms (personal / Marcuse I and Marcuse II), we try to give an answer to the question : which of this curves are appropriate ? We compare (by help of a mathematical computer program) our personal results with those which correspond to the exact characteristic equation form (5) (see Figure 2) .

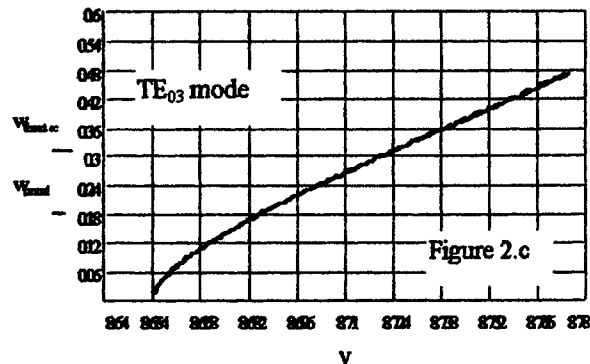
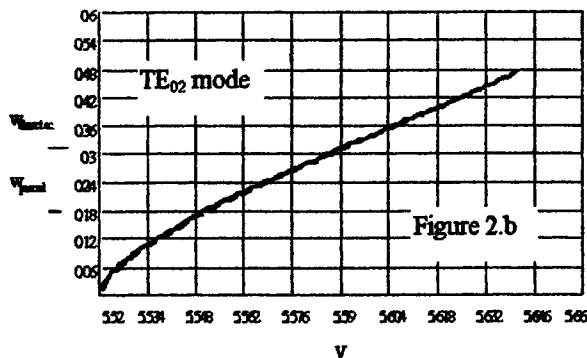


Figure 2. Comparative personal /exact characteristic equation near cut-off solutions for the first three modes TE_{01} , TE_{02} , TE_{03} .

We can formulate an important conclusion : the personal approximate equation (6) allows to calculate solution approached with the general solution of the characteristic equation near cut-off but - also - we can affirm that the Marcuse equation forms (7.a) and (7.b) are not correct.

1.2. Approximate solutions of the TM_{0m} modes

The characteristic equation : $n_1^2 \frac{J_1(u)}{uJ_0(u)} + n_2^2 \frac{1}{w^2 \ln(2/\gamma w)} = 0$ (8) with the cut-off condition $J_0(V_c) = 0$ takes the

$$\text{approximate form : } -\frac{w^4}{2V} \left[\frac{n_{12}}{V_c} \ln \frac{\gamma w}{2} + \frac{1}{2V} \right] + w^2 \cdot \left[1 - \frac{V_c}{2V} - n_{12} \cdot \frac{2V_c - V}{V_c} \ln \frac{\gamma w}{2} \right] - V \cdot (V - V_c) = 0 \quad (9)$$

where $n_{12} = (n_1 / n_2)^2$. We can observe that the presence of n_{12} is the only difference between Eq. (6) and Eq. (8). In our numerical computation, n_{12} have the value 1,1. This time, we compare our form with another Marcuse suggested form :

$$w^2 = \frac{-V_c \cdot (V - V_c)}{(n_1 / n_2)^2 \cdot \ln(\gamma w / 2)} \quad (10) \quad \text{The aspect of the dependence } w = f(V) \text{ and } u = g(V) \text{ is very close with those}$$

which was obtained in the TE_{0m} case. Some representative examples can be seen in Figure 3.

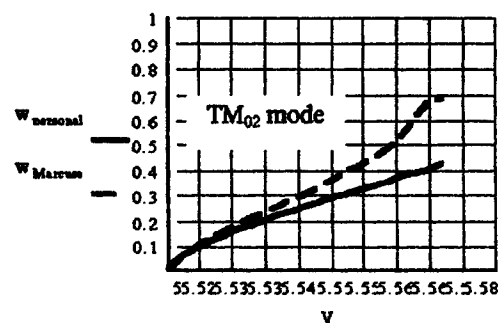
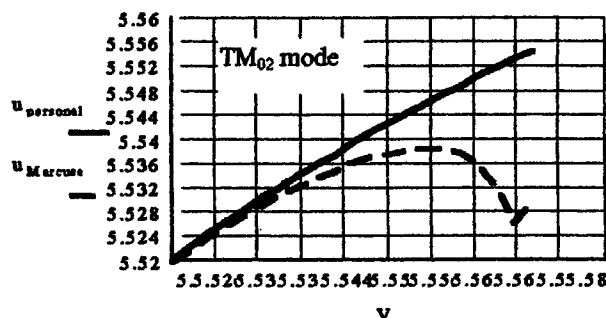
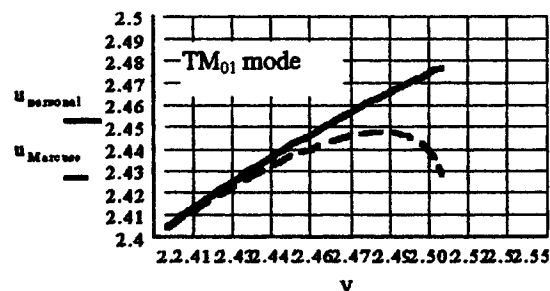
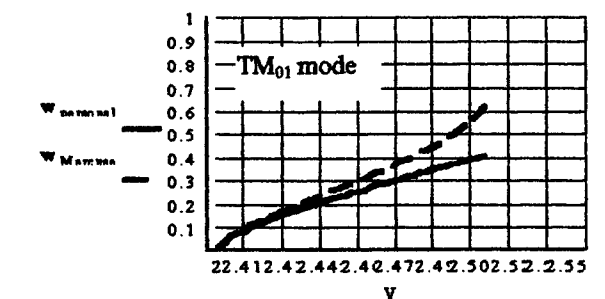


Figure 3. Comparative solutions (personal , Eq. (9) / Marcuse, Eq.(10)) for the first TM_{0m} modes

It can be observed substantial differences between the two sets of curves. Because (like in the TE_{0n} case) we can also present comparative curves for our solution (9) and for the general characteristic equation near cut-off (Eq. (8) with $n_{12} = 1, 1$), see Figure 4, we can easily observe the accuracy of our approximation.

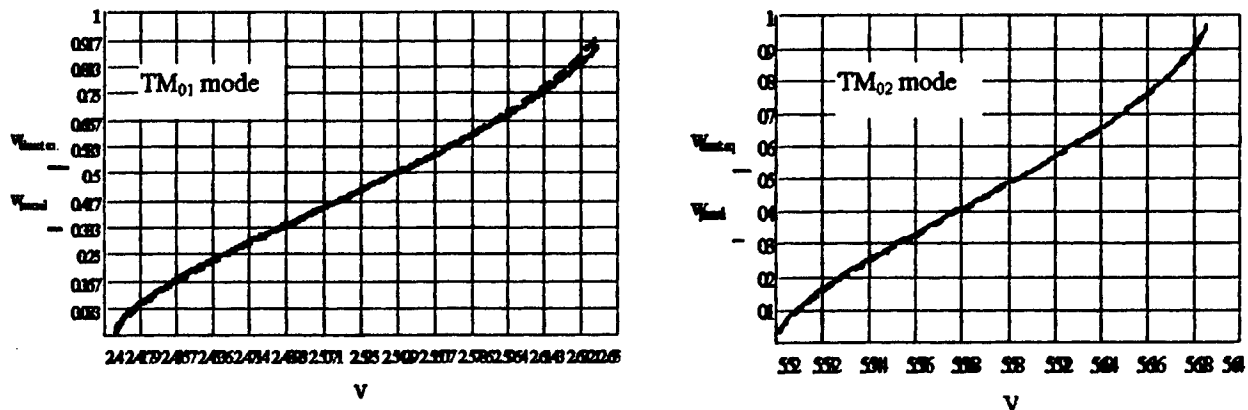


Figure 4. Comparative curves for the first two TM_{0n} modes which demonstrate the accuracy of our solution

V. The last problem we try to approach is to give an answer to the question: why and with which error our equations (6) and (9) can be used in the general frequency case (not only near cut-off)? For solving this problem we try to represent (also comparative) solutions of our equation and solution (calculated with computer) of the characteristic (eigenvalue) general equation having the form (1). The results can be observed in Figure 5 and 6.

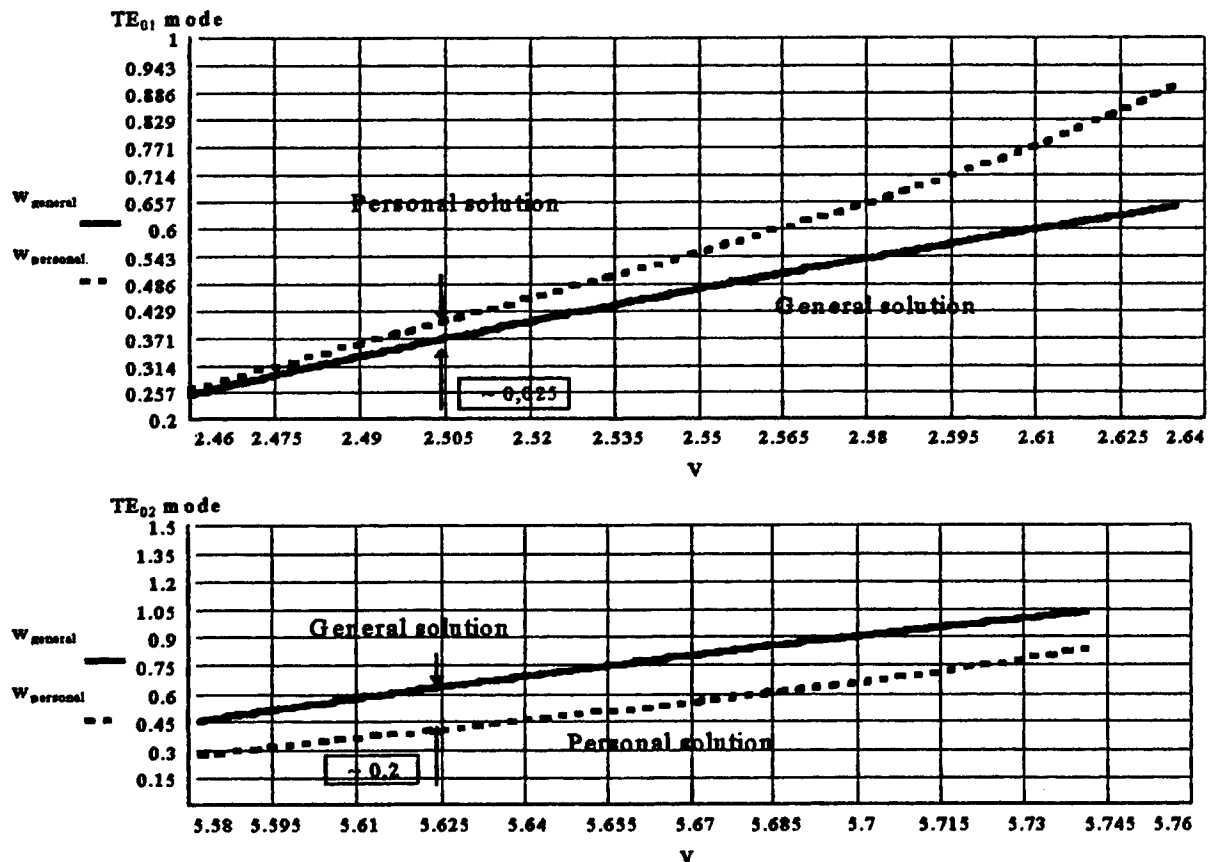


Figure 5. Comparative results for TE_{0n} modes.

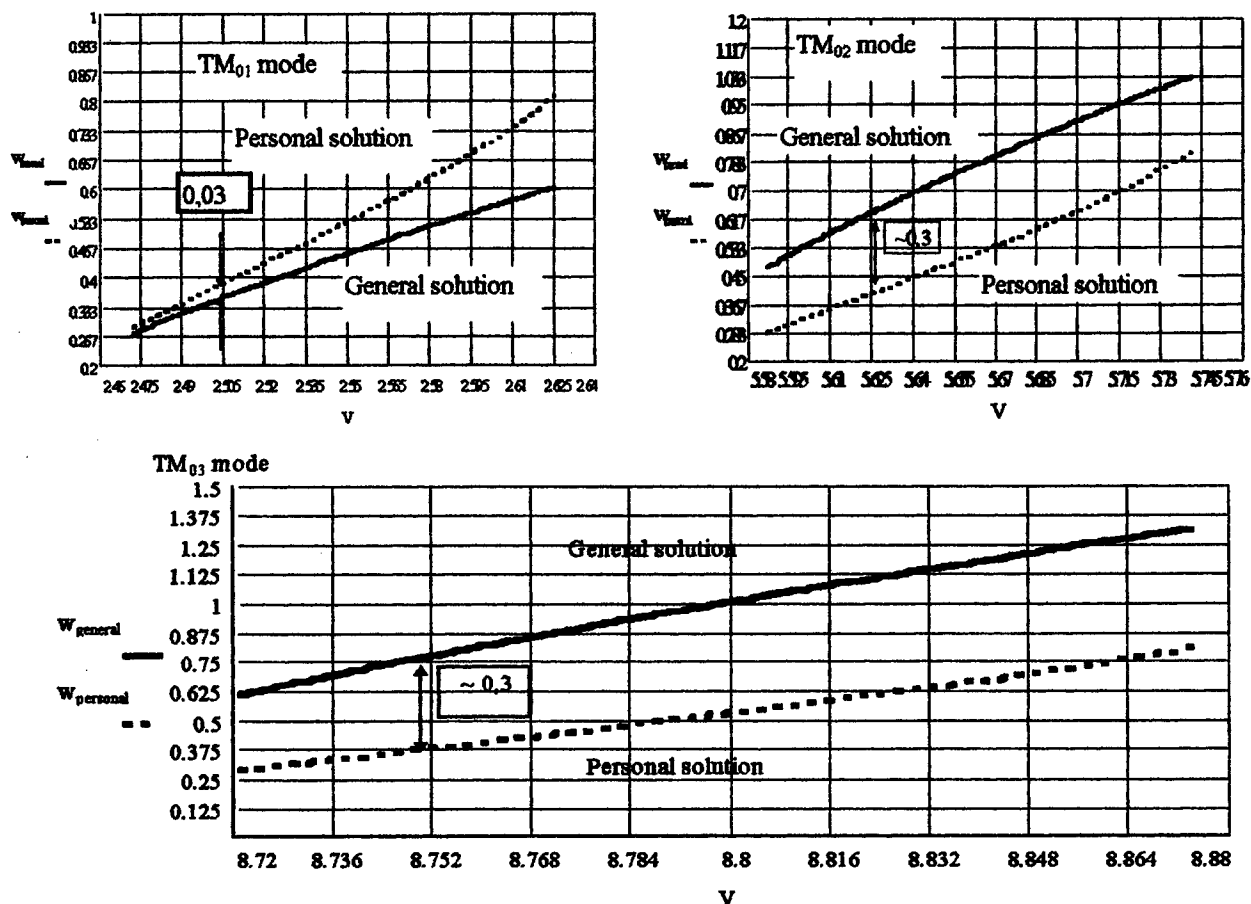


Figure 6. Comparative results for TM_{0m} modes.

2. CONCLUSIONS

The graphical dependencies from Figure 5 and Figure 6 shows that there are differences between the general and the approximate solution of the characteristic equation, but :

- we can find numerical results near cut-off (when $V - V_c \leq 0,1$) **only if we use the approximate equation** ; the general equation doesn't allow to have any solution if V is close to V_c , so we have no choice ;
- the numerical differences which are marked on the graphics have the explanation of growing the ϵ_r relative error value, which means that our Bessel function expand in terms on Taylor's series becomes incorrect.

In conclusion , this paper demonstrate that - near cut-off - the approximate Eq (6) and (9) are appropriate to be used like eigenvalue/characteristic equation for TE_{0m} and TM_{0m} modes. In the general case ($v \neq 0$) an extended analyse is presented in ⁷.

3. REFERENCES

1. D. Gloge, "Weakly guiding fibers", *Applied Optics*, No. 10, 1971
2. M.J. Adams, "An Introduction to Optical Waveguides", Wiley & Sons, Chichester, New York, 1981
3. M.K. Barnoski, "Fundamentals of Optical Fiber Communications", 2-nd ed., Academic Press, New York, 1981
4. P.K. Cheo, "Fiber Optics and Optoelectronics", 2-nd ed., Prentice Hall, London, 1990
5. D. Marcuse, "Theory of Dielectric Optical Waveguides", Academic Press, New York, 1974
6. D. Marcuse, "Light Transmission Optics", 2-nd ed., Van Reinhold, New York, 1982
7. C.L. Schiopu, "Studiul fibrelor optice pentru telecomunicatii", Teza de doctorat, mai 1997

Schiopu Paul

University "Politehnica", Department of Electronic Engineering, Bucharest, România

Dragnea Laurentiu

Institute of Microtechnology, Bucharest, România

ABSTRACT

In fiber optic communications the technique of wavelength division multiplexing (WDM) constitutes a means of increasing the information capacity of fiber optics in communication systems and allows the optimal usage of the capacity of optic fiber. This paper presents the concepts of wavelength division multiplexing (WDM) and high density wavelength division multiplexing (HD-WDM) from the point of view of developing a unitary theoretical analysis of necessary parameters for the design of optic integrated circuits with functions for optic signals multiplexing and demultiplexing, with planar diffraction gratings.

Keywords : wavelength division multiplexing (WDM), high density wavelength division multiplexing (HD-WDM), diffraction gratings

1. INTRODUCTION

In broadband applications, such as cable television (CATV) supertrunks, one needs to send multiple analog and digital signals over the same fiber. To do this one can employ a multiplexing technique where number of baseband signals are superimposed on a set of N subcarriers having different frequencies $f_1, f_2, f_3 \dots f_N$. In the standard fiber optics communication systems these modulated subcarriers combined electrically through frequency - division multiplexing (FDM) to form a composite signal that directly modulates a single optical source. Methods of achieving this include vestigial - sideband amplitude modulation (VSB - AM), frequency modulation (FM) and subcarrier multiplexing (SCM).

When multiple carrier frequencies pass through a nonlinear device such as a laser diode, signal products other than the original frequencies can be produced. These undesirable signals are called intermodulation products and they can cause serious interference in both in - band and out - of - band channels ; the result is a degradation of the transmitted signal. On the other hand this type of transmission make use of only a very narrow portion of the transmission bandwidth capability of a fiber, since the optical source has a narrow spectral width.

A dramatic increase of the information capacity of a fiber can thus be achieved by the simultaneous transmission of optical signals over the same fiber from many different light sources having properly spaced peak emission wavelengths. By operating each source at a different peak wavelength, the integrity of the independent messages from each source is maintained for subsequent conversion to electric signals at the receiving end. At the receiving end a demultiplexer is required to separate the signals into appropriate detection channels. Since the optical signals that are combined generally do not emit a significant amount of optical power outside of their designated channel spectral width, interchannel cross - talk factors are relatively unimportant at the transmitter end. The basic design problem here is that the multiplexer should provide a low - loss path from each optical source to the multiplexer output. A different requirement exists for the demultiplexer, since photodetectors are usually sensitive over a broad range of wavelengths which could include all the WDM channels. Thus, to prevent significant amounts of the wrong signal from entering each receiving channel, that is, to give good channel isolation of the different wavelengths being used, either the demultiplexer must be carefully designed or very stable optical filters with sharp wavelength cutoffs must be used.

In principle, any optical wavelength demultiplexer can also be used as a multiplexer. Thus, for simplicity, the word "multiplexer" is often used as a general term to refer to both multiplexers and demultiplexers, except when it is necessary to distinguish the two devices or functions.

WDM systems have potential application in telecommunication and computer networks. Several wavelength multiplexers and demultiplexers have been reported^{1-4, 6, 7} using a grating type multiplexer and demultiplexer. The difference between WDM and HG-WDM techniques consists in the fact that for WDM the channel spacing is much bigger than for the case of HD-WDM systems. For WDM the channel spacing is $25 \div 50 \text{ nm}$ ^{1, 7}, while for HD - WDM it can reach $1 \div 4 \text{ nm}$ ³.

The diffraction grating has the capacity of separating one wavelength from other wavelengths in the same bandwidth and of spatially dispersing different close wavelengths from a well-defined wavelength domain. The diffraction gratings used in HD-WDM have a much greater resolution than those used in WDM technique and also a much better linear dispersion. The characteristic parameter of diffraction gratings, the linear dispersion, explains these properties used in HD-WDM technique. This paper presents the characteristic parameters that limit or influence the design of diffraction gratings for coupling the radiation with the transmission or spectral (receiving) optical fiber.

2. GRATING DESIGN

Diffraction grating is an optical element in plan - parallel blade form or plan - cylindrical lens form with echidistant parallel bands of different profiles, opaque and transparent or reflective and absorptive on the surface. Groove spacing defines the constant of grating and the reverse represent spacing frequency of the number n of lines per millimetre. In gratings design some theoretical considerations regarding the propagation of waves in multimode waveguides must be taken into account (Figure 1).

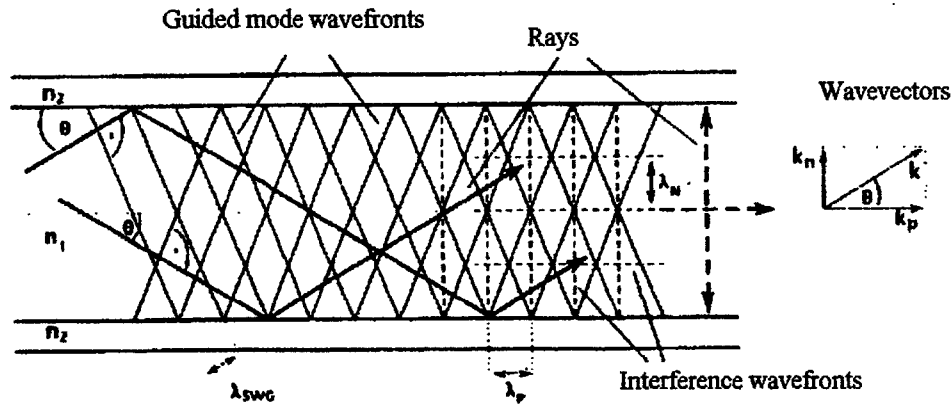


Figure 1. Scheme of the wave propagation in a multimode slab waveguide. Waves propagating under the same mode angles $\pm\theta_{SWG}$ interfere to a standing wave normal to and a propagating wave parallel to the guiding plane. The periodicity of the standing interference wave is λ_N and of the propagating interference wave λ_p .

Let $k_{SWG} = k_{VAC} \cdot n_1$ be the wave vector of the wave that enters the guide; k_{VAC} is the wave vector in vacuum, n_1 is the refraction index of the core of the guide; the wave is propagating only in the direction defined for discrete mode angles θ_{SWG} . The wave which propagates parallel with the guiding plan has the propagation factor⁷:

$$\beta = |k_{SWG}| \cdot \cos\theta_{SWG} = \frac{2n}{\lambda_{SWG}} \cdot \cos\theta_{SWG} = \frac{2n}{\lambda_p} \quad (1)$$

with :

$$1 > \cos\theta_{SWG} > \cos\theta_{max} = \left[1 - \left(\frac{NA}{n_1} \right)^2 \right]^{1/2}$$

where NA is the numerical aperture, $\lambda_{SWG} = \lambda_{VAC} \cdot n_1$ is the wavelength of the wave that propagates through the core material and λ_p is the effective wavelength (the spatial periodicity of the interference wave). Due to the discrete mode angles θ_{SWG} from equation (1), λ_p has a spectral bandwidth $\Delta\lambda_p$ ⁷:

$$\Delta\lambda_p(\theta) = \left(\frac{1}{\cos\theta_{\max}} - 1 \right) \cdot \lambda_{\text{SWG}} \quad (2)$$

so for λ_{SWG} it can be obtained a grating design independent of the grating linear dispersion. These considerations are true in the case of reflection gratings that are mostly used, especially for the spatial minimisation of chips.

Now, we will be preoccupied with the design of blazed gratings in the case of using them in the HD - WDM technique (Figure 2).

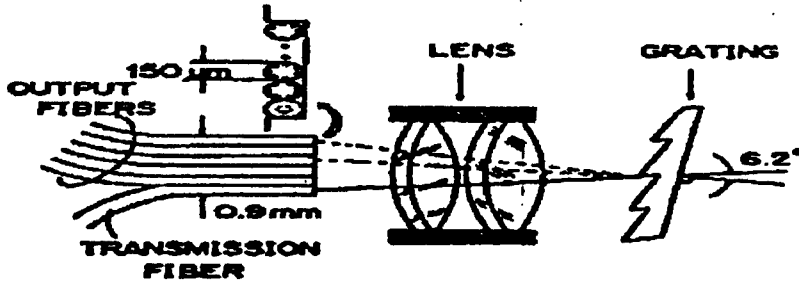


Figure 2. Schematic drawing of demultiplexer

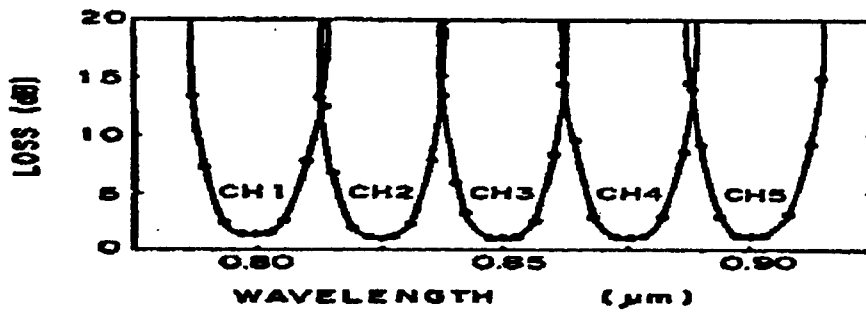


Figure 3. Demultiplexer branching characteristic of the output fiber

The blazed diffraction gratings are used in Littrow configurations. Taking into account the network equation :

$$2d \sin\phi_B = m\lambda_B \quad (3)$$

where d is the groove spacing (grating constant) , m is the diffraction order.

The grating linear dispersion is :

$$\frac{d\lambda}{dl} = \frac{d \cos\phi_B}{mL} \quad (4)$$

where L is the length of the network.

We consider the case ¹ in which five waves with wavelengths between $0.80 + 0.90 \mu\text{m}$ spaced at $25 \text{ nm} = \Delta\lambda_c$ propagate. We choose the optical fibers

having the cladding diameter of $d_c = 150 \mu\text{m}$ and are adjacent to one another having the faces placed in the same plan. We want to determine the core diameters of the optical fibers and of $\Delta\lambda_p$. The channel spacing is determined primarily by the linear dispersion of the grating ⁷ :

$$\frac{dl}{d\lambda} \geq \frac{d_c}{\Delta\lambda_c} \geq \frac{d_T}{\Delta\lambda_c} \quad (5)$$

where d_T is the core diameter of the transmission fiber. For the planar gratings the linear dispersion is generally limited also by $\Delta\lambda_p$ and by the core diameter region d_T and d_S of the transmission and spectral fiber ⁹.

$$\frac{|d_S - d_T|}{\Delta\lambda_p} \geq \frac{dl}{d\lambda} \quad (6)$$

This equation is valid for only one wavelength λ_{SWG} of negligible bandwidth. From this it results :

$$\Delta\lambda_c \geq \frac{d_c \cdot \Delta\lambda_p}{|d_S - d_T|} \quad (7)$$

In our case for $\Delta\lambda_c = 25 \text{ nm}$, $d_c = 150 \mu\text{m}$ it results :

$$\Delta\lambda_p \leq \frac{|d_s - d_T|}{d_c} \cdot \Delta\lambda_c \quad (8)$$

We choose $d_s = 100 \mu\text{m}$, $d_T = 60 \mu\text{m}$ and we obtain: $\Delta\lambda_p \leq 6,66 \text{ nm}$ (9)
So we can choose $\Delta\lambda_p = 6,5 \text{ nm}$.

In the equation (2) we put $\lambda_{\text{SWG}} = 900 \text{ nm}$; it results: $\cos\theta_{\text{max}} \approx 1 \Rightarrow \theta_{\text{max}} \approx 0$ (10)
So the optical fibers must be placed in the direction of the blazed angle.

From (5) it results that the linear dispersion of the grating is:

$$\frac{d\lambda}{dl} \leq \frac{\Delta\lambda_c}{d_T} = \frac{25 \text{ nm}}{60 \mu\text{m}} \quad (11)$$

From (4), considering $L = 10 \text{ mm}$, $d = 4 \mu\text{m}$ and $m = 1$, it results $\varphi_B = 6,2^\circ$.

If a system with lenses is interposed we must take into account ¹ (for choosing lenses):

$$f = \frac{d \cos\beta}{\frac{d\lambda}{dl}} \quad (12)$$

where f is the grating equivalent lens focal length, d is the grating constant, β is a diffraction angle with respect to the grating normal, and $d\lambda / dl$ is the linear dispersion in the focal plan.

The insertion attenuation obtained on the 5 channels in the presented example ¹ is 1,4 ; 1,1 ; 1,1 ; 1,1 ; 1,2 dB (Figure 3).

3. CONCLUSIONS

The diffraction networks design and the choosing of the volume characteristics (diameter core-cladding) for using them in wavelength division multiplexing and high density wavelength division multiplexing systems (optic integrated circuits) is directly dependent on the linear dispersion of the networks used. The linear dispersion of the diffraction network is a principal criterion in realising these goals.

Channel width of the particular optical source obtained for this type of multiplexer is very narrow and ensure that no interchannel interference results from source instability (for example, drift of peak operating output wavelength with temperature changes).

4. REFERENCES

1. Y. Fujii, K.-I. Aoyama, J.-I. Minowa, "Optical Demultiplexer Using a Silicon Echelette Grating", *I.E.E.E. Journal of Quantum Electronics*, Vol. Q.E.-16, No. 2, February 1980
2. I. Suhora, Y. Honda, H. Nishihora, J. Koyama, *Applied Phys. Lett.*, 40 (2), 15 January 1982
3. J.B. Sooh, A. Scherer, Y. Silberberg, H.P. LeBlanc, N.C. Andreadakis, K.R. Loguntke, *Electronics Letters*, Vol. 29, 18th March 1993
4. T. Aoyagi, Y. Aoyagi, L. Nomba, *Applied Phys. Lett.*, Vol 29, No. 5, 1 Sept 1976
5. S.T. Peng, I. Tamir, "Directional blazing of wave by asymmetrical dielectric gratings", *Optics Communications*, Vol 11, No. 4, pp. 408-409, 1974
6. C.A.M. Sternbergen, C. V. Ram, T.L.M. Scholtes, L. Shi, *Proc. 7th Eur. Conf. on Integrated Optics (ECIO '95)*
7. B. Anderer, W. Ehrfeld, D. Munchmeyer, S.P.I.E., Vol. 1014, 1988
8. M.C. Shutby, *Diffraction gratings*, Academic Press, Oxford, 1982
9. A. Reuki, "Resolving Power of Gratings in Planar Multimode waveguides", *Applied Phys.*, Vol. A-33, pp. 179-183, 1984

Modelling the passive and active LiNbO_3 optical waveguides

Niculae N. Puscas, Ion M. Popescu

University "Politehnica" Bucharest, Physics Department, Splaiul Independentei, 313, 77206, Bucharest, Romania

ABSTRACT

Based on several experimental measurements performed on Er^{3+} -doped Ti:LiNbO_3 optical waveguides, this paper presents some theoretical and experimental results concerning the refractive-index profile and the absorption spectra corresponding to the transition $^4I_{15/2} \rightarrow ^4I_{13/2}$.

The refractive-index profile of the above mentioned waveguide has been determined from near field intensity measurement using an optical fibre. A deconvolution algorithm for the original mode field of the waveguide reconstruction has been expanded and optimized for two-dimensional applications. By using the reported model it is possible to evaluate some parameters which characterize the optical waveguides like: the refractive-index difference Δn and the penetration depth d .

The homogeneous absorption and emission cross sections have been calculated from the transmitted spectrum around 1531 nm of the Er^{3+} -doped Ti:LiNbO_3 waveguide using the density matrix formalism.

KEYWORDS

Er^{3+} : Ti:LiNbO_3 optical waveguide, refractive-index profile, absorption and emission spectra

1. INTRODUCTION

Due to the potential use in compact and efficient monolithic devices (i. e. waveguide lasers, optical amplifiers, switches, etc.) which combine the rare-earth laser gain and the large range of integrated optical functions already demonstrated many theoretical and experimental papers concerning the characterization of the Er^{3+} -doped Ti:LiNbO_3 optical waveguides using nondestructive methods were reported in the last years^{1,2,3,4,5}. The exact knowledge of the field distribution and the absorption and emission spectra, respectively, are very important for the characterization of the integrated optical waveguides.

In Sec. 2 of this paper we review the basic equations used for the refractive-index profile reconstruction from deconvolved near field scanning measurement while in Sec. 3 we present some theoretical considerations for the determination of the homogeneous absorption and emission spectra. Sec 4 is devoted to the experimental techniques used for measurements and Sec. 5 to the discussion of the obtained results.

2. THE REFRACTIVE-INDEX PROFILE RECONSTRUCTION FROM NEAR FIELD MEASUREMENT

The most important advantages of refractive-index profile reconstruction from the near field measurement method are: the measurement method is direct, nondestructive and the single-mode waveguide is characterized at the operating wavelength. The major disadvantage is that the near field measurements are affected by many sources of errors, such as noise, errors due to the detection system, nonideal focusing, etc. This imposes the necessity to filter the experimental data of the near field measurements before to use them to determine the refractive-index profile.

In the scalar approximation the field is transversal and completely described by the linearly polarized mode, solution of the Helmholtz scalar equation:

$$\Delta_T \psi(x, y) + (k_0 n^2(x, y) - \beta^2) \psi(x, y) = 0. \quad (1)$$

where Δ_T is the traverse Laplace operator, $\psi(x, y)$ represents the transverse electric or magnetic field, $n(x, y)$ is the refractive-index profile, β is the propagation constant and k_0 is the wave vector of the vacuum.

The refractive-index profile may be determined from Eq. (1) as:

$$n(x, y) \approx \left(\frac{\beta}{k_0} \right) - \frac{1}{2n_s k_0^2} \frac{\Delta_T \psi(x, y)}{\psi(x, y)}. \quad (2)$$

In the case of a separable transversal field $\psi(x, y) = \psi(x)\psi(y)$ and assuming that the local field is known $I(y) = \psi^2(x_0, y)$ for a fixed position $x = x_0$ one obtained:

$$n(x_0, y) \approx \left(\frac{\beta}{k_0} \right) - \frac{1}{2n_s k_0^2} \frac{1}{\sqrt{I(y)}} \frac{d^2 \sqrt{I(y)}}{dy^2}. \quad (3)$$

The accuracy of the refractive-index profile reconstruction has been improved by using a deconvolution algorithm on the measured data. We consider the measured field profile $\psi_i(y)$ to be affected by different kind of errors. First of all, we took into account the influence of the experimental errors $\varepsilon(y)$, normally distributed with zero mean and known covariance so that:

$$\psi_1(y) = \psi_2(y) + \varepsilon(y). \quad (4)$$

The field $\psi_2(y)$ is the result of a combined effect of the unknown field profile $\psi(y)$ and the response function of the experimental setup which consists mainly of an optical fiber scanning the waveguide end face and a low noise detector:

$$\psi_2(y) = \int_{-\infty}^{\infty} \psi(y_1) F(y - y_1) dy_1 \quad (5)$$

where $F(y)$ is the mode profile of the monomode optical fiber. The problem to be solved is that to infer from the experimental data ψ_i the unknown $\psi(y)$ and this means to solve the Fredholm type integral equation of the first kind:

$$\psi_1(y) = \int_{-\infty}^{\infty} \psi(y_1) F(y - y_1) dy_1 + \varepsilon(y). \quad (6)$$

So special care has been taken and several procedures tested and modified to take advantage of the measured information using averaged formula for the deconvolution procedure. These procedures proved to be very sensitive to the initial shape of the field profile and not all the resulting deconvolved

fields could have been ascribed to a monomode waveguide. Therefore a new procedure which uses a numerical test function and which takes advantage of the full physical information has been implemented and tested. Each optical waveguide is characterized (both in width and in depth) by a refractive-index profile of the form:

$$n(y) = n_s + \Delta n f(y, p), \quad (7)$$

where n_s is the refractive-index of the substrate and $p = (p_1, p_2, \dots, p_m)$ is a vector of parameters for the index profile definition. Considering this refractive index profile (with $\Delta n f(y) \ll n_s$), the unidimensional form of the wave equation:

$$\frac{d^2 \psi(y)}{dy^2} + k^2 (n_s^2 - n_{ef}^2 + 2n_s n_o f(y, p)) \psi(y) = 0, \quad (8)$$

together with the boundary conditions $\psi(0) = 0$ and $\psi(d_{max}) = 0$ (for a given d_{max} value), represents a direct Sturm-Liouville problem. The eigenvalue equation was solved using a modified Fox-Goodwin algorithm⁶. This solution $\psi(y, p)$ was used to construct the test convolution function in the form:

$$E(y, p) = \int_{-\infty}^{+\infty} \psi(y_1, p) F(y - y_1) dy_1, \quad (9)$$

which was fitted to the measured convolved field. By minimization of the function χ in the equation:

$$\chi^2(p) = \sum_k [(E(y_k, p))^2 - \psi_k]^2, \quad (10)$$

with respect to the variables $(p_1, \dots, p_m) = p$, we determined the initial profile of the field.

3. THE ABSORPTION AND EMISSION CROSS SECTIONS

For the exact evaluation of the absorption and emission cross sections of the rare-earth doped LiNbO_3 optical waveguides, (i. e. Er^{3+}) the density matrix formalism must be applied³.

The experimental spectra can be numerically fitted with the formula^{3,5}:

$$I(\lambda) = \sum_i a_i \exp \left[-4 \log 2 \frac{(\lambda - \lambda_i)^2}{\Delta \lambda_i^2} \right]. \quad (11)$$

The inhomogenous cross sections $\sigma_{a,e}^I(\omega)$ are proportional to the experimental line shape $I_{a,e}(\lambda)$. The homogenous absorption and emission cross section $\sigma_{a,e}^H(\omega)$ may be determined from the experimental inhomogenous cross sections by inverse Fourier transformation as:

$$\sigma_{a,e}^H(\omega) = F^{-1} \left[\exp \left(\frac{\Delta \omega_{inh} x^2}{16 \log 2} F[\sigma_{a,e}^I(\omega); x] \right); \omega \right], \quad (12)$$

where $\Delta \omega_{inh} = 2\pi c \Delta \lambda_{inh} / \lambda^2$ is the inhomogenous bandwidth and $\Delta \lambda_{inh}$ the inhomogenous linewidth.

The fitting curve is not unique but the deconvolution expressed in $\sigma_{a,e}^H(\omega)$ has a unique solution. Once we have obtained the absorption cross section, the emission cross section can be obtained using the relation⁵:

$$\sigma_e(\nu) = \sigma_a(\nu) \exp\left[\frac{h(\nu - \varepsilon)}{k_B T}\right], \quad (13)$$

where:

$$h\varepsilon \equiv -k_B T \log\left(\frac{N_2}{N_1}\right). \quad (14)$$

4. EXPERIMENTAL SETUP

The experimental arrangement is shown schematically in Fig. 1³. We used a He - Ne laser ($\lambda = 0.63\mu\text{m}$) for alignment and a laser diode (L. D.) at $\lambda = 1.55\mu\text{m}$ for the optical signal, coupled together by a 3 dB coupler (C). The near field profile and the transmitted spectra of some Er:Ti:LiNbO₃ optical strip waveguides (W) have been measured.

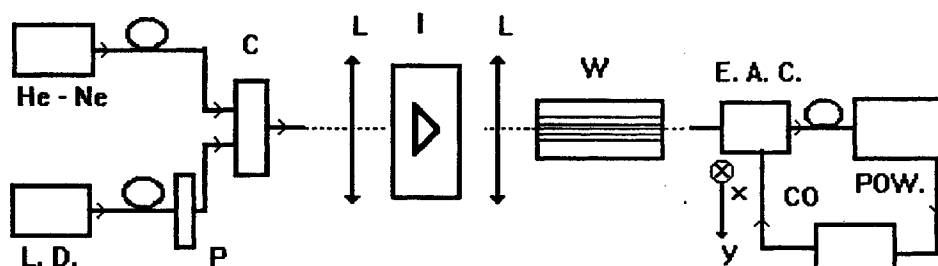


Fig. 1. Schematical experimental setup for the near field measurement

The measurement of the near field was performed using a standard optical fiber directly coupled with a powermeter (POW.). The displacement of the optical fiber mounted on a support was obtained with an electrostrictive actuator controller (E. A. C.) interfaced with computer to register the waveguide field intensity profile in depth and width for TE and TM polarizations selected by the polarization controller (P) and the isolator (I).

Using a optical amplifier as signal source in the range 1480 - 1620 nm the transmitted spectra of the above mentioned waveguides were registred using an optical spectrum analyser.

5. DISCUSSION OF THE RESULTS

Using the experimental arrangement presented in Fig. 1 we measured the near field intensity of an Er³⁺:Ti:LiNbO₃ 7.5 μm width and 52 mm long X-cut waveguide.

The measured field two-dimensional distribution (in the width and the depth of the waveguide) is presented in Fig. 2 a) while in Fig. 2 b) is presented the same distribution after the deconvolution procedure.

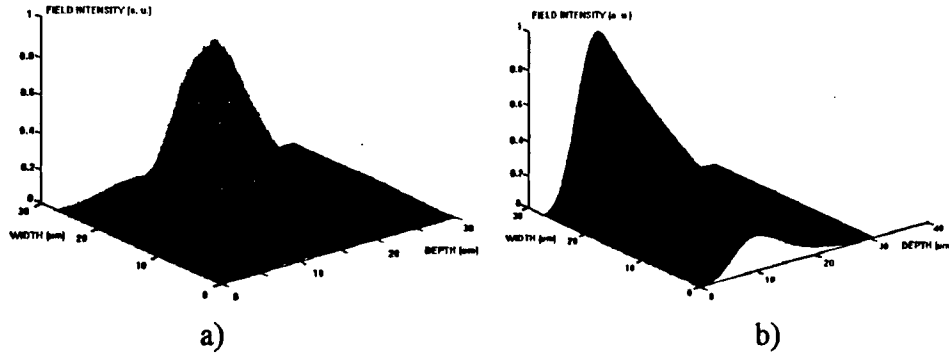


Fig. 2 a), b). The measured (a)) and deconvolved (b)) field two-dimensional distribution

Performing the deconvolution of the field distribution by using the procedure presented above we obtained the width and the depth refractive-index profiles (Fig. 3 a) and b)).

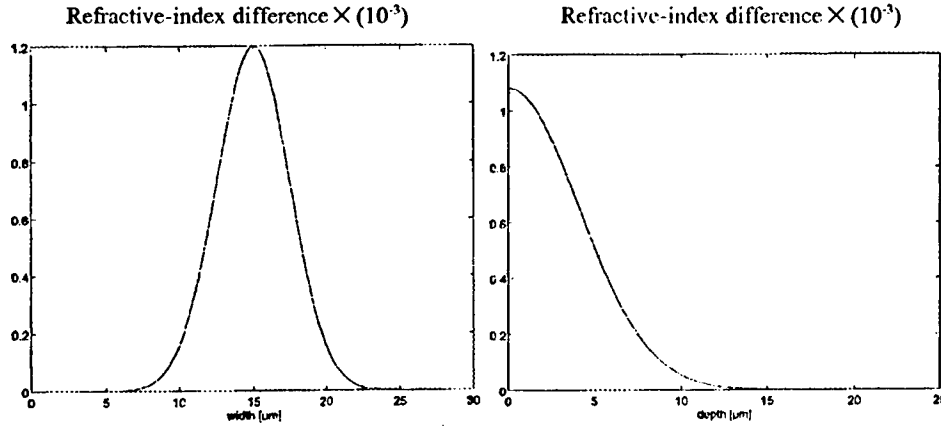


Fig. 3 a), b). The refractive-index profile after the application of the deconvolution method: a) width and b) depth

From the refractive-index profiles we obtained for the width refractive-index difference the value $\Delta n = 1.2 \times 10^{-3}$ and for the penetration depth $d_x = 3.5 \mu\text{m}$ while in depth the corresponding values are $\Delta n = 1.08 \times 10^{-3}$ and $d_y = 6.5 \mu\text{m}$, respectively.

In Fig. 4 a), b) are presented the unpolarised homogeneous absorption (a)) and emission (b)) cross section spectra of an $\text{Er}^{3+}:\text{Ti}:\text{LiNbO}_3$ waveguide for which, using the theoretical model presented in Sec. 3, we have obtained the peak values: $0.78 \times 10^{-24} \text{ m}^2$ and $0.84 \times 10^{-24} \text{ m}^2$, respectively. For the simulation of the inhomogenous absorption spectra we used eight Gaussian functions to assure the best fit with the experimental data.

The most significant peak in the absorption spectra is located around 1532 nm and corresponds to the transition $^4I_{15/2} \rightarrow ^4I_{13/2}$.

6. CONCLUSIONS

The measurement of the near field profile for the characterization of Er^{3+} -doped Ti in-diffused LiNbO_3 waveguides using nondestructive methods was performed by scanning the waveguide transversal section through a fiber probe. The measured data have been numerically deconvolved with a Gaussian-like function that approximates the fiber field profile. The near field profile has been used to obtain the refractive-index distribution in width and depth and to evaluate some parameters (i. e. the refractive-index difference and the penetration depth) which characterize the waveguide.

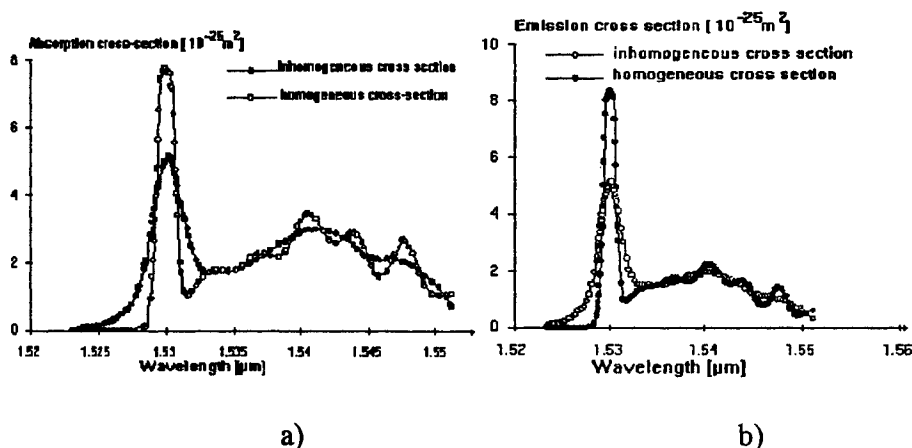


Fig. 4 a), b). The unpolarised inhomogeneous and homogeneous absorption (a)) and emission (b)) cross section spectra of an $\text{Er}^{3+}:\text{Ti}:\text{LiNbO}_3$ waveguide

Using the density matrix formalism we evaluated the homogeneous absorption and emission cross sections from the transmitted spectrum of the Er^{3+} -doped $\text{Ti}:\text{LiNbO}_3$ waveguide.

7. REFERENCES

1. W. Sohler: "Rare Earth Doped LiNbO_3 Waveguide Amplifiers and Lasers", in "*Waveguide Optoelectronics*"; J. Marsh and R. de la Rue (eds.), NATO ASI Series E: Applied Sciences, Vol. 226, pp. 361-394, Kluwer-Academic, Dordrecht, Boston, London (1992).
2. I. Baumann, R. Brinkmann, M. Dinand W. Sohler and S. Westenhofer: "Ti:Er:LiNbO₃ Waveguide Laser of Optimized Efficiency", *IEEE J. Quant. Electr.*, **QE 32**, 1695-1706 (1996).
3. E. Desurvire, *Erbium-Doped Fiber Amplifiers*, J. Wiley & Sons, Inc. New York 1994.
4. J. Helms, J. Schmidtchen, B. Schuppert and K. Peterman, "Error Analysis for Refractive-Index Profile Determination from Near-Field Measurements," *J of Lightwave Tehnology LT- 8* (5), 625-634, (1990).
5. N. N. Puscas, D. M. Grobnic, I. M. Popescu, M. Guidi, D. Scarano, G. Perrone, I. Montrosset; "Characterization of the Er^{3+} -Doped $\text{Ti}:\text{LiNbO}_3$ Waveguides: Losses, Absorption Spectra and Near Field Measurements", *Optical Engineering*, **35**(5), 1311-1318, (1996).
6. H. C. Rainsch, "Smoothing by spline function," *Numerische Mathematik*, **16**, 451-454, (1971).

EFFECTIVE INDEX METHOD FOR THE COMPUTATION OF THE PROPAGATION CONSTANT AND ELECTROMAGNETIC FIELD DISTRIBUTION IN Z-UNIFORM DIELECTRIC OR SEMICONDUCTOR WAVEGUIDES

Mihail Dumitrescu, Mircea Guina^(*)

Tampere University of Technology, Physics Department, SemiLab, P.O. Box 692, FIN-33101, Tampere

^(*) "Politehnica" University of Bucharest, Faculty of Electronics and Communications, TEF Department,
Blvd. Iuliu Maniu 1-3, 77202, Bucharest

ABSTRACT

The paper presents a numerical implementation of the Effective Index Method (EIM) for the determination of the propagation constants and field distributions in dielectric or semiconductor guiding structures that are uniform on the direction of propagation. The implementation proved to be applicable to a wide range of guiding structures (ridge, buried and diffused guides) and was tested against analytical solutions and against other methods' results proving good accuracy. The advantages and limitations of the EIM are discussed and a common waveguide problem result is presented as an example. From the practical applications of the method, the optical analysis of the ridge geometry and QW positioning of a 3W continuous wave GRIN SCH SQW laser diode in the 670 nm band is briefly discussed and the measured performances of the device are presented.

Keywords: modeling, Effective-Index-Method, Mode Solver, laser diode

1. INTRODUCTION

The dimension (3D, 2D, 1D) of the modeling of the electromagnetic field propagation has an important impact on the computational complexity of the implementation. Reducing the problem dimension while maintaining the accuracy is an important goal in deriving effective modeling methods. The general problem formulation for modeling the electromagnetic field propagation in dielectric or semiconductor guiding structures starts from the Maxwell equations. Assuming some general approximations^{1,2} the vectorial propagation equations are obtained. Solving this equations is a difficult 3D problem. A sensible reduction of the problem complexity is achieved when the guiding structures are (or can be considered) uniform on the direction of propagation (be z this direction). The distribution of any electric or magnetic field component in a z -uniform guiding structure has the form $\phi(x, y, z) = \phi(x, y) \exp(\pm j\beta z)$ and the methods aiming at the determination of field distribution $\phi(x, y)$, and associated propagation constant β , are grouped under the "Mode Solver" category.

Following from the presumed field distribution form and considering only progressive propagation, the vectorial propagation equations become:

$$\Delta_t \bar{E} + \nabla_t \left(\frac{\nabla_t [\epsilon_0 \bar{\epsilon}(x, y)]}{\epsilon_0 \bar{\epsilon}(x, y)} \bar{E} \right) + [k_0^2 \bar{\epsilon}(x, y) - \beta^2] \bar{E} = 0 \quad (1)$$

$$\Delta_t \bar{H} + \frac{\nabla_t [\epsilon_0 \bar{\epsilon}(x, y)]}{\epsilon_0 \bar{\epsilon}(x, y)} \times (\nabla_t \times \bar{H}) + [k_0^2 \bar{\epsilon}(x, y) - \beta^2] \bar{H} = 0 \quad (2)$$

Taking into account the coupling between the corresponding 6 scalar equations^{2,3} and the fact that only 2 of the 6 field components are independent, the problem comes to solving 2 coupled scalar equations derived from (1) and (2). At this point the problem is still a 2D vectorial problem. Further reduction in problem complexity can be achieved when the practical problem allows for the decoupling between the 2 scalar equations (like for example in the case of low contrast structures, $\nabla \epsilon(x, y) \cong 0$). Thus a single scalar wave equation has to be solved:

$$\nabla_t^2 \phi + [k^2 n^2(x, y) - \beta^2] \phi = 0. \quad (3)$$

If the gain/loss of the guiding structure can be neglected ($n(x, y)$ is real valued) the physically meaningful propagation constants β are real valued ($\beta = (2\pi/\lambda)n_{\text{eff}}$, n_{eff} being the effective index associated to a propagation mode). At this point

the problem is a scalar 2D problem having guided, radiative and leaky modes as solutions^{1,3}. Since the guided and radiative modes are orthogonal, any field distribution that propagates along the guiding structure is a linear combination of guided modes and any optical injection into the guide distributes its energy between guided modes (that propagate the energy along the guide) and radiative modes (which gradually evacuate their energy outside the guiding region). The obtained solutions allow for various analysis: modal analysis, transit time determination, modal and waveguide dispersion analysis, coupling coefficient analysis^{1,2}.

At this point there are many Mode Solver variants that reduce, 2D to 1D, the problem dimension, but most of them make it either at the expense of generality or at the expense of solution accuracy. The effective index method reduces the problem dimension (2D → 1D) maintaining a high degree of generality and good accuracy in the meantime.

2. EIM PROBLEM FORMULATION AND NUMERICAL IMPLEMENTATION

The basic assumption of the EIM approach is that the refractive index is slowly varying in at least 1 dimension of the transversal calculus window (let this direction be considered x). Consequently any field distribution can be assumed to be a product of a x -dependent function and a x and y dependent function slowly varying in the x direction :

$$\phi(x, y) = G(x)F(x, y) . \quad (4)$$

In view of the field distribution from (4) and due to the fact that $\frac{\partial F}{\partial x} \cong 0$ (F is dependent on x to assure coupling between the solutions on the two dimensions but is slowly varying on x , the rapid variation of ϕ with x being incorporated in G) the scalar equation to be solved, becomes:

$$\frac{1}{G} \frac{d^2 G}{dx^2} + \frac{1}{F} \frac{\partial^2 F}{\partial y^2} + (k^2 n^2(x, y) - \beta^2) = 0 \quad (5)$$

Since the second and third terms of (5) are x, y dependent while the first is only x dependent the problem can be decoupled in the 2 dimensions, by use of a separation function $\gamma(x) = kn_{\text{eff}}(x)$. Firstly the modeled structure has to be sliced in the x direction, and in each slice equation

$$\frac{\partial^2 F}{\partial y^2} + [k^2 n^2(y) - \gamma^2] F = 0 \quad (6)$$

is solved. Slicing the structure in the x -direction corresponds to decomposing the guiding structure into successive slab waveguides as is shown in Fig. 1. As can be observed, solving the equation (6) in each slice implies that the refraction index is not x -dependent inside the slice. To minimize the error introduced by this approximation the slicing step along x direction should be chosen so that the maximum refraction index variation along x direction in any slice is negligible.

Having the series of $F(y)$ and n_{eff} for each slice, the next step in assembling a 2D solution is to solve the equation :

$$\frac{d^2 G}{dx^2} + [\gamma^2(x) - \beta^2] G = 0 \quad (7)$$

for each distribution $\gamma(x)$ obtained from the effective indices solutions of (6). Some reduction of the computational complexity can be achieved by properly selecting the $\gamma(x)$ meaningful distributions considering the continuity conditions and the fact that the field continuity is proportional to Δn_{eff} across slice interfaces. Having all the equations solved, the 2D solution for the field distributions is obtained from (4) and the propagation constants from the eigenvalues of (7). In our implementation the equations (6) and (7) are solved using an 1D Finite Difference Method (with either constant or variable step). Our experience indicates that the reduction in computational complexity by using a variable step mesh is many times only apparent since the better conditioning (symmetrical and diagonal dominant) of the coefficient matrix of the eigenvalues and eigenvectors system to be solved, for the constant step variant, compensates the increased number of mesh points. The implementation uses either implicit boundary conditions ($\phi=0$) or absorbing boundaries (to avoid 'spatial aliasing'²) when the transversal calculus window cannot be made wide enough to accommodate implicit boundary conditions. The continuity conditions are implicitly taken into account by the way the matrix coefficients of the eigenvalues and eigenvectors system are derived and by the choice of $\gamma(x)$.

Besides the scalar EIM implementation we also tried a semi-vectorial one¹ but the supplementary vectorial information (polarization, mode conversions) did not justify (for our applications) the sensibly increased computational complexity. Also a Weighted Index Method (WIM) implementation was tried. In the WIM approach the field distributions are presumed to have the form $\phi(x, y) = X(x)Y(y)$ and the equation to be solved is :

$$\frac{d^2 A}{du^2} + \left[\frac{\int (k^2 n^2 B^2 - B'^2) dv}{\int B^2 dv} - \beta^2 \right] A(u) = 0 \quad (8)$$

where A,B,u,v are iteratively replaced by X,Y,x,y and Y,X,y,x until convergence is reached. Although some better accuracy is obtained for the same mesh, the increase of computational complexity introduced by the supplementary iteration in WIM is much more greater than the increase induced by the EIM mesh refinement needed to attain the same increase in accuracy.

3. RESULTS AND DISCUSSIONS

The EMI implementation was tested first by solving problems with analytical solutions. The EIM solutions converged very rapidly to the analytical solutions with mesh refinement. Furthermore the EIM implementation was tested for various guiding structures against solutions given by other methods (like 2D Finite Difference Method and 2D Finite Element Method based Mode Solvers) showing that for similar accuracy the EIM computational complexity is usually reduced by a factor around 2 (stemming from 2D to 1D reduction).

The effective index method is known to give solutions that have some discontinuities across slice borders when the refraction index has a sharp variation on x direction. However, if the slices dimensions and positions are carefully chosen, continuous distribution are obtained. For example we have chosen a rectangular burried waveguide structure given in Fig. 2.

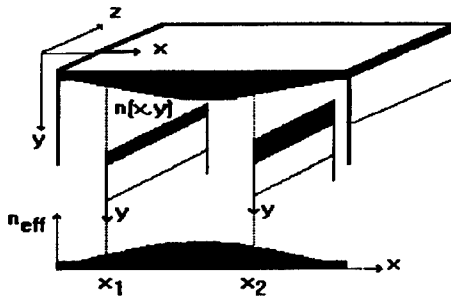


Fig. 1 Slab waveguide decomposition implied by EIM

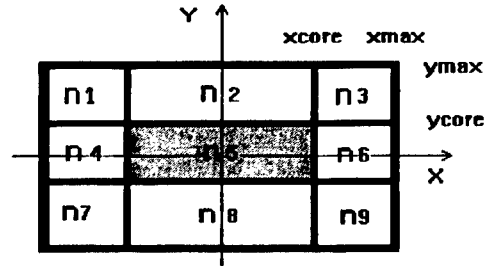


Fig. 2 Rectangular buried waveguide structure

The numerical values considered in the example are: $n_{1,2,3,7,8,9}=1.62$, $n_{4,6}=1.633$, $n_5=1.638$, $x_{\max} = 18\mu\text{m}$, $x_{\text{core}} = 6\mu\text{m}$, $y_{\max} = 6\mu\text{m}$, $y_{\text{core}} = 2\mu\text{m}$. The problem was solved for $\lambda = 0.8\mu\text{m}$ and the mesh was a $(32) \times (16)$ constant step. Some of the slab guide 1D solutions of (6), corresponding to the 12th slice, are shown in Fig. 3. Although the guiding structure has sharp refractive index variations, proper choice of the mesh led to continuous solutions as can be seen for example in Fig. 4 (smooth 2D solution for E_{11}), Fig. 5 (E_{12} 2D solution - with small discontinuities) and Fig. 6 (E_{13} solution with more pronounced discontinuities).

One interesting practical application of the EIM implementation was the determination of minimum ridge height and optimized QW position of a GRIN SCH SQW laser diode emitting in the 670 nm band⁴. While maximum ridge height was evaluated from solving the electric equations of the structure (since a too high ridge would lead to increased series resistance and decreased differential efficiency), the minimum height was evaluated in a first approximation using the EIM. The minimum ridge height was determined aiming at stable and narrow lateral far field and at negligible field values in the contact region (since significant field values in the contact region induce increased absorption losses and reflections). The first approximation of the ridge profile obtained using the EIM implementation proved accurate within 5% to the profile obtained using a much more sophisticated commercial package. Also the EIM-predicted far field distributions for the laser diode (approx. 42 degrees transversal and 5 degrees lateral) were very close to the measured far fields of the diode shown in Fig. 7. The measured performances of the laser diode are presented in Fig. 8. The diode, grown by Solid Source Molecular Beam Epitaxy at SemiLab, Tampere University of Technology had the following transversal structure: n-GaAs substrate, n-AlGaInP cladding, undoped-AlGaInP GRIN, 7 nm compressively strained undoped-Ga(0.42)In(0.58)P QW, undoped-AlGaInP GRIN, p-AlGaInP cladding, p-GaInP barrier reduction layer and p-GaAs contact. The diode was AR/HR 0.1/0.95 coated and 1mm long. Although little of the diode design (mostly of transversal nature) can be attributed to the optical analysis performed using the EIM implementation, some accurately modeled aspects (like near field distributions - used to evaluate the ridge geometry - far field distributions and maximum field position determination - used to evaluate optimum QW positioning) proved that EIM is an efficient approach for a first-approximation optical-evaluation of some practical structures.

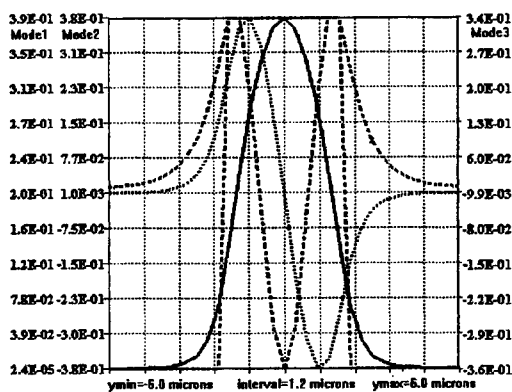


Fig. 3 Slab waveguide field distributions

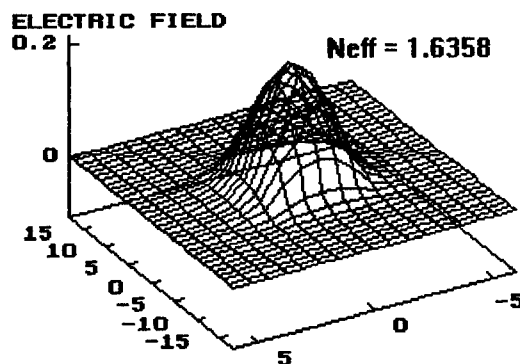


Fig. 4 E_{11} mode distribution obtained using EIM

ELECTRIC FIELD

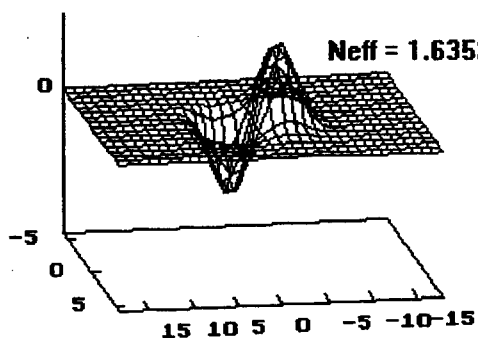


Fig. 5 E_{12} mode distribution obtained using EIM

ELECTRIC FIELD

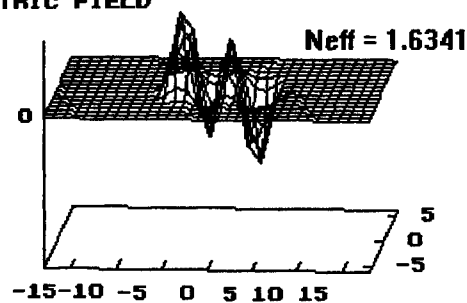


Fig. 6 E_{14} mode distribution obtained using EIM

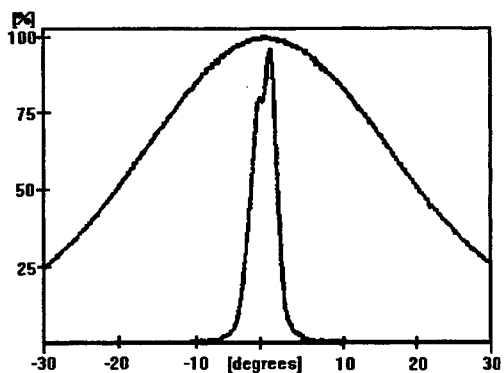


Fig. 7 Measured transversal and lateral far field for the EIM optically evaluated laser diode structure

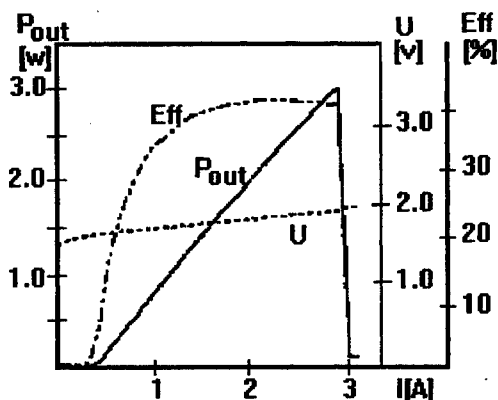


Fig. 8 Measured all mode laser power (P_{out}), differential efficiency (Eff) and forward voltage (U) with respect to current (I)

4. REFERENCES

1. Vasallo C., *Optical waveguide concepts*, Elsevier Science Publishers, 1991.
2. Dumitrescu M., Iancu O., Courtois B., Karam J.M., "Approximation choices for the numerical modeling of some optical guiding structures", *SPIE Photonics West, Physics and Simulation of Optoelectronic Devices III*, San Jose, 1995.
3. Tamir T. (Editor), *Guided-wave Optoelectronics*, Springer Verlag, 1988.
4. Savolainen P., Pessa M., "High-Power, High-Efficiency GaInP/AlGaInP Laser Diode", *Japanese Journal of Applied Physics - Part 2, Letters*, Vol. 35, No. 11B, pp. L1501-L1502, 1996.

About the real performance of image intensifier systems for night vision

Marinica Mirzu, Liviu Cosereanu, Mihai Jurba^{*}
George Copot, Daniel Ralea, Raluca Marginean^{**}

^{*} Army Institute for Research and Development, Bucharest, fax 7804863.

^{**} IOEL-S.A., 1 Atomistilor Street, Magurele, Bucharest, fax 4208632

ABSTRACT

The detection model based on the fluctuation theory can determine only the upper limit in the performance of image intensifier systems for night vision. Our laboratory and field experiments show that the signal to noise ratio(S/N) of the final image is influenced by the fluctuations in the number of incident photons on the image intensifier photocathode, the quantum efficiency of the photocathode, the value of noise generated in the amplification process and the modulation transfer function(MTF) for the atmosphere and optical components.

Keywords: image intensifier, fluctuation theory, signal to noise ratio, noise factor, detection range, recognition range, resolution, MTF.

1.THEORETICAL ASSUMPTIONS

The model for the detection of optoelectronic images developed by A.Rose on the base of fluctuation theory, establish the upper limit of the image intensifier systems performance. The value of S/N in the final image is calculated only on the base of statistical fluctuation in the number of incident photons that arrive from two adjacent resolution areas of the target and transformed in photoelectrons by the image intensifier photocathode . In these conditions the ideal system resolution R_{lim} is:

$$R_{lim} [lp/mm] = \frac{C}{(S/N)_p} \sqrt{\frac{S_{fk} \rho_a T_a E_t t \epsilon}{2(1+f_{nr}^2)(1+C)e}} \cdot 10^{-3}, \quad (1)$$

where: C is the target contrast, $(S/N)_p$ is the signal to noise ratio demanded by the final receptor for detection, S_{fk} is the photocathode luminous sensitivity(A/lm), ρ is the target reflectivity, T_a and T_o are the atmosphere and optics transmittance respectively, E_t is the target illumination(lux), t is the integration time(0.2 s), ϵ is the target shape factor, f_{nr} is the aperture number of the objective and e is the charge of electron.

The upper limit of the observation range L_{lim} is:

$$L_{lim} = \frac{H}{M} R_{lim} f'_{ob}, \quad (2)$$

where H is the target dimension, M is the observation difficulty function and f'_{ob} is the objective effective focal length.

2.EXPERIMENTAL RESULTS

Our laboratory and field experiments with second and 2^{plus} generation image intensifier systems for night vision demonstrate that the real performances are smaller than the ideal results given by relations (1) and (2).

The ideal and real observation ranges for a night vision sight with second generation image intensifier XX 1800 are given in table 1.

Table 1. The ideal and real observation ranges for a night vision sight for infantry weapon.

Observation range(m)	Ideal values	Real(field) values
Target		
Om 1.8x0.8m	3173	600
Om 1.6x0.5m	1138	500

We used two targets:

a) man, 1.8x0.8 m, with: $C=0.98$, $(S/N)_p=4$, $S_{fk}=308 \times 10^{-6} \text{ A/lm}$, $\rho=0.98$, $T_a=0.8$, $T_o=0.8$, $E_t=3 \times 10^{-3} \text{ lux}$, $t=0.2 \text{ s}$, $\epsilon=2.66$, $e=1.6 \times 10^{-19} \text{ C}$, $f'_{ob}=92 \text{ mm}$, $H=1.8 \text{ m}$, $M=3(\text{recognition})$;

b) man, 1.6x0.5 m, with: $C=0.40$, $(S/N)_p=4$, $S_{fk}=308 \times 10^{-6} \text{ A/lm}$, $\rho=0.32$, $T_a=0.8$, $T_o=0.8$, $E_t=3 \times 10^{-3} \text{ lux}$, $t=0.2 \text{ s}$, $\epsilon=0.625$, $e=1.6 \times 10^{-19} \text{ C}$, $f'_{ob}=92 \text{ mm}$, $H=1.6 \text{ m}$, $M=1(\text{detection})$;

The differences in the observation range given in table 1 appear because the real S/N of the final image is smaller than S/N calculated with the fluctuation theory. The cause is the image intensifier amplification process which introduces noise in the final image. The S/N value degradation in the image intensifier is characterised by the noise factor F :

$$F = \frac{\left(\frac{S}{Z}\right)_i^2}{\left(\frac{S}{Z}\right)_e^2} = \frac{F_A}{\eta} \quad (3)$$

where $(S/N)_i$ and $(S/N)_o$ are the signal to noise ratio at the image intensifier input and output, respectively, F_A is the amplification noise factor and η is the photocathode quantum efficiency. For the ideal systems $F_A=1$. We find that for second generation double proximity image intensifier XX 1800 $F_A=2.25$.

In this case relation (1) become:

$$R'_{lim} [lp/mm] = \frac{C}{(S/N)_p F \frac{1}{2} A} \sqrt{\frac{S_{flk} \rho T_a T_o E_t t \epsilon}{2(1+4 f_{nr}^2)(1+C)e}} \cdot 10^{-3}, \quad (4)$$

and L'_{lim} is:

$$L'_{lim} = \frac{H}{M} R'_{lim} f_{ob}. \quad (5)$$

With relations (4) and (5) the calculated observation ranges are 2115m and 758m respectively, but still persist differences between these theoretical values and those determined in the field. The only explanation is that the signal(contrast) is affected by the atmosphere and optical components of the optoelectronic system through the MTF. This theory was experimentally demonstrated. We used two optoelectronic systems with two sets of objectives and image intensifiers. First objective f'149/1.5 has a weak MTF and the second F'163/1.7 is very well corrected, with a good MTF. The image intensifiers are second generation XX1400 AEG and 2^{plus} generation XX1415 Phillips. We have measured resolution in lp/mm for the combinations between these components on the USAF 1951 target. The results are presented in table 2.

Table 2. Resolution(lp/mm), on USAF 1951 target, for different combination between image intensifier tubes and objectives.

Illumination level(lux)	Image intensifier	Objectiv f'149/1.5	Objectiv f'163/1.7
1	XX1400	17	24.5
	XX1415	19.1	27.5
10 ⁻²	XX1400	8.5	17.5
	XX1415	16.1	21.9

We observe that with the same objective, using different image intensifiers, the resolution is greater for 2^{plus} generation XX 1415. For the same image intensifier, say XX 1415 at 1 lux, the performance increase with 44% when we use well-corrected objective f'163/1.7. For illumination level 10⁻² lux the increase is 36%. On the other hand we determined that the quality of the final image is better when we use the f'163/1.7 objective.

3.CONCLUSIONS

1.The detection model based on the fluctuation theory determine only the upper limit in the performance of image intensifier systems for night vision.

2.The real performances of image intensifier systems for night vision are smaller than the ideal results given by the fluctuation theory.

3. The signal to noise ratio of the final image is influenced by the fluctuations in the number of incident photons on the image intensifier photocathode, the quantum efficiency of the photocathode, the value of noise generated in the amplification process and the modulation transfer function (MTF) for the atmosphere and optical components.

4. It is possible to generate a complex relation for correct determination of the real performance combining the factors above enumerated. Our results demonstrate that it is a good agreement between the theoretical and experimental results.

4. REFERENCES

1. Biberman, L., *Photoelectronic imaging devices*, vol. 1, 2, Plenum Press, London, 1971.
2. Copot G., Copot R., "Studies on the observation range of the night vision devices", *Proceedings SPIE*, vol. 2461, 491 (1995).
3. Curatu, E., *Quality of the optical systems. Optical Transfer Function (from rom.)*, Romanian Academy, Bucharest, 1992.
4. Magee P.E., Welsh B.M., "Characterisation of laboratory-generated turbulence by optical phase measurements", *Opt. Eng.*, 33(11), 3810 (1994).
5. Mirzu M., Cretu E., Nicoara I., *Physical and Fourier optics (from rom.)*, Military Technical Academy and Pro Transilvania, Bucharest, 1996.
6. Mirzu M., "Visual perception of the images delivered by optoelectronic systems", *Optoelectronica*, 3(4), 91 (1995).
7. Mirzu M., Cretu E., "Consideration on sources of night-time radiation for image intensifier systems", *Optoelectronica*, 4(2), 108 (1996).
8. Rose A., "The sensitivity performance of the human eye on an absolute scale", *JOSA*, 38(2), 196 (1948).

Control of laser spiking at Nd:YAG lasers with saturable absorbers

M.Jurba, V.Babin*, N.Baltateanu**, I.Gherghina V.Jipa, E.Popescu, L.Cosereanu and M.Mirzu
Army Research and Development Institute, Bucharest, Romania, *Institute of Optoelectronics,
Bucharest, Romania, **National Institute for Laser, Plasma and Radiation Physics,
Bucharest, Romania

ABSTRACT

Spiking behavior can be analytically described using laser rate equations. Control or suppress of spiking behavior can be obtained by placing suitable absorbers in the laser cavity. LiF:F_2^- saturable absorbers obtained by electron irradiation of LiF crystals were employed in control of laser spiking of pulsed Nd:YAG lasers. Experimental results are in good concordance with theoretical values.

Keywords: spiking control, saturable absorbers, electron irradiation, cavity loss.

1. INTRODUCTION

Considerable effort has been made to control spiking behavior at Nd:YAG lasers either by adding an optical component that introduces a loss mechanism within the laser cavity (whose loss increases with increasing photon number $n(t)$), or with an external feedback loop which controls a loss modulator within the cavity³.

It can be analytically shown that adding a small amount of fast-acting limiting effect or saturable gain element in a spiking laser, will strongly damp the spikes and relaxation oscillations¹. The problem is to find a fast low threshold optical limiter which can operate at the power density levels present in typical spiking lasers, and which will not add large amounts of optical loss at the normal operating point.

In the present paper are analyzed the conditions to control the spiking behavior of pulsed Nd:YAG lasers by employing saturable absorbers. Are also presented experimental results obtained by placing in the Nd:YAG laser cavities of specially prepared LiF:F_2^- saturable absorbers. F_2^- color centers were generated in LiF crystals by hard electron irradiation⁴. Irradiations were made in electron beam generated by a linear accelerator with average energy of 7MeV. Irradiation dose rates were of about 50MRads/h.

2. ANALYTICALLY PHASE PLANE DESCRIPTION

A modality to describe spiking behavior analytically, is to plot the photon number $X(t)$ and the population inversion $W(t)$ as points in a phase plane. It was considered a three level energetically scheme for the laser medium and a two levels model for the LiF:F_2^- saturable absorber, as shown in Figure 1.

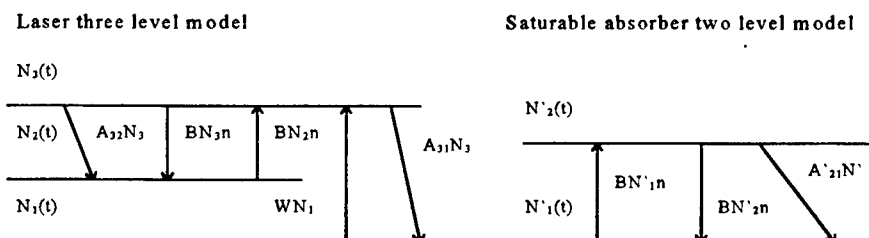


Figure 1. Laser and saturable absorber energetically scheme

In concordance with the energy level diagrams from Figure 1, laser rate equations can be written as equations for the photon number and population inversion in laser medium and saturable absorber:

$$\frac{dn}{dt} = B N n - B N' n - \gamma n \quad (1)$$

$$\frac{dN}{dt} = -2 B N n - (A_{32} + A_{31} / 2) N + (W + A_{32} + A_{31} / 2) N_1 - (A_{32} + A_{31} / 2) N_0 \quad (2)$$

$$\frac{dN'}{dt} = -2 B N' n - A_{21}' N' + A_{21}' N_0 \quad (3)$$

where:

n = photon density

$N = N_3 - N_2$

$N' = N'_1 - N'_2$

γ = loss rate in the laser cavity

Laser rate equations can also have the normalized form:

$$\frac{dX}{d\xi} = W X - X \quad (4)$$

$$\frac{dW'}{d\xi} = -2\sigma X W' - A W' + [C\sigma - A(\sigma + \sigma')] \quad (5)$$

where:

$W' = \sigma Y - \sigma' Z$; $X = n/N_0$; $Z = N'/N_0$; $A = A_{21}'/\gamma$; $\xi = \gamma t$

$$C = k \frac{2W + 2A_{32} + A_{31}}{2\gamma[2W + A_{31}]} \quad (6)$$

In the phase plane $\{X, W'\}$ there are two critical points having the coordinates:

$$P_1: \quad X_{10} = 0; \quad W'_{10} = \frac{C\sigma - A[\sigma + \sigma']}{A} \quad (7)$$

$$P_2: \quad X_{20} = \frac{C\sigma - A[\sigma + \sigma' + 1]}{A}; \quad W'_{20} = 1 \quad (8)$$

From the variety of "maps" in the phase plane we select the one which has stable oscillations (P_1 is an unstable point and P_2 a critical point in whose vicinity are generated oscillations).

The oscillation frequency will be:

$$\omega \approx \sqrt{C\sigma - A(\sigma + \sigma')} \quad (9)$$

The unnormalized form of the equation (6) is:

$$\Omega \approx \sqrt{B N_0 \left\{ k \frac{2W + 2A_{32} + A_{31}}{2W + A_{31}} - A_{21}' \right\}} \quad (10)$$

with the condition:

$$A_{21}' \approx k \frac{2W + 2A_{32} + A_{31}}{2W + A_{31}} \quad (11)$$

If we consider the values:

$$B \approx 2.8 \cdot 10^3 \text{ [cm}^3/\text{s]}$$

$$N_0 \approx 5 \cdot 10^{19} \text{ [cm}^{-3}\text{]}$$

$$N_0' \approx 1.4 \cdot 10^{16} \text{ [cm}^{-3}\text{]}$$

$$A_{21}' \approx 1.4 \cdot 10^7 \text{ [s}^{-1}\text{]} \quad (\text{the LiF:F}_2^- \text{ crystal length } l=3\text{cm the initial transmission } T_0=53\%, \text{ the final transmission } T_f=80\% \text{ and } \sigma=1.6 \cdot 10^{-17} \text{ cm}^2)$$

$$A_{32} \approx 4 \cdot 10^3 \text{ [s}^{-1}\text{]}$$

$$k \approx 10^7$$

The repetition frequency of the oscillations will be:

$$\Omega \approx \sqrt{BN_0 \frac{kA_{32}}{W}} \approx 170 \text{ kHz} \quad (12)$$

In the controlled oscillation regime obtained with suitable saturable absorber the frequency is proportional with the emission cross section and the ratio between the relaxation time of the laser medium and the saturable absorber.

For a laser in the free generation regime the repetition frequency of the spikes will be a function of the optical pumping and loss rates:

$$\Omega \approx \sqrt{\gamma(\gamma - W) + \frac{A_{21}}{2}\gamma} \quad (13)$$

In Figure 2 are represented values of the normalized photon number X function of the population inversion W' in a phase plane

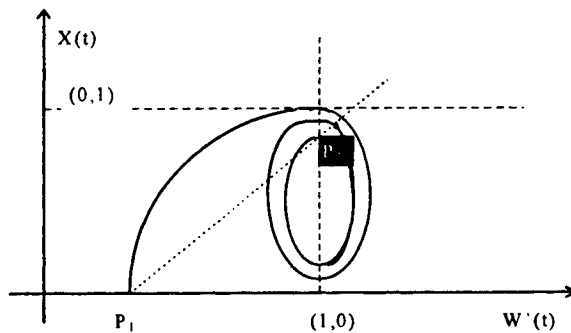


Figure 2. Phase plane representation of the photon number $X(t)$ function of population inversion $W'(t)$

3. EXPERIMENTAL RESULTS

The LiF:F₂⁻ crystals employed, were obtained by electron irradiation generated by a linear accelerator with 7 Mev average energy. F₂⁻ color centers generated in LiF crystals are characterized by

absorption and emission bands centered at 300 K, at 960 and 1130 nm. They consist in two anion vacancies located along the diagonal face of anion cell, with three captured electrons. Their most important application is Q-switching of pulsed Nd:YAG lasers.

The LiF:F_2^- crystals employed in spiking control experiment were obtained by hard electron irradiation of 3 cm long crystals at dose rates higher than 50MRads/h. The integrated doses were in the 100 to 150 MRads range.

The very high irradiation dose rates led to generation not only of F_2^- centers, but also an important number of other color centers and crystal defects. That was reflected by a low final transmission. The difference between final and initial transmission ($T_f - T_i$) was only of 5-14% compared with the crystals used as laser Q-switches with $T_f - T_i > 45\%$.

The experimental setup is shown in Figure 3.

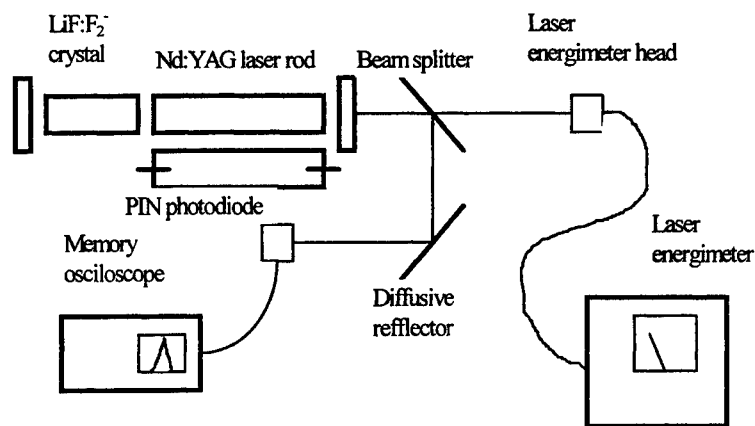


Figure 3. Experimental setup for study of spiking regime at Nd:YAG lasers

The LiF:F_2^- crystals were placed in the cavity of a Nd:YAG pulsed laser. The length of the laser cavity was of 15 cm. The optical pumping energy was varied from 18 to 40 J.

Output energy was measured with a laser energimeter and the trains of pulses were registered with a fast PIN photodiode and a memory digital oscilloscope Tektronix TDS 520.

In Figures 4, 5 and 6 is presented a train of pulses compared with the spiking free generation regime, and also the wave form of a single pulse in train. The pulses were obtained with a crystal having initial transmission $T_i = 77\%$ and final transmission $T_f = 82\%$.

The total energy of the train, E_t was of 64 mJ and the number of pulses of 32. The pulse width of a single pulse in train τ was of 28.8 ns. The average energy of a single pulse was of 2mJ and the average repetition frequency of about 280 kHz.

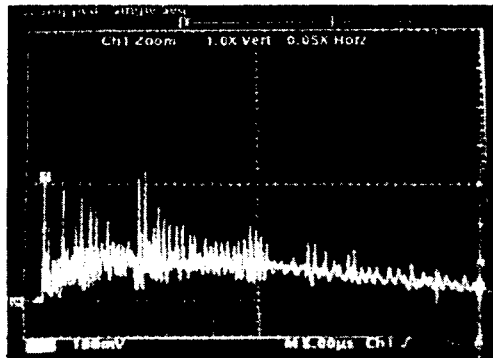


Figure 4. Spiking free generation regime of a Nd:YAG laser

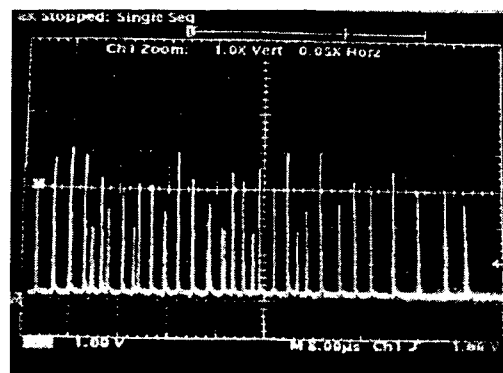


Figure 5. Controlled spiking regime

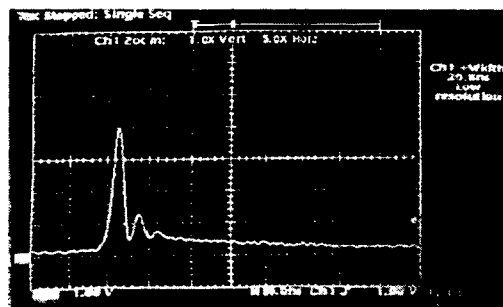
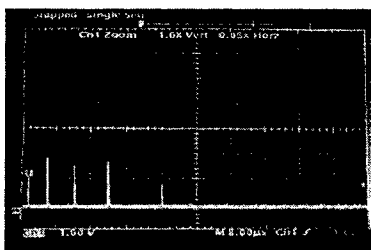


Figure 6. Pulsewidth in spiking regime

In Figure 7 (a, b) are presented trains of pulses obtained with a crystal (nr.4) with $T_i=47\%$ and $T_f=62\%$, at two pumping levels of 18 respectively 40. The pulsewidth grows with pumping level from 13.6 ns to 20.8 ns.

At this crystal the difference between T_i and T_f is higher than the one of the previous crystal and at the lower pumping level the number of pulses in train is only of 5, the pulsewidth approaching the value of the Q-switch regime. For example with crystals having initial transmission from 20 to 40% and the final transmission from 70 to 85%, introduced in the same laser cavity, were obtained pulses in the Q-switch regime with energies from 35 to 20 mJ and pulse width of about 10 ns.

a) Crystal No. 4 at 18 J pumping level



b) Crystal No. 4 at 40 J pumping level

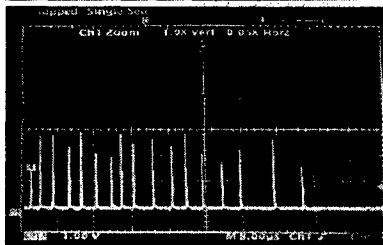


Figure 7. Trains of pulses and pulsewidth obtained at two optical pumping energies

In Table 1 are presented the parameters of trains of pulses obtained with four different crystals.

Crt. No.	T_i (%)	T_f (%)	E_t (mJ)	Number of pulses	τ (ns)	Repetition frequency (kHz)
1	77	82	64	32	20.8	400
2	70	77	93	21	21.6	280
3	72	78	84	25	24.8	310
4	47	62	28	17	20.8	210

Table 1. Parameters of pulses obtained with four different crystals.

The repetition frequency of the pulses is in the 210 to 400 kHz range, in concordance with the predicted values by (12).

4. CONCLUSIONS

In conclusion we can say that trains of pulses generated in Nd:YAG laser cavities using specially prepared LiF:F_2^- saturable absorber crystals have parameters in good concordance with the theoretical model. The average energy of the single pulses in train is of 1-2mJ and pulsewidth of 20-25ns. The trains of pulses have a good reproductibility. Due to their parameters they can be used in different applications as laser rangefinding or materials processing. Crystals with specific parameters allow a continues variation of the pulsewidth from 10 to 25 ns by a simple variation of the optical pumping energy. They are also suitable to be used in CW Nd:YAG lasers optically pumped with arc lamps or laser diodes.

5. REFERENCES

1. A.Siegman, "Lasers", Oxford Univ. Press, 1986.
2. W. Gellermann, A.Muller and D.Wandt, "Formation, Optical Properties and Laser Operation of F_2^- Centers in LiF Crystals", J. Appl. Phys. 61(4), 513-515, 1987.
3. T.T.Basiev, A.N.Kravets and A.V.Fedin, "Q-switching of a periodic-pulse-pumped industrial Nd:YAG laser by means of LiF:F_2^- crystals", Quantum Electron. 20, 513-515, 1993.
4. M.Jurba, N.Baltateanu, I.Spanulescu and G.Stoenescu, Balcan Phys. Lett. vol.2, 223-225, 1994.

About the optical transmission of ZnO thin films

I. I. Rusu, I. D. Bursuc*, I. Vascan

Bacau University, Calea Marasesti 157, Bacau, Romania

* "Al. I. Cuza" University, Iassy, Romania

ABSTRACT

ZnO films were prepared by d.c. reactive cathodic sputtering in a planar magnetron.

The structural properties of d.c. planar magnetron sputtered ZnO films are studied as a function of deposition parameters: substrate type, substrate temperature, sputter gas pressure, growth rate and sputtering power.

ZnO films growth has been carried out in an oxygen and argon atmosphere.

In dependence on the O₂ partial pressure in the argon sputtering gas there exists a narrow process window around a $p_{O_2}/(p_{Ar}+p_{O_2})$ ratio of 5-10% which yields transparent, low-resistance layers. The discharge voltage dependence on the oxygen partial pressure is a sensitive indicator for the oxidation state of the target surface and can be used for the regulation of the deposition process. Lower O₂ partial pressures yield metallic-like, opaque, but highly resistant layers. Higher oxygen partial pressures lead to transparent but highly resistant ZnO layers. Layers of lowest resistivity ($5 \times 10^{-4} \Omega \text{cm}$) and highest optical transmission (90%) have a stoichiometric ratio Zn:O of 1.0 and exhibit the largest grains.

These films are applied as piezoelectric transducers in micromechanical sensors and actuators.

1. INTRODUCTION

In the last 15-20 years, there has been a great deal of interest in piezoelectric and pyroelectric zinc oxide (ZnO) for use in acoustic, acousto-optic, and sensor device applications. One of the advantages of using ZnO instead of CdS is the ease with which it lends itself to vacuum deposition by either d.c. or r.f. sputtering. Consequently, several workers in the field used either diode or triode ZnO sputtering systems with varying degrees of success. The main difficulty in depositing ZnO has always been reproducibility, a problem which could be traced to the substrate temperature control which is affected by electron bombardment in the plasma, thermal conductivity of the substrate, and its contact to the substrate holder. Planar magnetron sputtering offers a solution to the above mentioned problems. The electron bombardment of the substrate is greatly reduced, and thus substrate temperature control can be more easily maintained by an external heater. Several workers in the field used a planar magnetron with a ZnO target and showed that higher sputtering rates, better quality films, easier control, and higher quality ZnO films can be obtained than with other deposition techniques.^{1,2}

In this work, we use a planar magnetron system with a zinc target and carry out

reactive sputter deposition in an oxygen atmosphere. Several additional advantages can be obtained using this technique. First, because a zinc target has a better thermal conductivity than a ZnO target, more power can be applied to the target and a higher sputtering rate can be obtained. Second, both the zinc target and the oxygen can be obtained with higher purity than a ZnO target. Thus the films obtained can be more pure than the ones obtained in direct ZnO sputtering. Third, either d.c. or r.f. sputtering can be used ; d.c. sputtering is usually preferred to r.f. sputtering because it is easier to control and may lead to higher sputtering rates for the same amount of input power.

2. EXPERIMENTAL DETAILS

ZnO films were obtained by d.c. reactive sputtering in an UVN-type planar magnetron. All the experiments have been carried out using an acceleration voltage of 550V and a discharge current of 300mA.

The substrate temperature was maintained constant at about 250°C using an external heating source. Zinc was used both as a sputtering target and as the cathode of the sputtering diode. The distance between the anode and the cathode was maintained at 3.8cm.

An oxygen and argon gas mixture, in different proportions, was used as the working gas. The pressure in the sputtering chamber was in the range of 5×10^{-2} - 10^{-1} torr during the deposition.

ZnO films were deposited on microscope glass substrates. The interferometric method was used for measuring the film thickness. The M II-2 Linnik interferential microscope was used. In order to obtain the monochromatic radiations, the microscope is equipped with two filters accordingly to radiations with wavelengths of 5535 Å and 4750 Å, respectively.

The studied films thickness was between 0.85 and 1.20µm. The band-gap thickness was determined taking into account that near the margin of the fundamental absorption, the absorption coefficient can be written as :

$$\alpha = A(h\nu - E_g)^{1/2}$$

where :

A is constant

$h\nu$ is the light quantum energy (the photon energy)

E_g is the gap energy

From the $\alpha^2=f(h\nu)$ graph, traced near the margin of the fundamental absorption, we were able to determine the gap energy. The transmission spectra for the ZnO films were recorded on a double-beam Specord U.V.-VIS, Carl Zeiss Jena spectrophotometer.(figure 1)

3. RESULTS AND DISCUSSION

The optical transmission of the ZnO thin films is connected with their stoichiometric composition, which is also influenced by the nature and the composition of the working gas.

In the case of using zinc as a target, the presence of the oxygen as a working gas is compulsory for obtaining ZnO films.

From the optical transmission spectra presented, (fig.1) it is observed that the

interferential spectrum is well outlined for an oxygen and argon mixture in equal proportions.

The structural analysis show that the high optical transmission films (above 90%) have better crystallographic orientation.

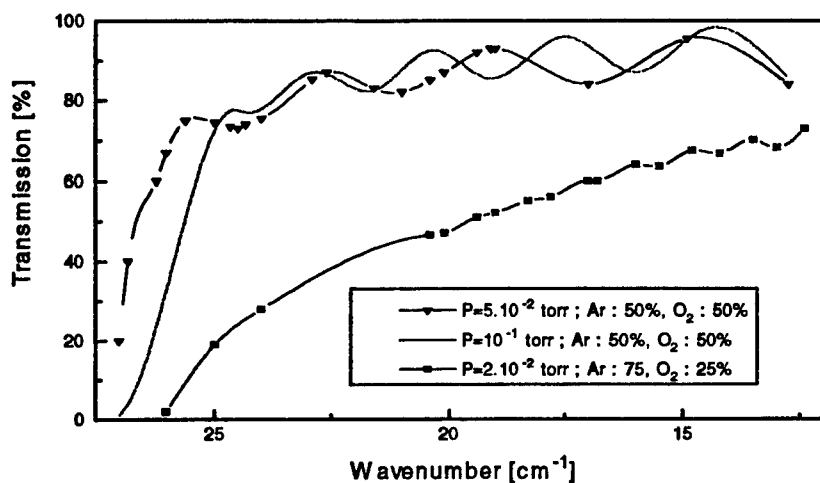


Figure 1: Optical transmission spectra of ZnO films deposited at different pressions

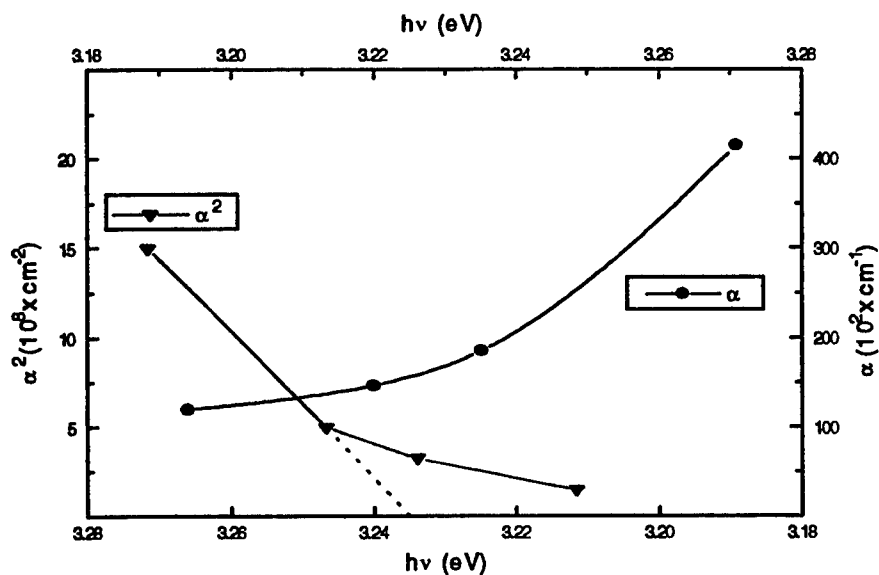


Figure 2: The absorption coefficient dependence on the radiation energy for O_2 -25%, Ar-75% $E_g=3.23$ eV

A decrease in the optical qualities and the crystallographic orientation is observed with decreasing oxygen percentage.

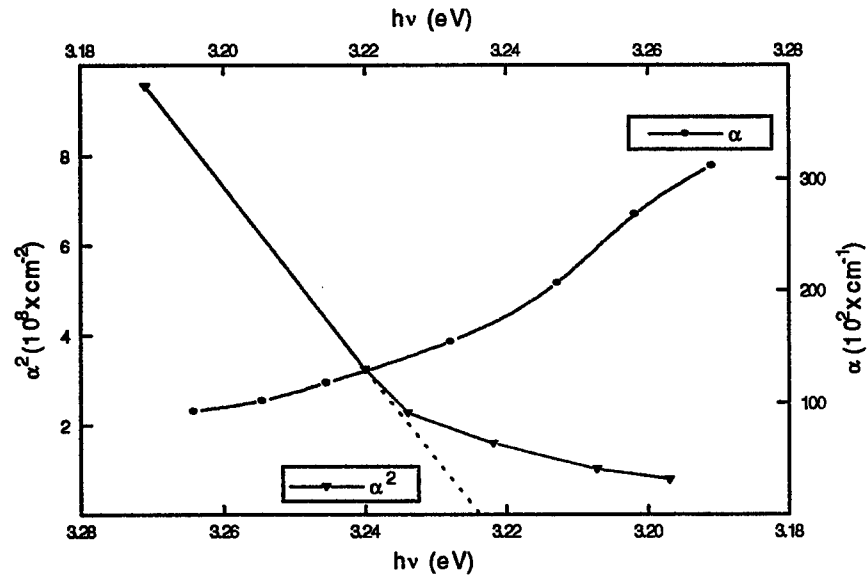


Figure 3: The absorption coefficient dependence on the radiation energy for O₂-50%, Ar-50%
E_g=3.22eV

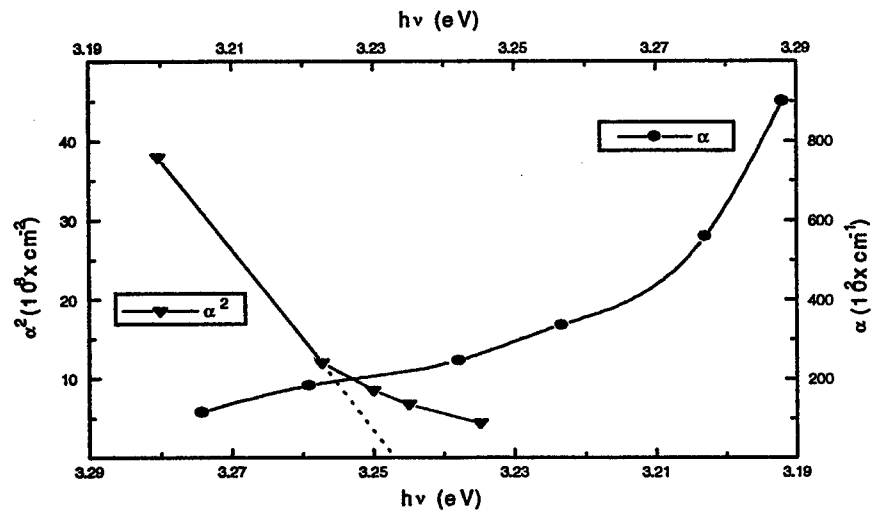


Figure 4: The absorption coefficient dependence on the radiation energy for O₂-75%, Ar-25%
E_g=3.24

ZnO crystals are transparent at room temperature. ZnO thin films with stoichiometric composition have the same property.

The band-gap thickness for ZnO films at room temperature is 3.2eV, when the films have stoichiometric composition, approaching to a dielectric. The band-gap thickness decreases with increasing temperatures. We were able to determine the band-gap thickness by optical absorption measurements. The values found are presented in figures 2,3 and 4, for different compositions of the working gas.

The results are according with those found by other authors.

4. CONCLUSIONS

ZnO thin films deposited by d.c. sputtering in planar magnetron are transparent at room temperature. The average transparency of the samples is above 90% in the visible range of the spectrum and does not change if the samples are heated in air up to temperatures of about 800°C.

The band-gap thickness, determined by absorption measurements was found to be about 3.2eV. ZnO films which do not have stoichiometric composition present deviations from this value.

Films with high transparency have good crystallographic orientation and stoichiometric composition.

5. REFERENCES

1. D. H. Zhang, D. E. Brodie, "Crystallite orientation and the related photoresponse of hexagonal ZnO films deposited by r.f. sputtering", *Thin Solid Films*, **251**, 151-156 (1994)
2. B. T. Khuri-Yakub and J. G. Smits, T. Barbee, "Reactive magnetron sputtering of ZnO", *J. Appl. Phys.*, **52** (7), 4772-4774 (1981)
3. D. H. Zhang, D. E. Brodie, "Effects of annealing ZnO films prepared by ion-beam-assisted reactive deposition", *Thin Solid Films*, **238**, 95-100 (1994)
4. M. Krunk, E. Mellikov, "Zinc oxide thin films by the spray pyrolysis method", *Thin Solid Films*, **270**, 33-36 (1995)
5. K. Ellmer, F. Kudella, R. Mientus, R. Schieck, S. Fiechter, "Influence of discharge parameters on the layer properties of reactive magnetron sputtered ZnO:Al films", *Thin Solid Films*, **247**, 15-23 (1994)
6. Ma Jin and Li Shu Ying, "Preparation of ZnO films by reactive evaporation", *Thin Solid Films*, **237**, 16-18 (1994)

Magneto-optical behaviour of ferronematics

C. Motoc, E. Petrescu, C. Dascalu

University "Politehnica", Department of Physics
313 Splaiul Independentei, 77206, Bucharest, Romania

ABSTRACT

The behaviour under magnetic fields of new types of ferronematics is examined. First, by using both optical and electrical method, an increase in the critical field for Freedericksz transition was noticed in cells containing ferronematics. Second we give an explanation of the relaxation processes occurring in ferronematics when the magnetic field was suddenly varied. When ferronematics are involved, the relaxation phenomena are described by lower time constants when compared to those of pure nematics.

Keywords : ferronematics, Freedericksz transition, birefringence

1 INTRODUCTION

The phenomena occurring in nematic liquid crystals (NLC) containing magnetic particles were first investigated by Brocchard and de Gennes.¹ Such systems were termed 'ferronematics' and it was shown that they exhibit peculiar properties when subjected to magnetic fields. One of these is concerned to an increase in the critical field for Freedericksz transition. This behaviour was explained by Burylov and Raikher which assumed that the magnetic moments of the magnetic particles are oriented perpendicular to the nematic director. The experimental data referring to the dependence of the critical field on magnetic particle size and concentration were in good agreement to the theoretical predictions.²

In this paper we examine the behaviour under magnetic field of new types of ferronematics obtained by mixing a NLC with a powder of organomagnetics.³ We report first changes in the critical field for Freedericksz transition occurring in ferronematics when using both optical and electrical methods. Secondly, we give an explanation of the relaxation processes when the magnetic field is suddenly varied. Such phenomena were noticed in case of pure nematics by Pieranski et al.⁴

We show that when ferronematics are involved, the relaxation phenomena are described by lower time constants when compared to those of pure nematics.

2 THEORETICAL BACKGROUND

2.1 Static behaviour

As it known, when a NLC is subjected to a magnetic field, a field-induced transition (Freedericksz transition) occurs for a critical values B_c .⁴ It consists in the parallel alignment of the molecular director to the magnetic field. If the nematic is homeotropically aligned and the field is perpendicular to the nematic director, at $B = B_c$ the homeotropic texture turns into a planar one. The nematic cell behaves as a magnetic field addressed light shutter which is similar to the electric field addressed shutter. The critical field is given by:

$$B_c = \frac{\pi}{d} \sqrt{\frac{K_i}{\mu_0^{-1} \chi_a}} \quad (1)$$

where d is the cell thickness, K_i an elastic constant, μ_0 the permeability of the free space and χ_a the magnetic anisotropy. The index i (1,2,3) refers to the three different geometries used in such experiments.

Burylov and Raikher² have shown that in ferronematics the critical field for Freedericksz transition \tilde{B}_C is given by :

$$\tilde{B}_C^2 = B_C^2 + G^2 \quad (2)$$

where the function G may be approximated as

$$G = \left(\frac{2Wf}{\mu_0^{-1} \alpha \chi_a} \right)^{\frac{1}{2}} \quad (3)$$

In (3) f is the volume fraction of the magnetic particles, a the mean particle diameter and W the surface density energy of the magnetic particles-nematic boundaries.

2.2 Dynamic behaviour

As it is shown in Fig. 1, when the magnetic field is suddenly varied, fluctuations in the light transmission are noticed. These phenomena were examined by Pieranski et al.⁴ and explained by assuming periodic distortions of the nematic director, giving rise to changes in the birefringence of the sample. They showed that when applying a field $B > B_C$, a phase difference δ between the ordinary and extraordinary waves is introduced. This is given by :

$$\delta = \frac{\pi d}{\lambda} \theta_m^2 (n_e - n_o) \quad (4)$$

where θ_m is the maximum distortion angle of the nematic director and λ the wave length of the incident light. As θ_m changes in time fluctuations in the light transmission (maxima and minima) are noticed. The extinction order (determined when $\delta = 2\pi N$) is given by :

$$N = \frac{d(n_e - n_o)}{2\lambda} \theta_m^2 \quad (5)$$

Pieranski et al. have shown that for pure nematics, the number of extinctions obeys the law :

$$N(t) = \alpha \theta_m^2(t) = \alpha \theta_m^2(0) \exp\left(\frac{t}{\tau_{A,B}}\right) \quad (6)$$

$\tau_{A,B}$ are time constants intervening when applying (τ_A) or suppressing (τ_B) the magnetic field. They may be obtained by measuring the time difference t_N (see Fig 1) between two neighbouring extinctions.

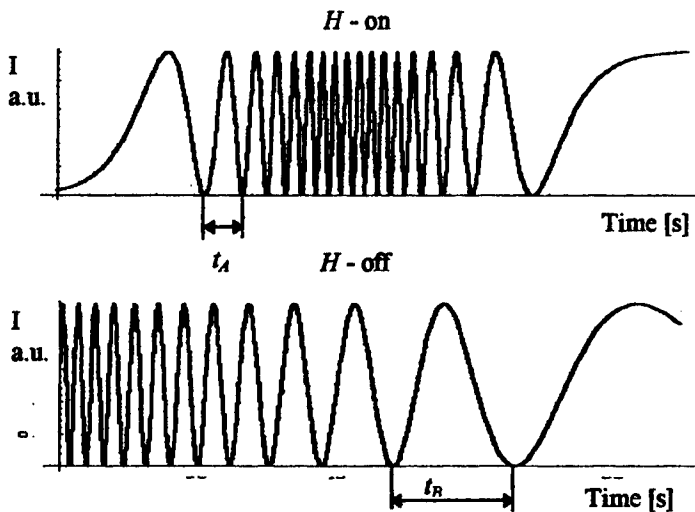


Fig. 1 Fluctuation in the light transmission when the magnetic field is suddenly varied

Therefore :

$$\tau_{A,B} = \frac{(t_N)_{A,B}}{\ln 2} \quad (7)$$

To obtain the behaviour of a ferronematic we solved the same variational problem introducing into the free energy of a pure nematic new terms, such as :

$$f_M = -\mu_0^{-1} M_s f(\tilde{m}\tilde{B}) + \left(\frac{fk_B T}{v} \right) \ln f + \left(\frac{fW}{a} \right) (\tilde{n}\tilde{m})^2 \quad (8)$$

In (8) M_s is the saturation magnetization, v the volume and \tilde{m} the magnetic moment of the particles. We assumed for the ferronematic a planar alignment. The distortions of the nematic director and magnetic moment are shown in Fig. 2

In this case the total free energy is :

$$f_t = \frac{1}{2} \left[(K_1 \cos^2 \theta + K_3 \sin^2 \theta) \left(\frac{\partial \theta}{\partial z} \right)^2 - \frac{1}{2} \mu_0^{-1} \chi_a B^2 \sin^2 \theta - \mu_0^{-1} M_s f B \cos \beta + \frac{fk_B T}{v} \ln f + \frac{fW}{a} (-\sin \beta \cos \theta + \cos \beta \sin \theta)^2 \right] \quad (9)$$

As f_t depends on θ and β we get two Euler Lagrange equations :

$$\mu_0^{-1} M_s f B \sin \beta + \frac{2fW}{a} (-\cos \beta \sin \theta - \sin \beta \cos \theta) (-\sin \beta \cos \theta + \cos \beta \sin \theta) = 0 \quad (10)$$

$$\begin{aligned} & (K_1 \cos^2 \theta + K_3 \sin^2 \theta) \frac{\partial^2 \theta}{\partial z^2} + (K_3 - K_1) \sin \theta \cos \theta \left(\frac{\partial \theta}{\partial z} \right)^2 + \mu_0^{-1} \chi_a B^2 \sin \theta \cos \theta - \\ & - \frac{2fW}{a} (\sin \beta \sin \theta + \cos \theta \cos \beta) (-\sin \beta \cos \theta + \cos \beta \sin \theta) = 0 \end{aligned} \quad (11)$$

Assuming small distortion ($\sin \theta \approx \theta$, $\sin \beta \approx \beta$, $\cos \beta \approx \cos \theta \approx 1$) we get from (10) :

$$\beta = \frac{1}{1 + \frac{M_s B a}{2\mu_0 W}} \theta \quad (12)$$

Introducing (10) in (11) gives:

$$K_1 \frac{\partial^2 \theta}{\partial z^2} + \mu_0^{-1} \left[\chi_a B^2 - \frac{2fM_s B W}{2W + \mu_0^{-1} M_s B a} \right] \theta = 0 \quad (13)$$

Assuming $\frac{2fW}{M_s B a} \ll 1$, and considering the relationship (3) the equation (13) may be written as :

$$K_1 \frac{\partial^2 \theta}{\partial z^2} + \mu_0^{-1} \chi_a [B^2 - G^2] \theta = 0 \quad (13')$$

When solving equation (13) the critical field (3) is obtained.

The dynamical problem is solved by equating the elastic and viscous torques (expressed in terms of the viscosity coefficient γ) It gives :

$$K_1 \frac{\partial^2 \theta}{\partial z^2} + \mu_0^{-1} \chi_a [B^2 - G^2] \theta = \gamma \frac{\partial \theta}{\partial t} \quad (14)$$

A rather good approximative solution of equation (14) satisfying the boundary conditions $\theta(z = \pm \frac{d}{2}) = 0$ is :

$$\theta(z, t) = \theta_m(t) \cos \frac{\pi z}{d} \quad (15)$$

Substituting (15) into (14) we get for θ the equation :

$$\frac{\mu_0^{-1} \chi_a \tilde{B}_c^2}{\gamma} \left[\frac{B^2}{\tilde{B}_c^2} - 1 \right] \theta_m(t) = \frac{d\theta_m}{dt} \quad (16)$$

The solution of (16) is :

$$\theta_m(t) = \theta_m(0) \exp \left[\frac{\mu_0^{-1} \chi_a \tilde{B}_c^2}{\gamma} \left(\frac{B^2}{\tilde{B}_c^2} - 1 \right) t \right] \quad (17)$$

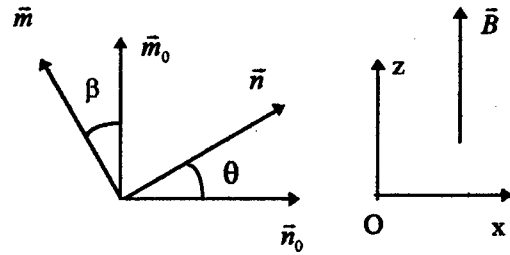


Fig. 2 Distortions of the nematic director and magnetic moment induced by the magnetic field

Therefore

$$\theta_m^2(t) = \theta_m^2(0) \exp\left(\frac{t}{\tau_A}\right) \quad (18)$$

where:

$$\tau_A^{-1} = \frac{2\mu_0^{-1}\chi_a\tilde{B}_c^2}{\gamma} (h'^2 - 1) \quad (19)$$

$$h'^2 = \frac{B^2}{\tilde{B}_c^2} \quad (20)$$

τ_A is the relaxation time intervening when the magnetic field was switched on. When suppressing the field we get :

$$\theta_m^2(t) = \theta_m^2(0) \exp\left(-\frac{t}{\tau_B}\right) \quad (21)$$

where :

$$\tau_B^{-1} = \frac{2\mu_0^{-1}\chi_a\tilde{B}_c^2}{\gamma} \quad (22)$$

The relationship (19) and (22) are similar to the ones obtained by Pieranski in case of pure nematics . When replacing h'^2 by $h^2 = \frac{B^2}{B_c^2}$ the time constant τ_A and τ_B characteristic for a pure nematic are obtained .

3 EXPERIMENTAL

The ferronematics were obtained by sonicating a magnetic powder of an organomagnetic substance³ termed PAN into nematic K15 . The solutions were introduced by capillarity into liquid crystal cells 180 μ m thick provided with ITO electrodes . Before filling , the cell's electrodes were chemically processed to obtain a planar texture .

In order to follow the phenomena occurring under magnetic field we used a common set-up described in.⁴ A photomultiplier and an X-t recorder was used to follow in time changes in the light transmission of He - Ne light source ($\lambda = 633$ nm) . The magnetic field was directed perpendicular to the cell 's electrodes . Changes in the capacitance were recorded by using a digital RLC meter E0711.

4 RESULTS AND DISCUSSION

In Fig 3 we give the magnetic field dependence of the capacitance (C) and intensity of transmitted light (I) for the pure nematic. Changes from the planar to the homeotropic textures at $B = B_c$ are revealed by sharp changes for I and C .

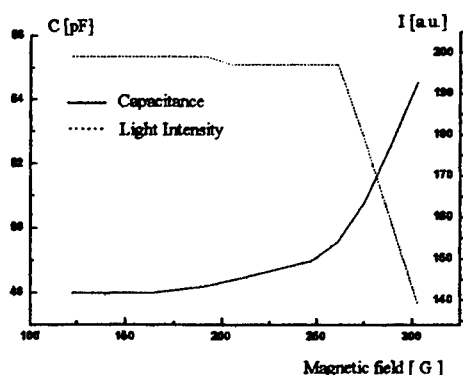


Table I
Specific parameters depending on f

$f \times 10^{-3}$	\tilde{B}_c [gauss]	G [gauss]	$G/f^{1/2}$	$\tau_B(s)$	\tilde{B}_c [gauss]
0	275	-	-	58	-
0.19	302	124.8	90	50	295
0.35	320	182.4	97	46	307
0.61	352	250	101	46.5	328

Fig . 3 Changes in the capacitance (C) and light intensity (I) as function of magnetic field

It increases when the volume fraction f was increased, as expected from equation (2). The ratio $G/f^{1/2}$ is the same for all ferronematics; this shows that \tilde{B}_c^2 varies linearly with f in accordance to equation (2) and (3). The critical field \tilde{B}_c in ferronematics is given in Table I.

The relaxation time $\tilde{\tau}_b$ was estimated by using the data given in Fig. 4 and equation (6). It decreased when f is increased. Using equation (22) we determined the critical field \tilde{B}_c . As shown in the last column of Table I, the results are in good agreement with those obtained before. The time constant $\tilde{\tau}_A$ varies linearly with h^2 (Fig. 5) as indicated by equation (19).

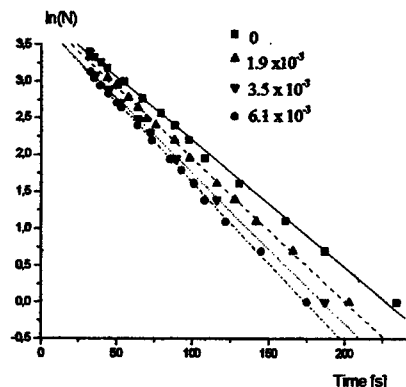


Fig. 4 Plot of $\ln(N)$ versus t for pure and doped nematics

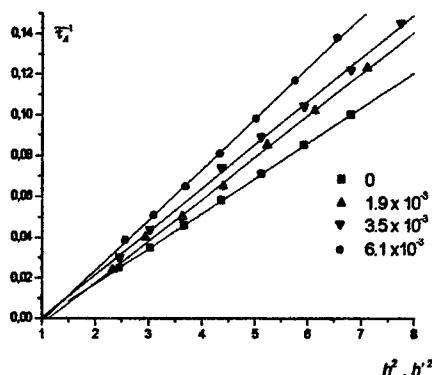


Fig. 5 The reverse of the constant $\tilde{\tau}_A$ versus the reduced field for pure and doped nematics

5 CONCLUSION

A theoretical model describing the dynamic behaviour of a ferromagnetic subjected to a magnetic field is proposed. We found that the relaxation phenomena are described by lower time constant when compared to those of pure nematics. Using this model, the critical field \tilde{B}_c was determined by means of the relaxation time.

6 REFERENCES

- 1 F. Brochard and P.D.Gennes, "Theory of magnetic suspensions in liquid crystals," *J. Physique*, Vol. 31, pp. 691-708, 1970
- 2 S.V Burylov and Yu. L.Raikher, "Magnetic Freedericksz transition in a ferronematic," *J. Magn Magn. Mater.* Vol. 122, pp. 62, 1993
- 3 Radu Setnescu, Silviu Jipa, Wilhelm Kappel, Shodo Kolbayashi and Zenjiro Osawa, "IR and X-ray characterisation of the ferromagnetic phase of pyrolysed polycrystalline nitrile," *Carbon* -in press
- 4 P. Pieranski, F. Brochard and E. Guyon, "Static and dynamic behaviour of a nematic liquid crystal in a magnetic field," *J.Physique*, Vol. 34, pp. 35-48, 1973

Optical bistability using nematic liquid crystals and polymer dispersed liquid crystals

D. Manaila-Maximean, C. Rosu, R. Bena, A. M. Albu and I. M. Popescu

"Politehnica" University of Bucharest, Spl. Independentei, 313, Bucharest, 76203, Romania

ABSTRACT

We present the experimental results concerning hybrid optical bistable devices without resonant cavity using as electro-optic modulators a nematic liquid crystal cell and a polymer dispersed liquid crystal film. Bistable operation was studied for different control voltages and multistable behaviour was studied for the polymer dispersed liquid crystal film as a function of the control voltage frequency.

Keywords: optical bistability, nematic, polymer dispersed liquid crystals

1. INTRODUCTION

An optical bistable device (OBD) has two possible stable states for the same value of an input parameter, usually the optical power; the system is in one of these states depending on its history. In order to obtain an OBD, two basic conditions must be fulfilled: the existence of a nonlinear mechanism and of a reaction mechanism.

The OBD can be classified as: active (in lasers) or passive, absorptive or dispersive, and intrinsic (all optic) or hybrid (optic and electronic)¹.

A special class of hybrid OBD's are those without an optical resonator. In this paper we present hybrid OBD's without optical resonator using as electro-optic modulator a nematic liquid crystal (NLC) cell and a polymer dispersed liquid crystal (PDLC) film.

2. EXPERIMENTAL

In fig. 1, we present the experimental set-up for obtaining bistability.

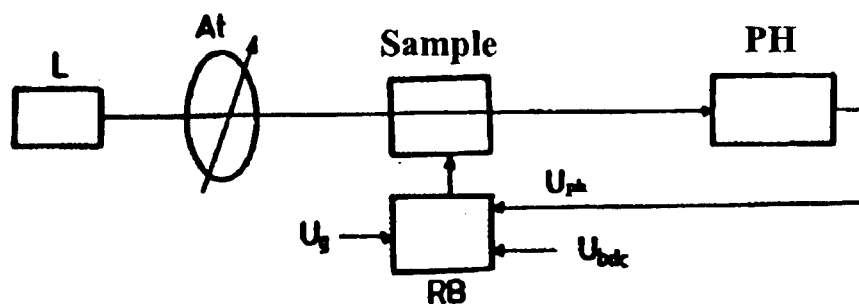


Fig. 1. Experimental set-up for obtaining bistable operation when applying the reaction voltage U_{ph} , the d.c. bias voltage U_{bdc} , and an a.c. sinusoidal voltage U_g .

The light source was a He-Ne laser (L); the input power was modified with a variable polarizer (At) and the emerging signal was detected by a photomultiplier (PH)². The reaction block (RB) sums three signals: the reaction signal from the photomultiplier (U_{ph}), the bias d.c. signal (U_{bdc}) and an a.c. sinusoidal control signal (U_g).

We used the following samples:

- a nematic liquid crystal E3 (BDH) - a mixture of cyanobiphenyl derivatives with $\Delta\epsilon > 0$
- a polymer dispersed liquid crystal composite film obtained using the same NLC and a polymer matrix (MMA - I)³ obtained from methyl methacrylate.

3. RESULTS AND DISCUSSION

The results obtained for the NLC sample are presented in figs. 2 and 3 a, b.

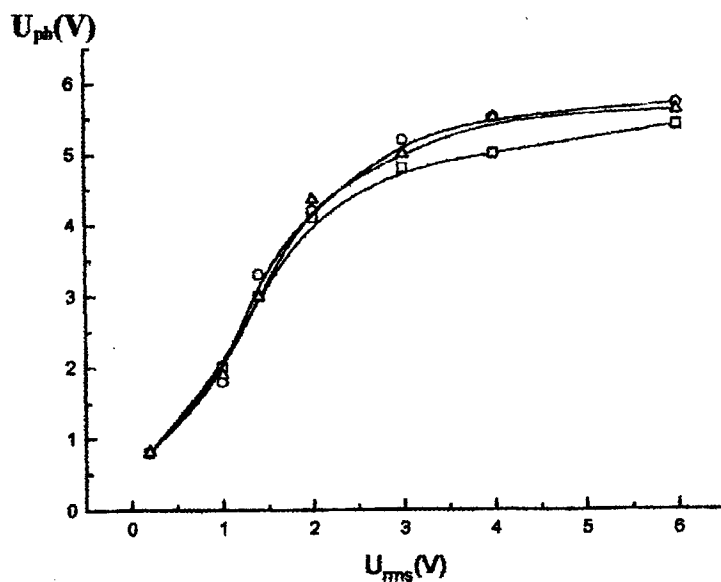


Fig.2. The photomultiplier output voltage versus the a.c. signals.

□ - $f = 40$ Hz; - ○ - $f = 200$ Hz; - Δ - $f = 1 + 20$ kHz

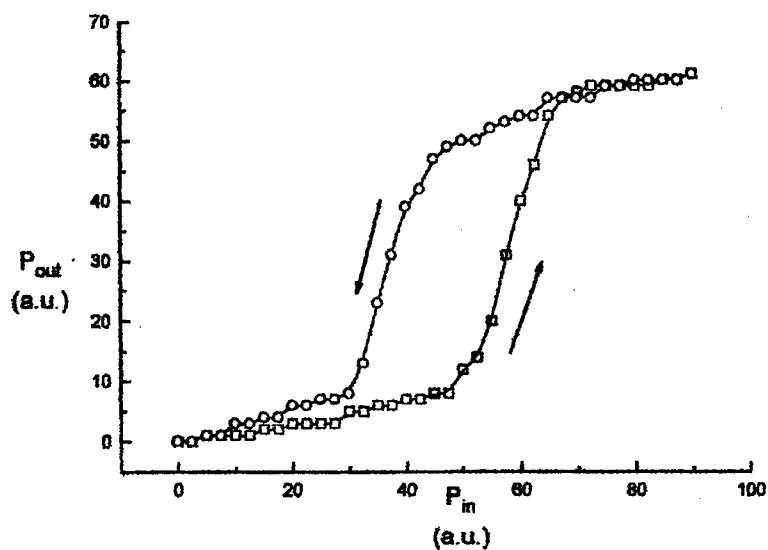


Fig. 3a. Bistability curve for E3 nematic liquid crystal sample ($U_{bdc} = 0V$, $f = 200Hz$)

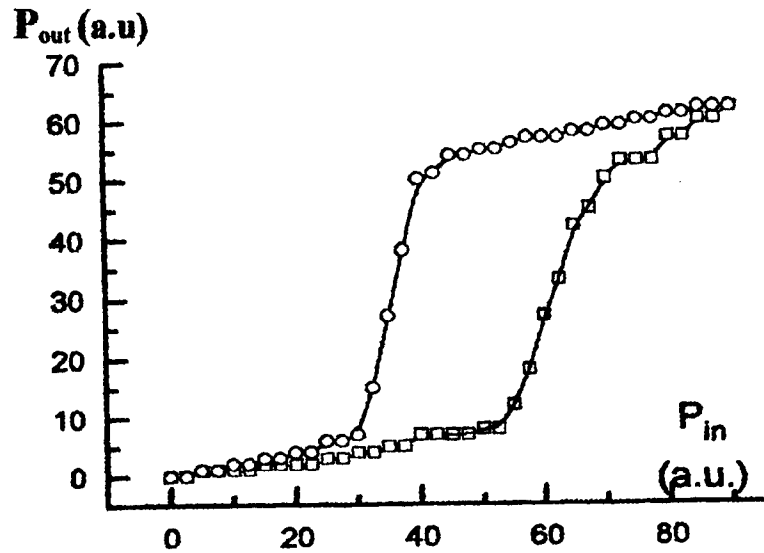


Fig. 3b. Bistability curve for E3 nematic liquid crystal sample ($U_{bdc}=0.1V$, $f=200Hz$)

In order to study the bistability of the PDLC sample, the transmission curve ($P_{out} = f(U_p)$) was obtained (fig.4). We observed maxima and minima of the output power. When applying the reaction voltage, they will lead to either bistability or multistability, depending of U_{bdc} .

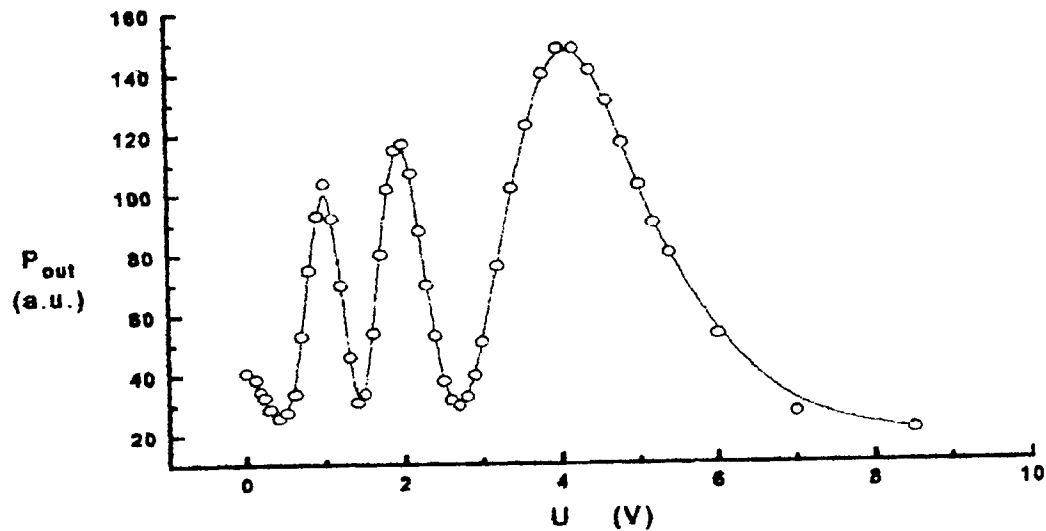


Fig. 4. Output power function of a.c. control signal voltage

In fig. 5 we present the output voltage U_{ph} , function of the alternative control voltage U_g , for different frequencies, in the high voltage range. For high frequencies, the transmission curve first rises, then reaches a saturation value; in the case of the low frequencies, the transmission curve first stays stationary, then rises. This behaviour is the result of competition between the aligning effects of the applied field and the restoring torques due to elastic and surface effects. The nonlinear dependence of the transmittance on the control voltage, is responsible for the characteristic nonlinear response of the system in the presence of linear feed-back.

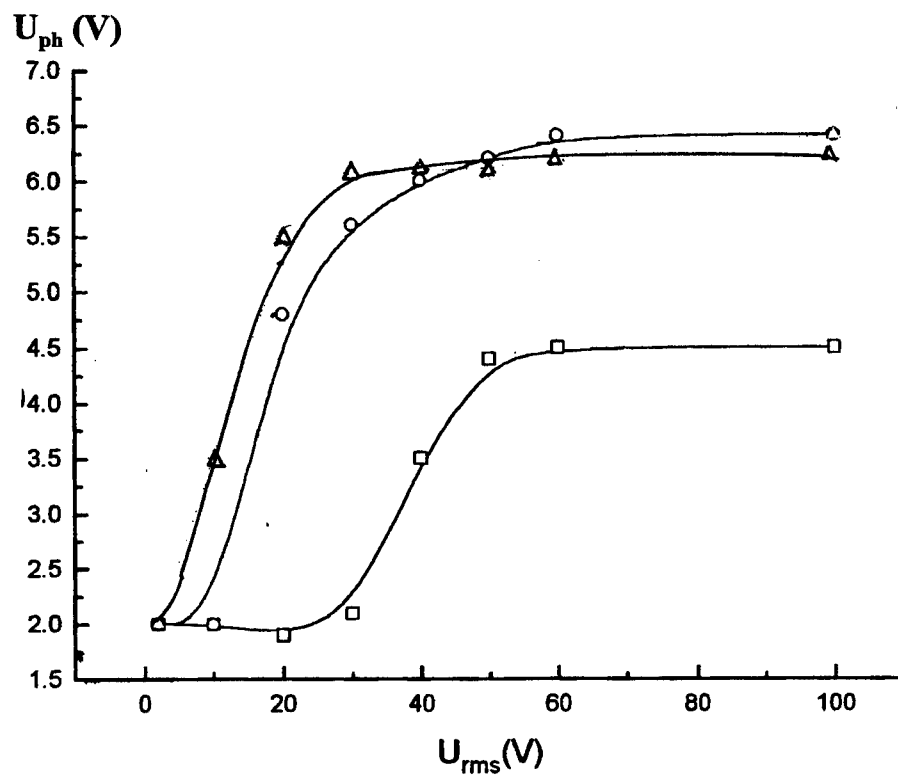


Fig. 5. Output voltage U_{ph} , function of the alternative control voltage U_g
 \square $f=40$ Hz; \circ $f=200$ Hz, Δ $f=1000$ Hz.

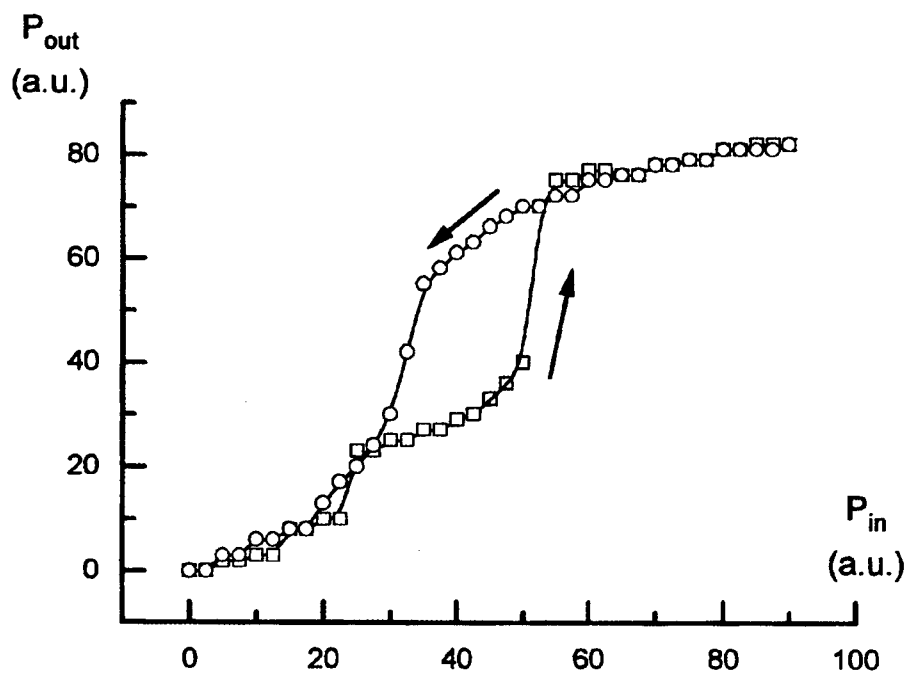


Fig. 6. Bistability curve $P_{out} = f(P_{in})$; $U_{bdc} = 0,1$ V; $f = 200$ Hz;

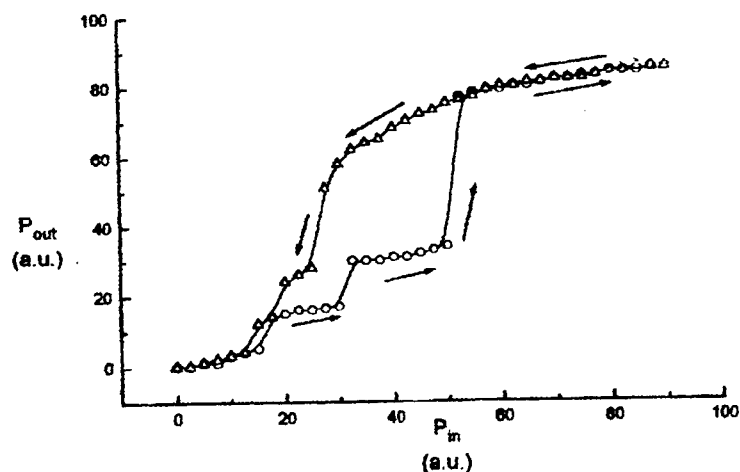


Fig. 7. Bistability curve $P_{out} = f(P_{in})$; $U_{bdc} = 0$ V; $f = 186$ Hz;

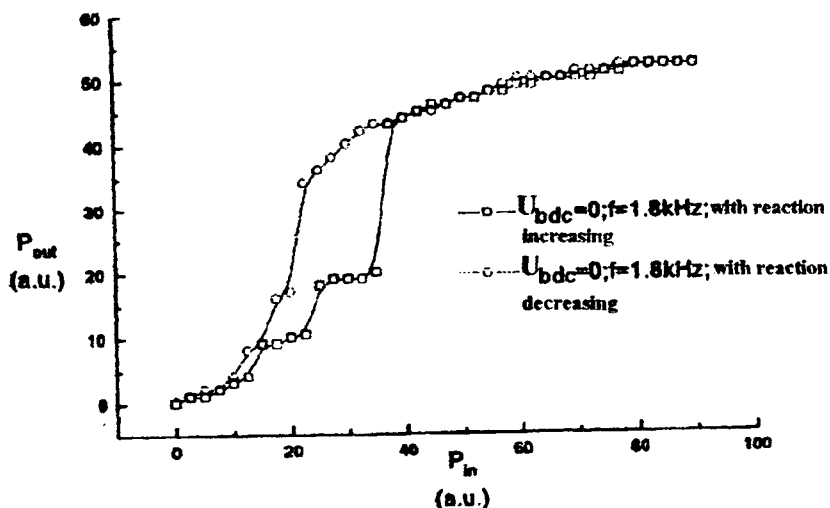


Fig. 8. Bistability curve $P_{out} = f(P_{in})$

Figs. 6, 7 and 8 show the bistable and multistable behaviour of the PDLC samples. Figs. 3 a, b and 6 show that the system can be in one of the two stable states ON-OFF, depending on its past history (hysteresis). The hysteresis area depends on the bias voltage U_{bdc} . Because of the weak dependence of U_{ph} on U_g frequency (figs. 2 and 5), the hysteresis area will not depend significantly on the frequency (figs. 3a, b and 7, 8). In PDLC films, the multistable behaviour is obtained because the transmission curve of the sample has more maxima and minima. These results suggest that PDLC films with feedback may be useful in optical protection and in optical memory applications.

4. REFERENCES

1. H. M. Gibbs, *Optical bistability: Controlling light with light*, Academic Press, New York (1985).
2. M. Okada and K. Takizawa, IEEE, "Optical regenerative oscillation and monostable pulse generation in electrooptic bistable devices", *J. Quantum Electron*, **16**, 770-776 (1980).
3. D. Manaila-Maximean, R. Bena, A. M. Albu, "Electric and electro-optic investigations on polymer dispersed liquid crystal films", *Modern Physics Letters B*, **11**, (9&10), 431-440 (1997).

I.R. absorption of TiO₂ thin films

M. Stamate , G.I. Rusu*, I. Vascan,

Bacău University, Calea Mărășești nr. 157, Bacau, Romania

*"AL.I.Cuza" University Jassy, B-dul Copou nr10, Romania

ABSTRACT

The titanium oxide films were deposited on glass by reactive sputtering system, in different oxygen partial pressure. In this paper we present the I.R. absorption of TiO_x thin films, deposited through a d.c. circular magnetron system. We found several common peaks of absorption located around 500 cm⁻¹, 530 cm⁻¹, 582 cm⁻¹, 638 cm⁻¹ and 800 cm⁻¹ that are corresponding to Ti-O_x links energy.

Keywords: d.c. magnetron sputtering , I.R. absorption, TiO₂ thin films,

1. INTRODUCTION

Titanium oxide films are extensively used in optical thin films devices applications owing to their desirable optical properties and good stability in adverse environments.

Many techniques can be used to deposit titanium oxide film. They include sol-gel process^{1,2} , chemical vapor deposition³, electron beam evaporation⁴ and sputtering⁵. The study of TiO₂ films prepared by reactive magnetron sputtering should be of interest because of high deposition rates and low substrate temperatures.

In this paper we present the I.R. absorption of TiO_x thin films, deposited through a d.c. circular magnetron system.

2. EXPERIMENTAL DETAILS

The titanium oxide films were deposited on glass by reactive sputtering system, in different oxygen partial pressure. Pure titanium (99.5%) of 130 mm diameter and 3 mm thickness has been used as a sputtering target. Pure argon (4N) and oxygen were used as the sputtering and reactive gases respectively. Base pressure system was 5x10⁻⁵ torr, total sputtering pressure (Ar+O₂) was 5x10⁻² torr, oxygen partial pressure was varied from 10⁻² torr to 10⁻³ torr. Sputtering current was kept at 200 mA and sputtering voltage was 550 V. The target substrate distance was 35 mm. The sputtering time was 60 min. The substrate temperature was held at 200 °C by using a quartz halogen lamp whose power was controlled by varying the input voltage of an external power supply. The thickness of the films was 3000 Å for films deposited at 10⁻³ torr oxygen partial pressure and 1800 Å for films deposited at 10⁻² torr oxygen partial pressure.

The X-ray diffraction was recorded with a Leybold -Didactic, X-ray apparatus, with Mo-K_α, of 42 kV and 1 mA. The I.R.- reflection spectra were recorded on a Specord I.R.-71 Carl Zeiss Jena, in a wavelength range between 4000 and 400 cm⁻¹

3. RESULTS AND DISCUSSION

X-ray diffraction results indicates that the films were amorphous.

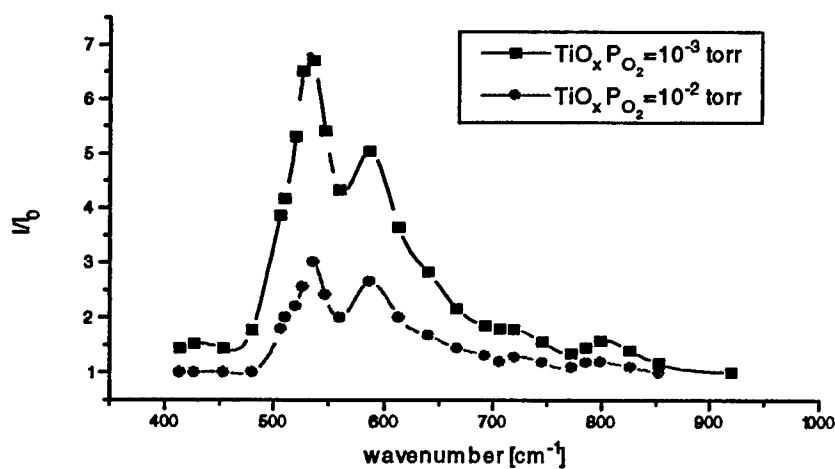


Fig.1
Ratio of reflection coefficient for substrate and TiO_x films

Figure 1. shows the I.R. absorption spectrum for TiO_2 deposited at 10^{-3} torr oxygen partial pressure and 10^{-2} torr oxygen partial pressure respectively.

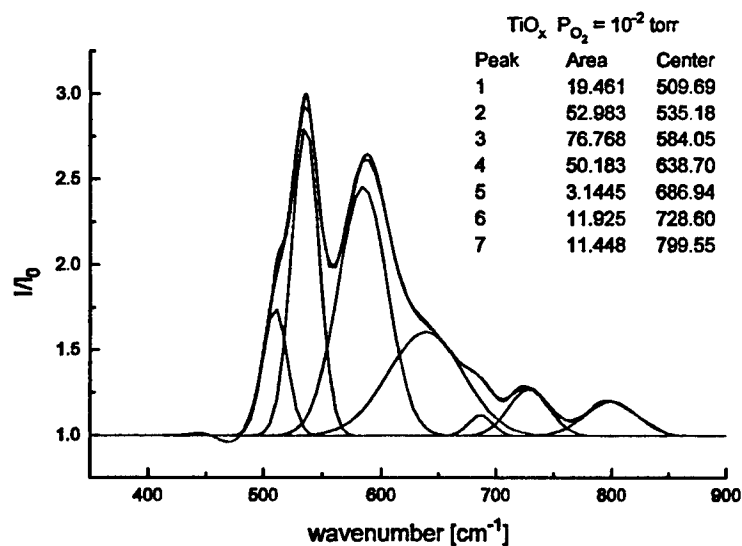


Fig.2
Multiple gaussian decomposition of IR absorption spectra for TiO_2 thin films deposited at low oxygen partial pressure

Figure 2. shows the results of the analysis and gaussian distributions decomposed spectrum of TiO_2 deposited at low oxygen partial pressure .

Figure 3. shows the results of the same analysis for TiO_2 deposited at high oxygen partial pressure.

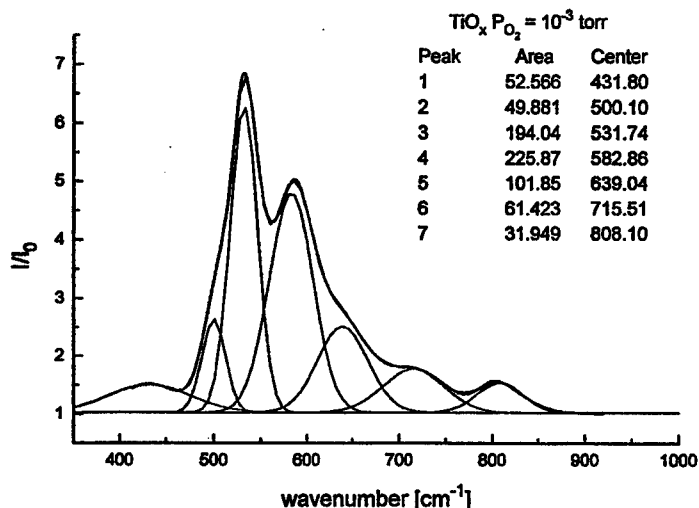


Fig.3
Multiple gaussian decomposition of IR absorption spectra for
 TiO_2 thin films deposited at high oxygen partial pressure

We found several common peaks of absorption located around 500 cm^{-1} , 530 cm^{-1} , 582 cm^{-1} , 638 cm^{-1} and 800 cm^{-1} .

The peaks are related to Ti-O bond and Ti-O_2 bond³ and are oxygen incorporation in film dependent. The refractive index calculated with an envelope technique of the measured transmission spectrum were 2,59-2,65. The optical band gap calculated were 3,1-3,3 eV. The resistivity measurement of films was find of the order of 10^9 - $10^{10} \Omega \cdot \text{cm}$.

4. CONCLUSION

From the analysis of I.R. absorption spectrum of TiO_x thin films we found several peaks of absorption located in 400 - 800 cm^{-1} range, that are related to Ti-O bond and Ti-O_2 bond. Also we found that there are thickness dependencies of the TiO_2 films reflection coefficient. The films with a large thickness has a higher I.R. reflection.

The peaks high is dependent by the oxygen incorporation in films. The I.R reflection analysis of the TiO_2 thin films may give some information about the film composition. This analysis may be used when other investigation techniques are not available.

5. REFERENCES

1. M.Gartner, C.Parlog and P.Osiceanu," Spectroellipsometric characterization of lanthanide-doped TiO₂ films obtained via the sol-gel technique", *Thin Solid Films*, **234**, 561-565 (1993)
2. K.A. Vorotilov , E.V.Drlova and V.I.Petrovsky, "Sol-gel TiO₂ films on silicon substrates", *Thin Solid Films* , **207**, 180-184 (1992)
3. Won Gyo Lee, Seang Ihe Woo, Jong Choul Kim, Soo Han Chioi, Kye Hwan Oh, " Preparation and properties of amorphous TiO₂ thin films by plasma enhanced chemical vapor deposition", *Thin Solid Films*, **237** (1994) 105
4. K.Narashima Rao, S.Mohan, M.S.Hegde, T.V.Balasubramanian, "Chemical composition of electron-beam evaporated TiO₂ films", *J.Vac.Sci.Technol.A*, **11**(2), 394-397 (1993)
5. Li-Jian Meng and M.P. dos Santos, " Investigation of titanium oxide film deposited by d.c. reactive magnetron sputtering in different sputtering pressures", *Thin Solid Films*, **226**, 22-29 (1993)

Computerized lateral-shear interferometer

Sorin A. Hasegan, Angela Jianu, Valentin I. Vlad

Institute of Lasers, Plasma and Radiation Physics, Lasers Dept., PO Box MG-36, R-76900, Bucharest, ROMANIA

ABSTRACT

A lateral-shear interferometer, coupled with a computer for laser wavefront analysis, is described. A CCD camera is used to transfer the fringe images through a frame-grabber into a PC. 3D phase maps are obtained by fringe pattern processing using a new algorithm for direct spatial reconstruction of the optical phase. The program describes phase maps by Zernike polynomials yielding an analytical description of the wavefront aberrations. A compact lateral-shear interferometer has been built using a laser diode as light source, a CCD camera and a rechargeable battery supply, which allows measurements in-situ, if necessary.

Keywords: lateral-shear interferometer, Zernike polynomials, phase demodulation.

1. INTRODUCTION

Methods and applications of shear interferometry have been summarized by Malacara¹. Recently, G. Harbers et al.² developed a modal phase-reconstruction method and studied the method error propagation using simulated images. Vlad and Malacara³ developed the direct spatial reconstruction of optical phase (DSROP) method that can be applied to many types of phase-modulated images obtained from different kinds of interferometers and holographic setups.

A lateral shearing interferometer uses a laterally shifted part of the wavefront to interfere with itself. The yielded fringe pattern gives information about the derivative of the wavefront phase profile (the fringes are the loci of constant average wavefront slope over the shear distance). The small optical path difference between the interfering beams leads to a relaxation in the coherence requirements, being possible to use a laser diode as a light source. A CCD camera is used to transfer the captured fringes images through a frame-grabber into a PC.

There are many types of shear interferometers^{1,4}, depending on the way the shear is performed: lateral shear; radial shear; rotational shear; reversal shear (as shown in Fig. 1).



Fig. 1 The principal four methods in shear interferometry

a) lateral shear (the interference pattern is produced in the striped zone); b) radial shear (the tested wavefront interferes with its contracted or expanded copy); d) rotational shear (the tested wavefront interferes with its rotated copy); e) reversal shear (the tested wavefront interferes with its symmetric copy)

Lateral shear can be obtained various ways. The simplest method (used in the present work) employs a plane-parallel plate. Other methods make use of a pair of diffraction gratings that divide and shift the tested wavefront⁵.

2. EXPERIMENTAL SETUP

Fig. 2 presents the interferometer setup. The laser diode beam is spatially filtered by passing it through a microscope objective ($\times 20$), microdiaphragm and then collimated by a good quality (with no aberrations) lens ($f = 83\text{mm}$). The collimated beam falls onto a plane-parallel plate (thickness $t = 10\text{mm}$) and the emerging wavefronts from the two sides of the plate interfere onto a screen. The shear is due to the non normal incidence.

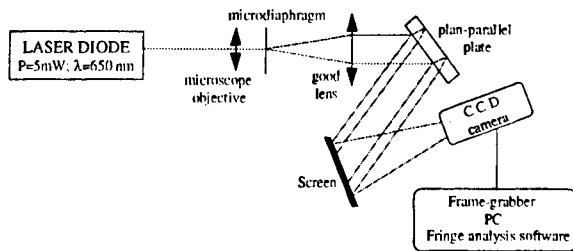


Fig. 2 The computerized lateral-shear interferometer

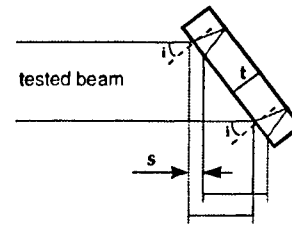


Fig. 3. Determination of the shear value

Lateral-shear value s is a function of the plane-parallel plate thickness t and the incidence angle i of laser beam wavefront onto the plate face. The plane-parallel plate geometry, shown in Fig. 3, gives the expression of lateral-shear as:

$$s = \frac{t \cdot \sin 2i}{\sqrt{n^2 - \sin^2 i}} \quad (1)$$

where n is the refraction index of the plane-parallel plate material.

This simple setup allows the obtaining of pure primary aberrations⁶.

The material refractive index n , for a given lateral-shear value s , when $I=45^\circ$, is given by:

$$n = \frac{\sin^2 i}{\sqrt{-\cos 2i}} \quad (2)$$

Eq. 2 shows that I must be greater than 45° in order to have a real value for refractive index.

The captured images (256×256 pixels) are stored in a digital format in PC and analyzed with a fringe analysis program. 3D phase maps are directly obtained using the DSROP algorithm developed by Vlad and Malacara³ and implemented in IDL® (Interactive Data Language). The fringe analysis program describes the phase maps encoded in the interferograms by Zernike polynomials. An analytical description of the wavefront aberrations is thus obtained. Zernike coefficients⁷ describe quantitatively wavefront aberrations caused by the non-collimated wavefront or the optical components imperfections.

To demonstrate lateral-shear method facilities a compact ($500 \times 150 \times 150$ mm) interferometer has been built. A rechargeable battery supply allows in situ measurements, if necessary. The battery autonomy is 20 hours before recharge.

3. DIRECT SPATIAL PHASE DEMODULATION OF OPTICAL INTERFEROGRAMS

DSROP in the space and Fourier domain has been implemented for interferogram analysis. DSROP uses single pattern analysis being faster than phase shifting methods.

A phase-modulated image can be defined as a two-dimensional function of the form:

$$I(x, y) = A(x, y) + B(x, y) \cos \Delta\phi(x, y) = A(x, y) + B(x, y) \cos [2\pi u_0 x + \Phi_m(x, y)] \quad (3)$$

where $A(x, y)$ is a positive, slowly-varying background, $B(x, y)$ is the positive, slowly-varying contrast, $\Delta\phi(x, y)$ is the phase spatial distribution, u_0 is the spatial carrier frequency and $\Phi_m(x, y)$ - the phase modulation.

(i) In the space domain, following the holographic analogy, one can accomplish the phase demodulation by the multiplication of the fringe pattern (4) with the reference:

$$R(x, y) = \exp(2i\pi u_0 x) \quad (4)$$

which is obtained from a weak phase modulation zone of the recorded fringe pattern.

The product $I(x, y) \cdot R(x, y)$ consists of two rapidly-varying functions (of frequencies u_0 and $2u_0$) and a slowly-varying term. By smoothing this pattern over a space interval with the dimension $\Delta_0 = 1/u_0$, it is possible to obtain only the slowly-varying term, $Y(x, y)$. The carrier frequency should be taken as high as the numerical resolution in the image allows, in order for $A(x, y)$, $B(x, y)$ and $\Phi_m(x, y)$ to be considered constant over one period.

It was demonstrated³ that the spatial phase distribution can be obtained as:

$$\Phi_m(x, y) = -\tan^{-1}\{\text{Im}[Y(x, y)]/\text{Re}[Y(x, y)]\}. \quad (5)$$

(ii) Phase demodulation in the Fourier domain relies on the description of the wavfront recording and reconstruction in holography. Thus, eq. (1) can be written as:

$$\begin{aligned} I(x, y) &= A(x, y) + [B(x, y)/2] \exp[i(2\pi u_0 x + \Phi_m(x, y))] + [B(x, y)/2] \exp[-i(2\pi u_0 x + \Phi_m(x, y))] = \\ &= A(x, y) + C(x, y) \exp[i(2\pi u_0 x)] + C^*(x, y) \exp[-i(2\pi u_0 x)] \end{aligned} \quad (6)$$

where:

$$C(x, y) = [B(x, y)/2] \exp[i\Phi_m(x, y)] \quad (7)$$

Taking the Fourier transform of eq. (7) and denoting the spectra with the same letters,:

$$\mathcal{J}(u, v) = \mathcal{J}(u, v) + \mathcal{C}(u - u_0, v) + \mathcal{C}^*(u + u_0, v) \quad (8)$$

After the band-pass filtering of the term $\mathcal{C}(u, v)$ and the computation of the inverse Fourier transform, the phase modulation can be obtained directly as:

$$\Phi_m(x, y) = -\tan^{-1}\{\text{Im}[C(x, y)]/\text{Re}[C(x, y)]\} \quad (9)$$

An expansion of a wavefront W in Zernike polynomials to order k has the general form⁸:

$$W(r, \theta) = \sum_{n=0}^k \sum_{m=0}^n A_{nm} R_n^{n-2m} \begin{cases} \sin \\ \cos \end{cases} (n-2m)\theta \quad (10)$$

where the sin function is used for $n-2m > 0$ and the cos function for $n-2m \leq 0$. (r, θ) are polar coordinates in the unit circle, and R_n^{n-2m} are the radial polynomials defined by:

$$R_n^{n-2m} = \sum_{s=0}^m (-1)^s \frac{(n-s)!}{s!(m-s)!(n-m-s)!} r^{n-2s} \quad (11)$$

A_{nm} are the coefficients of the Zernike polynomials.

The following table shows some of the polynomials that were used to fit the phase maps and their corresponding meaning in terms of optical aberrations.

Table 1: The meaning of the most important Zernike polynomials

n	m	Zernike polynomials	Meaning
0	0	1	Piston or constant term
1	0	x	Tilt about y axis
1	1	y	Tilt about x axis
2	0	2xy	Astigmatism with axis at $\pm 45^\circ$
2	1	$-1 + 2y^2 + 2x^2$	Focus shift
2	2	$y^2 - x^2$	Astigmatism with axis at 0° or 90°
3	0	$3xy^2 - x^3$	Triangular astigmatism with base on x axis
3	1	$-2x + 3xy^2 + 3x^3$	Third order coma along x axis
3	2	$-2y + 3y^3 + 3x^2y$	Third order coma along y axis
3	3	$y^3 - 3x^2y$	Triangular astigmatism with base on y axis
4	2	$1 - 6y^2 - 6x^2 + 6y^4 + 12x^2y^2 + 6x^4$	Third-order spherical aberration

4. EXPERIMENTAL RESULTS

Fig. 4 shows 3D phase map representations corresponding to the shear interferogram (a), obtained by DSROP in space domain (b) and in spatial frequency (Fourier) domain (c).

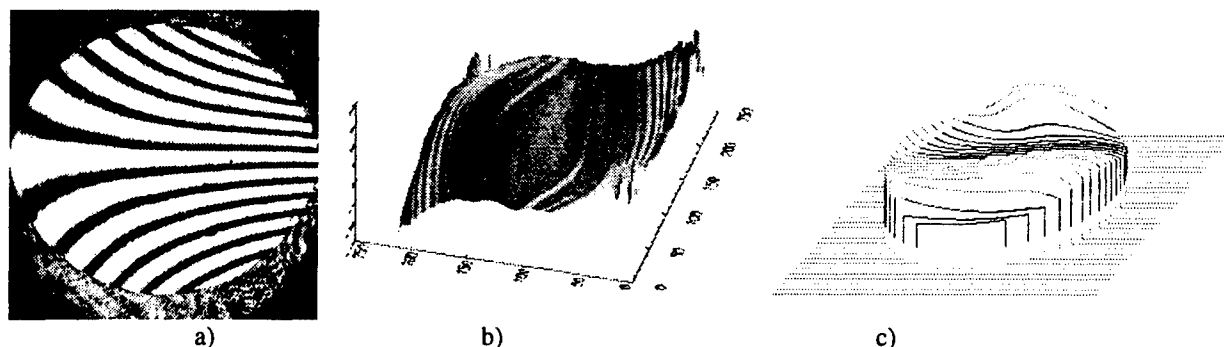


Fig. 4 (a) Fringe pattern obtained using a lateral-shear interferometer; (b), (c) 3D phase distribution, corresponding to the fringe pattern (a), obtained by DSROP in spatial domain and spatial frequency (Fourier) domain, respectively

Fig. 5. presents Zernike and Seidel coefficients for the phase map represented in Fig. 5 b, c.

ZERNIKE COEFFICIENTS				
	THIRD ORDER	FIFTH ORDER	SEVENTH ORDER	
SPHERICAL AB.	U8 = 0.00	U15 = -0.00	U24 = -0.00	
COMA	U7 = 0.15	U14 = -0.05	U23 = -0.05	
	U6 = -0.05	U13 = -0.01	U22 = 0.00	
ASTIGMATISM	U5 = -0.02	U12 = -0.01	U21 = -0.00	
	U4 = 0.02	U11 = -0.01	U20 = 0.00	
		U10 = -0.17	U19 = 0.04	
		U9 = 0.02	U18 = -0.00	
			U17 = -0.02	
			U16 = 0.03	
SEIDEL COEFFICIENTS				
SPHERICAL AB.	VALUE = 0.01			
COMA	VALUE = 0.49	ORIENTATION 199.5°		
ASTIGMATISM	VALUE = 0.05	ORIENTATION -44.6°		

Fig. 5. Zernike and Seidel coefficients for the phase map in Fig 5

5. ADVANTAGES AND APPLICATIONS

The advantages of lateral-shear interferometry over the conventional interferometry are the excellent experimental conditions: very few optical components; no isolation from external perturbations needed; different directions and values for lateral shear; independent wavefront tilts; no perfect reference wavefront needed; high rate of object inspection (scanning); video presentation of the entire inspection field; inspection of a large range at one moment; non-contact and non-contamination of inspected object; digital measurement of observation area; no high coherence needed; possibility of varying the interferometer sensitivity; possibility of varying the fringe frequency (by shear variation).

Lateral-shear interferometry suffers from the same limitation as conventional interferometry: the contrast of the interferograms decreases rapidly with the quality of object surface the tested wavefront comes from.

Lateral-shear interferometer has many applications: optical materials homogenities determination; glass and liquids refraction index measurement; laser wavefront collimation tests; optical distortion determination in transparent materials and glass windows; thermal flow (in plastic to metallic materials) non-destructive control and control of stresses arisen in fabrication (e.g. materials used in cars and airplanes construction industry).

6. REFERENCES

1. D. Malacara, Ed., "Radial, rotational and reversal shear interferometers" in "*Optical shop testing*" 2nd Edition, John Wiley&Sons, N.Y., 1992
2. G. Harbers, P.J. Kunst, G.W.R. Leibbrandt, "Analysis of lateral shearing interferograms by use of Zernike polynomials" *Appl. Opt.*, Vol. 35 (31), p. 6162-6172, 1996
3. V.I. Vlad, D. Malacara, "Direct spatial reconstruction of optical phase from phase-modulated images" in "*Progress in optics XXXIII*", Ed. E. Wolf, Elsevier Science B.V, Amsterdam, 1994
4. P. Hariharan, "Lateral and radial shearing interferometers: a comparison", *Appl. Opt.*, 27, 3594, 1988
5. J. Lewandowski, "Lateral shear interferometer for infrared and visible light", *Appl. Opt.*, 28, 2373, 1989
6. M. V. R. K. Murty, "The use of a single plane parallel plate as a lateral shearing interferometer with a visible gas laser source", *Appl. Opt.*, 3, 531, 1964
7. M. Born and E. Wolf, *Principles of optics*, 767-772, Pergamon, Oxford
8. D. Malacara, S. De Vore, "Interferogram evaluation and wavefront fitting" in "*Optical shop testing*", 2nd. Ed. Chapter No. 13, p. 455-499, ed. Daniel Malacara, John Wiley & Sons, Inc., 1992

AMORPHOUS Se/CdSe and SiO_x/CdSe MULTILAYERS

M. Popescu, F. Sava, A. Lörinczi, E. Vateva¹, D. Nesheva¹, G. Tchaushev¹, I. N. Mihailescu², P.-J. Koch³, S. Obst³,
H. Bradaczek³

National Institute of Materials Physics, P.O.Box Mg 7, 76900 Bucharest-Magurele, Romania.

¹G. Nadjakov Institute of Solid State Physics, 72 Tsarigradsko Chausse blv., 1784 Sofia, Bulgaria.

²Institute of Atomic Physics, Laser Department, P.O.Box Mg 6, 76900 Bucharest-Magurele, Romania.

³Institut für Kristallographie, Freie Universität - Berlin, Takustraße 6, 14195 Berlin, Germany.

ABSTRACT

Amorphous multilayers based on Se and CdSe alternated sublayers were successfully prepared by thermal vacuum evaporation and laser ablation with the periodicity of 22 nm.

The multilayer structure is stable up to ~70 °C. In the samples prepared by laser ablation a large contraction of the multilayer stacking occurs by annealing.

Amorphous SiO_x/CdSe multilayers with the periodicity of ~15 nm were successfully prepared by thermal vacuum evaporation. The structure is stable up to 400 °C annealing temperature. Pulse excimer laser irradiation of the SiO_x based multilayer produces an expansion of the interlayer distance with ~ 0.33%.

Keywords: multilayers, X-ray diffraction, CdSe, amorphous

1. INTRODUCTION

Amorphous quantum well structures or multilayers (ML) based on chalcogenide materials are important for the fabrication of electrophotographic and laser printer photoreceptors^{1,2}.

The main advantage of the amorphous ML is that the problems of lattice matching of different materials (typical for crystalline superstructures) do not exist for the amorphous semiconductor structures. That is why a great choice of material combinations is possible and new properties are expected. The stepwise behaviour observed in the transmission spectra of Se-Te / CdSe³ and Se/Se-Te⁴ ML with the periodicity of d~4.5-10 nm speaks in favour of quantum size effects.

The thermal stability, the boundary roughness and the intermixing of the sublayers in the ML structure are important parameters related to their electronic properties. On the other hand, the effect of high energy radiation (UV) is important in the control and fine tuning of the electro-physical properties of ML.

In this paper we report the thermal stability of the chalcogenide multilayers based on Se and the effect of UV laser radiation on the multilayers based on SiO_x.

2. EXPERIMENTAL

The multilayer structures were prepared by thermal and laser evaporation.

The Se/CdSe multilayers were prepared by thermal evaporation of Se and CdSe layers from two sources of preliminary synthesized glassy Se and powdered polycrystalline CdSe (suprapure, Merck). The sources were switched on only for the deposition of the corresponding layer⁵. Fourteen alternated Se/CdSe layers of ~22 nm periodicity were deposited. The deposition rate in a step-by-step vacuum evaporation procedure was 0.5 nm/s.

New Se/CdSe multilayers were prepared by the laser ablation procedure in the usual configuration.

The deposition of the layers has been performed in a vacuum chamber with a pulsed Nd laser (pulse energy was < 30 J and duration was ~2 ms) from two alternatively changed targets made of glassy or crystalline powder. Corning glass 7059 substrates held at room temperature have been used. The time interval between two laser pulses was ~ 15 s.

SiO_x/CdSe multilayers were prepared by thermal vacuum evaporation of SiO_x and CdSe from two independent Ta sources on Corning 7059 glass substrates kept at room temperature. Immediately after taking out the samples from the vacuum chamber, they were annealed in air for 1h at 400 °C. Samples with 21 SiO_x sublayers alternated by 20 CdSe sublayers were obtained.

X-ray diffraction measurements were carried out in the diffractometric method with Cu K_α radiation (Philips PW 1080 diffractometer) and Ni K_α radiation (TUR M62 diffractometer).

3. RESULTS

The X-ray diffraction structural results obtained on thermal vacuum evaporated (TE) and laser ablated (LA) Se/CdSe multilayers, show before annealing the formation of well-separated sublayers, expressed by narrow peaks accompanied by well-resolved satellites. The quality of the virgin samples is poorer in LA multilayers as proved by the lower intensity of the peaks. Figure 1a and 1b show the X-ray diffraction patterns of the as-prepared TE and LA samples.

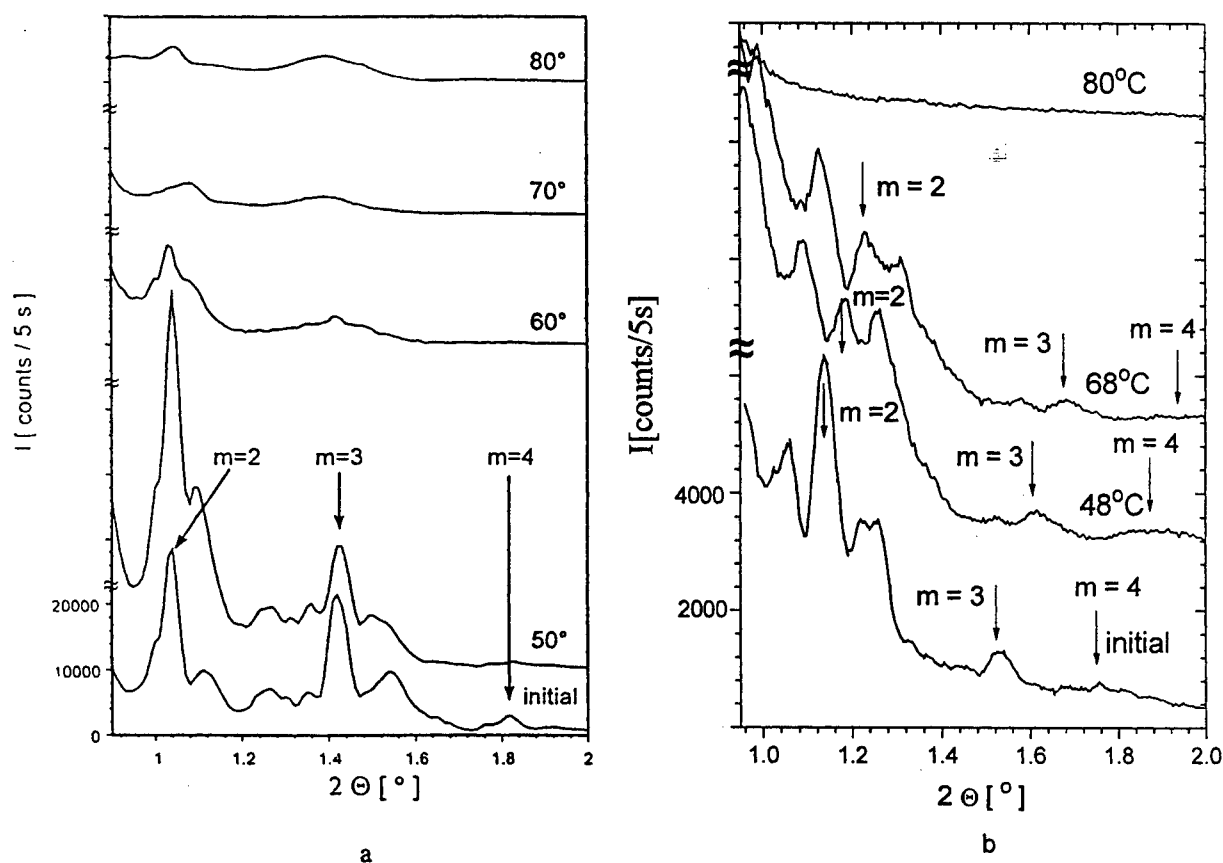


Figure 1. The X-ray diffraction patterns (Cu K_{α} radiation) of the TE (a) and LA (b) Se/CdSe multilayers (14 pairs)

The ML samples were annealed step by step at various temperatures up to 100 °C for times higher than 12 h for every step of annealing, and the change of structure was followed by X-ray diffraction.

Figure 1 shows the evolution of the diffraction pattern for both types of samples.

It is remarkable that the thermal stability of the chalcogenide ML is approximately the same for both types of ML and is ~ 70 °C. The periodicity in TE samples was calculated to be 22.4 nm. A periodicity of 15.5 nm was calculated in LA samples from the positions of the main diffraction peaks. From direct measurements with a Talystep instruments, there was obtained a stacking periodicity of ~ 14 nm.

The particular feature of the LA multilayers is the large contraction effect that occurs by thermal annealing. The decrease of periodicity with 0.6 nm for annealing at 48 °C and by still 0.6 nm for further annealing at ~ 68 °C was calculated from the X-ray diffraction patterns.

The SiO_x/CdSe multilayer samples were prepared and their structure has been studied. Figure 2 shows the X-ray diffraction of the ML sample. The ML exhibits a stacking periodicity of 10.5 nm. One of the samples was exposed to KrF⁺ excimer laser pulse radiation ($\lambda=248$ nm) in the following sequence: 10 pulses of power density 38 mJ/cm², 20 pulses of power density 36 mJ/cm², 20 pulses of power density 36 mJ/cm², 30 pulses of power density 24 mJ/cm² and 1000 pulses of power density 6 mJ/cm².

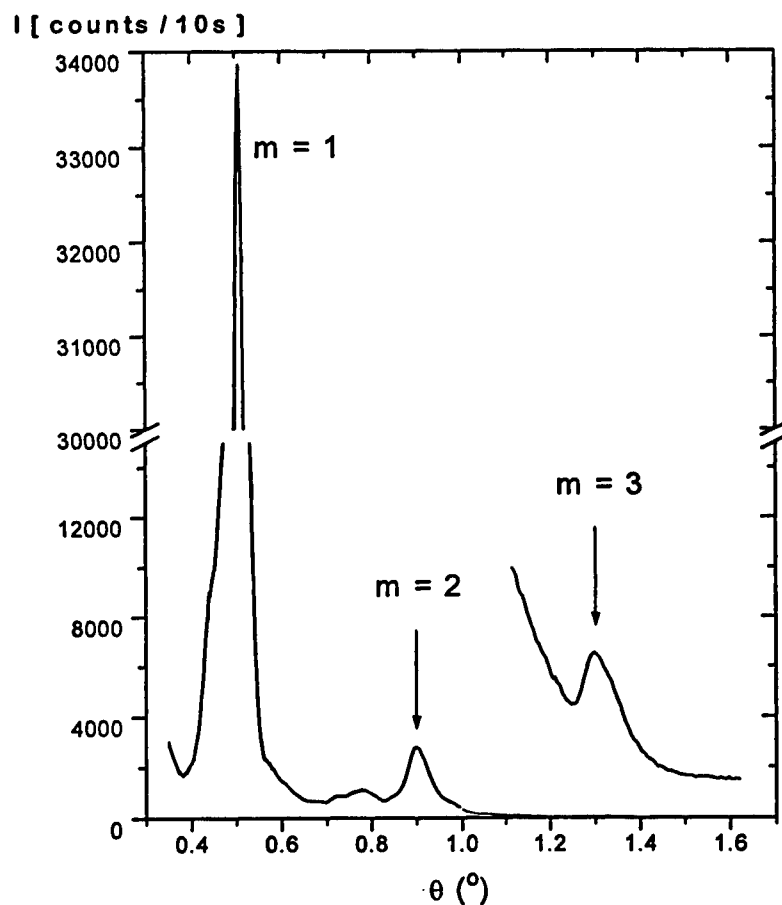


Figure 2. The X-ray diffraction pattern (NiK α radiation) of the SiO_x/CdSe multilayer sample (21/20 layers)

The X-ray diffraction pattern was recorded after each step of laser irradiation. The change of the peak position and intensity was carefully investigated by measuring accurately the position of the first and second order multilayer diffraction peaks.

A small change of interlayer distance was revealed from the X-ray diffraction data. Figure 3 shows the variation of the ML periodicity because of UV laser pulse irradiation. A maximum increase of inter-layer distance of ~0.33% was revealed.

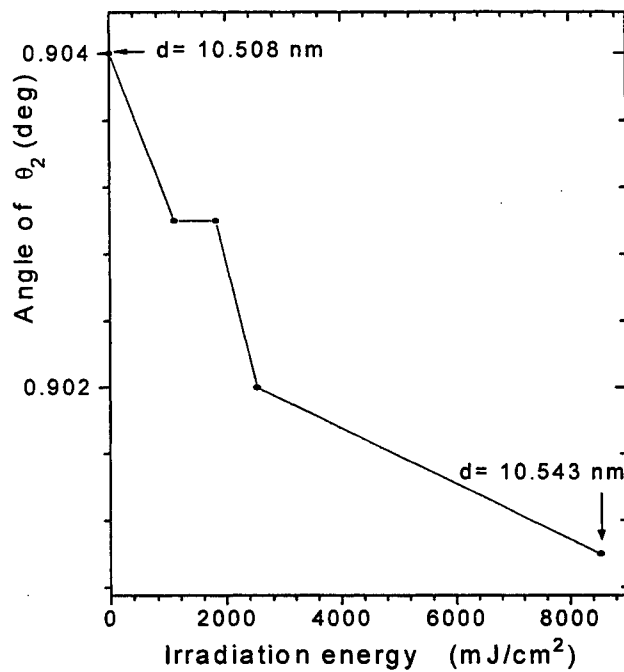
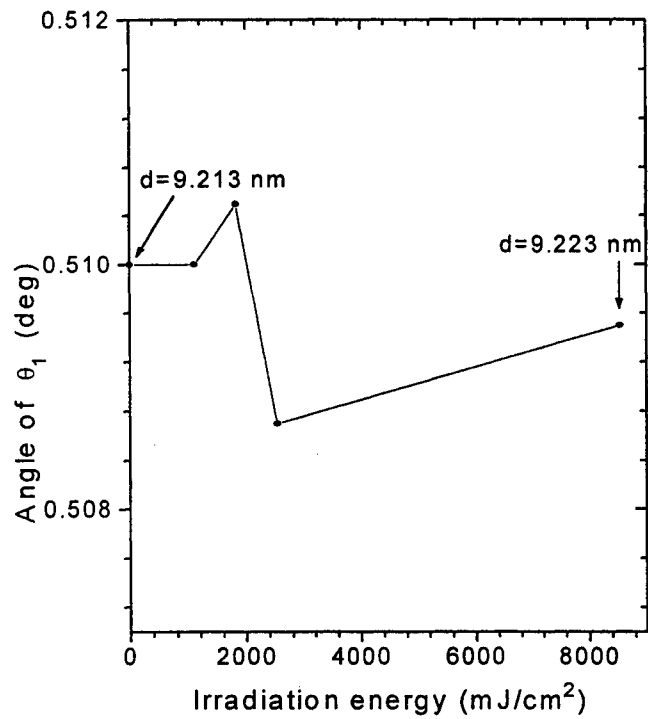


Figure 3 The evolution of the inter-layer distance because of laser pulse irradiation of ML SiO_x/CdSe samples:
a.-calculated from the first order diffraction peak
b.-calculated from the second order diffraction peak

4. DISCUSSION

The structural data obtained on ML samples of different compositions prove that ML structures based on chalcogenide materials are influenced by thermal annealing at not too large temperatures.

A stability limit of $\sim 70^\circ\text{C}$ has been established both for TE and LA multilayers. The TE multilayers do not exhibit significant modification of the interlayer distance by annealing⁶.

A particularly large contractions effect in LA Se/CdSe multilayers takes place by annealing and this effect may be due to the low density of the structure. This low density may be due to the significant amount of droplets embedded into the layers during LA deposition, which are accompanied by pores into the material. The droplets are known to be formed usually in the laser ablated films and their concentration is in relation with the distance target-substrate. Therefore, it is our suggestion that the low density structure can be avoided by changing the laser pulse parameters and the target-substrate distance.

The SiO_x/CdSe ML are influenced by UV radiation emitted by a KrF^* laser. A small expansion effect was detected. The magnitude of the effect is directly correlated with the total irradiation energy.

One important observation is the unequal variation of the X-ray diffraction peaks in different diffraction orders. This effect may be due to the phase slippage at the inter-layer boundaries. The effect leads to the smearing out and shift of the Bragg peaks as shown theoretically by Apostol⁷.

5. CONCLUSIONS

Amorphous multilayers based on selenium and on SiO_x sublayers alternated by CdSe sublayers have been successfully prepared. X-ray diffraction data show important features of the ML when annealed or laser irradiated.

The Se/CdSe ML are stable only up to $\sim 70^\circ\text{C}$ while SiO_x/CdSe ML are stable at least up to 400°C . Both types of MLs maintain their amorphous structure after annealing.

The large contraction of the quantum well structure obtained by LA is undoubtedly related to the low density of the material deposited by laser pulses. The compactness is obtained rather easily by low temperature annealing.

The SiO_x/CdSe multilayers are more stable than the Se/CdSe ones. The UV radiation determines a significant expansion of the periodicity distance.

Both effects are important for the control of the ML quantum well properties in optoelectronic devices.

ACKNOWLEDGEMENT

This work was partially supported by the Bulgarian Ministry of Science and Education under the Contract No. 505.

REFERENCES

1. R. Ionov, D. Nesheva, D. Arsova, "Electrical and electrophotographic properties of CdSe/SeTe and CdSe/Se multilayers", *J. Non-Cryst. Solids* **137&138**, 1151-1154 (1991).
2. D. Nesheva, D. Arsova, E. Vateva, "Xerographic multilayer photoreceptor based on Se", *Semic. Sci. & Technol.* **12**, 597 (1997).
3. R. Ionov, D. Nesheva, "Stepwise optical absorption in amorphous Se-Te/CdSe superlattices", *Superlattices and Microstructures* **11**, 439 (1992).
4. E. Vateva, I. Georgieva, "Optical properties of Se/Se₈₅Te₁₅ multilayers", *Proc. Intern. School "Electronic and Optoelectronic Materials for the 21st Century"*, eds. A. Vavrek and N. Kirov, World. Sci. Singapore, Varna, Bulgaria, 1992.
5. R. Ionov, D. Nesheva, "Preparation and characterization of amorphous SeTe/CdSe superlattices and their constituent thin layers", *Thin Solid Films* **213**, 230-234 (1992).
6. M. Popescu, F. Sava, A. Lőrinczi, E. Vateva, D. Nesheva, P.-J. Koch, T. Gutberlet, W. Uerbach and H. Bradaczeck, "Thermal stability of amorphous Se/CdSe multilayers", *Solid State Communications* **103**(7), 431-434 (1997).
7. M. Apostol, "X-ray scattering by a superlattice", *Superlattices and Microstructures* **17**(4), 419-420 (1995).

Aluminophosphate glass with $\text{CdS}_x\text{Se}_{1-x}$ microcrystallite for optoelectronics

Rodica Rogojan, Mihai Elisa, Paul Sterian*

MATPUR S.A. Sos.Garii Catelu nr.5, 73611 Bucharest, ROMANIA,

E-mail: rodica@prima.matpur.ro

*University "Politehnica" Bucharest, ROMANIA

ABSTRACT

Until now, all studies were done over the semiconductor glasses doped with $\text{CdS}_x\text{Se}_{1-x}$, in which the microcrystallite phase was grown into a vitreous silica matrix. Our study was made as for growing microcrystallites of $\text{CdS}_x\text{Se}_{1-x}$ into a vitreous aluminophosphate matrix. In the first step, the samples of semiconductor glass were obtained by melting the raw materials batch and then by adding sulphur selenium and cadmium into the molten glass. In the second step, the resulted glass was annealed in order to bring about the microcrystallite nucleation and growing process. Both linear and non-linear optical properties are deeply influenced by the microcrystallite size, which, on its turn is determined by the duration and temperature of the annealing treatment. By means of a spectrophotometer (SPECORD M-42), were drawn absorption, transmission and fluorescence spectra, in visible domain. From the shape and the absorption edge of these spectra, we are able to characterize the microcrystallite growing process. From these spectra it can be observed a shift of the absorption edge to red which depends on the microcrystallite size.

KEYWORDS: optical nonlinear materials, aluminophosphate glass, semiconductor-doped glasses, optical nonlinear semiconductor materials.

1. INTRODUCTION

Semiconductor doped glasses have recently attracted a large interest owing to their relevant non-linear optical properties. This paper presents the obtaining process of semiconductor doped glasses, which manifest non-linear optical properties, glasses applied to the fabrication of integrated optical structures, optical circuits with fast switching time (below 10^{-14} s) and planar channel wave guides¹. Besides semiconductors, crystals and organic materials, an increased attention is paid to $\text{CdS}_x\text{Se}_{1-x}$ semiconductor glasses². Up to the present, all the studies have been applied on semiconductor glasses, in which microcrystalline phase was grown in a silicate vitreous matrix. In the present paper we present our studies directed on the growth of $\text{CdS}_x\text{Se}_{1-x}$ microcrystallites into the aluminophosphatic vitreous matrix.

2. EXPERIMENTS

Consequently, the vitreous matrix composition was modified by adding of small amounts of Na_2CO_3 (NaOH), SiO_2 and ZnO, which can retain S, Se and Cd at high temperatures. Then, at low temperature, these elements are liberated in order to grow microcrystalline phase.

Two semiconductor glass compositions were experimented:

- SD1.1. which belongs to the system : $\text{Li}_2\text{O} - \text{P}_2\text{O}_5 - \text{Al}_2\text{O}_3 - \text{BaO} - \text{SiO}_2 - \text{La}_2\text{O}_3$, in which 1% (weight percent) $\text{CdS}_{0.5}\text{Se}_{0.5}$ and 1% (w. p.) ZnO are added;
- SD2.1. which belong to the system: $\text{Li}_2\text{O} - \text{Na}_2\text{O} - \text{P}_2\text{O}_5 - \text{Al}_2\text{O}_3 - \text{BaO} - \text{SiO}_2 - \text{La}_2\text{O}_3$, in which 1% (w. p.) $\text{CdS}_{0.5}\text{Se}_{0.5}$ and 1% (w. p.) ZnO are added.

It can be observed that the second composition contains some percentages of Na_2O , so that we emphasize the doped - semiconductor glass composition influence on the semiconductor and optical properties.

A brief description of the technological process will be presented below. The weighing of raw materials according to the glass molecular formula, damp homogenisation while chemical reactions of lithium, sodium, barium and aluminium phosphate obtaining take place, processes which occur simultaneously at about 200°C .

Then, the drying process and the preliminary heat treatment occur among $100 - 800^\circ\text{C}$, in order to obtain homogeneous phosphates. Melting process takes place at about 1200°C followed by the cleaning up of the molten glass during several hours, process that has the goal of obtaining a homogeneous glass lacked of defects (gases and fibrous inclusions, etc.).

After all these treatments, stoichiometric amounts of Cd, S and Se are added (for $x=0.5$) paying attention to introduce a supplementary amount of each element, in order to counteract the loss by volatilisation. After the casting process the colourless and transparent glass samples are treated at 425°C , 450°C and 475°C for 2h, 4h, 6h, heat treatments which bring about colouring of SD1.1. and SD2.1. glass samples.

The formation and estimation of the microcrystallite stoichiometry is further complicated by the presence of zinc³. There is some concern that zinc, which is present in all these glasses, may substitute to a small degree for cadmium, decreasing the average lattice constant. Because of this it would usually be better to deal with a four component system $\text{Zn}_y\text{Cd}_{1-y}\text{S}_x\text{Se}_{1-x}$ instead of the three-component system $\text{CdS}_x\text{Se}_{1-x}$. Some research on these questions has been carried out by Borelli et al. and by Potter et al.^{4,5}.

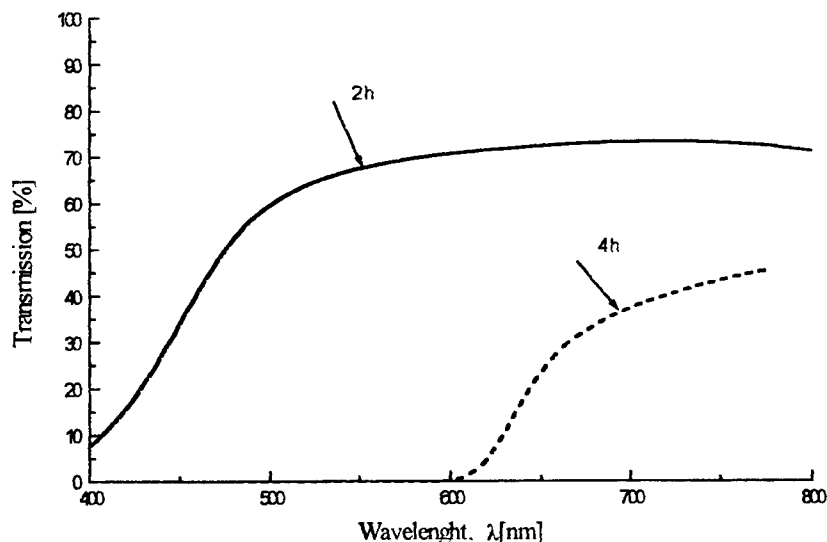


Fig. 1. The shift of absorption edge for SD1.1. sample (425°C treatment)

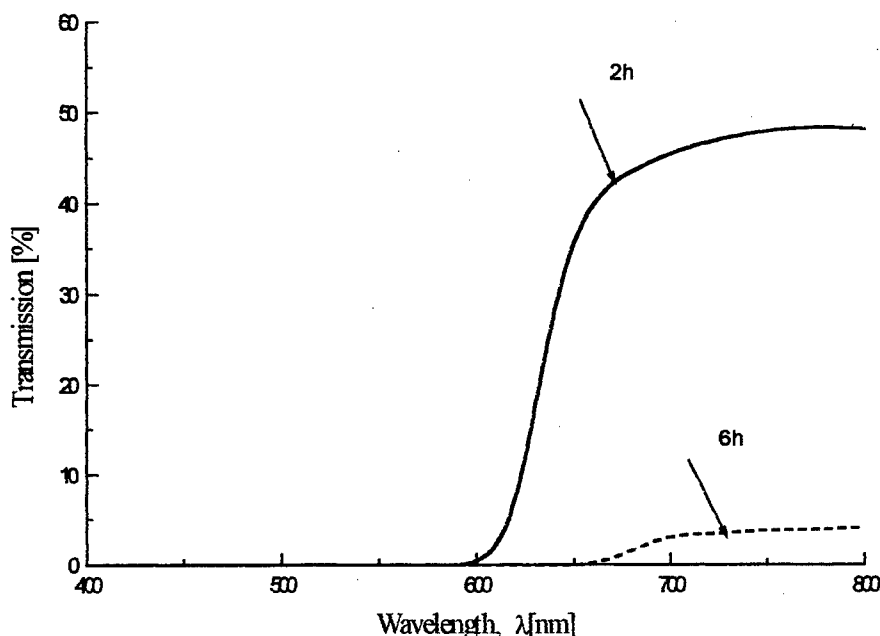


Fig. 2. The shift of absorption edge for SD1.1. sample (450°C treatment)

3. TRANSMISSION SPECTRA

For SD1.1. glass samples it is interesting to observe a large shift of the absorption edge from 400 nm to 600 nm, when the temperature and the time of the heat treatment increase from 425°C to 450°C and respectively from 2h to 4h. This phenomenon can be explained by the lack of Na_2O and by the growth of $\text{CdS}_{0.5}\text{Se}_{0.5}$ micro crystallites. Over 450°C and over 4h (time of heat treatment) the shift of absorption edge is very short (10 - 40 nm), both for SD1.1. and SD2.1. samples (show Fig. 1, 2, 3).

SD2.1. glass samples present a short shift of absorption edge (10-40 nm) to red, for all temperatures and all times of heat treatment, so that in this case, even at 425°C, the absorption edge is placed at about 600 nm. This fact can be explained by the growing process of the semiconductor particles, which takes place even before the heat treatment, namely after Cd, Se, S addition and the clearing up of the molten glass (show Fig. 4, 5, 6).

It can be observed that for a given temperature and a time of heat treatment, a short shift to red of the absorption edge appears, by changing the glass compositions. This shift is determined by the semiconductor particles growing process and we are demonstrating that we can modify the semiconductor microcrystallites growing mechanism by modifying the glass composition and the technological parameters⁶.

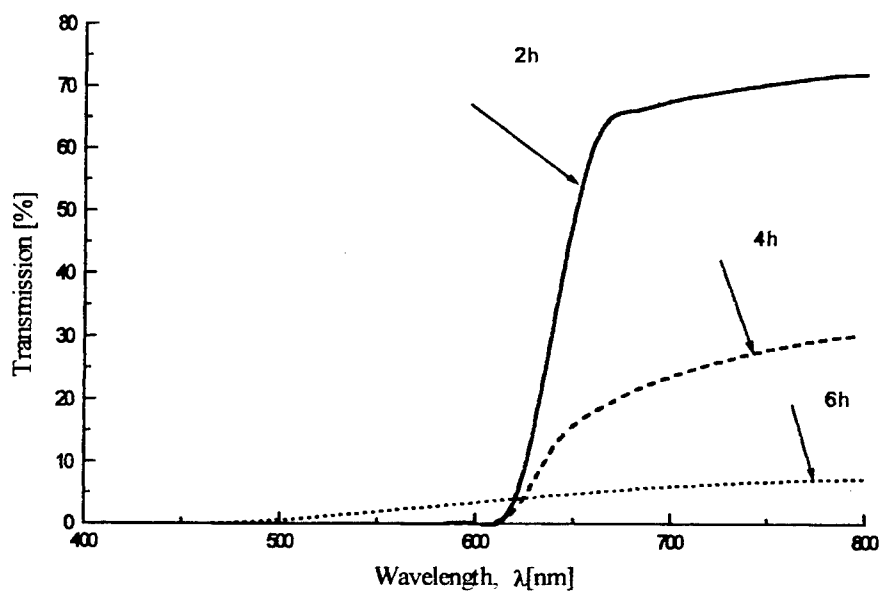


Fig. 3. The shift of absorption edge for SD1.1. sample (475°C treatment)

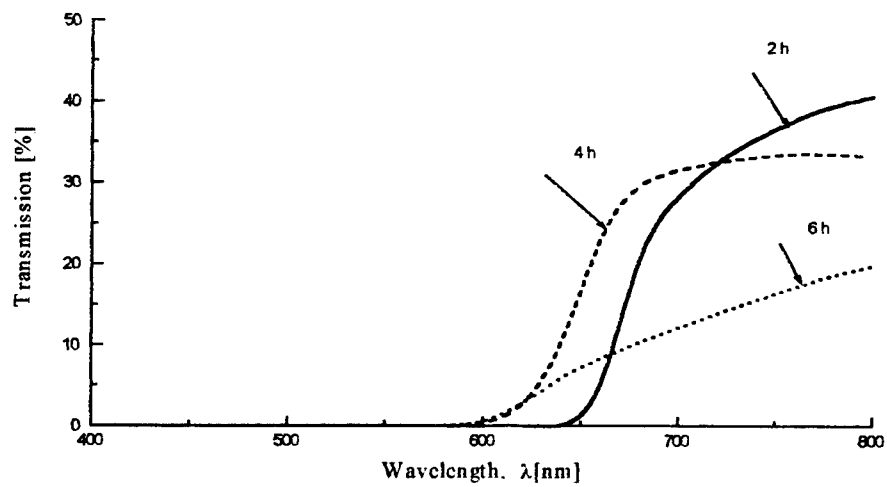


Fig. 4. The shift of absorption edge for SD2.1. sample (425°C treatment)

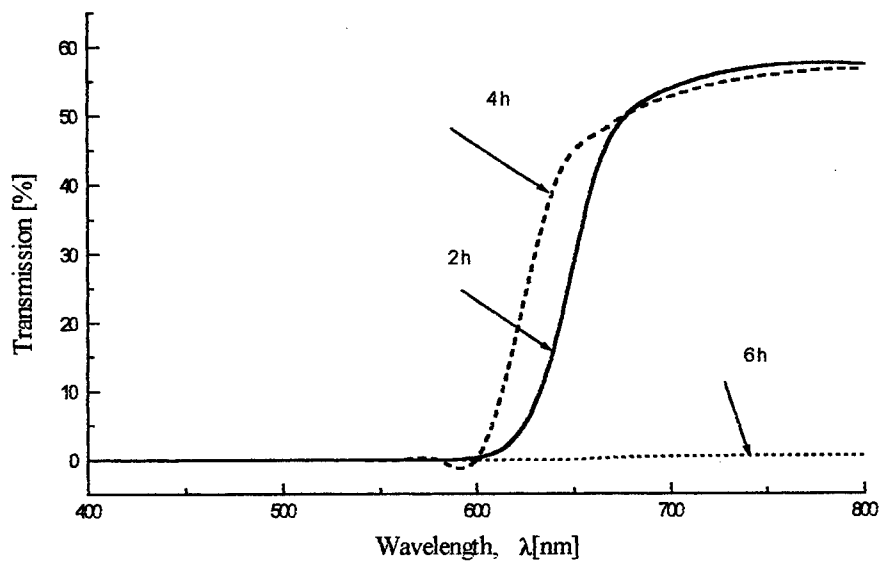


Fig.5. The shift of absorption edge for SD2.1. sample (450°C treatment)

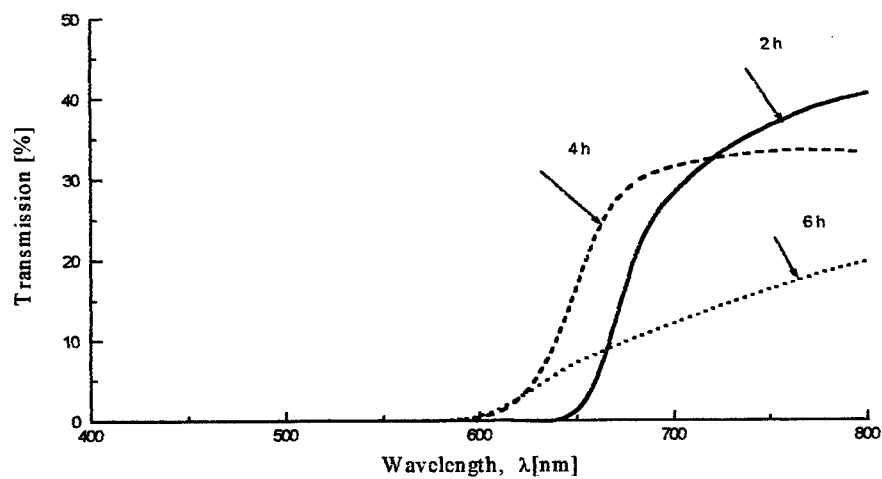


Fig.6. The shift of absorption edge for SD2.1. sample (475°C treatment)

4.CONCLUTIONS

It would be of a great interest to establish a correlation between "x" values (micro crystallites' composition) and several parameters as: vitreous matrix nature, temperature and time of heat treatment, etc.). We consider that it is very important to carry out some X-ray scattering experiments in order to determinate the quantitative and qualitative glass compositions. In the same time we are prevented to achieve high resolution microscopy measurements for estimating semiconductor micro crystallites' sizes.

In the next future, it will be necessary to make some experiments in order to emphasise the non-linear optical properties of these glasses and to estimate semiconductor micro crystallites' electron microscopy, small angle X- ray scattering, small angle neutron scattering, low frequency inelastic scattering of light, etc. We therefore think that aluminophosphate doped-glasses offers good possibilities as a non-linear material.

5. REFERENCES

1. G.C. Righini, G.P. Banfi, V. Degiorgio, F. Nicoletti, S. Pelli, "Semiconductor doped glasses: structural and waveguide characterization", *Materials-Science and Engineering*, Vol. B9, pp.397-403, 1991.
2. L. G. Zimin, " ", *Materials-Science and Engineering*, Vol. B9, pp.405-412, 1991.
3. K. E. Remitz, N. Neuroth, B. Speit, "Semiconductor-doped glasses as a nonlinear material", *Materials-Science and Engineering*, Vol. B9, pp. 413-416, 1991.
4. N. F. Borrelli, D. W. Hall, H. J. Holland, D. W. Smith, "Growth study concerning Cd(S,Se) nanocrystals", *J. Appl. Phys.*, Vol. 61(12), pp.5399-5406, 1987.
5. B.G. Potter and J.H. Simmons, "High resolution transmission electron microscopy", *Phys. Rev.B*, Vol. 37 (18), pp.10 838 -10957, 1988.
6. E. M. Vogel, S. C. Kosinski, D. M. Krol and J. L. Jackel, "Silicate doped glass", *J. Non-Cryst. Solids*, Vol.107, pp.10838-10850, 1989.

SESSION 7

Optical Sensors and Metrology

A new principle for self-calibration techniques in phase shift interferometry

Adrian Dobroiu, Dan Apostol, Victor Damian, Victor Nascov

National Institute for Laser, Plasma and Radiation Physics – Laser Department
PO Box MG-36, Bucharest-Măgurele, Romania

ABSTRACT

A new self-calibration principle for phase shift interferometry (PSI) is introduced, involving a whole-field consideration of the information contained by the interferograms. The principle is illustrated for the three-sample case, which was previously known as not having a self-calibration capability. Three related self-calibrating algorithms for phase shift interferometry are proposed, all of them based on this principle. The input of the algorithms is the set of three interferograms, and the output consists in both the correct phase shifts and the phase map of the wavefront being analyzed. No information on the actual phase shifts has to be supplied.

Keywords: phase shift, self-calibration algorithms, interferometry, fringe processing.

1. INTRODUCTION

Many self-calibrating algorithms for PSI have been designed to correct the effect of phase shifting errors. They can be divided into two categories, "pixel-by-pixel" and "whole-field" algorithms, based on whether the information in the interferograms is processed separately at every pixel or the images participate as a whole in calculating the correct phase shifts.

The algorithms in the first category¹⁻⁶ make the assumption that the phase shifting device is non linear, and its response can be described by a polynomial function of a certain order. Consequently, a larger number of phase-shifted samples are recorded at each point of the viewing field so as to provide a sufficient number of equations for all the unknowns involved. While three images are enough in the case of an error-free phase shifter, four images become necessary for a linear error, five for a parabolic error, and so on. Not only this principle demands more images for a higher order of the polynomial, but also in practice piezoelectric phase shifters usually suffer from hysteresis, so that unreproducible phase shifts are normally encountered.

Lately several algorithms in the second category have been proposed⁷⁻¹⁰ that succeed in correcting the phase shifting errors by an ellipse fitting or by iterative least-squares fitting. Drawbacks such as the extensive computational effort or the constraint on uniformity of illumination limit the application of these new algorithms.

We propose a new principle pertaining to this second category, based on a statistical consideration of the input interferograms. Given the set of three interferograms one can suppose some arbitrary phase shifts and calculate the map of a characteristic quantity, such as wrapped phase, contrast or intensity offset. According to the amount of phase shifting errors this map is affected more or less with respect to its ideal features. Then either the actual phase shifts are directly calculated or other supposed phase shifts are tested, until those feedback features match the ideal.

As there are more unknowns to be found than equations, additional assumptions have to be made. Hence some specific experimental care should be taken so that the assumptions be justified. This paper presents three related algorithms working on this principle, one for each quantity whose map is calculated and processed: phase, visibility, and intensity offset.

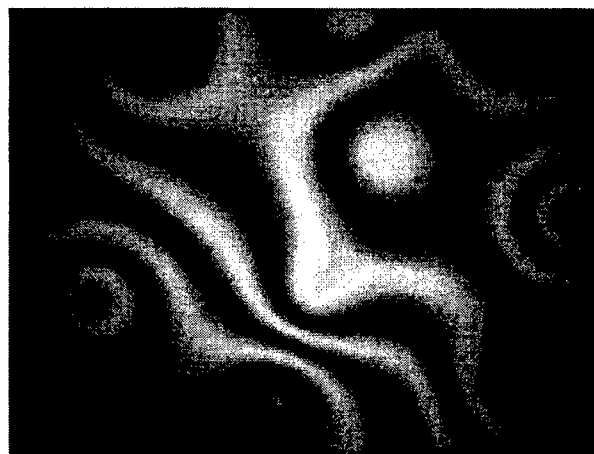
2. CALCULATION OF THE NECESSARY MAPS

The equation that gives the intensities measured at one pixel (x,y) as function of the phase, contrast and intensity offset is:

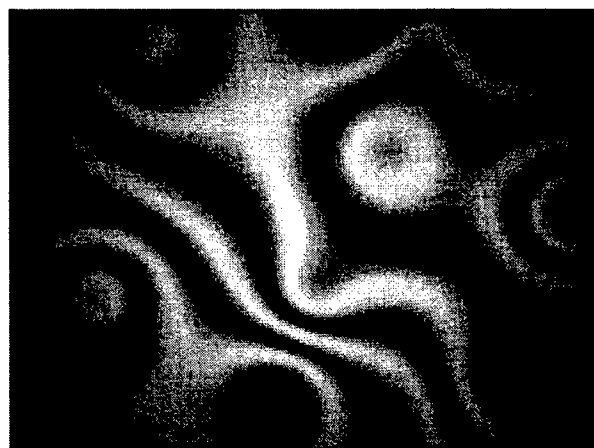
$$I_k = I_m [1 + V \cos(\varphi - \beta_k)], \text{ with } k = 0, 1, 2. \quad (1)$$

where $I_{0,1,2}(x,y)$ are the three intensities measured at pixel (x,y) , $\varphi(x,y)$ is the phase, $V(x,y)$ is the contrast, and $I_m(x,y)$ is the intensity offset. The quantities $\beta_{0,1,2}$ are the phase shifts, relative to the first interferogram. In the following, phase shift β_0 is taken arbitrarily zero.

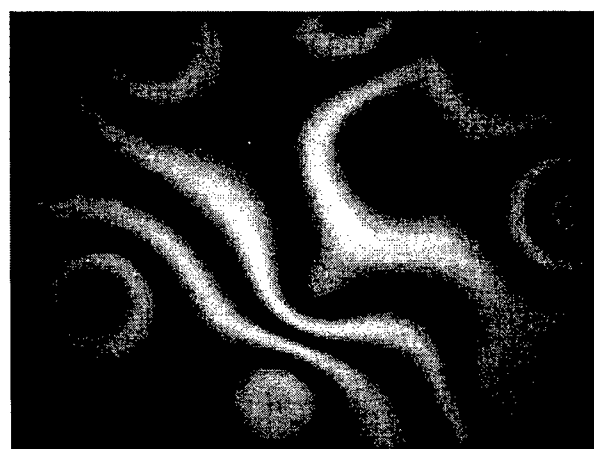
With a set of three phase-shifted interferograms (like those in figure 1) one can calculate the maps of the three quantities involved: the phase (mod 2π), the contrast, and the intensity offset. For this to be done one needs to know the values of the two phase shifts used, β_1 and β_2 .



(a)

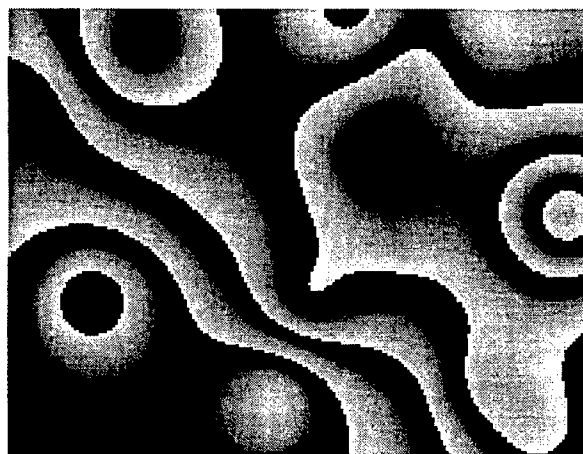


(b)

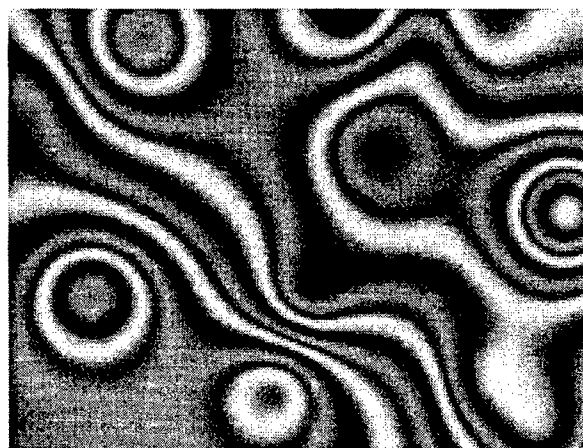


(c)

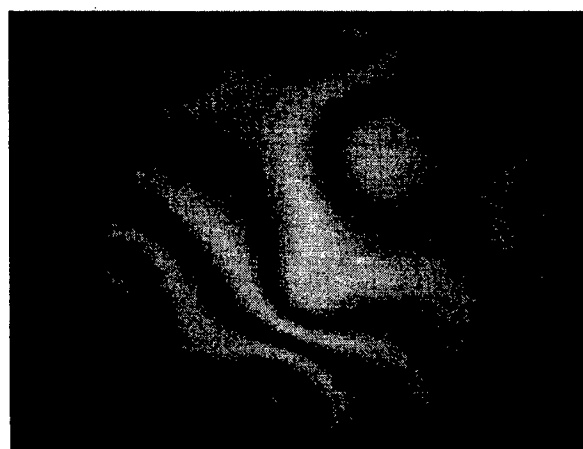
Fig. 1. Three phase-shifted interferograms. The simulations were carried out for phase shifts of: (b) 60° and (c) 250° . Noise (SNR = 15 dB) and non uniform intensity offset (decrease down to 20% at corners) were included.



(a)



(b)



(c)

Fig. 2. Maps of the quantities used in the algorithms, affected by phase shifting errors: (a) wrapped phase with two predominant shades of gray, (b) contrast with double pseudo-fringes, and (c) intensity offset with pseudo-fringes.

If the three intensities $I_{0,1,2}$ are given and the two phase shifts $\beta_{1,2}$ are known or supposed to have certain values, the equation system (1) can be considered as having the unknowns φ , V and I_m , in which case its solution becomes:

$$\begin{cases} \varphi = \arccos(c, s) \\ V = \frac{\sqrt{c^2 + s^2}}{I_0 - c} \\ I_m = I_0 - \sqrt{c^2 + s^2} \end{cases} \quad \text{with} \quad \begin{cases} c = \frac{(I_1 - I_0)\sin\beta_2 - (I_2 - I_0)\sin\beta_1}{(\cos\beta_1 - 1)\sin\beta_2 - (\cos\beta_2 - 1)\sin\beta_1} \\ s = \frac{(I_1 - I_0)(1 - \cos\beta_2) - (I_2 - I_0)(1 - \cos\beta_1)}{(\cos\beta_1 - 1)\sin\beta_2 - (\cos\beta_2 - 1)\sin\beta_1} \end{cases}, \quad (2)$$

where the function arc gives the angle within $[0, 2\pi)$ whose cosine and sine are proportional to the arguments. The maps corresponding to the interferograms in figure 1 are presented in figure 2.

3. STATISTICAL SELF-CALIBRATING ALGORITHMS

For all three algorithms that are to be described it was assumed that the phase shifts applied have constant values over the viewing field, that is, no tilts or deformations are induced, only pure longitudinal translations are allowed.

With the values given by (2) the maps of the phase, contrast and intensity offset can be calculated and used for the algorithms. Ideally, if the actual phase shifts are exactly known, these maps contain the exact values of the respective quantities (except for the phase which, because of the trigonometric functions, is only computed up to the modulo 2π).

If however the phase shifts used in this calculation differ from those that actually led to the interferograms some specific effects can be observed. These modifications (such as the appearance of parasite fringes, or a change in the values distribution) brought to the maps are used to find the actual phase shifts.

3.1. An algorithm based on the distribution of the calculated phase

One first algorithm¹¹ is based on the analysis of the calculated phase map. The assumption made for this algorithm is that the actual phase in the wavefront is uniformly distributed in the range $[0, 2\pi)$, that is, the histogram of the actual phase modulo 2π over the entire viewing field is uniform. This condition can be approximately met by having as many fringes in the field as possible.

Ideally, if there are no phase shifting errors, the calculated phase (modulo 2π) is uniformly distributed over the range $[0, 2\pi)$. The effect of phase shifting errors is that the calculated phase tends to concentrate around two values in this range so that its distribution comes to have two maxima and two minima (figure 3a). The position and the amplitude of the two maxima depends on the relationship between the actual and the supposed phase shifts.

The steps of the algorithm are as follows:

- (1) Suppose some arbitrary phase shifts;
- (2) Calculate the map of the phase based on these values of the phase shifts;
- (3) Build the histogram of the calculated phase map;
- (4) Calculate the Fourier transform of the histogram at frequency $1/\pi$, which gives a measure of the position and the amplitude of the two maxima;
- (5) Calculate the actual phase shifts from the Fourier coefficients.

For steps (4) and (5) of the algorithm the mathematical basis consists in an analytical estimation of the probability density function that gives a theoretical histogram that is to be expected when the actual and supposed phase shifts have certain values. This probability density function has the form:

$$P(\varphi'; \beta_1^e, \beta_2^e, \beta_1^s, \beta_2^s) = \frac{1}{2\pi} \cdot \frac{\sqrt{1 - A^2}}{1 + A \cos(2\varphi' - 2\alpha)}, \quad (3)$$

where φ' is the calculated phase, β_1^e and β_2^e are the actual phase shifts, β_1^s and β_2^s are the supposed phase shifts, A is a number within $[0, 1)$ that can give a measure of the amplitude of the maxima, and α gives the position of the maxima. A and α depend only on the phase shifts, actual as well as supposed, and are related to the Fourier coefficients C_p and S_p at frequency $1/\pi$ through the formulas:

$$C_P = -\frac{1-\sqrt{1-A^2}}{A} \cos 2\alpha \quad \text{and} \quad S_P = -\frac{1-\sqrt{1-A^2}}{A} \sin 2\alpha. \quad (4)$$

Once the histogram is calculated and its Fourier coefficients C_H and S_H extracted, the two actual phase shifts are found by searching their values that lead to $C_P = C_H$ and $S_P = S_H$. Even though an analytical way was not found to do this in one step, the computer solving routine used instead proved to work fast enough.

In figure 3 we present the histogram of the wrapped phase map, before and after the algorithm is run.

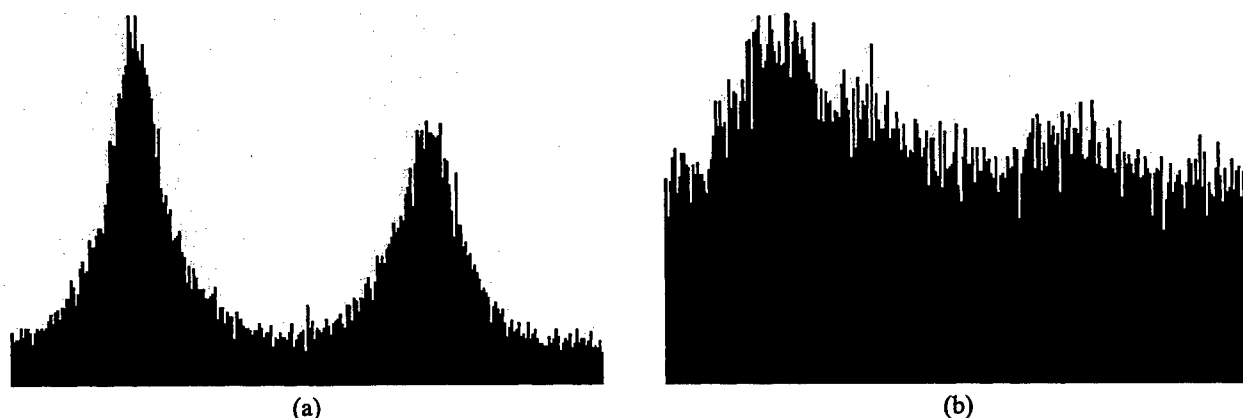


Fig. 3. The histogram of the calculated phase map (a) before and (b) after self-calibration. The position and the height of the two maxima in (a) depend on both the actual phase shifts and the supposed phase shifts.

Tests have been made to estimate the accuracy of the algorithm. For a precise handling of the parameters (noise, beam profile, fringe visibility, flatness of the wavefront) simulations were preferred to actual interferograms. Residual errors of retrieving the phase shifts have been found to lie in the $0.1^\circ \div 4^\circ$ range, depending on the number and the visibility of fringes in the field, the noise, and the flatness of the simulated wavefront.

3.2. An algorithm based on the calculated contrast uniformity

This algorithm¹² is based on the analysis of the calculated contrast map. The assumption made here is that the actual contrast of the interference pattern is constant. Many experimental setups readily satisfy this condition. Also there should be at least a few fringes in the interferograms to ensure a good accuracy.

The effect of phase shifting errors is that the calculated contrast map becomes "contaminated" with the fringe pattern in the interferograms (figure 2b). The histogram of the contrast map is no longer a narrow spike as it is in the ideal case of zero errors, but a broader distribution of values of the contrast is obtained, the usual shape of the histogram being made up by four peaks (figure 4a). As there is a monotonous relationship between the phase shifting errors and the width of the histogram, the latter can be used as the feed-back quantity for the algorithm, as suggested by the following steps:

- (1) Take a pair of supposed phase shifts as a departure point;
- (2) Calculate the resulting contrast map;
- (3) Construct its histogram and calculate the width of the contrast distribution;
- (4) Repeat steps (2) and (3) with two slightly different values of one phase shift, say β'_1 , and assume a parabolic dependence of the width on this phase shift, then choose for this phase shift the value that would lead to minimum width;
- (5) Repeat steps (2) ÷ (4) for the other phase shift, β'_2 ;
- (6) Repeat steps (2) ÷ (4) until the pair of phase shifts does not vary by more than a preset little amount, or the width of the histogram has reached its minimum.

The precision of this algorithm is very good, and considering the very loose condition of providing a uniform contrast we can foresee its widespread application. The only drawback is the longer time taken by the computation of the contrast map a considerable number of times.

Figure 4 presents the histogram of the contrast map, before and after the algorithm is run. In figure 4b this histogram corresponds to the case where the supposed phase shifts match their actual values, and the residual width of the calculated contrast is only due to noise.

Many tests have been carried out to check the dependence of the residual error on some parameters. Thus it has been established that the errors of estimating the actual phase shifts are expected to be above 1° in one of the following circumstances: the actual contrast is less than 0.2, the actual phase shifts are restricted to a 60° interval, the signal-to-noise ratio is less than 30, the frame contains less than 100 pixels or there is less than half a fringe within the viewing field. In normal conditions the residual error is less than 0.2° , or $2\pi/1800$ radians. If a He-Ne laser is used, that means less than 2 \AA in a reflective set-up. Even better precisions can be attained if special care is taken. We emphasize that this is an impressive achievement in the conditions of not having any information on the actual phase shifts, everything being inferred from the interferograms themselves.

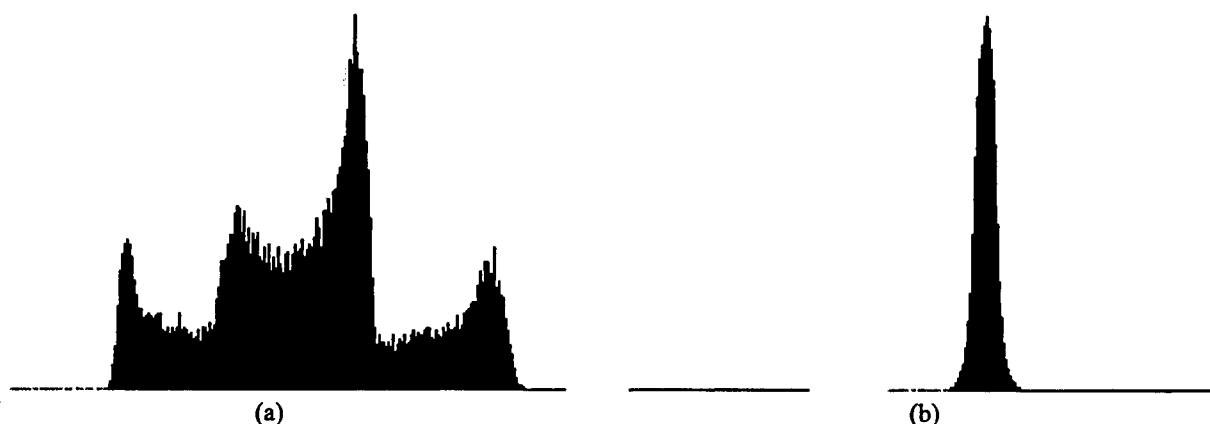


Fig. 4. The histogram of the calculated contrast map (a) before and (b) after self-calibration. A broad distribution with a characteristic shape is obtained when the supposed phase shifts are different from the actual ones. For noise-free interferograms four peaks are visible, while with increasing noise the structure of this distribution gets blurred. After self-calibration was achieved, the histogram contains a single peak, whose width is only determined by the amount of noise in the interferograms.

3.3. An algorithm based on the calculated intensity offset smoothness

The last algorithm in this series is based on the analysis of the calculated bias intensity map. No special assumption is made for this algorithm except that the actual bias intensity should not vary too steeply in the viewing field. The effect of phase shifting errors is that fringes, very similar to those in the interferograms, appear in the calculated intensity offset map. The profile of this fringes has been demonstrated to be sinusoidal, unlike the pseudo-fringes that affect the contrast map.

The feedback quantity used in this case is a measure of the variability of the calculated intensity offset map. This measure was taken as the sum of squared differences between neighbor pixels. As for the previous algorithm, after a starting pair of phase shifts is chosen the steps to be followed consist in repeatedly calculating the intensity offset map at different pairs of phase shifts, searching for the pair that leads to the minimum variability of the map.

If a uniform illumination in the interferometer can be realized, that is, a constant I_m is assumed in the interferograms, a more straightforward feedback quantity can be used.

The use of this algorithm is limited in the sense that there are some phase shifts for which the map of the calculated intensity offset becomes uniform even if the supposed phase shifts do not match the actual ones, so that the algorithm cannot work. These situations occur when one of the actual phase shifts is 180° , or when the difference between them is 180° .

The most important advantage of this algorithm is that its requirements are the most easily fulfilled. However the residual errors become important when the actual phase shifts are too close to the configurations mentioned before.

4. CONCLUSIONS

We presented a new approach to the problem of self-calibrating algorithms, by introducing a different principle, based on a statistical analysis of the interferograms. Three algorithms working on this new concept are described.

The first algorithm consists in calculating the histogram of the output wrapped phase and extracting the actual phase from a Fourier coefficient. The second algorithm calculates the contrast map and determines the amplitude of the pseudo-fringes that affect this map as a consequence of the phase shift errors. Finally the third algorithm analyzes the pseudo-fringes that contaminate the map of the intensity offset in order to cancel the phase shift errors.

None of the algorithms needs to be supplied with the approximate values of the phase shifts, the only input requested is the set of three interferograms. The output consists in the correct values of the phase shifts and in the wrapped phase map, theoretically free of errors. The residual errors are very low in many usual cases, and can be decreased down to as little as 0.2° .

5. REFERENCES

- [1] J. Schwider, R. Burow, K.-E. Elssner, J. Grzanna, R. Spolaczyk and K. Merkel, "Digital wave-front measuring interferometry: some systematic error sources," *Appl. Opt.* **22**, 3421-3432 (1983)
- [2] K. Kinnstaetter, A. W. Lohmann, J. Schwider and N. Streibl, "Accuracy of phase shifting interferometry," *Appl. Opt.* **27**, 5082-5089 (1988)
- [3] J. Schwider, O. Falkenstörfer, H. Schreiber, A. Zöller and N. Streibl, "New compensating four-phase algorithm for phase-shift interferometry," *Opt. Eng.* **32**, 1883-1885 (1993)
- [4] Y. Surrel, "Phase stepping: a new self-calibrating algorithm," *Appl. Opt.* **32**, 3598-3600 (1993)
- [5] B. Zhao and Y. Surrel, "Phase-shifting: six-sample self-calibrating algorithm insensitive to the second harmonic in the fringe signal," *Opt. Eng.* **34**, 2821-2822 (1995)
- [6] D. Apostol, P. C. Logofătu, V. Damian, A. Dobroiu, "Sensitivity analysis, using the Jacobian, of parameters determination from measurement of directly measurable quantities," *Opt. Eng.* **35**, 1288-1291 (1996)
- [7] K. Okada, A. Sato and J. Tsujiuchi, "Simultaneous calculation of phase distribution and scanning phase shift in phase shifting interferometry," *Opt. Comm.* **84**, 118-124 (1991)
- [8] C. T. Farrell and M. A. Player, "Phase step measurement and variable step algorithms in phase-shifting interferometry," *Meas. Sci. Technol.* **3**, 953-958 (1992)
- [9] C. T. Farrell and M. A. Player, "Phase-step insensitive algorithms for phase-shifting interferometry," *Meas. Sci. Technol.* **5**, 648-652 (1994)
- [10] G.-S. Han and S.-W. Kim, "Numerical correction of reference phases in phase-shifting interferometry by iterative least-squares fitting," *Appl. Opt.* **33**, 7321-7325 (1994)
- [11] A. Dobroiu, P. C. Logofătu, D. Apostol and V. Damian, "Statistical self-calibrating algorithm for three-sample phase-shift interferometry," *Meas. Sci. Technol.* **8**, 738-745 (1997)
- [12] A. Dobroiu, D. Apostol, V. Nascov and V. Damian, "Self-calibrating algorithm for three-sample phase-shift interferometry by contrast leveling", to be published.

Instruments and standard measurement procedures for laser beam characterization

R. Mästle, C. Schmitz, F. Varnik, A. Giesen, H. Hügel

Institut für Strahlwerkzeuge, Universität Stuttgart
Pfaffenwaldring 43, D-70569 Stuttgart

ABSTRACT

The EUREKA-project CHOCLAB (Characterization of Optical Components and Laser Beams), which was initiated in 1995, aims to investigate and develop instruments and standard measurement procedures for laser beam and laser optics characterization. From the start of the project, one of the main work items in the field of laser beam characterization has been the determination of the beam propagation parameters (beam width, divergence angle and beam propagation factor). The most common measurement devices for these purposes are 2d-matrix-cameras (i. e. CCD-cameras), 1d or 2d scanning devices (i. e. scanning pinholes and/or moving knife-edges) - both of them requiring further evaluation of the measured power density distribution to obtain laser beam parameters - and variable transmission/reflectivity optical elements, which allow the direct measurement of beam properties. The advantages and drawbacks of the different types of measurement devices, as well as measures to reduce systematical and statistical errors will be discussed.

The instruments and proposed standard measurement procedures are tested by „Round Robin“ experiments: different laboratories characterize the same laser beam source according to the standards. In 1996 and 1997 four different „Round Robin“ experiments on laser beam characterization were performed within the CHOCLAB project. The main goal of these „Round Robin“ experiments was to test the applicability of the proposed standard measurement procedures to different important types of industrial laser devices (in particular high power CO₂-lasers and pulsed Nd:YAG-lasers). The results of these experiments as well as the current status of CHOCLAB and of the draft international standards concerning laser beam characterization will be briefly reviewed.

Keywords: Laser beam characterization, Laser beam propagation, Laser beam width, CHOCLAB, ISO/DIS 11146

1. INTRODUCTION

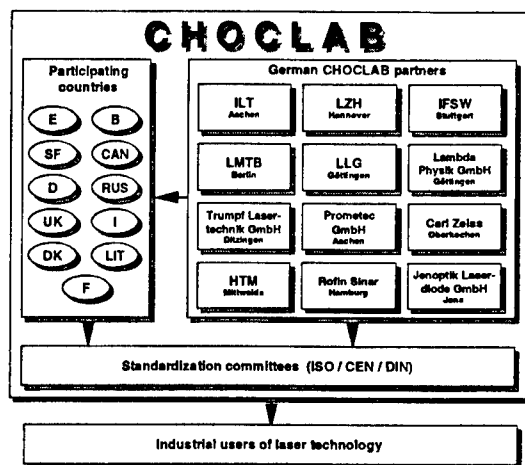


Figure 1: Structure of CHOCLAB.

The importance of laser technology in industrial applications as well as its progress crucially depend on well defined and easy to handle measurement procedures, which allow a unique characterization of laser beam performance parameters. Therefore, the development of test methods for laser beam characterization has been supported in national laser projects in different countries. First attempts of common definitions and measuring techniques were made in some European projects (e. g. EU 194). As a consequence, the international standardization committee started to work on the standardization of lasers in 1989. Nevertheless, it was found, that more thorough investigations are necessary before acceptable standards can be evaluated. In 1994 the idea was born to bring together all the different ideas in one European project: the EUREKA-project CHOCLAB was then initiated in 1995.

The main goals of the EUREKA-project CHOCLAB are to support the standardization efforts in the field of laser beam and laser optics characterization ([1] to [5]), the transfer of the standard measurement procedures to industrial users of laser technology and the basic research on the

proposed standard measurement procedures for laser beam and laser optics characterization. Figure 1 shows the structure of CHOCLAB. Today 37 partners from 11 countries are actively participating in the CHOCLAB project. The work of the CHOCLAB project is done in close cooperation with international standardization committees (CEN, ISO) in order to guarantee an immediate European wide embodiment of the results.

The instruments and proposed standard measurement procedures are tested and qualified with national and international „Round-Robin“ experiments, where partners from different laboratories and industrial companies characterize the same laser beam source according to the standards. In 1996 and 1997 four different „Round Robin“ experiments on laser beam characterization were performed within the CHOCLAB project, with up to ten participants from research facilities and industrial companies from all over Europe. The main goal of these „Round Robin“ experiments was to test the applicability of the standards ISO/DIS 11146 and ISO/DIS 11670 to different important types of industrial laser devices (in particular high power CO₂-lasers and pulsed Nd:YAG-lasers) and to give final conclusions concerning these two standards.

From the beginning of the CHOCLAB-project, especially the standard ISO/DIS 11146, which defines measurement procedures for the determination of beam widths and laser beam propagation parameters, has been one of the most important work items. The different beam width definitions proposed in ISO/DIS 11146, which will be discussed in the following are the:

- Second order moment beam width: which is from a theoretical point of view the beam width definition of choice and given by four times the variance of the power density distribution:

$$d_x = 4 \cdot \sigma_x \text{ with } \sigma_x^2 = \frac{\iint I(x, y) \cdot x^2 dy dx}{\iint I(x, y) dy dx} \quad (1)$$

- 86%-encircled energy diameter: which is defined by the minimum aperture which allows the transmission of 86,5% of the total beam power.
- Moving knife edge beam width: which is defined as a constant times the distance between the two positions of a knife edge which clips a certain percentage of the beam power from each side of the beam. According to ISO/DIS 11146 a clip level of 16% and a multiplier of two has to be used.

The laser beam propagation parameters are obtained according to ISO/DIS 11146 with a beam caustic measurement. This means the beam diameter has to be determined at different axial positions within one beam caustic, which has to be created artificially if not accessible for direct measurement.

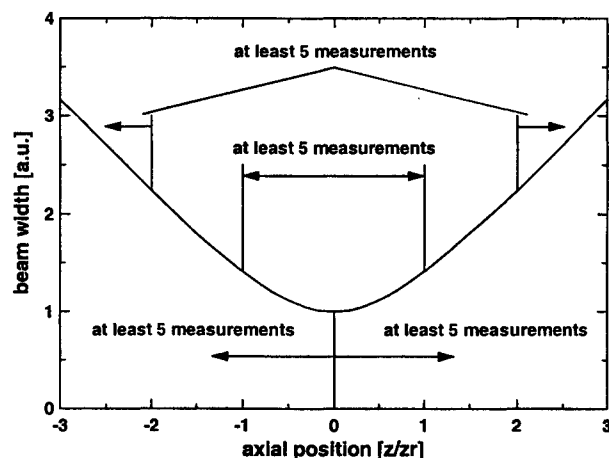


Figure 2: Combined determination of laser beam parameters with a beam caustic measurement.

Figure 2 shows the minimum requirements concerning the positions, where beam diameters have to be measured. The laser beam propagation parameters (waist diameter, waist position, divergence angle and beam propagation factor) are then obtained by fitting a hyperbola to the measured beam widths along the propagation. Note that meeting or exceeding these minimum requirements the maximum power density will change about a factor of ten and the beam diameter about a factor of three.

The measurement of the second order moment beam width can be performed using two basic principles:

- Numerical integration: Measurement of the power density distribution of a beam and subsequent evaluation of beam width.
- Optical integration: Direct measurement of laser beam parameters using variable transmission/reflectivity optical elements ([6], [7], [8]).

Using optical windows, for example with a parabolic transmission profile to determine the beam width, has several advantages, since the parabolic weighting (see equation (1)) can be performed in a noiseless manner, furthermore the measurement of beam width can be done by simple power measurements. However, the standard procedure most often used nowadays is the measurement of the power density distribution and subsequent determination of beam widths.

For measuring the power density distribution 1d or 2d scanning devices and especially 2d-matrix-cameras are widely used. Standard industrial grade 2d-cameras usually perform a 8bit digitizing, thus yielding 256 grey levels, and have relatively low spatial resolution of about 10 µm. Using these devices for a beam caustic measurement therefore requires a waist diameter of at least about 400 µm. To obtain reliable results the maximum signal of the measured power density distribution should be close to the saturation of the sensor, which requires at each axial measurement position adequate adaption of the beam power using attenuators. Scanning devices in general have a much greater dynamical range and may have a better spatial resolution,

which then allows automatic beam caustic measurement systems. However, the application of these devices is mostly restricted to the analysis of cw or quasi-cw beams and is more time-consuming. In the following the determination of laser beam widths by evaluating power density distributions, the potential sources of measurement errors, as well as measures to reduce systematical and statistical errors will be discussed.

2. EVALUATION OF POWER DENSITY DISTRIBUTIONS

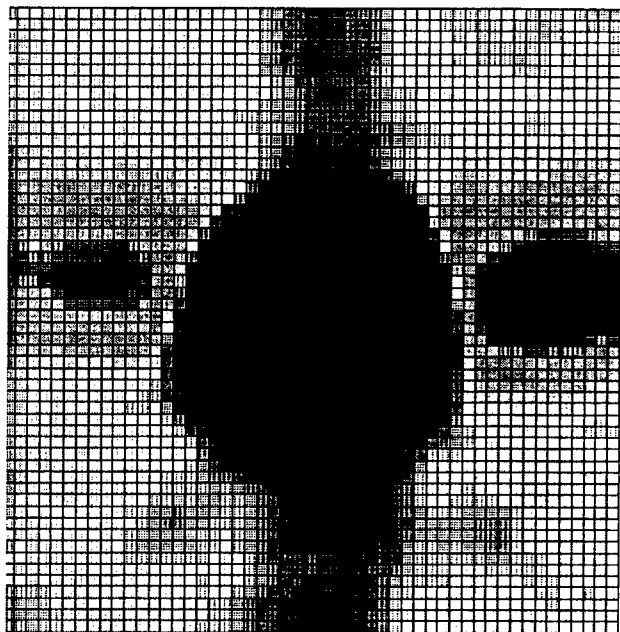


Figure 3: Typical image distortions of measured power density distributions.

The measurement of power density distributions may be affected by several potential sources of errors: image distortions due to detector properties (i. e. nonlinear response, inhomogenous background, baseline offset), distortions caused by the laser beam itself (like interference, vertical smear, too low Pixel values horizontally beside the laser beam, see figure 3) and distortions due to external light sources. The measured power density distribution is therefore composed of at least three contributions:

$$I_{\text{meas}}(x, y) = I_{\text{theo}}(x, y) + N(x, y) + I_{\text{off}} \quad (2)$$

where $I_{\text{theo}}(x, y)$ denotes the power density distribution of the laser beam, $N(x, y)$ the inhomogenous part of the background distribution and I_{off} the constant baseline offset. The two latter contributions have to be corrected or minimized to achieve highest reliability and accuracy. Since it is nearly impossible even to give an estimation of errors, caused by inhomogenous image distortion, these effects will be neglected in the investigations on measurement errors presented below. The investigations will be restricted to the influence of a constant baseline offset (see [12]). Therefore, it should be noted that for real measurement systems the errors will be in general higher than those given in the following. The accuracy of the laser beam parameters, calculated

from the measured power density distribution, moreover strongly depends on the beam representation, especially on the maximum signal and on the ratio of the beam diameter to the size of the measurement window. Figure 4 shows as an example the offset induced errors of different beam width definitions for a Gaussian beam with a maximum power density of 255 digits, dependent on the ratio of the beam diameter to the size of the measurement window. The relative window sizes chosen in figure 4 are those, that may typically appear when performing a beam caustic measurement.

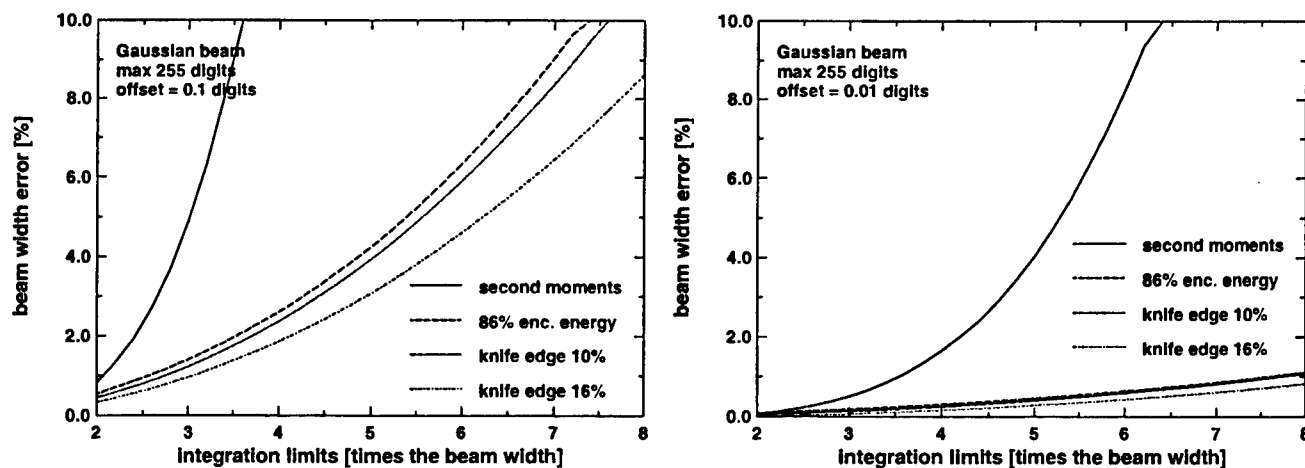


Figure 4: Offset induced errors of different beam width definitions for a Gaussian beam with a maximum intensity of 255 digits (left: offset = 0,1 digits; right: offset = 0,01 digits)

In order to reduce measurement errors two basic procedures have to be applied. At first image distortions and the baseline offset have to be minimized. The following procedures for this purpose have been proposed in the past and will be discussed in section 3 ([9] to [14]):

- reference frame subtraction, which may also correct for background inhomogeneities,
- fourier transform methods,
- histogram method,
- threshold method,
- statistical procedures.

Furthermore the integration domain, which is taken into account in the determination of the beam width, has to be chosen as small as possible using window functions, but without truncating the power density distribution of the beam too much (see figure 13). In general the measured power density distribution, can be divided in areas, which are illuminated by the laser beam (inner area), and others, that are not (outer area). Only the former ones have to be included in beam width calculations, the latter ones can be used for the correction of baseline offset and other errors. In the past mainly two types of window-functions have been proposed: Gaussian windows and Top-Hat windows. Both window functions require some iteration methods to obtain beam widths. The related problems as well as the properties of these beam width definitions are discussed in section 4.

3. METHODS FOR BASELINE OFFSET COMPENSATION

3.1. Reference frame subtraction

Reference frame subtraction is mandatory for most measurement devices to correct background inhomogeneities. Usually the contribution due to the offset level cannot be neglected, even if reference frame subtraction was applied. Reference frame subtraction reduces the offset level to smaller values (usually $\ll 1$ digit), but not necessarily to zero, due to scattered or incoherent light, image distortions caused by the laser beam itself, as shown in figure 3, or a drift of the baseline after the reference image was recorded. This is demonstrated in figure 5, where the signals of a CCD-camera, recorded in the focal spot of a Nd:YAG-laser, are summed over lines.

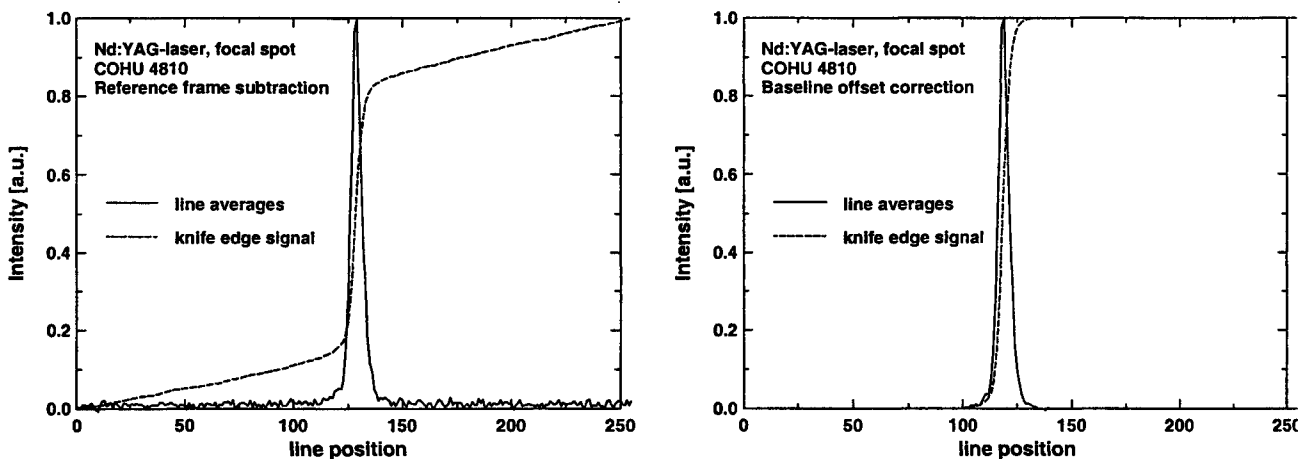


Figure 5: Power density distribution of the focal spot of a Nd:YAG-laser, measured with a CCD-camera, signals summed over lines (left: only reference frame subtraction applied; right: additional baseline offset compensation)

In the left image of figure 5, it can be clearly seen that the small baseline offset (which is about 0,03 digits) leads to a linear increase of the calculated moving knife edge signal even far away from the beam, which vanishes when an additional baseline offset correction is applied (right image). The second moment beam width gives 170 Pixels (only reference frame subtraction applied) and 12,3 Pixels (additional offset correction applied) respectively. Therefore to correct for the baseline offset level, additional procedures have to be applied to the measured power density distribution.

3.2. Fourier transform methods

One possible method for offset correction is using fourier transform techniques ([11], [14]). A constant baseline offset of the measured power density distribution results in a distinct peak at the spatial frequency zero, which is shown in figure 6. The interpolation of this value based on surrounding spatial frequencies nulls the offset.

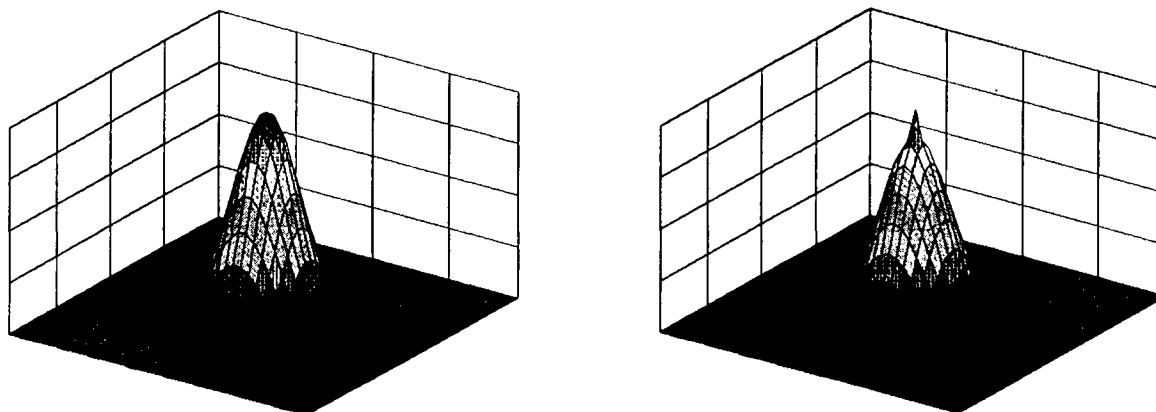


Figure 6: Gaussian beam with constant baseline offset: original distribution (left) and its fourier transform (right).

Due to the involved interpolation techniques in the frequency domain, it follows, that his method gives more reliable results for beams having a narrow spatial extension. The major advantage of fourier transform techniques is, that not only a baseline offset but additionally most of the image distortions can be identified and corrected, i. e. horizontal and vertical waves or a tilt of the baseline.

3.3. Histogram methods

Assuming a normally distributed detector noise, the offset is given by the maximum of a Gaussian distribution and can be consequently determined by fitting a gaussian distribution to the lowest peak of the histogram of a measured power density distribution [10]. The principle of this method is depicted in figure 7.

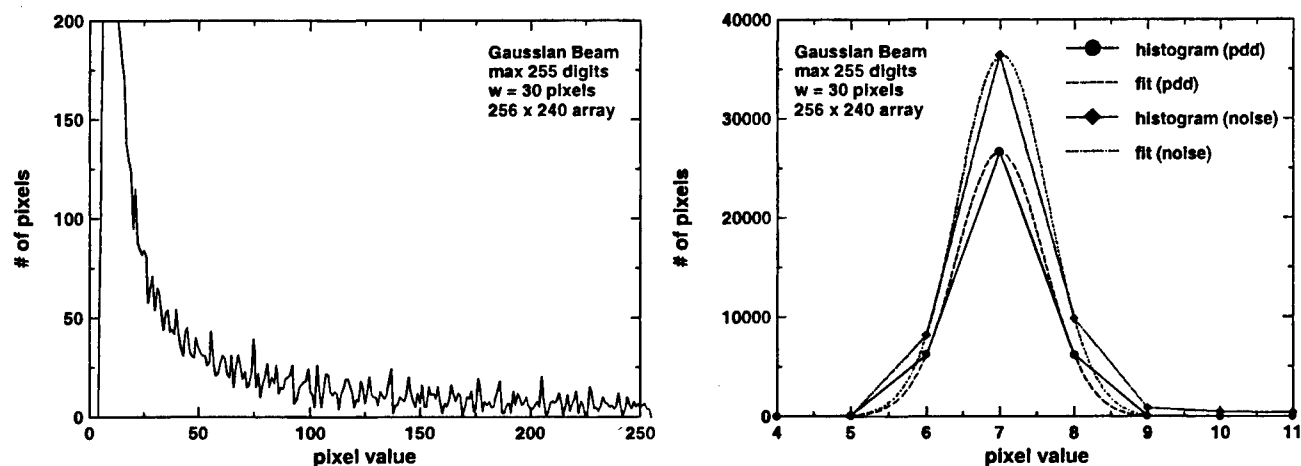


Figure 7: Histogram of a Gaussian beam (left: full histogram; right: zoom to values close to the baseline offset).

The determination of the histogram has to be restricted to regions of the measured power density distribution, which are dominated by the noise of the detector system (non-illuminated pixels), since using the complete measured power density distribution increases the histogram values above the baseline and then gives too high values for the baseline offset (in the example above the offset is increased by 0,035 digits). Furthermore, when using measurement devices with low noise, there are only about three to five values, which can be used for curve fitting, see right part of figure 7.

3.4. Threshold methods

Pixel values within the measured power density distribution which fall off below a certain threshold are set to zero [10]. This method transforms statistical errors into systematic errors, since with a proper choice of the threshold value the integration area and therefore statistical errors become very low, but due to the power truncation the resulting beam widths are always too small. Figure 8 shows the threshold induced errors of different beam width definitions for Gaussian beam with a maximum power density of 255 digits..

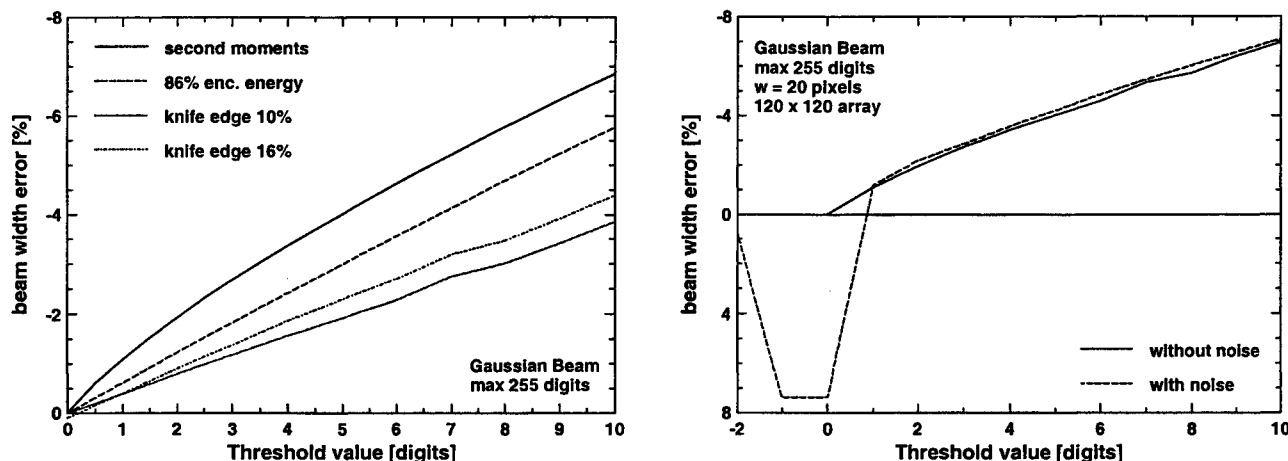


Figure 8: Threshold induced beam width errors for a Gaussian beam (left: theoretical calculations; right: second moment evaluation of a simulated power density distribution without and with noise).

The threshold induced beam width errors are constantly increasing with increasing threshold. In a noiseless system with a maximum power density close to the saturation the systematic beam width errors are still relatively small (below 5% for threshold values below 7 digits). From the right part of figure 8 it can be clearly seen, that the threshold value has to be chosen above the highest noise peaks of the detector background since cutting off only the negative noise amplitudes may create large errors. The best choice for the threshold value which fulfills this condition and gives the lowest errors, that can be achieved applying this method, will be in most cases 2 digits above the baseline.

3.5. Statistical methods

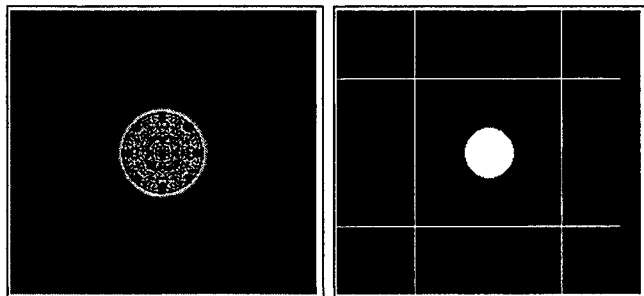


Figure 9: Windowing using the statistical method (left: original distribution; right: extracted window function, the white spot indicates the diameter).

Assuming a normally distributed detector noise, the background can be characterized by its mean value I_{off} and its standarddeviation σ_I . Calculating a running average of the power density distribution, where the mean values of subarrays of $N \times M$ pixels give the new pixel values, reduces the noise to [15]:

$$\sigma_{N \times M} = \sigma_I / \sqrt{N \cdot M} \quad (3)$$

but does not change the resolution. Only the pixel values of the running average which show statistically significant deviations compared to the background noise, i. e.

$$I_{N \times M}(x, y) > n_T \cdot \sigma_{N \times M} + I_{\text{off}} \quad (4)$$

are assumed to be illuminated and included in beam width calculations, the average of the non-illuminated pixels then gives the offset value ([12],[13]). Practical values of n_T are in the range between two and four. According to equation (4), this method is based on some threshold settings too, but allows to set a threshold value much smaller than 1 digit, which can be adapted the resolving power of the measurement device. Therefore it gives a limitation of the integration domain in a very natural way. The windowing properties are demonstrated in figure 9, where using this method the illuminated areas are extracted from a power density distribution. In the right image the black areas are considered to be non-illuminated, illuminated pixels are within the grey circle, the white spot indicates the beam diameter.

3.6. Comparison of different methods

In order to compare the different methods for offset correction a set of artificial power density distributions was created and subsequently evaluated. These power density distributions were composed of three distributions (according to equation (2)): a Gaussian distribution centered in an array of 256×240 pixels, a constant baseline offset of 7 digits and noise with a standard deviation of 0,5 digits, where the last value was chosen according to the noise of our 8 bit camera system. For calculating the Gaussian distributions different diameters (10, 20, 40, 60 and 80 pixels) and different maximum power densities (20, 100 and 255 digits) were used. The results of the second moment evaluation of this set of power density distributions using the different methods for offset correction is shown in figures 10 to 12.

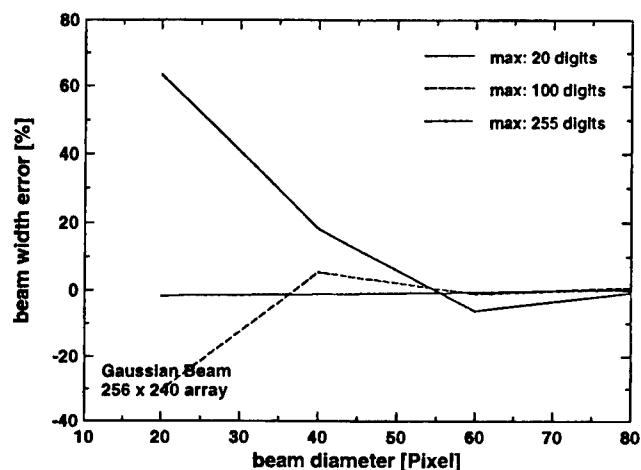


Figure 10: Evaluation using the histogram method.

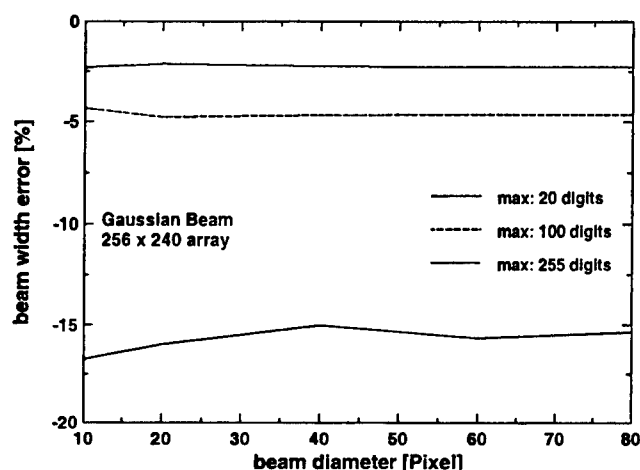


Figure 11: Evaluation using the threshold method.

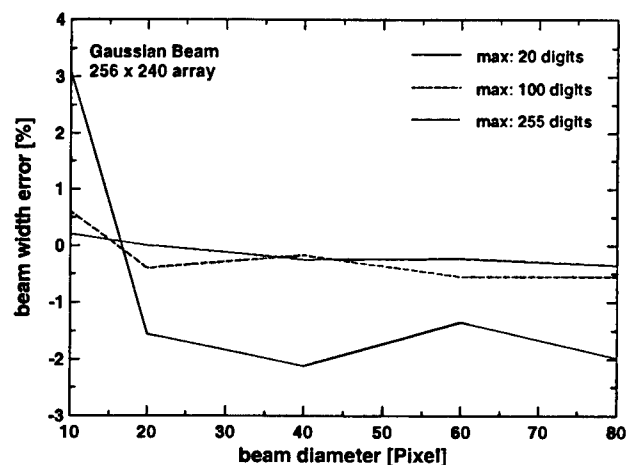


Figure 12: Evaluation using the statistical method.

The evaluation according to the histogram method (figure 10) reproduces the baseline offset of the test functions very good (better than 0,005 digits), but still gives very large errors for small beam width (or equivalently large relative window sizes) which has to be expected according to figure 4. Similar results have to be expected using the fourier transform method.

The beam width errors obtained with the threshold method (figure 11), where a threshold of 9 digits was used, are nearly independent from the actual beam size, but dependent on the maximum power density the systematic errors are increasing from about 2 % (max 255 digits) over about 5 % (max 100 digits) up to 17 % (max 20 digits).

The statistical method gives very low statistical and systematic errors (figure 12), due to its windowing properties, which are also nearly independent from the beam size and from the maximum power density. So this method seems to

be superior compared to the other methods, which usually require an additional limitation of the integration area to reduce the possible errors. Nevertheless for the evaluation of real measurements, even when using the statistical method, it is usually necessary to apply an additional window function to the power density distribution. The possible methods for this will be discussed in the next section.

4. WINDOW FUNCTIONS

Beside a proper offset compensation, the most powerful method to reduce errors is to limit the integration domain by using a window function. In the past, mainly two different kinds of window functions have been proposed: Gaussian windows and Top-Hat windows ([11], [16] to [19]). The modified second order moment can be written as:

$$\sigma_x^2 = \frac{\iint I(x, y) \cdot W(x, y) \cdot x^2 dy dx}{\iint I(x, y) \cdot W(x, y) dy dx} \quad (5)$$

The parameters of the window-functions cannot be chosen without taking into account the properties of the actual power density distribution. Therefore, using window functions implies the use of iteration methods. For both functions the integration limits may be chosen to enclose a constant fraction of the beam power or to be constant times the beam width. In the following the properties of a rectangular Top-Hat window function, with a size of k -times the beam width will be discussed, see figure 13. Assuming a centered window and a centered distribution (the first order moments vanish), the beam diameters are then defined by the solution of the system of equations (6) to (9):

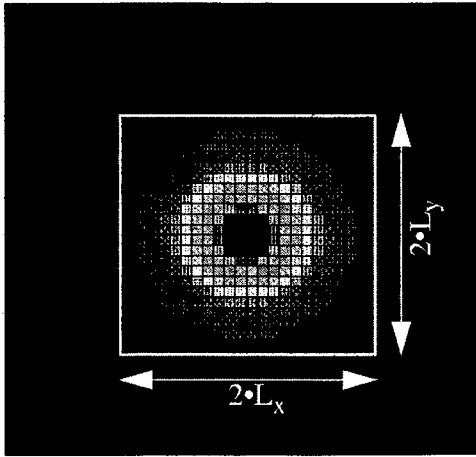


Figure 13: Rectangular Top Hat window function.

$$\sigma_x^2 = \frac{\int_{-L_x}^{L_x} \int_{-L_y}^{L_y} I(x, y) \cdot x^2 dy dx}{\int_{-L_x}^{L_x} \int_{-L_y}^{L_y} I(x, y) dy dx} \quad (6)$$

$$\sigma_y^2 = \frac{\int_{-L_y}^{L_y} \int_{-L_x}^{L_x} I(x, y) \cdot y^2 dx dy}{\int_{-L_y}^{L_y} \int_{-L_x}^{L_x} I(x, y) dy dx} \quad (7)$$

$$L_x = 2 \cdot k \cdot \sqrt{\sigma_x^2} \quad (8)$$

$$L_y = 2 \cdot k \cdot \sqrt{\sigma_y^2} \quad (9)$$

If the value of k is chosen greater than two, this system of equations has a unique solution for Laguerre-Gaussian and Hermite-Gaussian beams (nearly) independent of the choice of k . The differences to the „ordinary“ moments are less than 1 %, so no re-scaling factor is necessary. Furthermore, the result does not depend on the choice of the initial value of σ_x^2 . It is obvious that using this beam width definition the ABCD-propagation laws are valid for all beams which are shape-invariant during their propagation. Some investigations on the propagation properties of this beam width definition for diffracted beams are given below. For the evaluation of measured data k will be chosen usually between two and three.

Another question to be answered is whether the system of equations (6) to (9) is still converging when applied to measured power density distributions. The convergence in this case is mainly affected by a constant baseline offset. Introducing equation (2) in the system of equations (6) to (9) the resulting beam width can be shown to be:

$$\sigma_x^2 = \frac{3}{32} \cdot \sqrt{\frac{\sigma_{x, \text{theo}}^2}{\sigma_{y, \text{theo}}^2}} \cdot \frac{P_{L, \text{theo}}}{I_{\text{off}} \cdot k^2 \cdot (4 \cdot k^2 - 3)} \cdot \left(1 - \sqrt{1 - \frac{64}{3} \cdot \sqrt{\sigma_{x, \text{theo}}^2 \cdot \sigma_{y, \text{theo}}^2} \cdot \frac{I_{\text{off}} \cdot k^2 \cdot (4 \cdot k^2 - 3)}{P_{L, \text{theo}}}} \right) \quad (10)$$

with the assumption that, k is chosen large enough to reproduce the „real“ values for the second order moments $\sigma_{x, \text{theo}}^2$ and $\sigma_{y, \text{theo}}^2$ and the beam power $P_{L, \text{theo}}$. The convergence of the system of equations (6) to (9) is equivalent to the existence of a real and positive solution, therefore k has to be chosen according to equation (11).

$$k < \sqrt{\frac{3}{8} + \frac{3}{8} \cdot \sqrt{1 + \frac{1}{12} \cdot \frac{P_{L, \text{theo}}}{I_{\text{off}} \cdot \sqrt{\sigma_{x, \text{theo}}^2 \cdot \sigma_{y, \text{theo}}^2}}}} \quad (11)$$

A plot of this equation calculated for a Gaussian beam is shown in figure 14, where additionally the values of k are plotted which give errors of 5 % and 10 %. It can be clearly seen, that for practical values of k of about two to three, the baseline offset correction method applied must correct the offset to below one digit for an 8 bit measurement system. In figure 15 the possible error reduction applying this beam width definition is demonstrated, where the histogram method is used for offset correction and additionally a Top-Hat window with a value of $k = 2$ is applied. The evaluation of the same measurements without integration limits gave errors of up to 65 % (see figure 10), which are now reduced to about 5 %.

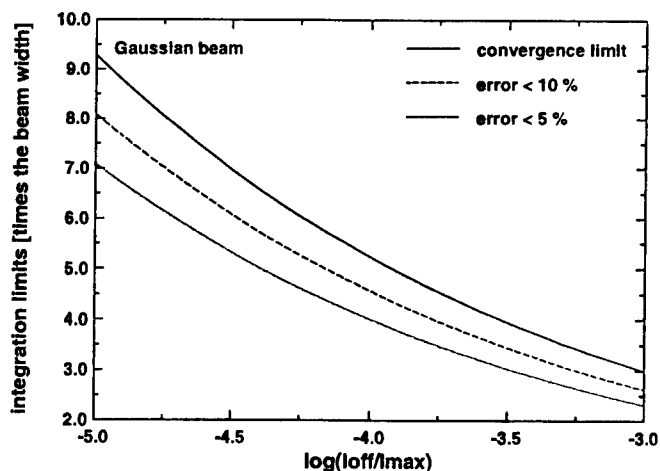


Figure 14: Convergence limit and beam width errors using a Top-Hat window function.

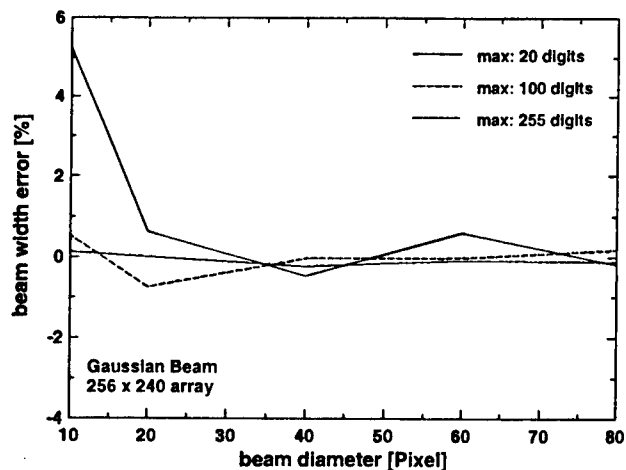


Figure 15: Error reduction using a Top-Hat window function with $k = 2$ (see figure 10).

It is well known that the influence of hard-edge diffraction yields infinite results for the second order moment of the power density distribution. So, an interesting question is, if this problem can be overcome using beam widths as defined by equations (6) to (9). Furthermore, the following questions have to be clarified:

- whether the beam propagation factor based on windowed moments remains invariant by the propagation through (nearly) lossless ABCD-systems,
- and whether windowed moments yield self-consistent results, i.e. whether data obtained at different positions can be transformed to each other by the appropriate paraxial propagation laws independent from the choice of k .

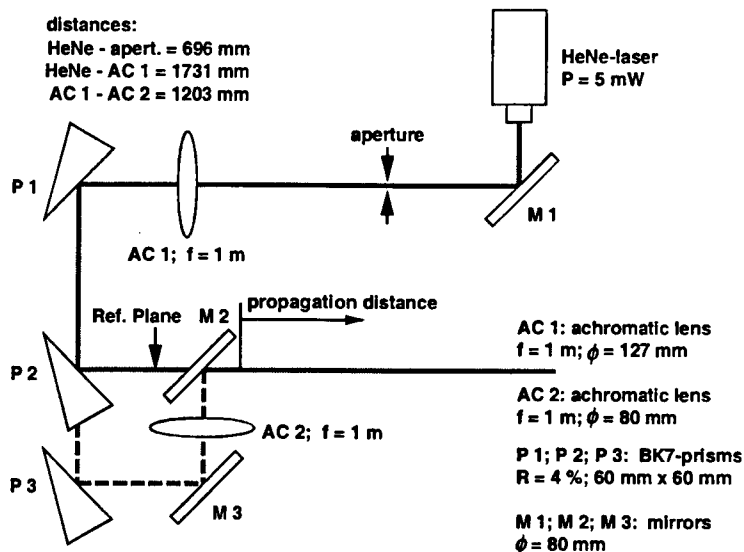


Figure 16: Experimental setup

The beam propagation measurements are performed on the propagation distance with a length of 3,5 m according to ISO/DIS 11146 using a high precision liquid nitrogen cooled 16 bit CCD camera, which has a dynamic range of 10^5 (single shot) and a dark current of only one electron per pixel and hour. The theoretical values are obtained by Kirchhoff-Fresnel calculations of the power density distribution and subsequent evaluation of the data according to equations (6) to (9).

To answer these questions experimental and theoretical investigations have been done ([18], [19]). Figure 16 shows the optical setup used for the measurements and the calculations.

As a beam source a 5 mW HeNe-laser with a semi-confocal resonator was used. The beam is specified to be TEM_{00} with a waist width of $800 \mu m$. A first beam caustic is generated by an aberration corrected achromatic lens AC1 with a focal length of $f = 1000$ mm. To investigate whether the ABCD-laws are valid a second beam caustic can be examined, that is generated by the achromatic lens AC2, which has again a focal length of $f = 1000$ mm.

For the systematic investigation of the propagation properties of windowed moments diffraction effects were created by introducing three different circular apertures, which were mounted between the laser and the achromatic lens AC1. The apertures are chosen so that 1,5 %, 5,9 % and 14,1 % of the total beam power are truncated.

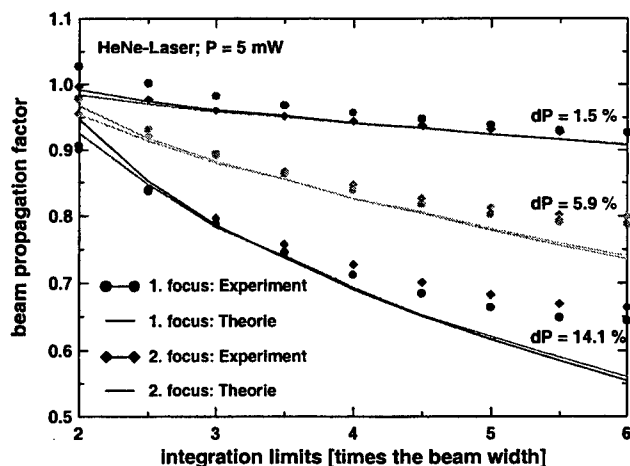


Figure 17: Beam propagation factors obtained for the different diffracted beams on the two beam caustics.

The results of these experimental and theoretical investigations are summarized in figure 17, where the beam propagation factors obtained for the first and second beam caustic are compared. The results show a reasonable agreement, even if slightly systematic deviations depending on the size of the integration area can be observed. For large integration areas the measured values are always greater than the theoretical calculated beam propagation factors, which is due to the limited resolving power of the CCD-camera. If the beam propagation factors measured on the first and the second beam caustic are compared the overall maximum error is below 3 %, the deviations between theoretical data obtained for the first and second caustic are below 1 %, which holds for the other beam propagation parameters as well. Taking into account all these results, it can be concluded that for the moments, as defined by equations (6) to (9), the ABCD-laws nearly hold, independent from the chosen integration limits. The achievable accuracy of a propagation calculation seems to be sufficient for most practical applications.

5. Results of „Round-Robin“ experiments

In 1996 and 1997 four different „Round Robin“ experiments on laser beam characterization were performed within the CHOCLAB project, with up to ten participants from research facilities and industrial companies from all over Europe. The main goal of these „Round Robin“ experiments was to test the applicability of the proposed standard measurement procedures to different important types of industrial laser devices (in particular high power CO₂-lasers and pulsed Nd:YAG-lasers) ([20], [21], [22]). In the following the results of a „Round Robin“ experiment held at the IFSW in Stuttgart will be discussed.

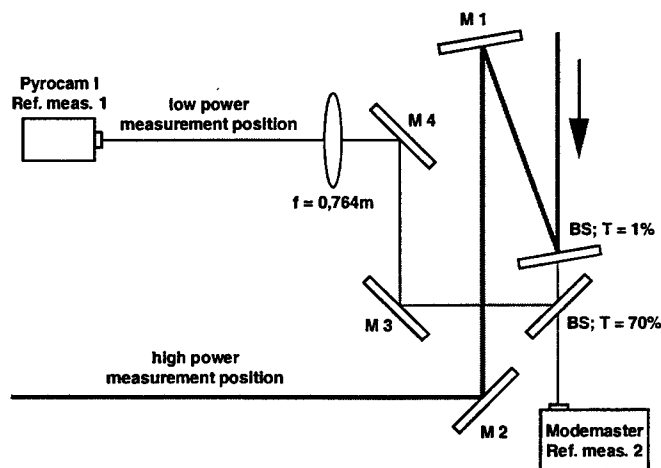


Figure 18: Experimental setup

The laser beam source under investigation was a Trumpf TLF1500 industrial CO₂-laser (hf-excited, fast axial flow) with a maximum output power of 1,5 kW where for the measurements an output power of 1,0 kW was used. The experimental setup which was used on the workshop is shown in figure 18. The laser beam is sampled by two beam splitters so that two low power beams and one high power beam can be investigated. The low power beams, with beam powers of 3 W and 7 W respectively, were used for the reference measurements. Participants made their measurements at the high power beam with a beam power of 0,99 kW (high power measurement position). Every optical element in the high power beam path was water cooled to minimize thermal distortion. The maximum beam diameter in the setup was below 18 mm. In order to avoid diffraction effects, the diameter of the optical elements was chosen to be at least 63,5 mm. The comparability of the results was ascertained by reference measurements which were performed during the measurements of each participant.

In this experiment ten partners from industrial companies and research facilities took part, which used the most common industrial devices for CO₂ laser beam characterization: the Prometec UFF 100, the Primes FocusMonitor, the IPU Modemaster, Spiricon Pyrocam I and the Coherent ModeMaster. Besides the different methods for data acquisition, the partners used different methods for determining laser beam parameters; this concerns especially the necessary background correction before calculating the beam width. The applied baseline offset correction procedure will be indicated in the following for each measurement result, since this may influence strongly the evaluated beam parameters. The participants in this experiment were supposed to use different beam diameter definitions, one power content based

86%-encircled-energy diameter				Second moment beam width			
measurement device	K_r	Comment	Ref. K_r	measurement device	K_r	Comment	Ref. K_r
Offset correction before recording the power density distribution							
UFF 100 A	0,579	device offset	0,533	UFF 100 A	0,424	device offset	0,533
UFF 100 B	0,541	device offset	0,524	UFF 100 B	0,343	device offset	0,524
UFF 100 C	0,546	device offset	0,515	UFF 100 D	0,430	device offset	0,521
UFF 100 D	0,512	device offset	0,521	UFF 100 F	0,650	device offset	0,532
UFF 100 E	0,569	device offset	0,526	UFF 100 E	0,486	device offset	0,526
mean	0,549		0,524	mean	0,467		0,527
std. dev. [%]	4,8		1,3	std. dev. [%]	24,5		1,0
Offset correction by evaluating the power density distribution							
UFF 100 D	0,523	threshold 2% of max.	0,521	UFF 100 A	0,496	fourier transform	0,533
FocusMonitor A	0,550	fit to histogram	0,522	UFF 100 D	0,612	threshold 2% of max.	0,521
FocusMonitor B	0,560	fit to histogram	0,532	FocusMonitor A	0,480	fit to histogram	0,522
				Modcamera	0,533	Butterworth filter	0,500
				Pyrocam I	0,534	non-illuminated pixels	0,521
				ModeMaster	0,584	calc. from knife-edge beam width	
mean	0,544		0,525	mean	0,540		0,519
std. dev. [%]	3,5		1,2	std. dev. [%]	9,4		2,3

Table 1: Measured beam propagation factors of a high power CO₂-laser (left: based on the 86%-encircled-energy diameter; right: based on the second moment beam width definition).

beam width (86%-encircled-energy diameter), which is less sensitive to noise, and the second order moment beam width. The resulting beam propagation factors based on the different beam width definitions are summarized in table 1.

The results of the reference measurements (based on the moving knife edge definition) given in table 1 prove the good stability of the laser beam parameters during the entire period (peak to peak < 7 %, std. dev. 2,3 %) of the „Round-Robin“ experiment. The results of the offset correction methods, which record the offset before acquiring the power density distribution give significantly higher noise compared to offset correction methods which determine the offset by evaluating the measured power density distribution. Furthermore, the resulting beam propagation factors are always somewhat smaller, which indicates that in general the baseline offset is a bit higher with the laser beam incident on the device (caused by incoherent and/or scattered light) and therefore the second order moment beam width is increased. A good agreement of the results can be stated, if the 86%-encircled energy diameter is used as the beam width definition. The uncertainty of the second order moments is a bit larger, which is mostly caused by the different methods for background correction. Therefore the ISO/DIS 11146 should give more detailed and precise provisions as to how background correction has to be done. It can then be expected that the 5% measurement uncertainty can be achieved.

6. CONCLUSIONS

The EUREKA-project „CHOCLAB“ aims to support the standardization efforts in the field of laser beam and laser optics characterization. This goal is to be achieved by pre-normative research and by testing the draft international standards with „Round-Robin“ experiments. From the beginning of the project one of the most important work items has been ISO/DIS 11146, the standard which defines the measurement procedures for the determination of laser beam propagation properties. This standard, the different beam width definitions as well as the different principles for the measurement of beam widths, i. e. optical and numerical integration, have been briefly reviewed.

The reliability of beam parameters obtained by evaluating measured power density distributions, may be affected by several potential sources of errors. In order to minimize measurement errors, image distortions and other measurement errors of the power density distributions have to be corrected. Furthermore the integration domain, which is taken into account in beam

width calculations has to be limited by using window functions, for example Gaussian windows or Top-Hat windows. The possible error reduction and the basic properties of the modified second order moment beam width, when applying a Top-Hat window, have been discussed.

Finally the results of a „Round-Robin“ experiment were presented. Dependent on the used beam width definition and on the applied error correction procedures, very large differences between the results of different participants could be observed. Therefore the ISO/DIS 11146 should give more detailed and precise provisions on procedures for error correction.

7. ACKNOWLEDGMENTS

This work was supported by the Bundesministerium für Forschung und Technologie under contract 13 EU 0138/2, within the frame of EUREKA EU 1269 (CHOCLAB).

8. REFERENCES

- [1] ISO/DIS 11146: Test methods for laser beam parameters: Beam width, divergence angle and beam propagation factor.
- [2] ISO/DIS 11670: Test methods for laser beam parameters: Beam positional stability.
- [3] ISO/WD 13694: Test methods for laser beam parameters: Power (energy) density distribution.
- [4] ISO/DIS 11554: Test methods for laser beam parameters: Power, energy and temporal characteristics.
- [5] ISO/DIS 12005: Test methods for laser beam parameters: Polarization.
- [6] Y. Champagne, et. al., „On the use of filters with transverse parabolic transmittance for measuring the spatial variance of laser beams“, in *Laser Beam Characterization*, H. Weber, et. al., editors, (FLI, Berlin, 1994), p. 17.
- [7] J. Alda, et. al., „Measurement of the moments of laser beams by means of polynomial transmissivity windows“, in *Laser Beam Characterization*, H. Weber, et. al., editors, (FLI, Berlin, 1994), p. 30.
- [8] M. W. Sasnett, et. al., „Techniques for measuring the moments of laser beam irradiance distributions“, in *Beam Control Diagnostics, Standards and Propagation*, L. W. Austin, et. al., editors, Proc. SPIE 2375, p. 214 (1995).
- [9] C. B. Roundy, et. al., „Compensating for performance deficiencies of CCD and VIDICON cameras for laser beam diagnostics applications“, in *Laser Beam Characterization*, P.M. Mejias, et. al., editors, (SEDO, Madrid, 1993), p. 381.
- [10] P. Apte, et. al., „Computational methods for beam amplitude characterization“, in *Laser Beam Characterization*, H. Weber, et. al., editors, (FLI, Berlin, 1994), p. 57.
- [11] C. Maier, et. al., „Test of the Standardization Draft of ISO/CD 11146 for industrial laser systems“, in *Beam Control Diagnostics, Standards and Propagation*, L. W. Austin, et. al., editors, Proc. SPIE 2375, p. 375 (1995).
- [12] B. Eppich, „Measurement of beam parameters with 2d matrix camera arrays“, in *Third international workshop on Laser Beam and Optics Characterization*, M. Morin, et. al., editors, Proc. SPIE 2870, p. 31 (1996).
- [13] B. Eppich, personal communication.
- [14] M. Scholl, H. Müntz, personal communication.
- [15] J. R. Taylor, „An introduction to error analysis“, University Science Books, Mill Valley, 1982.
- [16] C. Pare, et. al., „Propagation law and quasi-invariance properties of the truncated second order moment of a diffracted laser beam“, in *Optics Communications* **123** (1996), p. 679.
- [17] M. Scholl, et. al., „Description of diffracted beams by weighted moments“, in *Third international workshop on Laser Beam and Optics Characterization*, M. Morin, et. al., editors, Proc. SPIE 2870, p. 112 (1996).
- [18] R. Mästle, et. al., „Characterization of hard-edge diffracted beams“, in *Third international workshop on Laser Beam and Optics Characterization*, M. Morin, et. al., editors, Proc. SPIE 2870, p. 123 (1996).
- [19] F. Varnik, et. al., „Measurement of moments for diffracted beams: Comparison with theory“, in *Fourth international workshop on Laser Beam and Optics Characterization*, in press.
- [20] H. Bartels, et. al., „Beam characterization of an industrial CO₂-laser: results of a workshop within the EUREKA project EU-1269 „CHOCLAB“, in *Third international workshop on Laser Beam and Optics Characterization*, M. Morin, et. al., editors, Proc. SPIE 2870, p. 306 (1996).
- [21] U. Habich, et. al., „Evaluation of camera data: Results of a Round Robin Test“, in *Fourth international workshop on Laser Beam and Optics Characterization*, in press.
- [22] R. Mästle, et. al., „Results of two „Round Robin“-experiments on laser beam characterization within the EUREKA-project EU-1269 „CHOCLAB“, in *Fourth international workshop on Laser Beam and Optics Characterization*, in press.

Laser frequency comparisons involving Romanian length standard
and traceability

Gheorghe Popescu, * Jean-Marie Chartier, ** Fabrizio Bertinotto, *** Frantisek Petru

National Institute for Lasers, Plasma and Radiations Physics, Lasers Department, P.O.Box MG-36,
Bucharest 76 900, Romania

* Bureau International des Poids et Mesures, Pavillon de Breteuil, F-92312 Sevres Cedex, France

** Instituto di Metrologia " G. Collonetti ", Strada d. Cacce 73, 10135 Torino, Italia

*** Institute for Scientific Instruments, Kralovopolska 147, 612 64 Brno, Czech Republic

ABSTRACT

We present final results from four laser frequency comparisons involving the following He-Ne / Iodine lasers operating at wavelength $\lambda = 633 \text{ nm}$: the laser RO.2 from the National Institute for Physics of Lasers, Plasma and Radiation (Romania); the laser BIPM4 from the Bureau International des Poids et Mesures (France); the laser IMGC4/5 from the Institute for Metrology "Gustavo Collonetti" (Italy); the laser INVAR3 from the Institute for Scientific Instruments (Czech Republic); the laser NMS121 from the National Standards Laboratory (Norway). We report the results coming from matrix determinations on the lines d, e, f, g and then, by reducing all mean frequency differences to the same reference laser (BIPM4), we presented them as frequency traceability of a laser through that of the reference laser.

Keywords; metrology, fundamental units, laser frequency comparisons, traceability

1. INTRODUCTION

The adoption of the present definition of the metre¹ by the 17th Conference Generale des Poids et Mesures in 1983 allowed to the Comite International des Poids et Mesures (CIPM) to draw up recommendations for the practical realization of the definition, known as *mise en pratique* of the new definition of metre.

The definition was updated to take account of new measurements and improvements in techniques of laser stabilization in 1992. The CIPM decided to revise the 1983 *mise en pratique* and new recommendations were released. *Recommendation 3(CI-1992)* was adopted by CIPM at its 81st Meeting in October 1992 and it includes a list of recommended radiations². The values of frequency and wavelength given in the new list have considerably smaller uncertainties associated with value given in 1983. It worth to note that the values of the frequency f and of the wavelength λ are related exactly by the relation $\lambda f = c$, with $c = 299\,792\,458 \text{ m/s}$, but the values of λ are rounded.

It should be noted that each of the listed radiations can be replaced, without degrading the accuracy, by a radiation corresponding to another component of the same transition or by another radiation, when the frequency difference is known with sufficient accuracy.

One of the three methods specified for the practical realisation of the metre uses molecular transitions, six of them representing hyperfine transitions of $^{127}\text{I}_2$ iodine molecule. For many known reasons (as its wide commercial availability, its emission in the visible and the possibility of mechanical compactness) He-Ne lasers operated at 633 nm wavelength and frequency stabilized by saturated absorption in $^{127}\text{I}_2$, transition 11-5, R(127) are built in many laboratories all over the world and many nations are in the process of replacing their national length standards by iodine / He-Ne frequency stabilized lasers. Such a standard has been built at the National Institute for Laser, Plasma and Radiation Physics (NILPRP, former IFTAR).

The usual method used to stabilise a He-Ne laser with an iodine absorption cell placed inside the laser cavity is the third derivative technique³, where by modulating the laser frequency through the saturated absorption of the iodine vapour, a signal at three times the modulation frequency is detected to give a third derivative profile. By using the zero-crossing of line profile it is possible to stabilise the laser frequency very precisely onto a hyperfine component of the transition R(127) 11-5 of the $^{127}\text{I}_2$ molecular iodine, which precision then determines the precision of the frequency of the laser radiation.

2. FREQUENCY DIFFERENCE MEASUREMENTS

Such primary length standards are more technically complicated and their frequencies are vulnerable to uncontrolled perturbations and system malfunctions, so that a regular verification of its performance for reliable applications is made through international comparisons. The main objective of such a comparison is to verify the performance of each participating laser as a frequency standard, while operating properly under the specifications of the Recommendation 3 (CI-1992) /3/.

The Romanian laser RO.2 was used for frequency comparisons during measurements held at the Institute for Metrology "Gustavo Colonetti" (IMGC), Torino, Italy in 1994 (the compared laser: IMGC4/5), at the Bureau International des Poids et Mesures (BIPM), Paris-Sevres, France in 1995 (the compared lasers: BIPM4 and NMS121) and at the Institute for Scientific Instruments (ISI) Brno, Czech Republic in 1996 (the compared laser: INVVAR3).

It is important to assess the sensitivity of the frequency of each laser to the factors known to cause changes of frequency⁴. All measurements are made by the beat frequency technique which provides a very sensitive means of determining the behaviour of the stabilized lasers. Results from such determinations are used when some values of the laser parameters are slightly different from those in Recommendation 3(CI-1992).

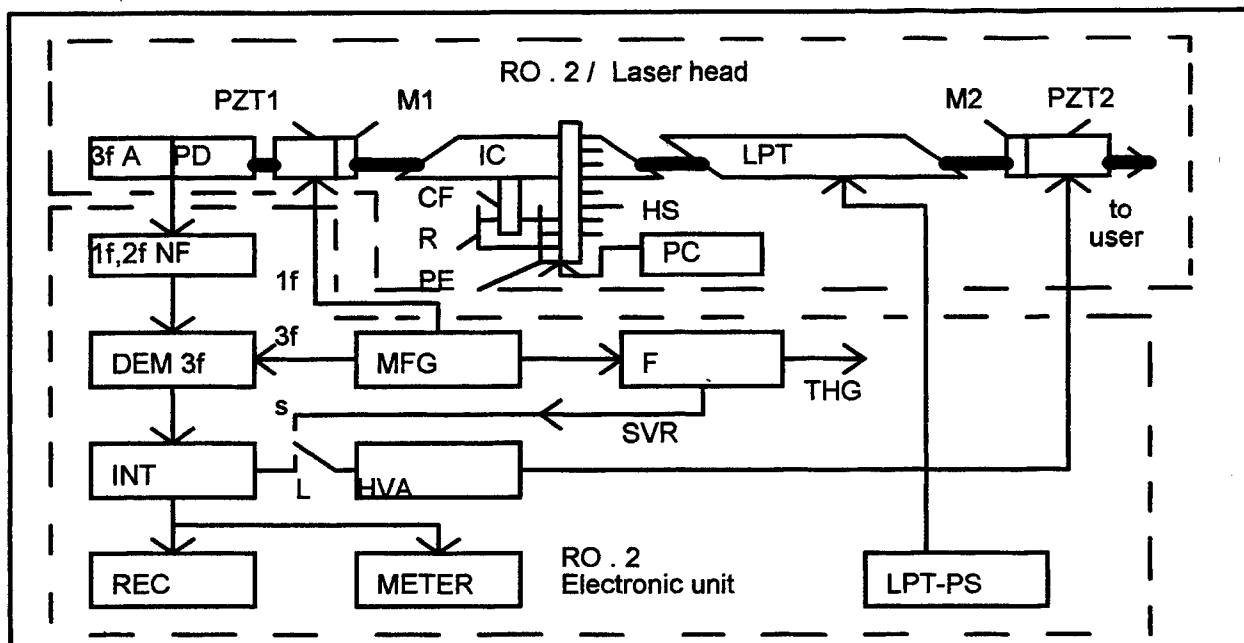


Figure 1. Diagram of the RO.2 laser head and electronic unit. 3f A, PD - selective detection on third harmonic; 1f, 2f NF - active notch filters; DEM 3f - synchronous detection on third harmonic; MFG - multiple function generator; INT - double integrator; HVA - high voltage amplifier; PZT1, PZT2 - piezoelectric transducers; M1, M2 - laser mirrors; LPT - laser plasma tube; LPT-PS - laser power supply; IC - iodine cell; C - cold finger; PE - Peltier-type cooler; PC - temperature controller; HS - heat sink; F - additional functions.

We present shortly details about the laser RO.2. The configuration of the laser head is based on a structure formed from three invar rods placed symmetrically around the optical axis of the discharge tube. The discharge tube is home made and it consists of a capillary tube (Pyrex glass; 190 mm long with 120 mm active discharge length) having Brewster windows at end parts and two large lateral reservoirs for longer life time. The iodine cell is BIPM 108 and its quality was checked at the BIPM. The laser cavity is protected by three dumping stages against mechanical vibrations. A light aluminium cover protects the laser head.

Both a current-stabilized high-voltage power supply for the plasma discharge tube and a servo-control system for the laser frequency stabilization form a separate electronic unit. The principle of the arrangement of the electronic circuits

of the iodine-laser RO.2 is shown in Figure. 1. Only a selective amplifier tuned on the third harmonic of the modulation signal (3f A, PD) and the circuits for the iodine cell cold finger temperature control (PC) are located inside of the laser head . Some additional circuits (F) are provided for adjusting selective amplifiers before measurements .

More details about lasers and their principal parameters could be found in the references^{5, 6, 7, 8}.

During the laser frequency comparison the largest possible number of frequency difference determinations was sought. A number of 23, 13, 10 and 2 frequency difference determinations were performed when the laser RO.2 was respectively compared with the laser IMGC4/5, the laser BIPM4, the laser INVAR3 and the laser NMS121.

One frequency determination consisted of a " matrix measurement " ⁹ in which the frequency intervals for all the combinations of the components d, e, f, g with the exception of the main diagonal of the matrix (which corresponds to the frequency intervals in which the lasers are stabilized on the same component) were measured . The frequency difference between the two lasers was then taken as the average of half of the differences of the symmetrical values obtained in the matrix .

The mean value of a number of independent matrix determinations on the group of lines d, e, f, g was computed when consider the frequency of the laser RO.2 as reference and the results are as follows :

$$\Delta\nu = \nu_{\text{RO.2}} - \nu_{\text{IMGC4/5}} = + 3.8 \text{ kHz ;}$$

$$\Delta\nu = \nu_{\text{RO.2}} - \nu_{\text{BIPM4}} = - 2.2 \text{ kHz ;}$$

$$\Delta\nu = \nu_{\text{RO.2}} - \nu_{\text{INVAR3}} = - 15.1 \text{ kHz ;}$$

$$\Delta\nu = \nu_{\text{RO.2}} - \nu_{\text{NMS121}} = -3.5 \text{ kHz .}$$

The conditions stated by Recommendation 3(CI-1992) " are by themselves insufficient to ensure that the stated standard uncertainty will be achieved. It is also necessary for the optical and electronic control system to be operating with the appropriate technical performance " ². Three from four frequency difference measurements have values inside the limits set for the estimated relative standard uncertainty of 2.5×10^{-11} , that represents an absolute frequency difference of 12.5 kHz, while the frequency difference for the measurements held at ISI proved to have a slightly larger value. We call for that difference as a first possible cause, the differences in absorption cell processing and filling procedures.

The frequency characteristics of a laser used as length standard are conventionally stated in terms of repeatability, reproducibility and stability, following the nomenclature recommended by the ISO ¹⁰.

Repeatability measurements were made by taking frequency difference measurements at intervals ranging from hours to days while keeping the parameters of the lasers as constant as possible. The modulation amplitude, iodine cell cold finger temperature, laser power and electronic offset were checked and adjusted as required before starting the set of independent matrix determinations.

Results from three frequency difference determinations involving the laser RO.2 are presented in Figure 2. Under the title *rough determination* we denominate the value before corrections has been applied for laser parameters known to cause laser frequency changes (when available, they were used for each laser comparison).

The standard deviation of the series of frequency difference measurements is taken as the frequency repeatability of each laser. The statistics of the above mentioned sets of 23 , 13, 10 or 2 independent measurements gives the following repeatability of the laser frequency measurements at IMGC, BIPM or ISI, respectively :

$$R [\text{RO.2} - \text{IMGC4/5}] = 5.7 \text{ kHz}$$

$$R [\text{RO.2} - \text{BIPM4}] = 6.7 \text{ kHz}$$

$$R [\text{RO.2} - \text{INVAR3}] = 2.5 \text{ kHz}$$

$$R [\text{RO.2} - \text{NMS121}] = 3.0 \text{ kHz}$$

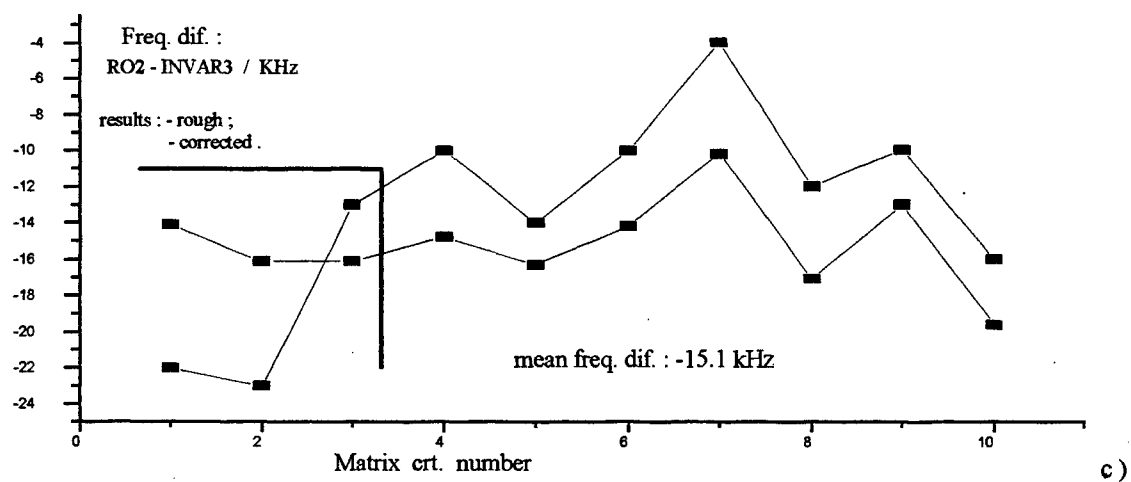
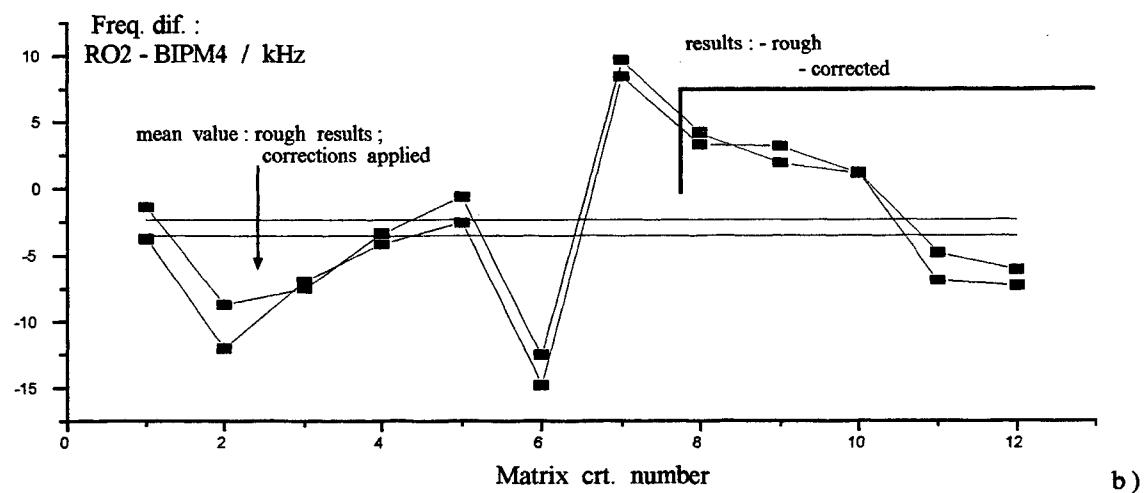
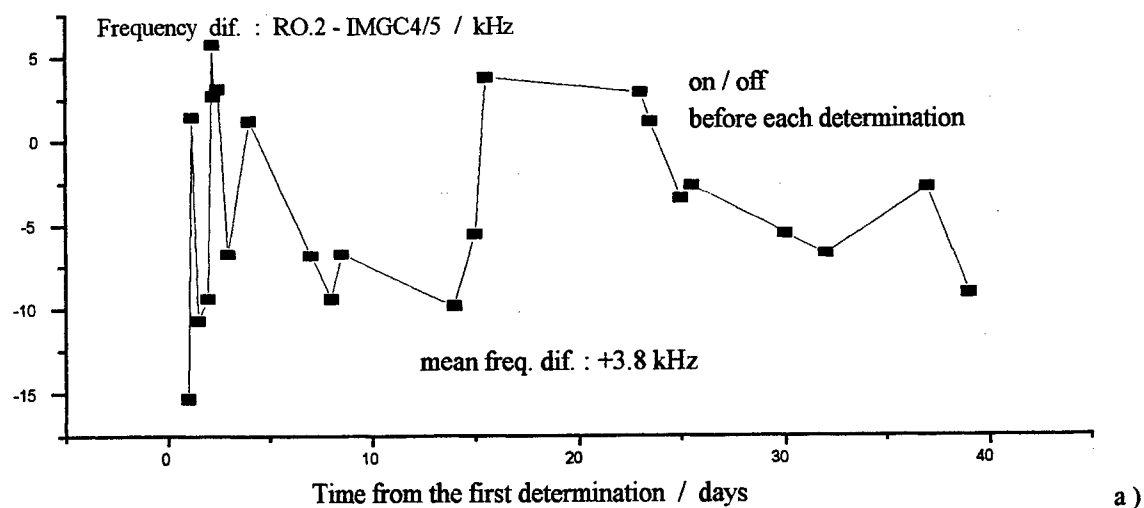


Figure 2. Frequency difference measurements considering the lasers " RO.2 - IMGC4/5 (a), RO.2 - BIPM4 (b) and RO.2 - INVAR3 (c). Matrix determinations on lines d, e, f, g.

3. FREQUENCY STABILITY MEASUREMENTS

The frequency stability of the lasers is characterized by the two consecutive samples variance called Allan variance¹¹. Usually, it is the square root of the variance normalized to the frequency which is given for different sampling times. In a logarithmic diagram, the representative curve presents, for low values of the sampling times a slope of -1/2 due to the white noise and, for higher values of the sampling times, a plateau due to flicker noise.

The frequency stability of the lasers was measured taking sampling times from 1 s to 3000s, and total times for

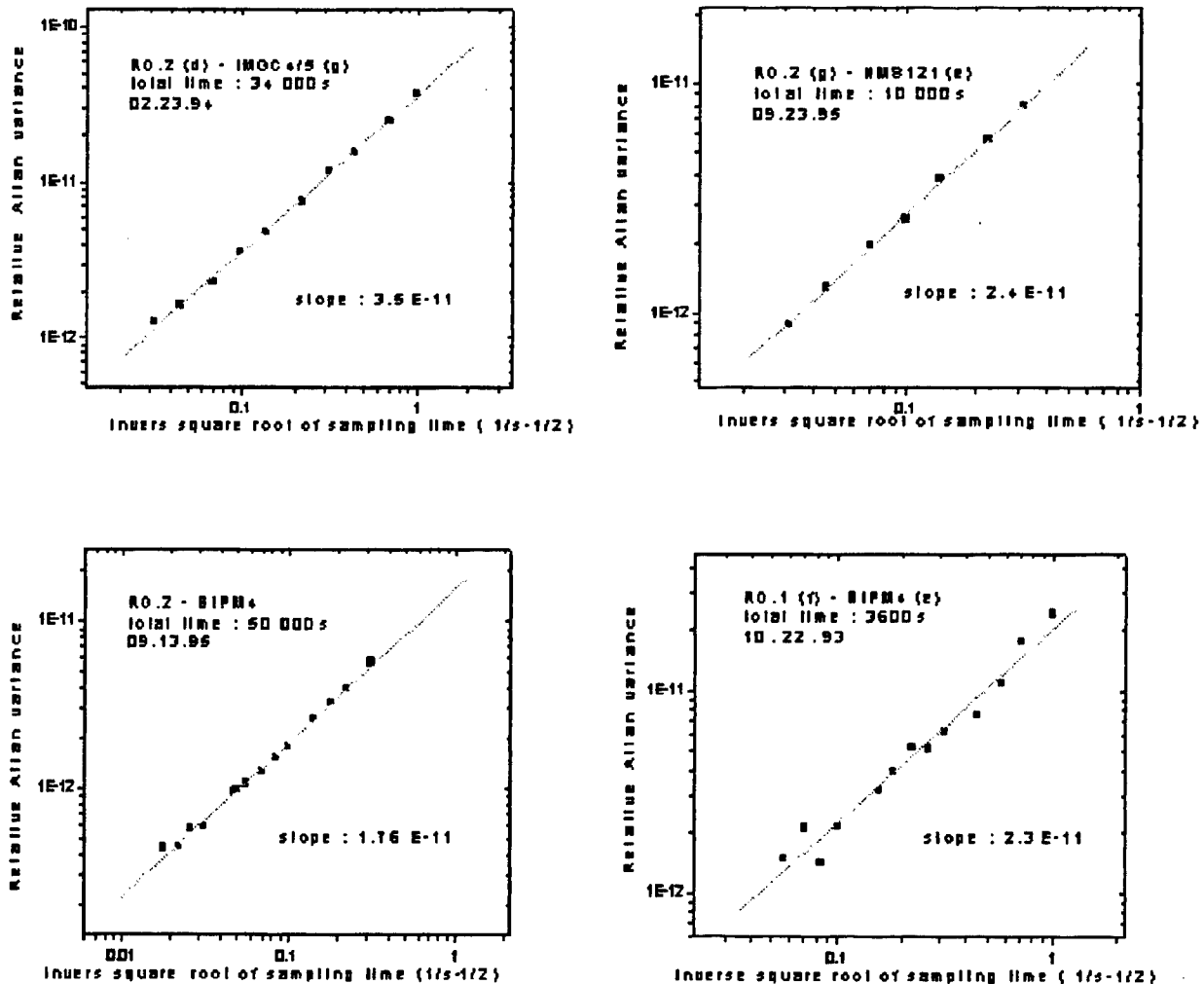


Figure 3. Frequency stability diagrams from comparisons involving Romanian length standards.

measurements from one hour to fourteen hours. A double logarithmic fitting gives the following linear expression for the relative Allan variance as a function of the inverse of the square root of the sampling time:

$$\sigma(v)/v = A + B \cdot \tau^{-1/2}.$$

Results regarding the frequency stability from four comparisons involving the lasers RO.1 and RO.2 are presented in Figure 3. In the frame of each graph, the value of B from the above equation is specified as the slope of a linear fitting to the experimental values. For long sampling times τ , one gets information about the limit value expected for the frequency stability. In our case, the limit A had values between $1.7 \cdot 10^{-14}$ and $6.4 \cdot 10^{-13}$, that could be considered as the above mentioned plateau.

4. FREQUENCY TRACEABILITY THROUGH BIPM LASERS

As a result of the adoption of the new *mise en pratique* of the definition of the metre in 1992, a lot of laser comparisons at wavelength 633 nm were carried out by involving bilateral or grouped comparisons¹². From the above mentioned frequency differences one could see their values lay inside the standard uncertainty (2,5 parts in 10^{11} , or as absolute frequency 12,5 kHz) as given in the *mise en pratique*.

The frequency differences between lasers without or with corrections applied for the factors known to cause changes of the laser frequency (the modulation amplitude, the iodine temperature or vapour pressure and the intracavity power) are presented as diagram Figure 4 or as a graph in Figure 5.

One good objective of frequency comparison involving lasers from three laboratories could be to verify the closing frequency of the bilateral comparisons.

In the upper half of the figure 4 are presented the frequency differences measured in bilateral comparisons between different laboratories and the BIPM. The mean frequency differences were computed from matrix measurements on the lines d, e, f, g.

In the lower half of the same figure are presented both the measured frequency difference from bilateral comparisons and the expected frequency differences as they results from considering the traceability through the BIPM lasers (calculated values considering previous bilateral comparisons).

It is worth to observe the small differences between measured value of the frequency difference from bilateral comparison and expected value calculated from bilateral comparisons with the reference laser BIPM4 for all three measurements where the laser RO.2 was involved :

- for the comparisons involving the lasers: RO.2, IMGC4/5 and BIPM4, the closing frequency is :

$$\Delta\nu_{\text{measured}} - \Delta\nu_{\text{expected}} = + 0,1 \text{ kHz ;}$$

- for the comparisons involving the lasers: RO.2, NMS121 and BIPM4, the closing frequency is :

$$\Delta\nu_{\text{measured}} - \Delta\nu_{\text{expected}} = -3,8 \text{ kHz ;}$$

- for the comparisons involving the lasers: RO.2, INVAR3 and BIPM4, the closing frequency is :

$$\Delta\nu_{\text{measured}} - \Delta\nu_{\text{expected}} = -4.4 \text{ kHz ;}$$

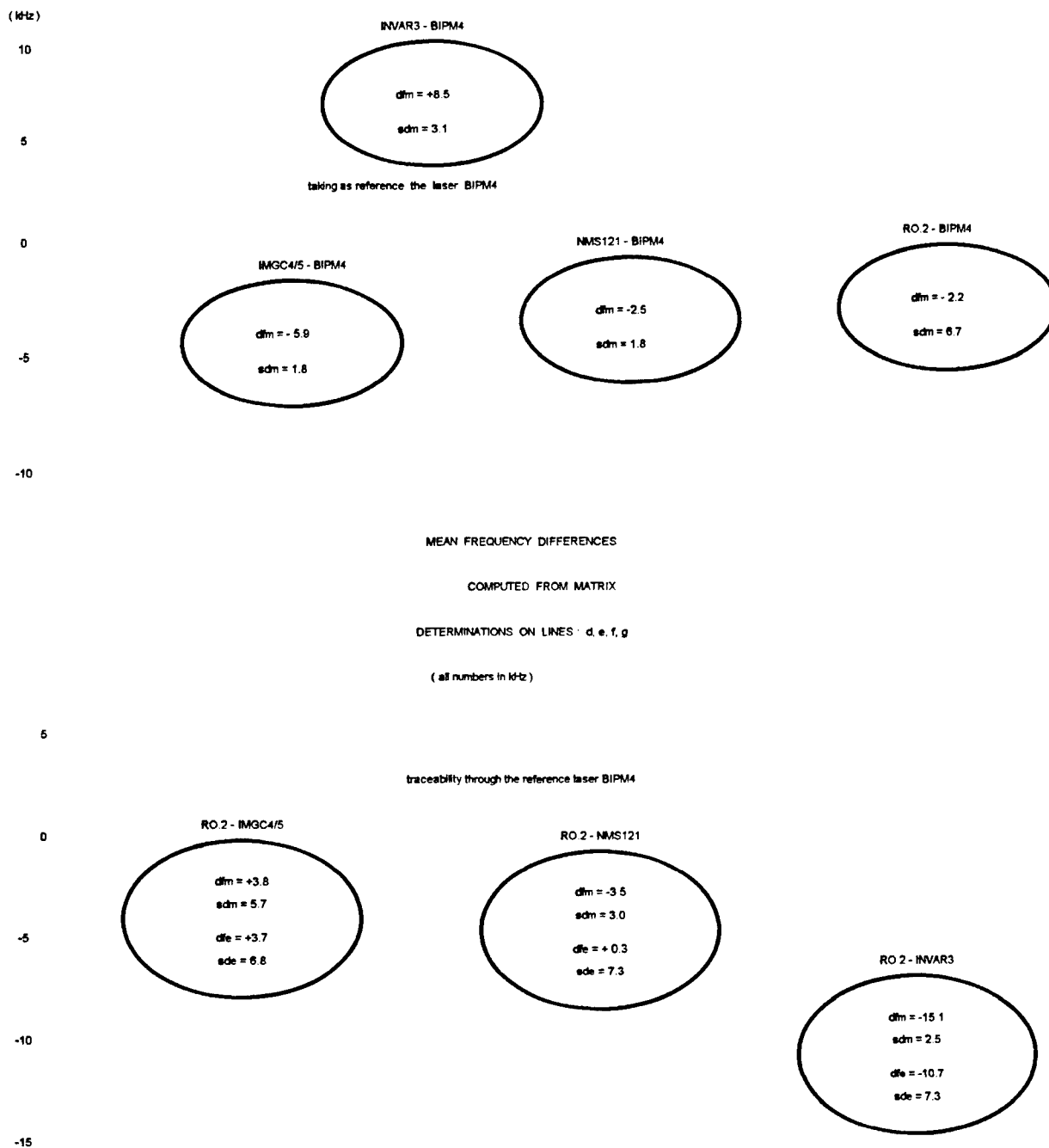


Figure 4. Frequency differences and traceability through the laser BIPM4. (dfm - frequency difference measured in bilateral comparison; sdm - standard deviation associated with the measured frequency difference dfm; dfe - frequency difference expected from previous comparisons with the reference laser BIPM4; sde - standard deviation associated with expected frequency difference dfe)

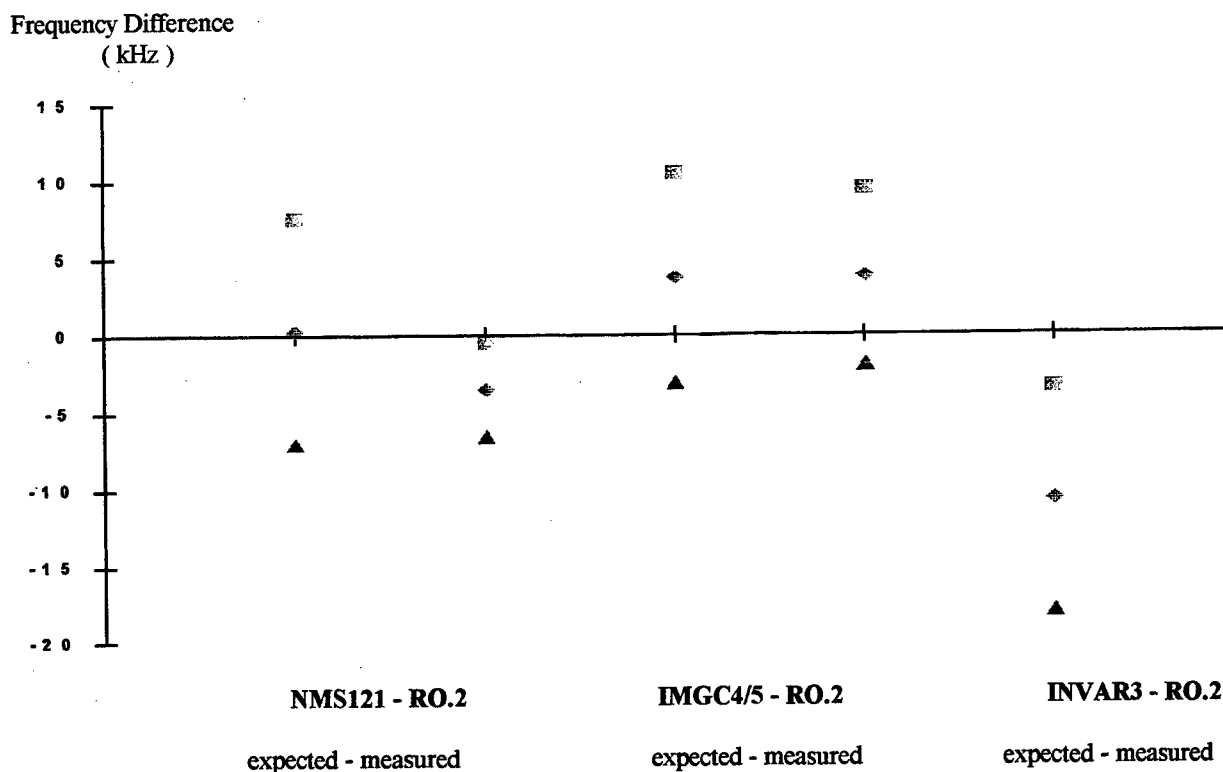


Figure 5. Frequency differences : measured and expected values as traceability through the BIPM lasers.

The higher standard deviations associated with the frequency difference expected values are in principle due to the standard deviation of the measured value of the laser RO.2 in bilateral comparisons. Also, we mention the time interval between first and last bilateral comparisons as part of this report: February 1994 - July 1996.

5. CONCLUSIONS

In the course of the systematic work of international laser comparisons a rich resource is being built up for future analysis. The extended picture thus obtained provides information valuable in revealing the ultimate of this type of laser standards. International comparisons^{12, 13} are also essential to test the reliability of national standards. This is especially true for laboratories which have recently introduced stabilized lasers as primary length standard; it is also a good example of transfer of technology by scientific exchange.

The comparisons of the NILPRP lasers against the BIPM, IMGC, ISI and NMS lasers show frequency differences within the limits predicted by the Recommendation 3(CI-92) of 12,5 kHz except for the frequency difference reported from the comparison held at the ISI.

The measurements also revealed a good traceability with other previous comparisons against the BIPM lasers. The closing frequency for three groups involving the NILPRP laser RO.2 were in the same low limits (frequency differences from + 0,1 kHz to - 4,4 kHz were reported between measured and expected values).

It was proved that even considering results obtained under various technical conditions and obtained at different locations and more than two years prior to the last mentioned bilateral comparison, lasers from the participating laboratories have preserved their performances near the limits set by last released documents² in order to be considered valid *mise en pratique* of the new definition of the metre.

Regarding the frequency stability measurements we should specify that there was a significant difference between previous results reported by NILPRP and ISI, but all the other reports give a good frequency stability, the flicker noise setting a limit around 5 parts in 10^{+13} , that is a value reported also in other international comparisons.

6. REFERENCES

1. BIPM Comptes Rendus 17th Conf. Gen. Poids et Mesures, p. 45-49, 97-98, (1983) ; Documents Concerning the New Definition of the metre, *Metrologia* 19, p. 163-177, (1984) ;
2. T. J. Quinn, " Mise en Pratique of the definition of the metre ", *Metrologia* 30, 523-541 (1993 / 1994)
3. A. J. Wallard, " Frequency stabilization of the helium-neon laser by saturated absorption in iodine vapour ", *J. Phys. E: Sci. Instrum.* 5, 926-930 (1972)
4. J. -M. Chartier, J. Helmcke, A. J. Wallard, " International intercomparison of the wavelength of iodine - stabilized lasers ", *IEEE Trans. Instrum. Meas.* IM-25, p.450-453, (1976) ;
5. F. Bertinotto, P. Cordiale, Gh. Popescu, " Preliminary results of the frequency comparison between iodine stabilized lasers at 633 nm from IMGC and IFA-IFTAR ", *Proc. SPIE* 2461,551-554 (1995)
6. Gh. Popescu, J. -M. Chartier, A. Chartier, " Iodine stabilized laser at $\lambda = 633$ nm : design and international comparison ", *Opt. Eng.* 35 (5), p.1348-1352, (1996) ;
7. J. de Vicente, A. M. Sanchez-Perez, F. Bertinotto, " Comparison of He-Ne lasers from the LMM and the IMGC stabilized on $^{127}\text{I}_2$ at 633 nm ", *Metrologia* 30, p.503-506, (1993) ;
8. F. Petru, B. Popela, Z. Vesela, " Iodine -stabilized He-Ne lasers at $\lambda = 633$ nm of a compact construction ", *Metrologia* 29, p. 301-307, (1992) ;
9. F. Bayer-Helms, J.-M. Chartier, A. J. Wallard, " Evaluation of the international intercomparison measurements (March 1976) with $^{127}\text{I}_2$ -stabilized He-Ne lasers: spacings of the hyperfine structure components ", *PTB-Bericht PTB-ME 17*, 139-146 (1977) ;
10. International Vocabulary of Basic and General Terms in Metrology, ISO 3, 15 (1984) ;
11. D. W. Allan, " Statistics of atomic frequency standards ", *Proc. IEEE* 54, 221-231 (1966) ;
12. T. J. Quinn, " Results of recent international comparisons of national measurement standards carried out by the BIPM, 1996 ", *Metrologia* Vol. 33, 271-287, (1996).
13. J.-M. Chartier, H. Darnedde, M. Frennberg, J. Henningsen, U. Karn, L. Pendrill, Jianpei Hu, J. C. Petersen, O. Poulsen, P. S. Ramanujam, F. Riehle, L. Robertson, B. Stahlberg, H. Wahlgren, " Intercomparison of Northern European $^{127}\text{I}_2$ - stabilized He-Ne lasers at $\lambda = 633$ nm ", *Metrologia* 29, 331-339 (1992) ;

All directions localizer of pulsed optical sources

P. P. Digulescu

Department of Electronics and Computer Science,
Technical Military Academy, 81-83 Regina Maria, Bucharest, Romania

P. E. Sterian

Department of Physics, "Politehnica" University,
313 Splaiul Independentei, Bucharest, Romania

ABSTRACT

There are many applications in which the direction to some pulsed optical sources have to be determined: pointing and tracking systems for laser based free-beam optical communications, laser warning systems, ECM and so on. A mathematical model of a localizer system intended for a laser warning system is developed based on the amplitude monopulse method. A linear transducer of the pulse energy into the time interval was used. The block diagram was designed and implemented based on general purpose devices and integrated circuits. The numerical results of the software simulation are presented. The system may be implemented using ASIC techniques and consequently its performance, especially the angular precision, can increase.

Keywords: angular measurements, optical sensors, laser warning systems

1. INTRODUCTION

The location of a radio-frequency source, whether it be a radar, a communication transmitter, or a navigational aid, is widely presented in literature. Basically, the problem consists in the determination of the geographic location of a radio signal source and can be solved with appropriate receivers.¹ For the optical domain this problem is quite complicated. Generally, the location of a laser-based source of radiation, as in the case of free-space communication or laser rangefinders, may be impossible because the high directivity of the transmitted beam. However, the angular location of a pulsed optical source is possible in the vicinity of the pointed object, because usually the beam is large enough here. Particularly, without any loss of the generality, the concomitance between the pointed object and the optical localizer may be assumed. In this case the problem consists in the great number of detectors required in order to obtain an appropriate accuracy, even if only a small field of view is required. For example, it may be used a CCD camera in conjunction with quite sophisticated computing resources.² In the following is demonstrated the possibility to find the direction to an irradiating optical source in a given solid angle with two optical detectors, and more, the possibility to cover all bearing space with a quite small number of discrete optical detectors. As we see, the required number of optical detectors will depend on the accuracy imposed for the system.

2. OPTICAL AMPLITUDE MONOPULSE METHOD: A BRIEF THEORY

It's widely known the radar monopulse method used in order to precisely determine the angular co-ordinates of a single-pulse irradiated target. Analogue to the pair of antennas used for each angular co-ordinate in the previous mentioned method, a dual linear converter of pulse energy into time intervals is

considered here as a part of the pulsed optical radiation sensor that is used. The analysis and the exact implementation of such a sensor was presented elsewhere.³ Here is enhanced only a brief theory of the optical amplitude monopulse method, that is necessary for the understanding of the localizer problem.

Basically, a linear converter of the optical energy into the time interval provides an electrical pulse with the pulsewidth T proportional to the energy of the optical pulse incident to the sensitive area of it's primary photodetector:

$$T \sim [\text{incident_pulse_energy}] \text{ or } T \sim q \quad (1)$$

where q represents the amount of the electrical charge freed in the photo-electric detection process.

Based on the equation 1, in this paragraph the electrical charge amounts are taken into account, this being equivalent with the pulsewidth of the dual converter outputs.

The dual converter that is supposed here is based on two identical p-i-n photodiodes that are simultaneously illuminated by an optical beam. The photodiodes are such spaced such that the distance between them may be neglected that is, the two photodiodes may be considered co-located in the centre of the coordinate system (Fig. 1.a). The two photodiodes are oriented with their optical axes, OA1 and OA2, in the horizontal plane and with an angular offset denoted by θ (Fig. 1.b). The direction of propagation of the optical beam is determined in a spherical coordinate system by the characteristic angles φ and ϵ , respectively.

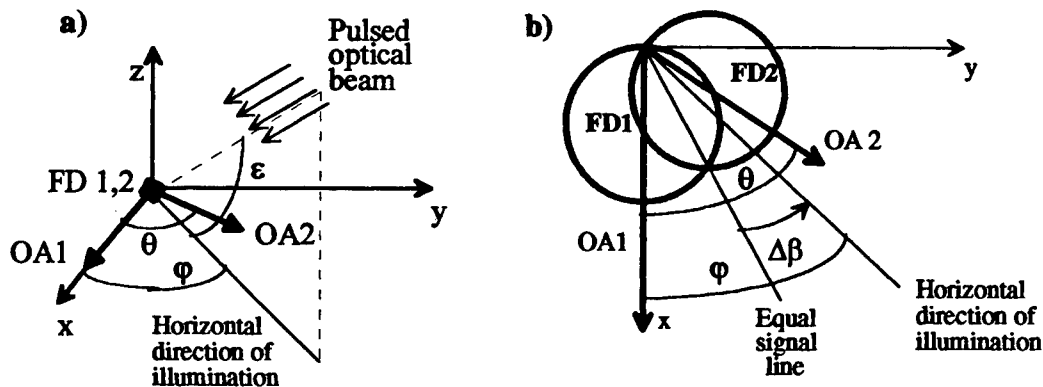


Figure 1 Coordinate system with the optical axes (a) and the horizontal receiving patterns (b) of the photodiodes used in the dual converter

In the horizontal plane (Fig. 1.b) is enhanced a particular direction denoted by "equal signal line" (ESL), characterized by the identical response of the two photodiodes if they are illuminated by a beam along this direction, that is, the horizontal angle of the beam is $\varphi = \frac{\theta}{2}$. More, we may define the horizontal angle $\Delta\beta$ of any beam, related to ESL as follows:

$$\Delta\beta = \varphi - \frac{\theta}{2} \quad (2)$$

Consequently, if an algorithm is given in order to find the angle $\Delta\beta$ then, the angular measurement does not depend anymore on the coordinate system. This is important for a generalization of the solution and will be used elsewhere in this work.

In this geometric arrangement, the amount of the electrical charge freed by each photodiode as a result of the illuminating pulsed beam may be as follows:

$$q_1 = E_0 \cdot R_D \cdot A_D \cdot \tau \cdot \cos \varphi \cdot \cos \varepsilon \quad (3)$$

$$q_2 = E_0 \cdot R_D \cdot A_D \cdot \tau \cdot \cos(\theta - \varphi) \cdot \cos \varepsilon \quad (4)$$

In the previous equations, E_0 represents the on-axis value of the radiant incidence of the beam, R_D and A_D are, respectively, the photodiode responsivity and the sensitive area and, τ is the pulsewidth of the optical pulse incident to the sensitive area of the photodiodes.

Applying the "classical" monopulse method that is, performing the sum and the subtraction between the two quantities provided by the equations (3) and (4), and then the ratio between the difference and the sum and, denoting the numerical result by N we may obtain:

$$N = \frac{q_1 - q_2}{q_1 + q_2} = \frac{\cos \varphi - \cos(\theta - \varphi)}{\cos \varphi + \cos(\theta - \varphi)} \quad (5)$$

or, by an algebraic evaluation omitted here, one may obtain:

$$N = \tan \frac{\theta}{2} \cdot \tan \left(\frac{\theta}{2} - \varphi \right) \quad (6)$$

Notice that in the equation (6) only the horizontal angle of the beam φ and the angular offset θ of the photodiodes axes are present. The other variables, including the elevation angle and the radiant incidence of the beam, were eliminated.

From equations (2) and (6) we may have as a result:

$$\operatorname{tg} \Delta \beta = -\frac{N}{\operatorname{tg} \frac{\theta}{2}} \quad (7)$$

or

$$\Delta \beta = -\operatorname{arctg} \frac{N}{\operatorname{tg} \frac{\theta}{2}} \quad (8)$$

If the angle $\Delta \beta$ is small enough then we may use some approximation equations such as:

$$\Delta \beta \approx -\frac{N}{\operatorname{tg} \frac{\theta}{2}}, \text{ in radians} \quad (9)$$

$$\Delta \beta \approx -\frac{180 \cdot N}{\pi \cdot \operatorname{tg} \frac{\theta}{2}}, \text{ in degrees} \quad (10)$$

Conclusively, if one can determine the first part of equation (5) then may be applied one of the equations (8), (9) or (10) in order to determine the horizontal angle of the illuminating beam. The determination of the electrical charge amount may be a quite difficult problem. Fortunately, we may apply the equation (1) which describe the converter supposed and, because the proportionality between the electrical charge freed in the detection process and the pulsewidth of the electrical pulse provided at the correspondent converter output, equation (5) is equivalent to the following equation:

$$N = \frac{T_1 - T_2}{T_1 + T_2} \quad (11)$$

In this way, we switched from the operation with the amount of the electrical charge, that is quite impossible, to the operation with the pulsewidth of some electrical signals, that is easier with an appropriate digital circuitry. An example for such an electrical circuit implementing equation (10) will be presented elsewhere in the paper (see paragraph 4).

3. ALL DIRECTION LOCALIZER: SYSTEM DEVELOPMENT

The angle $\Delta\beta$ in equation (10) is measured from the equal signal sight of a given pair of detectors. Therefore the numerical result is valid even the pair of detectors is rotated in the horizontal plane with an arbitrary angle. For simplicity let consider this rotation angle to be $n\theta$, n being an integer. Of course, the angle $\Delta\beta$ will be measured from the actual position of the equal signal sight, that is in the absolute coordinate system ($n\theta+\theta/2$). The position of the equal signal sight for each pair of detectors may be supposed known and constant.

Thus, if we provide a reasonable number of pairs then we can cover the whole azimuthal space.

For example, at the first sight, if $\theta=30^\circ$ then we need 12 pairs (24 detectors), if $\theta=45^\circ$ we need 8 pairs, and if $\theta=60^\circ$ we need 6 pairs. Of course the precision will be greater if the angular offset between the two axes of a detector pair will be smaller.

A strategy may be imagined such as the number of detectors is reduced to 12 even the angular offset between two consecutive detectors is 30° (or to 6 detectors if the offset is 60°). In this case the processing system will be more sophisticated a bit. In such a system each detector will be used in conjunction with two neighbours, as will be shown.

Let consider two sets of detectors, each of them containing 6. Each detector has it's optical axis rotated with 60° from it's neighbour's position in the set. By the other part, one set is rotated with 30° related to the other set. Denoting by convention the detectors from one of the sets by $C_1 \dots C_6$ (centre detectors) and the detectors from the other set by $L_1 \dots L_6$ (lateral detectors), then each centre detector will have as neighbours two lateral detectors rotated with 30° and -30° respectively. In Fig. 2 is illustrated such a triplet of detectors.

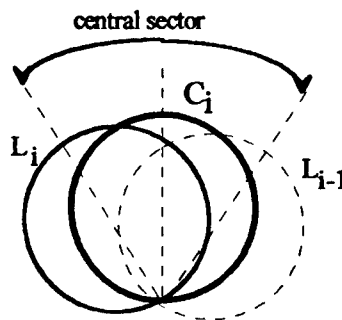


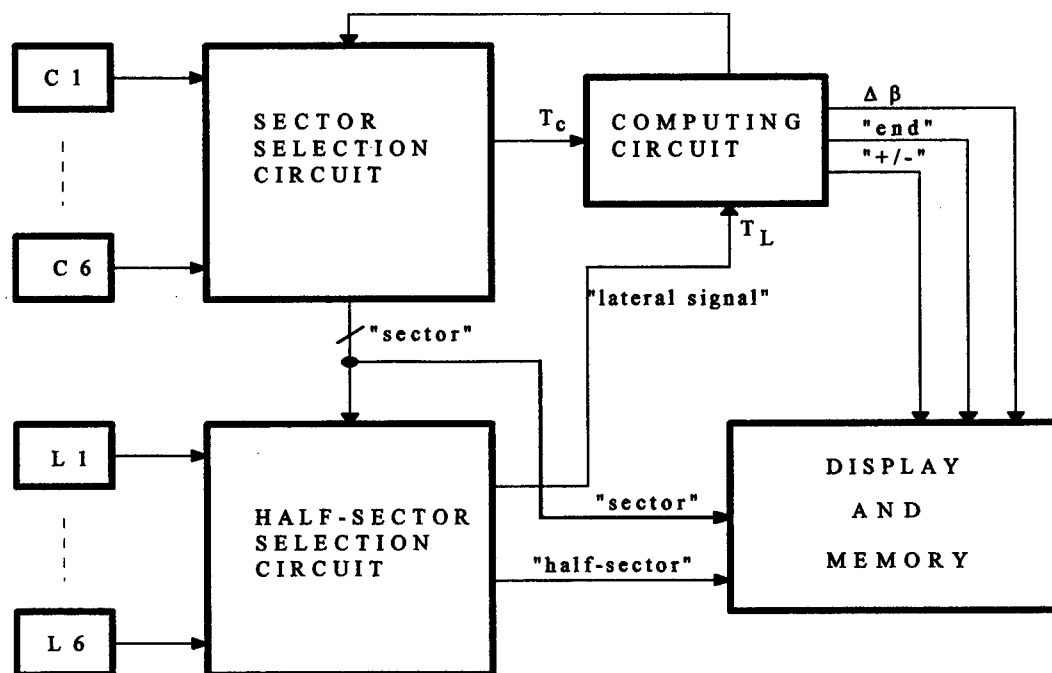
Fig. 2 The relative position of the receiving pattern of three neighbours detectors

A beam will be taken into account by a central detector C_i if it's projection on the horizontal plane is situated between the optical axes of the lateral detectors L_i and L_{i-1} .

In order to determine the sector that contain the beam, an analysis of the amplitudes of the signals provided by the detectors is necessary (the appropriate sector is that of the detector which provide the strongest signal).

In such a way, the whole azimuth space may be covered by 12 detectors. Of course, if the offset between two detectors is 60° , then the required number of detectors is 6, and each central detector will be "responsible" of 120° .

The block diagram is shown in the next figure.



Legend: C1 .. C6 - Center transducers
L1 .. L6 - Lateral transducers
Tc - Center signal
TL - Lateral signal

Fig. 3 THE ANGULAR LOCALIZER - BLOCK DIAGRAM

4. ELECTRICAL IMPLEMENTATION OF THE OPTICAL MONOPULSE METHOD

The determination of the quantity N implies a sum a subtraction and a ratio. Basically, these operations may be implemented by a circuit as shown in Fig. 4, based on two counters and a divider "attacked" by appropriate clock frequencies.

Because $T_1 - T_2 < T_1 + T_2$ then the division involved by the equation 10 is not possible by a simple digital division. Thus, is better to store not simply $T_1 - T_2$ but K times this value. This result is obtained by the use of a clock frequency of $K f_{\alpha}$.

Denoting by T_1 the pulse width of the signal provided by the central detector and by T_2 the pulse width of the signal provided by the lateral detector then in the binary counter BC_2 will stored a number of pulses equal to $[(T_1 + T_2) / f_{\alpha}]$, and in the binary counter BC_1 will stored a number of pulses equal to $[K (T_1 - T_2) / f_{\alpha}]$.

More, using the frequency $K'f_{ck}$ for the divider in the "computing" period, then we'll have as result at the output a number of pulses equal to $KK'N$. A resulting but very important advantage consists in the better resolution of the measurement of the difference $T_1 - T_2$. This is very important at small angles between the propagating direction and the equal signal sight. Thus, if possible, K is recommended to be greater than K' .

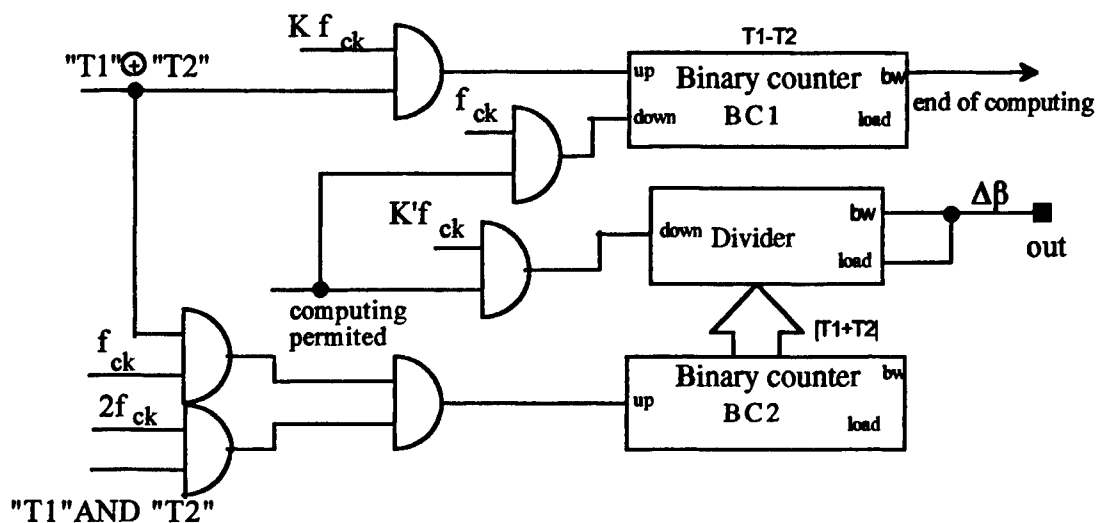


Figure 4. The "computing" circuit implementing monopulse method

5. ERROR ANALYSIS AND SYSTEM OPTIMISATION

The implementation of the exact equation (10) is not so easy because it implies a trigonometric function. Therefore an analysis of the errors involved by the approximate equation (12) is necessary.

In the previous paragraph was shown that we can obtain a number of pulses proportional with N . With a little chance we can obtain the azimuth itself given by the mentioned equation, in degree. The numerical analysis was performed with MATHCAD and the graphs shown in Fig. 5, 6, 7, 8 illustrate the results.

The required value of the coefficient that multiplies N is 213 for an angular offset of the detectors of 30° . This number equals the product 3×71 and the difference between the resulting clock frequencies is too large. Would be better if K and K' have the same order of magnitude. Can be observed that we can obtain the number of 210 as a product of 15 and 14. Fortunately, we can observe in Fig. 5 and 6 that this number is better than the exact value (213) because it provide an equalisation of the errors caused by the imprecision of the positioning of the sensor patterns.

The values of the clock frequencies used in Fig. 4 will be $15f_{ck}$ and $16f_{ck}$ with f_{ck} depending of the technology that is used (for TTL circuits may be used $f_{ck} < 2\text{MHz}$, and for CMOS circuits f_{ck} must be lower 1 MHz). The clock circuit will not be very simple because we'll need four frequencies quite unrelated (f , $2f$, $14f$ and $15f$).

For an angular offset between the detectors of 60° we obtain a coefficient with the value of 99, that may be approximated by 100. Then $K=K'=10$ and the clock circuit will be simpler but the method measure

errors will increase until 4° and it's inadmissible in the most of applications. If the coefficient is reduced at 90 (9x10), then the greatest error will be approximately 1 degrees, that is better again than the exact value.

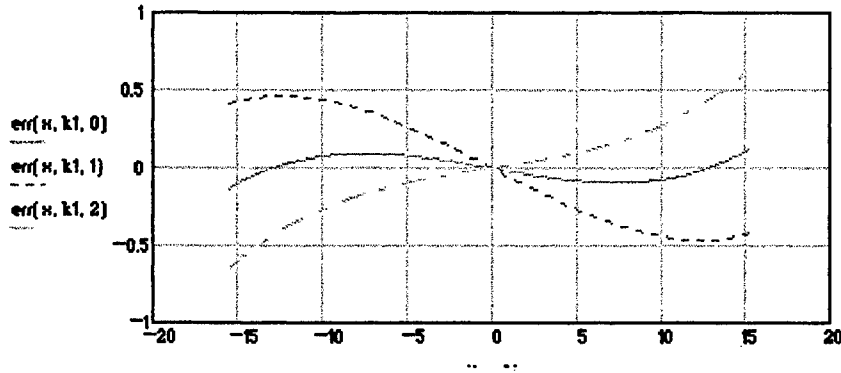


Fig. 5 Angular measurement accuracy versus the angle itself for three different positioning offset error (-1° , 0° and 1°). $K1=210$ and $\theta=30^\circ$

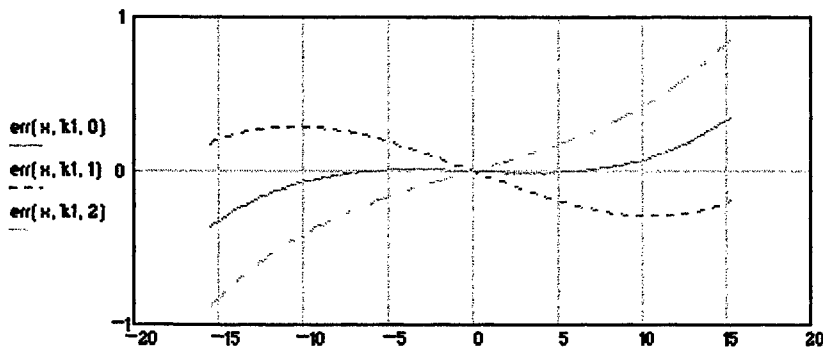


Fig. 6 Angular measurement accuracy versus the angle itself for three different positioning offset error (-1° , 0° and 1°). [$K1=213$ and $\theta=30^\circ$]

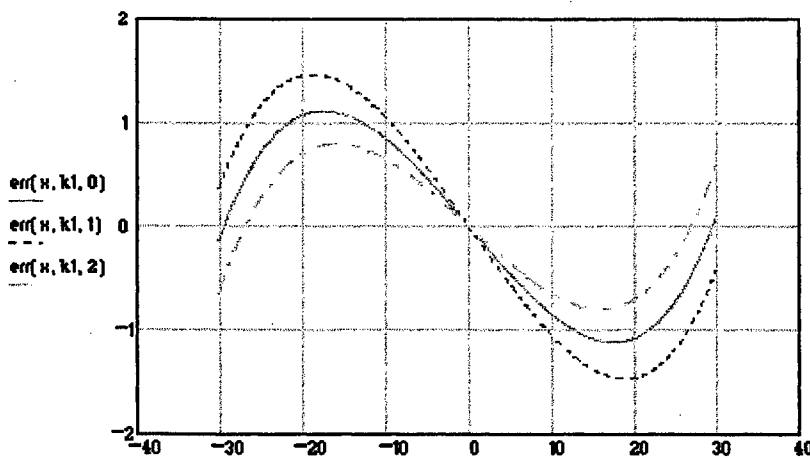


Fig. 7 Angular measurement accuracy versus the angle itself for three different positioning offset error (-1° , 0° and 1°). [$K1=100$ and $\theta=60^\circ$]

Conclusively, if the angular offset is selected to be 30° or 60° then the number of pulses provided at the output by the circuit shown in Fig. 4 can be equal (with a reasonable error to) the angle between the propagating direction of the beam and the equal signal sight, in degrees. The absolute value of the azimuth may be determined very easy because the azimuth of the equal signal sight has a known value.

If a counter that initially store the number of degrees of the equal signal sight is used, then this number may be increased or decreased by the number of pulses provided by the "computing" circuit from fig.3. As a result we'll have the azimuth in the absolute coordinate system, in degrees too.

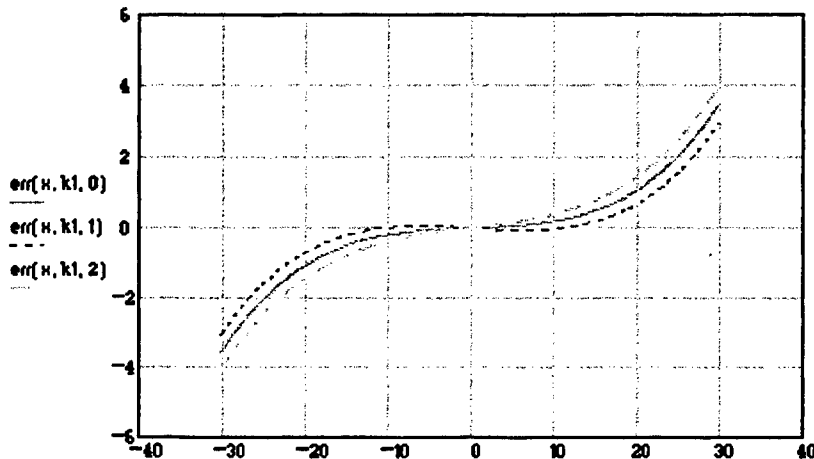


Fig. 8 Angular measurement accuracy versus the angle itself for three different positioning offset error (-1° , 0° and 1°). [K1=90 and $\theta=60^\circ$]

As was shown, we can cover the azimuth space with a number of 12 (if $\theta=30^\circ$) or 6 detectors ($\theta=60^\circ$). In order to use a single "computing" circuit, that is we suppose a single optical source at a time, some additional circuits are necessary to select the right pair of detectors that can provide the azimuth of the source.

This selection may be divided in two. Firstly, the center sector will be determined by the central detector that provide the first or the longer pulse. This detector will validate the lateral detectors that will be used at the right position and respectively at the left position. Secondly, will be established the lateral sector that contain the source by the lateral detector that provide the longest pulse. In this way is determined the equal signal sight to which will be related the result of computing and, simultaneously, will be filtered the parasitic pulses that may appear at the outputs of other detectors.

6. REFERENCES

1. L.A. deRosa, *Electronic Countermeasures*, Peninsula Publishing, Los Altos - California, 1961.
2. V. A. Skomin, C. R. Herman, M. A. Tascillo, D. N. Nicholson, "Mathematical modelling and simulation analysis of a pointing, acquisition, and tracking system for laser-based intersatellite communication", *Optical Engineering* 32(11), 2749-2763, November 1993.
3. P.P. Digulescu, *Convertisseur lineaire energie optique / time*, Session de Communications Scientifique de l'Institute de Recherche et Developpement de l'Armee, Bucarest, 1994.

UV radiation sensors with unitary and binary superficial barrier

V.Dorogan, T.Vieru, V.Kosyuk, I.Damaskin*, F.Chirita

Laboratory of Microelectronics, Technical University of Moldova,
bd. Stefan cel Mare 168, MD 2012 Kishinev, Moldova

*Institute of Applied Physics, Academy of Sciences of Moldova,
str. Academiei 5, MD 2028 Kishinev, Moldova

ABSTRACT

UV radiation sensors with unitary and binary superficial barrier, made on the basis of GaP - SnO₂ and GaAs - AlGaAs - SnO₂ heterostructures, are presented in the paper. Technological and constructive factors, which permit to realize a high conversion efficiency and to exclude the influence of visible spectrum upon the photoanswer, are analysed. It was established that the presence of an isotypical superficial potential barrier permits to suppress the photoanswer component formed by absorption of visible and infrared radiation in semiconductor structure bulk.

Keywords: Ultraviolet radiation sensor, heterostructures, A³B⁵ compounds, superficial potential barrier.

1. INTRODUCTION

The conversion efficiency and spectral sensibility of UV radiation sensors are determined by many factors, the most important being the band gap of utilized semiconductors. For the UV region the most perspective materials are semiconductors with band gap $E_g > 2.5$ eV ($\lambda < 0.49$ μm). Moreover, we have to consider the material reflection and refraction coefficients for $\lambda < 0.49$ μm , the defect density in potential barrier region, condition of structure surface. At present, the following semiconductor materials are utilized for UV sensors manufacturing: Si, A³B⁵ compounds and their solid solutions, A²B⁶ compounds, SiC etc.

The UV sensors need a high separating efficiency of charge carriers photogenerated by UV radiation at structure surface. Therefore, a small density of surface energetic states and presence of superficial potential barrier are required. The most spread are structures on the basis of p-n junction, Schottky barrier and on the basis of heterostructures with optic window.

Because Si is the most used semiconductor, sensors on the basis of single-crystal Si with superficial p-n junction (depth ~ 0.1 μm) and on the basis of MOS structures were realized. But in both cases the photosensitivity maximum is placed in near IR spectral region.¹

More efficient are the structures with Au - GaAs Schottky barrier.² Their photosensitivity spectrum has maximum for photons $h\nu \approx 2.5$ eV and external efficiency $\eta_e = 40\%$ in photosensitivity maximum.

The other way to extend the photosensitivity spectrum in UV region is utilization of Au - nGaAs_{0.6}P_{0.4} structures, on the basis of which an efficiency of 40% was obtained for photons $h\nu = 3.5$ eV ($\lambda = 0.36$ μm).³

Ga_{1-x}Al_xP ternary compounds permit to move the photosensitivity red boundary up to 3.1 eV. The quantum efficiency of Au - nGa_{1-x}Al_xP ($x = 0.5 \pm 0.1$) - nGaP structures is 30%.⁴

The structures with superficial barrier on the basis of GaP ($E_g = 2.27$ eV) are also intensive investigated. To form the Schottky barrier the following metals are used here: Au, Pt, Ni, Mo, Al, Cr, Ag, Cu, Mg. The potential barrier height varies from $\phi = 1.13$ eV (for Mo - GaP) to $\phi = 1.45$ eV (for Pt - GaP, Au - GaP) and depends on GaP surface quality and on metal deposition method.⁵ Au - GaP structure is the most studied and the most effective. The separating efficiency of charge carriers is 45% for photons $h\nu = 3.3$ eV.⁶

GaP - In₂O₃, GaP - SnO₂ and GaP - ITO structures are also studied. Sensors on nGaP - n⁺GaP epitaxial structures with charge carriers concentration $n \approx 10^{16}$ cm⁻³ and $\mu_n = 70 - 120$ cm²·V⁻¹·s⁻¹ have an absolute monochromatic sensibility of 1.5 times more than of Au - GaP sensors fabricated by Hamamatsu firm.^{7,8}

2. RESULTS AND DISCUSSION

The results in manufacturing the UV sensors on the basis of GaP - SnO₂ and GaAs - AlGaAs - SnO₂ heterostructures are presented in this paper.

n(p)-GaP with crystallographic orientation (111) was utilized as a substrate to prepare GaP - SnO₂ structures (Fig.1). Concentration of free charge carriers was $n(p) = 10^{17} - 10^{18}$ cm⁻³. The back ohmic contact was formed by electrolytic deposition of Ni. Current density in electrolyte was $j = 5 - 10$ mA/cm². To reduce the contact resistance, substrates were heated in hydrogen at $T = 600 - 650$ °C for 1-2 minutes. The frontal contact was formed by vacuum thermal deposition of metals and consisted of two layers (Ni + Cu).

SnO₂ layer was formed by two methods:

a) Pyrolysis from gas phase of tin acetylacetonate transported by a warm air flux. Temperature of heater was + 200 °C. GaP substrate temperature varied in interval 360 - 450 °C. Process duration was 30 - 60 min.

b) Multiple deposition (~ 10 times) of SnO₂ thin films by spraying and following pyrolysis of tin chloride solution in ethylic spirits. Substrate temperature was ~ 400 °C. One process duration - 3 min.

To improve the potential barrier properties we had utilized the epitaxial forming of crystalline films, which have more less structural defects and mechanical strains than initial GaP substrate. GaP epitaxial layers were formed on n-GaP, p-GaP, i-GaP (111) substrates by liquid phase epitaxy in temperature interval 800 - 950 °C.

The other way to form GaP - SnO₂ structures with high quality potential barrier is to reduce the concentration of noncontrolled dope impurities (background concentration). The melts was doped with rare elements (Er and Y) to reduce the concentration of electric active impurities in GaP epitaxial layers.

The concentration of free charge carriers in epitaxial layers was determined by Hall method. Epitaxial layers without rare elements have a background concentration $n = 5 \cdot 10^{16} - 6 \cdot 10^{17} \text{ cm}^{-3}$ and a mobility of free charge carriers $\mu = 20 - 60 \text{ cm}^2 \cdot \text{V}^{-1} \cdot \text{s}^{-1}$.

The presence of erbium (Er) in Ga + P melt causes an irregular growth of epitaxial layer with bad morphology.

Itrium (Y) has a more positive influence. The presence of 0.2 - 0.5 mg of Y in one gramme of melt and multiple utilization of melt reduce the concentration of electric active impurities in solid phase up to $n = 3.5 \cdot 10^{15} \text{ cm}^{-3}$. Moreover, in such mode we can invert the conductivity type (from n into p). Maximal mobility of free electrons is $\mu = 100 \text{ cm}^2 \cdot \text{V}^{-1} \cdot \text{s}^{-1}$ for charge carriers concentration $n = (3-6) \cdot 10^{16} \text{ cm}^{-3}$.

The influence of melt thermocycling with and without itrium upon the concentration of electric active impurities in epitaxial layer is presented in Fig. 2.

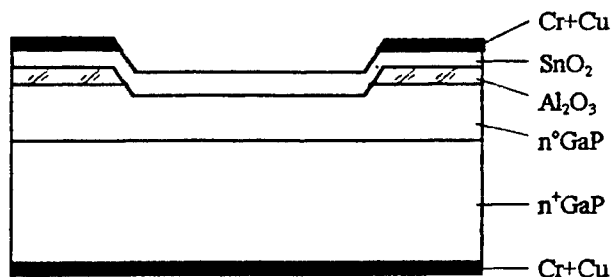


Fig. 1. Structure of UV radiation sensor.

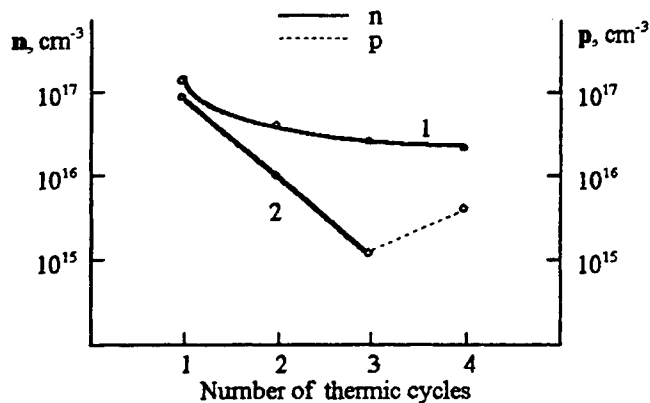


Fig. 2. Charge carriers concentration in dependence of melt thermocycling: 1 - without itrium; 2 - with itrium.

Thus, the optimum parameters of epitaxial layers were obtained using the Ga + P melt with rare elements (Y) and heating them after a special regime. During the heating the melt was homogenized (uniform distribution of P and Y in Ga). At cooling itrium formed with impurities any inactive compounds decreasing so their concentration in solid phase.

After epitaxial structure forming an Al₂O₃ layer was deposited on the frontal surface to limit the area of potential barrier which appears at GaP - SnO₂ interface. Windows with diameter 400 μm were opened in Al₂O₃ layer by photolithography.

2.1. Spectral characteristics.

Spectral characteristics of UV sensors with pGaP - nSnO₂ structure are presented in Fig. 3. nSnO₂ layer was made here by pyrolysis of tin acetylacetonate. Curves "a" and "b" represent the photoanswer measured in constant flux regime and in impulse regime (frequency 38 Hz) respectively. Curve "c" is the spectral photoanswer reported to spectrum of radiation source (lamp ДКЦIII-200). One can see that photosensitivity interval, determined at level 0.1 of maximal value, is 0.37 - 0.49 μm. Comparing the spectral sensibility of pGaP - nSnO₂ structure with that of pGaP - electrolyte barrier (Fig. 4) in interval 0.3 - 0.49 μm, we established that photoanswer is formed by charge carriers generated in GaP semiconductor crystal. The abrupt decreasing of photosensitivity for wavelengths $\lambda < 0.36 \mu\text{m}$ is caused by absorption of radiation in SnO₂ layer, by generation of charge carriers and by their recombination in the bulk or on the surface of SnO₂ layer (with thickness of 150 nm).

The spectral photoanswer of "electrolyte - SnO₂ - GaP" structure (Fig. 5) was measured to show that high recombination velocity of charge carriers in SnO₂ layer causes the practically zero sensibility in spectral region $\lambda < 0.36 \mu\text{m}$.

The maximum at 320 nm (SnO_2 band gap is 3.6 - 3.8 eV) is caused by charge carriers photogenerated in SnO_2 layer. Low intensity of this maximum demonstrates the small weight of generated in SnO_2 layer charge carriers in sensor's photocurrent forming. Cause can be only the imperfect structure of SnO_2 layer made on the basis of non-optimized technology.

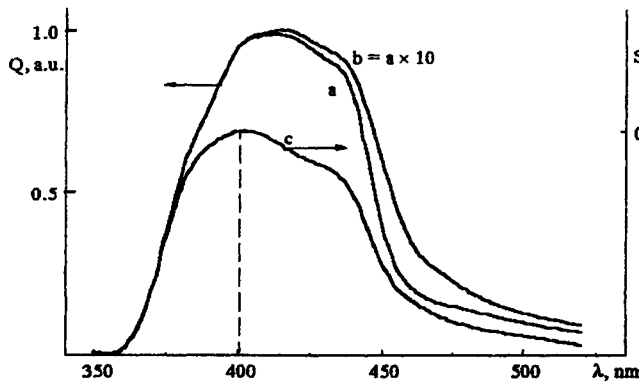


Fig. 3. Spectral characteristics of $p\text{GaP} - n\text{SnO}_2$ structure: *a* - in constant flux regime; *b* - in impulse regime; *c* - "*a*" reported to spectrum of radiation source.

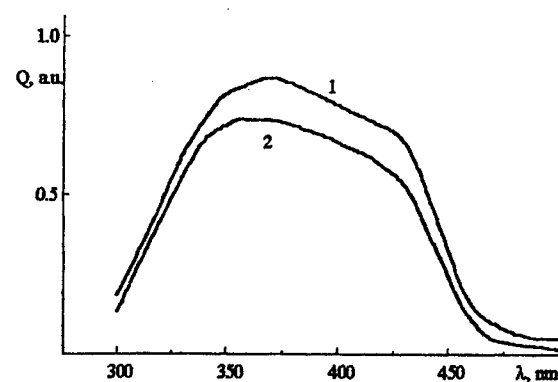


Fig. 4. Spectral characteristics of $\text{GaP} - \text{electrolyte}$ structure: 1 - $n\text{GaP}$; 2 - $p\text{GaP}$.

Fig. 6 shows the measured photoanswer spectrum (curve 1) of $n\text{GaP} - n\text{SnO}_2$ structure, emission spectrum of lamp ДКШ-200 (curve 2) and spectral photoanswer reported to emission spectrum of lamp, so the spectral sensibility of structure (curve 3). The photosensitivity interval extends here after 0.26 μm .

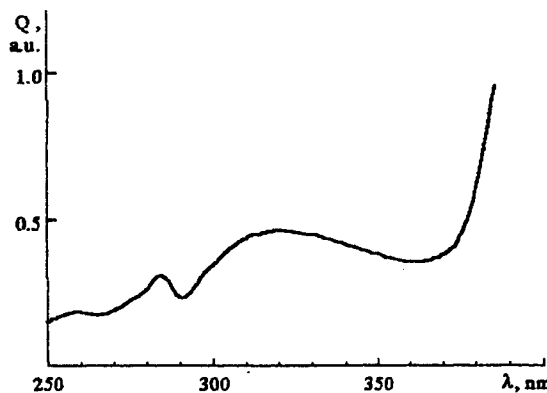


Fig. 5. Spectral characteristic of "electrolyte - SnO_2 - GaP " structure.

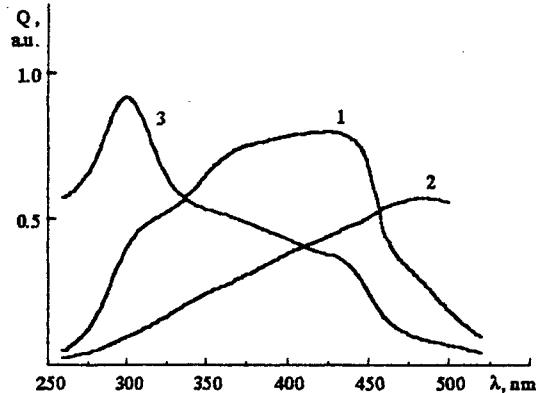


Fig. 6. Spectral characteristics of $n\text{GaP} - n\text{SnO}_2$ structure: 1 - measured; 2 - emission spectrum of lamp; 3 - measured spectrum reported to lamp spectrum.

Because of absence of a radiation source with wavelengths $\lambda < 0.26 \mu\text{m}$, we could not determine the left side of photosensitivity (on the wavelength scale), but we had established that the contribution of SnO_2 layer in photocurrent forming is more than GaP substrate's one. This demonstrates that one must give an exclusive attention to manufacturing technology of SnO_2 films to obtain a major sensibility in UV region.

2.2. Kinetics of photocurrent forming and relaxation.

Manufactured and studied $\text{GaP} - \text{SnO}_2$ structures are characterized by big times of photocurrent forming and relaxation. Fig. 7 illustrates the form of incident flux impulse (a) and the photocurrent form (b) determined by stroboscopic oscilloscope for photovoltaic regime. In initial moment t_1 the photocurrent increases abruptly up to its maximal value I_1 . During the 5 - 10 ms the photocurrent intensity decreases to $I_1/e = 0.37 \cdot I_1$ forming its stationary value I_{st} . After incident photoimpulse finishing, in the moment t_2 , the photocurrent changes suddenly its direction taking the value $-I_2$ and relaxes exponential. The ratio of photocurrents in positive and negative maximum to stationary photocurrent is: $I_1/I_{st} = 5-6$; $I_2/I_{st} = 3-4$. External quantum efficiency in impulse regime in photosensitivity maximum is about 50 - 60 %.

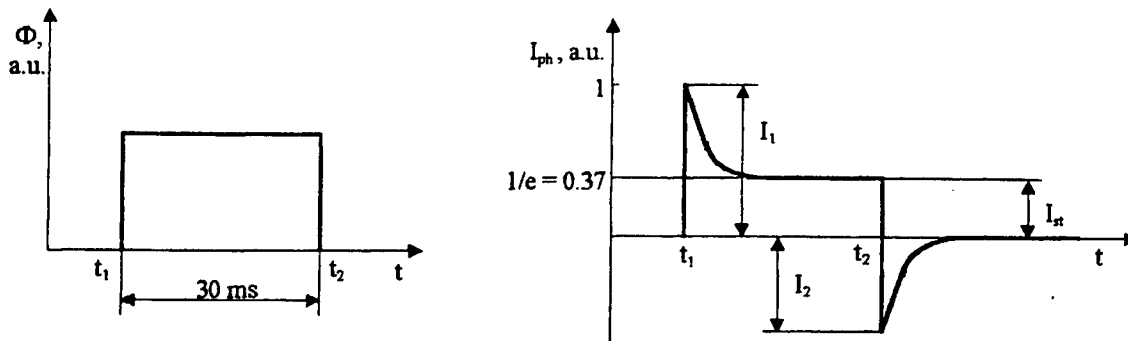


Fig. 7. Incident radiation impulse and the form of sensor photoanswer.

The photoanswer kinetics can be appreciate using ^{9,10}. In structures with intermediate dielectric layer the photocurrent forming is determined by two processes: by loading the structure capacity and by tunnel current through dielectric layer between GaP substrate and SnO₂ layer. The photocurrent kinetics is determined by relation:

$$I_{ph}(t) = q \cdot I \cdot \left[\frac{C_d}{C_d + C_{sc}} \cdot e^{-t/\tau} + \frac{S_{em}}{S_{em} + S_{rec}} \cdot (1 - e^{-t/\tau}) \right], \quad \text{for } t_1 < t < t_2$$

$$I_{ph}(t) = q \cdot I \cdot \left(\frac{S_{em}}{S_{em} + S_{rec}} - \frac{C_d}{C_d + C_{sc}} \right) \cdot e^{-t/\tau}, \quad \text{for } t > t_2$$

where: I_{ph} - photocurrent density;

I - flux of charge carriers generated in semiconductor;

C_d, C_{sc} - specific capacity (to a surface unit) of dielectric layer and of space charge region in semiconductor;

S_{em}, S_{rec} - effective velocity of charge carriers emission from semiconductor to SnO₂ layer and summary velocity of charge carriers recombination.

τ - time constant.

In dependence of parameters S_{em}, S_{rec}, C_d and C_{sc} a lot of relaxation variants are possible.

Let analyse the case $S_{em} < S_{rec}$. For $C_d > C_{sc}$ the photocurrent relaxation, according to relation $I_{ph}(t)$, has different directions. At the beginning of incident flux impulse the photocurrent increases quickly up to value qI , then relaxes to its stationary value $q \cdot I \cdot S_{em}/S_{rec}$ with time constant τ . At the photoimpulse end ($t > t_2$) the photocurrent changes its direction.

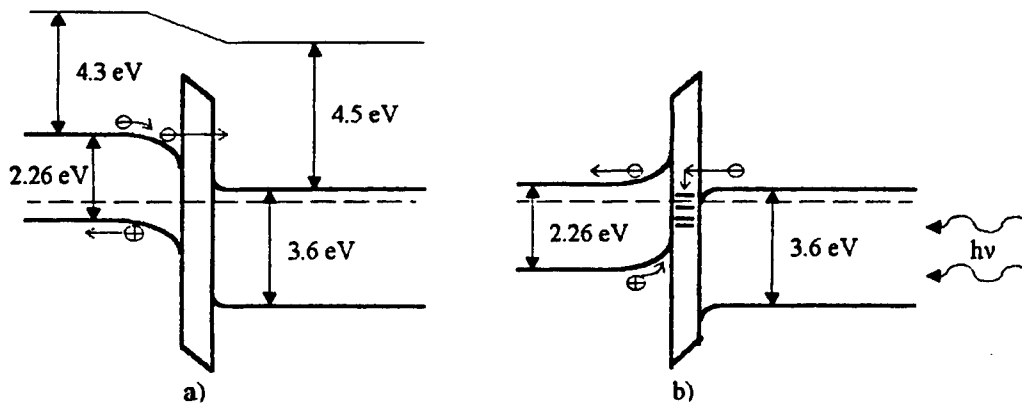


Fig. 8. Energetic diagrams:

a - pGaP - nSnO₂ structure; b - nGaP - nSnO₂ structure.

To better understanding the mechanism of photocurrent forming we had constructed the energetic diagrams of pGaP - nSnO₂ and nGaP - nSnO₂ structures with intermediate dielectric layer (Fig.8). In photocurrent impulse forming a considerable contribution is given by the transition of excessive minority charge carriers from GaP semiconductor through oxide layer to SnO₂ one. The presence of potential pits at semiconductor interface leads to accumulation in them of charge carriers whose concentration depends on dielectric layer transparency (that is on its thickness) and on dielectric constant ϵ . Thus, in the first moment t_1 the structure capacity is loading. At structure's reverse polarisation the layer transparency increases and the ratio I_1/I_{st} decreases. At direct polarisation the structure photocurrent decreases, what demonstrates the

presence of a big differential resistance. Cause is the increasing of potential barrier effective thickness for photogenerated minority electrons.

2.3. Volt-ampere characteristics.

Volt-ampere characteristics (VAC) in dark and light conditions are presented in Fig.9. VAC measured in temperature interval $-5 \div +80^\circ\text{C}$ have the same abruptness. It is characteristic for tunnel mechanism of the current through heterojunction.

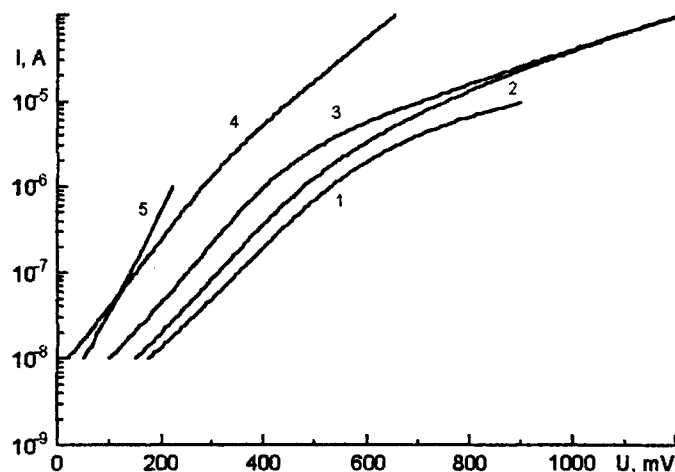


Fig.9. Volt-ampere characteristics:

1-4 - in dark, $n = 2.15$; $T, ^\circ\text{C}$: 1 - 0; 2 - 12; 3 - 20; 4 - 70; 5 - at illumination, $n = 1.33$.

Curve 5 represents the dependence $I_{sc} = f(U_{oc})$ constructed on the basis of characteristics I_{sc} , $U_{oc} = f(E)$. One can observe that VAC nonideality coefficient in dark conditions ($n = 2.15$) differs from that in light conditions ($n = 1.33$). It means that in studied structures the superposition principle, according to which injection current and photocurrent have the same forming mechanism, isn't fulfilled.

Effectuated investigations showed that GaP - SnO_2 structures can be successfully used for UV radiation sensors manufacturing. The following conditions are required to improve the conversion efficiency of optic radiation:

- An epitaxial layer with thickness $d > 5 \mu\text{m}$ have to be formed on GaP substrate to reduce considerable the density of superficial defects.

- To ensure the concentration of electric active impurities at level 10^{16} cm^{-3} , the epitaxial layer is growing from doped with rare elements liquid phase.

- The SnO_2 layer forming technology must exclude the forming on GaP substrate of an oxide layer, which determines the structure's total capacity.

- To reduce considerable the superficial recombination velocity of charge carriers, the potential barrier at semiconductors interface must be tunnel transparent.

- A superficial isotypical barrier for minority carriers from GaP has to be formed to reduce the contribution of charge carriers generated by photons with $h\nu \approx E_g^{\text{GaP}}$.

To exclude the influence of absorbed in semiconductor bulk radiation and to register only the charge carriers generated at surface by high energy photons, we realized a $\text{nGaAs} - \text{n}^+\text{Al}_{0.85}\text{Ga}_{0.15}\text{As} - \text{own oxide} - \text{SnO}_2$ structure with binary superficial barrier (fig.10). The $\text{n}^+\text{Al}_{0.85}\text{Ga}_{0.15}\text{As}$ layer with band gap $E_g \approx 2.1 \text{ eV}$ was grown on nGaAs substrate by liquid phase epitaxy. The concentration of free charge carriers changed in interval $4 \cdot 10^{17} \div 3 \cdot 10^{19} \text{ cm}^{-3}$ and the layer thickness varied within limits $0.1 \div 10 \mu\text{m}$. The space charge region with thickness W was localized at AlGaAs-SnO_2 interface. SnO_2 layer thickness didn't exceed 100 nm. An anodic oxide thin layer, tunnel transparent, was formed on the epitaxial layer to decrease the superficial states density.

The photons, absorbed at AlGaAs layer surface, generate charge carriers in excess, which are separated by AlGaAs-SnO_2 potential barrier. The charge carriers generated in the AlGaAs layer are similar separated. For holes generated in GaAs substrate there is a potential barrier, which brakes their diffusion to internal electric field of space charge region. Thus, the carriers generated in nGaAs substrate recombine without any contribution in photocurrent forming.

The separation coefficient of charge carriers Q depending on incident photons energy for different thicknesses of AlGaAs layer (d_{AlGaAs}) and of space charge region (W) is presented in fig.11. One can see that Q is maximal in interval $2.1 < h\nu < 4.4$ when d_{AlGaAs} and W have maximal values. The coefficient Q decreases non-uniform with d_{AlGaAs} and W decreasing:

quickly for low energies and slowly for high ones. It is due to absorption coefficient α , which decreases concomitant with photons energy. Particular is the second case, when the space charge region begins to extend also in nGaAs substrate, extracting the excessive carriers.

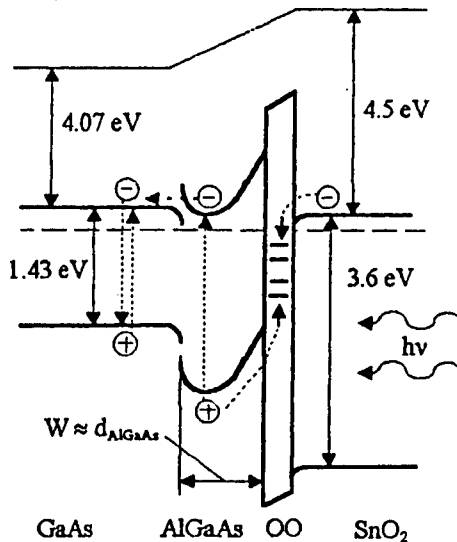


Fig. 10. Energy diagram of the structure with binary superficial barrier.

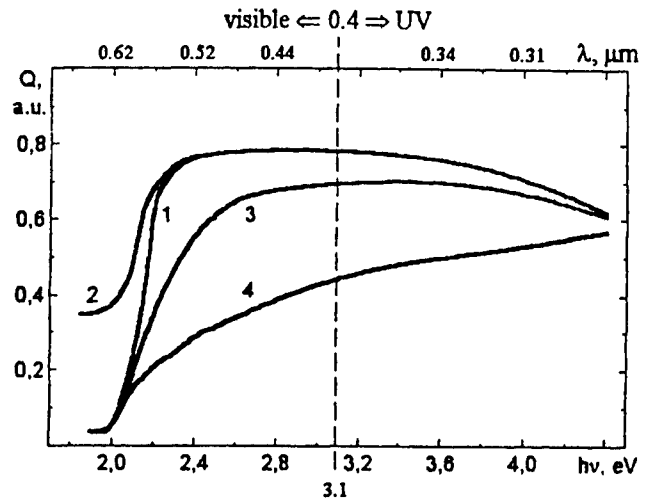


Fig. 11. Spectral dependence of separation coefficient:
1 - $d_{\text{AlGaAs}} > W = 1 \mu\text{m}$; 2 - $d_{\text{AlGaAs}} \approx W = 1 \mu\text{m}$;
3 - $d_{\text{AlGaAs}} \geq W = 0.5 \mu\text{m}$; 4 - $d_{\text{AlGaAs}} \geq W = 0.1 \mu\text{m}$.

Thus, varying the band gap width of AlGaAs frontal layer, its doping level and the thickness of AlGaAs layer, in which the space charge region is localized, we can change the structure sensibility to different energy photons. Even if some semiconductors with nonoptimized band gap less than threshold energy of UV region ($h\nu = 3.1 \text{ eV}$) are utilized, a photosensitivity with visible component less than UV one can be realized (fig. 11, curve 4). It was determined that the conversion efficiency of UV photons depends on perfection of AlGaAs-SnO₂ heterojunction, on intensity of barrier internal field which separates the photogenerated carriers, on thickness and transparency of SnO₂ layer. The visible component can be suppressed by realizing a structure in which the photons with energy $h\nu < 3.1 \text{ eV}$ are absorbed in a region with potential barrier, which brakes the excessive carriers separation.

3. REFERENCES

1. L. E. Klyachkin, L. B. Lopatina, A. M. Malyarenko, V. L. Suhanov, "Spektralnye karakteristiki selektivnykh FP dlya vidimoi i UF oblastei spektra", *Pisma v JTF* 11(6), 354-356 (1985).
2. A. A. Gutkin, M. V. Dmitriev, D. N. Nasledov, A. V. Pashkovski, "Spektry fotochuvstvitelnosti poverhnostno-bariernogo dioda Au-nGaAs v oblasti energii fotonov 1-5 eV", *FTP* 5(10), 1927-1933 (1971).
3. A. Berkeliev, Yu. A. Goldberg, D. Melevaev, B. V. Tsarenkov, "FP vidimogo i UF izlucheniya na osnove GaAs_{1-x}P_x poverhnostno-bariernykh struktur", *FTP* 10(8), 1532-1538 (1976).
4. A. R. Annaeva, A. Berkeliev, V. N. Bessolov, Yu. A. Goldberg, B. V. Tsarenkov, Yu. P. Yakovlev, "FP UF izlucheniya na osnove varizonnoi Ga_{1-x}Al_xP ($X_v = 0.5+0.1$) poverhnostno-bariernoi struktury", *FTP* 15(6), 1122 (1981).
5. T. F. Lei, L. Lee Chung, C. Y. Chang, "Metal-nGaP Schottky barrier heights", *Sol. St. Electron.* 22(12), 1035-1037 (1979).
6. B. V. Tsarenkov, G. V. Gusev, Yu. A. Goldberg, "Fotoelektricheskie svoystva poverhnostno-bariernykh struktur v UF polose spektra", *FTP* 8(2), 410-416 (1974).
7. A. I. Malik, G. G. Grushka, "Optoelektronnye svoystva geteroperehodov okisel metala GaP", *FTP* 25(11), 1691-1696 (1991).
8. A. I. Malik, V. A. Grechiko, V. E. Anikin, "Porogovye priemniki korotkovolnovogo izlucheniya na osnove diodov Schottky A³B⁵", *JTF* 59(11), 104-107 (1989).
9. O. Yu. Borkovskaya, A. T. Voroshenko, I. D. Dmitruk, A. K. Erohin, O. N. Mishchuk, "Fotoelektricheskie svoystva geteroperehoda IT/GaAs", *Optoelektronika i poluprovodnikovaya tekhnika* 18, 97-100 (1990).
10. A. Ya. Vul, A. G. Dideikin, Yu. S. Zinchik, K. V. Sanin, A. V. Sachenko, "Kinetika fotootveta tunnelnykh MDP struktur", *FTP* 17(8), 1471-1477 (1983).

A NEW TYPE SENSOR OF RADIATION IN WIDE RANGE OF ENERGY

Ac. Andriesh A.M. Malkov S.A. Verlan V.I. Bulgaru M.G.

Center of Optoelectronics of Institute of Applied Physics of Moldova Academy of Science, Academiei str. 5,
Chishinau, MD-2028, Moldova Republic, e-mail: andriesh@optoel.moldova.su

Abstract

The Me-Amorphous chalcogenide semiconductor (AChS) - dielectric- semiconductor ($Me - As_2Se_3 : Sn - SiO_2 - Si$)(*MChDS*) structure was obtained. There have been found that under the lighting in electric field the *MChDS* in dependence from applied external direction of electric field positive or negative are charged. There were found that quantity of accumulated charge from light intensity have been depended linear type $Q = Q_{max}(\alpha + \beta D)$, where D - is the dose of radiation ($D = I t$, where I is the intensity and t duration of radiation). There were studied and developed three different type of signal recording: by measuring of the photoempf, displacement photocurrent and accumulated charge, which allow to propose two type of sensors of radiation. The dose measuring and the image writing and readout processes in the real time and accumulation of the small signals regimes. The space functional separation of the recording and readout allows to carry out understroing repetition readout of the image and other operations.

Introduction

The amorphous chalcogenide semiconductors (AChS) are wide used in different domains of optoelectronic as active and passive elements for registration and memorization of the optical information etc. It have possessed some specific and advantage properties such as great photosensitivity in the large spectral range of the energy (from $h\nu > E_g$ to X-ray), the simple technology of preparation of the homogeneous layers on a large area, small independence from the impurities of the principal properties etc.

The some of the main peculiarities of amorphous and glass chalcogenides is to create under light action a special centers for capturing of the electrical charge and the formation of centers with

a new properties which are distinguished from the properties of the dopant centers in crystalline semiconductors [1]. The doping of the As_2Se_3 and As_2S_3 with electronic impurities type Sn are lead to grow of photosensitivity and decrease of the conductivity.

The direct application of the films were reduced because its high resistivity and of the small recombination time of the free charge. It is very promising the application of this materials in different devices for registration and memorization of the optical radiation, where the properties particularities of the AChS are to reinforcement and good reveal.

In present work we have studied the photoelectric properties of the *MChDS* structure type $Me - As_2Se_3 : Sn - SiO_2 - Si$.

The preparation of the *MChDS* structures

As substrates were used the monocrystalline plates of Si p-type of conductivity with the specific resistivity in range of $5 - 12 \text{ Ohm cm}$ and with concentration of carriers 10^{15} cm^{-3} . The plate have been polished and cleaned by standard technology and after that it were oxidiered in oxygen atmosfere at $1100^\circ C$. The thickness of the oxide was measured by elipsometric method and was changed in $600 - 2000 \text{ \AA}$ limits.

The preparation technology of the structures are described in detail in [2, 3, 4]. The *MChDS* structures were obtained by the consequent deposition on the monocrystalline Si plate with silicon bioxide, the amorphous chalcogenide films ($\alpha - As_2Se_3 : Sn$) and the top semitransparent contact from Al.

The scheme of the *MChDS* structure are shown in fig. 1a.

The results of the experiment

The charging and discharging characteristics of the structure were studied by the method of measuring high frequency (10^5 Hz) capacitance - voltage - characteristics ($C - V - Ch$) in dark and under lighting. At these frequencies $ACHS$ behaves like a dielectric. Fig. 1b shows $C - V - Ch$ of the structure, which were measured immediately after its preparation (curve 1). These dependencies are similar to the standard one of MDS structure [5], which are characterized by two boundary capacitances C_{max} and C_{min} and the transitive part, the width of which dependent on the thickness of the dielectric. In the multilayer case

$$C_{max} = \epsilon_0 \epsilon_x / d^*, \quad (1)$$

where $d^* = d_x + d_0 \epsilon_x / \epsilon_0$ and C_{min} is described by the formula

$$C_{min} = \epsilon / d_x^* + (\epsilon_x / (\epsilon_0 W_m)), \quad (2)$$

where $W_m = (\epsilon_s kT \ln(N_a/N_i))^{1/2}$, where N_a and N_i are the concentration of the impurity and of the carriers themselves in the silicon, ϵ_s is the silicon dielectric constant.

Under radiation of the $MChDS$ structure by the light with energy both from the absorption range and X-ray one [5] and application of the positive potential to Al $C - V - Ch$ move parallel towards the negative potential (curve 6). On the contrary the application of the negative potential in the same charge conditions $C - V - Ch$ move parallel to the positive bias part. Curve 2 corresponds to smaller lighting intensity than curve 3. The shift of the $C - V - Ch$ is connected with the charging of the $ACHS$ as dielectric under illumination. The position of the captured charge centroid on deep centers are obtained by formula [5]

$$X = \epsilon \epsilon_0 \Delta U_{fb} / Q, \quad (3)$$

where ΔU_{fb} is the shift of the flat bands voltage and Q is the accumulated charge in $ACHS$. The dependencies of the centroids of the positive and negative captured charge from temperature and voltage writing are shown on the fig. 2. For positive charging the lowering of the value of the charge centroid is observed with temperature decreasing in the range 215 – 295 K and by 225 K it have a value $X = 0.5 d_{ACHS}$ under photoexcitation by light with energy 3.76 eV. The positive charge centroid X linear decrease with growing the external electric field (0 – 20 V) at $T < 290$ K. At $T > 290$ K X is practically constant and is situated at 0.90 – 0.95 d_{ACHS} .

For negative charging the centroid of the charge weakly depended on wave length of the excited light, temperature in range (215 – 295 K), external voltage (0 – 20 V) and was placed at the $SiO_2 - As_2S_3$ boundary to 0.96 d_{ACHS} . The mechanism of the charging is connected with the creation of the captured charge deep centers under light action and of the current free charges, which under the electric field action move in space. The mobile free charge have extracted from layer of $ACHS$ or are captured on deep centers. In such way there are a charging of the $ACHS$.

The centroid characteristics show, that the accumulated positive charge disposes in dependence on temperature, electric field and length wave both in the As_2S_3 volume and at $SiO_2 - As_2S_3$ interface, but the negative charge places only at $SiO_2 - As_2S_3$ interface. The accumulation of the charge takes place until the accumulated charge compensates the external field in volume As_2S_3 . The kinetic of such charging process for $MChDS$ structure are experimentally described by the dose ($D = It$, where I is the light intensity) dependencies

$$\Delta V_{fb}(t) = \Delta V_{fb,sat}(\alpha + \beta D), \quad (4)$$

where α and β are coefficients, $\Delta V_{fb,sat}$ – the maximum shift of flat bands voltage at given external field. By increasing the external voltage the charging process are restored until the next saturation of the charging and the compensation in internal of $ACHS$ the external field. The quantity of maximum accumulated charge is linear with applied external field.

The dependence of the readout photoemf of the structure from charging time shown that characteristics of the charging in layer of $ACHS$. In all cases it have a form of curve with saturation. Under voltage growing and constant light intensity of illumination with energy $h\nu > E_{g2}$ the reached time of saturation of photoemf decrease and at $1.6 \cdot 10^{-2} \text{ W/cm}^2$ reaches 0.02 s at 6 V. The decreasing of the light intensity (fig. 3) at constant charging voltage brings to increase essential time of the maximal charging and for 100 times less intensity it is 30 s. Such strong dependence from intensity is characterized by dose dependence, which in all case is the same. The dependence of photoemf $U_i(t)$ has such form with saturation probably characterizes the inversion of the bands on Si surface.

Schema of energy-band diagram of $MChDS$ structure during the positive writing shown that in positive charging case the volume of As_2S_3 near the $As_2S_3 - SiO_2$ interface has positive charge and

induces through SiO_2 in Si the negative charge. As result the band profile bends down until they attain the surface inversion state of conductivity, the creation of p-n-junction. The creating of the p-n-junction probably determines the photoemf saturation.

The discharging decay characteristics of the $MChDS$ structure on temperature are sharply accelerated under increasing temperature and external voltage. It was determined that the relaxation of the accumulated charge due to the thermo-field emission of holes from traps according to the Pool-Frenkel law.

The increasing of the charge storage time can be attained by the way of the choosing the high specific resistance layer of $AChS$, and by improving the technology of the thin layers.

There are developed some methods to read out the accumulated charge, which corresponds of the writing signals, through:

- 1) the registration of the charge of the whole structures through the measuring of the shift of $C - V - Ch$ under $C = \text{const}$ from initial position;
- 2) the measuring of the photoemf of the structures by illumination of the silicon charged boundary space with light from range $E(\text{Si}) < h\nu < E_g(\text{chalcogenide})$;
- 3) the registration of the displacement photocurrent signal by same above described in 2) light.

In such way it is possible to read out the quantity of writing charge that are corresponded of the illuminated dose. Besides this by methods 2) and 3) can carry out the local readout of the writing signals by lighting with narrow spot of the light and to read out the relief of the writing signals (that corresponds of the image) by scanning of the light. The changing of the direction of electric field corresponds of writing of the positive or negative charging (positive or negative image).

The measuring of the quantity of part of the lighted area and transformation it in charge relief give the possibility to measure the area. In (fig. 3) is presented such process of measurement of the area in increasing order.

The equivalent scheme of measurements methods 2) and 3) are shown on (fig. 4a,b). The time resolution by this method is low and is limited of the RC structure.

The photocurrent are measured by scheme which are presented on (fig. 4b). In this case time resolution is limited by life time of non-principal free charge in Si and the $R_s C_{str}$ where C_{str} is the capacity of the local illuminated spot of the

readout light.

The dose dependence of the signals

The scheme of positive and negative charging of the $Me - ChDS$ structure is shown on fig. 4b, which are discussed down.

By the method 1) were realized the readout of the accumulated dose of radiation through the measuring of the quantity of charge. From linear dependence of charge and quantity of the quantity $Q - Nh\nu$ have been measured of the radiation dose which are falling on probe. Under $C = \text{const}$. it were measured the displacement ΔU from which is followed the quantity of charge $Q = C\Delta U$. It is necessary to mentioned that the capacity measuring is more precise than other one methods.

By writing of the light without external field because of existing of the contact potential (if the writing are place in contact domain) the writing are place until there are the complete compensation of the contact field by electric field of the charge.

The next charging are stopped because of the internal field absence.

For writing of more high dose in $MChDS$ structure it is necessary to increase the external field. It is clear that the charging are place until the internal field is less than external $E_{intern} < E_{extern}$. The maximum of the dose (charge) in such way is connected with external field and is less or equal $Q_{max} = E/\epsilon = U_{extern}/d$, where d is effective thickness of dielectric.

For preservation of the writing charge at long time it is necessary to hold constant the external electric field.

It is possible to provide a some cycle of the writing of the dose and its erase under light illumination without or opposite external field.

In another applying variant of the dosimeter it is uniformly illuminated with x-ray and are measured the displacement of the voltage at $C = \text{const}$, when the zone of the Si are plane.

The dose measurements of the radiation are carried out in a short time during of the radiation action or after memorization of dose by above described method.

Writing of the elementary bit of the information

In such way are place the transformation of illumination relief of the image in the charge relief of chalcogenide. It is mentioned that the space

generation of charged centers may be under lighting with energy of quanta $h\nu \geq E_g(\text{chalcogenide})$. The positive or negative charging depended from direction of the electrical field by illumination. If the electrical field is constant after illumination the writing relief are stored long time and relaxation characteristic in this case have been depended from the transition current through the dielectric (SiO_2).

To carry out the complete cycle of the writing and readout of the image it is necessary to illuminate the whole surface of the top semitransparent contact with uniform integral light (fig. 6b) (state 1). This procedure leads to the complete erasing of the charge. Then the polarity of the external voltage source is changed to opposite and by illumination through object the image writing takes place (state 2). The device permit to obtain the positive or negative image. If the writing is made from the state 1 to 2, the positive image will be formed. If the structure is in state 2 and transits to state 1, the negative image will be obtained. The processes occurred during the writing - erasing procedure are in principle the same physics, but in the first case the charging of the local centers brings to the formation of the potential relief and in case 2 the uniform distribution of the potential relief along the whole structure area takes place.

The writing of the elementary bit information is based on storage of the positive (+1), negative (-1) charge or noncharged (0) structure by above mentioned method. Under this written structures may be carry out consistent logical unitary operation bounded with exposures light and bias potential:

$(1, 0, -1) \rightarrow (-1, 0, -1) \xrightarrow{+} (0, +1, 0) \xrightarrow{+} (+1, +1, +1),$
 $(1, 0, -1) \xrightarrow{+} (0, +1, +1) \rightarrow (-1, 0, 0) \rightarrow (-1, -1, -1),$
 etc.

The density of storage elementary bits is connected with external reasons (diameter of light spot, electrical field etc.) and may be increased. The addressing to the definite bit can by the scanning light.

The writing and readout of the optical image

Below the processes of the writing and erasing of the optical image and its readout are described. During projecting the object image on the surface of the structure under simultaneous action of the

voltage, the charging of *ACHS* by positive or negative charge exists. In such way the light image is memorized by the structure in a relief charge kind. This relief of captured charge induces in *Si* substratum through dielectric SiO_2 the same charge relief of opposite sign as in *ACHS* or otherwise the relief of the surface potential. By connecting the top and down contacts by electric circuit and scanning the surface from top electrode side by laser beam with energy of the quanta $E_{g1} < h\nu < E_{g2}$, where $E_{g1,2}$ are the values of the forbidden band of the *Si* and *ACHS* respectively, we obtain the electric impulses, whose amplitude depends on quantity of the charge that is accumulated in *ACHS* layer. In such way we obtained the invisible image that is written through the charge relief. The space separation of the writing and readout processes permits us to provide the repeated readout of one image.

The readout of the optical information about the optical image by photoemf method had carried out by optical scan system depicted at fig. 7. The impulse signals of photoemf (U_i) generated by the carrier photoexcited in space charge range of *Si* were obtained with the help of point scan of the He-Ne laser ($\lambda = 6328 \text{ \AA}$) and were registered consequently. About charge in *ACHS* one can make the same conclusion from the flat bands shift but in this case one cannot carried out the local readout when we are used whole electrode on the area of the structure. If in the structure the big electric charge is memorized, which causes to depletion of the *Si* surfaces the U_i signal is observed without external potential. The value of the maximum signal was equal to 0.35 V. On the fig. 5b the dependence of the signal U_i and the quantity of the charge captured in *ACHS* is shown. In present case it can play the role of the characteristic curve of the image writing process. Between two saturation positions that are characterized by the transparency 1 and the maximum charge density 2 there is a domain of the charge with 10^{-8} Cl . The ratio $U_{i,max}/U_{i,min}$ is about 100.

The forms of readout impulses in the photoemf and photocurrent methods are shown on the fig. 8a,b. The speed action of the readout in the photoemf is limited by product of RC_{str} of the scheme (where R is the external load resistance and C_{str} is the capacitances of the structure) and there are reached the frequency 10^6 Hz . To decrease of the time readout is necessary to decrease sufficiently the parameters of the scheme (R and C_{str}).

The frequency dependences of photoemf and photocurrent signals are shown on fig. 9a,b.

The readout by measuring the recharging photocurrents is more promising for practical applications as compared with photoemf. The photocurrent readout consists to applying of the depletion voltage impulses and illuminating by the light impulses (fig. 8b). The maximum frequency of readout in this method is limited beside RC_{str} by the time of transition of the depletion voltage to a steady state and attains some MHz.

In our experiment we do not reach the space resolution, peculiar the photoconductive writing layer of $AChS$. The obtained resolution is limited by the laser scan beam diameter of used scan system (in our case it was 30 mkm). It is assumed that the resolution of $MChDS$ structures is analogous to one of optoelectronic memory element [6, 7] which reaches 10^8 bit/cm^2 . The usage of well focusing laser beam and more fast and precise electrooptic or acoustooptic scanning deflectors makes this possible. The maximal value the writing and reading rate of the optical information were limited by our measuring possibilities (10^6 Hz) and the silicon plate properties. The increasing of the sensibility of $\alpha\text{-As}_2\text{Se}_3 : \text{Sn}$ in comparisons with $\alpha\text{-As}_2\text{Se}_3$ were found.

The parameters of time resolution reached by us was: the whole cycle of writing – read out – erase procedures is 0.1 sec which are close with TV cycle and may be improved (fig. 10).

The operation under imagines

This applications is based on above mentioned process of a bit information writing but in this case whole imagine it is possible converted from positive in negative imagine and vice versa under uniform exposures of writing light after imagine storage and changing the electrical field in other direction.

It should be mentioned some direction realized by us:

- 1) Receiving of the direct (positive) and indirect (negative) imagine;
- 2) Put on some imagines by summing or difference and in this case is more interest the superposition of two appropriate imagines (two changing imagines etc). In this case it is possible to reveal or the contour of the object or the object moving trajectory.

CONCLUSION

For above mentioned effects of the writing and readout of the information we can proposed the following applications:

- 1) the dose sensors and the processing of the images in working in real time and accumulation regimes in a range of energy of quants more than 1.80 eV as the visible, ultraviolet and the X-ray ranges;
- 2) the realization of the bit regime processing of the information;
- 3) for measuring of the area;
- 4) for carrying out different operations under image as the making of positive or negative images, the measuring of sums and differences of the images and their areas, the recognition of the images and other operations such as the formation of the contour of the object, the obtaining of the moving object trajectories etc.

References

- [1] Anderson P.W. Phys. Rev. Lett. 1975. Vol. 24. P. 275.
- [2] Ac. Andriesh A.M., Malkov S.A., Verlan V.I. In Proceedings of SPIE in Recording Systems: High Resolution Cameras and Recording Devices and Laser Scanning and Recording Systems. 1993, v.1987, p. 171 – 178.
- [3] Ac. Andriesh A.M., Malkov S.A., Verlan V.I. in Solid State Sensor Arrays: Development and Applications conference, part. of IS T/SPIE's Symposium on Electronoc Imaging: Science, Technology, January 1996, San-Jose, USA, p.153.
- [4] Andriesh A.M., Verlan V.I. Ivashchenko Yu.N., Malkov S.A. et al. In book : "Mnogokomponentnye poluprovodniki". Chishiau, Moldova, ed. "Shtiintsa". 1985, p.118-123.
- [5] S.M.Sze. Physics of Semiconductor Devices, v.1. "John Wiley & Sons", 1981, p.455.
- [6] B.S. Borisov, B.I. Tselibin. Elektronnaia promyshlennost (USSR), 1977, N6, p.59 - 64.
- [7] Amorphous semiconductor. Technologies & devices. Ed. Y.Hamakawa, OHM, Tokyo-Osaka-Kyoto, 1982, p.38.

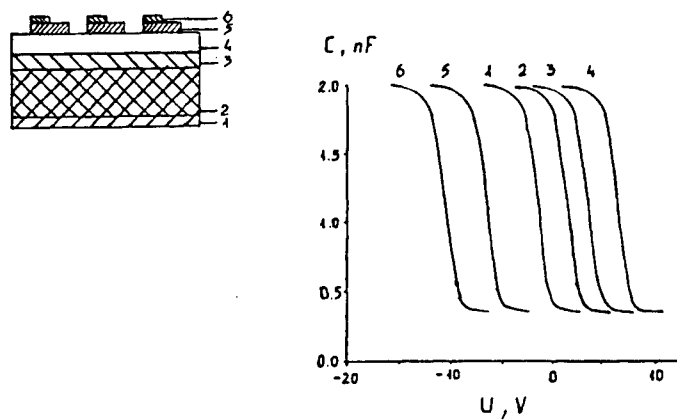


Figure 1: The scheme of MChDS structure (a). 1 - Si, 2 - SiO₂, 3 - AChS, 4 - the top semitransparent contact. $C - V - Ch$ of the Al - As₂Se₃ : Sn - SiO₂ - Si structure (b). 1 - no charged structure, 2, 3, 4 - negative charged, 5, 6 - positive charged.

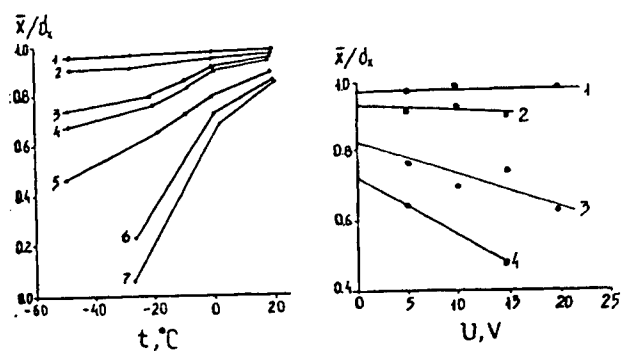


Figure 2: The dependence of the centroid of captured charges in As₂S₃ of MChDS structure from temperature under photogeneration with constant wave length (a) and from external voltage under constant temperatures (b). a: λ , mkm: 1, 2 - 0.48, 3 - 0.44, 4 - 0.40, 5 - 0.34, 6 - 0.51, 7 - 0.56, b: t , °C: 1 - -20, 2 - -17, 3 - -26, 4 - -51

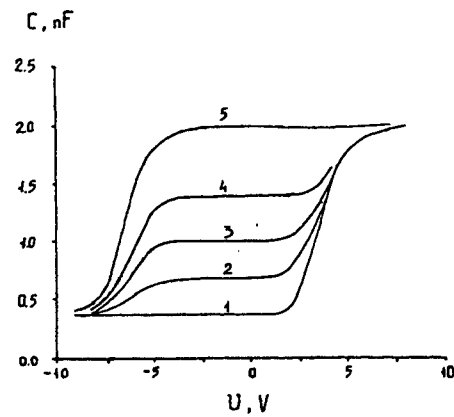


Figure 3: $C - V - Ch$ of the $Al - As_2Se_3 : Sn - SiO_2 - Si$ structure for different illuminated part of surfaces. The number of curves is placed in increasing value of illuminated surfaces.

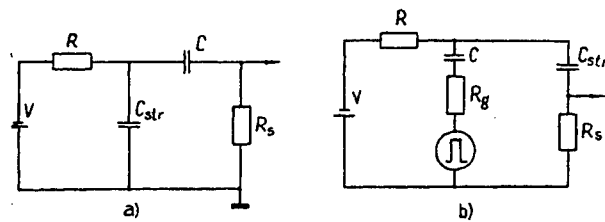


Figure 4: The equivalent scheme of the device in photoemf (a) and photocurrent (b) regimes of recording of storage charge in $MChDS$ structure.

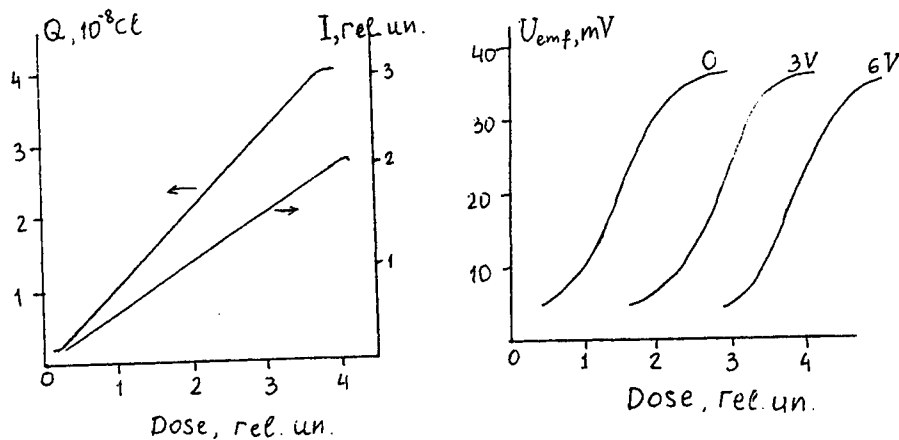


Figure 5: (a) The dependence of the photoemf signal amplitude from the writing dose for different constant applying voltages. (b) The dependence of the photocurrent signal amplitude from the writing dose for 3 V constant applying voltage.

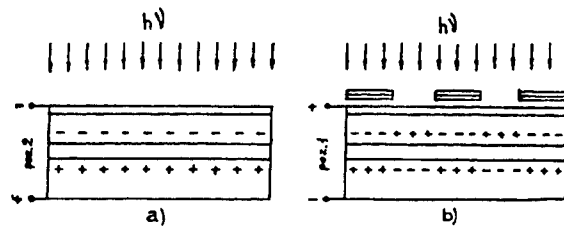


Figure 6: a) The schematic energy-band diagram of *MChDS* structure during the positive charge writing. b) Scheme of image writing: 1 - erasing, 2 - writing.

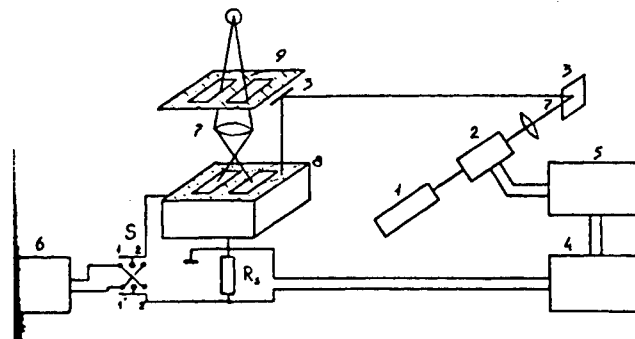


Figure 7: The scheme of complete writing and readout of image in *MChDS* structure. 1 - *He - Ne* laser (6328 Å) 2 - modulator, 3 - condensers, 4, 5 - the galvanometer mirrors, 6 - the mask (object), 7 - source of illumination, 8 - *MChDS* structure. Layers: a - semitransparent *Al*, b - *As₂S₃*, c - *SiO₂*, d - *Si*

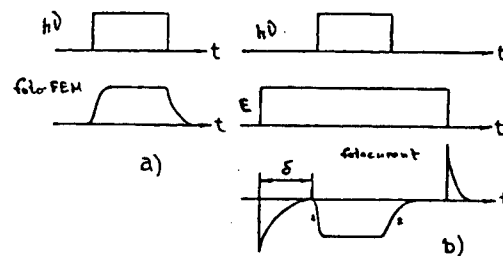


Figure 8: The time dependence of the signal form of the input (curves 1a, 1b, 2b) and output (curves 2a, 3b) signals in photoemf (a) and photocurrent (b) methods of the measures.

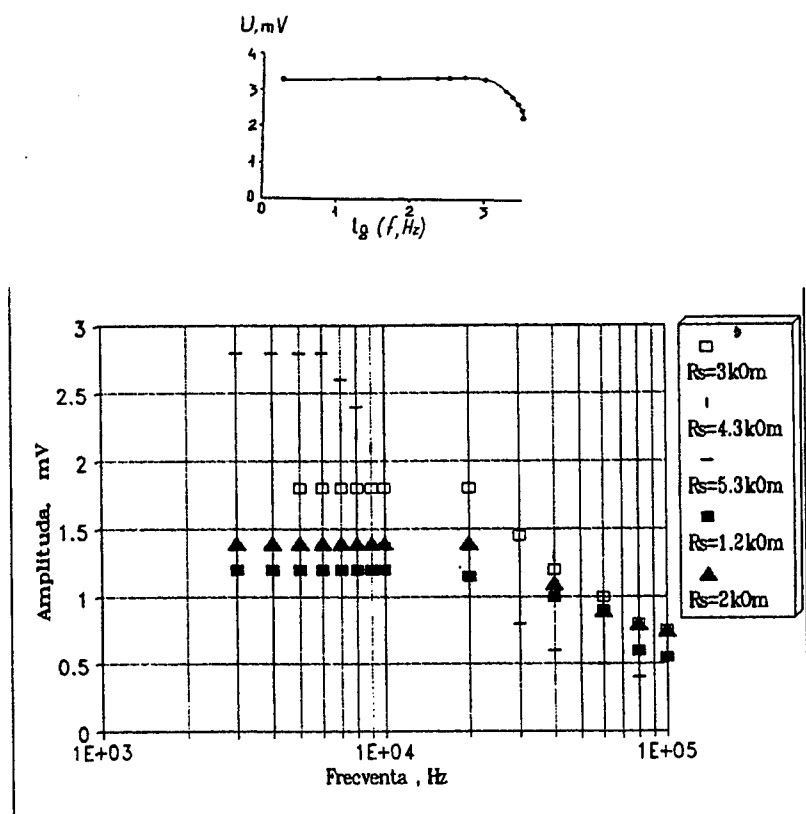


Figure 9: The dependencies of the photoemf (a) and photocurrent (b) from the frequency of the readout signal.

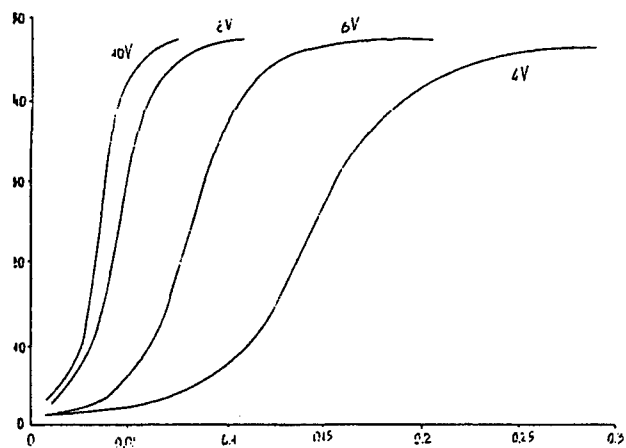


Figure 10:

Interference devices for noncontact diagnostics of arbitrarily shaped rough surfaces.

Peter P.Maksimyak

Correlation Optics Dept, Chernivtsy University,
2 Kotsyubinsky St., Chernivtsy 274012, Ukraine

ABSTRACT

The relationship between statistical structure parameters of rough surface and associated correlation parameters of scattered field is used to develop a method for rough surface diagnostics. The treatment is based on the model of random phase object with inhomogeneity phase dispersion $\sigma_{\varphi_0}^2 < 1$. The proposed diagnostic methods are applicable to surfaces with roughness period comparable to the radiation wavelength employed, low-reflectance and arbitrarily shaped surfaces, and surfaces of a thin plane-parallel plate. The sensitivity limit of the methods in measuring the standard deviation of surface profile from base line is about 0.003 mm.

Keywords: surface roughness, rms, low-reflectance and arbitrarily shaped surfaces, polarization interferometer, goniometer.

1. INTRODUCTION

The diagnostics of slightly rough surfaces has been the subject of considerable interest recently. A great deal of progress has been made in this field^{1,2}. A whole new class of optical diagnostics methods has been developed such as optical profiler total integrated scattering (TIS) angle-resolved scattering (ARS) speckle optics, interference and optical correlation techniques^{3,4} etc.

Several devices for surface roughness measurements based on these methods have also been developed⁵⁻⁹. Their efficiency is not always high enough, however, when applied to surfaces with roughness period comparable to the wavelength of the radiation employed. The difficulties in the former case are associated with the loss of information contained in the high-frequency component of the scattered field. Some difficulties also arise when measuring low-reflectance surfaces and arbitrarily shaped surfaces.

A number of interference methods for measuring surface roughness have been proposed which eliminate the above difficulties¹⁰. They are based on the RPS approach, which preassumes¹¹: (i) infinitely extended object (all spatial frequency components of the radiation scattered by the object are present in registration zone); (ii) phase variance of the object is small ($\sigma_{\varphi_0}^2 < 1$); (iii) the correlation length of the inhomogeneity is larger than the wavelength ($l_{\varphi_0} > \lambda$).

A unique relationship is known to exist within this approach among the statistical parameters describing the object structure and associated correlation parameters of the scattered field.

2. LOW-REFLECTANCE SURFACES

The method for measuring low-reflection surfaces is based on the measurement of the boundary field phase variance⁶.

The arrangement used for the measurement is shown in Fig.1. A telescope consisting of two objective lenses transforms a light beam from a single-mode laser source into a plane wave, which then undergoes amplitude splitting into a reference and an object wave by means of a beamsplitter. The object wave reflected by the beamsplitter is focused by an objective lens on the rough surface of a sample. The reflected radiation is then used to form the surface image in the plane of a 2x2 position-sensitive photodetector array. The radiation reflected by the mirror interferes with the object wave forming an interference pattern with fringes localized at infinity. The zeroth-order interference fringe is automatically kept within the 2x2 position-sensitive photodetector array by means of a transverse displacement of the micro-objective in the reference arm using two electric motors, and a longitudinal displacement of the mirror using a piezoceramic modulator which simultaneously accomplishes amplitude modulation of the resulting light beam. The output signal from the 2x2 position-sensitive photodetector array is fed into the phase comparators which generate control signals for the motors and

the piezoceramic modulator. The net signal is then transformed into a R_q value by means of the analogue processing unit, and is displayed on the indicator.

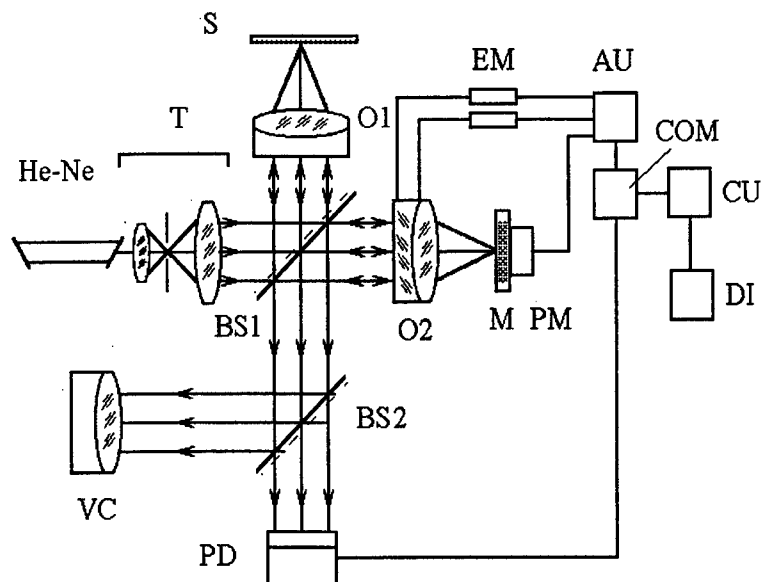


Fig.1. Experimental arrangement for measuring the degree of low-reflectance surface roughness:
He-Ne - laser, T - telescope, BS1, BS2- beam-splitters, O1,O2 - objective lenses, S - sample, M - mirror, PM - piezoceramic modulator, PD - 2x2 position-sensitive photodetector array, VC- visualization channel, EM - electric motors, AU - automatic zero fringe adjustment unit, COM - comparator, DI - digital indicator. CU - analog R_q calculation unit,

The mean height deviation is calculated using the formula:

$$R_q = \frac{\lambda}{4\pi} \sqrt{2 - \frac{I_{\max} - I_{\min}}{\sqrt{I_r} \sqrt{I_o}}}, \quad (1)$$

where I_{\max} and I_{\min} are the maximum and the minimum resulting intensities, respectively, and I_r and I_o are the reference and the object beam intensities, respectively.

The arrangement shown in Fig.1 can be custom designed to meet specific requirements for measuring objects of different sizes under various conditions. The above arrangement permits measurements of low-reflectance surfaces since allowance has been made for the relative reflectance coefficient of the surface measured with respect to the reference mirror. The lower limit of surface roughness measurements is $0.005 \mu\text{m}$. The surfaces in question class with optical surfaces such as optical element surfaces, crystal surfaces in microelectronics, machined surfaces etc.

3. MEASUREMENT OF ARBITRARILY SHAPED SURFACES

The transverse coherence function $\Gamma_{\perp}(\rho)$ is known to be given by the boundary field coherence function $\Gamma_v(\rho)$, and can be defined as

$$\Gamma_{\perp}(\rho) = \exp \left\{ \sigma_{\varphi_0}^2 [K_{\varphi_0}(\rho) - 1] \right\}, \quad (2)$$

where $K_{\varphi_0}(\rho)$ is the phase correlation coefficient. An important point is that, for objects with $\sigma_{\varphi_0}^2 < 1$, the transverse coherence function $\Gamma_{\perp}(\rho)$ is given by the boundary field transverse coherence function $\Gamma(\rho)$ in any recording zone. It is seen from Eq. (2) that, by taking logarithms of both sides, one can obtain an expression for the object phase variance. Thus, by measuring $\Gamma_{\perp}(\rho)$ and making the relative displacement ρ of optically mixed components larger than the correlation length of phase inhomogeneities l_{φ_0} , one can set $K_{\varphi_0}(\rho) = 0$, and get

$$\Gamma_{\perp}(\rho > l_{\varphi_0}) = \frac{I_{\max} - I_{\min}}{I_{\max} + I_{\min}} = \exp \left\{ -\sigma_{\varphi_0}^2 \right\}. \quad (3)$$

This relation is commonly used in rough surface diagnostics.

The general schematic of the device, which is intended for measuring the rms. height deviations of slightly rough surfaces is shown in Fig.2³.

A plane wave produced by the telescope T, consisting from a microobjective, a pinhole and an objective lens, undergoes a total reflection in the polarizer cube PBS, then passes through the quarter-wave plate $\lambda/4$ and falls upon the surface S to be measured. The double-pass of the plane wave through the quarter-wave plate results in the 90° rotation of the plane of polarization. Thus, all the reflected light passes through the polarizer cube. The cube, together with the two calcite wedges W, one of which is stationary, the other movable, and the analyzer A, make up a scanning polarization interferometer. The relative displacement of the interferometer beams is set by the separation between the wedges, and the displacement of the movable wedge results in the alternating resulting intensity minima I_{\min} and maxima I_{\max} , which are recorded by the photodetector PD. The rms. height deviation R_q that follows from (2), can be found from the relation

$$R_q = \frac{\lambda}{4\pi} \sqrt{-\ln \frac{I_{\max} - I_{\min}}{I_{\max} + I_{\min}}}. \quad (3)$$

The information contained in the resulting interference pattern is extracted by transforming the optical signals into electric ones, with their subsequent processing in the analogue electronic unit CU.

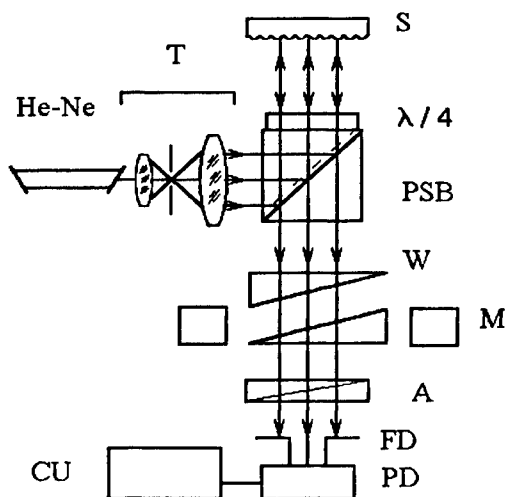


Fig.2. Experimental arrangement for measuring the degree of arbitrary surface roughness:

He-Ne - laser,
T - telescope,
PBS- polarizing beam- splitter,
S - sample,
W- calcite wedges;
M - electromechanical modulator,
A - analyzer;
FD - field-of-view diaphragm;
PD - photodetector,
CU - analog R_q calculation unit.

The device can be made either as a measuring head, or as a stationary instrument, depending on the size and the position of the object to be measured. The advantages of the device over those currently in use are its fast acting, high precision, non-contact nature of the measurement, and the possibility of averaging over a large number of roughness elements.

Therefore, in a shearing interferometer, the object field interferes with itself, rather than with the reference field, thus making possible the measurements of arbitrarily shaped surfaces with the radius of curvature larger than 0.2 m. This is especially important e.g. in the photochemical industry to monitor the quality of calender shafts, in the space industry to monitor the quality of mirrors fabricated by diamond micro-shaping etc. Being directly mounted at the polishing machine tool, this device was used for the surface quality control during making of the detail. Calender shafts and spherical mirrors under finishing of them by diamond micro-sharpening were controlled, and sensitivity on the rms height parameter down to $0,002 \mu\text{m}$ was achieved.

4. SURFACES WITH ROUGHNESS SPACING COMPARABLE TO λ

For roughness whose spacing exceeds λ , the diagnostics can be easily performed using a shearing interferometer (Fig.2), while if its spacing is comparable to λ , new approaches are needed to extract information contained in the high frequency component of the scattered field.

It has been proposed to separate the regular and the diffuse parts of the reflected beam, and then evaluate the degree of roughness by an interference measurement of the regular part and photometric measurement of the diffuse part of a beam⁷.

In the optical arrangement shown in Fig.3, a light beam from a single-mode He-Ne laser ($\lambda = 0.6328\mu\text{m}$) passes through a telescopic system forming a plane wave, which consists of a microscopic objective, a pinhole, and an objective lens. Then, a homogeneous component of the beam is separated by pinhole. Its polarization azimuth is in the transmission plane of the polarizer cube, making a 45° angle with the principal axis of the quarter-wave plate. The beam then passes into the integrating sphere to interact with the surface under study. The resulting beam intensity I_p is

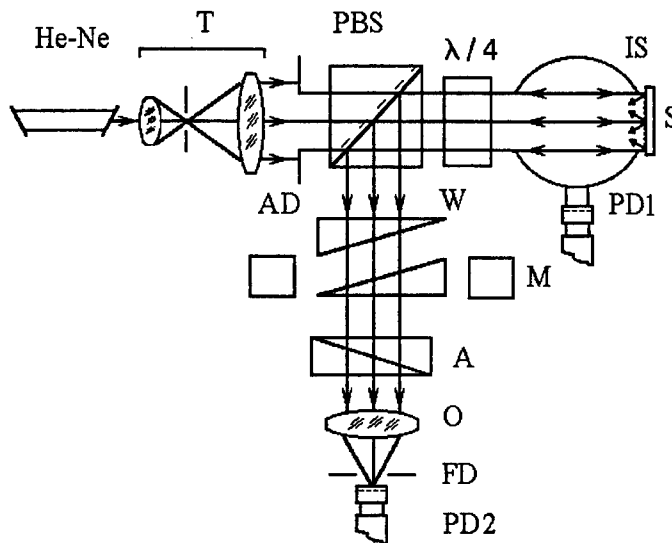


Fig.3. Optical arrangement for surface roughness measurements:
 He-Ne - laser,
 T- telescopic system,
 PBS - polarizing beam splitter,
 $\lambda/4$ - quarter-wave plate,
 IS - integrating sphere,
 S - sample,
 W- calcite wedges,
 M- electromechanical modulator,
 A - analyzer,
 O- objective lens,
 AD and FD - aperture and field-of-view diaphragms,
 PD1, PD2 - photodetectors.

composed of that of the coherent beam I_C which leaves the photometric sphere upon reflecting from the surface, that of the diffusely reflected light propagating within the coherent beam aperture I_S , and that of the diffusely reflected light which does not leave the photometric sphere I_d . The beams $I_C + I_S$ pass through the quarter-wave plate twice which results in 90° rotation of plane of polarization with respect to that of the incident beam. Thus, the above beams undergo a total reflection from the beam-splitting face of the cube and pass into the shearing interferometer. The image of the surface is formed at the plane of the field-of-view diaphragm, with a photodetector placed behind it. The diffusely reflected beam intensity I_d is measured by a photodetector. The transverse relative displacement of the beams mixed in the polarization interferometer, that is necessary for measuring $\Gamma_\perp(\rho)$, is achieved by means of an electromechanical modulator. The displacement is set to be larger than roughness period l_{ϕ_0} . Using (3), one has

$$\sigma_{\varphi 0}^2 = -\ln \left[\frac{I_{\max} - I_{\min}}{I_{\max} + I_{\min}} \right] - \ln \left[\frac{I_p - I_d}{I_p} \right]. \quad (4)$$

One can now go over from the phase variance values $\sigma_{\varphi_0}^2$ thus found, to height parameters such as the standard deviation R_q of the surface profile from the base line, by using the relation:

$$R_q = \frac{\lambda}{4\pi} \cdot \sigma_{\varphi_0}. \quad (5)$$

This method was applied to measure flat reflecting surfaces of electrolytic copper obtained by machining with a diamond tool. A feed pitch of the cutter was 1 to 4 μm . Surfaces were of different shape: plane, spherical or parabolic. Curvature radius of the surface was exceeding 0.3m. Roughness of the surfaces of interest has rms height deviation up to 0.006 μm .

Table 1 gives standard deviations obtained by a profilometric measurement, by standard shearing interferometry without recording high spatial frequencies, and by the above described method. It is seen that the discrepancy among the results obtained by our method and profilometric ones is about 15%, while standard interferometry results differ from ours by 30%. Besides, our method has the advantage of fast-acting and high resolution (0,003 μm).

Table 1. Standard deviation R_q of surface profile from the base line as measured by profilometric (R_{qp}) standard interference (R_{qi}) and the optical correlation (R_{qs}) methods.

Sample No	R_{qp} (μm)	R_{qi} (μm)	R_{qs} (μm)
1	0.0073	0.0054	0.0081
2	0.0112	0.00073	0.0134
3	0.0181	0.0130	0.0199
4	0.0224	0.0169	0.0238

ACKNOWLEDGEMENTS

This work was supported by the Ukrainian Scientific and Technological Center (USTC) under Project No. 230.

REFERENCES

1. T. Asakura, "Surfaceroughness measurement," 40, Chapter 3, 304-342 in "Speckle Metrology," *Academic Press*, 1978.
2. J. M. Bennett and Z. Mattsson Introduction to Surface Roughness and Scattering, *Opt. Soc. of America*, Washington, D. C., 1993.
3. A.A.Rusakov, *Roentgenography of Metal*, Atomizdat, Moscow, 1977 (in Russian).
4. O.V.Angelsky, I.A.Buchkovsky, P.P.Maksimyak and T.O.Perun, "A Fast Interference Method for Measuring the Degree of Surface Roughness," *J. Mod. Opt.*, 38, 1-4, 1991.
5. O.V.Angelsky and P.P.Maksimyak, "Interference Correlator for Measuring Surface Roughness," *J. Mod. Opt.*, 38, 1483-1486, 1991.
6. O.V. Angelsky and P.P. Maksimyak, "Interference Methods for Surface Roughness Measurement," *Proc. SPIE*, 2108, 246-252, 1993.
7. O.V.Angelsky and P.P.Maksimyak, "Optical Diagnostics of Slightly Rough Surfaces," *Appl.Opt.*, 30, 140-143, 1992.
8. O.V.Angelsky and P.P.Maksimyak, "Polarization-Interference Measurement of Phase-Inhomogeneous Objects," *Appl.Opt.*, 31, 4417-4419, 1992.
9. O.V. Angelsky and T.O. Perun, "Interference Method in the Studies of Turbulence in a Liquid," *Proc. of the 5-th EPS Liquid State Conference*, Institute for Problems in Mechanics USSR Academy of Sciences, Moscow, October 16-21, 83-88, 1989.
10. O.V.Angelsky and P.P.Maksimyak, "Optical Diagnostics of Random Phase Objects," *Appl.Opt.*, 29, 2894-2898, 1990.
11. S.M. Rytov, Yu. A. Kravtsov, and V.I. Tatarsky, *Introduction to Statistical Radiophysics, Part II, Random Fields*, Nauka, Moscow, 1978 (in Russian).

Optical studies on sedimentation of the suspensions

S. Anghel, I.Iova¹, Șt. Levai¹, I.Iorga Simăn, I. Iosub

The Faculty of Sciences, University of Pitești, V. Milea Square No. 1, Pitești - 0300, Romania.

¹ The Faculty of Physics, University of Bucharest, P.O.B. MG -11, Bucharest - 76900, Romania.

ABSTRACT

Sedimentation of the suspension process is important, especially in pollution, biologic liquids or polymers studies.

Unlike the usual methods, as those using pipettes, areometer or balances¹, the optical ones are nondestructive and more accurate.

During sedimentation produced by the braked fall of the solid particles in suspension, fluctuations produced by an opposite vertical diffusion occur; this process is lost using the chemical methods, which weigh the mass fallen on a submersed plate.

We used a scattering method, based on the attenuation of a laser beam which, in the absence of absorption, describes the variation of solid particles' concentration in the suspension.

Keywords: sedimentation, suspension, diffusion, scattering, fluctuations.

1. SEDIMENTATION OF THE SUSPENSION PROCESS

A suspension contains solid particles mixed in liquid. Gravitational sedimentation occurs under the action of the field of the gravitational force. The features of the process depend on the dimensions, form, concentration and the chemical nature of the particles in suspension².

During the sedimentation, two processes are important: the fall of the particles (under the action of the weight and of the resistant force in liquid) and the vertical diffusion produced by the difference of density which occurs as a result of the first process⁴.

We suppose that the initial concentration is the same in the whole volume of the suspension, the particles are approximately spheric and they do not chemically react.

Let us consider a small layer of dx thickness, at x depth in a suspension, $c(x)$ and $c(x+dx)$ concentrations of solid particles at the levels x and $x+dx$, v -the speed of particles crossing the layer (fig.1).

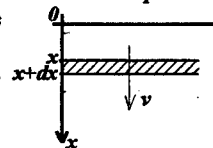


Fig. 1

The rate of the concentration change $\frac{\partial}{\partial t}(c dx)$ in the considered layer is produced by the diffusion

and the flow of the particles having the speed v :

$$\frac{\partial}{\partial t}(c dx) = \frac{\partial c}{\partial t} \cdot dx = D \left[\left(\frac{\partial c}{\partial x} \right)_{x+dx} - \left(\frac{\partial c}{\partial x} \right)_x \right] + v [c(x) - c(x+dx)] \quad (1)$$

where D - the coefficient of diffusion.

Using the developments $c(x+dx) = c(x) + \left(\frac{\partial c}{\partial x} \right)_x \cdot dx$ and $\left(\frac{\partial c}{\partial x} \right)_{x+dx} = \left(\frac{\partial c}{\partial x} \right)_x + \left(\frac{\partial^2 c}{\partial x^2} \right)_x \cdot dx$, it results:

$$\frac{\partial c}{\partial t} = D \cdot \frac{\partial^2 c}{\partial x^2} - v \cdot \frac{\partial c}{\partial x} \quad (2)$$

It is difficult to find a general and simple solution $c(x,t)$ of the equation (2). However, we can observe that $\frac{\partial c}{\partial t}$ can be

positive or negative (concentration increase or decrease as a function of time), as long as the term $D \cdot \frac{\partial^2 c}{\partial x^2}$ is bigger or smaller than

the term $v \cdot \frac{\partial c}{\partial x}$. During the sedimentation, fall or diffusion can prevail in different periods and the equilibrium between these processes is possible in some moments. Thus, fluctuations of the concentration can occur during the sedimentation.

2. EXPERIMENTAL METHOD

Scattering method uses the experimental set up shown in figure 2. The attenuation of the incident beam, describes the concentration of the solid particles in the suspension. Concentration as a function of time, in different "h" position, can be measured.

Let I_0 - incident, I_i and $I(t)$ - initial and at "t" moment intensities of the transmitted beam, c_i and $c(t)$ - initial and "t" moment concentrations. We can write:

$$I_i = I_0 \cdot e^{-A \cdot c_i} ; \quad I(t) = I_0 \cdot e^{-A \cdot c(t)} , \quad A - \text{constant} \quad (3)$$

where from:

$$\frac{c(t)}{c_i} = \frac{1}{\ln \frac{I_0}{I(t)}} \cdot \ln \frac{I_0}{I_i} \quad (4)$$

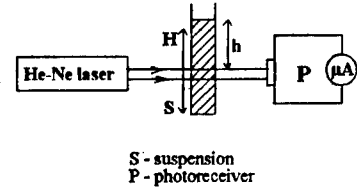


Fig. 2

concentration of solid particles can be determined as a function of time. The error in the determination of the concentration was about 2%.

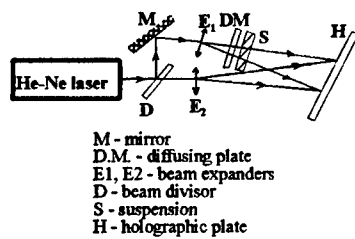


Fig. 3

A holographic method can be useful for sedimentation studies. It uses the experimental set up shown in figure 3.

Real time or double exposure method, produces fringe patterns that describes, by the variable distributions of the refractive index (as shown in fig. 4), the change rate of the concentration in the studied suspension³.

However, the fast fluctuations which occur during sedimentation, require very small exposure times, hence lasers over 100 mW power. The L.G.10 - He-Ne laser we used in scattering method, 10 mW power, with 20 seconds exposure time is useless.

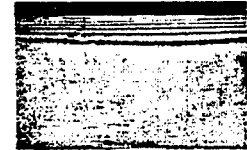


Fig. 4

3. EXPERIMENTAL RESULTS

We determined the dependencies $\frac{c(t)}{c_i}$ at several h depths, for different initial concentrations, using some suspensions of

SiO_2 , $\text{Al}(\text{OH})_3$ and $\text{Mg}(\text{OH})_2$ in water. The time of the gravitational sedimentation, as well as the sedimentation rate, depends on the dimensions of the particles in suspension, on the initial concentration and on the depth in suspension.

In the following figures are presented some experimental results we have obtained.

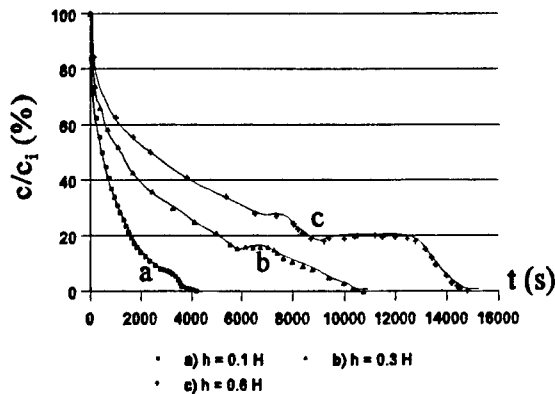


Fig. 5: Sedimentation curves (concentration as a function of time) at several depths (h)

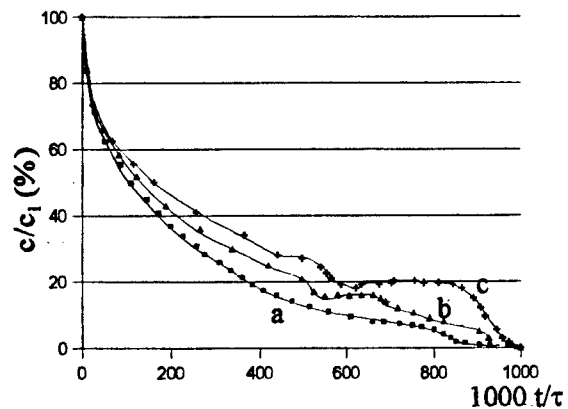


Fig. 6 Normalized curves from figure 5 (τ = sedimentation time).

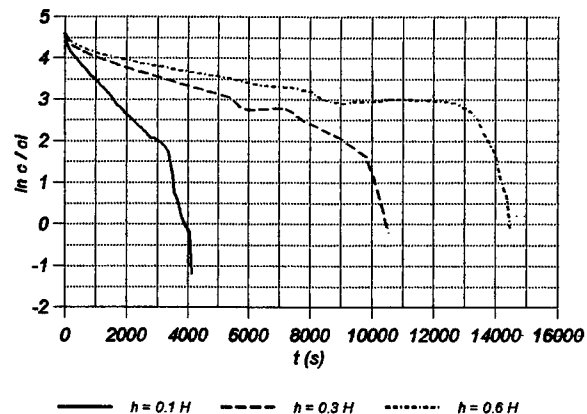


Fig. 7: Logarithmic representation of the curves from figure 5

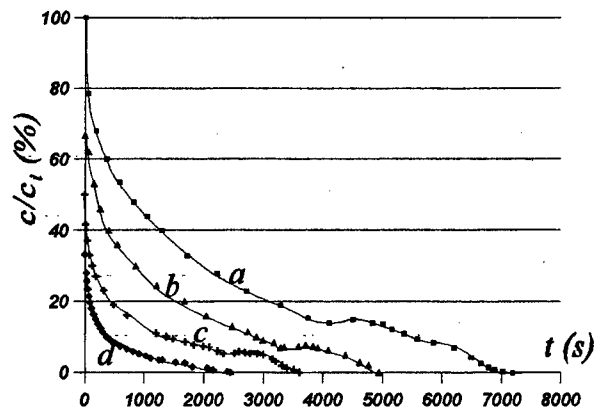


Fig. 8: Sedimentation curves for the same suspension at different initial concentrations ($h = 0.2H$; **a** - $c_{i1} = c_i$; **b** - $c_{i2} = 2c_i/3$; **c** - $c_{i3} = c_i/2$; **d** - $c_{i4} = c_i/3$.)

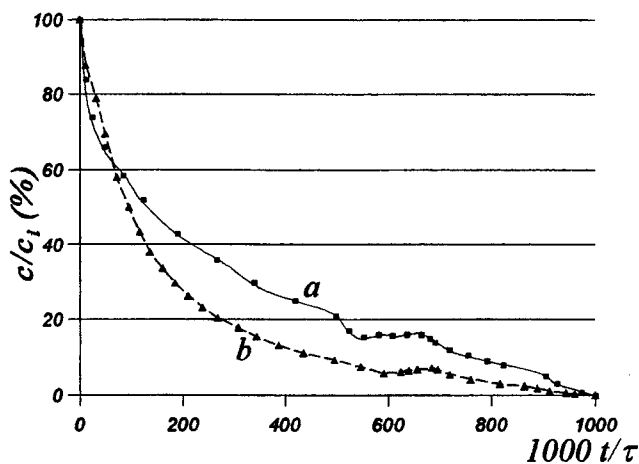


Fig. 9: The dimension of solid particles are bigger in the case **b** (30 μ m dimension) than in the case **a** (15 μ m dimension) ($h = 0.3H$)

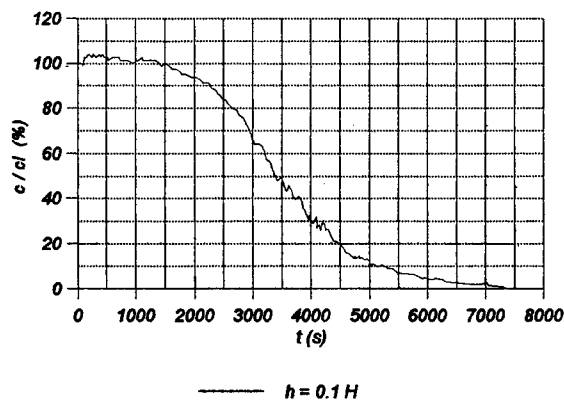


Fig. 10 (a): Sedimentation curves for small particles (6 μ m) in suspension.

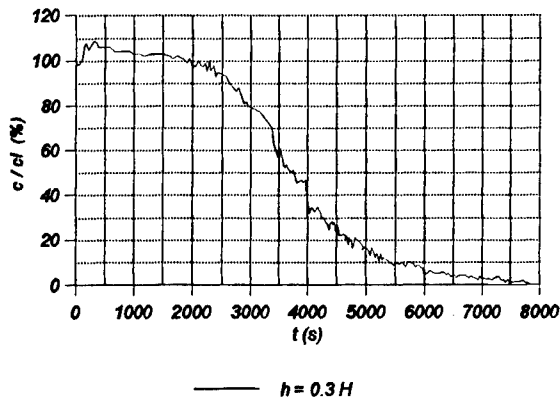


Fig. 10 (b): Sedimentation curves for small particles (6 μm) in suspension.

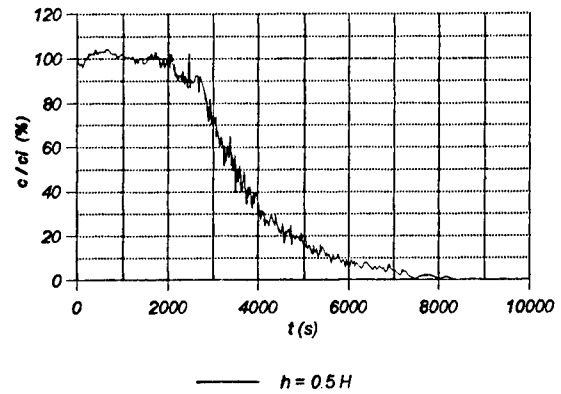


Fig. 10 (c): Sedimentation curves for small particles (6 μm) in suspension.

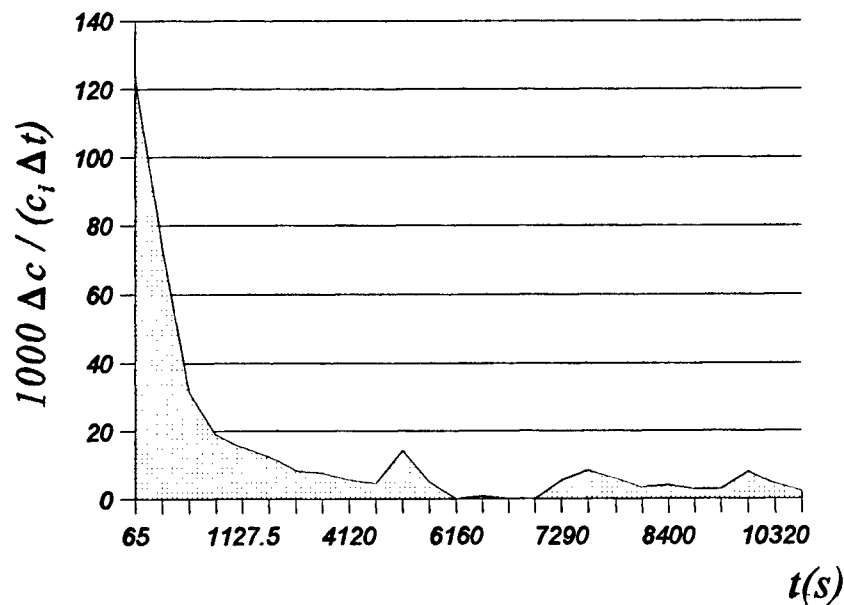


Fig. 11: Average rate of sedimentation as a function of time ($h = 0.3H$)

4. CONCLUSIONS

The experimental results we have obtained, suggest for the dependence on time of the concentration, a function as:

$$c(t) = c_i(t) \left\{ \exp\left(-\frac{t}{a}\right) + b \exp\left[-\frac{(t-c)^2}{d}\right] \right\} \quad (5)$$

where the first term describes the fall and the second the diffusion.

Positive parameters a , b , c , d depend on the features of the suspension, as it follows:

- a describes the sedimentation time τ which increases with the increase of " a ". Also " a " decreases as dimensions of the solid particles increase and as concentration and depth decrease.

- c express the moment when diffusion prevail (when concentration increase as a function of time); the second term in (5) is on the form of Gauss distribution and " c " corresponds to the moment when it has the maximum value. This maximum value is related to the parameter " b ", and " d " express the width of Gauss curve.

Experimental results shows that " b " increases as depth and concentration increase and as dimensions of solid particles decrease; " c " and " d " increase as depth and concentration increase. Also, " c " decreases and " d " increases as dimensions of the solid particles decrease.

The studies of sedimentation also point out the influence of the dimensions of the solid particles on the process. When dimensions are over 10 μm , the braked fall prevails and the dependence $c(t)$ is approximately an exponential decrease, as in figures 5, 6, 8 and 9. For dimensions under 10 μm diffusion prevails and $c(t)$ is a function as in figure 10; also, in case of small dimensions, fluctuations of concentration occur and intensify as dimensions decrease; so that for dimensions under 1 μm , sedimentation becomes a very slow process (because of the equilibrium between fall and diffusion); the movement of the solid particles in suspension becomes haphazard, like the Brownian movement.

5. REFERENCES

1. D. R. Mocanu - under coord. - "*Încercarea materialelor*" - Ed. Tehnică - București - pp. 275-278 - 1982.
2. I. Mândru, M. Leca - "*Chimia macromoleculelor și a coloizilor*" - E. D. P. - București - pp. 126-131 - 1977.
3. I. Cucurezeanu, R. Chișleag, P. Suci, D. Borza - "*Aplicații ale holografiei optice*" - Ed. Tehnică - București - 116-125 - 1984.
4. "*Laboratorii de fizică și chimie pe coloizii chimici*" - Ed. Chimia - Moscow - pp. 81-89 - 1986.

Quadrant-detector on the basis of InGaAsP heterostructures

V.Dorogan, V.Brynzari, T.Vieru, V.Kosyak

Laboratory of Microelectronics, Technical University of Moldova,
bd. Stefan cel Mare 168, MD 2012 Kishinev, Moldova

ABSTRACT

A new device called selective quadrant-detector, realized on the basis of InGaAsP heterostructures, is presented in the paper. It consists of a circular photodiode-quadrant with protective peripheric ring, having selective sensibility optimized for $\lambda = 1.06 \mu\text{m}$, in the center of which a photodetector integrated in the same crystal is formed. The photodetector has own capacity $C = 1\text{-}5 \text{ pF}$ and can be used for receiving the high frequency ($f > 1 \text{ GHz}$) optic signals and the small duration ($t \leq 1 \text{ ns}$) unitary signals. The presence of central photodetector decreases the coordinate characteristic abruptness ($K = 8 \cdot 10^3 \text{ V} \cdot \text{W}^{-1} \cdot \text{mm}^{-1}$) and photocurrent intensity with 8-10 %. Absolute spectral sensibility is $S_{\lambda=1.06} = 0.57 \text{ A/W}$ and photosensitivity spectrum semiwidth is $\Delta\lambda \leq 100 \text{ nm}$.

Keywords: photodiode, quadrant, InGaAsP heterostructure, infrared radiation, photosensitivity.

1. INTRODUCTION

Photodiode-quadrant (PDQ) with selective sensibility, elaborated and manufactured previously, is optimized for receiving the optic signals with $\lambda = 1.06 \mu\text{m}$ and is used in optoelectronic systems for orienting and directing the high velocity objects.^{1,2} According to calculations and measurements, the PDQ has an absolute spectral sensibility $S_{\lambda=1.06} = 0.57 \text{ A/W}$, an abrupt coordinate characteristic $K = 8 \cdot 10^3 \text{ V} \cdot \text{W}^{-1} \cdot \text{mm}^{-1}$ and can be successfully used for receiving the unitary optic signals with impulse duration $\geq 10 \text{ ns}$ and with incident optic power $\sim 1 \text{ mW}$ or for receiving the optic signals with limit frequency $\sim 20 \text{ MHz}$. The obtained values are limited here by relatively big area of PDQ, necessary to ensure the coordinate characteristic, which is the main characteristic of all photoreceivers with coordinate sensibility.

2. ESTIMATION OF PDQ LIMIT FREQUENCY AND ANSWER TIME

The photoanswer time of PDQ was determined for a standard load resistance $R_l = 50 \Omega$ to appreciate its limit possibilities. Two methods were utilized: after frequency characteristic and after transition characteristic of photodiode illuminated by a rectangular light impulse.

The photocurrent depending on frequency of optic signal throb was measured using the scheme presented in Fig.1.

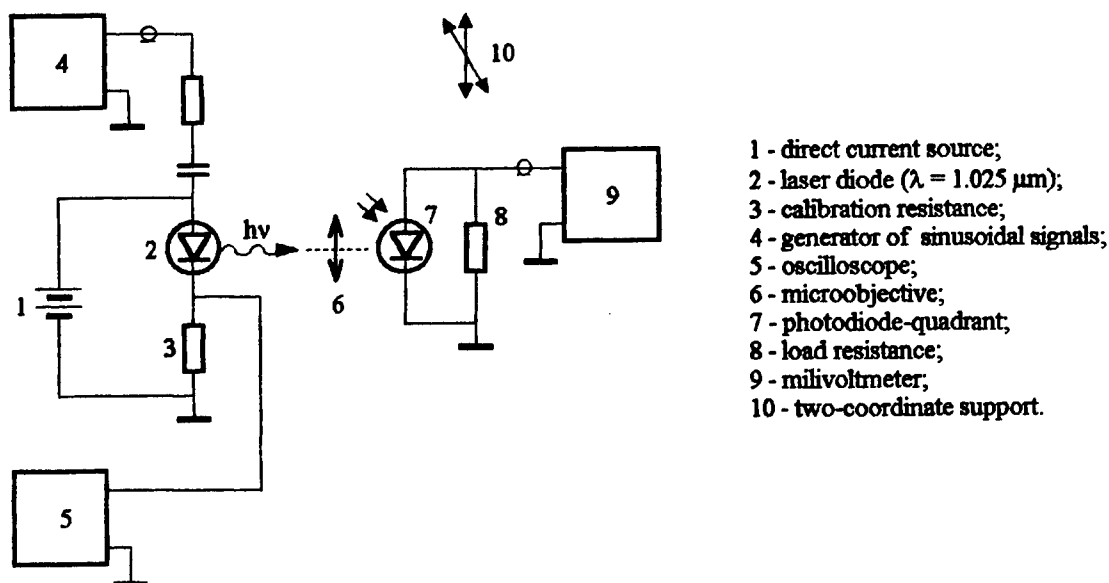


Fig.1. Scheme of instalation for measuring the photocurrent depending on frequency of optic signal throb.

The frequency dependence of photocurrent transmission coefficient (K) for different reverse polarisation are shown in Fig.2. The mathematical expression of this dependence is:

$$K = 1 / \sqrt{1 + (2\pi f\tau)^2} \quad (1)$$

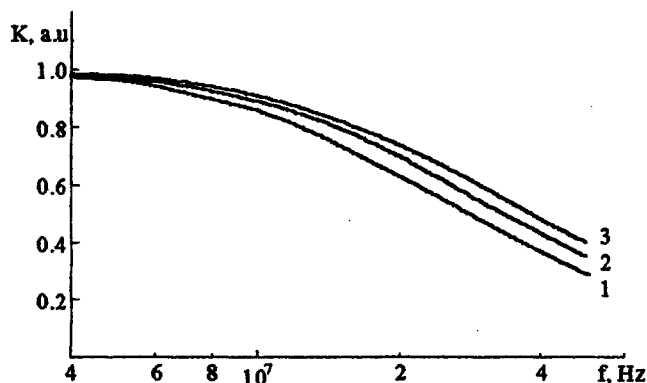


Fig.2. Frequency dependence of photocurrent transmission coefficient:
 U_{rev} , V: 1-0; 2-0.5; 3-1.0.

The photodiode transmission coefficient is determined practically as $K = U_f / U_o$, where U_f and U_o are photosignals at high and low frequency.

The photoanswer limit frequency is estimated from Fig.2 at level $K = 0.707$ and deals with time constant τ by expression:

$$\tau = 1 / (2\pi \cdot f_{lim}) \quad (2)$$

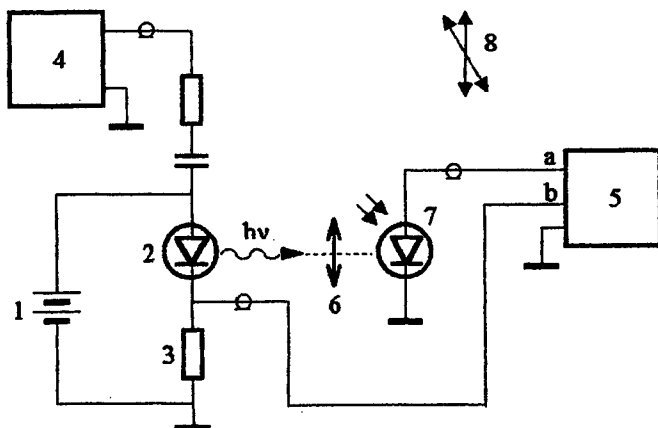
When the time constant is determined by p-n junction capacity and transition characteristic has an exponential form, the photoanswer time is determined at levels 0.1 and 0.9 of photocurrent maximum value or by relation

$$t_a = \tau \cdot \ln 9 \approx 2.2 \cdot \tau \quad (3)$$

Thus, measuring the limit frequency we determine the answer time for all quadrant sectors.

This method requires low intensity optic signals to ensure the straight sector of energetic characteristic $I_{ph} = f(\Phi_o)$. The minimizing of conductor capacity influence is also required. It have been observed for conductor total length $l < 0.4$ m, where conductor capacity is < 30 pF.

Measurements had showed that the time constant τ is determined by load resistance R and barrier capacity C. The p-n junction barrier capacity without polarisation is about $C = C_b \approx 200$ pF for each quadrant sector. The limit frequency is $f_{lim} = 16-18$ MHz and the answer time is $t_a = 22$ ns. Using the differential connecting of quadrant sectors we had decreased twice the answer time, practically equalizing it to $\tau = t_a \approx 10$ ns. Reverse polarizing the PDQ with $U_{rev} = 1$ V we had decreased the barrier capacity up to $C_b = 145$ pF and the answer time up to $t_a = 7$ ns.



- 1 - direct current source;
- 2 - laser diode ($\lambda = 1.025 \mu\text{m}$);
- 3 - calibration resistance;
- 4 - generator of nanosecond impulses;
- 5 - stroboscopic oscilloscope;
- 6 - microobjective;
- 7 - photodiode-quadrant;
- 8 - two-coordinate support.

Fig.3. Scheme of installation for study the photoanswer form.

The complete calculus of coordinate characteristics family $U(x, y_e)$ doesn't present a practical importance. Therefore, we had calculated the coordinate characteristic for the case $y = 0$, i.e. the light spot is symmetrical to axis "x". In this case the coordinate characteristic has four different domains with different mathematical expressions. They are:

- domain I - $0 \leq \bar{x} < 1 - \bar{r}$;
- domain II - $1 - \bar{r} \leq \bar{x} < 1$;
- domain III - $1 \leq \bar{x} < 1 + \bar{r}$;
- domain IV - $1 + \bar{r} \leq \bar{x}$,

where \bar{x} and \bar{r} are light spot coordinate and central detector radius reported to light spot radius ($\bar{x} = x/R$, $\bar{r} = r/R$). The characteristic points are $1 - \bar{r}$, 1 , $1 + \bar{r}$ and are noted in Fig.5 by "A", "O", "B".

Forming the mathematical expressions of coordinate characteristics, it was observed that domains 2, 3 and 4 are divided also in two parts with characteristic points $\sqrt{1 - \bar{r}^2}$ and $\sqrt{3}$.

Thus, the coordinate characteristic has a lot of domains with following analytic expressions:

- 1) $U(x) = 1/\pi (\pi + F_0)$, for $0 \leq \bar{x} < 1 - \bar{r}$;
- 2) $U(x) = 1/\pi (\pi + F_0 + F_1 + F_2)$, for $1 - \bar{r} \leq \bar{x} < \sqrt{1 - \bar{r}^2}$;
- 3) $U(x) = 1/\pi (\pi - F_1 + F_2)$, for $\sqrt{1 - \bar{r}^2} \leq \bar{x} < 1$;
- 4) $U(x) = 1/\pi (\pi - F_1 + F_2 + F_3 + F_4)$, for $1 \leq \bar{x} < 1 + \bar{r} < \sqrt{3}$;
- 5) $U(x) = 1/\pi (-F_1 + F_2 - F_3 + F_4)$, for $\sqrt{3} \leq \bar{x} < 1 + \bar{r}$ (if $1 + \bar{r} > \sqrt{3}$);
- 6) $U(x) = 1/\pi (\pi + F_3 + F_4)$, for $1 + \bar{r} \leq \bar{x} < \sqrt{3}$ (if $1 + \bar{r} < \sqrt{3}$);
- 7) $U(x) = 1/\pi (-F_3 + F_4)$, for $\sqrt{3} < 1 + \bar{r} < \bar{x} < 3$ (if $1 + \bar{r} > \sqrt{3}$).

$U(x)$ here is a parameter proportional with photocurrent through load resistance and show the relative difference of illuminated quadrant sectors, connected differential with load resistance.

The other parameters are:

$$\begin{aligned} F_0 &= -2 \arctg(b_0/a_0) + 2a_0 \cdot b_0; & F_1 &= \arctg(b_1/a_1) - a_1 \cdot b_1; \\ F_2 &= -\bar{r}^2 \cdot \arctg(b_2/a_2) + \bar{r}^2 \cdot a_2 \cdot b_2; & F_3 &= -\arctg(b_3/a_3) + a_3 \cdot b_3; \\ F_4 &= 4 \cdot \arctg(b_4/a_4) - 4 \cdot a_4 \cdot b_4; \\ a_0 &= \bar{x}; & b_0 &= \sqrt{1 - a_0^2}; \\ a_1 &= \frac{\bar{x}}{2} + \frac{1 - \bar{r}^2}{2\bar{x}}; & b_1 &= \sqrt{1 - a_1^2}; \\ a_2 &= \left| \frac{1}{\bar{r}} \left(\frac{\bar{x}}{2} - \frac{1 - \bar{r}^2}{2\bar{x}} \right) \right|; & b_2 &= \sqrt{1 - a_2^2}; \\ a_3 &= \left| \frac{3}{2\bar{x}} - \frac{\bar{x}}{2} \right|; & b_3 &= \sqrt{1 - a_3^2}; \\ a_4 &= \frac{3}{4\bar{x}} + \frac{\bar{x}}{4}; & b_4 &= \sqrt{1 - a_4^2}; \end{aligned}$$

We have to remark that these calculi are true for linear region of PDQ energetic characteristic $I_{ph} = f(Q)$. This region is characterized by low intensities of incident flux Q or by utilizing a load resistance more less than p-n junction resistance (short-circuit regime, $R_L < R_{pn}$).

The evolution of coordinate characteristic depending on central detector radius is presented in Fig.6. One can see that coordinate characteristic abruptness doesn't change practically up to $d/R_Q = 0.5$ and maximum voltage on the load resistance decreases with $< 10\%$ for central detector diameter $d \leq 400 \mu m$ ($d/R_Q = 0.4$). Therefore, the PDQ center can be used without any essential losses in coordinate characteristic to fabricate an integrated photodetector with low own capacity, capable to receive optic signals with high frequency (> 1 GHz) and unitary ones with impulse duration < 10 ns.

The second method permits to visualize the form of photoanswer impulse by a stroboscopic oscilloscope. The precision of this method is less because of difficulty in small duration rectangular photoimpulses forming and in measuring the low intensity (~ 10 - 20 mV) and duration (~ 1 ns) electric signals.

The scheme of instalation for study the photoanswer form is presented in Fig.3.

The photocurrent of one PDQ sector increases from $0.1 \cdot I_{\max}$ to $0.9 \cdot I_{\max}$ in $t_r \approx 20$ - 25 ns, what corresponds to result obtained by the first method.

Obtained values are extreme because the relatively big area of PDQ, necessary to ensure the coordinate characteristic, determines the big capacity of quadrant sectors. To extend the functional possibilities of PDQ we have elaborated and manufactured a new structure with an integrated central detector.

3. STRUCTURE, CHARACTERISTICS, PARAMETERS

The new structure ensures a selective spectral sensibility with maximum for $\lambda = 1.06 \mu\text{m}$, an abrupt coordinate characteristic, the detection of unitary optic signals with impulse duration < 10 ns or of optic signals with frequency > 1 GHz. Fig.4 shows the structure section (a) and the frontal view (b) of selective photodiode-quadrant with integrated detector.

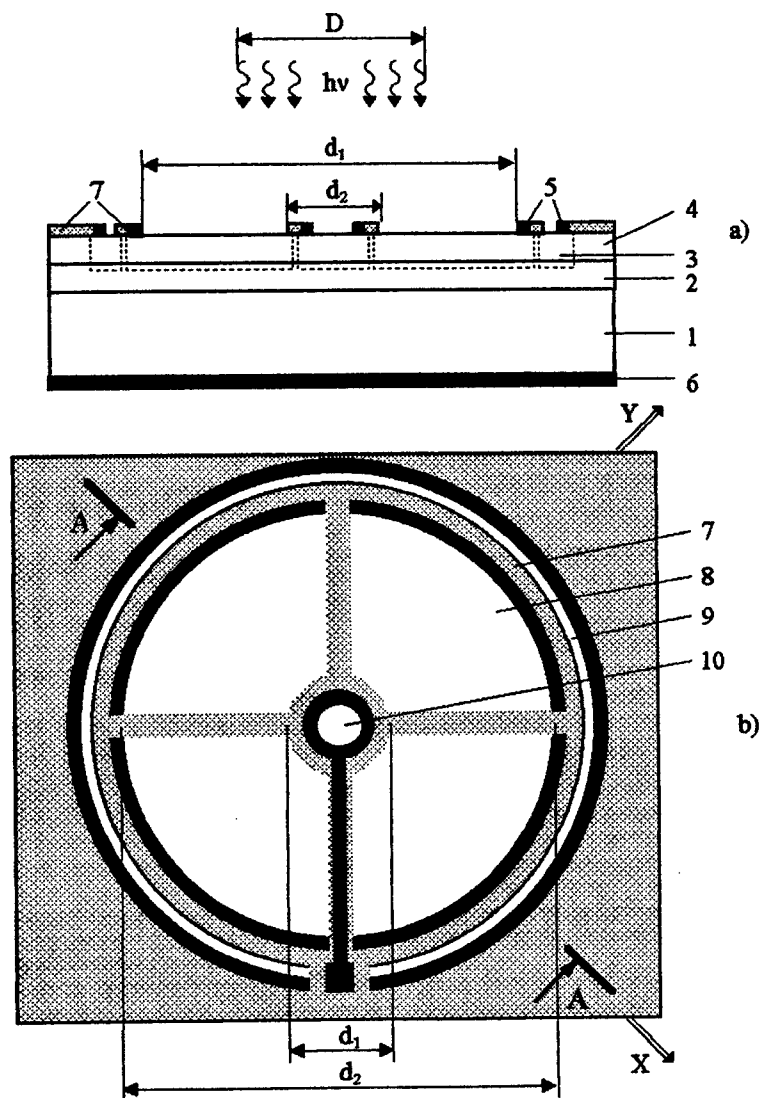


Fig.4. Selective photodiode-quadrant with integrated detector:
a - cross-section of structure; b - frontal view.

PDQ consists of $n^+ \text{InP}$ substrate 1, InGaAsP active layer 2, in which p-n junction 3 is placed, InGaAsP frontal layer 4, frontal metal contacts 5 and back contact 6. Separation of the whole surface into photosensible elements was made concomitantly with p-n junction forming by local diffusion of Zn through a SiO_2 mask 7. PDQ contains four elements 8 having circular sector form and a protective peripheric ring 9. A circular photoelement 10 with diameter $d_1 \leq 0.1 \cdot d_2$ (d_2 - diameter of PDQ active surface) was made in the center of PDQ.

The optic signal has a circular spot form with diameter $D = d_2/2$. When the optic signal is symmetrical respecting the center, photocurrents of those four circular sector elements 8 are equal. At optic signal moving after axes "x" or "y" the difference between photocurrents of two opposite sectors linear increases depending on coordinate. The peripheric ring 9 signals the moment when optic signal begin to go out the PDQ. Since the central detector 10 area is minimum 100 times less than PDQ one, the presence of central detector didn't change the coordinate characteristic abruptness. On the other hand, the central detector having a small area possesses a very low own capacity. It means that the time constant $\tau = R \cdot C$ gets small values, what permits to receive optic signals with frequency $> 1 \text{ GHz}$ and unitary ones with impulse duration $< 10 \text{ ns}$.

To determine the utilization fields of quadrant-detector we have to estimate the influence of central detector upon the PDQ characteristics and parameters. Since coordinate characteristic is the most important we study its evolution depending on central detector diameter.

The scheme of quadrant-detector surface is shown in Fig.5. Radius of photosensible sectors was $R_Q = 1 \text{ mm}$; radius of optic signal spot was $R = 0.5 \text{ mm} = R_Q/2$ and central detector radius "r" was variable. The coordinate of light spot center "x" was changing from zero (quadrant-detector center) to $3R = 1.5 \text{ mm}$ (spot completely went out the PDQ).

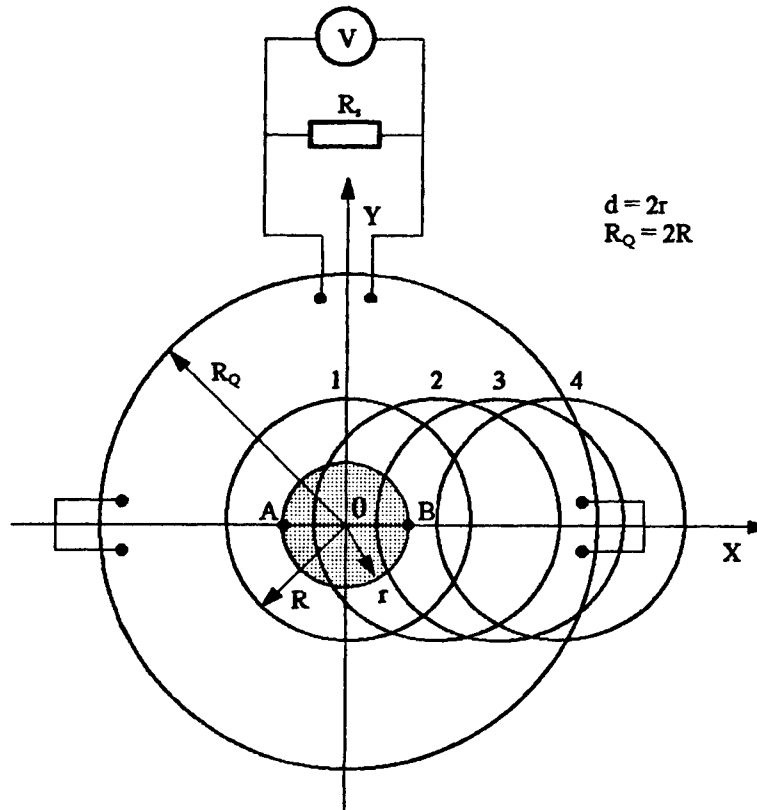


Fig.5. The scheme of quadrant-detector surface.

In general case, for PDQ with or without central detector, at differential connection of quadrant sectors, the electric signal on load resistance and, therefore, coordinate characteristic depend on both coordinate "x" and coordinate "y". To simplify the calculi, the dependence on "y" can be excluded by parallel connecting the sectors from the left and right side of axis "y" (see Fig.5). In this case the coordinate characteristic is transformed in a family of characteristics $U(x, y_0)$, where y_0 is a parameter.

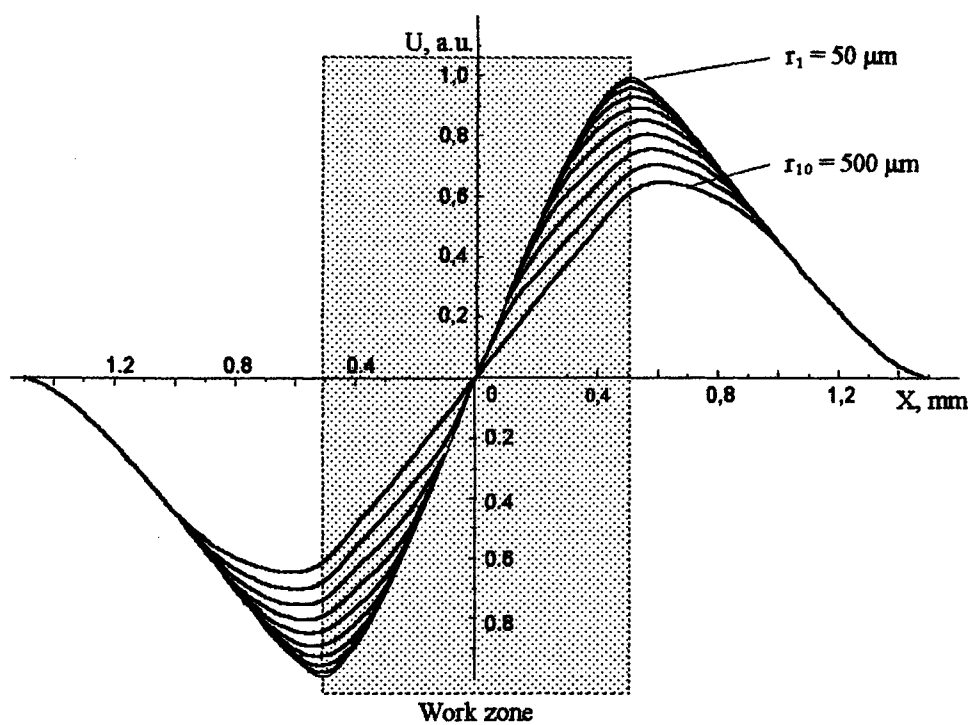


Fig.6. Evolution of coordinate characteristic depending on central detector radius.

A manufactured quadrant-detector encapsulated in capsule TO-5 is illustrated in Fig.7 and its main parameters are presented in the table.

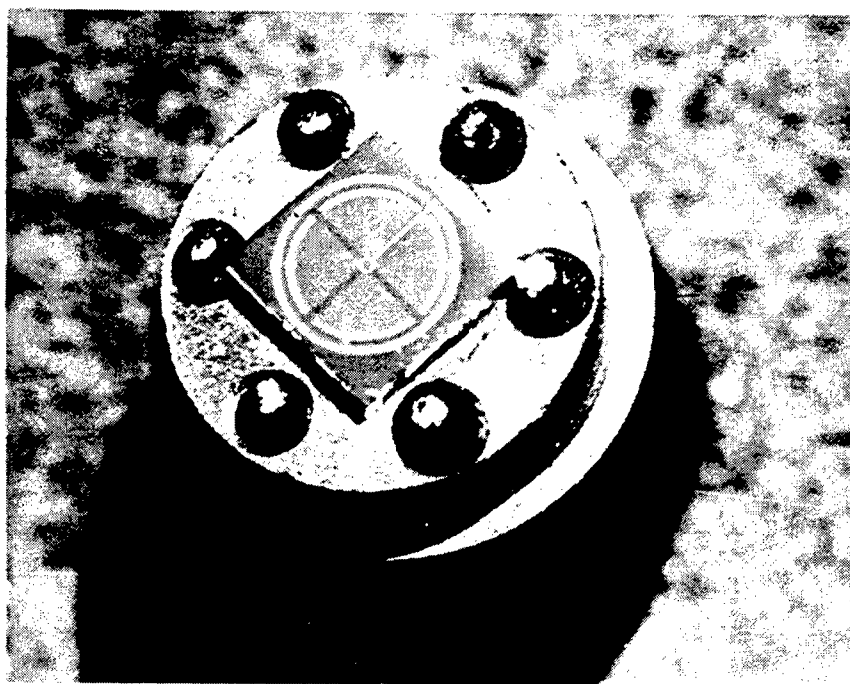


Fig.7. Quadrant - detector.

No.	Parameters	Value
1	Chip dimensions, mm × mm	3 × 3
2	Diameter of photodiode quadrant-detector, mm	2.6
3	Radius of photosensible sectors (R_0), mm	1
4	Diameter of central photodetector (d), μm	200
5	Width of protective peripheric ring, μm	150
6	Width of metal contacts: of quadrant, μm of central detector, μm	100 50
7	Width of SiO_2 separative strips, μm	100; 50
8	Radiation wavelength in maximum photosensitivity (λ_{max}), μm	1.06
9	Semiwidth of photosensitivity spectrum ($\Delta\lambda$), nm	< 100
10	Absolute sensibility ($S_{\lambda_{\text{max}}}$), A/W	0.57
11	Quantum efficiency (η), %	60
12	Own capacity of a quadrant photosensible sector (C_a^h), pF	190
13	One sector capacity for reverse voltage $U_{\text{rev}} = 1.5 \text{ V}$ (C_a^h), pF	145
14	Own capacity of central detector (C_c^v), pF	4
15	Own capacity of central detector for $U_{\text{rev}} = 1.5 \text{ V}$ (C_c^v), pF	1.5
16	Abruptness of coordinate characteristic (K), $\text{V} \cdot \text{W}^{-1} \cdot \text{mm}^{-1}$	$8 \cdot 10^3$

4. CONCLUSIONS

A new device called selective quadrant-detector with large functional possibilities was realized for the first time. It can successfully work in two regimes: detection of high frequency ($f > 1 \text{ GHz}$) optic signals, of small duration ($t \leq 1 \text{ ns}$) unitary signals and coordinate determination. It has coordinate characteristic abruptness $K = 8 \cdot 10^3 \text{ V} \cdot \text{W}^{-1} \cdot \text{mm}^{-1}$, absolute spectral sensibility $S_{\lambda=1.06} = 0.57 \text{ A/W}$ and photosensitivity spectrum semiwidth $\Delta\lambda \leq 100 \text{ nm}$.

5. REFERENCES

1. V.Dorogan, V.Kantser, A.Snigur et al, "Photodiodes with selective sensibility for control and space orientation of optoelectronic systems", IV Conference in Optics "ROMOPTO'94", V.2461, P.497-499, Bucharest, Romania, 5-8 September, 1994.
2. V.Dorogan, V.Brynzari, G.Korotchenkov and V.Kosyak, "Selective photodiodes with two-coordinate sensitivity (Quadrant) on the basis of InGaAsP quaternary compound", 20th International Conference on Microelectronics (MIEL'95), V.1, P.431-434, Nis, Serbia, 12-14 September 1995.

Photothermal method using a pyroelectric sensor for thermophysical characterisation of agricultural and biological samples

A.Frandas¹, D.Dadarlat¹, M.Chirtoc¹, H.Jalink², D.Bicanic³, D.Paris⁴, J.S.Antoniow⁴,
M.Egee⁴, C.Ungureanu¹

¹ Institute of Isotopic and Molecular Technology, POB 700, RO-3400, Cluj-Napoca, Romania,

² Centre for Plant Breeding and Reproduction Research (CPRO-DLO), Droevendaalsesteeg 1,
POB 16, NL-6700, The Netherlands

³ Laser Photoacoustic Laboratory, Department of Agricultural Engineering and Physics,
Wageningen Agricultural University, Bomenweg 4, NL-6703 Wageningen, The Netherlands

⁴ UTAP/Laboratoire d'Energetique et d'Optique, Universite de Reims, Moulin de la Housse
BP 1039, 51687 Reims Cedex 2, France

ABSTRACT

The photopyroelectric (PPE) method in different experimental configurations was used for thermophysical characterisation of agricultural and biological samples. The study appears important due to the relation of thermal parameters to the quality of foodstuffs (connected to their preservation, storage and adulteration), migration profiles in biodegradable packages, and the mechanism of desiccation tolerance of seeds. Results are presented on the thermal parameters measurement and their dependence on temperature and water content for samples such as: honey, starch, seeds.

1. INTRODUCTION

The photopyroelectric (PPE) method for thermal characterisation of materials is based on the measurement of the temperature increase of a sample due to absorption of radiation, by placing a pyroelectric sensor in thermal contact with the sample [1]. The PPE signal contains information on the thermal properties of the sample (conductivity, thermal diffusivity, thermal effusivity, specific heat) as well as on its optical properties (optical absorption coefficient, surface reflectance). Being a photothermal method, PPE signal is also sensitive to the nonradiative quantum efficiency of the radiation-to-heat conversion process [2].

The recently increasing interest in the thermal parameters measurement function of temperature or water content of agricultural and biological materials is due to their relation to the quality of foodstuffs (in relation to their preservation, spoilage, adulteration), migration profiles in biodegradable packages, or several mechanisms of biological systems like desiccation tolerance, freezing or chilling injuries. Thermophysical characterisation of these types of materials is not a simple task due to few problems encountered such as: first order phase transitions associated with volume change, inhomogeneities, coexistence of phases, instability in time, impossibility of

performing a good thermal contact due to sample's geometry, necessity of performing "in vivo" measurements.

For quantitative results, another set of problems comes from the necessity to calibrate the PPE measurements [3]. PPE is able to offer absolute values only for the thermal diffusivity [4]. In order to obtain the values of the other three thermal parameters (due to the relationships between them, only two are independent), the value of a second thermal parameter at a given temperature is necessary. For classical samples, values of the thermal conductivity or specific heat are usually available in the literature; this is not the case for foods or biological samples. This problem was partially solved by using special detection cells and by combining different PPE configurations.

2. BASIC CONFIGURATIONS OF THE PPE METHOD

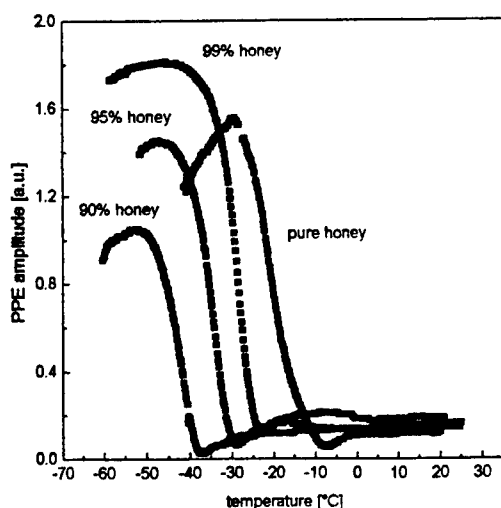
Basically, the PPE method is concerned with the measurement of the heat developed in a sample (due to absorption of a modulated light) with a pyroelectric sensor, situated in thermal contact with a sample.

Due to the characteristics of the investigated samples, two PPE configurations were selected as most suitable for calorimetric investigation (i) the back configuration (BPPE) with opaque sample and thermally thick sensor [4] and (ii) the front configuration (FPPE) with optically opaque and thermally thin sensor and thermally thick sample [5].

3. EXPERIMENTAL

The full description of the experimental cell and measuring setup are given elsewhere [6]. The newly designed cell made use of Peltier elements for changing the temperature. The entire measuring system was computer controlled.

1. Adulteration of honey



Pure honey and honey mixed with up to 15% water were measured by BPPE in the -60°C $+20^{\circ}\text{C}$ temperature range. The purpose was to detect the glass transition of honey and the influence of time and water content on the transition temperature. The results are presented in Fig.1 and the corresponding phase diagram in Fig.2 and 3.

Fig.1 The PPE signal amplitude for honey with different water contents. The temperature rate was $0.5^{\circ}\text{C}/\text{min}$.

As one can see in Fig.3, in time, the critical temperature of honey (kept in normal laboratory conditions, 1 atm, 20°C, 40% relative humidity) increases from -15.7°C to -9°C. The increase is faster in the first 5-6 hours, then a saturation appears. This shift in the critical temperature can be explained by a decrease of the water content. The influence of water content is more clear in Fig.2. A 15% water added to honey decreases the critical point with 40°C.

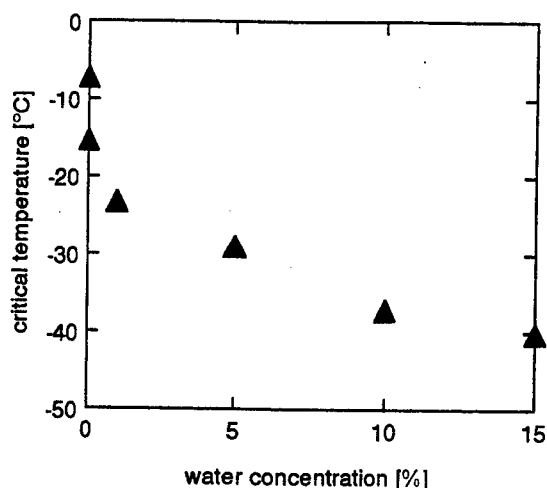


Fig. 2 Phase diagram of honey mixed with water

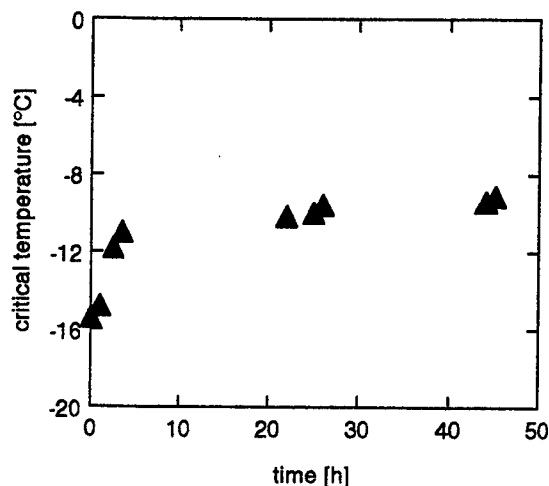


Fig.3 Phase diagram of honey in time

Another thermal parameter sensitive to water content is the thermal effusivity. Some values of this parameter for different water contents, as obtained in the front detection configuration are presented in Table I

Table I Thermal effusivity for honey mixed with water:

water	1600 Ws ^{1/2} m ² K
honey 50%	1380 Ws ^{1/2} m ² K
75%	1228 Ws ^{1/2} m ² K
85%	1166 Ws ^{1/2} m ² K
90%	1145 Ws ^{1/2} m ² K
95%	1111 Ws ^{1/2} m ² K
99%	1093 Ws ^{1/2} m ² K
100%	1088 Ws ^{1/2} m ² K

2. The influence of water content on starch

Starch samples with different water contents were obtained by equilibrating the samples in atmosphere containing saturated salt solutions. The frequency spectrum of an starch sample is presented in Fig.4 From the frequency dependence, the thermal diffusivity (α) and specific heat (C) of several samples were calculated (see Table II).

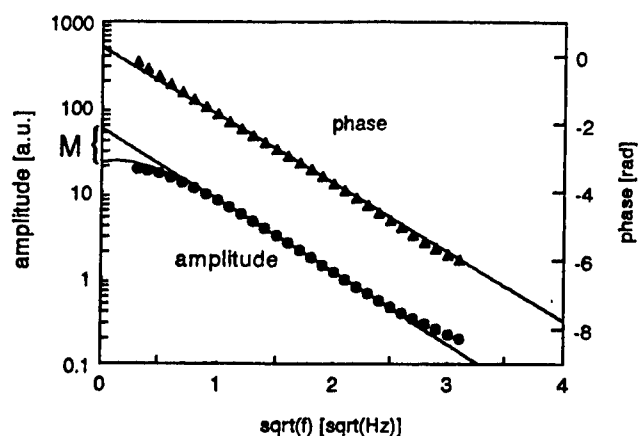


Fig.4 The frequency spectrum of PPE amplitude and phase for a dry starch sample.

Table II The thermal diffusivity and specific heat obtained from the frequency spectrum for samples equilibrated at different relative humidities

starch (0% RH)	$\alpha=11.3 \cdot 10^{-8} \text{ m}^2/\text{s}$	$C=2.20 \cdot 10^6 \text{ J/m}^3\text{K}$
starch (53% RH)	$\alpha=10.7 \cdot 10^{-8} \text{ m}^2/\text{s}$	$C=3.23 \cdot 10^6 \text{ J/m}^3\text{K}$
starch (98% RH)	$\alpha=11.0 \cdot 10^{-8} \text{ m}^2/\text{s}$	$C=5.50 \cdot 10^6 \text{ J/m}^3\text{K}$

The temperature dependence of the thermal diffusivity for starch samples equilibrated at different relative humidities were obtained in the back configuration. The results are shown in Fig.5.

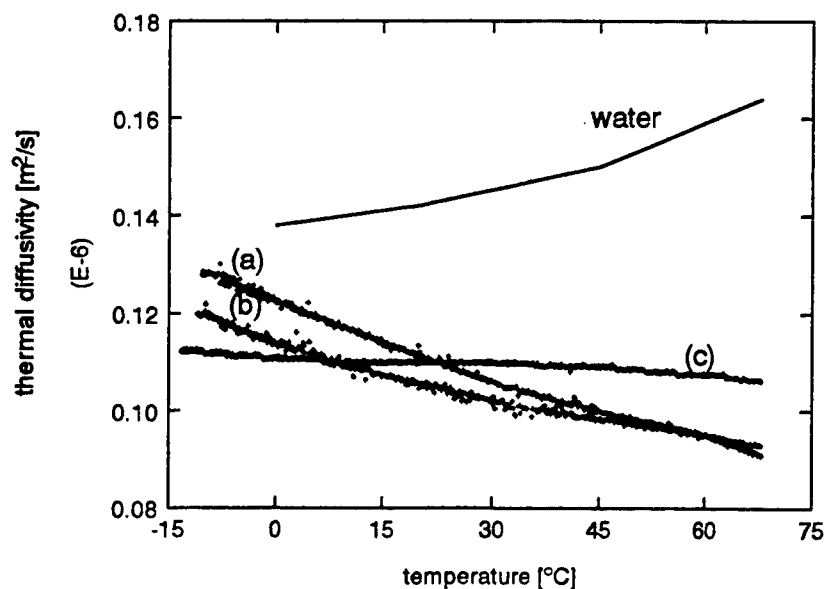


Fig.5 The thermal diffusivity of starch samples equilibrated at different relative humidities. (a) 0%, (b) 53%, (c) 98 %.

3. The phase diagram of Soybean seeds

The hypothesis that seed cytoplasm exists in a glassy state is widely accepted. Glasses have the advantages of stopping the chemical reactions that require molecular diffusion, limit the constituents tendency to crystallize and adds further resistance to dehydration. The investigated samples were soybean seeds, with different water contents. As a sample, an entire cotyledon was used in the front configuration. Fig. 6 shows the amplitude of the PPE signal for both heating and cooling for a soybean seed with 0.46 gH₂O/gDW. (DW=dry weight). The phase diagram of the soybean seeds with different water contents is shown in Fig. 7.

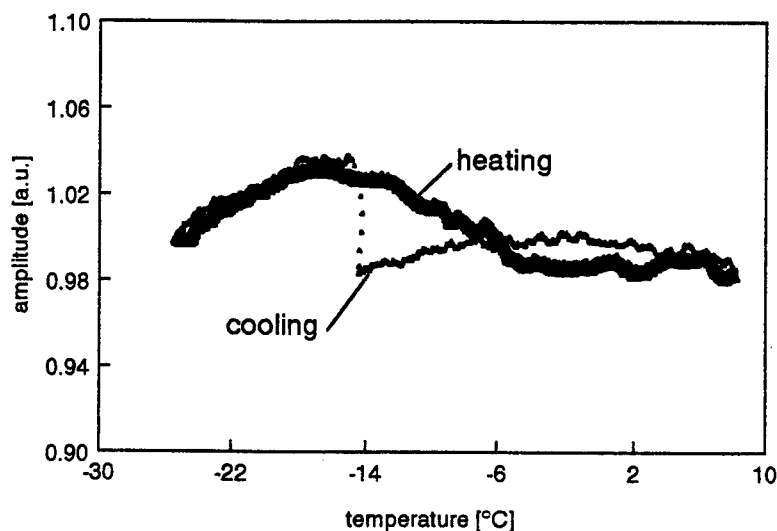


Fig.6 The amplitude of the PPE signal for a seed with water content of 0.46 gH₂O/gDW. The temperature rate was 0.6°C/min

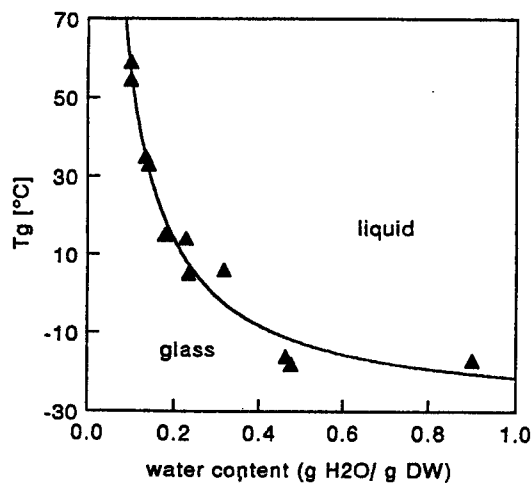


Fig.7 The phase diagram of the soybean seeds obtained by the FPPE configuration.

4. CONCLUSION

The versatility of the PPE method was proved by extending its application to agricultural and biological samples. We measured the thermal properties of honey in order to detect the most

sensitive parameter for spoilage and adulteration; in this case being the glass transition temperature. From the frequency dependence of the PPE amplitude and phase we measured the thermal diffusivity and specific heat of starch with different water contents, as a first step for measuring the water migration profile by photothermal methods. The phase diagram of soybean seeds, data relevant to storage protocols.

5. ACKNOWLEDGEMENTS

This research was partially supported by the Dutch Organisation for Scientific Research NWO, the International Agricultural Centre, The Netherlands, the INCO-COPERNICUS project ERBIC15CT961003 and the Humboldt Foundation, Germany.

REFERENCES

- [1] H.Coufal, Appl.Phys.Lett. **44**, 59 (1984)
- [2] M.Chirtoc, G.Mihailescu, Phys.Rev. **B40**, 9606 (1989)
- [3] D.Dadarlat, D.Bicanic, H.Visser, F.Mercuri, A. Frandas, J. Amer. Oil Chem. Soc. **72**, 273-279 (1995), **72**, 280-287 (1995)
- [4] M.Marinelli, U.Zammit, F.Mercuri, R.Pizzoferrato, J.Appl.Phys. **72** (3), 1096 (1992)
- [5] D.Dadarlat, A.Frandas, Appl.Phys. **A 56**, 235 (1993)
- [6] H.Jalink, A.Frandas, R. van der Schoor, D.Bicanic, Rev.Sci.Instrum. **67** (11), 3990 (1996)

Techniques for accurately measuring laser beam width with commercial CCD cameras

Carlos B. Roundy

Spiricon, Inc.
2600 North Main, Logan, Utah 84341 USA

ABSTRACT

CCD cameras are very useful instruments for the measurement of laser beam profiles and beam width. A principal advantage of CCD cameras is that they measure the entire beam cross-section simultaneously. However, camera noise and baseline offset can create significant errors in beam width measurements if not processed properly. Techniques have been developed that effectively compensate for both problems and enable very accurate measurements. These techniques are described, along with examples of the measurement accuracy under varying conditions. Additional signal processing is described that further enhances the ability to make accurate measurements.

Keywords: laser beam, measurement, CCD camera, accuracy, noise, baseline offset, signal processing

1. CCD CAMERAS FOR LASER PROFILE MEASUREMENT

1.1 Usefulness of CCD cameras

CCD cameras are very useful for laser beam profile analysis. The primary advantage of these cameras is the ability to capture the entire two-dimensional beam profile simultaneously. This is especially useful for pulsed lasers. The cameras are relatively uniform and linear in responsivity, which is very important for quantitative measurements.

1.2 Problems with CCD cameras

However, CCD cameras have two problems that inhibit their use. The cameras exhibit a drift of the DC baseline relative to the zero of the A to D converter. A positive camera baseline would suggest a false signal in the wings of a laser beam. A negative baseline drift cuts off energy in the wings of the beam. Thus a beam width measurement would be too large or too small, respectively.

Secondly, CCD cameras have a high level of random noise, typically 2 to 6 counts in an 8-bit digitizer. The RMS signal-to-noise ratio may be 100-300 but the peak-to-peak signal-to-noise ratio is as low as 50. Thus the signal in the wings of a laser beam is often buried in the random noise. Most digitizers truncate the noise below the mean of the noise distribution, which gives a false positive baseline shift. Digitizers that use background subtraction solve the baseline offset problem, but do not retain negative noise components to offset the positive noise.

1.3 Measurement accuracy considerations

To obtain accurate laser beam display and measurements it is essential that baseline drift and random noise be properly processed by the beam analyzer. Spiricon's patented Ultracal™ algorithms automatically compensate for these in all calculations.

2. BEAM WIDTH DEFINITIONS

Measurement methods to define the width of a laser beam include full-width-half-max, percent of peak, percent of energy, and knife-edge measurements. Each one of these has its place in certain applications. However, laser propagation theory has generated the Second Moment method, designated $D4\sigma$, which is used in the ISO standard for laser beams. It is considered to be more representative of the true width of a laser beam as it relates to beam propagation and focusing than are the other methods.

The Second Moment beam width algorithm integrates all energy in the camera field and gives particular weight to the noise and signal far into the wings of the beam. Noise generated by CCD cameras in the wings previously precluded this method from making accurate measurements. Spiricon engineers have generated new calculation algorithms in the PC Laser Beam Analyzer, Model LBA-300PC, that enable accurate Second Moment beam width measurements, even in the presence of high CCD camera noise.

3. THEORETICAL CALCULATIONS

To determine the effect of special measurement algorithms to enable $D4\sigma$ measurement, a simulated beam width calculation was performed. A mathematically generated Gaussian beam was computer generated so it would be a precisely defined width. To know the accuracy of a beam width measurement you must know the beam width to start with. Random noise with a Gaussian distribution of ± 8 counts at the 3 sigma level was then added to the mathematically generated beam. Measurements were then made using Spiricon algorithms to determine the accuracy of measuring the beam width under various conditions with a typical noise distribution included.

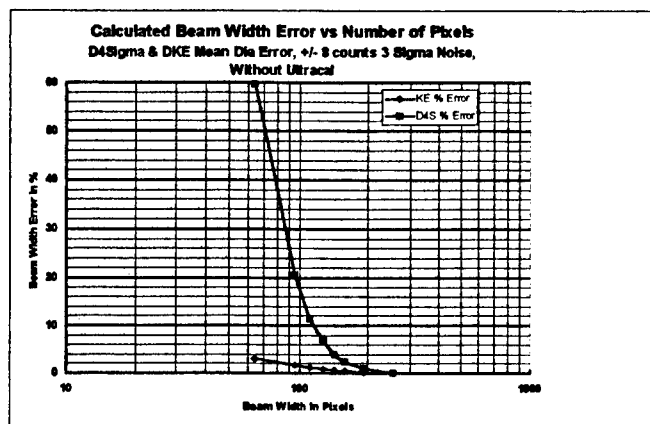


Figure 1. Theoretical beam width error vs. the number of pixels for both a $D4\sigma$ and a knife-edge measurement with a maximum size 256 pixel diameter beam in a 512X512 camera field.

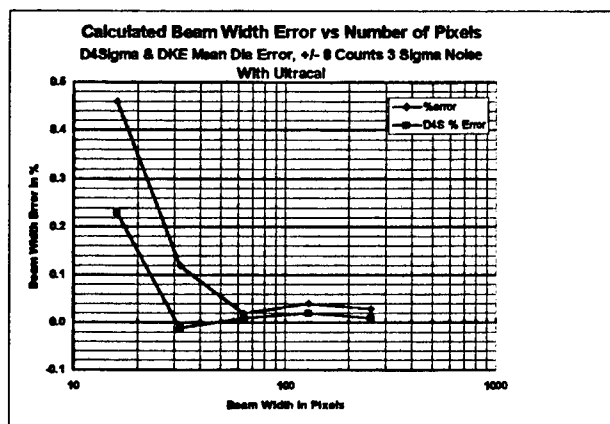


Figure 2. Theoretical beam width error for $D4\sigma$ and knife-edge measurements using an aperture of two times the width of the beam.

For example, Figure 1 illustrates the calculated beam width error vs. beam size using standard calculation algorithms. The beam started as a 256 pixel diameter beam in a 512x512 pixel camera field. Note that in a 512x512 camera array, a beam width only as small as 64x64 is calculated at 60% error using the $D4\sigma$ method. This theoretically confirms previous reports of the errors generated by the presence of noise in $D4\sigma$ measurements. Also shown in Figure 1 is the beam width error calculated using the conventional knife-edge method. It generates only 3% error at 64x64 beam size. Thus, while $D4\sigma$ is the theoretically correct way to measure a beam width, the practical problems of noise in the camera had precluded its use up to this point. The knife-edge technique, which is an approximation of the $D4\sigma$ method, is not nearly so affected by the noise and is able to provide a relatively accurate calculation as the beam width is reduced.

Using the knowledge gained from the simulations of Figure 1, Spiricon engineers have developed a new calculation algorithm, Ultracal, that enables accurate $D4\sigma$ and knife-edge measurements in the presence of camera noise. Under the same conditions of the simulations of Figure 1, the simulated measurement accuracy of the new algorithms is shown in Figure 2. A $D4\sigma$ calculation is now made with only 0.25% error down to a 16x16 beam width, vs. 60% at 64x64, even beating the knife-edge method error of 0.5%. These are astoundingly accurate results. In fact, these are the first reported indications that an accurate $D4\sigma$ measurement can be made with commercial grade CCD cameras.

4. ACTUAL BEAM WIDTH MEASUREMENTS

Many factors can contribute to the accuracy of a laser beam width measurement with CCD cameras. These factors are listed independently here, but they all interact with each other. These factors include:

1. Baseline offset
2. Negative noise components
3. The laser beam size
4. The intensity of the laser beam
5. The digitized number of pixels
6. The measurement method
7. The use of apertures around the laser beam

These factors have been investigated by measurements on a real laser beam. In all cases the baseline autocalibration was performed immediately prior to each beam width measurement, which insured proper baseline setting. Without proper baseline setting there is no way to predict the accuracy of the measurements. The effect of the other factors in measurement accuracy were then investigated.

It has been shown in the past that most beams, including Gaussian beams, have significant energy in the wings, up to 2 times the $1/e^2$ beam width. Any mechanical fixture that clips the beam smaller than twice the beam width can cause diffraction in the beam. If a measurement aperture is less than twice the beam width, then clipping of signal in the wings occurs, and a reported beam width smaller than the real beam width is calculated. At about 2 times the beam width the optimum measurement is made, wherein no significant clipping occurs, yet the maximum suppression of noise in the fringes of the camera field is obtained. Spiricon engineers have created an algorithm that automatically sets an aperture at 2 times the measured beam width.

The following graphs show the effects of measurement with and without an aperture. Measurements were also made wherein negative noise components were retained vs. when the noise is truncated at zero with no negative components. These measurements were made for 2 variable conditions, namely the number of pixels in the beam and the peak intensity of the beam relative to the camera saturation level. The number of pixels was varied, but not by focusing to a smaller spot because then there would be no reference size to compare to. Instead the sampling frequency was reduced from every pixel in every row and line to every second pixel in every second row, every fourth pixel in every fourth row, etc. This is analogous to having a small focused spot of only a few pixels width, but not exactly the same. A focused beam measurement would be the subject of a future study. The intensity was varied by inserting neutral density filters in the beam. In all cases 16 frames were processed and the beam width error was calculated by adding the standard deviation to the mean change in calculated beam width.

4.1 Beam width measurement error compared by the same measurement method

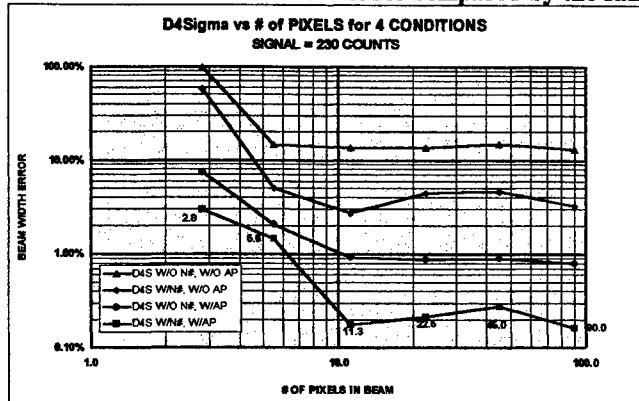


Figure 3. Beam width measurement error vs. number of pixels in the beam using D4σ method for 4 conditions of negative noise components and 2X apertures.

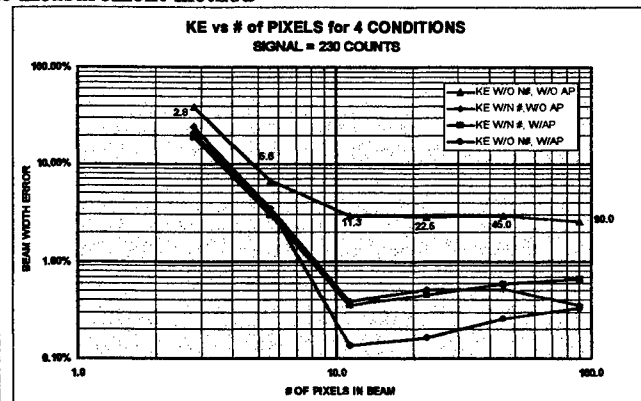


Figure 4. Beam width measurement error vs. number of pixels in the beam using knife-edge method for 4 conditions of negative noise components and 2X apertures.

Figure 3 shows a measurement using the Second Moment, or D4σ measurement method vs. the number of pixels in the beam, under 4 conditions. This beam was of high intensity, being about 230 digital counts out of 255 possible counts. This figure shows the wide diversity of accuracy obtained under the various conditions. Using negative numbers and 2X apertures an error of less than 0.3% is obtained down to only 10 pixels in the beam width, and an error as low as 3% with only 3 pixels in the beam width. Eliminating negative components of the noise increases the error from 0.3% to nearly 1%. Removing the 2X aperture increases the error to about 4%. Without negative noise components and without the aperture the error increases to over 10%. These curves show the importance of both negative noise and apertures in D4σ measurements. Nevertheless, with accurate baseline calibration and the automatic aperture, a 2% measurement is made with only 6 pixels in the beam width.

Figure 4 shows similar curves of error vs. pixels in the beam for a knife-edge measurement. Note that the knife-edge technique is less susceptible to noise than D4 σ . It yields a 3% error measurement under the worst condition of no aperture and no negative noise components. Excellent accuracy of less than 1% error are obtained under all other conditions from large beams down to beams with only 10 pixels in the width.

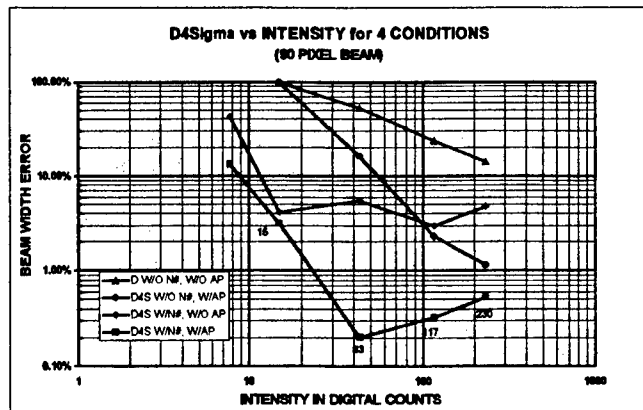


Figure 5. Beam width measurement error vs. beam intensity using D4 σ method for 4 conditions of negative noise components and 2X apertures.

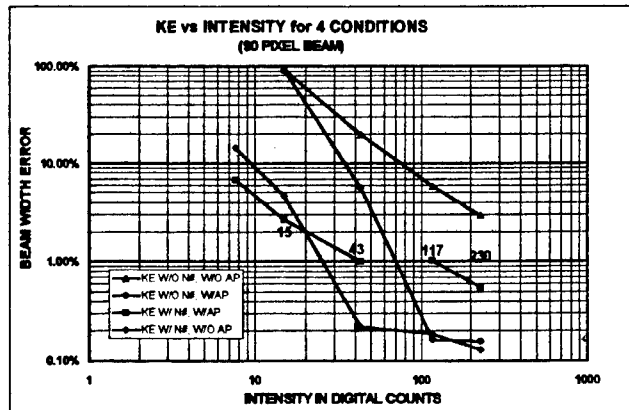


Figure 6. Beam width measurement error vs. beam intensity using knife-edge method for 4 conditions of negative noise components and 2X apertures.

Figure 5 shows beam width error vs. intensity. The beam width is about 90 pixels diameter in a 256x256 field. At full intensity the measurement is the same as in Figure 3. However, error increases rapidly as the intensity is reduced. Keeping negative noise components and with the 2X aperture, the error is less than 1% down to a signal level of 25 digital counts, or a beam peak of only 10% of saturation. The error is only 3% at 15 digital counts in the peak of the beam. The beam width error degrades very rapidly under the conditions of no negative noise components and/or without the 2X aperture. The D4 σ measurement is extremely sensitive to intensity because of the effect of noise in the wings of the beam. However, with a technique shown later, the D4 σ method makes a 7% measurement with a peak signal level less than 2 digital counts using negative numbers and an automatic 2X aperture.

Figure 6 shows the knife-edge measurement vs. intensity. The knife-edge measurement is much less sensitive to intensity than the D4 σ method and enables far more accurate measurements under all conditions.. Nevertheless, for multimode beams the knife-edge method may not measure correctly.

5. WIDTH MEASUREMENT ERROR COMPARISON BETWEEN SECOND MOMENT AND KNIFE-EDGE

5.1 Measurement Accuracy vs. the Number of Pixels in the Beam

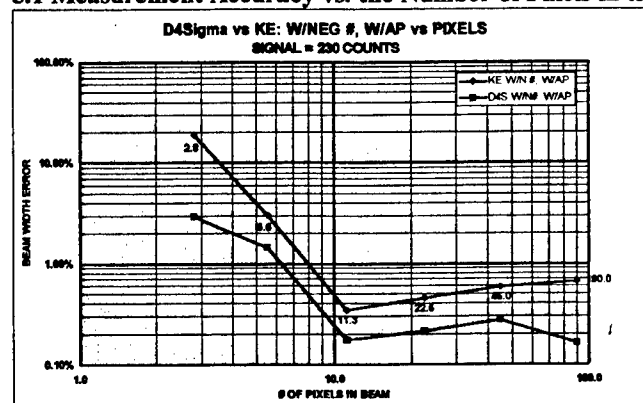


Figure 7. Comparison of the accuracy of D4 σ vs. knife-edge measurement with negative noise components and a 2X aperture in the beam.

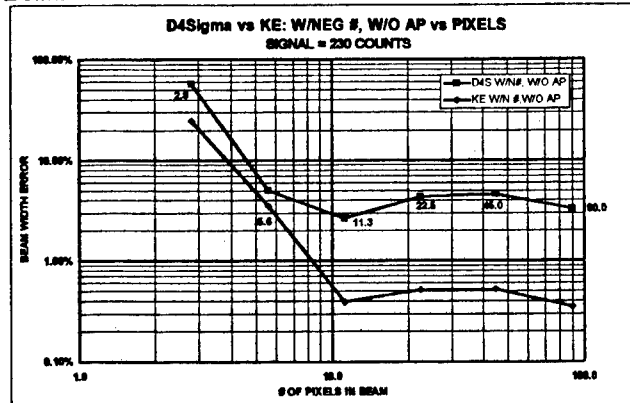


Figure 8. Comparison of the accuracy of D4 σ vs. knife-edge measurement with negative noise components but without an aperture in the beam.

Figure 7 shows a comparison of the $D4\sigma$ method of beam width measurement vs. the knife-edge method. When both an aperture and negative noise components are used, the $D4\sigma$ measurement is slightly more accurate than the knife-edge measurement, as predicted by Figure 2. It is seen that all of these measurements have less than 1% error to beam widths as small as 10 pixels in the beam. Even at 3 pixels in the beam the $D4\sigma$ measurement is only 3% error. In this case the $D4\sigma$ measurement is definitely superior. It is the more appropriate measurement method, and gives the best accuracy.

Figure 8 shows the measurement accuracy of knife-edge vs. $D4\sigma$ without an aperture. In this case, the knife-edge is considerably more accurate than the $D4\sigma$ measurement. This is expected because $D4\sigma$ is intrinsically susceptible to noise in the wings of the beam. The knife-edge method averages that noise, and is not nearly as susceptible to noise beyond twice the beam width. Even without the aperture the knife-edge measurement is less than 1% error down to 10 pixels beam width, which is totally acceptable, whereas the $D4\sigma$ measurement is in the 3-5% error range. This graph clearly shows, as compared with the previous graph, the value of an aperture in making $D4\sigma$ measurements.

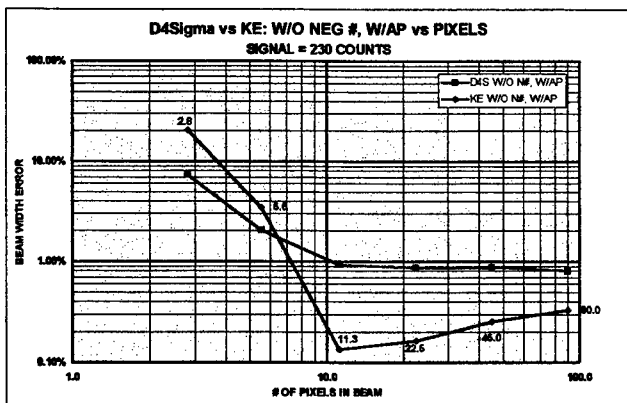


Figure 9. Comparison of the accuracy of $D4\sigma$ vs. knife-edge measurement without negative noise components but with a 2X aperture in the beam.

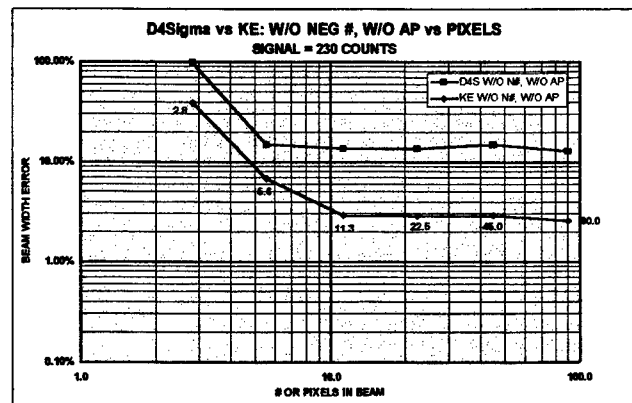


Figure 10. Comparison of the accuracy of $D4\sigma$ vs. knife-edge measurement without negative noise components and without an aperture in the beam.

Figure 9 shows a comparison of the $D4\sigma$ method and the knife-edge method when an aperture is maintained, but the negative numbers are not retained in the baseline. Here again the knife-edge method has considerably better accuracy than the Second Moment $D4\sigma$ method. This knife-edge accuracy is expected because without negative noise in the baseline the $D4\sigma$ will integrate positive noise components and will report a beam larger than the actual beam. Nevertheless, the $D4\sigma$ method maintains less than 1% error down to 10 pixels in the beam width, and as the beam gets even smaller, the $D4\sigma$ becomes slightly more accurate than the knife-edge.

Figure 10 shows the effect of not using the automatic 2X aperture and not maintaining the negative numbers in the baseline. Once again the knife-edge measurement is the most accurate, but in both cases the accuracy of measurement has deteriorated considerably. The knife-edge measurement provides 3% error down to 10 pixels, and the $D4\sigma$ measurement is about 12% error. Obviously this figure shows the real advantage of the two techniques of keeping negative noise and using the automatic aperture. Even with a large beam of full intensity neither method can maintain the accuracy that is obtained using the aperture and negative noise components.

5.2 Measurement accuracy vs. intensity

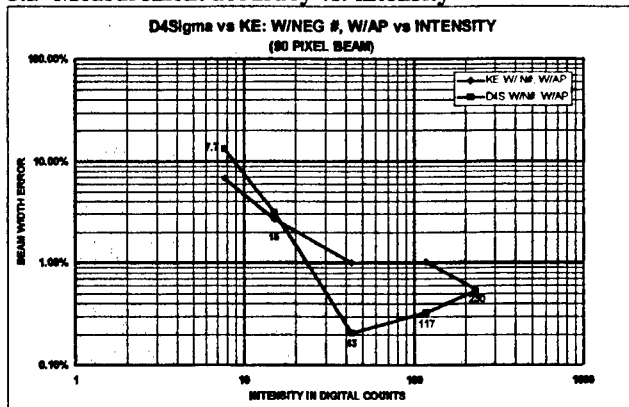


Figure 11. Comparison of the accuracy of D4 σ vs. knife-edge measurement with negative noise components and a 2X aperture in the beam. .

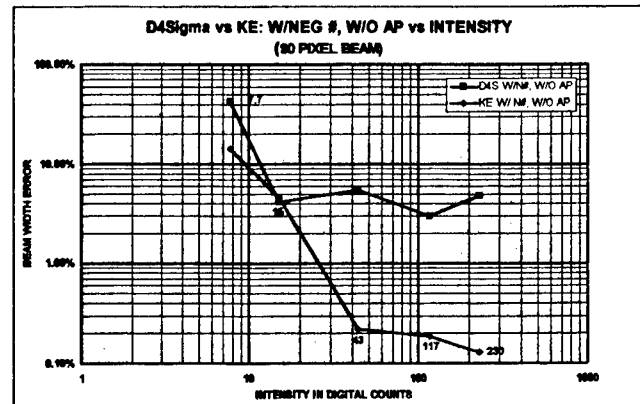


Figure 12. Comparison of the accuracy of D4 σ vs. knife-edge measurement with negative noise components but without an aperture in the beam.

Figure 11 shows a comparison of the knife-edge method vs. the Second Moment method as the peak intensity of the beam is reduced. In this figure negative noise components are retained and the 2X aperture is used to provide the most accurate measurement possible. This figure shows that D4 σ method is considerably more accurate than the knife-edge method when both error reduction techniques are used. D4 σ maintains an accuracy in the range of 0.2-0.5%, whereas the knife-edge measurement accuracy immediately goes to 1% as soon as the intensity is slightly reduced. At lower intensities of roughly 15 digital counts in the peak of the beam, both methods give an accuracy in the 3% range. Even this accuracy is quite good considering the low intensity of the beam.

Figure 12 shows what happens when the aperture is removed, even while the negative noise components are maintained. In this case the knife-edge measurement obtains accuracy far superior to the D4 σ method. This again is expected, since without the aperture D4 σ method is sensitive to noise in the wings of the beam and creates considerably greater error. Thus we see D4 σ measurement error in the 5% range down to 15 count peak intensity, whereas the knife-edge measurement is in the 0.2% range. Comparison between Figures 11 and 12 show that the knife-edge measurement is actually more accurate without the aperture, as long as the negative noise components are maintained. This is because with the aperture the knife-edge measurements estimates the beam slightly small. However, in either case the error is less than 1%, so this is somewhat academic.

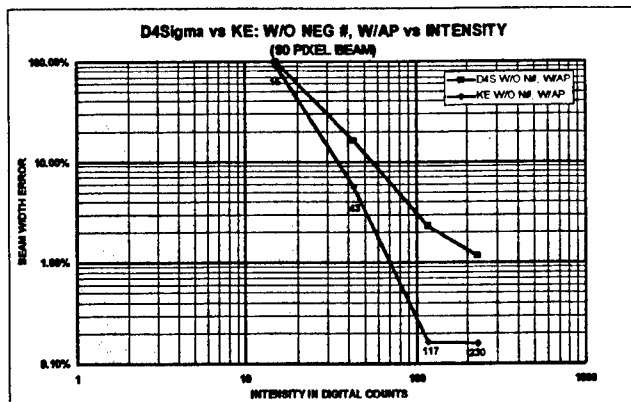


Figure 13. Comparison of the accuracy of D4 σ vs. knife-edge measurement without negative noise components but with a 2X aperture in the beam.

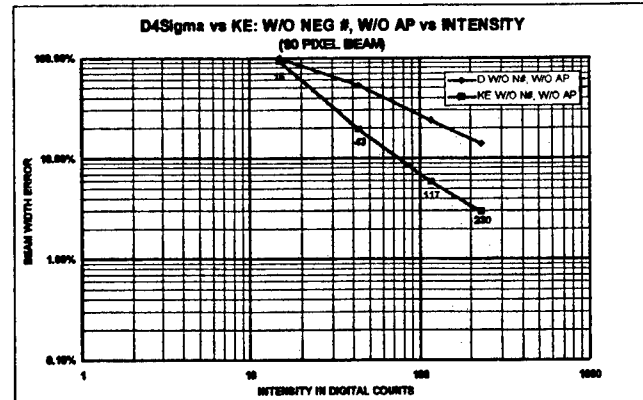


Figure 14. Comparison of the accuracy of D4 σ vs. knife-edge measurement without negative noise components and without an aperture in the beam.

Figure 13 shows the effect of keeping the aperture, but eliminating the negative noise components. Note that $D4\sigma$, even at high intensity, is over 1% error. Both $D4\sigma$ and the knife-edge methods cannot make accurate low intensity measurements without maintaining the negative noise components. At a peak signal level of 15 counts the error is already up to 100%.

Finally Figure 14 shows the effect of both removing the negative noise components and not using an aperture. Here the necessity of maintaining these two techniques is readily apparent. Neither the knife-edge measurement nor the $D4\sigma$ measurement give acceptable accuracy, even with a full intensity beam. The $D4\sigma$ of course is considerably worse at 15% error and full intensity vs. a knife-edge measurement at 3% error. Nevertheless, as the beam intensity is reduced, both measurements rapidly approach a totally unacceptable accuracy level.

Tables 1 and 2 summarize the results of the above 12 figures. It is seen from these two tables that the $D4\sigma$ measurement method is superior to the knife-edge measurement in only 2 out of 8 cases. This occurs in the two tables when both negative noise components and a 2X aperture are used. Once again this is because the $D4\sigma$ is especially susceptible to noise in the wings. In the other six cases the knife-edge measurement maintains greater accuracy than the $D4\sigma$ measurement. This is expected because of the greater effects of noise on the $D4\sigma$ measurement. If the beam is known to be of low mode content then the knife-edge technique yields greater accuracy without the error correction techniques. However, because a multiplying constant must be used with the knife-edge measurement, which may not be the correct number for higher mode content beams, the $D4\sigma$ method is superior. Since negative noise components and a 2X aperture can be used with greater precision, the $D4\sigma$ method is the measurement of choice.

Table 1
Accuracy of Two Measurement Methods vs. Number of Pixels

	W/N#, W/AP		W/N#, W/O AP		W/O N#, W/AP		W/O N#, W/O AP	
Pixels	90	3	90	3	90	3	90	3
$D4\sigma$	0.2%	3%	3.0%	60%	0.8%	8%	13%	99%
KE	0.7%	20%	0.4%	25%	0.3%	21%	2.5%	39%

Table 2
Accuracy of Two Measurement Methods vs. Intensities

	W/N#, W/AP		W/N#, W/O AP		W/O N#, W/AP		W/O N#, W/O AP	
Counts	230	8	230	8	230	15	230	15
$D4\sigma$	0.3%	14%	5%	45%	1%	100%	14%	100%
KE	0.6%	7%	0.1%	15%	0.2%	91%	3%	93%

6. SUMMARY OF MEASUREMENTS

These measurements illustrate the effects of various parameters of measuring beam widths. They show that it is possible to accurately measure a beam as small as just a few camera pixels in width, as long as other parameters are kept at their optimum. They also show that it is possible to measure a beam of fairly low peak intensity, using proper beam measurement algorithms. The parameters that should be under control of the operator are first, the number of pixels in the digitized camera field. Here the operator would want to minimize the digitized camera area and number of pixels to only incorporate what is needed to include the beam. This minimizes the amount of noise being contributed beyond the wings of the beam. Secondly, both $D4\sigma$ and knife-edge give relatively accurate measurements of low mode content beams. The $D4\sigma$ is preferred if the beam is not Gaussian. Third, an aperture placed around the beam increases the beam width measurement accuracy by nearly a factor of 10 in most cases. Retaining negative noise components can be extremely important. For high intensity beams that are large enough to fill the camera, the negative numbers are not as significant. However, if the peak beam intensity falls much less than saturation, or if a small beam of only a few pixels in a large field is measured, then retaining the negative noise gives more than a factor of 10 improvement in accuracy.

7. UNIQUE SIGNAL PROCESSING

7.1 Frame summing

Retaining the negative noise in the camera baseline field enables signal processing that would not otherwise be possible. One example of this processing is frame summing. When the negative noise components are eliminated, as is the case with most digitizers, frame summing causes all of the positive noise components to continually add, and ultimately produce a net positive baseline offset. However, with negative noise retained, the negative noise components subtract from the positive noise components on a frame-by-frame basis and keep the mean noise distribution near zero. The total noise adds roughly as the square root of the number of frames summed, the signal grows roughly as the number of frames, which gives a signal-to-noise ratio improvement roughly as the square root of the number of frames summed. Summing is used in the following example to show the dramatic effect that can be obtained with the retention of the negative noise.

7.2 Low intensity beam

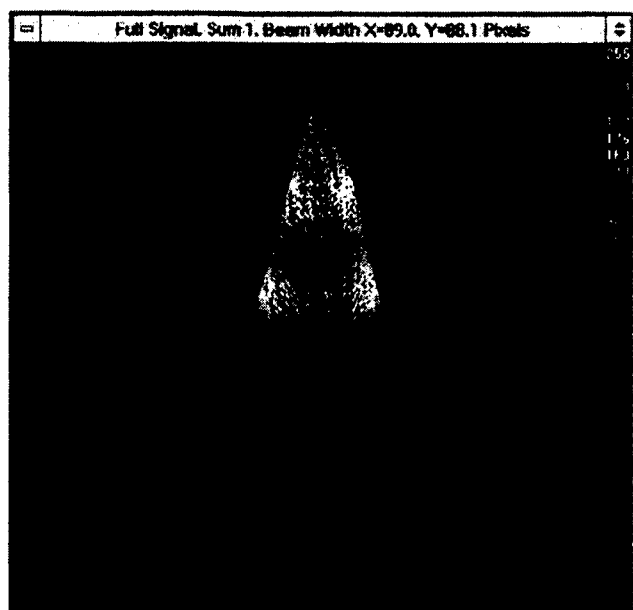


Figure 15. HeNe near Gaussian beam measured and displayed at full camera intensity.

The utility of frame summing signal processing is shown with a low intensity laser beam that was attenuated until it was buried in the noise so that the peak was approximately 1 digital count. The noise was approximately ± 3 digital counts. The signal-to-noise ratio at the beam peak is therefore about 0.3, and 0.003 in the wings of the beam. The beam was not even visible in the display. For reference, Figure 15 shows a 3D picture of the beam at its full intensity

7.3 Summing random noise

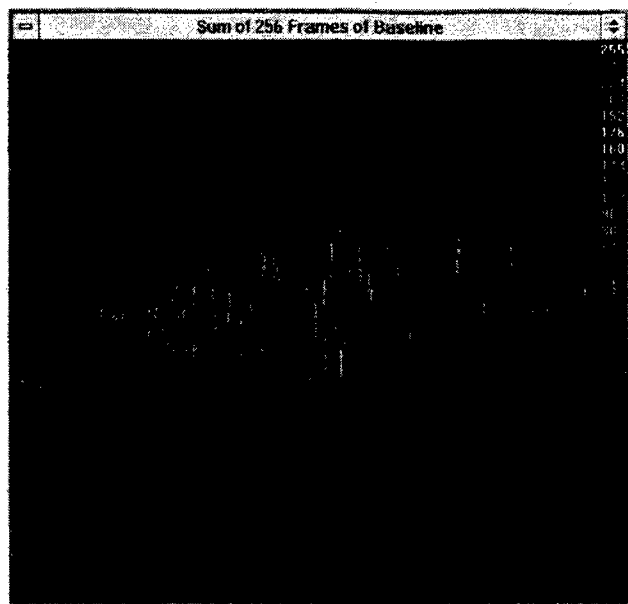


Figure 16. 3D display of noise field with summing of 256 frames.

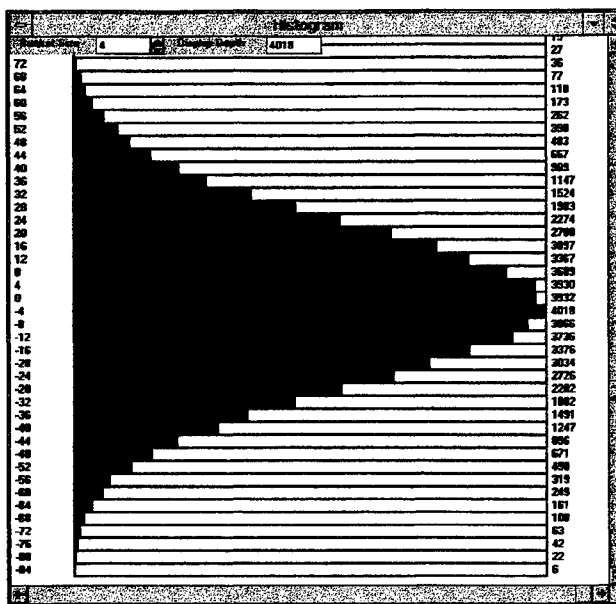


Figure 17. Histogram of the noise of Figure 16.
(Histogram shows the number of pixel counts at each intensity level.)

The accuracy of the baseline calibration is illustrated with the beam blocked and the baseline summed over 256 frames. Figure 16 shows a 3D picture of this noise field. The negative noise components are shown in gray, going below the colored positive noise components.

7.4 Noise histogram

The LBA-300PC produces a histogram of all signals. Figure 17 shows the histogram of the 256 sum of noise baseline from Figure 16. The histogram shows that the noise is centered at zero, with roughly a Gaussian distribution.

7.5 Beam with 256 frame summing

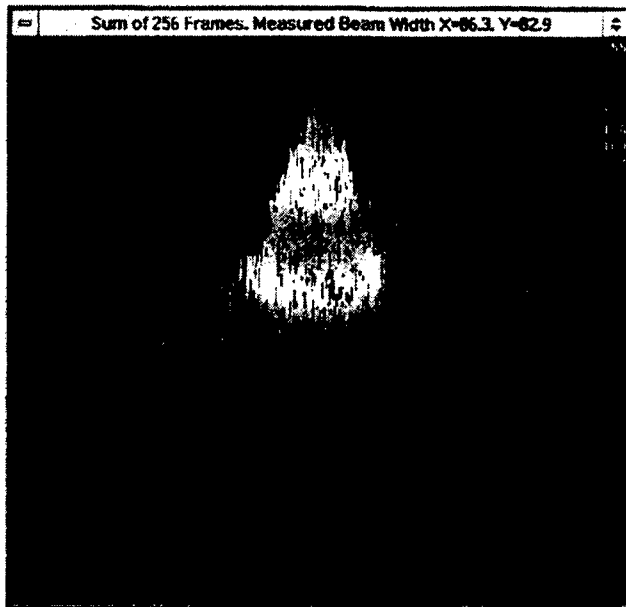


Figure 18. 3D image of laser beam of about 1 count intensity after 256 frames of summing.

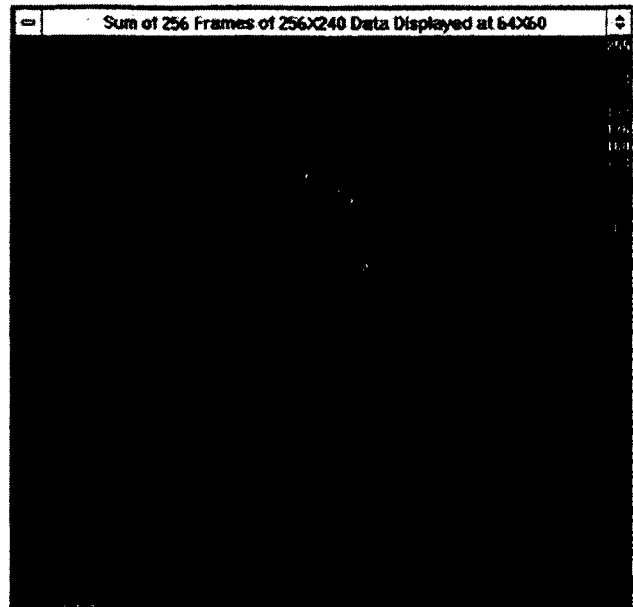


Figure 19. The beam of Figure 18 displayed with a 4X4 pixel averaging to create a single pixel.

Another Ultracal was performed, then immediately afterwards the 1 count beam was unblocked, and a sum of 256 frames of that beam was made. This beam profile is shown in Figure 18. The laser beam rises up out of the noise. The Ultracal algorithm enables fairly accurate beam width measurement even in this instance. The computed beam width error, from the unattenuated beam, is less than 5%.

One feature of the LBA-300PC is to average adjacent pixels for display purposes only. Thus with a 256X240 camera field, you can average 4X4 pixels into a single pixel, and display it as 64X60. This is shown in Figure 19. The beam of Figure 18 is now clearly discernible above the noise. One reason the knife-edge measurement algorithm can measure the beam accurately is that it uses an averaging technique to measure beam width. This figure illustrates why it is able to find and measure a beam in the midst of such large noise.

7.6 Convolution algorithm

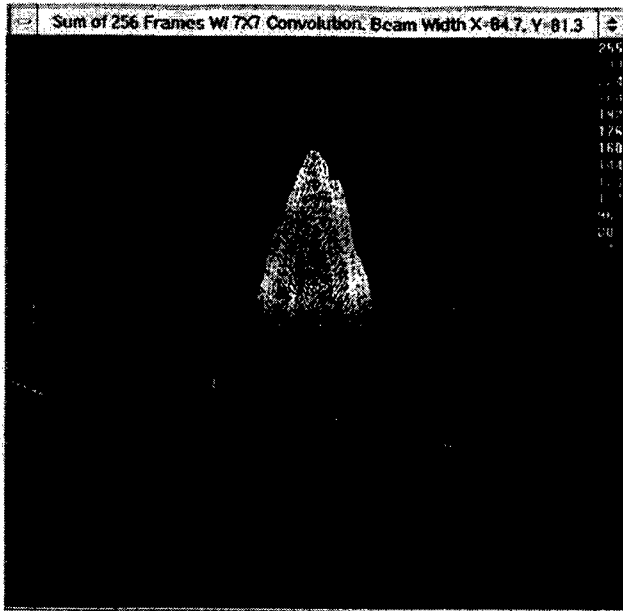


Figure 20. Convolution of 7X7 pixels of the beam of Figure 18.

The LBA-300PC has other signal processing algorithms that can be used to improve the measurement of beams and other objects. One of these is convolution, which can be used to suppress noise. Figure 20 shows the beam of Figure 18, with a convolution of 7X7 pixels. This clears up the noise extremely well, by processing of adjacent positive and negative noise components.

8. SUMMARY

There are many factors that contribute to the accuracy of laser beam width measurements. The operator must control the accuracy of the baseline (keeping it at zero), the negative noise components in the baseline, and the use of apertures to limit noise beyond the wings of the beam. Finally, being able to use the Second Moment measurement algorithm significantly improves the assessment of the actual beam width.

Keeping the negative noise components in the camera field enables other signal processing, such as averaging, summing, and convolution. These could be useful for machine vision, metrology, and other applications in addition to laser beam measurements.

Definition of a robust measure of similarity for the localization of small shapes in scenes.

Xavier Fernàndez, Josep Ferré-Borrull*, Salvador Bosch*.

Industrias de Optica, S.A. (INDO)
Sta. Eulàlia 181, 08902 L'Hospitalet (Barcelona), Spain
Tel.: 34 3 2982600 Fax: 34 3 4226181
E-mail: xavier@indo.es

(*) Laboratori d'Òptica. Dep. Física Aplicada i Electrònica
Universitat de Barcelona. Diagonal 647, 08028 Barcelona, Spain
Tel.: 34 3 4021203 Fax: 34 3 4021142
E-mail: pep@optica.fae.ub.es

ABSTRACT

After analyzing the problems related to finding a small shape in a scene, we introduce a nonparametric similarity measure based on the Kolmogorov-Smirnov statistic, which proves to be robust for template-matching problems where a target of binary characteristics is to be located inside a gray-scale image. We show that the Kolmogorov-Smirnov statistic gives the optimum thresholding level for the image and may be computed without actual thresholding of the image. Some interesting properties of the proposed similarity measure are exposed and compared to the corresponding properties of normalized correlation.

Keywords: Template matching, Similarity measures, Kolmogorov-Smirnov statistic, Normalized correlation.

1. INTRODUCTION

When the position of a small target having known characteristics (shape, size, orientation) is to be determined in a complex gray-scale scene, the template matching technique is widely used. Template matching uses a model of the target, and explores across the scene to find the regions which have (locally) a great similarity with the model, as computed by means of a properly defined similarity measure. The identification and localization of the target is assumed when the maximum value of the local similarity exceeds a threshold (decision) value.

Small targets, specially when they have been specially designed to be precisely located (as co-operative targets, fiducial marks, or synthetic references⁽¹⁾) have binary brightness characteristics: a shape defining a uniform foreground which is brighter (or darker) than the surrounding uniform background. Thus, the geometric design of the target, represented by its shape, is the distinguishing feature of the target.

The binary nature of the target suggests that an initial thresholding of the image acquired from the scene, followed by a searching procedure based on a binary-domain similarity measure^(2,3), would be a good choice for localizing the target. Binary similarity measures rely on match-and-mismatch pixel counting, so they have a low computing cost and a very simple implementation. Pixel counting is simply a kind of geometric similarity measurement, and the values obtained can be easily normalized.

(*) Address for correspondence.

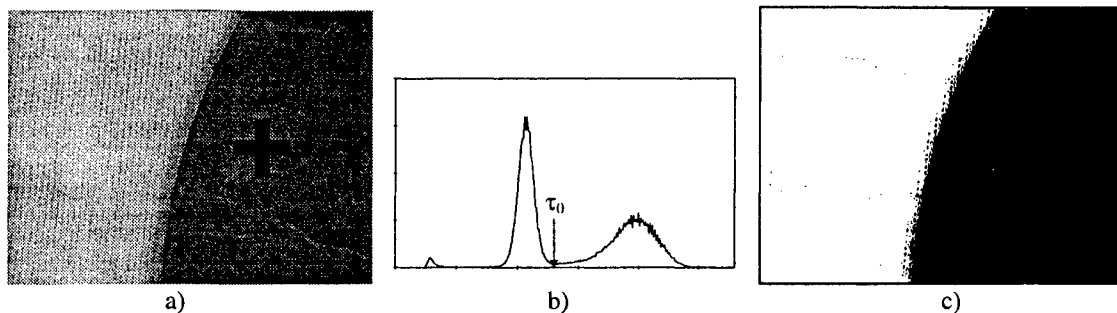


Fig. 1: Example showing the effect of binarizing a gray-scale scene with a small binary object using an algorithm for the selection of the threshold. a) Original scene. b) Optimal threshold selection. c) Binarized scene with the target embedded in the background.

This prior-binarizing schema, however, shows significant problems concerning the thresholding procedure for obtaining a binarized image from the scene. The choice of the binarizing threshold is usually based on the assumption of a bimodal Gaussian mixture for the image histogram⁽⁴⁾. If the target is small, luminances from other large objects appearing in the scene may dominate histogram densities, and there is a high risk that they lead to threshold values which leave the target embedded in the foreground or in the background of the binarized image (see for instance Fig. 1). In addition, binarization causes a great loss of the information contained in the gray-level values, and this may result in a lack of robustness when noise, blurring or spatial brightness gradients are present in the scene.

An alternative choice is the use of a similarity measure suitable for the gray-level domain, leading to a direct search on the original gray-level acquired image. This schema avoids thresholding and, thus, consequently, the above mentioned problems related to the binarization process will not be present.

Normalized Correlation⁽⁵⁾ (NC) is a well known and widely used gray-level similarity measure, which has two good properties: normalization of the values and invariance to linear luminance transformations. Normalization causes the similarity values to be in the interval $[-1, +1]$, irrespectively of the energy contents of the image and the model, and a full matching is uniquely represented by the $+1$ value. Invariance to linear luminance transformations allows the matching between model and target when they differ only in contrast and offset of the gray scale. Other gray-level similarity measures, such as standard (non-normalized) correlation and quadratic error⁽⁵⁾ do not possess these convenient properties.

The use of NC , however, requires a high computing cost as compared to the binary similarity measures. On the other hand, NC focuses on the gray-level contents of the target, instead of only on the geometric features of its shape. Thus, a target having a shape identical to the model, but with a non-uniform brightness in the foreground or in the background, is not detected as a perfect match (value equal to $+1$) by NC . Finally, NC fails to be invariant for some gray-level non-linear transformations (such as gamma compensations), which are quite common in visual perception.

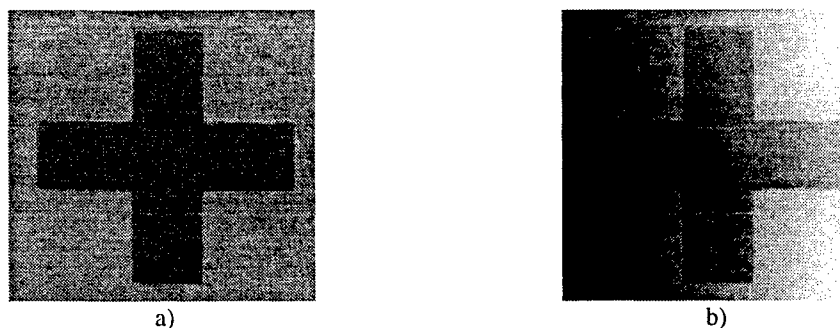


Fig. 2: Two targets having identical shape, (a) with uniform brightness, (b) with non-uniform brightness.

Properties	Similarity measure			
	Binary Type	Correlation	Normalized Correlation	Our Goal
Needs image binarization	Yes	No	No	No
Computing simplicity	Yes	(2)	No	Yes
Takes advantage of a binary model	Yes	No	No	Yes
Meets geometric similarity criteria	Yes	No	No	Yes
Uses whole gray-level information	No	Yes	Yes	Yes
Normalized range	Yes	No	Yes	Yes
Linear transformation invariance	(1)	No	Yes	Yes
Non-linear transformation invariance	(1)	No	No	Yes
Non-uniform brightness invariance	(1)	No	No	Yes

(1) Depends on binarization reliability
(2) Medium computing simplicity

Table 1: Properties of several similarity measures

Analyzing in detail how *NC* works, we realize that the model is taken as gray-valued, whereas in the problem we initially presented the model is essentially binary. In fact, some approaches have been reported which try to take advantage of the binary characteristics of the model while retaining all the information of the gray-scale values of the image⁽⁶⁻⁸⁾.

Summarizing, our goal is to define a new similarity measure which takes advantage of the binary character of the model (i.e., having the fast computing speed and the easy geometric interpretation of the binary similarity measures) while avoiding the thresholding of the whole scene. Besides, we will require normalization of the values, invariance to non-linear gray-level transformations and invariance to poor brightness uniformity in the scene (Fig. 2). Table 1 lists a summary of the characteristics of some of the existing measures of similarity and compares them with the characteristics we want to obtain from our new measure of similarity.

2. STATEMENT OF THE PROBLEM. DEFINITIONS.

We assume that the ideal target is small and its specific feature is shape, so it can be efficiently represented by a binary template T (Fig. 3), which is divided in two regions, the foreground T_1 and the background T_2 . When the template is displaced to every point of the image, each region T_1 and T_2 define corresponding regions I_1 and I_2 on the image window I . Let $h(gl_{I_1})$ and $h(gl_{I_2})$ the gray-level histograms of the I_1 , I_2 regions, respectively. Three situations may arise:

- There is no cluster of bright or dark pixels in I (Fig. 4a): histograms $h(gl_{I_1})$ and $h(gl_{I_2})$ are similar.
- Some clusters of pixels are present in I , but not exactly matching target's shape (Fig. 4b): now there is an overlapping between histograms $h(gl_{I_1})$ and $h(gl_{I_2})$.
- There is a target in I that fits exactly the shape of the template (Fig. 4c): histograms $h(gl_{I_1})$ and $h(gl_{I_2})$ are now disjoint and there is no overlapping, except when noise is present.

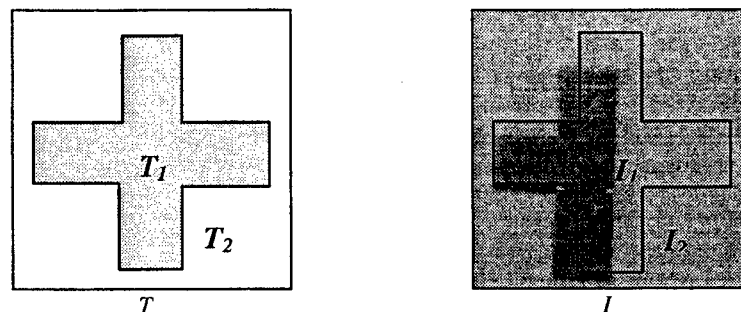


Fig. 3: Regions T_1 , T_2 of the binary template T , and the corresponding regions I_1 , I_2 of the image window I .

When I is binarized by a threshold τ , I' is obtained (see Fig. 5) and regions I'_1 and I'_2 can be defined for I' in the same way as I_1 and I_2 were, according to the template shape. Let $\alpha_1(\tau)$ be the fraction of I'_1 with a binary value of 0, and let $\alpha_2(\tau)$ be the fraction of I'_2 with a binary value of 1. We propose the following similarity measure:

$$J(\tau) = \alpha_1(\tau) + \alpha_2(\tau) - 1 \quad (1)$$

It can be shown that this is a modified form of the Yule similarity measure for binary images and templates⁽²⁾. Eq. 1 can be expressed in terms of the histograms of regions I_1 and I_2 :

$$J(\tau) = \sum_{g=0}^{\tau-1} h(g|I_1) + \sum_{g=\tau}^{M-1} h(g|I_2) - 1 \quad (2)$$

where M is the number of gray-scale quantization steps. The last term (-1) fits $J(\tau)$ into the interval $[-1, +1]$.

Now, let us call τ_0 the threshold which maximizes the absolute value of $J(\tau)$:

$$\tau_0: |J(\tau_0)| = \max_{0 < \tau < M} \left| \sum_{g=0}^{\tau-1} h(g|I_1) + \sum_{g=\tau}^{M-1} h(g|I_2) - 1 \right| \quad (3)$$

The absolute value enables the matching of both possible types of target: brighter and darker than background. When the sums of histograms in Eq. 3 are related to their respective cumulative distributions $H(g|I_1)$ and $H(g|I_2)$, the following expression is obtained:

$$|J(\tau_0)| = \max_{0 < \tau < M} |H(\tau|I_1) - H(\tau|I_2)| \equiv KS \quad (4)$$

The Kolmogorov-Smirnov statistic (KS) is recognized in Eq. 4; this statistic is used in the homonymous nonparametric test⁽¹⁰⁾ to check the hypothesis that two empirical distributions come from the same ground population.

Thus, the threshold value τ_0 computed in Eq. 3 for each image window maximizes the binary-domain similarity measure defined in Eq. 1. The value for this similarity measure may be obtained through the KS statistic of Eq. 4 and, besides, this equation can be computed directly from the cumulative distributions in the gray-scale domain (no need to threshold the window). The similarity measure between the target and the binarized image is simply the KS statistic computed through the regions I_1 and I_2 defined by the shape of the template.

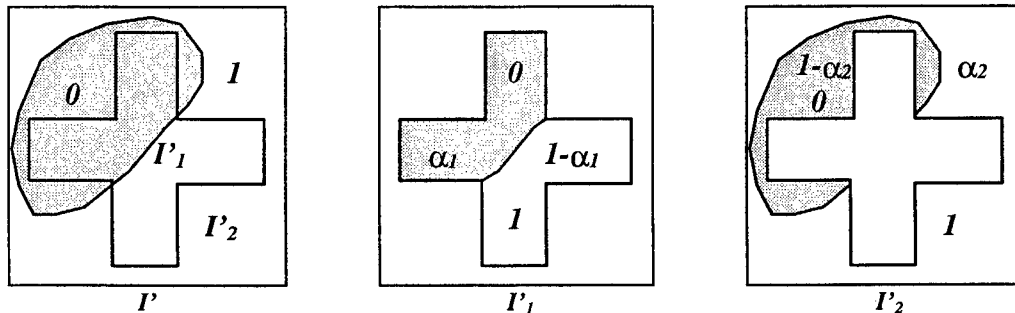


Fig.5: Defining area fractions α_1 , α_2 for the regions I'_1 , I'_2 in the binary image window I' .

3. PROPERTIES OF KS STATISTIC FOR MATCHING BINARY TARGETS IN GRAY-SCALE IMAGES. RESULTS.

In fact, the *KS* statistic is a figure of separability between the histograms $h(g|I_1)$ and $h(g|I_2)$. *KS* accounts for the overlapping area of both histograms by computing the maximum height difference between the cumulative distributions $H(g|I_1)$ and $H(g|I_2)$ (see Fig. 6). When the *KS* statistic is used as a template-matching similarity measure between binary templates and gray-scale images, as we propose, the situations illustrated in Fig. 4 may be reanalyzed. In case a where there is no target, a value near 0 is obtained, because distributions in regions I_1 and I_2 are very similar. When there is a target which does not match the shape of the template (case b), population mixtures cause a certain degree of overlapping, and *KS* takes values between 0 and 1, according to the fractions of area in I_1 and I_2 effectively covered by foreground and background pixels. A target that fits exactly the shape of the template (case c) has disjoint histograms, thus giving the maximum value 1 for *KS* statistic.

Two important properties of this *KS*-based similarity measure can be easily seen:

- 1) The nonparametric behavior of *KS* makes it invariant to any monotonically increasing transformation f of gray-level values: $g_1 < g_2 \Rightarrow f(g_1) < f(g_2)$.
- 2) *KS* yields a maximum value of 1 whenever target and template shapes are identical, and histograms of regions I_1 and I_2 are separable, irrespectively of their probability law.

Thus, *NC* is invariant to linear transformations of the gray-scale, but property 1 of *KS* is more general because it allows any non-linear monotonic function f . These transformations are frequently found in some image sensors, due to non-linear luminance responses, such as the gamma compensations used in TV cameras.

From property 2, a perfect matching (value 1) is reached for *KS*, even if the gray levels in the foreground or the background are not uniform, while *NC* requires uniformity to reach unity. Many real scenes may contain perfectly-shaped targets, but uneven lighting conditions, shadows or textured appearance prevent brightness to be uniform inside the background or foreground regions. Provided the local threshold simply preserves the target shape in the binarized image, *KS* will give value 1 (indicating a perfect match); by contrast, *NC* fails to reach a value of 1 in this situation.

It is not difficult to show that *KS* is computationally always much faster than *NC*, mainly when the template increases in size⁽¹¹⁾. Similarly, the invariance of *KS* with respect to monotonically increasing transformations of luminance proves to be stronger than for *NC*⁽¹¹⁾.

4. SUMMARY AND CONCLUSIONS

We have addressed the problem of the definition of a similarity measure for binary templates in gray-scale images. First, the relevant topics for this specific problems have been analyzed, mainly taking into account the requirements of good computing speed, retaining the information of the scene while taking profit of the binary character of the target.

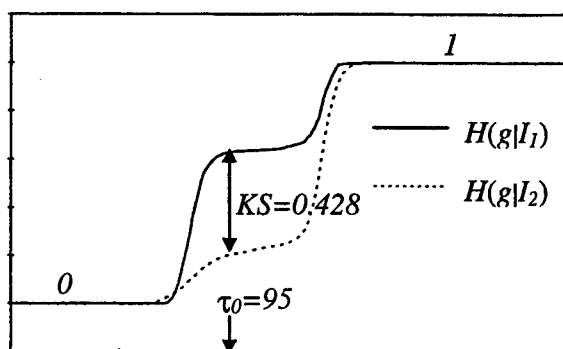


Fig. 6: Cumulative distributions for histograms in Fig. 4b, and the resulting *KS* statistic and optimum threshold τ_0 .

We show that for binary templates and gray-scale scenes, the proposed Kolmogorov-Smirnov-based method for template matching is a real alternative to the normalized correlation-based procedure. One important advantage of *KS* with respect to binary-domain template matching methods is avoiding the critical threshold-selection step, by assuming that a local threshold was selected according to the template geometrical constraints. The resulting value for *KS* statistic yields the optimized value for a properly defined binary-domain similarity measure. Regarding the performances of *KS* we may note that the computation speed of the *KS*-based algorithm is considerably faster than for the *NC* case; and the invariance to changes in brightness is better than for *NC*.

REFERENCES

1. X.Fernàndez, J.Amat, Detection of small-size synthetic references in scenes acquired with a pixelated device, *Optical Engineering* (in press, scheduled for Nov.97).
2. J.D.Tubbs, A note on binary template matching, *Pattern Recognition*, **22**, 359-365 (1989).
3. D.Bloomberg and P. Maragos, Generalized hit-miss operations, in *Image Algebra and Morphological Image Processing*, SPIE Vol. **1350**, 116-128 (1990).
4. S.U. Lee, S.Y. Chung and R.H. Park, A comparative performance study of several global thresholding techniques for image segmentation, *Comput. Vision Graphics Image Process*, **52**, pp. 171-190, (1990).
5. D.Ballard, C. Brown, *Computer Vision*, Prentice Hall, New Jersey (1982).
6. E.Chuang and D. Sher, χ^2 test for feature detection, *Pattern Recognition*, **26**, 1673-1682 (1993).
7. E.Chang and L. Kurz, Object detection and experimental designs, *Computer Vision, Graphics and Image Processing*, **40**, 147-168 (1987).
8. X.Fernandez and S. Bosch, Inspection of centring marks engraved on ophthalmic lenses by model-based numerical correlation, *Optical Engineering*, **34**(7), 2120-2125 (1995).
9. A.Rosenfeld, Image analysis: problems, progress and prospects, *Pattern Recognition*, **17**, 3-12, (1984).
10. T.Hettmansperger, *Statistical Inference Based on Ranks*, Wiley, New York (1984).
11. X.Fernandez, Template matching of binary targets in gray-scale images: a nonparametric approach, *Pattern Recognition*, Vol. **30**, pp.1175-1182, (1997).

ACKNOWLEDGEMENTS

This work has been partially financed under project TAP94-0303 of the spanish CICYT. J. Ferré-Borrull gratefully acknowledges the grant FI95-1113 from the Generalitat de Catalunya.

Light scattering in liquid crystals

M. Ursache, M. Socaciu, C. Sarpe-Tudoran

University of Craiova, Dept. of Physics
13 A. I. Cuza, Craiova 1100, Romania

ABSTRACT

In this paper we study the light scattering on the different mesophases of TBBA-CM mixture. We used He-Ne laser radiation and we derived a simple theoretical model of the diffusion process. The results are in good agreement with the data provided by other experimental methods.

Keywords: liquid crystals, light scattering

1. INTRODUCTION

The low power monochromatic light diffusion on different mesophases may provide information concerning the molecular orientation kinetics for the corresponding temperature intervals. The molecular orientation changes are also present at phase transitions and in droplet structure mesophases. Consequently, one can determine the droplet radius and its changing rate which depends on the temperature.

Light scattering was used as an experimental method to investigate the properties and the fluctuations that occur in liquid crystalline phases. The polarizability of the liquid crystal molecules has a large anisotropy at optical frequencies and by far the most intense light scattering effect comes from molecular reorientation.

It has been known that the nematic and cholesteric phases are strongly light scattering media. Quantitative light scattering experiments in nematic liquid crystals were initiated by Chatelain¹. The Orsay group then formulated a model which included the dynamics of the nematic director modes² by drawing upon anisotropic hydrodynamical theories developed by Leslie and Ericksen^{3,4}. This model was confirmed by light scattering experiments⁵. In the nematic phases, one can use light scattering to determine the elastic constants⁶, viscosities and to study electrohydrodynamic instabilities. Both static and dynamic properties in the vicinity of the second order, or weakly first order, nematic to smectic A transition have been studied from the experimental light scattering results. The thermally excited fluctuations are responsible for the light scattering in the S_C phase^{7,8}.

2. EXPERIMENTAL METHOD

In this paper, we studied the light scattering on different mesophases of smectic cholesteric terephthal-bis-butyl-aniline (TBBA) mixture and cholesteryl myristate (CM). At heating, this mixture presents the smectic A phase (68°C), the cholesteric phase (100°C) and the isotropic liquid phase. At cooling, only the cholesteric phase was recorded (120°C), followed by a series of smectic mesophases.

The changing of the diffusion image aspect indicates the modification of the mesophase. The theoretical proof is given only for the smectic and cholesteric phases. The results are in good agreement with the ones given by other experimental methods such as microstructural analysis, thermoelectric effect, differential thermal analysis.

The liquid crystal in the thermostated cells have homeotropic molecular orientation. The length of the liquid crystal molecule is about 100 Å. Due to the value of the optical length of our sample ($\tau = 1.2 \cdot 10^{-5}$ m), the multiple diffusion effect is avoided.

We recorded the intensity of the scattered light in a given observation plane, by using a 512 points CCD linear sensor coupled to the computer through a DAS 1601 interface. The sensor displacement was done in a xOy plane normal

to the incident laser beam direction (Oz). We used a He-Ne laser ($\lambda = 6238 \text{ \AA}$), the radiation being vertically polarized (V). The diffusion image was studied using an analyzer having the direction normal to the incident beam polarization direction (V_H) or parallel to the same direction (V_V). The obtained figures were slightly different, proving a high degree of depolarization for the scattered light, explained by the density and anisotropy fluctuations.

3. RESULTS AND DISCUSSIONS

For the smectic phase having a layered structure, the molecules being oriented parallel to each other, a symmetrical orientation with respect to the direction of the incident beam exists. Each layer gives a secondary wave : $E_k \sin(\omega t - \varphi_k)$.

The sum of the contributions given by all layers is:

$$E^S = \sum E_k \sin(\omega t - \varphi_k)$$

where $\varphi_k = \varphi_1 + \frac{2\pi}{n}k$ and $k = 0, \dots, n-1$.

If we consider the hole crystal sample as being formed by "n" layers having the width τ/n , then one has:

$$\begin{aligned} E^S &= E_1 \sum_{k=0}^{n-1} \sin\left(\omega t - \varphi_1 - \frac{2\pi}{n}k\right) = \\ &= E_1 \sin(\omega t - \varphi_1) + \frac{E_1}{2i} \left\{ \exp\left(i(\omega t - \varphi_1)\right) \sum_{k=1}^{n-1} \exp\left(-i\frac{2\pi k}{n}\right) - \exp\left(i(\omega t - \varphi_1)\right) \sum_{k=1}^{n-1} \exp\left(i\frac{2\pi k}{n}\right) \right\} = 0 \end{aligned}$$

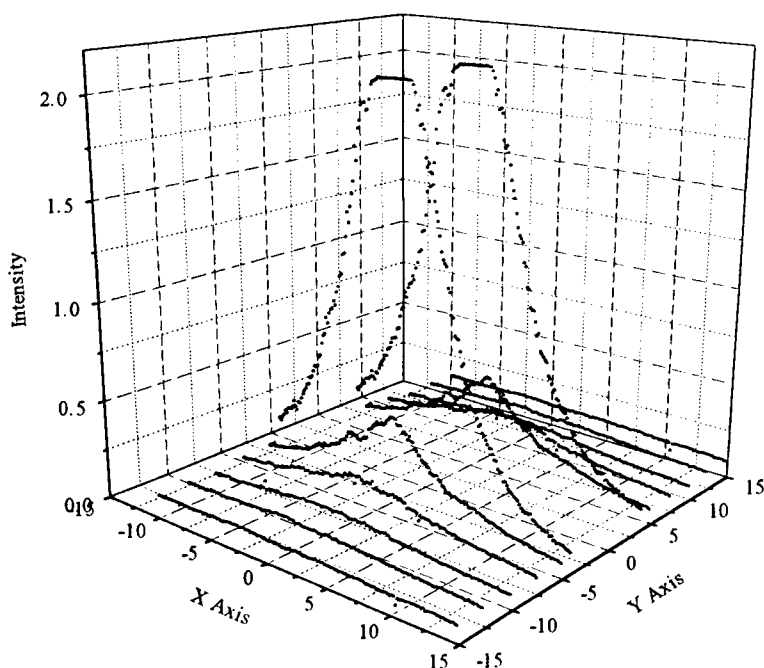


Fig. 1

Each layer that produces a scattered wave with a given phase corresponds thus to an other one which produces an opposite phase wave. We can explain therefore the lack of the diffusion for the homeotropic oriented smectic phase in its corresponding temperature domain. Actually, the scattering figure reproduces the Gauss distribution of the incident beam (Fig. 1).

The cholesteric phase has a helicoidal orientation, consequently the molecular direction in a given layer is clearly modified with respect to the direction corresponding to a neighbor layer.

Due to the dielectrical constant anisotropy $\Delta\epsilon$, the electric field of the scattered light has the following form:

$$E^s = \frac{\omega^2 \Delta\epsilon}{c^2 r 4\pi} E^0 v \sin \gamma$$

where "r" is the distance between the observation point to the position of the diffusing molecule. The angle between the corresponding position vector and the dipole axis is γ , while ω is the pulsation and v the diffusing volume. We consider that the fluctuations of the dielectric constant are only due to the density fluctuation, so:

$$\Delta\epsilon = \frac{\partial\epsilon}{\partial\rho} \Delta\rho$$

where ρ is the density of the cholesteric mesophase.

We obtained the following formula for the scattered radiation intensity on the cholesteric phase:

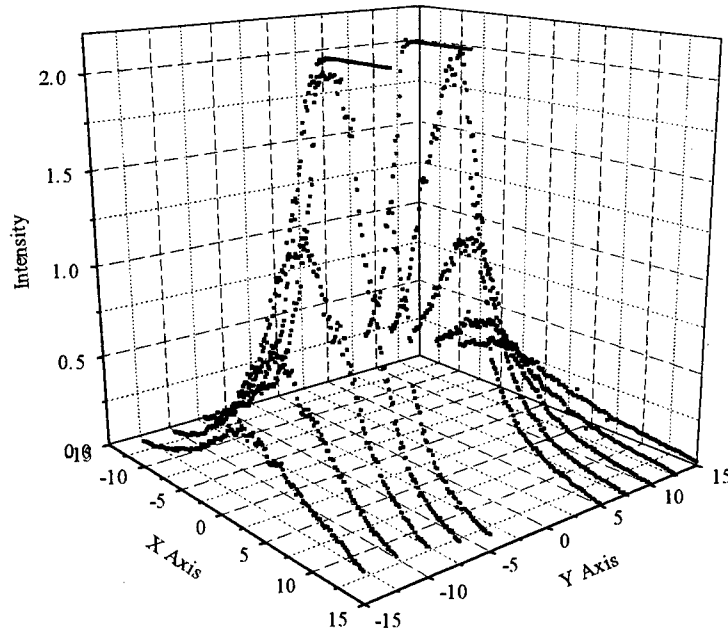


Fig. 3

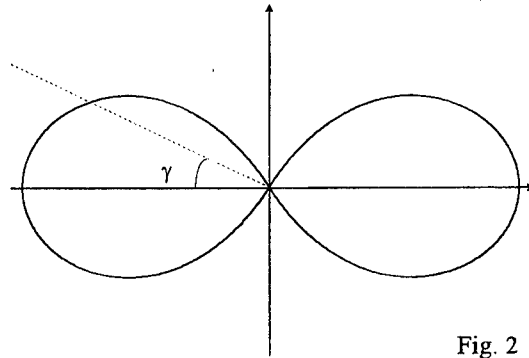


Fig. 2

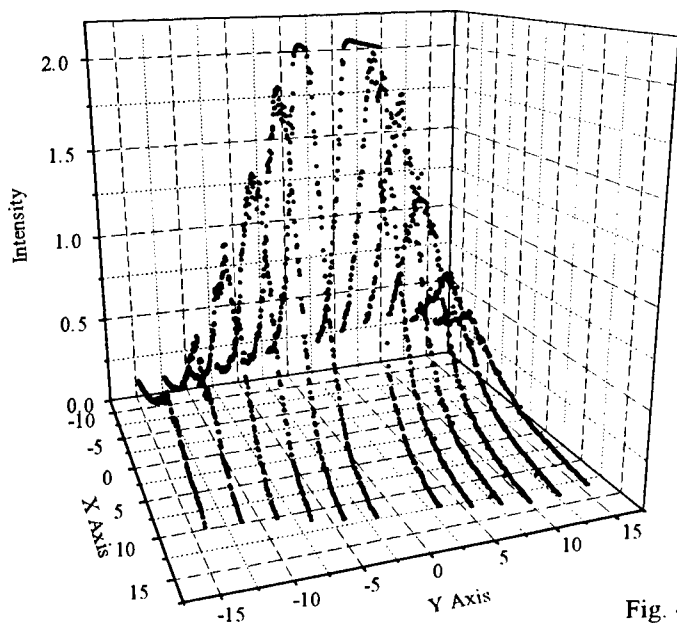


Fig. 4

Their radius grows when the temperature is decreased, until their dimension is comparable to the incident radiation wavelength. This fact was proved by the appearance of a diffraction image (an Airy disk) simultaneously with the diffusion one, around 120°C, at cooling, as one can see in Fig. 4.

4. CONCLUSIONS

Our experimental method allows to identify the phase transitions and the liquid crystal mesophases, by analyzing the diffusion images. The shape of the monochromatic light diffusion image may be explained by using a theoretical model similar to the Rayleigh-Gans one.

The occurrence of the Airy disk diffraction image on the diffusion figure characterizes the moment when the droplets radius becomes comparable to the laser radiation wavelength.

5. REFERENCES

- [1] Chatelain P., Acta Crystallogr., 1, 315, 1948.
- [2] Group d'Etude de Cristaux Liquides, J. Chem. Phys., 51, 816, 1969.
- [3] Leslie F. M., Q. J. Mech. Appl. Math. 19, 357, 1966.
- [4] Eriksen, Arch. Ration. Mech. Anal. 4, 231, 1960; 9, 371, 1962.
- [5] Orsay Liquid Crystal Group, Phys. Rev. Lett, 22, 1361, 1969.
- [6] Langevin D., Bonchiat M. A., J. Phys. 36, C 1-197, 1975.
- [7] Orsay Group on Liquid Crystals, Solid State Commun. 9, 653, 1971.
- [8] Rapini A, J. Phys., 33, 237, 1972.
- [9] Young C. Y., Pindak R., Clark N. A., Meyer R. B., Phys. Rev. Lett., 40, 773, 1978.
- [10] Bartolino R., Doucet J., Durand G., Ann. Phys 3, 389, 1978.

$$I_{\gamma}^s = \frac{\omega^4}{(4\pi r c^2)^2} (\epsilon - 1)^2 \frac{V}{N_1} I^0 \sin^2 \gamma$$

where V is the sample volume, N_1 is the particle number per unit volume. The dependence on $\sin^2 \gamma$ explains the two-lobes aspect of the diffusion figure for the cholesteric phase, showed in Fig. 2. The axis of the two lobes may rotate in the observation plane. The experimentally obtained scattering image in Fig. 3 has been analyzed in a plane which was normal to the incident light direction.

The projection of the diffusion maxima on the plane xOy shows the existence of a tilting angle of the two lobes and its variation with the temperature as well.

At cooling, the analyzed mixture presents droplets texture on the dark background of the isotropic liquid phase.

Digital laser powermeter

E. Smeu, N. Puscas, I. M. Popescu

"Politehnica" University of Bucharest, Physics Department,
Spl. Independentei 313, Bucharest 77206, Romania
E-mail: pnt@physics2.physics.pub.ro

ABSTRACT

A digital powermeter was developed for measuring the power of laser beams using an electrically calibrated thermopile. This choice allows metrological quality measurements in a broad spectral range and an accurate calibration, but the electronic readout must meet some severe specifications concerning internal fluctuation (generally, most of commercially available radiometers, even advanced, do not).

The reported powermeter has very low internal fluctuation (both drift and noise, in respect with its resolution). Original, yet simple circuitry was developed for low noise and for an accurate zero setting (even with a high background). The most important of these internal circuits is described. Statistical noise tests are also presented and some comparisons with advanced commercial powermeters. A large number of tests, each of them containing 500-900 measurements (values), revealed for the reported powermeter that "0" reading is the most probable noise value (i.e. the most often found), its probability being in all cases larger than 99% on the most sensitive range and equal to 100% on all other ranges.

Key words: electrically calibrated thermopile, statistical noise tests, low internal fluctuation

1. INTRODUCTION

Measuring laser beams power is not an ordinary problem, especially when requested power and spectral ranges are broad. In such cases, thermal detector heads are preferred. The thermopile is the most often choice when measuring the power of cw laser beams or the average power of laser pulses. This type of thermal detector was perfected in 1971 by Mefferd and others¹; meanwhile it became a true success. Its main advantages are: good response uniformity in a broad spectral range, broad power range (tens of μW to 100 W for some premium surface absorbing models) and also the possibility of electrical calibration (of the powermeter).

The width of the spectral range for good response uniformity (usually 2-3%) and the maximum power are closely connected. Low and medium power thermopiles (up to several hundred watts) are generally surface absorber types and their spectral range is broad (usually 0.2 - 20 μm or even larger). High power thermopiles (up to several kW) are volume absorber types and their spectral range is narrower (usually < 10 μm). Electrically calibrated thermopiles (ECTH) use an electrical power as the input, instead of an optical power². Since electrical standards are a lot more accurate than optical ones, this substitution procedure leads to lower calibration uncertainties and to smaller calibration difficulties (long time high stability optical standards are very expensive devices and they deliver only low optical power). High power thermopiles are not provided with electrical calibration, because of technological reasons.

Small responsivities, especially for medium and high power thermopiles (some mV/W or even lower) make the measurement process a rather difficult one. The total gain of the dc (exclusively used) amplification chain must be high on the smallest power range, so internal offsets (with the associate drifts), internal noise (especially low frequency), other parasitic voltages (such as connector-located thermoelectric ones) and background radiation as well add to the "useful" signal. Accurately subtracting these unwanted voltages is not quiet easy (only the signal representing the laser power must be measured).

2. BLOCK SCHEME DESCRIPTION

The block scheme of the reported powermeter is represented in Fig. 1.

The thermopile detector head is a RjP-30-CAL type (Laser Probe, Inc. - USA). This type was selected because it is a high quality one, being also provided with electrical calibration.

The dc voltage generated by the thermopile is fed into an amplifier. Its gain can be tuned in order to coarse calibrate the powermeter, but this tuning changes the offset (so it must be re-zeroed). A low noise (especially "pop-corn"), low thermal and time offset drifts operational amplifier was selected. It is used in the non-inverting configuration. Because of its very high input resistance, it is insensitive to the thermal drift of the internal resistance of the thermopile (which may become detectable at high incident laser power).

The next block, named " t_{resp} ", is a special circuit which changes the time response of the powermeter (0-90% of the output for a step input) from 1.5 seconds in the FAST regime to 10 seconds in the AVERAGE (AVG) regime. It is an originally modified proportional-derivative (PD) controller, performing a replacement of the time reponse corresponding to the thermopile alone (about 6 seconds) with another, which is set by the values of one resistor and one capacitor (some kind of "personality changing"). Its peculiar topology leads to low noise, unlike the D component of classical PD controllers. The AVG regime is useful when measuring average powers of laser pulses or cw fluctuating power beams. In this regime, the time constant of the circuit is strongly increased by connecting a large value capacitor in parallel with another using a simple panel switch. This function is generally present only on expensive powermeters.

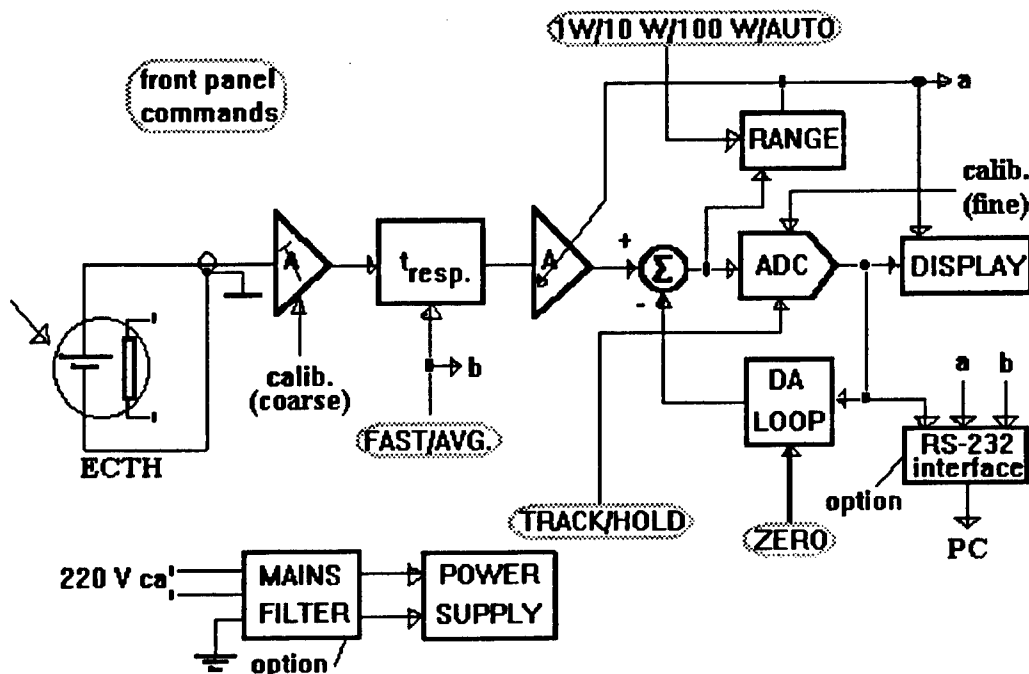


Fig. 1. Block scheme of the powermeter

The reported apparatus has three power ranges, each with the corresponding resolution: 0 - 999mW/1 mW, 0 - 9.99 W/10 mW and 0 - 99.9 W/100 mW, manually or automatically (AUTO) selectable. The ranging amplifier has three corresponding different gains, which are selected by the RANGE circuitry. The amplifier peculiar scheme makes its offset independent of the gain (it is also a low drift type). Unfortunately, this version does not use completely the 100 W range, because the maximum power is limited to 30 W by the thermopile.

The Autorange circuit is a sub-circuit of the RANGE circuitry. In order to improve ranging decision and range stability, the Autorange function uses a small "range overlapping", i.e. a hysteresis of about 20% of full scale for the higher range. So, the range is automatically switched from 1 W to 10 W when the incident laser power gets higher than 998 mW, but it is switched back to 1 W only when the power gets lower than 800 mW.

The analog-to-digital converter ADC delivers measured data to a 3-digit LED display. The ADC running is controlled by a TRACK / HOLD command. In TRACK position the ADC performs about 3.5 conversions/second and in HOLD an interesting value is displayed indefinitely. The HOLD command also disables all other commands of the powermeter. The **fine calibration** of the powermeter is achieved by tuning the full-scale (multiturn) potentiometer of the ADC. Only this tuning is used to periodically re-calibrate the apparatus (yearly), as it does not change any offset.

Zeroing the display is achieved rather fast, by simply pressing a push-button. A digital-to-analog loop (DA LOOP) subtracts the voltage corresponding to all internal offsets (including the ADC one) and external background (if any) from the "power" signal (a dc voltage too). The subtracted voltage grows only until the displayed value is 0. After this condition is accomplished the ZERO button may be depressed and the subtracted voltage is maintained until a new zeroing. Such a

facility is achieved by a simple front panel multiturn potentiometer on simple commercial powermeters, but only with a limited dynamic range, as the accuracy of the zeroing must be good. Consequently, a simple potentiometer zeroing solution can compensate only low background radiation. An accurate and also high dynamic range zeroing command can be found only on advanced (and, of course, high-priced) microprocessor-inside powermeters. On such apparatus, zeroing is accomplished by digital subtraction. The reported powermeter has no internal microprocessor, but its original simple zeroing circuit has both high accuracy and dynamic range. This circuit will be described in a dedicated section of the paper.

A serial RS-232 interface for connecting the powermeter to an IBM PC compatible computer and a mains filter are optional. The mains filter is very useful in pulsed lasers laboratories, as the mains is very noisy there. A former version of the apparatus was also equipped with an analog output for a plotter, but it seemed useless, so the actual version does not have it any longer.

The amplifier chain consists of one 725, 2 super- β usual operational amplifiers and a CMOS switch array (with their associated passive components). The logic consists of some CMOS and one TTL MSI integrated circuits. There are also a 3-digit ADC and an 8 bit DAC, three (7-segment) LED display elements, two measurement unit LED's (mW, W), 3 bipolar transistors, 2 voltage integrated stabilisers, a few diodes, 2 rectifier bridges, some more resistors and capacitors, panel switches, connectors, a ferrite coil and a mains transformer (excluding the optional RS-232 interface and the mains filter).

3. AUTOMATIC ZEROING DA LOOP

The block scheme of this original circuit is represented in Fig. 2.

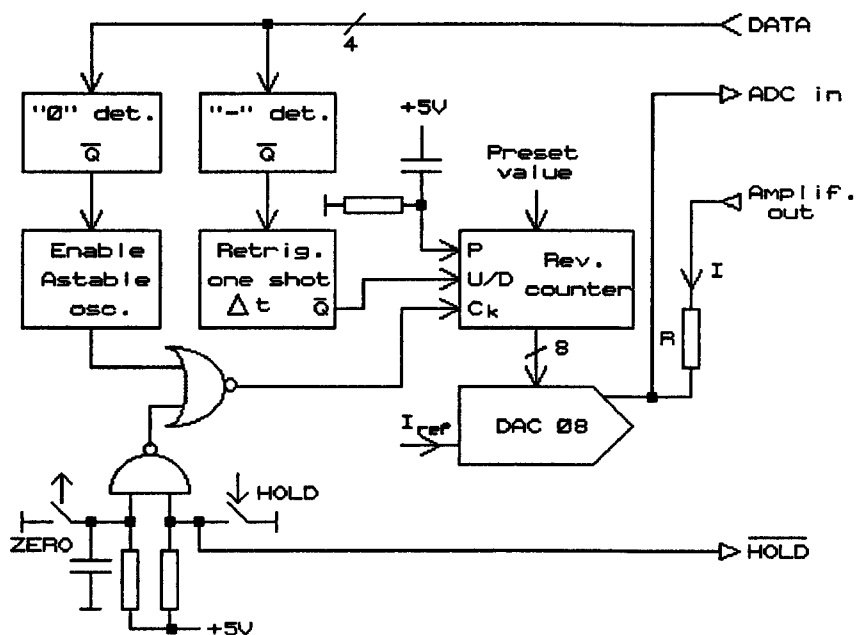


Fig. 2. Block scheme of the DA LOOP

Suppose that first the display shows a non-zero value, which represents the total internal offset plus the background (if any). The Astable oscillator is on and, if the ZERO button is pushed, clock pulses are fed into the reversible counter. The counter determines the evolution of a voltage on resistor R through an 8 bit current-output DAC. This voltage is subtracted from the ranging amplifier output (according to Ohm's wellknown law) and the result is fed into the ADC. Consequently, the displayed value decreases (in absolute value) till "0". When "0" is detected (digitally), the Astable oscillator is disabled and the compensation voltage remains constant on resistor R until a new zeroing. Now the ZERO button can be depressed and the "0" reading will be maintained on the display until the background changes or the internal offset drifts.

As the internal offset may be negative, a reversible counter was used (instead of a direct one) and provision has been made to compensate -4 mW of offset, by an appropriate Preset value. The counter is preset when power on by a pulse on the Preset (P) pin. Counting up (to compensate positive readings) or down (to compensate a negative offset) is "decided" by a "-

" detector (also digital) and a retriggerable one-shot, which maintains the "count down" decision long enough for a proper zeroing. "0" and "-" detectors are simple logic gates.

The ZERO command is disabled by the HOLD command, which acts on the ADC output and thus on the display, maintaining an interesting value indefinitely (till power off).

The circuit is an automatic "hibrid" tuning loop, having a digital input (4 bit data from the ADC) and an analog output (the voltage at the input of the ADC). As the voltage resolution of the ADC is 1 mV, a corresponding zeroing resolution of 0.25 mV was chosen for the loop. Stable, accurate and rather fast zeroing was obtained by choosing the frequency of the Astable oscillator: 5 units (i. e. mV)/sec. on any range. The maximum background which can be compensated is 60 units on any range (i.e. 60 mW on the 1 W range, 0.6 W on the 10 W range and 6 W on the 100 W range). The necessary compensation time for the max. background is thus 12 sec. on any range, in both FAST and AVG regime (because the loop is placed after the " t_{resp} " circuit, just in front of the ADC), but a 1 mW of offset takes only 0.2 sec. to be zeroed (this means practically instantly). It is worth noting that zeroing can take much longer, even on high-priced, μ P-inside radiometers: 10 sec. or even more for the 28-0925 Series Ealing Electro-Optics Research Radiometer³, **no matter how low the background is**. In contrast, zeroing the reported powermeter is achieved (with the enumerated facilities) by a small 6 ic's card (5 common 4000 series CMOS MSI ic's and a DAC).

4. CALIBRATING THE POWERMETER

The electrical calibration was used. The manufacturer of the thermopile indicates a very simple procedure: to inject an electrical power into the dedicated socket, to accurately measure it and to turn the calibration potentiometer (on the readout) until a 1.05 times higher power is displayed. The real equivalence factor was found to be 1.06 by the National Metrology Institute in Bucharest (the powermeter has a calibration certificate from this institute since 1996).

5. TECHNICAL POWERMETER DATA

- Display: 3 digits + 2 LED's (for measurement units)
- Manual / Auto-ranging
- Ranges / resolution:
 - 1 W / 1 mW;
 - 10 W / 10 mW;
 - 100 W / 100 mW
- ZERO - can compensate a background (including internal offsets) of 60 units on each range, i.e.:
 - 60 mW on the 1 W range;
 - 0.6 W on the 10 W range;
 - 6 W on the 100 W range
- Zeroing speed: 5 units/sec. on all ranges
- TRACK / HOLD
- Response time (to 90% of step-input):
 - approx. 1.5 seconds - FAST;
 - approx. 10 seconds - AVERAGING (AVG)
- Thermopile type: Rkt -30-CAL (Laser Probe, Inc. - USA) - electrically calibrated, air-cooled
- Spectral response: 0.19 - 20 μ m
- Sensing area: 2.5 cm², circular
- Max. total power: 30 W
- Max. irradiance: 200 W/cm²
- Noise equivalent power: max. 1 mW peak-to-peak on the 1 W range; 0 on other ranges
- Zero drift: max. 1 mW on the 1 W range after 30 min. operation; 0 on other ranges
- Active area uniformity: \pm 2%
- Nonlinearity (2 σ):
 - < 1% on the 1 W range;
 - < 1.5% on the 10 W range;
 - < 2% on the 100 W range
- Calibration uncertainty: \pm 3%
- Warm-up time: 1 hour

- Power supply / consumption: 220 V a.c. / approx. 4.2 W
- Readout dimensions: 22*18*10 cm
- Thermopile dimensions: Φ 8.5*4.5 cm (dia.*depth)

6. NOISE TESTS

When measuring a physical parameter with an electronic apparatus, it is pertinent to expect seeing an internal fluctuation (noise + drift) small enough in comparison to its declared resolution. Unfortunately, many optical powermeters, even advanced (μ P - inside) and expensive, are noisy, so that their declared resolutions are not real measurement resolutions, but correspond only to the displays.

A typical noise test performed with a Rm-3700 Universal Radiometer and the RkT-30-CAL Thermopile (Laser Probe, Inc., USA - the successor in radiometry of the well known Laser Precision) is presented above for the most sensitive range (300 mW). The time evolution of the readings is presented in Fig. 3.

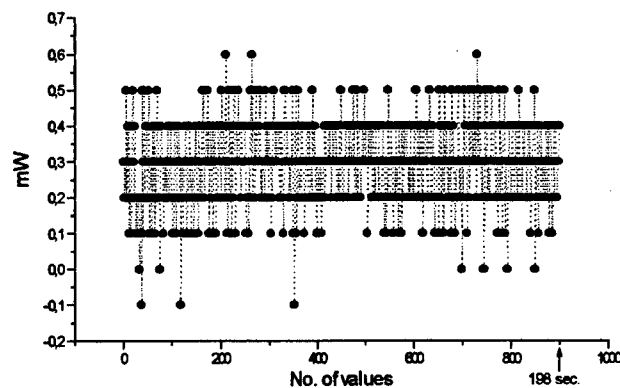


Fig. 3.

Avg = 293.56 μ W; SdtDev = 109.42 μ W

Noise histogram:

Total no. of values = 900 (198 sec.)

Value (mW)	No. of occurrences	Probability
-0.1	3	3.33e-3
0	7	7.78e-3
0.1	69	7.67e-2
0.2	225	0.25
0.3	320	0.35
0.4	217	0.24
0.5	56	6.22e-2
0.6	3	3.33e-3

The thermopile was well thermally isolated during the tests. The average (Avg) shows a combined effect of the offset and very low frequency noise and the standard deviation (SdtDev) represents the RMS noise⁴. The peak-to-peak noise can be immediately computed as (Max-Min) and it is several times higher than the declared resolution (0.1 mW on that range). More, the probability of the most probable value is smaller than 38% in all tests (this one is chosen randomly from some tens of such tests) and, in many cases, this value was not 0, although the Background Cancel command was used every time.

We had the opportunity to test also Rm-6600, which is more complex and, of course, more expensive than our Rm-3700 (it has two channels, more accepted detector heads and more internal μ P data analysis capabilities - even a graphical

display). We have used the same thermopile and we have observed the same behaviour (maybe just a little better, but unsatisfactory too).

We have concluded that, generally, it is hazardous to purchase commercial radiometers and to try performing metrological quality measurements, even if they have internal μP , are NIST traceable, etc.

For comparison, 6 representative noise tests are presented, which were performed on the most sensitive range of the reported powermeter (1 W), also with RkT-30-CAL thermopile. The time evolution of the readings for Test 1 is presented in Fig. 4.

Test 1: FAST

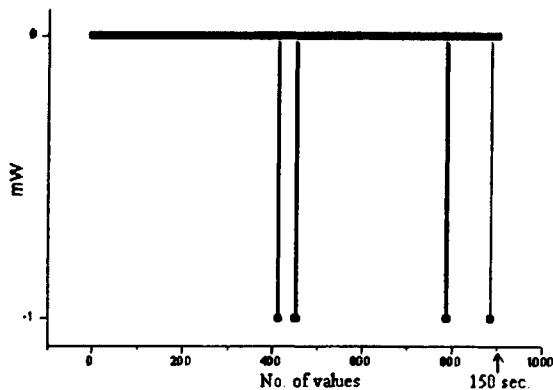


Fig. 4.

Avg = - 8.8 μW ; SdtDev = 93.9 μW

Noise histogram:

Total no. of values = 900 (150 sec.)

Value (mW)	No. of occurrences	Probability
-1	8	0.09
0	892	0.991

Test 2: FAST; 900 values; -1 mW (0.4%); 0 mW (99.6%); Avg = -4.4 μW ; SdtDev = 66.5 μW

Test 3: FAST; 900 values; 0 mW (99.4%); 1 mW (0.6%); Avg = 5.5 μW ; SdtDev = 74.3 μW

Test 4: FAST; 500 values (68 sec.); 0 mW (100%); Avg = SdtDev = 0

Test 5: AVG; 900 values; 0 mW (99.8%); 1 mW (0.2%); Avg = 2.2 μW ; SdtDev = 47.1 μW

Test 6: AVG; 900 values; 0 mW (100%); Avg = SdtDev = 0

Very low fluctuation can be observed for the reported powermeter. In all presented noise tests (and many others) only 2 values were present on the most sensitive range (0 and 1 mW or -1 mW). "0" is in all cases the most probable value, with probabilities higher than 99%. Even 100% for "0" reading can be obtained (i.e. no fluctuation) if AVG or a smaller time window (i.e. less data points) are used.

A similar stable "0" reading was observed for the HP 8152A Optical Average Powermeter with HP 81521B Optical Head (Hewlett Packard), which is Peltier cooled at -10°C. Its display has also (only) 3 digits.

7.CONCLUSIONS

The reported powermeter meets all needed requirements for laser beams power measurements in the specified ranges. It has parameters and facilities which are entirely comparable to those of advanced **high quality** models, but it is very cheap and convenient. It can be easily and accurately calibrated by electrical substitution. Its main feature consists in the very low internal fluctuation (in respect with its resolution). It is computer interfaced, so the acquired data can be processed. It is also very easy to operate and it needs no special conditions. It is rather small and has a low mains power consumption.

8. ACKNOWLEDGEMENTS

This apparatus was designed, built and tested under Contract INCO COPERNICUS no. IC15 - CT96 - 0820 (DG12 - MUYS) supported by the European Community and Contract no. 689/1996 supported by the Romanian Ministry of Research and Technology. The authors are grateful to the National Metrology Institute in Bucharest for carefully evaluating and certifying the reported powermeter.

9. REFERENCES

1. W. S. Mefferd, R. J. Rordeon and J. L. Hobart, *US Patent No. 3596514*, 1971.
2. E. Greenfiel, "Measuring laser power accurately", *Laser Focus*, March 1986, 134 - 142.
3. *28-0925 Series Ealing Electro-Optics Research Radiometer Instruction Manual*, 15 -16.
4. G. Eppeldauer and J. E. Hardis, "Fourteen-decade photocurrent measurements with large-area silicon photodiodes at room temperature", *Applied Optics* 30(22), 3094 - 3095, 1991.

Structured light in visual inspection

C. Blanaru, V. Vasiliu

National Institute for Laser, Plasma and Radiation Physics / Laser Department
P.O.B. MG-36, R-76900 Bucharest, ROMANIA

ABSTRACT

When a processed part is visually inspected along a projected line of several meters in length, generated by adequate cylindrical optics, the gaussian beam intensity profile along line length will create problems given by the fading edges of the intensity profile, the variation of the light level across the line and the presence of "hotspot" in the centre of the line.

In order to avoid these problems, we used the structured light generated by a special developed laser diode producing a non-gaussian (evenly illuminated) distinct line. The visibility of the projected line in real working conditions, depth of field and focusing performances of the beam are presented, as they have been evaluated.

Keywords: visual inspection, laser diode, structured light, non-gaussian line

1. INTRODUCTION

The *Automated Imaging Association* defines structured light as "the process of illuminating an object (from a known angle) with a specific light pattern. Observing the lateral position of the image can be useful in determining depth information". If an object is illuminated with light of a known "structure" (e. g., a line) and if the way this "structure" change is examined, then we'll get the information on the three-dimensional shape of the object, thus the term "structured light".

When the visual inspection is part of a technological process, the laser light is, in many cases, the only solving solution as the illuminating light source. This kind of applications takes full advantage of the laser light properties such as brightness and directionality.

If the processed part is visually inspected along a projected line of several meters in length, using the laser as a light source and the adequate cylindrical optics to generate the line does not mean that you've got the best structured light for the application, because not all line generators are created equally.

2. GAUSSIAN AND NON-GAUSSIAN LINES

If the projected line is generated by placing some adequate cylindrical optics at the optical output of the laser, the gaussian beam intensity profile along line length will create serious problems for the user¹. They are given by the fading edges of the intensity profile, the variation of the light level along the line and the presence of "hotspot" in the centre of the line (with impact on the level of safety ratings).

The gaussian intensity distribution along the structured light line means that it has a bright portion in the centre and the intensity profile fades away as you move towards the ends. So, especially in the case of visual inspection, it is hard to define where the line starts and ends. More than that, the operator's eyes will be captured and impressed by the brighter central portion of the line, making more difficult the inspection along the entire line projected light.

If an active detection (e.g., CCD) is going to be used for monitoring the structured light, the intensity variations will create serious problems to calibrate the detector. Certain pixels must be calibrated for the bright centre region, others for the mid regions (a little less bright) and still more for the end regions.

Finally, the "hotspot" in the centre of the line often has enough energy to push the laser into the next level of safety ratings.

In our particular application, we had to project a marking laser line of 12 m length from 1.5 m height. In such a case, the problems mentioned above became critical. More than that, as the main axis of the emitting laser beam would make an angle of approx. 20° with the projection surface, the depth of field and focusing performances had to be considered.

In order to solve the problem, we used the structured light generated by a special developed laser diode, producing a non-gaussian (evenly illuminated) distinct line. The line generator was a SNF Series focusable line projector made by

LASIRIS Inc., Canada. The beam shaping optics transforms the laser dot into a projected straight line by allowing one dimension to fan out, while maintaining tight control over the other. The result is an evenness of the illumination along the length of the line, so the points where the line starts and ends are well defined. This is of major importance in the case of visual inspection along projected lines of several meters.

3. EXPERIMENTAL RESULTS

The problem we had to solve was to position a laminate of up to 12 m long and 4 m wide before entering the edge scissors. To do that we had to project two parallel light lines, one of them in a fixed (reference) position, the other one displaceable across the width of the laminate according to the respective sheet dimension. The two projectors were to be held by a console of 1.5 m height, placed across the laminate rollers.

As light sources we used two SNF-701L-635-15-30° focusable laser diode line projectors, characterised by wavelength of 635 nm, power of 15 mW and fan angle of 30°. The reasons we chose this particular type of line projector were imposed by the specific geometrical requirements of line projection on site, in terms of fan angle, line thickness, projection distance and depth of field.

Projection distance (D) is the distance from the front end of the projector to the target plane. To project a line of length L from a projection distance D requires a fan angle F.A. given by the equation:

$$\text{F.A.} = 2 \tan^{-1}(L/2D).$$

This applies in the case of an orthogonal laser beam incidence on the target plane. We couldn't use such an orthogonal projection and we've got, in the plane of the laser pattern, an angle of 21° between the central emitting axis and the projected line. For a fan angle of 30°, this leads to a projected line that starts at 2 m from the console holding the laser head and ends at 15 m, resulting an equivalent projection distance of approx. 4 m and a projected line length of approx. 13 m. In these conditions, depth of field and line thickness have to be considered.

The depth of field is a measure of how well a focused line remains in focus. It is defined as twice the distance over which the line thickness increases from its minimum to a thickness equal to $\sqrt{2}$ times this minimum.

The projected line has a non-gaussian intensity distribution along its length, but it remains gaussian across the line. The line thickness is always measured at the $1/e^2$ points of the gaussian thickness profile. The $1/e^2$ points correspond to the points where the intensity is down at approximately 13.9% of the peak intensity (100%).

The SNF-701L line projectors were preferred because of their greater depth of field and focusing performances. For instance, the depth of field for minor axis configuration is approx. 20 m for a projection distance of 4 m and the minimum line thickness, at the same projection distance, is approx. 3.3 mm. These values were satisfactory for our application, where the variations from the equivalent projection distance were of +(10.7) m at the furthestmost projected point and -(1.8) m at the closest point versus the console.

The laser projectors have been separately mounted on two goniometric-type mounts, each of them allowing two rotations and one translation. The "reference" line projector mount assures a fine linear translation of ± 10 mm, while the displaceable projector mount is positioned by a servo-controller, electrically driven by a remote command.

First of all, we aligned the "reference" projected line in accordance with the rolling mill procedures. Then we placed the displaceable projector mount at a distance of 2 m versus the reference and aligned the laser line as to be emitted approximately at the same angle and parallel with the reference line. Using the remote commands, we positioned the displaceable projector mounts at different distances versus the reference line, checking the fact that the two emitted lines remain parallel and placed at the imposed intervals.

In the real working conditions we proceeded to evaluate the visibility of the projected lines, measuring the line thickness and depth of field along the entire line length. Using the focusing capability of the laser diodes, we adjusted the line thickness to an optimum corresponding to a projection distance of 10.7 m. The laser line width was measured with a photo-detector equipped with a slot diaphragm of 1.2 mm width. The photo-detector head was placed on a table driven by a micrometric screw in order to move the detector across the projected laser line. The output of the photo-detector was indicated by an electronic DC microvolt-ammeter type TR 1452-EMG.

Along each of the two lines (z co-ordinate) we moved from one end to the other in steps of 2 m length. In every resulting point we measured the laser power (P) versus the position (x) of the photo-detector head across the laser line. The corresponding results for the two projectors were tabled and the resulting laser intensity distributions are represented in Figure 1 and Figure 2, respectively.

Figure 1: Intensity distribution along projected line for SNF serial no. 706

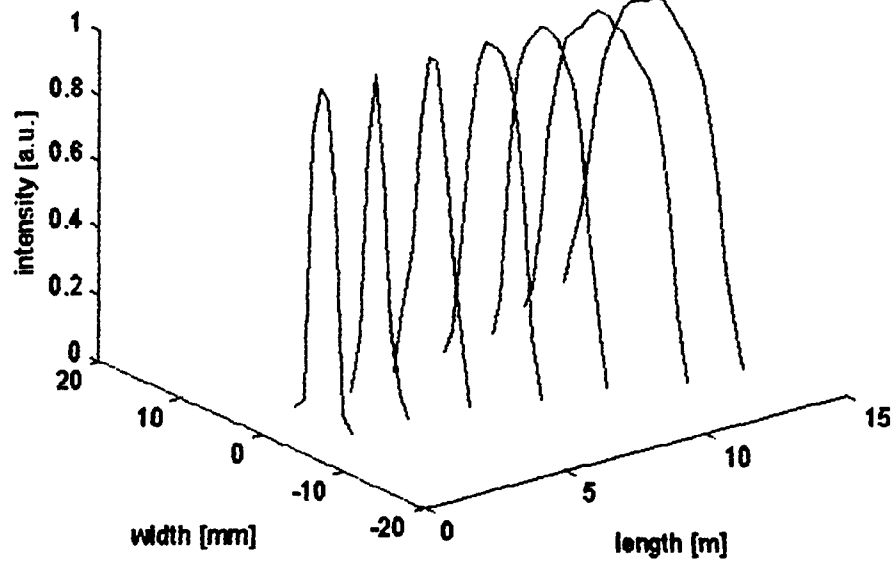
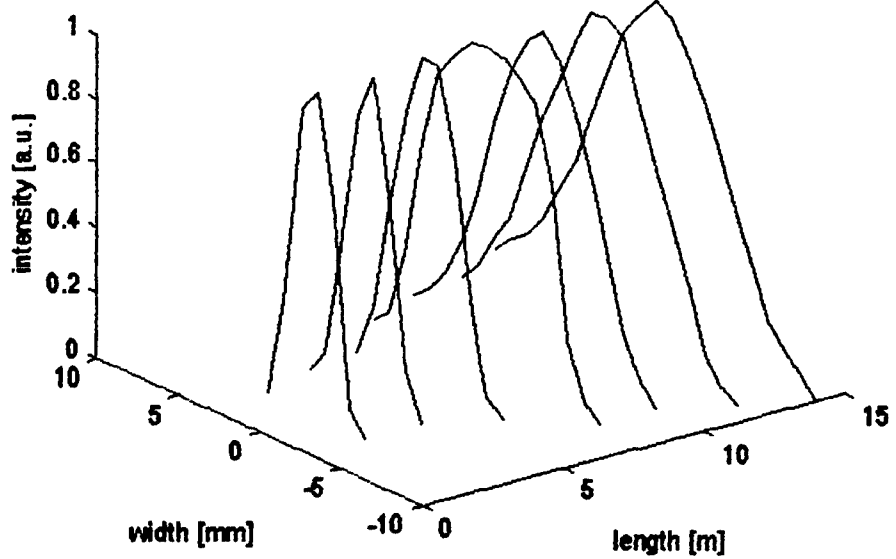


Figure 2: Intensity distribution along projected line for SNF serial no. 707



4. CONCLUSIONS

As you may notice from Figures 1&2, two laser lines were projected on the surface of the rolled sheet along a length of more than 12 m. The lines were obliquely viewed as scattered light with good visibility and intensity. This is because of the high output power of the diode laser and of the evenness of illumination along the length of the line. The result was an eye safe, brighter and sharper image. Limited by the depth of field and focusing performances of the laser projector, the line thickness varied along the entire length from 3 to 13 mm in the case of serial no. 707 projector and from 3 to 18.8 mm in the case of serial no. 706 projector. The larger thickness value for the second projector indicates the best focus was not obtained on site in this case.

Structured light applied for visual inspection, machine vision and alignment application needs represents a significant step forward in the transfer of high tech to real word problem solving.

5. REFERENCES

1. "Laser diode structured light products" Technical Brochure, Lasiris Inc., Canada, 1996

Romanian primary length standards
involved in international comparisons

Gheorghe Popescu

National Institute for Lasers, Plasma and Radiation Physics, Lasers Dept.,
Bucharest, P.O.Box MG - 36, R 76 900, Romania

ABSTRACT

One of the three methods specified for the practical realisation of the metre uses molecular transitions . He-Ne lasers operating at 633 nm wavelength and frequency stabilized by saturated absorption in $^{127}\text{I}_2$ were built at the National Institute for Lasers, Plasma and Radiation Physics (NILPRP), Lasers Department and their performances tested in international comparisons during last four years at the Bureau International des Poids et Mesures (BIPM. 1993, 1995), at the Institute for Metrology "Gustavo Collonetti " (IMGc, 1994) and at the Institute for Scientific Instruments (ISI, 1996) . Comparative results regarding frequency difference, repeatability and stability are presented . Results proved a good reproducibility of the performances during the time.

Keywords: He-Ne lasers, frequency stabilization, laser frequency comparison, metrology, fundamental units

1. INTRODUCTION

The new definition of the metre is based on a conventional value for the speed of light . One of the three methods specified for the practical realisation of the metre uses molecular transitions ¹. With the introduction of a fixed value for the speed of light, new and better laser systems are able successively to improve length standards, to an accuracy limited in principle by the uncertainty in the laser frequency, without having to change the definition of the metre.

Systematic errors exist that change the frequency of a given laser system with time and with conditions. To identify individual systematic errors , to improve understanding of system properties and to keep a stable value of frequency, it is important to make many relative frequency measurements.

Primary length standards are more technically complicated and their frequencies are vulnerable to uncontrolled perturbations and system malfunctions . A regular verification of its performance for reliable applications is made through international comparisons . The main objective is to verify the performance of each participating laser as a frequency standard while operating properly under the specifications of the *Recommendation 3 (CI-1992)* .

As many nations were in the process of replacing their national length standards by iodine / He-Ne frequency stabilized lasers , such a standard has been built at the National Institute for Lasers, Plasma and Radiation Physics, Lasers Department ² . It has compact construction, relative low weight and it is easy to operate . The method used to stabilise the frequency of He-Ne / iodine lasers was the third derivative technique ³ . The desired hyperfine components are found and set manually before frequency stabilization is completed.

2. DESCRIPTION OF LASERS

The Romanian lasers were involved in bilateral or international comparisons as follows :

- the laser RO.1 was compared at the Bureau International des Poids et Mesures (BIPM) , Paris - France (October, 1993);
- the laser RO.2 was compared: at the Institute for Metrology " Gustavo Collonetti " (IMGc) , Torino - Italy (February - March 1994) , at the BIPM (September, 1995) and at the Institute for Scientific Instruments (ISI) , Brno - Czech Republic (July, 1996) .

Comparative results are presented and discussed . The most important parameters of compared lasers are presented in Table 1, but more details could be found in references ^{4, 5, 6}.

Table 1. Principal parameters of the lasers participating in the comparisons : t represents the transmission coefficient of the mirror and r its radius of curvature (subscript index c is for the mirror facing the absorption cell and p for the mirror facing the gain tube).

Lasers	Cavity	Gain	Cell abs.	Cell identity /	Mirror on cell side		Mirror on tube side		Mean intracavity
	length	tube	length	producer	r _c	t _c	r _p	t _p	power
	(mm)	(type)	(mm)		(mm)	(%)	(mm)	(%)	(mW)
RO.1	290	NC-93/1	80	56d/BIPM	3000	0.13	600	0.9	12
RO.2	290	NC-93/2	80	108/BIPM	3000	0.15	600	0.92	11
IMGC4/5	400	GLT20-40	100	R/IMGC	1000	1	100	1	6.8
BIPM4	395	GLT20-40	80	76/BIPM	900	0.5	900	1	10.5
INVAR3	250	TK7	75	11/ BRNO	800	0.2	600	1.2	7.2

It is worth noting that Romanian lasers are equipped with BIPM absorption cells . They proved better qualities when compared with those made at NILPRP (former IFTAR)⁷.

3. FREQUENCY DIFFERENCE DETERMINATIONS

It is important to assess the sensitivity of the frequency of each laser to the factors known to cause changes of frequency ⁸. All measurements are made by the beat frequency technique which provides a very sensitive means of determining the behaviour of the stabilized lasers.

All lasers were locked to saturated absorption hyperfine components d, e, f, g of the $^{127}\text{I}_2$ intracavity cell systems using the third harmonic technique . Two copper - constantin thermocouples, linked between each lasers participating in comparison, gave information about cold finger temperature stability . We observed a good temperature stability of the cold point of the iodine cells .

For the comparison the parameters of each laser (modulation amplitude, cold point temperature, laser output power) were carefully adjusted to values given by Recommendation 3 (CI-92)¹ before the start of each matrix determination. A record of the output of the demodulator gave supplementary information about both electronic voltage offset and signal to noise ratio.

To study the variation in frequency difference, one laser worked under different settings of modulation amplitude, iodine temperature - pressure or intracavity power, while the other laser worked under fixed settings.

Variations in frequency difference for each of the four components were studied by measuring the frequency difference for the combinations [d-g], [e-g],[f-g] and [g-d] for each setting of the mentioned parameters when comparison were made at the BIPM. The combinations [h-d], [h-e], h-f] and [h-g] were used when comparisons held at the IMGC . In both cases , an average of the slope for the four individual components was then taken as a measure of the studied parameter dependence . The slope and its standard deviation from three comparisons are presented in Table 2, considering each four components and the mean value.

Apart from the parameters already mentioned, electronic voltage offsets were also studied for the laser RO.2, and a large difference has been noted in values obtained at the BIPM and at the IMGC. Also, for the laser RO.1 we observed a large slope for the cold point temperature dependence.

Results from one comparison are also presented in Figure 1. There are different contributions of each component to the mean frequency difference.

Table 2. The slope and its standard deviation for parameters known to cause changes in laser frequency are presented as follows : laser power ($\Delta v / \Delta P$), modulation amplitude ($\Delta v / \Delta m$), iodine pressure ($\Delta v / \Delta p$), cell cold finger temperature ($\Delta v / \Delta t$) and integrator offset ($\Delta v / \Delta v$). Determinations refer to components : d, e, f, g.

com- ponent	Slope and its standard deviation					compared lasers
	$\Delta v / \Delta m$ (kHz / MHz)	$\Delta v / \Delta p$ (kHz / Pa)	$\Delta v / \Delta t$ (kHz / °C)	$\Delta v / \Delta P$ (kHz / μ W)	$\Delta v / \Delta v$ (kHz / mV)	
d	-[7.8 \pm 2.2]	-	-[54.3 \pm 5.9]	-[0.06 \pm 0.02]	-	RO.1 - BIPM4
	-[7.7 \pm 3.3]	-[7.9 \pm 0.7]	-[11.6 \pm 1.3]	-[0.05 \pm 0.02]	-[3.8 \pm 1.3]	RO.2 - IMGC4/5
	-[6.4 \pm 1.4]	-[7.4 \pm 1.2]	-[11.8 \pm 2.1]	-[0.09 \pm 0.04]	-[34.4 \pm 0.3]	RO.2 - BIPM4
e	-[12.0 \pm 1.1]	-	-[50.4 \pm 2.9]	-[0.08 \pm 0.02]	-	RO.1 - BIPM4
	-[12.8 \pm 2.4]	-[9.8 \pm 0.5]	-[14.5 \pm 0.4]	-[0.05 \pm 0.04]	-[3.4 \pm 0.3]	RO.2 - IMGC4/5
	-[9.2 \pm 0.4]	-[8.1 \pm 0.5]	-[13.0 \pm 1.0]	-[0.16 \pm 0.05]	-[33.3 \pm 0.5]	RO.2 - BIPM4
f	-[11.1 \pm 1.4]	-	-[55.1 \pm 2.9]	-[0.11 \pm 0.23]	-	RO.1 - BIPM4
	-[13.4 \pm 2.8]	-[9.9 \pm 0.3]	-[14.5 \pm 0.7]	-[0.11 \pm 0.01]	-[3.7 \pm 0.6]	RO.2 - IMGC4/5
	-[10.0 \pm 1.3]	-[7.9 \pm 0.5]	-[12.7 \pm 1.0]	-[0.12 \pm 0.05]	-[34.0 \pm 1.0]	RO.2 - BIPM4
g	-[13.7 \pm 3.3]	-	-[55.2 \pm 2.6]	-[0.12 \pm 0.15]	-	RO.1 - BIPM4
	-[14.8 \pm 2.3]	-[10.2 \pm 0.3]	-[15.0 \pm 0.5]	-[0.08 \pm 0.02]	-[4.0 \pm 1.0]	RO.2 - IMGC4/5
	-[9.3 \pm 0.5]	-[8.3 \pm 0.4]	-[13.3 \pm 0.8]	-[0.16 \pm 0.09]	-[34.3 \pm 1.2]	RO.2 - BIPM4
mean	-[11.1 \pm 2.4]	-	-[53.7 \pm 2.2]	-[0.09 \pm 0.03]	-	RO.1 - BIPM4
	-[12.1 \pm 3.1]	-[9.4 \pm 1.0]	-[13.9 \pm 1.5]	-[0.07 \pm 0.03]	-[3.7 \pm 0.2]	RO.2 - IMGC4/5
	-[8.7 \pm 1.6]	-[7.9 \pm 0.4]	-[12.7 \pm 0.6]	-[0.13 \pm 0.03]	-[34.0 \pm 0.5]	RO.2 - BIPM4

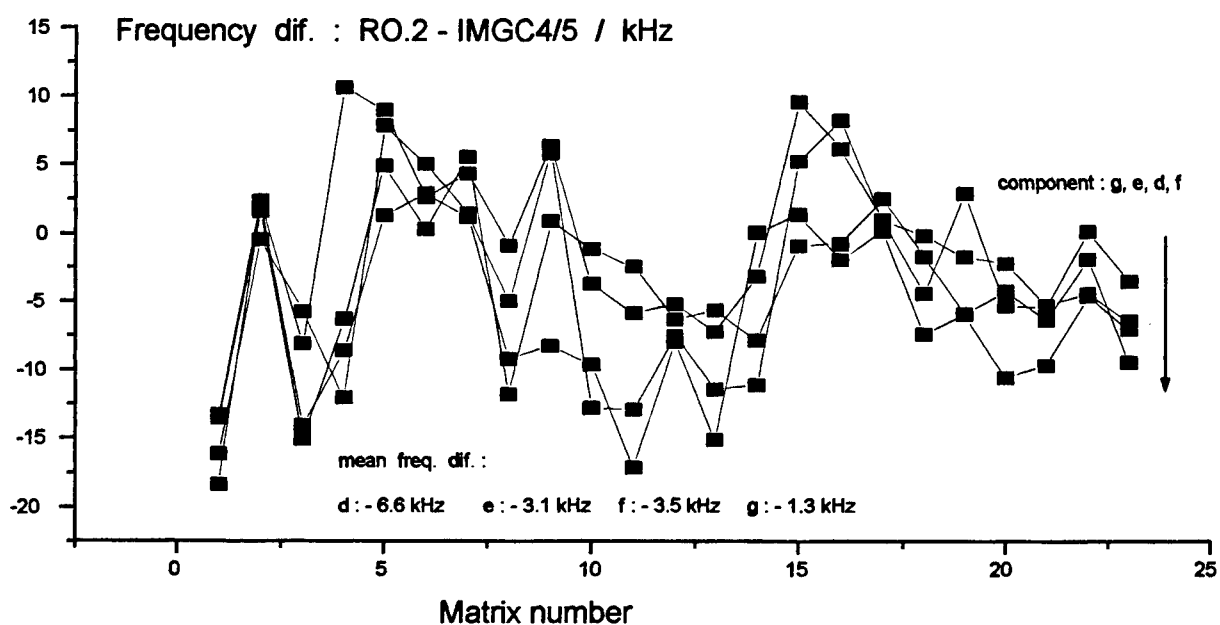


Figure 1. Frequency difference between lasers RO.2 and IMGC4/5 for components d, e, f, g. The mean frequency difference for the set of 23 determinations was calculated as : $f_{\text{RO.2}} - f_{\text{IMGC4/5}} = + (3.8 \pm 5.7) \text{ kHz}$

In Table 3 are presented mean values for frequency differences from different laser frequency comparisons involving lasers RO.1 and RO.2. During the comparisons the largest possible number of matrix determinations was sought. One frequency determination consisted of a "matrix measurement" in which the frequency intervals for all the combinations of the components d, e, f, g with the exception of the main diagonal of the matrix (which corresponds to the frequency intervals in which the lasers are stabilized on the same component) were measured⁹. The frequency difference between the two lasers was then taken as the average of half of the differences of the symmetrical values obtained in the matrix. Corrections were applied on final results using laser parameter dependencies mentioned in Table 2 when available.

Table 3. Mean frequency differences computed from matrix determinations involving the lasers RO.1 and RO.2. The standard deviation of a set of matrix determinations obtained during a comparison was considered as repeatability of the frequency difference.

Lasers participating in comparison	Number of matrix determinations	Frequency diff. [kHz]	Repeatability [kHz]
RO.1 - BIPM4	3	- 40.3	1.8
RO.2 - IMGC4/5	23	+ 3.8 *	5.7
RO.2 - BIPM4	13	- 2.2	6.7
RO.2 - INVAR3	10	- 15.1	2.5

* no corrections were applied.

3. LASER FREQUENCY STABILITY

The frequency stability of the lasers is characterized by the two consecutive samples variance called Allan variance¹⁰. A linear fitting of the data gives the following general expression for the relative Allan variance $[\sigma(\nu)/\nu]$ as a function of the inverse of square root of sampling time interval $[\tau^{-1/2}]$ as follows :

$$\sigma(\nu)/\nu = B \cdot \tau^{-1/2} + A$$

In Table 4 are presented some results for relative Allan variance determination for each bilateral comparison.

Table 4. Relative Allan variance determinations for comparisons involving Romanian lasers.

Laser (locking line)	B	A
RO.1 (f) - BIPM7 (e)	$2.3 \cdot 10^{-11}$	$4.9 \cdot 10^{-13}$
RO.2 (d) - IMGC4/5 (g)	$3.5 \cdot 10^{-11}$	$1.7 \cdot 10^{-14}$
RO.2 (g) - BIPM4 (d)	$1.76 \cdot 10^{-11}$	$6.4 \cdot 10^{-14}$

4. CONCLUSIONS

This type of laser is supposed to serve in metrological laboratories for testing other iodine-stabilized He-Ne lasers or for testing the wavelength of the frequency stabilized He-Ne lasers used in laser interferometers.

According to the last released documents¹, the relative frequency difference between the lasers should stay within a range of : $\pm 2.5 \times 10^{-11}$. That is valid for two-of-four of the results reported in Table 3.

The value for the mean frequency difference when lasers RO.2 and INVAR3 were compared should be judged from another point of view. So, from a previous comparisons with the laser BIPM4¹¹, resulted as mean frequency differences : $\Delta\nu_1 = \nu_{\text{INVAR3}} - \nu_{\text{BIPM4}} = + (8.5 \pm 3.1) \text{ kHz}$, respectively : $\Delta\nu_2 = \nu_{\text{RO.2}} - \nu_{\text{BIPM4}} = - (2.2 \pm 6.7) \text{ kHz}$. The expected value for frequency difference between lasers RO.2 and INVAR3 could be calculated from those values as : $\Delta\nu_e = \nu_{\text{RO.2}} - \nu_{\text{INVAR3}} = - (10.7 \pm 7.3) \text{ kHz}$. The expected frequency difference might be compared with that reported from direct measurements : $\Delta\nu_m = \nu_{\text{RO.2}} - \nu_{\text{INVAR3}} = - (15.1 \pm 2.5) \text{ kHz}$, so that their closing frequency (4.4 kHz) will stay within the same interval ($\pm 12.5 \text{ kHz}$) predicted by Recommendation 3 (CI-92).

There is a relative good agreement between values calculated for the coefficients reported in Table 2 when determined at IMGC and BIPM (measurements were against lasers having different constructions). That proves a good repeatability of the results obtained at a relatively long time interval (about 18 months), under different experimental conditions but using similar procedures.

Based on the above results, we could say that the Romanian laser RO.2 has well preserved its operating parameters during a period longer than two years, proving by international comparisons good and stable parameters as to be considered as a primary length standard, in accordance with last documents released in this field for the practical realisation of the new definition of the metre¹.

5. REFERENCES

1. BIPM *Comptes Rendus 17th Conf. Gen. Poids et Mesures*, p. 45-49, 97-98, (1983); *BIPM Proc.-Verb. Com. Int. Poids et Mesures*, 1983 **51**, 25-28, Recommendation 1 (CI -1983); Documents Concerning the New Definition of the metre, *Metrologia* Vol. **19**, 163-177, (1984); T. J. Quinn, " *Mise en Pratique* of the definition of the metre ", *Metrologia* Vol. **30**, 523-541 (1993 / 1994)
2. Gh. Popescu, J. -M. Chartier, A. Chartier, " Iodine stabilized laser at $\lambda = 633 \text{ nm}$: design and international comparison ", *Opt. Eng.* Vol. **35** (5), 1348-1352, (1996);
3. A. J. Wallard, " Frequency stabilization of the helium - neon lasers by saturated absorption in iodine vapour ", *J. Phys. E: Sci. Instrum.*, Vol. **5**, 926-930, (1972);
4. F. Petru, B. Popela, Z. Vesela, " Iodine - stabilized He-Ne lasers at $\lambda = 633 \text{ nm}$ of a compact construction ", *Metrologia* Vol. **29**, 301-307, (1992);
5. J. de Vicente, A. M. Sanchez, F. Bertinetto, "Comparison of He-Ne lasers from LMM and IMGC stabilised on $^{127}\text{I}_2$ at 633 nm ", *Metrologia* Vol. **30**, 503-506, (1993);
6. S. Iwasaki, J. -M. Chartier, " Comparison of the $^{127}\text{I}_2$ stabilized He-Ne lasers at 633 nm wavelength of the National Research Laboratory of Metrology of Japan and the Bureau International des Poids et Mesures ", *Metrologia* Vol. **26**, 257-261, (1989);
7. G. Popescu, M. Necsoiu, J.-M. Chartier, S. Picard, A. Chartier, " A study on the spectral characteristics of the iodine cells from IFA-IFTAR used in the He-Ne / $^{127}\text{I}_2$ lasers ", *Roum. Journ. Phys.*, Vol. **40**, 493-497, (1995);
8. J. -M. Chartier, J. Helmcke, A. J. Wallard, " International intercomparison of the wavelength of iodine-stabilized lasers ", *IEEE Trans. Instrum. Meas.* Vol. **IM-25**, 450-453, (1976);
9. F. Bayer-Helms, J.-M. Chartier, A. J. Wallard, " Evaluation of the international intercomparison measurements (March 1976) with $^{127}\text{I}_2$ -stabilized He-Ne lasers: spacing of the hyperfine structure components ", *PTB-Bericht* **PTB-ME 17**, 139-146 (1977);
10. D. W. Allan, " Statistics of atomic frequency standards ", *Proc. IEEE* Vol. **54**, 221-231 (1966);
11. T. J. Quinn, " Results of recent international comparisons of national measurement standards carried out by the BIPM, 1996 ", *Metrologia* Vol. **33**, 271-287, (1996).

Calibration procedures for a 10.6 μm laser calorimeter

Michael Kennedy, Detlev Ristau, Gabriel Dumitru*, Dan G. Sporea*, Clementina Timus*

Laser Zentrum Hannover e.V., Department of Laser Components,
Hollerithallee 8, 30 419 Hannover, Germany

*National Institute for Laser, Plasma and Radiation Physics,
PO Box 52-36, 76900 Bucharest, Romania

ABSTRACT

The paper presents the theoretical background of laser calorimetry as a method to investigate the absorptance of optical components, according to the recently adopted ISO Standard 11 551. An experimental set-up for optical absorption measurements, including a cw CO₂ laser and a calorimetric chamber, is presented. The calibration of the laser calorimetric set-up is also described. The calibration involved several steps: laser power calibration, evaluation of chamber sensitivity, electrical calibration using electrically heated samples and optical calibration utilizing 100 % absorptance samples. There were measured the conversion factors for the laser power and for the sample temperature; there were calculated over-all correction factors for the different substrates and they could be placed within ± 4 % around their mean value.

Keywords: laser optical component, absorptance, ISO standard, laser calorimetry, calibration

1. THEORETICAL BACKGROUND

The evaluation of optical absorption for laser components is becoming more and more important, due to the increasing laser powers needed in various scientific and technical domains. A wide range of laser optical components are used in different applications and, at the present moment, important scientific efforts are dedicated to the development of standard test procedures for determining the absorptance of optical components.

The international standard ISO 11 551, which stipulates test and evaluation methods for the optical absorption of laser components, has been recently accepted.

1.1. ISO Standard 11 551

The theoretical approach included in this document uses some simplifying assumptions:

- (i) one temperature characterizes the whole sample;
- (ii) the entire absorbed laser power is converted into heat;
- (iii) the heating energy is fast and homogeneously distributed over the sample;
- (iv) the environment temperature is constant;
- (v) the temperature rise is small comparing to the sample temperature.

Using these assumptions, the heat diffusion equation becomes very simple:

$$\frac{\partial u(t)}{\partial t} = \frac{\alpha P(t)}{mc + C_h} - \gamma u(t), \quad (1)$$

and

$$C_0 \equiv mc + C_h. \quad (2)$$

- $P(t)$ - incident laser power,
- $u(t)$ - difference between the sample and the environment temperatures,
- α - sample's absorptance,
- m - sample's mass,
- c - sample's specific heat,
- C_h - holder's heat capacity,
- γ - general losses coefficient.

1.2. Heating process

The laser irradiation of the optical component starts at the time $t=0$ and stops at the moment $t=t_0$. Due to the absorbed laser energy, a temperature rise occurs, and it is described by the dependence $u_h=u_h(t)$. For the approximation of constant laser power, $P(t)=P_0$, the solution of equation (1) is:

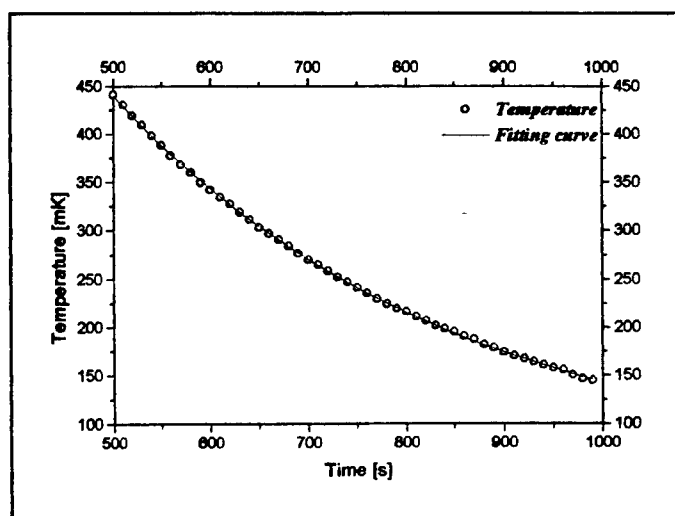
$$u_h(t) = \frac{\alpha P_0}{\gamma C_0} (1 - e^{-\gamma t}). \quad (3)$$

The average laser power (P_0) and the heat capacity (C_0) are known; during an optical absorption measurement, the dependence $u_h(t)$ is determined. Hence, if the losses coefficient (γ) is found - usually by monitoring the cooling process - the absorptance (α) of the optical component can be calculated.

1.3. Cooling process

After the laser heating, the optical component is allowed to cool and the temperature decrease during this process must be recorded, permitting the calculation of the losses coefficient (γ). The cooling starts at $t=t_0$ and it is described by the solution of equation (1), $u_c(t)$:

$$u_c(t) = u_0 e^{-\gamma(t-t_0)}. \quad (4)$$



Temperature decrease and its exponential fit

The experimental dependence $u_c(t)$ must be fitted by an exponential decay and from the analytical expression of the fitting curve, the losses coefficient (γ) is deduced.

1.4. Evaluation methods

With respect to the discussed theory, two methods for the evaluation of calorimetric were used: the exponential method and the pulse method.

The exponential method: the heating and cooling curves are fitted with exponential functions:

$$f_h(t) = A_h + B_h e^{-C_h t}, \quad (5)$$

$$f_c(t) = A_c + B_c e^{-C_c t}. \quad (6)$$

and from the fitting coefficients, all the relevant parameters can be calculated by comparing equations (5) with (3) and (6) with (4).

The pulse method: this technique of evaluation uses only the cooling curve and performs its extrapolation up to a temperature u_e and the time t_e given by:

$$u_e = \frac{\alpha P_0 t_0}{C_0}, \quad (7)$$

and

$$t_e = \frac{t_0}{2}. \quad (8)$$

The exponential curve that fits the cooling process is:

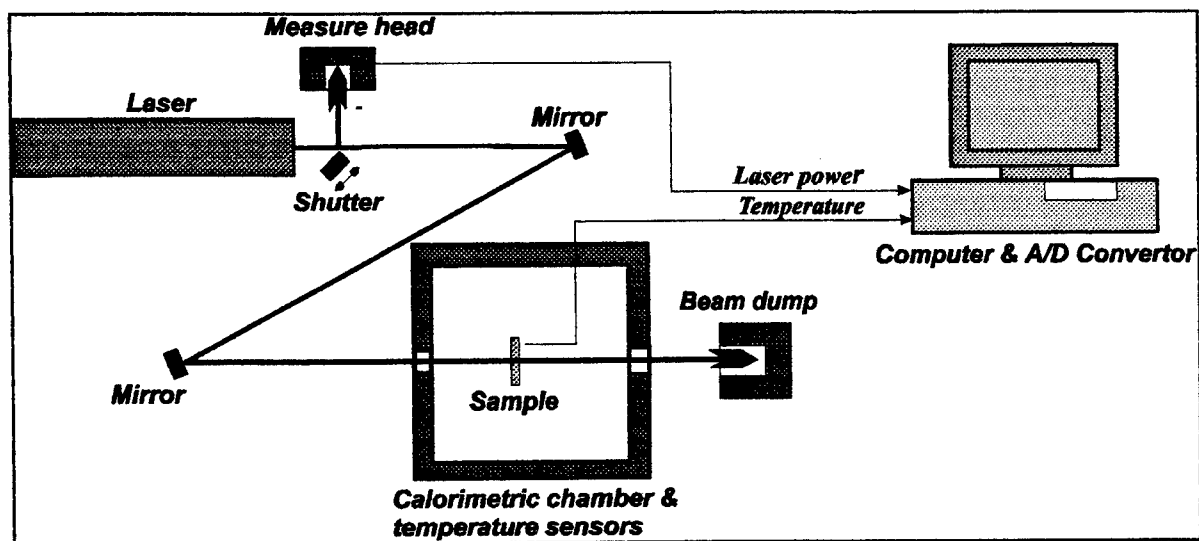
$$f_e(t) = u_e e^{-C_e(t-t_e)}. \quad (9)$$

and by comparing (9) with (4), the sample's absorptance can be calculated.

2. EXPERIMENTAL SET-UP

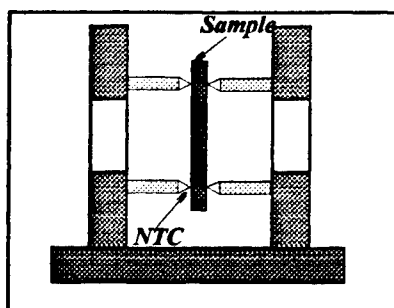
The investigated optical component is exposed to laser radiation and the temporal evolution of its temperature must be recorded. The sample has to be allowed to cool, insulated from the environmental fluctuations; hence the component is placed inside a calorimetric chamber with walls having a high thermal mass. The laser power has to be monitored, to determine the exact amount of laser energy that is incident on the sample; the temperature and power signals are acquired and stored using a PC compatible computer.

The source of radiation for the laser calorimetric set-up was a continuous wave CO₂ laser, with a maximum output power of 25 W; the typical operating level was 15 W. Plane copper mirrors were used to guide the laser beam and the optical path of the beam was visualized with a He-Ne laser, coupled with the main laser. The power level was continuously measured using a power-meter.



Laser calorimetric set-up

The calorimetric chamber has walls with high thermal mass and it contains the sample holder that is used for optical component fastening and which embeds the temperature sensors. The holder has three thermal sensors with small area (NTC resistors), each of them situated at 8 mm from the central axis.



The sample holder

The signals from the NTC resistors and from the laser power-meter are converted into digital values by the A/D converter and stored as data files for further processing, according to §1.4.

3. CALIBRATION

The digital parameters obtained after the A/D conversion (both for laser power and temperature) have to be calibrated with respect to their actual values and also the dependence between the incident laser power incident on the sample and the laser output power (monitored with the power-meter) must be determined.

The data processing basically involves fitting procedures for the heating and cooling curves and it leads to a value for the absorbance of the investigated optical component. The computing algorithm can be tested with known power measurements (electrical calibration) and with known absorbance measurements (optical calibration).

3.1. Power calibration

During an absorption measurement, the actual laser power incident on the sample can not be measured, but it can be calculated from the output laser power. The purpose of the calibration procedure is to find, as accurate as possible, the conversion factor between the laser power that impinges on the sample and the voltage signal after the A/D conversion.

This measurement is performed using a second power-meter, placed inside the calorimetric chamber. The conversion factor between the output and the incident laser powers was determined by measuring (for 100 s) both of them at several power levels and by linear fitting the time average values. The linear fitting of the experimental data leads to the following conversion factors:

- 0.92 between the laser power which is actually irradiating the optical component and the total output laser power;
- 471 mW/V between the incident laser power and the voltage recorded from the power-meter used for power monitoring.

3.2. Chamber sensitivity

The laser beam must pass through the chamber without hitting any component, because this leads to scattered radiation and to direct heating of the NTC resistors. During the empty holder measurements, performed with no sample inside the calorimetric chamber, no temperature increases occurred.

3.3. Electrical calibration

With an especially designed sample, there was performed an electrical calibration of the experimental set-up: a ZnSe sample was placed in the holder and it was heated with a resistor. The electrical power was assimilated with an incident laser power and the absorbance for the specific sample was calculated.

Several results for the electrical calibration

Absorbance [%] (theory: 100 %):	90.8	125.6	110.4	104.9
---------------------------------	------	-------	-------	-------

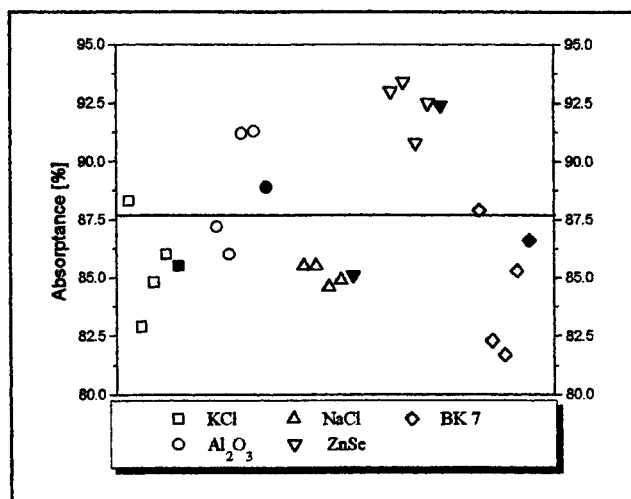
3.4. Optical calibration

The following step in the characterization of the calorimetric set-up was the calibration of the experimentally obtained values for the optical absorption. For this purpose, optical components with known absorbance must be measured and obtained values must be compared with that value.

Different samples with near 100% absorbance, obtained by blackening several optical substrates were measured using the laser calorimetric set-up. The samples were checked by measuring their transmittance and reflectance, using a FTIR 1900 Perkin-Elmer spectrometer.

Samples used for optical calibration			
Substrate	Mass [g]	Specific heat [J/g·K]	Thermal conductivity [W/cm·K]
Al ₂ O ₃	2.82	0.754	0.46
BK 7	7.75	0.858	0.011
KCl	7.15	0.68	0.065
NaCl	7.71	0.85	0.051
ZnSe	6.96	0.338	0.18

If the sum between transmittance and reflectance at 943 cm⁻¹ was greater than 0.5%, the sample was cleaned, blackened and checked again. The black coating should be thin (to let the thermal mass unchanged) and the thermal contact should be made between the thermal sensors and the sample itself, by removing small parts from the coating surface.



Results for the 100 % absorbance measurements.

Mean absorbance values						
Sample:	KCl	Al ₂ O ₃	NaCl	ZnSe	BK 7	Average
Absorbance [%]:	85.5	88.9	85.1	92.4	86.6	87.7

After the optical calibration, with the calculated conversion factors for laser power and temperature, for a 100 % absorbance the obtained value is 87.7 %. Therefore the over-all correction factor which has to be used is 1.14

4. ACKNOWLEDGEMENTS

The research was performed at the experimental facilities of the Laser Zentrum Hannover e.V., in the frame of the PECO project ERBCIPDT 940609.

5. REFERENCES

1. U. Willamowski, T. Groß, D. Ristau, H. Welling, "Calorimetric Measurement of Optical Absorption at 532 nm and 1064 nm according to ISO/FDIS 11551", *Proc. SPIE*, **2870**, pp. 483-494, 1996.
2. D. Ristau, U. Willamowski, H. Welling, "Evaluation of a round robin test on optical absorption at 10.6 mm", *Proc. SPIE*, **2870**, pp. 502-514, 1996.
3. ISO 11 551: "Optics and optical instruments. Lasers and laser related equipment. Test methods for absorbance of optical laser components".

Marius Nicola, Eugen Darvasi, Despina Gomoiescu, Emil Cordoş

Research Institute for Analytical Instrumentation,
Cluj-Napoca, Romania

ABSTRACT

The effect of the composition and of the grain size of Fe, Cu and Sn metallic powders on the reflectance spectra in VIS range have been studied. Calibration curves for determination of the percentage composition of Fe-Cu mixtures and for determination of the medium grain sizes for Fe, Cu and Sn powders were plotted.

1. INTRODUCTION

The grain size is an important physical characteristic of powders. For example, in the powder metallurgy process for obtaining structural parts from metal powders, a number of stages will be influenced by the particle size of starting powder, and its size distribution¹.

There is a variety of techniques available for determining particle sizes and size distributions. Sieving is the oldest and appears to be the most widely used method for size analysis. Other size analysis methods are: sedimentation², light scattering or diffraction phenomena of particles, the use of time-of-flight, the phase LDA signal measurement³, scanning with electronic microscope⁴, video images processing⁵ etc.. The selection of these methods is made depending on the specific needs⁶.

In this paper authors show how the results obtained from the investigation of the visible radiation reflected by the surface of some metallic powders can be used, to estimate the minimum sizes of their grains and to establish the proportion of some homogeneous mixtures based on two metallic powders with different colors.

2. THEORY

The investigation of the radiation reflected by a surface is a non-destructive procedure which can offer important information about the characteristics of studied surface. Thus the intensity and the spectral composition of reflected radiation depend on many factors as: the measurement geometry⁷, packing density, the form and the size of the micro-crystals which compound the surface⁸, the refractive index and the absorbance of studied surface⁹.

When a radiation is incident to a surface, two kinds of reflection can occur: A regular (specular) reflection, for smooth surfaces, and a diffuse reflection, for ideal matte surfaces. For these two extreme cases two fundamentally different theories are developed. But in practice all the situations are between these two extremes and an exact theoretical description can be difficult, that's why simplifying assumption which can never be exactly fulfilled must be made.

In the case of powders, diffuse reflection model is of interest. The diffuse reflectance assumes that the angular distribution of the reflected radiation is isotropic: that is, when the density of the reflected radiation (surface brightness) is directionally independent. This involves the validity of the Lambert Cosine Law. Two conceptions are possible for the occurrence of this isotropic angular distributions: For particle diameters much greater than the wavelength, the radiation is partly reflected by means of regular reflection at elementary mirrors¹⁰ (crystal surfaces) inclined statistically at all possible angles to the macroscopic surface, and partly penetrates into the inside of the samples where it then undergoes numerous reflections, refractions and diffractions at the irregularly located particles, finally emerging diffusely from the surface¹¹. For particle diameters of the order of the wavelength, scattering occurs. According to Mie's theory of single scattering at gases or colloids this scattered radiation is angular distributed and is by no means isotropic.

One of the physical amount which expresses the properties of quantitative reflection of some surface is the reflectance.

The reflectance R is defined by the relation $R=J/I_0$, where I_0 is the reflected flux of a Lambertian surface and J is the reflected flux of sample surface in the same conditions. R is a wave length λ or wave number ν function.

In this paper we use R^* defined as the reflectance of a layer of material of which thickness is enough to prevent the transmission (usually R^* is noted R_∞).

In practice R and R^* are not an absolute amount but a relative one because the measurements are made using MgO or $BaSO_4$ as standard and not an ideal standard such Lambertian surface.

The powders reflectance, R^* , depends on grain size and this dependence can be explained based on the variations of the absorption coefficient K and scattering coefficients S with the grain size¹²⁻¹³. Assuming negligible scattering, *Felder*¹⁴ demonstrated that the absorption coefficient in transmission K_T increases with diminishing of grain size and gives for a system of monodispersed particles the formula

$$K_T = -\frac{3}{2d} \varphi(P_m) \ln \left[1 - \frac{P}{\varphi(P_m)} (1 - T_d) \right] \quad (1)$$

in which d = particle diameter; P = packing density of particles, defined by $P = (N/V) \cdot (\pi d^3/6)$; $\varphi(P_m)$ is the function of a maximum possible packing density P_m , defined by the limit to which the particles can approach one another [$\varphi(P_m) \sim P_m < 1$]; T_d is the transmittance of a single particle, given according to *Duyckaerts*¹⁵ by

$$T_d = \frac{2}{(kc_0d)^2} \left[1 - (1 + kc_0d) \cdot e^{-kc_0d} \right] \quad (2)$$

in which $k = 2.303 \cdot \epsilon$ is the natural extinction coefficient of the molecules, while c_0 is their concentration in moles per liter in the particle.

It has been experimentally demonstrated that the absorption coefficient in reflection K_R is proportional with K_T , therefore K_R also decreases with increasing grain sized d .

In practice, studying not too strongly absorbing materials, we meet the opposite situation: the absorbance increases with grain size increasing (e.g. the powders become more dark). This is due to the fact that, in addition to the absorption coefficient, the scattering coefficient S is a function of particle size, increasing with particle sizes $d \geq 1\mu$ in proportion to d^2 which compensates the particle size dependence of K_R . The scattering therefore diminishes with increasing d , the radiation can penetrate deeper into the powder, the average traversed path becomes grater, and the absorbance also increases. This means that grinding absorbing materials in general cause them to become paler. A well known example is $\text{Cu SO}_4 \cdot 5 \text{ H}_2\text{O}$ which appears practically white in the finely triturated form.

Based on the previous consideration, we can made a model for metallic powder reflection. Thus we can consider that the metallic powder surface is formed from elementary-mirrors (grain faces) inclined statistically at all possible angles to the macroscopic surface. However, in this case, regular reflection can occur, mainly for great angle of incident radiation. This regular reflection can be partly compensated by shadowing effects, but for removing it, diffuse incident radiation (e.g. $D/8^\circ$ measurement geometry) must be used. Added to this is the radiation coming back through the surfaces of the sample from its interior. The density distribution of this radiation can be assumed as largely isotropic and should according fulfill the requirements of the Lambert Law. The average path of radiation trough the interior of powder becomes greater with the increasing of the metallic powder grain size and the quantity of diffusely reflected radiation decreasing. Thus, the diffuse reflectance of the metallic powder depends on grain size. We must mention that this mode to approach the reflection can be applied only if the wavelength of the incident radiation is much lower than the grain size.

The VIS reflectance spectra of a metallic powder contain also the information about its color. Using the color differences, the proportion of homogenous mixtures of two metallic powders can be determined.

3. EXPERIMENTAL

The reflectance spectra of metallic powder in the spectral range 380-700 nm (VIS), was measured with a double-beam spectrophotometer specialized in colorimetric measurement (wavelength accuracy ± 2 nm; bandwidth ≤ 10 nm; photometric range 0-100%R; photometric repeatability %R < 0.3). The geometry of measurement was $D/8^\circ$. This means that diffuse illumination of metallic powder samples was made with an integrating sphere (sphere diameter 150mm; windows diameter 25mm), and the observation angle was 8° . BaSO_4 was used as standard. With a PC and a home soft the apparatus can display and printout reflectance spectra and can determine specific colorimetric parameters.

For the measurements the following metallic powders for sintering were used: homogenous mechanical mixtures of Fe and Cu (to determine the powder proportion using color differences); Sn, Fe and Cu (for grain size estimation). The grain size range of measured powders is between 30 and 200 μm and the form of the grains is approximately spherical.

Five homogenous mechanical mixtures of Fe and Cu with known proportion was made. With data obtained from reflectance spectra of these mixtures at a chosen wavelength the proportion of Fe as function of reflectance R^* (a calibration curve) was plotted.

Grains of metallic powders with known size range were obtained by sieving. Every range of grain size was replaced with a medium dimension of the grains. The reflectance spectra of these fractions of metallic powders with known medium grain size were plotted. Using the data of these spectra the grain size as function of reflectance R^* at a chosen wavelength (a calibration curve) was plotted.

The wavelength used for calibration is selected to assure a best resolution (greatest distance between reflectance spectra) for an optimal signal-noise ratio. This criterion was used for all the measurements presented in this paper.

For measuring, the metallic powder was introduced in a special support with a glass window. This was necessary because the sample window of integrating sphere was vertically. The layer thickness of metallic powder samples was approximately 7 mm, enough to prevent transmission.

4. RESULTS AND DISCUSSION

Due to the color differences between Fe and Cu powders it is possible to determine the proportion in a mechanical mixture of Fe and Cu powder using reflectance measurements. In Fig. 1 the reflectance spectra for different proportions of Fe-Cu homogenous mechanical mixtures are shown. It can be observed that the metallic powder of Fe has no selective absorption band while the

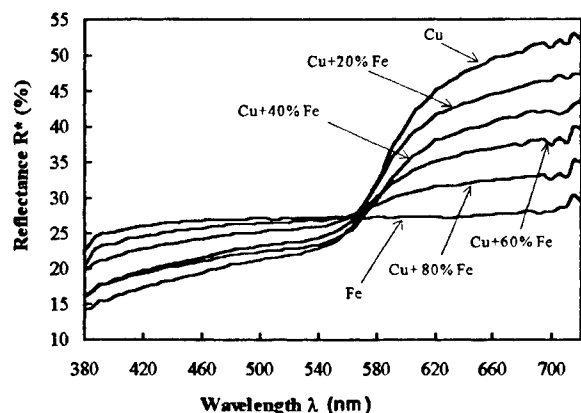


Fig. 1. Reflectance spectra of mechanical mixtures of Fe and Cu metallic powders

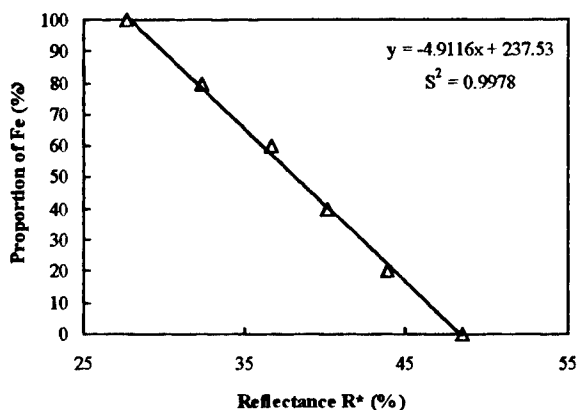


Fig. 2. Calibration curve (at 650 nm) for the proportion of Fe

metallic powder of Cu has a selective absorption band in green spectral domain. The data obtained from reflectance spectra were used for plotting the calibration curve. The calibration curve was plotted for 650 nm wavelength, where the distance between the reflectance spectra is the greatest. Fig. 2 shows the calibration curve, its equation and correlation coefficient S^2 . This calibration curve can be used to estimate the proportion of a mechanical mixture of Fe-Cu powder using reflectance measurements. It is very important to know the grain-size distribution of mixture, because the calibration curves can be used only for the same grain-size distribution of powders.

For grain size estimation of Sn powder, calibration curve was made using five powder fractions with medium grain size diameter of: 30 μm (where the grain-size range obtained by sieving was 25-35 μm), 40 μm (35-45 μm), 56 μm (45-67 μm), 71 μm (67-75 μm) and 80 μm (75-85 μm). Fig. 3 shows the reflectance spectra obtained for these fractions. It can be observed that

the reflectance increases with the diminishing of medium grain size of powder. The calibration curve and its equation, plotted for 540 nm wavelength, are shown in Fig. 4. With correlation coefficient of $S^2 = 0.9946$, the calibration curve has a good linearity.

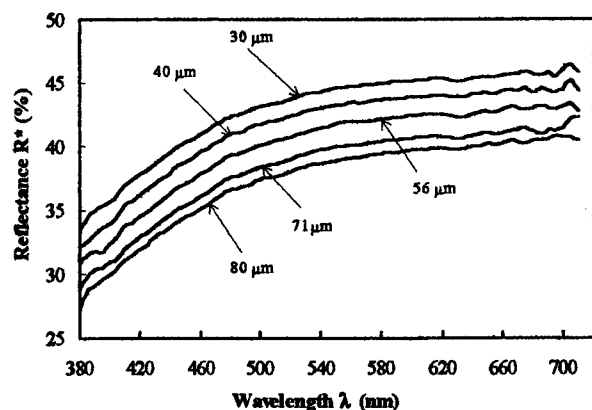


Fig. 3. Reflectance spectra for different grain sizes of Sn metallic powders

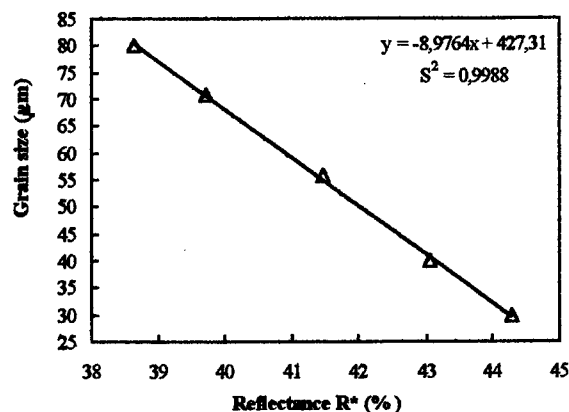


Fig. 4. Calibration curve (at 540 nm) for the estimation of grain size of Sn metallic powder using R^* measurements

The same method was applied for Fe powder (Fig. 5), where the medium grain sizes of used fractions to plot calibration curve were: 40 μm (35–45 μm), 71 μm (67–75 μm), 80 μm (75–85 μm), 125 μm (120–130 μm) and 160 μm (155–165 μm). The calibration curve was plotted at 590 nm (Fig. 6).

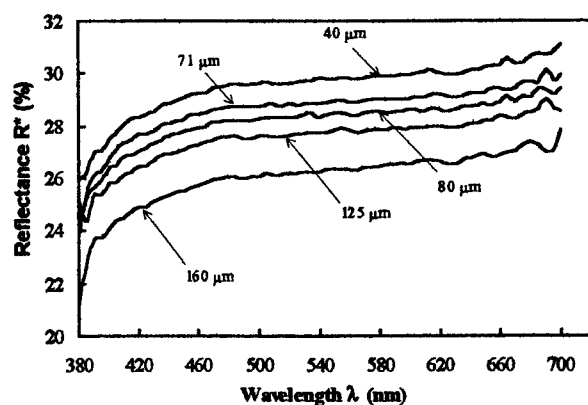


Fig. 5. Reflectance spectra for different grain sizes of Fe metallic powders

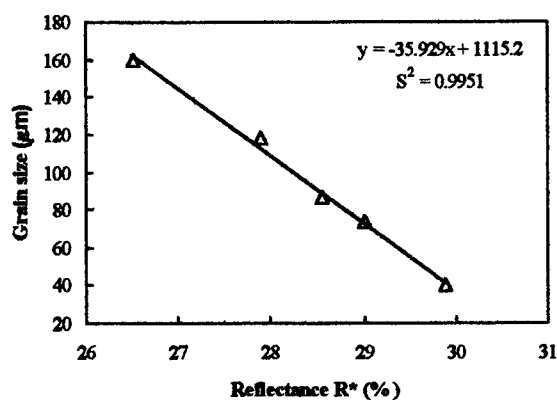


Fig. 6. Calibration curve (at 590 nm) for the estimation of grain size of Fe metallic powder using R^* measurements

For Cu powder (Fig. 7) the fractions used for calibration were: 56 μm (45–67 μm), 71 μm (67–75 μm), 100 μm (95–105 μm), 140 μm (135–145 μm), 180 μm (175–185 μm). In this case, due to the absorption band, the proper wavelength for calibration is above 620 nm. Below this wavelength the distances between reflectance spectra are very small and a good resolution of measurements is not possible. The used wavelength for calibration is 690 nm (Fig. 8). An increasing of distances between the fraction reflectance spectra can be observed for higher wavelengths of visible range.

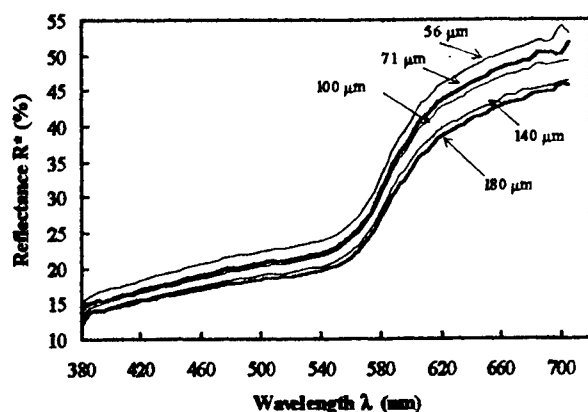


Fig. 7. Reflectance spectra for different grain sizes of Cu metallic powders

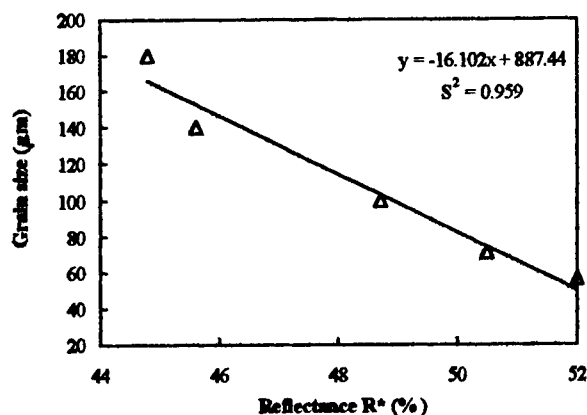


Fig. 8. Calibration curve (at 690 nm) for the estimation of grain size of Cu metallic powder using R^* measurements

5. ACCURACY AND ERROR SOURCES

The accuracy for proportion determination of two mechanical mixture powders depends strongly on the color difference between powders, thus the procedure is limited. The accuracy can be seriously affected if the mechanical mixture is not homogenous. For presented determination, the calibration accuracy is better than 2.47 (% Fe).

For a good accuracy in powder grain size estimation an important condition is the precision of calibration. The calibration accuracy increases with the narrowing of the grain size range. For presented determination the calibration accuracy is better than 4.29 μm (for Sn), 4.97 μm (for Fe), 13.9 μm (for Cu).

Error sources which affect the both types of determinations are the powder contamination and oxidization and the reaction with other substances. These processes can seriously modify powder reflectance spectra.

For very strong absorbing materials, the estimation of the grain size with the reflectance measurements is not recommended because the ratio signal - noise is small, so the accuracy of the measuring is small.

The insufficient thickness of the powder layer is also a possible error source. It is important to avoid the radiation penetrating through the powder layer. Another source of error is the non-uniformity of the surface.

6. CONCLUSION

The reflectance measurements in visible spectral range can give us important information about some opaque or strongly absorbing and scattering substances. The main advantages of the reflectance measurements are the rapidity and non-destructive character. These advantages make the reflectance measurements suitable for on-line measurements. We can use this kind of measurement to estimate the powder grain sizes, with good precision, the obtained results suggesting the possibility to use the VIS reflectance measurement in powder industrial application.

7. REFERENCES

1. "Particle size analyzers", *Metal Powder Report*, **51**(11), 42 (1996)
2. D. Hewitt, D. Mulcahy, J. Ralston, G.T. Wilkinson, "Rapid particle sizing by photosedimentometry", *Meas. Sci. Technol.* **2**(4), 271-275 (1991).
3. M. Safman, "Optical particle sizing using the phase LDA signals", *Dantec Inf.*, pp. 8-13, Sept. 1987.
4. S. A. Ditsman, I. A. Mikhailova, "Measuring the dimensions of spherical particles in scanning electron microscopy", *Bull. Acad. Sci. USSR Phys. Ser.* **51**(3), 78-81 (1987).
5. K. Deguchi, "An image processing technique for high-speed measurement of particle size distributions", *Measurement* **4**(4), 128-131 (1986)

6. B. B. Weiner, D. Fairhurst, "How to choose a particle size analyzer: considering quantitative and qualitative needs", *Powder-Bulk-Eng.* **6**(2), 22-27 (1992).
7. G. Kortum, D. Oelkrug, *Z. Naturforsch.*, **19a**, (28) (1964).
8. G. Kortum, D. Oelkrug, *Naturwiss.*, **53**, 600 (1966).
9. G. Kortum, "*Reflectance Spectroscopy*", Springer-Verlag Berlin . Heidelberg . New York (1969).
10. D. Bouguer, "*Traite d'optique sur la gradation de la lumier*", Paris (1760).
11. R. v. Seeliger, *Munch. Akad. II. Kl. Sitzungsber.*, **18**, 201 (1888).
12. R.J. Gledhill, D. B Julian, *J. Opt. Soc. Am.* **53**, 236 (1963).
13. J.W. Otvos, H. Stone, W.R. Harp, *Spectrochim. Acta*, **9**, 148 (1957).
14. B. Felder, *Helv. Chim. Acta*, **47**, 488 (1964).
15. G. Duyckaerts, *Spectrochim. Acta* **7**, 25 (1955).

Method for small birefringence evaluation

Anca Maria Beldiceanu

S.C. Pro Optica S.A, Aleea Bucovina, 4, 74404, Bucharest, Romania

ABSTRACT

A simple experimental method for evaluating small birefringences is reported. This method is based on the amplification of low phase retardation values using a rotary λ plate in conjunction with the birefringent sample. The new value of retardation is readily evaluated in white light with the sensitive λ plate or is measured with a system of a compensating plate and wedge in monochromatic light. The initial small retardation is determined by interpolation from theoretical curves. This unexpensive method can be applied in any biological, chemical or mineralogical laboratory where simple polarizing accessories are available.

key words : optical anisotropy, compensation methods, chromatic polarization, uniaxial crystal, retardation plate, photoelasticity, polariscope-polarimeter, residual birefringence, stress birefringence, sensitive plate

1. INTRODUCTION

Small values of birefringence appear in microscopic samples in biology, mineralogy, crystallography and in optical components in optoelectronics, polarimetry, ellipsometry.

The classical methods for evaluating the phase retardation due to birefringence make use of optical compensators with half-shadow devices,[1] and do not have high sensitivity and accuracy. Modern sensitive methods are based upon sophisticated modulation and evaluation techniques of retardation,[4],[5],[6].

We propose a method for the visualisation and the evaluation of small anisotropies in white light with a simple λ plate and an ordinary quartz wedge. There exist azimuth values of the tint λ plate for which the amplification of retardation takes place ;vivid, beautiful colours appear and the measurement can easily be done with a microscope quartz wedge.

2. THEORY

The method is based on the interference phenomena in the polariscope. The photodetector being the human eye the laws of polarized light interference must be completed with the psycho-physiological laws of vision.

For a system of two crystalline plates with retardations, δ_1 , δ_2 , and azimuthal angles ν_1 , ν_2 , between crossed polarizers, the resultant phase difference and the intensity of light that emerges from the analyser are given by, [1],[2] :

$$\delta = \delta_2 \pm \tan^{-1} \frac{\sin 2\nu_1 \cdot \sin \delta_1}{\sin 2(\nu_2 - \nu_1) \cdot \cos 2\nu_1 + \sin 2\nu_1 \cdot \cos 2(\nu_2 - \nu_1) \cdot \cos \delta_1} \quad (1)$$

$$I = \sin^2 2\nu_1 \cdot \sin^2 \frac{\delta_1}{2} + \sin^2 2\nu_2 \cdot \sin^2 \frac{\delta_2}{2} + 2 \sin 2\nu_1 \cdot \sin 2\nu_2 \cdot \sin \frac{\delta_1}{2} \cdot \sin \frac{\delta_2}{2} \cdot [\cos \frac{\delta_1}{2} \cdot \cos \frac{\delta_2}{2} - \cos 2(\nu_2 - \nu_1) \cdot \sin \frac{\delta_1}{2} \cdot \sin \frac{\delta_2}{2}] \quad (2)$$

It is evident that the intensity of interference in polarized light reduces when the azimuth is small. The well known laws of Weber -Fechner and Purkinje state that the colour sensitivity and the contrast sensitivity of the eye increase when the brightness of the field of view decreases.

3. EXPERIMENT

The usual principles of evaluating birefringences of the order of 15-20nm follow the colours of a Λ plate in the standard $\pm 45^\circ$ azimuth or the compensation of the phase retardation from a performant instrument. A new procedure based on these known methods can be obtained by the rotation of the λ plate toward small values of azimuth until birefringences of the order of 5nm become visible and measureble. The observed effect is produced at the same time by the amplification of the phase, eq.1, and by the luminance reduction, eq.2. Two simplified equations for describing the the method are immediately obtained if the values of interest in the proposed experiment, $\nu_1 = 45^\circ$ and $\delta_2 = 360^\circ$, are introduced in eq.1 and 2.

3.1 Experimental set - up

In order to develop and certify the method we used the experimental arrangement in fig.1

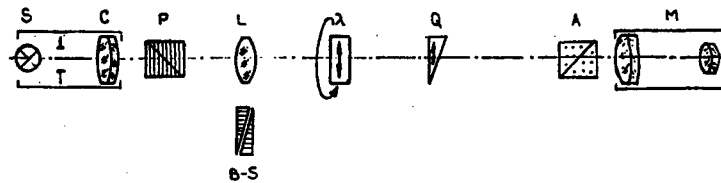
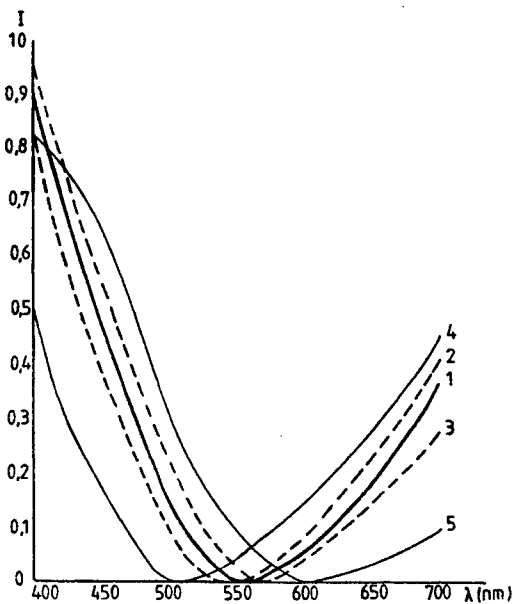


Fig.1 Optical scheme

- S - powerful light source with variable intensity ; C - collimating lens with moderate focal distance
P,A - polarizers with good extinction factor ; L - lens under the test of birefringence (1)
B-S - Babinet-Soleil compensator ; Λ - sensitive plate made from quartz crystal, in a rotary mount (2)
Q - quartz compensation wedge ; M - tele-microscope with micrometric reading ocular scale

3.2 Amplification of retardation

To illustrate the visual effect of the phase difference amplification, the intensity of interference in the visible part of the spectrum, in the classical arrangement and in the new one, was computed and represented in fig. 2.



The important feature of this graph is the great displacement of curves 4 and 5 compared with that of curves 2 and 3, relative to curve 1. The large differences in the position of the minima of intensity produce drastical changes in the computed thrychromatic coordinates. The resultant changes in the sensation of colour, in the two experimental situations, were computed in section 4 in order to demonstrate the objective amplification of the method proposed. To avoid errors in colour evaluation due to luminance differences caused by azimuthal changes we amplified the intensity in case of small angle ; the amplification factor, A, can be determined both experimentally and from calculus, and is realized in practice by raising the electrical voltage. of the light source.

Fig.2 Distribution of intensity for a small birefringence
1- λ plate alone; 2-sample and λ plate in standard azimuth;
3-sample in stdard azimuth and λ plate in reduced azimuth

3.3 Qualitative evaluation

Qualitative evaluation of birefringence is based on the well known correspondence between colour and phase difference given by the Newton scale.

In order to prove the validity of the Newton scale of colours in our experimental arrangement the computed distribution of luminous intensity, in the ideal and in the experimental case, is followed in graphs fig. 3.

For the same sample, i. e. the same δ_1 , we compare the standard intensity, given by :

$$I = \sin^2 (\delta_2 + \delta_{12}) / 2 \quad (3)$$

with the intensity given by eq.2.. and amplified by the determined value of the amplification, A. δ_{12} is the amplified value of the sample retardation, namely the result of \tan^{-1} in eq. 1. Differences between these curves are smaller than the least perceptible ones for the human eye, which appear in fig. 2 between curves 1 and 2. The distribution of light for the amplified phase retardation, supposed to have the same azimuth as the λ plate, can be approximated by the formula

$$I = A^* \sin^2 2v_2 \sin^2 \delta_{12} / 2 \quad (4)$$

For usual values of retardation and amplification the values of A and A^* do not differ very much.

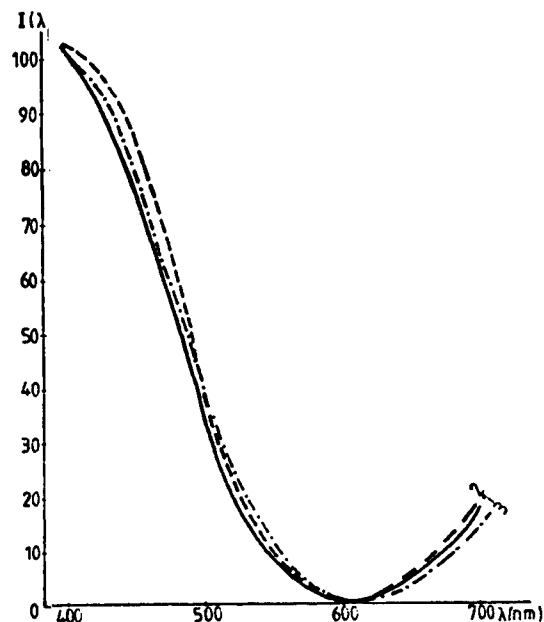


Fig.3 Intensity of light for an usual birefringence, of 10 nm
1-intensity distribution after the amplification of eq. 2
2-intensity distribution for amplified δ_{12} from eq.3
3-approximate intensity distribution given by eq.4

3.4. Compensation method

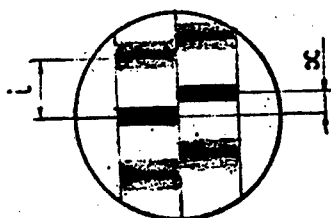
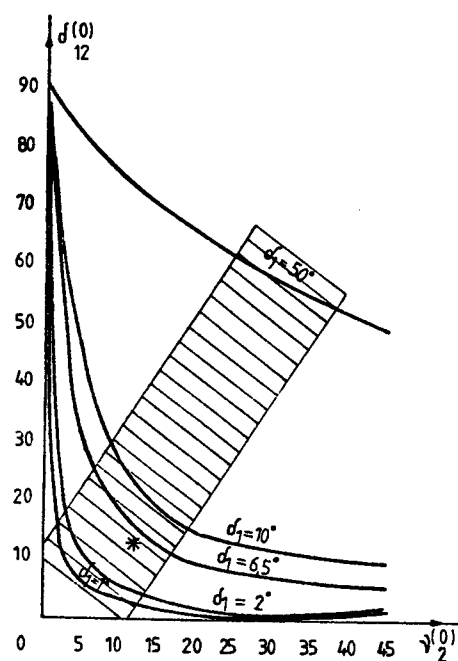
For the measurement of the resultant value of retardation, δ in eq. 1, one can use the well known compensators of Babinet or Senarmont.

A simplified way of operation appears to be possible, based on the experimental observation that the system of λ plate and wedge, in the same azimuth, differing by sign, can play very well the role of a Babinet compensator; in white light a sharp black fringe appears in the place where the wedge has the value of the λ plate retardation and the value of the amplified retardation can readily be measured. The retardation δ_{12} is computed for different interesting experimental values of δ_1 and of v_2 .

The initial small value is determined by interpolation from theoretical curves like those represented in figure 4. The values of δ_{12} and of v_2 are measured by compensation with the aid of the wedge and by direct reading on a mechanical scale. The displacement of the compensating wedge is read on a micrometric scale.

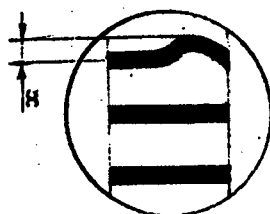
The procedure of measurement with the microscope and the quartz wedge, calibrated formerly with a Babinet - Soleil compensator, is illustrated for two of our samples: a cristal thin plate with uniform birefringence and an isotrope stressed plate with local birefringence, in fig 5a, 5b.

Fig.4 Theoretical curves of amplified phase difference δ_{12} , as a function of the v_2 azimuth of the λ plate and with δ_1 as parameter



5a. The measurement of the displacement x of the black fringe. In white light, the central fringe is black and the lateral ones have the red colour of the first order of interference

Fig.5 Measuremet of δ_{12}



5b. The measurement of the deformation x of one of the black fringes in any monochromatic laser light, except green

4. RESULTS

Many experimental observations were made on samples with residual birefringence caused by defects like stresses, striae and inclusions in the optical parts. For small values of retardation these defects are not visible in the standard arrangement of the polariscope and appear as coloured regions in an azimuth of the λ plate of $1-2^\circ$.

Experimental work was done in order to find which are the best components for the optical scheme. The most convenient are: halogen lamp, 100w, Superflux with optical fiber, polaroid polarizer and analyzer with HN-22, collimator lens with focal distance 300mm, microscope objective 1^* , He-Ne laser, medium power, quartz wedge with $.5$ and 1° angle. The mechanical adjustment of the experimental arrangement was simplified to the establishment of typical figures in the field of view of the microscope easy to be obtained by the rotation of the mechanical mounts.

The compensator wedge and the colour scale for the optical components without optical coatings were calibrated with a Babinet - Soleil compensator. All data in the table below are calculated from 3-5 readings in white light.

Table of quartz wedge calibration

wedge reading	1	2	3	4	5	6	7	8	9	10
Babinet reading	.45	3.27	6.16	9.00	11.92	9.1	11.94	14.73	17.60	20.48
Correspondence		2.82	2.89	2.94	2.92		2.80	2.80	2.87	2.87

Measurements of small values of retardation were made on a sample with well known values of birefringence, namely a Babinet-Soleil compensator delivered by Melles-Griot and calibrated in the laboratory with a Hg spectral lamp. The azimuth of the λ plate was fixed at a value of $5 \pm 0.1^\circ$ which gives an amplification of about 5 times for the original retardation. For a chosen value of retardation, $\delta_1 = 6.5^\circ$, given by the reading .254 on the compensator scale, the experimental results, in the two possible ways of evaluation, were the following. The colour of interference with the halogen lamp corresponds to an approximate optical path difference of 600 nm, which means 11 nm for the sample and a phase retardation of 7° , if the wavelength is supposed to be $\lambda = 550$ nm. Readings with the quartz wedge gave the following values of retardation: $\delta_{12} = 30^\circ$, $\delta_1 = 6^\circ$, the corresponding optical path differences being 601 nm and 9 nm. An informative value of the same phase retardation measured with a red light filter, was about 6° fringes being not sharp enough.

These measurement results are in good agreement with each other and with the predicted value of birefringence. Within these measurements were verified both the principle and the accuracy of the experimental method.

The results of colorimetric calculations with the values of the intensity of interference given by eq.2, in case of fig.2, with a theoretical light source of I.C.I. Illuminant C type are as follows. For curves 2 and 3 chromaticity changes ΔE and ΔC are of the order of 4 units while for curves 4 and 5 the same parameters are 10 times greater. Colour differences are represented in NBS units.

All calculations were accomplished with Fortran and Basic programs for HP-3000 and Wang computers.

5. SENSITIVITY AND APPLICABILITY RANGE

Qualitative evaluation has the sensitivity of the known purple red of interference, namely 15 nm, for the amplified value of birefringence, which means a sensitivity of about 2 nm for the actual value of optical path difference. In order to sustain this sensitivity, the results of computation for chromaticity changes introduced when the optical path is increased with 1 nm from the nominal value, are given. For any of the interesting values of 540, 550, 560 and 570 nm, representing the minima in fig.2, practically the same colorimetric sensitivities, ΔE and ΔC , were obtained; hence, in the range of small retardations, the sensitivity of 2 nm is theoretically available. These value was experimentally verified with samples of fine annealed optical glass, delivered with birefringences of 1 nm/cm.

With sharp interference fringes, obtained with intense source of light and good quality optical components, the sensitivity of the wedge method can be as good as $\lambda/100$.

The best range of amplification is shadowed in the graph of fig.4. For small values of the azimuthal angle the method loses its applicability because for $\nu_2 < 2^\circ$, mechanical errors play an important role. For great values of sample retardations the method loses its utility while the amplification is not significant (if δ_1 is greater than 30 degrees). The recommended value of amplification for usual evaluations is of about 5 times. One can use a higher magnification, only to visualize small birefringences, without making any precise measurement, in the region of 1-2nm.

The obtained precision of $\pm 0.5^\circ$ in the measurement of retardation is better than that reported by [6].

Computations on the parameters of interest, the intensity of light and the resultant phase retardation indicate for the mechanical accuracy in azimuthal angles of the sample and of the polarization components, a value of $\pm 5^\circ$ to be accepted.

6.CONCLUSIONS

A simple method was proposed and demonstrated. The method was developed from empirical observations, simulated data for light intensity and measured values of retardation. The method is characterized by good sensitivity, simplicity and low cost of application. One can obtain good results with tungsten lamps of 15w and 30w, and with components from an old polarisation microscope. The best results are obtained by colour evaluation in white light or by wedge compensation with a He-Ne laser.

Following the idea that the λ plate introduces a modulation of the polarized intensity of light we intend to develop the experiment with photodetection and modulation. The simplified assumptions made during the development of the method are the unity value of the incident intensity of light for all wavelength in the visible range, the value of 555nm for λ in white light, the parallelism of intensity curves, the dispersion not taken into account.

7.ACKNOWLEDGEMENTS

The author wishes to thank for helpful discussions on colorimetry to C.Visan, and for aid to prepare the manuscript to L.Regman and D.Ursu.

8.REFERENCES

- 1.H.G.Jerrard, "Optical compensators for measurement of elliptical polarization" J.O.S.A., 1,35, (1948)
- 2.H.G.Jerrard, "A quarter wave compensator with a sensitive Half-Shadow device", J.O.S.A., 4, 249, (1951)
- 3.H.Kubota and T.Ara, "On the sensitive colour of chromatic polarization", J.O.S.A.,8,537, (1951)
- 4.F.A.Modine and R.Major, "High frequency polarization modulation method for measuring birefringence", Appl. Opt.,3, 757, (1975)
- 5.S.Nagae, K.Iwata, "Measurement of surface strain distribution by means of color display using optical spatial filtering",4,970, (1975)
- 6.Y.Otani,T.Shimada,, "Two dimensional birefringence measurement using the phase shifting technique", Opt. Eng., 5,1604,(1994)

Circularity measurement by laser triangulation

Victor Damian, Constantin Blanaru, Dan Apostol, Adrian Dobroiu, Victor Nascov

National Institute for Laser, Plasma and Radiation Physics
Laser Department
Magurele P.O.Box MG-36
76 900 Bucharest, ROMANIA
E-Mail: DAMIAN@ROIFA.IFA.RO

ABSTRACT

The method and experimental results of circularity measurements by optical triangulation are presented. The measuring system is a laser based one, using a bi-cell detector with rectangular active surface shape and diagonal gap.

The measured data were fitted with a parametric function depending on the position of the tested object centre, relative to the centre of the rotating table.

A resolution of 2.5 $\mu\text{m}/\text{mV}$ is reported. This sensitivity is satisfactory for the majority of industrial applications - circularity measurement and centring.

Keywords: measurement, optical triangulation, circularity

1. INTRODUCTION

The advantages of using optical imaging systems for the determination and control of position are very apparent. One may quote the simplicity of the laws of reflection and refraction. The noncontact instruments using these laws do not wear and are unaffected by backlash and other ills that plague mechanical references.

The variety of surfaces and materials to be inspected require the use of versatile, noncontact systems and for this purpose optical or laser-based systems have clearly proved their merits. Targets having a dull surface, which is the general case in industrial applications, mainly reflect diffuse-reflection components of incoming light. The linear displacement measurement for a diffuse-reflection object uses the optical triangulation measuring principle, which is illustrated in fig. 1.

A point of light from a laser diode L is projected onto a target O and reflected diffusely. This point is focused onto a position sensor (PSD) by a lens placed in M. The PSD element supplies a position-dependent, analogue output voltage proportional to the position of the light spot on the detector surface. When the object moves from position A to B, the diffuse-reflected spot moves from a to b on the PSD active area. Applying the geometrical principle of similar triangles, one can determine the displacement of the object from its initial position:

$$\Delta ABO \approx \Delta abO \Rightarrow |AB| / |ab| = k,$$

where k is a characteristic of the practical set-up. One can measure for instance, $k = |AO| / |aO|$.

As it was mentioned, the PSD output is a measure of the $|ab|$ spot movement, so the object displacement results as:

$$|AB| = k \cdot |ab|$$

This paper deal with a particular case of form measuring and determination: circularity and centering of a rotating object.

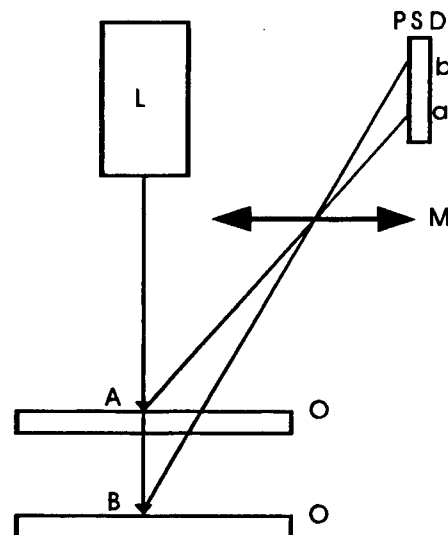


Figure 1

Triangulation measuring principles

2. THEORETICAL CONSIDERATION

The problem for circularity is the measurement of the radius variation and its representation. The radius variation, in the industrial applications is small compared with the radius value. That's why, for the graphical representation it is useful to use the magnification of the radius variations.

The graphical representation for the roundness assessment are plotted on polar or Cartesian coordinates¹. Generally the polar representation are more useful because of their realistic display and that it could be immediately related with the workpiece.

A general representation of the radius variation with the rotating angle could be written as

$$\rho(\theta) = M(r(\theta) - R) + S \quad (1)$$

where

- $\rho(\theta)$ - radius variation
- $r(\theta)$ - local radius
- R - mean radius
- M - magnification
- S - representation radius

In real application the rotating axes not corresponds with the workpiece axes under test. The theoretical function that describes the movement of an off-axis object is given by the equation (fig.2)

$$y(\theta) = -(\Delta C) \cdot \cos(\theta - \theta_0) + \sqrt{(\Delta C)^2 \cdot \cos^2(\theta - \theta_0) + R^2 - (\Delta C)^2} \quad (2)$$

where: ΔC - is the measure of the off axis position vector of the center of the tested object relative to the rotational center;
 R - the mean radius of the object
 θ_0 - the initial angles of the off-axis position vector
 θ - rotational angles

From this equation we determine the function of measured values as

$$\delta y = y_0 - y(\theta) \quad (3)$$

where: y_0 - is the reference value and

$y(\theta)$ - is current value of the motion function.

Using a χ^2 procedure, and fitting the measured data we can obtain the best value for y_0, θ_0 and ΔC .

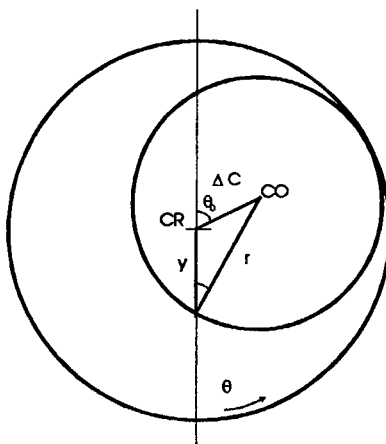


FIGURE 2
Elements of an off-axis object

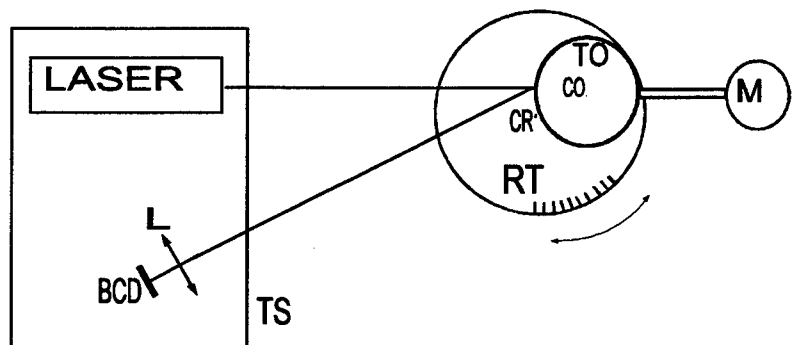


FIGURE 3
Experimental set-up

3. EXPERIMENTAL RESULTS

The experimental set up presented in fig. 3, allows to measure the δy values for different rotational angles^{2,3}, θ . Data were measured using two methods: by laser based triangulation system (TS) and by a micrometer (with a resolution of $1\mu\text{m}$). The tested object (TO) with its physical centre in (CO), is rotated with the aid of the rotating table (RT) with its physical centre in (CR).

The laser based triangulation system (TS) uses as light source a visible laser diode ($\lambda = 670\text{ nm}$, $P = 3\text{ mW}$) and as position detector a bi-cell detector (BCD) with rectangular active surface shape and diagonal gap. The scattered light from the object surface is focused on the (BCD) by a collecting lens (L). The displacement of the incoming spot on (BCD) active surface is proportional to the displacement of the target object.

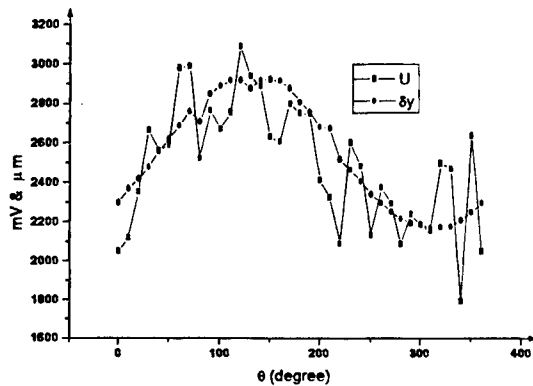


FIGURE 4
Cartesian representation of experimental data

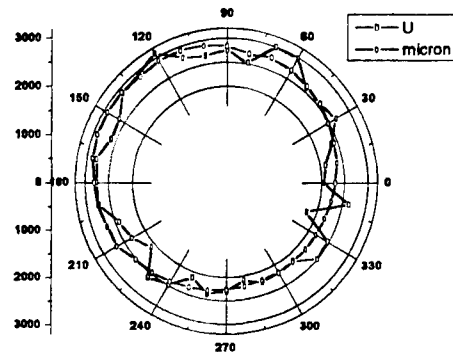


FIGURE 5
Polar representation of experimental data

The low-level current mode outputs of the bi-cell detector are changed into higher-level voltage signals by two corresponding transimpedance amplifiers. A third amplifier inverts one of the detector signals. An analog divider then performs the necessary computation to provide a signal U proportional to the position of the incident beam on the PSD.

Figure 4 presents a set of experimental data in Cartesian coordinates, where U represents the output voltage (in mV) of the (TS) system and δy is the position variation (in mm) of the tested object as measured by the micrometer.

Figure 5 represents the same set of measurements but in polar coordinates.

Displacing the object by means of a micrometric screw driven table, we have determined the sensitivity of the system. The best value obtained was $2.5\mu\text{m/mV}$ (fig.6).

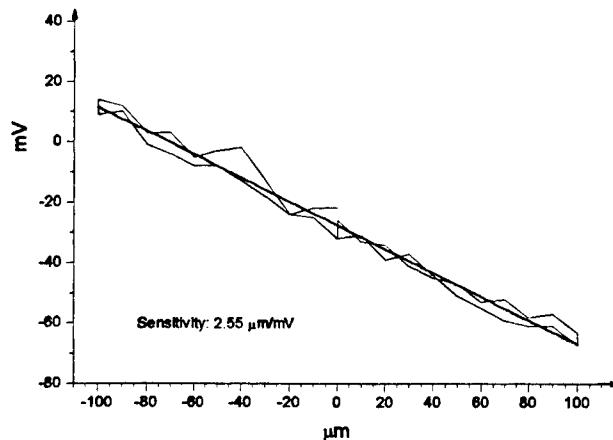


FIGURE 6
Sensitivity representation

4. CONCLUSIONS

The use of optical triangulation method for measuring of circularity and other geometrical parameters proves to be an efficient and cost effective solution for today industrial measurements. The position information obtained through the detection of the diffuse light coming from the target sweeps away the requirements regarding industrial processed surface quality.

Main advantages of the method are related to its simplicity, non-contact measuring principle and on-line processing capability.

The experimental data recorded for circularity measurements of an industrial processed body present a resolution of $2.5 \mu\text{m/mV}$ on a measuring range of $\pm 1 \text{ mm}$, when the target was placed at a distance of 300 mm from the laser head.

5. REFERENCES

- [1] D.J.Whitehouse, *Handbook of Surface Metrology*, IOP Publishing, Bristol, (1994)
- [2] S.Tanwar, H.Kunsmann, "An electro-optical sensor for microdisplacement and control", *J.Phys. E. Sci. Instr.*, **17**, 864, (1984)
- [3] M.F.M. Costa, "Surface inspection by an optical triangulation method", *Opt.Eng.* **35**, 9, 2743, (1996)

SESSION 8

Optical Components

Polarizing interference coatings made with anisotropic thin films

François Flory, Céline Defay

Laboratoire d'Optique des Surfaces et des Couches Minces
Ecole Nationale Supérieure de Physique de Marseille - Aix Marseille III
Domaine Universitaire de St Jérôme - 13397 Marseille cedex 20 - France
Tel : (33) 04 91 28 80 64 - Fax : (33) 04 91 28 80 67

ABSTRACT

It is now well known that the microstructure of materials in thin film form can be slightly different from that of corresponding bulk materials. Conventional evaporation (EC) using a heated crucible or an electron beam gun generally leads to a lacunar structure in columns. Some consequences of this microstructure on the optical properties of the films are well-known. The refractive indices are slightly smaller than that of the bulk material; water adsorption-desorption in the voids leads to variations of the spectral reflection and transmission of the coatings. But apart from these disadvantages, the columnar structure can present advantages because it also induces anisotropy of refractive index. When deposited with an ion beam assistance (IAD) the microstructure of the material is modified and so is its anisotropy. The anisotropy can then be controlled through the ion energy, making it possible to construct multilayer filters combining both isotropic films and anisotropic films. This opens the way for the making of components acting on the polarisation state of light. Results of calculation for different components are presented. Planar non absorbing monochromatic polarisers or polarisation rotators can be made in this way. The difficulty in controlling the deposition comes from the fact that the anisotropic layers must be deposited on non rotating substrates. This problem is discussed and examples of measured optical properties of multilayer filters will be given.

KEYWORDS : anisotropy, thin films, polariser, rotator, Ion Assisted Deposition

1. INTRODUCTION

Optical coatings are very often an important part of the optical systems. They can be used to make anti-reflection, mirrors, pass-band filters, etc. They are composed of thin amorphous layers deposited one on top of the other on the optical surfaces. Generally the layer materials are assumed to be isotropic and, in normal incidence the coatings are supposed not to change the polarisation state of the light.

However, most of the materials deposited by conventional e-beam evaporation under vacuum exhibit a columnar microstructure¹. It has been shown that such columnar materials present a form birefringence².

After briefly recalling the formalism^{3,4} used to calculate the optical properties of multilayers of such anisotropic materials we give a summary of measured anisotropy of TiO₂ films deposited under different incidence by conventional technique⁴. We also give the anisotropy of TiO₂ films obtained by Ion Assisted Deposition (IAD)⁵.

We are then concerned with examples of multilayer stacks including an anisotropic layer. Two different kinds of components are presented. Both a plane, non absorbing polarizer capable of working in normal incidence and a polarisation rotator acting in reflection are studied.

2. THEORY

Several years ago Horowitz and Macleod² proposed a model to describe the properties of films with columnar microstructure. In this model the principal axes of the films, considered as biaxial material, are connected to the columns (Fig. 1). One -ON3- is taken as the column direction; a second one -ON2- perpendicular to the first is taken in the plane of incidence on which the material arrives on the sample during deposition; the third -ON1- is perpendicular to ON2 and ON3 in such a way to obtain a direct reference.

Starting from Maxwell's equations for a monochromatic plane wave we can determine the so-called 4x4 transfer matrix. The theory of the propagation of an optical wave in an anisotropic dielectric medium in thin film form deposited on an isotropic substrate has been described by several authors.

We use this formalism of the propagation of an optical wave in an anisotropic thin film to express the so-called transfer matrix. This matrix links the tangential components of the total field on one interface delimiting a layer to those of the total field on the layer other interface. Reflection and transmission coefficients can be derived from this matrix formalism. These calculations can be performed whatever the orientation of the propagation plane in front of the principal planes of the thin film material.

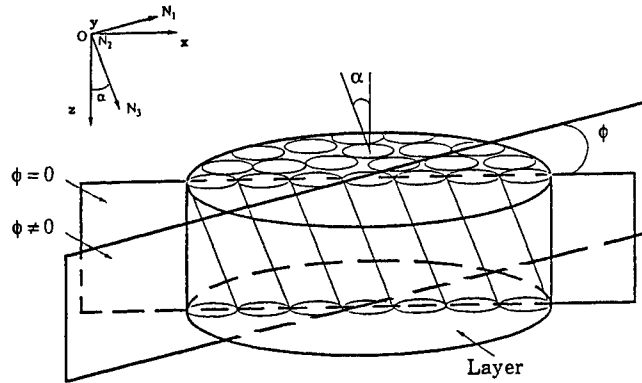


Figure 1: Anisotropic layer model (F. Horowitz and H.A. Macleod): α is the angle between the axis of the columns and the normal to the layer surface. ϕ is the angle between the plane of propagation and the plane containing the axes of a row of columns.

Let us consider a three-medium system made up of a non absorbing, homogenous, anisotropic dielectric thin layer, the thickness of which is d , limited with respect to z , infinite with respect to x and y , surrounded by two isotropic media.

The propagation of a monochromatic electromagnetic plane wave in an anisotropic layer, whose dielectric tensor is (ϵ) (its magnetic permeability is μ_0 , that of vacuum), can be studied by using the four by four matrix formulation given. This leads to a generalisation for the isotropic case. The principle of this method is to express the vector constituted by the four tangential components of the electric and magnetic fields on one interface limiting the layer in relation to the same vector on the other interface. By doing so we obtain the four by four transfer matrix.

Accordingly we can consider the propagation of an electromagnetic field in the anisotropic medium. We can use the following Maxwell equations:

$$\text{rot } \mathbf{E} = - \partial \mathbf{B} / \partial t \quad (1)$$

$$\text{rot } \mathbf{H} = \partial \mathbf{D} / \partial t \quad (2)$$

The plane of the incident light is the plane (Ox, Oz) ; the partial derivative with respect to y is then zero. To solve the equations we look for progressive waves in the form:

$$\begin{bmatrix} \mathbf{E} \\ \mathbf{H} \end{bmatrix} = \Gamma(z) \exp(i\omega(t - sx/c))$$

$$\begin{bmatrix} \mathbf{D} \\ \mathbf{B} \end{bmatrix} = \Lambda(z) \exp(i\omega(t - sx/c)) \text{ with } s \text{ the normalised propagation constant, } c \text{ the speed of light, } \omega \text{ the}$$

pulsation of the progressive wave,

$$\Gamma(z) = \begin{bmatrix} E_x(z) \\ E_y(z) \\ E_z(z) \\ H_x(z) \\ H_y(z) \\ H_z(z) \end{bmatrix} \text{ and } \Lambda(z) = \begin{bmatrix} D_x(z) \\ D_y(z) \\ D_z(z) \\ B_x(z) \\ B_y(z) \\ B_z(z) \end{bmatrix}.$$

Using Maxwell's equations (1) and (2) one can obtain two linear algebraic equations and four linear first order differential equations linking together the six components of the electromagnetic field in our anisotropic medium. From the two linear equations we can express H_z in relation to E_y and E_z in relation to H_y , E_x and E_y .

Carrying the expressions of E_z and H_z into the four differential equations and omitting the factor $e^{i\omega t}$, we reduce the number of variables from six to four. We can then write these four equations in the form:

$$\frac{\partial}{\partial z} \begin{bmatrix} E_x \\ E_y \\ H_x \\ H_y \end{bmatrix} = i\omega/c \begin{bmatrix} C_{11} & C_{12} & 0 & C_{14} \\ 0 & 0 & C_{23} & 0 \\ C_{31} & C_{32} & 0 & C_{34} \\ C_{41} & C_{42} & 0 & C_{44} \end{bmatrix} \begin{bmatrix} E_x \\ E_y \\ H_x \\ H_y \end{bmatrix} \quad (3)$$

That is:

$$\frac{\partial}{\partial z} \varphi(z) = \frac{i\omega}{c} C \varphi(z) \quad (4)$$

The layer is assumed to be homogenous in its thickness, so the coefficient of the matrix C are independent of z . Then we can look for four independent solutions to equation (4) in the form:

$$\varphi_j(z) = \varphi_j(0) \exp(-i\omega q_j z/c) \quad (5)$$

The equation (4) then gives a system of algebraic equations. To have a non trivial solution to this system it is necessary for the determinant to be equal to zero:

$$\det(C + qI) = 0 \quad (6)$$

I is the 4x4 identity matrix.

One eigenvector $\varphi_j(0)$, a particular solution to equation (4), corresponds to each eigenvalue q_j solution of (6):

$$C \varphi_j(0) = -q_j \varphi_j(0).$$

We look for a solution for $z = d$ in the form:

$$\varphi(d) = L(d) \varphi(0)$$

That is, for four independent vectors φ_j :

$$\Psi(d) = L(d) \Psi(0) \quad (7)$$

where Ψ is the 4x4 matrix constructed with the vectors φ_j .

The matrix $L(d)$ is the 4x4 transfer matrix which links the electric and magnetic fields on one interface to the fields on the other interface. This matrix is obtained from (5) and (7):

$$\Psi(d) = \Psi(0) K(d) = L(d) \Psi(0) \quad \text{with}$$

$$K(d) = \begin{bmatrix} e^{-i\omega q_1 d/c} & 0 & 0 & 0 \\ 0 & e^{-i\omega q_2 d/c} & 0 & 0 \\ 0 & 0 & e^{-i\omega q_3 d/c} & 0 \\ 0 & 0 & 0 & e^{-i\omega q_4 d/c} \end{bmatrix}.$$

The four eigenvectors $\varphi_j(0)$ are a reference of the vector space of solutions. So the matrix $\Psi(0)$ constructed with these vectors is regular and can then be inverted. The transfer matrix is then given by the relation:

$$L(d) = \Psi(0) K(d) \Psi(0)^{-1}.$$

So, through the layer, the tangential components of the electric and magnetic fields in one polarisation are obviously coupled to the tangential components in the other polarisation.

This matrix gives the link between the four tangential components of the electromagnetic field on one interface and the tangential components on the other interface bounding the layer. The dielectric tensor is obtained by applying two rotations to the matrix of the material which is diagonal in the reference corresponding to the main axis. One (α) corresponds to the orientation of the columns in front of the normal to the layer's boundaries ; the other (ϕ) corresponds to the orientation of the propagation plane in front of the principal plane (n_1, n_3).

Reflection and transmission coefficients as well as guided mode propagation constants (β_s) can be calculated from this formalism. The comparison between measured and calculated transmission in normal incidence and measured and calculated β_s performed versus the orientation of the principal plane of the layer material in front of the incident plane can be used to determine the anisotropy of thin films.

3. REFRACTIVE INDICES OF SINGLE TiO₂ LAYERS

3.1 Anisotropy of TiO₂ films deposited by e-beam gun under oblique incidence

3.1.1 Deposition conditions

The 4 layers studied have been obtained by conventional evaporation-condensation process in vacuum on non rotating BK7 substrates; the partial pressure of oxygen in the chamber is maintained to $1 \cdot 10^{-4}$ hPa; the deposition rate is controlled with a quartz microbalance (of course it depends on the position of the sample in the evaporation plant); the temperature of the substrates is approximately 250°C. The incidence of the material is 16.1° on sample 1, 20.3° on sample 2, 24.5° on sample 3 and 31.8° on sample 4.

3.1.2 Results

Table 1 gives the values of n_1 , n_2 , n_3 , d , $\Delta n_{13} = n_3 - n_1$, $\Delta n_{12} = n_2 - n_1$, $\Delta n_{23} = n_3 - n_2$ for the four samples. We can notice that n_1 is decreasing more rapidly with the angle of incidence of the material than n_2 and n_3 ; in consequence Δn_{13} and Δn_{12} increase with this angle; on the other hand Δn_{23} is practically constant. When the incident angle of the material increases a uniaxial model is not sufficient and the material behaves like a biaxial one.

	$\gamma(^{\circ})$	n_1	n_2	n_3	d (nm)	Δn_{13}	Δn_{23}	Δn_{12}
Layer 1	16.1	2.289	2.306	2.356	496.0	0.067	0.050	0.017
Layer 2	20.3	2.281	2.301	2.355	444.0	0.074	0.054	0.020
Layer 3	24.5	2.269	2.297	2.349	407.6	0.080	0.052	0.028
Layer 4	31.8	2.236	2.283	2.334	291.5	0.098	0.051	0.047

Table 1 : Anisotropy and thickness of layer deposited under oblique incidence by conventional technique
($\Delta n_{13} = n_3 - n_1$, $\Delta n_{23} = n_3 - n_2$, $\Delta n_{12} = n_2 - n_1$)

3.2 Anisotropy of IAD TiO₂ films

3.2.1 Deposition conditions

TiO₂ films which are studied here are obtained in a Balzers BAK 750 equipped with a cryogenic pump. The background pressure is 1×10^{-6} hPa. An argon pressure of 5×10^{-5} hPa is introduced through the ion gun (8 cm Kaufman-type ion gun) and a total pressure of 1.5×10^{-4} hPa is maintained adding O₂ also through the ion gun. The starting material is TiO tablets and the deposition rate of 0.2 nm/s is regulated with a quartz crystal. The substrates (BK7 glass) are not rotating during deposition. The substrate temperature is not controlled and is less than 373 K. The vapour incidence is 20.3° on all the studied samples. The ion beam is centred on the substrate and the angle of incidence of the ions on the substrate is 23°. The distance between the output grid of the ion gun and the substrate is 400 mm. The ion current density is approximately 230 $\mu\text{A}/\text{cm}^2$ on the substrate.

3.2.2 Results

Fig. 2 gives the dependence of the differences $n_3 - n_1$ and $n_2 - n_1$ measured in air with the ion energy. So we show that the anisotropy of TiO₂ films can be varied when using IAD by changing the ion energy.

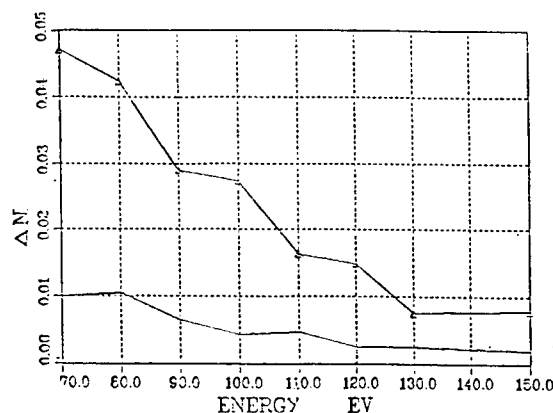


Figure 1: Dependence of $\Delta n_{31}=n_3-n_1$, $\Delta n_{21}=n_2-n_1$ on ion energy.

4. MULTILAYER POLARISING COMPONENTS

4.1 Polariser

4.1.1 Choice of a design

Polarisers can be made with isotropic thin films used in oblique incidence⁶ because the equivalent refractive index of a layer of refractive index n is $n \cos \theta$ for TE polarisation and $n/\cos \theta$ for polarisation TM with θ the incidence in the layer.

To make polarisers working in normal incidence it is necessary to use anisotropic thin films. In this last case the refractive index n_{\perp} for TE polarisation is n_2 and the refractive index n_{\parallel} for TM polarisation is given by: $1/n_{\parallel}^2 = \sin^2 \theta/n_1^2 + \cos^2 \theta/n_3^2$ when the incident plane is the plane $\phi = 0^\circ$.

Such a layer can be used to make a polariser by using it as a spacer layer of a Fabry-Perot filter. The centring wavelength λ_0 of a Fabry-Perot filter in normal incidence is given by the relation $2nd = k\lambda_0$ (d thickness of the spacer layer, k positive integer). Such a filter has a two different centring wavelengths λ_1 and λ_2 for the two polarisations :

$$2n_{\perp}d = k\lambda_1 \quad 2n_{\parallel}d = k\lambda_2 \quad \text{with} \quad |\lambda_1 - \lambda_2| = 2d |n_{\perp} - n_{\parallel}|/k.$$

For a given birefringence $|n_{\perp} - n_{\parallel}|$, depending on the width of each peak, the transmission peaks for the two polarisations are well separated or not. The transmission bandwidth of a Fabry-Perot filter is mainly depending on both the number of layers composing the mirrors and the thickness d of the spacer layer for a couple of defined high and low refractive indices. As an example, the spectral transmissions of filters of two slightly different designs are shown on Fig. 3. The calculation is performed for the two polarisations (plane $\phi = 0^\circ$) with the refractive indices of a typical anisotropic TiO_2 spacer layer ($n_1 = 2.27$, $n_2 = 2.28$, $n_3 = 2.32$). The designs considered are silica substrate/M6 20H M6/air (Fig. 3-a) and silica substrate/M8 18H M8/air (Fig. 3-b) where Mp ($p = 6$ or 8) represents a mirror composed of p alternated high and low refractive index layer (isotropic) of optical thickness $\lambda_1/4$ and qH ($q = 20$ or 18) represents an anisotropic layer of optical thickness $q\lambda_1/4$ for TE polarisation ($n_{\perp}d = q\lambda_1/4$).

It can be seen that the filter of design silica/M8 18H M8/air has the narrowest bandwidth. We consider this design for a first realisation. Designs with more layers can give better theoretical results but we limit ourselves to the simplest multilayer presenting some interest for applications which can be made. The realisation of such a filter is already not easy. The bandwidth is of only 1 nm and this is close to the limit of what can be made with isotropic thin films.

4.1.2 Realisation conditions.

The filter has been made by Ion Assisted Deposition. The materials used are TiO_2 and SiO_2 . For the mirrors the TiO_2 is deposited at ~ 0.2 nm/s with a partial pressure of O_2 of $\sim 1.5 \times 10^{-4}$ hPa ; the O_2 is injected in the chamber through the ion gun ; the ion energy is of 250 eV and the ion current density is ~ 230 $\mu\text{A}/\text{cm}^2$ on the sample. For the anisotropic TiO_2 films the deposition conditions are the same but the substrate is not rotating (incidence of the material on the substrate $\sim 20^\circ$) and the ion energy is reduced to 100 eV. For the SiO_2 the deposition rate is ~ 0.6 nm/s with no O_2 ; only Ar ions are used to assist the deposition (pressure of 5×10^{-5} hPa). The substrates are at room temperature during deposition.

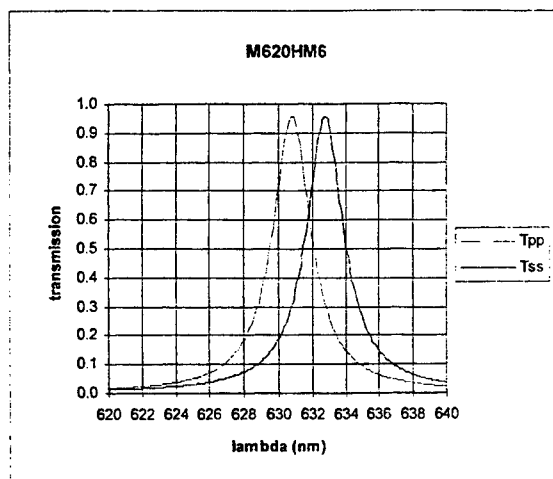


Figure 3-a : Tpp and Tss calculated versus the wavelength

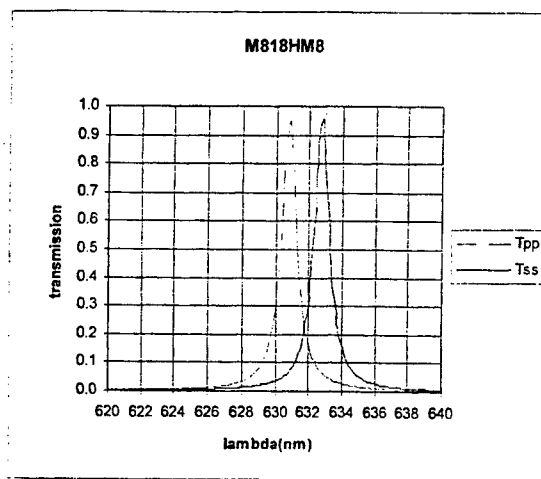


Figure 3-b : Tpp and Tss calculated versus the wavelength

A performing transmission optical monitoring⁷ is used and the multilayer is deposited in two times. First a M8 mirror and the 18H anisotropic layer are deposited. The sample is then directly used for the monitoring. A new bare substrate is positioned on the optical axis of the monitoring to deposit the second M8 mirror ; the studied sample is placed as close as possible to the monitoring glass. In this first attempt to make a polariser we choose to use a monitoring wavelength of 634 nm and to measure its performances at 632.8 nm. The centring wavelength of the filter is larger than the measuring wavelength to be sure that the transmission peaks can be measured by tilting the sample even if the centring wavelength slightly decreases after the deposition.

4.1.3 Results

The transmissions Tss and Tpp measured versus the angle of incidence θ for an incidence plane $\phi = 0^\circ$ at 632.8 nm are shown on Fig. 4. The maxima of transmission are obtained at 14° and 12° respectively instead of 7.5° and 5° expected. This could be due to some water adsorption phenomena which tend to increase the refractive indices of the materials. These maxima are of 22% and 37% respectively instead of ~96% given by the calculation (Fig. 5). Both some absorption and errors in the thicknesses of the layers can give such a decrease in transmission. However the maxima for the two polarisations are effectively separated and the difference in the incidence for the peaks is 2° , close to the 2.5° expected. It can also be noticed that Tss is smaller than Tpp. This could be due to some dichroism of the anisotropic layer.

In summary of this first experiment it appears that, even if the transmission peaks are smaller than expected and shifted toward greater incidences, the polarising function of the coating is demonstrated with a ratio between Tpp and Tss of more than 3 at $\theta = 12^\circ$.

4.2 Polarisation rotator in reflection

4.2.1 Design

In a single anisotropic layer the two polarisations are coupled when the waves propagate in a planes $\phi \neq 0^\circ$. This effect is enhanced in a resonant structure like a Fabry-Perot. As an example Tsp is of a few times 10^{-3} for a typical anisotropic 18H layer; for the Fabry-Perot previously considered this transmission increases to 7% (measured). Instead of a symmetric Fabry-Perot structure we consider an asymmetric one; the mirror close to the substrate is composed of more layers than that close to the air. Such a structure behaves like a mirror but for the centring wavelength the resonance in the spacer layer of the Fabry-Perot is stronger than with a symmetric structure. For a sack of simplicity in the realisation we choose to study a multilayer of design silica/M8 4H M4/air where 4H is the anisotropic layer. The calculated reflection between cross polarisers for $\phi = 45^\circ$ is ~ 0.09 for an anisotropic layer of refractive indices $n_1 = 2.215$, $n_2 = 2.225$, $n_3 = 2.257$.

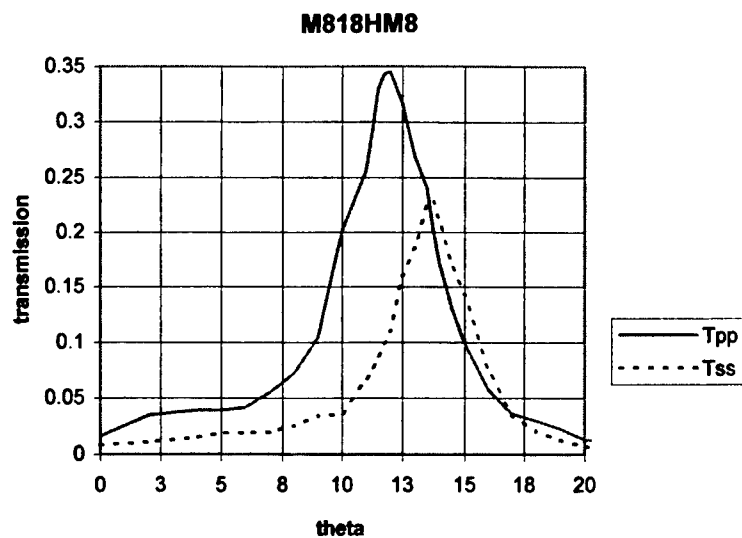


Figure 4: Tpp and Tss measured versus the angle of incidence theta

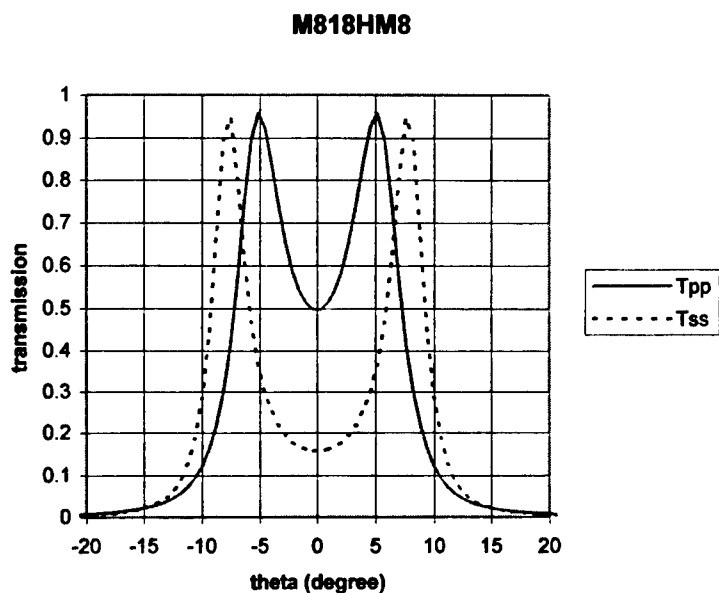


Figure 5 : Tpp and Tss calculated versus the angle of incidence theta

4.2.2 Realisation conditions

The deposition conditions of the layers composing this structure are quite the same than those of the symmetric Fabry-Perot polarising structure. Only the centring wavelength is changed (634.5 nm) and the ion energy during the deposition of the anisotropic layer (80 eV). The optical monitoring is performed directly on the sample, in one run.

4.2.3 Results

The measured reflection between cross polarisers $R_{ps}(\phi = 45^\circ)$ versus the angle of incidence exhibits a strong peak at $\theta = 14^\circ$. The measured reflection between cross polarisers $R_{ps}(\theta = 14^\circ)$, versus ϕ , is shown in Fig. 6.

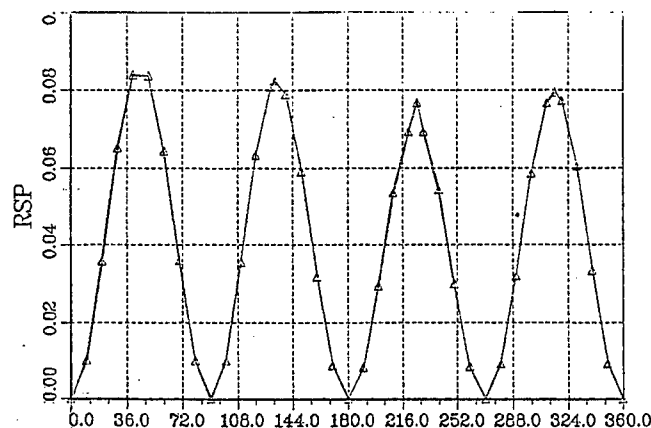


Figure 6 : measured $R_{ps}(\phi)$ for the sample odf design substrate/M8 4H M4/air

$R_{ps}(\phi)$ is modulated between 0 for $\phi = 0^\circ$ and $\sim 9\%$ for $\phi = 45^\circ$. The behaviour of the filter is what was expected : for the resonance $R_{ps}(\phi = 45^\circ)$ is much stronger than for an equivalent single anisotropic layer ($R_{ps}(\phi = 45^\circ) < 1 \cdot 10^{-3}$). The peak of $R_{ps}(\theta)$ is obtained for 14° instead of 6° expected. Like for the symmetric Fabry-Perot this could be due to water adsorption in the anisotropic layer. However the measured $R_{ps}(\phi = 45^\circ)$ is well explained by the theory.

5. CONCLUSION

The transfer matrix formalism used to study the measured optical properties is well suited to determine the refractive index of single layers. IAD is a good deposition technique to make low losses multilayer stacks composed of isotropic TiO_2 and SiO_2 thin films as well as anisotropic films.

We demonstrate the possibility of making two different multilayer components by this means. A monochromatic polariser based on a symmetric Fabry-Perot structure has been made and a polarisation rotator has also been made by using an asymmetric Fabry-Perot.

In both cases the performances obtained are not as high as expected by calculation but the functions are demonstrated. Better results can be expected by refining the monitoring of the filters and by taking into account the water adsorption phenomena. We will now focused our attention on such technical problems.

Plenty of other components acting on the polarisation of the light can be made by associating isotropic and anisotropic thin films but the problem of uniformity also needs to be studied for medium sized substrates and, of course, for large substrates.

6. ACKNOWLEDGMENTS

The authors thank G. Albrand, M. Bayle and B. Lazaridés for their technical support.

7. REFERENCES

- 1 A. G. Dirks, H. J. Leamy, "Columnar microstructure in vapor deposited thin films," *Thin Solid Films*, **47**, 219-222, 1977
- 2 F. Horowitz, H. A. Macleod, "From birefringence in thin films," *Proc. Soc. Photo-Opt. Instrum. Eng.*, **380**, 83-87, 1983
- 3 F. Flory, D. Endelega, E. Pelletier, I. Hodgkinson, "Anisotropy in thin films. Modelization and measurement of guided and non guided optical properties. Application to TiO_2 films", *Applied Optics*, **32**, n°28, 5649-5659, 1 October 1993.
- 4 F. Flory, "Guided Wave Techniques for the Characterization of Optical Coatings," in *Thin Films for Optical Systems*, F. Flory ed., Marcel Dekker Inc. USA, vol 49, Optical Engineering Series, 393-454 (1995)
- 5 F. Flory, "Consequences of the microstructure of thin films on their optical properties," *SPIE Proceedings, Thin Film Physics and Applications*, 2364, pp 27-35, (1994).
- 6 F. Varnier, E. Pelletier, "Filtres optiques multidielectriques adaptés pour l'incidence oblique: méthode de contrôle et tolérances de réalisation," *J. Optics (Paris)*, **11**, 169-177 (1980)
- 7 R. Richier, A. Fornier, and E. Pelletier, "Deposition Techniques and Related Topics: Optical Monitoring," in *Thin Films for Optical Systems*, F. Flory, ed., Vol. 49 of Optical Engineering Series (Marcel Dekker, Inc., New York, 1995), pp. 57-90.

Special mirrors for c.w. CO₂ high power lasers

R.V. Medianu, I. Gutu, G. Georgescu, M. Lazarescu*

National Institute for Laser, Plasma and Radiation Physics, Laser Department, P.O.Box MG-36, Bucharest, Romania

*National Institute of Material Physics, P.O.Box MG-6, Bucharest, Romania

ABSTRACT

"Special mirror" concept is presented as a "spare module" for a GaAs extracting mirror technological processed with GaAs thin films, mounted within two kinds of c.w. CO₂ laser resonators: U-type resonator (with optical pathlength $L_r \approx 4\text{m}$) and U-type folded resonator with V-discharge on each branch, reversal mirror provided (with the optical pathlength $L_r \approx 8\text{m}$), experimentally used to obtain good quality laser beam. The extracting mirror presents variable reflectivity, acting as a super-Gaussian mirror and working as an output coupler in the resonator, providing total compensation of the refractive index and of the small gain asymmetries.

Keywords: GaAs thin films, variable reflectivity mirror, high power laser.

1. INTRODUCTION

A "special mirror", designed as a variable reflectivity mirror (VRM), presents a particular interest for continuous wave (c.w.) CO₂ laser simple optical resonator equipped, conceived to use the active medium as efficiently as possible. This optical component was obtained by depositing GaAs thin films on GaAs substrate by r.f. magnetron-sputtering technique and experimentally used as an extracting mirror within laser resonators. Stoichiometry measurements of GaAs thin films deposited by this technique were made using an EDAX system. The laser we consider is a c.w. CO₂ transversal flow gas laser (TFL) with cylindrical geometry, existing as a technological device^{1,2}, for which the requirements were to include an as small as possible number of optical components within resonator and providing a good quality TEM_{00/01} laser beam. In this paper we report the technological data about a special GaAs extracting mirror thorough designed for a c.w. CO₂ high power laser (HPL) which delivers a multimode structure beam at 10.6 μm at power levels up to 2.5kW.

2. CO₂ LASER REQUIREMENTS

The laser described in detail elsewhere² is a CO₂ transverse flow gas (TFL) with optical pathlength of the U-type resonator $L_r \approx 4\text{m}$. The advantages of the TFL CO₂ laser are well known: relatively small dimensions and weight, reliability, compactness, low price, simplicity in the construction, high power capability, high small signal gain coefficient. For such a CO₂ laser type, the Fresnel number (N_F) is higher than 10 and the electrical discharge has a non-circular shape. Due to this, the beam intensity distribution is non-uniform and non-circular in shape too, being good for thermal treatments. A good quality laser beam is characterised by a TEM_{00/01} intensity distribution irrespective of laser power. Considering the total losses of the resonator $\Sigma q \leq 10\%$ (for 6 mirrors configuration), to extract the laser power out of the active medium volume, whose transverse diameter is in the range of 20mm÷26mm, a special structure of output coupling mirror M_1 was used.

Our experimental work is focused on state of the art of producing a good quality laser beam with high efficiency for a c.w. TFL laser dedicated for different industrial purposes like cutting, hardening and surface cladding, hardening and texturing of metal sheet, welding, production of nanopowder from hard materials. We are using a CO₂ laser with cylindrical geometry and two discharge ways. This design presents a good matching coefficient of the active medium section respective to plasma section (good energetic efficiency) for a Fresnel number $N_F < 2$ corresponding to a TEM_{00/01} laser beam intensity distribution. This type of laser, working in real industrial conditions, is a compact unit allowing total compensation of the both types of the active medium asymmetries.

A real resonant cavity is described in Fig. 1.

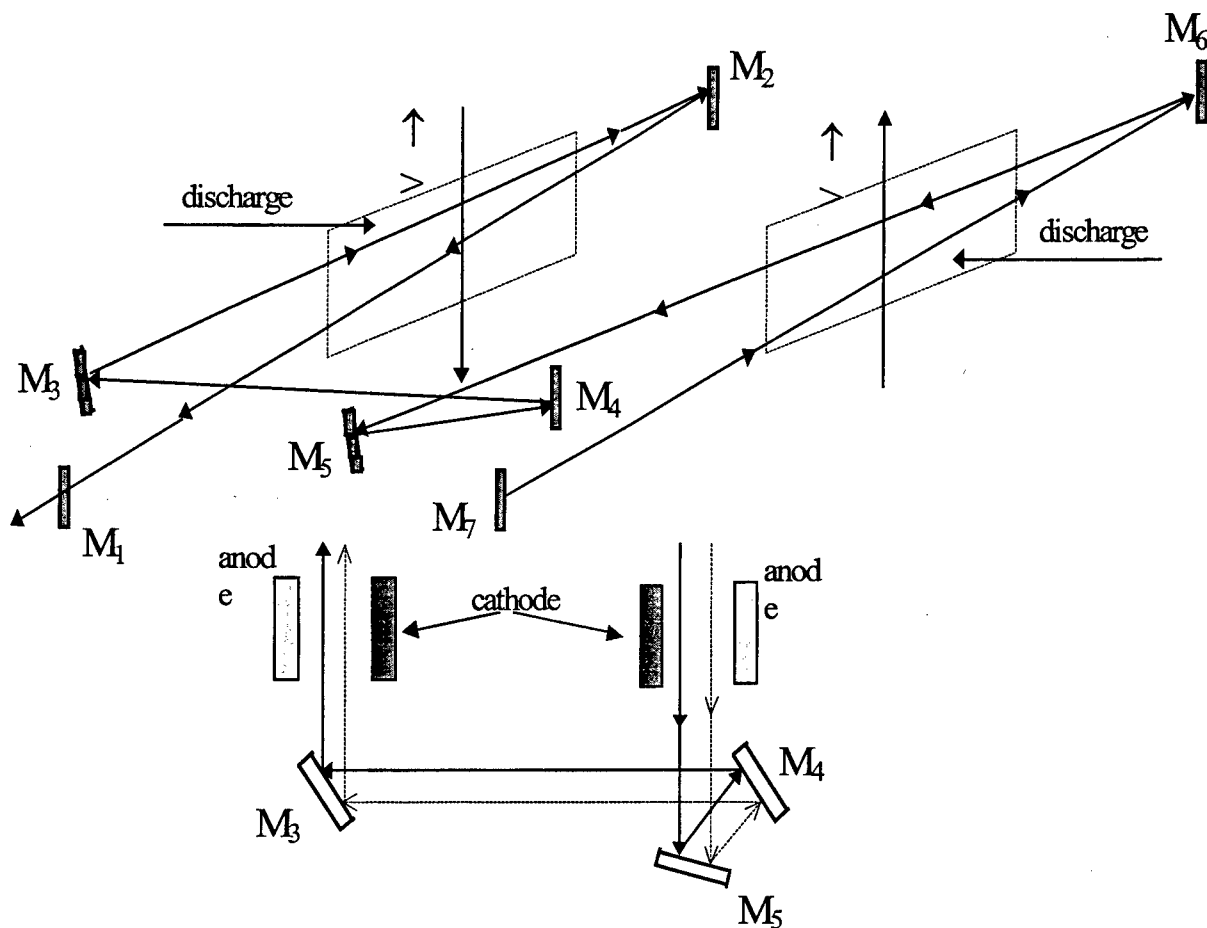


Fig.1- Schematic drawing of the double V resonator with "inverse" wave front mirror-M₄; M₁- output mirror GaAs, T=27%, R=∞; M_{2,3,4,5,6}-Cu deposited with Au mirrors; M₇-end mirror Cu deposited with Au, R= 21m± 1m.

As far as the resonant cavity we should like to stress that:

- it is provide with a special mirror M₄ for the reversal of the wavefront;
- in the same time, the group of mirrors (M₄, M₅) gives, in this configuration, a total compensation even in the case of the decreasing anode-cathode distance;
- it is reach a total compensated active medium, parallel and perpendicular to the flow direction;
- a matching coefficient $\eta_m = 0.8$ where

$\eta_m = \text{cross section of the laser beam} / \text{cross section of the plasma}.$

Consequently to this upgrade we are expecting 2.5kW on the multimodal beam TEM_{00/01}. Extracting mirror M₁ exhibits a particular interest for c.w. CO₂ laser that includes simple optical resonator conceived to use the laser medium as efficiently as possible. The extracting mirror is the most important optical component in determining beam quality. A special mirror M₁ could be designed as a variable reflectivity mirror for reaching monomodal structure for the laser beam. A transversal distribution of super-Gaussian of the laser intensity is defined by

$$I = I_0 \exp\left[-2\left(\frac{r}{w_0}\right)^n\right] \quad (1)$$

where I - is the current laser beam intensity within a transverse section through the beam measured on a plane perpendicular to it, I_0 - is the maximum beam intensity within the same section, r - is radial coordinate within the same section and w_0 is the laser beam waist; $n \geq 2$ is the order of super-Gaussianity.³

To keep this beam intensity distribution it is necessary that the reflectivity profile of the VRM obeys the same law:

$$R(r) = R_0 \exp[-2(r/w)^n] \quad (2)$$

where R_0 - is the maximum value of the VRM reflectivity, r - is the radial cardinal coordinate of the VRM surface and w is the linear dimension of the laser spot on the mirror surface.⁴

For a stable resonator, like a U-type cavity design, VRM allows a lower diffraction of the resonator coupling mirror to be obtained, and finally a better quality laser beam, as well as high modal volume of laser radiation. The value for the Fresnel number (N_F) usually is 1.2-2.5 and the laser power is up to 1kW for TEM_{00/01}.

A coupling mirror in the case of multimodal working structure of the laser beam can be produced as a normal extracting mirror described in Fig. 2.

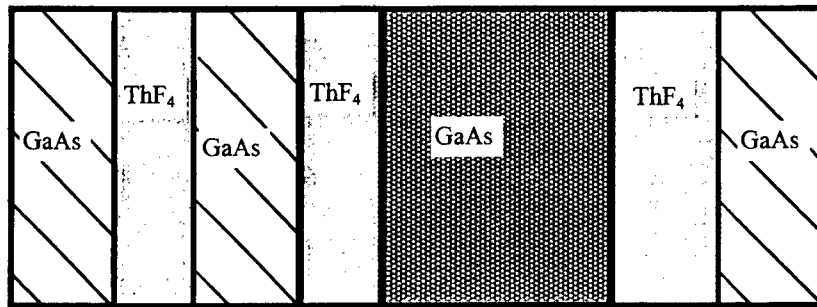


Fig. 2- Schematic structure of mirror M_1

The mirror structure, designed and improved by us, is schematically described as follows:

$$\begin{array}{ccccccc} \text{(Air)} & / & \text{(ThF}_4\text{)(GaAs)(ThF}_4\text{)} & // & \text{(GaAs)} & // & \text{(ThF}_4\text{)(GaAs)} & / \text{Air} \\ & & \text{antireflection} & & \text{substratereflection} & & & \\ & & \text{contribution} & & & & \text{contribution} & \end{array}$$

where candidates materials for being pair or correction layers could be ZnS, ZnSe, BaF₂, ThF₄, CeF₃/IRX.

3. GaAs EXTRACTING MIRROR M_1

Why we need a GaAs substrate for the extracting mirror M_1 ?

The industrial c.w. CO₂ laser can be characterised by two main conditions, always true conditions and probably never will change:

- ever better beam quality beam / a conservative good coherence;
- ever higher power levels.

Glenn H. Sherman⁵ said that the continuation of the second ensure the perpetuation of the first. Beam quality is determined, mostly, by the output mirror. The two optical materials historically used for the output mirror within c.w. CO₂ industrial lasers are zinc selenide and/or gallium arsenide. For choosing a correct solution depending on the level of the power we want to get, we have to consider the qualitative information give to us by figure of merit (F):

$$F = K / A[dL / dT + dn / dT] \quad (3)$$

where K - is the thermal conductivity ($\text{W/cm}^0\text{K}$), A - is the total absorption (cm^{-1}), dL/dT - the thermal expansion coefficient ($10^{-6}/^\circ\text{K}$) and dn/dT -refractive index temperature coefficient ($10^{-6}/^\circ\text{K}$).

Table 1. Physical properties for ZnSe and GaAs

Substrate material	Absorption coefficient (cm^{-1})	Thermal conductivity ($\text{W/cm}^0\text{K}$)	dn/dT ($10^{-6}/^\circ\text{K}$)	dL/dT ($10^{-6}/^\circ\text{K}$)
ZnSe	0.0005	0.18	64	8.5
GaAs	0.008 (the best)	0.49	149	5.7

Substrate material is becoming of secondary importance with 99.8% reflective coatings.

Table 2. Figure of merit for some IR materials

Substrate material	F for enhanced $R=99,8\%$	F for Au plated mirror $R=98,5\%$
Si	3	0.40
SiC	2.35	0.31
Mo	1.25	0.17
Cu	1.15	0.15

Performance will be limited by other cavity components. With less reflective coatings substrate become more important, i.e.

-GaAs output mirror with $R \approx 65\%$ has $F \approx 0.24$;

-ZnSe output mirror with $R \approx 65\%$ has $F \approx 0.11$;

-Ge end mirror with $R \approx 99,5$ has $F \approx 0.22$.

A new concept of design is considering the possibility of GaAs thin layer deposition on GaAs optical substrate. This "spare module" is clear described in Fig. 2.

The idea was to use GaAs substrate material and GaAs as a thin film material, optical compensated by ThF_4 films, to produce a "bulk material" with an equivalent complex refractive index which can confer a desired reflection for the extracting mirror. We have used GaAs as substrate material, produced in the National Institute of Material Physics⁶, with a refractive index 3.26-3.3 for $10.6\mu\text{m}$ and an extinction coefficient between 0.7×10^{-6} and 3×10^{-6} while the refractive index of GaAs as thin film was considered (by spectrophotometrical measurements) in the range of 3.16-3.26 with a very good stoichiometry according to substrate material.

The absorption coefficients of GaAs determined by laser calorimetry at $10.6\mu\text{m}$ were found to be $0.015 \pm 0.005 \text{ cm}^{-1}$ in good accordance with the values obtained from spectrophotometrical measurements obtained by scanning in a Fourier Transform Infrared (FTIR) Perkin-Elmer spectrometer over the spectral range 2.5-20 μm . In this condition we consider that oxygen doped GaAs investigated make this material suitable to be used as substrate in $10.6\mu\text{m}$ laser optics for c.w. CO_2 industrial lasers and also for the target material within the technological process of thin film deposition

GaAs thin films were deposited, with a very good reproducibility, by radio-frequency magnetron-sputtering into a special equipment designed and realised by ELETTRORAVA S.p.a. VARIAN ER3119. The main characteristics of the sputtering process used in our specific case are shown in Table 3.

Table 3. Technological parameters used in the sputtering deposition

Active Power (W)	Reactive Power (W)	Intensity (A)	Evaporation Rate ($\text{\AA}/\text{s}$)
1	0	<0.1	0.1
5	0	<0.1	0.4
25	3	0.1	1.5
60	9	0.1	3-3.2
75	12	0.1	3.5-4
100	17	0.1	4.5

GaAs thin films observe, in a very good approximation, the stoichiometry of the substrate material. The measurements were done using an EDAX system and the final results for two probes are given in the next table which represent the proportions of Ga and As within GaAs thin film:

Table 4. Composition of GaAs films according EDAX

Ga (%)	As (%)
54.7	45.3
56.47	43.53

The theoretical spectral characteristic for the extracting mirrors we proposed is shown in Fig. 3:

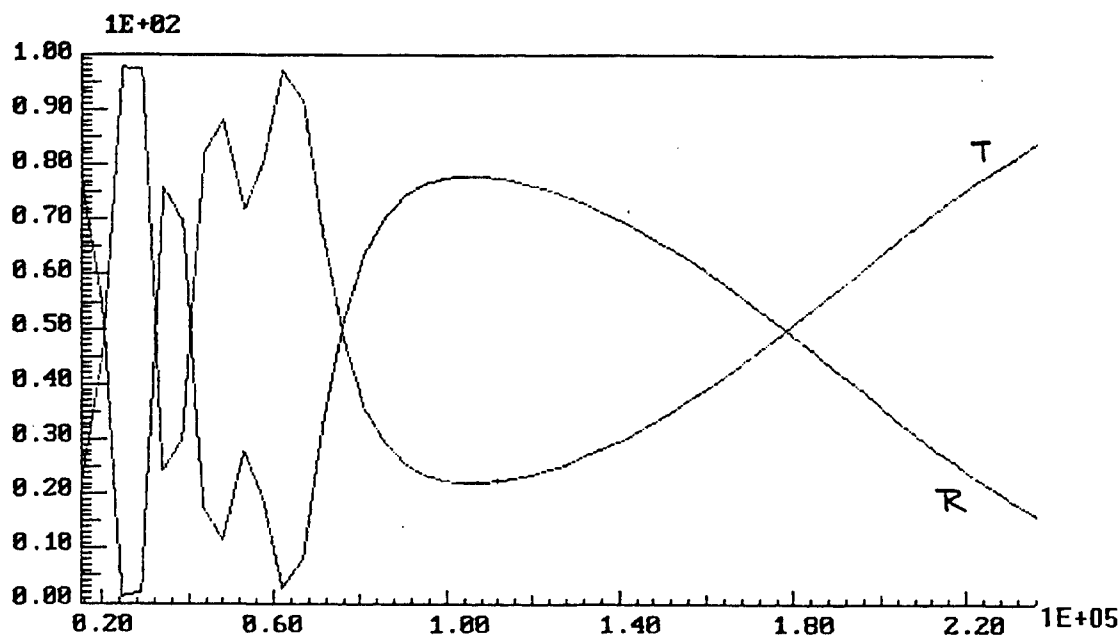


Fig. 3- Computed spectral characteristic of mirror M_1

The computed characteristics were done using a quarter wavelength optical thickness (QWOT) structure for refractive coatings and a non-QWOT for the anti-reflective coatings. Using this technique we can reach a maximum desired reflectivity at $10.6\mu\text{m}$ for the experimental laser cavity we are referring to.

4. CONCLUSION

Our final goal, starting from this simple concept of "special mirror", is to realise a good quality of laser beam $\text{TEM}_{00/01}$ at a power level no more then 800W, suitable with laser technological equipment dedicated for nonconventional cutting technologies.

5. ACKNOWLEDGEMENTS

The authors thank to Dr. Clementina Timus for peculiar measurements and Dr. Claudian Georgescu for helpfully discussions and constant assistance.

6. REFERENCES

1. I. Gutu and M.L.Pascu, "A new design for high power transverse flow CO₂ lasers", *Laser Optoelektronik*, Vol.24 (4), pp. 37- 43 (1992).
2. I. Gutu ,T.Julea, V.Draganescu , D.Dumitras, I.N. Mihailescu and V.R.Medianu, "Development of a high power gas transport CO₂ laser with cylindrical geometry", *Optics and Laser Technology*, Vol.18,(6), pp. 307-312 (1986).
3. A. E. Siegman, "Lasers", pp. 913-920, Oxford University Press, 1986.
4. R. Medianu, M. L. Pascu and I. Gutu, "Coating method for variable reflectivity mirrors to be used in high power c.w. CO₂ lasers", *Pure and Applied Optics*, Vol.3, pp. 449-455 (1994).
5. G. H. Sherman, E. J. Danielewicz and J. Earl Rudisill, "Optics for CO₂ lasers", *Laser & Optronics*, Vol.7,pp. 556-562 (1988)
6. C. Timus, M. Lazarescu, R. Medianu and M. L. Pascu, "Optical investigation on oxygen doped GaAs", *Optica Applicata*, Vol.XXII, nr. 3-4,pp. 187-193 (1992).

Spectrophotometry, ellipsometry and computer simulation in thin film developments.

S. Bosch

Laboratori d'Optica, Departament de Física Aplicada i Electrònica. Universitat de Barcelona
Diagonal 647, 08028 Barcelona, SPAIN.

ABSTRACT

Thin film deposition techniques are widely used in industry because of the variety of practical applications where they may be appropriate. The manufacture of thin film coatings normally requires high vacuum equipment, with additional attachments such as electron beam evaporators, ion guns, quartz oscillator microbalance, etc.

Besides the technological problems involved in the deposition of the films, the optical characterization of the coatings obtained is a major issue. For example, for wideband antireflection coating of lenses a precise control of the refractive indices and thicknesses obtained is required, together with a good uniformity inside the whole vacuum chamber. Thus, techniques for the measurement of refractive indices and thicknesses of thin films have to be available in laboratories related to the deposition plants. Several characterization apparatus are quite standard in industry, because their wide range of applications and relative low cost (spectrophotometer is the typical example). Other apparatus are much more specific and much more expensive like ellipsometers, secondary ion mass spectrometers (SIMS), transmission electron microscopes (TEM) ... , although monochromatic ellipsometers may sometimes be accessible because of its moderate cost. Finally, very powerful desk computers are really cheap nowadays, so computation facilities are always available at any laboratory.

The aim of the present work is to illustrate the combined use of three basic laboratory techniques -spectrophotometry, monochromatic ellipsometry and computer simulation- in the development of thin film coatings and filters.

Keywords: thin film coatings, spectrophotometry, ellipsometry, computer simulation.

1. INTRODUCTION

The manufacture of thin film coatings for optical applications requires a precise control on thicknesses and optical constants of all the component layers. Considering, for example an antireflection (AR) coating on glass for ophthalmic applications, it is known¹ that lenses have to be coated (both sides) with at least 4 layers that have to be controlled in thickness with a precision of about 1 nm each. The manufacture of band-pass or edge filters, where many more layers are involved, requires a much more precise control, although practical procedures for error compensation have been developed². Besides the intrinsic difficulty of achieving the preceding requirements, there are other important issues to overcome before the industrial manufacturing process is satisfactory. For example, the stability of the whole process and the elimination of differences between the diverse samples coming from a single batch process (for different positions in the evaporation chamber, for example).

Our aim is to focus on some of these production problems which may be adequately dealt with by using simple (not very expensive) laboratory equipment. We will discuss how spectrophotometric and ellipsometric measurements, together with simulation techniques for better coating uniformity, allow the adequate development of the whole manufacturing process of thin film filters. Other characterization techniques will not be considered since they are less widespread. Similarly, thin film design will not be addressed because, although it is a computer simulation task, it has to be considered a specific topic.

We may note that our analysis will not be complete: more practical problems have to be addressed in before practical production, even using the same kind of equipment we consider here, but we will try to cover the more prominent aspects related to the manufacturing task.

Finally, we may point out that, for conciseness, we usually refer to topics related to AR coating developments using high vacuum thermal evaporation equipment (with crucibles or e-beam guns). It should be evident, however, that most of the problems we will devise are common to the high vacuum coating procedures and the adaptation of the techniques presented to other different practical applications should be straightforward.

2. THE CENTRAL PROBLEM IN MANUFACTURING

Simply stated, the central problem in manufacturing is, in most of the cases, to know the correspondence between what is programmed in the control unit of the evaporation bench and what is really being deposited in the different layers of the coating. More precisely, to know with enough precision the refractive indices n_i (and extinction coefficients k_i if one deals with non transparent materials) and the thicknesses d_i of each layer i forming the coating. We may note that: a) this is not a trivial task and, b) once accomplished (and only in this case) the remaining procedures are much simpler. An striking example illustrating these points is presented in Ref. 3, where an inverse synthesis method is developed for analyzing the variations in multilayers obtained from different coating runs. The most prominent results of this work, dealing with a 6-layer wideband AR coating, are summarized here as they may be considered very significant for our general purposes:

- 1) when only small deviations are expected, near-normal incidence reflectance measurements are enough to determine the differences within the component layers.
- 2) the required accuracy in reflectance measurements is of the order of 0.01 %.
- 3) the numerical procedure for inverse synthesis has to be adequate to guarantee the uniqueness of solution.

With this information available, a first conclusion may be deduced: if one of the above conditions is not fulfilled, the other ones must be reinforced to guarantee meaningful results. For example, if the required accuracy in measurements is not achieved one may try to use not only reflectance measurements but also other complementary data (as transmittance data or ellipsometric measurements). This kind of procedure will be clearly illustrated in the following paragraphs.

Once the central problem is mastered, the rest of the manufacturing task is simpler, because adjusting the process parameters (thicknesses) is easy with the help of a standard thin film computations program. Let us analyze a complete practical case, where the full process of developing a thin film filter prototype is considered in detail⁴. The aim of the work was the manufacture of an AR coating on glass, starting from a theoretical design taken from the literature and ending with the set of parameters to be introduced in the controller of the high vacuum evaporation bench in order to deposit the coating on lenses. As pointed out in Ref. 5, the actual optical behavior of individual layers usually differs from the assumed homogeneous and isotropic refractive index condition. This fact is an additional feature to the well known dependence of the refractive index on the deposition process⁶, specially noticeable for high index dielectric materials. Thus, important differences between theoretical designs and deposited coatings should be expected even for a moderate number of layers.

The following four-layer AR coating design⁷ was our starting point:

$$1.000 \text{ L } | 2.108 \text{ H } | 0.331 \text{ L } | 0.225 \text{ H } | 1.520$$

where L and H design quarterwaves for $\lambda_0=520$ nm, $n_H=2.08$, $n_L=1.38$. Assuming homogeneous and non-dispersive materials, the computed reflectance in the visible range is presented in Fig. 1.

The dispersion in the refractive indices of existing materials that may be effectively used to make the coating will clearly originate noticeable differences that may not be considered, of course, due to a non-ideal behavior of materials. Since our final goal is the manufacture of the coating, we have to determinate not only the dispersion of the components but also any other relevant optical properties to define any non-ideal behavior observed in experiments. To this end, the proposed "Optimized procedure..." described in Ref. 4 comprised the following steps:

- 1) Deposit single layers of the components and determine their dispersive refractive indices.
- 2) Deposit selected combinations of the individual layers forming the coating.

3) Adjust experiments with models for the layers.

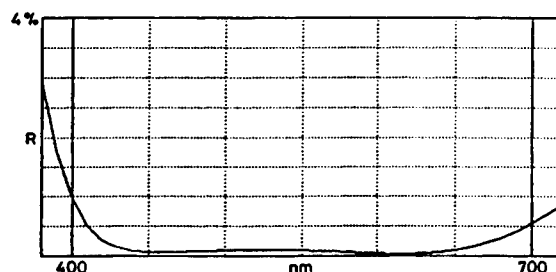


Fig. 1. Computed reflectance (at normal incidence) of the starting AR coating design.

The following laboratory equipment was required:

- Three wavelength ellipsometer.
- A multiple sectors reversible calotte for substrates.
- Spectrophotometer with reflection attachment.
- Standard thin film computations program.

Once the real substrate (Crown glass) and coating materials (MgF_2 for L and HfO_2 for H) were selected, the procedure started with step 1 above, using the three wavelength ellipsometer (with wavelengths 405, 546 and 633 nm in our case) for single layer samples of optimal thicknesses (see § 4 below, about monochromatic ellipsometry). This leads to the determination of the dispersion of the materials, which will be defined by the refractive indices at 405, 546 and 633 nm and the following dispersion formula (for any other λ in the visible range)

$$n(\lambda) = A + B/(\lambda - C).$$

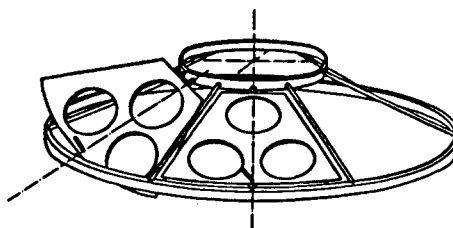


Fig. 2. Multiple sectors reversible calotte.

We are ready to start step 2, using a multiple sectors reversible calotte (as the one shown in Fig. 2). This attachment is easy to adapt to most thermal evaporation plants, allowing different substrates to be coated with different combinations of layers produced in a *single* coating run, thus eliminating uncertainties due to different run processes. Now, by using a standard spectrophotometer (not high precision required) and common thin film computations tools, we are ready for an accurate optical characterization of the individual layers forming the coating (step 3). The example presented in Ref. 4 illustrates an additional difficulty in the development of step 3, namely, the marked inhomogeneity of HfO_2 already indicated in Ref. 8. The final optical characterization of the coating, which fully described the behavior of the samples, was done as follows. Each material was defined by its refractive index at the three wavelengths, which for our deposition conditions (substrate temperature, evaporation rate...) are summarized in Table 1, and the refractive index values given by the previous dispersion formula for any other λ in the visible range.

Table 1. Refractive indices of the materials used.

	405 nm	546 nm	633 nm
MgF ₂	1.390	1.383	1.379
HfO ₂	2.050	2.000	1.990
substrate	1.520	1.505	1.502

Then, the optical behavior of each layer was defined by its dispersive index, its thickness and also by means of a multiplicative factor for the refractive index. This is a value (always close to 1, of course) which may be different for different layers of the same material, thus expressing differences with respect to the nominal index data of the material. Moreover, since it is multiplicative, may define both a gradient in refractive index (see below) or a void fraction in the layer. This multiplicative factor must be deduced for each layer by comparing the experimental reflectance curves from the test coatings with the computed (simulated) ones and fitting the results. For example, from curves like those presented in Fig. 3 a) and b) we found that a complete description of the coating, whose measured reflectance is shown in Fig 3 a), was given by the following data

Air | 82.5 nm MgF₂ (1.00) | 45.0 nm HfO₂ (0.98) | 47.0 nm HfO₂ (0.99) |

47.0 nm HfO₂ (1.00) | 26.0 nm MgF₂ (0.99) | 18.0 nm HfO₂ (0.95) | Substrate

where the figures in parenthesis are the cited multiplicative factors for the refractive index.

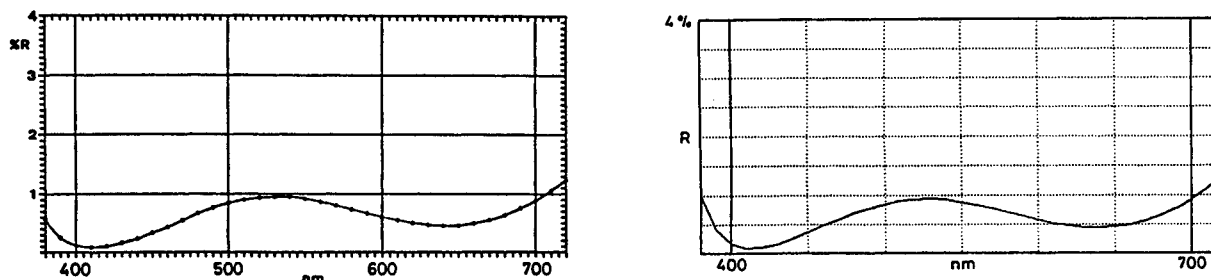


Fig. 3. a) (left) Experimental reflectance (at 15 deg. incidence) of an early stage coating. b) (right) Computed reflectance at 15 deg. incidence of a multilayer structure which modelizes the sample.

The most visible feature of our results is the marked inhomogeneity of the HfO₂ thick layer, represented here by its subdivision in three different layers of the same HfO₂ with multiplicative factors 0.98, 0.99 and 1.00. Although this result is in good agreement with Ref. 8, the accuracy of this assumption was independently tested and proved by measuring the reflectance of the single layer on glass, following the method presented in Ref. 9.

From the precise optical characterization just given, it is easy to optimize the reflectance shown in Fig. 3 a) in order to obtain a curve like Fig. 4 by easy adjustments of layer thicknesses. In the present case, for example, the only differences between Fig. 3 b) and Fig. 4 are the thicknesses of the two outermost layers which are (for Fig. 4) 91.5 nm of MgF₂ and 40 nm of HfO₂. Thus, this optimization may be achieved in the coating chamber by, simply, a -3.6 % (for HfO₂) plus a +10.9 % (for MgF₂) thickness variations in the two outer layers. The multilayer producing a reflectance as in Fig. 4 may be considered a good wideband AR coating for ophthalmic lenses, specially considering that only uses 2 different materials in 4 layers. Summarizing, it has been demonstrated that the procedure allows the satisfactory development of a thin film filter prototype through the analysis of a reduced number of samples obtained from a few trial coatings.

As indicated, the practical procedures presented in Refs. 3-4 may be considered as the basic references for our objectives. In the rest of the paper, the relevant topics to implement adequately the above approach will be considered in more detail.

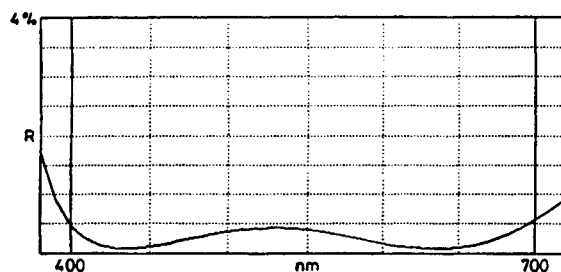


Fig. 4. Computed reflectance at 15 deg. incidence for the optimized structure.

3. SPECTROPHOTOMETRIC METHODS

Spectrophotometric measurements are the usual control and characterization procedures in many optical laboratories. For thin films, the final performance requirements are normally defined in terms of transmittance or reflectance values. Thus, the use of the spectrophotometer for the optical characterization of materials is convenient and adequate. The fundamental application in the coating environment is the determination of the optical constants $n(\lambda)$ and $k(\lambda)$ and thickness d of a layer deposited on a substrate when both are transparent (or only slightly absorbing). We outline the basics of a procedure for this optical characterization with an example case of a TiO_2 film on a glass substrate, using the transmittance spectrum (Fig. 5) and assuming that the substrate is well known beforehand.

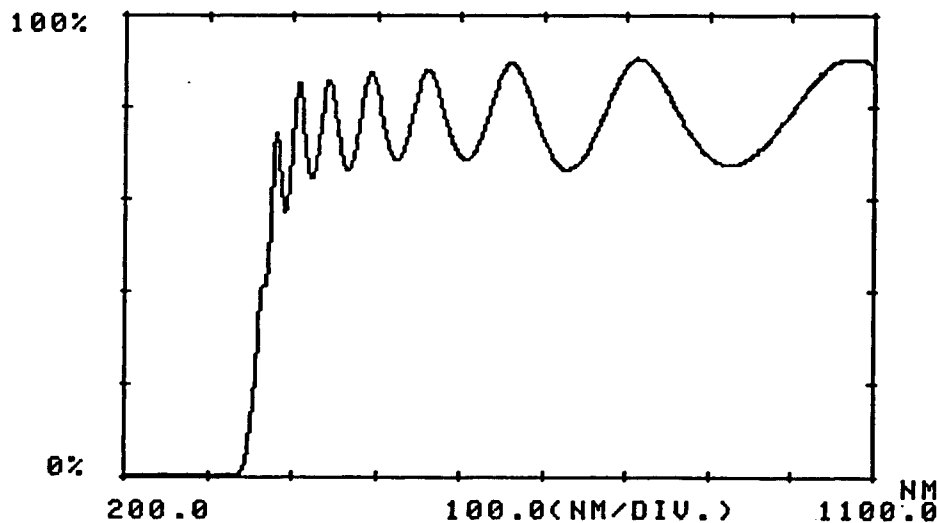


Fig. 5. Spectral transmittance curve, at normal incidence, of a glass plate coated with a TiO_2 film on one side.

The data (λ, T) for all extrema in Fig. 5 are given in Table 2.

Table 2. Transmittance data corresponding to the extrema of the curve in Fig. 5.

λ	T (%)	λ	T (%)
1070.0	91.4	914.0	68.0
809.0	91.4	722.0	67.2
657.0	90.3	602.0	68.6
559.0	88.4	523.0	67.9
492.0	87.6	465.0	65.3
442.0	85.9	423.0	63.3
407.0	84.8		

To take into account the two sides of the substrate when only one is coated, it is a good approximation to assume $T = T_f \cdot T_s$, where T is the measured transmittance, T_f the transmittance of the air-film-substrate side assuming a semiinfinite substrate and T_s the one corresponding to a bare semiinfinite substrate¹⁰. We will define the order m of the transmittance extrema in terms of $\lambda/4$ from the expression

$$n(\lambda) \cdot d = m \cdot \lambda / 4$$

In the present example, since TiO_2 is a high index dielectric material, odd orders always give values below the substrate transmittance (minima) and the refractive index $n(\lambda)$ is known to be smoothly decreasing with wavelength in the range considered. The extinction coefficient will have similar behavior, with a negligible value ($k \approx 0$) in the IR range. Thus, starting by the lower orders (longer λ) where we know that the index of the substrate is $n_s = 1.51$ (for $\lambda > 700$ nm), we have at this zone

$$T_s = \frac{4n_s}{(1+n_s)^2} = 0.959$$

and at odd extrema⁹

$$T_f = \frac{4n^2 n_s}{(n^2 + n_s)^2}$$

Using the measured value $T(914 \text{ nm}) = 0.680$ from Table 2 and using $T/T_s = T_f$, one can easily compute n at this wavelength. This is, $n(914 \text{ nm}) = 2.245$. If one knows the order of the corresponding extremum, the thickness of the film may be deduced. In our case, from the two rightmost maxima and assuming $n(809 \text{ nm}) \approx n(1070 \text{ nm})$, we note that

$$\frac{1070}{809} \approx \frac{8}{6}$$

and the transmittance extrema may be labeled 6, 7, 8,... from right to left with total certainty. Then, for order 6,

$$d = 6 \frac{1070}{4} \frac{1}{2.245} = 715 \text{ nm}$$

The values $n(914 \text{ nm}) = 2.245$ and $d = 715 \text{ nm}$ are quite precise, since the near IR zone of dielectric materials like TiO_2 is highly transparent and only slightly dispersive. To find $n(\lambda)$ for the whole spectrum we must assume a dispersion relation, as well as a certain $k(\lambda)$, and try to fit the transmittance data. There are many references where this topic has been developed in full, including also inhomogeneous films (with refractive index variable in depth)¹¹⁻¹³ and we do not develop this topic further.

It is important to note that, as in the example just analyzed, spectrophotometric methods are applicable for layers giving several transmittance (or reflectance) extrema, thus having thicknesses of the order of the central wavelength of the range considered (i.e., at least half micron for the visible). For thinner films, spectrophotometry alone is not suitable.

Regarding instrumentation, the normal equipment for the visible and near IR range is the (dispersive) double beam spectrophotometer, whereas for the medium and far IR the Fourier transform spectroscopy (FTIR) is the most common. This last instrument is, in fact, an adaptation of a Michelson interferometer and this technique has proven to be the most suitable in the IR range. We do not give more details since our interest is not on the spectroscopic techniques but in the applications for thin films, where we start from the spectrum of the sample.

Since transmittance is the usual measurement, determining reflectances of samples requires an additional attachment in the spectrophotometer. The most interesting case is normal incidence but, in practice, near-normal attachments are standard since they are easier to manufacture and do not originate important differences in reflectance for small incidence angles (less than 10 deg., for example). One of the simpler designs one can conceive for double beam spectrophotometers is presented in Fig. 6. In this case the measurements are really made by comparison with those of a reference sample placed along the reference beam, which has to be known with high precision.

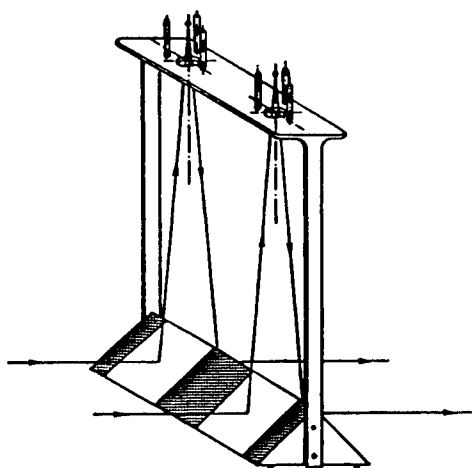


Fig. 6. Sketch of a reflectance attachment for a double-beam spectrophotometer.

Of course, either for transmittance or reflectance measurements, only plane-parallel substrates may be used in principle to have meaningful results. It may be convenient in some circumstances to measure the reflectance of spherical surfaces or the transmittance of curved substrates. In fact, the reflectance attachment shown in Fig. 6 is suitable for the measurement of spherical surfaces (either concave or convex) by means of a simple practical procedure, since it holds the samples by a three-point set up¹⁴. In Fig. 7 we can see the differences in reflectance due to the convex shape of a lens side, which approaches its center about 1 cm to the evaporation sources (respect to a plane substrate). Similarly, a method for the measurement of transmittance of non-plane samples, requiring only the additional use of a limiting diaphragm along one beam, was developed primarily for the case of lenses¹⁵.

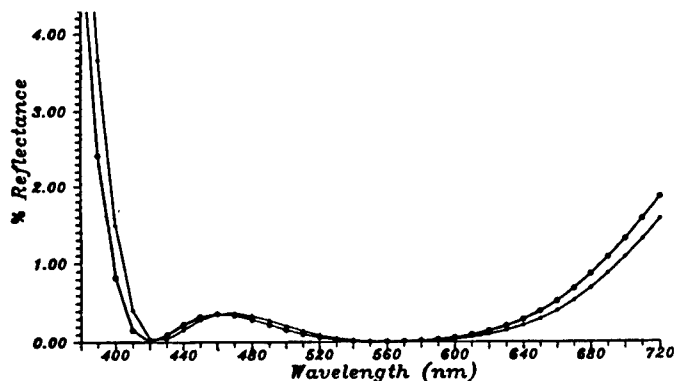


Fig 7. Reflectances of a convex (*) and a plane (o) sample coated in equivalent positions inside the vacuum chamber. The differences correspond to the displacement of the convex surface towards the evaporation sources.

4. MONOCHROMATIC ELLIPSOMETRY IN MANUFACTURING

Ellipsometry is a standard characterization technique for thin film coatings both in research and industrial environments. The basis of reflection ellipsometry is the change in the polarization of the light upon reflection on the sample. A simple and useful introduction to ellipsometry is given in Refs. 16-17. A complete treatment of the topic is developed in the classical book of Azzam¹⁸ which also deals with different instrumental designs and methods. Transmission ellipsometry could be commented on equivalent physical basis but is not a common technique and will not be treated here. An experimental measurement gives, for each wavelength, two real values Δ and Ψ which may be interpreted as the change produced by the reflection in the phase (thus, $0 \leq \Delta \leq 2\pi$) and in the amplitude ratio E_p/E_s ($0 \leq \tan(\Psi) \leq \infty$, or $0 \leq \Psi \leq \pi/2$), where the subscripts 'p' and 's' for electric field amplitudes stand for the usual designation 'parallel' and 'perpendicular' with respect to the incidence plane (see Fig. 8).

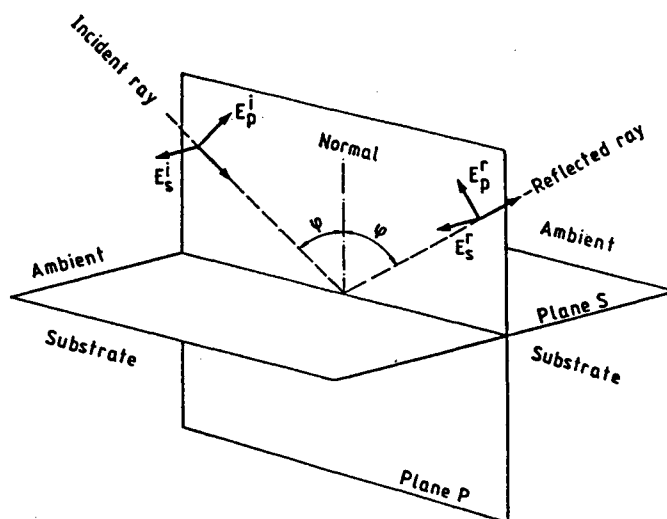


Fig. 8. Illustrating the reflection of a plane electromagnetic wave.

The fundamental equation of ellipsometry is, casting Δ and Ψ in the usual complex form,

$$\rho \equiv \tan(\Psi) \exp i(\Delta) = R_p / R_s$$

where R_p and R_s are the reflection coefficients for the sample. In practice, starting from the measurement (Δ, Ψ) it is then necessary to relate it to some characteristic property of the reflecting surface. The standard notation designates the different layered media from the ambient to the substrate with subindices 0, 1, 2 ... Then, for a bare substrate its complex refractive index $\underline{n}_1 \equiv n_1 - ik_1$ may be computed directly from the knowledge of Δ and Ψ (i.e., ρ)¹⁸:

$$\underline{n}_1 = n_0 \tan(\varphi_0) \left[1 - \frac{4\rho}{(1+\rho)^2} \sin^2(\varphi_0) \right]^{1/2}$$

where n_0 is the ambient refractive index and φ_0 the incidence angle. For a single perfectly parallel layer on a semi infinite substrate the corresponding fundamental equation of ellipsometry is

$$\tan(\Psi) \exp(i\Delta) = \frac{r_{01p} + r_{12p} \exp(-i2\beta)}{1 + r_{01p} r_{12p} \exp(-i2\beta)} \frac{1 + r_{01s} r_{12s} \exp(-i2\beta)}{r_{01s} + r_{12s} \exp(-i2\beta)}$$

where r_{01p} , r_{12p} , ... are the corresponding Fresnel reflection coefficients and $\beta = 2\pi(d_1 / \lambda)(n_1 - ik_1) \cos(\varphi_1)$ (in computations Snell law is valid with complex indices and angles). It is important to note that coefficients r_{01} and r_{01} depend only on $(n_0 - ik_0)$, $(n_1 - ik_1)$, $(n_2 - ik_2)$ and φ_0 ; the only term which depends on d_1 is β ¹⁸.

To find the refractive index and thickness of the layer (n_1, k_1, d_1) from ρ requires inverting the above equation for these three quantities, having measured only two real quantities Δ and Ψ . Clearly this is not possible unless one of the three quantities is known (for example, for transparent layers $k_1=0$), or ellipsometric data at different angles of incidence are available, having several (Δ, Ψ) pairs to invert. Moreover, a suitable numerical inversion method is required for the different cases.

In the simplest case where $k_1=0$, adequate inversion procedures have been developed. The most basic method, suitable even for small desk calculators (it was published in 1972) is due to Reinberg¹⁹. The basis of the procedure is as follows. Assuming a tentative (approximate) value for n_1 , solve the last equation for the exponential $X = \exp(-i2\beta)$, which leads to an equation of the form $AX^2 + BX + C = 0$.

When $k_1=0$, it is easy to see that $|X|=1$ when one has chosen the right n_1 . Thus, varying the assumed n_1 one may obtain the right value by searching for $|X|=1$. The key point of the procedure is that the iteration to find the exponential X needs only to be done on n_1 , computing d_1 once one has found n_1 and X . This reduction from two dimensions (n_1, d_1) to simply one (n_1) makes the iteration method very simple and easy to converge.

In the light of this initial idea, many different algorithms have been developed to cope with the different situations of practical interest. First, for a single absorbing layer, when more than one angle of incidence may be used in measurements, we will have in principle overdetermination of the unknowns (n_1, k_1, d_1). This is not realistic, however, since the different measurements (which will correspond to not very different incidence angles) are usually correlated and affected of a significant experimental error. Thus, numerical methods for absorbing layers have to be considered with caution²⁰⁻²¹. An interesting approach, which also gives confidence limits when experimental errors are known is presented in Ref. 22.

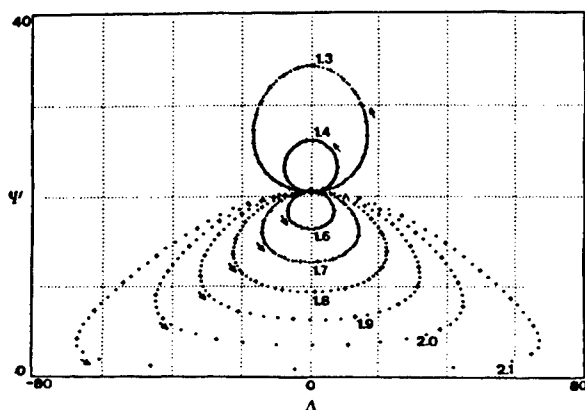


Fig. 9. Iso-refractive index curves for a transparent film on glass.

Like for spectrophotometric methods, there are some restrictions on the index and thickness of the layer to have good accuracy in the optical characterization using ellipsometry. A very useful procedure for illustrating the limitations of ellipsometry for a transparent layer on a known substrate is plotting the iso-refractive index curves. These are obtained by representing the (Δ, Ψ) values which correspond to increasing thickness, for a family of fixed values of the index n_1 . Fig. 9 shows the iso-refractive index curves on glass (with index 1.505) for $\lambda=546.1$ nm and incidence angle 70 deg. The refractive indices of the layer are 1.3, 1.4, ... 2.1 and the increment in thickness is 2.5 nm. We note that all curves pass through a common point which corresponds to the bare substrate, so, when experimental measurements are close to this common (Δ, Ψ) value, data inversion will be intrinsically difficult.

These plots also show, for example, that for a single transparent film there is a cycle thickness given by the quantity

$$\frac{\lambda}{2\sqrt{n_1^2 - n_0^2 \sin^2(\varphi_0)}}$$

and the optimum thickness range is around 1/2, 3/2, ... times this value, whereas thicknesses near 1, 2, ... times the cycle are difficult to determine¹⁶. Besides, thicknesses of several cycles may also give difficulties due to inhomogeneity in depth. So, recalling the cited intrinsic limitations of spectrophotometry for very thin layers, advantages and disadvantages of spectrophotometry and ellipsometry complement themselves since spectrophotometry requires relatively thick layers and ellipsometry is more suitable for thin ones.

For more than one layer the equations are more involved¹⁸, and the physical model assumes an increasing number of hypothesis which are difficult to assess (smoothness of all the interfaces, parallelism, ...). In fact, from the numerical point of view it is possible to invert the equations in a number of cases²³⁻²⁹ even for a sample having any number of layers³⁰. This last method has been used for the important industrial problem of the characterization of oxide-polysilicon-oxide on silicon³¹. Summarizing, efficient numerical methods are available for more than one layer on a known substrate but the conclusions are difficult to be tested and meaningful results will only be obtained when we consider the adequate model for the sample.

The above comments were made assuming monochromatic ellipsometry. Spectroscopic ellipsometry is much more powerful but in industrial environment single wavelength apparatus are common practice, because of the big differences in cost. Sometimes two or three wavelength ellipsometers, with more than one incidence angle, are a good choice regarding the ratio cost/performances. This last case allows both the application of multiple incidence angle methods²² and multiple wavelength ones⁴.

5. LIMITING THE DIFFERENCES WITHIN A SINGLE COATING RUN

In production processes, usually many samples will be coated in a single coating run. A typical example may be the coating of ophthalmic lenses where not only many pieces have to be manufactured together but coating both substrate sides without opening the chamber by means of reversible calottes is also advantageous for reducing production time. As long as different positions within the evaporation chamber are considered, differences between the coatings obtained will arise. Following the analysis of our spectacle lens case, the differences in thicknesses of the deposited layers will originate different reflectances which, although not giving very different lens performances, cause a very anti-aesthetic effect due to important variations in the resulting reflected color³². Of course, it is necessary to be able to quantify the differences and to measure reflectance differences (see § 3) but, anyway, it is evident that differences in thicknesses should be avoided as much as possible in any application.

When thermal evaporation plants are considered, crucibles or e-beam guns are used for producing the vapor. The directional emissive properties of these sources will originate important gradients in layer thicknesses, unless additional care is taken. The use of rotating calottes (the supports of the substrates to be coated) for better thickness homogeneity and well adapted heating devices for controlling the temperature of the samples is a standard practice in manufacturing³³.⁶ For compensating the remaining differences in the thicknesses deposited, static correcting shutters are placed inside the chambers for screening the parts of the calotte which are still receiving too much vapor. The normal practice is the trial-and-error correction, which works well for materials and configurations already known.

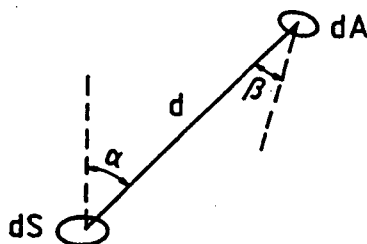


Fig. 10. Elementary geometrical configuration.

A computer-aided approach for optimization of thickness uniformity may be developed by using the equations presented in Ref. 6. The basic assumptions are the characterization of the emissive properties of the evaporation source through a fixed exponent n (depending on the type of crucible, evaporation rate, etc.) and the supposition that any particle moving away from the source will follow a straight line (in accordance with the mean free path of the molecules at the very low pressure of the chamber). Then, referring to Fig. 10, if dS designates the evaporation source (it may be considered a surface element because of its actual small size) and dA a surface element to be coated, the amount of evaporated material deposited per unit time may be expressed as

$$dm = \frac{K \cos^n(\alpha) dA \cos(\beta)}{d^2}$$

where K is a constant proportionality factor and n is an exponent used to define the directionality of the source dS (to be determined)⁶. Any geometrical configuration and any deposition conditions may be considered as a process of many differential terms dm . For example, for a rotating dome-shaped calotte (Fig. 11 a) it will be necessary to describe the simultaneous variations of d , α , β , etc. as the angle ϕ is varied. For other calotte shapes the geometrical relations may be more complicated, as for the plane-sectors reversible holder sketched in Fig. 11 b)³⁴.

Since the radial position of the source at the bottom of the evaporation bench is usually adjustable, it should be placed at the point where it naturally gives the best uniformity on the calotte. A complete procedure for optimization of thickness uniformity all over the calotte may readily be devised by using a simulation program able to compute Σdm for a whole

turn of the calotte³⁴. In fact, the more difficult case of a plane sectors reversible lens holder (Fig. 11 b) has also been addressed there. The procedure is as follows:

- determine the emissive properties of the source (i.e., the exponent n).
- find the best radial position for the evaporation source dS by simulation.
- design static correcting shutters for final uniformity.

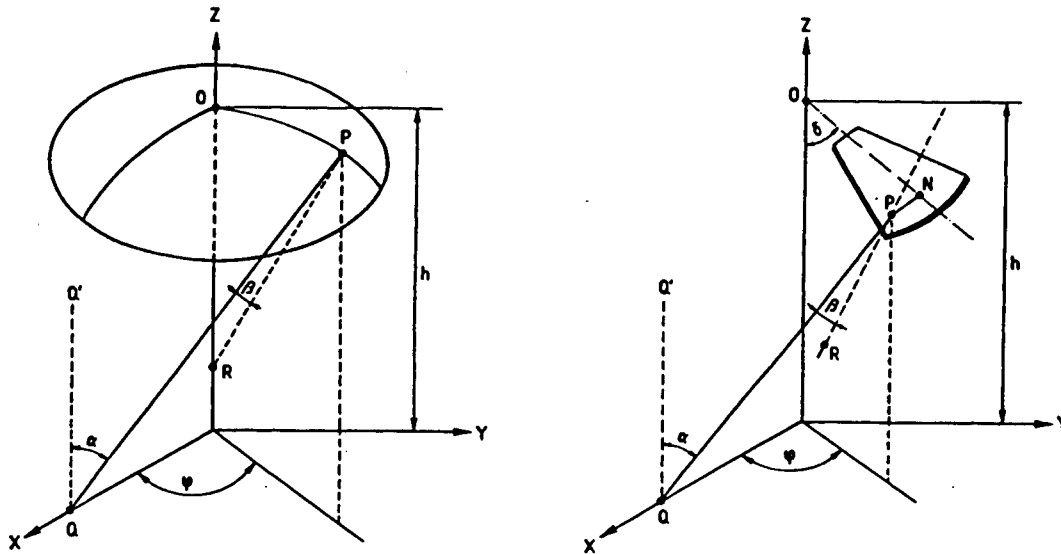


Fig. 11. a) (left) The dome-shaped calotte. b) The plane sectors reversible lens holder.

Of course, the development of the three steps requires several experimental coating tests, but the number of trials required to achieve a good uniformity is greatly reduced with respect to other non computer-assisted procedures.

In case one is dealing with new evaporation plants and with changes in the evaporation materials used, having the above mentioned computer tools to simulate the deposition processes (according to the positions of the crucibles) and to design the final static correcting shutters, is highly advisable. In fact, in the process of assembling a new bench, the choice of the position for the evaporation sources, according to the expected application, may be greatly improved by means of these computation tools. A particular example, again in the field of lens coating is developed in Ref. 35. In this case, the differences in layer thicknesses arising from the very shape of the substrate are analyzed. Since the curvature of lenses is intrinsic, in this case the only possibility to reduce differences is only to optimize the position of the evaporation source.

6. CONCLUSIONS

We have analyzed the manufacturing of thin film coatings in relation to the optical characterization of the component layers. The proposed procedures address some of the fundamental problems in fabrication, requiring only common thin film laboratory equipment: spectrophotometer, monochromatic ellipsometer and personal computer. Besides, a review of the two cited optical characterization techniques (those based in spectrophotometry and ellipsometry) is given, with indications of relevant applications in the field of optical coatings and related references. Similarly, the basis for computer-aided simulation tools to enhance coating uniformity inside the evaporation chambers is studied.

It has been illustrated that the complementary use of computer simulation tools together with spectrophotometric and ellipsometric optical characterization methods is advisable for optimum manufacturing because it overcomes the intrinsic limitations of each single technique.

7. ACKNOWLEDGMENTS

The author wishes to thank his collaborators in the works cited in the text. Special thanks are given to the research staff of INDO, S.A. (L'Hospitalet de Llobregat, Spain) and to the Thin Film Laboratory of ENEA (Roma, Italy).

8. REFERENCES

1. Rancourt, J.D. *Optical thin films user's handbooks*, Macgraw-Hill, USA 1987.
2. Bousquet, P., Fornier, A., Kovalczyk, R., Pelletier, E., and Roche, P. 1972, *Thin Solid Films* 13, 285.
3. Klug, W., Boos, M., Herrmann, R., and Schwiecker, H. 1986, *Proc. SPIE*, 652, 118.
4. Bosch, S. 1992, *Appl. Phys. A* 54, 431.
5. Machorro, R., Macleod, H.A., and Jacobson, M.R. 1986, *Proc. SPIE*, 678, 84.
6. Pulker, H.K. *Coatings on glass*, Elsevier, Amsterdam 1984, ch. 6.
7. Thelen, A. *Design of optical interference coatings*, Macgraw-Hill, New York 1988, ch. 4.
8. Baumeister, and P., Arnon, O. 1977, *Appl. Opt.* 16, 439.
9. Piegari, A., and Emiliani, G. 1989, *Thin Solid Films* 171, 243.
10. Vriens, L., and Rippens, W. 1983, *Appl. Opt.* 22, 4105.
11. Denton, R.E., Chambell, R.D., and Tomlin, S.G. 1972, *J. Phys. D: Appl. Phys.* 5, 852.
12. Borgogno, J.P., Lazarides, B., and Pelletier, E. 1982, *Appl. Opt.* 21, 4020.
13. Montecchi, M., Masetti, E., and Emiliani, G. 1995, *Pure Appl. Opt.* 4, 15.
14. Bosch, S., and Roca, J. 1993, *Meas. Sci. Technol.* 4, 190.
15. Bosch, S., and Roca, J. 1991, *Meas. Sci. Technol.* 2, 946.
16. Bosch, S. 1991, *European Microscopy and Analysis* 9, 13.
17. Tompkins, H.G. *A user's guide to ellipsometry*, Academic Press Inc., San Diego 1993.
18. Azzam, R.M.A., and Bashara, N.M. *Ellipsometry and polarized light*, North Holland, Amsterdam 1977.
19. Reinberg, A.R. 1972, *Appl. Opt.* 11, 1273.
20. Easwarakhanthan, T., Michel, C., and Ravelet, S. 1988, *Surf. Sci.* 197, 1988.
21. Urban III, F.K. 1993, *Appl. Opt.* 32, 2339.
22. Bosch, S., Monzonís, F., and Masetti, E. 1996, *Thin Solid Films* 289, 54.
23. Charlot, D., and Maruani, A. 1985, *Appl. Opt.* 24, 3368.
24. Yoriome, Y. 1983, *J. Opt. Soc. Am.* 73, 888.
25. So, S.S. 1976, *Surf. Sci.* 97, 56.
26. Kinoshita, K., Nishibori, M., Yamamoto, M., and Yokota, K. 1970, *Optica Acta* 17, 115.
27. Wei, H.F., Henning, A.K., Slinkman, J., and Hunter, W.R. 1992, *J. Electrochem. Soc.* 139, 1783.
28. Bosch, S. 1993, *Surf. Sci.* 289, 411.
29. Bosch, S., and Monzonís, F. 1994, *Surf. Sci.* 321, 156.
30. Bosch, S., and Monzonís, F. 1995, *J. Opt. Soc. Am. A* 12, 1375.
31. Bosch, S., and Monzonís, F. 1995, *Semicond. Sci. Technol.* 10, 1634.
32. Klug, W., Herrmann, R., and Sauer, G. 1990, *Proc. SPIE*, 1270, 278.
33. Macleod, H.A. *Thin film optical filters*, Adam Hilger, Bristol 1986.
34. Bosch, S. 1992, *J. Vac. Sci. Technol. A* 10, 98.
35. Bosch, S. 1993, *J. Phys. D: Appl. Phys.* 26, 124.

Structure Investigations of Optical Coatings on GaAs Substrate

C. A. Timus, R. V. Medianu, G. Georgescu, E. Vasile*

National Institute for Laser, Plasma and Radiation Physics, Laser Department,
P.O.Box MG-36, Bucharest, R-76 900, Romania, e-mail: timus@roifa.ifa.ro

* METAV S.A., Bucharest, Romania

ABSTRACT

ZnS, BaF₂ and GaAs thin films on NaCl and GaAs substrates, produced by thermal evaporation and r.f. magnetron sputtering as antireflective and reflective coatings for 10.6μm are investigated. Optical and electronic microscopy (TEM and SEM) with EDAX and SAED had been approached to study the structure and morphology of optical coatings, corroborated with the technological parameters of the deposition. The columnar structure of the thermally evaporated BaF₂ film was observed. Uniformity and deposition rate for r.f. magnetron sputtering deposition, without ion assistance turns out to be very critical, since the induced mechanical stresses could compromise the optical film.

Keywords: thermal evaporation, r.f. magnetron sputtering deposition, columnar structure, optical coating

1. INTRODUCTION

GaAs is an A^{III}B^V intermetallic compound largely used in microelectronics, but also in IR optics as substrate for transmission optical components^{1,2}, in some applications, due to its high thermal conductivity. The reflective and the antireflective coatings are realized by using BaF₂, ZnS, ZnSe and also GaAs films. Two deposition methods have been used: thermal evaporation in Balzers BA 510 unit and r.f. magnetron sputtering in VARIAN ER 3119 equipment.

GaAs thin films, deposited by sputtering, without ion assistance is a priority proposed³, to enhance the reflectivity of the coatings for 10.6μm.

The interest in this paper was on the investigation of optical coatings by transmission and scanning electron microscopy, and X-ray diffraction to obtain information on the structure and reproduction of the coatings.

2. DEPOSITION OF OPTICAL COATINGS - CONSIDERATIONS

The lifetime of the optical components is depending on the optical properties and mechanical resistance at high power/energy laser levels, as well. In order to obtain high-quality optical components, the absorption coefficient of the single layer must be as low as possible consistently with the deposition system. This is a particularly important request for laser coatings because the optical losses decrease the damage threshold and reduce the reflectivity.

The mechanical stability of a thin film is related to the normally present residual stress, that could be of two kinds: 1. thermal stress due to the different thermal expansion coefficients of the substrate and the thin film; 2. intrinsic stress caused by the deposition characteristics: epitaxial growth, metastable phase occurring during deposition or large defects concentration. The absorption of humidity in microvoids, or in the void spaces among the microcolumns eventually present in the film causes an increase of the stress, after the exposure to the atmosphere of the coating till to, in some circumstances, the destruction of the optical component.

The stoichiometry of the compound is the main factor, that governs the optical absorption. In thermal deposition the evaporated particles have lower energy, about some eV and the characteristic is the columnar structure of the film and quite a low compactness.

In sputtering deposition method the characteristic feature is the preferential sputtering: when an ion beam impinges on a multicomponent target the different components of the target are sputtered with a different proportion. In the collision cascade the momentum and energy is differently distributed to each component (with different mass) resulting in different ejection probabilities for atoms⁴. As a consequence the target surface could be enriched of one component after the ion bombardment even if there are other effects to concur at the stoichiometric alteration. Transport phenomena as for instance thermal diffusion, recoil implantation or cascade mixing, radiation enhanced segregation can occur, when using high energy ions. If the target is a growing thin film, the preferential sputtering represents the main difficulty in order to obtain stoichiometric coating. In Sigmund's theory⁵ the sputtering yield is described by the relation:

$$Y = \Lambda F_D(E, \theta, 0) \quad (1)$$

where the two terms Λ and $F_D(E, \theta, 0)$ contain all specific material properties and the type, energy and direction of the incident ions.

The first term Λ is a constant and contains the atomic mass, the atomic number, the density and the binding surface energy of the target. The second term

$$F_D(E, \theta, 0) = \alpha N S_n(E) \quad (2)$$

represents a target particles flow through the surface (i.e. the zero in the first term of the equations 1 and 2 indicates the surface as the origin of the coordinate) and takes into account by the dimensionless parameter " α " of the dependence of the sputtering yield on the angle of incidence θ , the mass ratio of the target atoms, ion mass and the ion energy E . The meaning of the term $S_n(E)$, called the nuclear stopping cross section, can be found in Sigmund's theory⁶. In this theory the assumption is that the atoms are randomly distributed, in order to treat the atom collision cascades by the equation of transport theory, particularly in the framework of Boltzman formulation. When an energetic ion impinges on the target, the atoms can receive sufficiently energy to recoil and break the bonds and begin a collision cascade process in which both the incident ions and moving atoms spend a fraction of their energy.

Thin film formation by r.f. sputtering depends on the target sputtering yield and thus on the energy of bombarding ions that, in turn, will be influenced by the gas pressure in the chamber and the applied voltage. The control of all parameters is the main problem of the sputtering process.

The problem of stoichiometry is critical in both deposition methods thermal deposition and r.f. magnetron sputtering and to check for the characteristics of the coatings depending on the technological parameters is a problem of high interest. The thermal characteristics and lattice dimensions for materials used in our experiments are presented in the table 1.

Table 1. Characteristics of materials used for 10.6 μ m

material	thermal expansion 10 ⁻⁶ / K	thermal conductivity W / cm ² K	melting temperature ° C	lattice constants Å
GaAs	5.7	0.48	1237	f.c.c. 5.65
NaCl	44	0.0648	801	f.c.c. 5.63
KCl	36	0.0652	776	f.c.c. 6.28
BaF ₂	18.4	0.12	1280	f.c.c. 6.2
ZnS	7.8	0.155	1830	h.c.p 3.82
ZnSe	7	0.13	1526	f.c.c. 5.667

3. EXPERIMENTAL

It is the purpose of these investigations to establish the influence of the different deposition methods on the structure and properties of the films used in laser optics at 10.6 μ m wavelength, in order to improve the quality of output mirrors.

Optical quality⁷, oxygen doped GaAs grown⁸, by liquid encapsulation Czochralski (LEC) at dimensions up to 48 mm diameter, was used as substrates for optical coatings.

Transmission electron microscopy was approached for investigations of films structure with selected area electron diffraction (SAED). Special samples were deposited on NaCl substrates, using similar parameters as in the deposition on GaAs substrates :

Samples :

1. ZnS films on cleaved NaCl deposited by thermal evaporation
2. ZnS films on NaCl wafer deposited by r.f. magnetron sputtering
3. GaAs deposited by r.f. magnetron sputtering on NaCl substrate
4. ZnS film deposited by thermal evaporation on GaAs substrate
5. BaF₂, ZnSe as reflective coating on GaAs substrate deposited by thermal evaporation

ZnS is usually the high index refractive material in IR $n=2.1$ at 10.6 μ m. The parameters of the thermal deposition of sample 1, ZnS on NaCl: unheated substrate, uniform deposition rate 30Å/s, layer thickness $\lambda/4$ at 10.6 μ m .

At optical inspection the film is a uniform layer reproducing the characteristics of the cleaved surface. The film is floated off in water and put on TEM grids. The bright field TEM images using a TEM CM 30 show the deposition has a microcrystals structure of nanometer dimension Fig. 1(a) with quite a low density of greater crystals. The selected area electron diffraction (SAED) pattern shown in Fig. 1(b) is a confirmation- that the film consists of crystal grains of nanometer dimension and the density of higher grains (around 50nm) is rather poor.

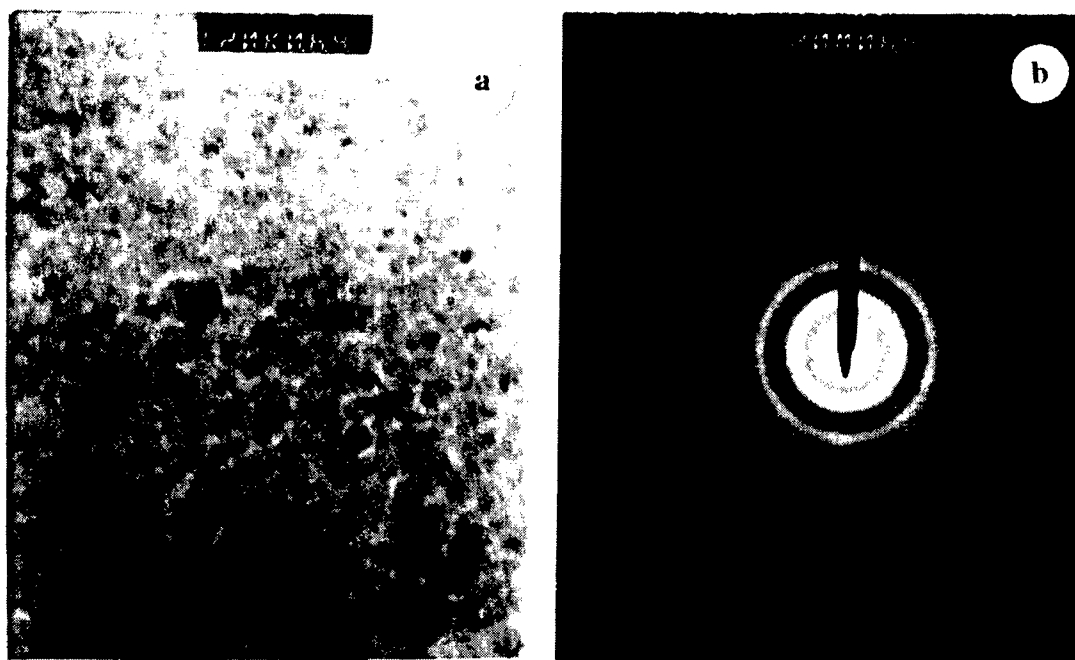


Fig. 1. Bright field TEM image of thermally deposited ZnS film on NaCl substrate (a), corresponding SAED pattern (b)

Sample 2 is ZnS on NaCl substrate and the deposition method r.f. magnetron sputtering, with following deposition parameters: unheated substrate, distance between target and substrate 10cm, argon flow rate 30sccm, pressure 5.5×10^{-4} mbarr, deposition rate was fluctuating in the range 4.1-6.1 Å/s, according the fluctuation of the reactive power at the magnetron.

The investigation by TEM in bright field put into evidence a stratified structure, which is justified by the nonuniform rate of the deposition. Fig.2 (a) shows the polycrystalline structure, with grains of about 40-50nm. The density of microcrystals is much higher in this case. The SAED pattern Fig.2(b) is a lauegram and comparing the measured interplane distances with the ASTM list the coating is ZnS. We believe the higher density of the microcrystals is due to the higher energy of the evaporated particles in the case of magnetron sputtering.

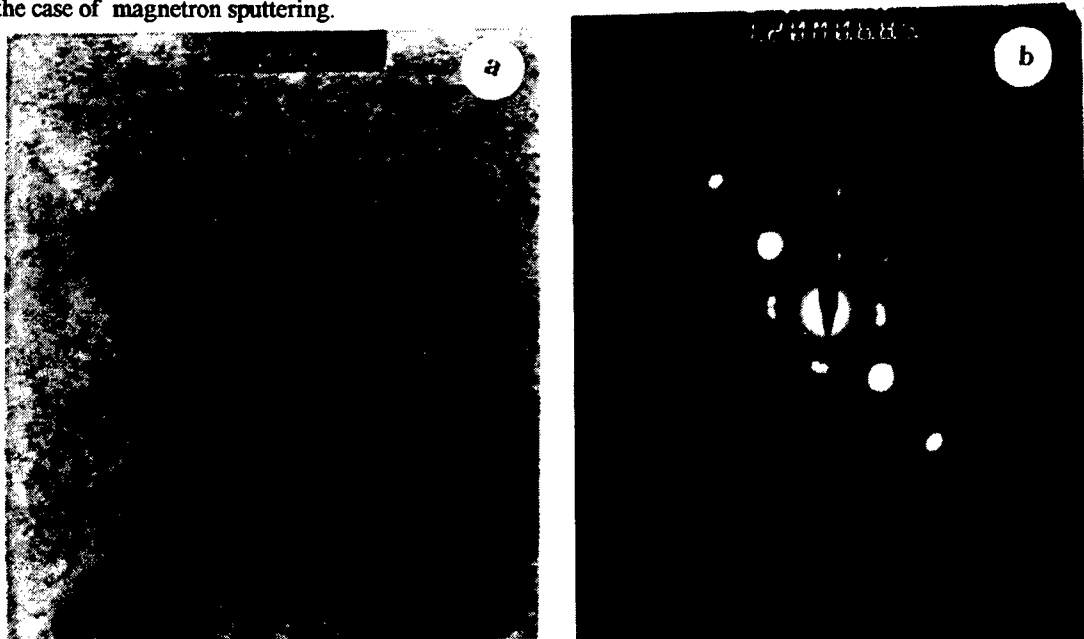


Fig. 2. TEM bright field image of an r.f. magnetron sputtered ZnS film on NaCl substrate, (a) and corresponding SAED pattern for hexagonal crystals (b)

In the second case of sample 2 it was possible to observe a stratified structure of the film, when investigating by TEM, due to fluctuation of the evaporation rate induced by the fluctuating reactive power of the magnetron. The variation of the deposition rate induces mechanical stresses, which could, in some circumstances produce the damage of the coating.

GaAs layers, deposited by sputtering on different substrates NaCl (sample 3) and GaAs (sample 4) were investigated in order to establish the best deposition conditions to obtain a stable coating for IR optics. The samples 3 consists of GaAs, deposited on recently cleaved NaCl surfaces. Previously the deposition process the surface was bombarded about 7 minutes with an argon ion beam for final cleaning and also surface activation, in order to improve the adhesion of the film to the

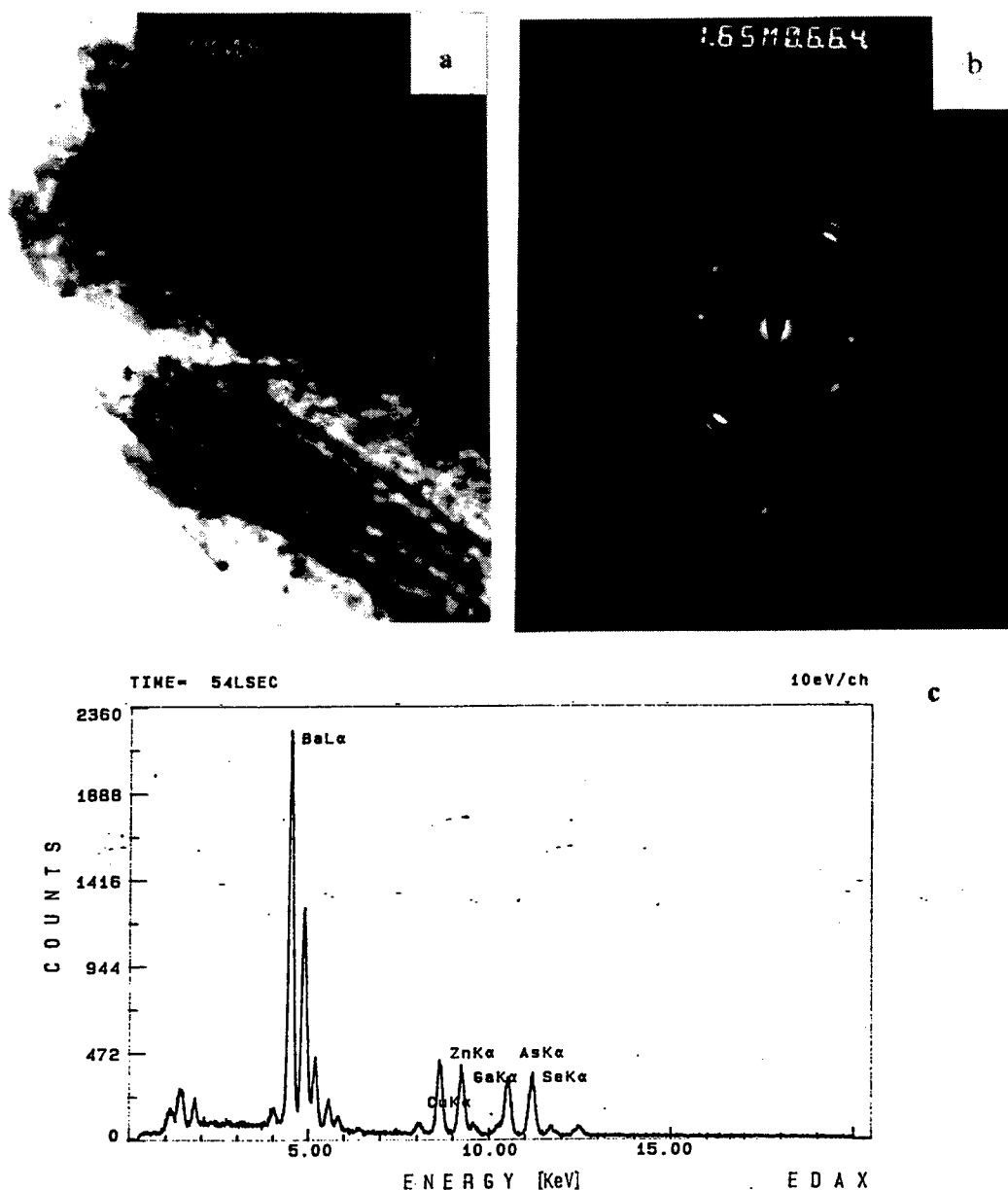


Fig.3 Bright field TEM image of thermally deposited BaF_2 film on GaAs substrate (a), corresponding SAED pattern (b), and EDAX on the same sample(c)

substrate. 500Å and 1000Å thickness GaAs on NaCl surface was investigated by X-ray diffraction (XRD), but the result is an amorphous film. The IR spectrum of the sample with NaCl reference is not specific for low absorption GaAs. When immersed in water to float off the film for TEM investigation it was observed the film to tear, a consequence of a low mechanical resistance.

Sample nr. 4 is ZnS on GaAs substrate, deposited by thermal evaporation. The deposition parameters were the following: substrate GaAs, substrate temperature 100°C, pressure: 1.33×10^{-5} mbarr, layer thickness 12 800Å.

A large interest had been paid to the investigation of sample 5 a double layer structure of $\lambda/4$ BaF₂ / ZnSe on GaAs substrate, the reflective coatings for the output mirror in the industrial CO₂ laser, delivering up to 1.5kW in c.w. working regime. BaF₂ is the low index material for IR $n=1.395$, and the high index material is ZnSe $n=2.4$ at 10.6µm.

The parameters for thermal evaporation were the following: substrate temperature 150°C, deposition rate 10-20Å/s, thickness $\lambda/4$ at 10.6µm.

The double layer of BaF₂ and ZnSe on GaAs substrate has a reddish color, but sometimes a milky reddish tint could be observed, probably due to some hydroxyl residues. In thermal evaporation, generally a columnar microstructure is occurring. Microstructure allows penetration of water into the film, due to its porosity.

The film had been erased from the surface and fragments put on beryllium TEM grids, to avoid errors, when using energy disperse x-ray analysis (EDAX). TEM was chosen to investigate the morphology of different fragments of the film and SAED and EDAX were used to make the identification of specific selected areas. In Fig.3(a) the bright field TEM image, identified by EDAX (Fig.3.c) to be BaF₂ shows the polycrystal structure (Fig.3.b) and the columnar disposition of the microcrystals, which is quite specific for thermally evaporated fluorides.

4. CONCLUSIONS

The different behavior of transmissive optical components in CO₂ laser determined the interest to investigate the optical coatings deposited by different physical methods and correlate the results with the deposition parameters.

The deposition method is highly influencing the quality of the film, as concern the absorption and mechanical resistance. In thermal deposition, the columnar structure and the poor compactness produce a higher absorption and lower mechanical resistance.

Sputtering deposition without ion assisted produces films of higher cristallinity, but the stoichiometry is rather poor.

5. REFERENCES

- 1 I. Gutu, T. Julea, V. Draganescu, D. Dumitras, I. N. Mihailescu and V. R. Medianu, "Development of a high power gas transport CO₂ laser with cylindrical geometry", *Optics and Laser Technology*, Vol. 18, pp. 307- 312 (1986).
- 2 I. Gutu and M. L. Pascu, "A new design for high power transverse - flow CO₂ lasers", *Laser und Optoelektronik*, Vol. 24, pp. 37- 43 (1992).
- 3 V. R. Medianu, A. S. Manea and M. F. Lazarescu, "IR optically active structure obtained by plasma assisted deposition (PAD) of III-V and II-VI binary compound thin layers", *Proc. SPIE* Vol. 2461, pp. 571-575 (1994).
- 4 G. Betz and G. K. Wehner, "Sputtering by particle bombardment II", *Topics in Applied Physics. Sputtering by Particle Bombardment II*, Vol. 52, Ed. R. Behrish, pp.11-90, Springer-Verlag, Berlin (1983).
- 5 P. Sigmund, "Theory of sputtering I. Sputtering yield of amorphous and polycrystalline targets", *Phys. Rev.*, Vol. 184 (2), pp.383 - 416 (1969).
- 6 P. Sigmund, "Sputtering by Ion Bombardment: Theoretical concepts", in *Topics in Applied Physics. Sputtering by particle bombardment I*, Vol. 47, Ed. R. Behrish, pp. 9 -71 Springer Verlag, Berlin (1981).
- 7 C. A. Timus, M. F. Lazarescu, V. R. Medianu and M. L. Pascu, "Optical investigations on oxygen doped GaAs", *Optica Applicata*, Vol. XXII, (3-4),pp. 187 - 193 (1992).
- 8 M. F. Lazarescu, E. Elena, A. Manea, C. A. Timus and M. L. Pascu, "Optical quality GaAs from quartz crucible ", *Cryst.Res. Technol*/Vol. 28, (4),pp. K19 -K 23 (1993).

Characteristics of a carbon/nickel multilayer structure for soft X-ray optics deposited by R.F. magnetron-sputtering

M.Ulmeanu, G.Georgescu, R.Medianu, N.Nastase*, C.Ghica**, V.Vasiliu

National Institute for Laser, Plasma and Radiation Physics, Laser Department, P.O. Box MG-36,
Bucharest, R-76900, Romania

* National Research and Development Institute for Microtechnology, P.O. Box 38-160,
Bucharest, R-72225, Romania

** National Institute for Materials Physics, P.O. Box MG-6, Bucharest, R-76900, Romania

ABSTRACT

In order to make X-ray-UV interference mirrors, we tried to obtain a periodic multilayer structure with thin films of two materials, a high absorption material (Ni) and a low absorption material (C) on a quartz substrate.

We present theoretical approaches to determine the optimum values of the thicknesses of each thin film and the number of periods required for maximum reflectivity at normal incidence of a soft X-ray mirror working at $\lambda=50\text{\AA}$.

We also described the experimental procedures used for obtaining the multilayer structure and the microscopically investigations.

Keywords: X-ray interference mirrors, r.f. sputtering, microscopically investigations.

1. INTRODUCTION

By the use of multilayer coating theoretically we can enhance the reflectivity at any soft X-ray wavelength for normal incidence. For this spectral region, the multilayer consists of a succession of alternately high absorption layers separated by spacer low absorption layers. An R.F. magnetron-sputtering system is a good choice providing film purity, process repeatability, uniformity of deposition, ability to cover complex shapes and where numerous periods are needed. Due to the very small thicknesses of the layers required, it is necessary to have a proper deposition control and a good deposition rate, too.

In this paper, we describe the experimental procedure and characterization of a C-Ni multilayer for the 50\AA wavelength. The most suitable optical constants for high reflectivity multilayer around 50\AA for normal incidence are obtained from the transition elements (V, Cr, Mn, Fe, Co, Ni) combined with space layers of carbon.¹

2. THEORETICAL CONSIDERATION

In the X and X-UV ranges, the usual form of the refractive index is:

$$n = 1 - \delta - i\beta \quad (1)$$

where δ and β are directly related to the scattering power of a given element and to its linear or mass absorption, respectively.

It is also common to use the complex atomic scattering factor $f = (f_1 + i f_2)$ on the range where one has tables of atomic scattering factors for the constituent atoms.²

All the different units are linked together and connected to the atomic properties, so the complex refractive index is given by:

$$n = 1 - \delta - i\beta = 1 - (r_0 \lambda^2 / 2\pi) N (f_1 + i f_2) \quad (2)$$

where r_0 is the classical radius of an electron, N is the volume concentration of the atoms from a layer, λ the wavelength and f_1 and f_2 are the tabulated atomic scattering factors. Noticing that the values for δ and β are small (between 10^{-2} and 10^{-9}), the reflectivity at normal incidence from Fresnel formulas is no more than 10^{-4} .

For noticeable increase in reflectivity response, an optical component has to be made using a stack of interfaces set at the right spacing. This leads to a constructive interference obtained from the partially reflected waves of each interface thus the absorption loss should be lower than reflectivity per interface.

In order to find the best parameters -the optimum thicknesses layers and the number of periods required- we just followed the first good approximate calculation proposed in 1977 by Vinogradov et al.³ and refined in 1987. We considered that such simplified formulas can be used with confidence for general predictions. For the wavelength $\lambda=50\text{\AA}$ the optical constants are:

$$\text{nickel} \quad \tilde{n}_C = n_1 - ik_1 = 0.9832 - 0.00903i$$

$$\text{carbon} \quad \tilde{n}_{Ni} = n_2 - ik_2 = 0.996 - 0.000926i$$

We assume that the nickel thin film takes the share α of all period l , with $0 < \alpha < 1$. Following the simple transcendental equation³ we found the optimum value for $\alpha=0.4$. Thus, the number of periods should be 100, the thicknesses of the carbon and nickel layers 15\AA and 10\AA respectively, in order to obtain a maximum of the reflectivity, around 28.4%⁴, for $\lambda=50\text{\AA}$ at an incidence angle of 4.5° .

For the same reason of maximum reflectivity, it is necessary to form smooth, stable boundaries between thin films. Is known that spacer thin films of carbon are better for X-rays $45\text{\AA} < \lambda < 100\text{\AA}$ forming stable interfaces without interdiffusion with most metals and with an effective roughness $\sigma_{rms}=3\text{\AA}$.

According to the Bragg law for constructive interference $2d\sin\theta=N\lambda$ the shortest possible wavelength is $\lambda=2d$ and corresponds to the normal incidence case. We can observe the wavelength must be in a range larger than about 44\AA . For smaller periods, even if Bragg peaks can be obtained, one observes a very fast decrease of the ratio between measured and the calculated reflectivity that is not predicted for a stack with perfect interfaces. This is because for such thin individual layers, a roughness or an interdiffusion over a few atomic layers is sufficient to decrease the index modulation necessary to obtain a noticeable reflectivity per period. However, carbon has a major absorption edge near 44\AA , which reduces the X-ray reflectance drastically.

3. TECHNOLOGICAL METHOD

One of the most known and used optical coating deposition technique is that based on R. F. sputtering. Sputtering is a process operating on an atomic or molecular scale whereby an atom or molecule of a surface is removed when the surface itself is struck by an energetic incident particle. This process is governed by the momentum transfer of incident atoms to the target material atoms and this momentum transfer can lead to the ejection of a surface atom (sputtering). Since in this kind of process the atoms arrive individually, it is an appropriate technique for growing films of atomic thicknesses or small multiples thereof or molecule-by-molecule also.

For proper thin film adhesion and desorption of adsorbed water vapour, hydrocarbons and other gas atoms, the 23.6mm diameter quartz substrates were cleaned by Ar ion beam etching pre-treatment process, at normal incidence, for 10min prior the deposition. We used an ANATECH IS-300 5cm filamentless ion source providing a beam uniformity of $\pm 5\%$ with constant parameters, shown in Table 1, during all the time of the process.

Etching parameters	Voltage(V)	Intensity(mA)
DES	391	173
BEAM	590	8.6
ACCELERATOR	103	0.86

Table 1

The pressure inside vacuum chamber was 3.3×10^{-4} Torr and flow of Ar gas 15sccm.

C-Ni multilayer structure was made using an R.F. sputtering plant with two 100mm discs targets of nickel and graphite 99.99% purity. The multilayer structure was obtained by growing alternatively C and Ni thin films at a fixed substrate-target distance $D=10\text{cm}$. During the fabrication an initial layer of C (15\AA) was deposited on the substrate. Then 16 layers of Ni (10\AA), alternating with 15 layers of C (15\AA) were deposited. For deposition rate control we used a quartz system with a 0.1\AA/s accuracy.

Deposition parameters were reproducible and are shown in Table 2.

Deposition parameters	C	Ni
Initial evacuation pressure	10^{-5} Torr	10^{-5} Torr
Operating pressure	1.1×10^{-2} Torr	0.9×10^{-2} Torr
Gas (Ar) flow	75sccm	60sccm
Power of discharge	250W	67W
Current intensity	0.5A	0.1A
Deposition rate	0.2Å/s	0.1Å/s

Table 2

The Ar flow was measured with a mass flow controller of 0.2% accuracy. The temperature of the collector was 25°C. Due to the great number of periods required, at this stage of our work we choosed to deposit fewer periods in order to have a prior knowledge about thin films and interfaces characteristics for this method.

4. MICROSCOPICALLY INVESTIGATIONS

4.1 TEM results

Transmission Electron Microscopy (TEM) investigations have been performed on JEOL 200CX installation operating at 200 kV. Samples have been prepared by the extraction replica technique.

Figure 1 shows the corresponding diffraction pattern of the multilayer. The diffraction rings indexing revealed the complete oxidation of the Ni layers leading to the fcc NiO structure (bunsenite) with the cell parameter $a=4.1769\text{\AA}$. The NiO layers consist of small crystallites (few nanometers sizes) which determine the diffuse aspect of the diffraction rings.

The micrograph presents the cross-section of 32 alternative C-Ni layers (Fig. 2). A certain roughness is visible especially for the first deposited layers because of the collector's surface irregularities. The fact that the interface between successive NiO and C layers is not quite well defined indicates a certain interdiffusion. The limiting factor for reflectivity is the intrinsic roughness of the carbon/nickel interface. It is worth to mention that the layers smoothness and the uniformity increase with the distance from the substrate. These values seem to reach a minimal stationary value after the first 10 deposited layers.

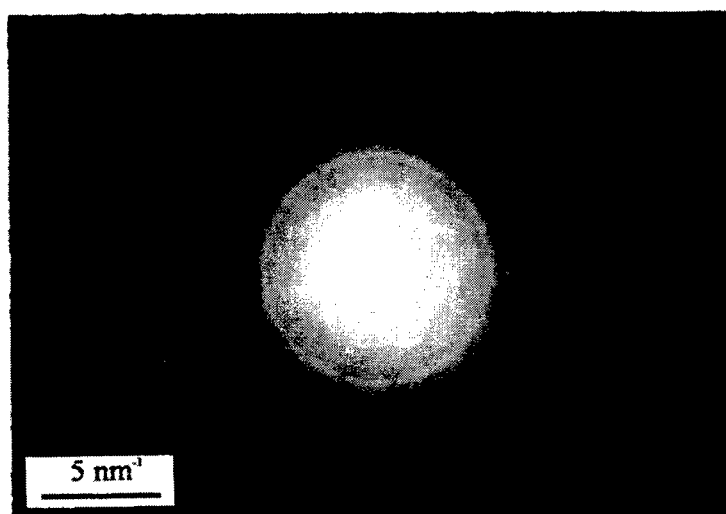


Fig. 1 Diffraction pattern of multilayer structure by TEM



Fig. 2 Cross section of multilayer structure by TEM

4.2 AFM results

Atomic Force Microscopy is one of the new scanning surface technologies that allow the investigation at nanometric resolution of surfaces. It acts like a profilometer with a sensing tip, which follow nondestructively the surface features. The tip is mounted on a side of a soft cantilever sensible to short and long-range forces. The analyses of the surfaces were made in air at room temperature, in constant-height mode. We used a commercial Si_3N_4 tip with a radius of 500\AA .

AFM image of a single C layer (Fig. 3), 100\AA thick on quartz substrate, shows an uniform surface with a granular morphology characterized by a roughness root mean square $\sigma_{\text{rms}}=2.49\text{nm}$ at a surface area of $\sim 0.7\mu\text{m} \times 0.7\mu\text{m}$. Following the profile of an ordinary line from the surface investigated, the histogram shows a Gaussian distribution (Fig. 4). That indicates a smooth ideal surface with very small granulation (the fractal dimension $d_f=2.00$) with atoms situated almost symmetrically (symmetry $S \approx 0.07$) related to a mean surface profile.

We have measured pores height (in the limit of AFM measurements) $h = 4.05\text{nm}$ with a diameter in the range of $\sim 100\text{nm}$.

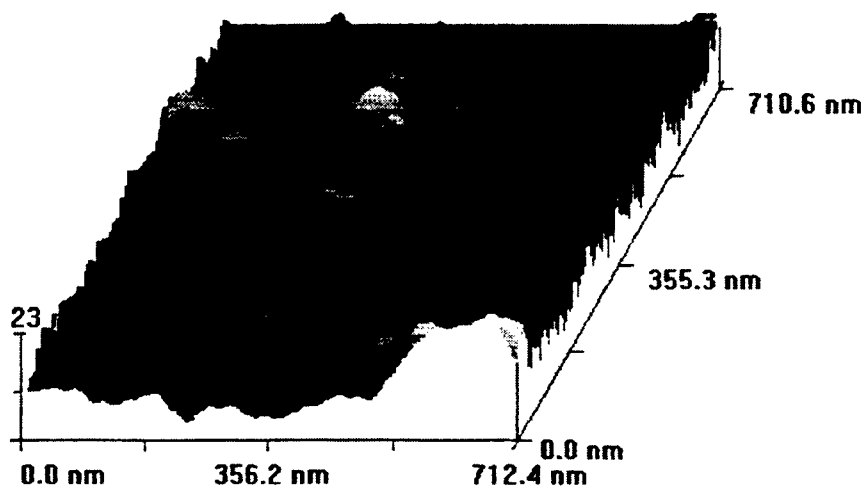


Fig. 3 AFM - 3D image of a carbon surface

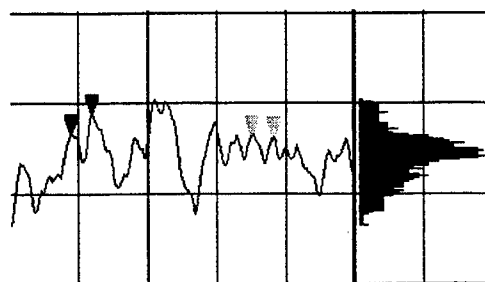
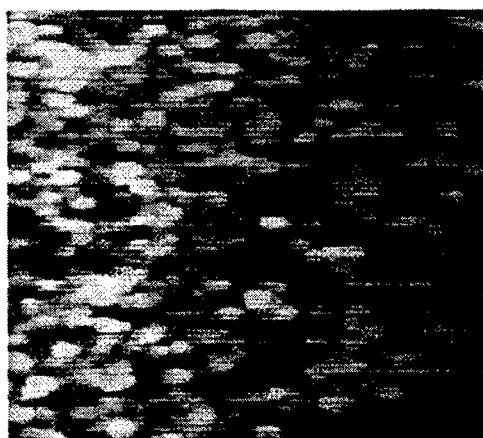
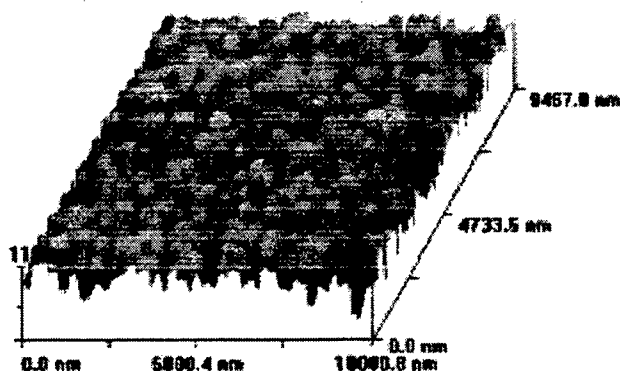


Fig. 4 The histogram realized from a line of the carbon surface (Gaussian profile)

The images of the top nickel thin film surface from the multilayer structure show a topography with a relative uniform distribution of small granules with an average roughness in the domain of 9-22nm and the σ_{rms} of 11-26nm. Symmetry about mean is $S \approx -0.4$ and kurtosis about mean is ~ 3 for a $22 \times 22 \mu m^2$ surface that means a Gaussian distribution approximately symmetric about mean of surface profile.



(a)



(b)

Fig. 5 2D (a) and 3D (b) AFM images of the top nickel thin film surface from a carbon-nickel multilayer structure

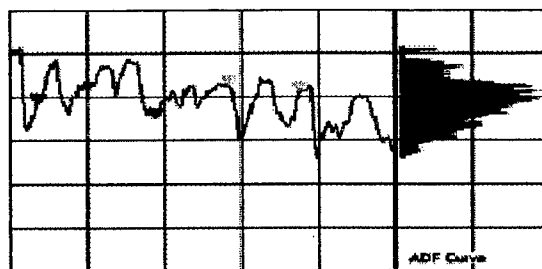


Fig. 6 Profile and amplitude density function (the histogram) of a line from fig. 5 (a)

5. CONCLUSIONS

We have shown that under the deposition conditions we were able to obtain smooth and uniform layers of C and Ni. The C grew amorphous and the Ni with the layer thickness limited crystallite size. The main problem to accomplish is

to avoid the oxidation of the nickel layer. Some solutions might be to decrease the argon flow used in deposition process and to protect with a carbon layer as a last thin film of the multistrukture.

From the TEM measurements results that the multilayer has a continuous aspect and for larger periods the smoothing effect increases together with the uniformity of the layers.

The AFM measurements indicate smooth ideal surfaces with a relative uniform distribution of small granules.

The degrade of the multilayer nearby the quartz substrate indicated by the TEM image, indicates that other microscopically smooth surface should be used (e.g. float glass, Si wafers) and a good control of etching rate and microroughness if this kind of cleaning process is used.

We note that with the knowledge about the film characteristics afforded by the complementary characterization techniques used in this work it should now be possible to improve the quality of the mirrors and so its reflectance.

6. REFERENCES

1. Troy W. Barbee Jr., "Sputtered Layered Synthetic Microstructure (LSM) Dispersion Elements," *Low Energy X-Ray Diagnostics*, ed. D.T. Attwood and B.L. Henke, AIP Conf. Proc. No. 75, AIP, New York, 131 (1981)
2. B.L. Henke, E.M. Gullikson and J.C. Davis, "X-ray interactions," *Atomic Data and Nuclear Data Tables* **54**(2), 218-260 (1993)
3. Vinogradov A.V. and Zeldovich B. Ya, "X-ray and far UV multilayer mirrors: principles and possibilities," *Appl. Opt.* **16**, 89-93 (1977)
4. V.G. Kohn, "On the theory of reflectivity by an X-ray multilayer mirror," *Phys. Stat. Sol. (b)* **187**, 61-70 (1995)

New method for automatically optimization of glasses combination
in optical systems working in visible range

Daniel Ralea*, Raluca Marginean*, Marinica Marzu**

*Institute of Optoelectronics, Department of Nightvision Apparatus, PO Box MG6-22, 1 Atomistilor Street, Magurele,
Bucharest 76900, Romania

**Army Institute for Research and Development, fax 7804863

ABSTRACT

The algorithm presented in this paper proposes a way to find the optimum glasses that assure a better correction for optical apparatus with the human eye as a final receiver. The model (N_e , v_1 , v_2), based on the Buchdahl formula, gives an approximation error for the refraction index less than $5 \cdot 10^{-5}$ for visible domain. We introduced in the merit function used for optimizing the optical system an operand that describes the existence of an optical glass. This operand was defined so that the obtained value for N_e , v_1 and v_2 can be closed to some values for a real glass. A definition for this operand is obtained using the PN_e , Pv_1 , Pv_2 , probabilities of existence for a glass with a certain parameter N_e , v_1 or v_2 . Another possibility to define this operand is to describe the volume occupied by the optical glass in (N_e , v_1 , v_2) space with some elliptical functions. The probabilities and the elliptical functions were found after an analysis for all optical glasses listed in the Schott catalogues was made.

Keywords: optical design software, optical glasses, color-correction, automatically glass selection

1. INTRODUCTION

The problem of color-correcting optical systems is one of the most difficult problems facing optical designers. One solution for getting the optimum glasses combination in an optical system is to mathematically model the glass and to vary its parameters during the optimization routine.

The common method for selecting optical materials is to describe these materials by the pair (N_d , V_d), where N_d is the index of refraction for "d"-light ($0.5876 \mu\text{m}$) and V_d the Abbe number for "d"-light. This method has two major defects:

- 1) it can't calculate the index of refraction with a good enough precision for the ending zones of the visible domain;
- 2) it is possible to find a pair (N_d , V_d) which is not close enough to some values for a real glass.

As a result, after a good solution is found using this method, a conversion must be made back to real glasses and for many optical systems the new design will perform worse than the initial design.

2. THE MATHEMATICAL MODEL

A great variety of dispersion formulae has been developed over the years to express refractive index as a function of wavelength¹. For the development of a mathematical model which express the material characteristics in the terms of its dispersion properties we needed a dispersion formula in the form:

$$N = \sum c_n x^n \quad (1)$$

where the coefficients c_n are characteristic for a particular glass and are independent of the wavelength λ , and where the variable x is a function of the wavelength λ . A formula of this kind was proposed by Buchdahl²:

$$N = N_0 + v_1 \omega_1 + v_2 \omega_2 + v_3 \omega_3 + \dots + v_n \omega_n \quad (2)$$

where: - N_0 is the refractive index at a selected base wavelength λ_0

- ω is the color coordinate defined as:

$$\omega = (\lambda - \lambda_0) / [1 + \alpha(\lambda - \lambda_0)] \quad (3)$$

- v_n are the dispersion coefficients

The term α is a constant independent of the dispersion characteristics and its calculated value by Buchdahl is 2,5. The dispersion coefficients are independent of the wavelength and differ from an optical material to another. By using the equation (2) we keep the main advantage of the (N_d, V_d) model: $N(\lambda_0)$ describes the image quality for the base wavelength (like N_d in the common model) and v_n describe axial color correction state (like V_d)³.

Because the great majority of the optical systems working in visible range has as primary wavelength the "e"-light, we choose in (2) $\lambda_0=0.5461 \mu\text{m}$. We kept only the first and the second terms in the sum in (2). The values for v_1 and v_2 were obtained by minimizing the function:

$$F = \sum [N_s(\lambda_i) - N_c(\lambda_i)]^2 \quad (4)$$

where N_s is the index of refraction for λ_i presented by the Schott catalogue and N_c is the index of refraction calculated with (2). The sum was calculated over 90 wavelengths λ_i in the $0.4 - 0.9 \mu\text{m}$ domain. The resulting maximum absolute error was only $2 \cdot 10^{-4}$ for the $0.4 - 0.9 \mu\text{m}$ domain and only $5 \cdot 10^{-5}$ for the $0.48 - 0.65 \mu\text{m}$ domain. These values are less than the production tolerances for optical glasses.

3. OPTIMIZING THE GLASS COMBINATION USING THE PROPOSED MODEL

We introduced in the merit function used for optimizing the optical system (with the damped least-squares method) an operand that describes the existence of a glass. In order to define this operand, an analysis for all optical glasses listed in the Schott catalogue was made. We calculated v_1 and v_2 for every glass in this catalogue. We have two possible definitions for the operand:

1. using the probabilities of existence for a glass with a certain parameter N_e , v_1 , or v_2 .
2. describing the volume occupied by the optical glasses in the (N_e, v_1, v_2) space.

3.1. The calculus of the probability of existence for an optical glass

A statistical analysis over the obtained values for N_e , v_1 and v_2 was made. In Fig1a, Fig1b and Fig1c, we have the histograms for the number of glasses with N_e , v_1 or v_2 varying between the minimum and the maximum obtained values with a step of 0.005. By dividing the numbers of glasses with parameters within every interval at the total number of glasses (from the Schott catalogue), we can obtain the existence probabilities P_{N_e} , P_{v_1} and P_{v_2} for a glass. Because rough data is affected by statistical fluctuations, the use of un-smoothed numerical derivatives in minimization procedure could frequently lead to a false minimum (local minimum), as we can see in Fig.1d. In order to prevent this, the distributions of glasses were approximated by continuous functions, namely normalized sums of two or three gaussians:

$$P = (A / w\pi^{1/2}) \exp[-2(x-x_c/w)^2] \quad (5)$$

These continuous approximations are presented also in fig. 1. The parameters that define the gaussians are presented in table 1.

Table 1: The parameters of the gaussians that describe the probabilities of existence P_{N_e} , P_{v_1} and P_{v_2}

	x_{c1}	w_1	A_1	x_{c2}	w_2	A_2	x_{c3}	w_3	A_3
P_{N_e}	1.5225	0.00515	0.02795	1.6203	0.00972	0.5036	1.6479	0.2279	0.4685
P_{v_1}	-0.0964	0.0789	0.7142	-0.0647	0.02087	0.2858	0	0	0
P_{v_2}	0.0096	0.0135	0.4313	0.0429	0.0594	0.5687	0	0	0

The operand that describe the existence condition for an optical glass can be specified in the form:

$$V^{(j)} = P_{N_e} \cdot P_{v_1} \cdot P_{v_2} \quad (6)$$

Obviously, this operand has as a target value $T=1$.

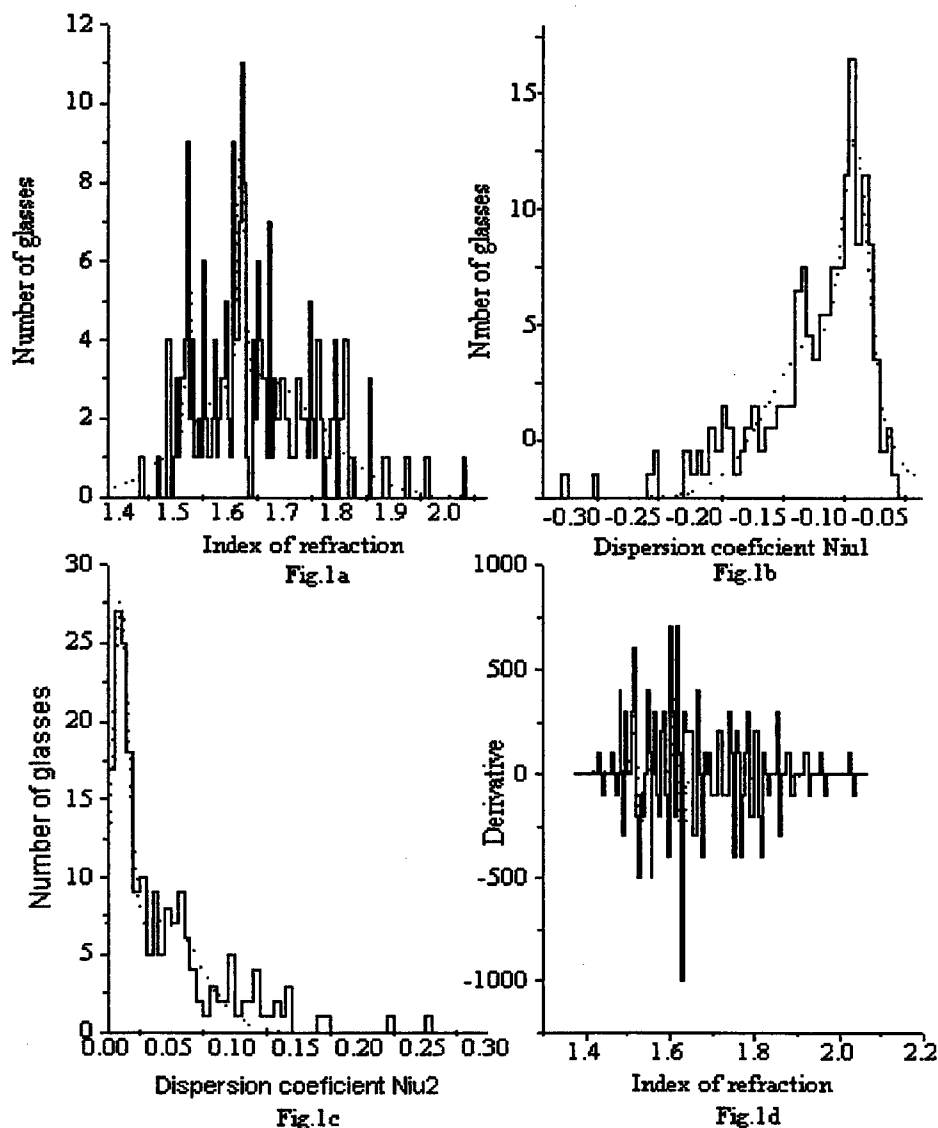


Fig.1: The index of refraction N_e (a); the dispersion coefficients N_{iu1} (b) and N_{iu2} (c) versus the number of glasses; the derivative of the glasses distribution function as a function of the index of refraction N_e .

3.2. The volume occupied by optical glasses in (N_e, v_1, v_2) space

The volume occupied by glasses in the (N_e, v_1, v_2) space can be established by casting it on the three coordinate planes (N_e, v_1) , (N_e, v_2) and (v_1, v_2) . An AutoLisp software read from a file the calculated values for N_e , v_1 , v_2 and plotted in the graphics presented in Fig. 2a, Fig. 2b and Fig. 2c the points that represent the glasses parameters. If we know the position of a glass in two of these planes, we can easily obtain its position in the third plane. This interdependence allow us to restrict our analysis to only two planes (N_e, v_1) and (v_1, v_2) .

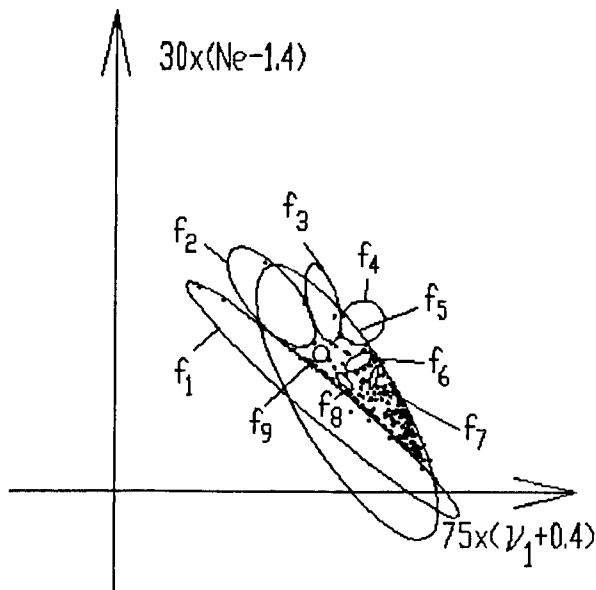


Fig. 2a

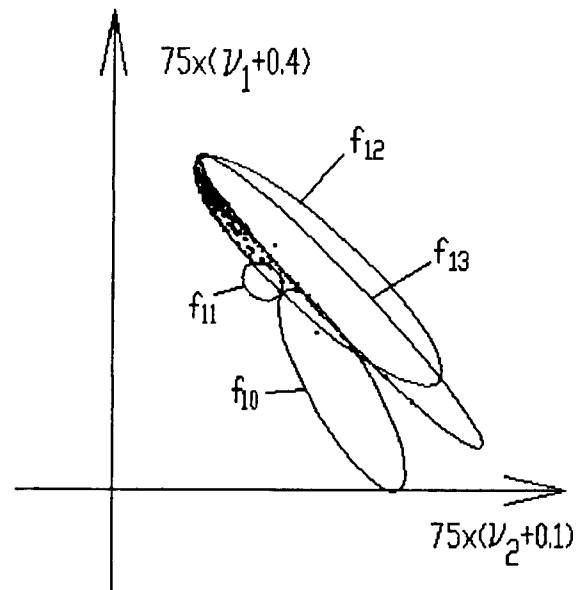


Fig. 2b

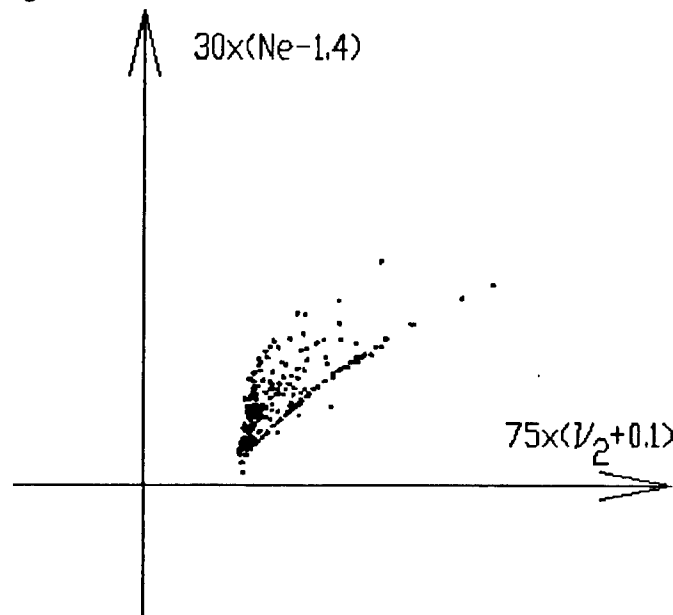


Fig. 2c

Fig.2: The areas occupied by de glasses in the (N_e, Niu_1) (fig.2.a), (Niu_1, Niu_2) (fig.2.b), (N_e, Niu_2) (fig.2.c) planes and the elliptical functions that we used for describing the volume occupied by the glasses in the (N_e, Niu_1, Niu_2) space

The volume that interested us was described by 13 elliptical functions f_j . For defining this volume, we used the property that, for a point inside the ellipse, the function has a negative value and, for a point outside the ellipse, the function has a positive value. We trace in the planes the ellipses that delimit the areas occupied by glasses. With the "LIST" command available in AutoCAD, we read the values for the ellipses parameters: major and minor axis coordinates and the center coordinates. The most convenient form for the elliptical equations is:

$$f_j = A_0x^2 + A_1y^2 + A_2xy + A_3x + A_4y + A_5 \quad (7)$$

The coefficients A_{ji} for the elliptical functions f_j , $j = 1 \dots 13$ are given in table 2, together with the conditions that every equation has to fulfill. These coefficients were calculated from the ellipses parameters, taking into account the rotation and translation given the coordinate system's origin.

Table 2: The conditions to fulfill for elliptical functions; the coefficients of the functions that describe the volume occupied by glasses in the (N_e, N_{iu1}) , (N_{iu1}, N_{iu2}) planes; the inverse of the ellipses major diameters

j	Condition	A_{0j}	A_{1j}	A_{2j}	A_{3j}	A_{4j}	A_{5j}	$1/D_j$
1	$f_1 \geq 0$	0.14495	0.22313	0.357	-8.1134	-9.8212	109.37	0.329
2	$f_2 \geq 0$	0.1363	0.11533	0.17675	-6.5235	-6.0987	92.1043	0.959
3	$f_3 \geq 0$	0.59202	0.1283	0.28137	-25.59	-9.0428	298.65	1.491
4	$f_4 \geq 0$	0.27778	0.30595	-0.0624	-10.952	-7.2386	166.244	2.538
5	$f_5 \leq 0$	0.04243	0.02073	0.04678	-2.0535	-1.2485	24.2796	0.381
6	$f_6 \geq 0$	1.38695	2.81324	-2.5278	-31.117	-7.3969	365.861	4.028
7	$f_7 \geq 0$	12.2806	2.35878	-7.4414	-477.83	121.421	4757.76	5.288
8	$f_8 \geq 0$	5.32694	5.02441	8.13535	-285.41	-253.07	3982.83	5.256
9	$f_9 \geq 0$	2.23336	2.19353	-0.2578	-76.479	-45.503	938.687	7.216
10	$f_{10} \geq 0$	0.09732	0.04499	0.10918	-4.8366	-2.95	60.0687	0.515
11	$f_{11} \geq 0$	0.3462	0.41923	0.19254	-12.455	-16.983	227.443	2.645
12	$f_{12} \leq 0$	0.0376	0.04924	0.07589	-2.7408	-3.1641	52.5637	0.354
13	$f_{13} \geq 0$	0.12645	0.1319	0.25169	-9.0447	-9.2087	162.33	0.288

The operand that describe the existence condition for a glass has the value:

$$V^{(2)} = \sum e_j, \quad j = 1 \dots 13 \quad (8)$$

where: $e_j =$

$$\begin{aligned} &0, \quad \text{if the "j" condition is fulfilled;} \\ &f_j^2, \quad \text{if the "j" condition is not fulfilled;} \end{aligned} \quad (9)$$

Obviously, this operand has as a target value $T=0$.

When the "j" condition is not fulfilled, the value for the $f_j(x, y)$ equation divided to the distance between the (x, y) point and the "j" ellipse depends on the major diameter D_j of the "j" ellipse. In order to eliminate this dependence, we normalized the elliptical equation by dividing the values for A_{ji} to the corresponding major axis diameters.

4. DISCUSSIONS AND CONCLUSIONS

When using the operand defined with probabilities of existence for an optical glass, the obtained solutions are acceptable only for unpretentious optical systems (i.e. systems with "low speed" and corrected in maximum 3 wavelengths). Because the probabilities have bigger values for common glasses, this method has the advantage that the optical systems designed with it are cheaper. That's why this definition for the operand can be recommended at the beginning of the system design, in order to determine if the system can be realized with common glasses.

The advantage when using the operand defined taking into account the volume occupied by optical glasses in the (N_e, v_1, v_2) space, is that it will always exist one or more real glasses with parameters closed enough to the calculated parameters. When we convert the model glasses to real glasses, we can preserve the aberrations values calculated for primary wavelength by preserving the N_e value for the model glass. By preserving the values for v_1, v_2 , we can preserve the paraxial color-correction. If we keep the lens powers when this conversion is made, the real optical system is quite similar to the ideal calculated one.

For comparison, we optimized an optical system working in visible range using a merit function that includes an operand including the glass parameters defined with the proposed model or with the (N_d, V_d) model. As we can see in Fig.3-5, the results obtained with our model are superior to those obtained with the common model. The color-correction (Fig.3) is better and the aberrations values are smaller.

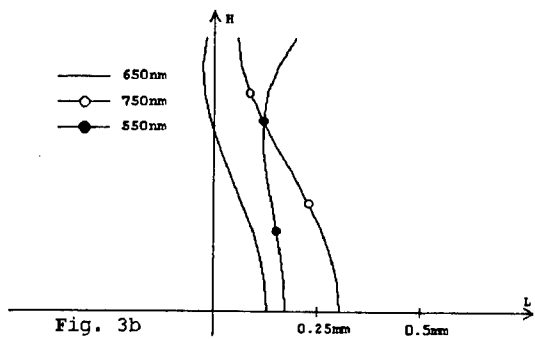
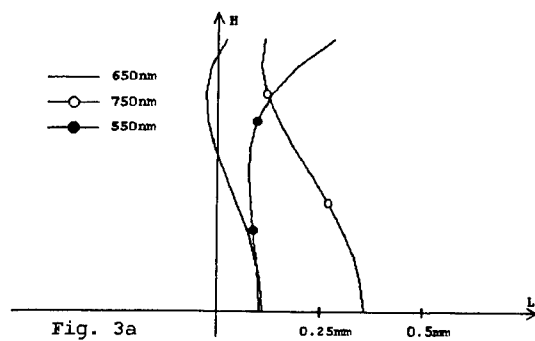


Fig.3: Longitudinal aberration obtained using:
a) N_d, V_d model and b) N_e, v_1, v_2 model

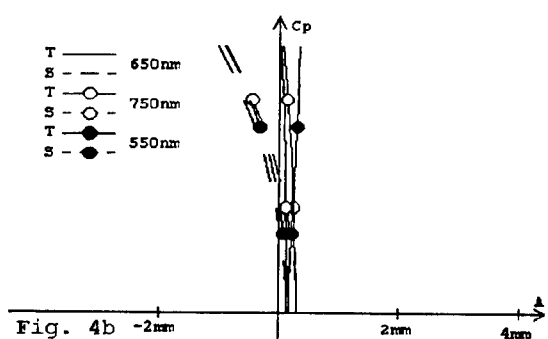
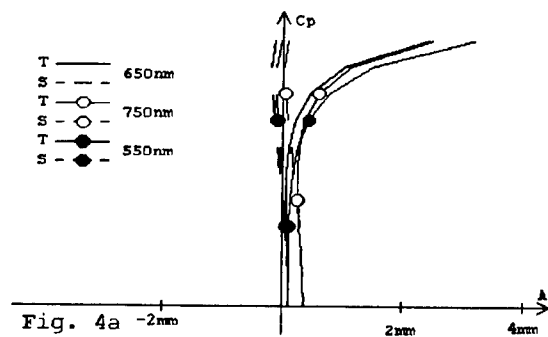


Fig.4: Field curvature obtained using:
a) N_d, V_d model and b) N_e, v_1, v_2 model

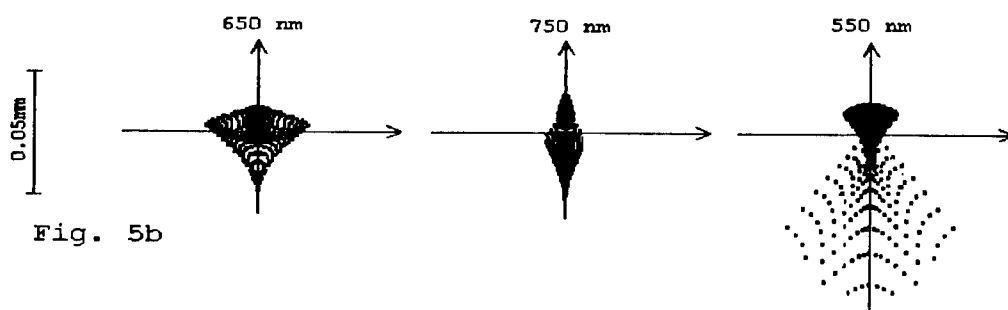
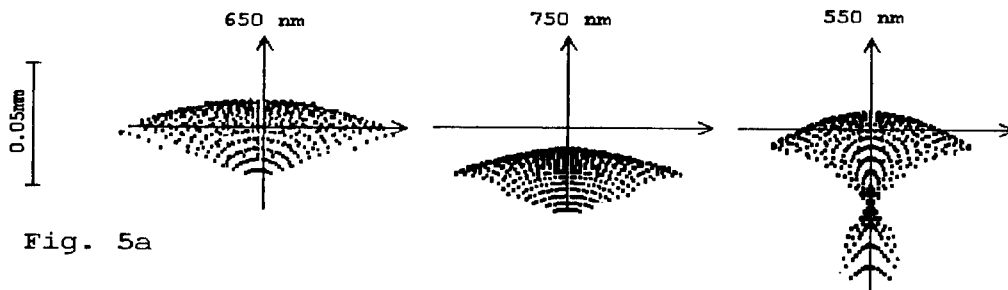


Fig.5: Spot diagram for 2/3 of maximum fields obtained using:
a) N_d, V_d model; and b) N_e, v_1, v_2 model

Although the determination of gaussians and f_j functions is difficult, the method based on equation (2) offers a powerful tool for automatically optimization of glass combination. With the global optimization methods, it also ensures a very good chance to find the global minimum for a certain system configuration.

5. REFERENCES

1. M. J. Smith, "*Modern Optical Engineering*", pp.147-148, Mc.Graw Hill Book Company, New York, 1966
2. H.A. Buchdahl, "*Optical Aberration Coefficients*", Dover Publications Inc., New York, 1968
3. Romeo I. Mercado, Paul N. Robb, "*Color corrected optical systems*", US Patent no.5,020,889, 4 jun.1991

Interferometric characterization of GRIN lenses for ophthalmic uses

J. R. de F. Moneo, I. Juvells, S. Vallmitjana, S. Bosch, A. Carnicer, I. Labastida and J. Pérez
Universitat de Barcelona, Laboratori d'Òptica, Departament de Física Aplicada i Electrònica
Diagonal 647, E08028 Barcelona (Spain) E-mail: sbp@hermes.fae.ub.es

ABSTRACT

The proposal of this work is the study of a method for characterization of the focal of ophthalmic lenses whose surface refraction index has been modified by diffusion techniques based on thermal ion exchange in glass. In particular the aim is the measurement of the variations in focal length of ophthalmic lenses after undergoing a diffusion process. An interferometric technique has been used and computer simulations have also been carried out.

1. Introduction

The inclusion of gradient-index technology in optical elements has become a very impressive field in applied optics. The possibility of totally or partially changing the index of refraction in lenses designed for vision purposes is a very attractive subject. The proposal of this work is the study of a method for characterization ophthalmic lenses of which the surface refraction index has been modified by diffusion techniques based on thermal ion exchange in glass. In particular the aim is the measurement of the variations in focal length of ophthalmic lenses after undergoing a diffusion process. As these variations are extremely small, an interferometric technique is needed. Among the different architectures of lateral shearing interferometers we have chosen the Mach-Zehnder interferometer (MZI) as a powerful tool for optical testing.^{1,2} A method for the calculation of the focal length derived from the interferograms is described. In order to obtain the best work conditions and to test the method of measurement, a computer simulation has been also carried out.

2. Method

The method of calculation of the focal length is based on the analysis of the interference pattern between a plane wave and the corresponding spherical wave after passing through the lens. This interference is carried out by means of a MZI and is recorded through a CCD camera and a frame grabber.

Once the focal length of the test lens has been calculated, the surface index of this lens is modified by a diffusion technique and a new measurement of the focal length is realized by the analysis of the interference pattern. The final difference between both calculated focal lengths will give the influence of the gradient index variation on the lens.

The basis of the calculation of the focal length (see Figure 1) is the obtention of the distance z , which is the distance between the interference plane and the center of the converging spherical wave. The distance between the back principal plane of the lens and the interference plane is d . The addition of z plus d will give this focal, as can be seen in the same Figure. In the setup, a plane wave interferes with the converging one to its focus, giving concentric circles, as seen in Figure 2.

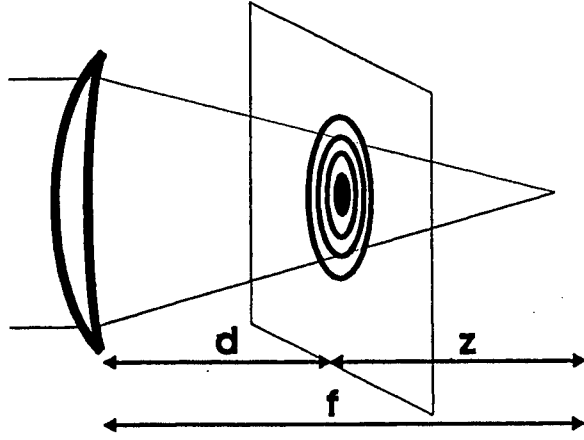


Figure 1: Focal length measurement

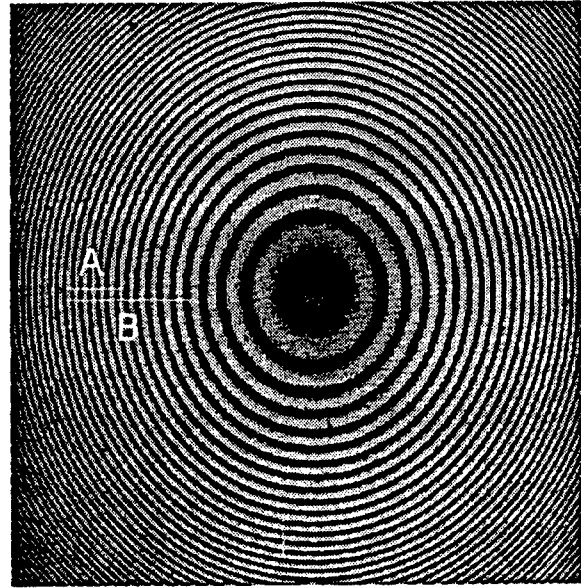


Figure 2: A and B measurement

By analyzing the interference rings between a plane wave and a spherical wave converging (or diverging) to the distance z behind (or before) the plane, the radius of the interference circles follow the relation³:

$$\rho_n^2 = 2n\lambda z \quad (1)$$

where n is the interferometric order of the ring. Theoretically, measuring the radius of the rings in the interference plane would be enough to obtain z . This is not correct because the last equation is only true when the phase at the centre is zero (or there is a maximum at the centre). In general, the correct equation which gives the relation between radius of maxima of order n and z is:

$$\rho_n = 2\lambda z(n \pm p) \quad \text{where } 0 \leq p < 1 \quad (2)$$

This now gives an extra unknown p , but moreover there is another difficulty that appears when z is large. This case implies a large value of the radius which in the practical case could be longer than the actual size of the captured area taken by the CCD and the frame grabber. Another practical problem arises for the determination of the centre of the radius on the pixelated images because the circles are in grey levels and they are not perfect circumferences. As a result, all these experimental problems lead to make a very inaccurate measurement of z .

In order to overcome these drawbacks we propose a method of measuring based on subtraction so, the central phase does not affect the results and, in addition, for large z the CCD can be laterally displaced. This gives more rings regardless of the situation of the centre.

Starting from a certain ring (Figure 2), which is of a unknown order n , and measuring the distances A and B , between n and $2n$ rings, we obtain,

$$\begin{aligned} \rho_n - \rho_{n-m} &= A = \sqrt{2\lambda z n} - \sqrt{2\lambda z (n-m)} \\ \rho_n - \rho_{n-2m} &= B = \sqrt{2\lambda z n} - \sqrt{2\lambda z (n-2m)} \end{aligned} \quad (3)$$

Solving the system:

$$\frac{m}{n} = \frac{12AB - 8A^2 - 4B^2}{4AB - 4A^3/B - B^3/A}$$

$$z = \frac{A^2}{2\lambda n(1 - \sqrt{1 - \frac{m}{n}})^2} \quad (4)$$

To this distance z (from the interference plane to focus) the distance from the lens to the interference plane has to be added, in order to obtain the focal length. For simplicity in the latter equations, we have supposed that there is a maximum in the centre (initial phase p zero). In the general case (see equation 2) the integer corresponding to the order must be substituted by a real number $n \pm p$, but the system 3 remains the same and now n is real. It is important to remark that once the system is solved, Equation 2 is useful for checking and refining the results.

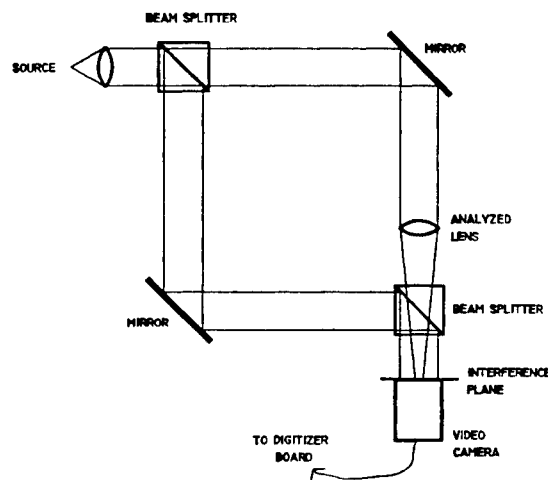


Figure 3: Mach-Zehnder interferometer

3. Experimental

3.1. Setup

This interference is carried out by means of a MZI on an isolated optical table, the arrangement of which is represented in Figure 3. By adjusting the collimator a coherent plane wave coming from a He-Ne laser crosses the first cube beam-splitter. In one of the arms the lens under study is placed and the wave plane is changed into convergent or divergent after passing through. In the other arm the plane wave remain the same. The interference between the two arms in the exit of the cube beam-splitter is grabbed in a 8 bit by means of a CCD camera.

3.2. Optimization of the precision

In this method it is very important to minimize all sources of error. First of all the optical quality must be good enough to avoid unwanted deformations of the wavefronts. In particular the resolution has to be high in the

digitized rings. Theoretically, the longer the distances A and B measured the better precision in the results, but also the imprecision on the fainter and more concentrated rings affects negatively. Conversely if shorter distances are measured the results also begins to decay. In order to deal with this, an optimum range of distances has been found after a study based on a series of measurements over known tests. The exact situation of the maxima is another important element to be defined which also depends on the resolution of the frame grabber.

In order to reduce to the minimum the influence of these sources, a good $\lambda/20$ was used in the mirrors, $\lambda/10$ in the cubes, a special collimator and a microscope objective corrected for infinity was used on a compressed air active-isolated optical table. After trial error tests we have found an optimal compromise between the digitation, the precision and the counted number of rings. Other error sources due to the experimental limitations are derived from the fact that each lens is measured twice (before and after the difusion) and the conditions of the interferometer are not the same. These sources are: interference pattern without lens, conditions of room temperature, conditions of illumination and saturation of the CCD. Other problems arise from the fact that the digitation is squared over a rectangular sensitive surface.

Finally, in order to deal with these other sources, the same experimental protocol was used each time, and checking first the room conditions and the initial interference pattern, its verticality, and the photometric conditions.

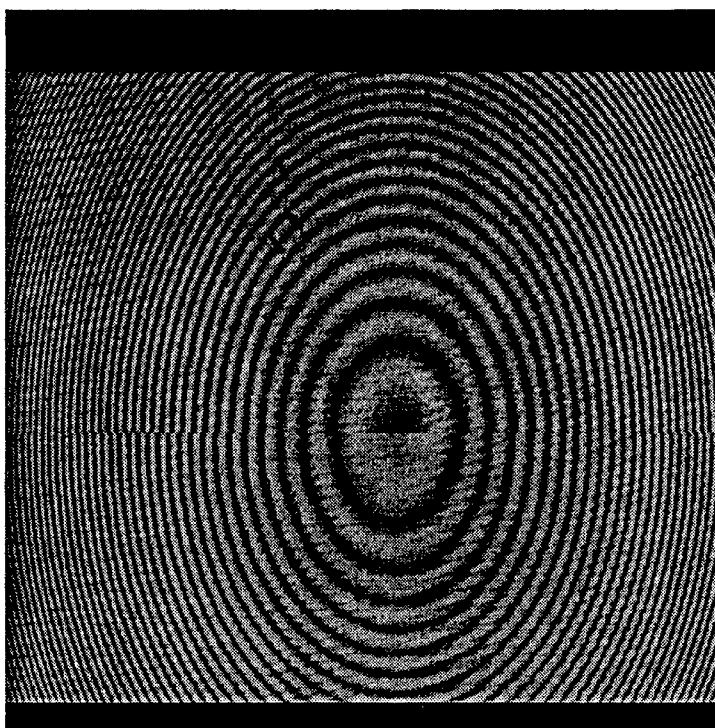


Figure 4: Superposition of two interferograms

4. Results

For each ophtalmic lens the procedure has been the same. First the lens is placed in the MZI within the aforementioned conditions and from its interferogram the focal length is measured. Afterwards the lens is treated

by diffusion techniques based on thermal ion exchange with a view to changing the surface refractive index. A second measurement in the MZI gives the variation on the focal length. Figure 4 shows the superposition of two interferograms of the same lens before (upper part) and after (lower) the diffusion bath. The fringe displacement is due more to the different central initial phase than to the difference on the gradient of the refractive index. In all the experiments the variations on the surface index of refraction give unaffected values of the power of the lens. The appreciated increments are so faint that they are inside of the range of imprecision. Our initial precision was a dispersion of ± 0.025 dioptres over several measurements of a positive meniscus lens of a power of +2 dioptres. Now we have improved the method of measurement giving a dispersion of ± 0.010 dioptres around the power tested.

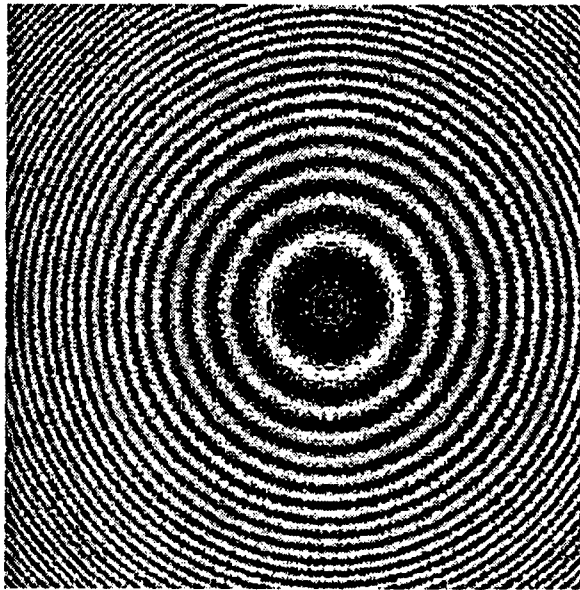


Figure 5: Simulated interferogram

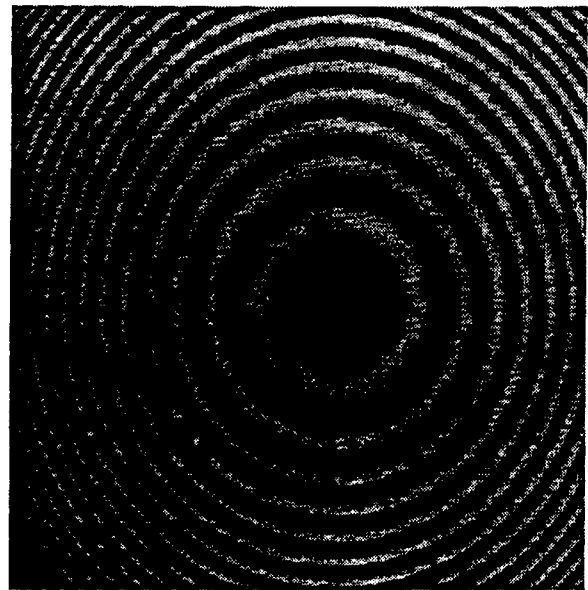


Figure 6: Experimental interferogram

5. Simulated results

Another way to test the method of obtaining the focal length has been carried out by simulation. A computer program which simulates the MZI has been designed. The parameters of the ophtalmic lens as curvature radii, index of refraction and thickness are introduced. The program calculates and displays the simulated interferogram after entering the exact position of the lens. By measuring the same distances *A* and *B* over the rings as in the experiment, the program computes the focal power. In order to compare and simulate the experimental conditions, two meniscus of +1 and +2 dioptres (nominal value) are measured in the MZ interferometer. The two curvature radii and thickness were measured through a precision spherometer ($\pm = .001mm$) and a precise value of the refraction index is given by the commercial supplier. With all these values the program in the computer calculates the interference rings and display the interferogram, with an accurated scale factor. The distances *A* and *B* are measured by the same method and with the same *m* number, finally a focal length results for the simulated interferometer. Figures 5 and 6 show respectively the simulated and the experimental interferograms obtained from the same lens. In the simulated interferogram the distances *A* and *B* are measured by the same method and with the same *m* number. The results are as follows:

1. Lens of +1 dioptré (nominal)

- Simulation: Obtained value: 0.958 dioptrés
- Actual measurement in the MZI 0.967 dioptrés. Error 0.009

2. Lens of +2 dioptré (nominal)

- Simulation: Obtained value: 1.960 dioptrés
- Actual measurement in the MZI 1.979 dioptrés. Error 0.019

The accordance is excellent because the difference between the measured and simulated values are within the tolerable range of precision according to the data values and the experimental method.

6. Conclusions

An interferometric method for obtaining the power focal of an ophthalmic lens with a precision better than one hundredth of dioptré has been developed. The method is based on the analysis of the interference pattern between a plane wave and the corresponding spherical wave after passing through the lens. This interference is obtained in a Mach Zehnder interferometer and recorded through a CCD and a 8 bit frame grabber. A computer programme that simulates the interferometric behaviour has also been developed. The method has been applied to measuring the variations of the focal power of a lens after undergoing a thermal ion exchange treatment in order to modify the surface variations of the refraction index.

Acknowledgements

This work has been supported by INDO, S.A., under project FBG/2216-10/95.

7. REFERENCES

- [1] D. T. Moore and D. P. Ryan, "Measurement of the optical properties of gradient index materials", *J. Opt. Soc. Am.* **68**, 1157-1166 (1978).
- [2] H. El-Kashef, G. E. Hassan and I. El-Ghazaly, "Mach-Zehnder optical system as a sensitive measuring instrument", *Appl. Opt.* **33**, 3540-3544 (1994).
- [3] D. Malacara, "Optical Shop Testing", John Wiley Sons, New York (1978).

Ray tracing for ophthalmic optics. Specific developments for GRIN materials.

J.R. de F. Monco, I. Juvells, S. Vallmitjana, S. Bosch, A. Carnicer, I. Labastida, J. Pérez.

Universitat de Barcelona. Laboratori d'Òptica. Departament de Física Aplicada i Electrònica.
Diagonal 647, 08028 Barcelona (Spain). E-Mail: sbp@hermes.fae.ub.es

ABSTRACT

In this work we present the developments for the simulation of image formation through an ophthalmic lens. The procedure is, essentially an exact ray tracing taking into account the particular mobility conditions of the exit pupil. This leads to the computation of astigmatism as a function of the field angle considered. In the computer program, the use of a commercial glass with a gradient in the refractive index (GRIN material) is foreseen. This latter feature proves to be useful for two practical objectives: modifying the power and the astigmatism of the lens. To illustrate these points, an example based on a lens made by deforming a plane parallel plate of GRIN material will be presented.

Keywords: Gradient-index lenses, ophthalmic lenses, optical design.

1. Introduction

Graded-Index (GRIN) optics has been widely studied for improving optical properties of many kinds of lenses. The use of GRIN elements in optical design provides powerful additional degrees of freedom for the correction of aberrations [1]. Lenses with GRIN profiles have been adapted to a wide range of applications such as imaging and transforming systems; coupling, connecting and collimating devices in optical communications and so on. Applications of GRIN optical materials include rod lenses, multifocal contact lenses, low chromatic aberration lenses, and high-bandwidth optical fibers.

Most of the applications of GRIN to optical systems deal with the design and manufacture of small lenses and with the correction of aberrations in optical systems consisting of several lenses [2] [3] [4]. There are only a few references where the different aspects related to the design of single (individual) lenses, having higher aperture, have been reported. Several of these applications are intended for ophthalmic use [5] [6].

The aim of this work is to study the potential use of GRIN materials for the design of ophthalmic lenses. We will show results obtained by means of a computer simulation program which implements the image formation through an ophthalmic lens manufactured using a GRIN media. The basis of our program is a ray tracing procedure which tries to reproduce the working conditions of an ophthalmic lens, i.e., the eye (operating under its particular optical requirements) is always placed behind. In fact, the program allows the simulation of lenses either homogeneous or manufactured with different kinds of GRIN conditions. In this case, the program allows the optimization of the lens design in study by means of the modification of the GRIN. This latter feature proves to be useful for two practical objectives: modifying the power and the astigmatism of the lens. To illustrate these points, an example based on a lens made by deforming a plane parallel plate of GRIN material is presented.

2. Image formation

2.1. Working conditions.

The optical properties of an ophthalmic lens are closely related to their conditions of use. Basically, these conditions are defined by the presence of the eye behind the lens and by the allowed relative position between lens and eye. The two main characteristics of the ophthalmic uses of a lens are:

- 1) The exit pupil of the lens will always be quite small (a few millimeters in diameter), due to the presence of the eye pupil in all practical cases.
- 2) The position of the exit pupil moves as the eye pupil rotates around the center of the eye, when looking at different points.

The two previous constraints lead to important conclusions:

- An ophthalmic lens must be designed to work with large field angles.
- The most significant aberration in the design of an ophthalmic lens is the astigmatism.

2.2. Determination of the entrance pupil.

Once the optical elements forming the system are geometrically defined, the first step in computations is finding the entrance pupil. This is done by means of an inverse exact ray tracing (i.e., computed from the eye to the object) in the two different cases (on axis and off axis, rotating the eye). This calculation is implemented within the program by means of the following simplified procedure. We take two points in the actual pupil of the eye: one is at the center and the other 1 mm apart. By an exact inverse ray tracing, the two images in the object space are determined. These automatically define the position, orientation and size of the entrance pupil. This procedure is illustrated in Figure 1.

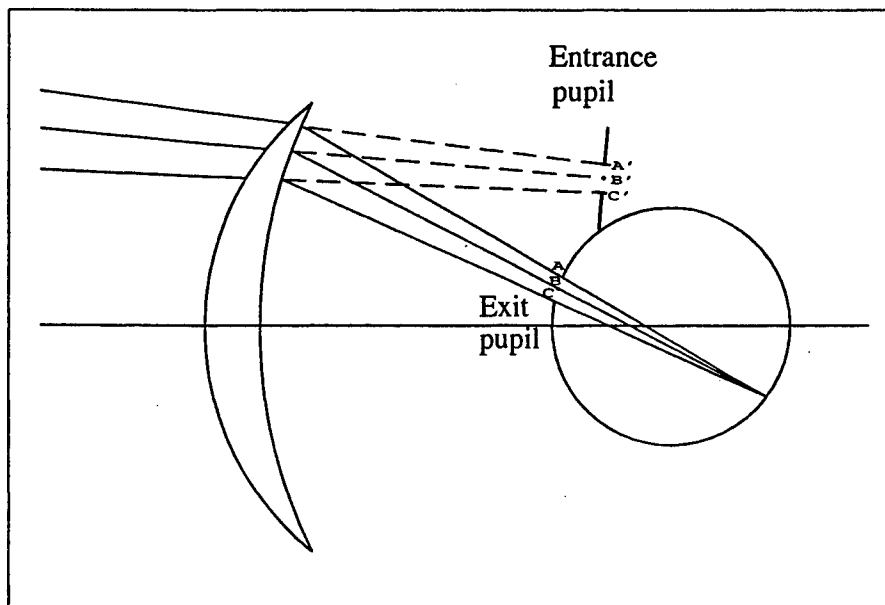


Figure 1: Schematic of ophthalmic lens and eye performance.

2.3. GRIN types.

For GRIN materials three different types have been implemented:

- 1) Radial variation: the changes in refractive index are of the form $n(r)=n_0+Ar^2+Br^4$, where r is the distance from the optical axis.
- 2) Axial variation: the refractive index changes as $n(z)=n_0+Az^2+Bz^4$, where z is the position along the optical axis.
- 3) Depth variation: the index changes in depth, from the surface of the lens, according to $n(d)=n_0+Ad^2+Bd^4$, where d is the distance from the surface. This is the kind of variation one may expect by ion exchange (diffusion) of glass within a liquid media. [7].

2.4. Ray tracing and aberrations.

The spot diagrams corresponding to two far point objects (axis and field zone) are computed. This is done by considering an uniform distribution of rays in the entrance pupil and by exact ray tracing through the lens (which may be homogeneous or made with any of the three kind of inhomogeneous media explained).

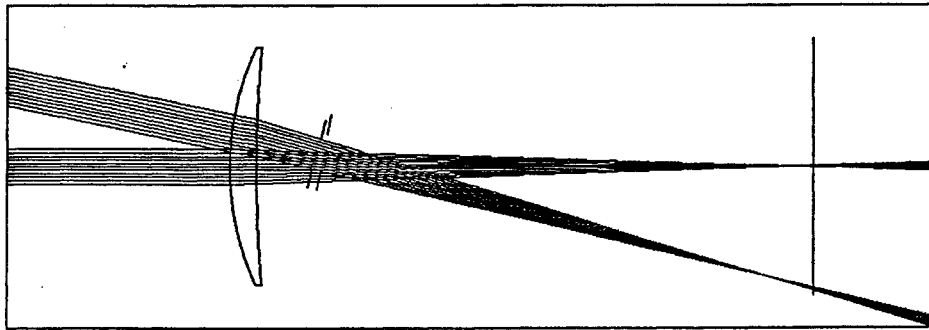
Exact ray tracing through a GRIN media has been implemented using the Runge-Kutta numerical method, in the form of the algorithm proposed by Sharma et al. [8]. This procedure consists of dividing the ray path into small steps, computing for each one the director cosines and the coordinates of the ray. The problem of computing the intersection of the rays with the surfaces between the different media has been addressed by interpolation, following the idea suggested by Stone et al. [9]. As indicated, our ray tracing procedure always takes into account the fact that, when looking at a field angle, the eye pupil moves accordingly. Thus, in these conditions the rays will cross the lens obliquely.

The assessment of the quality of the lenses is done by computing the tangential and sagittal foci for a certain field angle (and also the axial focus). These tangential and sagittal focal points are determined as those giving minimum distance between two closely spaced rays, traced in the directions sagittal and tangential, since there will be no actual intersection between two rays traced in a general case. Astigmatism is defined as the distance between the two focal points [10]. Astigmatism and field curvature may be combined to give a figure of merit for the quality of the lens.

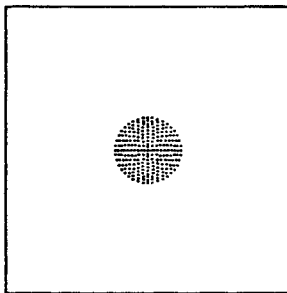
2.5. Results from the program.

Here we will present the results corresponding to the working conditions described above, although the same computer program would be useful for other practical applications. For example, designing contact lenses by using GRIN materials would be possible; in this case the merit function to optimize has to be mainly the spherical aberration [6].

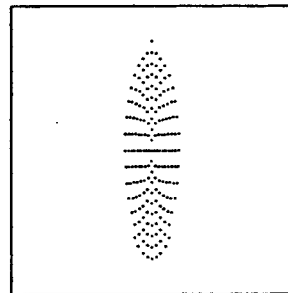
Figure 2 a) shows a plot of the meridian rays traced through a lens having a radial variation in refractive index, and the corresponding spot diagrams on axis and field zone. The procedure for finding the entrance pupil is illustrated (image of the eye pupil calculated backwards through the lens). While running, the program allows moving the image plane and the scale for plotting the spot diagrams. Figures 2 b) and c) are spot diagrams on axis and field zone in a plane close to the paraxial focal plane of the lens. The field spot diagram shows the typical shape due to the astigmatism which induces the commented visual conditions (small aperture, large field angle). Figures 2 d) and e) show the spot diagrams in the sagittal plane, whereas f) and g) correspond to the tangential plane. The distance between them is the astigmatism corresponding to the part of the lens where the light rays cross.



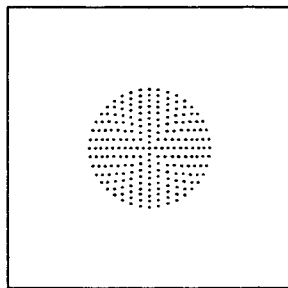
a



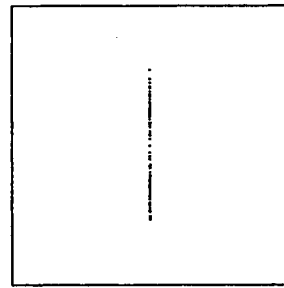
b



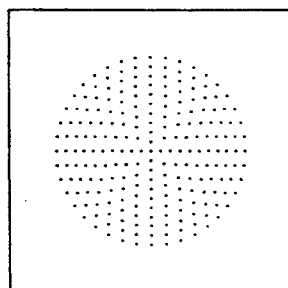
c



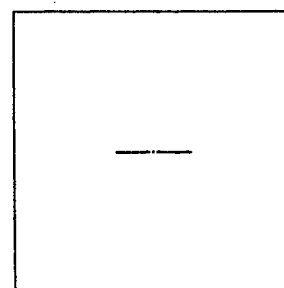
d



e



f



g

Figure 2.- Ray tracing through a GRIN lens.

3. Designing a GRIN ophthalmic lens

To show the potential use of GRIN materials for manufacturing ophthalmic lenses, an example case has been developed. A plane-parallel slab of material of 2mm thick (say plastic or glass) is curved to give two 5.25 dioptre surfaces and 60 mm diameter. We will work with a field angle of 25 deg. We will assume a radial variation in the refractive index given by $n(r)=1.5+Ar^2+Br^4$. Here, the second order term introduces a variation in optical path length which is equivalent to a spherical surface, thus inducing a variation in optical power similar to a common change of surface curvature for homogeneous materials. The fourth order term is equivalent to the substitution of a spherical surface by an aspherical one, thus modifying the resulting aberrations (mainly astigmatism).

The design procedure has been oriented to find the two parameters A and B which define the GRIN. The results obtained show that A is mainly related to the final power of the lens, whereas B controls the astigmatism. For example, $A=-0.001$ gives a lens of about 4 dioptres; if $B=0$, the astigmatism is -0.007 dioptres, while making $B=8E-8$ the astigmatism reverses sign (0.007 dioptres), indicating that B may virtually eliminate it with proper adjustment.

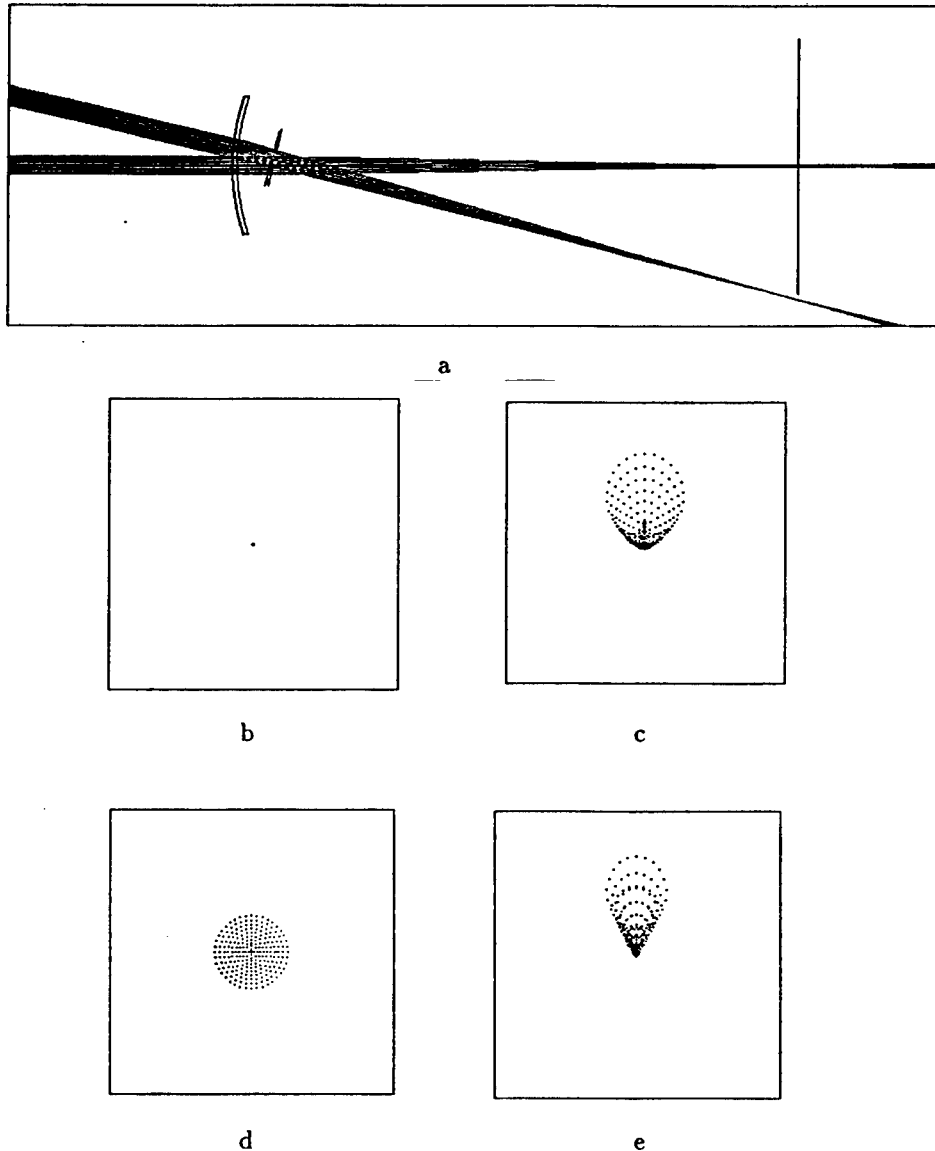


Figure 3.- Ray tracing through a curved slab.

Figure 3 illustrates the behaviour of the lens in the initial case ($A = -0.001$ y $B = 0$). For the other case ($A = -0.001$ y $B = 8E-8$) the plots are very similar. Figure 3a corresponds to the ray tracing through the lens (in fact this is only a curved slab with a radial variation in the refractive index). Figures 3b and 3c are the spot diagrams (on axis and in field zone, respectively) in the focal plane of the lens. Finally, Figure 3d and 3e are the spot diagrams in an intermediate plane between the sagittal and tangential foci. One may note, in the focal plane, that the axial image is virtually a point while in field zone shows the typical comma shape. The same kind of phenomenon, even more noticeable, is visible in 3 c. Both images evidence the absence of astigmatism, which implicitly leads to a small comma, practically a third order one.

4. Conclusions

In this work we have addressed several aspects related to the potential use of GRIN materials for the manufacture of ophthalmic optics. First, we have analyzed the working conditions of ophthalmic lenses, according to the eye characteristics, and the relevance of the different aberrations. Consequently, a computer program was developed to implement the above ideas: taking into account the role of the eye in the process and evaluating the astigmatism as the more important merit function.

The program begins by finding the entrance pupil, from the actual position of the eye pupil, performing an exact ray tracing for lenses which may be manufactured with several different kinds of variations in the refractive index (either radial, axial or in depth). Then, the program computes the aberrations (particularly astigmatism) and allows the user to take this factor into account in the design of the ophthalmic lens.

As an example, we present the results obtained with a lens formed by a curved slab (i.e., initially a plane parallel piece) of material having a radial variation in the refractive index. We show that this kind of GRIN allows a significant increase in optical power (by variation of the first coefficient) while the second coefficient allows a good control of the astigmatism (it may be virtually zero).

5. Acknowledgements

This work was supported by INDO, S.A., under project FBG/2216-10/95.

6. References

- [1] K. Iga. "Evaluation and reduction of aberrations in distributed-index lenses: a review", *Appl. Opt.* **21**, 1024-1029 (1982).
- [2] L.G. Atkinson, S.N. Houde-Walter, D.T. Moore, D.P. Ryan, J.M. Stigman. "Design of a gradient-index photographic objective". *Appl. Opt.*, **21**, 993-998 (1982).
- [3] J.P. Bowen, J.B. Caldwell, L.R. Gardner, N. Haun, M.T. Houk, D.S. Kindred, D.T. Moore, M. Shiba, D.Y.H. Wang. "Radial gradient-index eyepiece design". *Appl. Opt.*, **27**, 3170-3176 (1988).
- [4] K. Siva Rama Krishna, A. Sharma. "Low-power gradient-index microscope objective: design", *Appl. Opt.* **28**, 5636-5641 (1996).
- [5] J. Liñares, C. Montero, X. Prieto. "Graded-index bifocal spectacle lenses produced by ion-exchange in glass: paraxial designing", *Pure Appl. Opt.* **4**, 695-699 (1995).
- [6] Y. Koike, A. Asawada, A.P. Wu, E. Niheil. "Gradient-index contact lens", *Appl. Opt.* **34**, 4669-4673 (1995).
- [7] D.S. Kindred. "Gradient-index silver alumina phosphate glasses by exchange of Na for Ag", *Appl. Opt.*, **29**, 4051-4055 (1990).
- [8] A. Sharma, D.V. Kumar, A.K. Ghatak. "Tracing rays through graded-index media: a new method", *Appl. Opt.* **21**, 984-987 (1982).
- [9] B.d. Stone and G.w. Forbes. "Optimal interpolants for Runge-Kutta ray tracing in inhomogeneous media", *J. Opt. Soc. Am. A*, **7**, 248-254 (1990).
- [10] E.W. Marchand. "Photographic gradient singlet", *Appl. Opt.* **19**, 1044-1051 (1980).

On the solutions of the single layer synthesis with symmetrical three layer periods

Andreea Dincă, Paul Miclea, Voicu Lupei

National Institute for Laser, Plasma and Radiation Physics
Solid State Quantum Electronics Laboratory
P. O. Box MG-36, RO-76900 Bucharest, Romania

Mihai Dincă

University of Bucharest, Faculty of Physics
P. O. Box MG-11, RO-76900 Bucharest, Romania

ABSTRACT

Admittance matching is generally used in the design of optical components which require in the same time high reflectance and high transmission bands. The matching is done at the both sides of the basic stack by synthesizing an equivalent layer with symmetrical three layer periods. In order to obtain a broad transmission band, a quasi-matching is necessary around the matching wavelength. The paper studies the solutions provided by analytical synthesis of the matching stack for a number of one to three periods.

Keywords: optical coatings, admittance matching

1. INTRODUCTION

In order to obtain a high transmittance band, the multilayer system has to be admittance matched at a certain wavelength (λ_m) and also a quasi-matching must be fulfilled in a region around this wavelength. Thus, we shall consider here basic stacks of the form $(H/2 L H/2)^n$ or $(L/2 H L/2)^n$ which will be optically matched with the substrate and incident medium. The matching structures will consist of a periodic structure of the form $(aH bL aH)^m$ or $(aL bH aL)^m$ depending on the basic stack type.

2. DESIGN METHOD

If one denotes by E_b the equivalent refractive index of the basic stack at λ_m and E_{ad} the refractive index of the considering adjacent medium, the period of the matching stack must have the equivalent refractive index E and phase thickness γ given by $E = \sqrt{E_b E_{ad}}$ and $\gamma = \frac{(2k+1)\pi}{n}$, where $k = 0, 1, 2, \dots$. Only the matching with $m = 1, 2$ and 3 periods will be studied in the following. In this cases the possible values of γ^1 are shown in Figure 1.

By imposing the values of E and γ to the matching period, and denoting

$$B = \frac{\frac{n_a}{E_m} - \frac{n_a}{n_b}}{\frac{n_a}{E_m} - \frac{n_a}{n_a}} \quad F = \frac{1}{2} \left(\frac{n_a}{E_m} + \frac{E_m}{n_a} \right) \quad S = \frac{1}{2} \left(\frac{n_a}{n_b} + \frac{n_b}{n_a} \right) \quad (1)$$

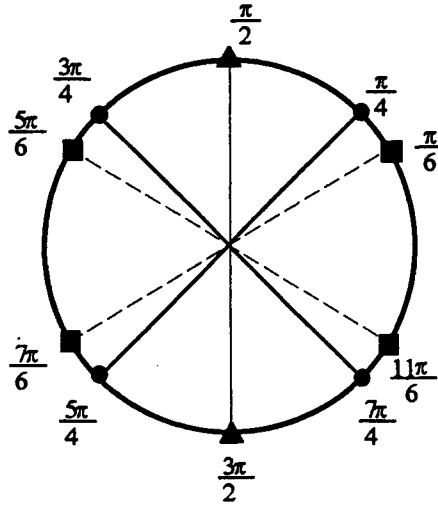


Figure 1. Values for phase thickness of the matching period, for $m=1$ (triangle), $m=2$ (circle), and $m=3$ (square)

one obtain that the phase thickness $\phi_a = \frac{\pi}{2} ag$ and $\phi_b = \frac{\pi}{2} bg$ obey to the equations:

$$\begin{aligned}\sin \phi_b &= \sigma_s M_s B \\ \cos \phi_b &= \sigma_b \sqrt{1 - B^2 M_s^2} \\ \sin 2\phi_a &= \sigma_s M_s \frac{\sigma_b F \sqrt{1 - B^2 M_s^2} - \sigma_c B S \sqrt{1 - M_s^2}}{1 + M_s^2 (F^2 - 1)} \\ \cos 2\phi_a &= \frac{\sigma_c \sigma_b \sqrt{1 - M_s^2} \sqrt{1 - B^2 M_s^2} + M_s^2 S B F}{1 + M_s^2 (F^2 - 1)}\end{aligned}\quad (2)$$

where $M_s = \sin \gamma$, σ_s and σ_c are the sign of $\sin \gamma$ and $\cos \gamma$, respectively. It must be outlined that the constants B , F and S are not independent.

$$F^2 - 1 = B^2 (S^2 - 1) \quad (3)$$

and F and S are always greater than unity. For a given the equation set (2) can have two solutions corresponding to the two possible signs σ_b and $\cos \phi_b$, or none.

In the case of one period matching, as resulted from Figure 1, two values of γ are possible, $\gamma = \frac{\pi}{2}$ and $\gamma = \frac{3\pi}{2}$. For them $M_s = 1$ and the equations (2) reduce to

$$\begin{aligned}\sin \phi_b &= B \sigma_s \\ \cos 2\phi_b &= \sigma_b \sqrt{1 - B^2} \\ \sin 2\phi_a &= \sigma_b \sigma_s \frac{\sqrt{1 - B^2}}{B F} \\ \cos 2\phi_a &= S \frac{B}{F}\end{aligned}\quad (4)$$

with $\sigma_s = \pm 1$, $\sigma_b = \pm 1$.

For ϕ_b two solutions are obtained for each value of σ_s , corresponding to the sign of $\cos \phi_b$. Consequently, the four solutions will be denoted with subscripts referring to the signs of $\sin \gamma$ and $\cos \phi_b$, respectively. On the other hand the solutions for ϕ_a depends only on the product $\sigma_s \sigma_b$ and the corresponding optical thickness are denoted consequently (Table 1).

Table 1. Solutions of the equations (4) for $m = 1$

Solution number	σ_s	σ_b	Optical thickness	
			b	a
1	+	+	b_{++}	a_+
2	+	-	b_{+-}	a_-
3	-	-	b_{--}	a_+
4	-	+	b_{-+}	a_-

Considering the signs of $\sin \phi_b$ and $\cos \phi_b$ one can show that the optical thickness b are indexed in the order of value increasing if $B > 0$ and value decreasing if $B < 0$; on the other hand $a_+ < a_-$. Thus, if $B > 0$ the lower total optical thickness ($2a + b$) is provided by the first solution. If $B < 0$ the lower total optical thickness is given either by solution 3 or solution 4.

In the case of matching with two or three periods the results are different. For each of these situations, four values for γ are possible with $\sin \gamma = \pm M_s$ and $\cos \gamma = \pm M_c$ where M_s and M_c depends on the number of periods (2 or 3). For each combination of signs σ_s and σ_c of $\sin \gamma$ and $\cos \gamma$, respectively, two solutions with $\sigma_b = \pm 1$ can be obtained. In this way, a total number of eight solutions are obtained for each period number (Table 2).

Table 2. Solutions of the equations (2) for $m = 2$ or 3

Solution number	σ_s	σ_c	σ_b	Optical thickness	
				a	b
1	+	+	+	a_{+++}	b_{++}
2	+	+	-	a_{-+-}	b_{+-}
3	+	-	+	a_{+--}	b_{++}
4	+	-	-	a_{--+}	b_{+-}
5	-	+	+	a_{--+}	b_{-+}
6	-	+	-	a_{+--}	b_{--}
7	-	-	+	a_{-+-}	b_{-+}
8	-	-	-	a_{+++}	b_{--}

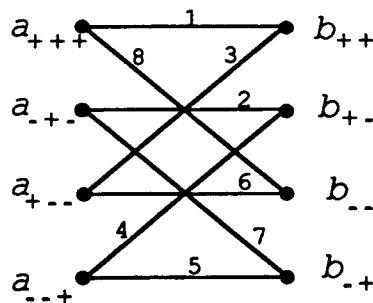


Figure 2. Schematic representation of the solutions of equations (2)

The optical thickness b depends on σ_s and σ_b , and only four different values are obtained for this eight solutions. Again, they are denoted by subscripts referring to σ_s and σ_b , respectively. The optical thickness a depends on the products $\sigma_s \sigma_b, \sigma_s \sigma_c$ and $\sigma_c \sigma_b$. Also, four different values are obtained, denoted with subscripts referring to the three products above mentioned.

For the values of b the same order relationship as in the previous case apply and $a_{-+-} > a_{+--}$. The overall order for the values of optical thickness a depends on the specific values of n_a, n_b and γ . From Table 2 one can observe that the eight solutions could be arranged in the "butterflies" shown in Figure 2. Also, the solutions ϕ_a and ϕ_b present interesting symmetry properties which were studied elsewhere.² In order to find the solution with the lowest total optical thickness, the solving of the system (2) for the given values n_a, n_b, E and γ becomes necessary.

Thus, a maximum number of twenty different solutions can be obtained. Besides the overall optical thickness, the spectral dependence of $E_m(g)$ must be investigated in order to select the most promising one. Among the matching stacks with low total optical thickness, those which better verify $E_m(g) \cong \sqrt{E_b(g) n_{ad}}$ have to be preferred. The solutions for which these admittances have different sense of variation around λ_m must be rejected.

If it is necessary to perform a matching procedure on both sides of the basic structure, one can obtain in our conditions $m \leq 3$ up to 400 solutions. According to the above discussed criteria, from each set corresponding to matching with the adjacent media only few solutions are selected. Combining the solutions of these reduced sets, several global solutions are obtained, for which the reflectance behaviour is calculated. In the final selection, the stop-band preservation (height and width) is taken into consideration, too. A detailed analysis on the criteria used in the selection procedure will be later published.³

3. EXAMPLE OF METHOD APPLICATION

Using this method a mirror for a high power Nd:YAG laser, with high reflectance band at $\lambda_0 = 1.064 \mu\text{m}$ and high transmittance band at $\lambda_m = 0.6324 \mu\text{m}$ was designed. The structure

$$\left(\frac{L}{2} H \frac{L}{2} \right)^{11} \quad (5)$$

was selected for the basic stack in order to provide lower ripple in the shorter wavelength region. The used materials

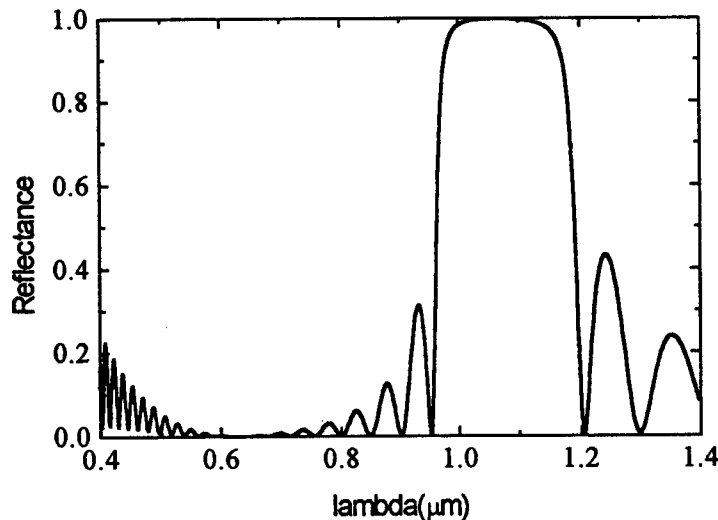


Figure 3. Spectral dependence of the reflectance for the matched structure

were ZrO_2 ($n_H = 1.91$) and SiO_2 ($n_L = 1.45$) deposited on a Nd:YAG crystal ($n_s = 1.82$). Since the equivalent refractive index of the basic stack at λ_m is 1.24 the matching with both surrounding media is necessary and the constant B is negative on the air side and positive on the substrate side. For a matching stack of the form $(aL bH aL)^n$ with $m = 1 \div 3$, a number of twenty solutions were obtained and for each of them, the dependence of the matching stack equivalent index versus g were calculated. For the final decision, the spectral dependence of the reflectance for the entire system *air-matching stack-basic stack-matching stack-substrate* (Figure 3) was computed. Thus, the lowest reflectance in the considered spectral range was obtained for the structure

$$\text{air } (0.541L \ 0.704H \ 0.541L)^1 (0.5L \ H \ 0.5L)^{11} (0.472L \ 1.279H \ 0.472L)^1 \text{ substrate} \quad (6)$$

with $m = 1$, σ_s and σ_b being both negative on the air side and positive on the other one.

REFERENCES

1. A. Dincă, M. E. Trifan, V. Lupei, M. P. Dincă, "Dichroic mirror design by complete admittance matching", *Opt. Eng.* **35** (5), 1284–1287 (1996).
2. A. Dincă, P. T. Miclea, V. Lupei, M. P. Dincă, "Regularities observed among the solutions obtained for optical admittance matching", *Proc. Suppl. Balkan Physics Letters* **5** (1997), in press.
3. A. Dincă, P. T. Miclea, V. Lupei, T. Skettrup, M. P. Dincă, "Multiple solutions provided by analytical synthesis in admittance matching: application to dichroic mirrors", *J. Mod. Optics* (June 1997), in press.

Yield optimisation of multilayer optical coating by modelling of monitoring process

G.L.Muscalu

Pro Optica ,str.Bucovina,nr.4,74404,Bucharest

ABSTRACT

In this paper,one investigated the yield of some optical coatings with a nonquarterwave structure within the classical vacuum systems by modelling of the monitoring process.The correlation of the synthesis and modelling process, allows to set the optimum monitoring process for different types of coatings.The experimental results tested on antireflection coatings are according to the theoretical ones.

Keywords : modelling of monitoring process,photometer, photometric monitoring wavelengths ,yield of a coating production

1.INTRODUCTION

To produce some optical coatings with a nonquarterwave structure within a vacuum system equipped with a classical photometer working at a single wavelength,with as high as possible yield,is a difficult problem¹. The coatings with such structures are actually produced by using the wideband monitoring system ,based on fast scanning spectrophotometers connected to computers operating in a real time². However,the classical photometric systems are still usable also for producing of some nonquarterwave structure coatings^{1,3}. To increase the production yield, assumes the modelling of the monitoring process to produce coatings within the respective vacuum system⁴. The deduction of the optimum monitoring strategy by using the elaborated model can be done during the coating synthesis³ or after it⁴.

In this paper one shows the optimisation process of one coating production yield by using a classical photometer operating at a single wavelength and it consists in correlating the synthesis and modelling process necessary for monitoring the coating production.The method provides the partial compensation of the classical deficient mode,for producing an optical coating (without monitoring in a real time)⁵.

2.MODELLING OF FOTOMETRICAL PROCESS AT A SINGLE WAVELENGTH

The model takes into account the following types of static errors : in the refraction index value of the vacuum and air layer as well as in determining the final value of the monitoring parameter. The errors of the layer refraction index value were considered only of a random type. In the monitoring parameter value,both random and systematic errors were considered ; a total positive error implies the overshoot of the final value of the monitoring parameter and the negative one implies its undershoot. The random errors were described as usual by a normal distribution having a zero mean and a corresponding standard error (experimentally determined)⁴.The method presumes that for each "i" layer on the test plate,the realized thickness is the result of thickness and index errors in the previous layers and of inherent errors of the same type in the actual layer.The real thickness of each layer is calculated starting from the determined value of its thickness on the monitoring plate by means of the configuration factor.

Based on this model within the afferent calculating programme,the process was divided in two stages :

-stage I - the actual layer thickness is the result of the disturbances inside the previous layer index and thickness and inside its index ;

-stage II - the actual layer thickness is the result of the disturbances inside the monitoring parameters at its end.

Taking into account the variation mode of the monitoring parameter related to thickness,periodic variation with upper and lower limits,measurement specific character and error sizes during the process,the following four possible situations are treated :

-turning value monitoring - the value of the monitoring parameter is attainable both in stage I and in stage II ;

-level monitoring method - the value of the monitoring parameter is attainable both in stage I and in stage II ;

-level monitoring - in stage I the value of the monitoring parameter is unattainable.The monitoring parameter passes through an extreme before attaining the predetermine value ; as a result the undisturbed value of the monitoring

parameter is replaced with its value in extreme;

-level monitoring following - the value of the monitoring parameters attainable in stage I becomes unattainable in stage II ; the value is changed according to the significance of the error sign above mentioned.

3. OPTIMISATION METHOD OF PHOTOMETRIC MONITORING PROCESS

The study of the coating monitoring process intends to produce a coating with properties within the pre-determined limits in the vacuum system at a maximum yield. For this reason, the method developed within this paper uses the modelling of the monitoring process and tries to find the optimum combination of structure - monitoring strategy. The method organigramme for studying the process is given in Fig. 1.

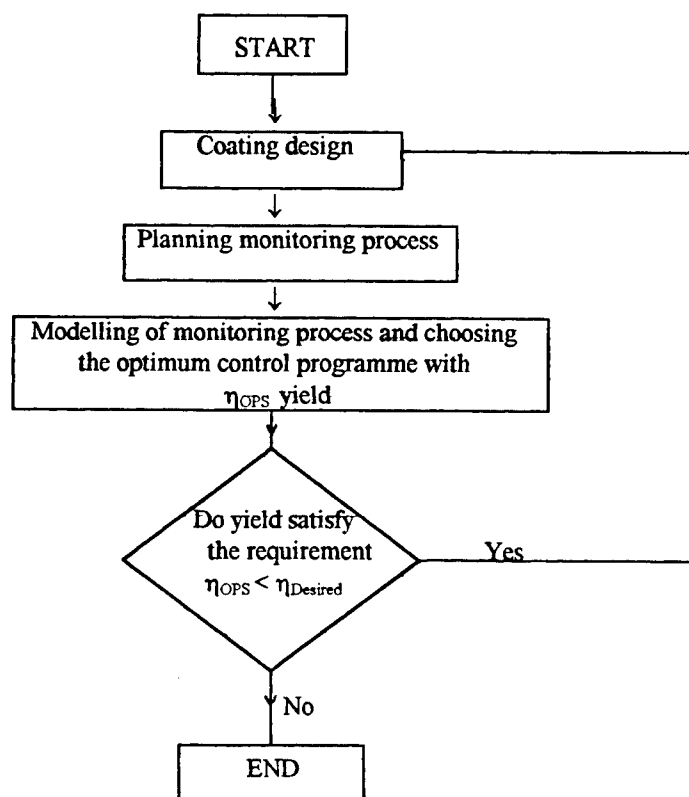


Fig.1 Optimisation method organigramme for photometric process

So, as a result of the synthesis activity specifically developed, one can get the structure meeting the imposed properties. Further, the study of the monitoring process contains two stages : to plan the monitoring process and to choose the optimum monitoring programme for the given structure (yield η_{OPS}). If $\eta_{OPS} < \eta_{Desired}$ the coating structure is changed and the process is retaken until it attains the yield desired value ($\eta_{Desired}$).

During the planning process one proposes to choose the photometric monitoring wavelength as those for which the thickness measurement uncertainty, σ_t is minimum. This definition takes into account the definition of the most sensitive wavelength of the respective literature (values $\partial R/\partial t$ or $\partial T/\partial t$) great⁶ but it makes it complete considering both the features of the used photometric system (σ_{Nm}) and the other parameters ($\partial P/\partial n$).

Indeed, taking into account the measurement of the layer thickness by using a classical photometer, the measurement process ends when the value of the monitoring parameter at the respective wavelength $P_m(\lambda)$ attains the predicted value P_t :

$$P_m(\lambda) = P_t(n, t, \lambda) \quad (1)$$

with n, t, λ representing the refractive index, the thickness and respectively wavelength.

Based on the calibrating relation, the equation (1) is written :

$$N_m(\lambda) = N_t(n, t, \lambda) \quad (2)$$

with $N_m(\lambda)$, $N_t(\lambda)$ representing the adequate values of the monitoring parameter expressed in scale divisions.

Out of the relation (2) one can infer the expression for the thickness measurement uncertainty (σ_t) depending on the uncertainty of determining the monitoring parameter in division (σ_{Nm}) and the uncertainty of measuring the layer refraction index (σ_n).

$$\sigma_t^2 = \frac{\sigma_{Nm}^2 + \left(\frac{\partial N_t}{\partial n} \right)_\lambda \cdot \sigma_n^2}{\left(\frac{\partial N_t}{\partial t} \right)_\lambda} \quad (3)$$

$$\left(\frac{\partial N_t}{\partial t} \right)_\lambda = \frac{N_i}{P_i} \cdot \left(\frac{\partial P_t}{\partial t} \right)_\lambda \quad (4)$$

$$\left(\frac{\partial N_t}{\partial n} \right)_\lambda = \frac{N_i}{P_i} \left(\frac{\partial P_t}{\partial n} \right)_\lambda \quad (5)$$

with P_i, P_t the values of the monitoring parameter (R/T) at the beginning, respectively at the end of the layer execution.

The determination of the photometric monitoring wavelengths just as above, leads to the increase of the thickness measuring precision according to the simulations done, reflected in a decreased value of thickness standard deviation.

The selecting criterion proposed for choosing the optimum monitoring programme is the yield obtained as a result of simulating the monitoring process errors developed according to the conceived programme. The simulation uses the developed model, the values of the respective errors being experimentally determined.

4. APPLICATIONS AND EXPERIMENTAL RESULTS

By means of the above-mentioned method, one optimised the yield of producing some antireflection and filter coatings under classical vacuum systems that use photometric monitoring method at a single wavelength. As a title of example, let's consider the yield optimisation of optical coating with the following structure :

$$S|k_1 H k_2 L k_3 H k_4 L k_5 H k_6 L k_7 H k_8 L|A \quad (6)$$

with $n_H=2.02, n_L=1.385, k_1=0.135, k_2=0.556, k_3=0.380, k_4=0.436, k_5=0.821, k_6=0.192, k_7=0.702, k_8=1.026, \lambda_d=550\text{nm}$.

The main elements considered in choosing the free parameters of the photometric process were: equipment implementing the photometric method within vacuum installation (GSM 210 photometer), features of photometric monitoring process according to references data⁴, coating structure and definition adopted for photometric monitoring wavelengths. Three monitoring programmes were developed based on it; their features and the production yield deduced by modelling of the monitoring process are given in Tab.1. The standard deviation of the considered vacuum and air refraction indexes were experimentally determined : $(\sigma)_{ZrO_2}=0.02$ respectively $(\sigma)_{MgF_2}=0.001$. The errors of determining the reflection factor at the end of each layer (σ_{R_i}) were calculated based on the relation :

$$\sigma_{R_i} = \frac{R_i}{N_i} \sigma_{N_i} \quad (7)$$

deduced from photometric measuring equation; N_i is the photometer indication value corresponding to the layer starting reflection R_i , and (σ_{N_i}) is the uncertainty of displayed indication value on the photometer monitor; in calculation, (σ_{N_i}) was considered 1.

Tab.1 Main Monitoring Programmes and some of their Features

Monitoring Programme No.	Seq. No. of Test Plate	Seq. No. of layers on test plate according to structure counting	Monitoring wavelengths	Yield for criterion $R_{(440-650)} \leq 0,3\%$
1	1	1...8	355	40%
2	1	1...4	401	60%
	2	5	377	
	3	6	401	
	4	7	546	
	5	8	401	
3	1	1...4	401	50%
	2	5...7	377;377;441.	
	3	8	401	

The data used in calculation are given in Tab.2.

Tab.2 Constants values used for obtaining the data of Tab.1

Material	Sellmeier Dispersion Coefficients				Ratio of geometrical thickness in a vacuum-air transition
	under vacuum		in air		
	A	B	A	B	
Zr O ₂	3.220	107.0x10 ³	3.62	135.2x10 ³	1.10
Mg F ₂	1.918	0	1.907	0	1.18
support BK 7	2.263	12.8x10 ³	2.263	12.8x10 ³	-

By analysing the results of the programme 2, one note that the greatest errors are obtained in monitoring of the layer 7; as a result a decision was taken for the layer to pass from level monitoring to turning value monitoring with overshoot error and it needs a coating redesigning. The optimisation programme was used with the method of the damped least squares with restrictions on the thickness of layers 7 (because the new monitoring mode) and 1 (small thickness of a layer). An antireflection coating with similar optical features was obtained; the geometrical thickness of the coatings layers (they are numbered from the substrate) deduced after the optimisation are: 9.3; 59.1; 25.0; 44.4; 57.8; 13.9; 54.2; 98.9. For the new structure, an optimum monitoring programme 3 was elaborated (Fig.1). The monitoring is indirect and it uses five control plates (for the layers of 1..4, respectively 5,6,7,8), the monitoring wavelengths being 401, 377, 401, 360 and 420. The coating yield for the criterion $R_{(440-650)nm} \leq 0.3\%$ is 95%. The results of error simulation is given in Fig.2.

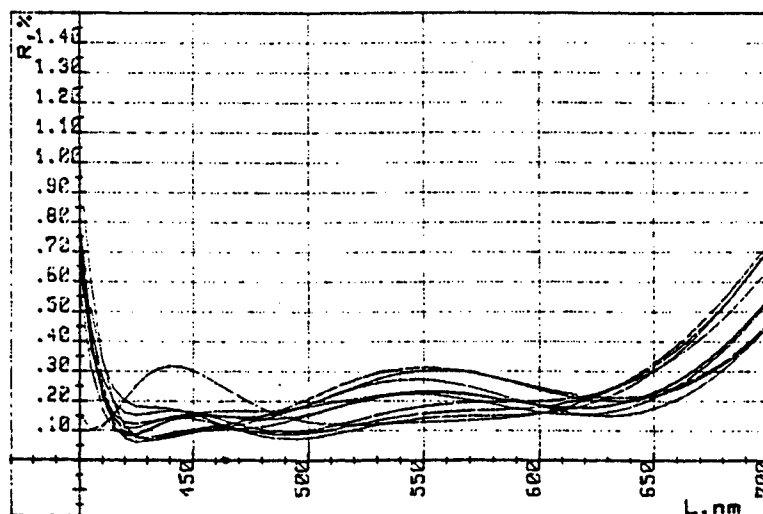


Fig.2 Result of error simulation during the monitoring process for production antireflection coating according to the monitoring programme 3

With an experimental coating (BAK 550,GSM 210 photometer) the yield for obtaining the spectral feature with $R_{(440-650)\text{nm}} \leq 0.35\%$ in 20 cycles was 95 % (Fig.3).

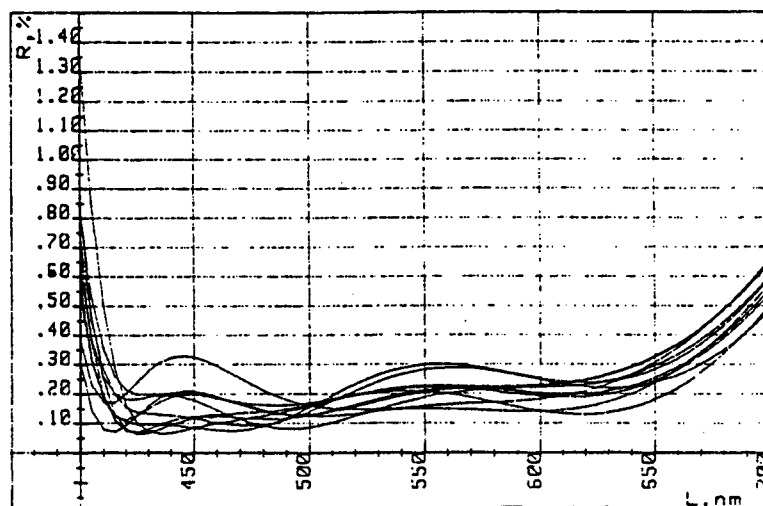


Fig.3 Reflection factor of antireflection coatings, experimentally produced according to the monitoring programme 3

The result confirm the possibility of the yield optimisation for producing a coating by modelling the monitoring process and its correlation to the synthesis process.

5.CONCLUSIONS

In this paper, by modelling of the photometric process at a single wavelength, the coating yield was optimised by means of the correlation of the synthesis and optimisation process. The proposed method provides the partial compensation of the classical deficient model for producing an optical coating (without monitoring in a real time). The application of the method in the case of the yield optimisation for production a wide band antireflection coating in the visible spectral range led to good results: yield >95 % for $R_{(440-650)\text{nm}} \leq 0.35\%$ according to experimental results.

6. REFERENCES

1. C.J. van der Laan, "Optical monitoring of nonquarterwave stacks", *Applied Optics*, Vol. 25, No. 5, pp. 753-760, 1986
2. B.T. Sullivan, J.A. Dobrowolski, "Deposition error compensation for optical multilayer coatings II. Experimental results-sputtering system", *Applied Optics*, Vol. 32, No. 32, pp. 2351-2360, 1993
3. 4. Y.F. Zheng, J.F. Tang, "New automatic design technique for optical coatings", *Applied Optics*, Vol. 26, No. 8, pp. 1546-1549, 1987
4. H.A. Macleod, "Monitoring of optical coatings", *Applied Optics*, Vol. 20, No. 1, pp. 82-89
5. D.E. Efremov, "Printipi postroenia automatizirovannoi sistemi upravlenia izgotovleniem tonkosloinich pokritii", *O.M.P.*, No. 7, pp. 23-24, 1979
6. J.A. Dobrowolski, "Versatile computer program for absorbing optical thin film systems", *Applied Optics*, Vol. 20, No. 1, pp. 74-81

Interferential filter design with continuously variable refractive index

Andreea Dincă, Voicu Lupei

National Institute for Laser, Plasma and Radiation Physics
Solid State Quantum Electronics Laboratory
P. O. Box MG-36, RO-76900 Bucharest, Romania

Mihai Dincă

University of Bucharest, Faculty of Physics
P. O. Box MG-11, RO-76900 Bucharest, Romania

ABSTRACT

The paper briefly presents an original method for design of inhomogeneous thin films which takes into consideration from the beginning the finite character of the optical thickness. At the beginning, the best solution is obtained in terms of the value of a complex function on a certain spectral grid. At the second step, the design is converted in terms of refractive index profile. Special care is taken to minimize the variations of this profile. Then, a program using this method, written as Windows application, is described together with a design example providing a spectral dependence of the reflectance having the shape of Romanian Athenaeum building.

Keywords: optical coatings, inhomogeneous films, inverse Fourier transform method, finite optical thickness

1. INTRODUCTION

In the early works of Delano and Pegis,^{1,2} where the Fourier transform method for inhomogeneous films synthesis was proposed, the finite thickness of the inhomogeneous layer was taken into consideration and, exploiting the sampling theorem, the spectral functions were expressed by their values on a certain grid. However, subsequent developments of the method introduced the finite character of the optical thickness at an intermediate design step and took no advantage of the special properties of spectral functions. A new method which considers from the first begin the finite character of the optical thickness, was recently proposed³ and its efficiency in design inhomogeneous layer with almost any arbitrary reflectance profile was demonstrated. Here, we will briefly review the method basis and present the computer program written for design inhomogeneous layers by using this method, together with an example of interferential filter design.

The index profile is expressed by function $n(\delta)$ where δ is twice the optical thickness variable. An important role has the function

$$q(\delta) = \frac{1}{2} \frac{d[\ln n(\delta)]}{d\delta} \quad (1)$$

and its Fourier transform

$$Q(k) = \int_{-\infty}^{\infty} q(\delta) \exp(2\pi i k \delta) d\delta \quad (2)$$

where $k = 1/\lambda$ is the wavelength number. Due to finite total optical thickness, denoted by Δ , the $Q(k)$ function can be expressed by its values, Q_m on a grid $k = m/(2\Delta)$ with m integer as

$$Q(k) = \sum_{m=-\infty}^{\infty} Q_m \operatorname{sinc}[\pi(2k\Delta - m)] \quad (3)$$

Thus, for any sequence Q_m , the corresponding index profile has a total optical thickness equal or less than Δ . The Q_m complex numbers are the natural freedom degrees in the search for an index profile which comes closest by the required performances. Moreover, for low reflectance values, the Q function can be simply expressed by $f_2 = r/t$, where r and t are the reflection and transmission coefficients, respectively

$$Q(k) \cong f_2(k) \quad (4)$$

On its turn, $f_2(k)$ may be expressed by its values f_{2m} on the grid points

$$f_2(k) = \sum_{m=-\infty}^{\infty} f_{2m} \text{sinc}[\pi(2k\Delta - m)] \quad (5)$$

The numbers f_{2m} are the freedom degrees for the reflectance curve which can be reached with the finite optical thickness Δ .

2. METHOD DESCRIPTION AND APPLICATION

The proposed method consists of two steps. First, the f_{2m} numbers are modified till the corresponding reflectance curve fulfill the requirements. At this stage, an optimal phase algorithm proposed by Guan,⁴ can be used in order to assure low variations in the resulting index profile. At the second step, this sequence is converted in an index profile. Since no exact relationship between f_2 and Q exist, the conversion is made by using the approximate equation (2) and then the Q_m sequence is corrected with a procedure similar with that proposed by Sossi.⁵ At last, the obtained index profile provides a reflectance curve practically identical with that found at the first method step.

Since by expressing the synthesis solution in terms of f_{2m} assures that the total optical thickness will be less or equal to Δ , the conversion which has to be performed at the second step is always possible. Its accuracy is limited only by the number of the homogenous layers used in discretization of the continuous index profile. We found that with this number equal or greater than $8\Delta k_0$, where k_0 is the central wavenumber in the interesting spectral range, the conversion accuracy provides reflectance curves practically identical with those predicted in the first step.

For method application, a computer program has been written as Windows application using Borland Delphi. The program consists of three units, each of them corresponding to a graphical forms which is displayed and the user can interact with.

In the TARGETS unit the requirements on the reflectance profile are set. Each target consists in a spectral range, the maximum and minimum reflectance. In Figure 1 is presented the graphical form. The targets can be edited either numerically, in a table, or graphically by selecting and dragging with the mouse on the plot. The user can select to display the table, the plot or both. Using the form menu the target set can be saved and loaded as a target file. When the target editing is accomplished the user updates the targets in the main unit and the synthesis process can be continued. The form buttons, which can be operated by mouse, have suggestive pictures and, in the same time, when the mouse passes over them explicit hints are displayed, making the interaction with this form very friendly.

In the F2 unit the f_{2m} numbers are modified until the corresponding reflectance curve meet the requirements stated by the targets set. The graphical form is shown in Figure 2. The total optical thickness (TOT), and consequently the grid step, as well as the positions number between two grid points where the reflectance is checked can be interactively modified. All buttons have the features above described and the interaction with his form is friendly, too.

The MAIN unit makes the conversion of f_{2m} numbers previously found into a refractive index profile using the algorithm above mentioned. Due to specific way in which the design was made at the first step, the conversion is always possible with the imposed total optical thickness. From here all options an results can be saved or loaded as project files. Also, the program automatically saves at exit the options and results in a WORK project file which is loaded at the new start. From the MAIN form the TARGETS or F2 forms can be called, allowing a very flexible navigation during the synthesis.

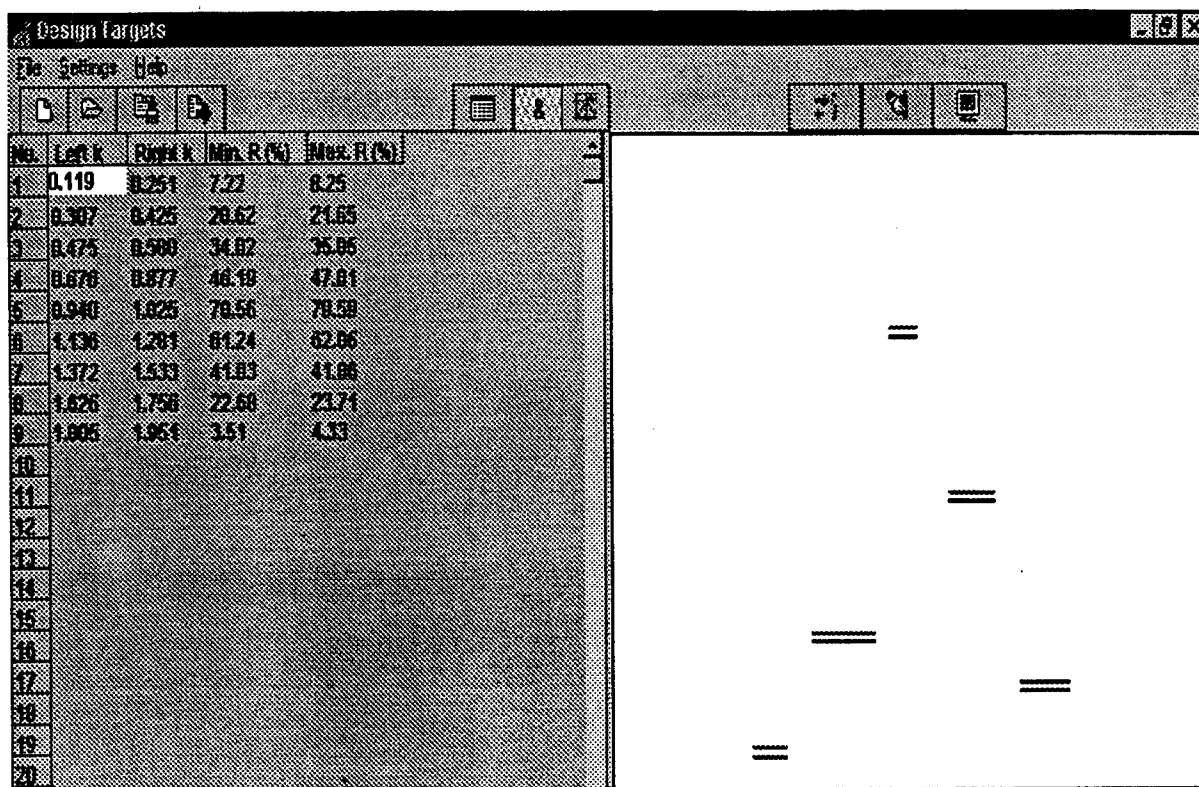


Figure 1. Graphical form of the TARGETS unit

Using this program a sharp stop-band filter with reflectance 0.9 between 0.95 and 1.05 μm and less than 0.002 beyond this interval was designed. The total optical thickness was imposed to be 40 μm . In Figure 3 are represented the values of numbers f_{2m} , as obtained in the first method step and after the conversion performed at the second step. Figures 4a and b present the obtained reflectance and the corresponding index profile, respectively.

In order to test the capability of the program to synthesized almost any arbitrary reflectance dependence, an interferential filter having a spectral dependence of reflectance of the shape of Romanian Athenaeum building was designed with a total optical thickness $\Delta = 12.5 \mu\text{m}$. Figure 5 present the index profile and corresponding reflectance, respectively.

REFERENCES

1. E. Delano, "Fourier synthesis of multilayer filters", *J. Opt. Soc. Am.* **57**, 1529–1533 (1967).
2. E. Delano, R. J. Pegis, "Methods of synthesis for dielectric multilayer filters", *Progress in Optics* **7**, 67–137 (1969).
3. A. Dincă, "Optical components with distributed properties performed by vacuum deposition", PhD Thesis, Institute of Atomic Physics, July 1996 (in Romanian). A resume of the PhD thesis translated in English is available on request from author.
4. S. Guan, R. T. Melver, "Optimal phase modulation in stored wave from inverse Fourier transform excitation for Fourier transform mass spectrometry. I. Basic algorithm", *J. Chem. Phys.* **92**, 5841–5844 (1990).
5. L. Sossi, "A method for the synthesis of multilayer dielectric interference coatings", *Eesti. NSV Tead. Akad. Toim. Fuus. Mat.* **23**, 229–237 (1974).

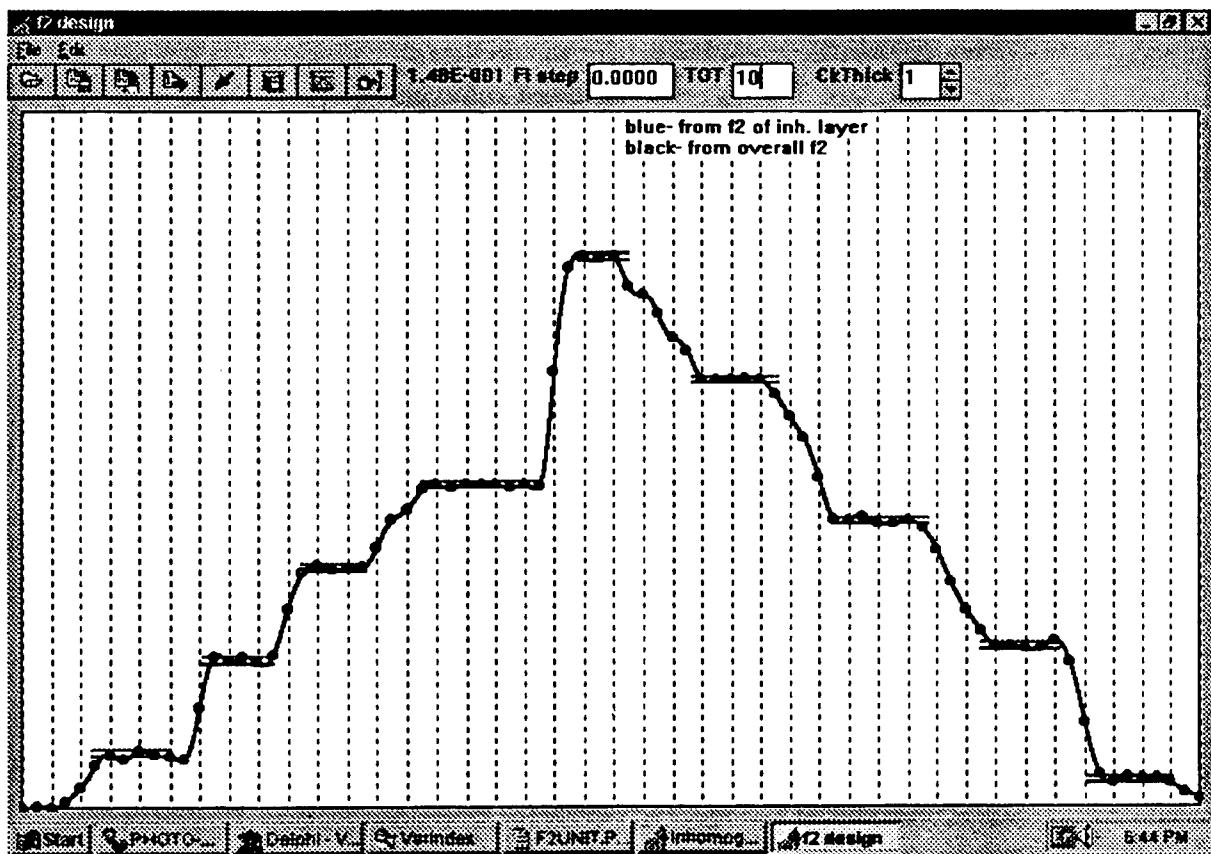


Figure 2. Graphical form of the F2 unit

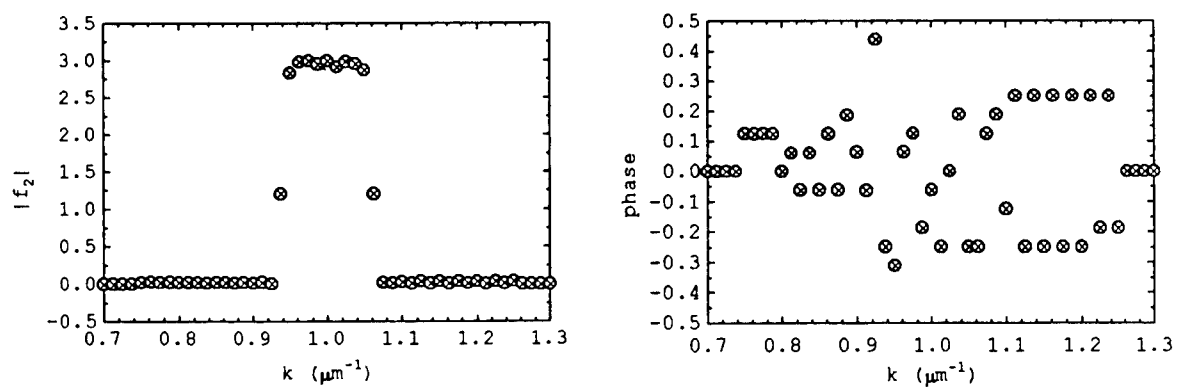


Figure 3. Set of complex numbers f_{2m} obtained at the first method step (circles) and after conversion performed at the second step (cross)

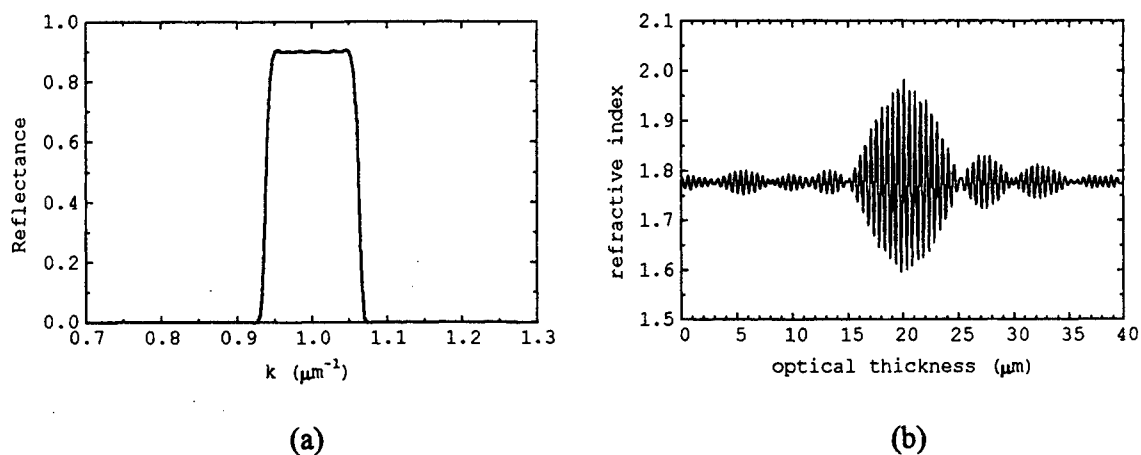


Figure 4. Dependence of the reflectance (a) and refractive index profile (b) for the designed stop-band filter

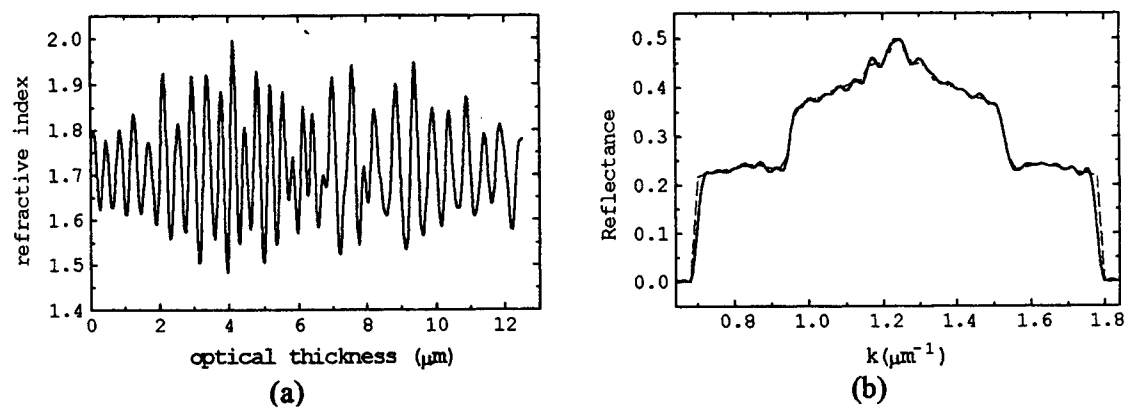


Figure 5. Interferential filter with a reflectance curve having the shape of Romanian Athenaeum building: (a) refractive index profile; (b) required (dashed line) and obtained (solid line) reflectance

Filters with induced transmission

Honciuc Gheorghe
S.C. Pro Optica S.A., Bucharest,
Aleea Bucovina, nr. 4, 74404, Romania

ABSTRACT

Some problems appeared during the production of induced transmission filters are analysed in the case of some technological limits. One can reveal the dependence between the performances of induced transmission filters and production technological parameters. The experimental results are compared to those ones characteristic to other types of narrow band interference filters.

Keywords: Optical coatings, narrow band transmission filters.

1. INTRODUCTION

The advantages of interference filters with induced transmission (IT) are well known opposite to the other type of interference filters with narrow band transmission. These advantages are: no side bands of transmission; great peak transmission; a very good blocking; a very clear transition between transmission and blocking spectral zones.

The IT filters can also form combinations with some other types of narrow band interference filters (generally all dielectric Fabry-Perot interference filters - ADFP) to get superior performances.

The theory and methods for designing IT filters are well known^{1,2,3}, as there are certain articles^{2,3,4,5} where some aspects concerning the production of these filters are shown.

All the optical coatings further analysed contain thin layers of the following materials:

- zinc sulphide (ZnS) considered dispersive, absorbent under 430nm and it is referred to in coating structures by H (quarter wavelength optical thickness);
- cryolite (Na_3AlF_6) considered nondispersive, nonabsorbent, and it is referred to in coating structures by L (quarter wavelength optical thickness);
- silver (Ag) dispersive, absorbent⁶ and it is referred to in coating structures by M (nd = quarter wavelength optical thickness, $n=n-ik$);

The solutions for IT filters are:

$$\begin{array}{lll} \text{IT}_1 & (\text{HL})^3 0.765\text{L } 0.03\text{M } 0.765\text{L } (\text{LH})^3, & \lambda_0=550\text{nm} \quad (\text{I}) \\ \text{IT}_2 & (\text{HL})^3 2.765\text{L } 0.03\text{M } 2.765\text{L } (\text{LH})^3, & \lambda_0=550\text{nm} \quad (\text{II}) \end{array}$$

with the spectral transmission factors shown in Fig. 1.

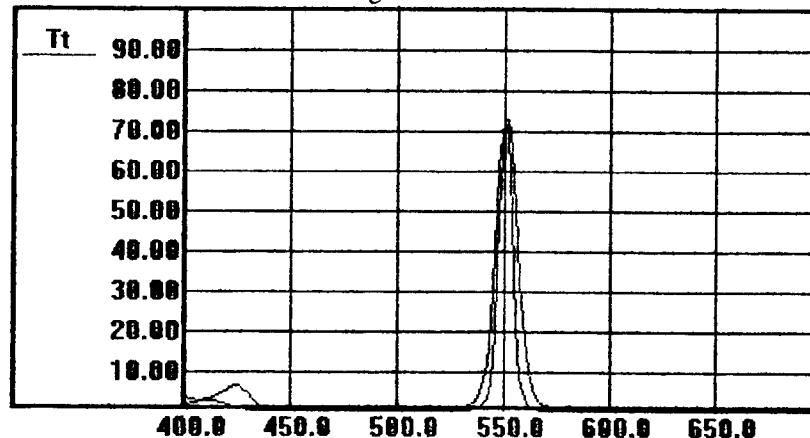


Fig. 1 Spectral transmission for IT_1 and IT_2 filters.

2. EXPERIMENT

The optical coatings have been performed on an AVI 80 FAN - Romania vacuum installation specially equipped for this type of coatings, the measuring system being formed of a GSM 210 Balzers photometer connected to a digital voltmeter and an Oriel Corporation Model 7420 monochromator. One can notice the evaporation of zinc sulphide and cryolite of their tantalum sheet crucibles with 0.1mm in thickness with a shape similar to Balzers DB 482054 type and of silver of its tungsten crucible with 0.1mm in thickness with a shape similar to Balzers DB 482051 type. The measurement has been performed in transmission on a fixed test glass (all layers⁵) by turning-value monitoring method and the elements are rotating around the symmetry axis of the evaporating geometry (see Fig. 2). All the layers are monitored at a wavelength λ , except the first nonquarterwave layer monitored at wavelength $\lambda_1 < \lambda$ (due to the phase shift on the silver layer undeposited yet). All the dielectric layers were monitored following the extremes. The stopping of the evaporating process are made by hand. The silver layer was produced in maximum 15 seconds, the material being firstly heated at the evaporating regime under a shutter screen. Because of the evaporating rates relatively great and of the manual stopping of the evaporating process, it is possible that the silver layer should be produced with some errors. These errors influence the filter transmission. By little experience, this layer can be monitored within the reasonable limits. One can check up if the geometric thickness of the silver layer was realised by measuring the reflection factors of the coating on both sides. For the theoretical thickness, the reflection factors for the center wavelength must be zero. If there are errors at this layer, it is better that they lead to experimental thickness greater than the theoretical ones. The pressure inside the technological chamber was lower than 2×10^{-5} mbar. As it has already been said, the monitoring of the optical coating is achieved on a single test glass on which all the layers are deposited. The advantages of this method have been already presented in various papers^{4,5}, that's why we do not insist on them. One can notice that in a measuring system, a monochromator is very useful.

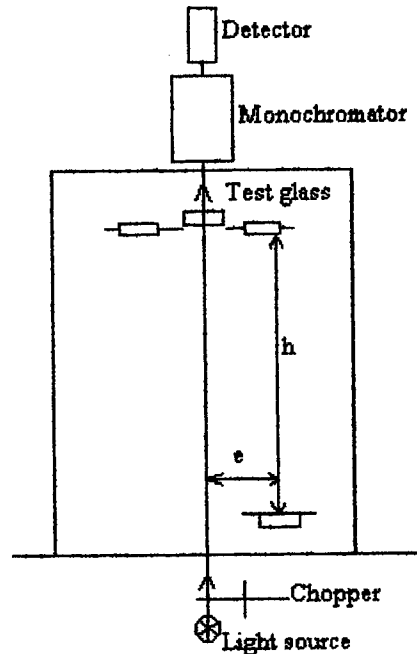


Fig. 2 Experimental geometry

3. INFLUENCE OF PHOTOMETER SENSITIVITY

Unlike the case of filters ADFP⁵, the compensation of error is not done in the same manner. The errors produced in the dielectric layers that are preceding the metallic layer cannot be compensated by the dielectric layers that are following the metallic layer. If at the producing of the metallic layer, the signal measured cannot be changed with minimum one specified range (meaning that the first cavity was achieved at the desired wavelength), then the process for producing the rest of layers must be abandoned because they cannot compensate the errors of the first package of dielectric layers. This may happen either when λ_1 is not correct or when the photometer sensitivity is low. So, each layer must be produced with a maximum precision, being a minimum precision imposed by the reproductibility of the technological process. As the monitoring of coating is achieved by following extremes, the precision for producing a layer is as greater as the variation of the measured signal is greater during the production of the layer. It imposes the use of a photometer at maximum sensitivity for the monitoring of each layer. To determine the minimum variation range of the measuring signal for each layer, one can simulate the measuring

process where the errors considered are those closely related to the stopping of the evaporating process (extreme detection closely related to the photometer sensitivity and to the operator's errors).

An interference filters is as better as its bandwidth is smaller and it presents a passing as clearer as possible between the spectral zones of transmission and blocking and also a transmission as greater as possible. The filter performances increase if the number of dielectric layers increases having e.g. the following solution:

$$(HL)^4 1.765L 0.038M 1.765L (LH)^4, \quad \lambda_0=550nm \quad (III)$$

If a minimum variation of the measured signal is imposed at the achievement of each layer, e.g. of 100 div/digits, using a GSM 210 photometer type which has a scale of 600 div for maximum sensitivity (the maximum signal obtained during the production of a layer is of 600 div), one can notice that the number of layers of solution (I, II) cannot be surpassed. The solution with $(HL)^4$ imposes a photometer with a scale of 1000div. at a maximum sensitivity. It is important that this sensitivity should be ensured for the whole spectral range where the filters are produced. The solution with a great number of layers can be used even in the existing endowment but with a high technological rejecting coefficient. The above mentioned considerations are also valid for the multicavity total dielectric interference filters .

4. INFLUENCE OF EVAPORATING GEOMETRY

The geometrical thickness on the test glass and on the substrate can be different, the ratio between them being called the coefficient of the evaporating geometry.⁷

$$C = (\text{thickness on substrate}) / (\text{thickness on test plate})$$

To have a better correspondence between the optical coating on the test glass and on substrate, it is better for C to be as close to 1 as possible. The more different from 1 C is the lower performance of the coating on the substrate is, due to the dispersion of the used materials.

Because the section of the light beam on the test plate is not neglectable, one must also take into account the nonuniformity on the test glass. It is better that the section of the light beam on the test glass should be as smaller as possible and if it is not circular (e.g. the image of a filament), the length of the section should be positioned on the uniformity direction. The uniformity on the test glass is maximum when $e=0$, a nonpractical solution because there are three fixed crucibles and for this value of e the nonuniformity on the substrate is great (on the substrate, the uniformity increases for $e > 0$). Also, the uniformity on the test glass and on the substrate increases if h is great. Even if for the great values of h , there is a greater consumption of material, the technological advantages are great. The shape of the crucibles for zinc sulphide and cryolite imposes that the solid angle pointing the crucible and including the substrate during the rotation should be as smaller as possible. (the sources are different from a flat source, also, because of the evaporation of the crucible material, it is possible that C should be changed during the evaporation process and also it is better that the incidence of the vapours on the substrate should be as closer as to the normal).

The uniformity on the test glass is important peculiarly for zinc sulphide and cryolite due to the nonuniformity which for these layers influences the filter performances as much as possible. If there is a nonuniformity at the layers of these materials it is better that this nonuniformity should be as lower as possible and the nonuniformities of the layers should be identical (nonuniformities of the same magnitude but differently positioned lead to more important nonuniformities of coatings). So, the crucibles for zinc sulphide and cryolite must be put as closer as possible to each other without "seeing" each other.

A solution for all the problems is that the test glass should rotate around the symmetry axis of the evaporating geometry. However it imposes that the parallelism of the test glass surfaces should be very good (without producing deviation of the light beam which by rotation can modulate the measured signal) and its rotation should be without errors. The incidence angle of the light beam on the test glass should be constant. If the incidence angle on the test glass is changed, then at the achievement peculiarly of the layers in the second half of the optical coating (with a maximum at the last layers), we have a modulation

of the intensity of the light beam that makes difficult the detection of the extremes where the evaporation stops.

The nonuniformities of the layers made of zinc sulphide and cryolite on the substrate are practically the same (the shape of the crucibles and the values of e and h are coinciding). The nonuniformity on the substrate leads to a maximum diameter for the interference filters that can be produced in a certain evaporating geometry. To impose a maximum given variation $\Delta\lambda$ for λ_0 on the filter surface means to impose a nonuniformity allowed on the filter surface, so a limitation of the filter surface. The evaporating geometry must be optimised (e, h , the rotating radius of the substrate, the tilting angle of the substrate to the horizontal) in order to have C as closer as possible to 1 and uniformity imposed by $\Delta\lambda$. To increase the uniformity on the substrate, a planetary movement can be given to it.

5. EXPERIMENTAL RESULTS

The evaporating geometry used has the following parameters: $h=395$, $e=110$, the rotating radius of the substrate $r=50$, the tilting angle of the substrate $\alpha=11^\circ$. The selection of these parameters was limited by the constructive parameters of the technological chambers of the vacuum installation AVI 80. The maximum diameter of the filters that can be produced in this geometry and have a variation $\Delta\lambda$ for λ_0 on the filter surface smaller than 4nm, is of 25mm. In the Fig. 3 one can see the spectral transmission of a filter with an induced transmission produced in the above mentioned conditions as well as a metal-dielectric-metal filter (MDM) by comparison.

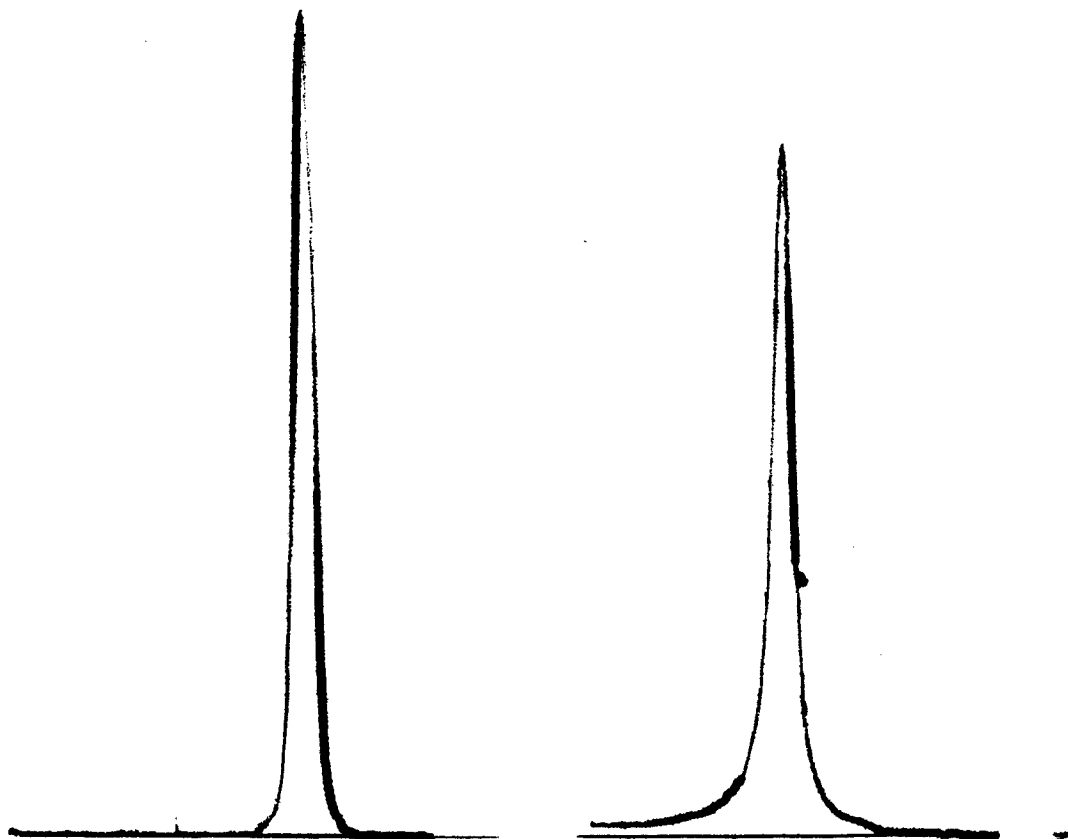


Fig.3 Transmission factors for IT and MDM filters.

As one can see of the Fig. 3, the advantages of IT filters related to MDM filters are: a better transmission (T_0) for the central wavelength and a narrow bandwidth between the points with $T=T_0/50$.

The spectral range where the filters can be executed on the installation AVI 80, is 430 - 1070nm, with a very good reproductibility in the spectral ranges where the sensitivity of the measuring system is great (photomultiplier sensitivity and transmission of measuring optical system are great, providing an indication of 600 div for the maximum signal obtained during the achievement of each layer), the reproductibility increasing with the increasing of the measuring system sensitivity.

6. REFERENCES

1. R.J. Holloway and P.H. Lissberger, "The design and preparation of induced transmission filters", *Appl. Opt.* **8** (3), pp. 653-660, (1969).
2. John Macdonald. *Metal-Dielectric Multilayers*, Adam Hilger Ltd, London, 1971.
3. P.H. Lissberger, "Coatings with induced transmission", *Appl. Opt.* **20** (1), pp. 95-104 (1981).
4. H. A. Macleod, "Absorption in turning value monitoring of narrow band thin-film optical filters", *Opt. Acta* **20**, pp. 493-500 (1973).
5. E. Pelletier, R. Kowalczyk, A. Fornier, "Influence du procede de controle sur tolerances de realisation des filtres interferentiels a bande etroite," *Opt. Acta*, **20**, pp. 509-513 (1973).
6. *American Institute of Physics Handbook*, pp. 6-116, McGraw-Hill, New York, 1963.
7. C.J. van der Laan, "Optical monitoring of nonquarterwave stacks", *Appl. Opt.* **25** (5), pp. 753-760 (1986).

Software for optical coatings design

Honciuc Gh.
S.C. Pro Optica S.A., Bucharest,
Aleea Bucovina, nr. 4, 74404, Romania

Singurel Gh.
Univ. "Al. I. Cuza" Iassy, Romania

ABSTRACT

A Windows 3.1 application is shown for editing, analysing, optimising, designing technologies and determining the optical constants out of the (R,T) measurements. A dynamic arborescent structure of data (optical coatings) has been used, allowing a great flexibility in describing the optical coatings. The optical coatings of the arborescent structure are defined on the same thin layers (defined in root), the change of a layer being detected by all the optical coatings of the arborescent structure, containing that layer. The layers are seen by coatings by means of some groups (structures) of layers and some scale factors, the groups being the elements that describe the coating. So, one can study an optical coating or parts of coating (e.g. optical monitoring) under different conditions.

Keywords: optical coatings design

1. INTRODUCTION

When one is designing an optical coating, a computer assisted programme for exploiting the new hardware and software facilities is a strong and indispensable tool. Such a programme must cover all the activities implied in the designing and manufacturing of optical coatings. The Windows 3.1 application, also called STRAT V5.1, written in Borland C 3.0 has been performed (The previous versions¹ have been written in FORTRAN 77 for a CORAL 4021 - PDP 11 minisystem). The functions of this software were created to be used in the optical industry for designing coatings and production technologies of optical coatings in a simpler and faster manner. To develop this software application, the following things were considered:

- that one who is exploiting the application, has enough knowledge in designing and producing optical coating;
- one can use only optical materials with relatively well controlled properties and for this reason, the optical constants are not considered as explicit variables;
- a considerable effort must be made to eliminate the errors of the fabrication process and to reduce their magnitude and not to take into account a great number of considerable error in the designing step;
- a user-computer interface must be friendly, simple and the application should be compatible with other applications used in the optical industry.

2. DATA STRUCTURE

Very important for this application is the data structure. Such a structure of data has been searched in order to describe so flexibly the types of optical coatings and to allow their study under various environments.

The data that describe the optical coatings have a dynamic arborescent structure. The first level is composed of root coatings. The first optical coating created is a root coating. Such a coating defines a structure of thin layers (of a solution type): number of layers, parameters of thin layers, group of layers, structures of thin layers that define the coating, optical material for layers, etc. It's possible to have more root optical coatings, so more solutions for the same problem in the same time. Starting from a root coating, one can define branch optical coatings defined on the layers and the optical materials of the root coating and they contain the structure or a part of the root structure. The branch optical coating can have other media of incidence, emergence, other angles of incidence, other polarisation state of the incident light and they can be

defined with a number of layers at most equal or smaller than that one of the root optical coating. Also, the layer materials of the branch optical coatings can have optical constants changed (n, k and dispersion). If a layer is changed in a coating, this change is seen by all the optical coatings of the arborescent structure containing (pointing to) that layer. In fact, the branch optical coatings have not their own layers, they are pointing to the layers of the root coating. The layers are seen by coatings by means of some groups (structures) of layers and some scale factors, the groups being the elements that describe the coating. The most commands of editing, analysis and optimisation can be done on the branch optical coating. The branch optical coatings cannot change the structure or parts of the structure of the root optical coating on which is defined. Each optical coating has its own windows through which the interface with the user is ensured.

More root optical coatings may exist. The root optical coatings are totally independent, between them as there is no connection as regards the optical coating structures (layers, materials, groups of layers, etc.). For example, it might be a root optical coating of a multilayer antireflection type and a root optical coating of a band-pass filter type.

3. APPLICATION FUNCTIONS

3.1 Editing

The optical materials are characterised by:

- type of material: homogeneous / inhomogeneous, respectively the parameters of equation describing inhomogeneity;
- type of equation of dispersion for n , respectively the coefficients of the equation of dispersion and the spectral range for which the equation of dispersion is valid;
- type of equation of dispersion for k , respectively the coefficients of the equation of dispersion and the spectral range for which the equation of dispersion is valid.

Each optical coating can use 10 optical materials (also including the substrate and the incidence medium). To each material corresponding a symbol (a letter) by means of which the material is referred in the structure of coating. E.g. for the materials:

TiO_2 - A, SiO_2 - B

the structure can be written as follows:

BAB 6(AB) A

In the case of this structure, there are 16 layers but they are classified in 6 groups as follows:

- group 1: layer 1
- group 2: layer 2
- group 3: layer 3
- group 4: layers 4, 6, 8, 10, 12, 14;
- group 5: layers 5, 7, 9, 11, 13, 15;
- group 6: layer 16.

The groups are the parameters that are to be optimised. They can be declared constant (the layers of that groups are not changed) or variable. The geometrical thickness of the group layers are scaled by a scale factor (e.g. a nonuniform coating can be studied). The branch optical coatings cannot have other groups but those defined in the root (so, they cannot define other structure but that defined in the root), excepting the branch optical coating on the test glasses. When the branch optical coatings on the test glass are generated, the root optical coating has redefined groups, each group containing a single layer because, by simulating the monitoring process, some errors of the layer geometrical thickness appear that make a total unmatching between layers and structure. Some structures can be preserved but this limits the disposal of the layers on the test glass and the liberty of producing errors (simulated).

Each layer has limits for the geometrical thickness. The inhomogeneous layers are considered to be composed of a specified number of elementary homogeneous layers with a constant index given by the position of the elementary layer in the inhomogeneous layer.

Symmetrical structures can be used with a certain (real) index and certain phase thickness. In the above mentioned structure, one can select e.g. the layers BAB and he can impose that these layers should have a certain equivalent index and a certain phase thickness.

3.2 Analysis

The following elements can be analysed::

- R, T, A, A*, R* for s and p polarisation;
- A_j - absorption in layers;
- ρ, ρ*, τ, phase changes on transmission and reflection ;
- distribution of electric field in layers;
- $\partial R/\partial l_j$, $\partial T/\partial l_j$, where l_j is the geometrical thickness of layer j;
- trichromatic coordinates.

The major part of the analysis functions are actualised when a change of the optical coatings is detected.

3.3 Optimization

A gradient method^{1,2,3,4} is used where the merit function for the optical coatings can have the following forms:

$$F = \sum_i w_{(\lambda_i)} Q_{(\lambda_i)}$$

$$F = \sum_i w_{(\lambda_i)} (Q_{(\lambda_i)} - Q_{0(\lambda_i)})^2$$

where: w - weight;

Q - actual value of optimised parameter;

Q₀ - target value of optimised parameter .

Q can be R, T for s and p polarisation.

More optical coatings can be simultaneously optimised, namely, the active optical coating and the branch optical coatings (if they are) that are starting from the active optical coating, only the selected ones. In this case, the optimised merit function is:

$$F = \sum_j w_j F_j$$

where : w_j - weight for coating j;

F_j - merit function for coating j.

For example, an antireflection coating can be optimised on more optical glasses and for more incidences.

3.4 Technology

Includes:

- analysis of the evaporating geometry; uniformity study of thin layers produced on various types of surfaces in different evaporating geometries. The evaporating geometry of a planetary type⁵ where the substrate surface is described by a quadric includes the major part of geometries as particular cases.
- setting of geometric coefficients for crucibles (representing the scale factors through which the coatings on the test glass can see the layers of the root optical coating);
- generating of branch optical coatings on test glasses;
- setting optical constants for materials of branch optical coatings on test glasses;
- setting of monitoring parameters⁶ and simulation of the monitoring process. The layer producing is monitored following that the extremes should be obtained (minimum and maximum), just like some absolute values of the measured signals, some values related to some extremes that are preceding them;
- analysis of errors produced during the monitoring process established as a result of the photometer sensitivity, variation range of optical constants and the errors produced during the stopping of the evaporating process. After the parameters of single wavelength monitoring have been set, one can study the errors produced when the photometer sensitivity is changed (peculiarly when following extremes), the optical constants are changed or some errors are produced during the stopping of the evaporating process.

In the root optical coating, the spectral answer is analysed. With this function, one can also analyse technological process experimentally produced.

3.5. Determination of optical constants out of (R,T) measurements

The determination of optical constants of evaporating materials is decisive for designing of the optical coatings and of their fabrication technologies. The easier mode of determining the optical constant is that out of spectral-photometric measurements ((R,T) method⁷). Starting from the premises that the layers is homogeneous and geometrical thickness is known (for nonabsorbent materials with extremes in the spectral range the geometrical thickness can be determined). The determination of optical constants can be done according to the following procedure:

1 - determinations done within an optical coating (root or branch) with a single layer, (R,T) values being targets for optimisation;

2 - measured values are introduced and respective corrections are made (linearity lines of 0% and 100%, reference for 100%, elimination of second surface if it is);

3 - for each wavelength introduced, the constant reflection and transmission lines equals to the measured values are represented in the plane (n,k), the lines containing all the points (pixels of the representing windows) whose reflection and transmission are in the measuring tolerance for R and T (Fig. 1).

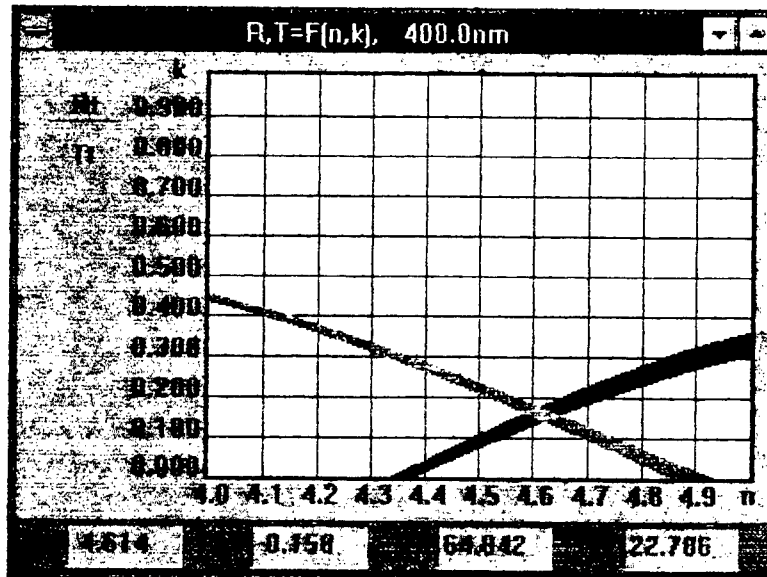


Fig. 1 $R=(64.21\pm1)\%$, $T=(22.8\pm0.5)\%$, geometrical thickness = 60nm, $\lambda=400\text{nm}$.

A thick line signifies great errors in determining the optical constants. The solution (n,k) for (R,T) is at the intersection of the two lines. Pointing by mouse to that zone, the values for (n,k) and (R,T) are to be displayed. Also, some information are got concerning the precision of determining the pair (n,k) at that wavelength. By maximising the window or by reducing the domains for n and k, the precision of determining the pair (n,k) is increased. If these values are not satisfying, then they are starting values in a searching process by means of Rosenbrock method.

4 - by using the determined optical constants, the experimental values (R,T) are compared to the theoretical ones. The geometrical thickness being measured with errors, one can search the geometrical thickness that generates the closest values (R,T) to the experimental ones (with determined optical constants), after then, with the new geometrical thickness, the optical constants can be redetermined. An incorrect optical thickness is easily detected (especially with nonabsorbent materials) as a result of the dispersion of material. With an arborescent structure, one can analyse more experimental measurements.

5 - a type of equation of dispersion is selected for n and k and the coefficients of the equation are determined;

6 - the material is saved in a file from where it can be used later;

4. CONCLUSIONS

The application Windows 3.1 was checked up by designing and implementing many optical coatings of different types in fabrication. It has a friendly interface, easy to be exploited. An image of the application interface is shown in Fig. 2.

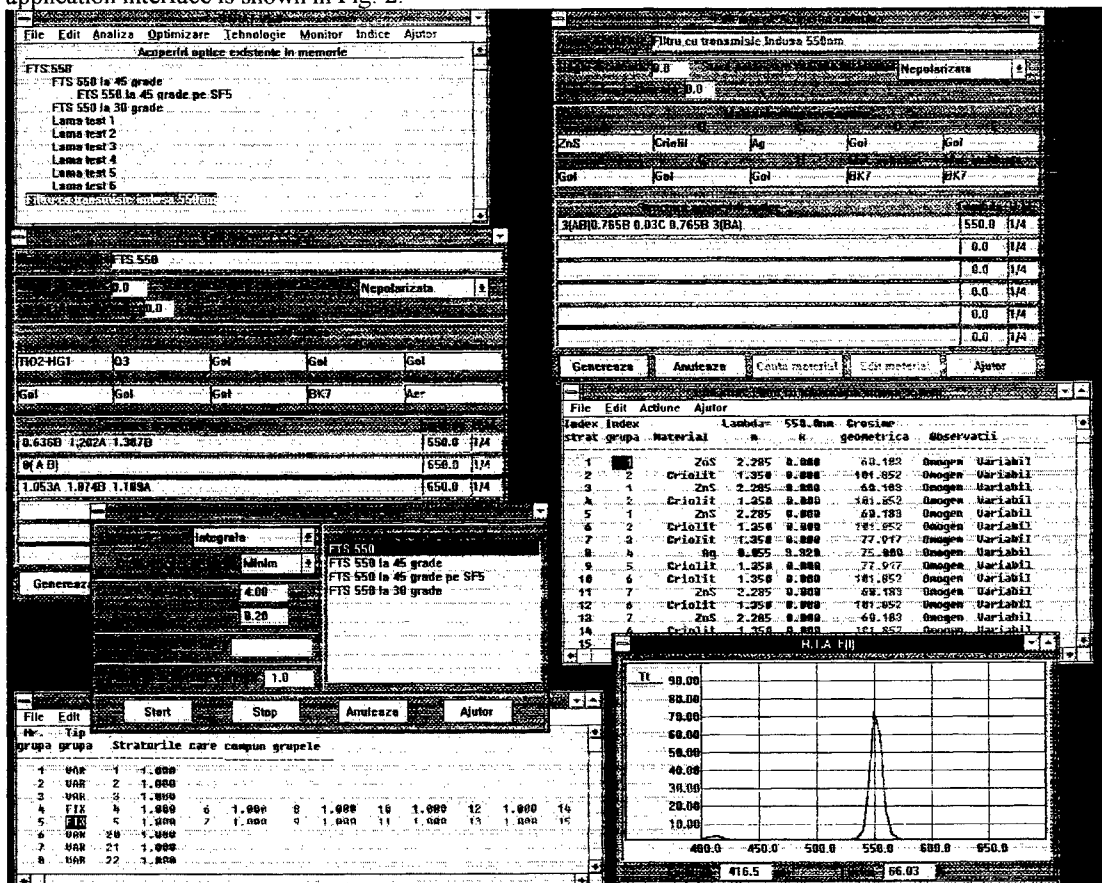


Fig. 2 STRAT V5.0 interface.

The future efforts are to be directed to the development of new functions that will exploit better the arborescent structure of data, to an increased security in exploiting and to an improvement of the user-computer interface. The programme is part of a coherent series of Windows 3.1. applications developed by PRO OPTICA S.A. and used in the optical industry. The optical coatings created with this application can be used by the application WINOPTIC V1.0 for designing optical systems.

5. REFERENCES

1. Honciuc Gh. "Optimization of optical coatings", 50th Anniversary Scientific Symposium IOR, Bucharest, 1986.
2. Philip W. Baumeister, "Methods of altering the characteristics of a multilayer stack", *JOSA* 52 (9) pp. 1149 - 1152 (1962)
3. A.L.Bloom, "Refining and optimization in multilayers" *Appl. Opt.* 20 (1), pp. 66 - 73 (1981).
4. J.A.Dobrowolski, R.A.Kemp, "Refinement of optical multilayer systems with different optimization procedures", *Appl. Opt.* 29, 2876 - 2893 (1990).

5. Honciuc Gh., Gaceff St., Georgescu C, "Determination of distribution of thin layer thickness on aspheric surfaces describing a planetary movement", Optics National Congress, Bucharest, 1984.
6. C.J. van der Laan, "Optical monitoring of nonquarterwave stacks", *Appl. Opt.* **25** (5), 753-760 (1986)
7. J.M.Bennett, M.J.Booty, "Computational method for determining n and k for a thin film from the measured reflectance, transmittance, and film thickness", *Appl. Opt.* **5**, pp. 41-43 (1966).

Electrostatically-driven dynamic focus system

Horățiu Țoția and Marius Micluța

National Institute for Laser, Plasma and Radiation Physics
P. O. Box MG-36, RO-76900 Bucharest, Romania

ABSTRACT

Real-time accurate positioning of laser beams and optical images on three-dimensional targets, as well as focus correction in flat field laser scanning, are provided by dynamic focus systems. Commonly used zooming devices involve rather complex driving mechanisms to control the relative motion of the lens systems. A possible, cost-effective alternative to this approach is to use a lens with variable focal length. The design of a dynamic focus system based on this principle is presented, and a suitable driving method, using electrostatic interactions, is also proposed. Dimensional design formulae are given, together with performance evaluation calculations.

Keywords: laser scanning, beam positioning, focus correction, adaptive optics

1. INTRODUCTION

Dynamic focus systems are required in various applications, such as real-time accurate positioning of laser beams and optical images on three-dimensional targets, or reading optical information from moving or stationary fields. They may also be used for focus correction during flat field laser scanning, as a distortion-free substitute for field-flattening lenses. Such zooming devices are generally quite complex and involve a controlled translation motion of a lens system, achieved through sophisticated and expensive mechanisms.

A dynamic focus system with a simpler architecture, inspired by the principles underlying human sight, is proposed in the present paper. It allows a fast variation of the focal length within a range of a few centimeters, which covers the needs of most vision and beam positioning applications. The design of the optical system is outlined, as well as an adequate driving method, based on electrostatic interactions. Some dimensional design and performance evaluation calculations are also provided.

2. OPTICAL SYSTEM DESIGN

The optical system is composed of two lenses, one having a fixed focal length f_1 , while the focal length of the other, f , is variable. For a distance T between the two lenses, the focal length of the system, t , may be easily evaluated by matrix methods,¹ which lead to the formula:

$$\frac{1}{t} = \frac{1}{f} + \frac{1}{f_1 - T}. \quad (1)$$

Thus, for given f_1 and T , the position of the secondary focal plane of the optical system depends only on f . If one could modify the value of f between the limits $f_{\min} < f < +\infty$, then

$$\frac{f_{\min}(f_1 - T)}{f_{\min} + f_1 - T} < t < f_1 - T. \quad (2)$$

By using a thin plane-convex lens with variable curvature radius, its focal length f may be changed, leading to a variation of the focal length of the optical system over a wider range than that achievable through a relative axial translation of the two lenses. This is important in order to ensure a maximum versatility of the overall system by applying very small changes to the curvature radius of the active lens.

The lens with variable focal length is built as a pneumatic cell, filled with a transparent fluid and bounded by two parallel windows. The input window is plane and rigid, while the curvature radius of the output window may be continuously varied from infinity to a minimum value by increasing the fluid pressure. The minimum curvature radius is determined by the maximum value of the pressure in the cell.

Considering the output window as a clamped-edge circular plate with radius R and thickness h , the dependence of the curvature ρ in the vicinity of the optical axis (i.e., for radial distances $r \ll R$) on the applied pressure p is given by^{2,3}:

$$\rho = \frac{p}{16D} R \left[1 - \left(\frac{r}{R} \right)^2 \right], \quad (3)$$

where D is the flexural rigidity of the plate, defined as

$$D = \frac{E h^3}{12(1 - \nu^2)}, \quad (4)$$

with E —the elastic modulus and ν —the Poisson ratio.

The corresponding deflection is

$$W = \frac{p R^4}{64 D} \left[1 - \left(\frac{r}{R} \right)^2 \right]^2, \quad (5)$$

and, although it depends on r^4 , the shape of the curved plate is very close to a spherical surface in the vicinity of the optical axis. This approximation is valid for further considerations as long as laser beams, having diameters of a few millimeters and very low divergences, are involved.

The focal length of the thin lens formed by the fluid of refractive index n enclosed in the pneumatic cell may be evaluated by introducing equation (3) with $r = 0$ in the lens formula, which yields:

$$f = \frac{16 D}{(n - 1) p R^2}. \quad (6)$$

The allowed values of the focal length f range from infinity (corresponding to a null pressure) to a minimum value imposed by the strength of the plate material. For a given geometry of the output window (R , h), made of a material with an allowed tensile yield stress σ_a , the pressure cannot exceed the value³

$$p_{max} = \frac{4}{3} \frac{\sigma_a h^2}{R^2}. \quad (7)$$

Equations (6), (7), and (4) lead to the following value of the minimum focal length f :

$$f_{min} = \frac{E h}{\sigma_a (n - 1) (1 - \nu^2)}. \quad (8)$$

For a thickness $h = 0.7$ mm of the output window, the above equation gives a minimum value $f_{min} = 1.86$ m for fused silica and $f_{min} = 2.22$ m for optical glass. However, these limits might be further decreased due to other technical considerations involved by a specific method used to control the pressure.

Special care must be taken when selecting the fluid, in order to ensure a good optical quality of the focus system. Siliconic oil could be an almost ideal choice. The high value of its refractive index ($n = 1.56$) allows a smaller focal length for a given curvature radius and also matches well with the refractive indexes of the adjacent media, while its absorption coefficient is very low in both visible and infrared wavelength domains.

3. ELECTROSTATIC DRIVING METHOD

3.1. Principle of operation

The pressure in the pneumatic cell may be modified in various ways from the outside, in order to control the focal length f . A simple and cost-effective driving method has been devised to this end and is presented in the following. The output window of the pneumatic cell is made of a thin plastic film with radius $R = 30$ mm, coated with colloidal graphite on the external surface, except for a small central circular disc. A metal-coated diaphragm is mounted parallel to the output window at a distance $d = 1$ mm and is provided with a small circular hole in the center. A plane capacitor is thus obtained from the two conductive layers and the dielectric fluid contained between them. By

applying a potential difference U to this capacitor, an electrostatic attractive force develops between the two plates and the elastic output window is bent under the action of the resulting pressure.

For an optical system with $f_1=50$ cm and $T=5.8$ cm, a variation of the total focal length t with 25 mm implies a minimal value of 7385 mm for the modulus of the variable focal length f . The corresponding curvature radius is 3692.5 mm and the deflection along the optical axis is of only 60 μ m. The necessary driving pressure is equal to the pressure of the electrostatic field, given by

$$p = \frac{\sigma^2}{2\varepsilon}, \quad (9)$$

with ε —the dielectric constant of the fluid. The surface charge density σ is related to the applied difference of potential by the equation

$$U = \frac{\sigma d}{\varepsilon}, \quad (10)$$

which is a valid approximation since $d \ll R$ and $W \ll d$, as outlined above. It follows from (9) and (10) that the value of U necessary to induce a pressure p on the elastic plate is

$$U = d \sqrt{\frac{2p}{\varepsilon}}. \quad (11)$$

In order to obtain a desired curvature of the output window in the vicinity of the optical axis, the potential difference U must induce a pressure

$$p = \frac{16 D \rho}{R^2}. \quad (12)$$

In our case, $p = 0,534 \text{ Nm}^{-2}$, which involves a value $U = 155,44$ V for the potential difference applied to the cell. It is worth mentioning that an alternative power supply may be used as well, since the pressure depends only on the square of the applied potential. A potential difference of this order of magnitude does not imply special technical problems and can be easily controlled by a computer, through a D/A interface, in conjunction with the motion of an $X - Y$ scanning device.

3.2. Response time

The use of the described system for real-time focus correction in flat field laser scanning requires a sufficiently fast response, so as to ensure a synchronous operation with the scanning devices. The following estimation is intended to investigate this aspect.

For the purpose of evaluating the influence of the viscous fluid resistance on the output window movement, we shall neglect the small elastic deformation and consider a simplified model, consisting of two parallel circular plates of radius R and thickness h , separated by a distance d , the space between them being filled with a fluid of dynamic viscosity η . The force of resistance exerted on one of the plates when it is subject to a small translation movement towards the other plate is given by⁴

$$F = \frac{3\pi\eta R^4}{2d^3} u, \quad (13)$$

where u is velocity of the plate.

The equation of motion for the respective plate may be written as

$$m \dot{u} + \delta u = F_0, \quad (14)$$

$m = \pi R^2 h \rho$ being the mass of the plate, ρ —its density, F_0 —the driving force (having a step function time dependence), and $\delta = \frac{3\pi\eta R^4}{2d^3}$.

The time constant corresponding to this damped motion is

$$\tau = \frac{m}{\delta} = \frac{2}{3} \frac{d^3 h \rho}{\eta R^2}. \quad (15)$$

For the case of using a thin polyethylene window with $R = 30$ mm, $h = 0.2$ mm, and $\rho = 0.96$ g cm⁻³, the gap of thickness $d = 1$ mm between the windows being filled with siliconic oil ($\eta = 8.5$ g s⁻¹ cm⁻¹), one obtains from (15) a time constant $\tau \approx 1.67 \cdot 10^{-7}$ s. This value is much smaller than the response times of the fastest state-of-the-art scanning devices. The proposed driving method is thus suitable for high-speed scanning applications.

4. COMMENTS

A dynamic focus system has been designed, intended primarily to flat field laser scanning applications. The optical system, composed of a convergent lens with fixed focal length and a plane-convex lens with variable curvature radius, allows a wide range of variation for the position of the secondary focal plane, superior to that resulting from the relative axial translation of the two lenses. This solution proves to be highly versatile, as by changing the lens with fixed focal length, the system may be adapted to fit the needs of various applications.

An experimental model of the proposed system has been built, using as variable curvature lens a pneumatic cell filled with siliconic oil. This system was tested with various elastic window materials, the driving pressure being controlled manually in the first instance. Focal lengths of the system ranging from infinity to several meters, depending on the elastic window material, were obtained, in good agreement with the theoretical estimations.

Automatic control of focal length is a key feature in modern vision and laser scanning applications. To this end, a simple driving method has also been conceived. It is based on the electrostatic field pressure obtained by applying a potential difference to the capacitor formed by the conducting walls of the pneumatic cell and the dielectric fluid layer enclosed between them. This method proved successful upon test, although driving voltages greater than those theoretically calculated were required, most probably due to inaccurate evaluation of some material constants. Several mechanical assembly solutions were compared, in order to maximize the overall performances. A detail worth mentioning is that siliconic oil, which possesses excellent optical qualities, is also a hygroscopic liquid. This may cause in time an alteration of its dielectric properties, so special handling and sealing care must be taken into account.

REFERENCES

1. A. Gerrard, J. M. Burch, *Introduction to Matrix Methods in Optics*, J. Wiley & Sons, London, 1975.
2. S. Timoshenko, S. Woinowsky-Krieger, *Theory of plates and shells*, McGraw-Hill, New York, 1959.
3. H. Țoția, M. Micluța, "Adaptive mirrors for power-laser cavities", in *ROMOPTO '94: 4th Conference on Optics*, V. I. Vlad, Editor, Proc. SPIE 2461, pp. 65-67, 1994.
4. L. D. Landau, E. M. Lifshits, *Course of Theoretical Physics*, Vol. 6: *Fluid Mechanics*, Second Edition, Pergamon Press, London, 1987.

SESSION 9

Optics and Environment

III-V compounds and piezoelectric ceramics thin films deposited by reactive PLD: application to sensor buildingM. Dinescu, P. Verardi¹, F. Craciun¹, C. Stanciu, R. Dinu, C. Gerardi², L. Mirengi², M. Gartner³, V. Sandu⁴

INFLPR, Lasers Dept., P.O. Box MG-16, RO 76900, Bucharest V, ROMANIA

¹Institute of Acoustics "O.M. Corbino", CNR, Via Cassia 1216, I-00189, Rome, ITALY²PASTIS CNRSM, SS7 Appia, 72100 Brindisi, ITALY³ICF "I.G. Murgulescu", Spaiul Independentei 202, Bucharest, ROMANIA⁴INFIM, PO. Box MG-26, RO 76900, Bucharest V, ROMANIA**ABSTRACT**

High quality AlN, GaN, ZnO and PZT thin films were deposited on different substrates by laser ablation of metallic or PZT targets in nitrogen or oxygen reactive atmosphere. A YAG laser ($\lambda=1.06\ \mu\text{m}$, $t_{\text{FWHM}}=10\ \text{ns}$, $0.3\ \text{J/pulse}$) was used as laser source. The target collector distance was varied in the range 3-8 cm, the gas pressure in the range 10^{-3} - 10^{-1} mbar, the collectors were heated at temperatures between 200 and 400 °C. The influence of the process parameters on the physical properties of the deposited films was analyzed. The profile of atoms inside the film was evidenced by SIMS analysis. Depth profile XPS and AES confirm the presence of Al-N, Ga-N and Zn-O bonds inside the films. X-ray diffraction studies revealed different crystalline orientation depending on deposition conditions. The recorded spectra show the crystalline orientation of the layers, at collector's temperatures lower than the best results reported in literature. Optical absorption spectroscopy studies in the UV and visible range evidenced a high transparency (over 80% transmission) for the AlN, GaN and ZnO deposited films. For PZT a particular result consists in the piezoelectricity of the deposited films "as received", without any subsequent thermal or electric treatment.

1. INTRODUCTION

Since the first years after the construction of the first laser, lasers have been widely applied to the synthesis and deposition of thin films¹. One of the most successful methods was shown to be pulsed laser deposition (PLD). This method has emerged as an excellent technique (sometimes unique) for the deposition of thin films with complicated stoichiometry, being an excellent "carrier" of the stoichiometry from the target to the film^{2,3}. Another interesting version of the method is reactive PLD, which offers the possibility of one step synthesis and deposition of new compounds. The material to be reacted, is ablated in a reactive gas atmosphere, the new compound being collected on a substrate placed either parallel or perpendicular to the target. Thus, PLD was found to be effective for producing a large variety of thin films.

We report here the successful deposition of III-V compounds (AlN and GaN) and piezoelectric thin films (ZnO and PZT) by employing the PLD technique. The III-V nitrides, in either crystalline or amorphous films have received an increasing interest for their potential applications in the active and passive device fields, in thermal management and high speed circuitry, protective wear, resistant hard coatings⁴. AlN is one of the most widespread III-V nitride, with a combination of very interesting properties: large direct band-gap (5.4-6.3 eV)^{5,6}, large thermal conductivity ($3.19\ \text{W/cm}^2$ at $T=300\text{K}$), high acoustic velocity (6000 m/s), high melting point (2273 K)⁷, high Knoop hardness (1300 kg/mm), low dielectric loss etc. It is used as insulator in metal-insulator-semiconductor devices, heat sink in electronic packaging applications, component for acoustic wave device in the range of 215 nm until the blue end of the spectrum. For the deposition of AlN thin films, we ablated Al targets in nitrogen reactive atmosphere. The realization of gallium nitride LEDs and more recently laser diodes⁸ makes GaN an important candidate semiconductor for optoelectronic applications. It offers the potential for replacing the traditional vacuum light tubes and moreover, the conventional GaAs, GaP and GaAlAs III-V compounds, which are toxic for humans. Although the major part of semiconductor devices has now been realized, the material is far from being mastered. We deposited GaN thin films by laser ablation of liquid phase Ga in nitrogen atmosphere, on low temperature substrates.⁹ In some of our experiments, we used ZnO as a buffer layer between the silicon or sapphire substrates, to improve the crystallinity of the deposited layers.

PLD was also successfully applied for the deposition of crystalline and highly oriented piezoelectric thin films. Zinc oxide, widely used for surface and bulk acoustic wave generation and detection devices, for sensors and actuators¹⁰⁻¹², was deposited by laser ablation of a Zn target in oxygen reactive atmosphere. Lead zirconate-titanate (PZT) is a prime candidate for thin film applications like infrared devices, surface acoustic waves delay lines, ultrasonic sensors and actuators, electro-optic displays, atomic force microscopy sensors etc¹³⁻¹⁵. Thin films were deposited by the ablation of an already prepared PZT target, in oxygen atmosphere, on substrates heated at lower temperatures than those reported in literature¹⁴.

2. EXPERIMENTAL

The experiments were performed in vertical PLD set up, that allows the ablation of liquid phase targets. The beam of a Q-switched Nd-YAG laser (350 mJ/pulse at 1064 nm) operating at 10 Hz was directed in a stainless steel vacuum chamber and focused on the different targets. The incident laser fluence was set at approx. 25 J/cm². The materials used as targets were: a) high purity Al cylindrical plates, 20 mm diameter and 3 mm thick; b) high purity liquid phase Ga, put into a fused silica vessel, 15 mm diameter and 6 mm height; c) 99% purity Zn cylinders of 20 mm diameter and 3 mm thickness and d) commercially available PZT sintered targets. During the deposition the targets were rotated in order to avoid the crater formation. The ablated material was deposited on the substrates fixed at distances varying from 2 to 8 cm away from the target. The substrates are mechanically attached to a heater and the temperature monitored with a chromel-alumel thermocouple embedded in the heating block. The measured deposition temperatures represent therefore the block temperature and not the substrate surface temperature, which is actually lower. After loading the sample, the irradiation chamber is several times evacuated by a turbomolecular pump down to 10⁻⁶ mbar and refilled to atmospheric pressure with the reactive gas of interest. The working pressure was varied in the range 10⁻³-10⁻¹ mbar.

Different techniques were used to characterize the deposited layers. XPS and X-ray excited Auger electron spectra (XEAES) analyses were done using a VG ESCALAB 210 instrument. An X-ray Mg non-monochromatic source was used to generate photoelectrons from the surface region of the sample. A 3 kV Ar⁺ beam was used to sputter the surface to remove the contamination. SIMS analyses were performed on a CAMECA ims4f magnetic sector instrument by using a Cs⁺ beam to sputter the sample surface. The depth scale calibration was carried out by measuring the erosion rate both in film and substrate, respectively. A TENCOR ALPHASTEP 200 stylus profilometer was employed to measure the eroded depth. XRD studies were performed to investigate the crystallinity of the deposited films by using the CuK α line (with an average wavelength value of 1.54 Å) produced by a DRON 20 diffractometer with nickel filter. The optical transmission of the films was measured in the range of 200-800 nm and the optical band-gap was calculated from the relation: $(\alpha h\nu)^2 \sim (h\nu - E_g)$. Spectroellipsometric (SE) measurements were performed in air, at room temperature, using a null ellipsometer in PCSA (Polarizer-Compensator-Sample-Analyzer) arrangement.

Having in view the building of sensors, appropriate electrodes were deposited on the substrates before depositing the piezoelectric materials. Thus, for both ZnO and PZT films, prior to their deposition, a layer of Au of about 50 nm was evaporated on the silicon, sapphire and Corning glass substrates, after a flash of Cr used to improve the adhesion of the Au layer.

3. RESULTS AND DISCUSSION

3.1. III-V compounds

3.1.1. AlN

AlN thin films were deposited by the ablation of Al in nitrogen atmosphere, on Si(100) and sapphire(0001) substrates. The temperature of the collector was varied from 280 to 400°C.

Optical transmission spectra were recorded for the films deposited on sapphire. The transmission of the films had values of around 75%, while the band gap from these spectra was superior to 5.5 eV for all the films deposited at temperatures over 350°C.

XPS and XAES investigations were performed on these films, deposited on sapphire heated at 350°C, at $p = 5 \cdot 10^{-2}$ mbar, $d_{\text{target-collector}} = 5$ cm. Al2p, N1s and AlKLL regions were scanned from the survey spectrum, to obtain more information about the stoichiometry of the compound. On the surface, N1s exhibits a double peak, one at 397 eV, specific to Al-N bond, and the other, at higher binding energy, being due to NOOH contamination groups. In the depth of the film, the contamination component disappears. The Al2p exhibits a single component, no homomorphie or Al-O bonds being identified. The film was sputtered with Ar⁺ ions, accelerated at 3 kV, in order to investigate the chemical bonding of Al at different depths from the surface. The Auger parameter (related to the ALKLL – Fig1a and Al2p positions) was calculated at different steps of the sputtering process. At a certain depth, after overcoming the surface region affected by oxygen, its value stabilizes around the typical value for Al-N chemical bond (Fig1b). The film deposited at $p=7 \cdot 10^{-2}$ mbar, $d=4,5$ cm and $T=350^\circ\text{C}$ but in a perpendicular geometry is inferior to all the others deposited parallel to the target, having a refractive index of 1,83 and a ratio Al/Al+N of 0,69. The oxygen level is in the order of 2-3 atomic percent.

SIMS profiles of Al, N and O confirm the uniformity of the stoichiometry along the 270 nm thickness of the film. The oxygen signal is higher at the surface, decreasing in the depth of the film at a constant level, indicated quantitatively by XPS.

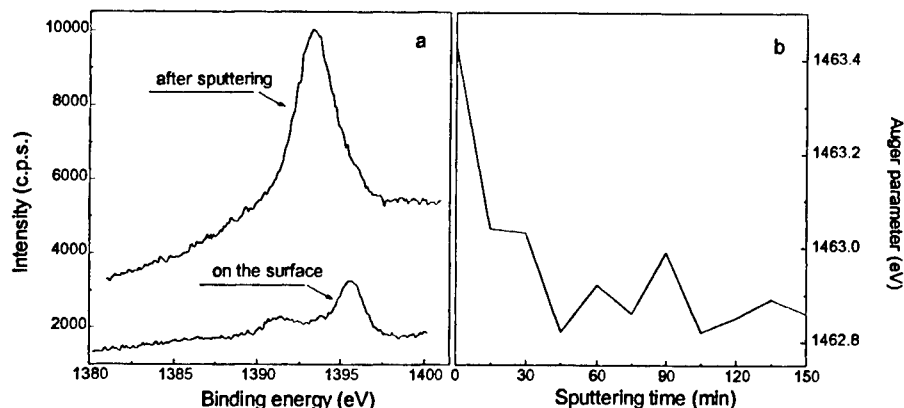


Fig.1. Al KLL X-ray excited Auger line for the surface as received and after 80 minutes of sputtering.

The AlN compound's properties, for the films deposited on silicon, were investigated by FTIR and SE. All the films show typical AlN FTIR spectra, with two broad peaks positioned at 679 and 644 cm^{-1} , shifted toward higher energies compared with the reference data for the bulk material.

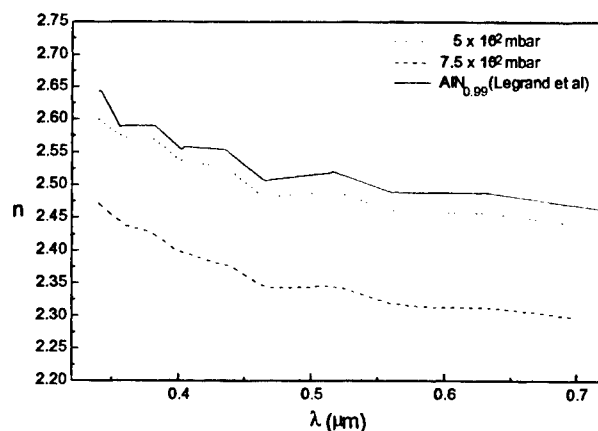


Fig.2. The refractive index spectra for two films deposited on Si(100), compared with the reference data used in the simulations.

For the estimation of the compositional and optical properties of the films, the experimental spectroellipsometric spectra, acquired in the range 400-700 nm, were fitted using a theoretical model. The model was that of a multilayer and multicomponent film with sharp parallel interfaces, where the optical properties of each layer are calculated in the Bruggeman Effective Medium Approximation. For the simulations, we used as reference data the refractive index of $\text{AlN}_{0.99}$ and $\text{AlN}_{0.83}$ reported by P.B.Legrand et al¹⁶. We used for every sample a model of a three-layer structure laying on 10 Å of native silicon oxide. The interfacial layer is affected by this native oxide of the silicon wafer, while the surface one is rough (up to 50%) and oxidized. The interfacial and the surface layers are very thin compared to the main (middle) layer of the deposit (around 150 Å for a total thickness of 2500 Å). The values of the refractive index, calculated from the best fit show that for the main layer refractive indices are about 9% smaller than the reference values and indicate a good quality of the compound (Fig.2). The absorption index k has very small values (the order of 10^{-2} - 10^{-3}), yet different from 0 - possibly due to the slight non-stoichiometry of the AlN compound. According to the composition of the layers, the Al/Al+N ratios for these samples vary from 0.506 (for a film deposited at $5 \cdot 10^{-2}$ mbar, $d=5$ cm, $T=400$ °C) to 0.525 (for deposition conditions: $7.5 \cdot 10^{-2}$ mbar, $d=5$ cm, $T=400$ °C). The film deposited at $3 \cdot 10^{-2}$ mbar, $d=4.5$ cm and $T=350$ °C but in a perpendicular geometry is inferior to all the others deposited parallel to the target, having a refractive index of 1.83 and a ratio of 0.69.

The rate of deposition in this case was four times smaller than for the parallel configuration. The rate of deposition also decreases at the highest pressure.

The crystallinity of the films strongly depends on the substrate type and nature, the distance target-collector and the pressure of the reactive gas. The films deposited on sapphire exhibit two main peaks in their XRD spectra, at $2\theta=33.28^\circ$ and $2\theta=38.17^\circ$, corresponding to AlN(100) and AlN(101), respectively. The two peaks are shifted towards bigger values of the diffraction angle, one possible explanation being the difference between the thermal expansion coefficient of AlN and that of sapphire. Depending on the distance target-collector, the orientation of the films is modified as follows: while for a film deposited at 5 cm only a well evidenced (101) peak was detected, for the sample deposited at 4 cm (the other deposition parameters being identical) both (101) and (100) peaks are present in the spectrum, broadened and with smaller intensities, indicating a weaker degree of the crystallization.

The situation is different when using silicon wafers as substrates. For a film deposited at a pressure of $p = 3 \cdot 10^{-2}$ mbar on Si(100) only one peak is present, at $2\theta = 33.18^\circ$ and it corresponds to the (100) film orientation. Reducing the reactive gas pressure at 10^{-2} mbar (with the temperature, target-collector distance and laser fluence kept constant), the orientation of the deposited film is changed: the (100) peak is broadened and its intensity decreases, while a more intense peak appears, at $2\theta = 59.40^\circ$ - corresponding to the (110) orientation. At the same pressure, a film deposited on Si(111) instead of Si(100) wafer shows a higher degree of orientation, exhibiting only the peak (110), well evidenced at 59.40° .

3.1.2. GaN

GaN films were deposited by the ablation of liquid gallium in nitrogen atmosphere. In order to improve the crystallinity of the films, ZnO buffer layers were deposited by magnetron sputtering on the sapphire(0001) and Si(100) substrates. The most appropriate set of parameters for the deposition of GaN was found to be: N_2 pressure $5 \cdot 10^{-2}$ mbar, distance target-collector 5 cm, $T_{\text{collector}} = 300^\circ\text{C}$, laser fluence 25 J/cm^2 .

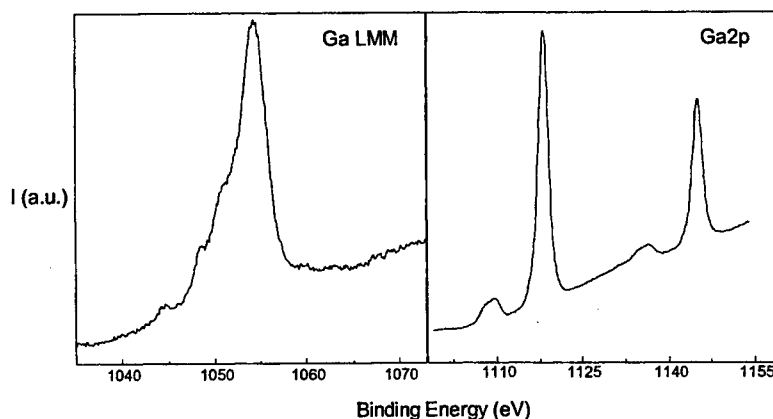


Fig.3. GaLMM line and Ga2p doublet of the XPS spectrum.

XPS investigations performed on the films deposited in the conditions mentioned above indicate the good quality of the compound. The calculated Auger parameter (as the distance between the photoelectron Ga3d peak and the X-ray excited Auger GaLMM peak) is 1083.9 eV, value that corresponds to the GaN compound. The Ga2p_{3/2} peak is situated at 1118 eV, typical for the Ga-N bond (Fig.3). A scanning of the N1s region revealed that beside the N-Ga peak, situated at 397.3 eV, there are two (low-level) contamination signals, corresponding to NO₂ and N₂H₄.

An elemental depth profiling was performed by SIMS. Along the 130 nm thickness of the film, the distributions of Ga and N are uniform. The film-substrate (sapphire) interface is abrupt, showing no interdiffusion. The oxygen level is higher at the surface of the film, decreasing after the first 15 nm at levels of 3 atomic percent, as indicated by XPS evaluations.

XRD analyses were performed on the films deposited with or without ZnO buffer. All the films have a good crystallinity, having the main orientation with the c axis perpendicular on the substrate. The peak centered at $2\theta = 34.3^\circ$, corresponding to the (0002) orientation, is present in the spectrum of each film. The best results were obtained for the structure GaN/ZnO/Si, where the GaN film has exclusively the (0002) orientation. As the ZnO buffer film, deposited prior to the GaN one, was also c-oriented (Fig.4) and taking into account the similarity of the two wurzite structures of ZnO and GaN, we can suppose that the growing of GaN(0002) onto ZnO(0002) was an epitaxial one. Surprisingly, the use of the

ZnO buffer layer on sapphire substrates did not improve the film orientation. Whenever using a sapphire plate as substrate, besides the (0002) peak, some (1010) and (1011) contributions appear in the XRD pattern.

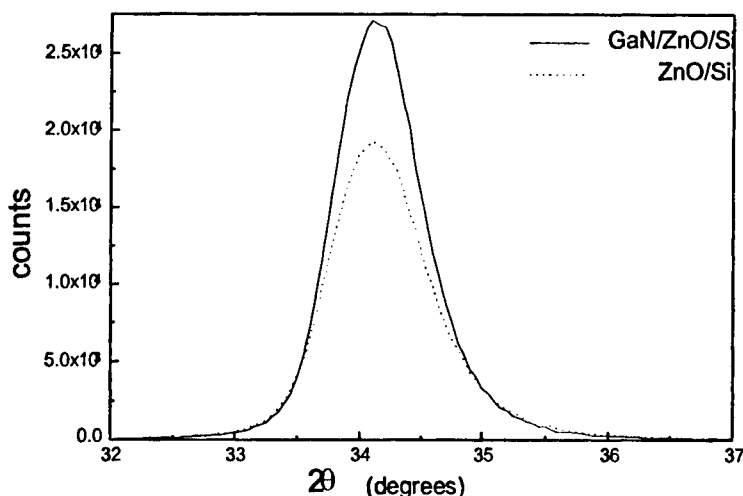


Fig.4. XRD spectrum of a GaN/ZnO/Si structure, compared to the spectrum of the initial ZnO/Si support.

Optical transmission measurements indicate transmission values of 80-85% for films deposited on sapphire and of only 70% for the films deposited on ZnO/sapphire (in this last case, we used ZnO/sapphire as reference for the background correction). From these transmission spectra, we obtained values for the energy band gap larger than 3.6 eV.

3.2. Piezoelectric ceramics

3.2.1. ZnO

Optical microscopy and scanning electron microscopy evidenced the smooth appearance of the deposited films. The number of droplets and their dimension were diminished by increasing the distance target-collector, although this leads to smaller deposition rates.

The optical transmission of the films was found to be higher than 90% in the visible range, with a step falloff at 380 nm. The band gap, calculated from the transmission spectra, increases from 2.9 eV for the samples deposited at low temperatures (20-100°C) to 3.2 eV for 250°C.

The stoichiometry of the deposition was investigated by XPS, for a film deposited at 10⁻¹ mbar oxygen pressure and 8 cm distance from the Zn target to the Corning glass collector, the laser fluence being set at 3.8 J/cm². The deconvolutions performed on the O1s region of the spectrum (Fig.5) indicate the major presence of O-Zn bonds (at 530 eV). Only a small amount of oxygen is absorbed in hydroxidic form.

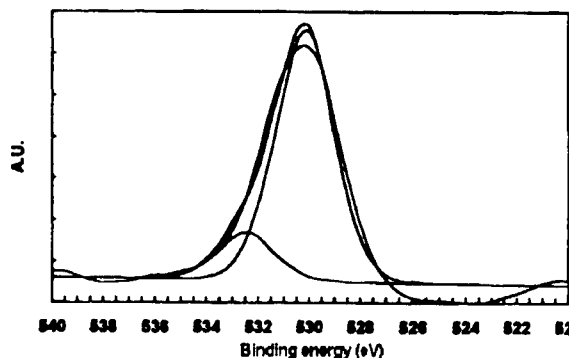


Fig.5. O1s region from the XPS spectrum of a ZnO film deposited on Corning glass.

XRD studies evidenced an excellent crystallinity of the films. For the same deposition parameters ($p=10^{-2}$ mbar, $T_{\text{collector}}=350^{\circ}\text{C}$, $d_{\text{target-collector}}=4$ cm, laser fluence 25 J/cm^2), the orientation with the c-axis perpendicular to the substrate surface does not depend on the substrate nature. The (002) peak is slightly shifted (with only $2\theta = 0.2^{\circ}$) for a film deposited on Corning glass, compared to a film deposited on Si wafer. As calculated from the line width at half maximum of the (002) peak, the average crystallite size was of 20 nm when using a Corning glass substrate, and 35 nm when using a Si(100) wafer.

Cross-section SEM images show a columnar structure of the deposited film. For the transmission electron microscopy, the samples were prepared by the extraction replica technique. As a result, the film splits into separated groups of columns (Fig.6), confirming the columnar character of the deposited layer. The columns have the base diameter of 50-100 nm and the height of 600-700 nm, corresponding to the thickness of the film as measured from the cross section SEM images.



Fig.6. TEM image of a ZnO film deposited on an Au/Cr/Si structure, that confirms the columnar growing of the film.

As mentioned before, for the evaluation of the piezoelectric properties of the ZnO films, an appropriate Al/ZnO/Au/Cr/Si structure for bulk acoustic waves was built. This was a metric structure (3×3) of 2 mm diameter discs separated by 4 mm distance between centers. The measured piezoelectric component d_{33} has a mean value of $8 \cdot 10^{-12} \text{ C/N}$, very closed to the bulk value, while the propagation velocity of the longitudinal wave was 8440 m/s. This confirms the excellent quality of the deposited ZnO films, suitable for electroacoustic applications.

3.2.2. PZT

Commercially available PZT sintered target was used for the deposition of PZT thin films on (111)Au/Si(111). During the PLD process the pressure of the oxygen ambient was set at $2 \cdot 10^{-1}$ mbar. The oxygen pressure is important for maintaining the Pb content in the film. It has been shown that usually the Pb content of the deposited film decreases dramatically at a low oxygen pressure¹. For ambient O_2 pressures above $1.33 \cdot 10^{-1}$ mbar, Pb, Ti and Zr atoms are well oxidized to PZT compound, and the PZT films can be formed without stoichiometric change.

The effects of the substrate temperature are very important in obtaining a particular crystal structure and orientation. PZT thin films have been deposited on different substrates, either non-heated or heated at different temperatures (typically below the temperature where extensive vaporization of volatile film constituents occurs). In general, at low temperatures the pyrochlore phase dominated the film structure, temperatures as high as 600°C being necessary for obtaining a stable perovskite phase.

In our experiments, we succeeded in the deposition of perovskite phase PZT at temperatures as low as 350°C .¹⁷ We have performed the deposition for two different temperatures: 375 and 500°C . The laser fluence was 25 Jcm^{-2} , the distance target-substrate 4-5 cm, and the deposition time 10-40 min.

EDS and X-ray diffraction were used to determine the composition and crystal structure for deposited films. XRD spectrum for the deposited films at 375°C has been compared with those for the original target.

Fig.7 shows the X-ray diffraction spectra of the original target of commercial PZT, before and after irradiation. One can observe that the sample presents a tetragonal structure. In the lower part of the graph, the X-ray diffraction spectrum for

PZT films deposited on Au(111)/Si(111) is presented. The Au(111) peak, normally evident, is masked in this spectrum, because the PZT film absorbs a great part of the X-rays.

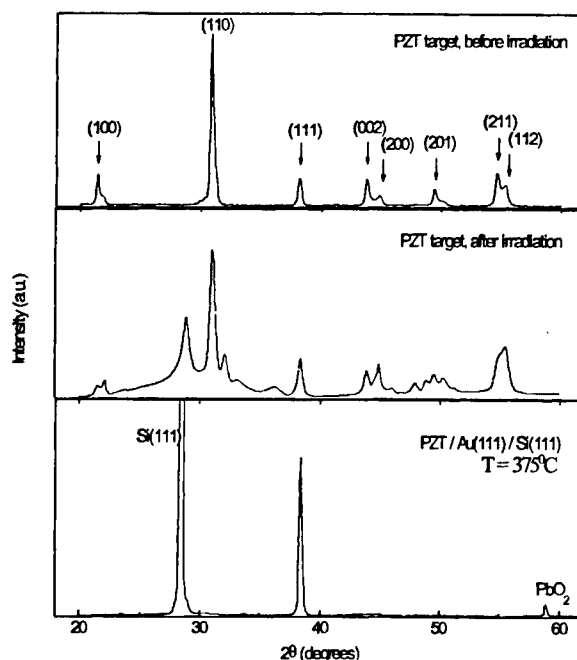


Fig.7. X-ray diffraction pattern for the PZT film deposited on Au(111)/Si(111) at a substrate temperature of 375°C; in the upper part, the graph of the PZT target used for its deposition, before and after irradiation.

From this diffraction spectrum one can observe that the films exhibited a preferential alignment of the (111) planes parallel to the film surface; the perovskite composition of the films is highly oriented. If the temperature is increased at 500°C we have obtained that the PbO₂ content is not a minor one and a PbO compound is generated. Definitely, the content of non-perovskite phases in the sample obtained at a higher temperature has increased.

SIMS analysis presented evidenced that the films deposited at lower substrate temperature (Fig.) have an almost uniform composition along the layer, with reduced interdiffusion. Strong penetration of the elements in the substrate can be instead observed in the other case (Fig.8) due to the much higher temperature, which favors diffusion. As one can observe, PZT/Au interface is drastically modified in this later case, too.

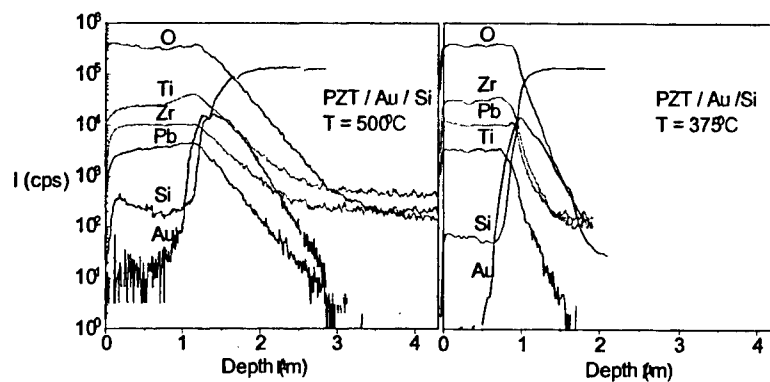


Fig.8. SIMS depth profiles of two PZT films, deposited at 500°C and 375°C, respectively.

The measurements that we have done for investigate the piezoelectric properties of PZT films revealed that they were all piezoelectric without poling. This fact is due to the epitaxial nature and (111) preferred orientation of the films. The measurements that have been performed in many different points on a large area ($2 \times 1 \text{ cm}^2$) evidenced the same polar orientation in all regions. The measured d_{33} piezoelectric constant values varied slightly between different measurements points and it was of 40 pC/N for the film deposited at 375°C and of 30 pC/N for the film deposited at 500°C. This value represents only approx. 20% of the PZT bulk constant, but it is adequate for many thin film applications. This fact and the deposition temperature, which was very low, make the obtained thin films useful in many integrated piezoelectric devices.

4. CONCLUSIONS

Pulsed Laser Deposition in reactive atmosphere was found to be effective for obtaining thin films of III-V compounds and piezoelectric ceramic as well. The experiments were performed at low collector temperatures (under 400 °C), using available and less expensive combination laser-gas target. The layers properties as high crystallinity and orientation, good adherence, make them suitable for sensors building.

5. REFERENCES

1. D.B. Chrisey and G.K. Huber, "Pulsed Laser Deposition of Thin Films", John Wiley & Sons, Inc., New York, Chidrester, Brisbane (1994).
2. R.K. Singh and J. Narayan, "Pulsed laser evaporation technique for deposition of thin films: Physics and theoretical model", *Phys. Rev. B*, **41** (13), 8843-8859 (1990).
3. R.K. Singh, O.W. Holland and J. Narayan, "Theoretical model for deposition of superconducting thin films using pulsed laser evaporation technique", *J. Appl. Phys.*, **68** (1), 233-246 (1990).
4. P.J. Gielisse and H. Niculescu, "Wide Band Gap Electronic Material", M.A. Prelas et al., Kluwer Academic Publisher, Netherlands, **401** (1995).
5. A. Saxler, P. Kung, C.J. Sun, E. Bigan and M. Razeghi, "High quality aluminium nitride epitaxial layers grown on sapphire substrates", *Appl. Phys. Lett.*, **64** (3), 339 (1994).
6. P. Verardi, M. Dinescu, C. Stanciu, C. Gerardi, L. Mirengi and V. Sandu, "A parametric study of AlN thin films grown by pulsed laser deposition", *Materials Science & Engineering B* (1997) (in press).
7. G. Radhakrishnan, "Properties of AlN films grown at 350 K by gas-phase excimer laser photolysis", *J. Appl. Phys.*, **78** (10), 6000 (1995).
8. Shuji Nakamura and Gerhard Fasol, "The Blue Laser Diode", Springer-Verlag, Berlin, Heidelberg, New York, (1997).
9. M. Dinescu, P. Verardi, C. Boulmer-Leborgne, C. Gerardi, L. Mirengi and V. Sandu, "GaN thin films deposition by laser ablation of liquid Ga target in nitrogen reactive atmosphere", *Applied Surface Science* (in press).
10. S.B. Krupanidhi and M. Sayer, *J. Appl. Phys.* **56**, 3308 (1984).
11. M. Dinescu, P. Verardi, "ZnO thin film deposition by laser ablation of Zn target in oxygen reactive atmosphere", *Appl. Surface Science* **106**, 149-153 (1996).
12. P. Verardi, M. Dinescu, A. Andrei, "Characterization of ZnO thin films deposited by laser ablation in reactive atmosphere", *Appl. Surface Science* **96-98**, 827-830 (1996).
13. J.J. Lee, C.L. Thio, S.B. Desu, *J. Appl. Phys.* **78**, 5073 (1995).
14. K. Sreenivas, M. Sayer, D.J. Baar, M. Nishioka, *Appl. Phys. Lett.* **52**, 709 (1988).
15. T. Fujii, S. Watanabe, M. Suzuki, T. Fujiu, *J. Vac. Sci. Technol.* **B13**, 1119 (1995).
16. P.B. Legrand, M. Wautelet, B. Dugnoille, J.P. Dauchot and M. Hecq, "Optical properties of sputter-deposited aluminium nitride films on silicon", *Thin Solid Films*, **248**, 220-223 (1994).
17. P. Verardi, F. Craciun, M. Dinescu, C. Gerardi, "Epitaxial piezoelectric thin films obtained by pulsed laser deposition", *Applied Surface Science* (in press).

Laser monitoring of pesticides in water

M.L. Pascu, N. Moise, L. Voicu, T. Negoita*, G. Manolescu**, A. Smarandache

National Institute for Laser, Plasma and Radiation Physics, Bucharest

*Polar Research Center, Bucharest

**Institute of Physical Chemistry, Bucharest

ABSTRACT

Pesticides monitoring at low concentrations using optical absorption, laser induced fluorescence (LIF), fluorescence lifetime measurements and gas chromatography are reported.

The studied pesticides were chlortriazines (athrasine, propasine and simasine) and organophosphoric pesticides (dichlorvos and parathion).

Since in normal conditions the chlortriazines show absorption spectra in ultraviolet (around 250 nm), to obtain fluorescence spectra in the visible they were treated with pyridine and ethyl ester of cyanacetic acid in basic medium.

The LIF spectra of chlortriazines are measured at concentrations of pollutants between 5 ppm and 20 ppm. The molecular complex fluorescence spectrum induced by pulsed laser radiation at 545 nm, available from a tunable dye laser, exhibited a maximum at 577 nm; it remained unchanged for three hours, following which the intensity decreases as a consequence of the complex destruction (decomposition)

The fluorescence lifetime of the molecular complex measured using a fast photodetector was 2.6 ns, immediately after complex formation.

The organophosphoric pesticides were monitored using a rather different initial chemical treatment, at the end of which a quinino-vanado-molibdophosphoric complex $(\text{PMo}_{10}\text{V}_2\text{O}_{39})_2(\text{C}_{20}\text{H}_{24}\text{O}_2\text{N}_2\text{H}_2)_3$ was formed. The fluorescence spectra of these pesticides induced by pulsed laser radiation at 337.1 nm available from a pulsed nitrogen laser (700 ps pulse time width, 300 $\mu\text{J}/\text{pulse}$ energy) exhibited a maximum at 445 nm with a FWHM of 80 nm.

The low concentration detection limits were 0.2 ppm for P in dichlorvos (dichlorvos concentration 14.18 ppm) and 0.2 ppm for P in parathion (parathion concentration 17.8 ppm).

These methods in correlation with optical absorption, classical fluorescence and gas chromatography methods were applied to monitor pesticides in water samples collected from the North Pole zone following two expeditions dated March-April 1995 to Severnaia Zemlia Archipelago and July-August 1996 to Spitzbergen Archipelago. Comments about the monitoring of pesticides content of these samples are made.

1. INTRODUCTION

The pesticides belong to the category of the most oftenly encountered pollutants in water and soil and last very long time in environment (more than 30 years). Their biodegradability within soil or water is extremely low¹. This is why there is a significant interest in their concentration measurements, particularly in water; on the other hand, the standards about the limits of pesticides concentrations in water and soil issued by EEC, are imposing maximal allowed concentrations for these pollutants in environment, of 0.01 ppm.

Many standard or unconventional experimental techniques including absorption, laser emission spectroscopy and chromatography were developed to monitor pesticides pollutants in environment. They may be applied either in laboratory or "in situ", using dedicated equipment. For "in situ" measurements laser induced fluorescence (LIF) techniques are currently used based on elementary processes previously specified². LIF spectroscopy has proved to be one of the most sensitive detection methods and became a powerful tool in analytical chemistry, biology and medicine. LIF has a great potential to qualitatively and quantitatively measure the pollutants due to its sensitivity (small quantities of studied samples and usually, low concentrations of fluorophores) and in the same time, to the undestructive character of the measurements with the possibility to perform remote monitoring using optical fibers. Since fluorescence emission is affected by fluorophores nature and concentrations and their surrounding environment, different polluted samples are expected to yield different fluorescence signals, both in spectral and temporal range.

Usually, the absorption spectra of pesticides are reported in UV range, below 250 nm³, so that laser monitoring is difficult due to the lack of tunable laser radiation available in this spectral range. To measure easier the absorption peaks and the related fluorescence spectra it is necessary to chemically treat the pesticide samples with different substances using different methods in order to obtain new complexes which are optically active in the visible range. Taking into account the difficulties to monitor pesticides in water using standard methods, we have developed laser absorption and spectrophotofluorimetric methods for their concentration measurements.

The organophosphoric pesticides have a very high toxicity affecting the nervous system at the synapse level and inhibiting the activity of the enzymes.

Besides the chromatographic methods for monitoring organophosphate pesticides, in the last years were developed spectrophotometric and spectrophotofluorimetric methods either.

The detection limit for parathion and paraoxone using these techniques was 0.05 - 0.1 µg/ml⁴.

With excitation at 350 nm the fluorescence emission of gibberelic acid is around 455 nm⁵.

Using optical excitation at 300 nm, thiabendazol in acid solution shows a fluorescence maximum at 360 nm⁶.

LIF method was used to monitor other phosphorus complexes in water, soil, plants and rocks using fluorescence reagents such as lyvanol (lactic acid-6,9 diamino-2 etoxiacridina).

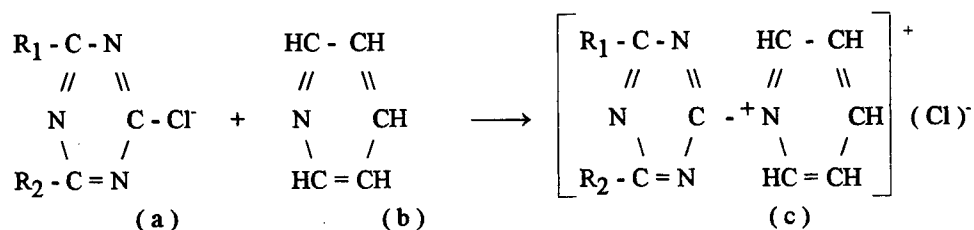
2. MATERIALS

The pollutant samples which were studied using absorption, laser emission spectroscopy and gas chromatography were classified in the following categories: samples containing chlortriazine pesticides, organophosphoric pesticides and water samples collected during two expeditions at North Pole zone.

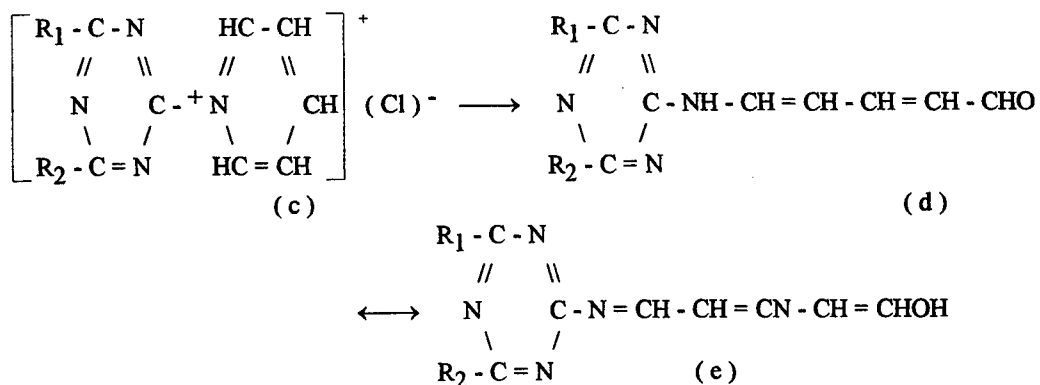
2.1 Samples of untreated and treated solutions in water containing different concentrations of chlortriazines.

Since absorption spectra of chlortriazine samples in water are showing significant peaks in UV at 224 nm and 260 nm, laser monitoring of chemically untreated samples is difficult as mentioned. Consequently, chlortriazines were processed using a chemical method to be optically active in the visible spectral range.

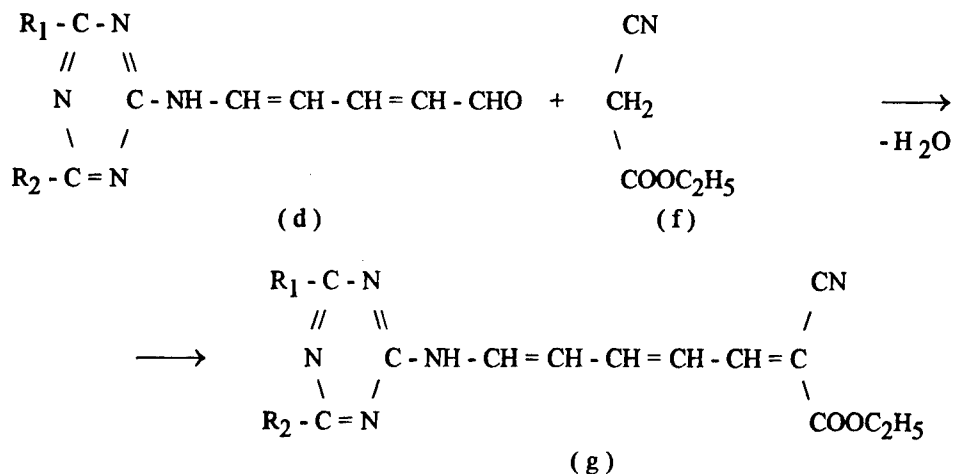
The chlortriazines, particularly simasine, propasine and athrasine (a), were treated with pyridine (b) obtaining a quaternaire chloride of pyridinium (c) following a nucleophile substitution reaction.



In basic medium, the pyridine cycle is opened and an anyl of the glutathionic aldehyde (d), in equilibrium with the enol form (e) are obtained:



The mixture (d) + (e) has a strong absorption peak in the visible range in the presence of ethyl ester of cyanacetic acid (f). The complex molecule (g) exhibits an absorption maximum at 545.5nm.



2.2 The organophosphoric pesticides samples consist of dichlorvos and parathion and were monitored using a rather different initial chemical treatment, at the end of which a quinino-vanado-molibdophosphoric complex $(PMo_{10}V_2O_{39})_2(C_{20}H_{24}O_2N_2H_2)_3$ was formed.

Amounts between 0.2 and 1 μ g phosphor contained in organophosphoric pesticide may be measured using a phosphoric complex produced following the reaction between molibdofosfate and quinine alkaloid. The quinino-vanado-molibdophosphoric complex is precipitated in 0.5 M H_2SO_4 medium. The excess of quinine is removed by cleaning with 0.5 M H_2SO_4 and the phosphoric complex is dissolved in a mixture formed by acetone - 0.5 M H_2SO_4 (9 + 1 V/V).

2.3. The water samples were divided in two categories. The samples of series I were picked up following the expedition of T. Negoita dated March-April 1996 to Severnaia Zemlia Archipelago - North Pole zone from the points:

- 89°59'57" North latitude and 70°42' East longitude
- 88°50' North latitude and 100°15' East longitude
- 89°42' North latitude and 48°20' East longitude.

The samples of the first series were picked up from:

1. In pack
2. Ocean
3. Ocean
4. In pack
5. In pack
6. In pack

The samples of series II were picked following the expedition of T. Negoita dated July-August 1996 from Spitzbergen Archipelago:

1. Bjorndalen - snow river
2. Grumantdalen - in pack water
3. Zachariassendalen - snow river
4. Brattdalen - snow river
5. Grondalen - valley river
6. Bjorndalen - snow river
7. Bjorndalen - valley river
8. Adventfjordan - ocean water
9. Longjerdalen - snow water river
10. Longjerdalen - valley river (snow + ice pack).

3. METHODS AND EXPERIMENTAL RESULTS

3.1.1. Absorption spectroscopy. Chlortriasine (simasine, propasine and athrasine) samples diluted in water at different concentrations between 1ppm and 10ppm were studied by classic UV and visible absorption spectroscopy. The spectra were measured using a Specord UV-VIS spectrophotometer (Carl Zeiss Jena).

The measured spectra have shown that the chemically untreated chlortriasines exhibit in water UV absorption spectra which are characterized by one or two maxima. There is not a significant difference between the absorption spectra of simasine, propasine and athrasine.

From Fig.1 one observes that untreated chlortriasines exhibit a higher absorption peak at 244nm and a relative maximum at 266nm. Another conclusion is that the absorption spectra obtained at different concentrations show the same peaks which are decreasing in intensity with concentration decreasing.

To obtain an absorption signal in the visible, the chlortriasine samples were processed using pyridine complexation. In basic media and in the presence of ethyl ester of cyanacetic acid, the mixture changes its colour and exhibits an absorption maximum at about 545nm.

The absorption spectra performed on treated simasine, propasine and athrasine samples (at concentrations between 1ppm and 10ppm) are similar; it is to be observed that the three complexed chlortriasines show only one absorption maximum at 545nm.

In Fig.2 is shown the transmission spectrum of complexed atrasine (1ppm concentration). According to our observations the absorption and fluorescence spectra of treated chlortriasines are time dependent, so that stable optical properties are noticed within a time interval not longer than 3 hours after the chemical treatment.

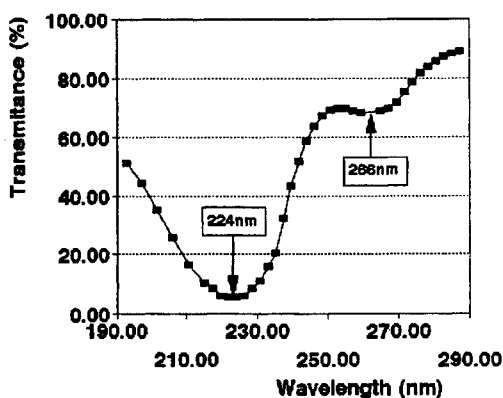


Fig.1 Transmission spectrum of atrasine at 10ppm (classical spectrophotometer).

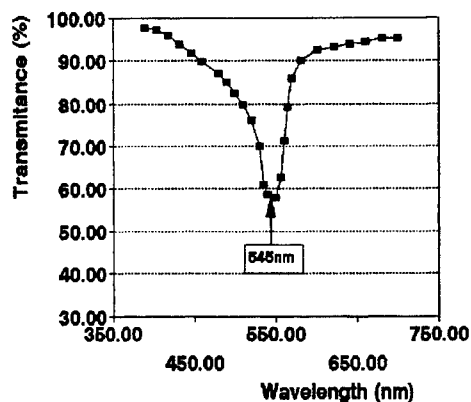


Fig. 2 Transmission spectrum of complexed atrasine at 1ppm (classical spectrophotometer)

The absorption spectra of the treated chlortriasines active in the visible range and at low concentrations may be measured using a tunable dye laser. The absorption spectra of chlortriasines between 1ppm and 0.001ppm were measured using a laser spectrophotometer developed specifically for this purpose³. The radiation of the tunable dye laser is introduced in an optical bridge which contains the absorption cell (chlortriasine sample) and the reference cell. In this way was obtained an absorption signal for each emitted radiation wavelength.

In Fig.3 is shown the laser transmission spectrum for atrasine at 0.01ppm exhibiting, also, an absorption maximum at 545nm. It is to be observed a good sensitivity of the device in the range of low concentrations. To determine the chlortriasine concentration in water, a data library is introduced in the computer's memory for concentrations in the 0.001ppm to 1ppm range.

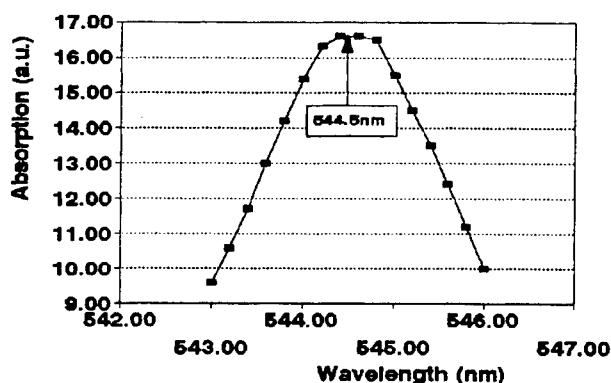


Fig.3 Laser absorption spectrum of complexed athrasine (0.01 ppm).

3.1.2. Laser induced fluorescence spectroscopy. Taking into account that the complexed chlortriasines absorption maximum is at 545nm, to induce laser fluorescence is necessary to use a laser radiation with a wavelength closed to this value but lower than it, which may be available from a tunable dye laser. The nitrogen pulsed laser used to pump the dye works at atmospheric pressure and emits an UV radiation at 337.1nm. The emitted energy per pulse is about $150\mu\text{J}$ and the laser beam power fluctuations are less than 5%, inducing relatively small fluctuations of fluorescence signal. The pulse time width of pumping laser is 700 psec and the pulse repetition rate is chosen between 0.5pps and 10pps. The experimental set-up for LIF measurements is shown in Fig.4. The nitrogen laser radiation is focused into a quartz cell (C1) which contains the dye (coumarin or Na-fluorescein) using a system of two quartz lenses (L_s and L_c).

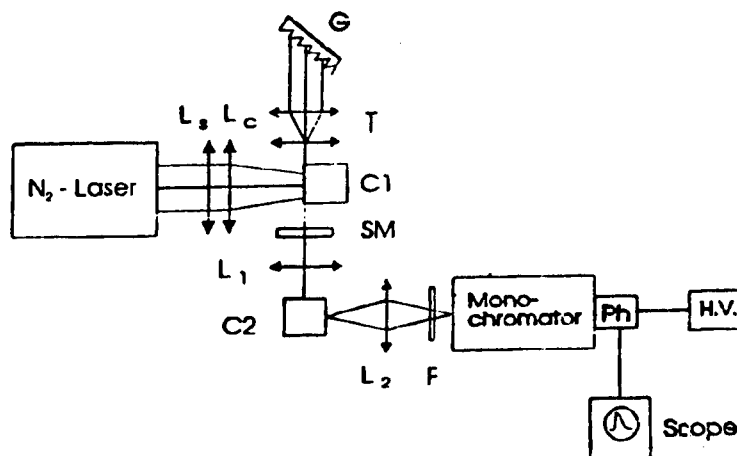


Fig.4 Experimental set-up for LIF measurements on chlortriasines

The UV laser radiation is absorbed by the dye and its fluorescence radiation is emitted along the pum-ping filament. The fluorescence radiation is amplified and analysed using a diffraction grating (G) so that one obtains a tunable laser radiation at the output of the optical cavity, within the spectral range of the fluorescence radiation, for the given dye solution. Dye laser beam is focused on a quartz cell (C2) which contains the chlortriasine sample (simasine, propasine or athrasine), whose fluorescence is excited. Dye laser wavelength is chosen to be 530nm. The fluorescence radiation yielded by chlortriasines is focused on the $25\mu\text{m}$ input slit of a SPM2 monochromator (Carl Zeiss Jena) equipped with a 1302 grooves/mm diffraction grating. The analysed spectrum was measured with a 1P28 (RCA) photomultiplier and sent to a 7904 Tektronix scope obtaining point by point the fluorescence spectrum. An UV absorption filter is introduced before the monochromator input slit, avoiding UV radiation input into the monochromator. The fluorescence

spectra of the three chlortriasines at different concentrations (10ppm, 15ppm and 20ppm) were measured. We noticed that the fluorescence maximum for all the chlortriasines is at 577nm and their spectra are emitted between 550nm and 600nm with a FWHM of about 30nm. In Fig. 5 are shown LIF spectra for athrasine at the three mentioned concentrations (10ppm-empty square, 15ppm-filled triangle, 20ppm-filled square). The linear distribution of fluorescence intensity maximum function of concentration for all the three chlortriasines was observed. This may be used as calibration curve to determine samples' concentrations.

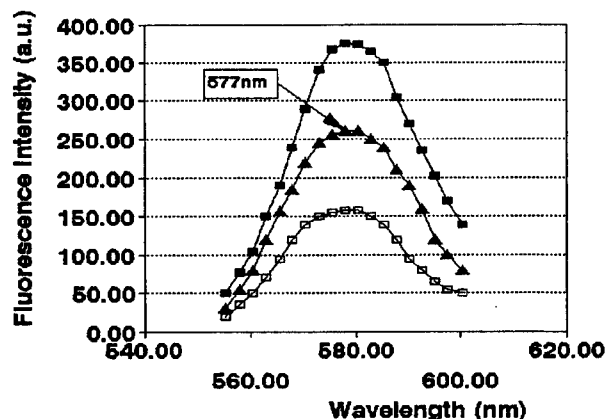


Fig.5 LIF (excited with 530 nm laser radiation) for complexed athrasine (10, 15 and 20 ppm), respectively.

For fluorescence lifetime measurements, the fluorescence signal of chlortriasine samples was focused on a fast PIN photodiode with a rise time of about 0.2nsec. The photodiode yielded signal was observed on a Tektronix scope; the image obtained reproduces the time behavior of fluorescence intensity. Fig.6 exhibits an exponential decay of fluorescence intensity for all the complexed chlortriasines. The fluorescence lifetime, measured as the time required for the intensity to decay to 1/e of its initial value, was 2.6 nsec for athrasine, simasine and propasine immediately after their complexation. The overall error was about 6%.

We observed that, in time, all the complexed chlortriasines became colourless and, at the same excitation wavelength (530 nm), their fluorescence is vanished. The LIF time evolution has shown that the fluorescence maximum emitted by the treated samples of chlortriasines is shifted after 24 hours from 545nm to 428nm in direct connection with the modification of the excitation wavelength from 530nm to 337.1nm. The LIF spectrum of treated athrasine sample (10 ppm) after 24 hours from preparation is shown in Fig.8. We noticed that the fluorescence peak is at 428nm and the full width at half maximum (FWHM) is about 100nm. On the other hand, the fluorescence lifetime of treated chlortriasines increases in 24 hours to 6.6 nsec. In Fig.7 is shown the decay time of fluorescence intensity for treated athrasine (10 ppm, 24 hours after preparation).

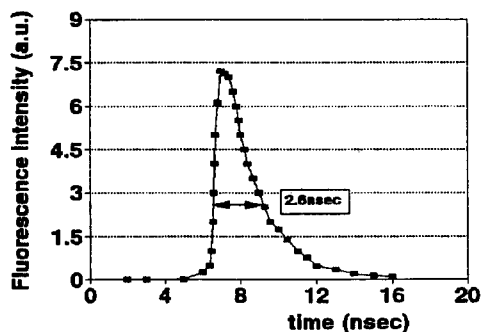


Fig. 6. Fluorescence intensity decay time for complexed chlortriasines

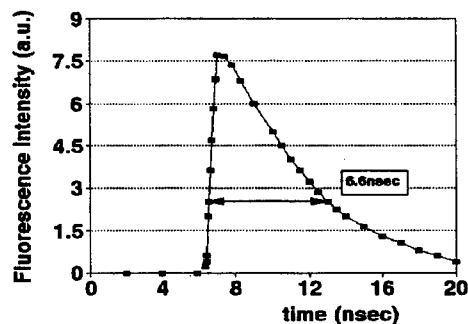


Fig. 7. Fluorescence intensity decay time for chlortriasines (24 hours after preparation)

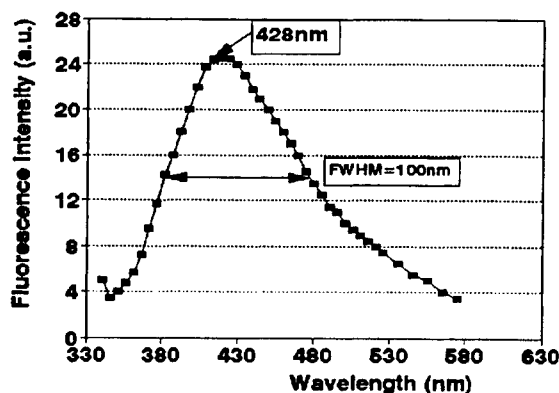


Fig.8 LIF (excited with 337.1 nm) of complexed atrasine (10 ppm) after 24 hours

3.2. The fluorescence excitation of the quinino-vanado-molibdophosphoric complex was made using pulsed laser radiation available for pulsed TEA nitrogen laser (emitting at 337.1 nm, pulse full time width of approximately 700 ps, peak energy per pulse of 300 μ J); the pulse repetition rate was chosen between 0.5 pps and 10 pps). The laser beam power fluctuation were less than 5%, inducing relatively small fluctuations of the fluorescence signal.

The experimental set-up used to measure the fluorescence of phosphoric complex is shown in Fig. 9.

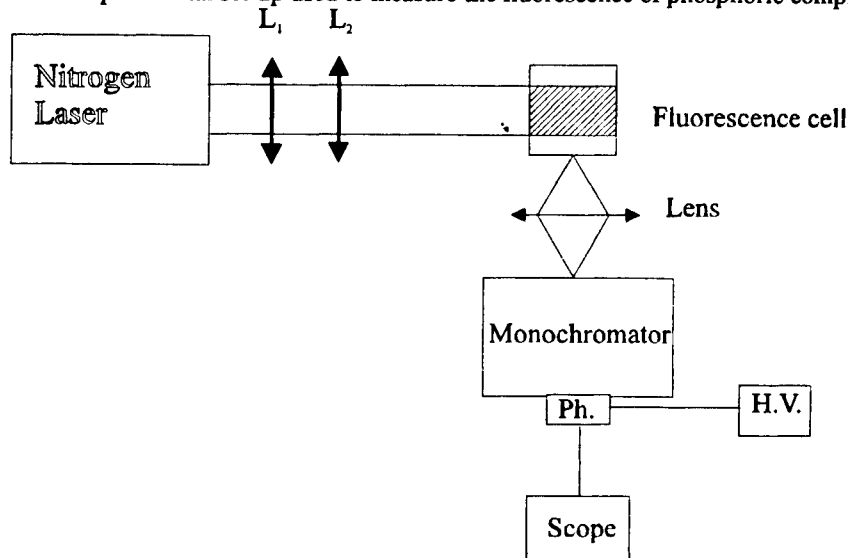


Fig. 9. The experimental set-up for LIF measurements for organophosphoric pesticides

The fluorescence radiation emitted by the complex is optically analyzed by a monochromator and measured by a 1P28 (RCA) photomultiplier. An UV absorption filter was introduced before the monochromator input slit to avoid UV radiation input into the monochromator.

The fluorescence spectra of an etalon sample and of the phosphoric samples at different concentrations (0.2 ppm, 0.5 ppm, 0.8 ppm) are shown in Fig. 10 exhibiting a maximum of fluorescence at 445 nm with a spectral width at half maximum of about 80 nm.

The low concentration detection limits were 0.2 ppm for P in dichlorvos (dichlorvos concentration 14.18 ppm) and 0.2 ppm for P in parathion (parathion concentration 17.8 ppm).

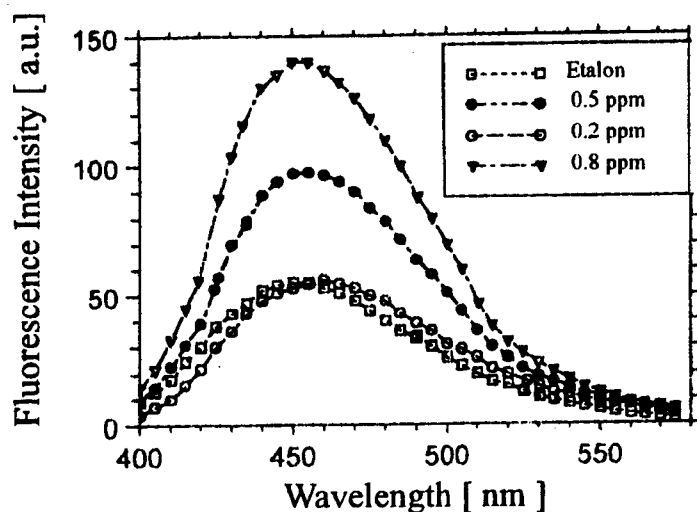


Fig. 10. Fluorescence spectra of phosphoric samples at different concentrations.

3.3. The water samples picked-up during the two expeditions at North Pole zone were analyzed by standard absorption, classical fluorescence, laser induced fluorescence and gas chromatography.

3.3.1. The absorption spectra of water samples were made with a standard spectrophotometer SPECORD UV-VIS (Carl Zeiss Jena) in UV and visible range between 200 nm - 800 nm.

The absorption spectra of the six samples of series I at room temperature (Fig. 11) and ten samples of series II at room temperature (Fig. 12) are showing different spectral behaviours.

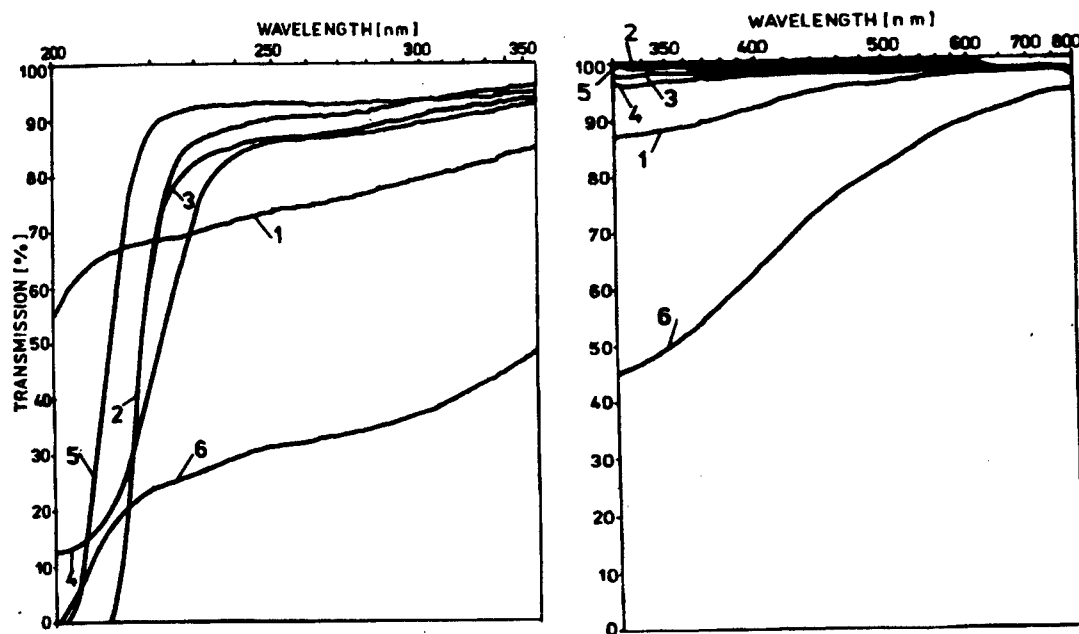


Fig. 11. UV and VIS absorption spectra of series I samples.

Only the sample no. 6 of series I shows an increasing of the absorption with time. The absorption spectra of sample no. 6 were measured within a time interval of 4 hours.

The same sample was studied from the point of view of the properties variations induced by the temperature modifications.

The absorption spectra were measured in a temperature range between 0°C and 50°C showing an increasing of absorption with the increasing of temperature.

The modifications of sample no. 6 absorption may be due to *Bacillus Subtilis* bacteria.

This sample was boiled in order to destroy the bacteria. In this respect we observed a decreasing of absorption which confirms our hypothesis.

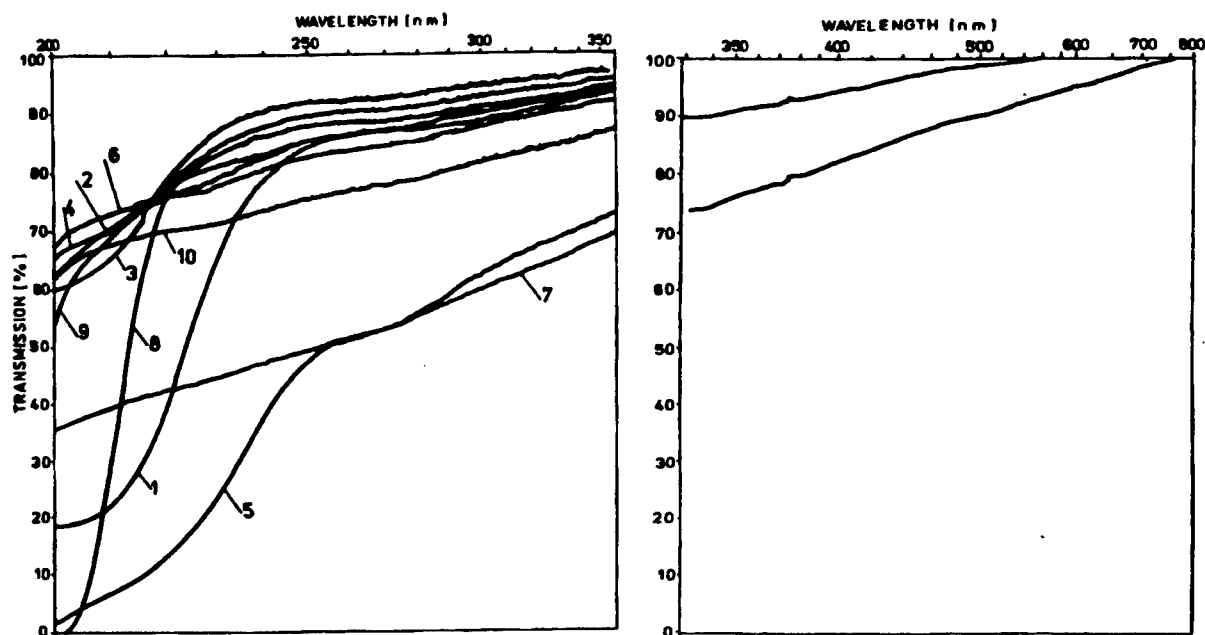


Fig. 12. UV and VIS absorption spectra of series II samples.

3.3.2. The classical fluorescence spectra of samples of series I were measured with a spectrophotofluorimeter AMINCO-BOWMAN using optical excitation at 300nm and 337nm. The fluorescence maximum is in the range (430 - 510)nm. The sample no. 6 has the higher fluorescence intensity.

3.3.3. The laser induced fluorescence of water samples was obtained using pulsed laser radiation available from a pulsed TEA nitrogen laser with the following characteristics: wavelength 337.1nm, pulse full time width 700ps, peak energy per pulse of 300μJ, pulse repetition rate from 0.5pps to 10pps, power fluctuations less than 5%. The fluorescence radiation emitted by the samples is collected by an optical fiber and transmitted to the entrance slit of a monochromator SPM 2. The analyzed fluorescence spectrum is measured by a 1P28 (RCA) photomultiplier and sent to a Tektronix scope.

In Fig. 13 (a) and (b) are shown the LIF spectra of sample no. 1 (series II) filtered and unfiltered and respectively of sample no. 2 (series II) filtered and unfiltered.

The fluorescence maximum of filtered sample no. 1 is around 405nm and is higher than the fluorescence of the unfiltered sample which show two peaks at 385nm and 420nm with a minimum at 405nm. The fluorescence maximum of filtered sample no. 2 is around 407nm and is higher than the fluorescence of the unfiltered sample which has a maximum at 385nm.

Since the filtered samples show a higher intensity of fluorescence one may conclude that the impurities of these samples are fluorescence quenchers.

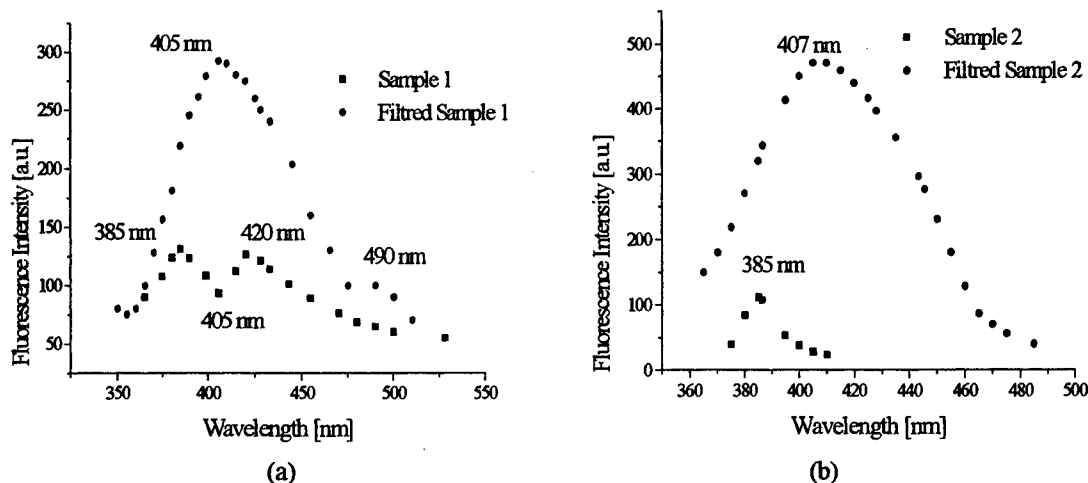


Fig. 13 Fluorescence spectra of sample 1 (series II) (a) and 2 (series II) (b), filtered and unfiltered.

3.3.4. Gas chromatography measurements.

In this study we explore the presence and identity of organochlorinated pesticides in water samples using two different detection techniques. The samples were concentrated using solid-phase extraction cartridges (SPE) in which analytes of interest were initially absorbed by a solid support and subsequently desorbed with an appropriate solvent.

Solid-phase extraction. Immediately before use, the SPE cartridges (Bakerbond SPE-500, 6ml (500mg) packed with 500mg of C18 material) are conditioned by eluting with 6ml hexane and dried under vacuum for 1-2 minutes. Then we aspirate 12ml methanol, followed by 6ml bidistilled water treated with KMnO_4 . The sample water (250ml) is filtered using a glass filter, then is sent to pass through the preconditioned cartridge in about two hours in vacuum conditions; we add 1ml hexane to column, allow the solvent to percolate into the column for 1 minute and then slowly aspirate it through the column. All solvents obtained from Supelco were of pesticide grade (free of pesticide residue detected by electron capture detector - ECD or mass spectrometry - MS).

1 μl of this solution containing organochlorinated pesticides eluted from the cartridge is injected in gas chromatograph.

Gas chromatography analysis. The presence of chlorinated pesticides residues in water sample 1 was established using Hewlett-Packard 5890 gas chromatograph (GC) in conjunction with an electron capture detector (ECD). The chromatograph operating conditions were as follows: column PASS 5: 30m x 0.25mm x 0.2 μm ; stationary phase: 5% phenyl methyl silicon; column temperature: 85°C for 1 minute, 30°C/min to 190°C, 3.6°C/min to 240°C; detector temperature: 340°C; nitrogen flow rate 2.3ml/min. The detection limit was 1ng/l for DDE, dieldrin, DDT.

GC-ECD chromatogram of water sample 1 (series II) and GC-ECD chromatogram of reference substance are shown in Fig. 14 and Fig. 15.

The concentrations of detected organochlorinated pesticides (Table 1) were determined by comparison of each peak area with a reference standard. The standard organochlorinated pesticide mixture containing α -HCH (0.2ng/ μl), β -HCH (0.2ng/ μl), γ -HCH (0.2ng/ μl), heptachlor (0.2mg/l), aldrin (0.2ng/ μl), pp'DDE (0.2ng/ μl), dieldrin (0.2ng/ μl), ppDDT (0.2ng/ μl) was obtained from Alltech Associates.

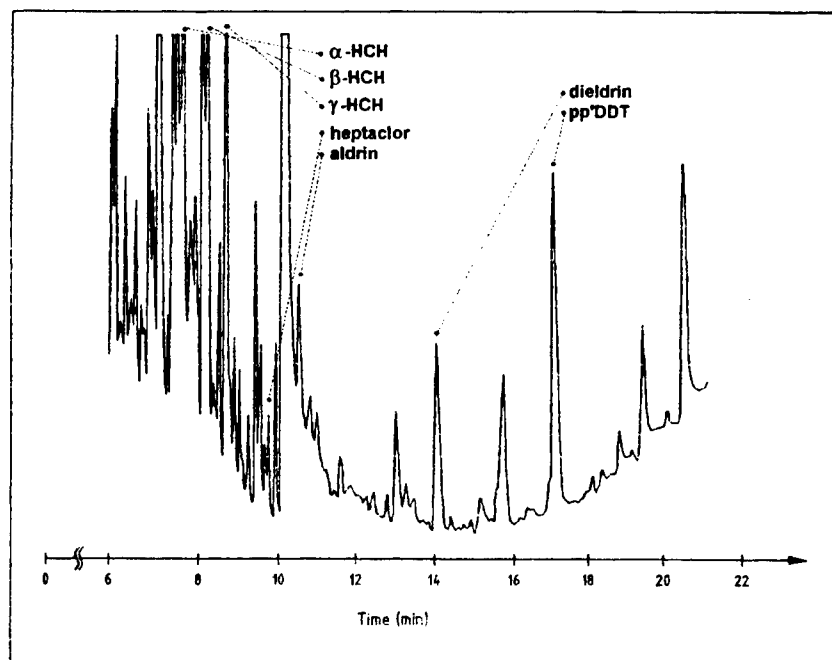


Fig. 14 GC-ECD chromatogram of water sample no. 1
 α -HCH (t_R : 7.50), β -HCH (t_R : 8.08), γ -HCH (t_R : 8.59), Heptachlor (t_R : 9.78),
 Aldrin (t_R : 10.75), Dieldrin (t_R : 14.01), pp'DDT (t_R : 17.08)

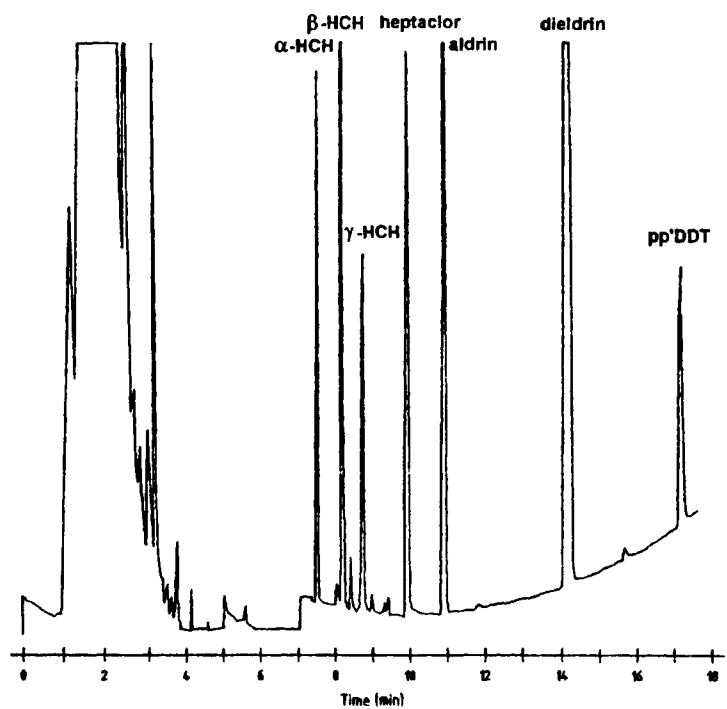


Fig. 15 GC-ECD chromatogram of reference substances
 α -HCH (t_R : 7.41), β -HCH (t_R : 8.06), γ -HCH (t_R : 8.59), Heptachlor (t_R : 9.78),
 Aldrin (t_R : 10.76), Dieldrin (t_R : 14.01), pp'DDT (t_R : 17.08)

Table 1. The concentration ($\mu\text{g/l}$) of detected chlorinated pesticide in the water samples prelevated from series II (see Introduction)

Organochlorinated pesticide	The concentration ($\mu\text{g/l}$) of detected chlorinated pesticide in sample no. 1	The concentration ($\mu\text{g/l}$) of detected chlorinated pesticide in sample no. 2	The concentration ($\mu\text{g/l}$) of detected chlorinated pesticide in sample no. 3
α -HCH	0.168	0.0043	0.010
β -HCH	0.169	0.0056	0.0237
γ -HCH	0.203	0.0037	0.0287
γ -HCH	0.203	0.0037	0.0287
δ -HCH		0.0121	
Heptachlor	0.026		
Aldrin	0.126		
Heptachlor epoxid		0.0437	
pp'DDE		0.0225	0.005
Dieldrin	0.053	0.1837	
pp'DDD		0.7525	
Endrin aldehida		0.08	0.0362
pp'DDT	0.236	0.0625	0.0187

The positive results were then confirmed using GC- mass spectrometry (MS). The extracted chlorinated pesticides residues from water samples 2 and 3 were analysed using GC-mass spectrometry. The chromatographic operating conditions were as follows: Hewlett-Packard 5890 series II gas chromatograph; mass spectrometer HP 5972; column HP5MS: 30 m x 0.25 mm x 0.2 μm ; stationary phase: 5% phenyl methyl silicon; column temperature: 280°C; helium flow rate: 1.48 ml/min.

The standard organochlorinated pesticide mixture containing α -HCH (0.2ng/ μl), β -HCH (0.2ng/ μl), γ -HCH (0.2ng/ μl), δ -HCH (0.2ng/ μl) heptachlor (0.2ng/ μl), aldrin (0.2ng/ μl), heptachlor epoxid (0.2ng/ μl), endosulphat I (0.2ng/ μl), pp'DDE (0.2ng/ μl), dieldrin (0.2ng/ μl), endrin (0.2ng/ μl), endosulphat II (0.2ng/ μl), ppDDD (0.2ng/ μl), endrin aldehida (0.2ng/ μl), endosulphat sulphat (0.2ng/ μl), pp'DDT (0.2ng/ μl) was obtained also from Alltech Associates. The chromatogram of water sample 2 and 3 acquired using GC-MS coupled with an IBM computer are shown in Fig. 16 and Fig. 17.

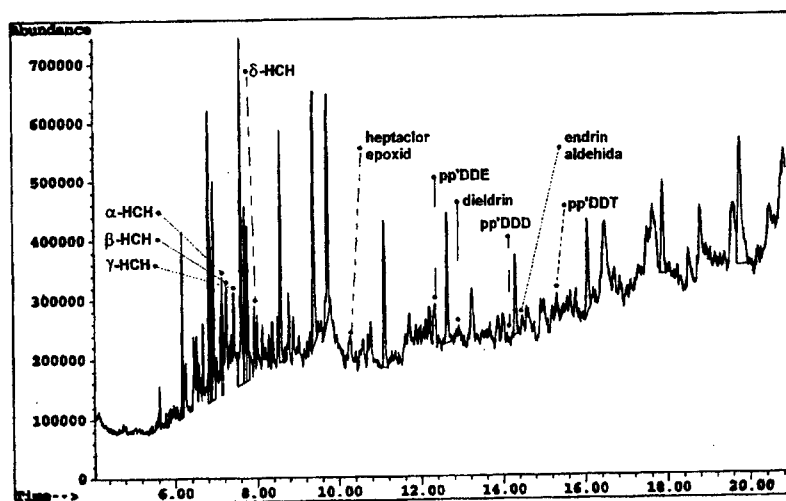


Fig. 16 GC-MS chromatogram of water sample no. 2

α -HCH (t_R : 7.16), β -HCH (t_R : 7.44), γ -HCH (t_R : 7.56), δ -HCH (t_R : 7.95), Heptachlor epoxid (t_R : 10.89), pp'DDE (t_R : 12.58), Dieldrin (t_R : 12.64), pp'DDD (t_R : 14.33), Endrin aldehida (t_R : 14.32), pp'DDT (t_R : 15.35)

The concentrations of detected organochlorinated pesticides for the sample 2 and 3 determined by comparison of the peak area with the reference standard are shown in Table 1. Each chromatographic peak has an unique mass spectrum that can be compared with a reference standard library for peak identification.

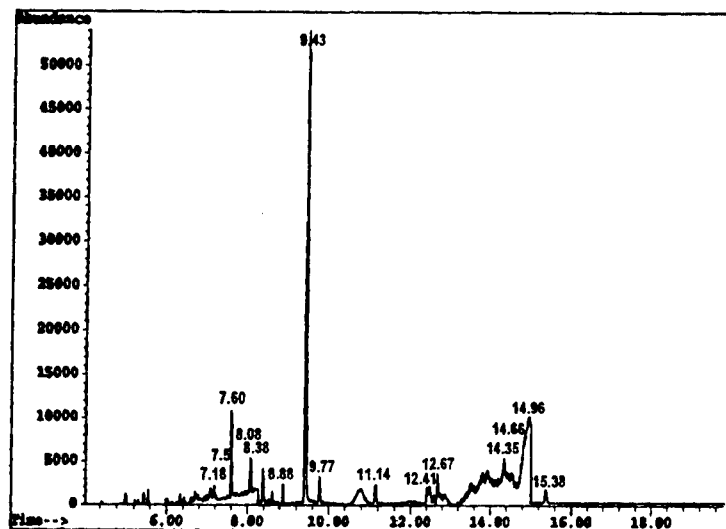


Fig. 17. GC-MS chromatogram of water sample no. 3 : α -HCH (t_R : 7.18), β -HCH (t_R : 7.50), γ -HCH (t_R : 7.60), pp'DDE (t_R : 12.60), Endrin aldehyda (t_R : 14.35), pp'DDT (t_R : 15.38)

4. CONCLUSIONS

The reported results are covering a relatively large area measured water samples polluted with pesticides and in the same time are showing the capabilities in pesticides monitoring of the optical absorption (both classical and laser) laser induced fluorescence and gas chromatography.

The laser methods are proved to be usefull for low concentration pesticide monitoring, particularly when laser induced fluorescence is used. For chlortriasines detection, LIF may be used down to sub-ppm concentration level; the same is true for phosphorate pesticides.

Another kind of results are regarding chlorinated pesticides presence in water samples collected at the North Pole zone. The measureenmts were made using gas chromatography and are showing typical concentrations in the range $0.04\mu\text{g/l}$ to $0.7\mu\text{g/l}$.

Further studies /measurements are required on polar water samples to fully characterize their pollution state.

5. REFERENCES

- 1."Cleaning Our Environment. A Chemical Perspective. A Report by the Committee on Environmental Improvement", American Chemical Society, Washington D.C., pp.188-274, 1978.
2. N.Moise, A.Vasile, M.L.Pascu "Measuring of soil contamination with oil components using LIF transmitted through optical fibres", Vol. SPIE 2461, pp.636-643, 1995.
- 3.Gunther A. and Blinn R., "Analysis of Insecticides and Acaricides", Interscience Publishers Inc.N.Y.,pp. 628,1955.
- 4.Martin A., *Ca. J. Pharm. Sci.*, 7 (1), pp.21, 1972.
- 5.Pesticide Analitical Manual, Vol. 11, *Pesticide Reg. Sec.* 120.224, 7/15/68.
- 6.Pesticide Analitical Manual, Vol. 11, *Pesticide Reg. Sec.* 180.242, 11/7/73.
- 7.Rongua Li, Zhauro Zhou, "Determination of trace amounts of phosphorous by laser excited time resolved fluorometry", *Analist*, 118, pp.563, 1993.

Detection of atmospheric pollutants by pulsed photoacoustic spectroscopy

Miruna Roman, M.L.Pascu, A. Staicu

National Institute for Lasers, Plasma and Radiation Physics; Lasers Department
P.O. Box MG-36, Bucharest 76911

ABSTRACT

Pulsed laser photoacoustic detection of NO_2 and SO_2 is reported. The laser source is a pulsed molecular nitrogen laser emitting at 337.1 nm. The average energy per pulse is about 350 μJ and the pulse duration 10 nsec. For detection we used a piezoelectric transducer (TUSIM- N.I.M.P., resonance frequency 4 MHz) and an electret condenser microphone (Trevi EM 27). The photoacoustic cell was a nonresonant one, with a cylindrical shape. The laser beam was centred along the cylinder axis. Linear dependence of the photoacoustic signal on pollutant pressure was obtained. This linearity is in a good agreement with theoretical considerations. The photoacoustic signal was measured for pollutants pressure between 1 torr and 100 torr for NO_2 and between 35 torr and 100 torr for SO_2 .

Keywords: pulsed laser photoacoustic detection, atmospheric pollutants, NO_2 , SO_2 , pulsed molecular nitrogen laser

1. INTRODUCTION

Laser photoacoustic spectroscopy (PAS) has been used as a very sensitive technique in detection of a wide range of molecules¹. PAS exhibits an important spectral selectivity and for this reason this technique is widely used for individual detection of a certain substance in mixture² such as pollutants detection in atmospheric air.

Pulsed laser excitation is an alternative experimental approach to photoacoustic spectroscopy and detection, relative to modulated cw lasers. The technique provides temporal resolution of the photoacoustic signal (phase resolution in modulated cw technique), which makes it able to separate the molecular gas absorption signal from the window and cell wall absorption. Since the sensitivity of the photoacoustic detection is mainly limited by the magnitude of the background signal, rejection of a large portion of it by temporal resolution leads to a high signal/noise ratio³.

2. THEORETICAL CONSIDERATIONS

The photoacoustic effect is the process of generating pressure waves in a sample resulting from the absorption of modulated light radiation. In the particular case of laser induced photoacoustic techniques the excitation sources are modulated c.w. laser beams or pulsed laser beams.

When visible or ultraviolet radiation is used to excite a molecular electronic state, the number of possible deactivation pathways is greatly increased. Some of the possible photoinduced processes are illustrated schematically in Figure 1.

Light absorbed by a sample will excite a fraction of ground-state molecular population into higher energy levels. These excited states will subsequently relax through a combination of radiative and nonradiative pathways. The nonradiative component will finally generate a pressure wave that propagates away from the source. The pressure wave is then detected with a suitable sensor such as a microphone or a piezoelectric transducer⁴.

Light absorbed by molecules is converted to heat, luminescence or chemical energy, obeying the general condition of energy conservation (Figure 2). A relevant percentage of energy absorbed as light by matter is dissipated as heat by various molecular mechanisms and is consequently lost to optical studies. In this sense we can refer to photoacoustic methods as complementary to fluorescence and phosphorescence measurements.

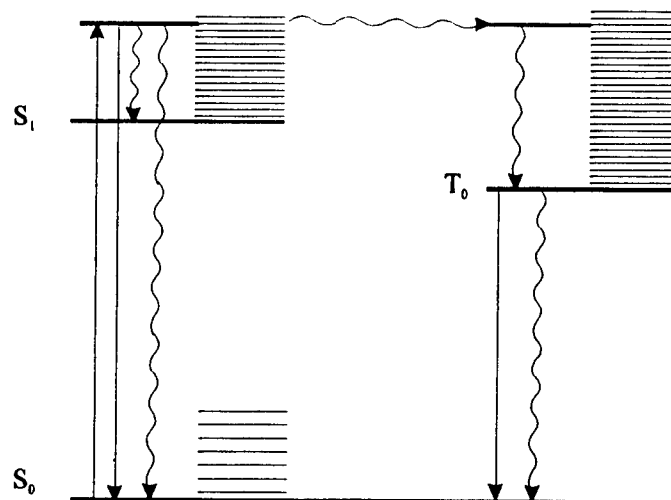


Fig.1 Electronic energy level diagram indicating some possible photophysical processes.

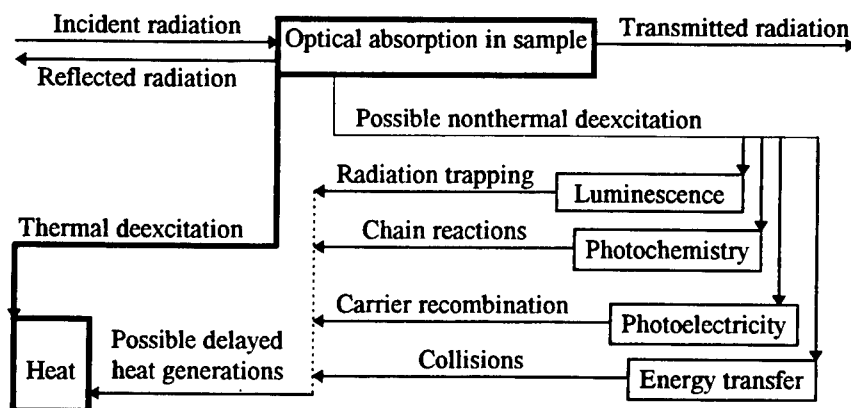


Fig.2 Block diagram showing the main processes bearing on the generation of heat following the absorption of light by a photoactive sample.

The time resolution of the method depends on the possibility of separating the heat emitted in the fast processes (i.e. internal conversion, for example) from the heat produced by slow processes (luminescence, photochemistry, photoelectricity and energy transfer).

When using a pulsed laser, with an input pulse energy of E_0 per pulse, the energy absorbed by the medium having an absorption coefficient of α [cm^{-1}] and length l [cm] is given by Equation (1):

$$E_{abs} = E_0 (1 - e^{-\alpha l}) \quad (1)$$

For $\alpha l \ll 1$ we obtain:

$$E_{abs} = E_0 \alpha l \quad (2)$$

Since we are assuming that nonradiative relaxation predominates in the medium, the thermal energy E_{th} is given by

$$E_{th} = E_{abs} = E_0 \alpha l \quad (3)$$

Under the conditions mentioned above it will be obtained a relation between optoacoustic signal V_{oa} and absorption coefficient of the sample α given by the following equation¹:

$$V_{oa} = \text{const. } \beta v_a C_p^{-1} E_0 \alpha = K \alpha \quad (4)$$

where v_a is sound velocity, β is the volumetric expansion coefficient, C_p is the specific heat at constant pressure.

Thus a measurement of the optoacoustic signal for a given substance gives direct information regarding the absorption coefficient α . Equation (4) contains most of the important parameters necessary for the practical use of optoacoustic spectroscopy for quantitative measurements of small absorption coefficients.

We can also know the concentration C [mol/l] of an absorbing sample in its solution, if we take into account the relation between the absorption coefficient α and sample concentration in solution C .

$$\alpha(\lambda) = \varepsilon(\lambda) C \quad (5)$$

where ε is the extinction coefficient.

The extinction coefficient ε is a constant for a certain wavelength. For this reason it exists a linear dependence between optoacoustic signal V_{oa} and the concentration of the sample C .

$$V_{oa} = K \alpha = K \varepsilon C = K' C \quad (6)$$

3. EXPERIMENTAL SET-UP

Experimental arrangement (Figure 3) contains a pulsed N_2 laser adjusted to deliver 350 μ J per pulse as light source. Pulse duration is 10 nsec. The wavelength of emission radiation is 337.1 nm (UV).

The photoacoustic cell is of cylindrical shape, sealed with quartz windows (length 100 mm, diameter 18 mm). Pulsed excitation allows the use of a nonresonant cell which simplifies the set-up construction and alignment. The laser beam was centred along the cylinder axis. For focalisation is used a quartz lens (focal distance 15 cm). At the focal level of the lens laser beam section is about 2 mm diameter.

An electret condenser microphone Trevi EM 27 (bandwidth 16-18000 Hz) or a piezoelectric transducer (TUSIM-National Institute for Materials Physics, resonance frequency 4 MHz) were used to monitor the acoustic signals. Their active surface is parallel with laser beam axis, such as shown in Figure 3.

To visualise the signals a 7904 Tektronix oscilloscope was used. To reduce the extraneous noise the obtained photoacoustic signal is filtered. When we used the piezoelectric transducer the optoacoustic signal's bandwidth is about 1-10 KHz. For microphone this bandwidth was between 1 Hz and 30 KHz.

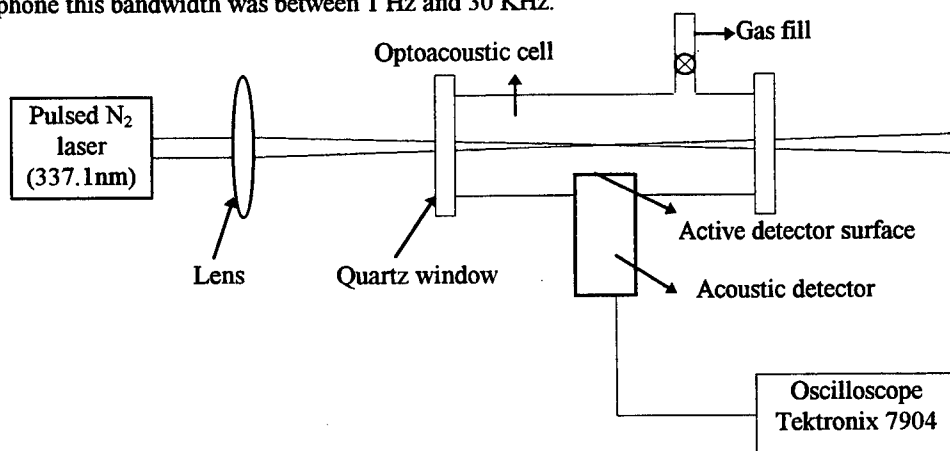


Fig.3 Experimental set-up

4. EXPERIMENTAL RESULTS AND DISCUSSIONS

The photoacoustic signal was measured for pollutants pressure between 1 torr and 100 torr for NO_2 and between 35 torr and 100 torr for SO_2 . The photoacoustic cell was previously emptied to 10^{-3} torr. The photoacoustic cell was then filled with pollutant at a known pressure and photoacoustic signal was recorded.

Linear dependence of the photoacoustic signal on pollutant pressure was obtained and this linearity is in good agreement with theoretical considerations presented above.

A plot of the photoacoustic signal versus pollutant pressure is shown in Figure 4 for NO_2 and SO_2 .

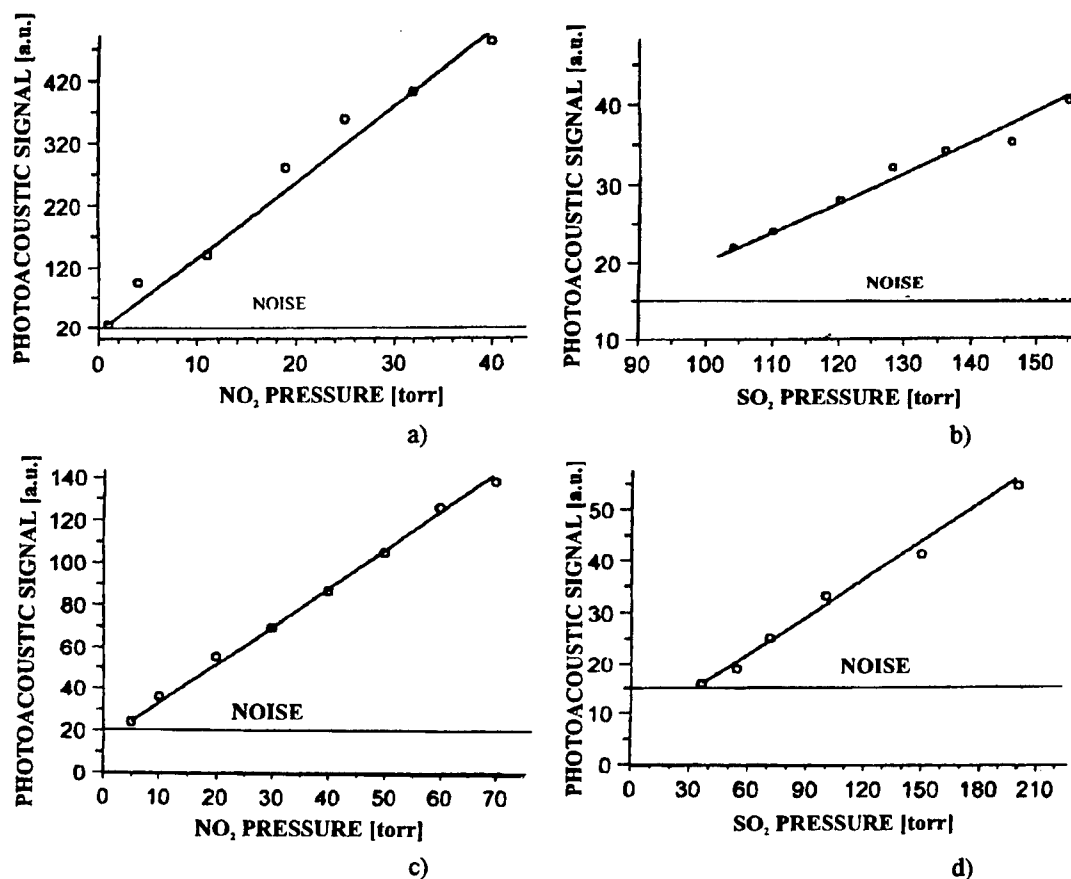


Fig.4 Photoacoustic signal versus pollutant pressure a) NO_2 detection with piezoelectric transducer. b) SO_2 detection with piezoelectric transducer. c) NO_2 detection with microphone. d) SO_2 detection with microphone.

5. CONCLUSIONS

The absorption of radiation at 337.1 nm for SO_2 is low and for this reason the photoacoustic detection of this pollutant has not a very good sensitivity under these conditions. Also, for both pollutants the laser energy must be higher to increase the detection sensitivity.

The sensitivity of SO_2 detection was better using microphone than piezoelectric transducer, but the NO_2 detection has a similar sensitivity for both detectors.

A better accuracy in pressure pollutant estimation using optoacoustic detection is obtained if the normalised optoacoustic signal S is considered.

$$S = V_{oa} / E_0 \quad (7)$$

The spectral selectivity of pulsed photoacoustic is also studied in order to quantitatively determine individual component concentrations in a mixture of several components.

Individual determination of a component concentration in a mixture of several components needs optoacoustic signal measurement for different wavelength of monochromatic light used for excitation of photoacoustic signal.

6. REFERENCES

1. D.A.Gilmore, G.N.Atkinson, Quantitative Detection of Atmospheric Pollutants by Pulsed Laser Photoacoustic Spectroscopy,
2. P.C.Claspy, Infrared Optoacoustic Spectroscopy and Detection, in Optoacoustic Spectroscopy and Detection, Yoh-Han Pao (editor), Acad. Press, New York San Francisco London 1977, pp. 133.
3. C.K.N.Patel, A.C.Tam, Pulsed optoacoustic spectroscopy of condensed matter, *Rev. Mod. Phys.*, **53**(3), July 1981.
4. Garry A. West, Joseph J. Barrett, Donald R. Siebert, K.Virupaksha REDDY, "Photoacoustic spectroscopy", *Rev.Sci.Instrum.*, 1983, vol.54, no.7, pp 797-817.
- 5.Tam A.C., "Applications of photoacoustic sensing techniques", *Rev. Mod. Phys.*, 1986, vol. 58, no. 2, pp. 381-431.

Modelling of atmospheric effects on the angular reflectance characteristics of vegetation canopies

Gheorghe Stancalie

National Institute of Meteorology & Hydrology
97 Soseaua Bucuresti-Ploiesti, Sector 1, 71552 Bucharest, Romania

ABSTRACT

The capabilities for off-nadir satellite observing directional variations in terrestrial surface reflectance, not yet sufficiently present in operational satellite series, are expected to be developed in the near future. The main objective of the paper is the study and modelling the atmospheric effects on the typical angular reflectance characteristics of vegetation surfaces in the visible and near-infrared regions. For the evaluation of the atmospheric contribution to the satellite data, radiative transfer model simulations, with ground radiometric measurements have been performed. The paper discusses the signatures that the atmosphere imposes on the angular distribution of the emerging solar radiation above aerosol-loaded atmosphere. The model calculations have also showed that some atmospheric -invariant features of the angular reflectance distribution, like the aerosol forward scattering peak or the hot spot in the antisolar direction, may be used as discriminant surface reflectance characteristics in the case of low aerosol-loaded atmosphere.

Keywords: remote sensing, atmospheric effects, off-nadir satellite observations, angular reflectance signatures

1. INTRODUCTION

The monitoring of agricultural crops performance and accurate prediction of crops yields required high quality information on the state of the vegetation. Relevant information may be retrieved through remote measurements, using satellites sensors in the solar reflective spectrum.

The information content of a measured reflected radiative field distribution about a remotely sensed surface may be subdivided into some distinctly different scene reflectance characteristics: spectral, spatial, angular, temporal and polarised. Either one of these features may be used as an identifier for a certain surface characteristic. The influence of the atmosphere must be taken into account in the case of remote sensing from satellites. An essential condition for satellite-sensed feature identification is that the discriminating reflectance features are either cvasi-invariant to atmospheric effects or are such that atmospheric perturbations can be modelled and removed from the image.

Our paper concentrates on the analysis and modelling of atmospheric effects that are included in satellite-sensed angular reflectance distribution. We have limited our study to passive remote sensing where unpolarized solar radiation is assumed to be the only radiative source.

2. POSSIBILITIES OF IDENTIFYING VEGETATION SPECIES OR CROPS TYPES FROM SATELLITE IMAGE DATA

The spectral reflectance characteristics of plants canopies are typical for the green vegetation components such leaves and stems.¹ In the visible region the reflectance is small, but in the 700 - 800 nm it rapidly increases and in the near-infrared has the greatest values. The 650 - 700 nm region is useful for the detection of chlorophyll state as well as for initial stress detection; the 700 - 780 nm is of value for senescence detection and for vegetation state monitoring. The reflectance in the 800 - 870 nm domain is related to leaves anatomy and state of hydration.

When these types of data from different crops are quantitatively compared it appears that their spectral responses are almost identical, although large characteristics peaks and valleys are present. Such comparison indicates a low feature discrimination between different species on the basis of spectral characteristics alone.

The atmospheric influence on the image data, in the visible region is high, especially because of aerosol scattering effects.

Although the atmospheric perturbations are generally small in near-infrared, the end result is still a poor feature identification of crop types from satellites sensed spectra.

Better feature identification on the basis of spectral signatures is expected where higher spectra resolution such as below 10nm bandwidth, is assumed for the sensing instrument.² For spatial characteristics a similar conclusion may be drawn because typical row structures and other vegetation patterns are "a priori" poor discriminators for different species although the atmospheric perturbations of these characteristics, such as the adjacency effects, may be considered small.

The angular reflectance characteristics of vegetation canopies may be called a good feature discriminator as far as the identification of different crop types is concerned. The large difference in the angular reflectance distributions for different crops are a direct result of the plant canopy's geometric structure which therefore appears to be a better identifier for plant types than its spectral or spatial reflectance characteristics.

The atmospheric perturbations of angular reflectance features are generally small for azimuthal variations of the viewing direction and large, but correctable, for view zenith-angle variations.³

The combination of good features discrimination and small atmospheric perturbations may lead to a high degree of vegetation feature identification from satellite-sensed angular reflectance characteristics.

The angular reflectance features may be obtained from off-nadir measurements; such observations also need an increased flexibility of the observing instruments on board the satellite systems. Presently, there are limited possibilities of using angular signatures extracted from satellite data (NOAA-VHRR, HRT-SPOT). For example, the AVHRR can detect a part of the angular reflectance characteristics for homogeneous, large vegetation surfaces, if the scanning angle is greater than the solar zenithal angle. For the determination of some particular angular reflectance characteristics, especially in the backscattering region, measurements in the solar principal plane, at observing angles close to the solar zenithal angle are necessary.

Experimental sensors such as the Polarisation and Directionality of the Earth's Reflectance (POLDER) on ADEOS satellite, are now in progress. In the near future more off-nadir satellite-data will be available once the NASA Earth Observing System (EOS), orbital platform is lanced.

It appears that only the remote sensing of angular reflectance characteristics, obtained from off-nadir observations of vegetation, promises to allow good and cvasi-constant identification of vegetation features (especially for the agricultural crops), if the additional complexities that the acquisition of multiangle data faces can be resolved.

3. REPRESENTATION OF ANGULAR REFLECTANCE CHARACTERISTICS

To describe the angular geometry defining solar and sensor view angles we used a standard co-ordinate system (fig.1). Ω_s represents the unit vector of direct solar radiation and Ω_v the unit vector into the view direction. θ_s is the sun zenith angle and θ_v the view zenith angle, respectively; Φ_v is the view azimuth angle, measured with respect to principal plane defined by the vectors of the solar incident direction and the z-axis: Ω_v is always defined with a position view zenith angle between 0° and 90° , while the view azimuth angle Φ_v is taken relative to the Sun and varies from 0° , observing the forward scattering lobe of the solar radiation to $\pm 180^\circ$ for the backscattering.

A complete description of the angular reflectance from a surface is given by the bi-directional reflectance distribution function (BRDF) which is defined as:

$$BRDF_{i,r} = \frac{dL_r(\Omega_i, \Omega_r)}{L_i(\Omega_i) \cos \theta_s d\Omega_i} \quad (1)$$

where : $dL_r(\Omega_i, \Omega_r)$ is the reflected radiance into direction Ω_r , which is due to an incident irradiance from direction Ω_i , within the solid angle $d\Omega_i$.

The total radiance that emerges from the surface in direction Ω_r can then be calculated by integration over incident directions Ω_i :

$$L_r(\Omega_r) = \int_{2\pi} \text{BRDF}(\Omega_i, \Omega_r) L_i(\Omega_i) \cos \theta_i d\Omega_i \quad (2)$$

where the element of solid angle is $d\Omega_i = \sin\theta_i d\Omega_i d\Phi_i$

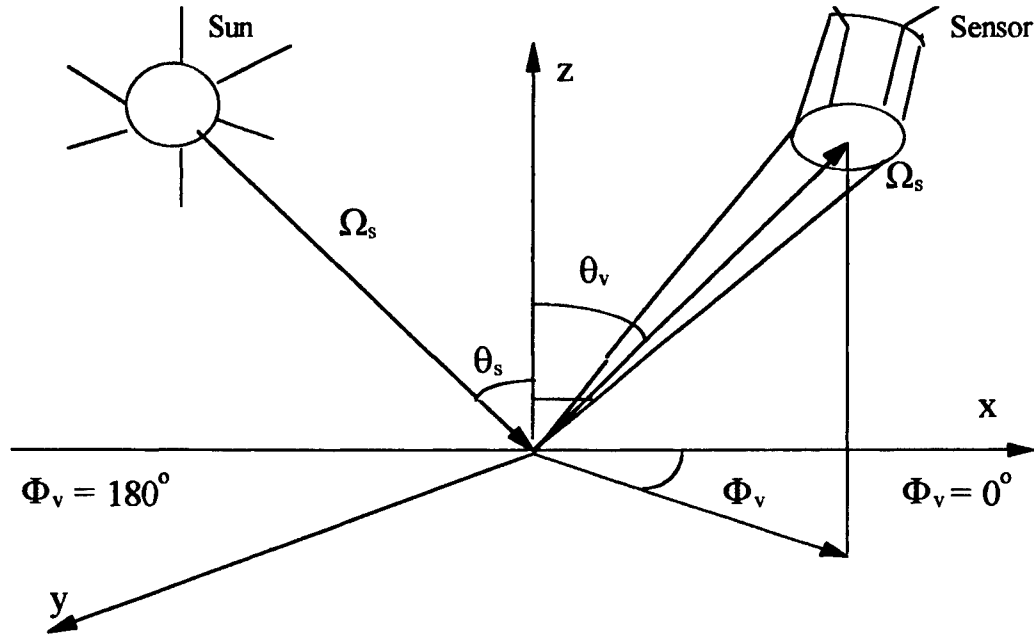


Fig.1. The angular geometry for the Sun - target - satellite system

The BRDF may be interpreted as a boundary condition relating the upwelling radiance distribution to the downwelling flux distribution at a reflecting surface. It is preferable to use a directional reflectance factor (RF) which is defined as the irradiance reflected into a finite solid angle divided by the radiance that would be reflected into the same solid angle by a perfect diffuse (Lambertian) reflector. The RF are measured in the field and incorporate the diffuse illumination of a scene, while the BRDF is specific for a monodirectional illumination and is thus independent of diffuse skylight.

Satellite scanning instruments have a very small instantaneous field of view (IFOV) and measure the radiance within a small cone $\Delta\Omega_r$. Therefore, it seems most appropriate to use the radiance distribution of the reflected radiation, $L_r(\Omega)$. In order to present the measurements independent of the intensity of the incident radiation, we used reflected radiance distributions that are normalised to the incident solar flux above the atmosphere:

$$R(\Omega) = \frac{\pi L_r(\Omega)}{S_0 \cos\theta_s} \quad (3)$$

where: S_0 is the solar constant.

This normalised reflected radiance, called shortly the reflectance $R(\Omega)$, which also represents the angular reflectance distribution, may be interpreted as the ratio of the satellite-sensed radiance $L_r(\Omega)$ to the radiance that a perfect Lambertian reflector at the top of the atmosphere would produce:

$$L_r^* = (1/\pi) S_0 \cos\theta_s \quad (4)$$

$R(\Omega)$, taken at the top of the atmosphere, called the apparent reflectance $R_{app}(\Omega)$, is identical to BRDF of the atmosphere-surface system times π . $R_{app}(\Omega)$ is also equal to the RF, when only infinitesimal cones of incident and reflected radiation are considered.

The reflectance $R(\Omega)$, taken directly above the reflecting surface is not equivalent to the RF or the $BRDF \times \pi$. This follows because the denominator in the definition for $R(\Omega)$ (ec. 3) is the constant solar flux that provides a normalisation of the reflected radiance values, while the denominator in the BRDF definition (ec.1), as well as that of the RF, is the incident flux at the location where the BRDF or the RF are defined. This incident flux on the reflecting surface below an atmosphere incorporated already the scattered radiation and the absorption that the solar radiation has suffered in propagating through the atmosphere and may differ substantially from the value $S_0 \cos \theta_s$ above the atmosphere. Therefore it is more appropriate to compare values of the upwelling radiance, $R(\Omega)$, than RF or the BRDF values.

4. MATERIALS AND METHODS

The spectroradiometric measurements have been carried out using the Field Multi-channel Visible and Infrared Radiometer (RMCT-VIR) ⁴, designed and produced by the National Institute of Meteorology and Hydrology and the National Institute of Metrology in Bucharest. The RMCT-VIR radiometric measurement system uses the conic geometry recommended by the Working Group of the Commission VII of the International Society of Photogrammetry and Remote Sensing on Radiative Measurements. This radiometric system is made up of two interconnected devices simultaneously working:

- a radiometer designated to measure into the nadiral geometry the radiance reflected by the natural bodies, under a 35° acceptance angle, for the ground level measurement and 1° for the aerial regime;
- an identical radiometer oriented towards the sky, equipped with 180° opening field of view, in order to detect the global incident radiation, in irradiance values.

Because the angular response of the receiver is not Lambertian it was equipped with cosinus correction devices.

The measurements are carried out into four spectral channels of the visible and near-infrared region of the spectrum: channel A (0.5 - 0.6 μm), channel B (0.6 - 0.7 μm), channel C (0.7 - 0.8 μm) and channel D (0.8 - 1.1 μm). These spectral channels are identical with the ones with which the MSS scanner of LANDSAT satellites operates.

The device has the possibility to measure under a continuous instantaneous and simultaneous regime on the four channels. In order to observe and recognise the bodies studied in case of the aerial regime, the device is equipped with a terrestrial telescope.

The RMCT-VIR radiometers is part of the category of instruments which do not produce an image, but can spacially, timely and on a spectral interval integrate the signal, finally leading to the curve of spectral response or to a series of spectral indices, which characterise the field reflected by the measured target.

The RMCT-VIR radiometer was fixed at between 3 m and 3.5 m as compared to the terrestrial surface; the observed ground area, for the nadiral geometry has a circle shape with environ 2 m diameter. The instrument was attached to a mount capable of movement in the horizontal (azimuth) and vertical (zenith) planes. Field stops were used to restrict the angular field of view to 10° .

5. DETERMINATION OF THE ATMOSPHERIC EFFECTS ON THE ANGULAR REFLECTANCE CHARACTERISTICS OF THE TERRESTRIAL SURFACES

Due to the forward scattering characteristics, typical for the atmospheric aerosol, in the visible region of the electromagnetic spectra, the radiation field of the diffuse component of the solar flux is anisotropic.

In the case of data obtained from satellite measurements, the perturbing effect of the atmosphere act both on the descendent and ascendant path of the incident and respectively reflected radiation.

In order to emphasise the atmosphere effect on the angular reflectance characteristics of the terrestrial surfaces and to separate out the surface and atmosphere signatures, we first considered the radiative transfer of solar radiation through the

atmosphere for a surface with Lambertian reflector properties. The simulations for the surface-atmosphere system were carried out in the LANDSAT-MSS channels, with a modified version of the '6S' radiative transfer code and with a Gauss-Seidel numerical iteration algorithm⁵. We used a standard mean latitude summer atmospheric model for different aerosol-loaded atmospheres.

The distribution of the radiative field reflected by the Lambertian surface is perturbed by aerosol scattering effects, as against the isotropic distribution. We have observed that the atmospheric perturbation in the angular reflectance distribution is strongest when the sensor looks at large zenith angles, in the principal plane towards the Sun, that means a viewing azimuth near zero. The observed perturbation peak is attributed to the strong forward scattering properties of aerosols. This peak persists at $\Phi_v = 0^\circ$, but shifts to smaller view zenith angles as the total atmospheric aerosol optical depth increases.

When surface remote sensing is intended, this atmospheric signature on $R(\Omega)$ is a perturbation that does not contain any information about the surface reflectance. The features associated with the atmospheric aerosol scattering are mostly depending on the viewing geometry and influence consistently the intrinsic reflectance of the surfaces.

In order to study the influence of atmospheric conditions on the surface reflectance and to establish the possibility of surface feature identification from satellite off-nadir observations we compared results of atmospheric radiative transfer where some measured angular reflectance characteristics at ground level are considered as a bottom boundary condition. The measurements were carried out in the in Padina region of the Bucegi Mountains.

Fig. 2 illustrates an example of the the angular reflectance distribution in the solar principal plane, for a pasture surface, measured above the canopy and simulated at the top of the atmosphere, in the "red" LANDSAT-MSS B channel (situated in red) for three atmospheric conditions: clear atmosphere with a total atmospheric optical depth $\tau_{\text{atm}} = 0.1$, moderated aerosol-loaded atmosphere with $\tau_{\text{atm}} = 0.25$ and a heavy aerosol-loaded atmosphere with $\tau_{\text{atm}} = 0.4$.

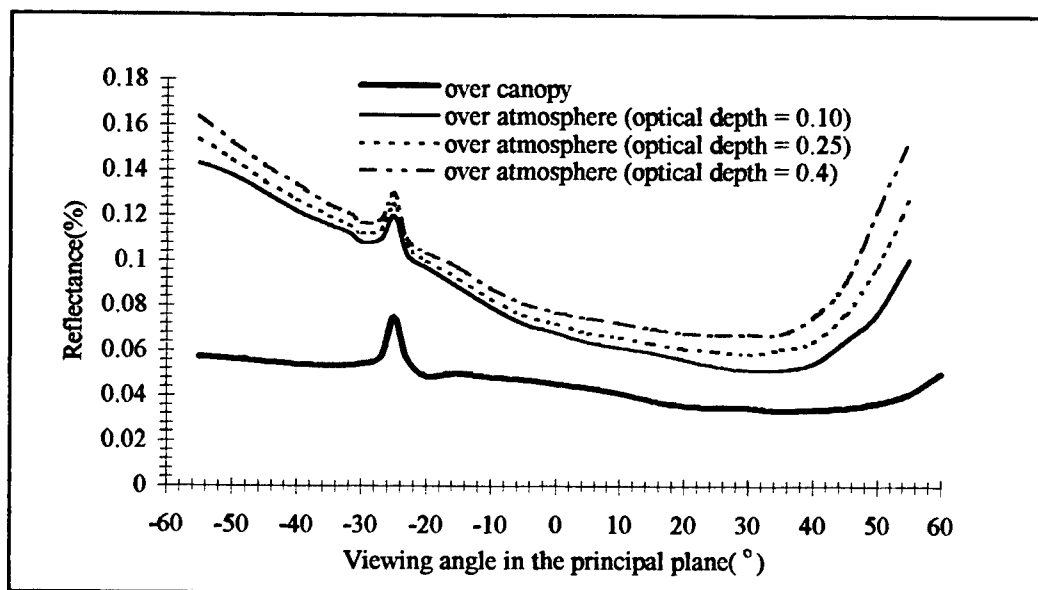


Fig. 2. Reflectance distribution in the solar principal plane, in the LANDSAT MSS channel B (600 - 700 nm), above the canopy and at the satellite level for different aerosol-loaded atmospheres

In the red region the angular distribution of radiance above the atmosphere do not reflect the surfaces features but the atmospheric path radiance characteristics. The results present as a dominant feature the characteristic aerosol forward scattering peak in the reflectance distributions at the top of the atmosphere.

Fig. 3 shows similar angular distribution in the LANDSAT-MSS channel D, situated in the near-infrared.

In the near-infrared region, the vegetation has a higher reflectance and the aerosol scattering effects are much smaller. In this case the reflected radiance received by the sensor above the atmosphere mainly depend on the canopy radiative field. For larger viewing angles an increasing attenuation in the backscattering direction is also emphasised.

In all reflectance distributions where the measured data at the ground level showed the hot-spot effect, represented by a distinct increase in reflectance in the backscattering region⁶ (caused by the hiding of shadows at low phase angles), we noticed that generally this peak in the reflectance distribution, remains distinct in the antisolar direction above the aerosol-loaded atmospheres. In the visible the atmosphere attenuation effect reduces the hot-spot amplitude.

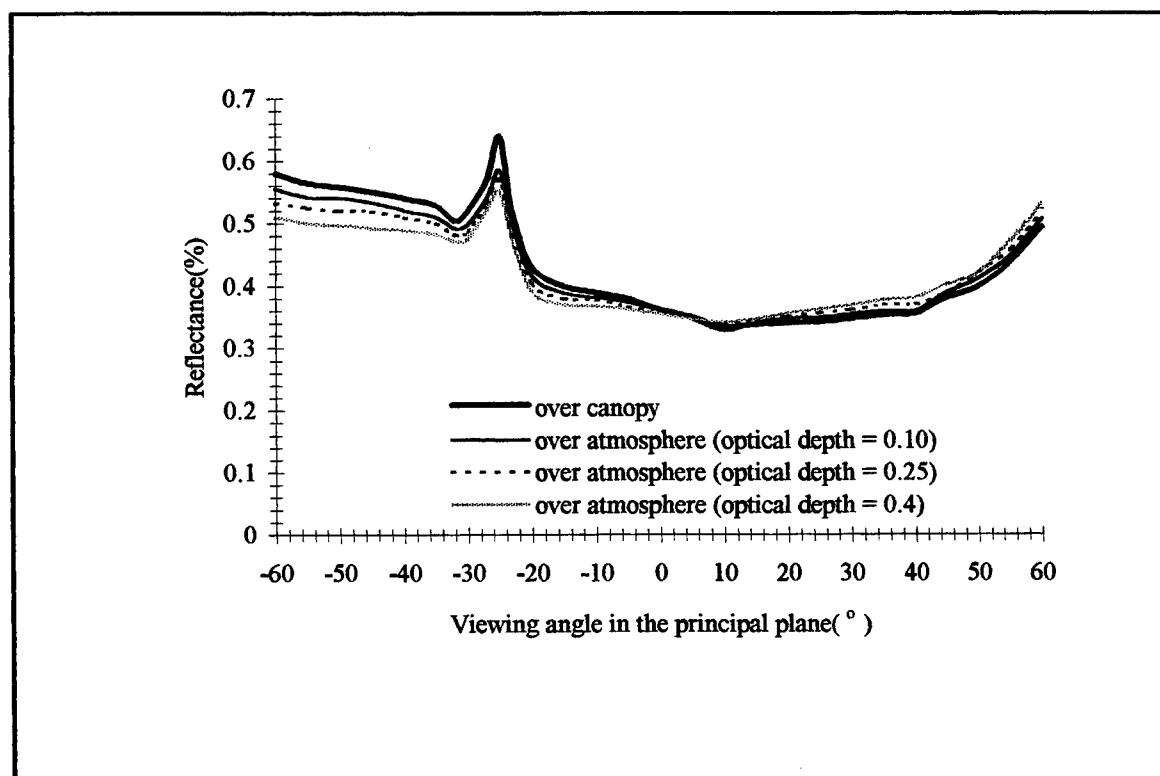


Fig. 3. Reflectance distribution in the solar principal plane, in the LANDSAT MSS channel D (800 - 1100 nm), above the canopy and at the satellite level for different aerosol-loaded atmospheres

The angular reflectance characteristics can provide a good discrimination of the terrestrial surface features obtained from the remotely sensed data, on condition that they remain cvasi-invariant as compared to the atmospheric effects. In order to identify these atmosphere-invariant angular reflectance features, simulations of the realistic ground reflectance characteristics through several different atmospheric conditions have been achieved. Thus we can compare results of atmospheric radiative transfer calculations where "in situ" angular reflectance distribution at ground level are entered as a bottom boundary condition.

The simulations was performed in the visible and near-infrared LANDSAT-MSS channels, for homogeneous surfaces; under these circumstances the adjacency effects could be neglected. We determined the variation of the reflectance function of the view azimuth angle, obtained from ground measurements and from simulations for different aerosol-loaded atmospheres.

The reflectance profiles at the top of the atmosphere for constant view zenith angle, through the hot spot, in the opposite direction, back to the Sun have presented some interesting characteristics:

- for a large aerosol loads the reflectance values increase due to multiple scattering effects in the atmosphere;

- increasing aerosol loads tend to reduce the height of the hot spot peak due to atmospheric absorption; the backscattering peak in the aerosol phase function can balance this reduction and the end result is that the hot-spot effect is maintained above the aerosol-loaded atmospheres.

- the reflectance profiles for a constant view zenith angle, through the hot spot are cvasi-invariant to atmospheric effects, but only for reasonably low aerosol loads, for atmosphere with a visual range $V > 10$ km .

6. CONCLUSIONS

The conclusions drawn out from the analysis of the angular reflectance distributions for vegetation canopies, for the achieved calculations and measurements are the following:

- The atmospheric effects on the angular reflectance distribution $R(\Omega)$ are mainly additive;
- For the turbid atmosphere the reflectance values increase due to the multiple scattering in the atmosphere;
- The atmospheric perturbation peak associated with the forward characteristics of aerosols remains a dominant feature, for the different aerosol loaded atmospheres. The characteristics aerosol forward scattering peak in the reflectance distributions emerging from the top of the atmosphere remains a dominant feature for all the atmospheric conditions.
- In all reflectance distributions where the measured surface data show a distinct hot spot, we notice that this peak in $R(\Omega)$ in the antisolar direction remains a distinct peak in the same view direction above the aerosol loaded atmosphere; the hot spot effect may be considered as a feature that is quite invariant to atmospheric effects;
- The atmospheric absorption leads to the reduction of the hot spot effect amplitude and therefore the reduction of the reflectance values for the $\pm 180^\circ$ azimuthal viewing angle (in the antisolar direction);
- The reflectance profiles for a constant view zenith angle, through the hot spot may be considered as a cvasi-invariant feature to atmospheric effects, only for reasonably low aerosol - loaded atmospheres.

Off-nadir satellite remote sensing of the vegetation land surfaces which consists almost exclusively of non-Lambertian surfaces may provide very valuable information for surface feature identification. Radiative transfer modelling capabilities can provide the basis to analyse the off-nadir satellite observations, especially for the atmospheric effects in the visible and near-infrared wavelength regions.

The values of the angular signatures can be considered complementary to the well known spectral signatures in the vegetation canopies identification.

6. REFERENCES

1. G. Guyot, "Les signatures spectrales des surfaces naturelles", *Télédétection spatiale*, nr.5, ed. Paradigme, Caen, France, (1989).
2. G. Guyot and F. Baret, "Utilisation de la haute resolution spectrale pour suivre l'état des couverts végétaux", *Proc. 4-th Intern. Colloq. in Remote Sensing*, Aussois, p.279 - 283 (1988).
3. T. Lee and Y. J. Kaufman, "The effect of non - lambertian surface on remote sensing of surface reflectance and vegetation index", *IEEE Trans. Geosci. Remote Sens.*, **24**, p. 699 -708 (1986).
4. Ileana Sândoiu and G. Stăncălie, "Rezultate preliminare obținute cu radiometrul de teren RMCT - VIR în investigarea agrometeorologica", *The 3-rd National Conference of Geodesie, Comunicari si referate*, vol.III, p.241, CNIT, Bucuresti, (1988)
5. S. Liang and A.H. Strahler, "Calculation of angular radiance distribution for a coupled atmosphere and canopy", *IEEE Trans. Geosci. Remote Sens.*, **31**, p. 491 - 502.
6. N.S. Goel, "Models of vegetation canopy reflectance and their use in estimation of biophysical parameters from reflectance data", *Remote Sensing Rev.*, **4**, p. 1 - 212 (1988).

Author Index

- Abu-Taha, M. I., 578
 Aiftimiei, Cristina, 779, 891
 Akimova, Elen A., 790
 Al-Jourani, M. M., 578
 Albu, Alexandru M., 902, 946
 Aldea, E., 831
 Alexandrescu, Rodica, 122, 174, 199, 218
 Alexe, M., 846
 Allott, Ric M., 162
 Andrei, A., 182, 199, 831
 Andriesh, Andrei M., 258, 385, 1013
 Aneculaese, Maria, 632
 Anghel, Sorin, 1027
 Antipa, Ciprian, 696, 739, 747
 Antoniow, Jean S., 1039
 Apostol, Dan, 972, 1100
 Apostol, Ion G., 702
 Apostol, Silvia, 665, 713
 Ashurov, Mukhsin Kh., 837
 Babin, Vasile, 45, 498, 865, 930
 Baibarac, M., 623
 Baltateanu, N., 75, 930
 Baltog, I., 205, 623
 Balucani, M., 762, 784, 831
 Barb, D., 311
 Barba, N. A., 790
 Battaglin, Giancarlo, 533
 Băzăvan, M., 524, 636
 Beldiceanu, Anca Maria, 1094
 Bena, Rodica, 946
 Bertinetto, Fabrizio, 990
 Bertolotti, Mario, 335
 Bicanic, Dane D., 1039
 Biloiu, C., 524, 636
 Bivol, Valery V., 790
 Blanaru, Constantin, 1074, 1100
 Boerasu, I., 846
 Bondarenko, V., 762, 784
 Borsella, E., 533
 Bosch, Salvador, 1056, 1120, 1150, 1156
 Bota, M., 727
 Botez, C. E., 462
 Boyd, Ian W., 225, 272
 Bradaczek, H., 960
 Braescu, Cora Lucia, 779, 891
 Bratescu, M. A., 603
 Bratulescu, G., 619
 Braverman, Ada Livia, 106
 Brojbeanu, Gabriela, 692
 Bruckner, Ion I., 696, 739
 Brynzari, Vladimir, 1032
 Buca, D., 233, 267
 Bulgaru, M. G., 1013
 Bulinski, M., 636
 Bunesco, M. C., 225, 272
 Bunița, Daniela, 739
 Burke, V. M., 39
 Bursuc, I. D., 936
 Buzdugan, Arthur I., 258
 Calian, Violeta, 278, 494
 Calin, Mihaela, 727, 733, 801, 860
 Carnicer, Arturo, 1150, 1156
 Carp, C., 717
 Cârstocea, Benone, 665, 713
 Chan, H. L., 122
 Chartier, Jean-Marie, 990
 Chelu, Mariana, 252
 Chera, Ionel, 524
 Chilibon, Irinela, 813, 883
 Chirita, F., 1007
 Chirtoc, Mihai, 1039
 Chiș, Ioan, 153, 188, 282, 702
 Chumash, Valentin N., 446
 Cicala, Eugen F., 246, 293, 299
 Cimpoa, Valerica, 75
 Ciobu, V. E., 570
 Ciotaru, D., 727
 Cireasa, Raluca, 199
 Ciuchita, Tavi, 747
 Ciurea, M. L., 205, 623
 Cojoc, Dan, 425
 Cojocaru, Laurentiu, 498
 Cojocaru, S., 199
 Constantinescu, B., 311
 Constantinescu, T., 524
 Copot, Gheorghe, 819, 926
 Copot, Rodica, 819
 Cordoș, Emil, 1088
 Cosereanu, Liviu, 926, 930
 Craciun, Doina, 225, 272
 Craciun, F., 1194
 Craciun, Valentin, 225, 272
 Craiu, M., 252
 Cristea, M., 524
 Cristescu, Constantin P., 65
 Cristescu, Simona M., 627
 Cristian, Petre, 99
 Crunteanu, A., 199
 Dabu, Razvan V., 81, 225, 454, 702
 Dadarlat, Dorin, 1039
 Damaskin, I., 1007
 Damian, Victor, 972, 1100
 Darvasi, Eugen, 1088
 Dascalu, Constanta, 796, 941
 Dascalu, Traian, 70, 233, 267, 713
 David, Ion, 246, 299

- Daviti, Maria, 241
 Defay, Céline, 1106
 de F. Moneo, J. R., 1150, 1156
 De Marchi, Giovanna, 533
 de Vries, Hugo S. M., 556
 Digulescu, Petre P., 825, 999
 Dima, Stefan V., 686
 Dima, Vasile F., 686
 Dincă, Andreea G., 1162, 1173
 Dincă, Mihai P., 1162, 1173
 Dinescu, Gheorghe H., 831
 Dinescu, Maria, 831, 1194
 Dinu, R., 1194
 Dobre, Mara, 722
 Dobroiu, Adrian, 972, 1100
 Dolghier, V., 258
 Dolocan, V., 887
 Dorogan, Valerian, 1007, 1032
 Dragnea, Laurentiu, 912
 Dragoi, V., 846
 Dragulinescu, Dumitru, 188
 Ducariu, Adrian, 483
 Dumitras, Dan C., 627, 654
 Dumitrescu, Mihail, 922
 Dumitru, Gabriel, 17, 81, 1083
 Dumitru, Mihaela A., 10
 Dutu, Doru C. A., 627, 654
 Egee, Michel, 1039
 El-Kahlout, A. M., 578
 Elisa, Mihai, 965
 Enaki, Nicolae A., 399
 Enaki, V. N., 570
 Enculescu, Ionut, 262, 897
 Ersen, Simion, 498, 865
 Farcas, Ana-Florica, 45
 Fenic, Constantin G., 81, 252, 454, 702
 Fernández, Xavier, 1056
 Ferrari, A., 762, 784, 831
 Ferré-Borrull, Josep, 1056
 Flory, François, 1106
 Forgaciu, Flavia, 288
 Frandas, A., 1039
 Furuhashi, M., 32
 Gafencu, Luiza, 665
 Gafencu, Otilia L., 713
 Gaivan, S. L., 469, 473
 Galeata, G., 205
 Gartner, Mariuca, 887, 1194
 Gasanov, Eldar M., 837
 Georgescu, Geo, 1114, 1132, 1137
 Georgescu, Serban, 2, 112, 612
 Gerardi, C., 1194
 Gherghina, Ion, 930
 Gherman, Valentin V., 483
 Ghica, C., 218, 252, 702, 1137
 Ghica, D., 831
 Ghita, C., 887
 Ghita, R. V., 75
 Giesen, Adolf, 978
 Girardi, R., 24
 Giubileo, Gianfranco, 642
 Gomoiescu, Despina, 1088
 Gonella, Francesco, 533
 Gostian, Doina, 678
 Grigore, Maria, 498
 Grigorescu, Cristiana E. A., 860, 897
 Grigoriu, Constantin, 153, 188, 282
 Groß, Tobias, 17
 Gruia, Ion, 524
 Guina, Mircea, 922
 Guja, Victor B., 439
 Gutu, Iulian, 99, 1114
 Guzun-Stoica, Anicuta, 489
 Gyorgy, Eniko, 182, 218
 Hapenciuc, Claudiu, 2
 Harren, Frans J. M., 556
 Hasegan, Sorin A., 955
 Hening, Alexandru, 218, 678
 Herisanu, Nicolae-Alexandru, 81
 Heumann, E., 51
 Honciuc, Gheorghe, 1178, 1183
 Huber, Guenter, 51
 Hugel, Helmut, 978
 Huq, Syed E., 162
 Hutsanu, V., 887
 Iancu, Ovidiu D., 439, 852
 Ibragimova, E. M., 837
 Iftimia, Nicusor, 865
 Ilie, Gheorghe, 524, 636
 Iliescu, Brandusa, 262, 897
 Ioncea, A., 225, 272
 Ionescu, Elena, 696, 739, 747
 Ionescu-Pallas, Nicholas, 375
 Ioniță, M., 713
 Ioniță-Mânzatu, V., 713
 Iordache, Gh., 81
 Iorga Siman, Ion, 1027
 Iosub, I., 1027
 Iova, Iancu, 524, 636, 1027
 Iovu, Michael S., 258
 Ishimov, B. M., 790
 Ispasoiu, Radu G., 58, 462
 Ivan, R. V., 825
 Ivana, Eugenia, 252
 Jalink, Henk, 1039
 Jeloica, L., 311
 Jiang, Weihua, 153, 188
 Jianu, Angela, 511, 517, 955
 Jipa, V., 930
 Jurba, Mihai, 926, 930
 Juvells, Ignacio P., 1150, 1156
 Kasuchits, N., 762
 Kato, Kiyoshi, 393
 Kennedy, Michael, 1083
 Khadzhi, P. I., 406, 469, 473
 Kim, Nam Seong, 162
 Klein-Douwel, R. J. H., 143
 Kobayashi, Takao, 32

Koch, P.-J., 960
 Kopica, Mirosław, 756
 Koswig, H. D., 796
 Kosyak, V., 1007, 1032
 Krieger, W., 432
 Kumar, Ashok, 122, 199
 Kurzeluk, Mona, 489
 Labastida, I., 1150, 1156
 Labes, U., 796
 Lăcătușu, Veronica, 252
 Lainé, Derek C., 578
 Laky, Dezideriu, 686
 Lamedica, G., 762, 784, 831
 Lazarescu, Mihail F., 860, 1114
 Leinfellner, N., 541, 584
 Levai, Stefan, 1027
 Lisi, Nicola, 162
 Logofatu, B., 860
 Logofatu, C., 897
 Logofatu, Michaela F., 860
 Lörinczi, A., 960
 Luculescu, C., 81, 454, 702
 Lupei, Aurelia, 563, 570, 589
 Lupei, Voicu, 2, 51, 70, 89, 112, 563, 570, 589, 612, 713, 1162, 1173
 Macovei, M., 399
 Maddison, B. J., 162
 Maksimyak, Peter P., 1022
 Malkov, Sergei A., 1013
 Manaila-Maximean, Doina, 946
 Manea, Stefan A., 860, 897
 Mann, C. M., 162
 Manolescu, G., 1202
 Marcu, A., 153, 188, 282
 Marginean, P., 252
 Marginean, Raluca, 926, 1143
 Marian, A., 233, 267
 Marica, F., 548
 Marin, Gheorghe, 182, 218
 Marom, Emanuel, 363, 418
 Martin, C., 218, 272, 708
 Marzu, Marinica, 1143
 Mästle, Ruediger, 978
 Matei, Consuela-Elena, 654
 Mattei, G., 533
 Mazets, I. E., 541, 584
 Mazzoldi, Paolo, 533
 Medianu, Victor Rares, 85, 99, 1114, 1132, 1137
 Mel'nikov, Igor V., 353
 Mendlovic, David, 363, 418
 Mereutza, Alexandru Z., 462
 Miclea, M., 603
 Miclea, Paul T., 1162
 Micloș, Sorin, 45, 807
 Micluța, Marius, 1189
 Mihailescu, Ion N., 182, 218, 272, 305, 678, 708, 960
 Mihalache, Dumitru, 353
 Mihut, L., 623
 Mincu, Niculae E., 722, 831
 Mirenghi, L., 1194
 Mirzu, Marinica, 926, 930
 Mitrea, Mihai, 477
 Miu, Catalin, 241
 Miu, Dana, 153, 188, 282
 Miyamoto, Kenji, 603
 Mocofanescu, Anca, 45
 Moise, N., 665, 717, 1202
 Moldovan, Adrian, 498, 865
 Moldoveanu, Vladimir, 696
 Montrosset, Ivo, 24, 439, 873
 Moon, S. W., 162
 Morjan, Ion G., 174, 199
 Moroseanu, A., 713
 Motoc, Cornelia, 796, 941
 Motta, Gabriella, 873
 Munteanu, Ion I., 860
 Musa, G., 603
 Muscalu, G. L., 454, 1167
 Nacu, Mihaela, 739
 Nascov, Victor, 972, 1100
 Nastase, N., 1137
 Neamtu, Johnny, 182, 305, 619
 Necsoiu, Teodor, 733
 Negoita, T., 1202
 Nelea, V. D., 218, 708
 Nemes, Miloslava, 288
 Nesheva, D., 960
 Nichici, Alexandru, 246, 293
 Nicola, Marius, 1088
 Ninulescu, V., 10
 Nishiura, K., 153
 Nistor, Leona C., 218, 252, 702
 Nitulescu, Gabriel, 483
 Obst, S., 960
 Oomens, Jos, 556
 Osiac, E., 51, 89
 Oud, J. L., 241
 Panoiu, Nicolae-Coriolan, 353
 Pantelica, D., 182
 Paris, D., 1039
 Parker, David H., 556
 Pascu, Mihai L., 665, 717, 739, 1202, 1215
 Pavel, Nicolaie I., 32, 70
 Pavelescu, Gabriela, 205, 623
 Pentia, E., 205
 Pérez, J., 1150, 1156
 Perrone, Alessio, 130
 Perrone, Guido, 873
 Persijn, S., 556
 Petrache, M., 589
 Petraru, A., 563, 589
 Petre, D., 846
 Petrescu, Emil, 796, 941
 Petris, Adrian, 511, 517
 Petru, Frantisek, 990
 Pintilie, Ioana, 846
 Pintilie, Lucian, 846

Pîrc ălăboiu, Daniel, 852, 873
 Piscureanu, Mihai C., 10
 Polychronyadis, E. K., 241
 Popa, Carmen, 517
 Popa, Dragos, 517
 Popescu, Aurelian A., 902
 Popescu, C. R., 174
 Popescu, E., 930
 Popescu, F. F., 548
 Popescu, Gheorghe, 665, 990, 1078
 Popescu, Ion M., 58, 211, 916, 946, 1067
 Popescu, Mihai A., 960
 Popovici, Elisabeth-Jeanne, 288, 632
 Popovici, Maria-Ana, 722
 Poterasu, M., 267
 Poterasu, M., 233
 Preda, A. M., 65, 211
 Preda, Liliana, 65, 211
 Preoteasa, V., 678
 Presura, C., 570
 Prisacari, A. M., 790
 Puscas, Niculae N., 24, 58, 462, 483, 916, 1067
 Puzewicz, Zbigniew, 756
 Quaranta, Alberto, 533
 Radu, G., 548
 Radu, Liliana, 678, 708
 Radu, Mihaela, 727, 733, 801, 860
 Radu, S., 678
 Radu, S., 619
 Răducanu, Dan, 891
 Radulescu, Irina, 678, 708
 Rădvan, Roxana N., 733, 801
 Ralea, Daniel, 926, 1143
 Ricciardelli, A., 784
 Ristau, Detlev, 17, 1083
 Ristici, Iosefina, 85
 Ristici, Marin, 85
 Robea, Bogdan, 807
 Robu, Maria, 801, 813, 883
 Robu, Shtefan V., 790
 Roger, Jean P., 205
 Rogojan, Rodica, 965
 Roman, Miruna, 665, 1215
 Rosu, Constantin, 796, 946
 Rotaru, A. H., 411
 Roundy, Carlos B., 673, 768, 1045
 Rusca, Nicolae, 696
 Rustamov, Igor R., 837
 Rusu, G. I., 951
 Rusu, Ioan I., 936
 Sakai, Yosuke, 603
 Sandrock, T., 51
 Sandu, V., 831, 1194
 Sarpe-Tudoran, Cristian, 278, 494, 619, 1063
 Sava, F., 960
 Savastru, Roxana, 801
 Savi, G., 727
 Scarano, Danilo, 24
 Scarlat, E., 65, 211
 Schiopu, Carmen Liliana, 906
 Schiopu, Paul, 906, 912
 Schmitz, C., 978
 Serbanescu, Ruxandra, 708
 Shabtay, Gal, 418
 Shemer, Amir, 418
 Sibilia, Concita, 335
 Singurel, Gh., 1183
 Smarandache, A., 1202
 Smeu, Emil, 58, 462, 1067
 Socaciu, Margareta, 278, 494, 619, 1063
 Soergel, E., 432
 Sorescu, M., 311
 Sporea, Dan G., 17, 81, 1083
 Staicu, Angela, 1215
 Stamate, Marius D., 951
 Stancalie, Gheorghe, 1220
 Stancalie, V., 39
 Stanciu, Angelia, 241
 Stanciu, Catrinel A., 831, 1194
 Stanciu, George A., 241
 Stefan, Levai, 489
 Stefanescu, Eliade N., 877
 Sterian, Paul E., 10, 825, 877, 965, 999
 Stoian, Razvan, 702
 Stoica, Axente, 891
 Stratan, Aurel, 81, 252, 454, 702
 Stroila, Carmen, 727
 Strzelec, Marek, 756
 Sureau, Alain, 39
 Suruceanu, Grigore I., 58, 462
 Suteanu, S., 692
 Taira, Takunori, 32, 70
 Tanaka, Eiko, 393
 Tchaushev, G., 960
 Teodorescu, Valentin S., 182, 218
 ter Meulen, J. J., 143
 Ticos, C. M., 665
 Timus, Clementina A., 17, 1083, 1132
 Tkachenko, D. V., 406
 Toacsan, M. I., 311
 Tomescu, M., 733
 Toția, Horațiu, 1189
 Triduh, G. M., 790
 Tronciu, V. Z., 411
 Tsaranu, A., 902
 Tudor, Tiberiu S., 504
 Turcu, I. C. E., 162
 Udrea, M. V., 692
 Ulmeanu, M., 1137
 Ungureanu, Costica, 596, 1039
 Ungureanu, M., 596
 Ursache, Marcela, 278, 494, 619, 1063
 Ursu, Veronica, 288, 632
 Usurelu, Mircea, 747
 Vallmitjana, Santiago R., 1150, 1156
 Varnik, F., 978
 Vascan, Ioan, 936, 951
 Vasile, E., 75, 225, 272, 1132

Vasiliu, Virgil V., 686, 692, 696, 1074, 1137
Vateva, Elena, 960
Veltman, R. H., 556
Verardi, P., 1194
Verlan, Victor I., 1013
Vieru, T., 1007, 1032
Vinkler, Istvan, 504
Vlad, Adriana, 477
Vlad, L. A., 790
Vlad, Valentin I., 375, 432, 511, 517, 955
Vlaiculescu, Mihaela, 696, 739, 747
Voicu, Ion N., 174
Voicu, L., 1202
Volvoreanu, C., 717
Vorozov, N., 762
Wallas, Gordon, 17
Walther, Herbert, 320
Werckmann, J., 218
Windholz, Laurentius, 541, 584
Yakovlev, Vladimir P., 462
Yatsui, Kiyoshi, 153, 188, 282
Yukawa, T., 153, 188, 282
Yuldashev, Bekzad S., 837
Zalevsky, Zeev, 363, 418
Zisu, Tudor, 807
Zoran, Maria, 779, 891
Zsivanov, Delia, 293